

APPENDIX A AERB

STANDARD PROBLEM EXERCISE ON **PERFORMANCE OF CONTAINMENT VESSEL UNDER SEVERE ACCIDENT CONDITIONS**

Phase -1 Analysis Report

Model – 2

EXERCISE UNDERTAKEN BY



**ATOMIC ENERGY REGULATORY BOARD
MUMBAI**

MARCH 2011

A-1

INTRODUCTION

The U.S. Nuclear Regulatory Commission (USNRC) and SANDIA National Lab, USA are participating in a round robin analysis with the Atomic Energy Regulatory Board of India (AERB). The round robin analysis, called the Standard Problem Exercise (SPE) No. 3, involves the structural analysis of local effects of a prestressed concrete containment vessel (PCCV) under severe accident conditions. The detail of the scope is furnished in white paper. The SPE3 has two phases, Phase-1 and Phase-2. Phase-1 analysis consists of three models, Model-1, Model-2 and Model-3.

This document describes the details of Model-2 study. Model-2 analysis has three parts, (i) Model-2a, (ii) Model-2b and (ii) Model-2c. The main objective of Model-2 is to study the effect of steel-concrete (liner and cylindrical wall) interfacial behavior. The brief details of Model-2 are furnished below:

- (i) Model-2a: Liner is integrally connected to concrete cylindrical wall
- (ii) Model-2b: Liner is connected to concrete cylindrical wall by means of friction
- (iii) Model-2c: (optional): best estimate of interfacial behavior, liner is connected to concrete cylinder by anchors only.

The outcome of analysis (i) and (ii) are furnished in this report. Analysis of Model-2c could not be completed, hence not furnished in this report.

A study of crack propagation in steel liner based on fracture mechanics approach is also a part of this study. However, this study will be taken up in subsequent Phase, i.e. Phase-2.

Report on Model-2a is furnished in page no. A-3 to A-30

Report on Model-2b is furnished in page no. A-30 to A-46

MODEL 2A (LINER IS INTEGRALLY CONNECTED TO CONCRETE INNER SURFACE)

2.1 Description of Model

The geometry and boundary condition are defined in SPE3-white paper. The portion of cylindrical wall from 324° azimuth to 18° azimuth is chosen for analysis. The elevations are selected as 15.34' to 26.42'. The FE meshed geometry of the wall is furnished in Figure A 1. Wall is meshed with 8 node solid elements. The 'Damage plasticity concrete material' of ABAQUS is used for this study.

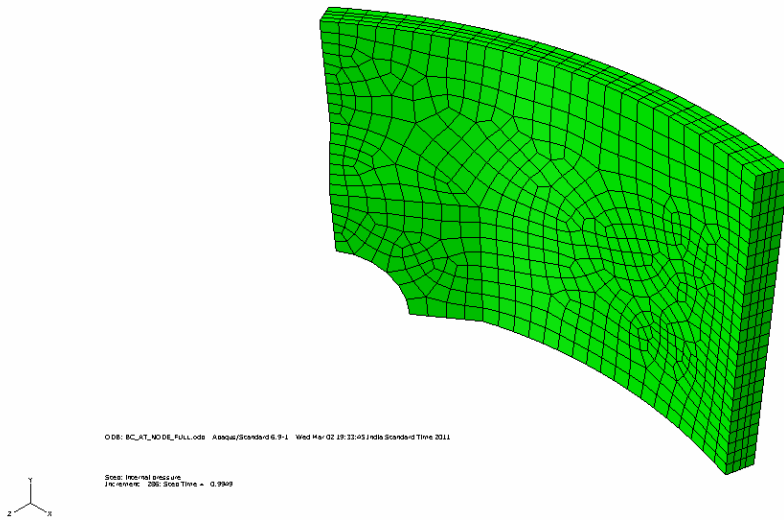


Figure A 1 FE meshed cylindrical wall portion

The liner and pipe sleeve are modeled using 4 node shell element. ‘Metal plasticity’ model was used for this purpose. The pipe sleeve is assumed to span up to concrete wall thickness only. The liner is modeled at the inner surface of concrete wall. The liner is assumed integrally connected to concrete surface (i.e. tied with concrete). The sleeve is integrally connected to liner only. Frictionless interaction is modeled between concrete surface at hatch and sleeve. Figure A 2 shows the liner with sleeve meshed geometry. The rebars (vertical and horizontal) are modeled as sub elements of solid concrete element in the form of smeared surfaces embedded into concrete solid element. The individual stirrups are modeled exclusively as 2- node truss element. Figure A 3a shows the rebar sub-element along with stirrups.

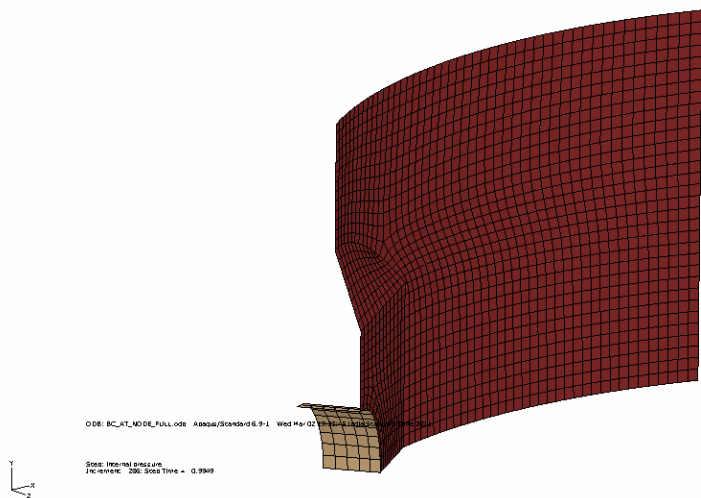


Figure A 2 Liner with pipe sleeve (meshed with shell elements)

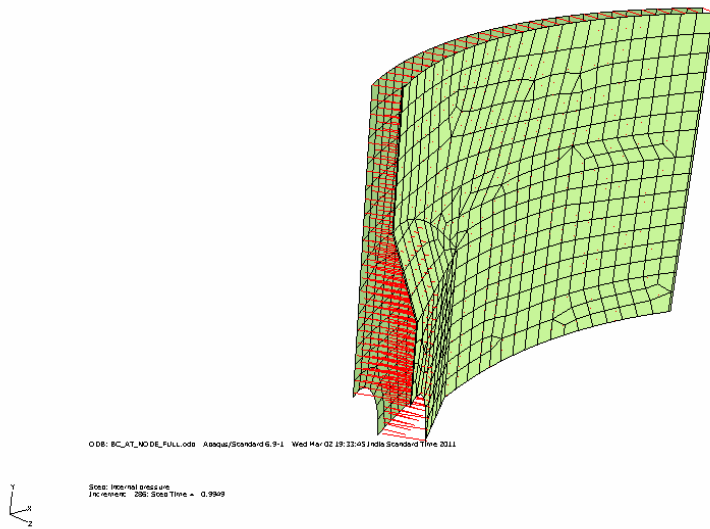


Figure A 3 Rebar sub-element with stirrups

The prestressed cables are modeled exclusively as per the cable profile shown in construction drawing. The horizontal cables are modeled as '2 in 1', (i.e. one cable with double cross sectional area). So, number of cables in horizontal direction is half of the actual number keeping total cross-sectional area same. In the vertical direction all the cables are modeled. Cables are meshed with truss element and these are embedded into solid concrete element. No friction interaction is modeled between concrete and cable. Cable and concrete will have perfect strain compatibility till concrete cracks. Figure A 4 shows the vertical and horizontal cable profile. Prestress is simulated as 'initial condition, type=stress' option in ABAQUS. The average initial stresses of $8.0E+08$ Pa and $12.0E+08$ Pa was applied to horizontal and vertical cables respectively.

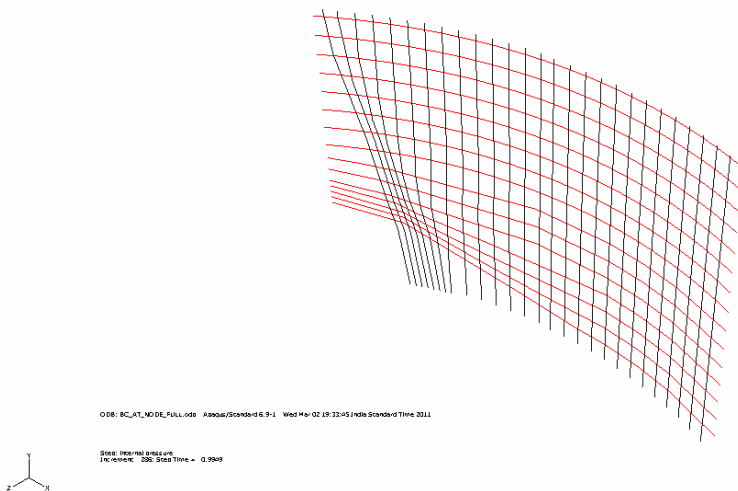


Figure A 4 Vertical and horizontal prestress cables

The material properties are considered as per tech-memo of Model1 (circulated by Mr. Dameron). Symmetric boundary conditions are applied to two vertical surfaces. Bottom surface is kept vertically restrained. Two horizontal rotations at the top surface are restrained and it is allowed to move vertically as plane surface by applying constrain equation. The analysis is done in two steps; in the first step, prestress is applied and model is allowed to reach equilibrium. In the second step, internal pressure is applied along with meridional pull at top surface, which is a function of internal pressure (i.e. $0.144 \cdot p \cdot 8.27$) MPa as provided in tech-memo of Model2 (circulated by Mr. Dameron). The ultimate pressure is derived to be 3.44 times design pressure, i.e. $3.44 P_d$ for Model-2a.

The deformed shapes of cylindrical wall after prestress, at design pressure and at ultimate pressure are shown in Fig Figure A 5, Figure A 6 and Figure A 7 respectively.

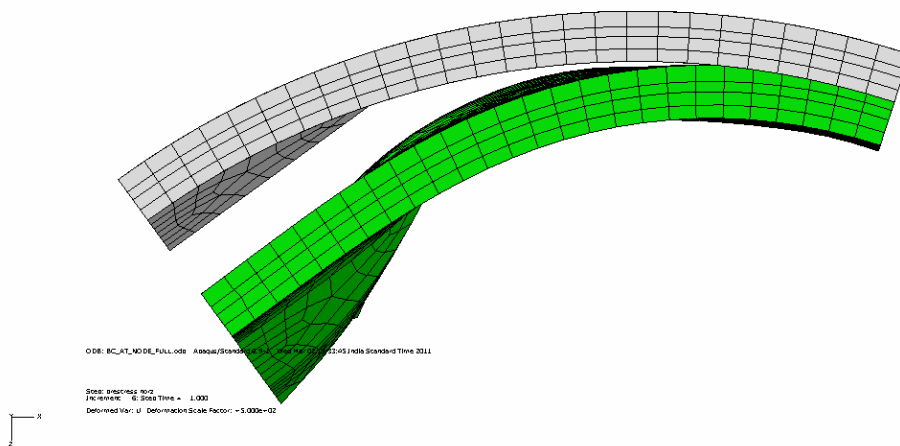


Figure A 5 Deformed shape of wall after the prestress (x 500)

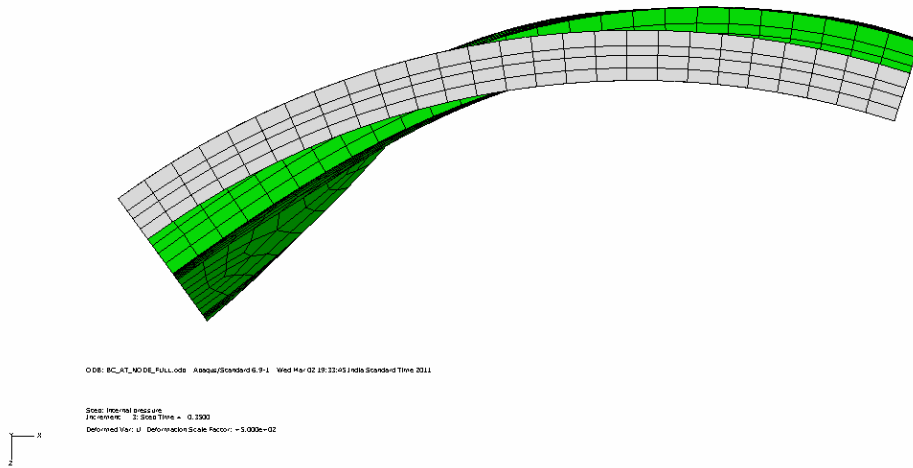


Figure A 6 Deformed shape of wall at design pressure (x 500)

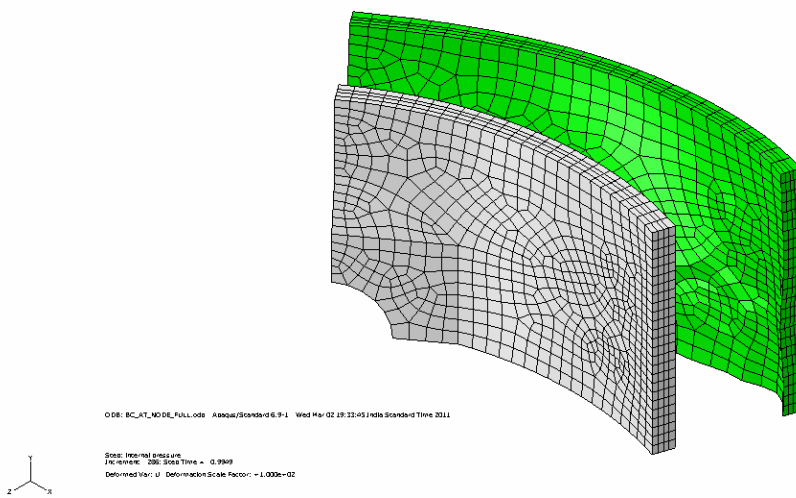


Figure A 7 Deformed shape of wall at ultimate pressure 3.44Pd (x 100)

Figure A 8 and Figure A 9 show the minimum principal stress at prestress and maximum principal stress at design pressure respectively.

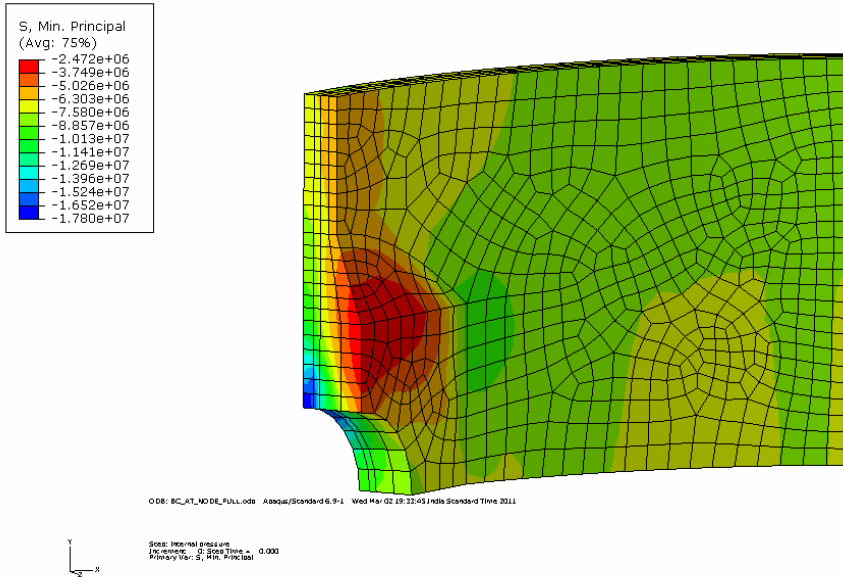


Figure A 8 Min principal stress in concrete (contour) after prestress

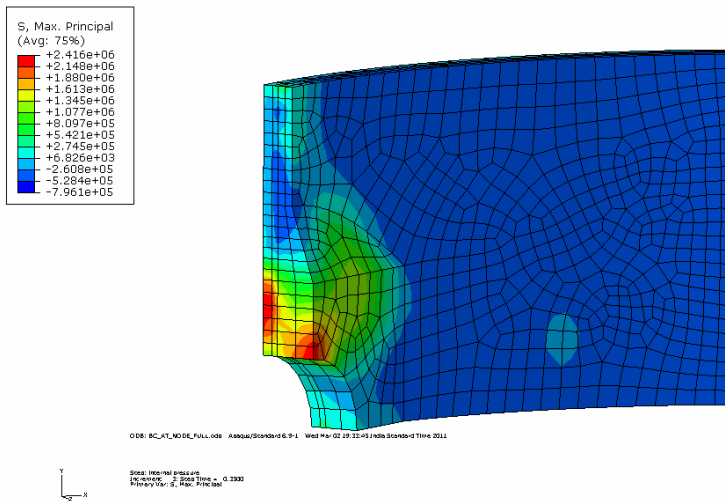


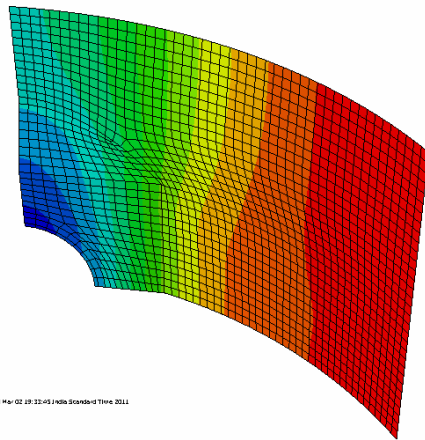
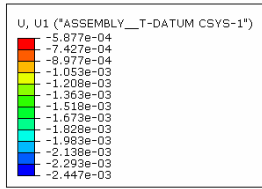
Figure A 9 Max. principal stress in concrete (contour) at design pressure

2.3 Pressure Milestone: Applied pressure when:

- Concrete Hoop Cracking Occurs and report where: *at pressure 0.64 MPa, i.e 1.64 Pd at 0° azimuth.*
- First tendon Reaches 1% strain and report where: *maximum tendon strain reached 0.312% at ultimate pressure at horizontal tendons near 0° azimuth*

2.4 Deformed shape and liner strain distribution

The radial deformations of liner at different load steps are shown in following figures. (+) sign indicates deformation radially outward.

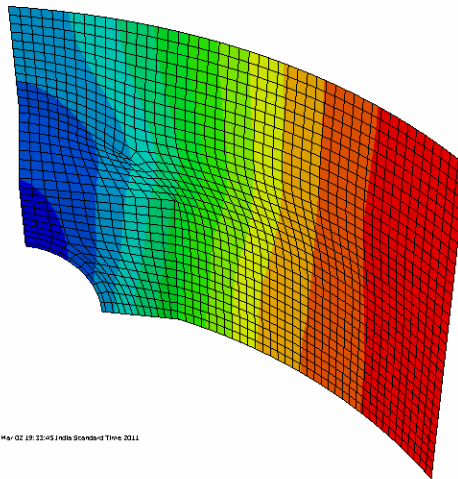
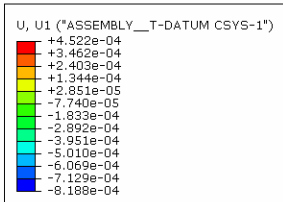


ODB: BC_AT_NO DE_FULL.odb A894a/Stand:d 6.9-1 Wed May 02 17:22:45 India Standard Time 2011



State: Internal pressure
 In. name: 0.000 Time = 0.000
 Primary Var: U, U1 (*ASSEMBLY__T-DATUM CSYS-1*)

Figure A 10 Liner deformed shape (contour) at 0.0P



ODB: BC_AT_NO DE_FULL.odb A894a/Stand:d 6.9-1 Wed May 02 17:22:45 India Standard Time 2011



State: Internal pressure
 In. name: 1.000 Time = 0.100
 Primary Var: U, U1 (*ASSEMBLY__T-DATUM CSYS-1*)

Figure A 11 Liner deformed shape (contour) at 1.0P

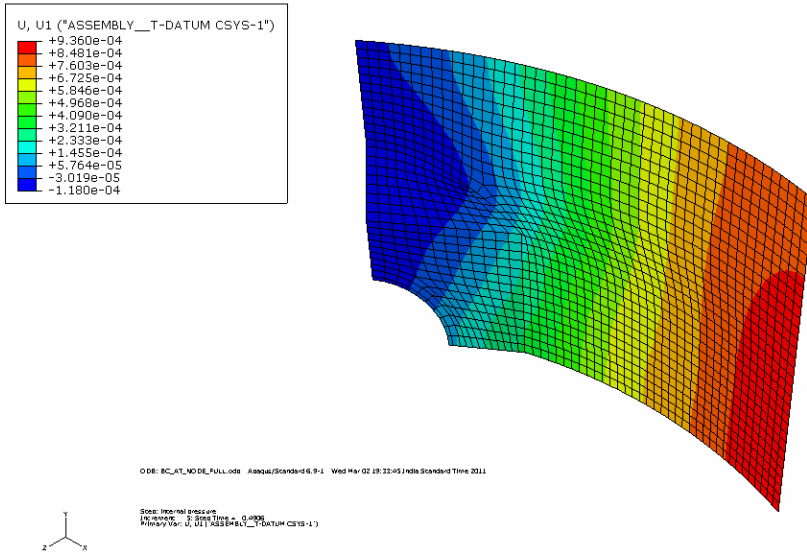


Figure A 12 Liner deformed shape (contour) at 1.5P

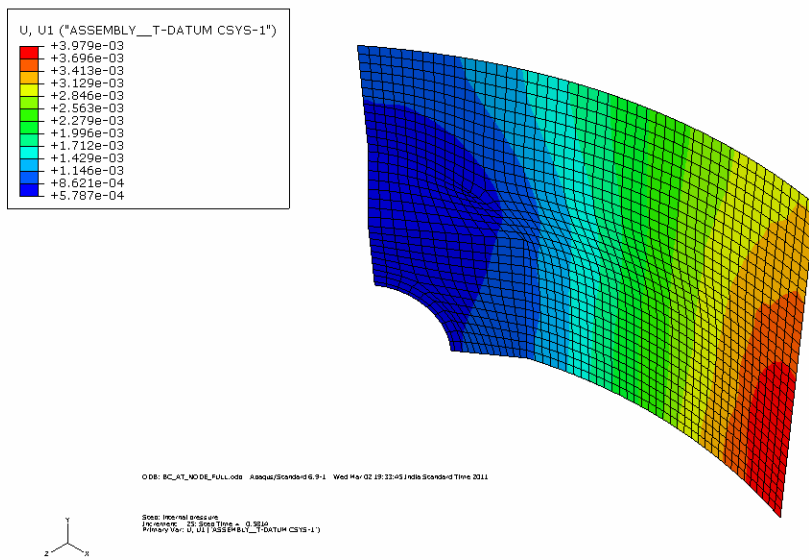
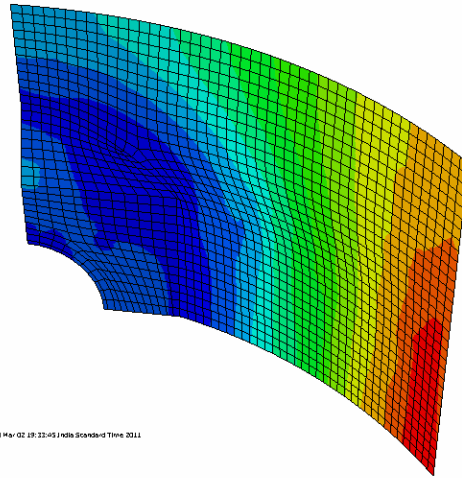
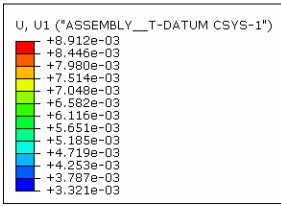


Figure A 13 Liner deformed shape (contour) at 2.0P

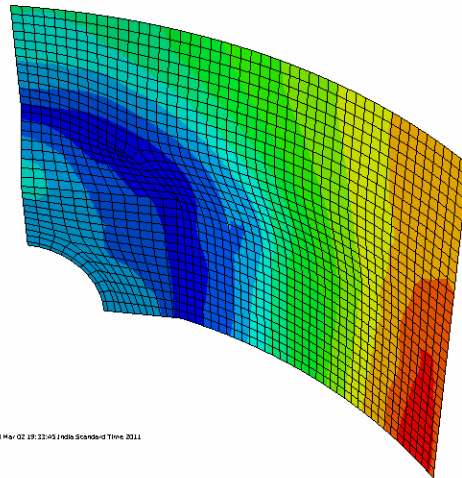
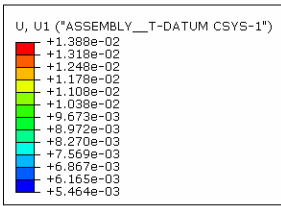


ODB: BC_AT_NODE_FULL.odb A8994/Scnds=6.9-1 Wed Mar 02 19:22:05 | rds Scnds=1 Time 2311



Plot: Internal Pressure
 W/Nodes: 117, 2663 Time = 0.228
 Primary Var: U, U1 (*ASSEMBLY__T-DATUM CSYS-1*)

Figure A 14 Liner deformed shape (contour) at 2.5P



ODB: BC_AT_NODE_FULL.odb A8994/Scnds=6.9-1 Wed Mar 02 19:22:05 | rds Scnds=1 Time 2311



Plot: Internal Pressure
 W/Nodes: 117, 2663 Time = 0.317
 Primary Var: U, U1 (*ASSEMBLY__T-DATUM CSYS-1*)

Figure A 15 Liner deformed shape (contour) at 3.0P

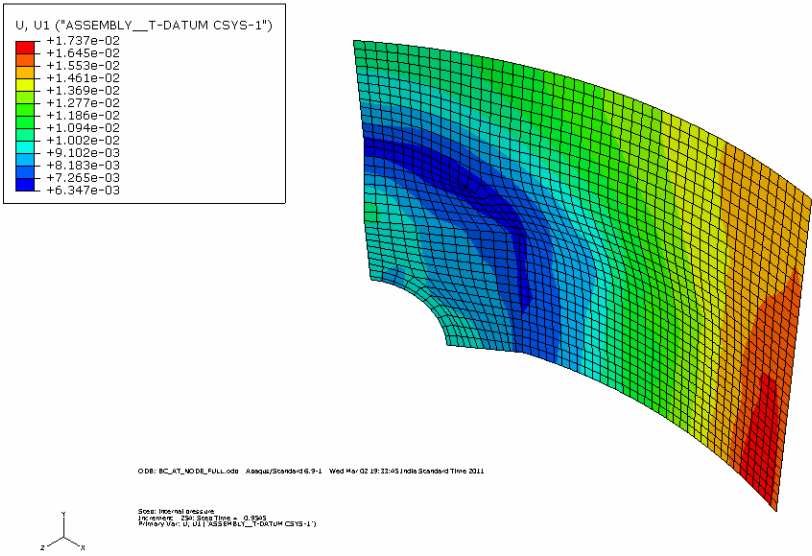


Figure A 16 Liner deformed shape (contour) at 3.3P

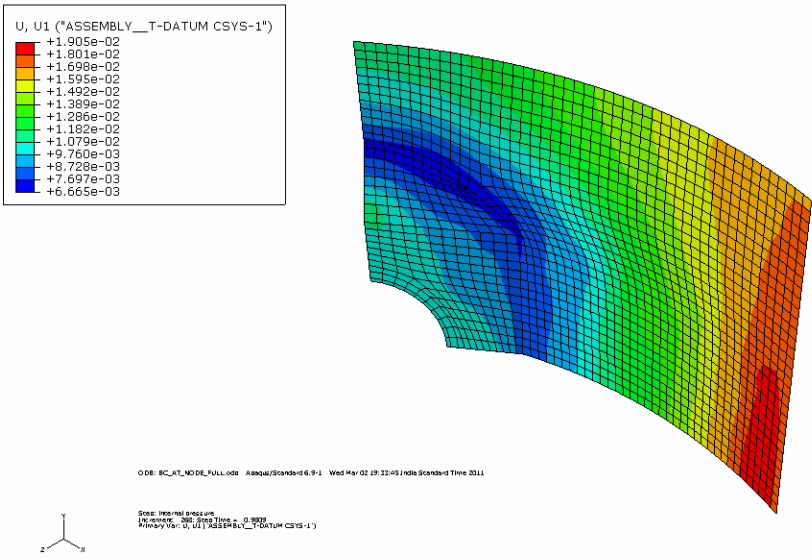
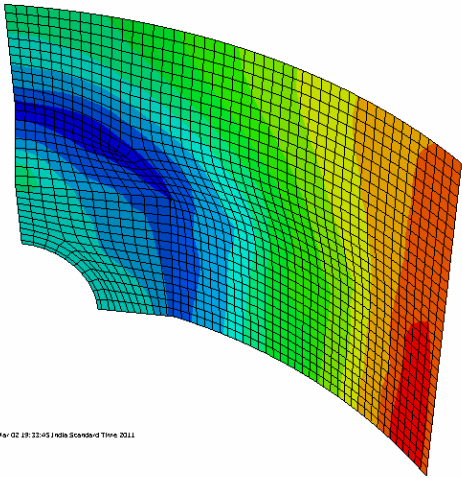
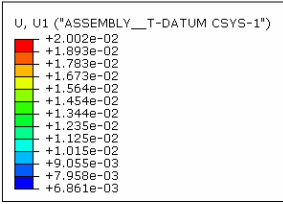


Figure A 17 Liner deformed shape (contour) at 3.4P

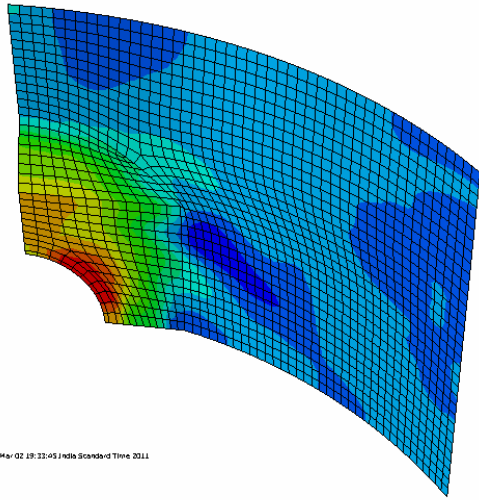
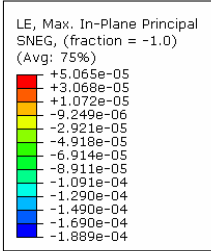


ODB: BC_AT_NO_DE_FULL.odb Aabaq/Standard6.9-1 Wed Mar 02 19:32:05 India Standard Time 2011



Scan: Internal pressure
Increment: 0.001
Primary Var: U, U1 (*ASSEMBLY__T-DATUM CSYS-1*)

Figure A 18 Liner deformed shape (contour) at ultimate P

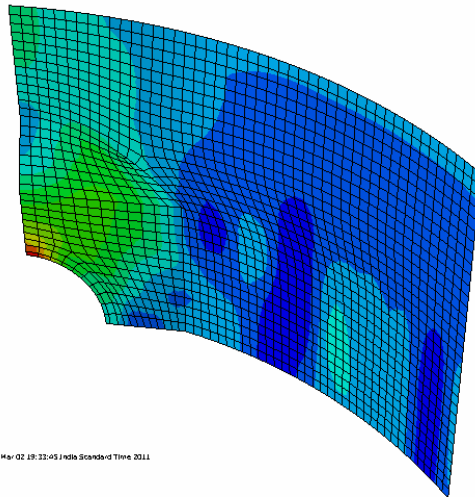
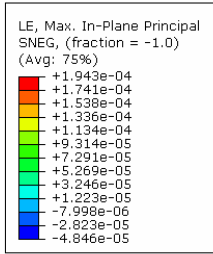


ODB: BC_AT_NO_DE_FULL.odb Aabaq/Standard6.9-1 Wed Mar 02 19:33:05 India Standard Time 2011



Scan: Internal pressure
Increment: 0.001
Primary Var: LE, Max. In-Plane Principal

Figure A 19 Liner strain (contour) at 0.0P

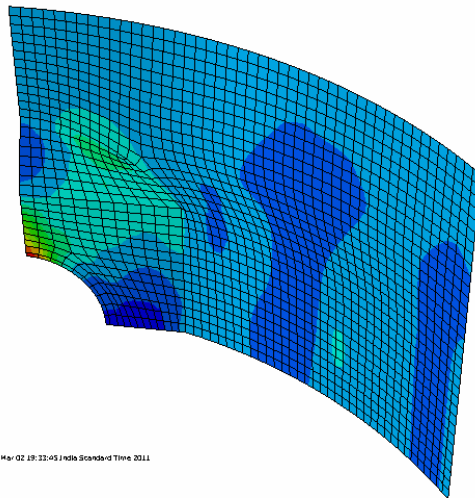
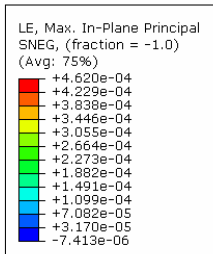


ODB: BC_AT_NO DE_FULL.odb Abaqus/Standard 6.9-1 Wed Mar 02 19:32:05 India Standard Time 2011



Plot: Internal pressure
 Increment: 1 Step Time = 0.1000
 Primary Var: U, Max. In-Plane Principal

Figure A 20 Liner strain (contour) at 1.0P

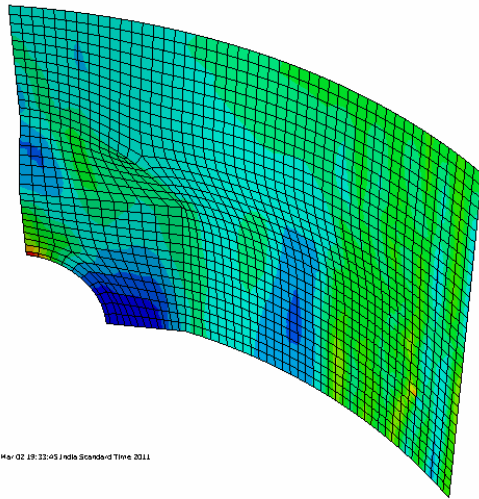
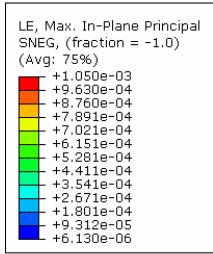


ODB: BC_AT_NO DE_FULL.odb Abaqus/Standard 6.9-1 Wed Mar 02 19:32:05 India Standard Time 2011



Plot: Internal pressure
 Increment: 1 Step Time = 0.0000
 Primary Var: U, Max. In-Plane Principal

Figure A 21 Liner strain (contour) at 1.5P

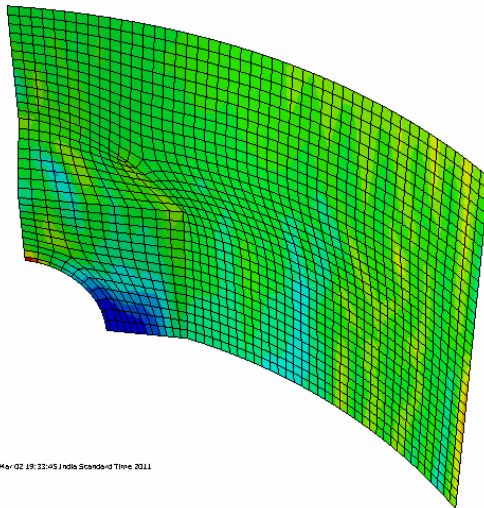
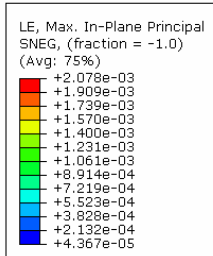


ODB: BC_AT_NODE_FULL.odb Abaqus/Standard 6.9-1 Wed Mar 02 19:32:45 India Standard Time 2011



Step: Internal Pressure
 Inc. number: 11, Step Time = 0.0550
 Primary Var: LE, Max. In-Plane Principal

Figure A 22 Liner strain (contour) at 2.0P

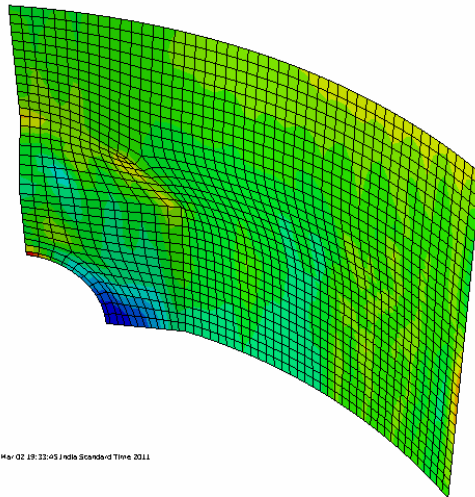
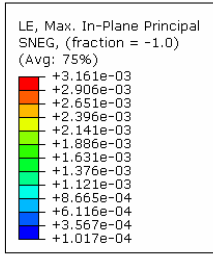


ODB: BC_AT_NODE_FULL.odb Abaqus/Standard 6.9-1 Wed Mar 02 19:32:45 India Standard Time 2011



Step: Internal Pressure
 Inc. number: 11, Step Time = 0.1200
 Primary Var: LE, Max. In-Plane Principal

Figure A 23 Liner strain (contour) at 2.5P

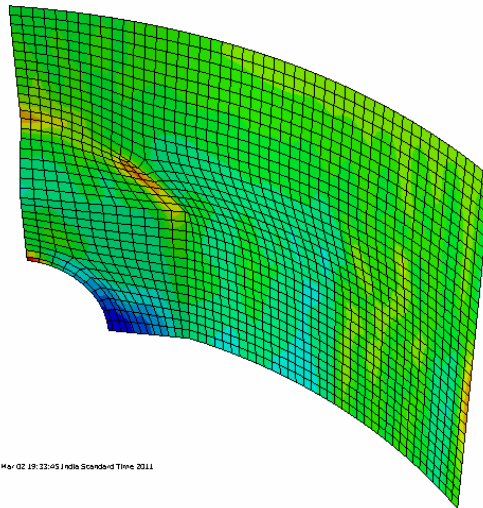
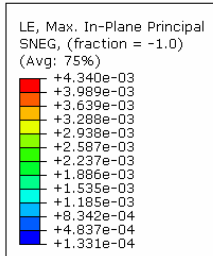


ODB: BC_AT_MODEL_FULL.odb Abaqus/Standard 6.9-1 Wed Mar 02 19:33:05 India Standard Time 2011



State: Internal Pressure
 Increment: 237; Step Time = 0.8717
 Primary Var: U, Max. In-Plane Principal

Figure A 24 Liner strain (contour) at 3.0P

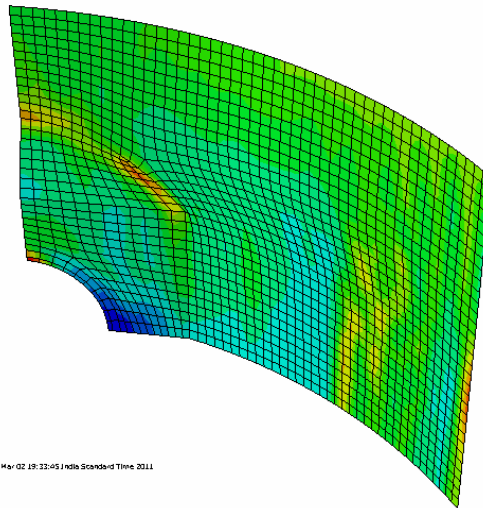
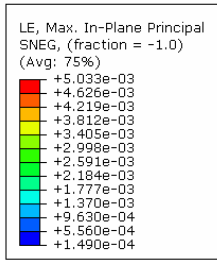


ODB: BC_AT_MODEL_FULL.odb Abaqus/Standard 6.9-1 Wed Mar 02 19:33:05 India Standard Time 2011



State: Internal Pressure
 Increment: 237; Step Time = 0.9233
 Primary Var: U, Max. In-Plane Principal

Figure A 25 Liner strain (contour) at 3.3P

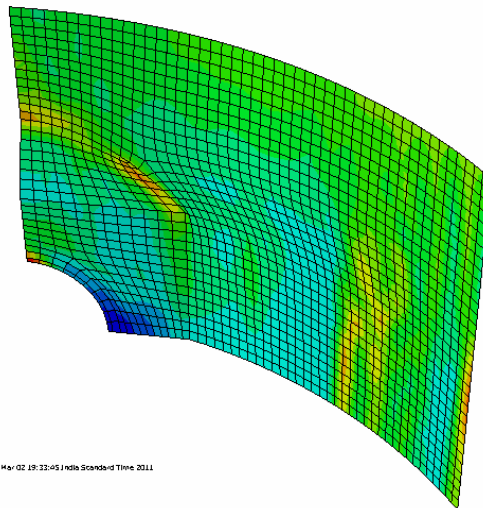
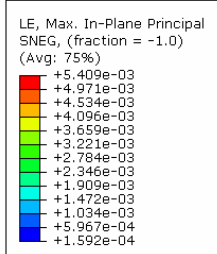


ODB: BC_AT_NO DE_FULL.odb Araqq/Stand/d 6.9-1 Wed Mar 02 19:22:45 India Stand/d Time 2011



Step: Internal Pressure
Increment: 200; Step Time = 0.9018
Primary Var: LE, Max. In-Plane Principal

Figure A 26 Liner strain (contour) at 3.4P



ODB: BC_AT_NO DE_FULL.odb Araqq/Stand/d 6.9-1 Wed Mar 02 19:22:45 India Stand/d Time 2011



Step: Internal Pressure
Increment: 200; Step Time = 0.9909
Primary Var: LE, Max. In-Plane Principal

Figure A 27 Liner strain (contour) at ultimate P

2.5 Liner strain magnitudes (hoop direction) at locations indicated in Figure11 (white paper)

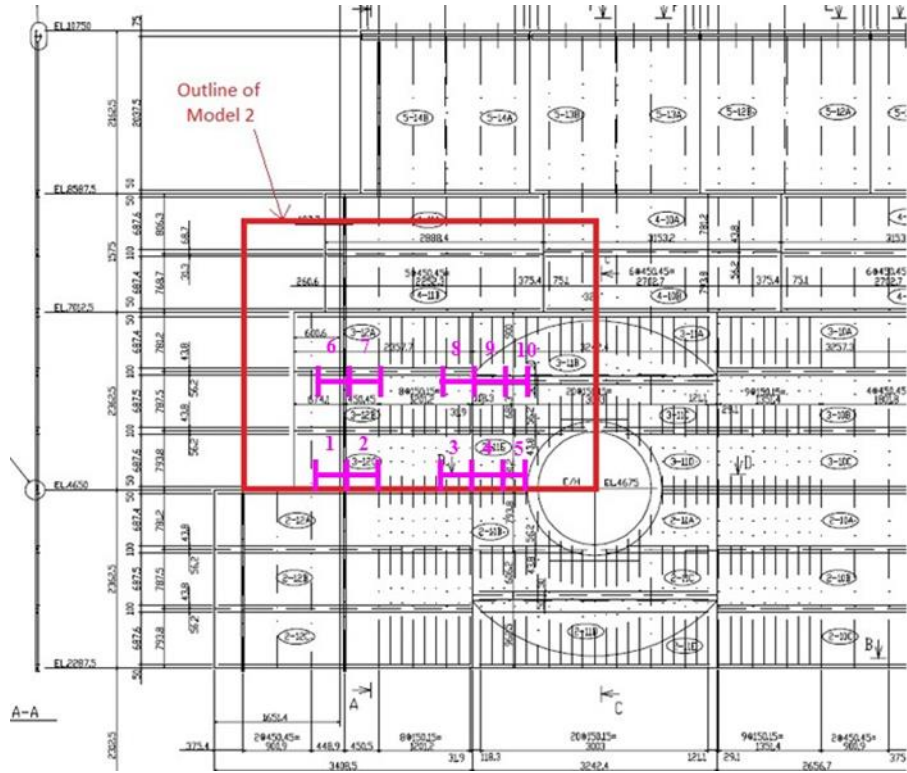


Figure A 28 Liner strain measuring locations (Fig.11 of white paper)

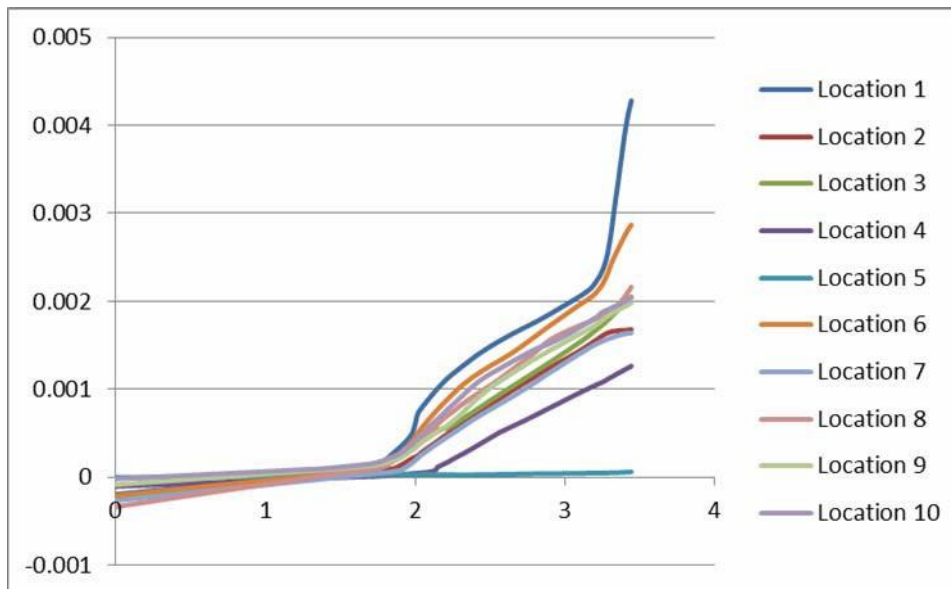


Figure A 29 Liner strain (Y-axis) vs pressure (X-axis), multiples of design pressure

2.6 Radial displacement

Figure A 30 shows the comparative study of radial deformation with respect to multiple of design pressure, where (+) sign indicates radially outward.

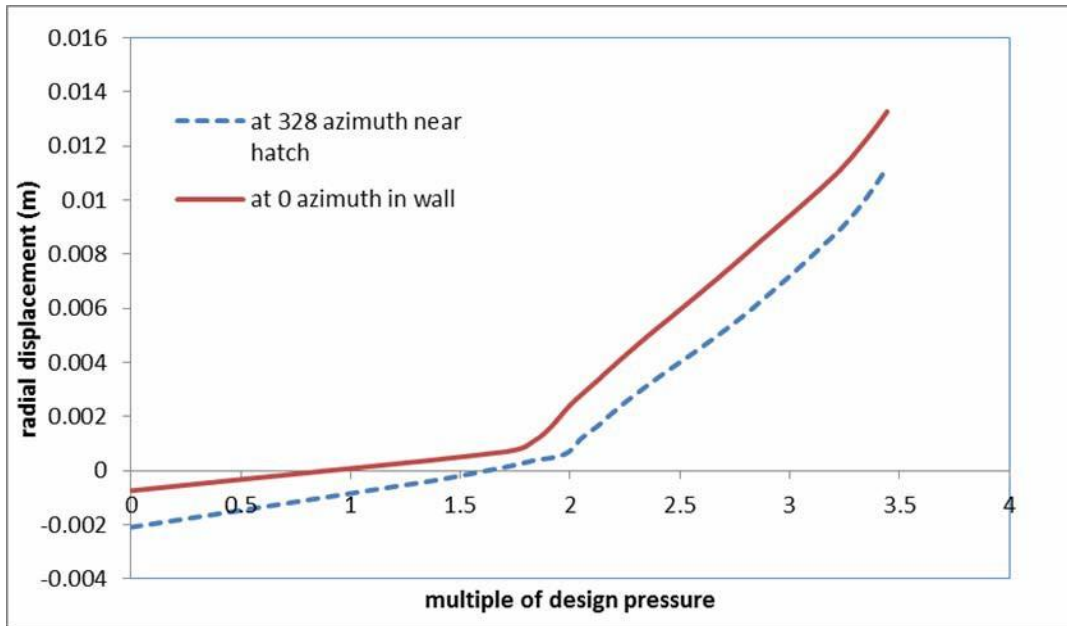


Figure A 30 Radial displacement at 328° and 0° azimuth

2.7 Tendon stress distribution

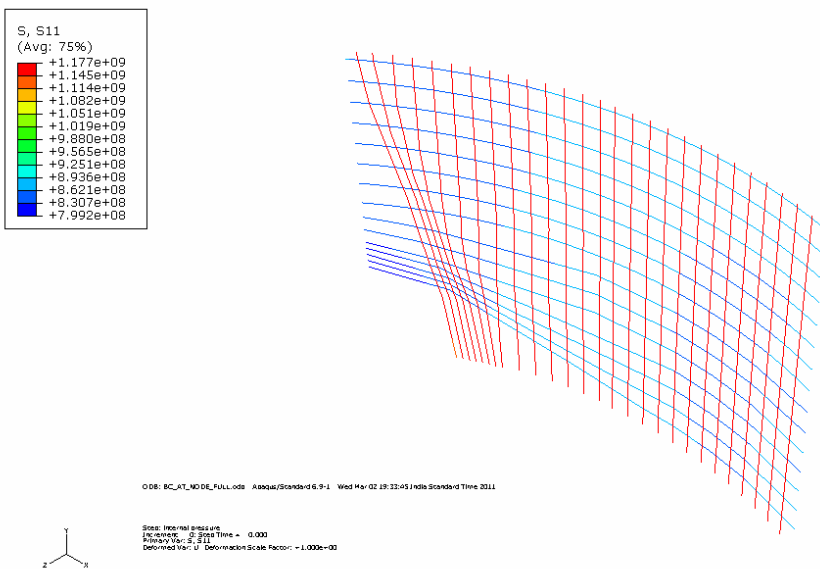
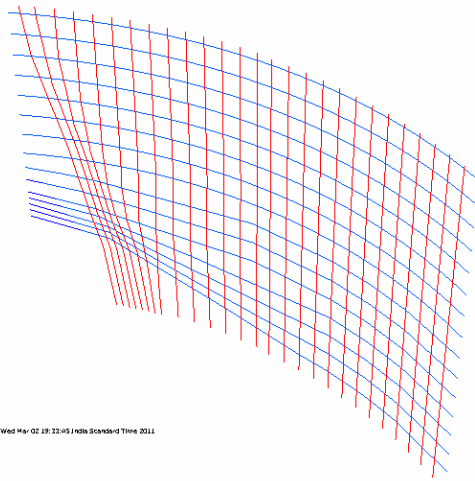
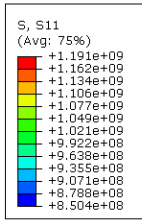


Figure A 31 tendon stress distribution at 0.0P

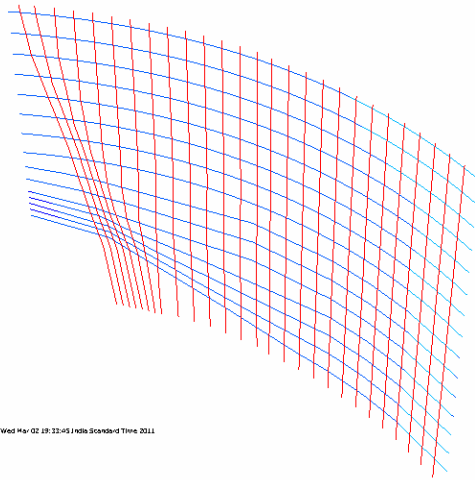
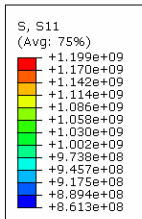


ODB: BC_AT_NODE_FULL.ods Abaqus/Standard-6.9-1 Wed May 02 19:32:45 India Standard Time 2011



Step: Internal pressure
Increment: 2, Step Time = 0.2000
Display Var: S, S11
Deformed Var: U, Deformation Scale Factor = 1.000e+00

Figure A 32 tendon stress distribution at 1.0P



ODB: BC_AT_NODE_FULL.ods Abaqus/Standard-6.9-1 Wed May 02 19:32:45 India Standard Time 2011



Step: Internal pressure
Increment: 2, Step Time = 0.4900
Display Var: S, S11
Deformed Var: U, Deformation Scale Factor = 1.000e+00

Figure A 33 tendon stress distribution at 1.5P

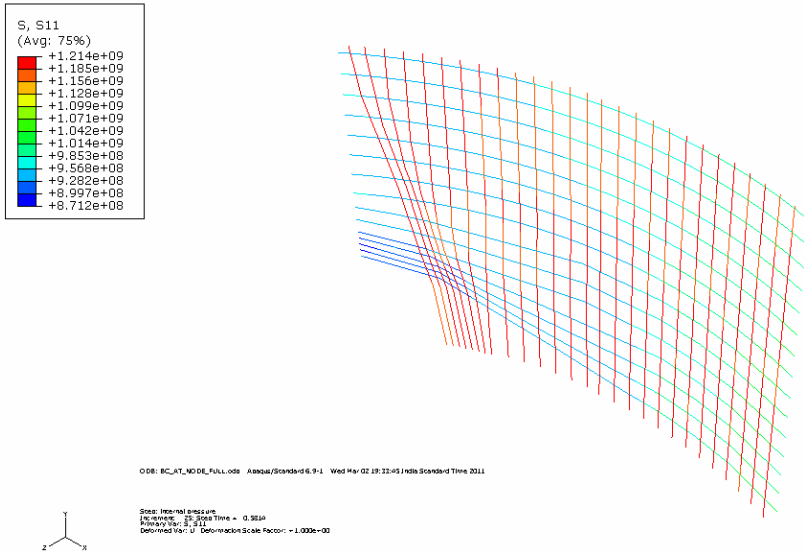


Figure A 34 tendon stress distribution at 2.0P

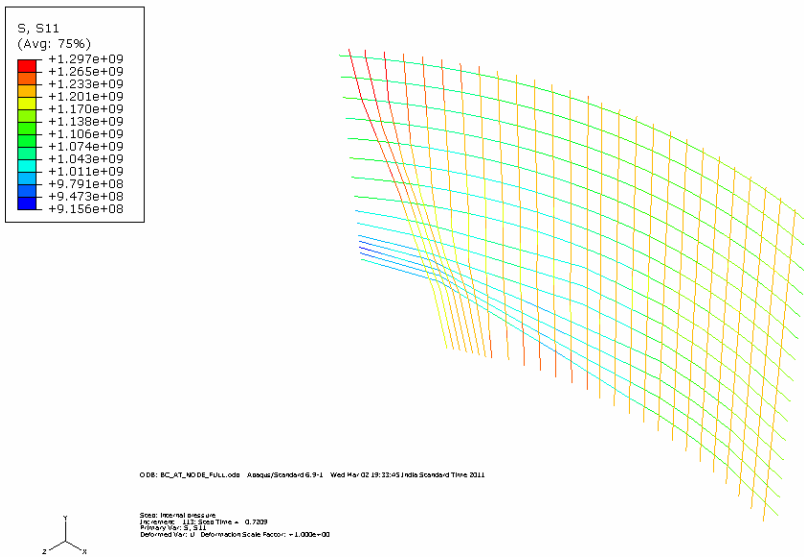
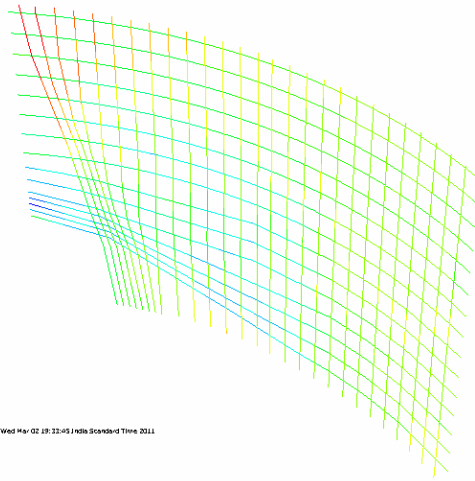
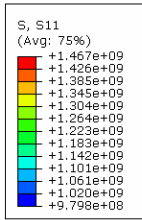


Figure A 35 tendon stress distribution at 2.5P

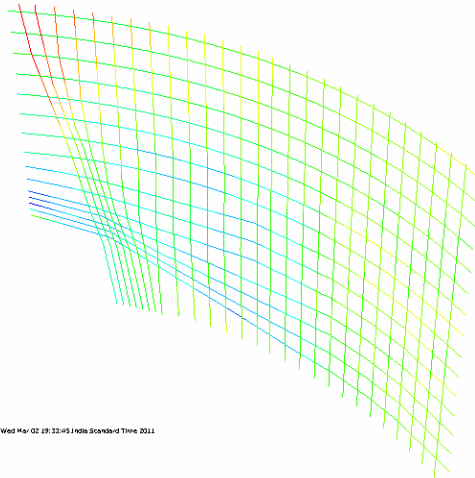
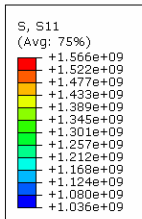


ODB: BC_AT_NODE_FULL.ods Abaqus/Standard-6.9-1 Wed May 02 19:32:45 India Standard Time 2011



Step: Internal pressure
Increment: 307
Time: 0.8717
Primary Var: S, S11
Deformed Var: U Deformation Scale Factor: -1.000e+00

Figure A 36 tendon stress distribution at 3.0P



ODB: BC_AT_NODE_FULL.ods Abaqus/Standard-6.9-1 Wed May 02 19:32:45 India Standard Time 2011



Step: Internal pressure
Increment: 313
Time: 0.9311
Primary Var: S, S11
Deformed Var: U Deformation Scale Factor: -1.000e+00

Figure A 37 tendon stress distribution at 3.3P

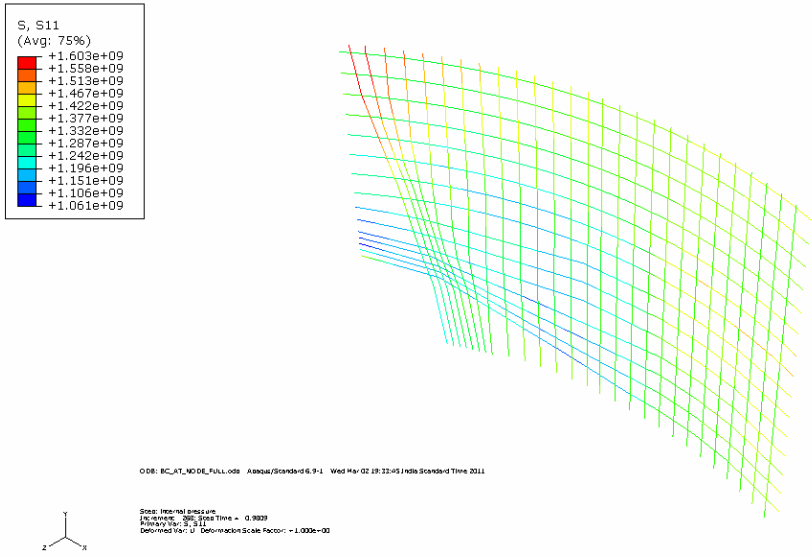


Figure A 38 tendon stress distribution at 3.4P

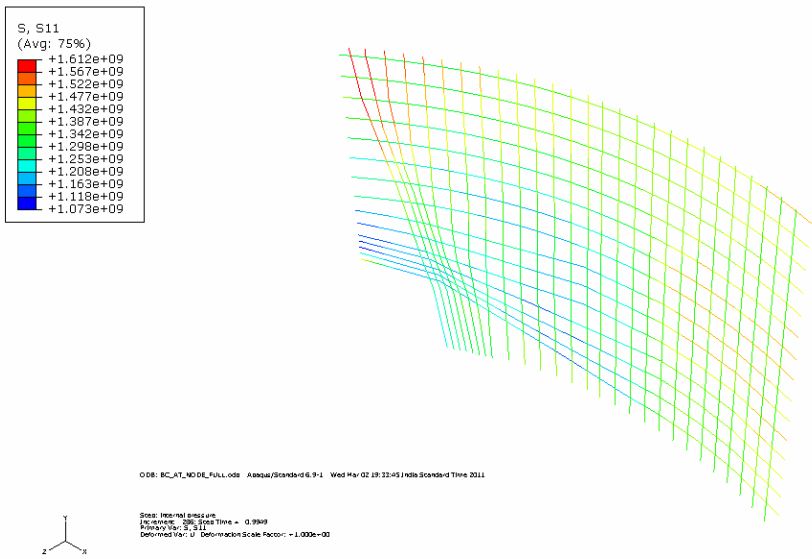


Figure A 39 tendon stress distribution at ultimate pressure

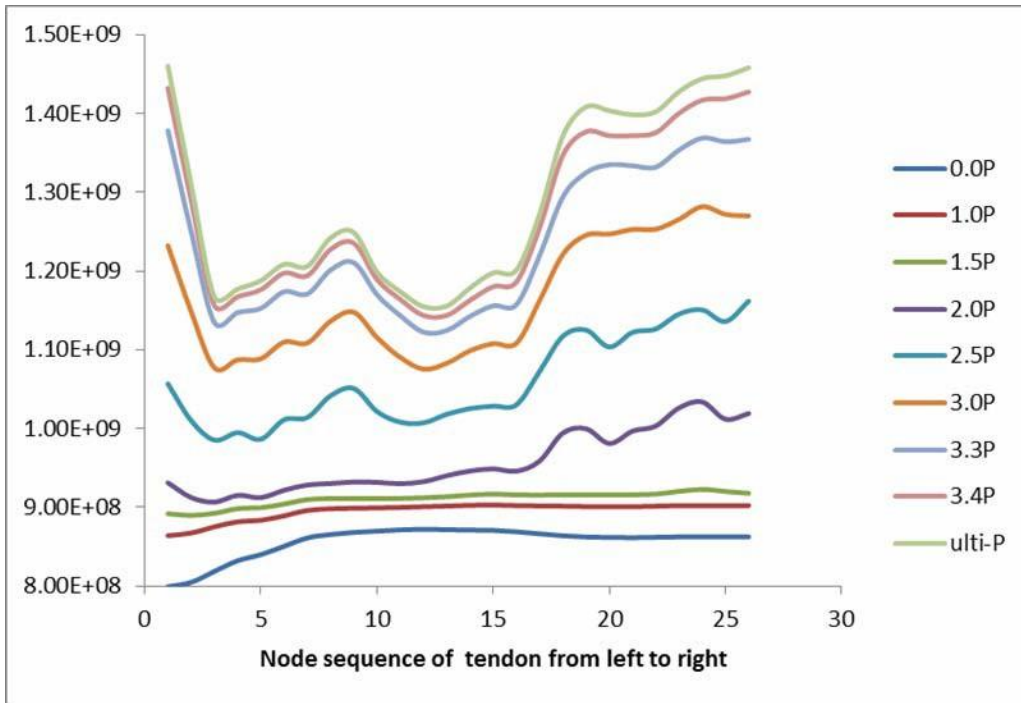


Figure A 40 Stress (Pa) distribution of hoop tendon nearest the penetration at different multiples of Pd

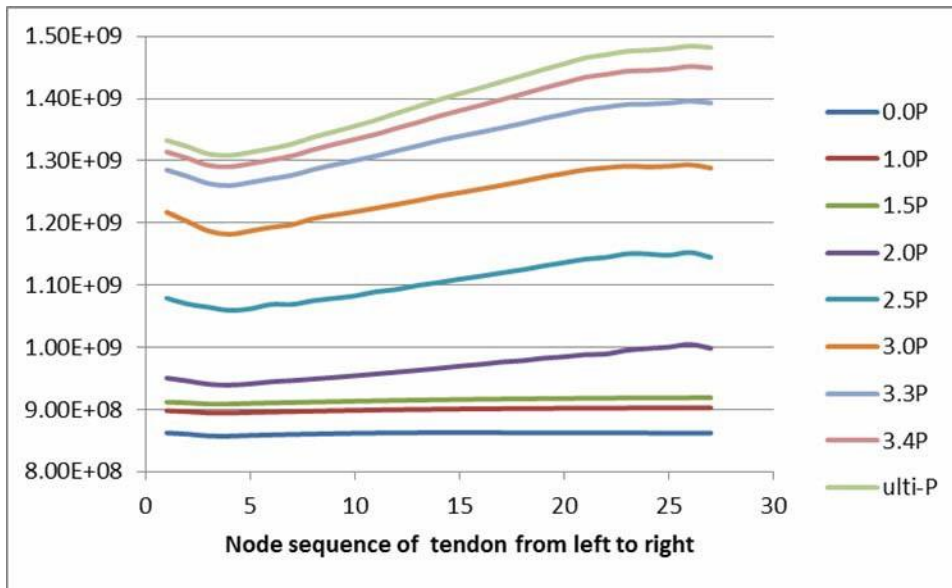


Figure A 41 Stress distribution of hoop tendon at top of the model at different multiples of Pd

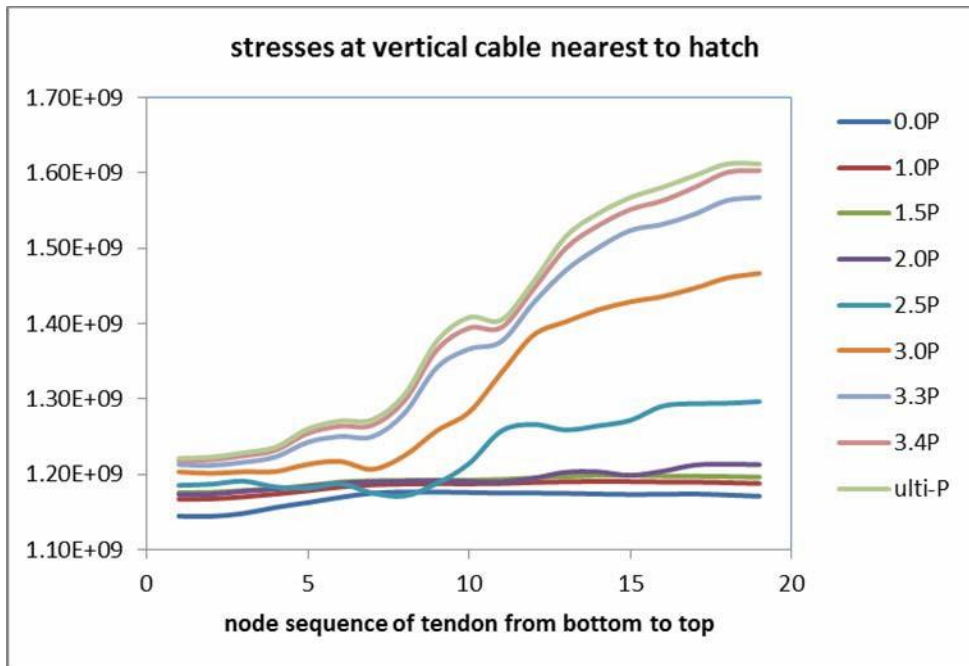


Figure A 42 Stress distribution of vertical tendon nearest to hatch at different multiples of Pd

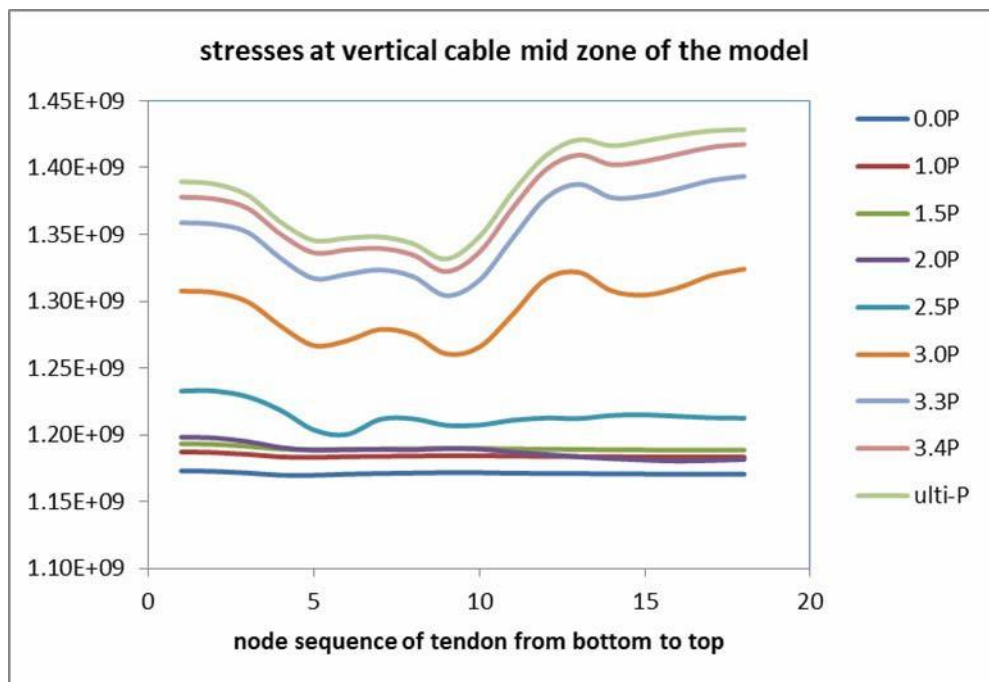


Figure A 43 Stress distribution of vertical tendon at mid zone of the model at different multiples of Pd

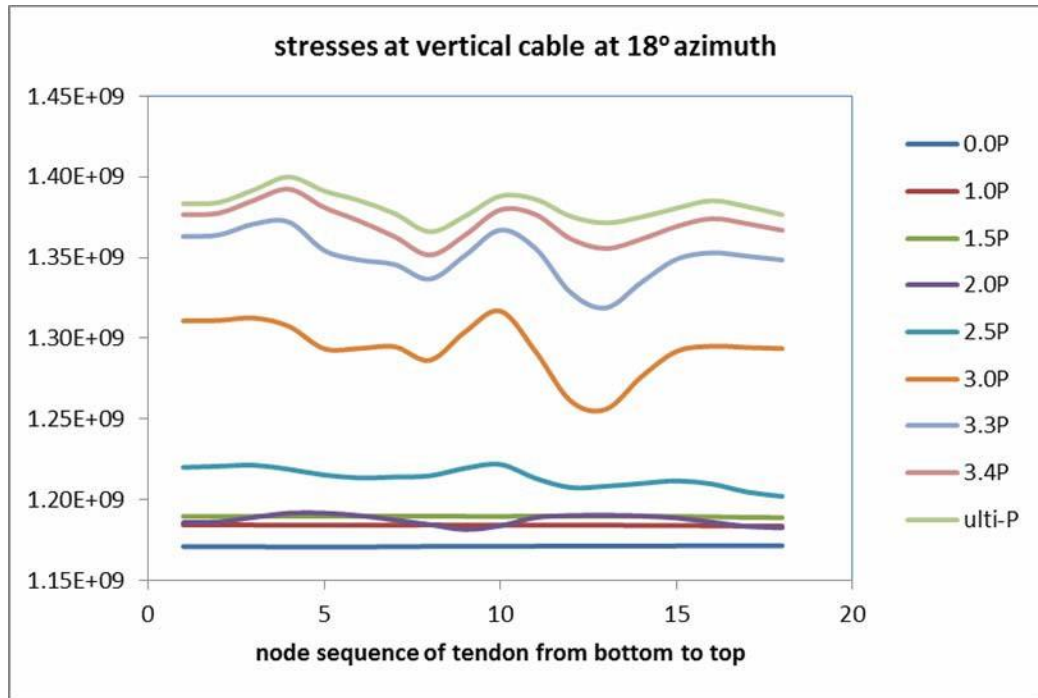


Figure A 44 Stress distribution of vertical tendon at 18° azimuth at different multiples of Pd

2.8 Separation plot of pipe sleeve, (+)ve sign indicates separation

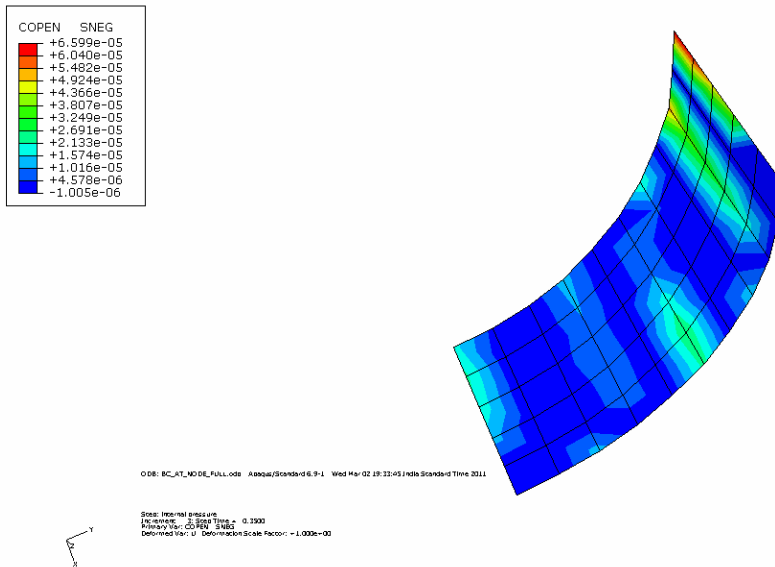
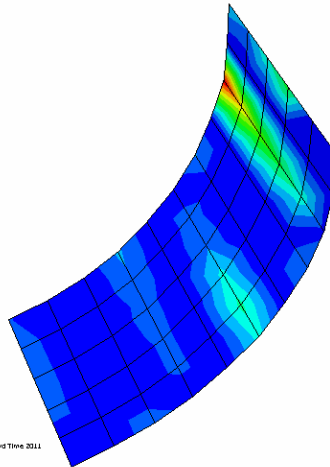
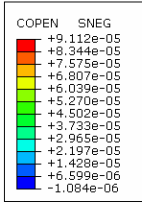


Figure A 45 pipe separation (contour) at 1.0P

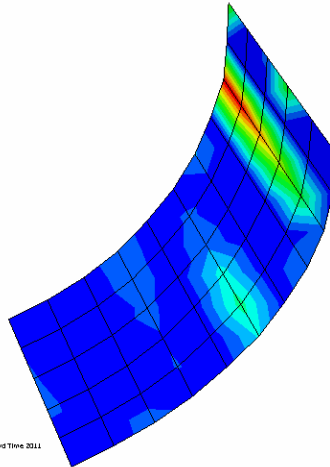
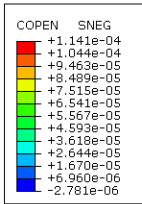


ODB: RC_AT_MO DE_FULL.odb Aqaq/Standar 6.9-1 Wed Mar 02 19:32:05 India Standard Time 2011



Scale: Internal pressure
 Element: 25 (80) Time: 0.9998
 Primary Var: COPEN, SNEG
 Deformed Var: U Deformation Scale Factor: 1.000e+00

Figure A 46 pipe separation (contour) at 1.5P

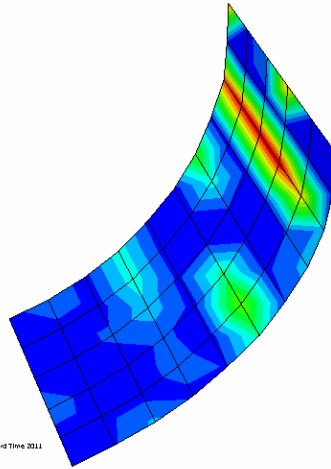
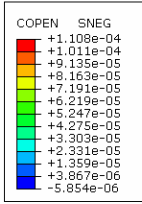


ODB: RC_AT_MO DE_FULL.odb Aqaq/Standar 6.9-1 Wed Mar 02 19:32:05 India Standard Time 2011



Scale: Internal pressure
 Element: 25 (80) Time: 0.9814
 Primary Var: COPEN, SNEG
 Deformed Var: U Deformation Scale Factor: 1.000e+00

Figure A 47 pipe separation (contour) at 2.0P

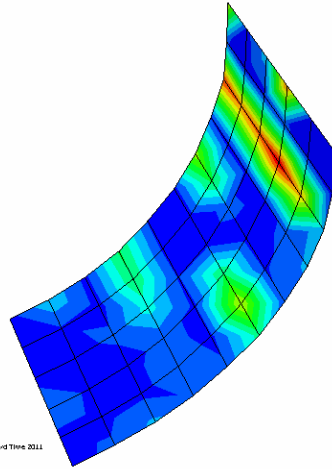
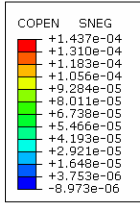


ODB: BC_AT_NO DE_FULL.ods Abaqus/Standard 6.9-1 Wed Mar 02 19:22:03 India Standard Time 2011



Scale: Internal Pressure
 Element: U2, SNEG Time = 0.7229
 Primary Var: COPEN, SNEG
 Deformed Var: U, Deformation Scale Factor = 1.000e+00

Figure A 48 pipe separation (contour) at 2.5P

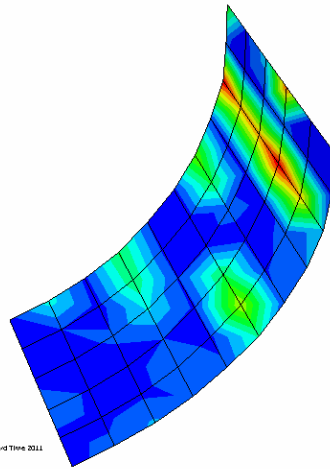
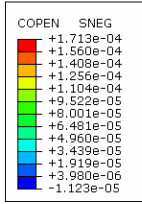


ODB: BC_AT_NO DE_FULL.ods Abaqus/Standard 6.9-1 Wed Mar 02 19:22:03 India Standard Time 2011



Scale: Internal Pressure
 Element: U2, SNEG Time = 0.8717
 Primary Var: COPEN, SNEG
 Deformed Var: U, Deformation Scale Factor = 1.000e+00

Figure A 49 pipe separation (contour) at 3.0P

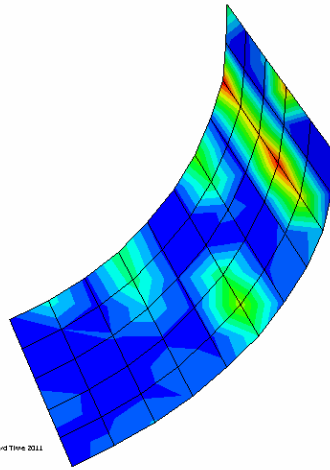
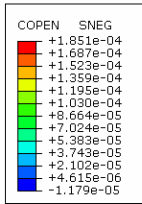


ODB: BC_AT_NO DE_FULL.ods Ahsaal/Scanda-d-6.9-1 Wed Mar 02 19:22:45 India Scanda-d Time 2011



Scale: Internal pressure
 Engineering: 200, 0.0001 Time = 0.9545
 Reference Var: CD MIN = 3.980
 Deformed Var: U Deformation Scale Factor = -1.000e-00

Figure A 50 pipe separation (contour) at 3.3P



ODB: BC_AT_NO DE_FULL.ods Ahsaal/Scanda-d-6.9-1 Wed Mar 02 19:22:45 India Scanda-d Time 2011



Scale: Internal pressure
 Engineering: 200, 0.0001 Time = 0.9829
 Reference Var: CD MIN = 3.980
 Deformed Var: U Deformation Scale Factor = -1.000e-00

Figure A 51 pipe separation (contour) at 3.3P

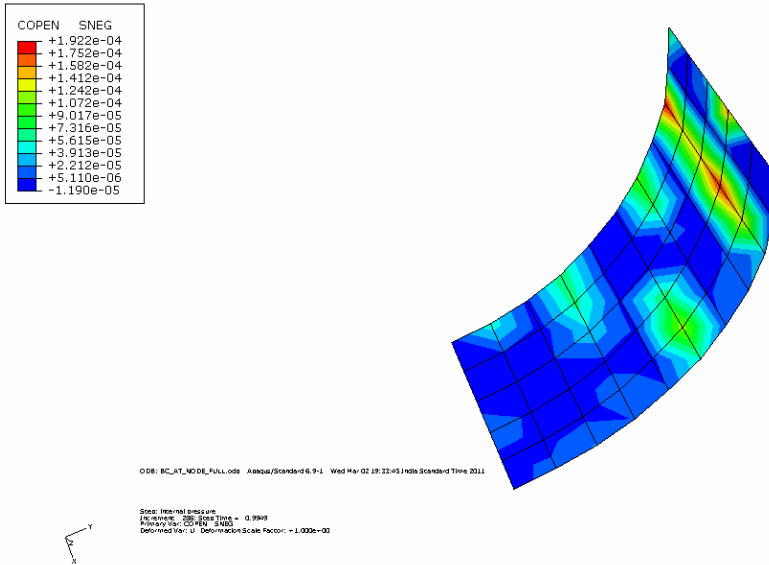


Figure A 52 pipe separation (contour) at ultimate P

MODEL 2B – LINER IS ATTACHED TO CONCRETE SURFACE DUE TO FRICTION ONLY

Description of the model

This model is similar to Model-2a considering liner and sleeve are connected to concrete by means of friction (co-efficient is 0.5). In this case the analysis could not proceed beyond 3.05 times the design pressure. The ultimate pressure, wherever is mentioned in this report is assumed to be 3.05 Pd for Model-2b. Figure A 1b and Figure A 2b show the minimum principal stress at prestress and maximum principal stress at design pressure respectively.

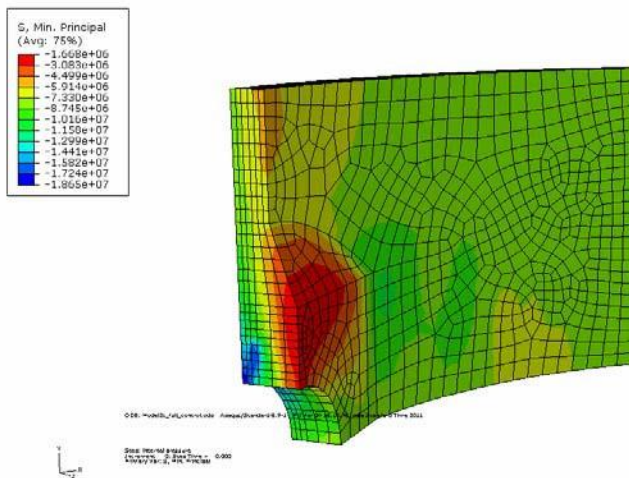


Figure A 53 Min principal stress in concrete (contour) after prestress

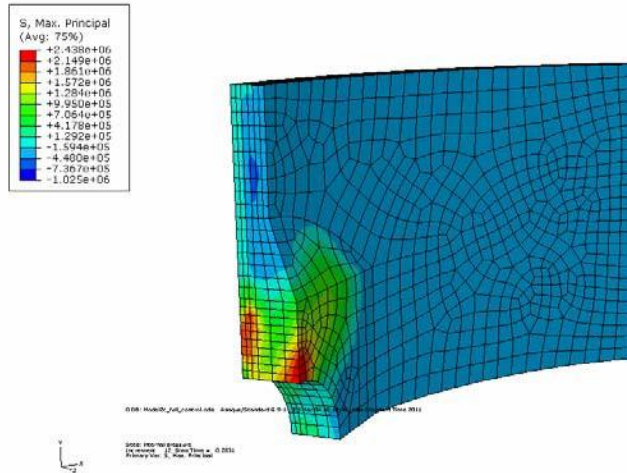


Figure A 54 Max. principal stress in concrete (contour) at design pressure

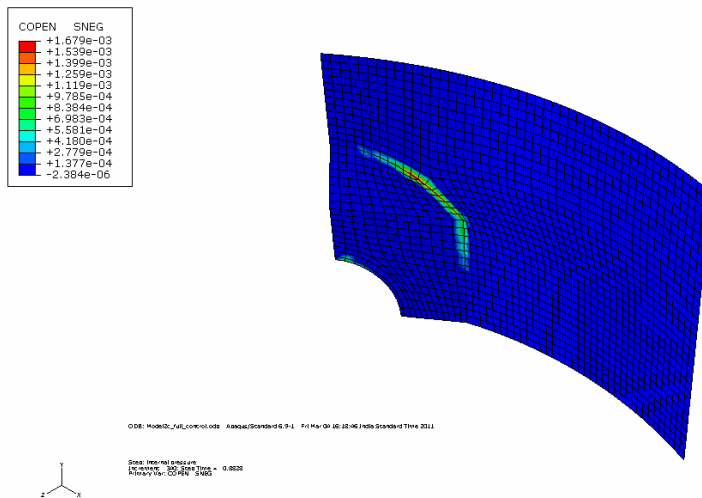


Fig. Figure A 55 shows the contact open at ultimate pressure (3.05pd), (+)ve sign indicates separation from concrete surface.

Pressure Milestone: Applied pressure when:

- Concrete Hoop Cracking Occurs and report where: *at pressure 0.64 MPa, i.e 1.64 Pd at 0° azimuth.*
- First tendon Reaches 1% strain and report where: *maximum tendon strain reached 0.312% at ultimate pressure at horizontal tendons near 0° azimuth*

Deformed shape and liner strain distribution

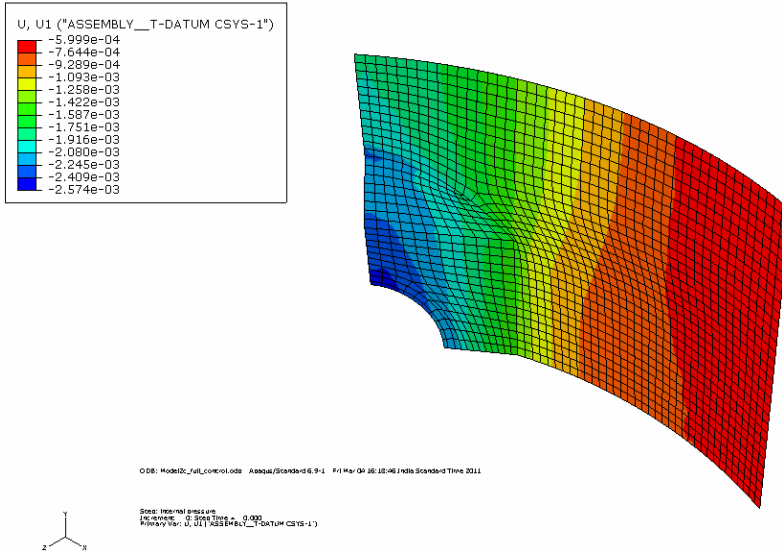


Figure A 56 Liner deformed shape (contour) at 0.0P

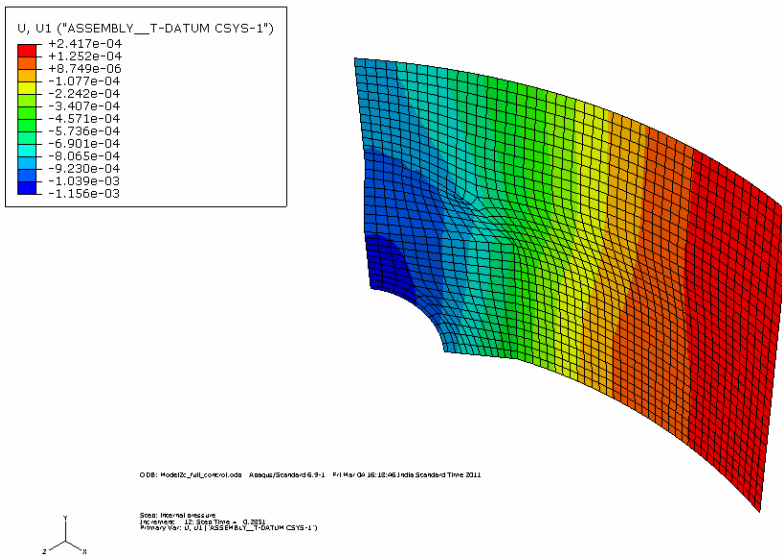


Figure A 57 Liner deformed shape (contour) at 1.0P

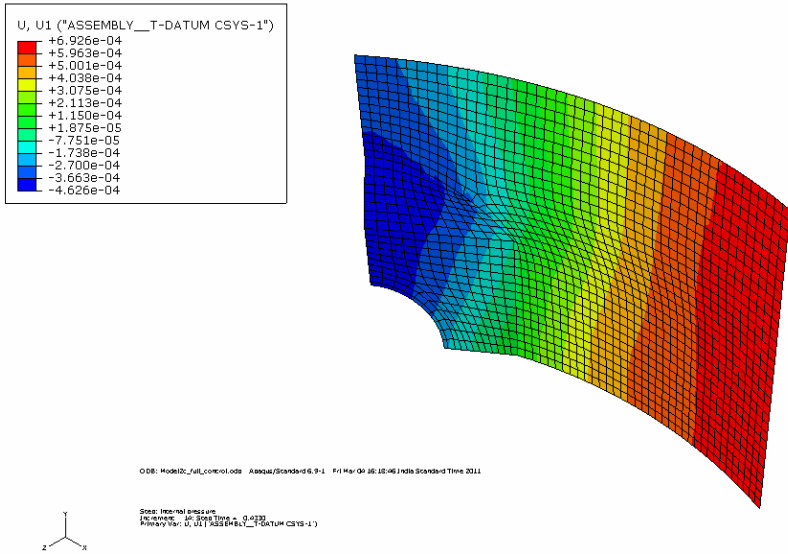


Figure A 58 Liner deformed shape (contour) at 1.5P

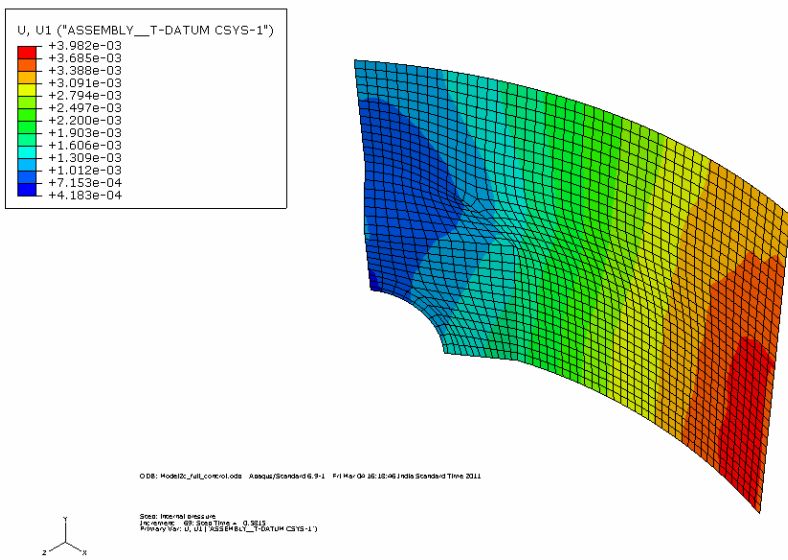
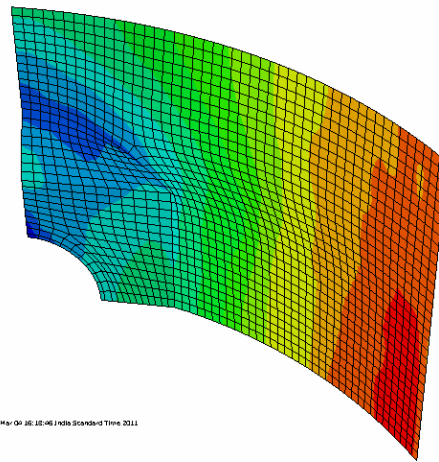
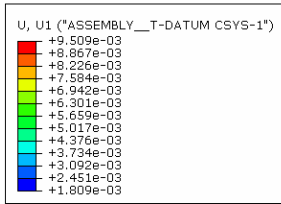


Figure A 59 Liner deformed shape (contour) at 2.0P

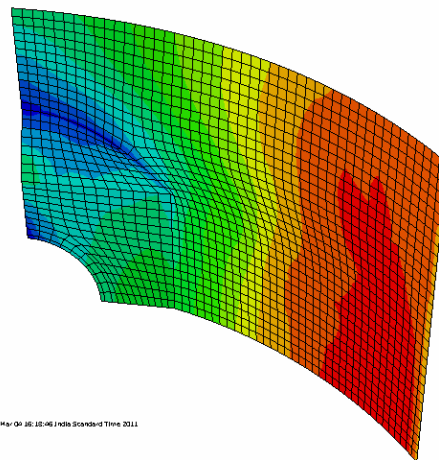
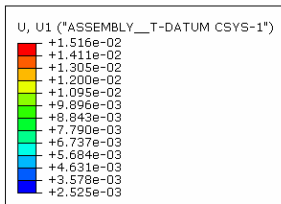


ODB: ModelID_full_conc1.odb Abaqus/Standard 6.9-1 Fri Mar 09 16:18:46 India Standard Time 2011



Step: Internal pressure
 Increment: 126 (Step Time = 0.2201)
 Primary Var: U, U1 (*ASSEMBLY__T-DATUM CSYS-1*)

Figure A 60 Liner deformed shape (contour) at 2.5P

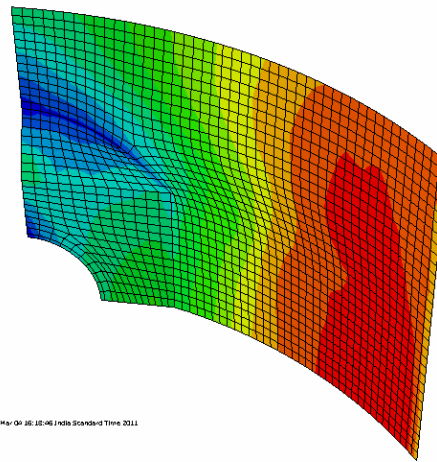
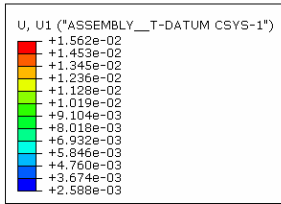


ODB: ModelID_full_conc1.odb Abaqus/Standard 6.9-1 Fri Mar 09 16:18:46 India Standard Time 2011



Step: Internal pressure
 Increment: 126 (Step Time = 0.3075)
 Primary Var: U, U1 (*ASSEMBLY__T-DATUM CSYS-1*)

Figure A 61 Liner deformed shape (contour) at 3.0P

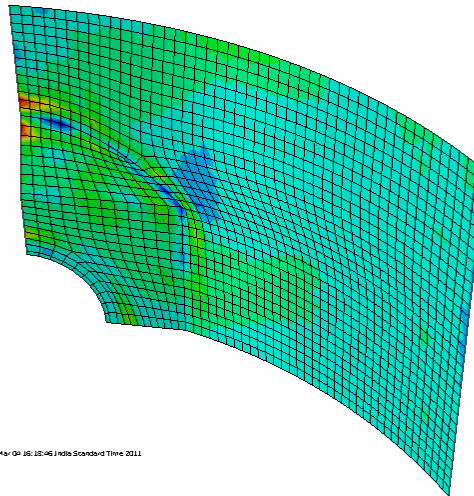
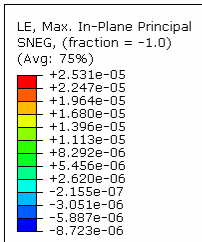


ODB: ModelID_full_conc1.odb Abaqus/Standard 6.9-1 Fri Mar 04 16:18:46 India Standard Time 2011



Scale: Internal pressure
 Location: 0.000 Time = 0.0000
 Primary Var: U, U1 (*ASSEMBLY__T-DATUM CSYS-1*)

Figure A 62 Liner deformed shape (contour) at ultimate P

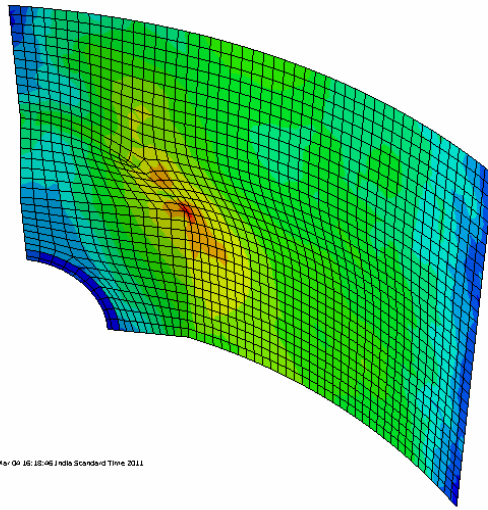
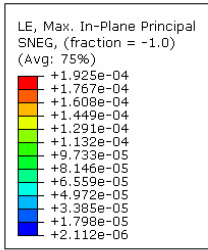


ODB: ModelID_full_conc1.odb Abaqus/Standard 6.9-1 Fri Mar 04 16:18:46 India Standard Time 2011



Scale: Internal pressure
 Location: 0.000 Time = 0.000
 Primary Var: LE, Max. In-Plane Principal
 Deformed Var: U Deformation Scale Factor: -1.000e+00

Figure A 63 Liner strain (contour) at 0.0 P

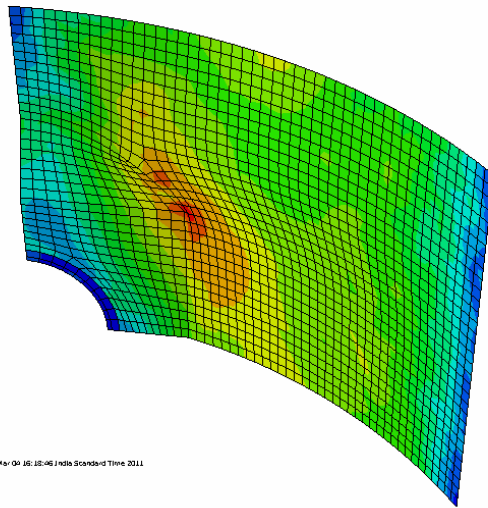
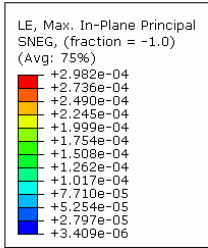


ODB: Model2_full_control.odb ABAQUS/Standard 6.9-1 Fri Mar 09 16:22:46 India Standard Time 2011



Session: Principal Stress
Increment: 15 Step Time = 0.2511
Principal Str: LE, Max. In-Plane Principal
Deformed Str: 0 Deformation Scale Factor: = 1.0000e+00

Figure A 64 Liner strain (contour) at 1.0 P

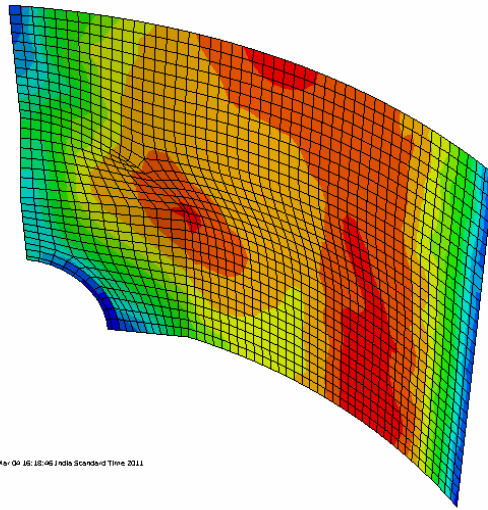
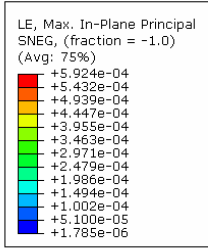


ODB: Model2_full_control.odb ABAQUS/Standard 6.9-1 Fri Mar 09 16:22:46 India Standard Time 2011



Session: Principal Stress
Increment: 16 Step Time = 0.3732
Principal Str: LE, Max. In-Plane Principal
Deformed Str: 0 Deformation Scale Factor: = 1.0000e+00

Figure A 65 Liner strain (contour) at 1.5 P

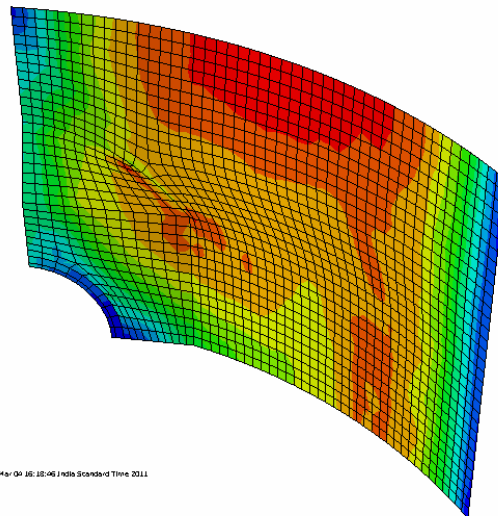
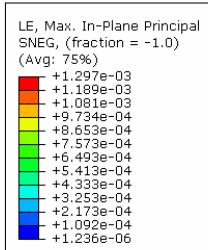


ODB: Model2_full_control.odb Abaqus/Standard 6.9-1 Fri Mar 04 16:18:46 India Standard Time 2011



Step: Internal Pressure
 Increment: 49, Step Time = 0.3215
 Primary Var: LE, Max. In-Plane Principal
 Deformed Var: U, Deformation Scale Factor: = 1.000e+00

Figure A 66 Liner strain (contour) at 2.0 P

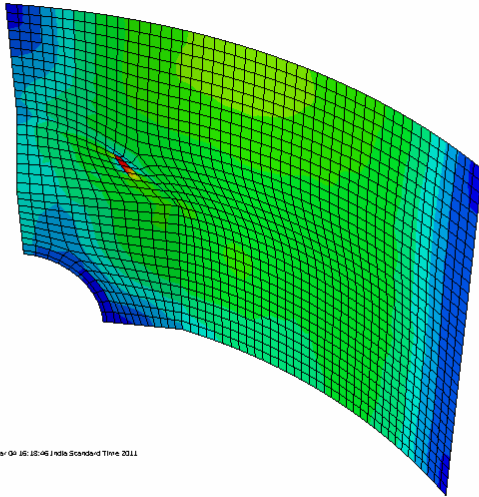
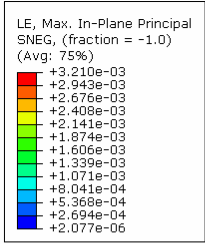


ODB: Model2_full_control.odb Abaqus/Standard 6.9-1 Fri Mar 04 16:18:46 India Standard Time 2011



Step: Internal Pressure
 Increment: 49, Step Time = 0.7201
 Primary Var: LE, Max. In-Plane Principal
 Deformed Var: U, Deformation Scale Factor: = 1.000e+00

Figure A 67 Liner strain (contour) at 2.5 P

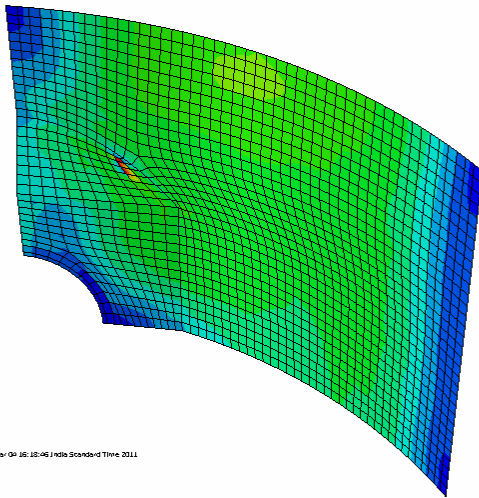
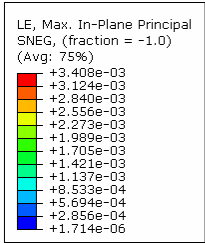


ODB: Model2_full_contour.odb Aabaq/Stand:d:6.9-1 F:\Ms\04\05.18\06\nda\Stand:d\Tme.3011



Scale: Internal pressure
 In-plane: 300 Scale Time = 0.0200
 Primary Var: LE, Max. In-Plane Principal
 Deformed Var: U Deformation Scale Factor = 1.000e+00

Figure A 68 Liner strain (contour) at 3.0 P



ODB: Model2_full_contour.odb Aabaq/Stand:d:6.9-1 F:\Ms\04\05.18\06\nda\Stand:d\Tme.3011



Scale: Internal pressure
 In-plane: 300 Scale Time = 0.0200
 Primary Var: LE, Max. In-Plane Principal
 Deformed Var: U Deformation Scale Factor = 1.000e+00

Figure A 69 Liner strain (contour) at ultimate P

2.5 Liner strain magnitude (hoop direction) at location indicated in figure 11 (white paper)

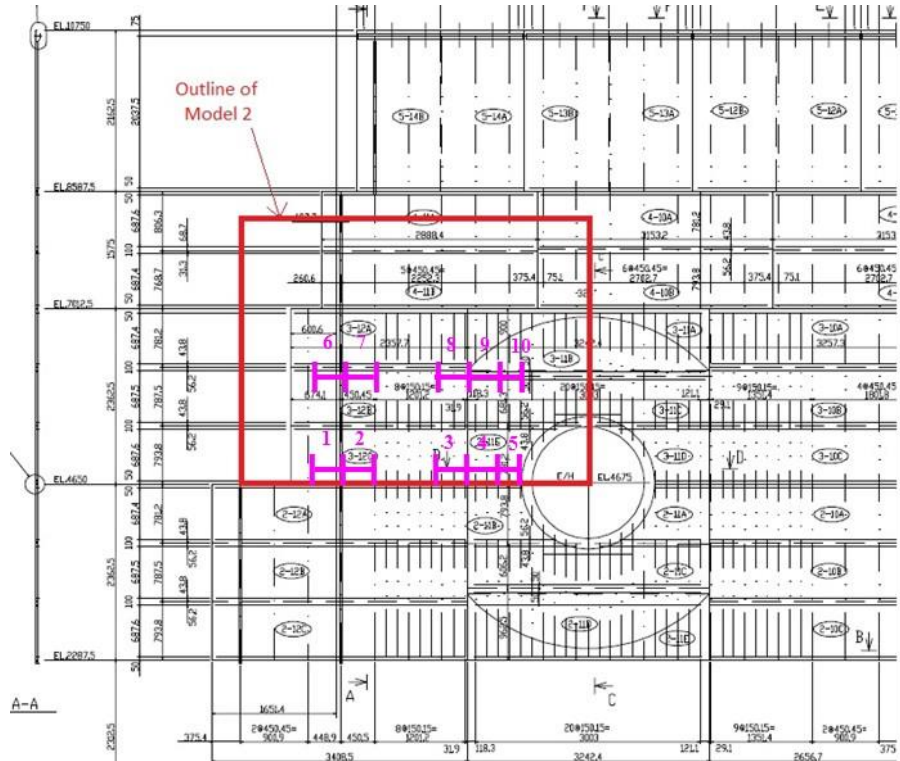


Figure A 70 Liner strain measuring locations (Fig.11 of white paper)

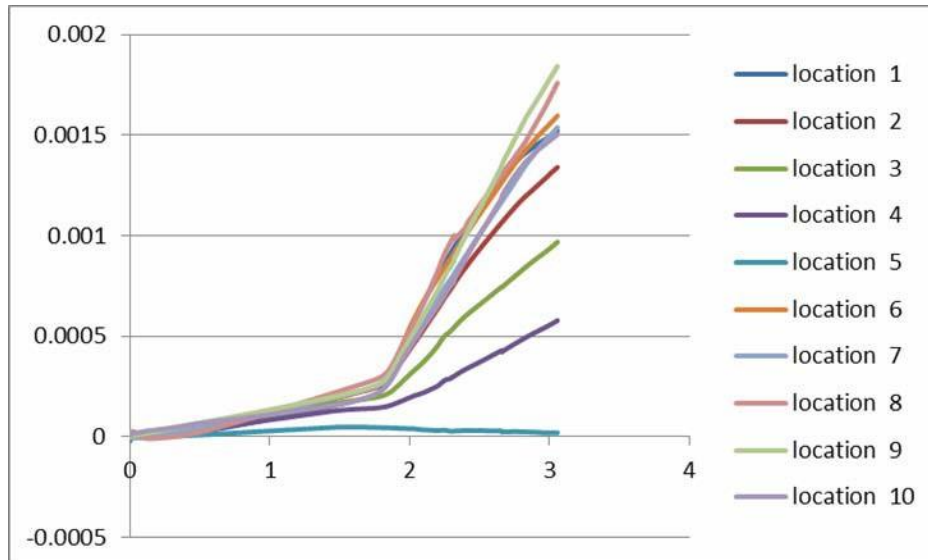


Figure A 71 Liner strain (Y-axis) vs multiple of design pressure (X-axis)

2.6 Radial displacement

A fig. 2.6.1b show the comparative study of deformation with respect to multiple of design pressure, where (+) sign indicates radially outward.

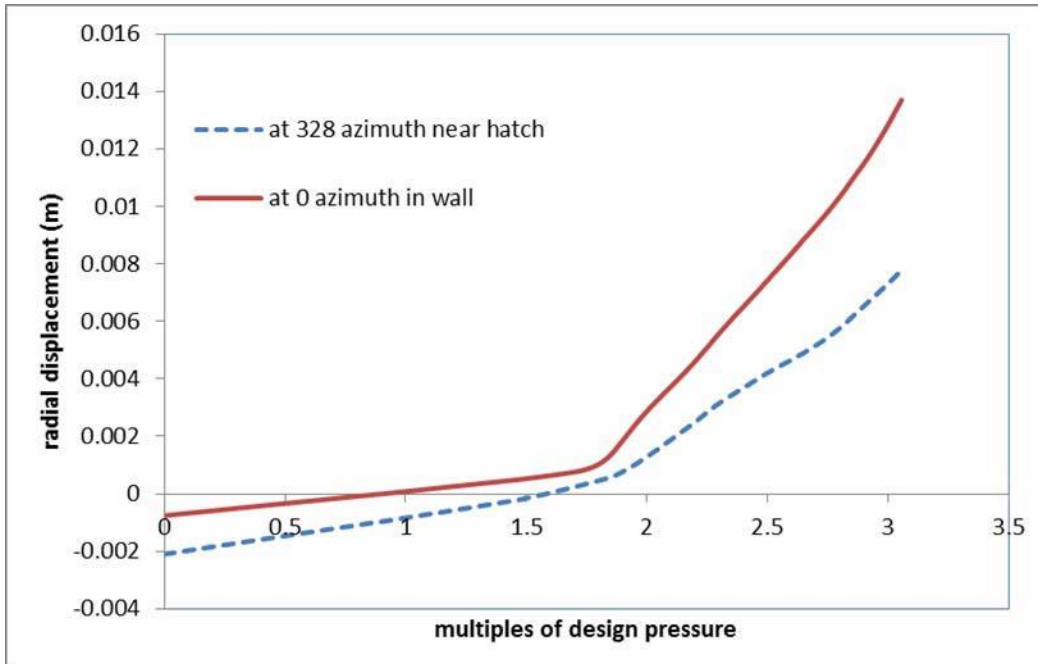


Figure A 72 Radial displacement at 328° and 0° azimuth

2.7 tendon stress distribution

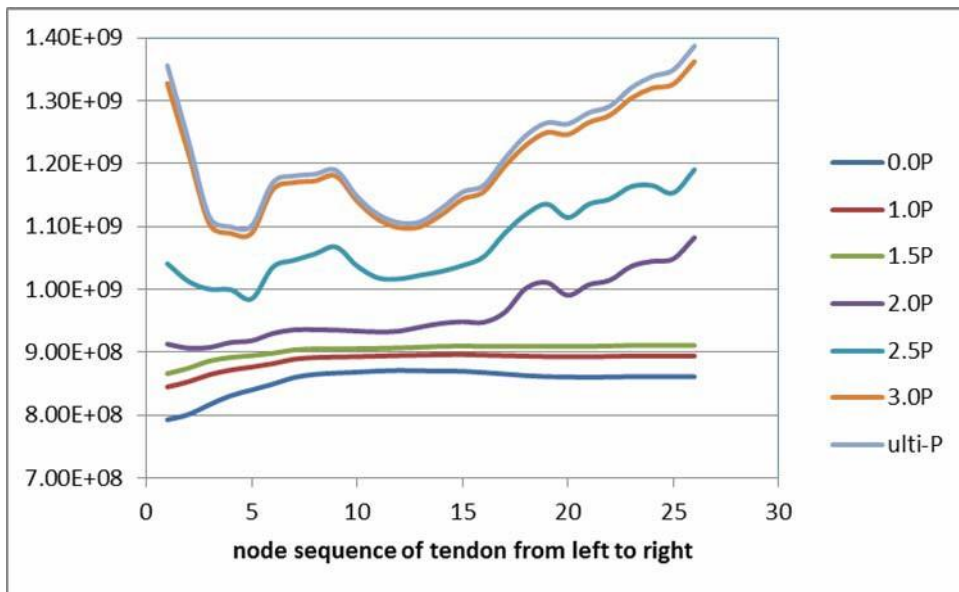


Figure A 73 stresses (N/m2) in hoop tendon nearest the penetration hatch

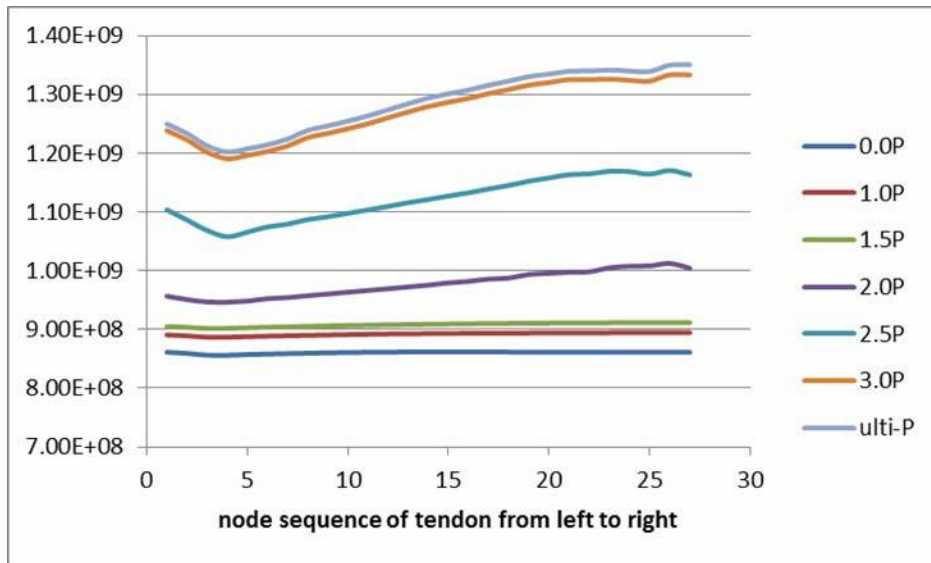


Figure A 74 stresses (N/m²) in hoop tendon at top of the model

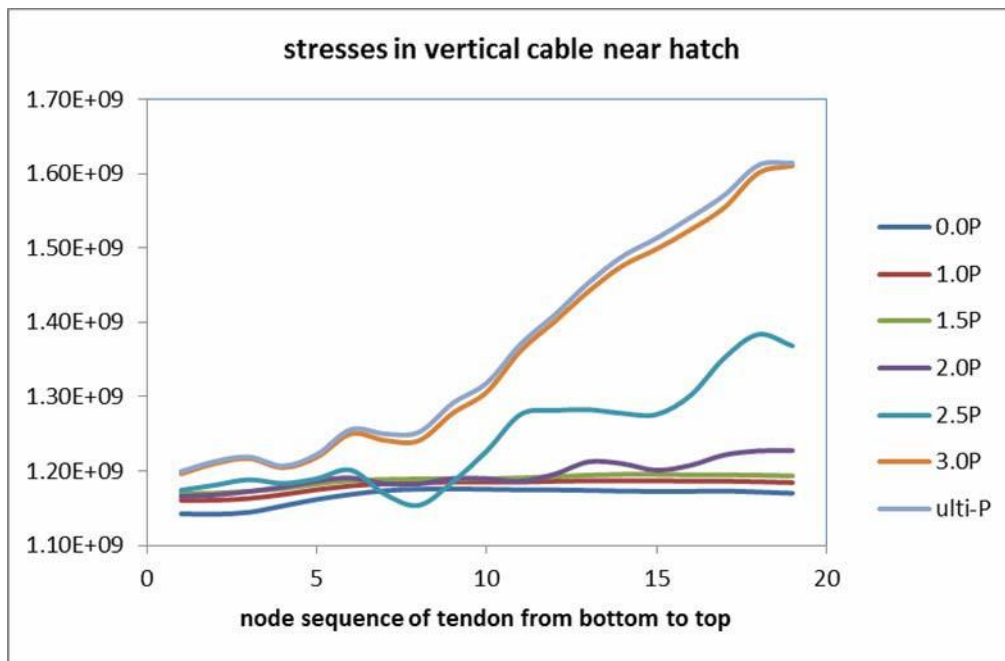


Figure A 75 stresses (N/m²) in vertical tendon near hatch

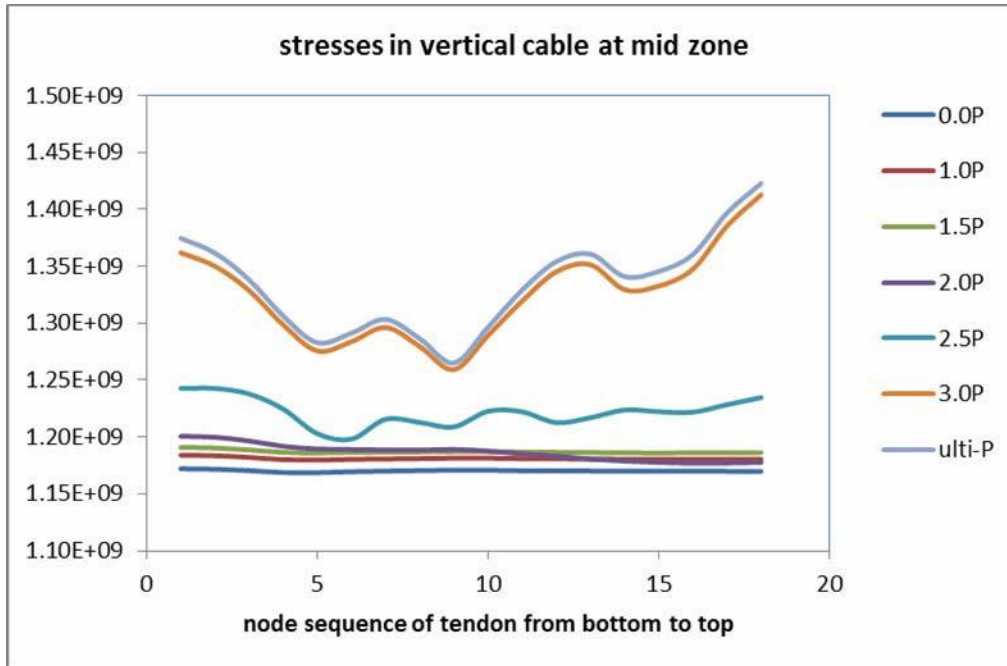


Figure A 76 stresses (N/m2) in vertical tendon at mid zone

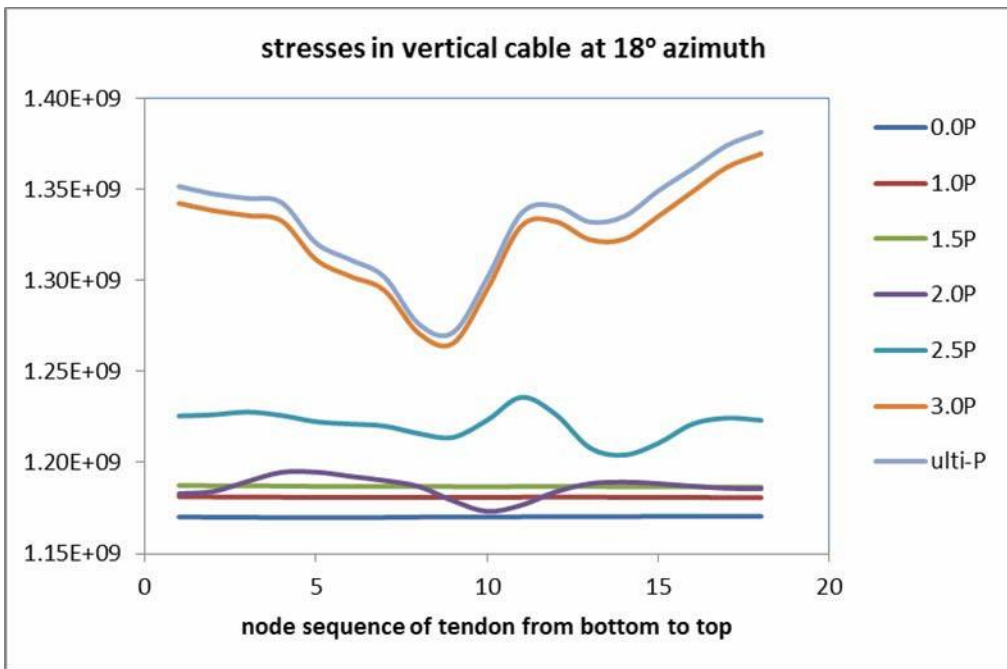
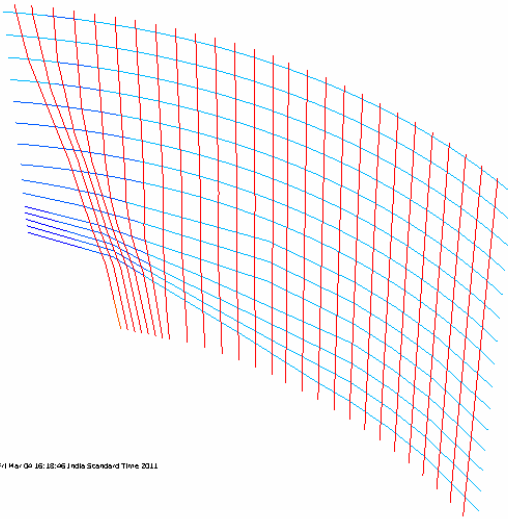
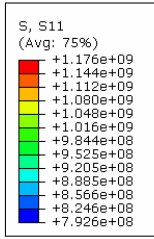


Figure A 77 stresses (N/m2) in vertical tendon at 18° azimuth

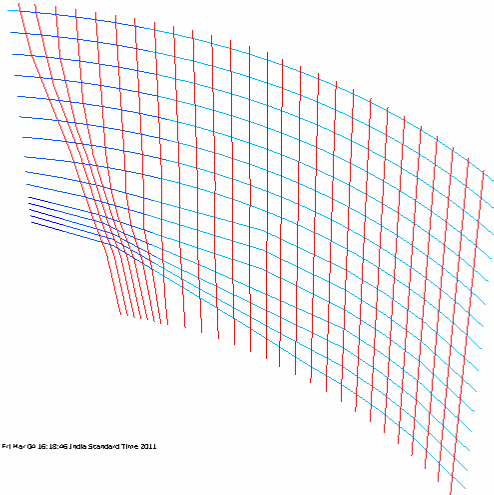
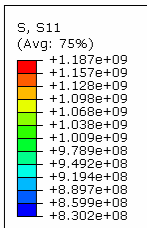


ODB: Model2_all_control.odb Abaqus/Standard 6.9-1 Fri Mar 09 16:18:46 India Standard Time 2011



Plot: Internal pressure
 Element: 31, Step Time = 0.000
 Primary Var: S, S11
 Deformed Var: U, Deformation Scale Factor: = 1.000e+00

Figure A 78 tendon stress (contour) at 0.0P

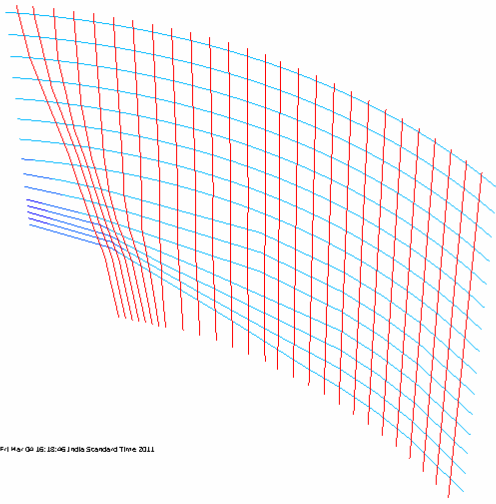
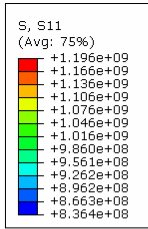


ODB: Model2_all_control.odb Abaqus/Standard 6.9-1 Fri Mar 09 16:18:46 India Standard Time 2011



Plot: Internal pressure
 Element: 31, Step Time = 0.2011
 Primary Var: S, S11
 Deformed Var: U, Deformation Scale Factor: = 1.000e+00

Figure A 79 tendon stress (contour) at 1.0P

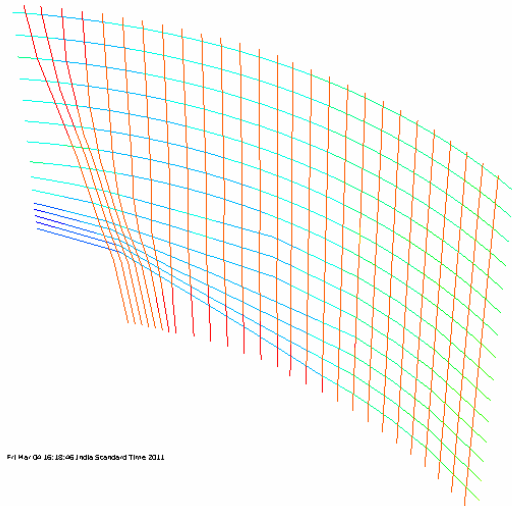
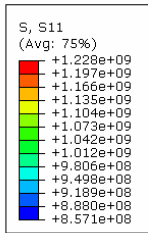


ODB: Model02_full_control.odb Abaqus/Standard 6.9-1 Fri Mar 04 16:18:46 India Standard Time 2011



Scale: Internal pressure
 Element: 89 Step Time = 0.4233
 Primary Var: S, S11
 Deformed Vis: U Deformation Scale Factor: = 1.000e+00

Figure A 80 tendon stress (contour) at 1.5P

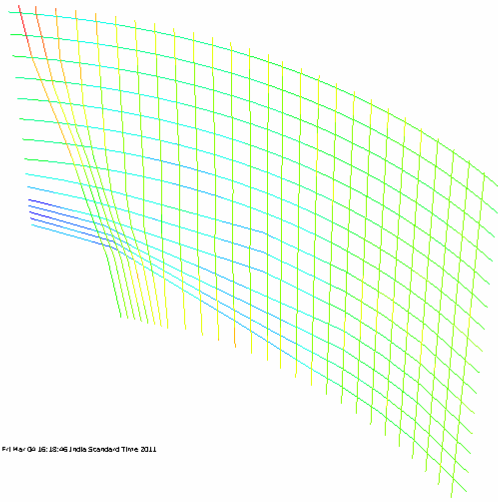
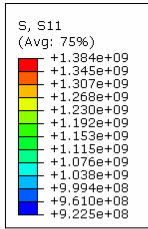


ODB: Model02_full_control.odb Abaqus/Standard 6.9-1 Fri Mar 04 16:18:46 India Standard Time 2011



Scale: Internal pressure
 Element: 89 Step Time = 0.5613
 Primary Var: S, S11
 Deformed Vis: U Deformation Scale Factor: = 1.000e+00

Figure A 81 tendon stress (contour) at 2.0P

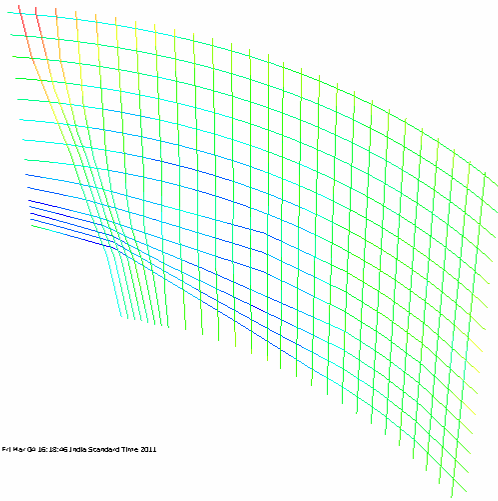
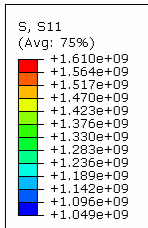


ODB: Model2_full_contour.odb Abaqus/Standard 6.9-1 Fri Mar 04 05:18:46 India Standard Time 2011



Scale: Internal pressure
 Increment: 395, Step Time = 0.7303
 Primary Var: S, S11
 Deformed Var: U, Deformation Scale Factor = 1.000e+00

Figure A 82 tendon stress (contour) at 2.5P



ODB: Model2_full_contour.odb Abaqus/Standard 6.9-1 Fri Mar 04 05:18:46 India Standard Time 2011



Scale: Internal pressure
 Increment: 395, Step Time = 0.8704
 Primary Var: S, S11
 Deformed Var: U, Deformation Scale Factor = 1.000e+00

Figure A 83 tendon stress (contour) at 3.0P

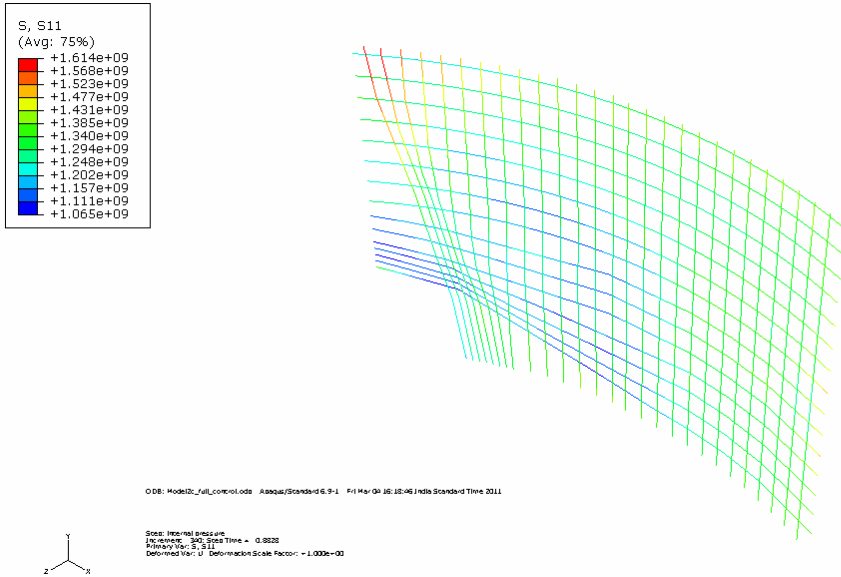


Figure A 84 tendon stress (contour) at ultimate P

2.8 Separation of pipe sleeve, (+)ve sign indicates separation/contact open

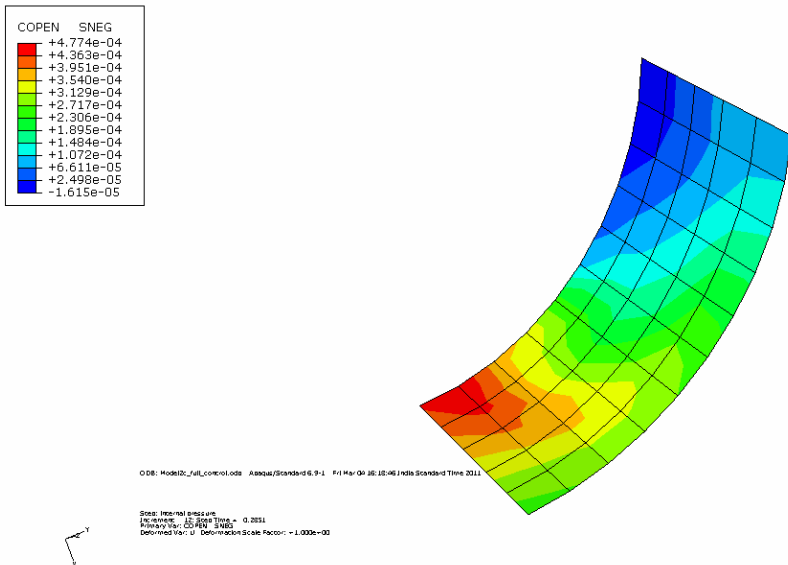
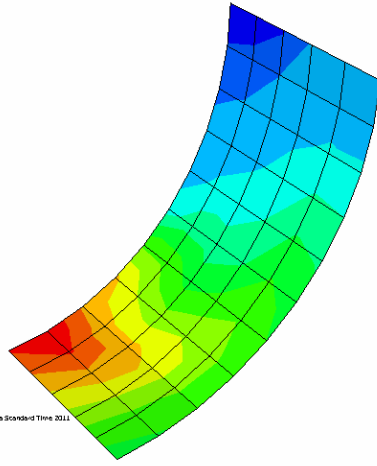
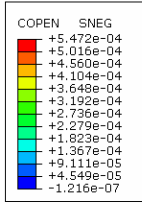


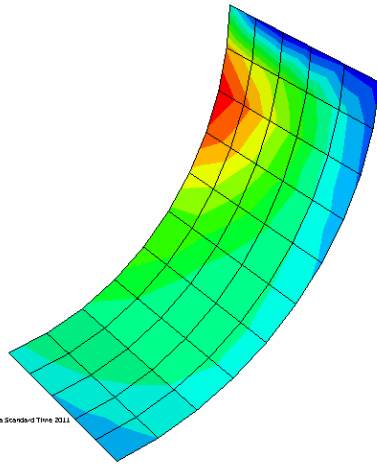
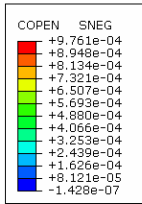
Figure A 85 contact open (contour) at 1.0P



ODB: Model2_full_contact.ods Abaqus/Standard 6.9-1 Fri Mar 09 16:18:46 India Standard Time 2011

Scale: Internal pressure
 Element: 65 2008 Time: 0.4133
 Primary Var: COPEN SNEG
 Deformed Var: U Deformation Scale Factor: -1.000e-00

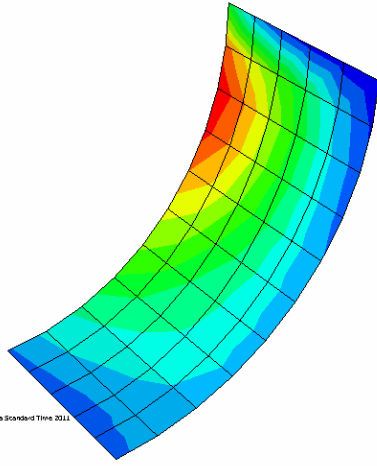
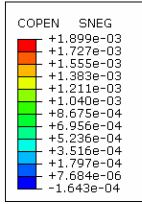
Figure A 86 contact open (contour) at 1.5P



ODB: Model2_full_contact.ods Abaqus/Standard 6.9-1 Fri Mar 09 16:18:46 India Standard Time 2011

Scale: Internal pressure
 Element: 65 2008 Time: 0.5615
 Primary Var: COPEN SNEG
 Deformed Var: U Deformation Scale Factor: -1.000e-00

Figure A 87 contact open (contour) at 2.0P

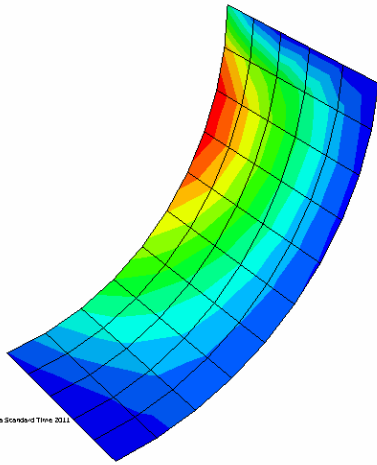
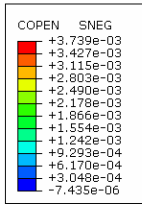


ODB: Model2_full_contact.ods Ansys/Standard 6.9.1 Fri Mar 09 16:18:46 India Standard Time 2011

Scale: Internal pressure
 Engineering Units: SI Units Time = 0.7321
 Reference Vx: CD MIN = 1.983
 Determined Vx: U Deformation Scale Factor = -1.000e-00



Figure A 88 contact open (contour) at 2.5P

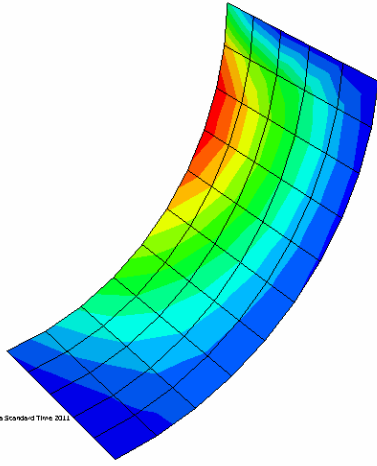
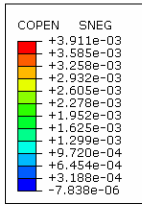


ODB: Model2_full_contact.ods Ansys/Standard 6.9.1 Fri Mar 09 16:18:46 India Standard Time 2011

Scale: Internal pressure
 Engineering Units: SI Units Time = 0.8739
 Reference Vx: CD MIN = 1.983
 Determined Vx: U Deformation Scale Factor = -1.000e-00



Figure A 89 contact open (contour) at 3.0P



ODB: ModelID_full_contact.ods Ansys/Standard 6.9.1 Fri Mar 09 16:10:46 India Standard Time 2011



Scale: Internal Pressure
 Maximum: 392.000 Scale Factor = 0.0025
 Primary Var: COPEN SNEG
 Deformed Var: U Displacement Scale Factor = 1.0000e-01

Figure A 90 contact open (contour) at ultimate P

STANDARD PROBLEM EXERCISE
Performance of Containment Vessel Under
Severe Accident Conditions

Results of First Phase Analysis

MODEL - 3



Siting & Structural Engineering Division ATOMIC
ENERGY REGULATORY BOARD Mumbai, India

March-2011

A-50

CONTENTS

Introduction	A-52
General	A-52
First stage analysis.....	A-52
Scope	A-52
Structure of report.....	A-53
Model description.....	A-53
General	A-53
PCCV model description	A-53
Finite element model.....	A-54
Modeling of Rebars.....	A-54
Modeling of tendons	A-54
Modeling of penetrations	A-54
Boundary condition.....	A-55
Failure prediction criteria.....	A-55
Loading	A-56
Modeling of prestress	A-56
Modeling of internal pressure	A-56
Results of global model analysis.....	A-57
General	A-57
Results	A-57
Deformed shape.....	A-57
Liner strains	A-57
Tendon stress distribution.....	A-58
Ultimate capacity.....	A-58
Output at 55 standard output locations	A-58
Summary	A-103

INTRODUCTION

General

The AERB-USNRC Standard problem Exercise on "Performance of Containment Vessel Under Severe Accident Conditions—" has been floated with the objective of improving knowledge in the following areas:

1. local containment behavior under beyond design basis pressures
2. characterization of leakage behavior as a function of pressure and temperature
3. probabilistic aspects of containment response

The analysis on Containment Performance involves the assessment of the ultimate load capacity of a Prestressed Concrete Containment Vessel (PCCV), and this is done in two stages. The first stage examines local effects in the containment model. The second stage will focus on characterization of leakage behavior of containment vessels as a function of pressure and temperature.

First stage analysis

In the first stage, assessment of those local effects which were observed to require more study during the previous round robin analyses, is included. The assessment include an examination into the effects of containment dilation on prestressing force, slippage of prestressing cables, steel-concrete interface, failure mechanisms, and the use of nominal versus in-situ conditions in the previous round robin analyses. Analysis results from this stage is also expected to help in calibrating the model in stage two of the analysis.

Three model studies were proposed as part of the first stage analysis.

1. Tendon behavior model
2. Local model of equipment hatch
3. Global analysis model

Scope

This report contains the details of analysis performed and the results obtained from model-3, the global analysis model. Global Analysis Model is aimed at incorporating lessons learned from Models 1 and 2, and to provide PCCV response information at any and all locations of the structure.

However, in the present study the lessons from Models 1 and 2 are not incorporated. The results in this report are a baseline on the global model using the design information of the PCCV. The assumptions made in mathematical modeling of the PCCV are detailed in Chapter 2. Further

analysis incorporating the lessons from models 1 and 2 will be carried out by refining the current global model.

Structure of report

The report contains four chapters including the introductory Chapter. The analysis model and failure prediction approach are detailed in Chapter 2. Chapter 3 brings out the results of the global model analysis. A summary of the study carried out and the results of the study is presented in Chapter 4.

MODEL DESCRIPTION

General

Global Analysis Model incorporating lessons learned from Model Exercises 1 and 2 is expected to provide PCCV response information at all locations of the structure. For the first stage analysis the model was required to provide output at the 55 standard output locations originally requested for the 1:4 Scale model round robin analysis. A 3D model was encouraged as axisymmetric results alone will only provide a limited set of strain information.

PCCV model description

The PCCV model, Figure A - 2.1 consists of a 10.8m diameter cylinder with a wall thickness of 325mm, a 3.5m thick basemat and a hemispherical dome of thickness 275mm. The structure is made of pre-stressed concrete. The cylinder and dome have a concrete grade of M45. The prestressing is accomplished with hairpin shaped meridional tendons and circular hoop tendons. The meridional tendons are anchored in stressing gallery. The anchorages of the hoop tendons are staggered in the buttresses located at 90 and 270 degrees. Two major openings in the cylinder represents the openings for equipment hatch and the airlock.

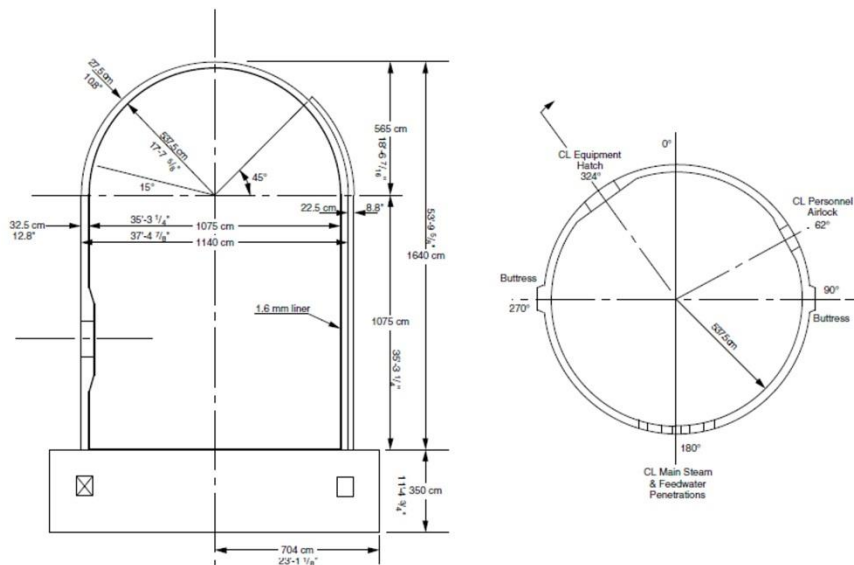


Figure A 2.1: Model of the prestressed concrete containment vessel

Finite element model

The finite element model of the containment vessel is developed from the gross dimensions available in NUREG reports. The model has been developed in ABAQUS using layered shell element. 4-node, quadrilateral, stress/displacement shell element with reduced integration and a large-strain formulation has been used for the present study. Centreline modeling has been adopted for modeling the concrete sections. The gradual change in thickness from cylinder to dome and general section of cylinder to thickened areas are not modeled. The gross cross section is modeled as two layers; layer - 1: concrete having nine integration points along the thickness and layer - 2: liner having three integration points along its thickness. The general sketches of the model are included as Figure A - 2.2.

Modeling of Rebars

Reinforcement in the structure comprise of an inner and an outer layer of both hoop and meridional reinforcement. These reinforcements have been simulated in the finite element model as rebar layers using the provision available in ABAQUS. These rebar layers are considered as uniformly distributed reinforcement layer with thickness equal to the ratio of the rebar area to the spacing.



Figure A 2.2: Model of the prestressed concrete containment vessel

Modeling of tendons

Prestressing tendons are also modeled as rebar layers.

Modeling of penetrations

Only two major openings are considered in the present model. These openings correspond to

1. The equipment hatch: Diameter 1.54m, at 324° and elevation of centre being 4.675m
2. The airlock: Diameter 0.661m, at 62° and elevation of 4.525m.

Boundary condition

The structure is assumed to be fixed at the base. Hence the raft has not been modeled.

Failure prediction criteria

The concrete damage plasticity model available in ABAQUS was used to model the non-linear properties of concrete. The main failure mechanisms assumed in the model are tensile cracking and compressive crushing of the concrete material. The failure surface is controlled by two variables representing the equivalent plastic strains in compression and tension.

The degradation of elastic stiffness in the model is characterized by damage variables (d_t or d_c), which are functions of plastic strains. The damage variables can take values from zero, representing undamaged material, to 1.0, which represents total loss of strength. If E is the initial elastic stiffness of the material, the stress-strain relations under uniaxial tension and compression loading are given by:

$$\sigma_t = (1 - d_t)E(E_t - \bar{\epsilon}_t^p) \quad (2.1)$$

$$\sigma_c = (1 - d_c)E(E_c - \bar{\epsilon}_c^p) \quad (2.2)$$

If damage is not specified, the model behaves as a plasticity model. In the present study the effect of damage has not been included. This aspect could be considered in further refinements of this analysis.

The reinforcement bars are defined as embedded oriented surfaces inside the concrete layer. The rebars are superposed on a mesh of shell elements used to model the concrete. The rebar material behaviour is represented by metal plasticity models available in ABAQUS. In this modeling approach, the concrete behavior is considered independent of the rebar. Effects associated with rebar/concrete interface, such as bond slip and dowel action are modeled approximately by introducing the tension stiffening into the concrete model to simulate the load transfer across cracks through the rebar.

The compressive and tensile stress-strain curves specified for the concrete material in the study is given in Figure A 2.3. The stress-strain curves of prestressing steel, rebar steel and liner steel are also given in Figure A - 2.3.

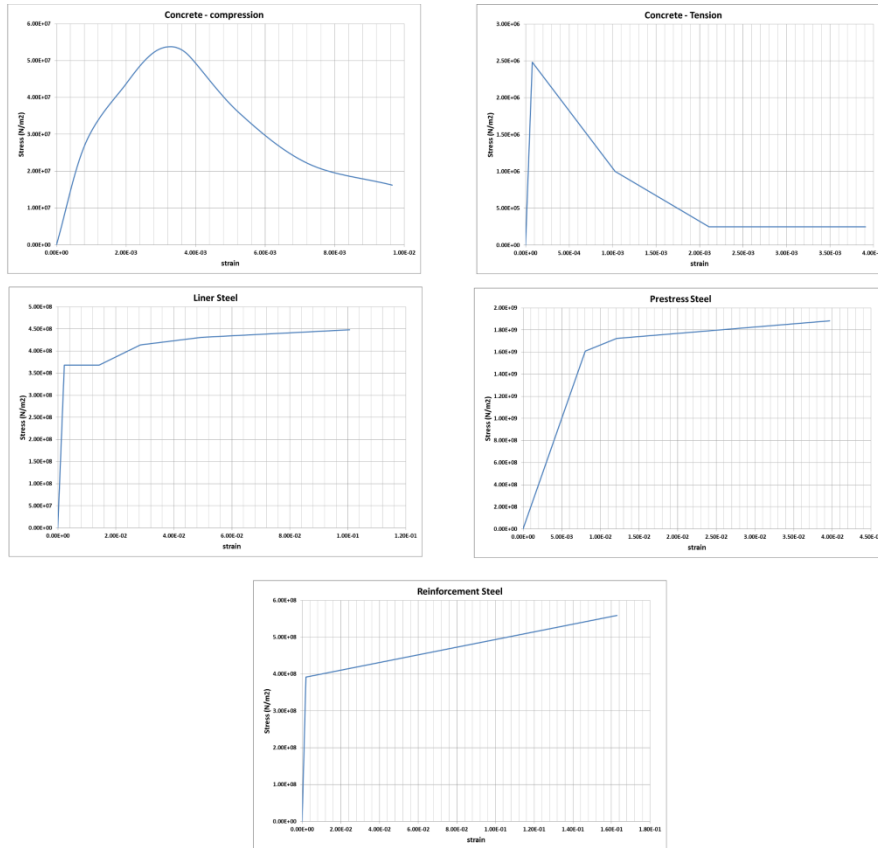


Figure A 2.3: Stress strain curves for different materials used in the model

Loading

The two loads considered in the analysis are the prestress load and the internal pressure.

Modeling of prestress

Prestress is introduced into the model by specifying it as an initial stress. The value of this stress is taken from NUREG6810 based on the values of stress at the beginning of the pressure test. The variation of prestress along the length of cables and effect of deviation of cables around the openings are not included. The stress values used are

- Hoop cables $8.41 \times 10^6 \text{ N/m}^2$
- Hairpin cables $12.5 \times 10^6 \text{ N/m}^2$

Modeling of internal pressure

Internal pressure was applied in incremental static load steps. The initial condition of the structure before application of pressure was the one obtained after application of prestress. The load steps were increased until the solution failed to converge, which was considered as the ultimate capacity.

The effect of dilation of prestressing cables, which in turn is expected to induce some additional prestressing is not modeled in the current study. The inclusion of this effect will result in some

increase of the ultimate capacity of the structure over the one determined using the current computational model.

RESULTS OF GLOBAL MODEL ANALYSIS

General

The expected output from global model analysis was specified to be the following:

1. A subset of the response information defined by the "55 standard output locations" of the 1:4 Scale PCCV round-robin exercise.
2. Plots of response versus pressure for Standard Output Locations:
 - 1-15 (displacements)
 - 22-29 (rebar strains)
 - 36-42 (liner strains)
 - 48-55 (tendon strains and stresses)
3. Contour Plot of Peak Strains in the Liner at the following pressure milestones
 - $P = 0$ (prestress applied);
 - $1 \times P_d$;
 - $1.5 P_d$;
 - $2 P_d$;
 - $2.5 P_d$;
 - $3 P_d$;
 - $3.3 P_d$;
 - $3.4 P_d$;
 - Ultimate Pressure
4. Average Strains Over 450.45 mm Regions as shown in Figure A - 3.1, locations 3, 4, 5 plotted as a Function of Pressure.
5. Tendon stress distribution at different pressure increments for
 - Hoop Tendons H35, H53, H68
 - Vertical Tendon V37 and V46

Results

Deformed shape

The deformed shape of the pccv at different pressure stages is depicted in Figure A - 3.2

Liner strains

The contour plots of liner strains in hoop and meridional directions for the required pressure stages are given in figures - 3.3 and 3.4.

The liner strain distribution over the gauge length of 450mm for the requested locations are given in Figure A - 3.5.

Tendon stress distribution

The distribution of tendon stress for different pressure stages for the requested tendons are plotted in figures 3.6 through 3.10. The stress distribution in the tendon layer, approximately at the height of the specified tendon and following grossly the profile of the tendon is reported.

The contour plot of hoop and meridional stress distribution in the layer of hoop and vertical prestressing is depicted in figures - 3.11 through 3.16

Ultimate capacity

The model solution successfully converged until the internal pressure equivalent of 3.59 times the design pressure. Hence this pressure is considered as the ultimate pressure obtained from this computational model. The deformation pattern of the structure at different pressure stages is depicted in Figure A - 3.2. The maximum principal stress distribution in different layers of concrete is presented in Figure A - 3.17

It is to be recognized that the refinements to include dilation effect, tendon load distribution with respect to length of tendon and also with respect to regions in the model needs to be considered in further refined studies.

Output at 55 standard output locations

Table A- 3.1 reproduces the results expected at the 55 standardized output locations. The locations specified in the problem and the locations considered based on the limitations of meshing in the model are also tabulated in Table A- 3.1. In all, output has been reported at 52 locations of the 55. Salient features of deriving these output are as follows:

1. Tendon stress distribution for a particular tendon is not available from the present model, as individual tendons are not modeled. Hence the stress distribution in the tendon layer, approximately at the height of the specified tendon is reported.
2. For reporting of rebar strains, the specification does not always differentiate between outer layer or inner layer of rebars. In general, where only one output is requested, the same has been provided for the outer layer.
3. Liner was modeled as a layer in the shell element and this layer comprised of three integration points. Liner strain is reported corresponding to the central integration point.
4. For reporting the liner strains over gauge length of 450mm at locations specified in Figure A 11 of SPE problem statement, an average of the strains approximately corresponding to the requested location, over a length of about 450mm has been considered.
5. The displacements at the centre of E/H opening and A/L opening has been evaluated as the average of the displacement at the four nodes on the edge of the openings.
6. The output at the base liner (location 47) is not provided as base liner is not modeled.
7. The outputs at locations 54 and 55 are not provided as the prestressing tendons are modeled as a layer and hence no anchorage locations are available.

The plots of pressure versus the response at all these locations are presented in figures- 3.18 through 3.70.

Table A 3.1: Standard output locations in the PCCV model

Loc.	Type	Orientation	Az(deg)	EI(m)
1	Displacement	Vertical	135	0
2	Displacement	Radial	135	0.25
3	Displacement	Radial	135	1.43
4	Displacement	Radial	135	2.63
5	Displacement	Radial	135	4.68
6	Displacement	Radial	135	6.2
7	Displacement	Radial	135	10.75
8	Displacement	Vertical	135	10.75
9	Displacement	Radial	135	14.55
10	Displacement	Vertical	135	14.55
11	Displacement	Vertical	135	16.13
12	Displacement	Radial	90	6.2
13	Displacement	Radial	90	10.75
14	Displacement	Radial	324	4.675
15	Displacement	Radial	62	4.525
16	Rebar Strain	Meridional	135	0.05
17	Rebar Strain	Meridional	135	0.05
18	Rebar Strain	Meridional	135	0.25
19	Rebar Strain	Meridional	135	0.25
20	Rebar Strain	Meridional	135	1.43
21	Rebar Strain	Meridional	135	1.43
22	Rebar Strain	Hoop	135	6.2
23	Rebar Strain	Meridional	135	6.2
24	Rebar Strain	Hoop	135	10.75
25	Rebar Strain	Meridional	135	10.75
26	Rebar Strain	Meridional	135	10.75
27	Rebar Strain	Hoop	135	14.55
28	Rebar Strain	Meridional	135	14.55
29	Rebar Strain	Meridional	135	14.55
30	Rebar Strain	Meridional	90	0.05
31	Rebar Strain	Meridional	90	0.05
32	Rebar Strain	Hoop	90	6.2
33	Rebar Strain	Meridional	90	6.2
34	Liner Strain	Meridional	0	0
35	Liner Strain	Hoop	0	0
36	Liner Strain	Meridional	135	0.25
37	Liner Strain	Hoop	135	0.25
38	Liner Strain	Meridional	135	6.2
39	Liner Strain	Hoop	135	6.2

40	Liner Strain	Meridional	135	10.75
41	Liner Strain	Hoop	135	10.75
42	Liner Strain	Meridional	135	16.13
43	Liner Strain	Meridional	90	6.2
44	Liner Strain	Hoop	90	6.2
45	Liner Strain	Hoop	334	4.675
46	Liner Strain	Hoop	58	4.525
47	Base Liner	Radial	135	0
48	Tendon strain	Hairpin	180	15.6
49	Tendon strain	Hairpin	135	10.75
50	Tendon strain	Hoop	90	6.58
51	Tendon strain	Hoop	180	6.58
52	Tendon strain	Hoop	280	6.58
53	Tendon strain	Hoop	0	4.57
54	Tendon force	Hairpin	241	-1.16
55	Tendon force	Hoop	275	6.58

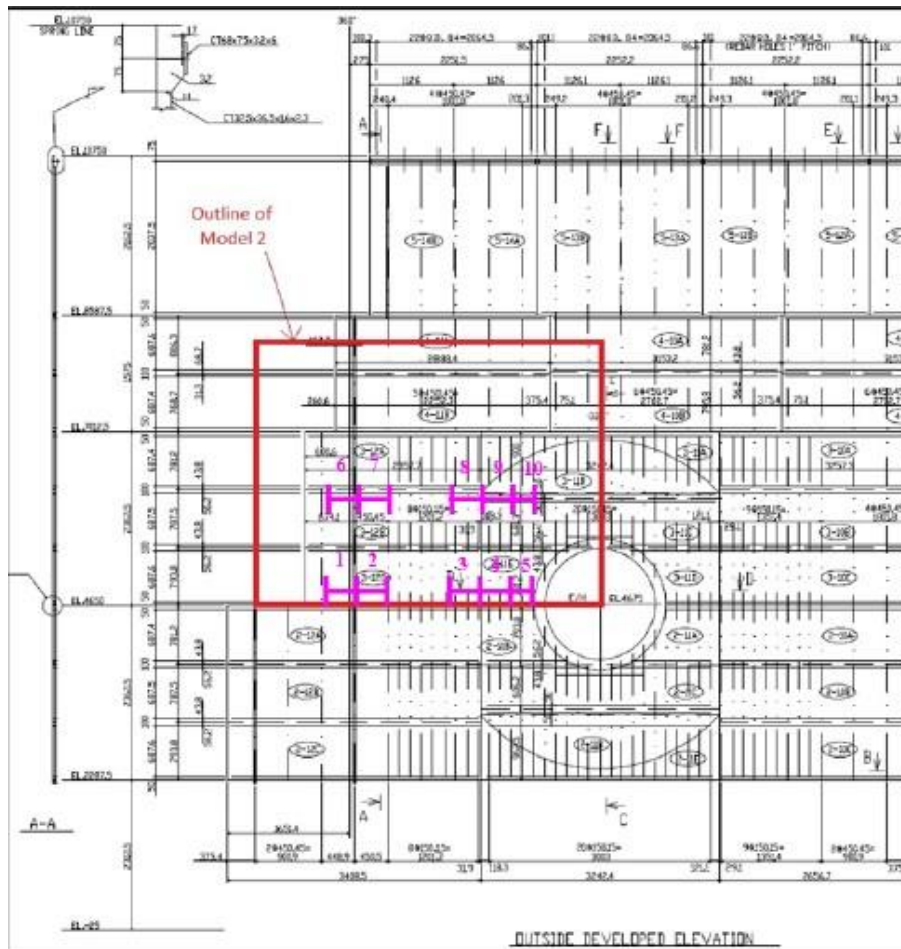


Figure A 3.1: Locations for strain reporting over gauge length of 450mm in liner

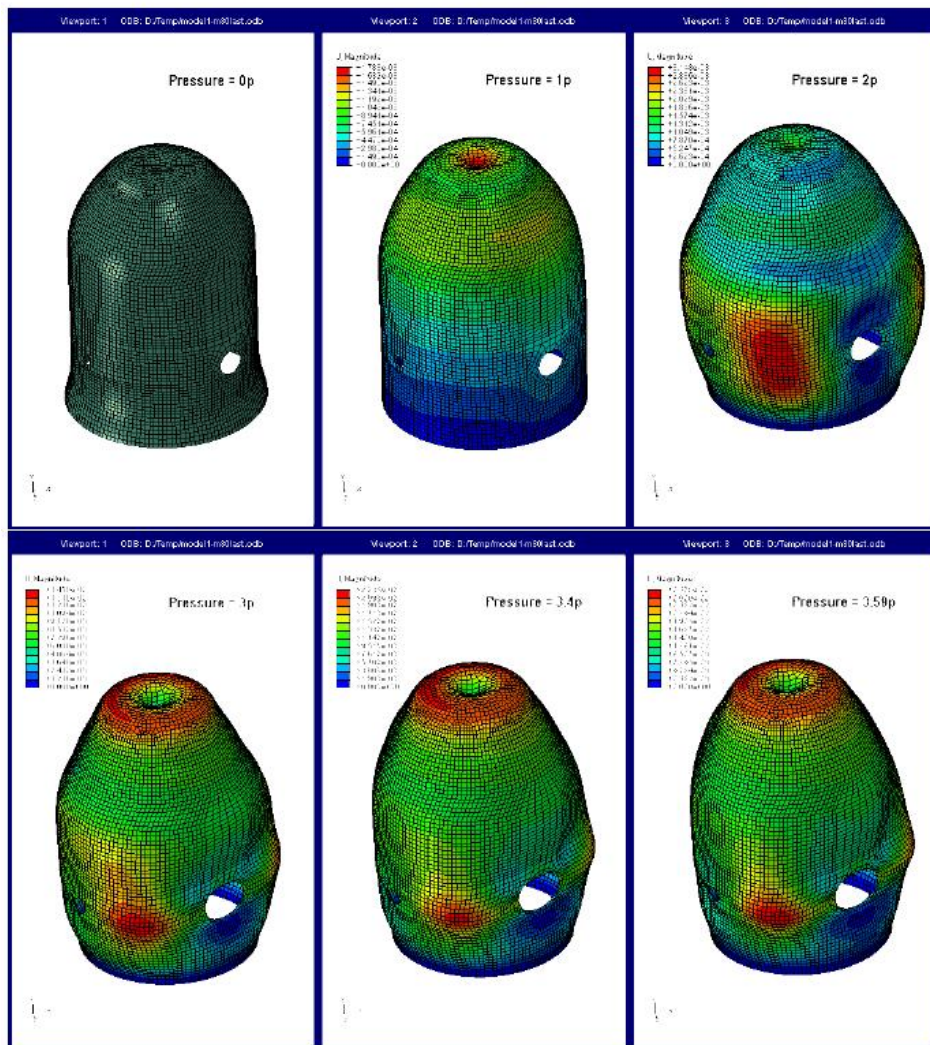
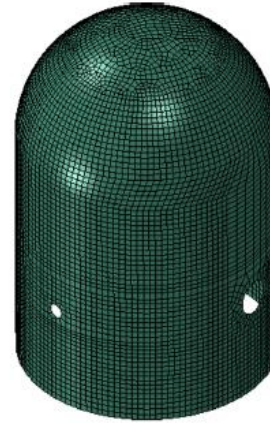


Figure A 3.2: Deformation of the structure for various pressure stages

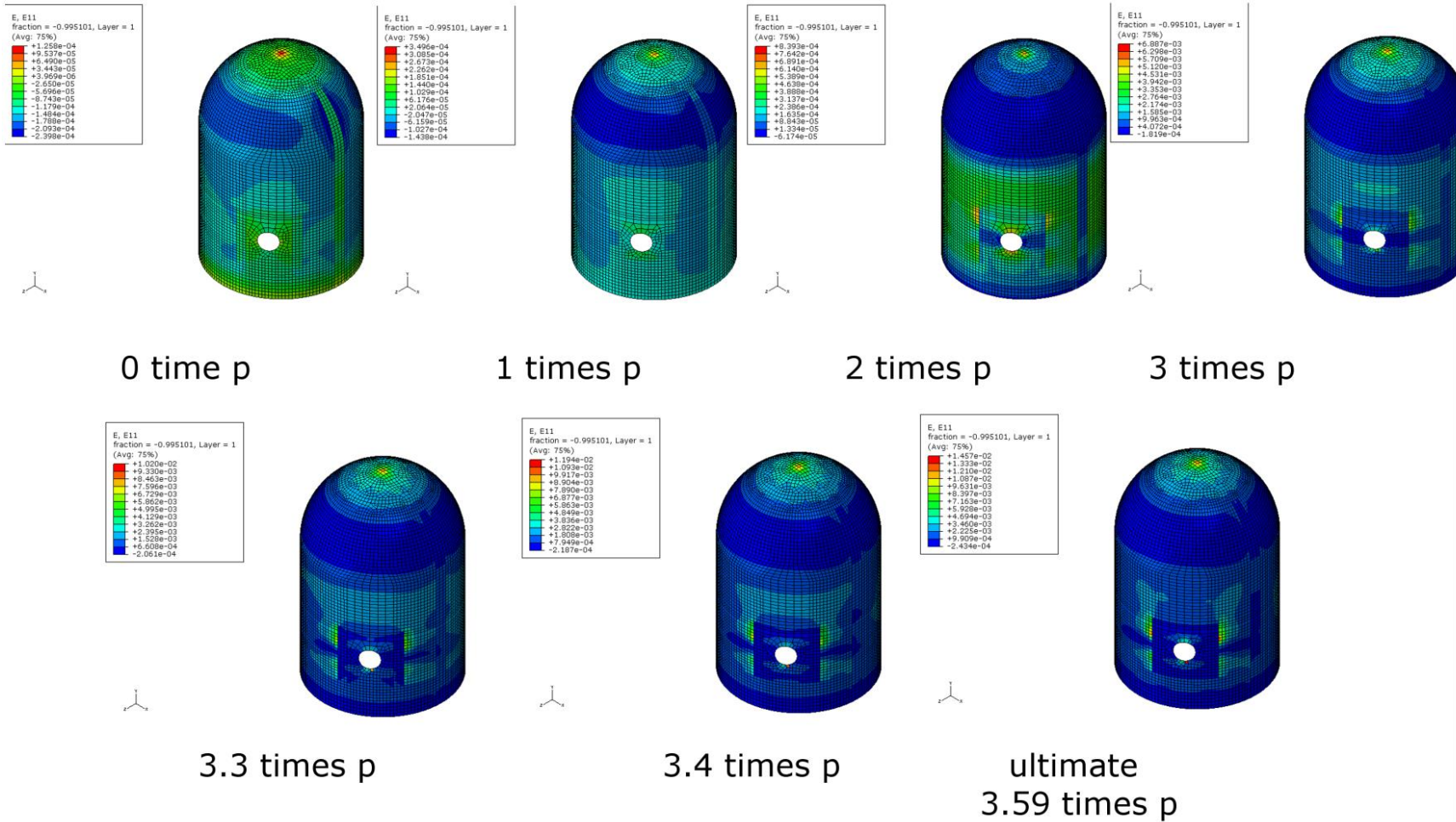


Figure A 3.3: Hoop strain distribution in liner at differnt pressure stages

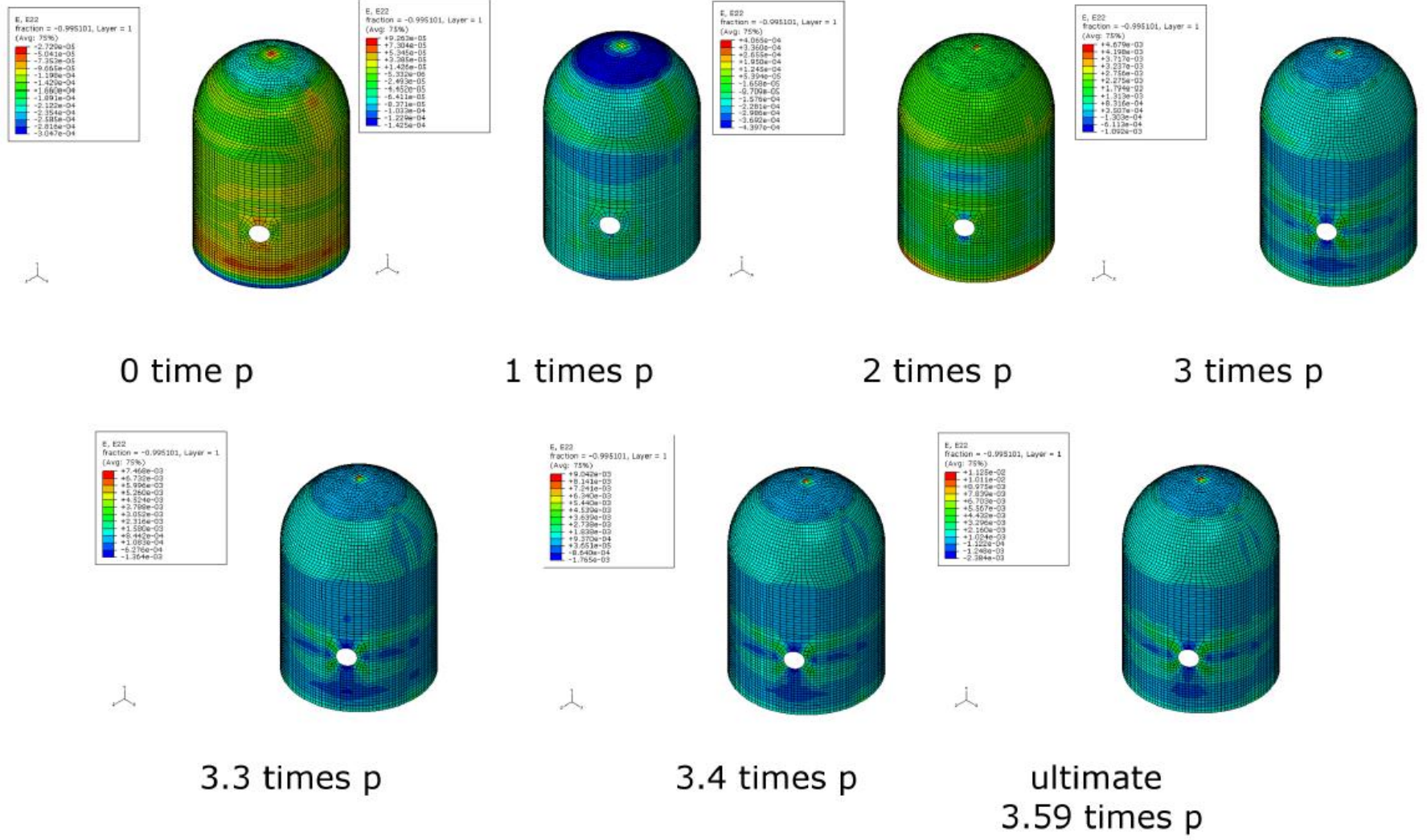


Figure A 3.4: Meridional strain distribution in liner at differnt pressure stages

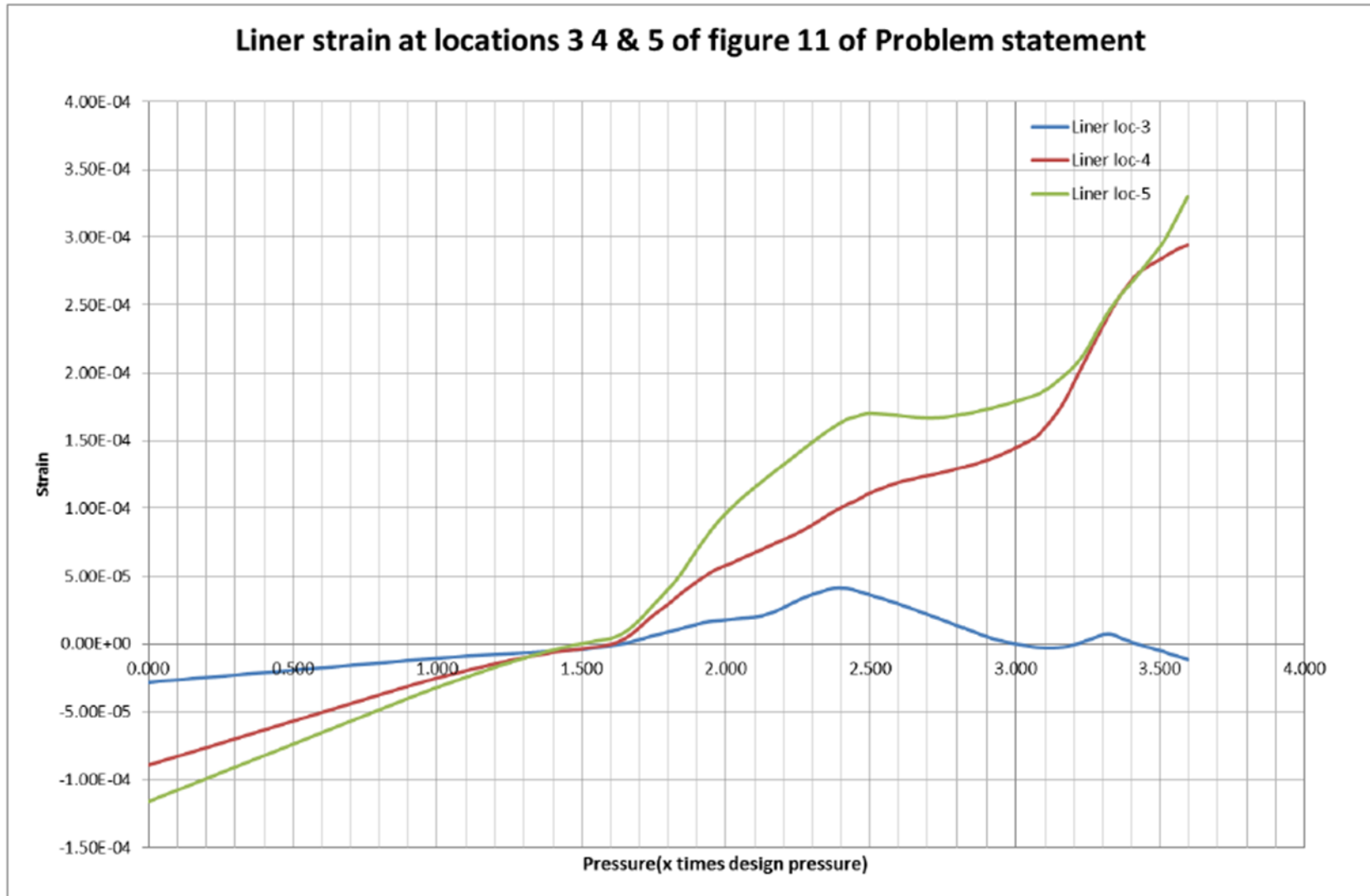


Figure A 3.5: Strain distribution in liner across standardized gauge length as shown in Figure A 11 of problem statement

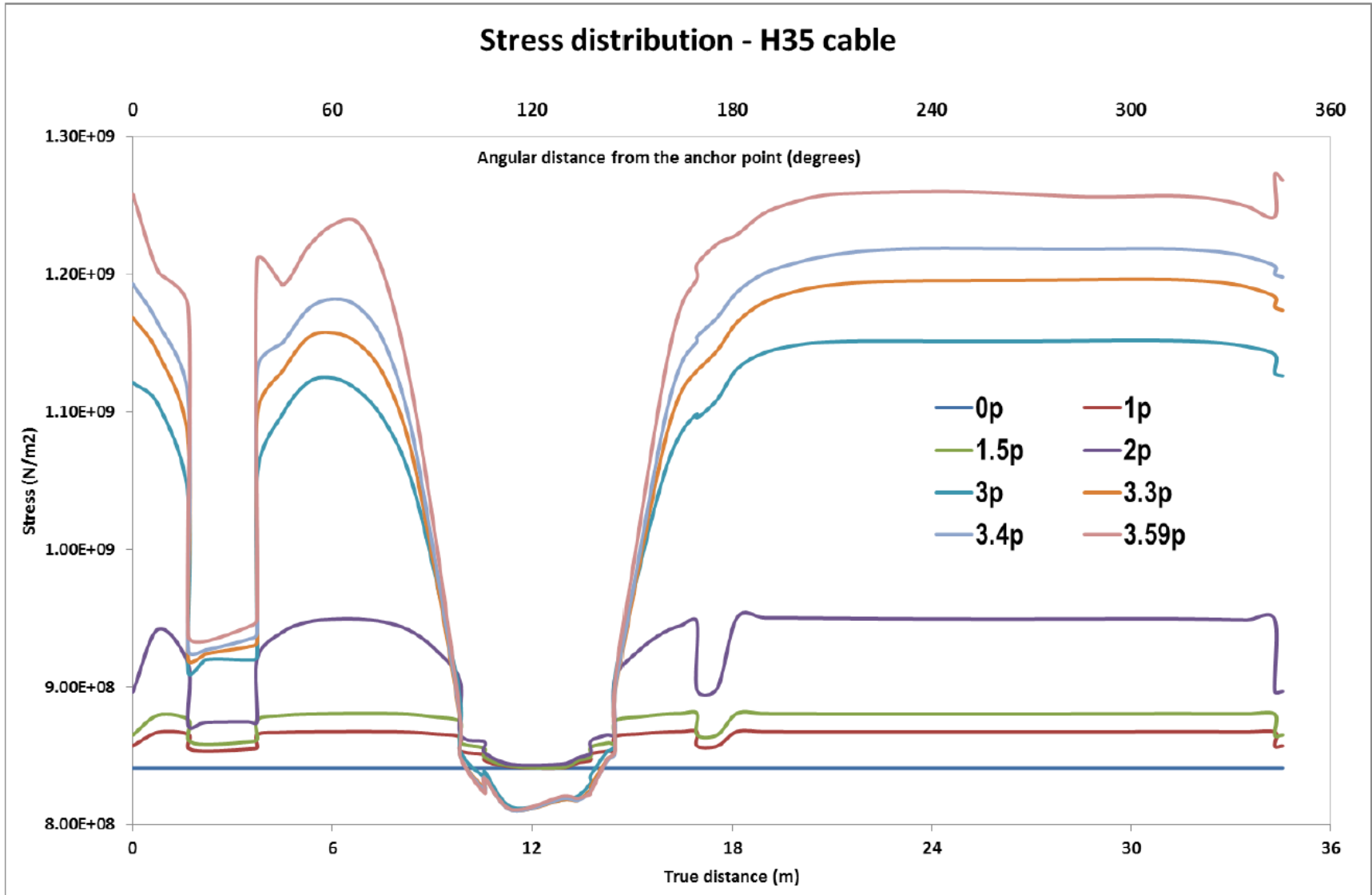


Figure A 3.65: Stress distribution in hoop tendon at elevation of H53 tendon (x axis = length in m)

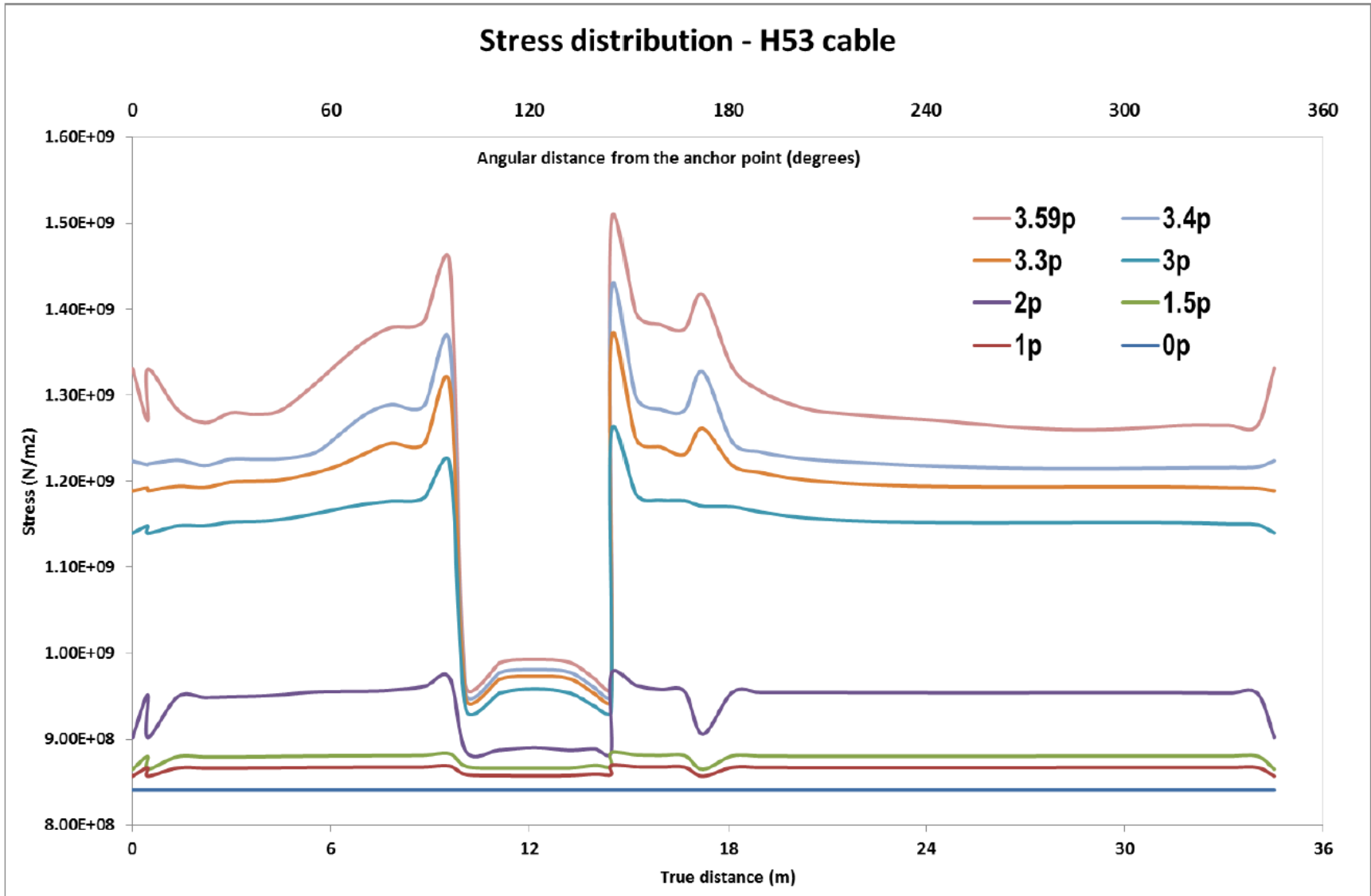


Figure A 3.7: Stress distribution in hoop tendon at elevation of H53 tendon (x axis = length in m)

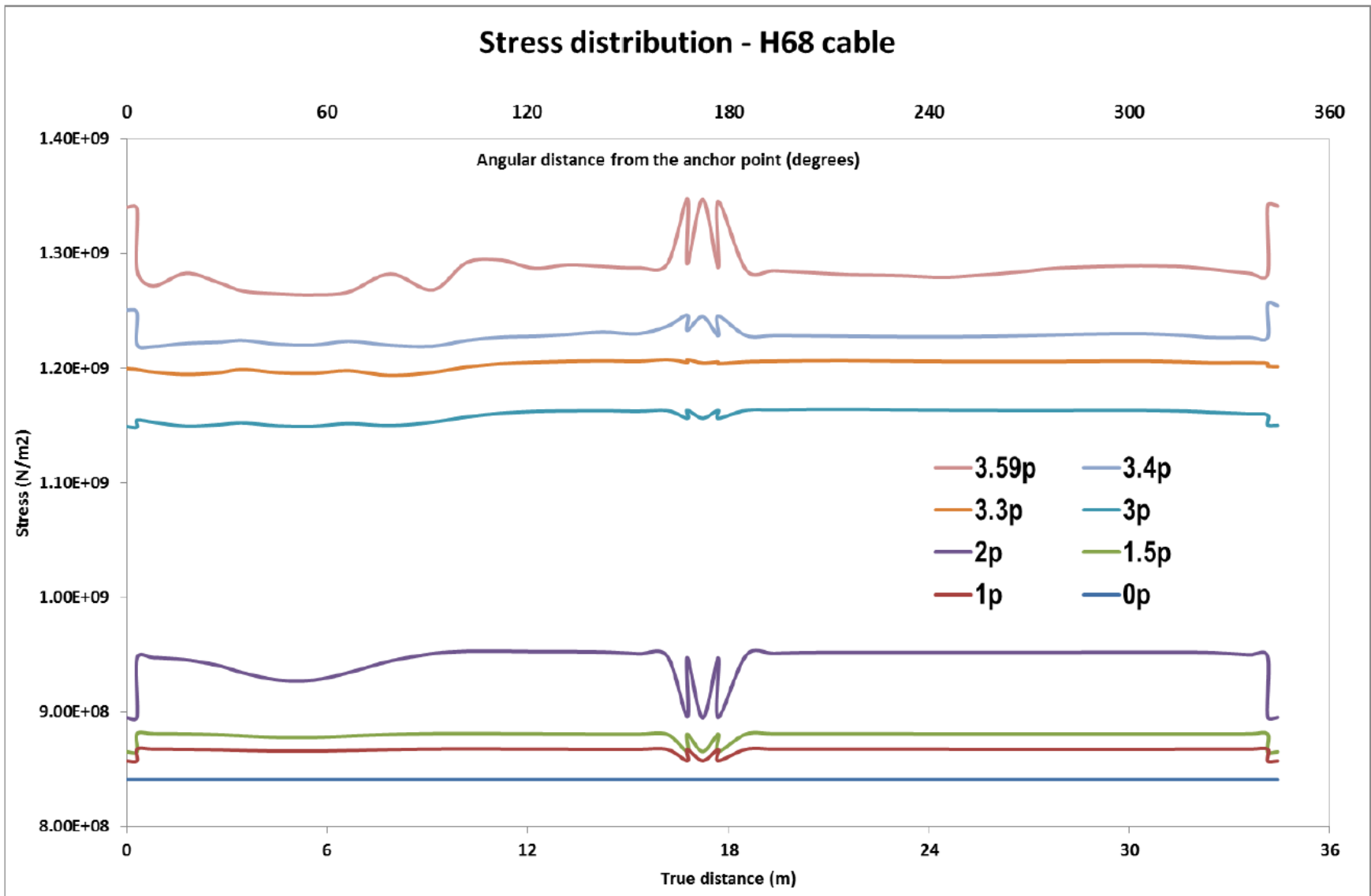


Figure A 3.8: Stress distribution in hoop tendon at elevation of H68 tendon (x axis = length in m)

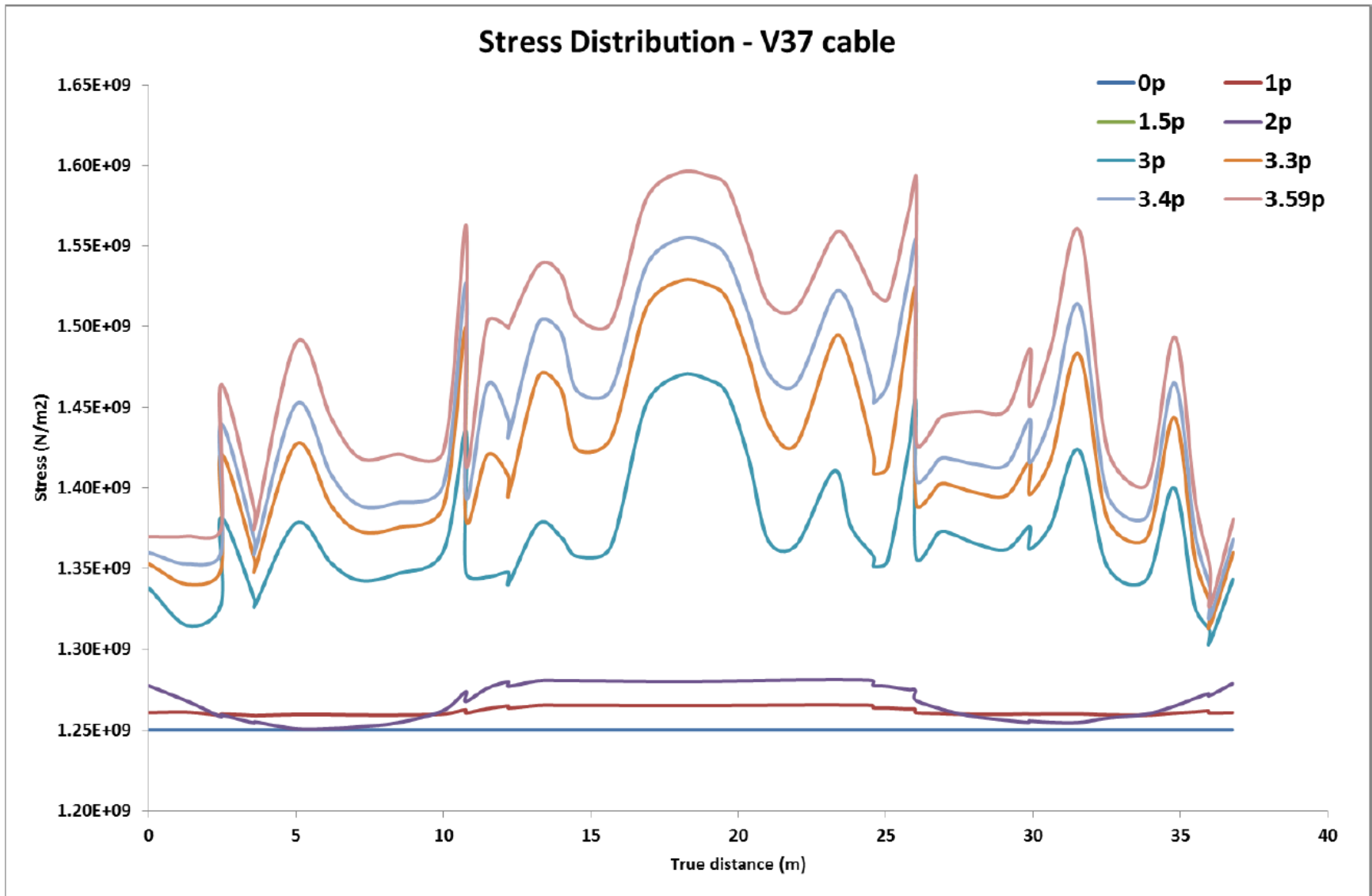


Figure A 3.9: Stress distribution in hoop tension at elevation of V37 tendon (x axis = length in m)

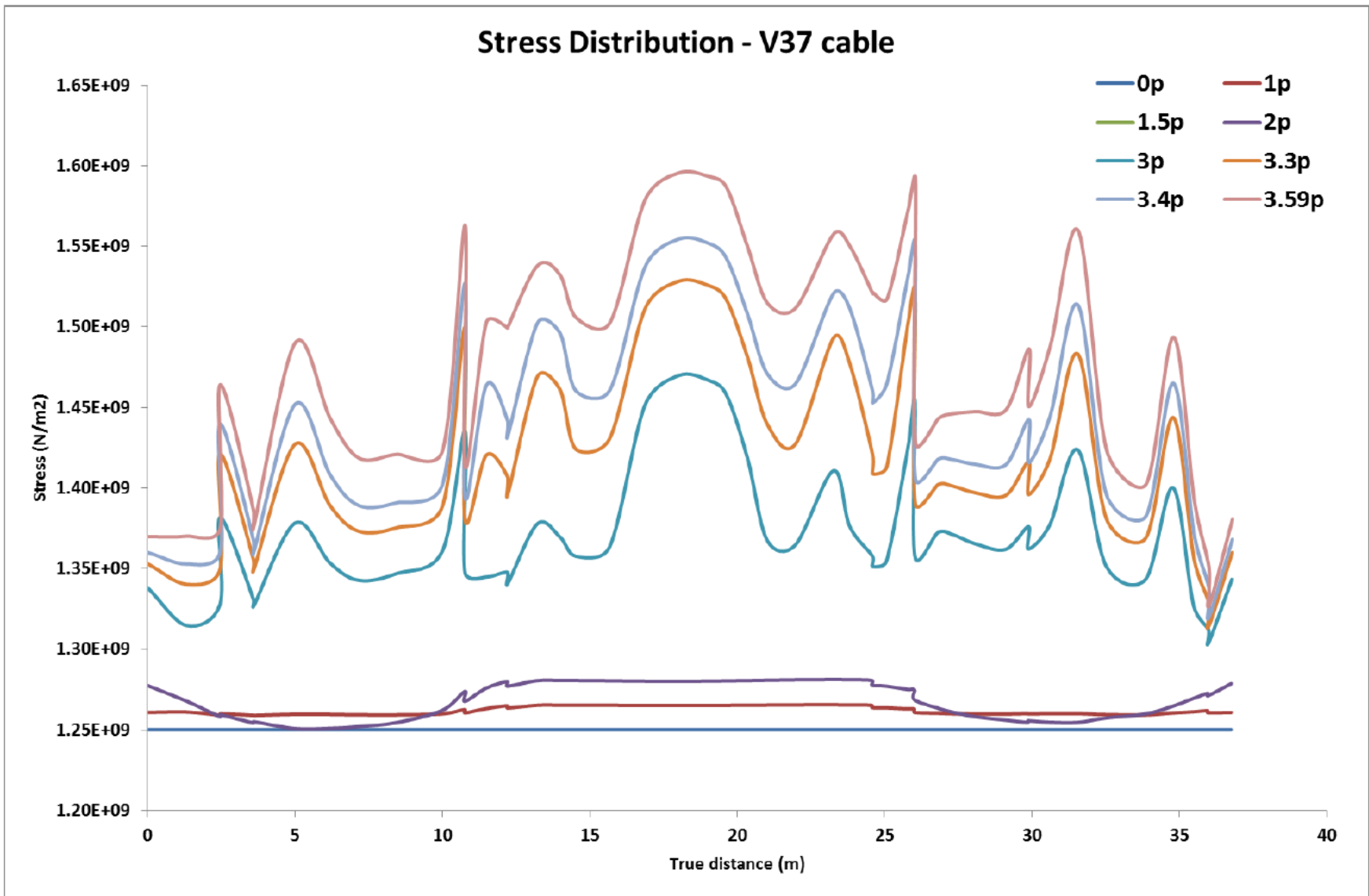


Figure A 3.10: Stress distribution in hoop tendon at elevation of V46 tendon (x axis = length in m)

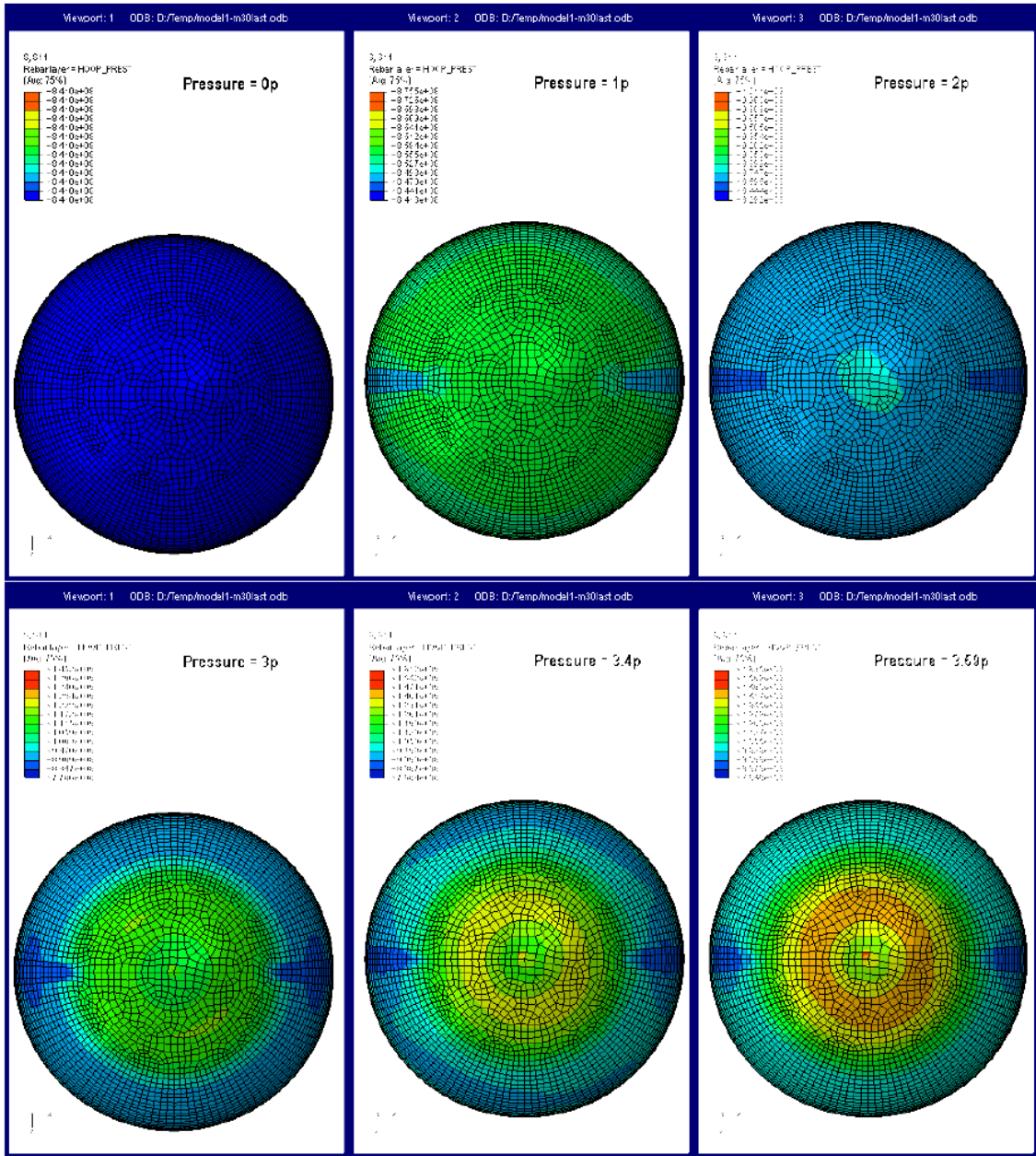


Figure A 3.11: Stress distribution in hoop prestressing tendons – plan

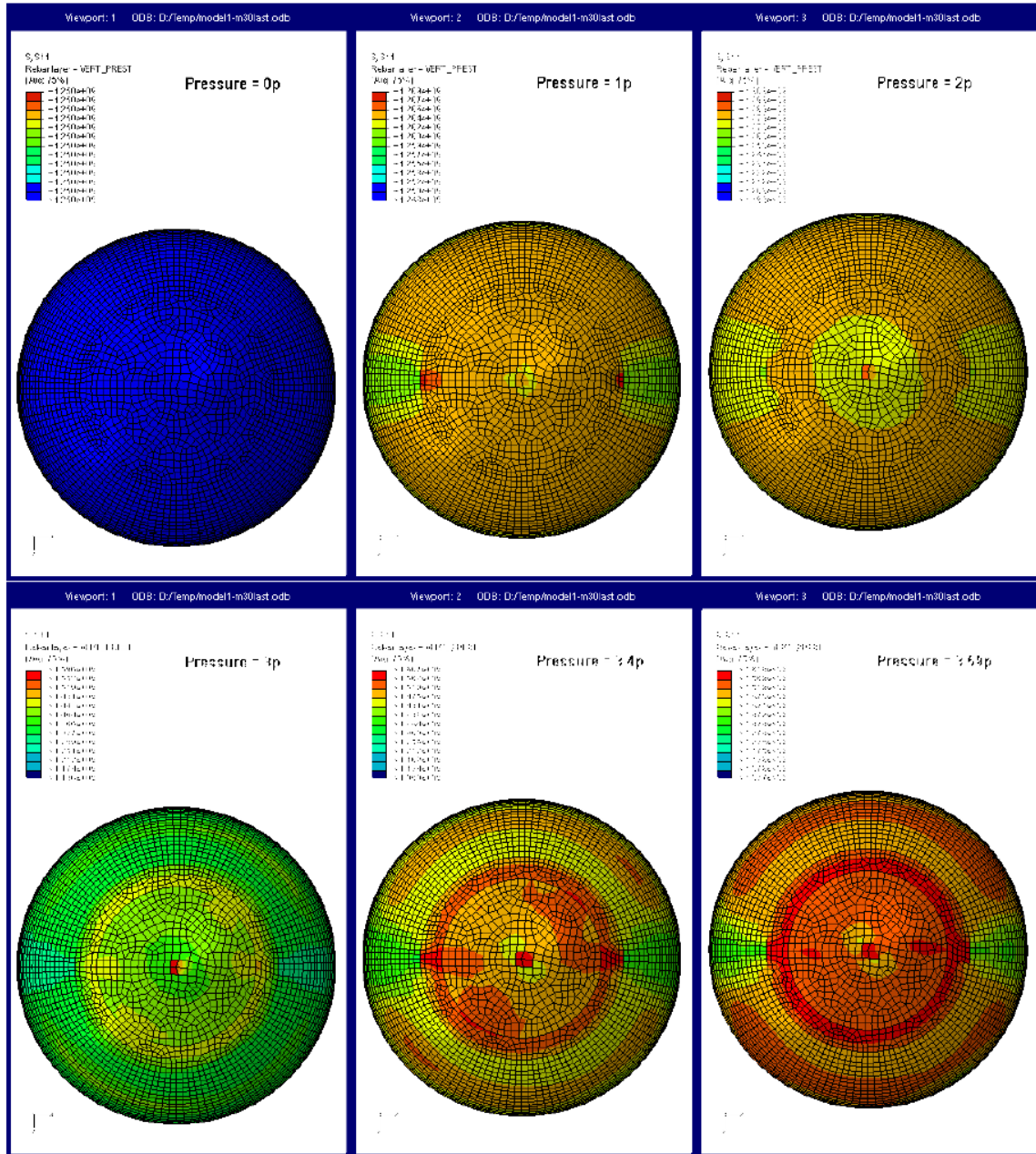


Figure A 3.12: Stress distribution in hairpin prestressing tendons – plan

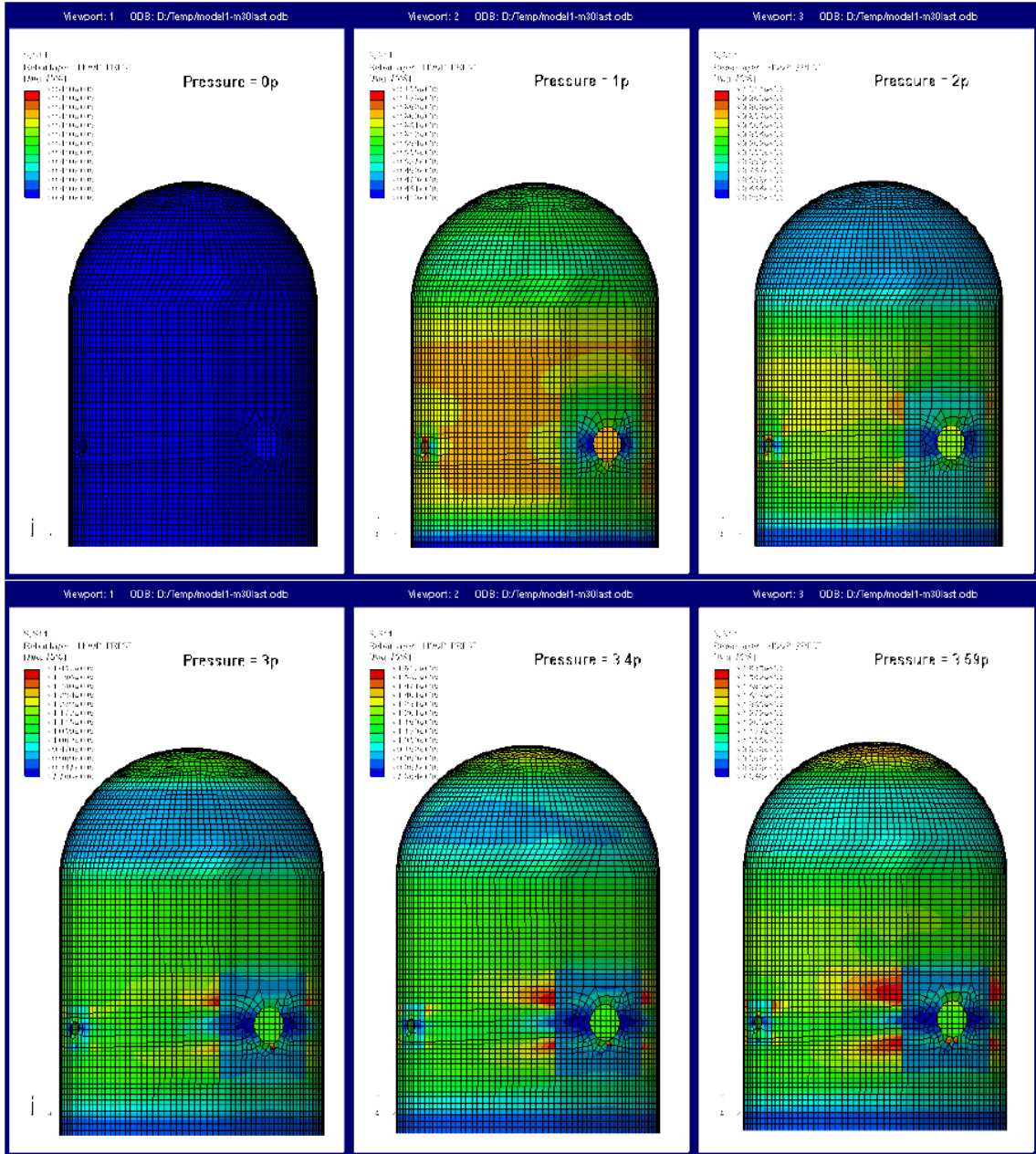


Figure A 3.13: Stress distribution in hoop prestressing tendons - elevation (major opening side)

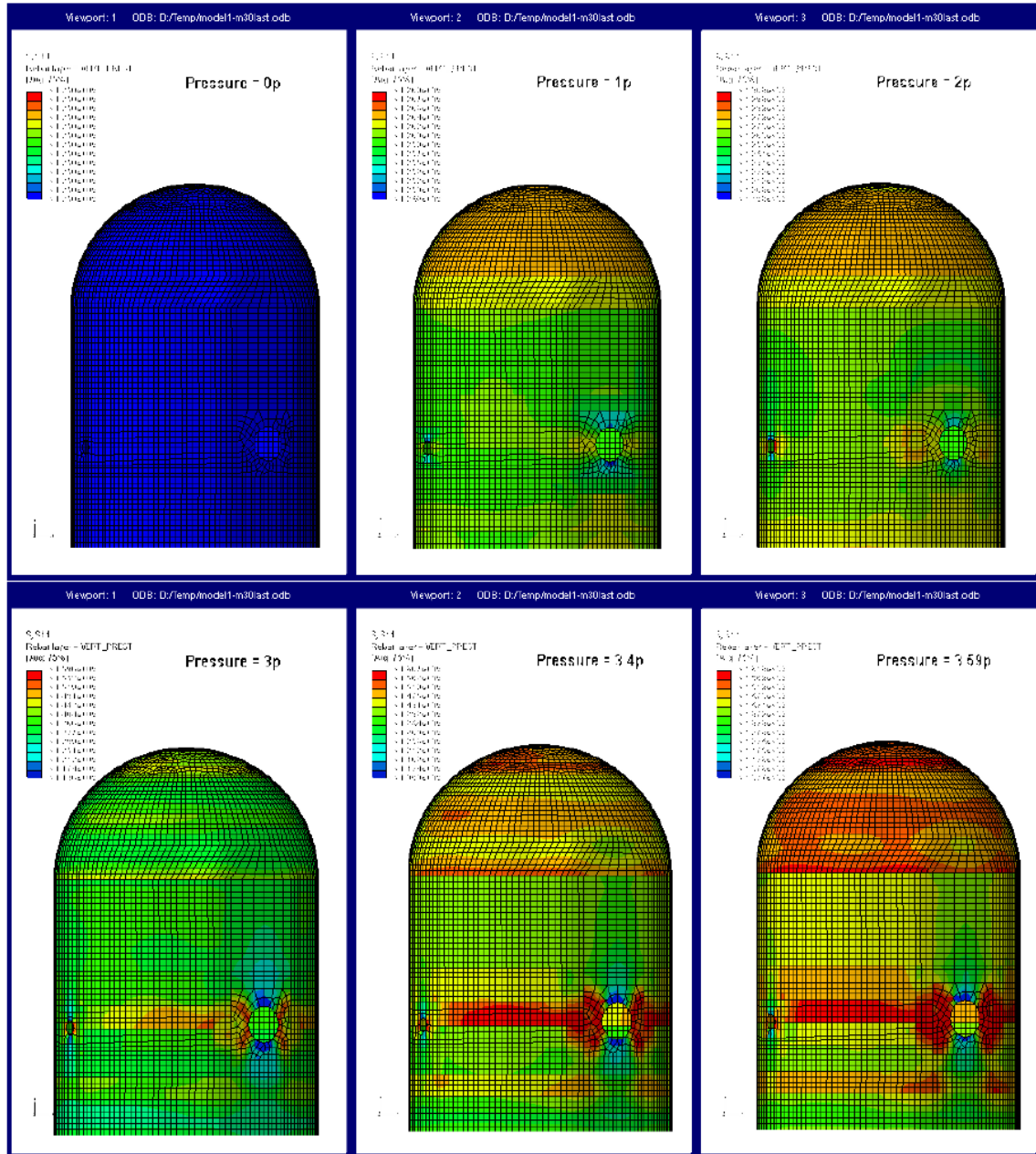


Figure A 3.14: Stress distribution in hairpin prestressing tendons - elevation (major opening side)

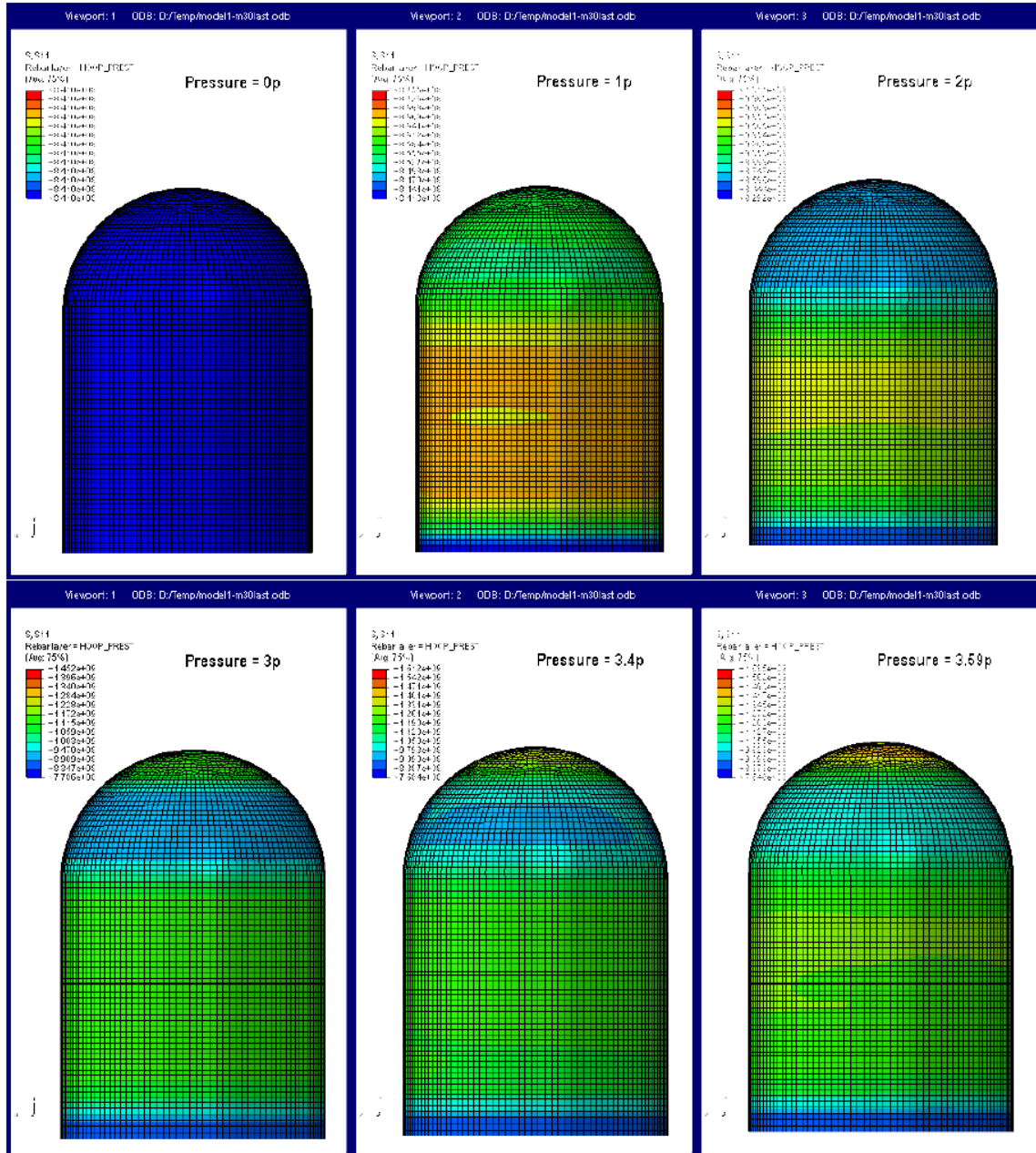


Figure A 3.15: Stress distribution in hoop prestressing tendons - elevation (other side)

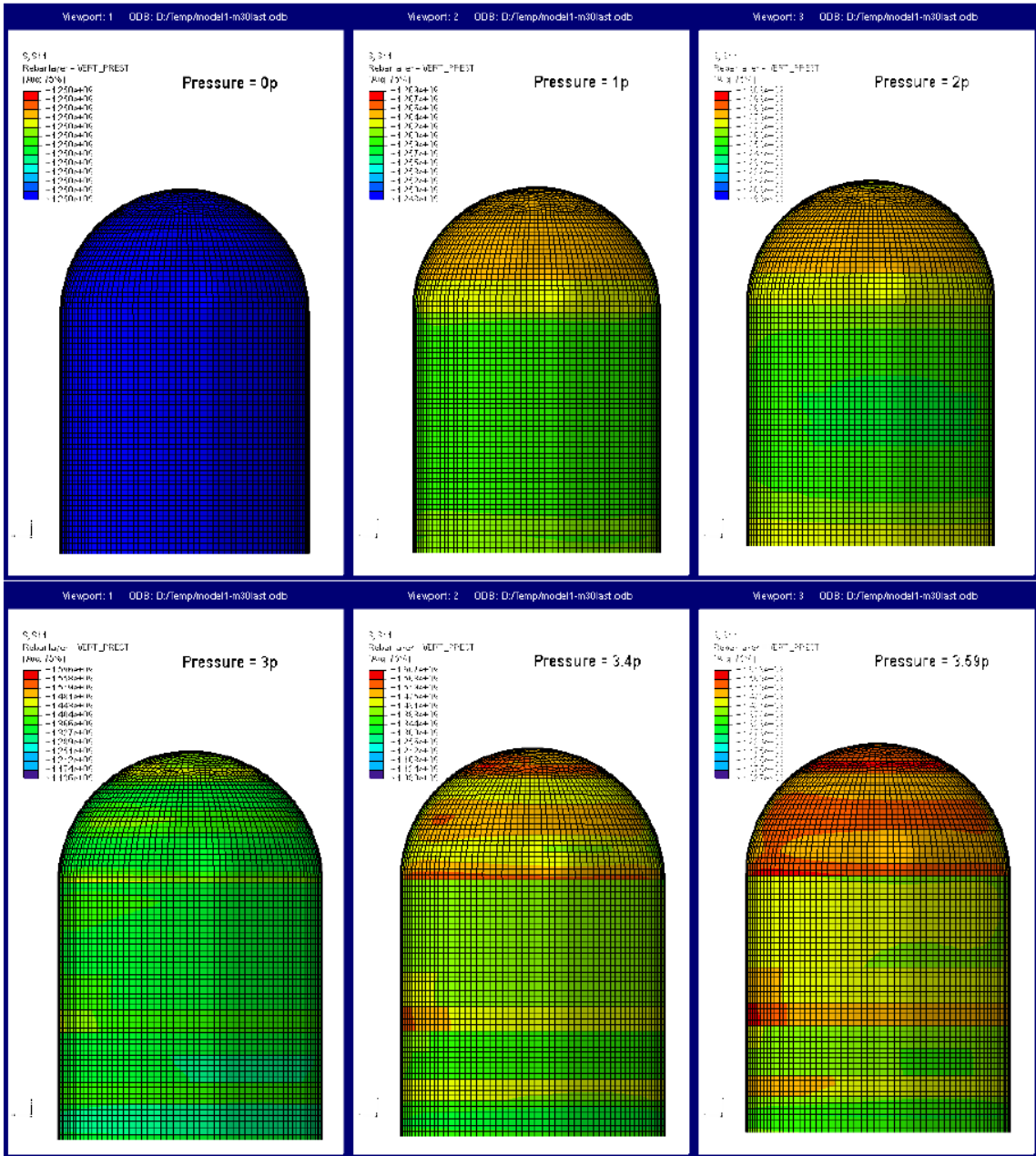


Figure A 3.16: Stress distribution in hairpin prestressing tendons - elevation (other side)

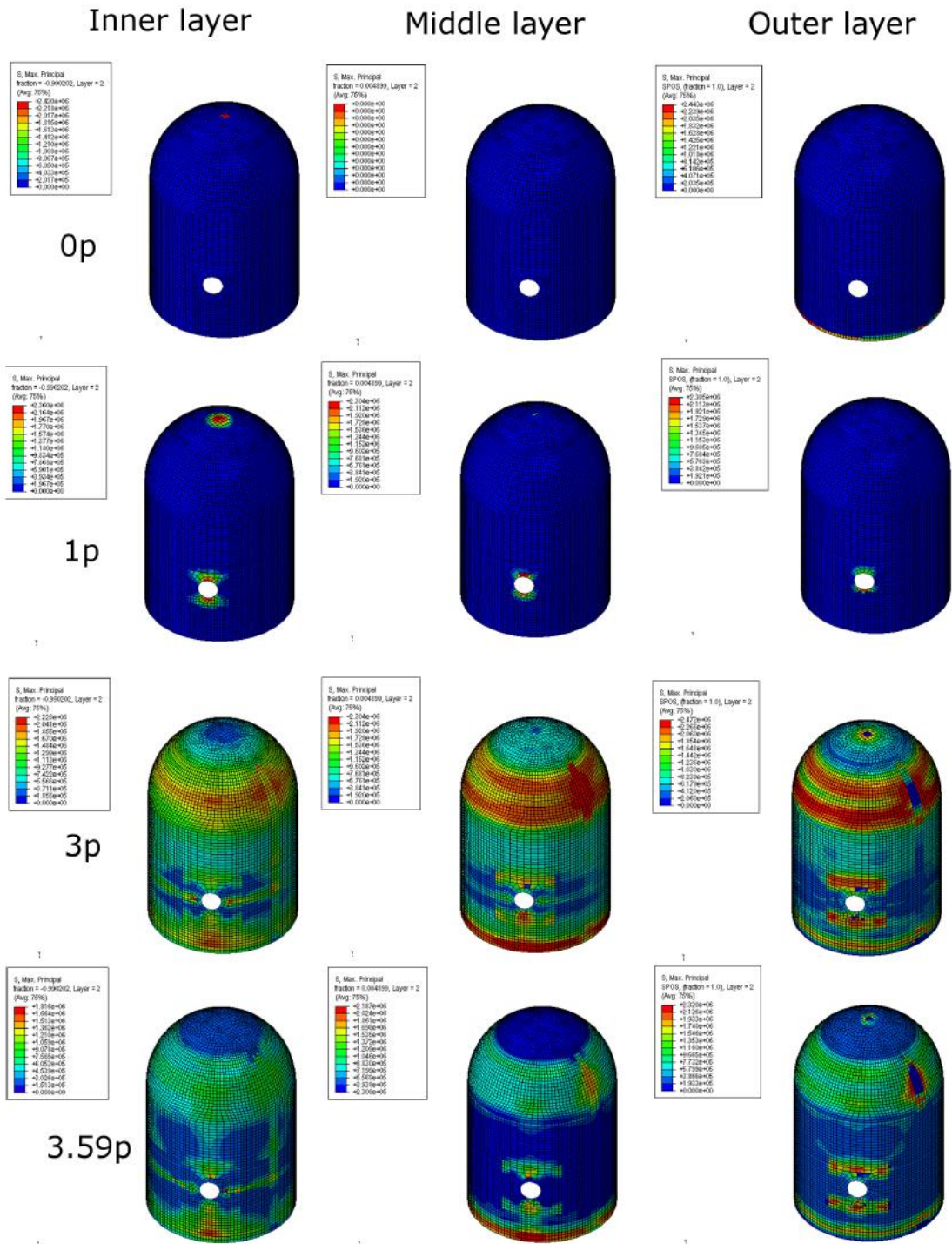


Figure A 3.17: Maximum principal stress distribution in concrete layers

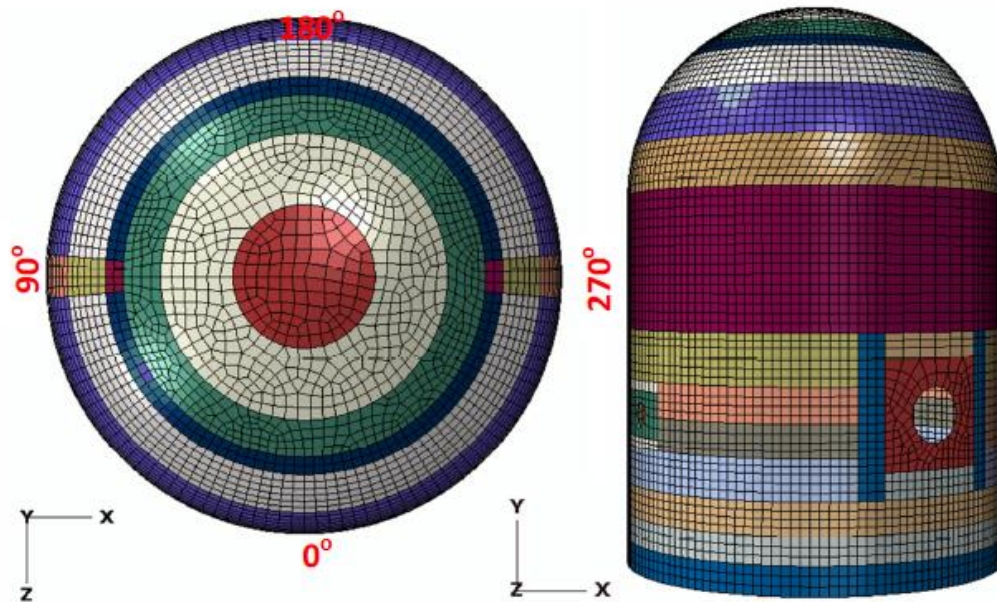


Figure A 3.18: Model of containment vessel indicating the coordinate directions

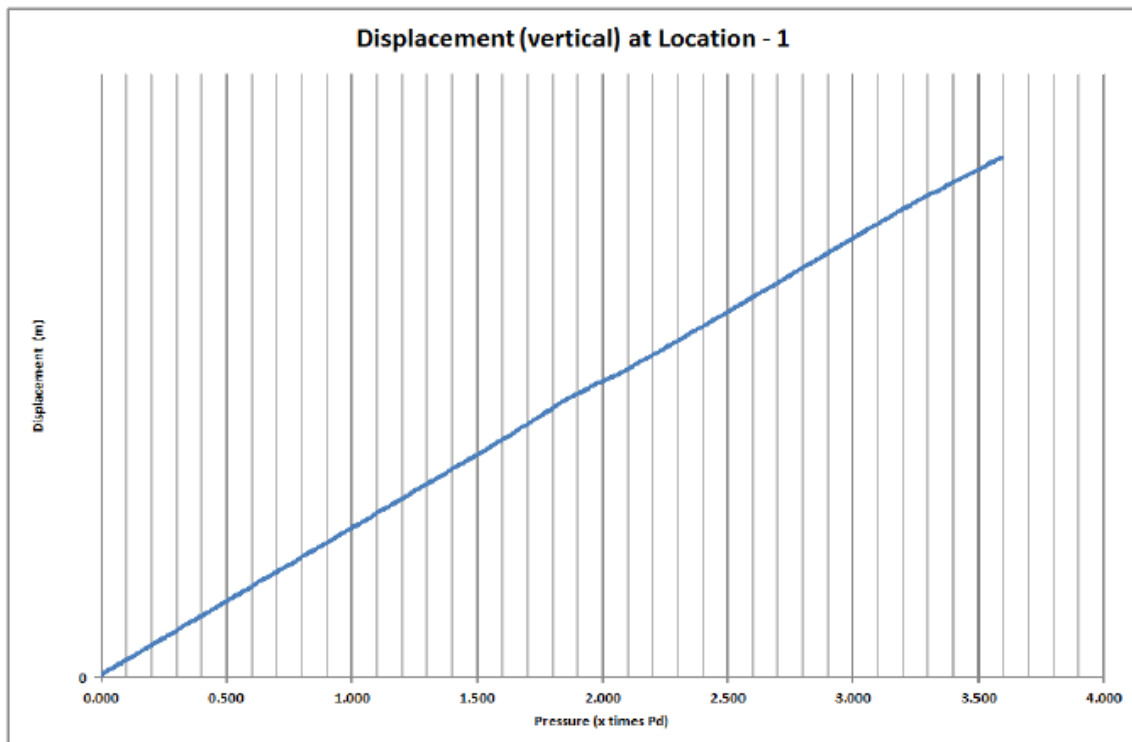


Figure A 3.19: Response at Location - 1

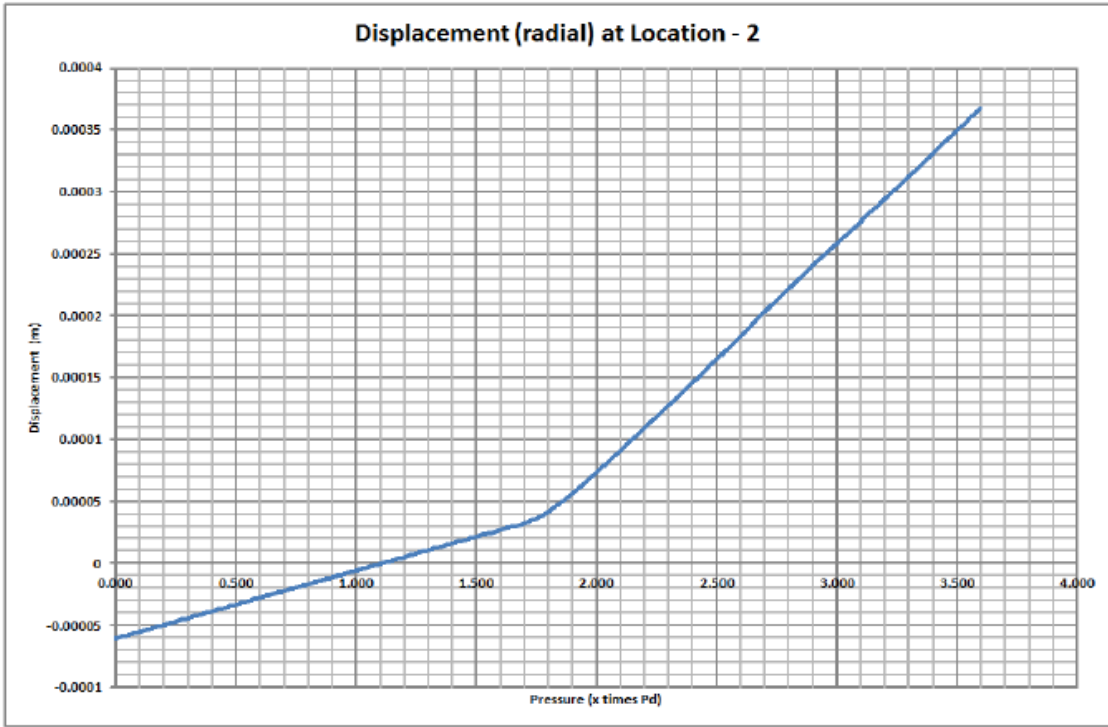


Figure A 3.20: Response at Location – 2

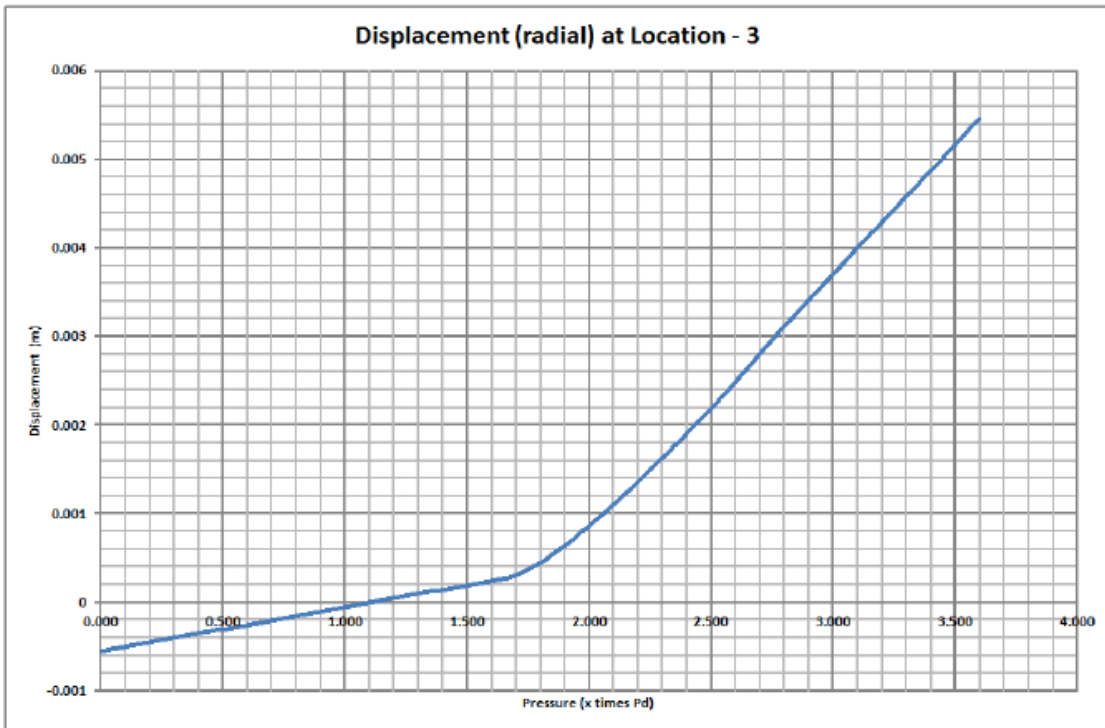


Figure A 3.21: Response at Location – 3

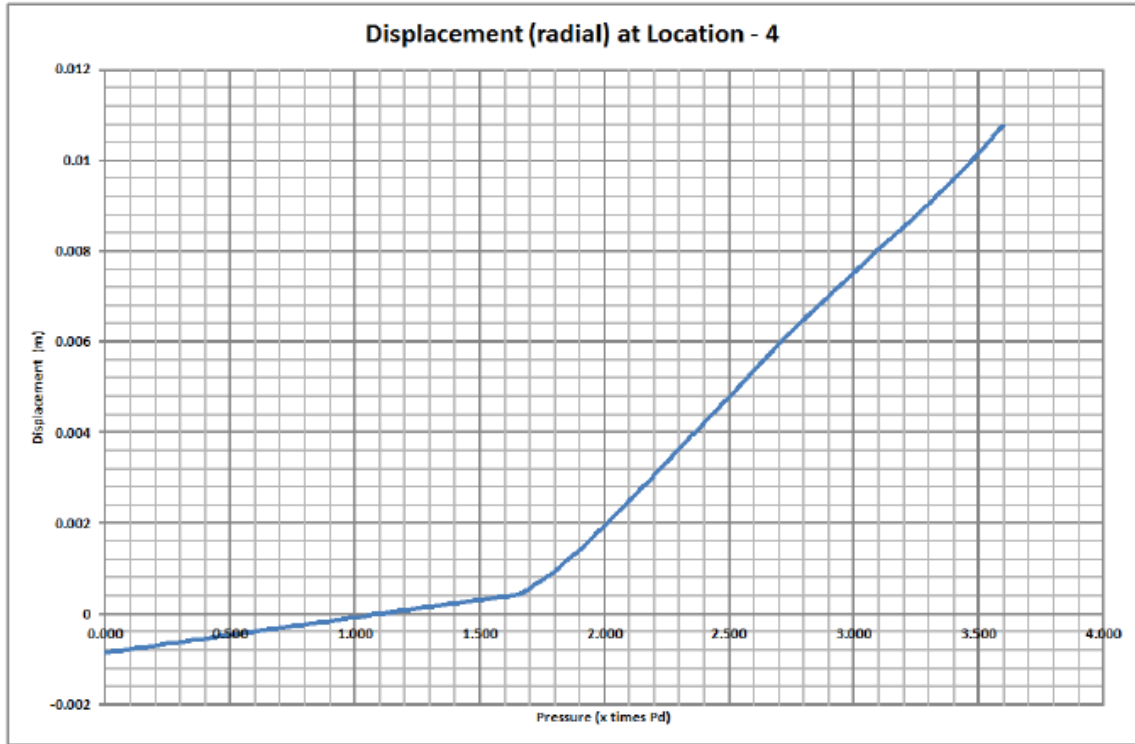


Figure A 3.22: Response at Location – 4

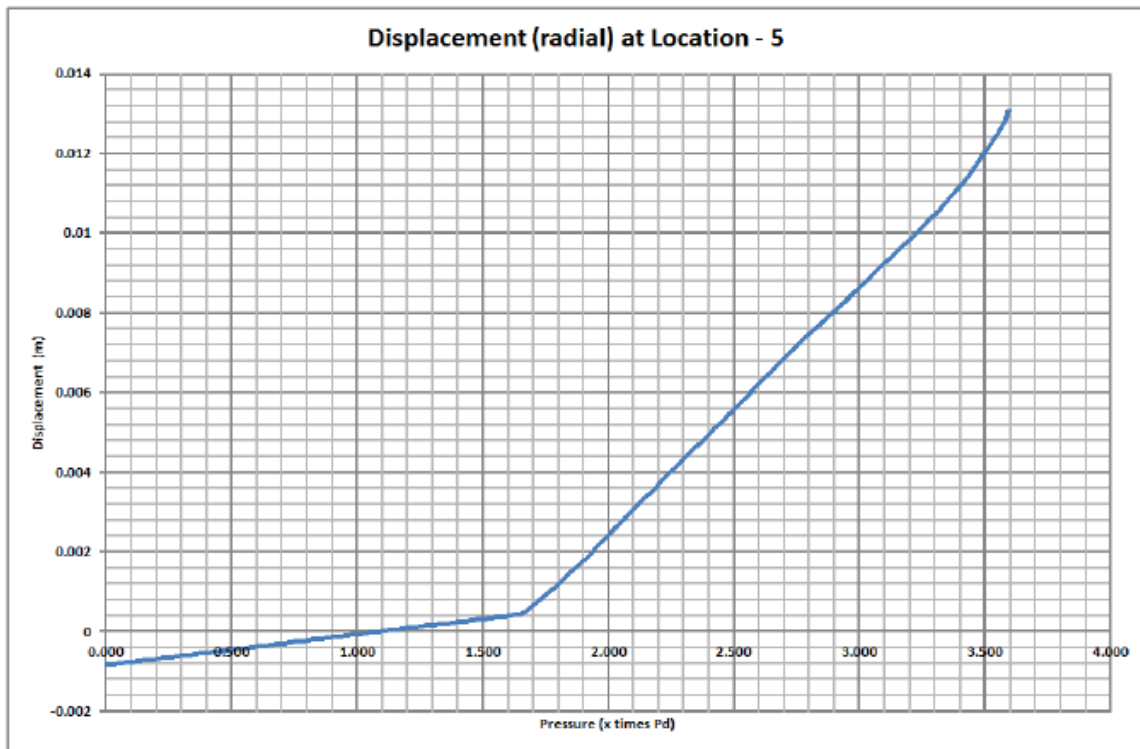


Figure A 3.23: Response at Location – 5

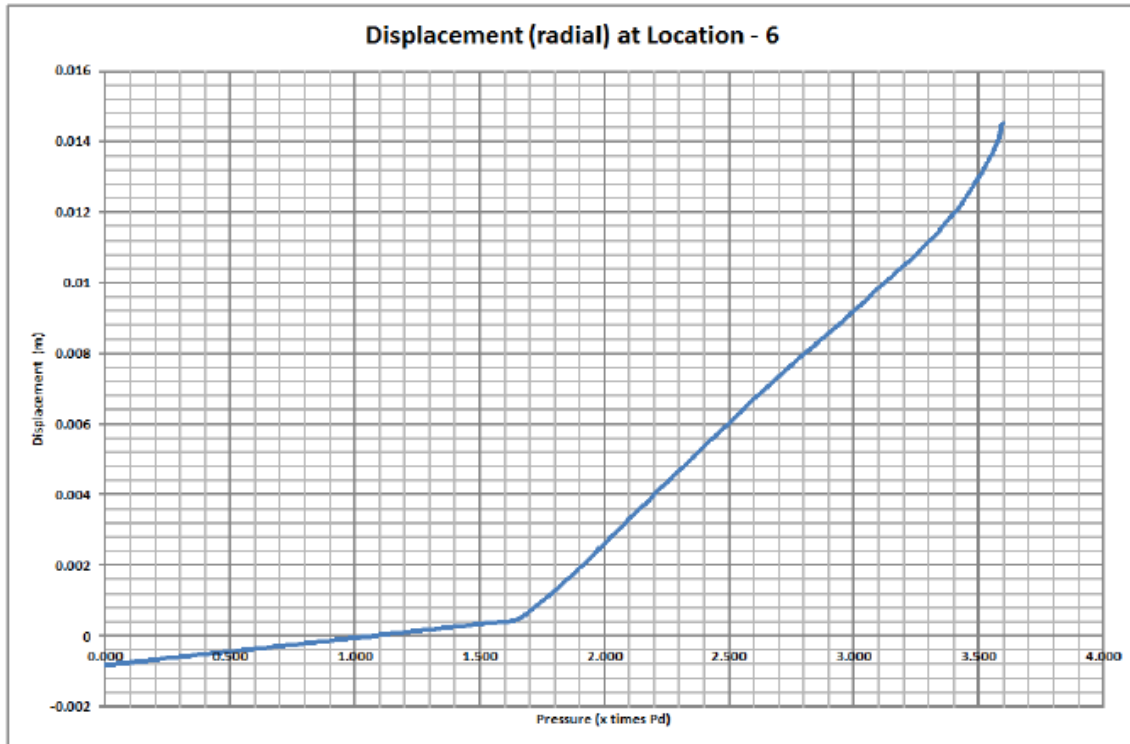


Figure A 3.24: Response at Location – 6

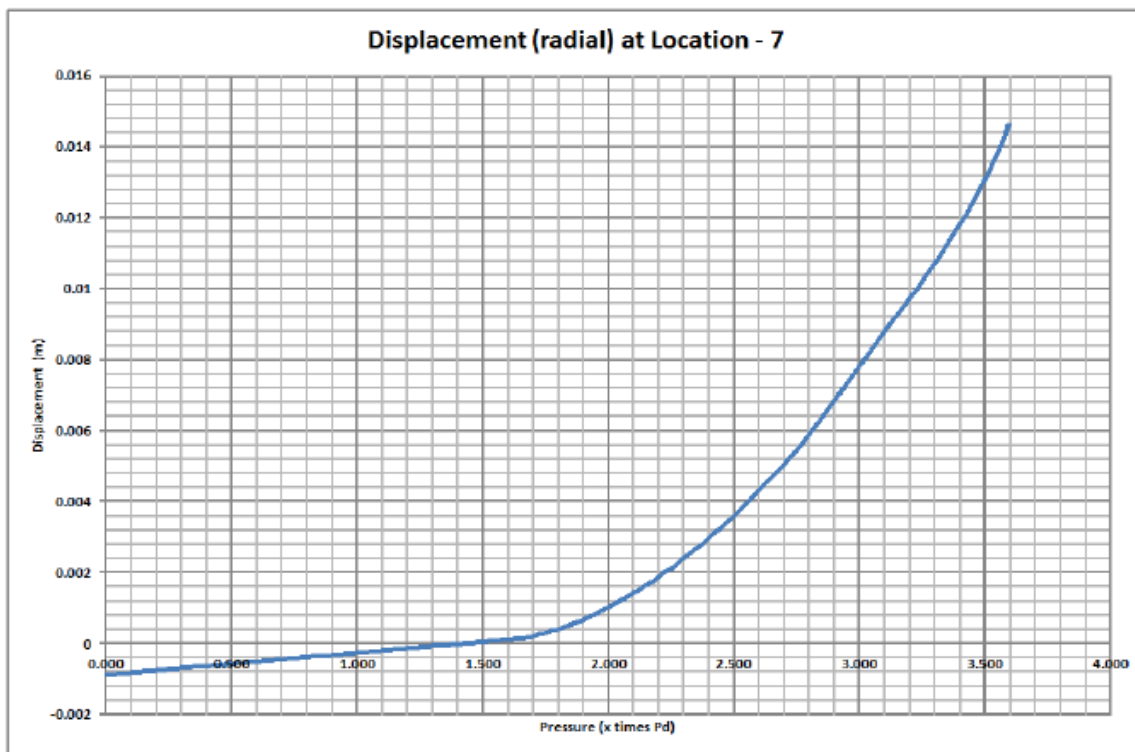


Figure A 3.25: Response at Location – 7

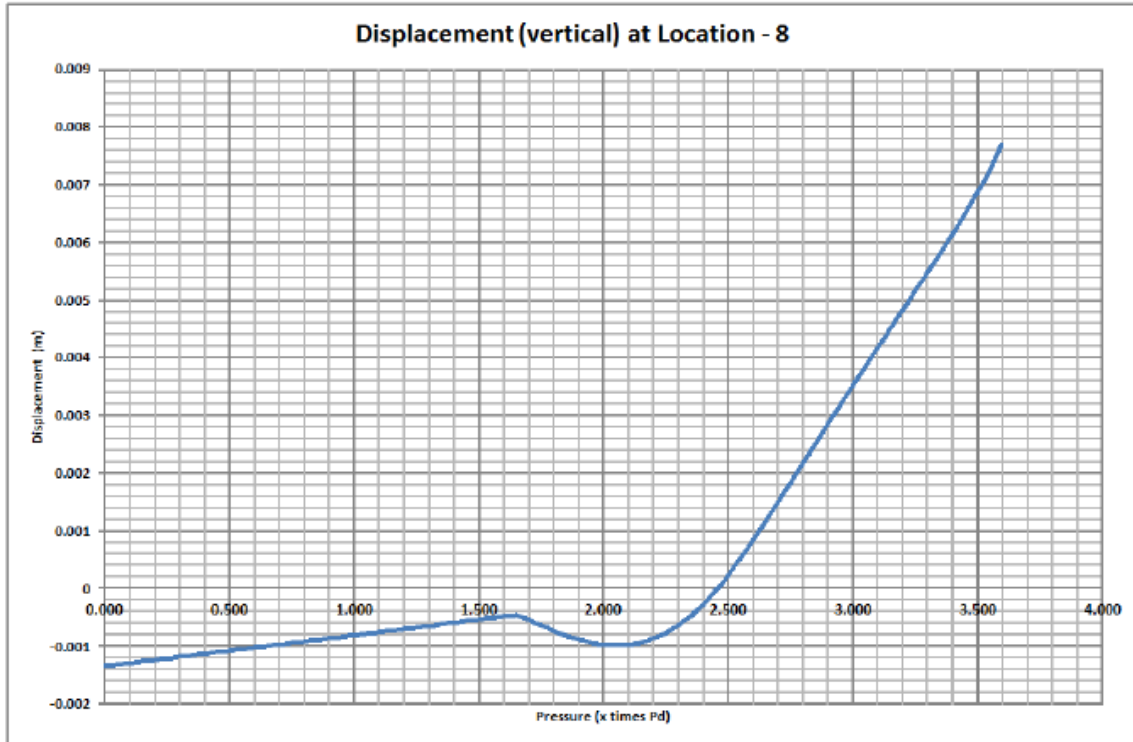


Figure A 3.26: Response at Location – 8

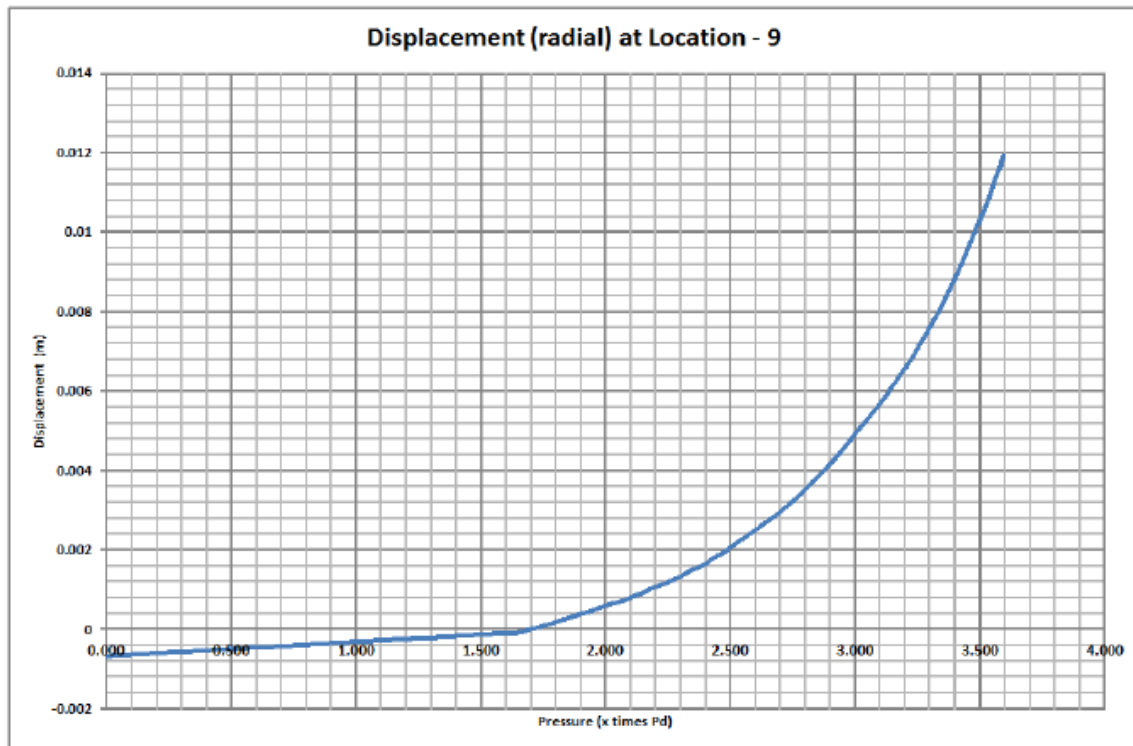


Figure A 3.27: Response at Location – 9

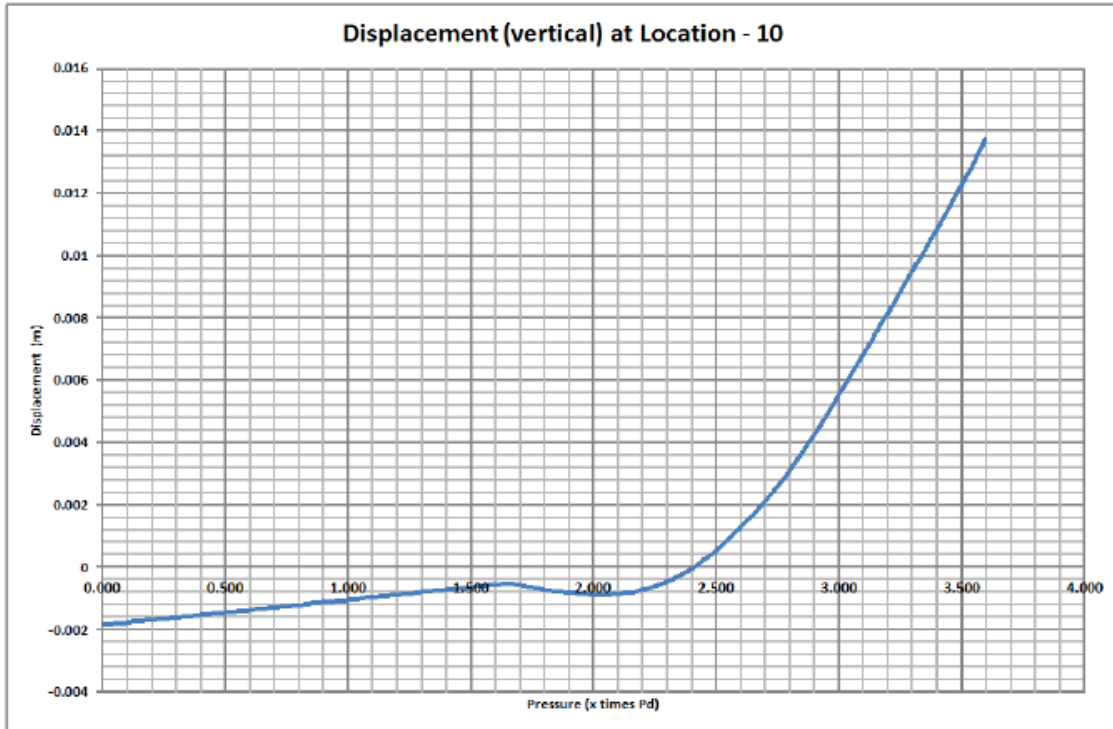


Figure A 3.28: Response at Location – 10

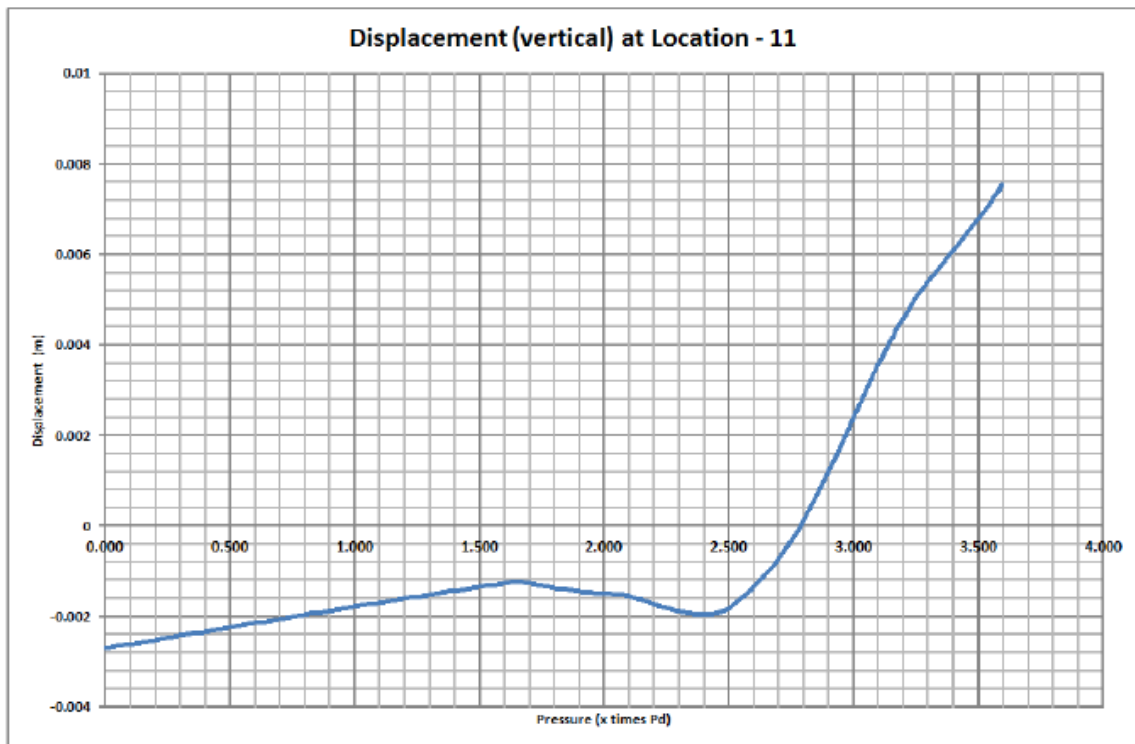


Figure A 3.29: Response at Location – 11

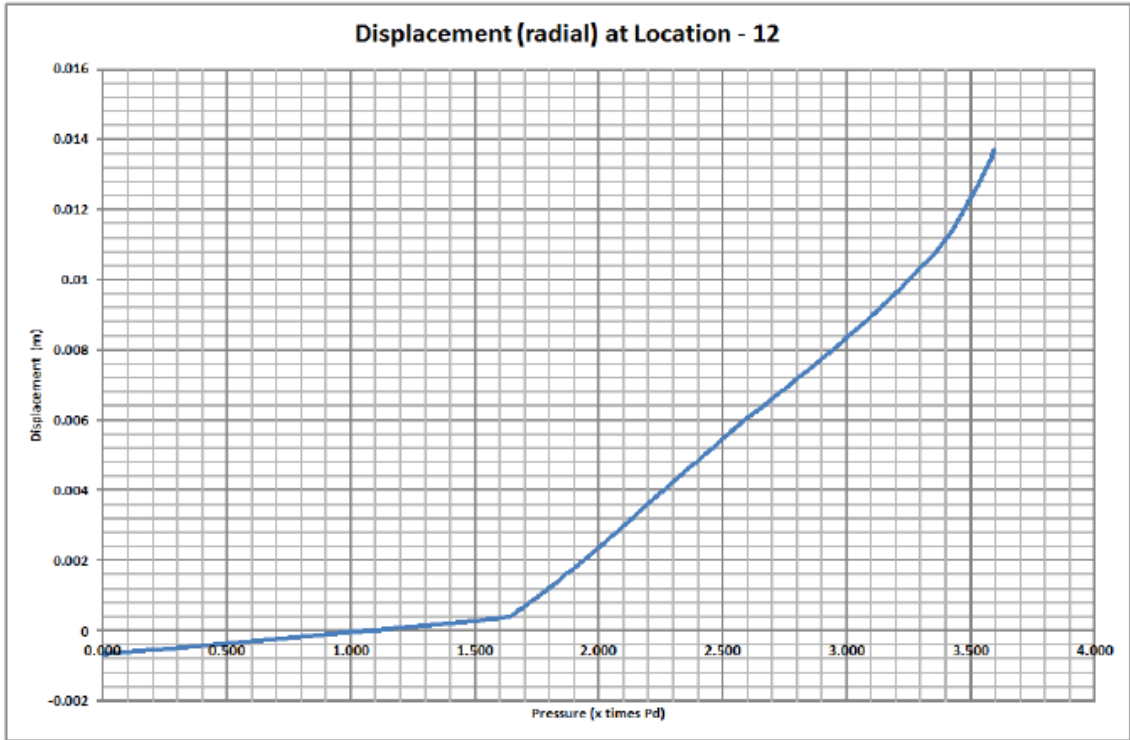


Figure A 3.30: Response at Location – 12

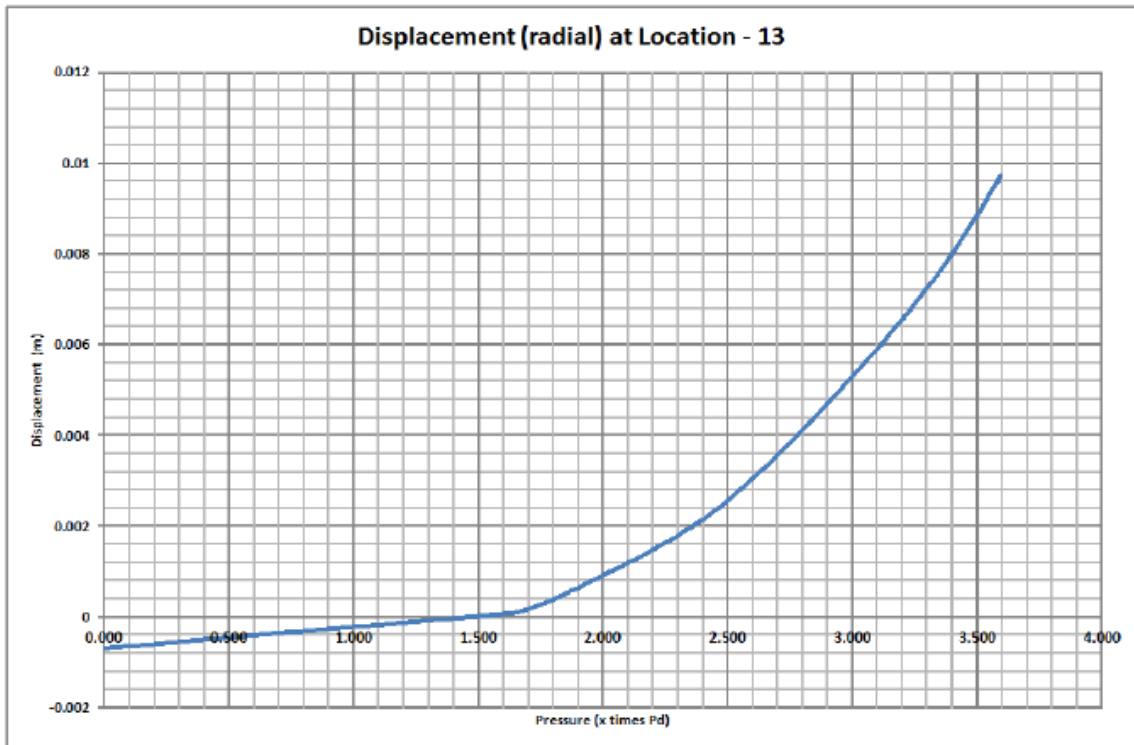


Figure A 3.31: Response at Location – 13

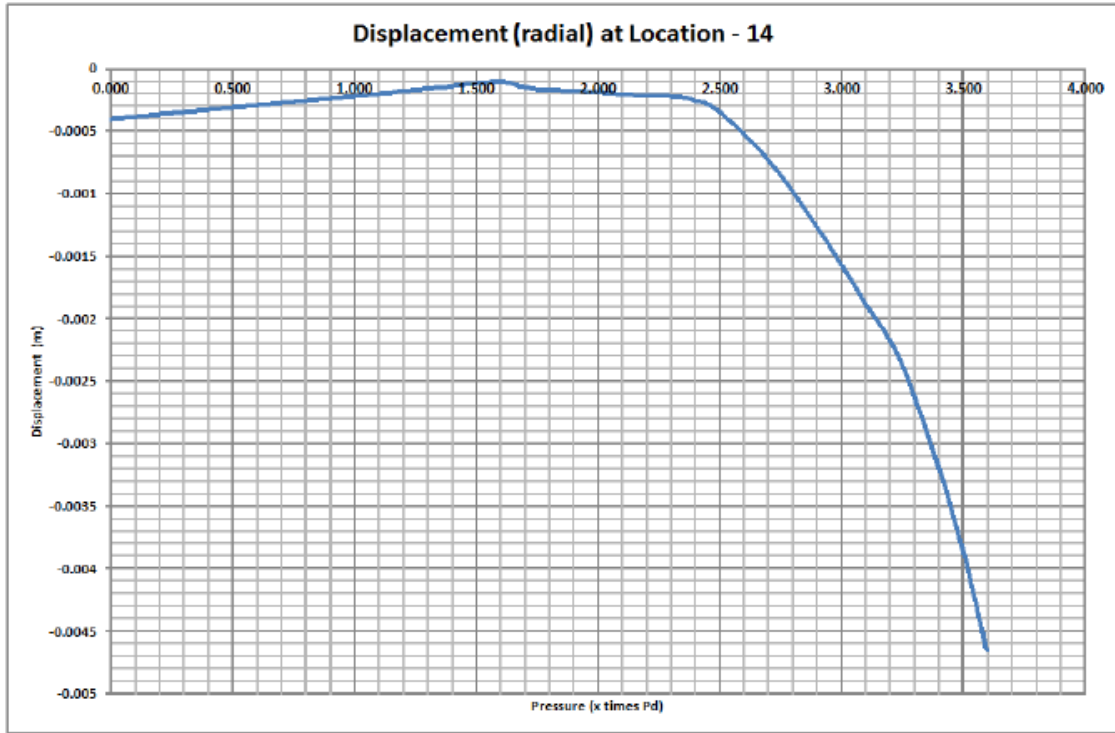


Figure A 3.32: Response at Location – 14

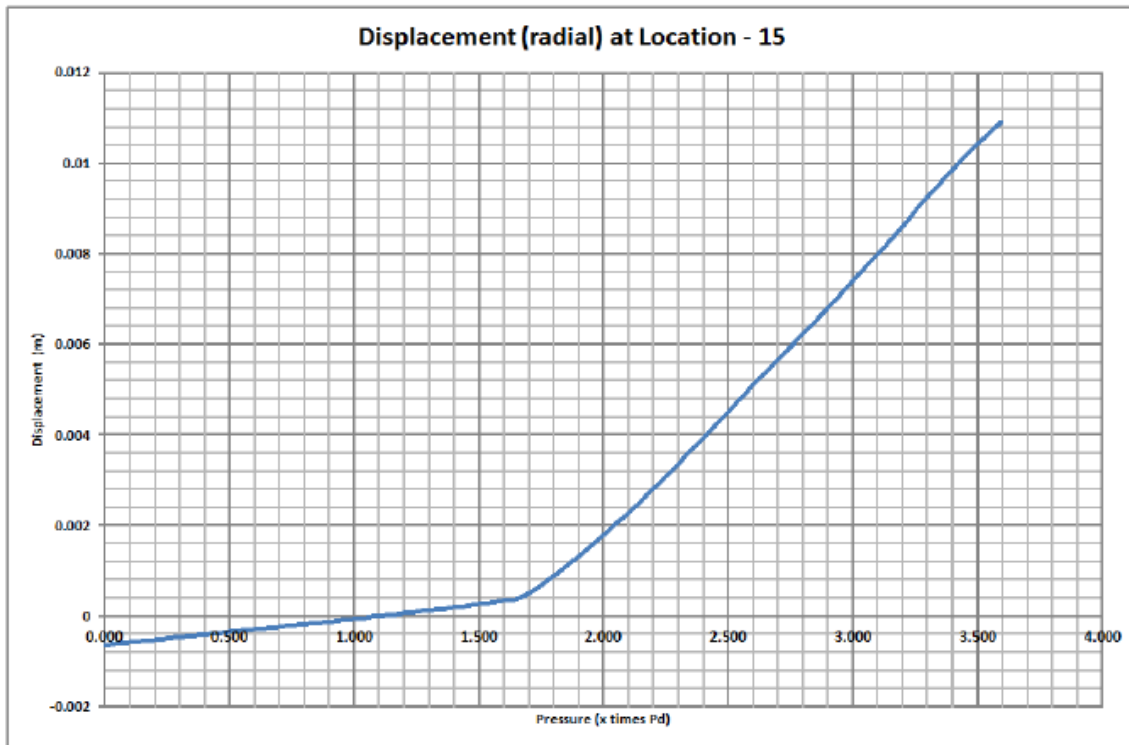


Figure A 3.33: Response at Location – 15

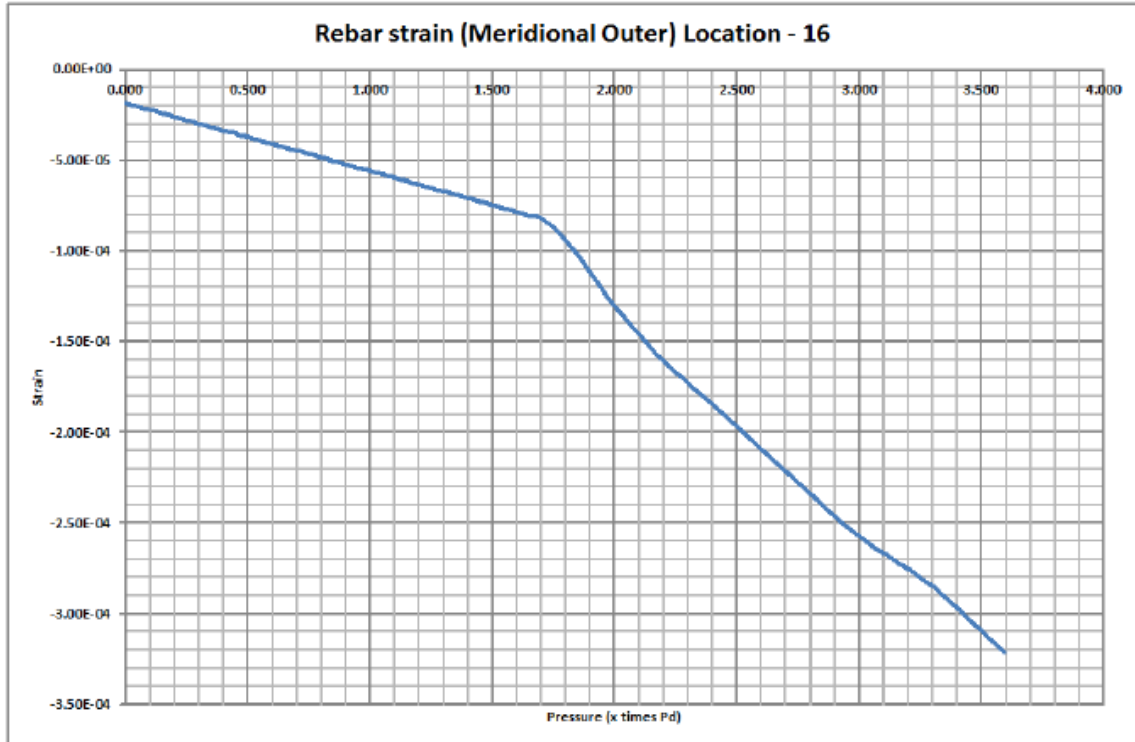


Figure A 3.34: Response at Location – 16

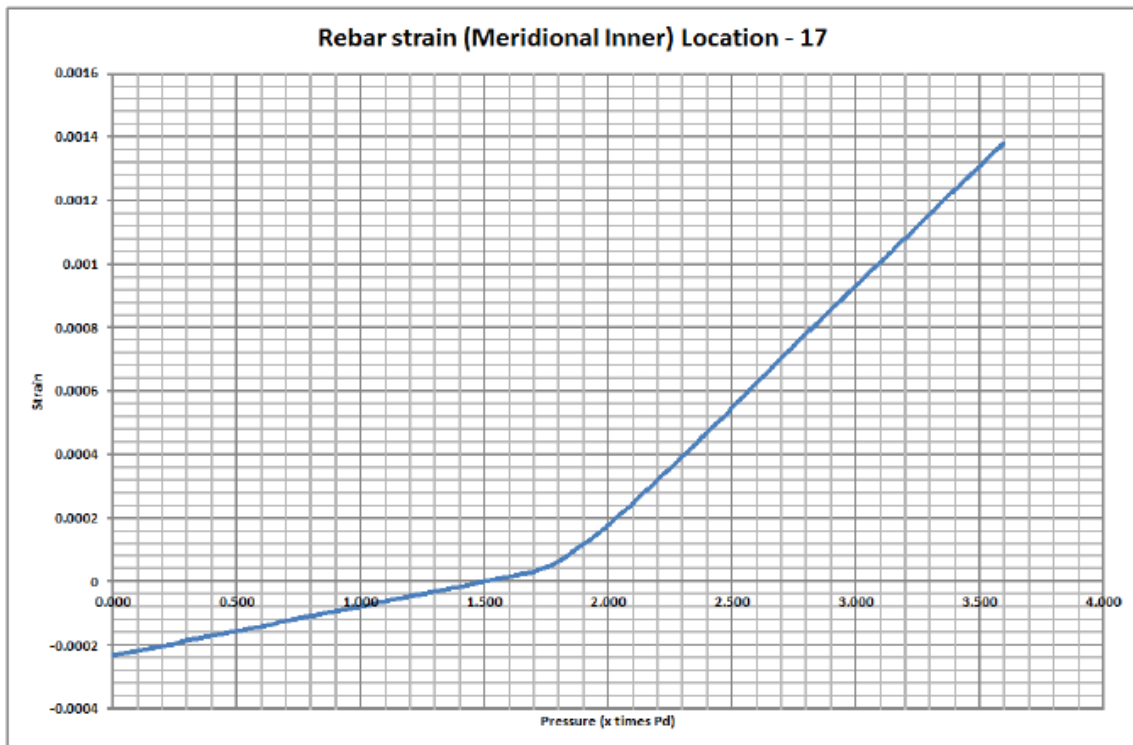


Figure A 3.35: Response at Location – 17

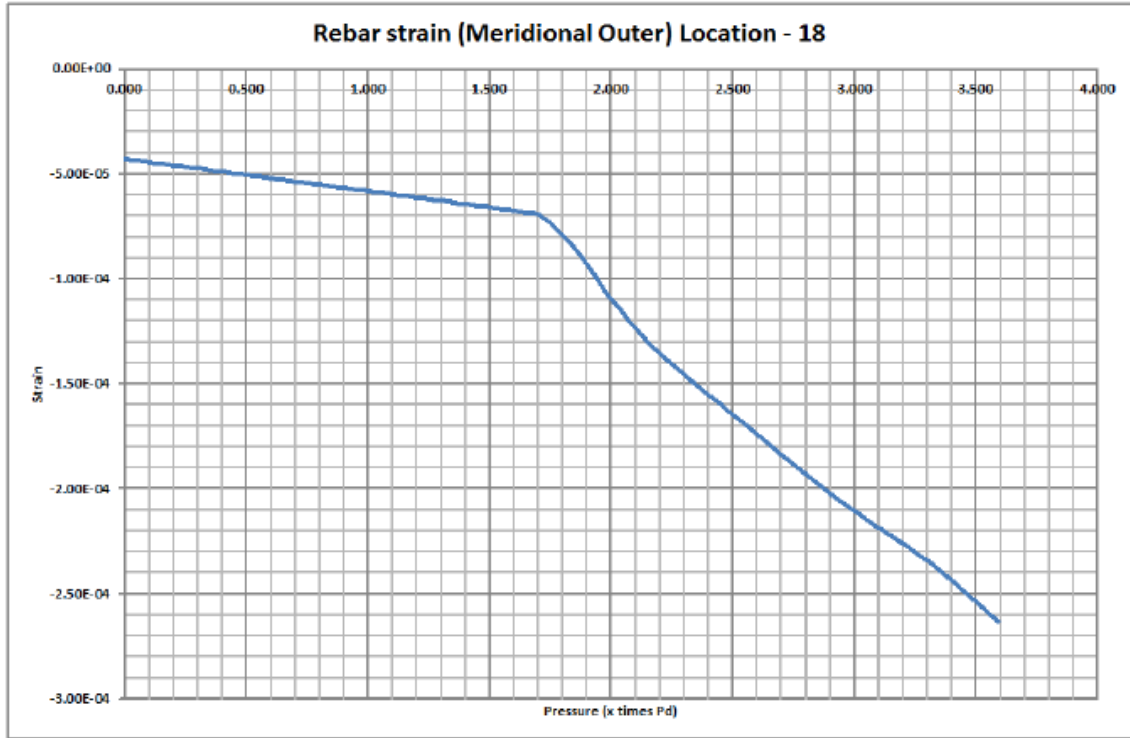


Figure A 3.36: Response at Location – 18

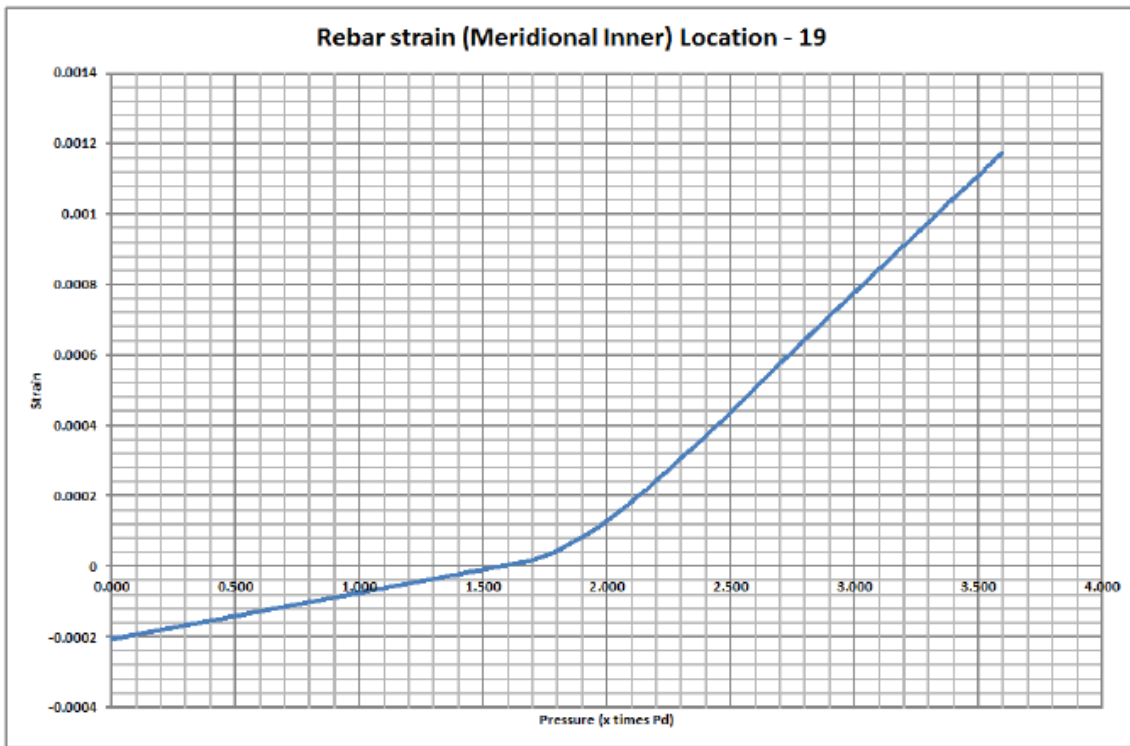


Figure A 3.37: Response at Location – 19

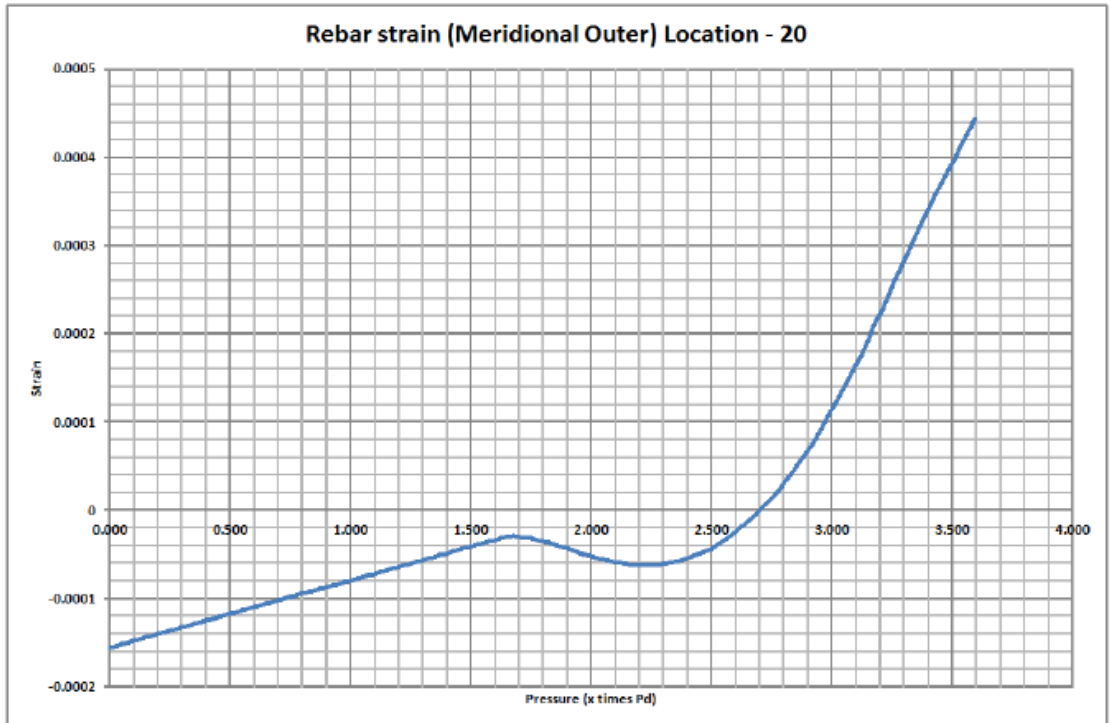


Figure A 3.38: Response at Location – 20

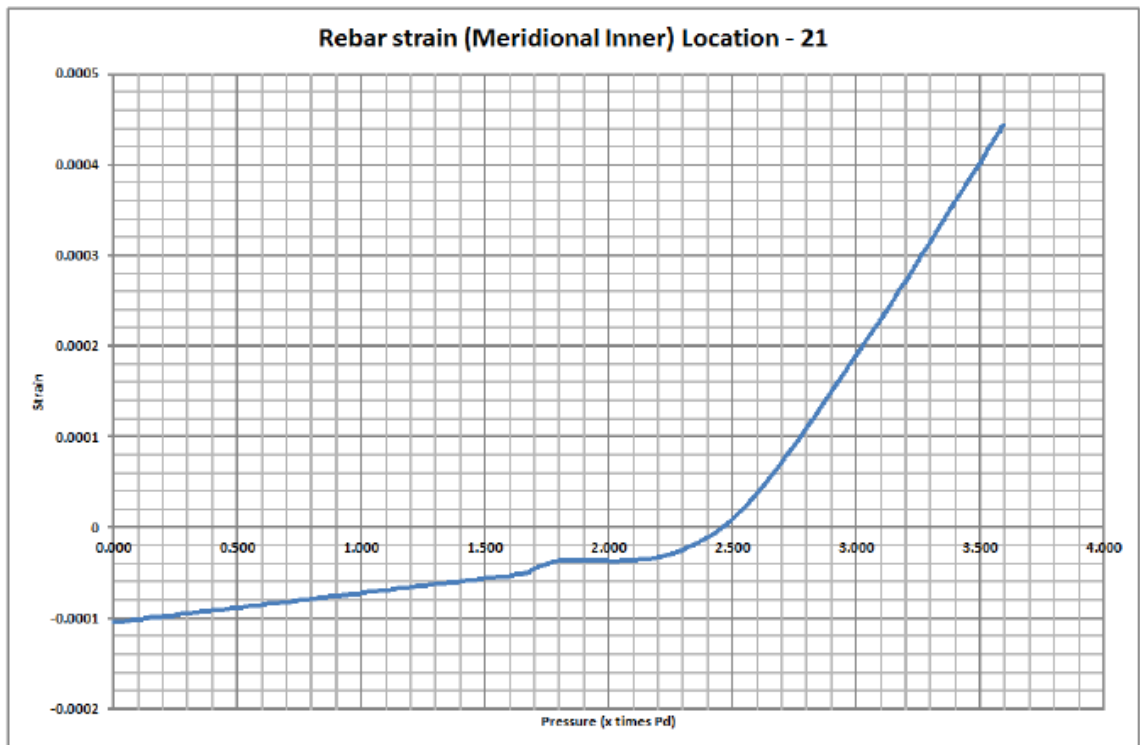


Figure A 3.39: Response at Location – 21

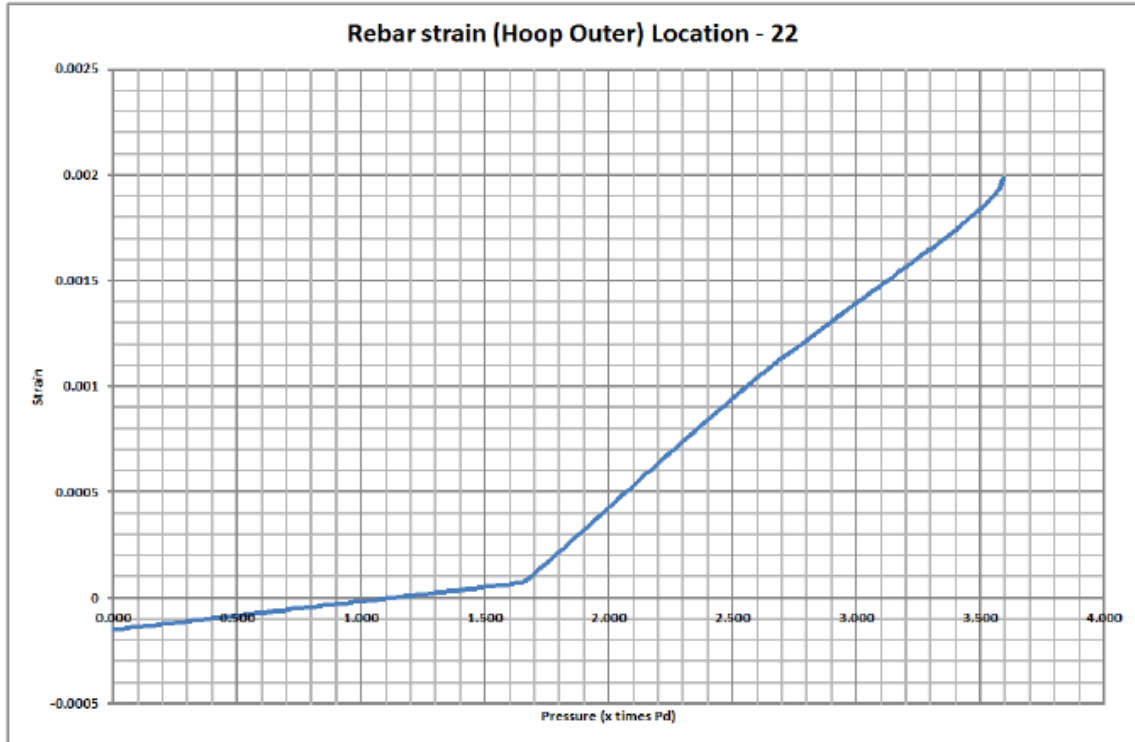


Figure A 3.40: Response at Location – 22

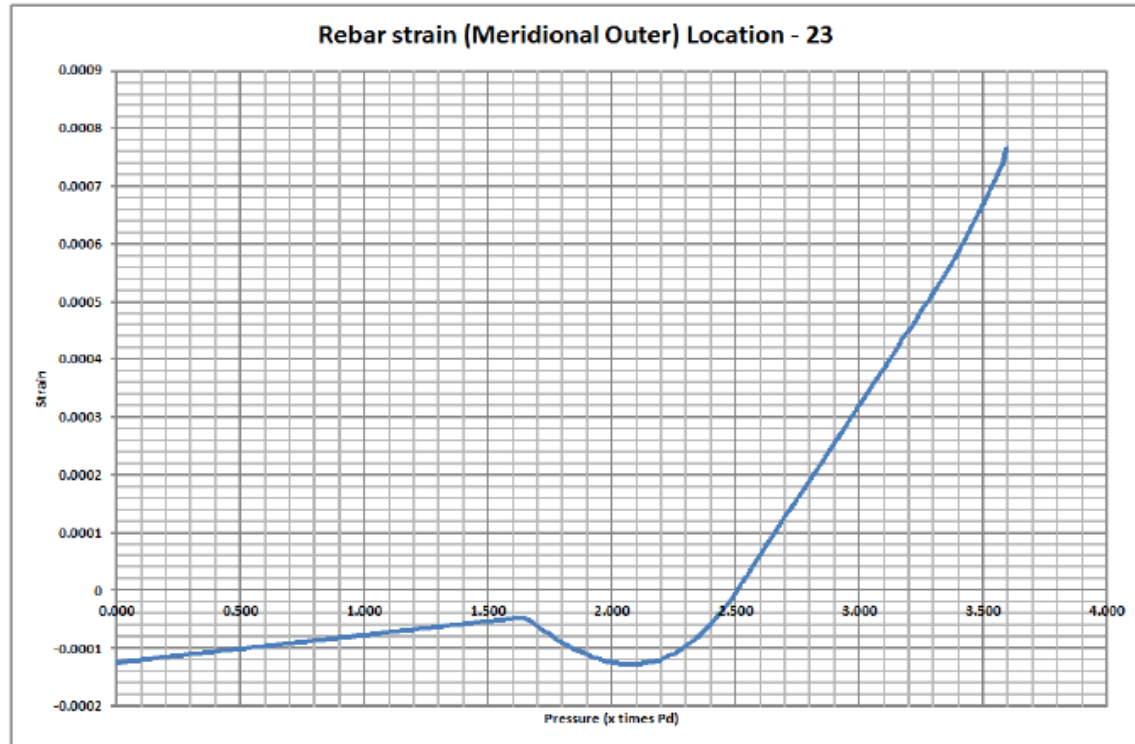


Figure A 3.41: Response at Location – 23

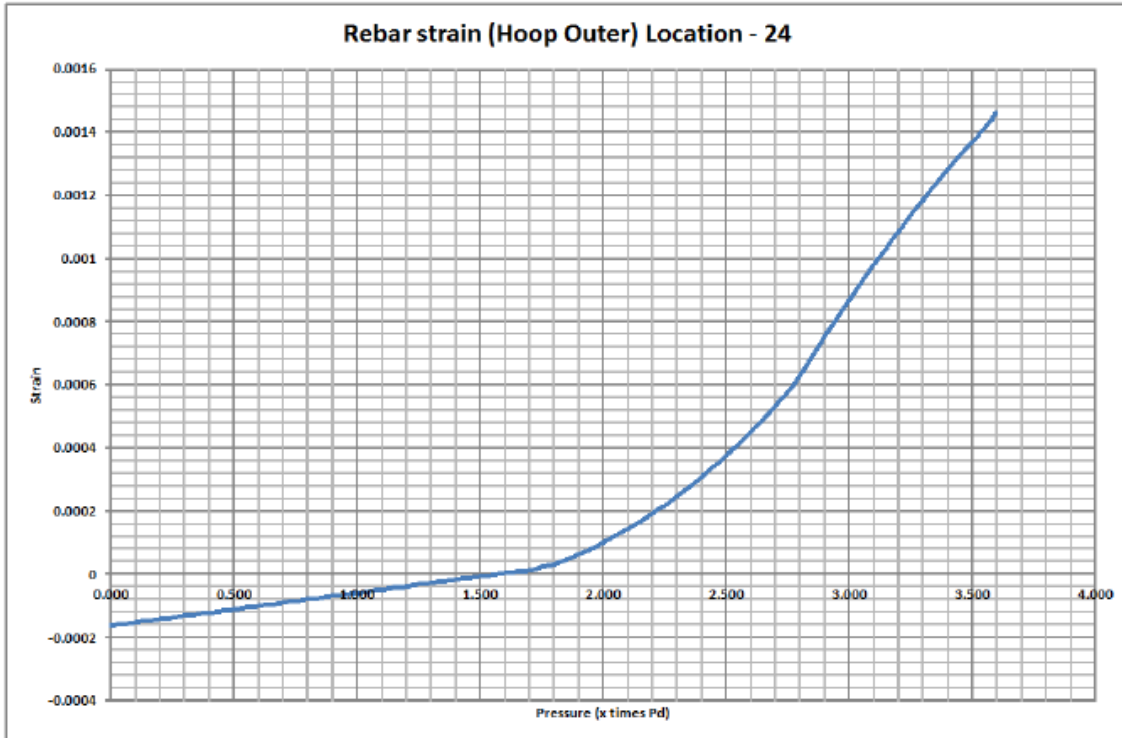


Figure A 3.42: Response at Location – 24

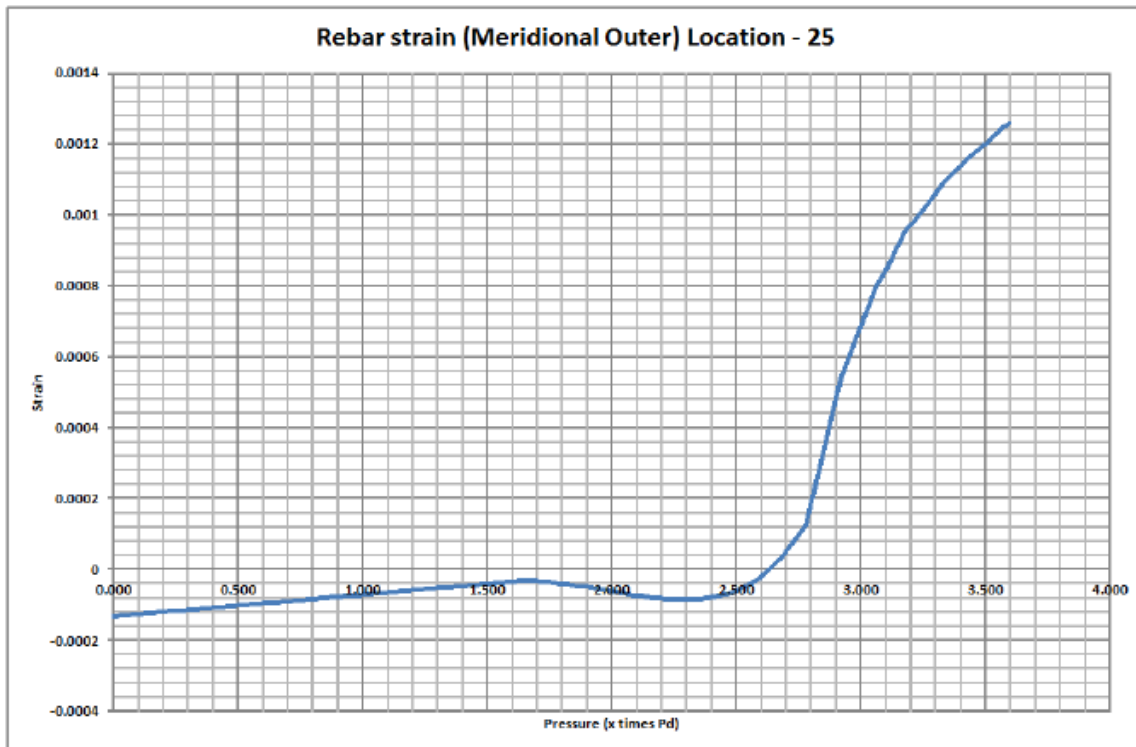


Figure A 3.43: Response at Location – 25

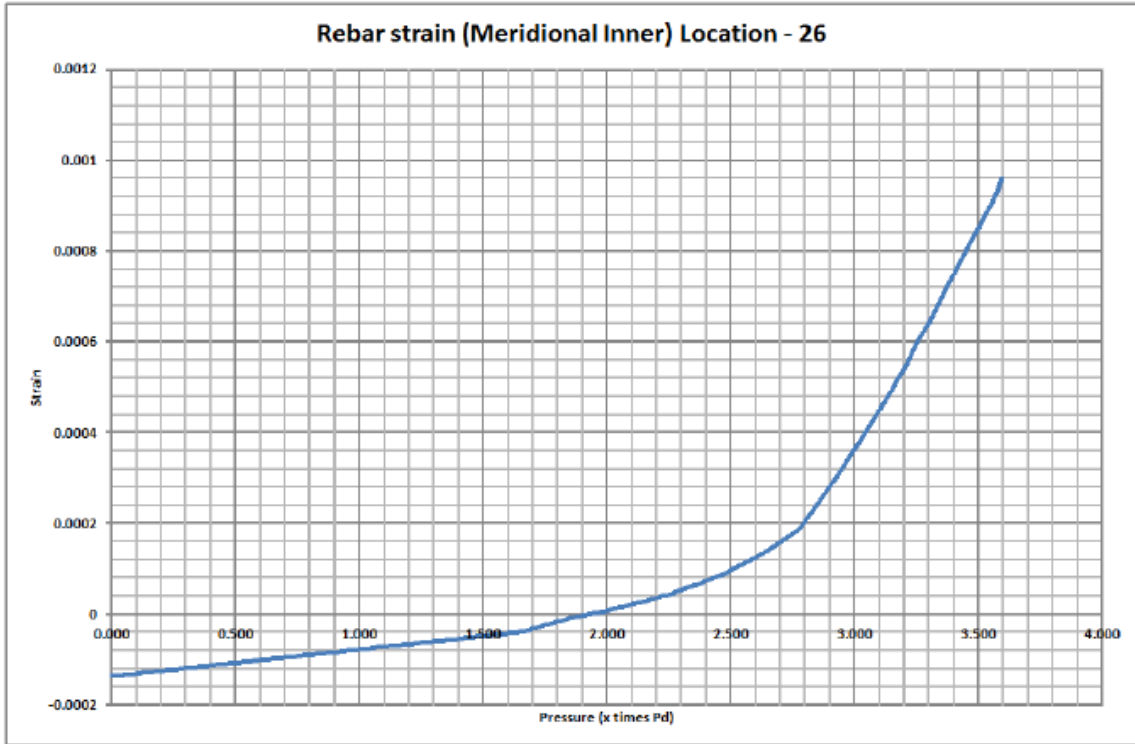


Figure A 3.44: Response at Location – 26

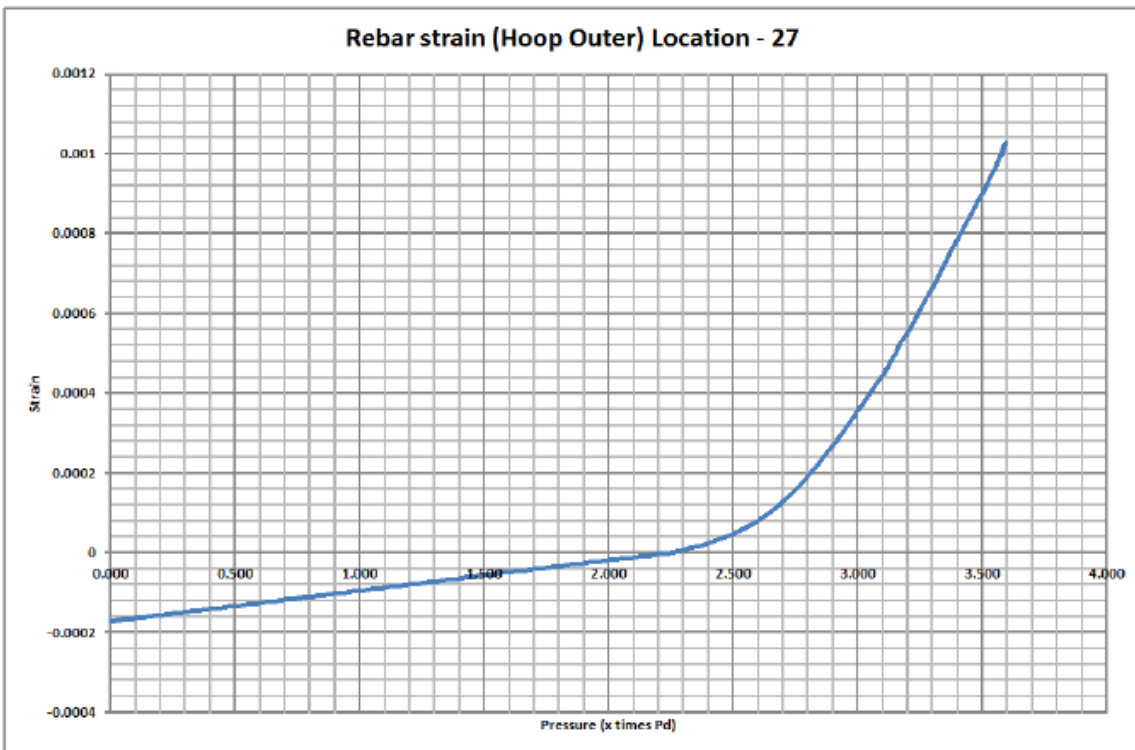


Figure A 3.45: Response at Location – 27

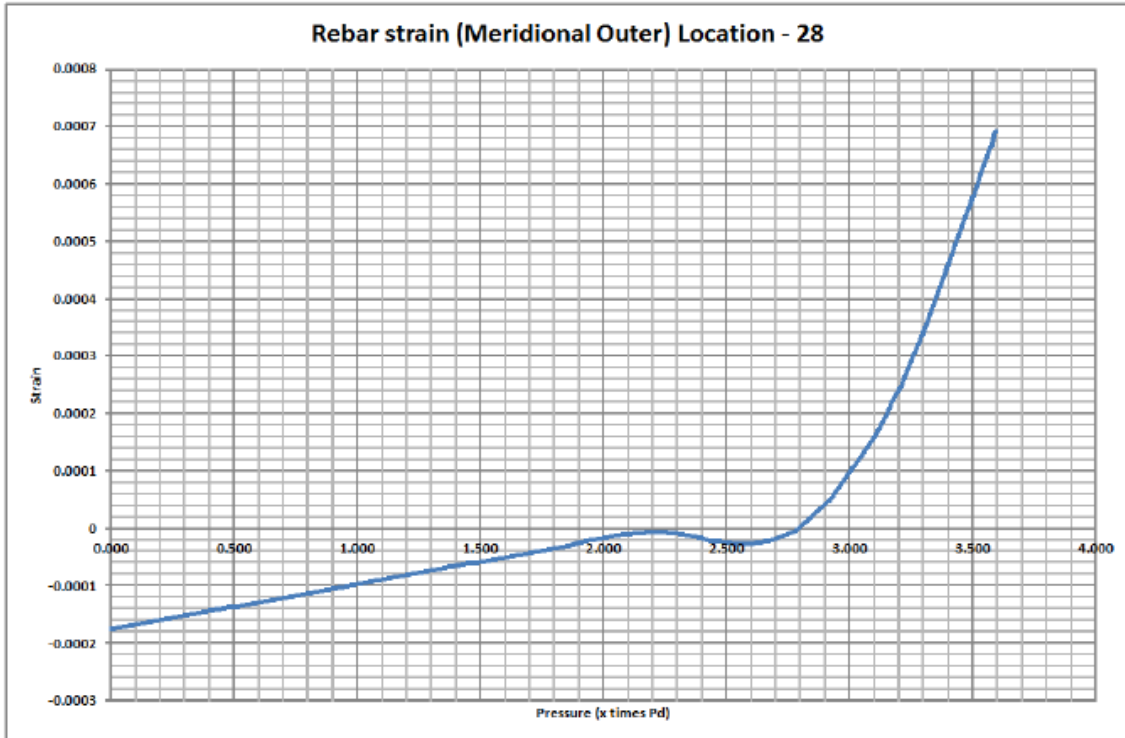


Figure A 3.46: Response at Location – 28

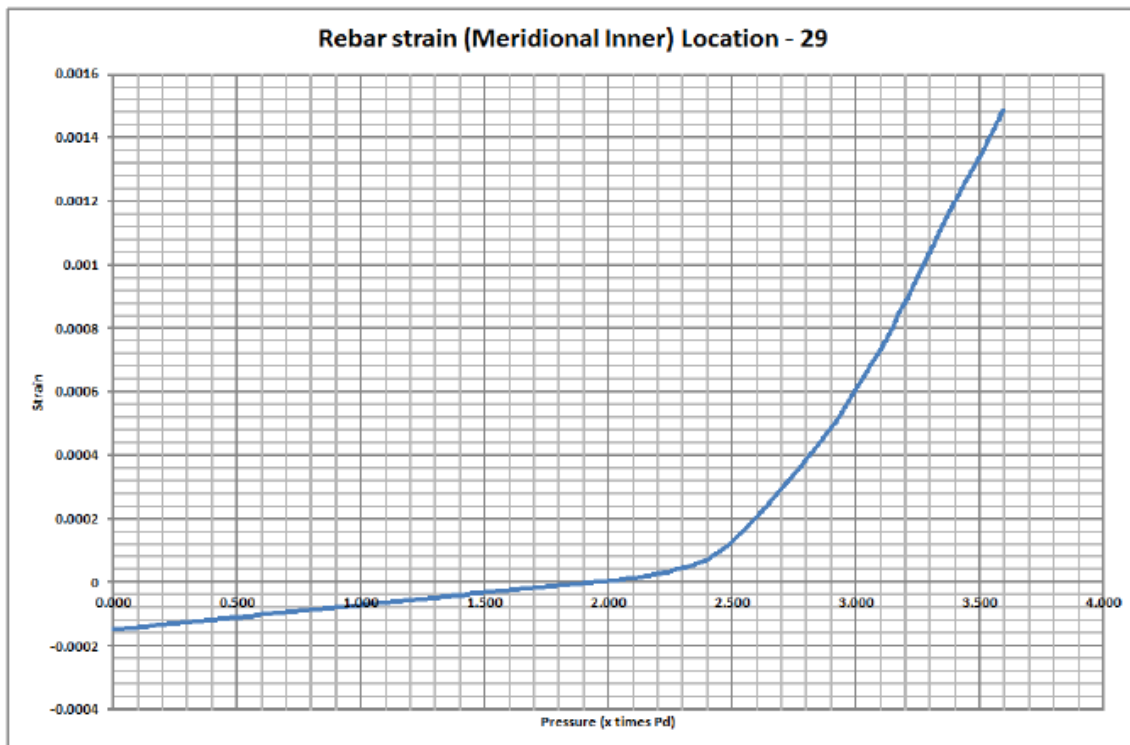


Figure A 3.47: Response at Location – 29

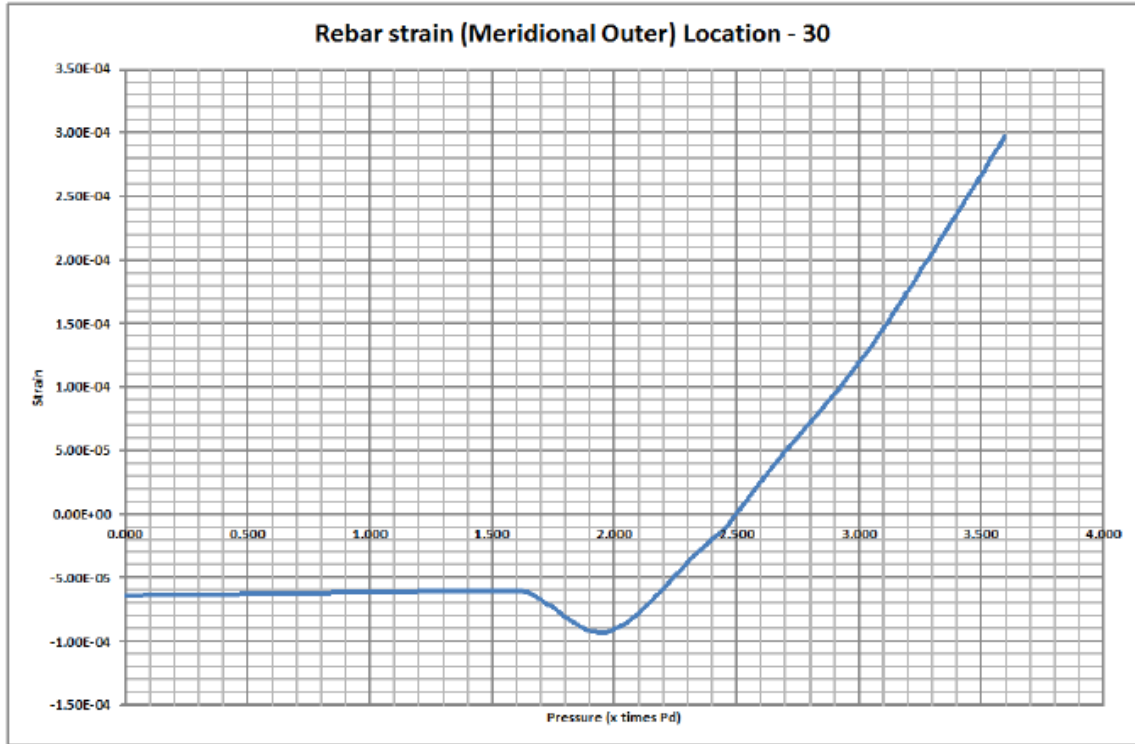


Figure A 3.48: Response at Location – 30

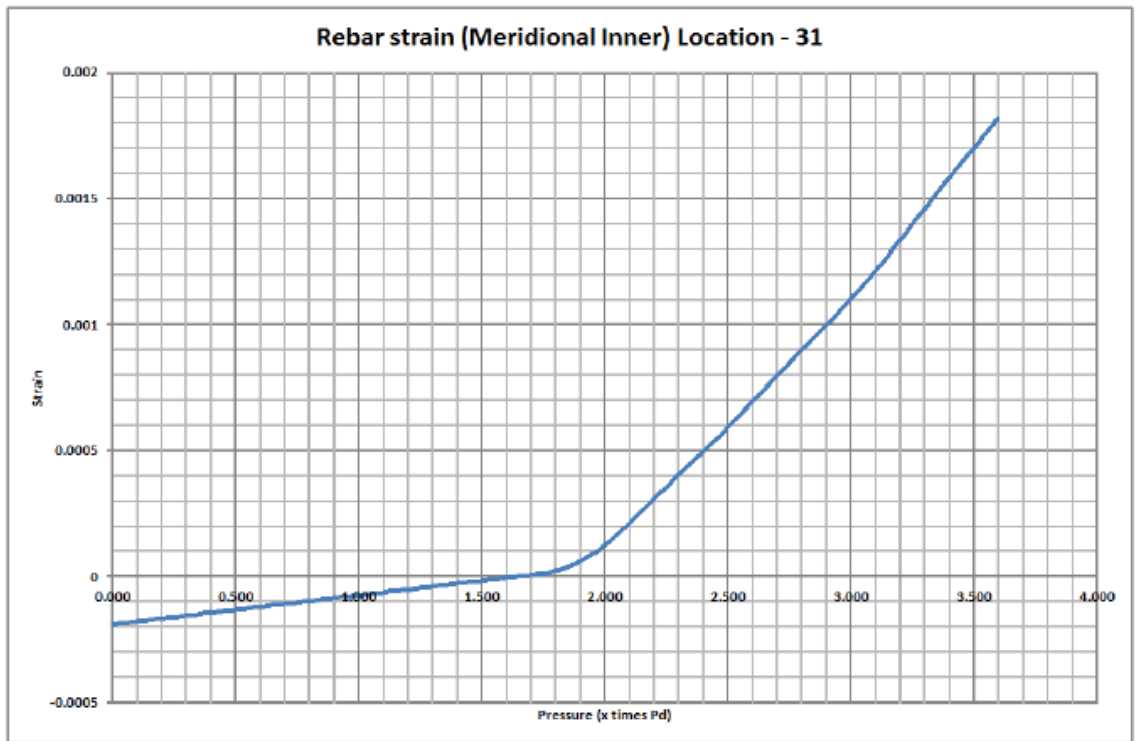


Figure A 3.49: Response at Location – 31

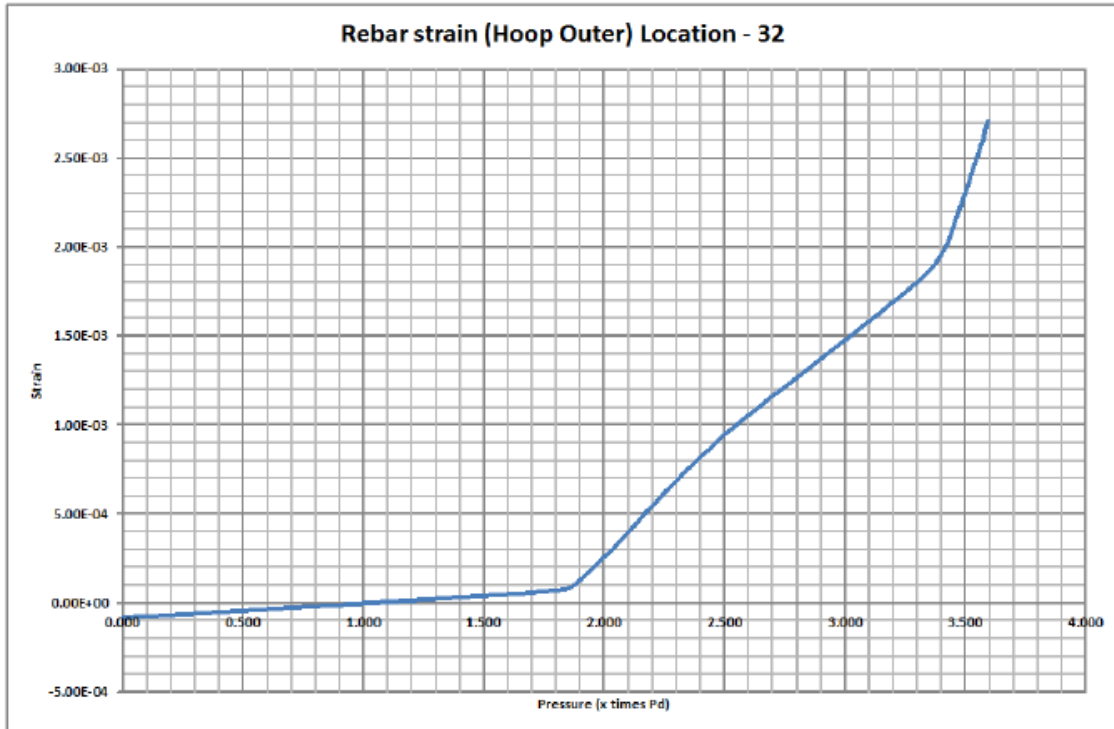


Figure A 3.50: Response at Location – 32

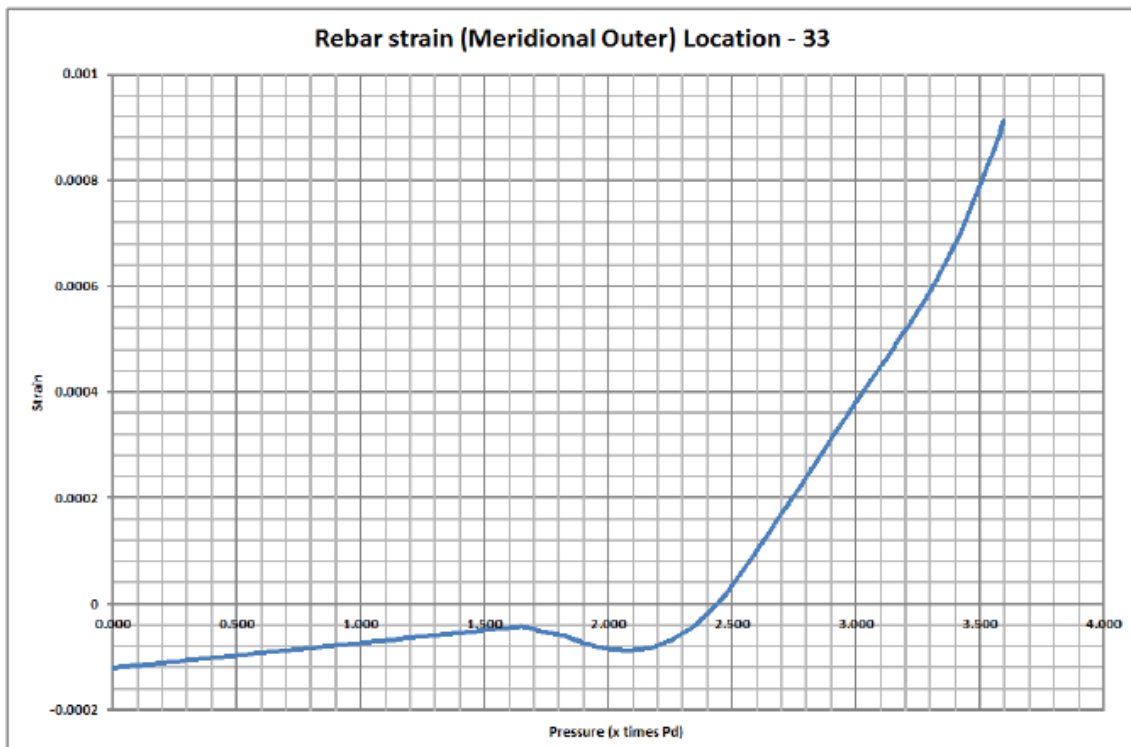


Figure A 3.51: Response at Location – 33

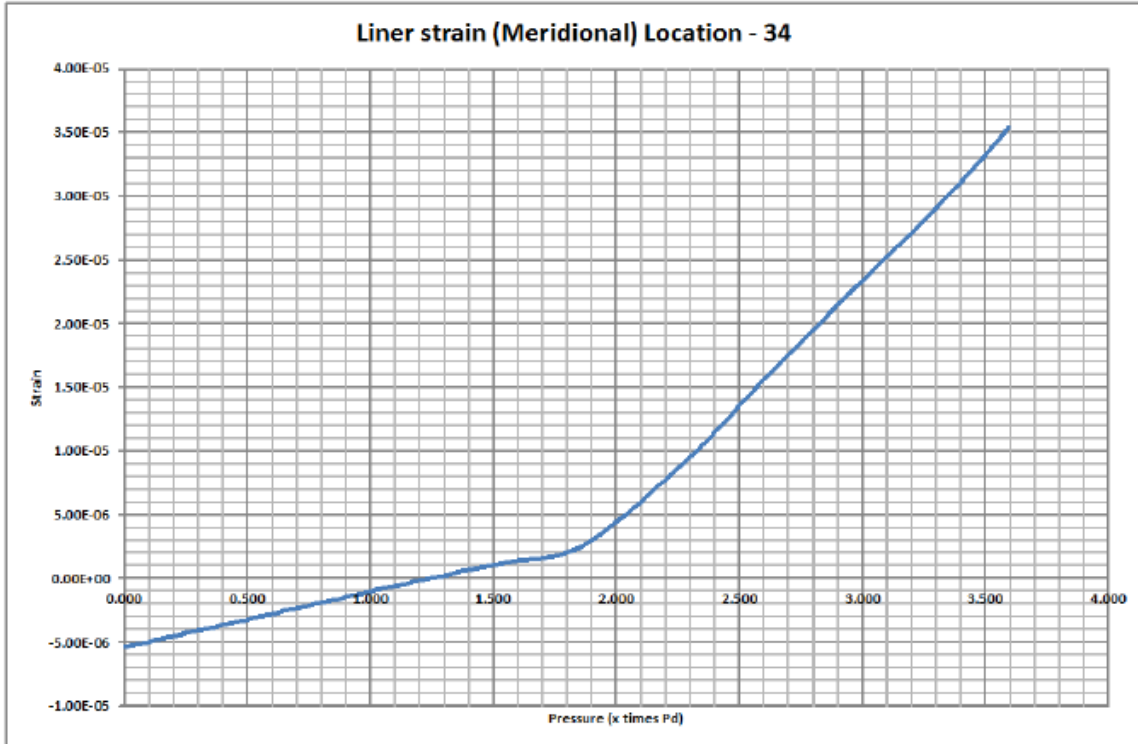


Figure A 3.52: Response at Location – 34

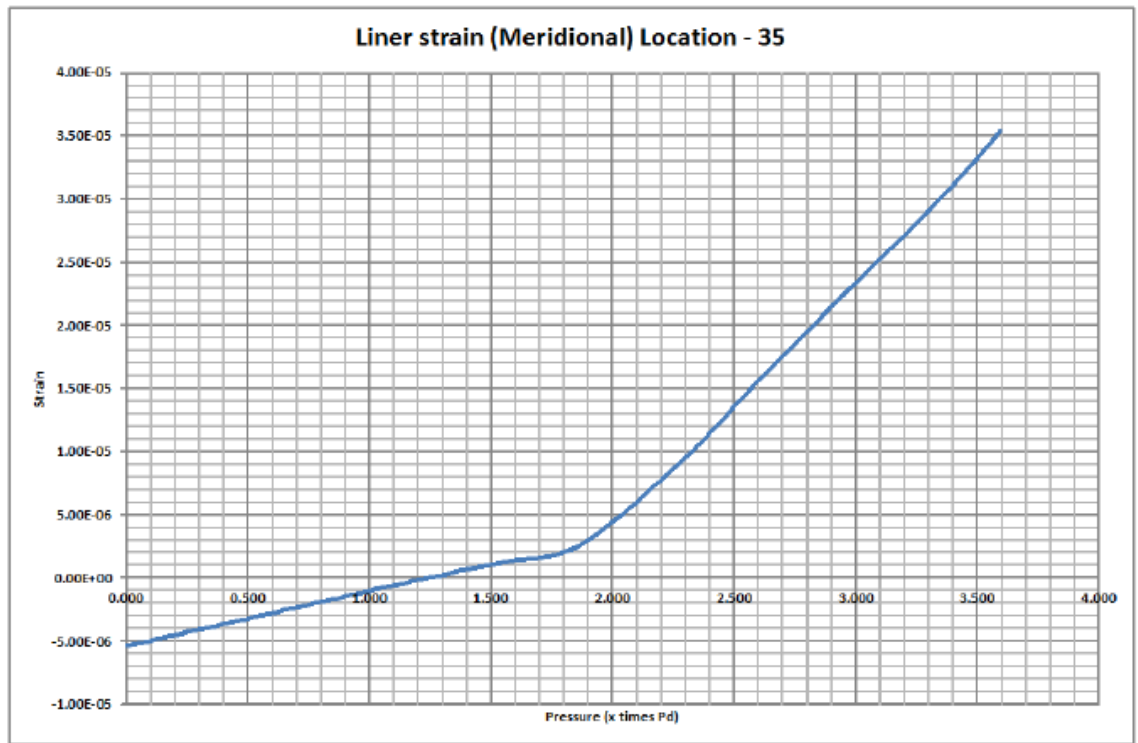


Figure A 3.53: Response at Location – 35

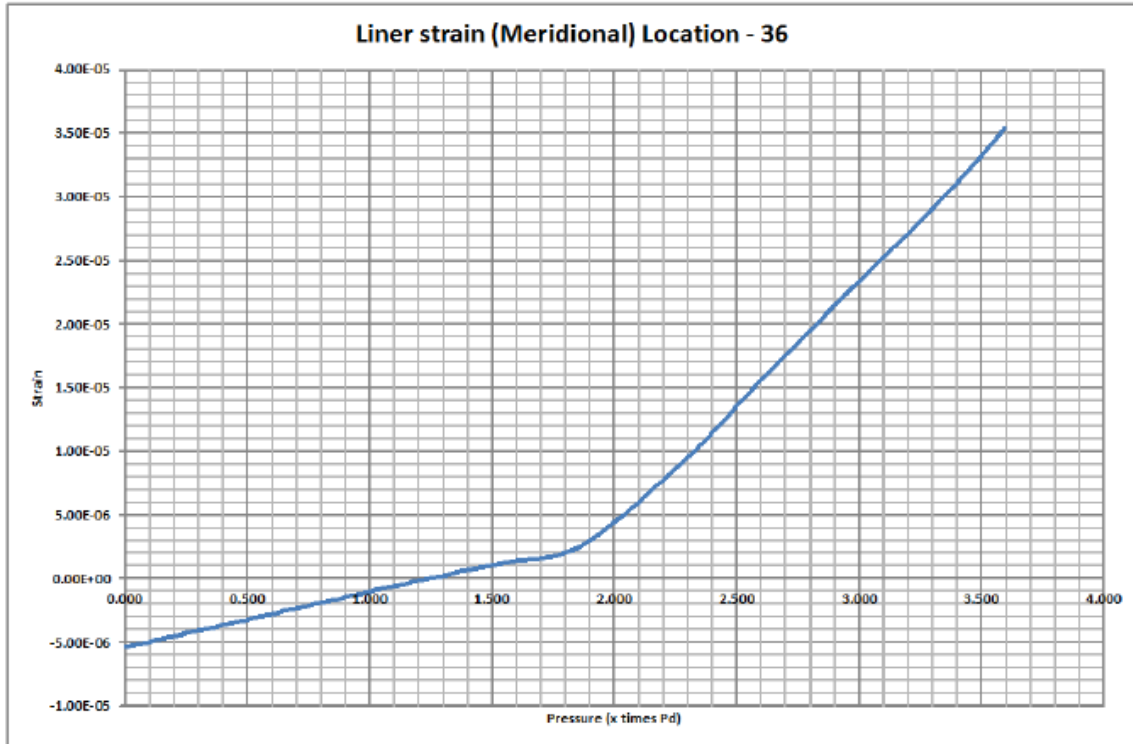


Figure A 3.54: Response at Location – 36

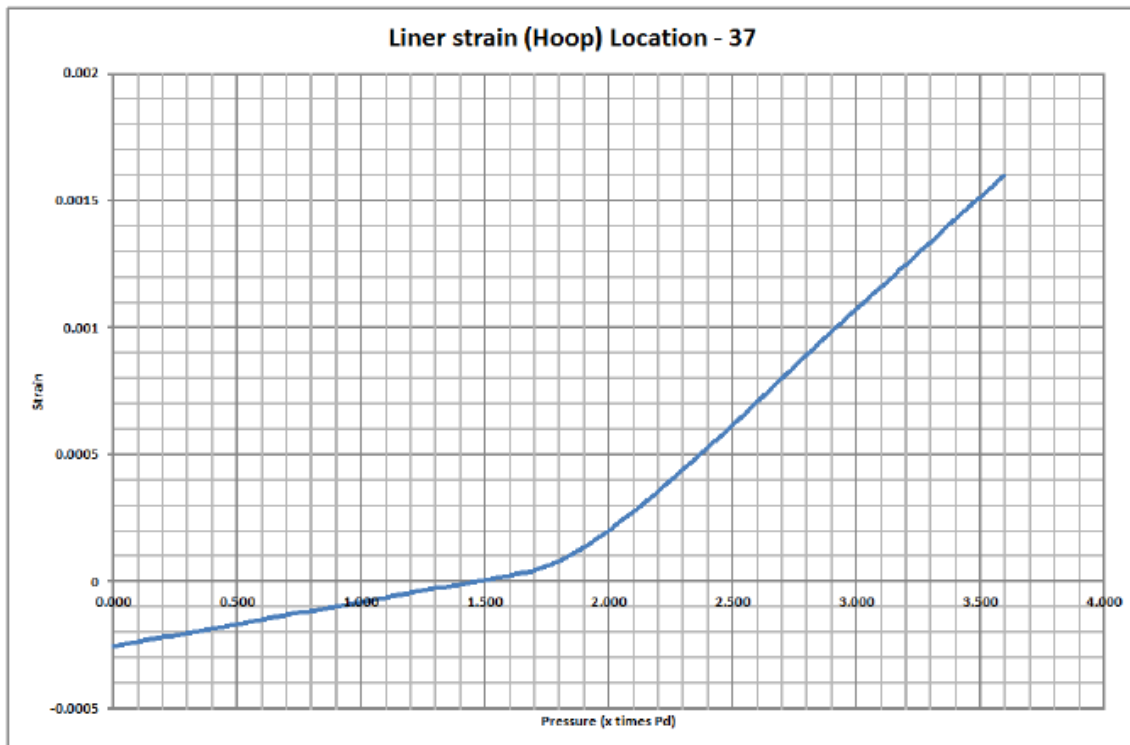


Figure A 3.55: Response at Location – 37

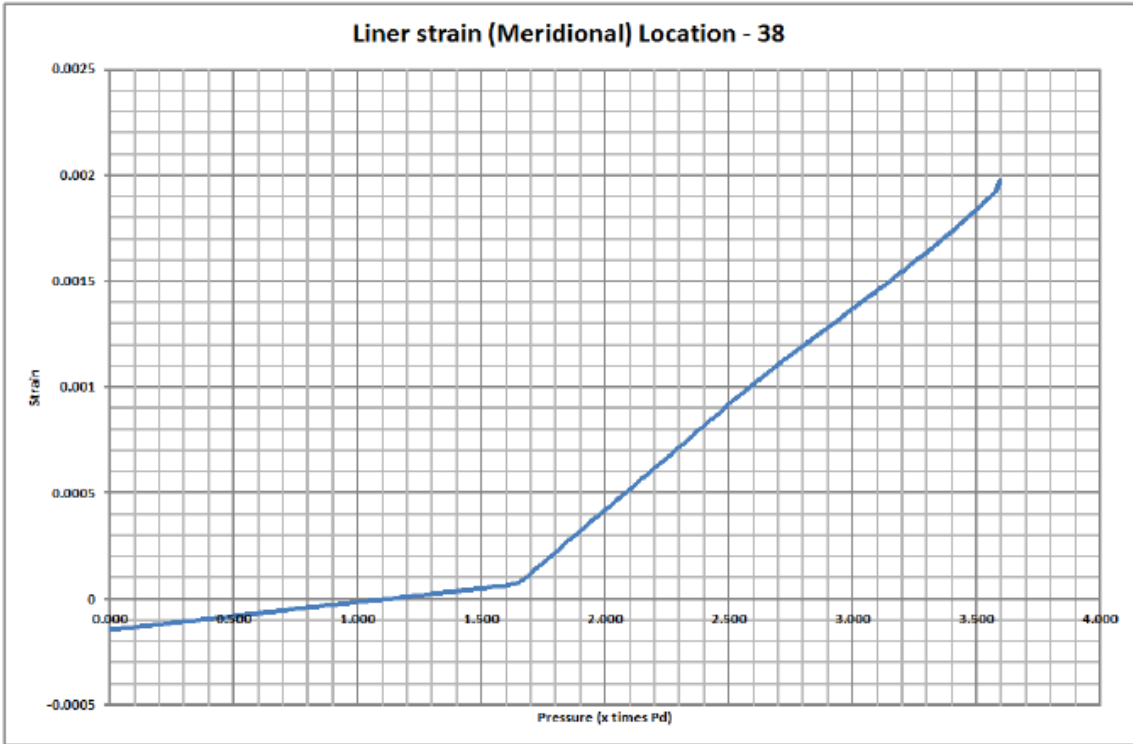


Figure A 3.56: Response at Location – 38

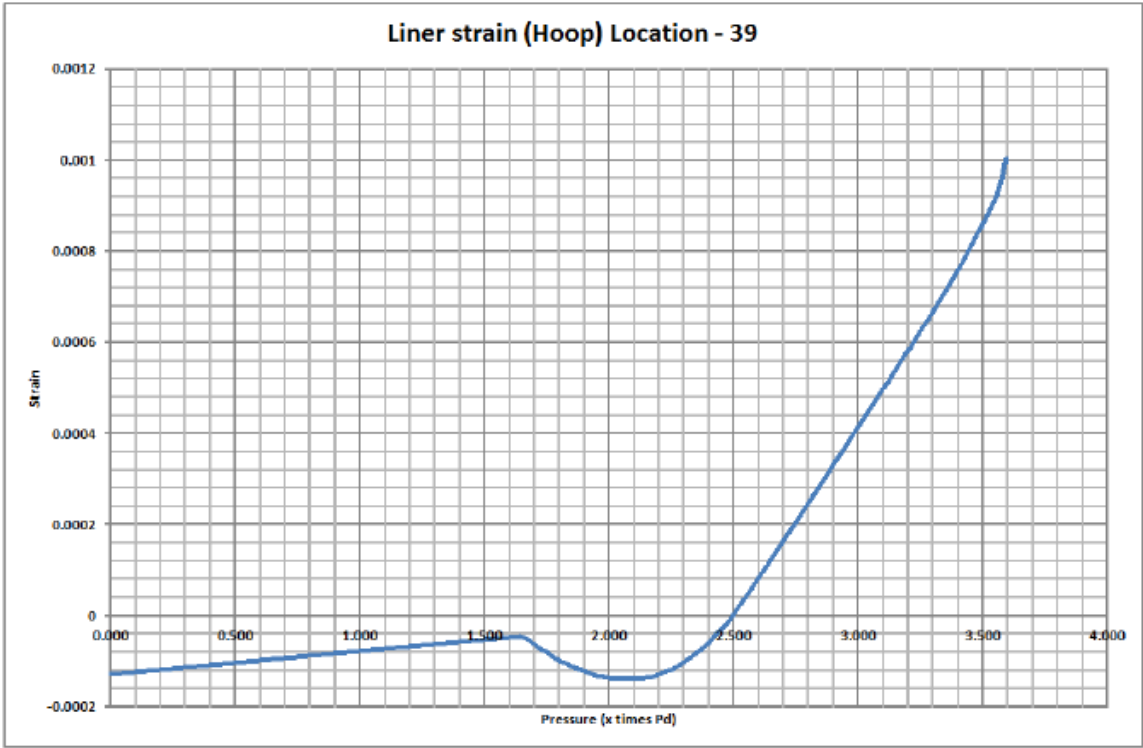


Figure A 3.57: Response at Location – 39

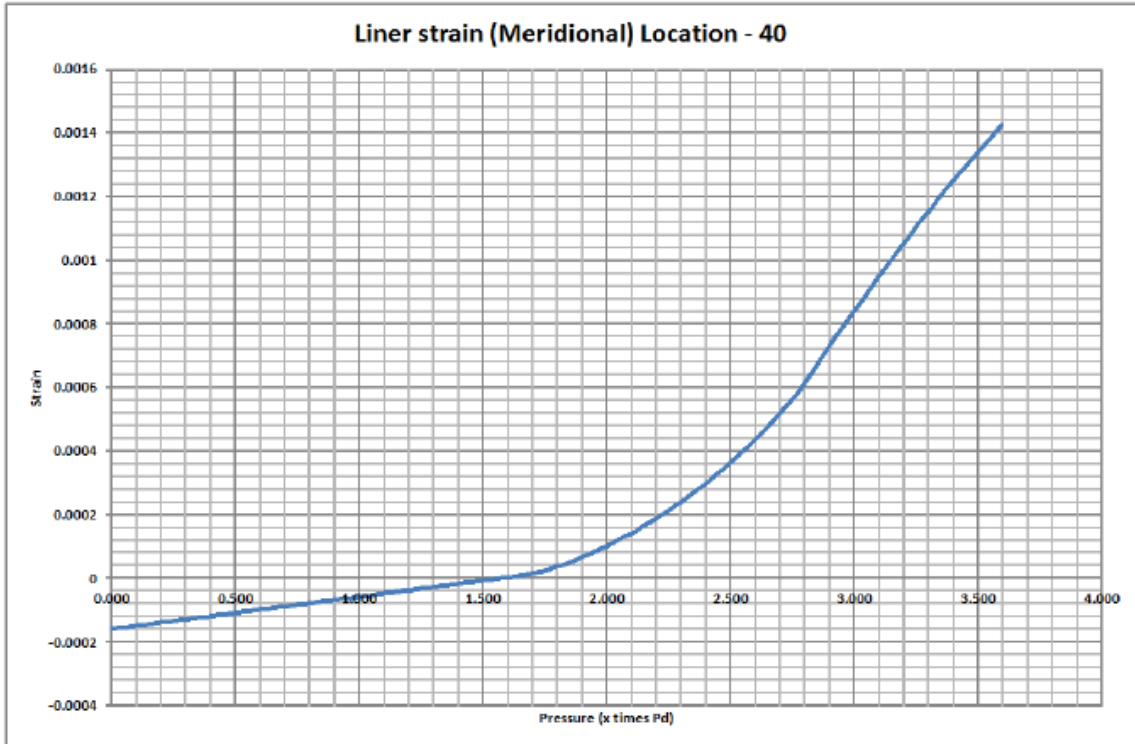


Figure A 3.58: Response at Location – 40

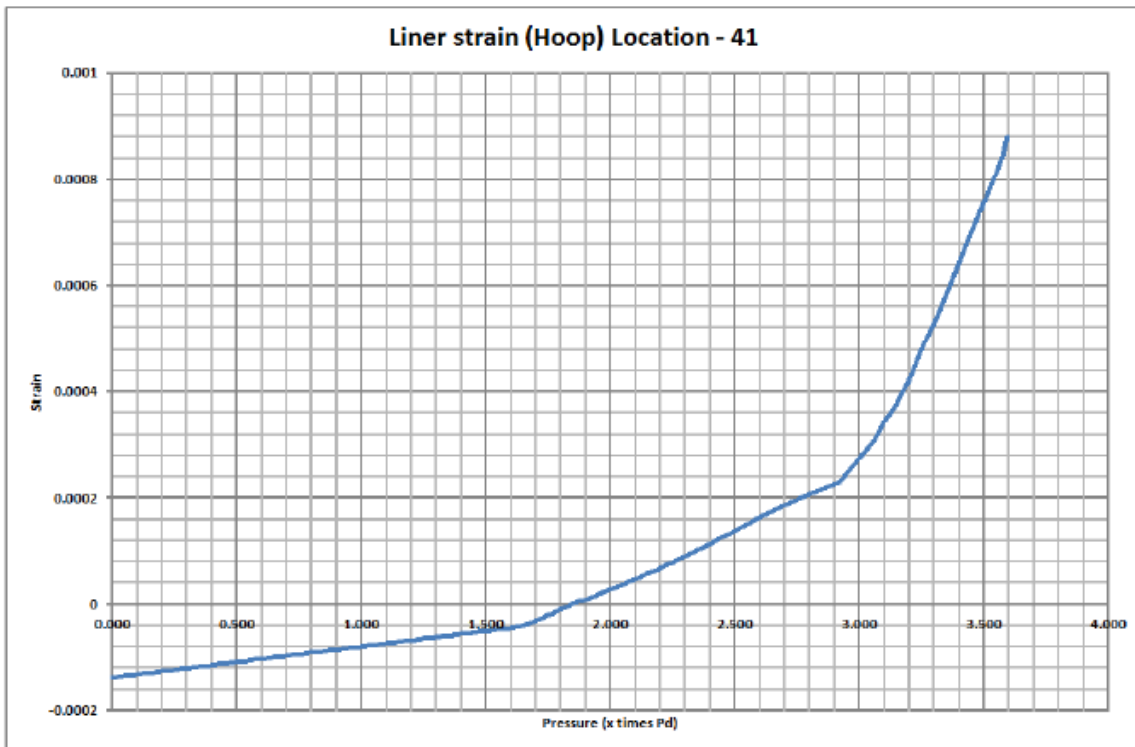


Figure A 3.59: Response at Location – 41

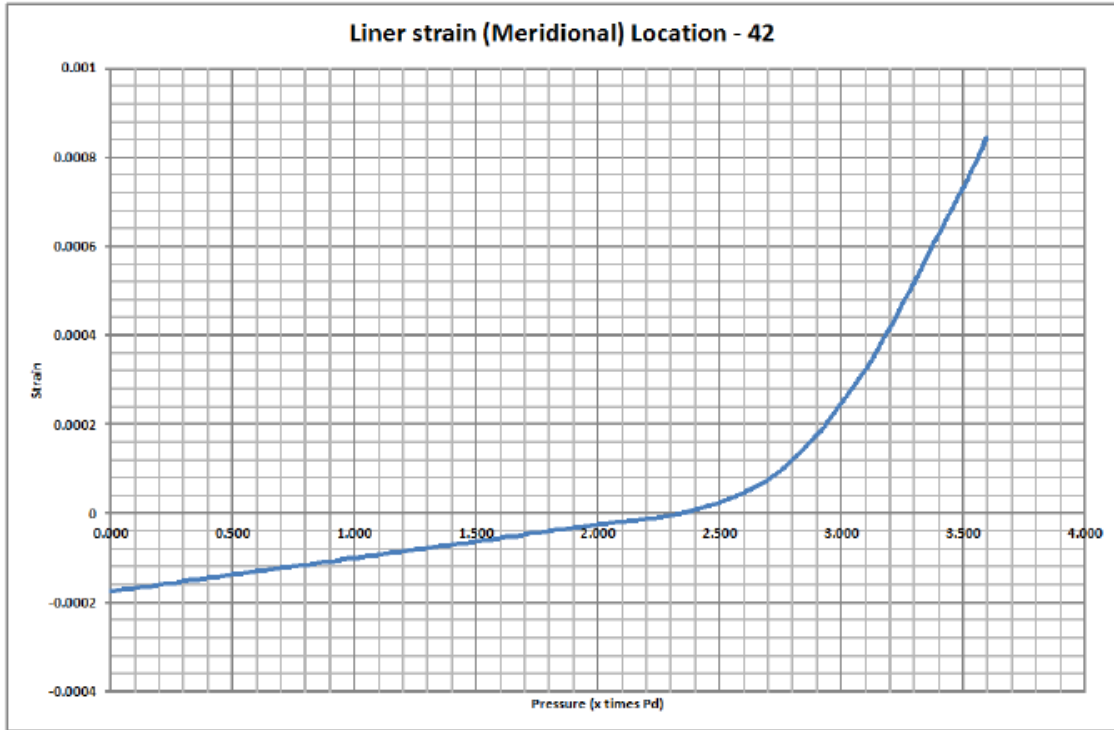


Figure A 3.60: Response at Location – 42

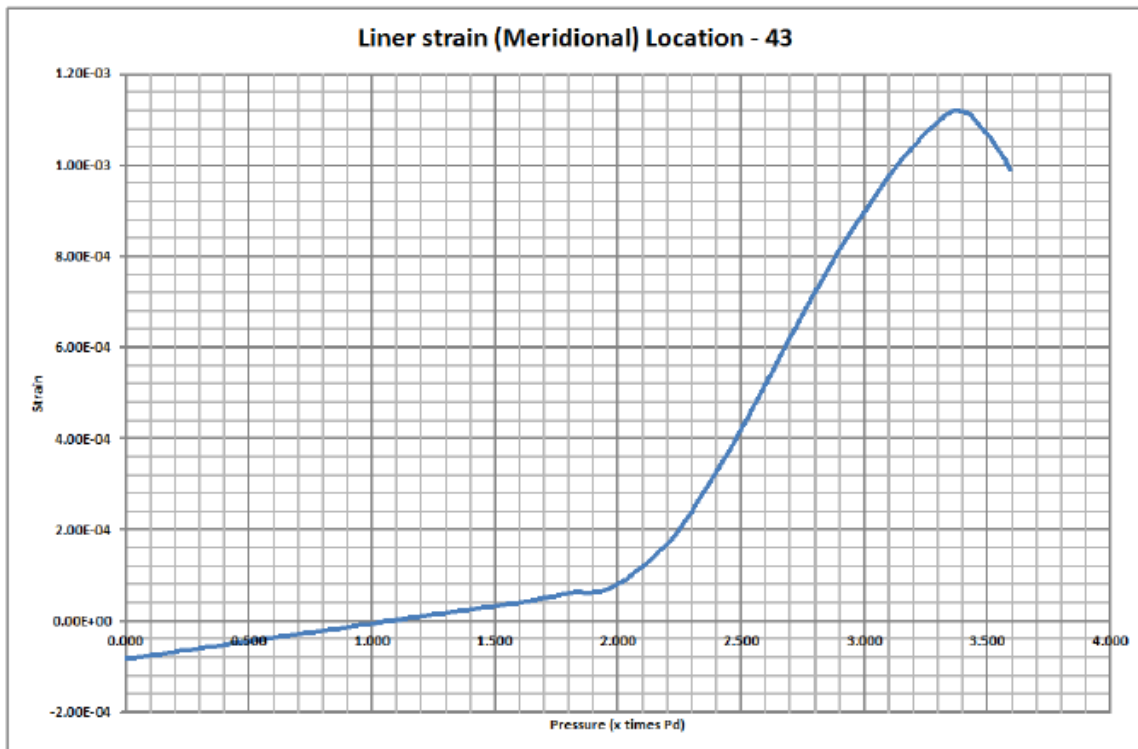


Figure A 3.61: Response at Location – 43

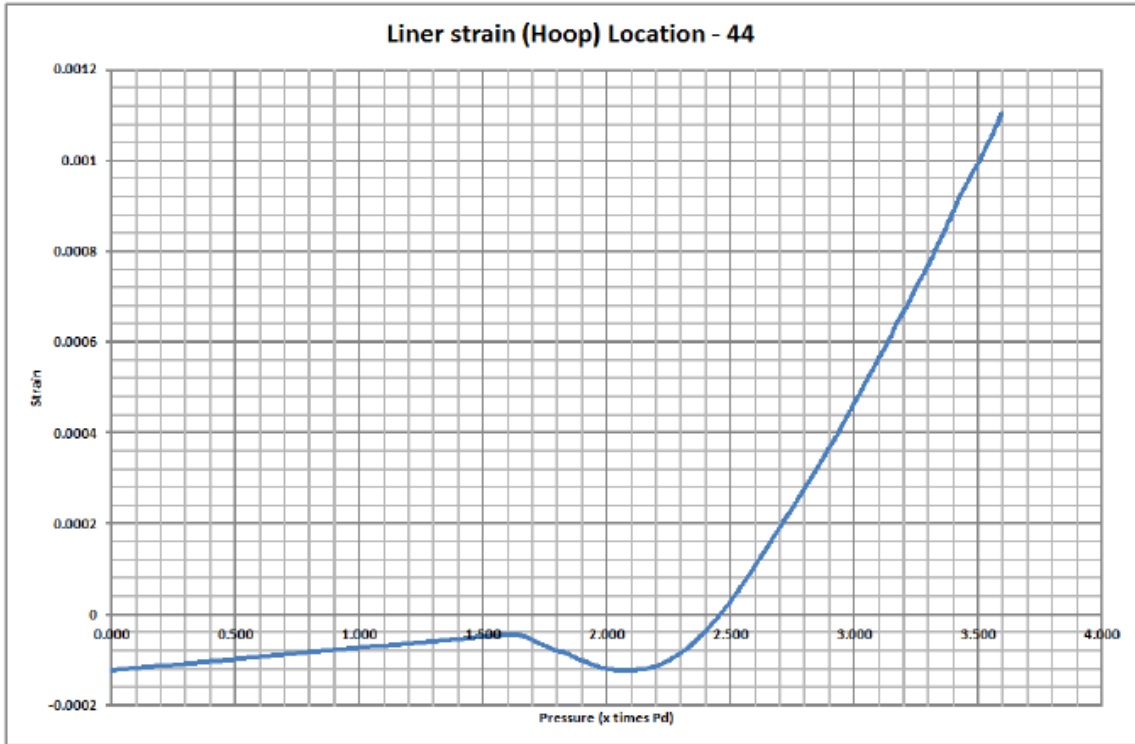


Figure A 3.62: Response at Location – 44

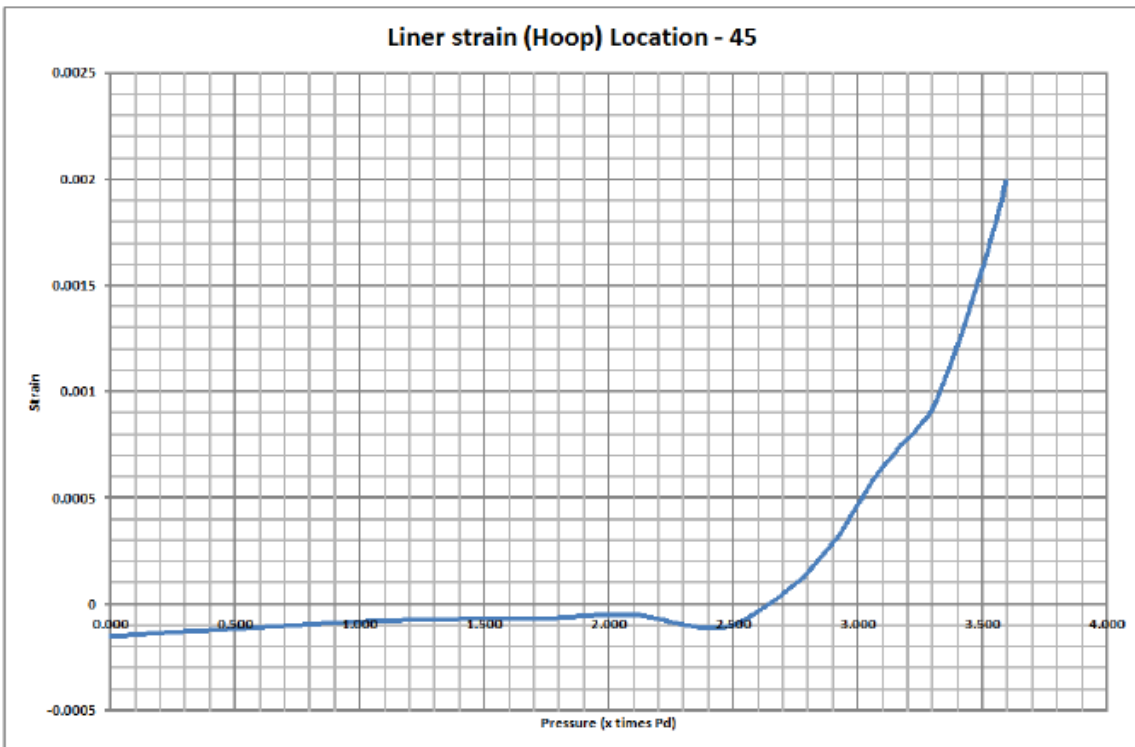


Figure A 3.63: Response at Location – 45

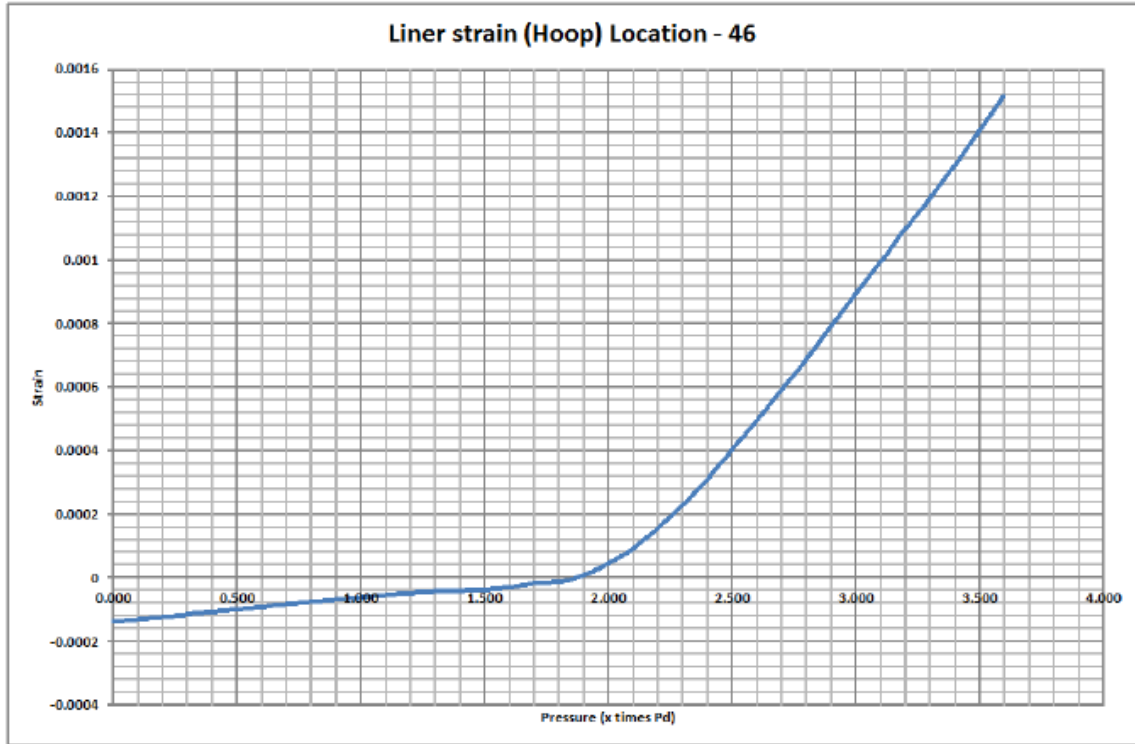


Figure A 3.64: Response at Location – 46

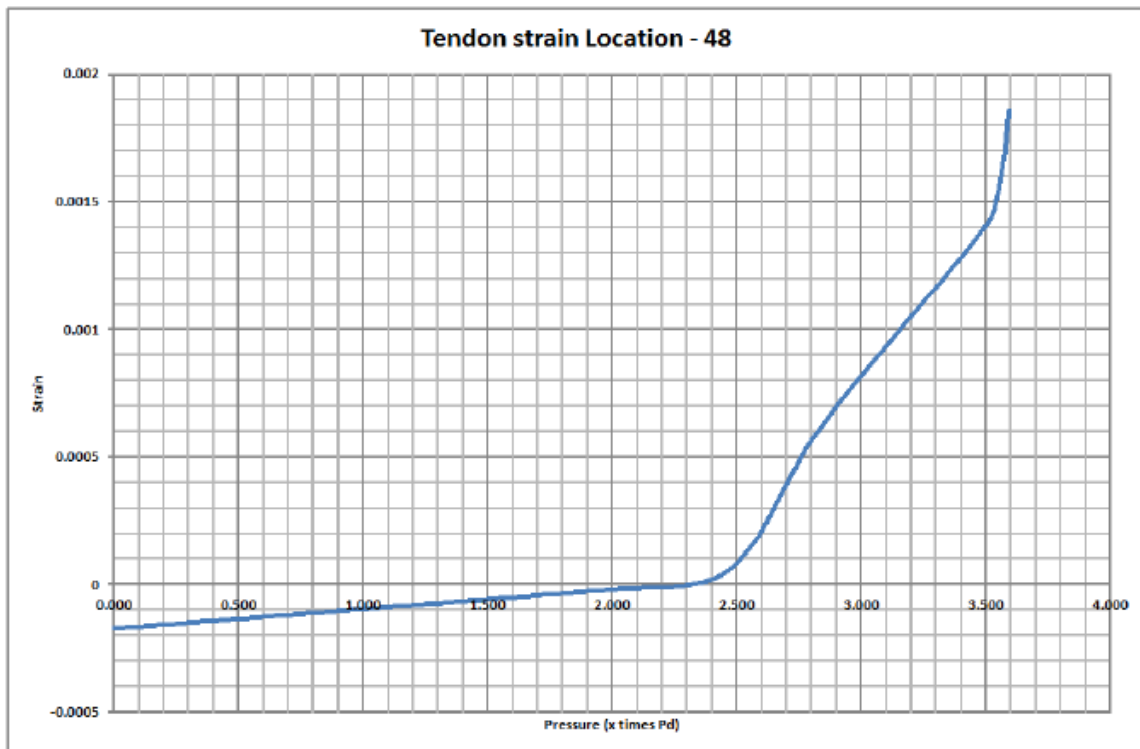


Figure A 3.65: Response at Location – 48

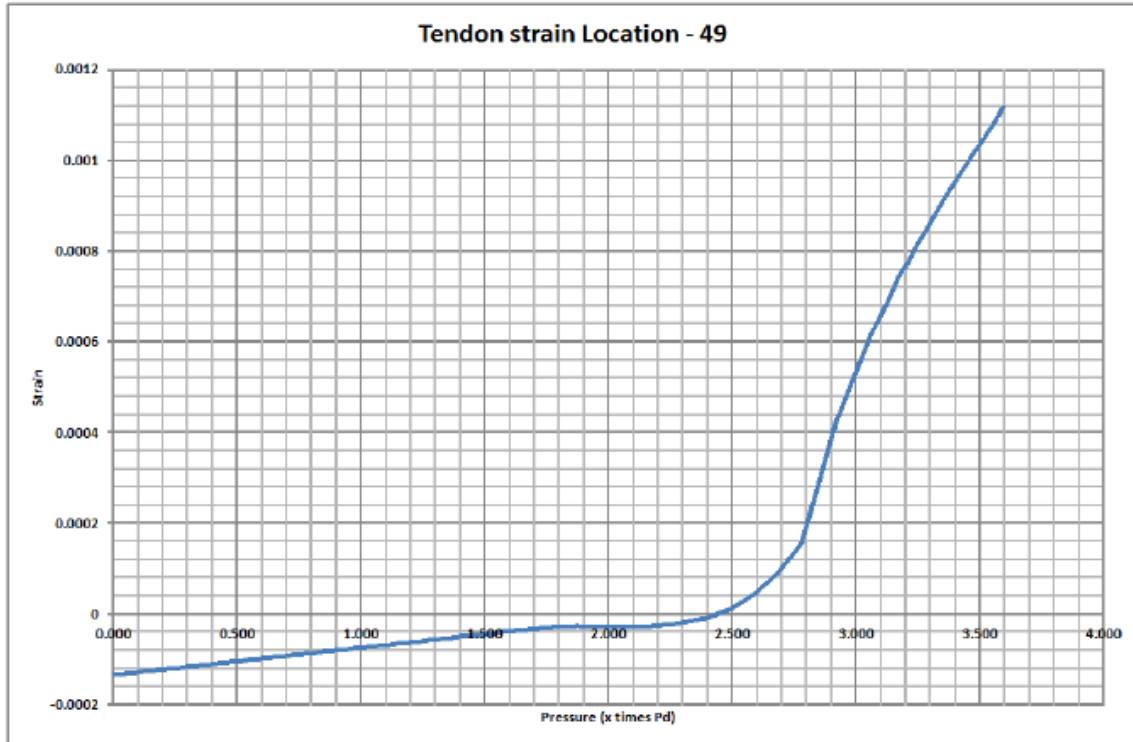


Figure A 3.66: Response at Location – 49

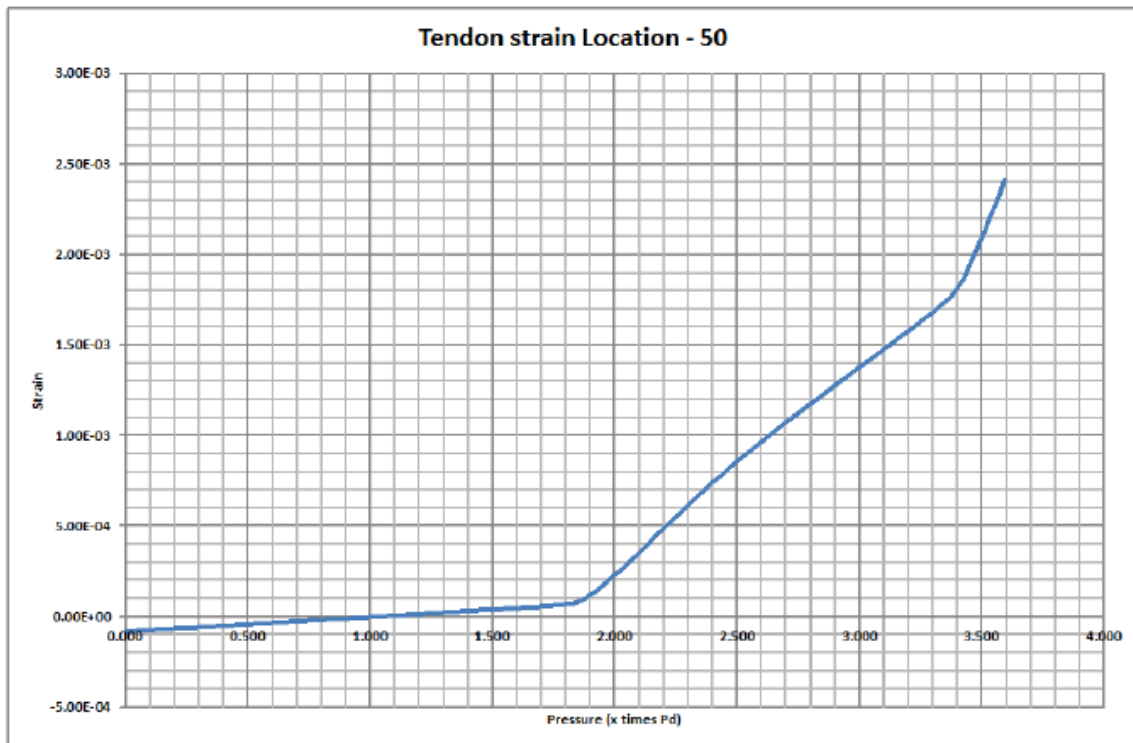


Figure A 3.67: Response at Location – 50

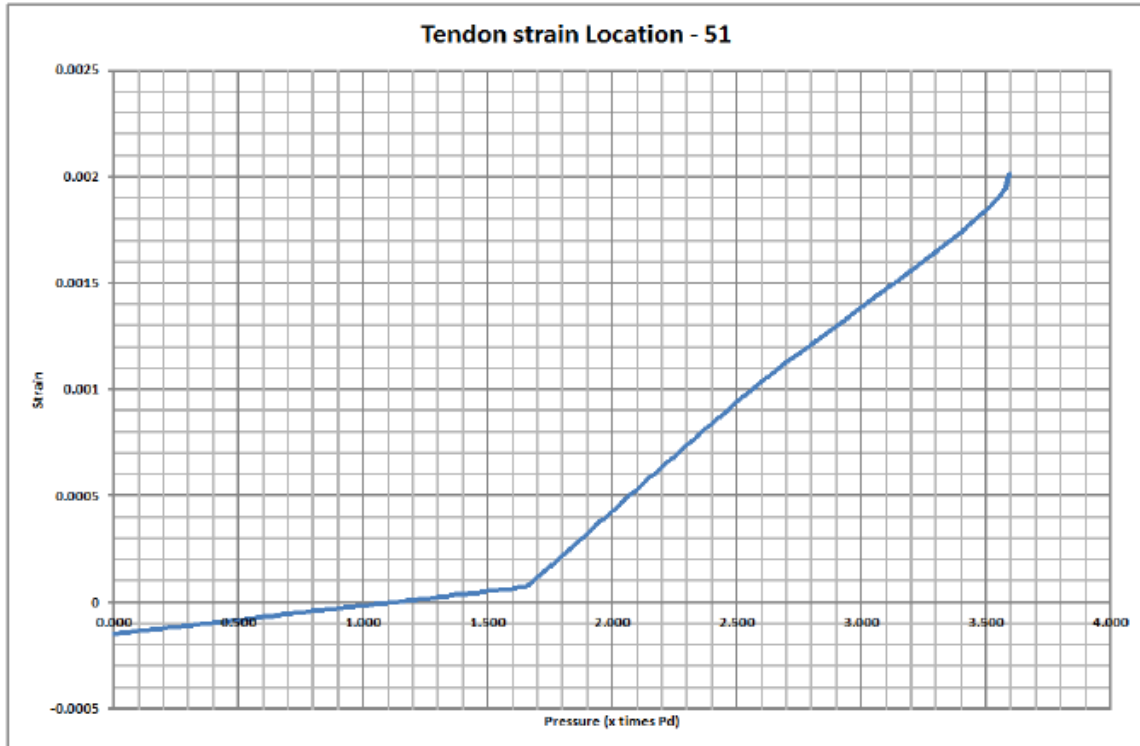


Figure A 3.68: Response at Location – 51

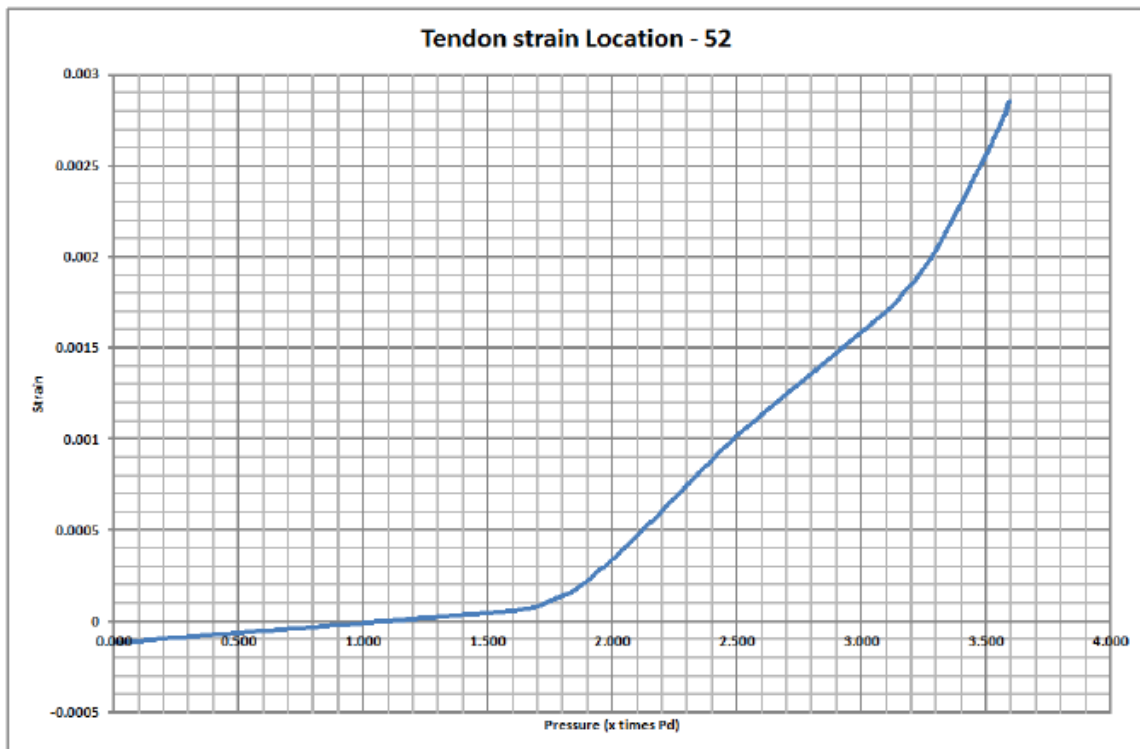


Figure A 3.69: Response at Location – 52

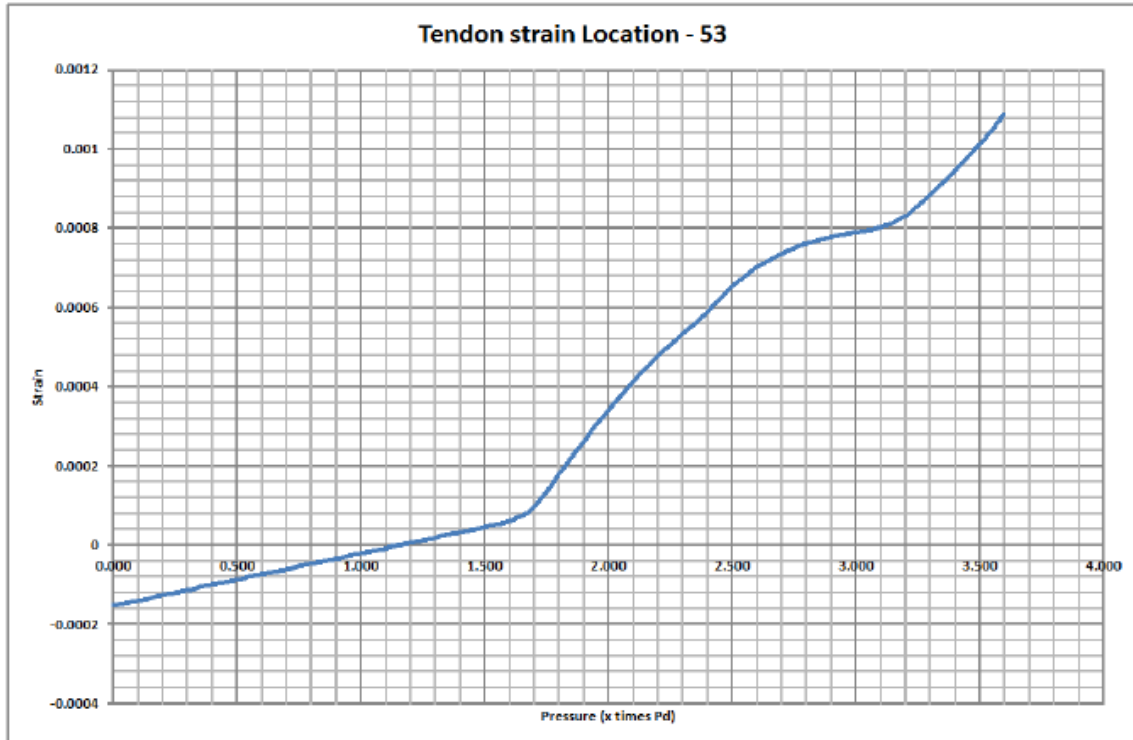


Figure A 3.70: Response at Location - 53

SUMMARY

Global analysis model has been developed based on the dimensions and material properties specified. The cross section is modeled using layered shell elements and reinforcement is included as an embedded oriented surface inside the shell.

For the initial study, results of which were presented in Chapter - 3, the effect of tendon slippage and liner concrete interaction, obtained from the results of model studies 1 and 2 are not included. These effects would be considered in refined analysis planned for the future.

The ultimate capacity of the PCCV is estimated as 3.59 times the design pressure of 0.39MPa.

Failure is initiated around the equipment hatch opening, mainly in the region between equipment hatch and airlock.

The output as requested has been obtained and included in Chapter - 3.

APPENDIX B EDF

study title PERFORMANCE OF CONTAINMENT VESSEL UNDER SEVERE ACCIDENT CONDITION SPE #3	
client EDF	
document reference N002_A210_2011_EDF_A2	offre reference D311_ET_EDF_B
type of document TECHNICAL REPORT	
document title PHASE 1 : Ring model and tendon behaviour	



Ind.	Date	State	Modifications	Prepared by	Verified by	Approved by
A2	25.08.2011	GFO	First release	M. MOZAYAN	S. MICHEL-PONNEL	S. GHAVAMIAN

A vertical line on the right margin of the page indicates modified parts

GFO: Good for observation

GFD: Good for release

SUMMARY

Appendix B EDF B-1
Summary B-2
INTRODUCTION..... B-3
METHODOLOGY B-3
GEOMETRIC DESCRIPTION..... B-4
DESCRIPTION OF THE FINITE ELEMENT MODEL..... B-6
MATERIAL PROPERTIES AND CONSTITUTIVE MODELS..... B-7
TENDON AND PRESTRESSING MODEL..... B-12
RESULT ANALYSIS..... B-13
Deflection of the model for different load steps B-14
Tendon stress distribution at different load steps B-19
Tendons' strain evolutions at azimuth 135° at different load steps..... B-26
Concrete damage index mapping at different load steps B-27
CONCLUSIONS B-29
REFERENCES..... B-30

INTRODUCTION

Within the frame-work of the SPE #3 “Performance of Containment Vessel Under Severe Accident Condition, this report concerns the analysis carried out to simulate the mechanical behaviour of a ring model of the SANDIA PCCV mock-up (phase 1.1).

Information indicated in this report are:

- a full geometrical description of the structure
- mechanical material data
- modelling methodology
- constitutive laws
- boundary conditions and loadings
- simulation results and their comparison to experimental measures and simulation results provided by other participants of the project

METHODOLOGY

The study is carried out base on the following methodology:

- The structure is modelled using different type of finite elements to represent each constituents (concrete, tendons, rebars, liner, ...)
- The behaviour of each material is non linear, using specific constitutive law
- Loads are applied in the same order as in reality: body weight, prestressing, internal pressure
- Prestressing is modelled using finite element internal forces. Tendon nodes are separated from the surrounding concrete, which allows their slippage. A friction law determines the profile of prestressing along each tendon. Prestressing is applied as fixed internal load which induces their contraction
- Non linear analyses are performed using Code_Aster (EDF [1]), using a implicit resolution algorithm, linear research resolution technique, geometrical second order effect (large displacements and rotations)
- Results are extracted at specific locations and load intensity, as indicated by the SPE#3 program specification

GEOMETRIC DESCRIPTION

The structure is a ring, corresponding to the cylindrical part of the tested SANDIA mock-up. The following indicates its characteristics.

Table B 1. Geometrical characteristics of the model

Concrete cylinder wall		
Internal radius	m	5.375
External radius	m	5.700
Vertical height	cm	22.5
Thickness	cm	32.5
Steel liner		
Thickness	mm	1.6
Reinforcement steel rebars		
		13.3
Horizontal outer layer section	cm ² /ml	14.8
Horizontal inner layer section		
Vertical outer layer section	cm ² /ml	9.8
Vertical inner layer section		
Prestressing tendons		
Tendon section	cm ² /tendon	3.393

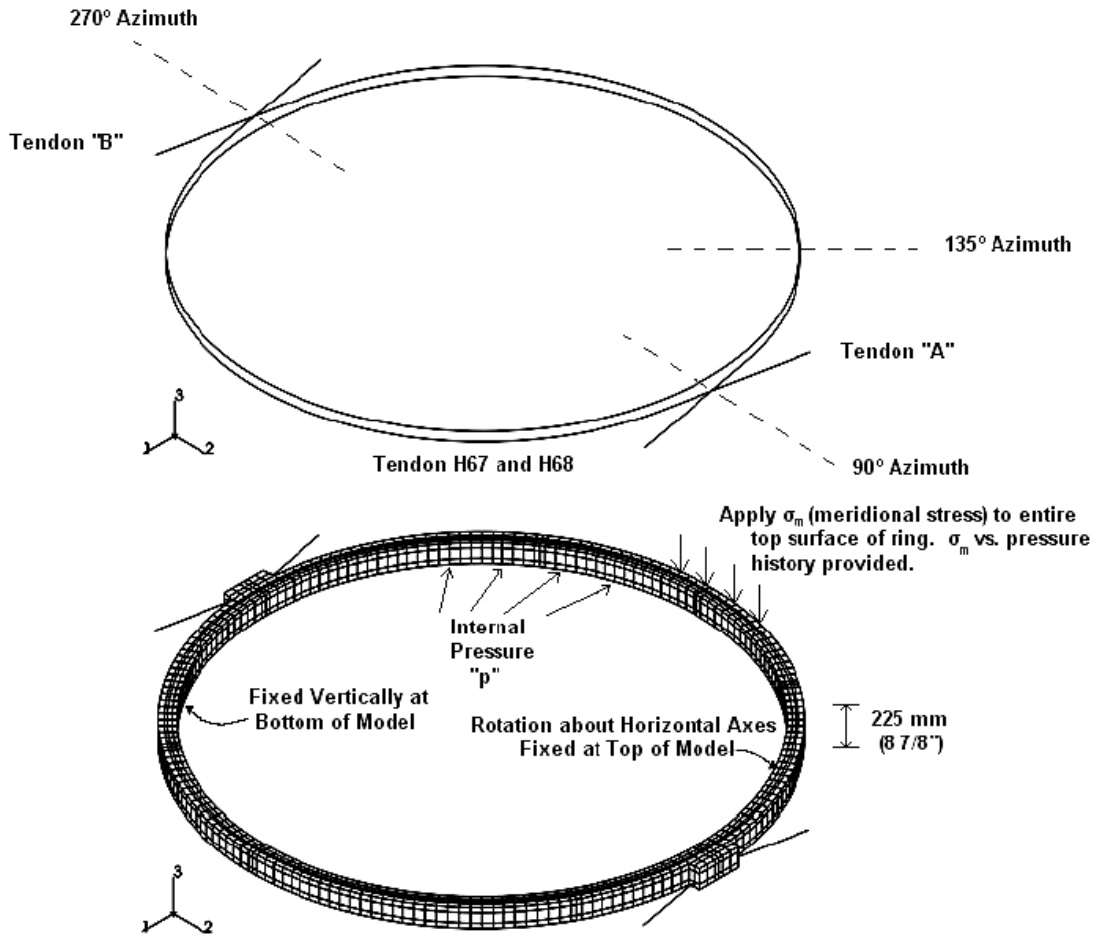


Figure B 1. Geometrical characteristics of the model

DESCRIPTION OF THE FINITE ELEMENT MODEL

Each constituent of the model is represented by different type of finite elements. The following Table B indicates their characteristics, as well as their material behaviour model:

Table B 2. Different mesh groups in the model

Constituent	Mesh group	FE	Behaviour law	Material name
Concrete cylinder wall	JUPE	Linear 8-node hexahedral solid element	Non-linear damage mechanics	BETON (EIB)
Concrete buttress	NERV_D NERV_G	Linear 8-node hexahedral solid element	Linear elastic	BETON (ELAS)
Steel liner	INT	Linear 4-node quadrangle shell element with uniaxial ⁽¹⁾ behaviour One element for hoop and one for vertical direction	Non-linear elasto-plastic	ACILI
Reinforcement steel rebars				
- Horizontal outer layer	ARMAEXTH	Linear 4-node quadrangle shell element with uniaxial behaviour	Non-linear elasto-plastic	ACIRN_H
- Horizontal inner layer	ARMAINTH			
- Vertical outer layer	ARMAEXTV	Linear 4-node quadrangle shell element with uniaxial behaviour	Non-linear elasto-plastic	ACIRN_V
- Vertical inner layer	ARMAINTV			
Prestressing Tendon	CB_67 CB_68	Linear 2-node truss element	Non-linear elasto-plastic	ACIPR

(1) Using two uniaxial shell elements is equivalent to an orthotropic element, with no interaction between the two directions. This is obviously not a natural choice, since liner behaviour is realistically represented by a classical shell element. Our choice was dictated by the FE code, since classical shell element is not compatible with large displacement (2nd order effect) algorithm essential for these analyses.

MATERIAL PROPERTIES AND CONSTITUTIVE MODELS

The various materials used in the finite element model and their properties are shown below.

Table B 3. List of material characteristics

Material model	Constituent	Mesh group	Characteristics		Value	Unit
BETON (EIB)	Concrete cylinder wall	JUPE	Young' modulus	E	26 900	MPa
			Poisson ratio	ν	0,21	-
			Density	ρ	2 176	kg/m ³
			Tensile strength	σ_t	2.4	MPa
			Linear post-pic softening modulus ⁽¹⁾	E _D	-1000	MPa
Behaviour law: Non linear damage model ENDO_ISOT_BETON Parameters: SYT = 2.4E6 , D_SIGM_EPSI = -1.0e9						
BETON (ELAS)	Buttress	NERV_D NERV_G	Young' modulus	E	26 900	MPa
			Poisson ratio	ν	0,21	-
			Density	ρ	2 176	kg/m ³
Behaviour law: Linear elastic model						
ACILI	Liner	INT	Young' modulus	E	210 000	MPa
			Poisson ratio	ν	0,3	-
			Density	ρ	7 850	kg/m ³
			Tensile Yield strength	σ_t	400	MPa
			Plastic hardening modulus	E _p	700	MPa
Behaviour law: Non linear elasto-plastic GRILLE_ISOT_LINE Parameters: SY= 370.0E6 , D_SIGM_EPSI = 927.0E6						
ACIRN_H	Rebar	ARMAEXTH ARMAINTH ARMAEXTV ARMAINTV	Young' modulus	E	185 000	MPa
			Poisson ratio	ν	0,3	-
			Density	ρ	7 850	kg/m ³
			Tensile Yield strength	σ_t	445	MPa
			Plastic hardening modulus	E _p	1 250	MPa
Behaviour law: Non linear elasto-plastic GRILLE_ISOT_LINE Parameters: SY= 445.0E6 , D_SIGM_EPSI = 1250.0E6						
ACIRN_V	Rebar	ARMAEXTH ARMAINTH ARMAEXTV ARMAINTV	Young' modulus	E	185 000	MPa
			Poisson ratio	ν	0,3	-
			Density	ρ	7 850	kg/m ³
			Tensile Yield strength	σ_t	460	MPa
			Plastic hardening modulus	E _p	1350	MPa
Behaviour law: Non linear elasto-plastic GRILLE_ISOT_LINE Parameters: SY= 460.0E6 , D_SIGM_EPSI = 1350.0E6						

ACIPR	Prestressing Tendon	CB_67 CB_68	Young' modulus	E	191 000	MPa
			Poisson ratio	ν	0.3	-
			Density	ρ	7 850	kg/m ³
			Tensile Yield strength	σ_t	1 750	MPa
			Plastic hardening modulus	E_p	3 350	MPa
			Guaranteed ultimate tensile strength	f_{prg}	1 857	MPa
				ν	0.21	-
			Coefficient of friction	k	0.001	-
			Coefficient for wave effect	Δs	3.95	mm
			Anchorage slip	T_0	444	kN
			Initial prestressing force			
Behaviour law: Non linear elasto-plastic VMIS_ISOT_LINE						
Parameters: SY= 1750.0E6 , D_SIGM_EPSI = 3350.0E6						

(1) The softening tangent stiffness of concrete was initially estimated at 5 600 MPa, based on the following calculation, taking into account tension stiffening mechanism. However we decided to use the same value as the one from MOFFAT & NICHOL report (1 000 MPa), in order to avoid discrepancy in FEM comparisons.

Hoop rebars diameters $\phi_s = 14$ mm (D13 and D16) and spacing $e = 11.3$ cm, RC cross section $b = 22.5$ cm; $h = 32.5$ cm, Concrete cover $c = 2.6$ cm

Crack spacing $S_{r,max}$ estimated using Eurocode 2:

$$e < 5 (c + \phi_s/2), \text{ therefore } S_{r,max} = c k_3 + k_1 k_2 k_4 \phi_s / \rho_{p,eff}$$

$$\rho_{p,eff} = A_s / A_{c,eff}$$

$$k_1 = 0.8$$

$$k_2 = 1 \text{ (pur tension)}$$

$$k_3 = 3.4$$

$$k_4 = 0.425$$

$$A_s = \text{steel section}$$

$$A_{c,eff} = b \times \min (2.5 (h-d) , h/2) = 0.225 \times (2.5 \times 0.0363, 0.325/2) = 0.0204 \text{ m}^2$$

$$A_s = (13.3+14.8) \times 0.225 \times 10^{-4} / 1.0 = 0.0006 \text{ m}^2$$

$$\rho_{p,eff} = A_s / A_{c,eff} = 0.0006 / 0.0204 = 0.0309$$

$$S_{r,max} = 0.026 \times 3.4 + 0.8 \times 1 \times 0.425 \times 0.014 / 0.0309 = 0.24 \text{ m}$$

$$n = G_f \times 2 \times E / (S_{r,max} \times f_{t2})$$

$n =$ see diagram bellow

$G_f = 150$ j/m² fracture energy

$f_t = 2.4$ MPa tensile strength

$E = 26\,900$ MPa Young's modulus

$$n : 150 \times 2 \times 26\,900 \times 10^6 / (0.24 \times (2.4 \times 10^6)^2) = 5.8$$

$$E_{\text{softening}} = -E / (n-1) = -26\,900 / (5.8-1) = 5\,604 \text{ MPa}$$

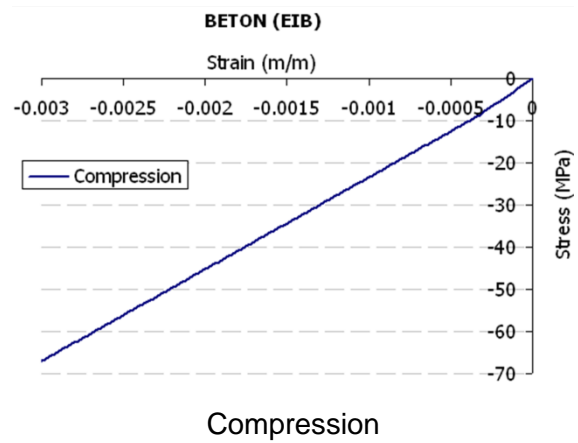
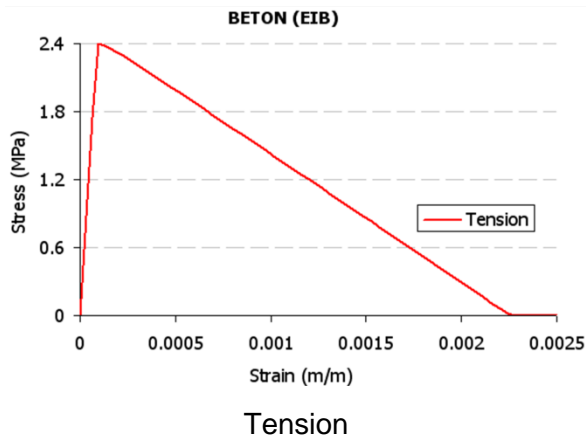
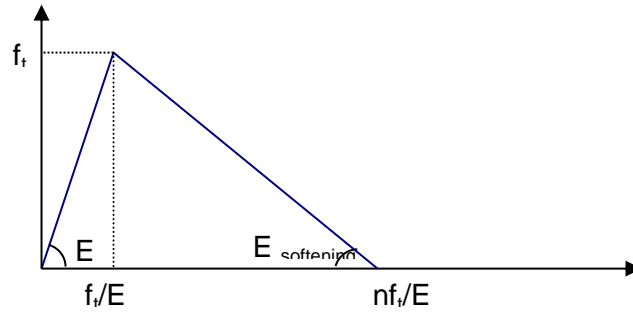


Figure B 2. Concrete damage model. Uniaxial stress/strain behaviour

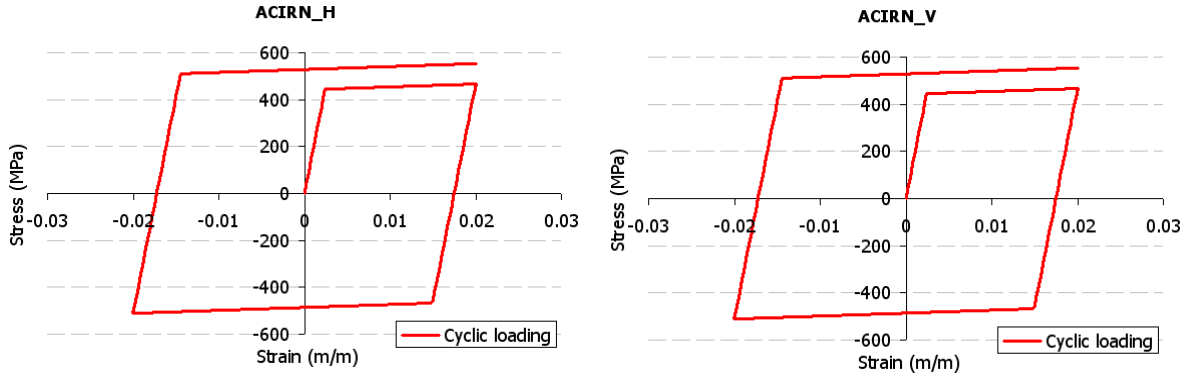


Figure B 3. Reinforcement horizontal and vertical rebar steel model. Uniaxial stress/strain behaviour. Cyclic loading

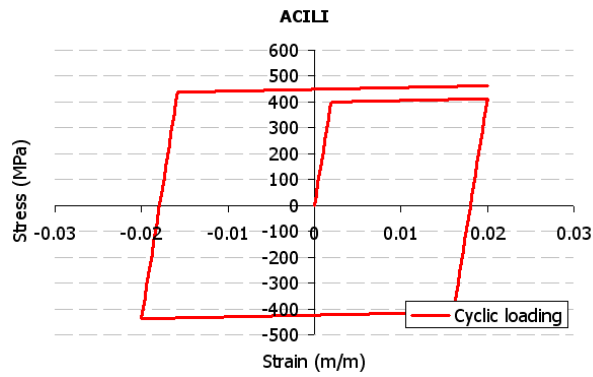


Figure B 4. Liner steel model. Uniaxial stress/strain behaviour. Cyclic loading

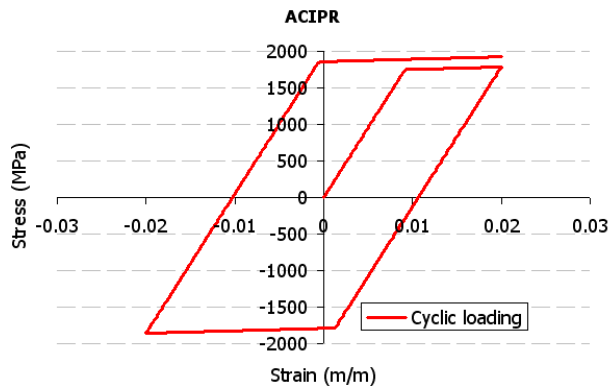
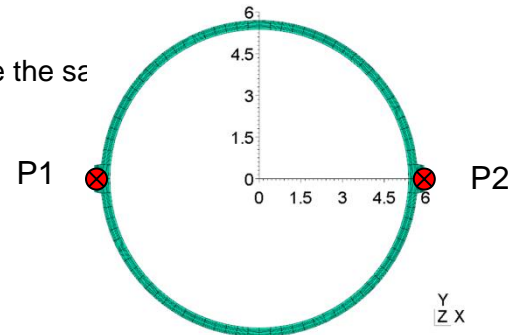


Figure B 5. Tendon steel model. Uniaxial stress/strain behaviour. Cyclic loading

LOADING AND BOUNDARY CONDITIONS

Boundary conditions:

- Top surface remains horizontal: all DOF of the top surface have the same ϵ
- No vertical movements of the bottom surface: $U_z = 0$
- Constrained rigid body motions:
 - o Point 1 ($X = -$ external radius , $Y = 0.0, Z = 0$):
 - $U_Y = 0$
 - o Point 2 ($X = +$ external radius , $Y = 0.0, Z = 0$):
 - $U_Y = 0$,
 - o Points 1 and 2: $U_{X \text{ Point 2}} = - U_{X \text{ Point 1}}$



Load cases:

Body weight	<p><u>Structural elements:</u> Automatically calculated by the program using mesh and density.</p> <p>The rest of the upper part of the reactor building is represented by a vertical pressure applied on the top surface of the model:</p> <p style="text-align: right;">$p_{DL} = 0.16 \text{ MPa}$</p>																				
Prestressing	<p><u>Vertical prestressing:</u> Represented by a vertical pressure applied on the top surface of the model:</p> <p style="text-align: right;">$p_{VP} = 6.86 \text{ MPa}$</p> <p><u>Horizontal prestressing:</u> Represented by internal forces applied to truss elements corresponding to 2 tendons</p> <p style="text-align: right;">$F_{HP} = 444 \text{ kN per jack}$ (see §0 for more details)</p>																				
Internal pressure	<p><u>Increasing pressure applied on the inner surface of the model:</u></p> <p style="text-align: right;">$p_{int} = \text{from } 0 \text{ to } 1.4 \text{ MPa}$</p> <table border="1" style="margin-left: auto; margin-right: auto;"> <thead> <tr> <th>x pd</th> <th>MPa</th> </tr> </thead> <tbody> <tr><td>0,0</td><td>0,00</td></tr> <tr><td>1,0</td><td>0,39</td></tr> <tr><td>1,5</td><td>0,59</td></tr> <tr><td>2,0</td><td>0,78</td></tr> <tr><td>2,5</td><td>0,98</td></tr> <tr><td>3,0</td><td>1,17</td></tr> <tr><td>3,3</td><td>1,29</td></tr> <tr><td>3,4</td><td>1,33</td></tr> <tr><td>3,6</td><td>1,40</td></tr> </tbody> </table> <p style="text-align: right;">(1 $p_D = 0.39 \text{ MPa}$) (2.56 $p_D = 1 \text{ MPa}$)</p> <p><u>Increasing pressure applied on the top surface of the model:</u></p> <p style="text-align: right;">$p_{int-top} = -p_{int} \times 8.27 \text{ MPa}$</p>	x pd	MPa	0,0	0,00	1,0	0,39	1,5	0,59	2,0	0,78	2,5	0,98	3,0	1,17	3,3	1,29	3,4	1,33	3,6	1,40
x pd	MPa																				
0,0	0,00																				
1,0	0,39																				
1,5	0,59																				
2,0	0,78																				
2,5	0,98																				
3,0	1,17																				
3,3	1,29																				
3,4	1,33																				
3,6	1,40																				

TENDON AND PRESTRESSING MODEL

Tendons are represented by truss elements, separated from the concrete. When a concrete node and a tendon node are positioned at the same location in space, they are connected to each other through a friction element, and two kinematic equations. They allow longitudinal displacement of tendon in its duct, and disable any lateral movements.

Where ever tendon and concrete nodes do not overlap, a node located at the same coordinates to the tendon node is created and connected to concrete by kinematic constrains. Again friction element and lateral kinematic equation are added to represent the tendon/duct interaction.

In this way, a tendon can slide over the concrete, depending on the characteristics of the friction element. Friction forces are calculated by the non-axial force components at tendon nodes.

Figure B 6 is a schematic diagram of the sliding surface between the friction element, which transmits frictional force between the tendon and the reinforced concrete skeleton. The friction element, which connects the tendon to the reinforced concrete skeleton, consists of 3 axial springs, which transmit frictional force as well as normal stress. The first spring is in tendon's slide direction and the two other springs are oriented perpendicular to the tendon's slide direction. The frictional force is calculated using Coulomb's Law.

Figure B 7 and Figure B 8 show the stress-displacement relationship of the friction element, represented by an elastic perfectly plastic evolution law. The initial stiffness is relatively high. Normal stress needed for the calculation of friction force is obtained by the other two spring elements.

Prestressing is applied as internal forces. The distribution of the initial prestressing is evaluated by a classical formula (BPEL, French prestressed structures standard). Once friction elements are activated in the model, any further evolution in prestressing may create slippage and thus stress evolution.

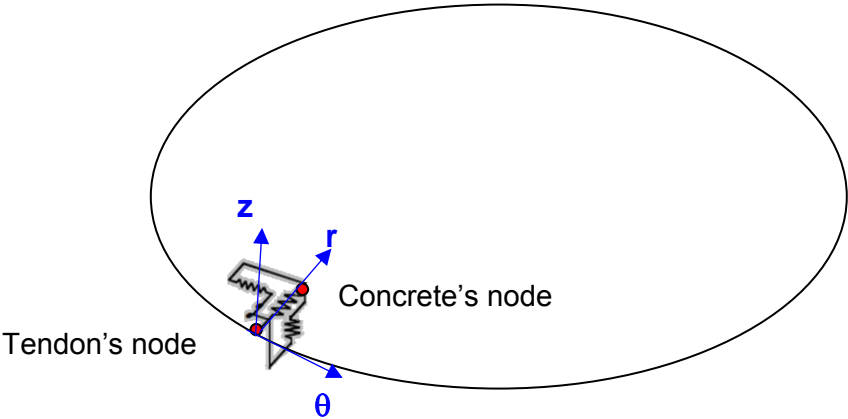


Figure B 6. Tendon friction element

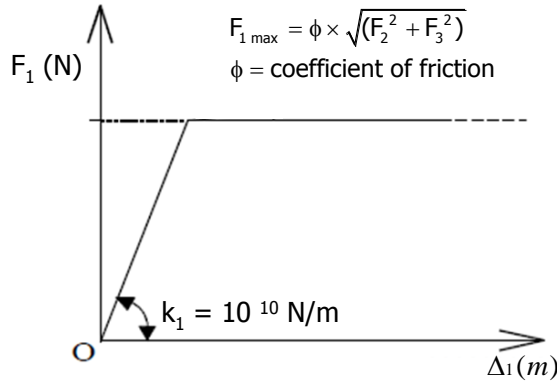


Figure B 7. Slip and friction force, model

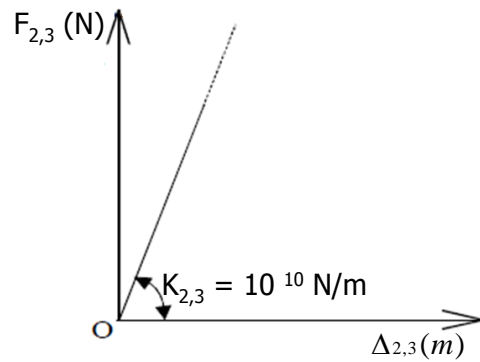


Figure B 8. Lear elastic spring elements for other perpendicular directions to tendon

RESULT ANALYSIS

Table Bau 4. Results summary

Time	Results	Pressure	
		(MPa)	P _d
1	Concrete Hoop Stress (at 135° azimuth) Equals Zero	0.57	1.5
2	Concrete Hoop Cracking Occurs (at 135° azimuth)	0.78	2.0
3	Tendon A Reaches 1% Strain (at 135° azimuth)	1.31	3.4
4	Tendon B Reaches 1% Strain (at 135° azimuth)	1.31	3.4
5	Tendon A Reaches 2% Strain (at 135° azimuth)	1.33	3.4
6	Tendon B Reaches 2% Strain (at 135° azimuth)	1.33	3.4

Results presented in this report are:

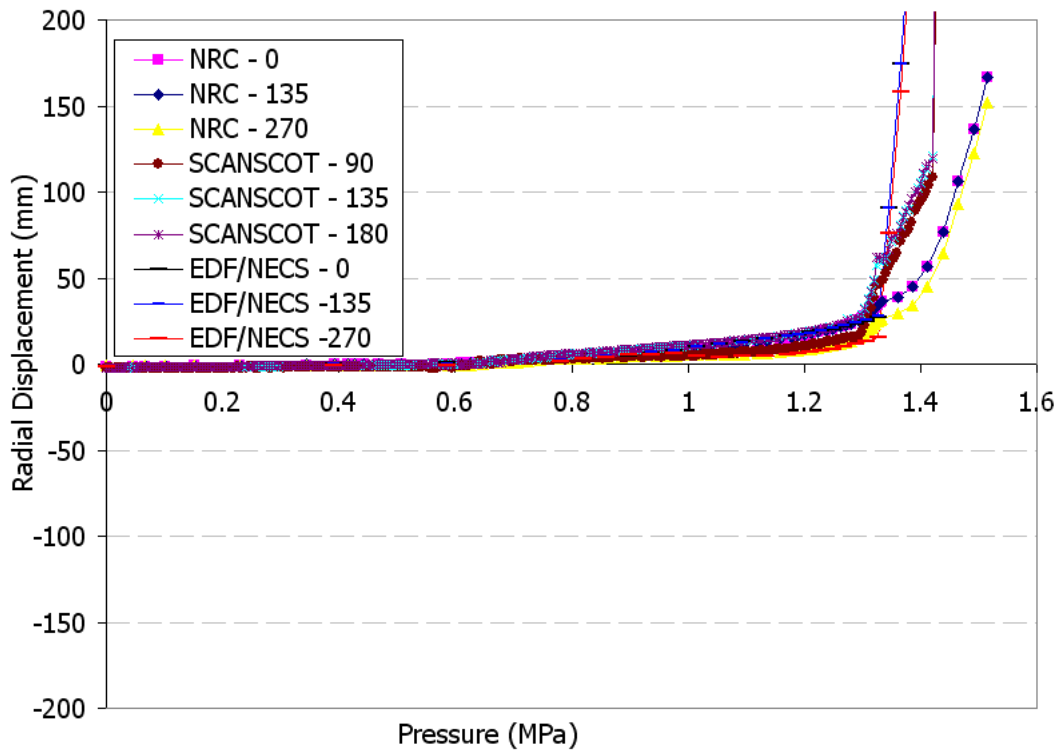
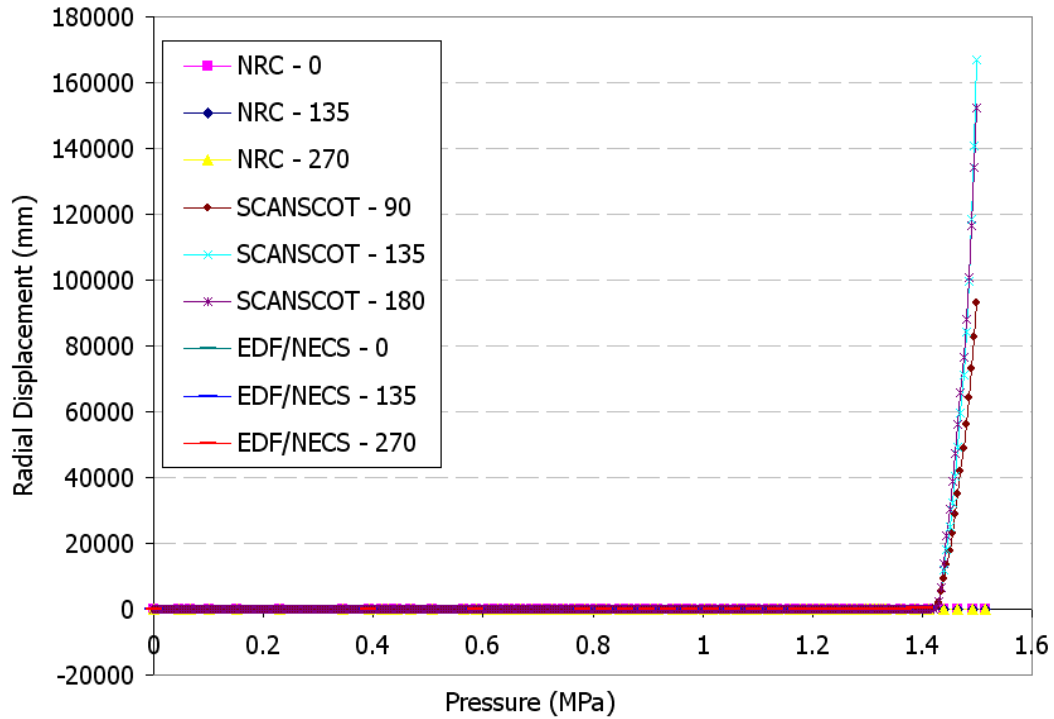
- Deflection of the model at several internal pressure values
- Tendon stress distribution at different load steps
- Tendons' strain evolutions at azimuth 135° at different load steps
- Concrete radial displacement at azimuths 0°, 135°, 270° at different load steps
- Concrete damage index mapping at different load steps
- Tendon / concrete slippage at different load steps

Deflection of the model for different load steps

These plots indicate the shape of the ring model at different internal pressure values.

From these results we can draw the following observations:

- At the beginning, due to the prestressing, the vessel is deflected towards the centre
- It is at 1.5 pd that the deflection reaches back the initial geometrical state of the model
- Buttresses were kept linear elastic to avoid local damaging caused by tendon anchorages. Different analyses with nonlinear buttresses indicate very little change in results, however computation costs tend to increase significantly
- Compared to experimental measures (see Figure B 10) and other analyses results (



- Figure B 11), it appears that the model behaviour is quite consistent at all pressure values. From several sensitivity analyses we conclude that yielding thresholds and post elastic tangent stiffness of tendons and rebars have great influences on the rapid increase in deflections and strains.

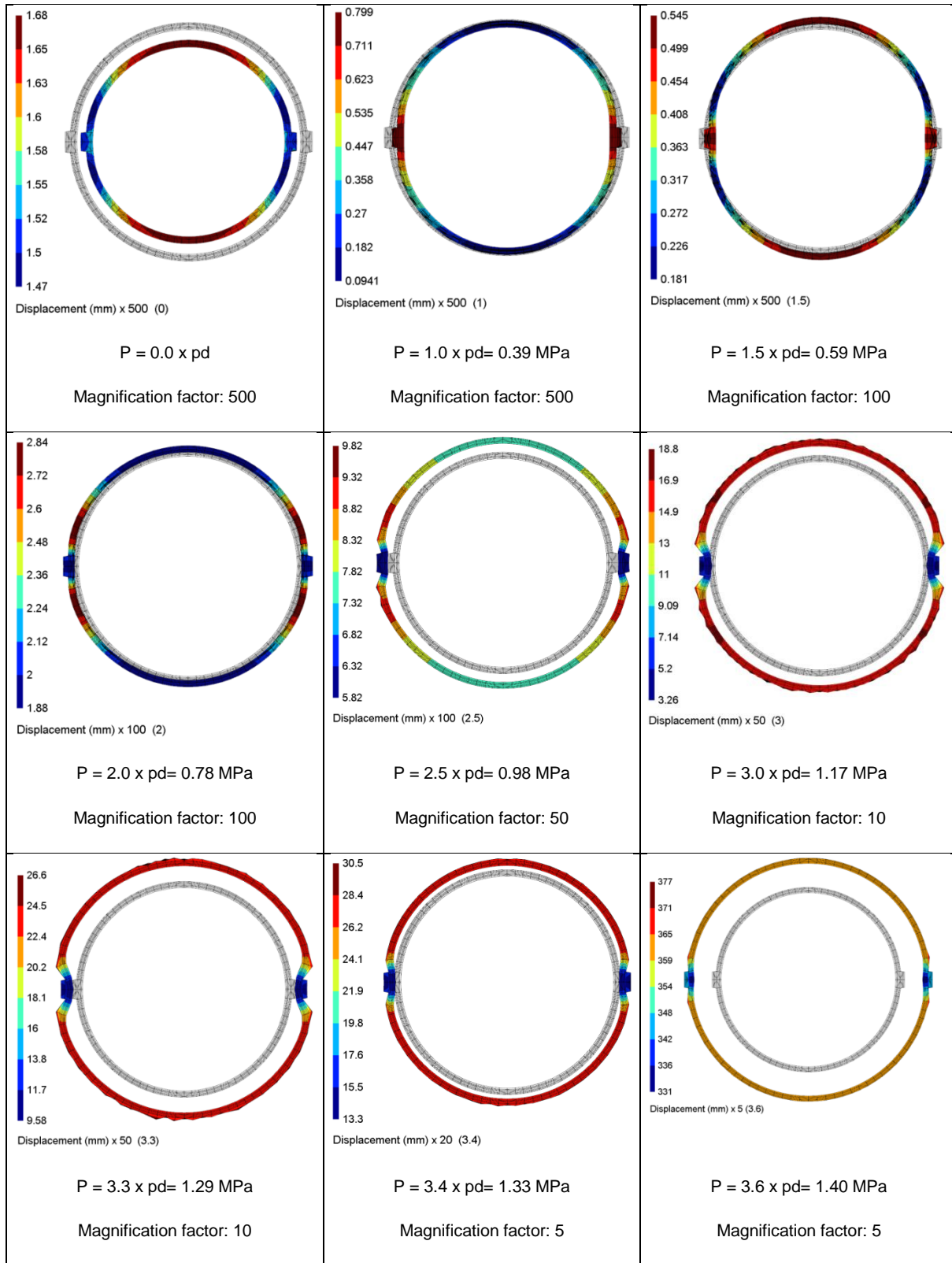


Figure B 9. Deformed shape at different pressures

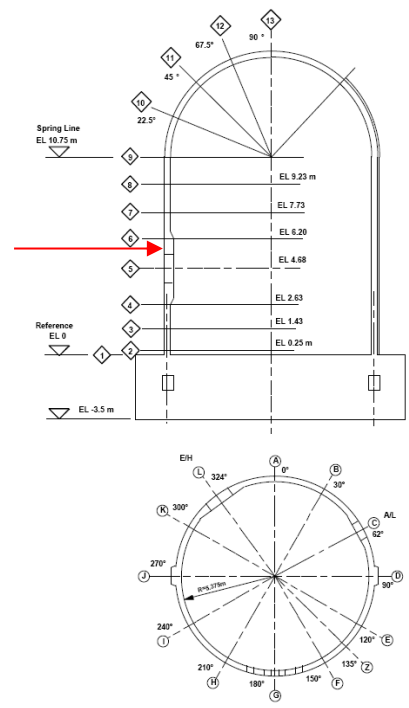
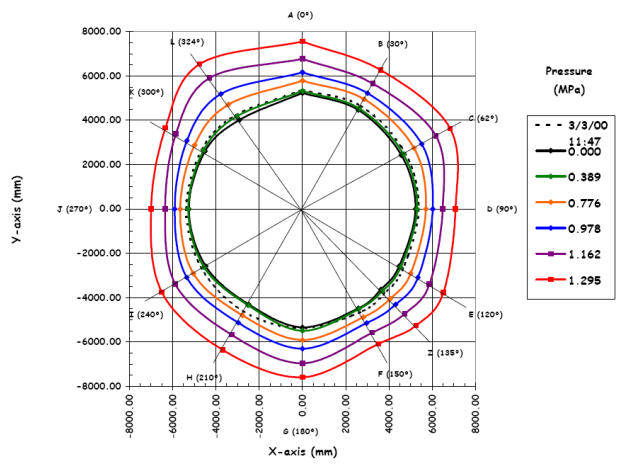


Figure B 10. Experimentally measured deflection of the containment wall LST, observation at elevation 4680 (5) x 100 (from NUREG/CR-6810 SAND2003-0840P, pp 5-40)

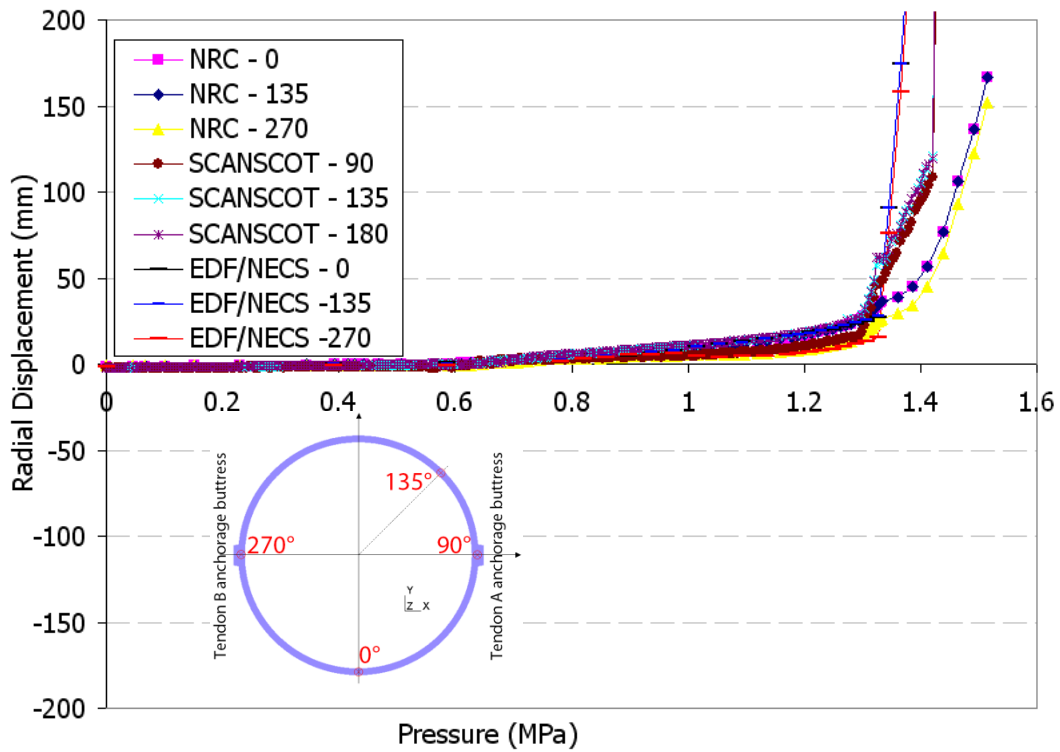
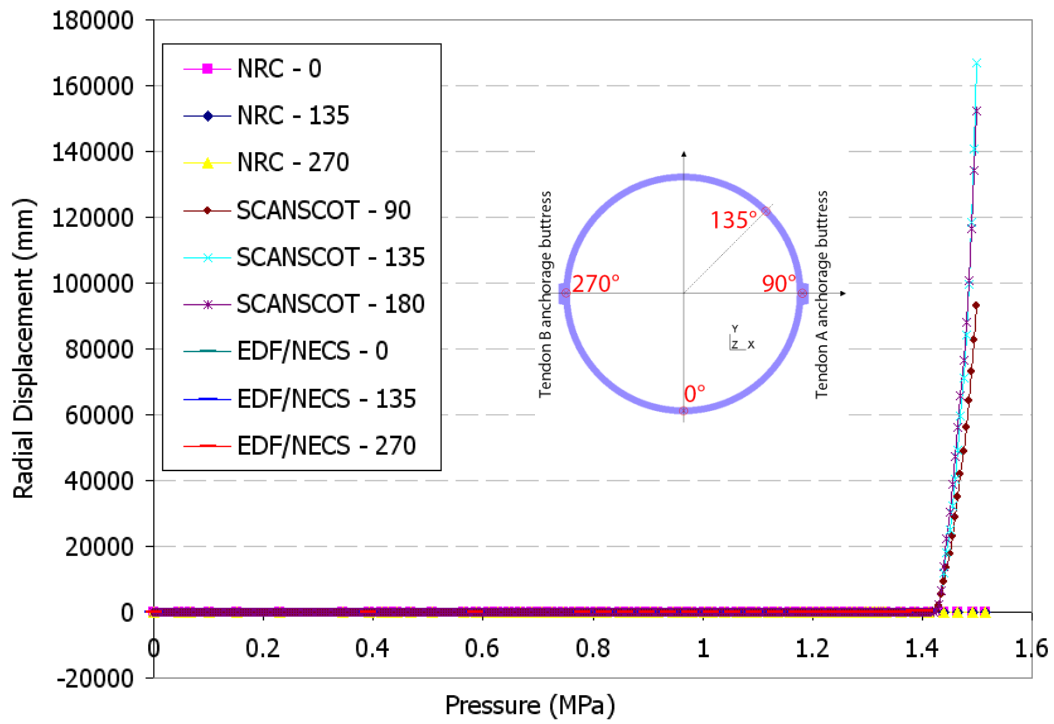


Figure B 11. Concrete radial displacement at azimuths 0°, 135°, 270° at different load steps full range and zoom

Tendon stress distribution at different load steps

The following plot indicates the evolution of tendon B stress as the internal pressure increases. Simulation results are compared to measures recorded during the test. From these plots we can observe:

- that the initial stress state of the tendon is quite standard and close to the measures made on site. However, it should be recalled that the initial state of the model does not encounter for the consequences of age effect (concrete drying, shrinkage, creep, ...).
- that with the raise in internal pressure, the local hoop elongation of concrete and the slippage of tendon, tend to increase the stress, and finally reach a uniform distribution. Local amplifications or reductions can be explained by two phenomena:
 - o at endings where tendon leaves the wall to reach its anchors, the low elongation of the buttress added to the force of friction, tend to lower the raise of stress in tendon (Figure B 12 close to azimuths -270° and 90°). Figure B 13 indicates the slippage of tendon, where we see that they are most active in these areas
 - o where concrete remains elastic in buttresses, elongations are too low to raise the stress in tendon. On Figure B 12 this can be observed at azimuth 90°
 - o close to azimuth 90° buttress, the raise in tendon stress is due to the bending of the wall, clearly visible on Figure B 9. This tends to diminish as the internal pressure raises and damage spreads all around reducing the bending effect

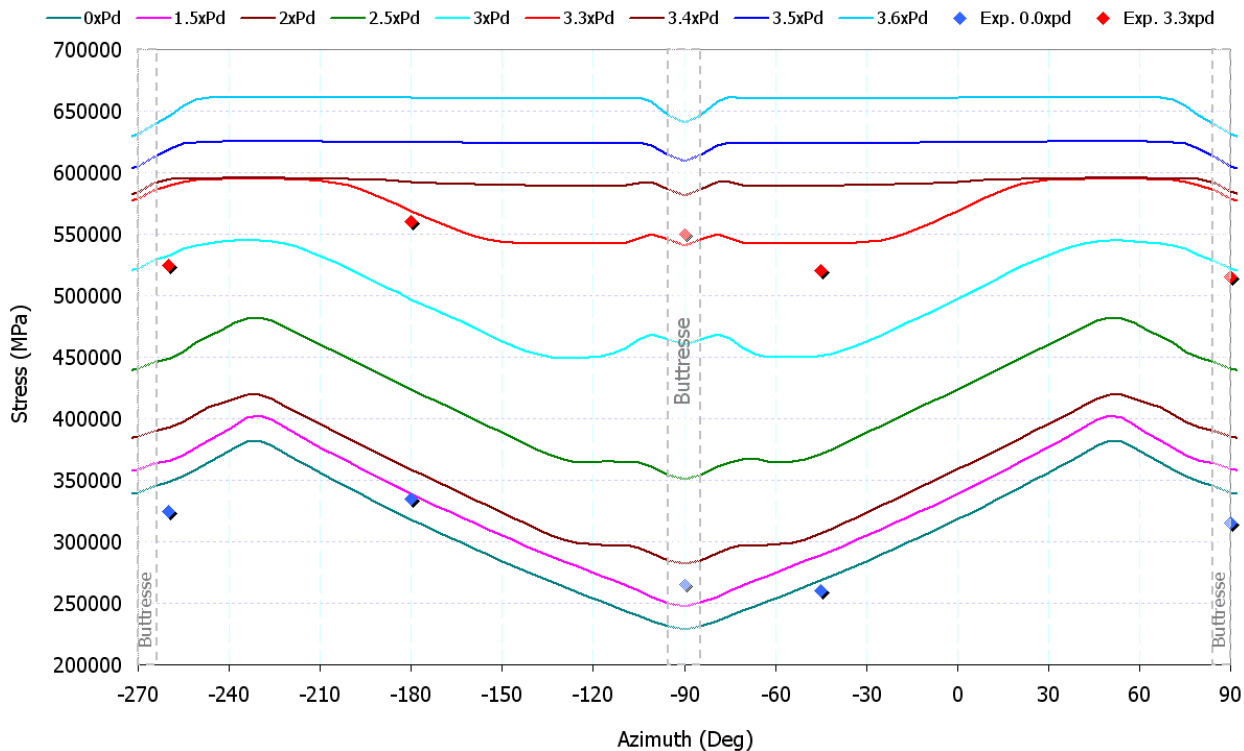


Figure B 12. Tendon B stress distribution at different internal pressure

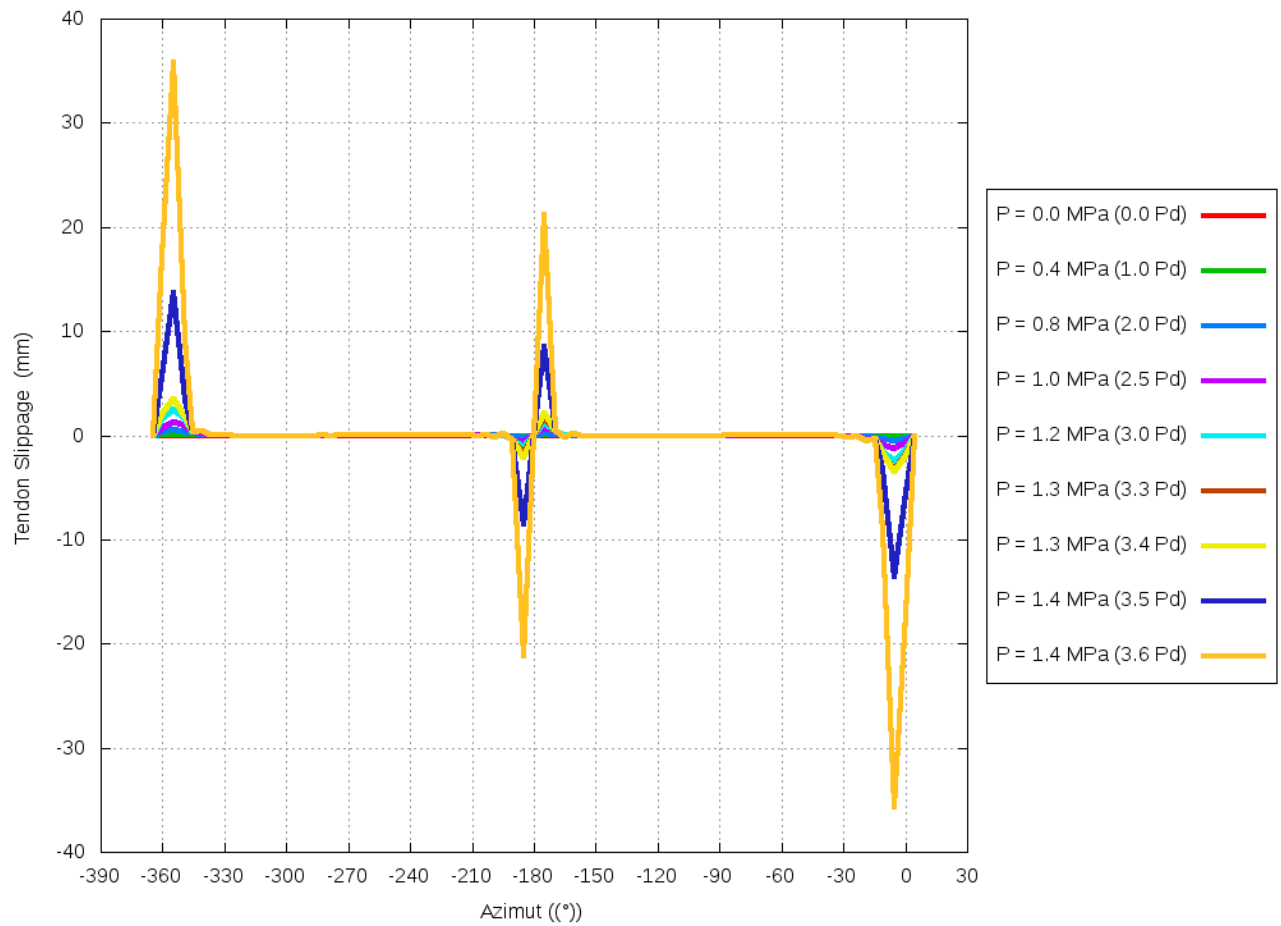
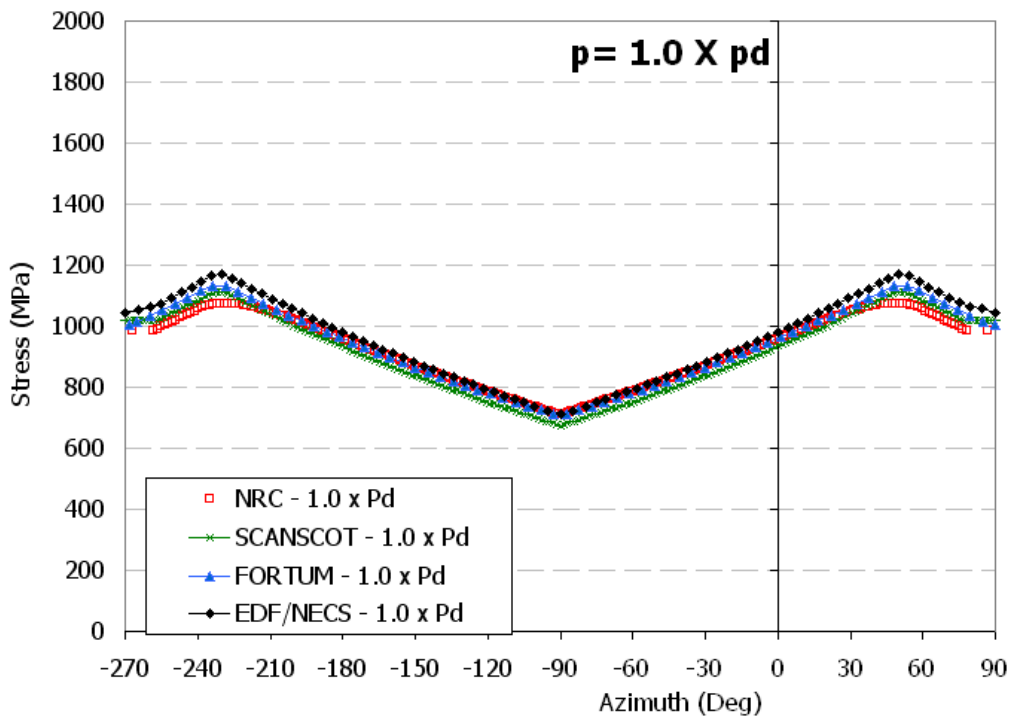
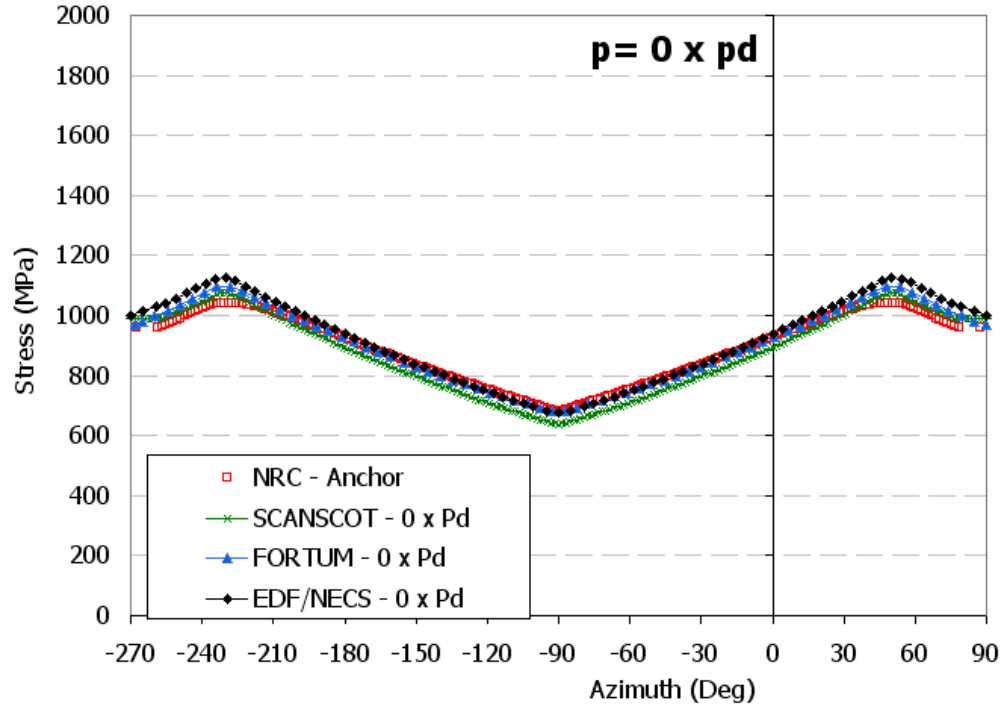
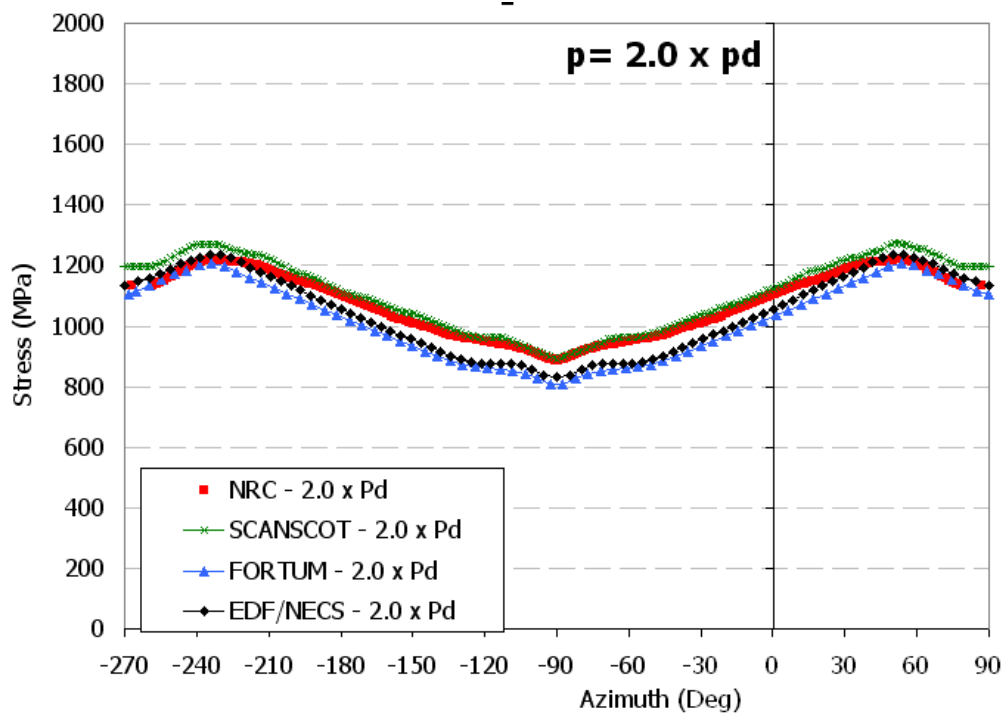
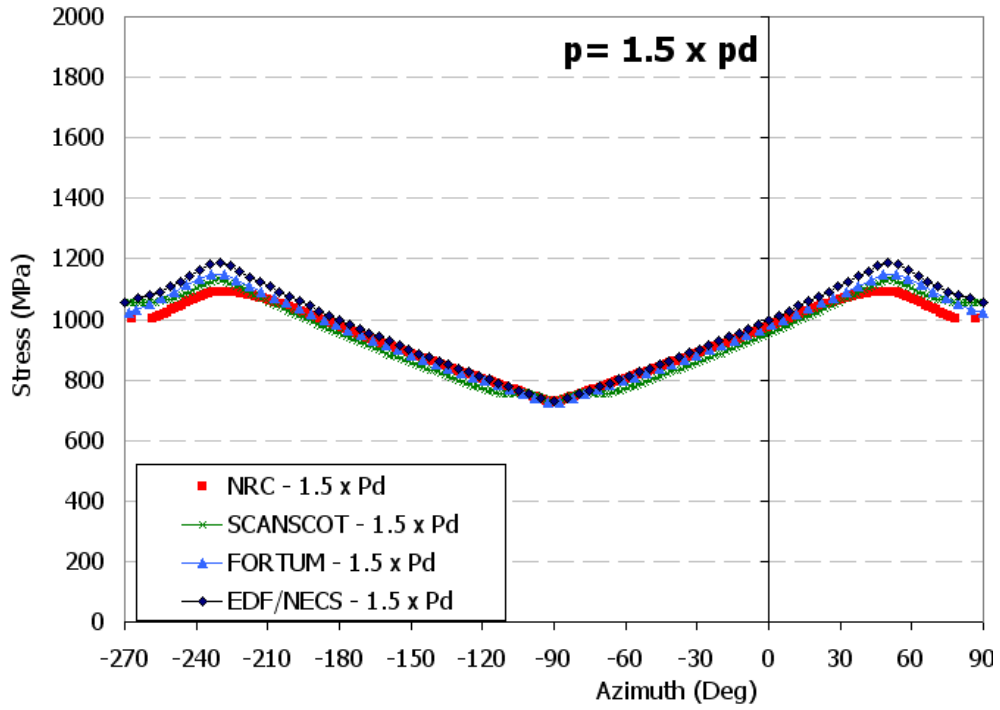
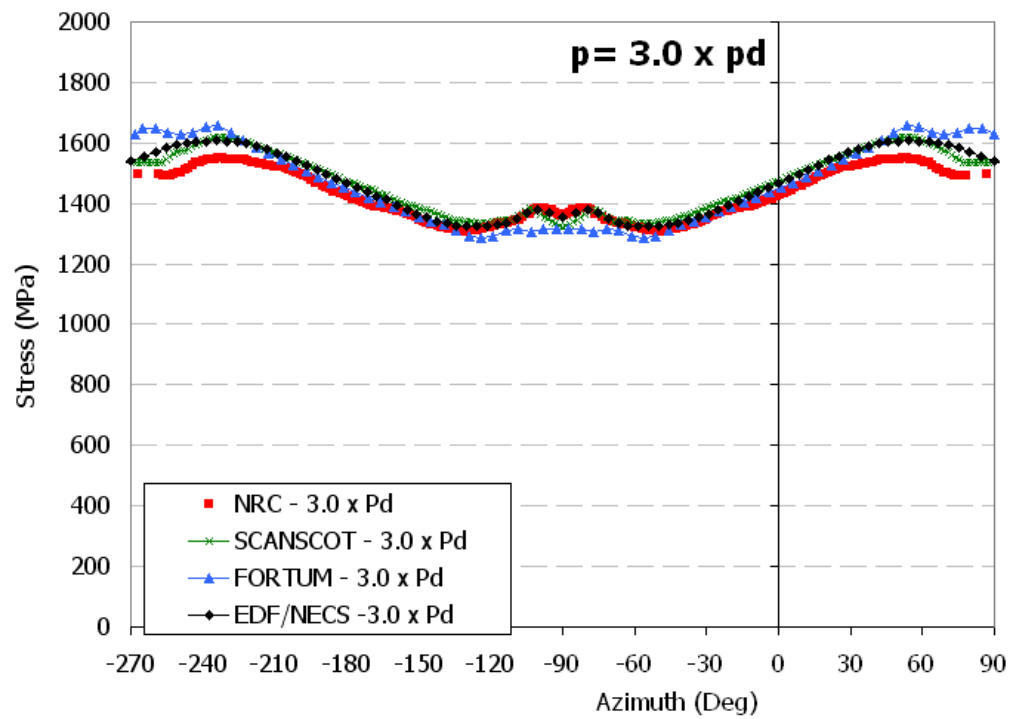
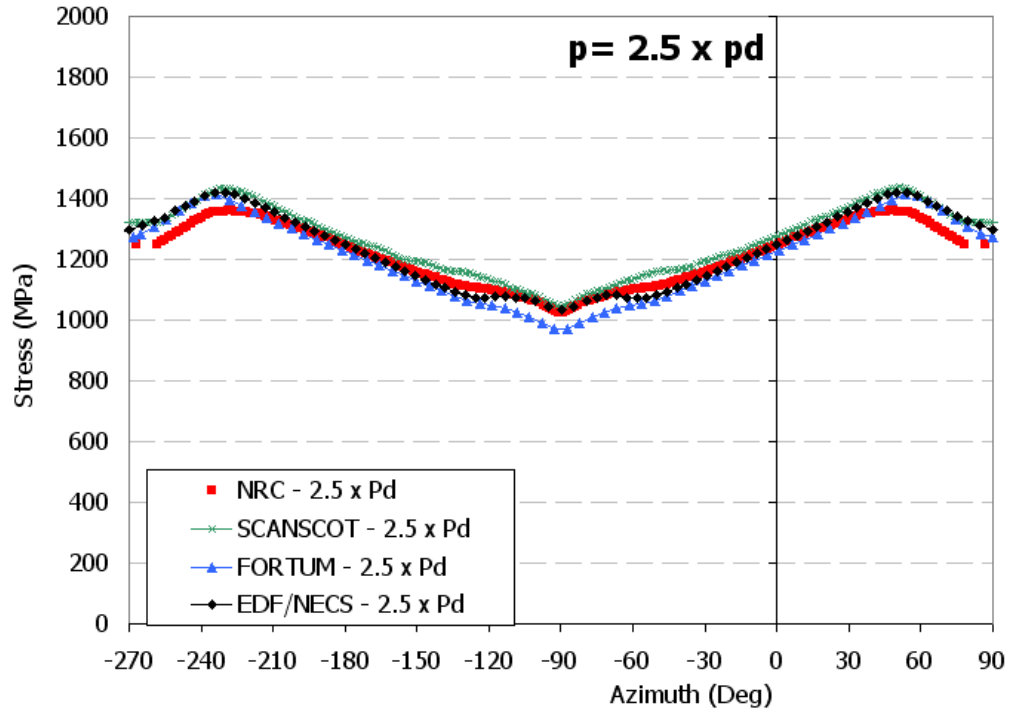


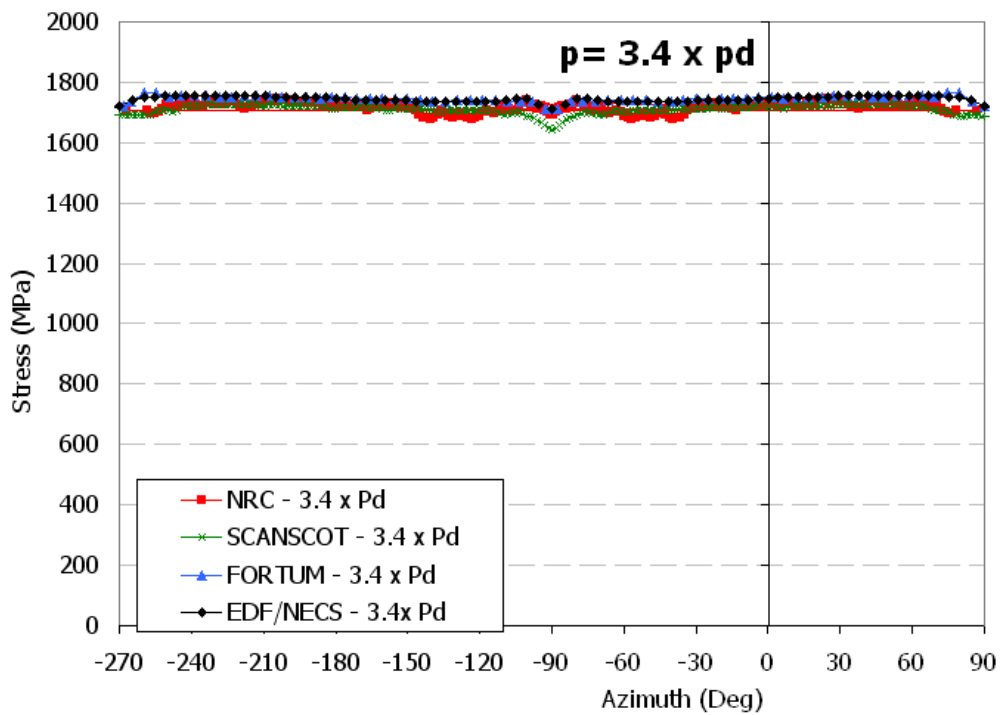
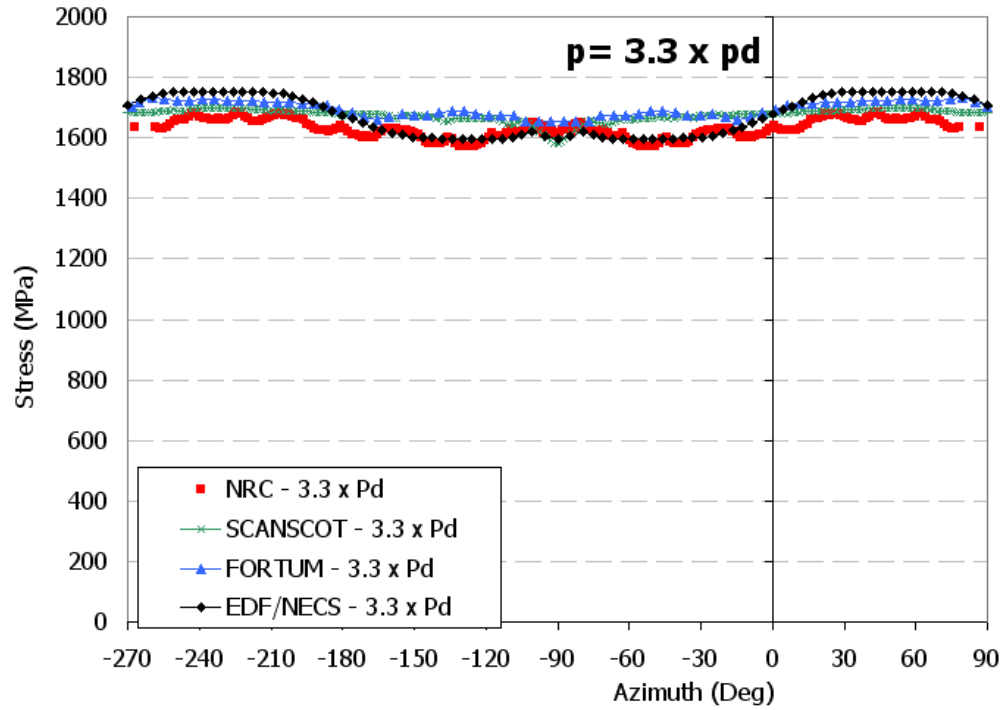
Figure B 13. Tendon Slippage at different pressures

The following plots compare tendon stress results with other analyses performed by other participants of the project.









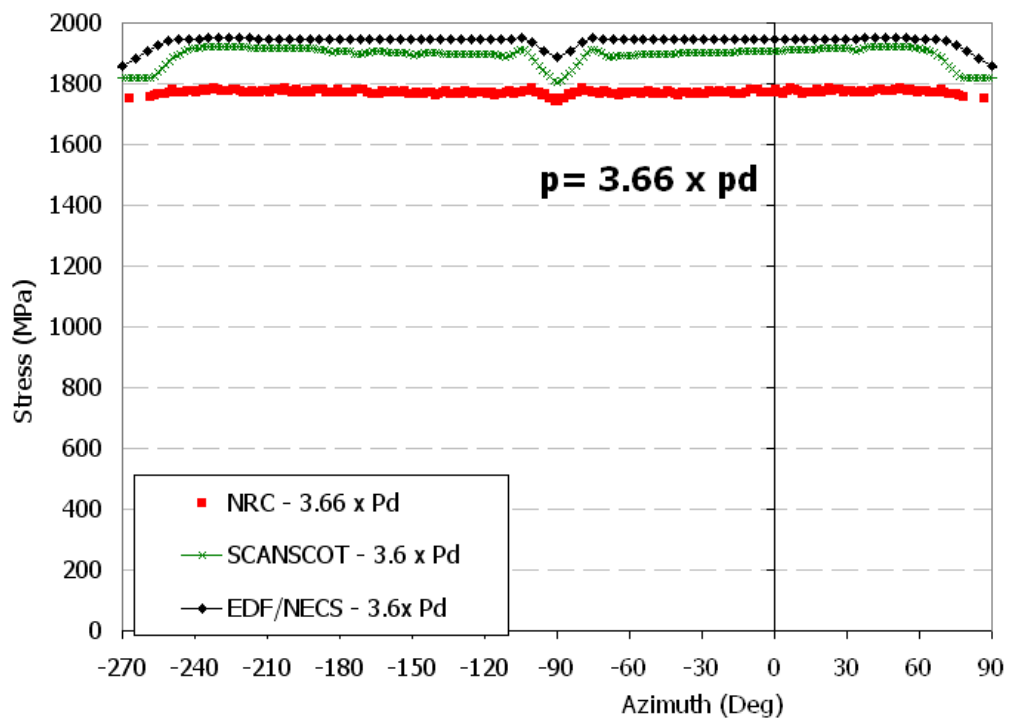
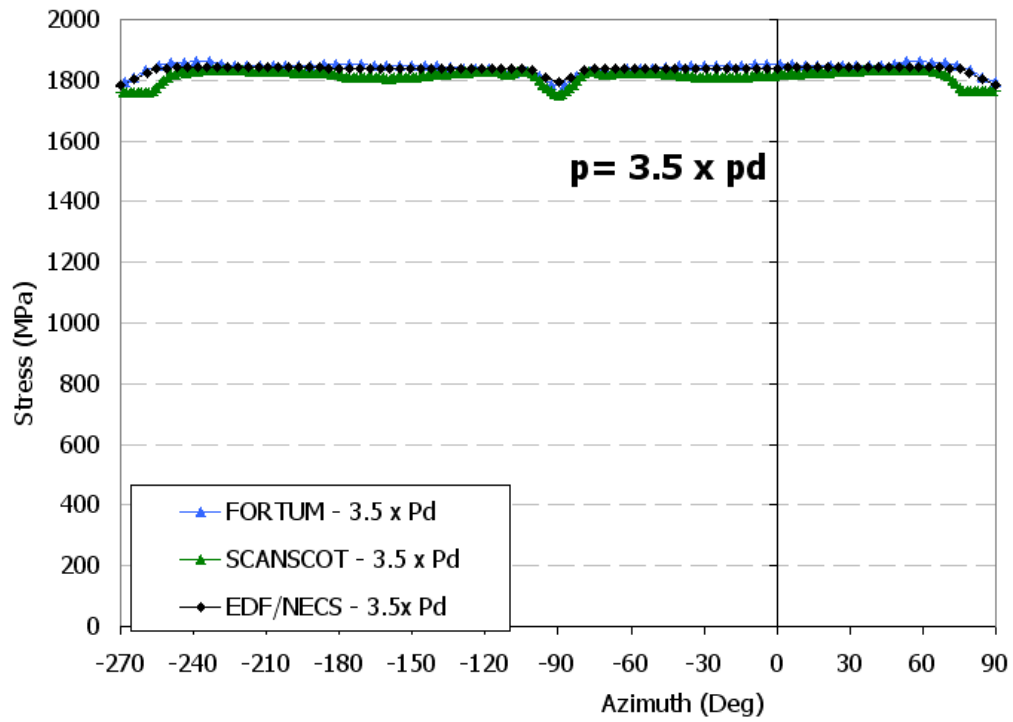
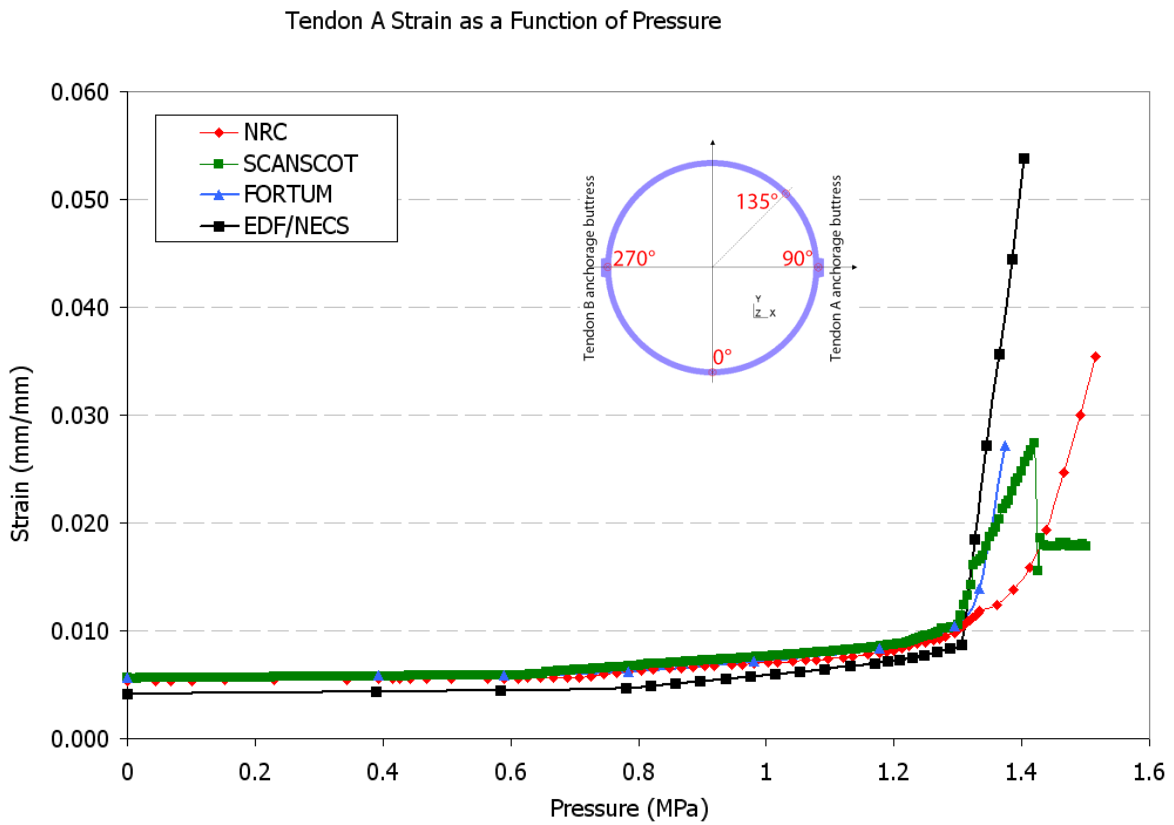


Figure B 14. Tendon Stress Distribution at different pressures. Comparison with other analyses results

Tendons' strain evolutions at azimuth 135° at different load steps



Tendon B Strain as a Function of Pressure

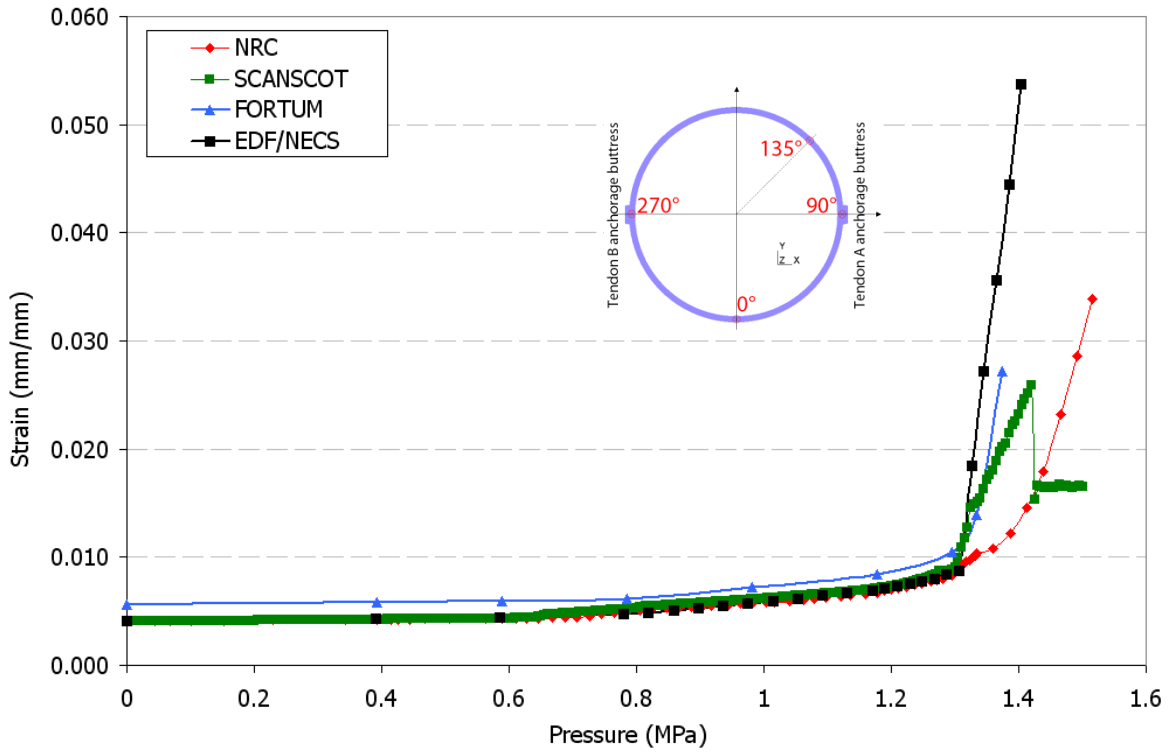
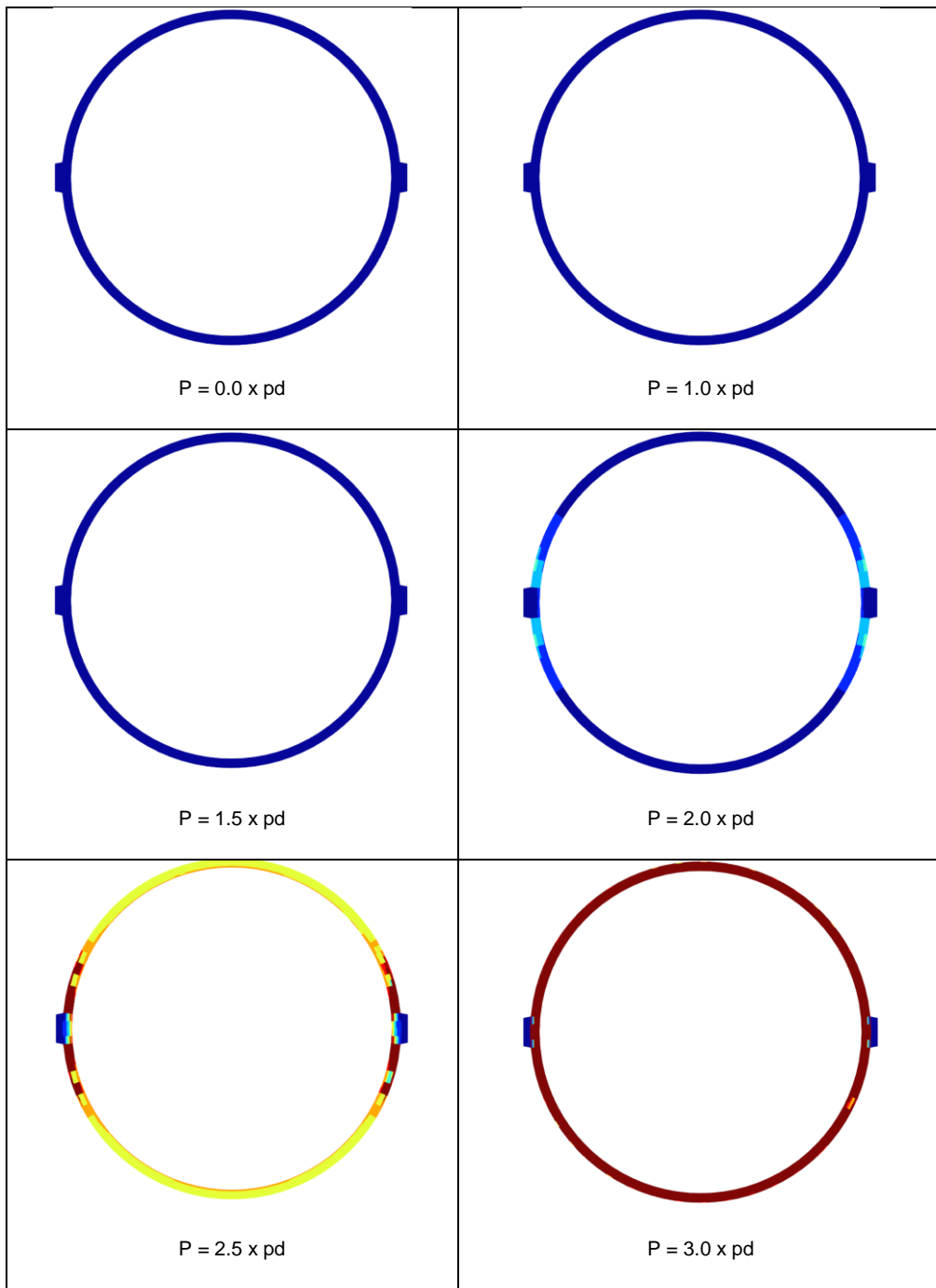
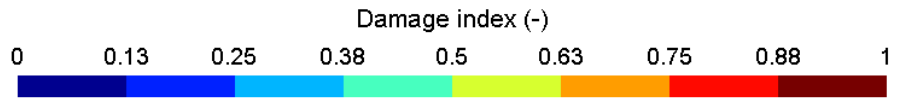


Figure B 16. Tendon B Strain at 135° azimuth versus pressure

Concrete damage index mapping at different load steps

The evolution of damage index of the concrete constitutive law is indicated here bellow. From these graphics we can see that damage initiates around buttress areas, due to the deflection created by the prestressing. Damage then increase in these regions and spreads all over the wall beyond $3 p_d$, except linear elastic portions of buttresses.



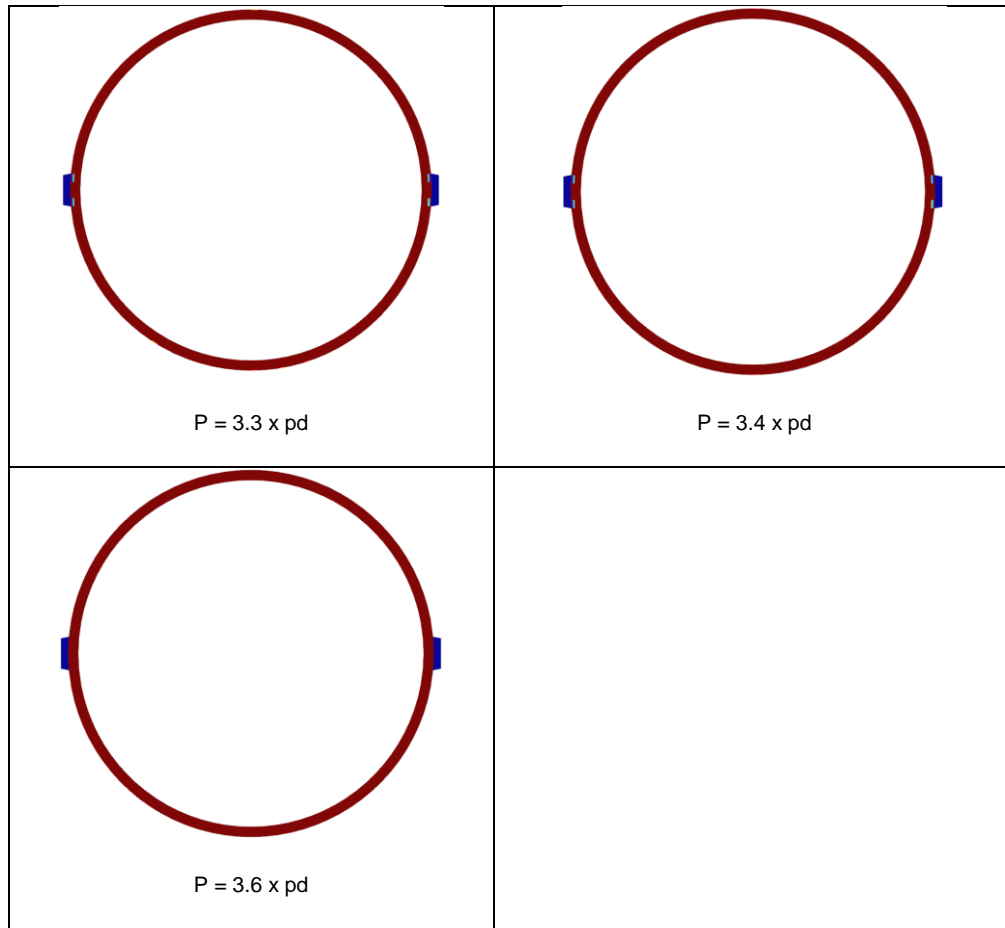


Figure B 17. Concrete damage at different pressures values

CONCLUSIONS

The work carried out in this phase allowed us to elaborate a suiTable B simulation methodology, in order to capture non-linear mechanisms involved in this test case, especially when internal pressure reaches high values above design pressure.

The simulation technique was then validated thanks to comparisons made to both experimental measures and other analysis results from participants of SPE3.

To reach this quality in results, many different strategies were tested, and fruitful lessons learnt. Other phases of SPE3 will be studied using the methodology presented in this report.

REFERENCES

- [1] Code_Aster EDF SA
Thermo-mechanical analysis of structures (www.code_aster.org)

APPENDIX C FORTUM

PCCV SPE3

PHASE 1 SIMULATIONS:

FORTUM LTD

TABLE OF CONTENTS

LIST OF FIGURES	C-5
LIST OF TABLES	C-8
INTRODUCTION	C-9
TENDON BEHAVIOR MODEL	C-10
Model description	C-10
Used code	C-10
FE-model	C-10
Boundary conditions	C-11
Tendon-concrete interaction	C-11
Reinforcement and vertical tendons.....	C-12
Applied load	C-14
Material models	C-15
Concrete	C-15
Tendon steel.....	C-16
Rebar steel	C-17
Liner steel	C-18
Results	C-19
Pressure milestones.....	C-19
Deformed shape.....	C-19
Tendon stress.....	C-24
Discussion	C-25
GLOBAL MODEL	C-26
Model description	C-26
Used code	C-26
FE-model	C-26
Boundary conditions	C-27
Tendon-concrete interaction	C-27
Applied load	C-27
Material models	C-28
Concrete	C-28
Tendon steel.....	C-28
Rebar steel	C-28
Liner steel	C-28
Steel for the patches of the penetrations	C-28
Results	C-28
Response of the model.....	C-28
Displacements.....	C-28
Rebar strains.....	C-36
Liner strains	C-46
Tendon strains and forces	C-53

Peak strains in the liner C-58
Strains near the penetrations..... C-67
Global deformation at failure..... C-68
Discussion C-70
LINER FRACTURE NEAR THE EQUIPMENT HATCH C-70
Model description C-70
Submodeling C-70
Fracture C-71
Results C-72
Discussion C-75
CONCLUSIONS C-75
REFERENCES C-75

LIST OF FIGURES

Figure C 1. Tendon behaviour model. [1]	C-8
Figure C 2. Global model	C-9
Figure C 3. The FE-model. Model 1	C-10
Figure C 4. Tendon-concrete connectors.	C-11
Figure C 5. Slot connector.	C-11
Figure C 6. Rebar layers used to modes the reinforcement and vertical tendons.	C-12
Figure C 7. Rebar layers near azimuths 90° and 270°	C-12
Figure C 8. Measured tendon H53 force distribution. [2]	C-13
Figure C 9. Applied load	C-14
Figure C 10. Stress-strain behaviour of the concrete model.	C-15
Figure C 11. Stress-strain behaviour of the horizontal tendons	C-16
Figure C 12. Stress-strain behaviour of the vertical tendons.	C-16
Figure C 13. Stress-strain behaviour of the reinforcement steel model	C-14
Figure C 14. Stress-strain behaviour of the liner steel model.	C-18
Figure C 15. Deformation (x10) at applied pressure $P = 0.0 \times P_d$	C-20
Figure C 16. Deformation (x10) at applied pressure $P = 1.0 \times P_d$	C-20
Figure C 17. Deformation (x10) at applied pressure $P = 1.5 \times P_d$	C-21
Figure C 18. Deformation (x10) at applied pressure $P = 2.0 \times P_d$	C-21
Figure C 19. Deformation (x10) at applied pressure $P = 2.5 \times P_d$	C-22
Figure C 20. Deformation (x10) at applied pressure $P = 3.0 \times P_d$	C-22
Figure C 21. Deformation (x10) at applied pressure $P = 3.3 \times P_d$	C-23
Figure C 22. Deformation (x10) at applied pressure $P = 3.4 \times P_d$	C-23
Figure C 23. Deformation (x10) at applied pressure $P = 3.5 \times P_d$	C-24
Figure C 24. Force distribution of tendon A in prestressing	C-26
Figure C 25. Stress distribution of tendon A as the pressure increases.	C-26
Figure C 26. The FE-model. Model 3	C-27
Figure C 27. Vertical displacement at Standard output location 1.	C-29
Figure C 28. Radial displacement at Standard output location 2	C-29
Figure C 29. Radial displacement at Standard output location 3	C-30
Figure C 30. Radial displacement at Standard output location 4	C-30
Figure C 31. Radial displacement at Standard output location 5	C-31
Figure C 32. Radial displacement at Standard output location 6	C-31
Figure C 33. Radial displacement at Standard output location 7	C-32
Figure C 34. Vertical displacement at Standard output location 8.	C-32
Figure C 35. Radial displacement at Standard output location 9	C-33
Figure C 36. Vertical displacement at Standard output location 10.	C-33
Figure C 37. Vertical displacement at Standard output location 11.	C-34
Figure C 38. Radial displacement at Standard output location 12	C-34
Figure C 39. Radial displacement at Standard output location 13	C-35
Figure C 40. Radial displacement at Standard output location 14	C-35

Figure C 41. Radial displacement at Standard output location 15.....	C-36
Figure C 42. Rebar strain at Standard output location 16.	C-37
Figure C 43. Rebar strain at Standard output location 17.	C-37
Figure C 44. Rebar strain at Standard output location 18.	C-38
Figure C 45. Rebar strain at Standard output location 19.	C-38
Figure C 46. Rebar strain at Standard output location 20.	C-39
Figure C 47. Rebar strain at Standard output location 21.	C-39
Figure C 48. Rebar strain at Standard output location 22.	C-40
Figure C 49. Rebar strain at Standard output location 23.	C-40
Figure C 50. Rebar strain at Standard output location 24.	C-41
Figure C 51. Rebar strain at Standard output location 25.	C-41
Figure C 52. Rebar strain at Standard output location 26.	C-42
Figure C 53. Rebar strain at Standard output location 27.	C-42
Figure C 54. Rebar strain at Standard output location 28.	C-43
Figure C 55. Rebar strain at Standard output location 29.	C-43
Figure C 56. Rebar strain at Standard output location 30.	C-44
Figure C 57. Rebar strain at Standard output location 31.	C-44
Figure C 58. Rebar strain at Standard output location 32.	C-45
Figure C 59. Rebar strain at Standard output location 33.	C-45
Figure C 60. Vertical liner strain at Standard output location 34.	C-46
Figure C 61. Vertical liner strain at Standard output location 35.	C-47
Figure C 62. Vertical liner strain at Standard output location 36.	C-47
Figure C 63. Hoop liner strain at Standard output location 37.	C-48
Figure C 64. Vertical liner strain at Standard output location 38.	C-48
Figure C 65. Hoop liner strain at Standard output location 39.	C-49
Figure C 66. Vertical liner strain at Standard output location 40.	C-49
Figure C 67. Hoop liner strain at Standard output location 41.	C-50
Figure C 68. Vertical liner strain at Standard output location 42.	C-50
Figure C 69. Vertical liner strain at Standard output location 43.	C-51
Figure C 70. Hoop liner strain at Standard output location 44.	C-51
Figure C 71. Hoop liner strain at Standard output location 45.	C-52
Figure C 72. Hoop liner strain at Standard output location 46.	C-52
Figure C 73. Radial liner strain at Standard output location 47.	C-53
Figure C 74. Tendon strain at Standard output location 48.	C-54
Figure C 75. Tendon strain at Standard output location 49.	C-54
Figure C 76. Tendon strain at Standard output location 50.	C-55
Figure C 77. Tendon strain at Standard output location 51.	C-55
Figure C 78. Tendon strain at Standard output location 52.	C-56
Figure C 79. Tendon strain at Standard output location 53.	C-56
Figure C 80. Tendon force at Standard output location 54.	C-57
Figure C 81. Tendon force at Standard output location 55.	C-57

Figure C 82. Peak strains in the liner at applied pressure $P = 0.0 \times Pd$	C-58
Figure C 83. Peak strains in the liner at applied pressure $P = 1.0 \times Pd$	C-59
Figure C 84. Peak strains in the liner at applied pressure $P = 2.0 \times Pd$	C-60
Figure C 85. Peak strains in the liner at applied pressure $P = 2.5 \times Pd$	C-61
Figure C 86. Peak strains in the liner at applied pressure $P = 3.0 \times Pd$	C-62
Figure C 87. Peak strains in the liner at applied pressure $P = 3.3 \times Pd$	C-63
Figure C 88. Peak strains in the liner at applied pressure $P = 3.4 \times Pd$	C-64
Figure C 89. Peak strains in the liner at applied pressure $P = 3.5 \times Pd$	C-65
Figure C 90. Peak strains in the liner at applied pressure $P = 3.6 \times Pd$	C-66
Figure C 91. Locations 3, 4 and 5 of the E/H.	C-67
Figure C 92. Maximum in-plane principal strain at locations 3, 4 and 5 of the E/H as a function of pressure.	C-67
Figure C 93. Locations 3, 4 and 5 of the A/L.	C-68
Figure C 94. Maximum in-plane principal strain at locations 3, 4 and 5 of the A/L as a function of pressure.	C-68
Figure C 95. Global deformation ($\times 50$) at applied pressure $P = 3.5 \times Pd$	C-69
Figure C 96. Submodel of the E/H	C-71
Figure C 97. Submodel of the E/H and the global model 3.	C-72
Figure C 98. Fracture criterion as a contact property.	C-73
Figure C 99. Crack propagation. $P = 3.034 Pd$. No cracking.	C-73
Figure C 100. Crack propagation. $P = 3.280 Pd$. Crack initiation.	C-74
Figure C 101. Crack propagation. $P = 3.284 Pd$	C-74
Figure C 102. Crack length at $P = 3.284 Pd$	C-75

LIST OF TABLES

Table C 1. Material parameters for concrete.C-14
Table C 2. Material parameters for tendon steel. C-15
Table C 3. Material parameters for reinforcement steel.C-17
Table C 4. Material parameters for the liner steel.C-18
Table C 5. Pressure Milestones..... C-19
Table C 6. Material parameters for the liner steel.C-28

INTRODUCTION

The standard problem exercise on the performance of containment vessels under severe accident conditions [1] studies an overpressurization test of a prestressed concrete containment vessel [2]. The first phase of the exercise focuses on the local effects of the containment. Within phase 1 three models of the containment are examined. The local tendon behaviour is studied with model 1. The model 1 is presented in Figure C 1. Model 2 is a local model of the equipment hatch that focuses on the steel-concrete interface and on the liner tears. Model 3 is a global model of the containment. With model 3 the focus is on the global response of the containment and on the liner tears. The model 3 is presented in Figure C 2.

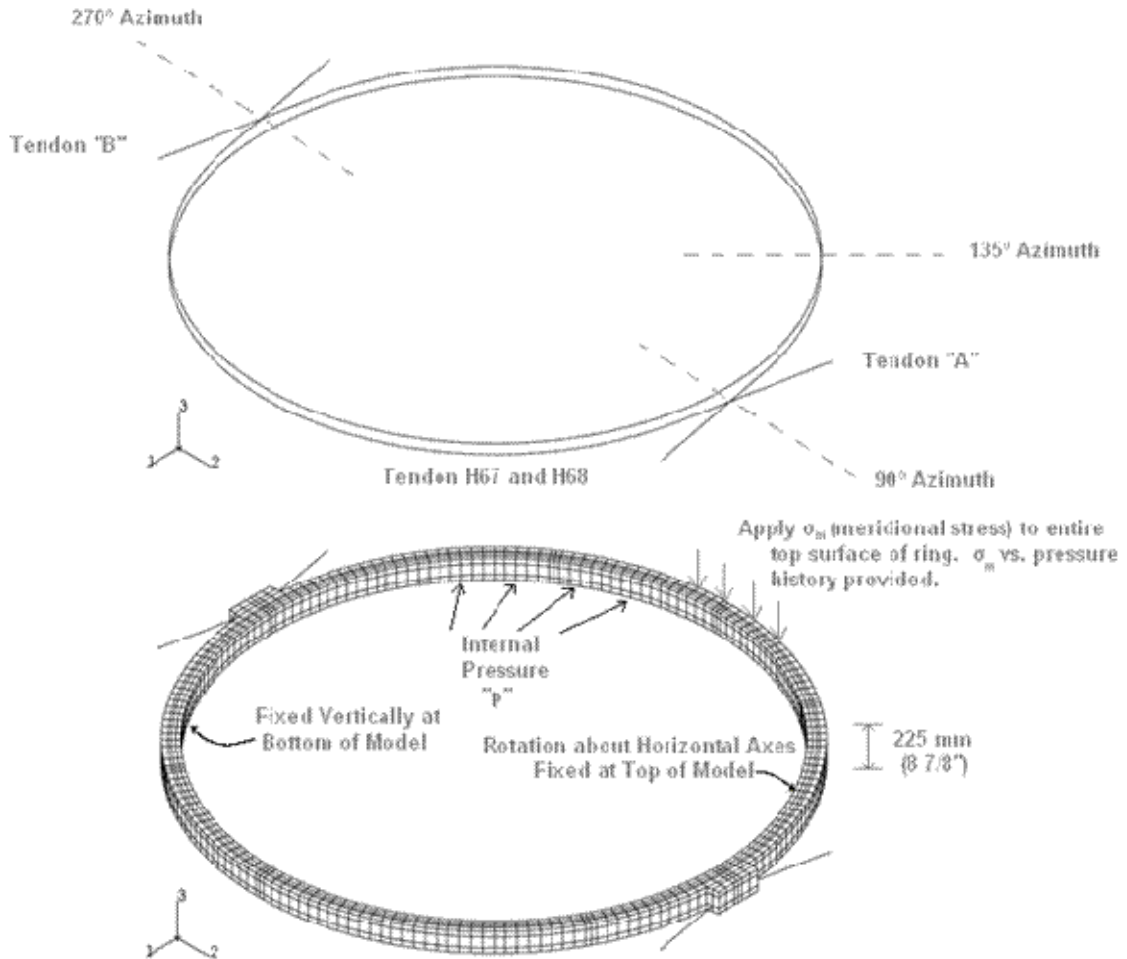


Figure C 1. Tendon behaviour model. [1]

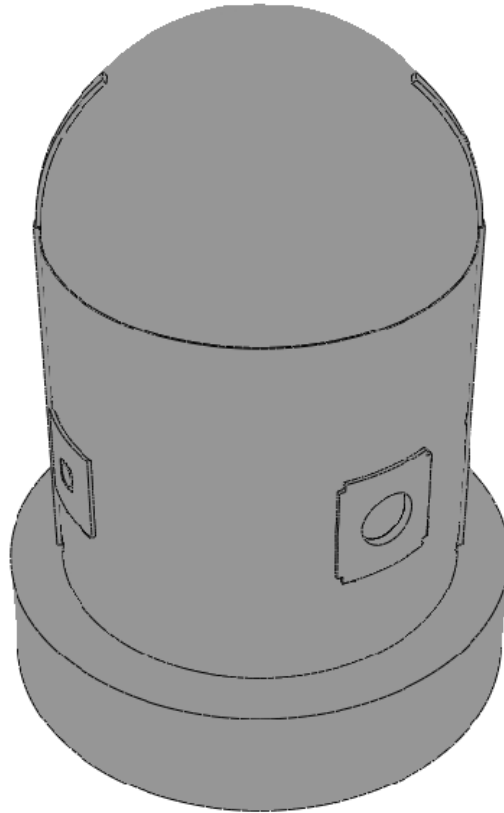


Figure C 2. Global model.

Fortum has participated in the first phase of the exercise with simulations of models 1 and 3. The local behaviour near the E/H is studied with a submodel based on the global model 3. In this report the analyses of the models 1 and 3 are presented. In addition, some examination on the liner fracture near the equipment hatch is presented.

TENDON BEHAVIOR MODEL

Model description

Used code

Model 1 is studied with Abaqus 6.10. Implicit dynamic code is used.

FE-model

The finite element model consists of 978 nodes and 1118 elements. Concrete is modelled with 420 shell elements (S4R). The concrete element thickness is 325 mm. In the azimuths 90° and 270° the shell thickness is 650 mm. Reinforcement and vertical tendons are modelled as rebar layers in the concrete section. The liner is modelled with 420 shell elements (S4R) that share the same nodes

as the concrete elements. The liner elements are offset to the inner surface of the concrete elements. The liner element thickness is 1.6 mm. The horizontal tendons are modelled with 138 beam elements (T3D2). The connection between the concrete and the tendons is modelled with 140 connector elements (CONN3D2). The FE-model is presented in Figure C 3.



Figure C 3. The FE-model. Model 1.

Boundary conditions

The bottom nodes of the concrete ring are constrained in vertical direction. The rotations around the horizontal axes are constrained in the upper nodes of the ring.

Tendon-concrete interaction

The tendon-concrete interaction is modelled with slot connectors. The slots connect tendon nodes to the nearest concrete node. The slots allow tangential movement of the tendon nodes. The allowable movement direction is modelled with local coordinates. Friction value of 0.21 is used in the slot. The connectors are presented in Figure C s 4 and 5.

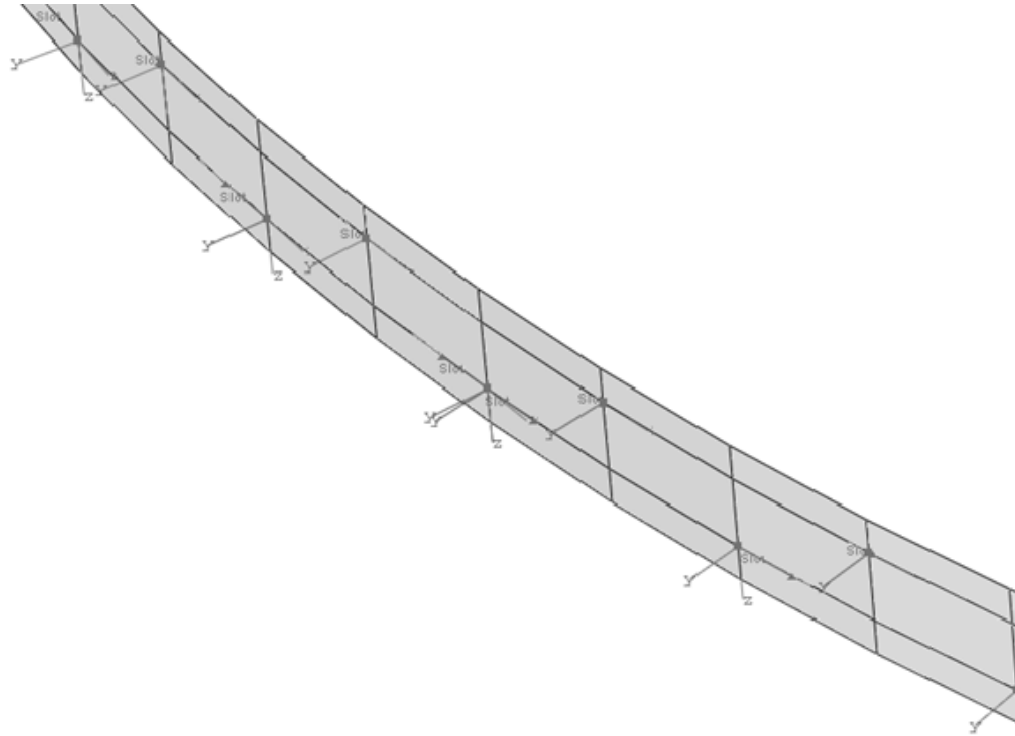


Figure C 4. Tendon-concrete connectors.

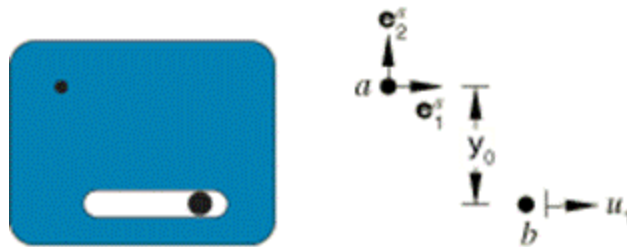


Figure C 5. Slot connector.

Reinforcement and vertical tendons

Reinforcement and vertical tendons are modelled as rebar layers in the concrete elements. The prestressing of the vertical tendons is not modelled. The rebar layers are presented in Figure C s 6 and 7.

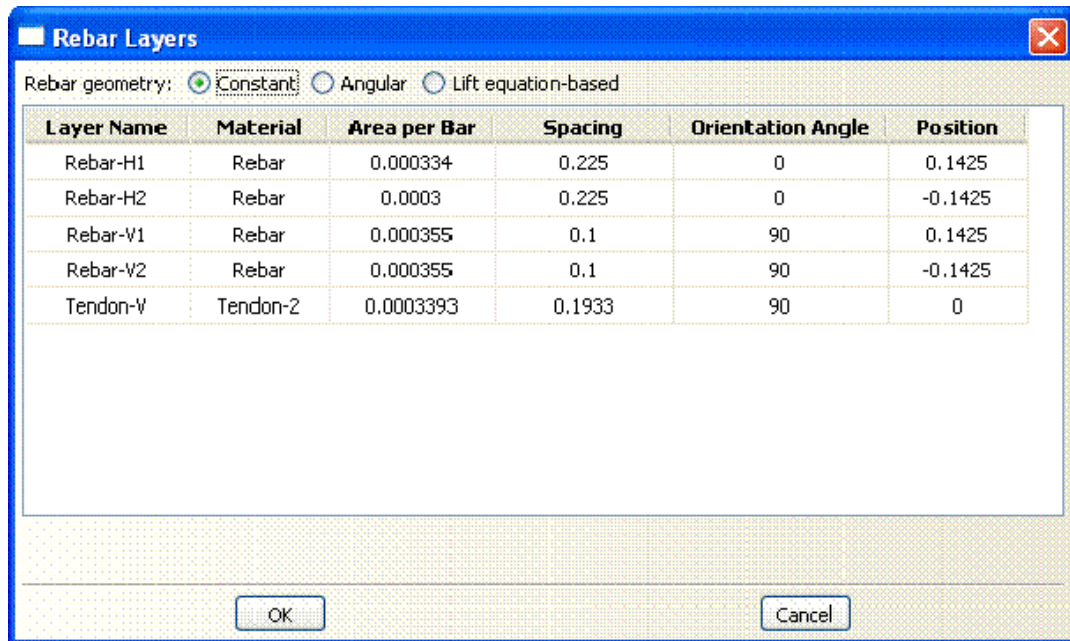


Figure C 6. Rebar layers used to model the reinforcement and vertical tendons.

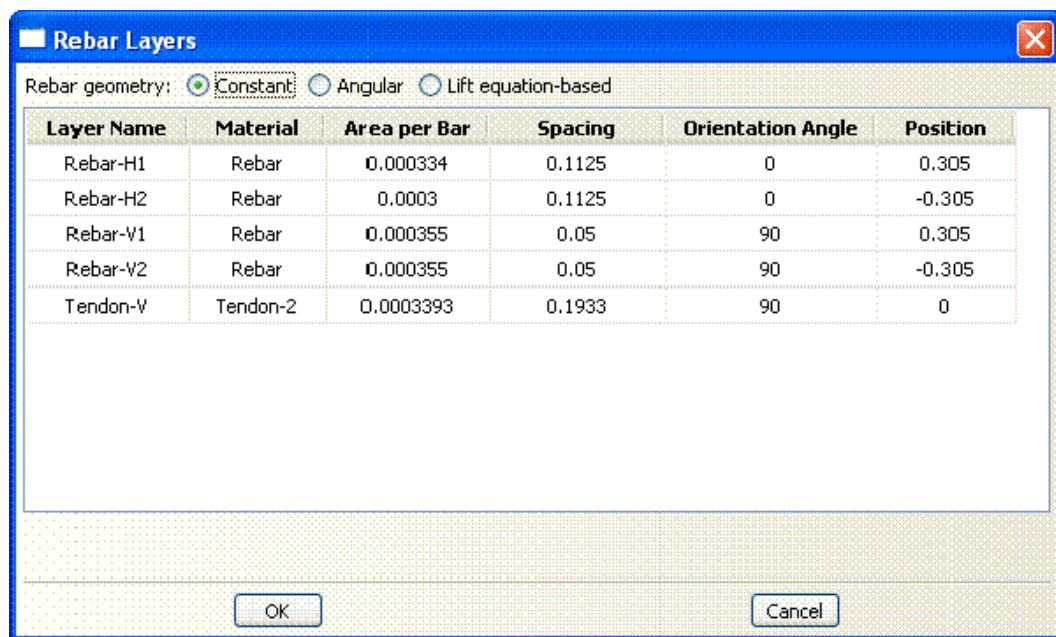


Figure C 7. Rebar layers near azimuths 90° and 270°.

Applied load

The prestressing load is given as a connector displacement in the connectors at the end nodes of the tendons. The connector displacement value is chosen to give a similar tendon stress distribution in jacking and after seating as presented in Figure C 8.

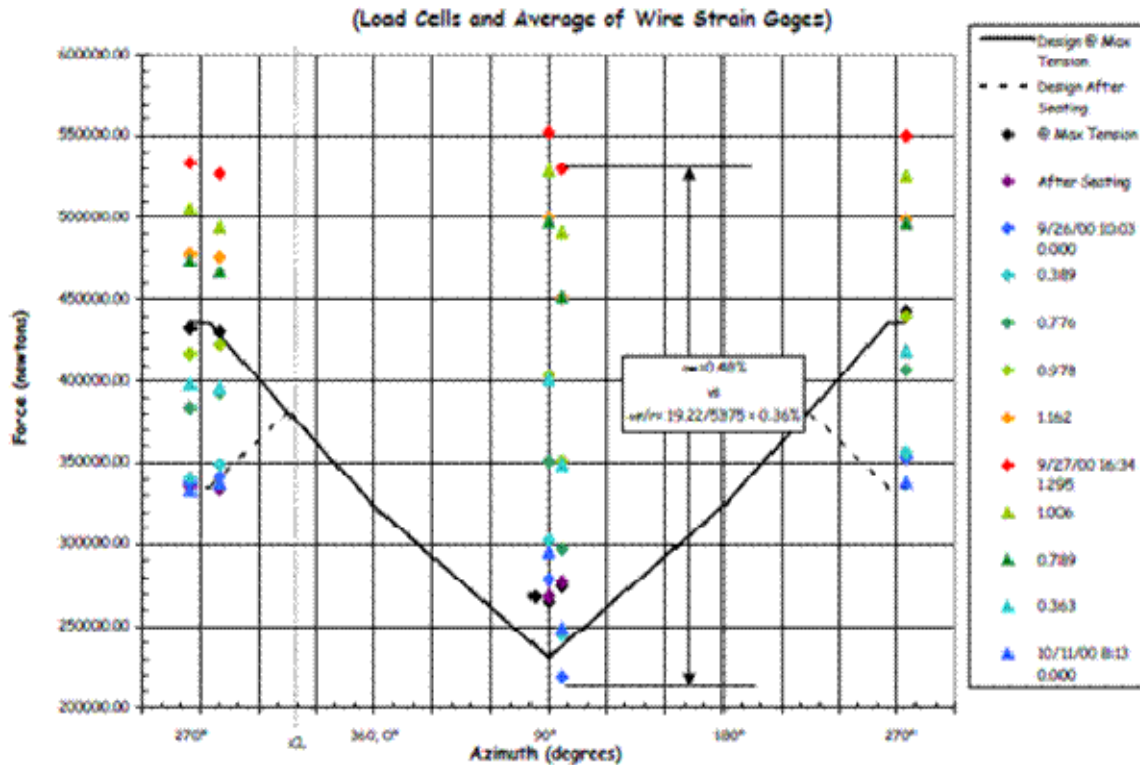
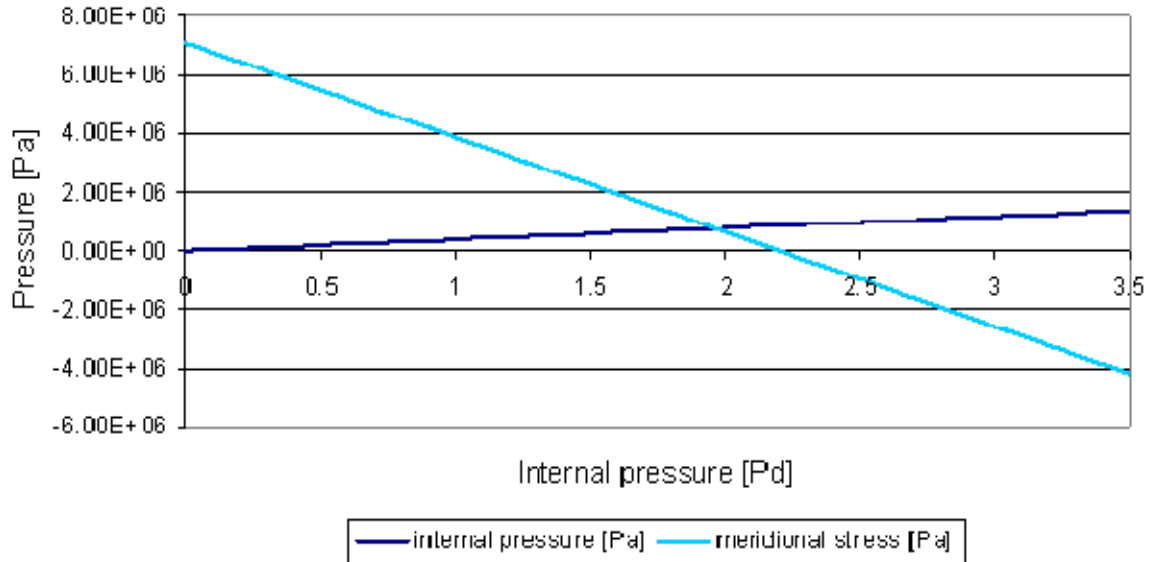


Figure C 8. Measured tendon H53 force distribution. [2]

The internal pressure is modelled as a pressure load on the liner shell elements. The meridional stress is given as point loads on the upper surface of the containment ring. The relation between the meridional stress and the internal pressure is calculated with the same method as presented in [3]. The applied pressure is presented in Figure C 9.



Material models

In the following, the used material models are presented. The presented stresses and strains are engineering values.

Concrete

Concrete is modelled with the concrete damage plasticity model found in Abaqus. The material model is presented in Table C 1 and in Figure C 10.

Table C 1. Material parameters for concrete.

Density	2500 kg/m ³
Young's modulus	28 GPa
Poisson's ratio	0.2

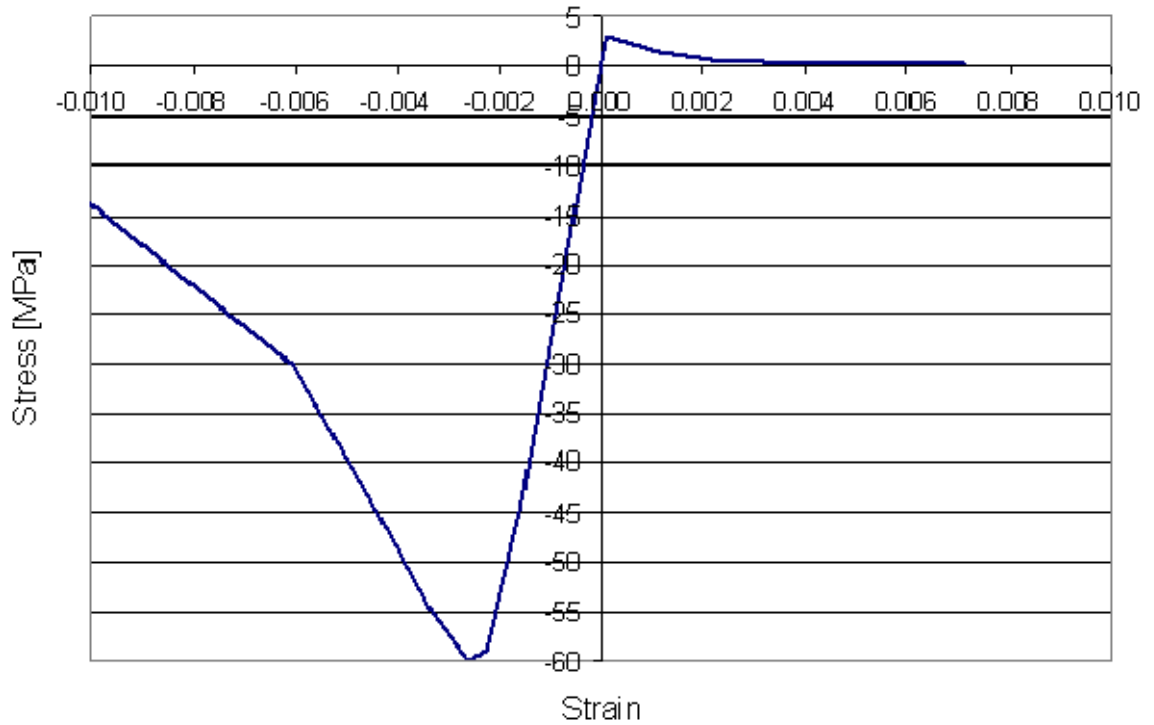


Figure C 10. Stress-strain behaviour of the concrete model.

Tendon steel

The material model for the horizontal tendons is presented in Table C 2 and in Figure 11. The material model for the vertical tendons is presented in Table C 2 and in Figure C 12.

Table C 2. Material parameters for tendon steel.

Density	7850 kg/m ³
Young's modulus	191 GPa
Poisson's ratio	0.3
Fracture strain	0.04

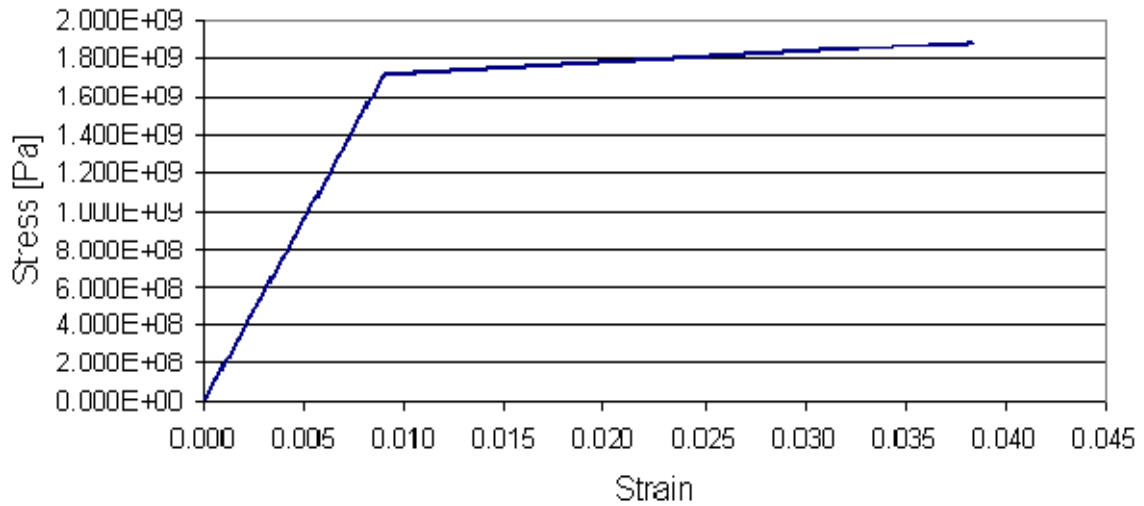


Figure C 11. Stress-strain behaviour of the horizontal tendons.

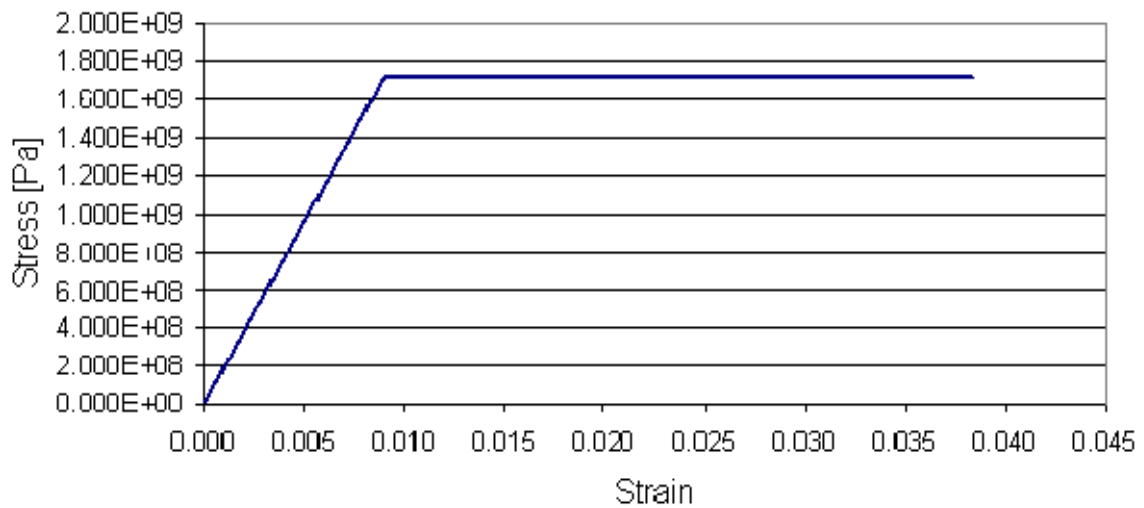


Figure C 12. Stress-strain behaviour of the vertical tendons.

Rebar steel

The material model for the liner steel is presented in Table C 3 and in Figure C 13.

Table C 3. Material parameters for reinforcement steel.

Density	7850 kg/m ³
Young's modulus	200 GPa
Poisson's ratio	0.3

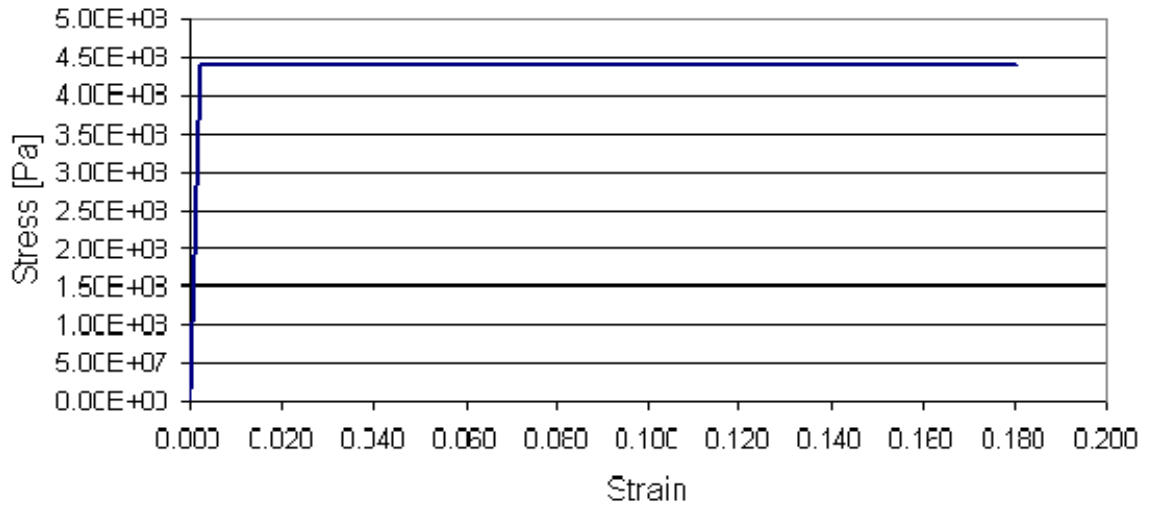


Figure C 13. Stress-strain behaviour of the reinforcement steel model.

Liner steel

The material model for the liner steel is presented in Table C 4 and in Figure C 14.

Table C 4. Material parameters for the liner steel.

Density	7850 kg/m ³
Young's modulus	219 GPa
Poisson's ratio	0.3
Fracture strain	0.18

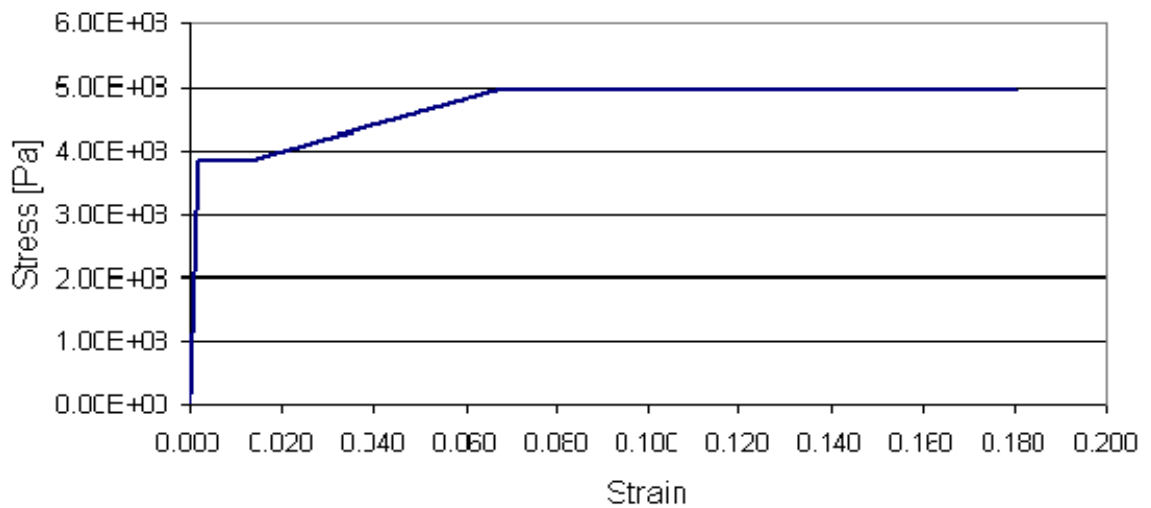


Figure C 14. Stress-strain behaviour of the liner steel model.

Results

Pressure milestones

Model behaviour at the pressure milestones given in [1] is presented in Table C 5.

Table C 5. Pressure Milestones.

	Applied pressure
Concrete Hoop Stress (at 135° azimuth) Equals Zero	1.4 x Pd (0.55 MPa)
Concrete Hoop Cracking Occurs (at 135° azimuth)	1.9 x Pd (0.74 MPa)
Tendon A Reaches 1% Strain (at 135° azimuth)	3.3 x Pd (1.29 MPa)
Tendon B Reaches 1% Strain (at 135° azimuth)	3.3 x Pd (1.29 MPa)
Tendon A Reaches 2% Strain (at 135° azimuth)	3.4 x Pd (1.33 MPa)
Tendon B Reaches 2% Strain (at 135° azimuth)	3.4 x Pd (1.33 MPa)

Deformed shape

The deformed shape of the ring as the pressure increases is presented in Figure C s

15 to 23. From the Figure C s it can be seen that the ring breaks near azimuths 0° and 180°. From Figure C 23 it can be seen that at pressure 3.5 x Pd the ring has broken. In the test the final rupture occurred at azimuth 6° with an effective pressure of 3.63 x Pd.

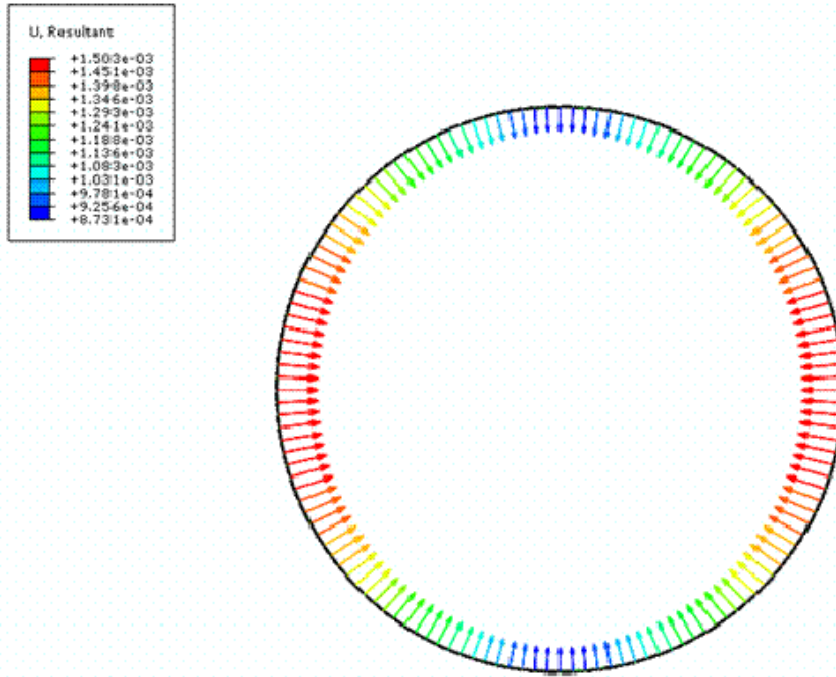


Figure C 15. Deformation (x10) at applied pressure $P = 0.0 \times P_d$

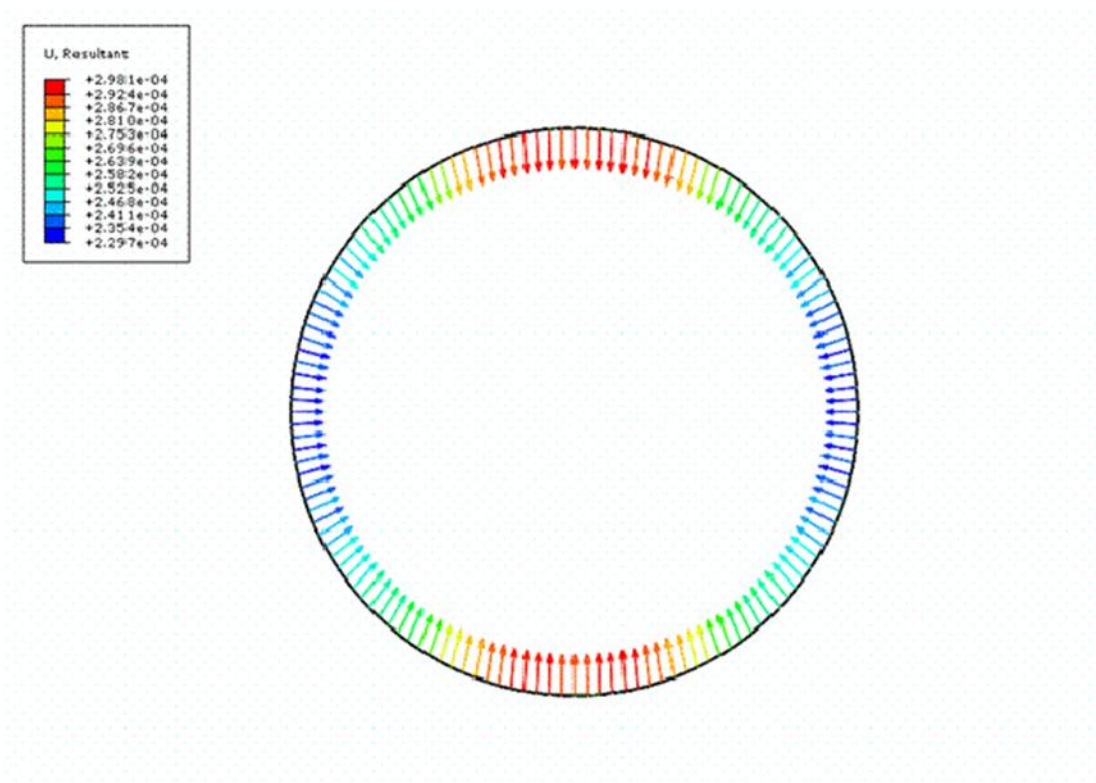


Figure C 16. Deformation (x10) at applied pressure $P = 1.0 \times P_d$

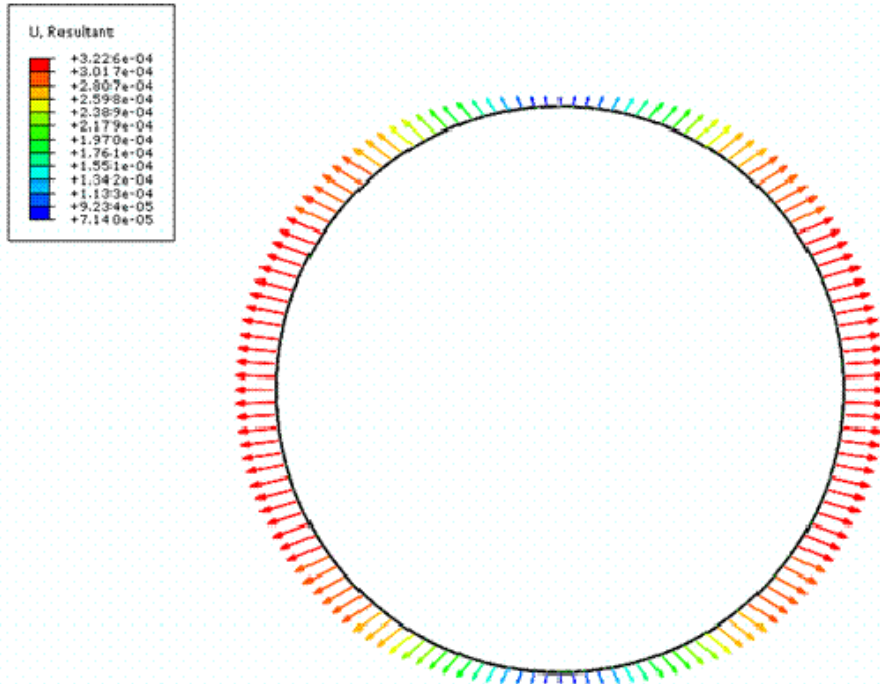


Figure C 17. Deformation (x10) at applied pressure $P = 1.5 \times P_d$

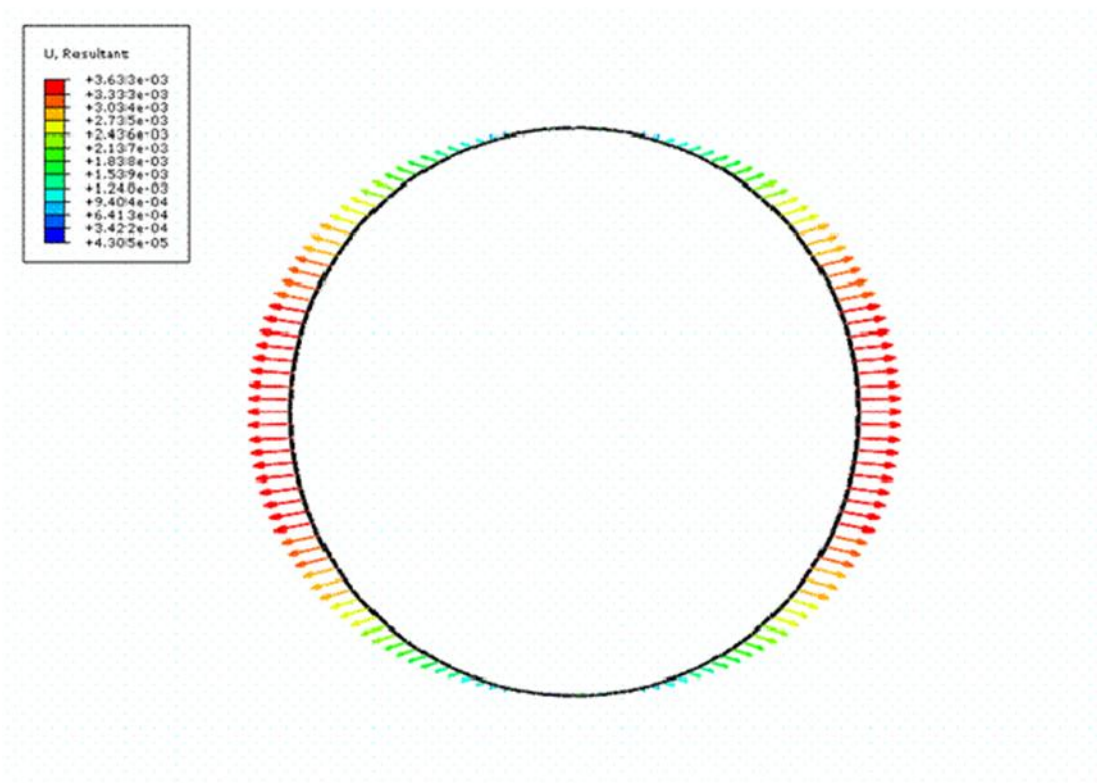


Figure C 18. Deformation (x10) at applied pressure $P = 2.0 \times P_d$

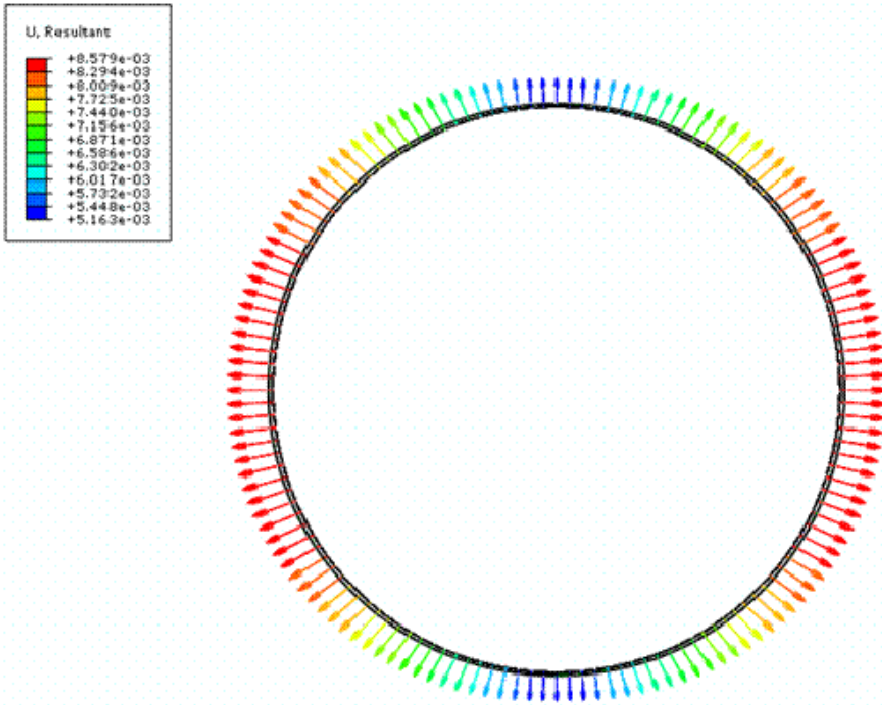


Figure C 19. Deformation (x10) at applied pressure $P = 2.5 \times Pd$

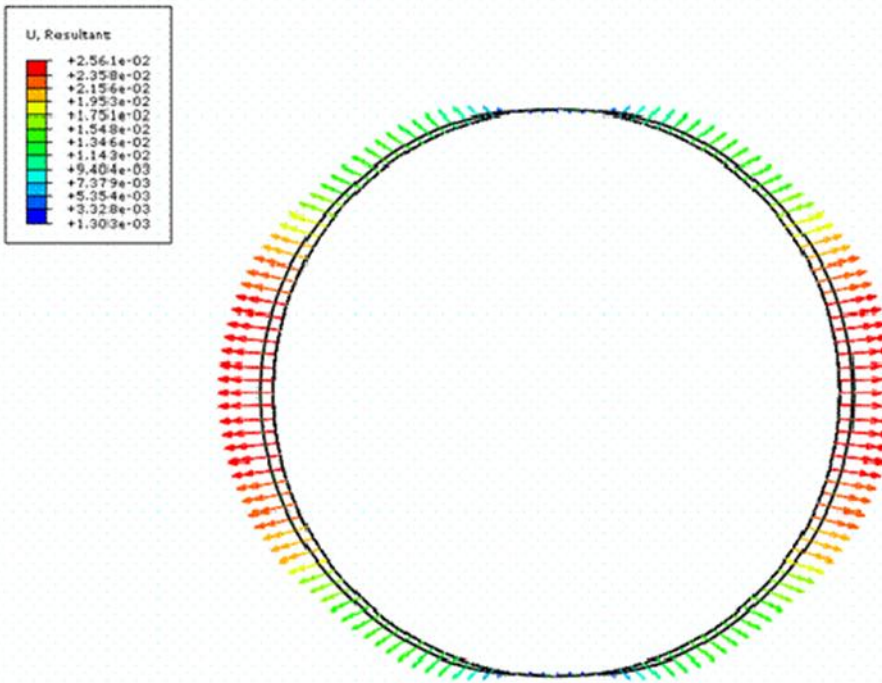


Figure C 20. Deformation (x10) at applied pressure $P = 3.0 \times Pd$

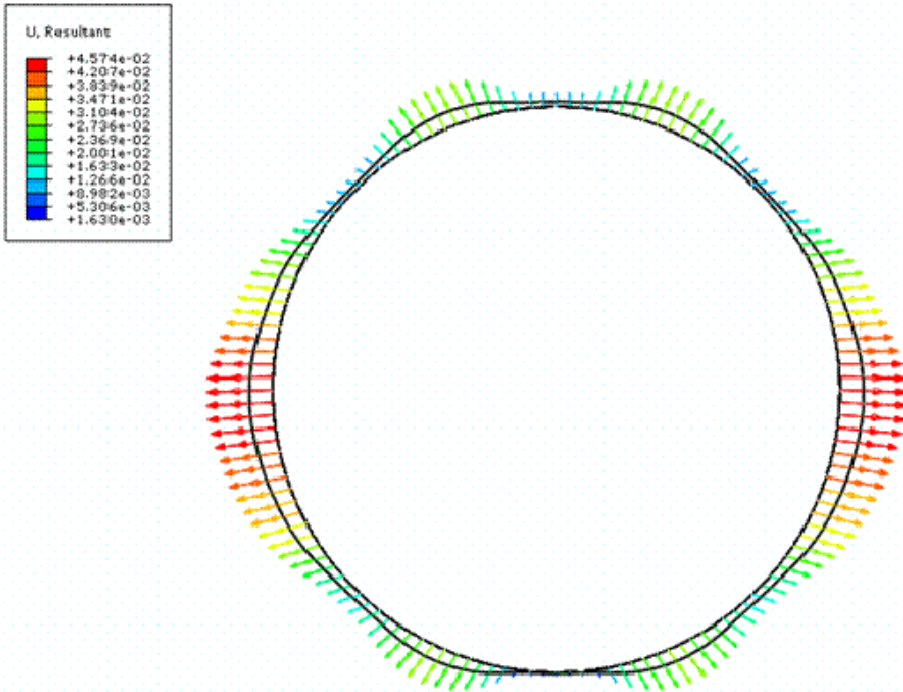


Figure C 21. Deformation (x10) at applied pressure $P = 3.3 \times Pd$

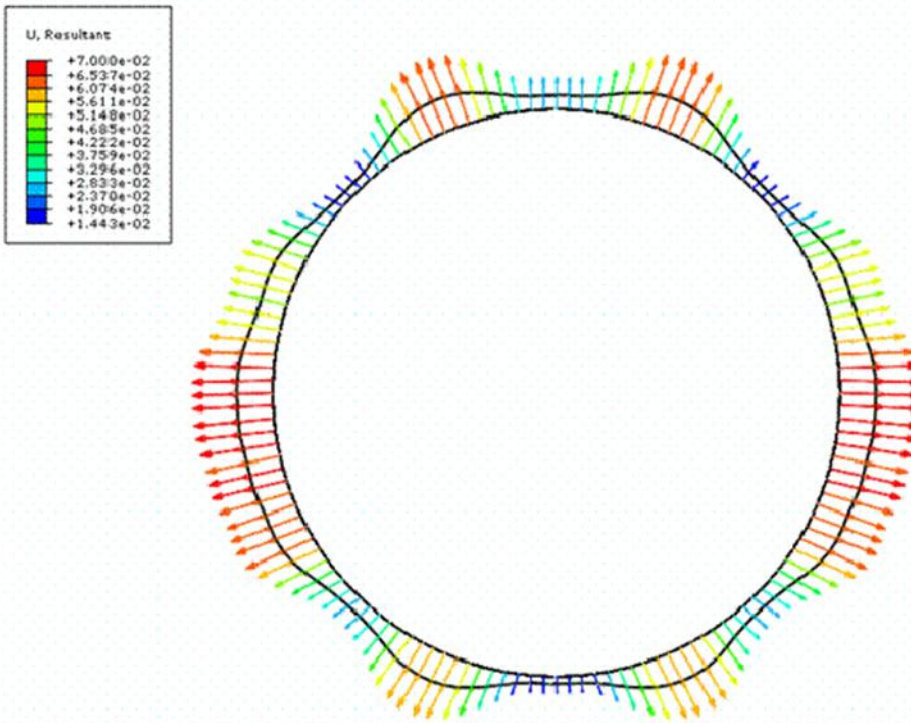


Figure C 22. Deformation (x10) at applied pressure $P = 3.4 \times Pd$

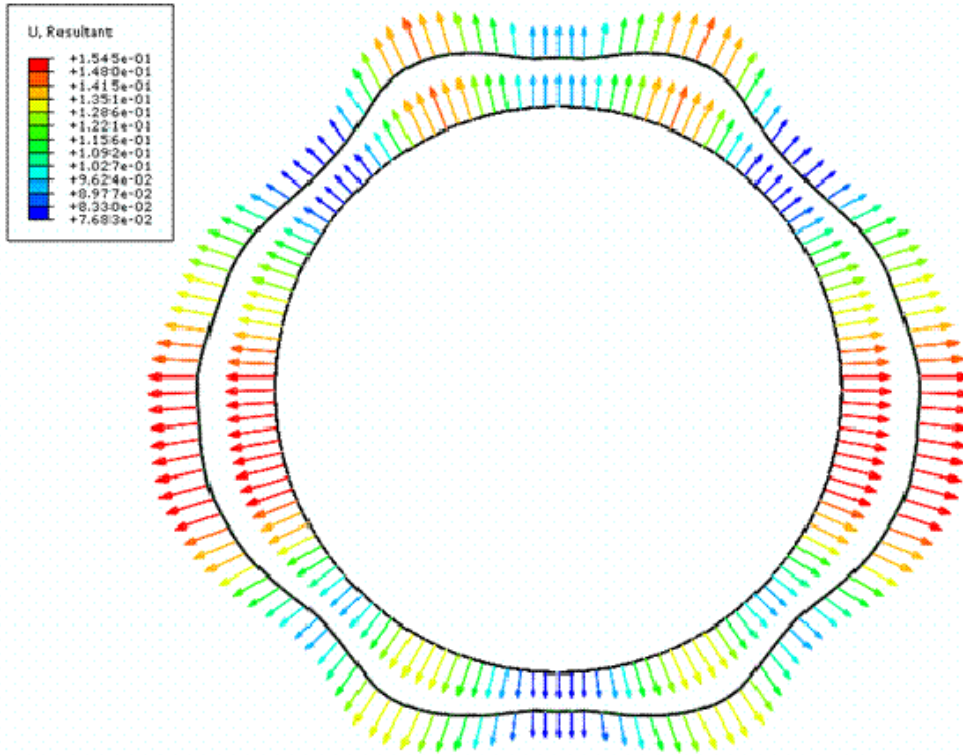


Figure C 23. Deformation (x10) at applied pressure $P = 3.5 \times P_d$

Tendon stress

The tendon force distribution in prestressing compared to the measured values is presented in Figure C 24. The tendon stress as the pressure increases is presented

in Figure C 25. The presented values are for tendon A. Tendon B behaves similarly. From the Figure C 25 it can be seen that the model captures the tendon stress dependency on the internal pressure. As the pressure increases, the tendon stress rises up to the ultimate capacity of the tendon.

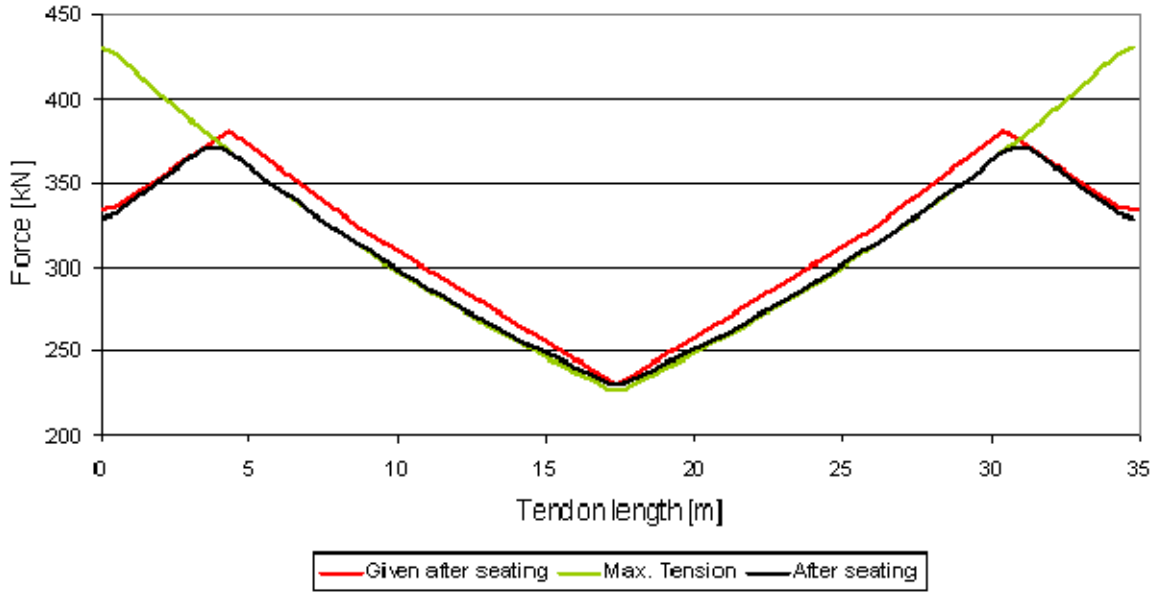


Figure C 24. Force distribution of tendon A in prestressing.

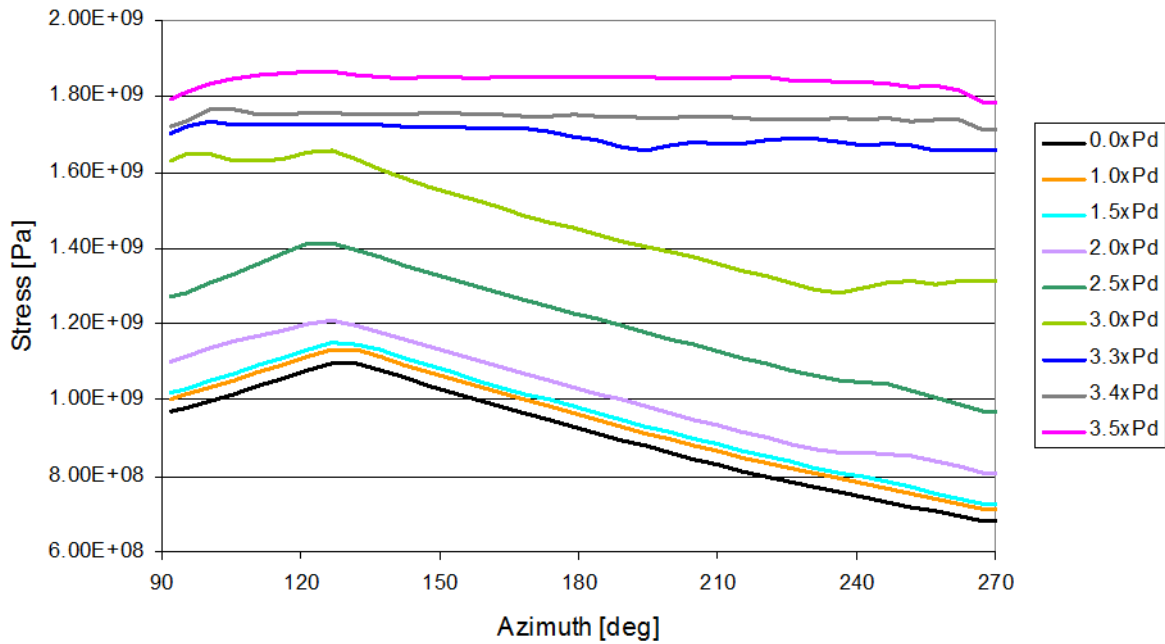


Figure C 25. Stress distribution of tendon A as the pressure increases.

Discussion

The behaviour of the model is consistent with the test results. Slot connectors are able to model the tendon-concrete interaction.

GLOBAL MODEL

Model description

Used code

Model 3 is studied with Abaqus 6.10. Implicit dynamic code is used.

FE-model

The finite element model consists of 175603 nodes and 257580 elements. The concrete part of the containment is modelled with 22153 shell elements (S4R and S3R). The concrete element thickness is 325 mm at the cylinder part of the containment and 275 mm at the dome part of the containment. In the azimuths 90° and 270° the shell thickness is 650 mm at the cylinder part of the containment and 550 mm at the dome part of the containment. Near the equipment hatch (E/H) and the air lock (A/L) the element thickness is 550 mm. Reinforcements are modelled as rebar layers in the concrete section. The liner is modelled with 22153 shell elements (S4R and S3R) that share the same nodes as the concrete elements. The liner elements are offset to the inner surface of the concrete elements. The liner element thickness is 1.6 mm. The tendons are modelled with beam elements (T3D2). The horizontal tendons consist of 19370 elements, and the vertical tendons are modelled with 23280 elements. The connections between the concrete and the tendons are modelled with connector elements (CONN3D2). The base of the containment is modelled with 42028 solid elements (C3D8R). The base is modelled as 3.5 m thick. The patches of the penetrations E/H and A/L are modelled with 52 1 mm thick shell elements (S3R).

The FE-model is presented in Figure C 26.

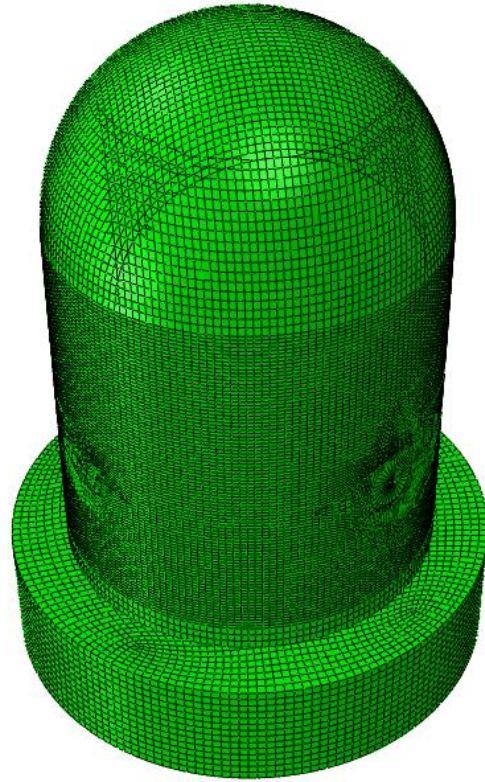


Figure C 26. The FE-model. Model 3.

Boundary conditions

The bottom nodes of the concrete base are constrained.

Tendon-concrete interaction

The tendon-concrete interaction is modelled with slot connectors. The slot connectors are similar to the tendon behaviour model (see Figure C A 4).

Applied load

The load is applied to the model in four steps. In the first step, the gravity load is applied. Second, the prestressing load is added. The prestress is given as a connector load in the connectors at the end nodes of the tendons. For the horizontal tendons the load is 432 kN, and for the vertical tendons the load is 483 kN. In the third step, the anchorage loss is modelled by lowering the connector loads by 25 %. In the fourth step, the internal pressure load is applied. The internal pressure is modelled as a pressure load on the liner shell elements. The pressure is increased linearly over time (0.039 MN / s). The model is analyzed up to four times the design pressure $P_d = 0.39$ MN. Before the internal pressure is applied, the end nodes of the tendons are locked to the concrete shell elements.

Material models

Concrete

Concrete is modelled with the concrete damage plasticity model found in Abaqus. The material model is the same as with the tendon behaviour model. It is presented in Table C 1 and in Figure C 10.

Tendon steel

The material model for the tendons is similar to the tendon behaviour model.

The material model for the horizontal tendons is presented in Table C 2 and in Figure C 11. The material model for the vertical tendons is presented in Table C 2 and in Figure C 12.

Rebar steel

The material model for the rebar steel is the same as with the tendon behaviour model. The model is presented in Table C 3 and in Figure C 12.

Liner steel

The material model for the liner steel is the same as with the tendon behaviour model. The model is presented in Table C 4 and in Figure C 13.

Steel for the patches of the penetrations

The patches of the penetrations E/H and A/H are modelled with linear steel pre- sented in Table C 6.

Table C 6. Material parameters for the liner steel.

Density	7850 kg/m ³
Young's modulus	210 GPa
Poisson's ratio	0.3

Results

Response of the model

In the following, the response output from the 55 standard output locations is presented. The standard output locations are presented in [2].

Displacements

Figure C s 27 to 41 present the measured and simulated displacement histories of the standard output locations 1 to 15. The simulation results are in accordance with the test results.

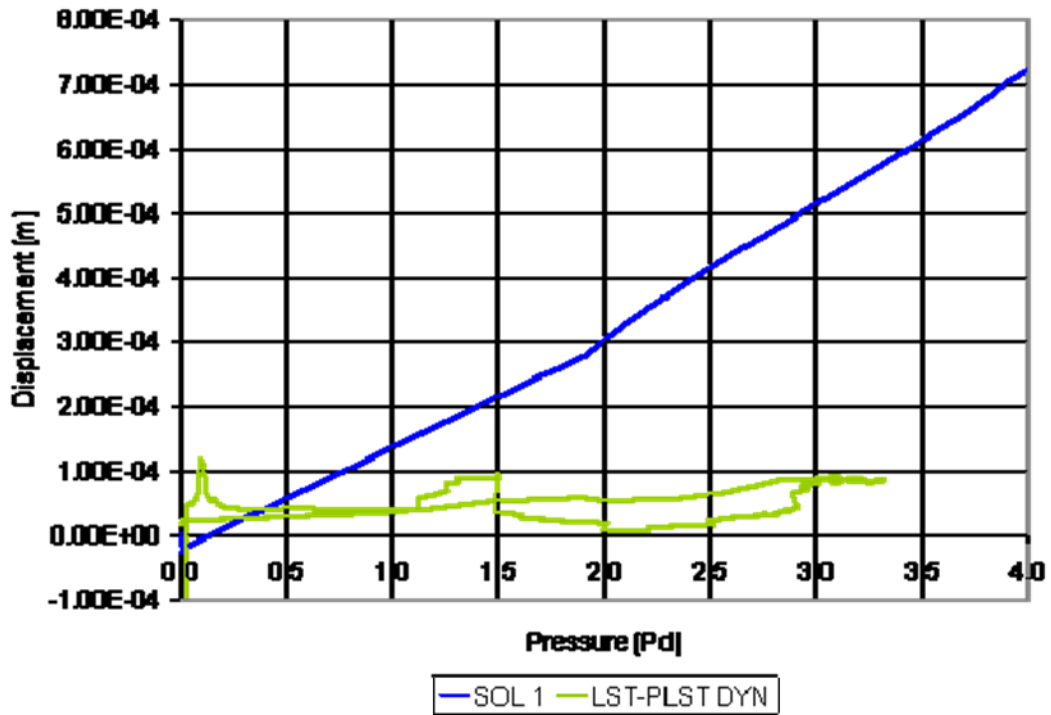


Figure C 27. Vertical displacement at Standard output location 1.

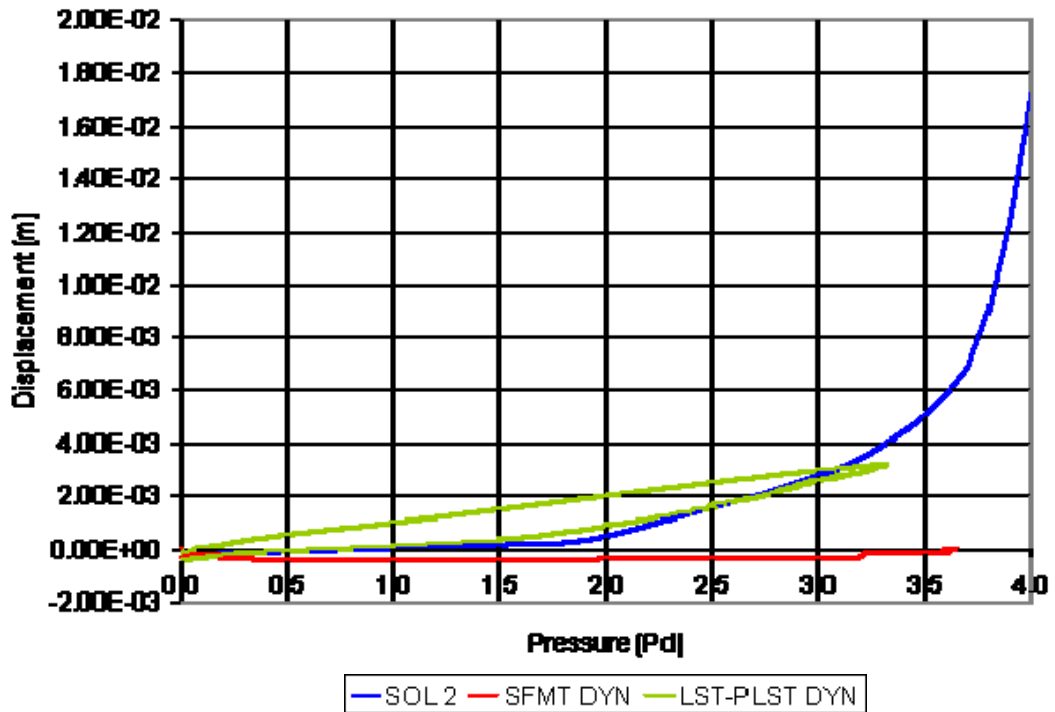


Figure C 28. Radial displacement at Standard output location 2.

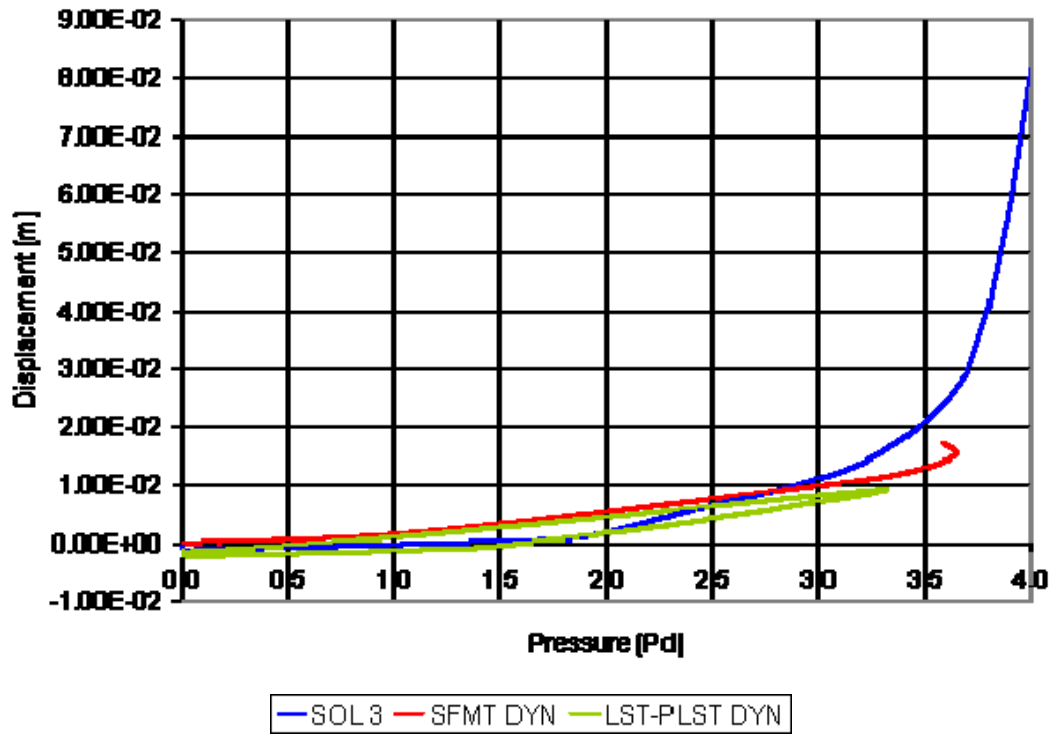


Figure C 29. Radial displacement at Standard output location 3.

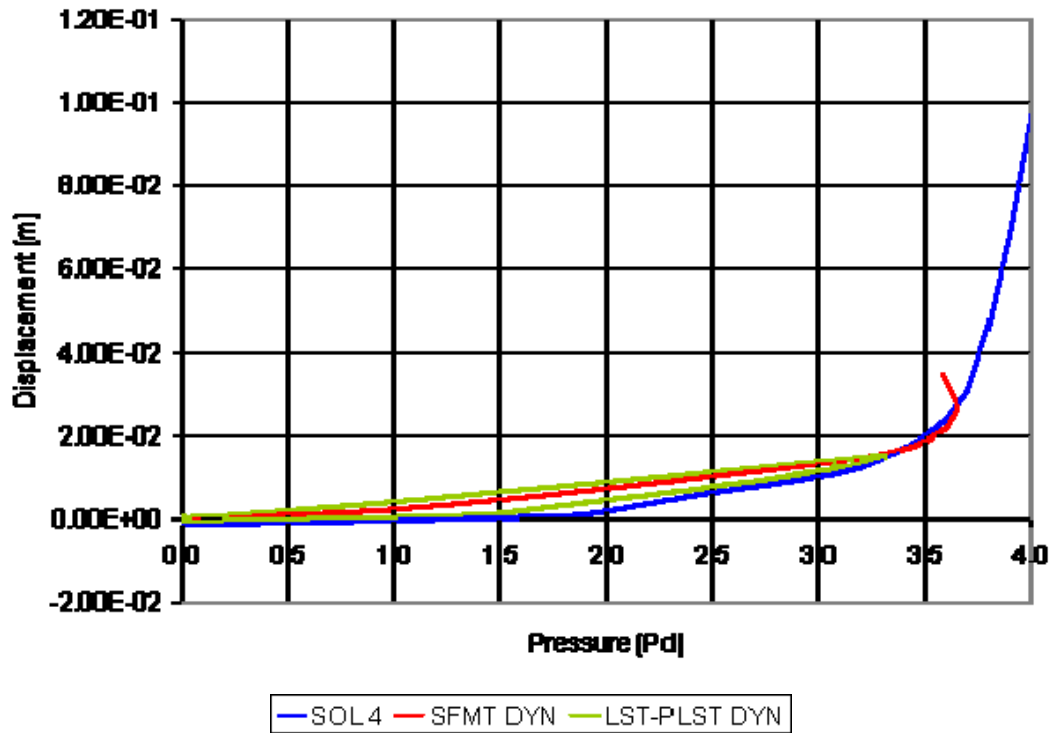


Figure C 30. Radial displacement at Standard output location 4.

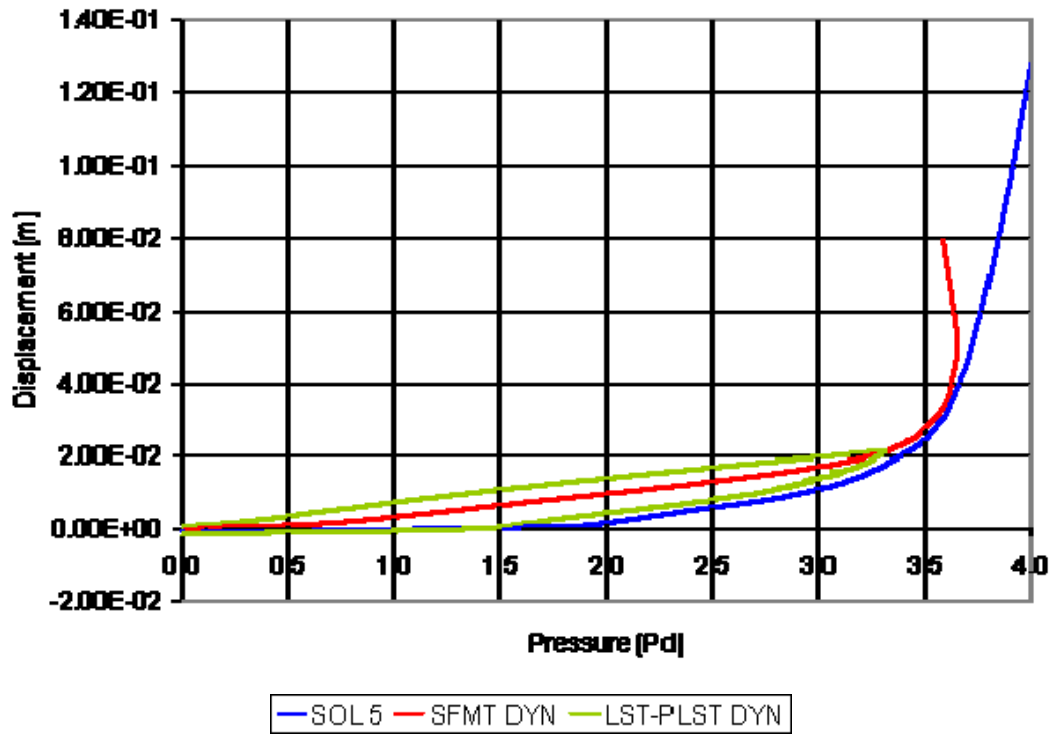


Figure C 31. Radial displacement at Standard output location 5.

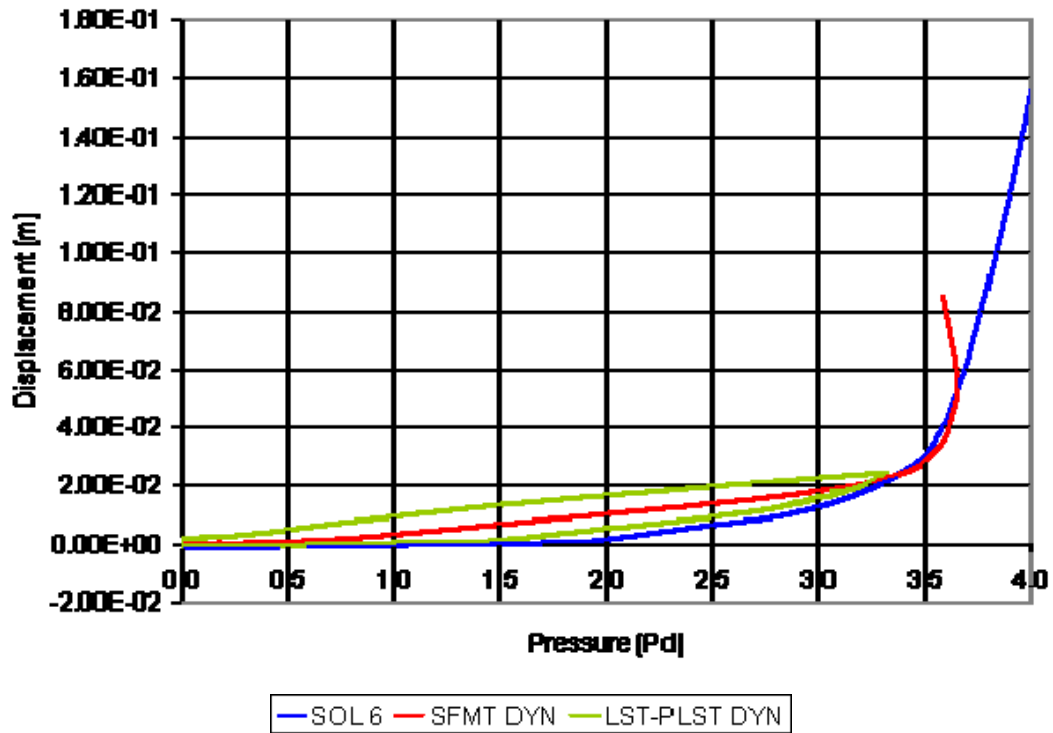


Figure C 32. Radial displacement at Standard output location 6.

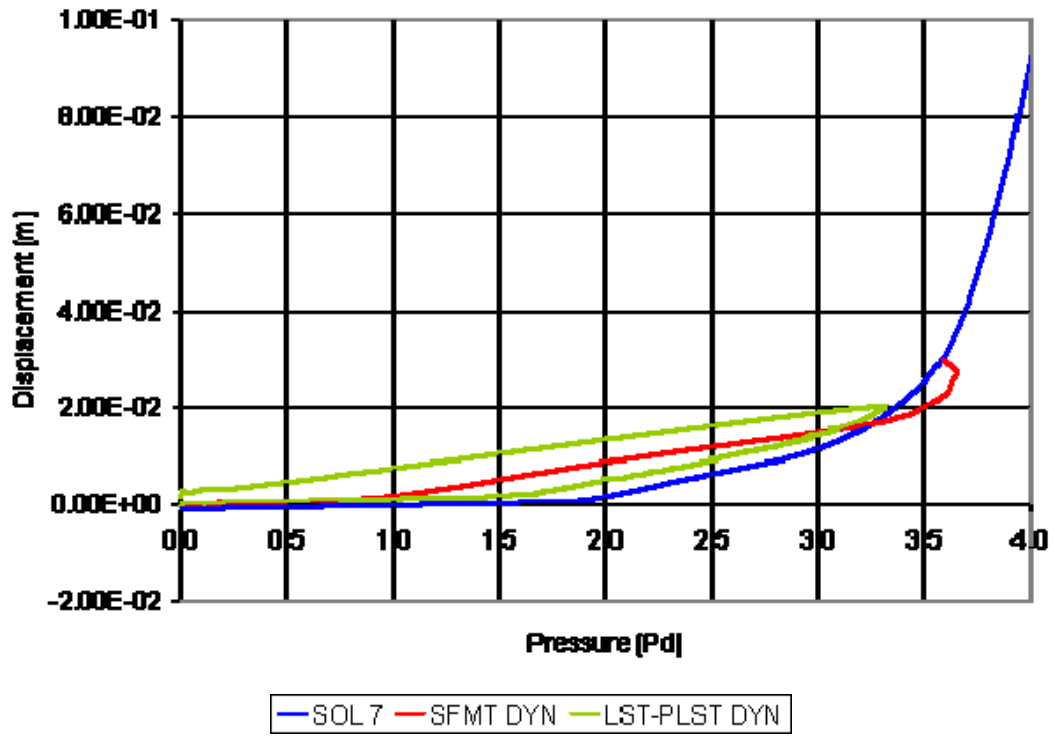


Figure C 33. Radial displacement at Standard output location 7.

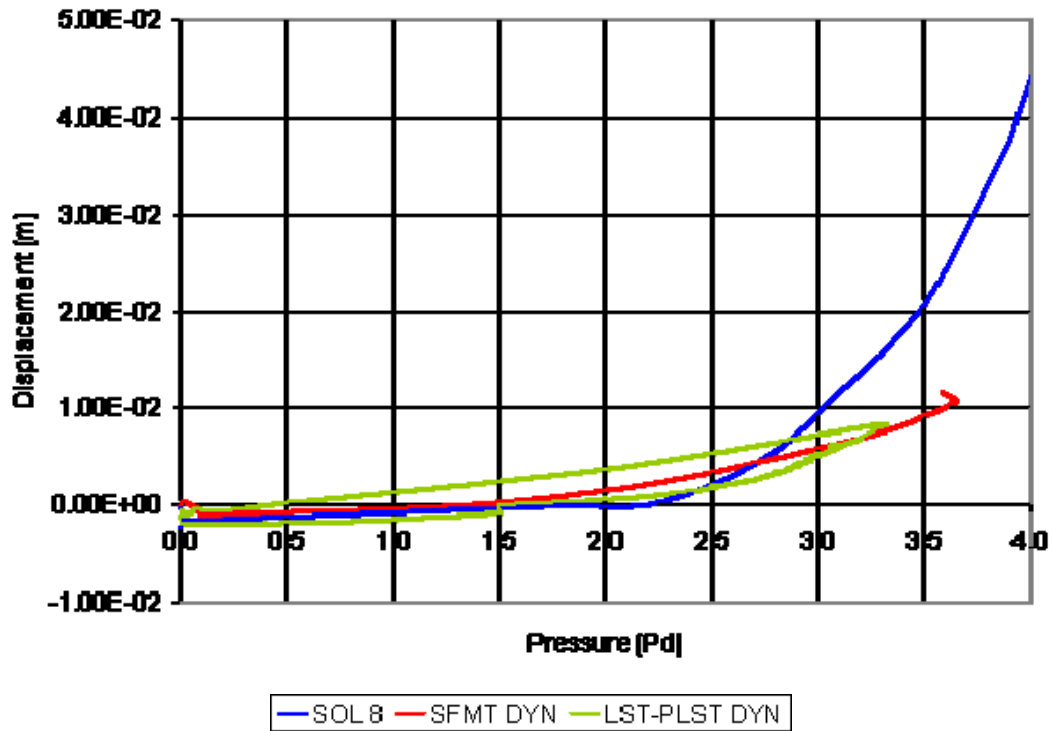


Figure C 34. Vertical displacement at Standard output location 8.

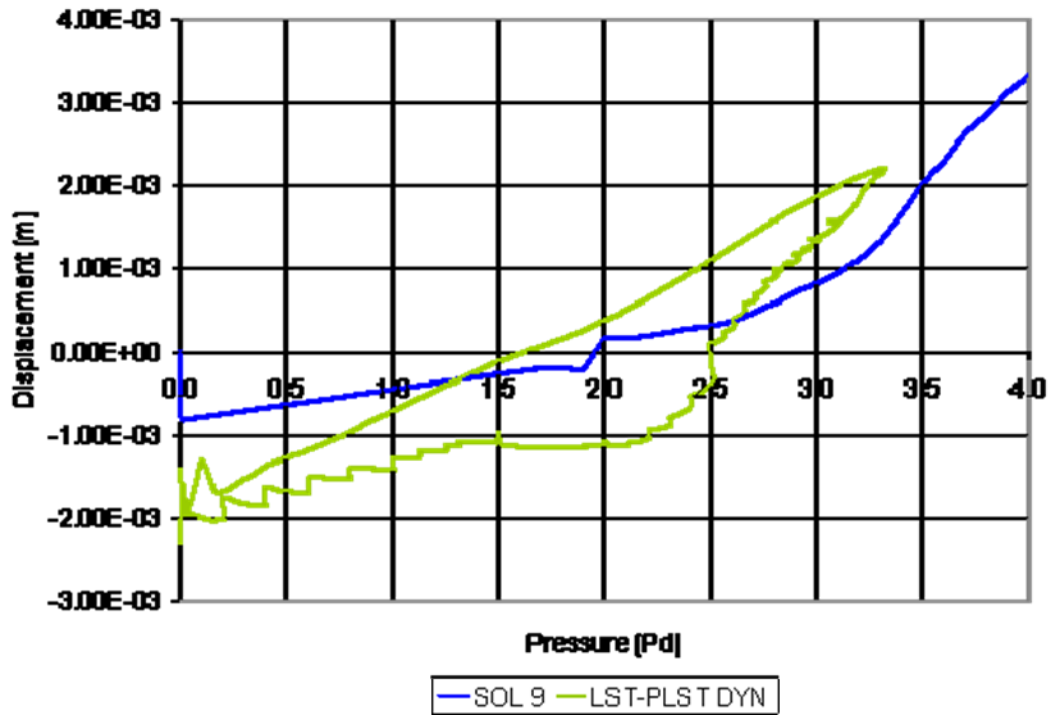


Figure C 35. Radial displacement at Standard output location 9.

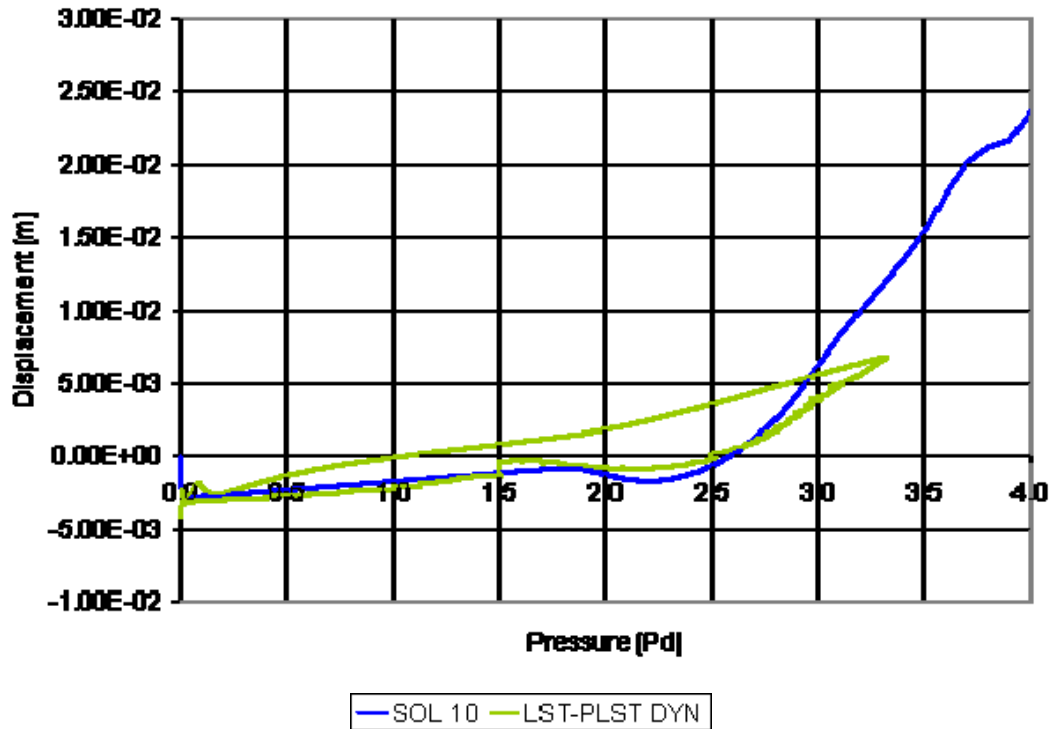


Figure C 36. Vertical displacement at Standard output location 10.

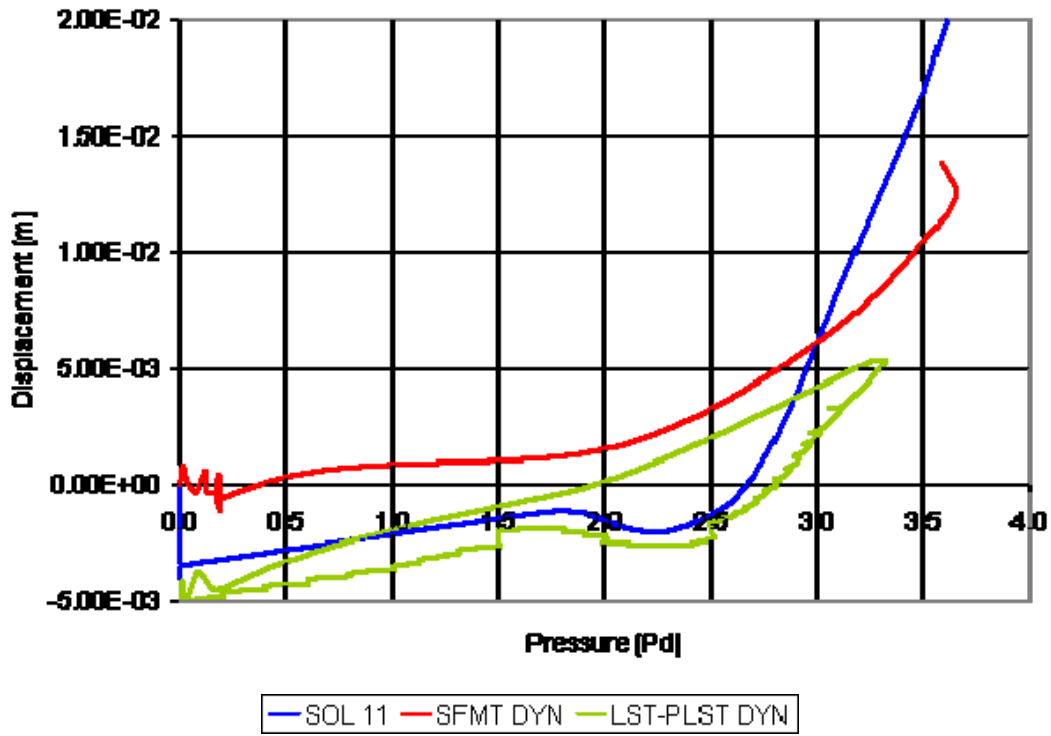


Figure C 37. Vertical displacement at Standard output location 11.

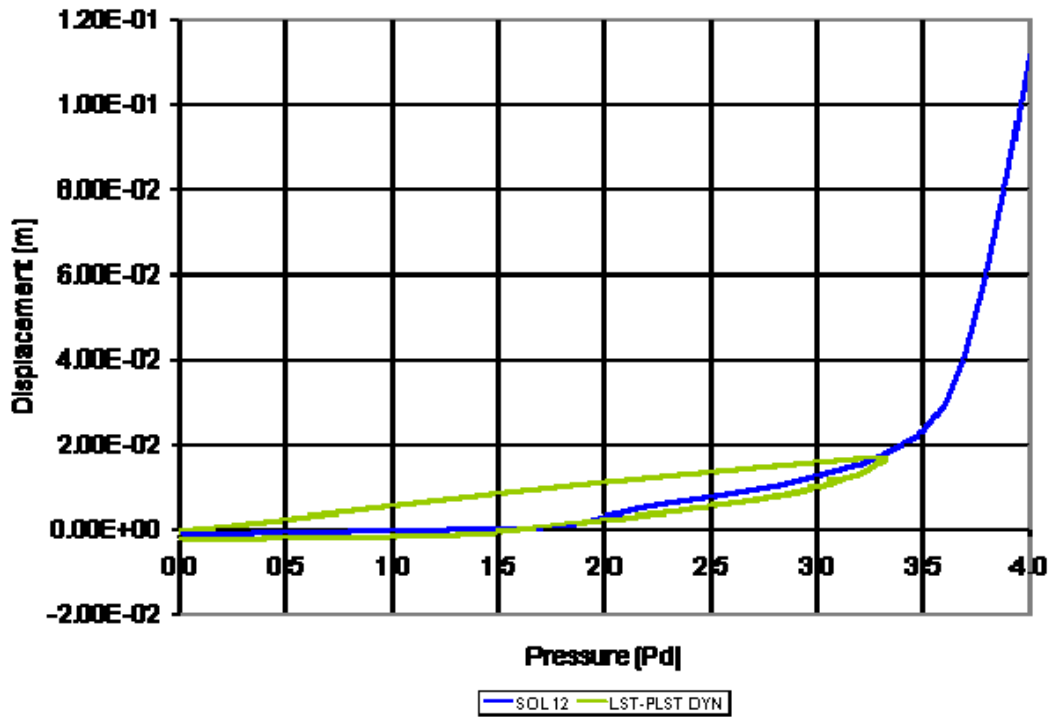


Figure C 38. Radial displacement at Standard output location 12.

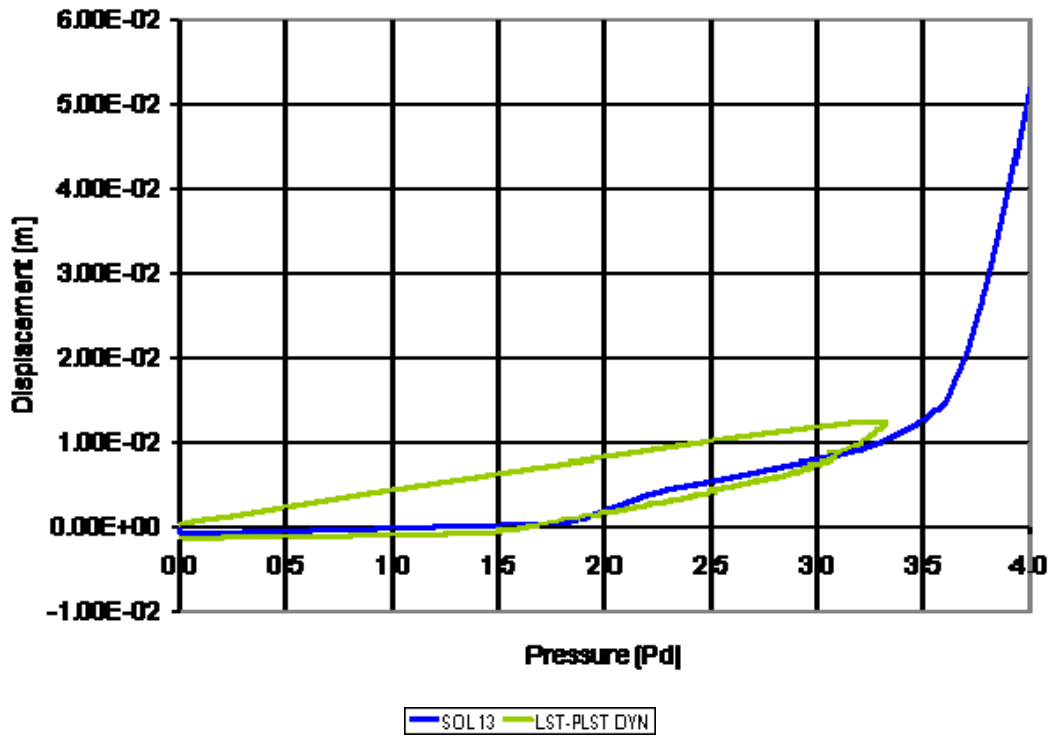


Figure C 39. Radial displacement at Standard output location 13.

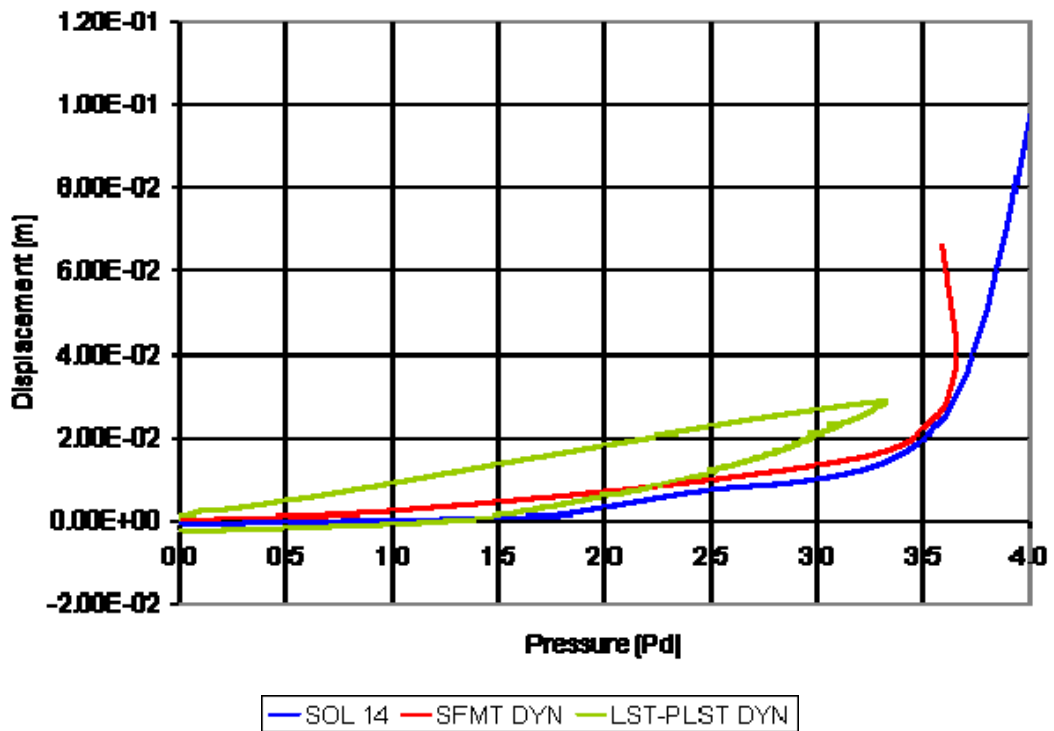


Figure C 40. Radial displacement at Standard output location 14.

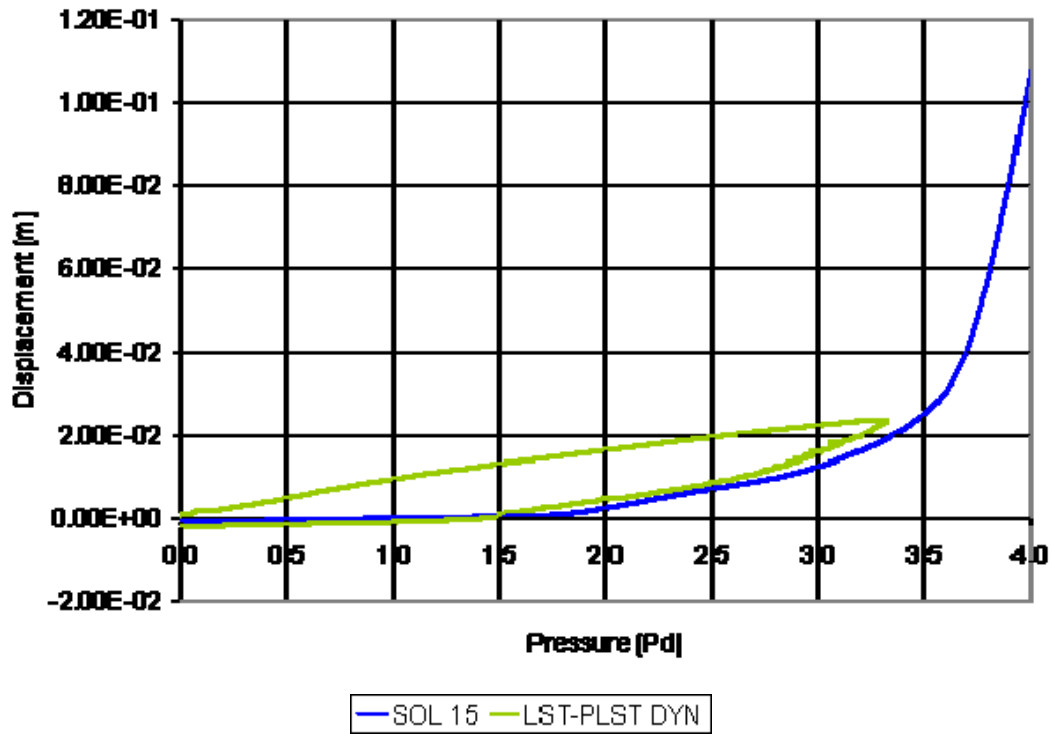


Figure C 41. Radial displacement at Standard output location 15.

Rebar strains

Figure C s 42 to 59 present the measured and simulated rebar strains at the standard output locations 16 to 33. The simulation results do not correspond to the measured values at all cases. However, in most cases the orders of magnitude of the simulation results correspond to the test results.

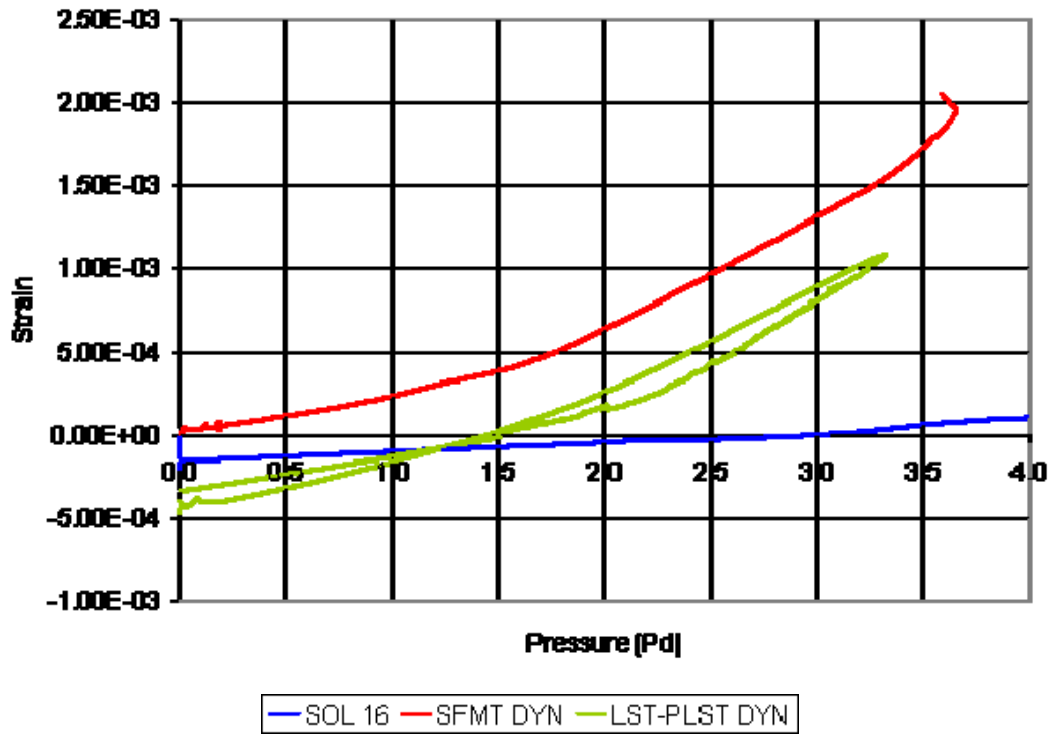


Figure C 42. Rebar strain at Standard output location 16.

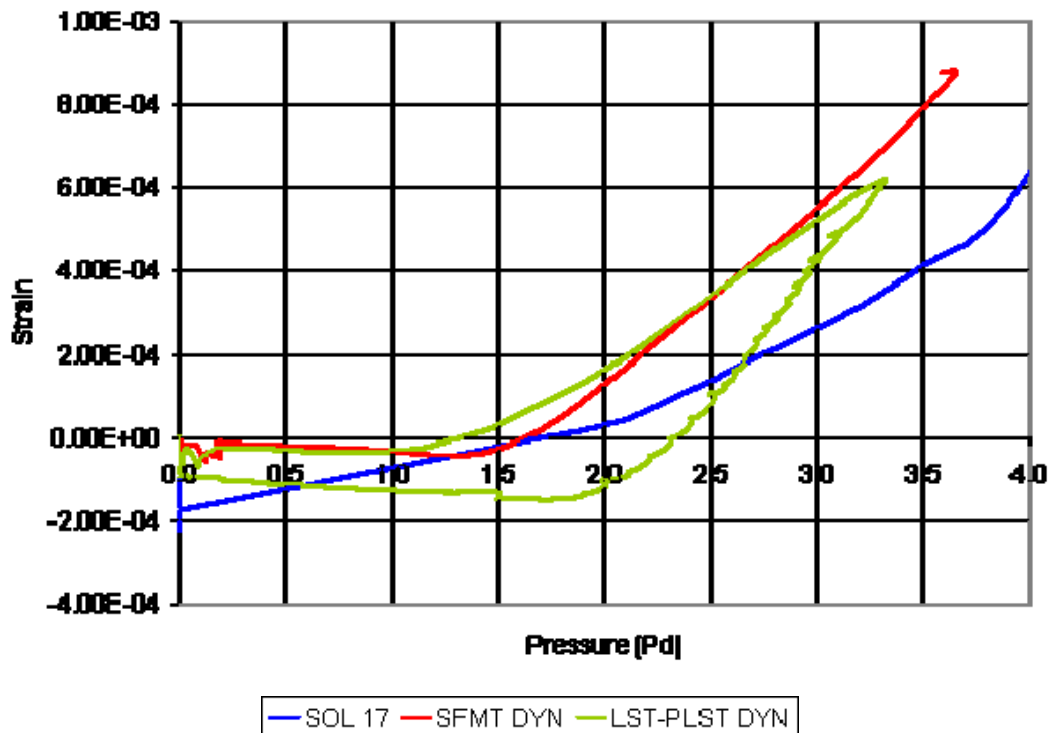


Figure C 43. Rebar strain at Standard output location 17.

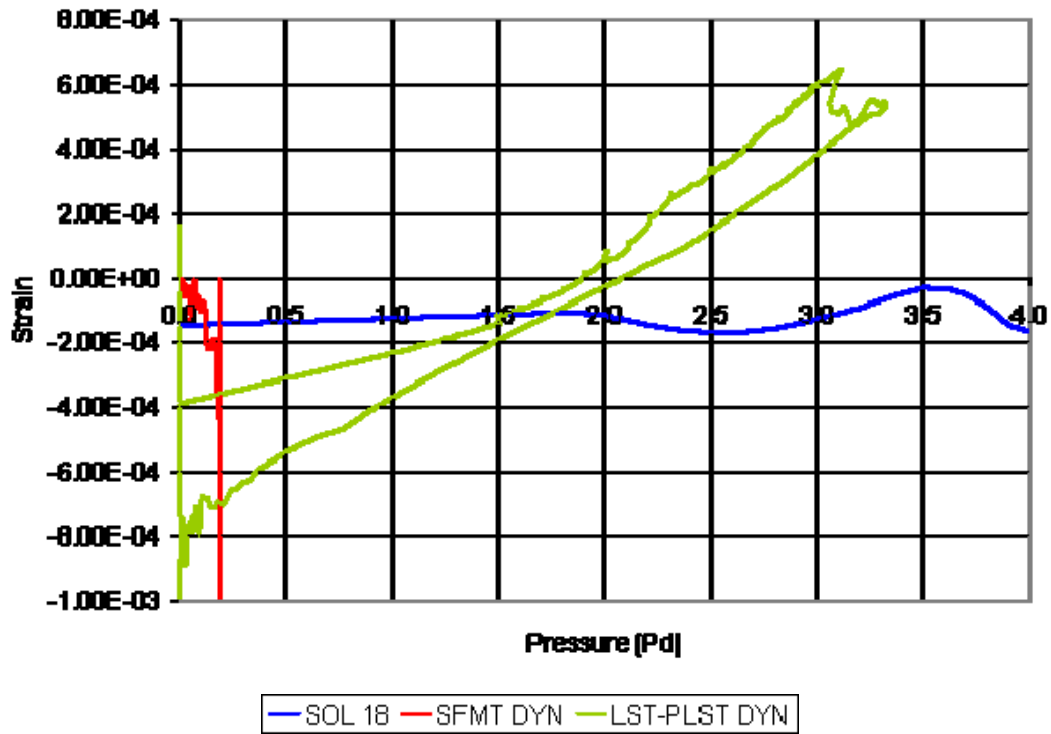


Figure C 44. Rebar strain at Standard output location 18.

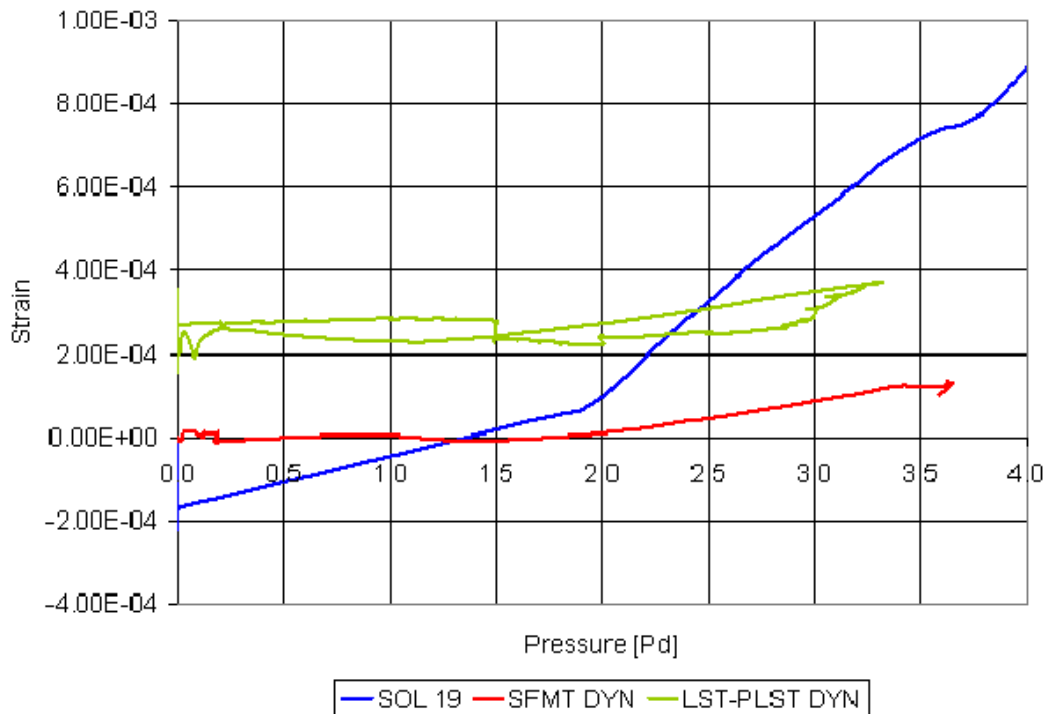


Figure C 45. Rebar strain at Standard output location 19.

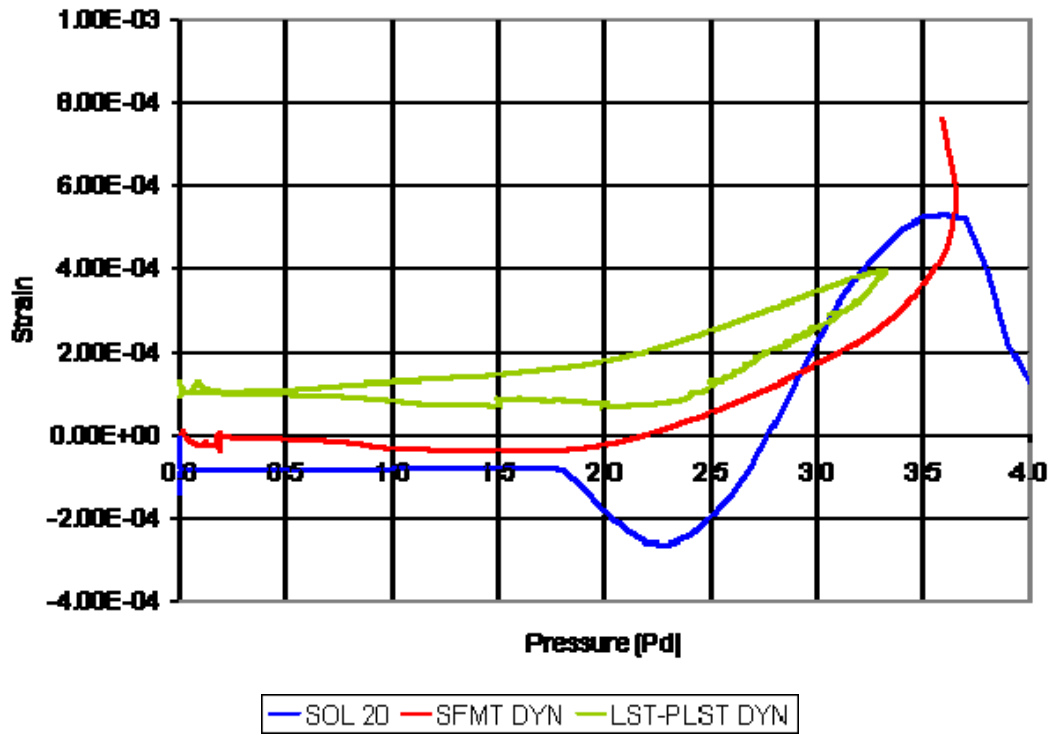


Figure C 46. Rebar strain at Standard output location 20.

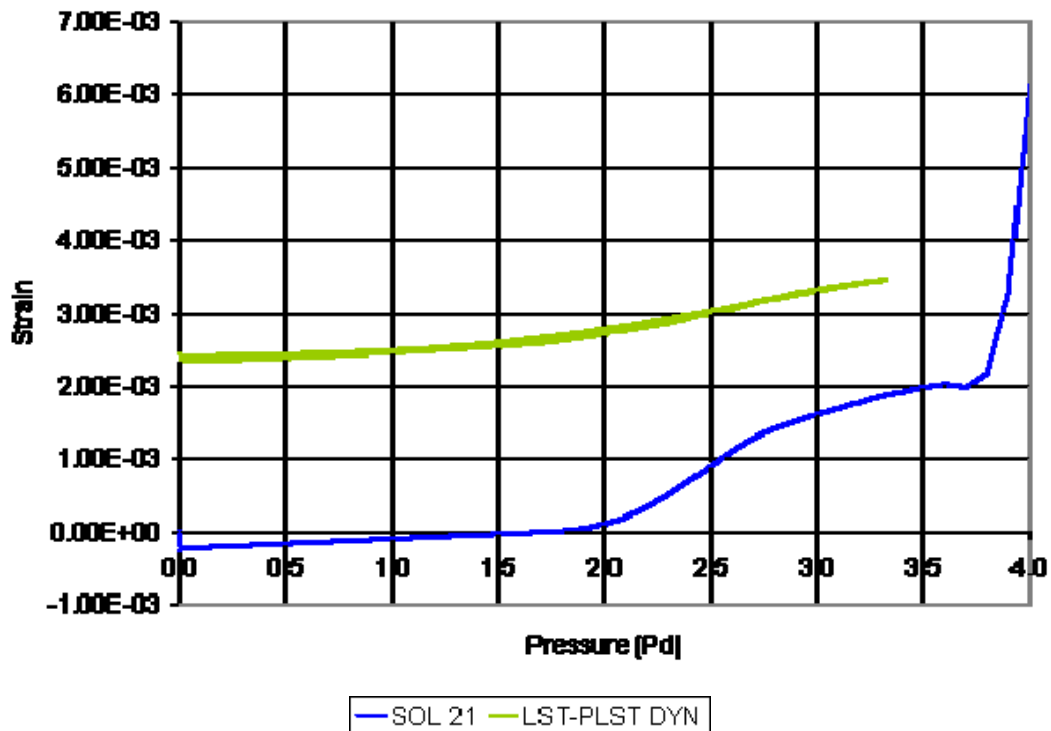


Figure C 47. Rebar strain at Standard output location 21.

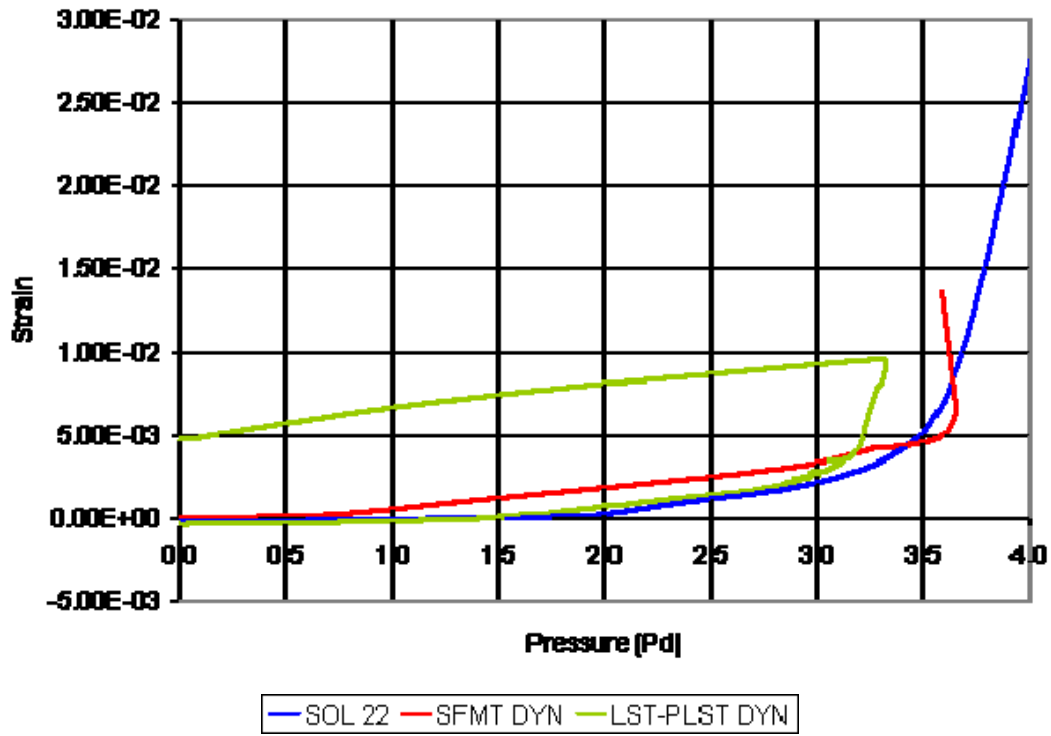


Figure C 48. Rebar strain at Standard output location 22.

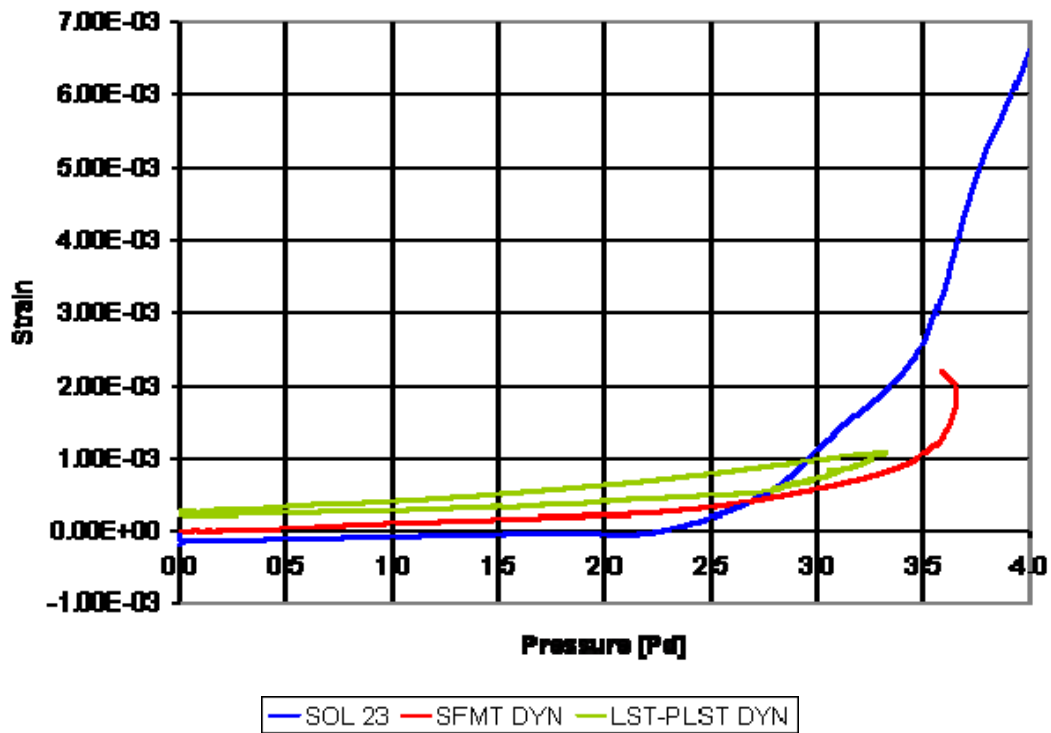


Figure C 49. Rebar strain at Standard output location 23.

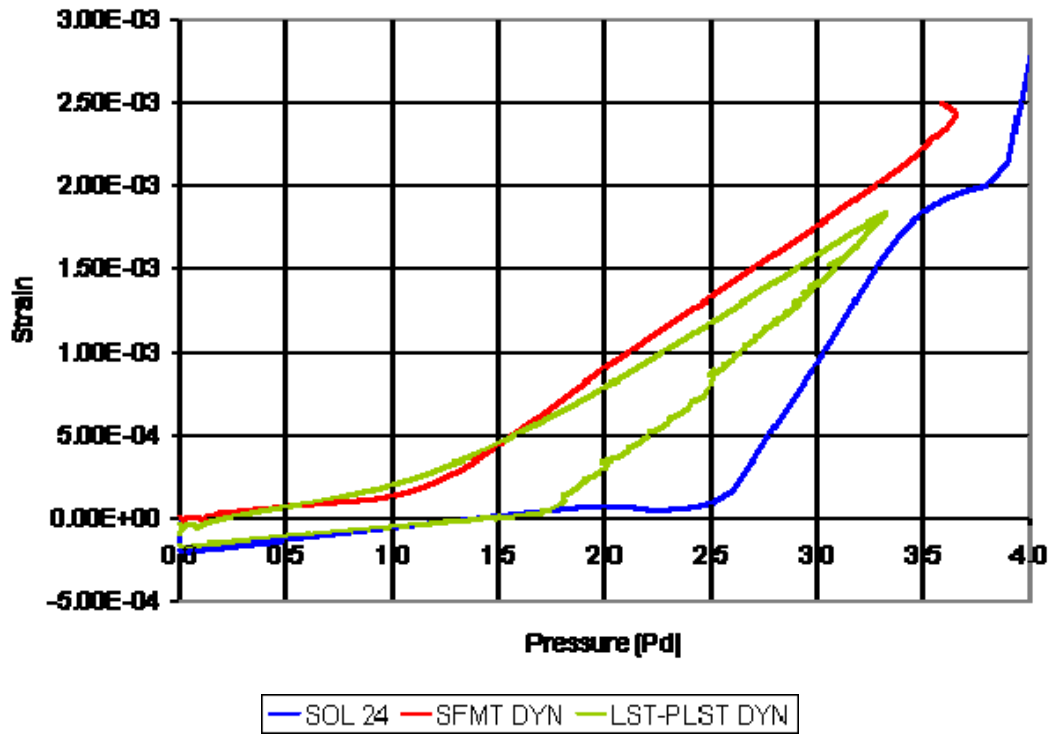


Figure C 50. Rebar strain at Standard output location 24.

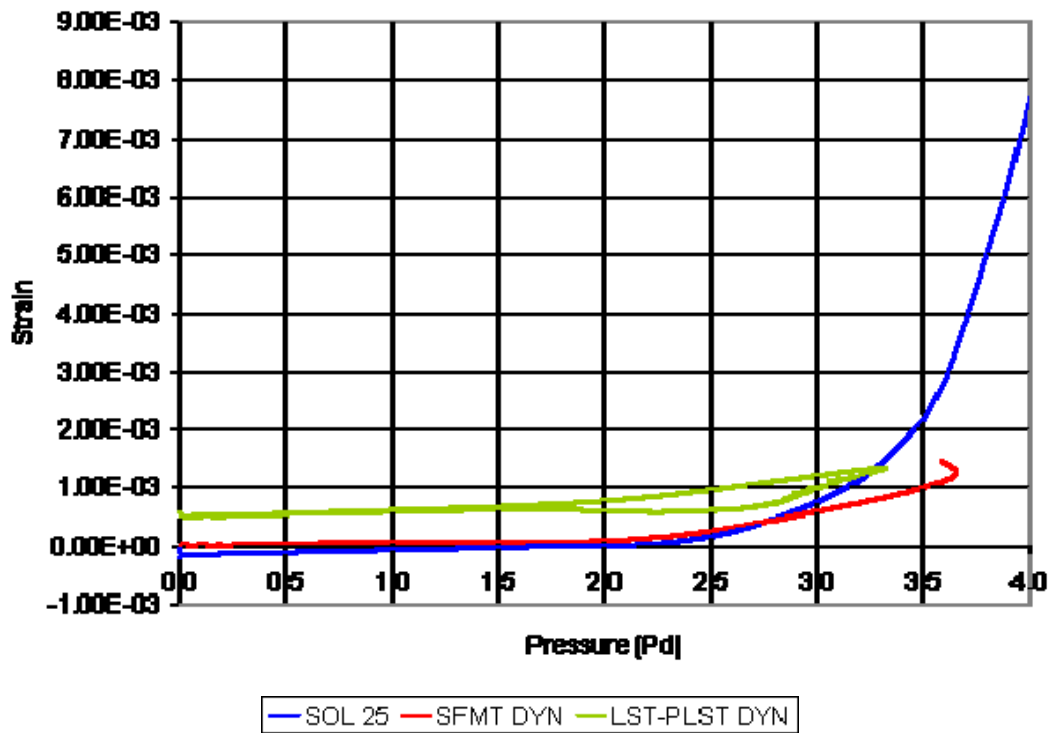


Figure C 51. Rebar strain at Standard output location 25.

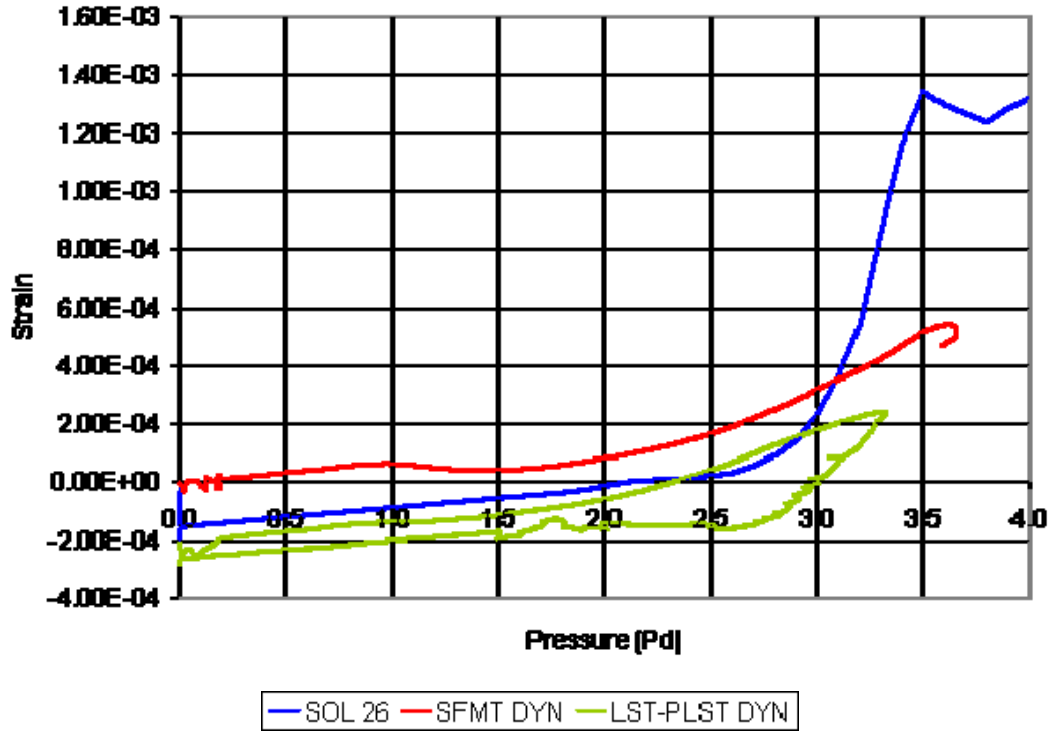


Figure C 52. Rebar strain at Standard output location 26.

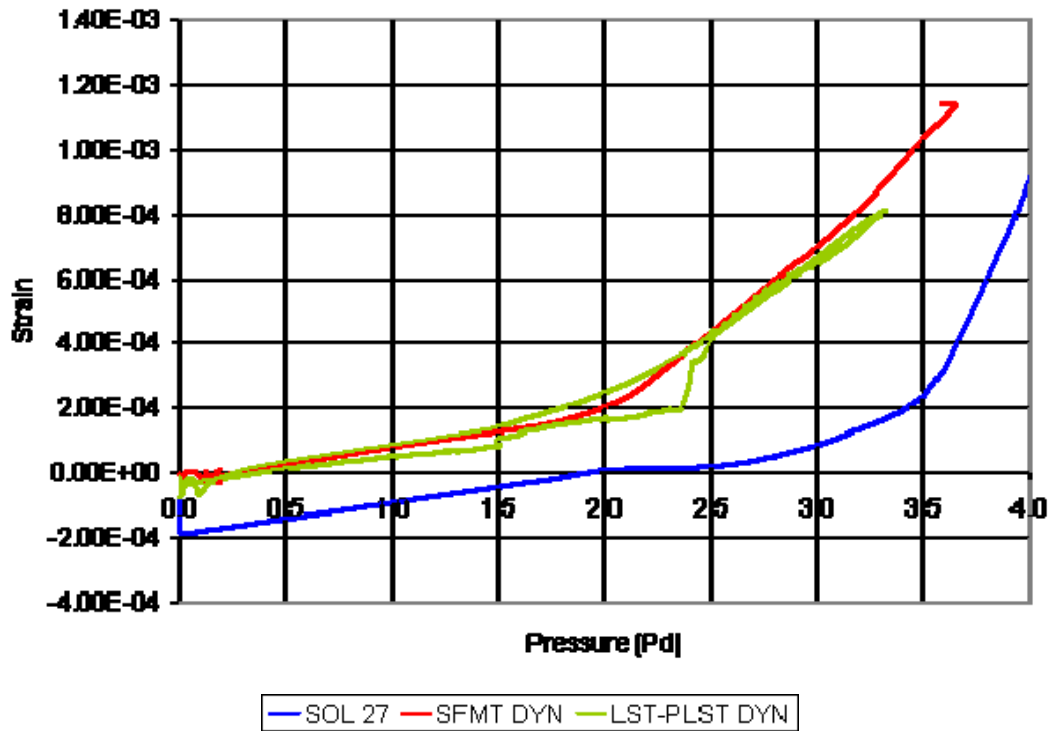


Figure C 53. Rebar strain at Standard output location 27.

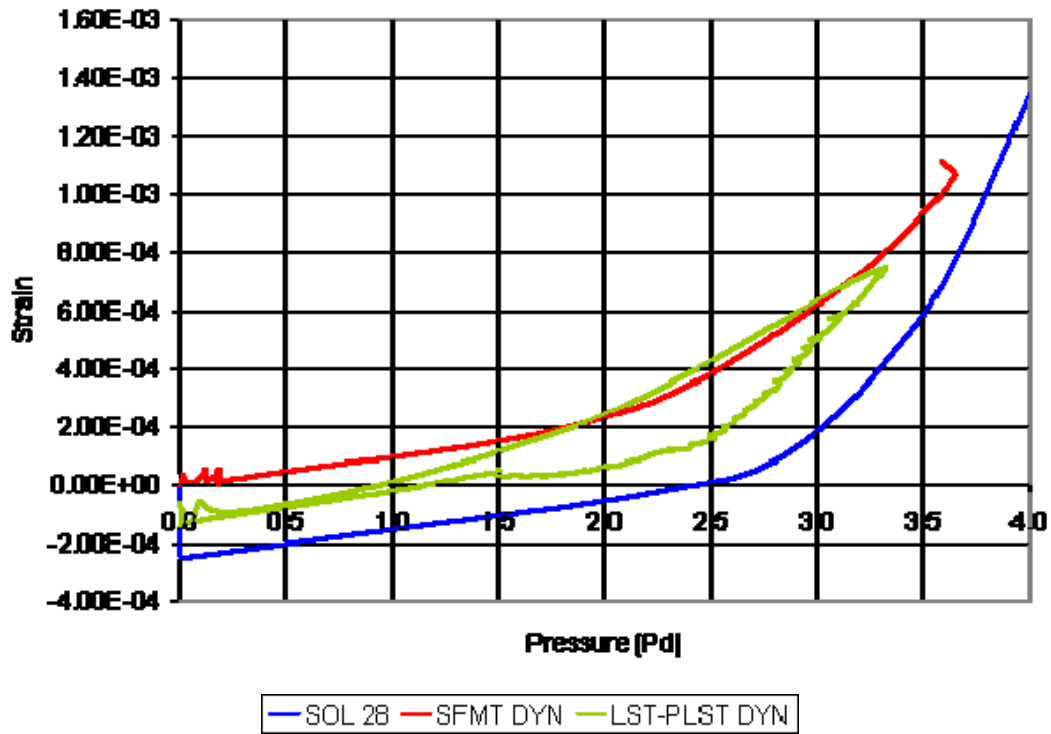


Figure C 54. Rebar strain at Standard output location 28.

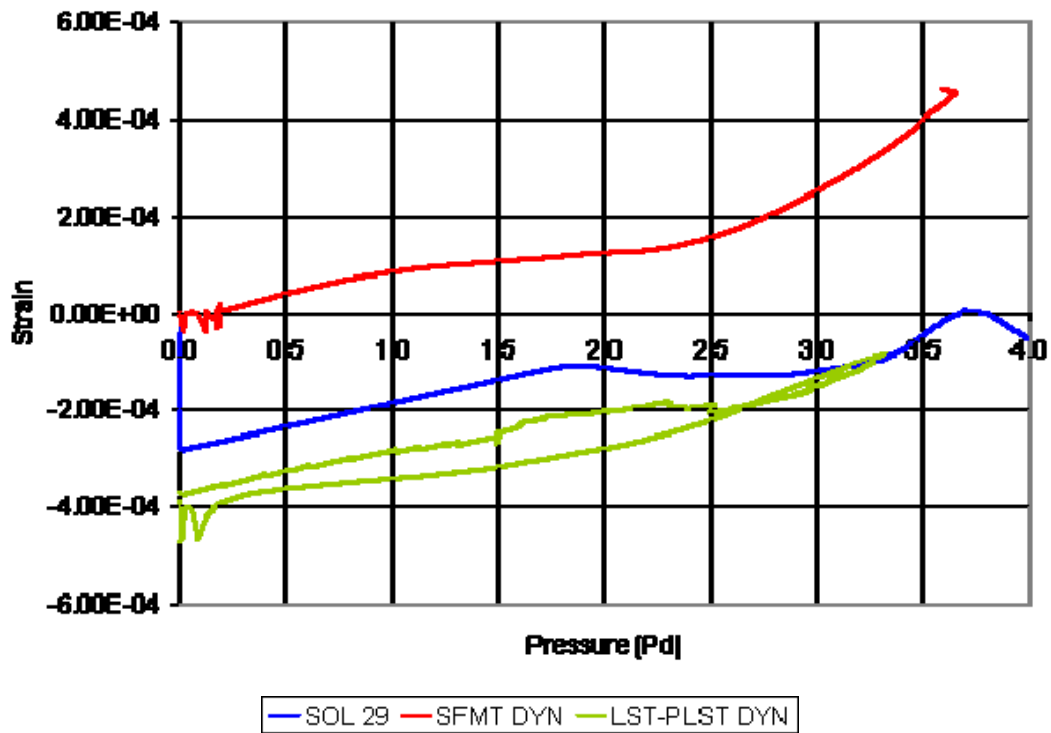


Figure C 55. Rebar strain at Standard output location 29.

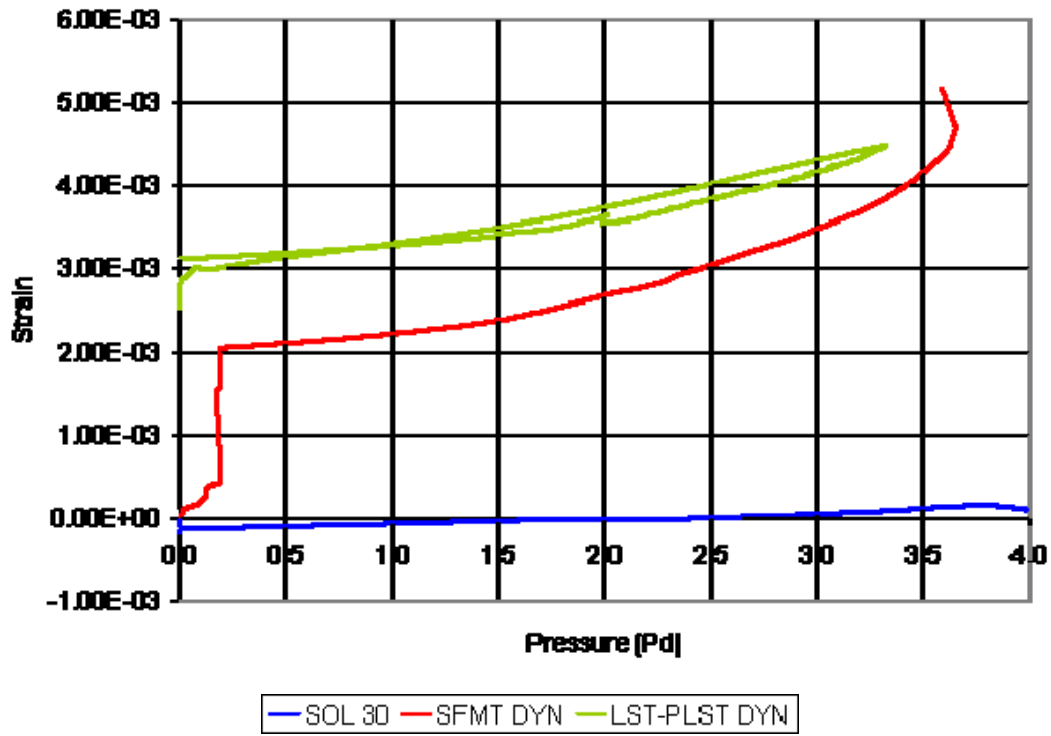


Figure C 56. Rebar strain at Standard output location 30.

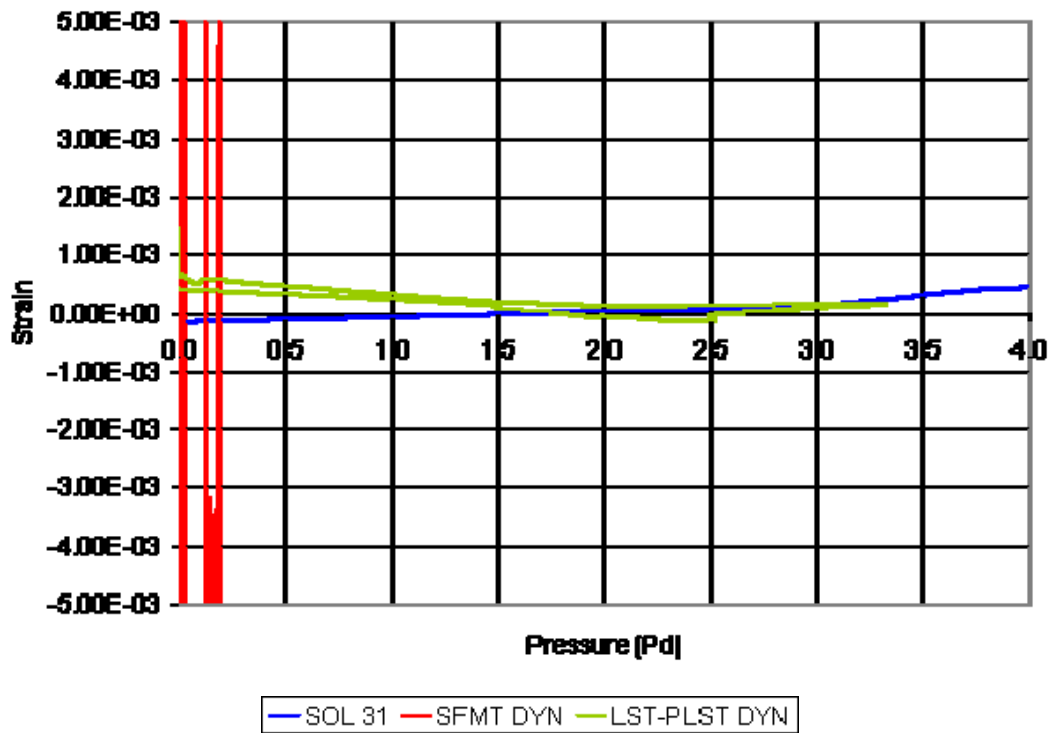


Figure C 57. Rebar strain at Standard output location 31.

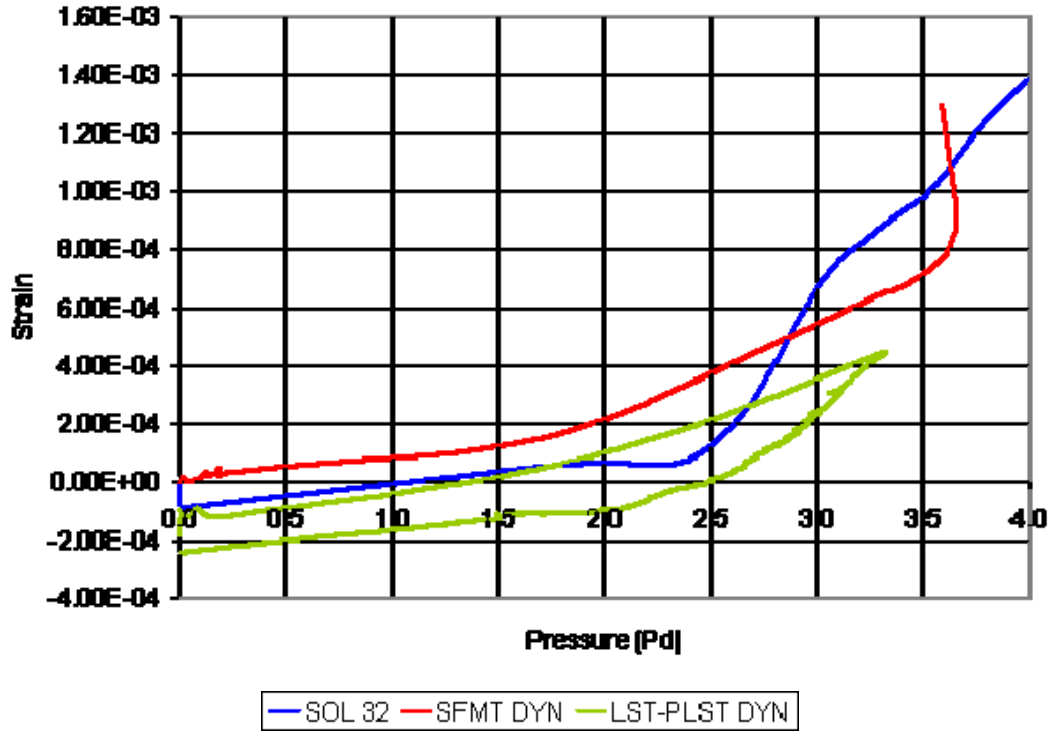


Figure C 58. Rebar strain at Standard output location 32.

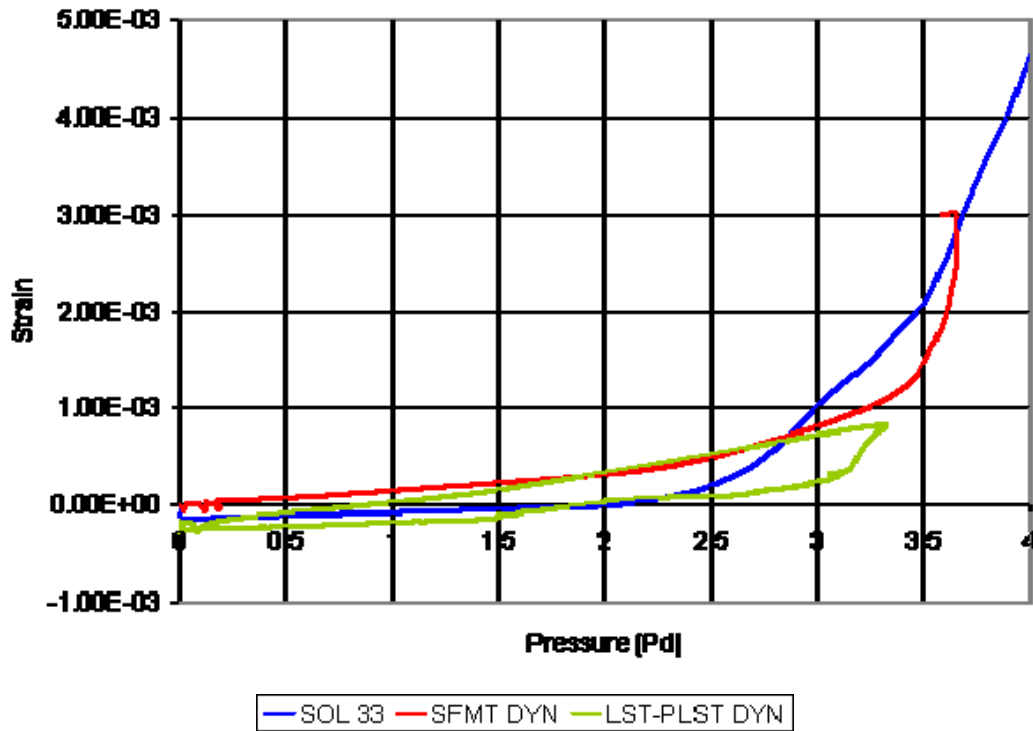


Figure C 59. Rebar strain at Standard output location 33.

Liner strains

Figure C s 60 to 73 present the measured and simulated rebar strains at the standard output locations 34 to 47. The simulation results do not correspond to the measured values at all cases.

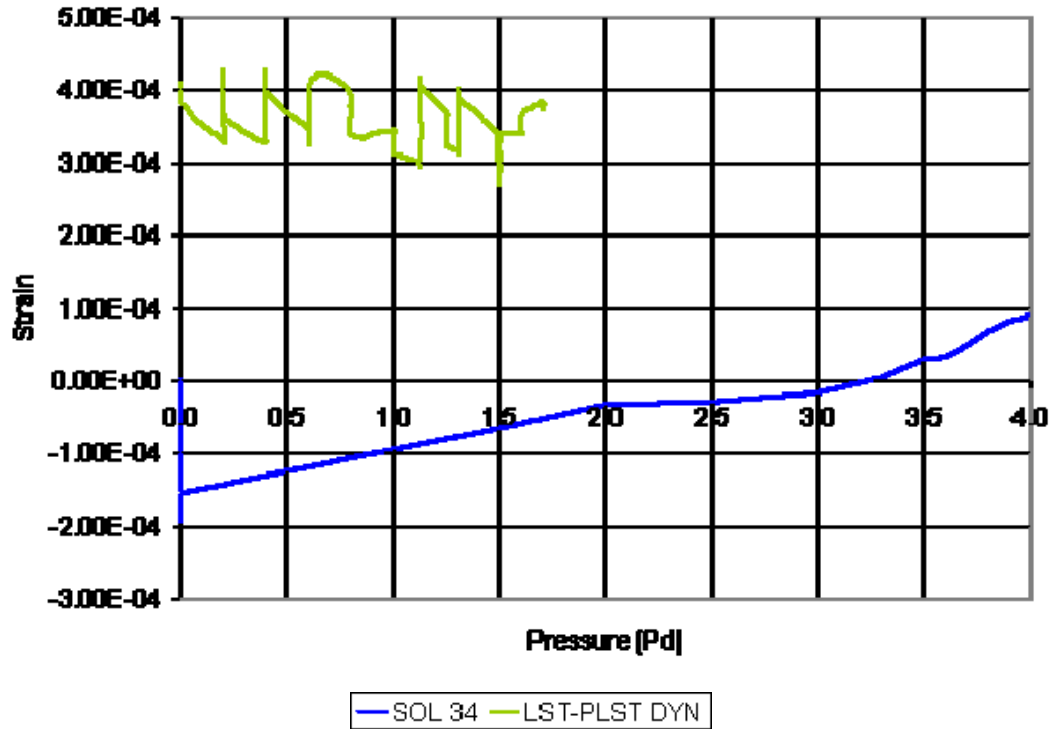


Figure C 60. Vertical liner strain at Standard output location 34.

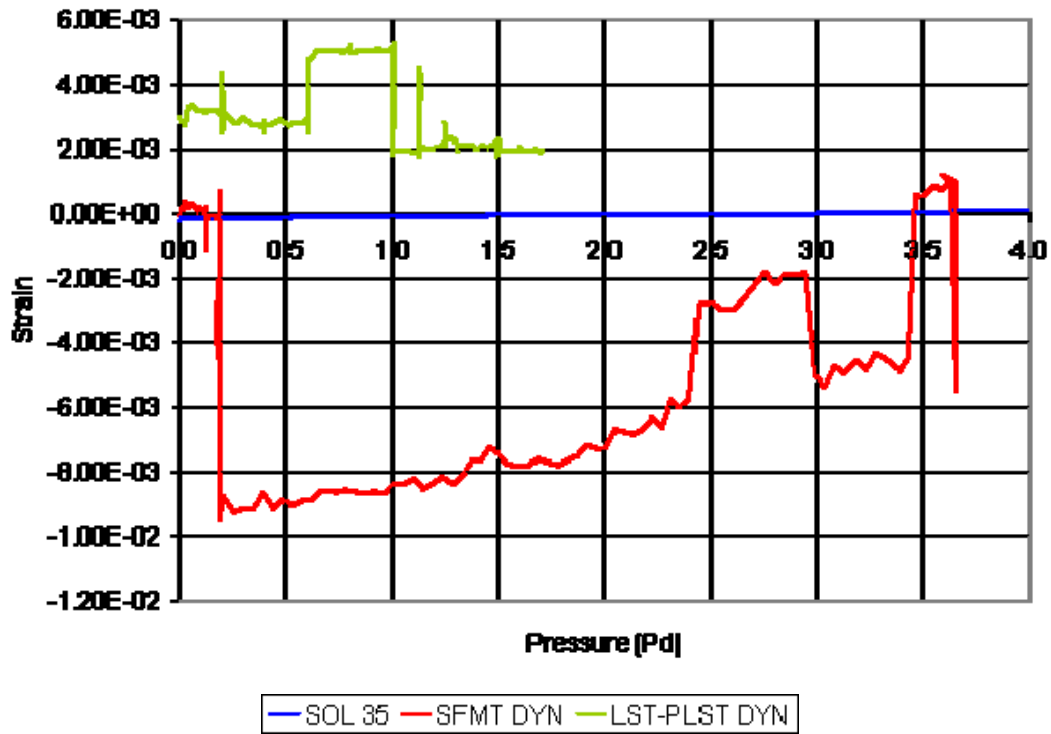


Figure C 61. Vertical liner strain at Standard output location 35.

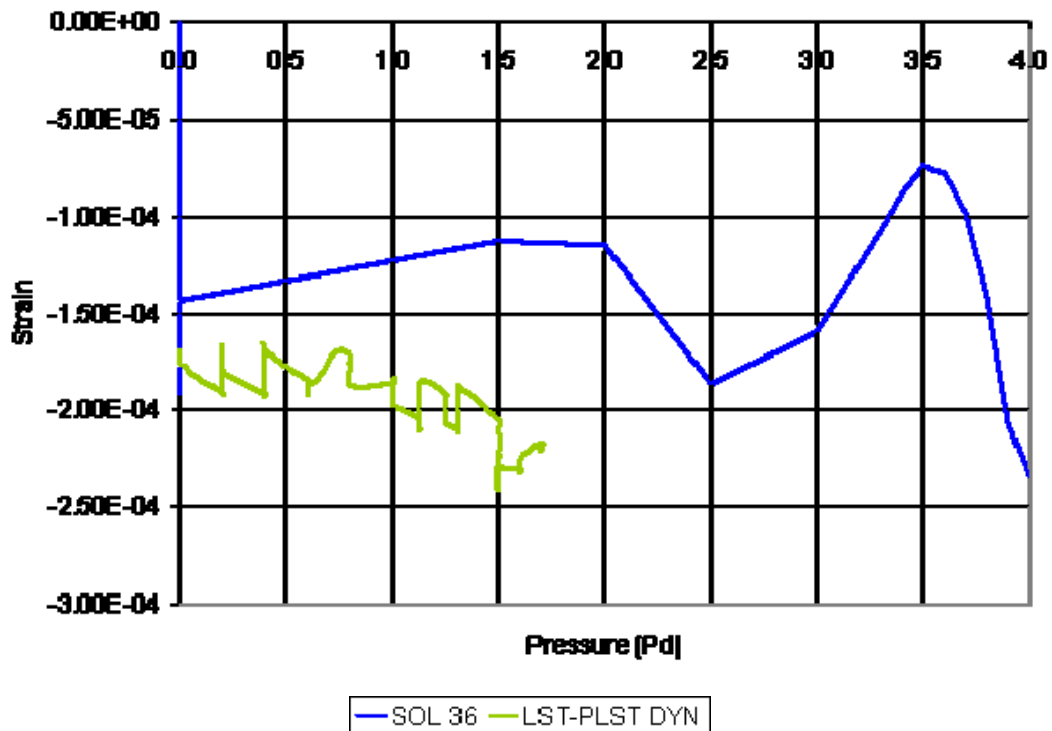


Figure C 62. Vertical liner strain at Standard output location 36.

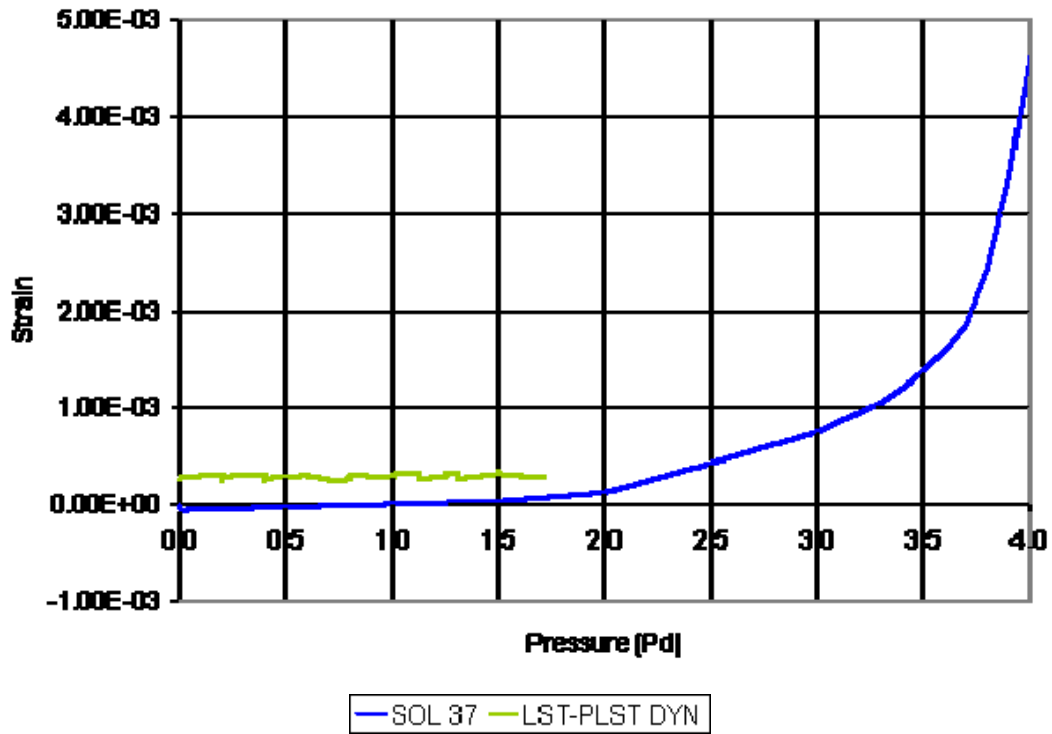


Figure C 63. Hoop liner strain at Standard output location 37.

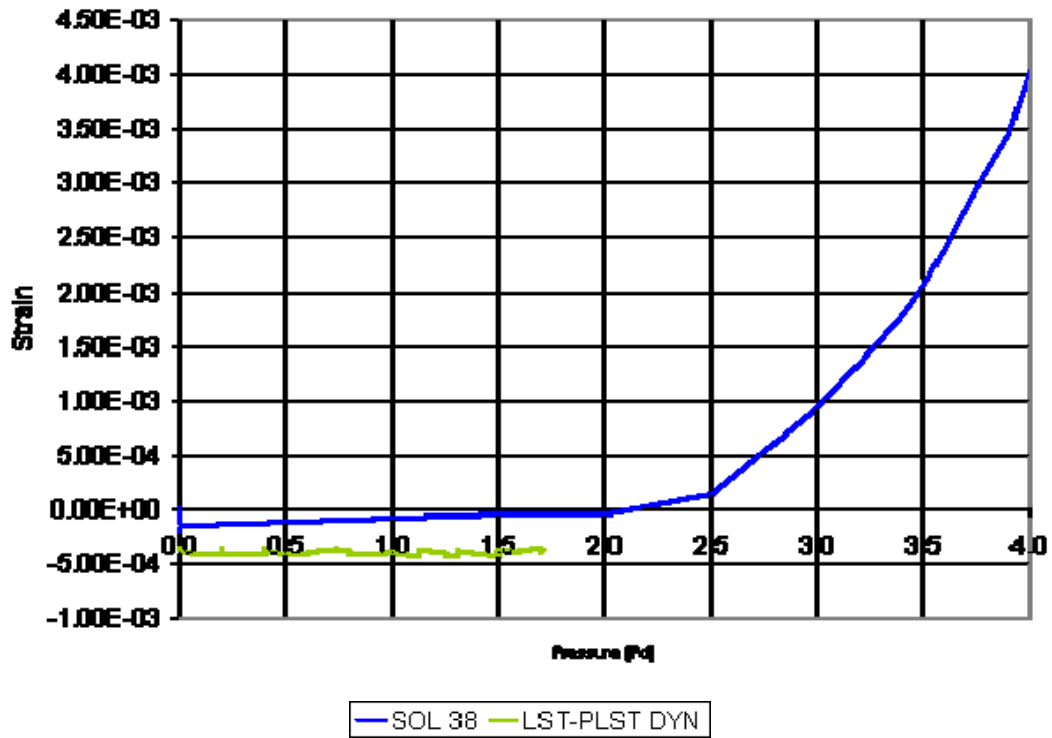


Figure C 64. Vertical liner strain at Standard output location 38.

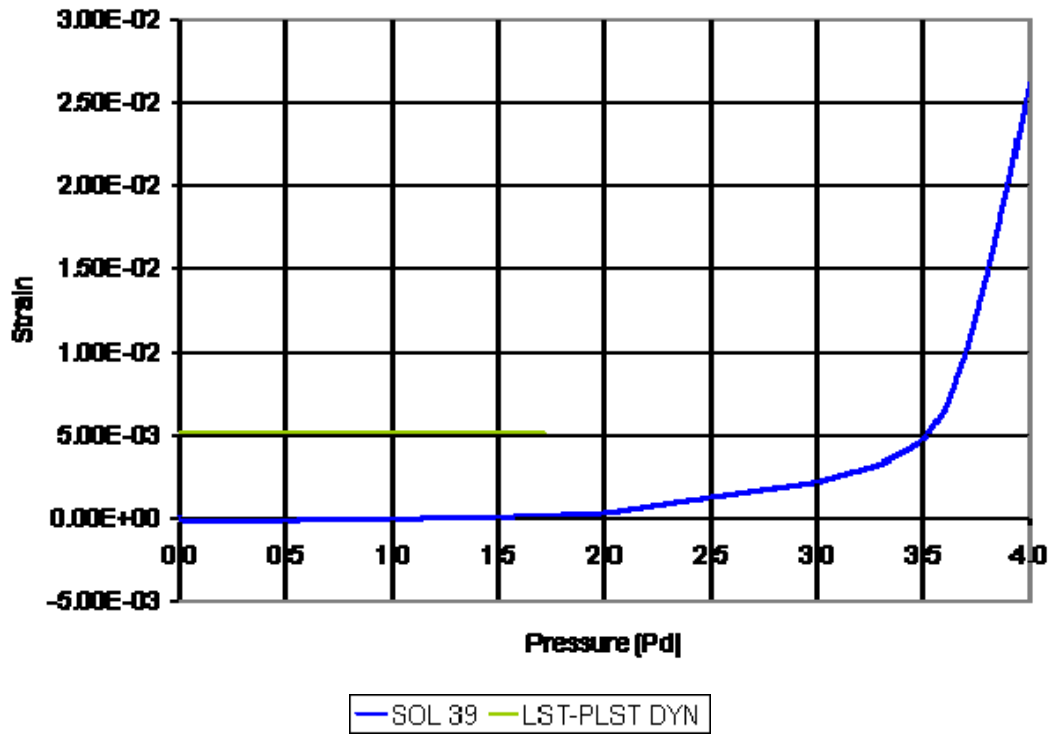


Figure C 65. Hoop liner strain at Standard output location 39.

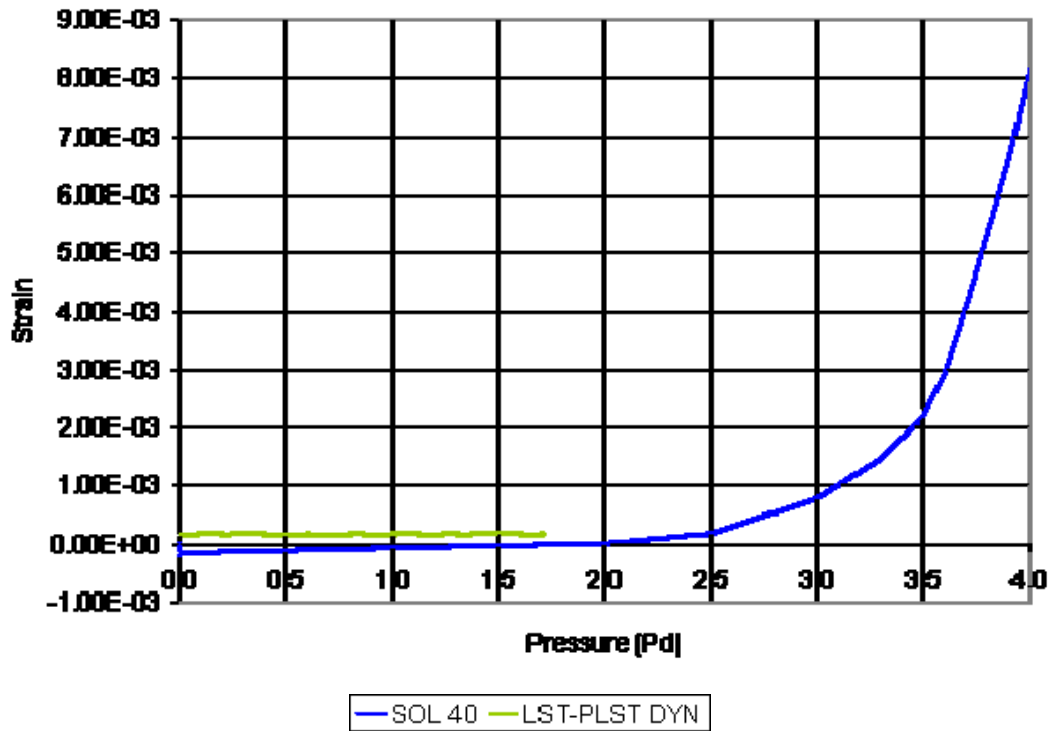


Figure C 66. Vertical liner strain at Standard output location 40.

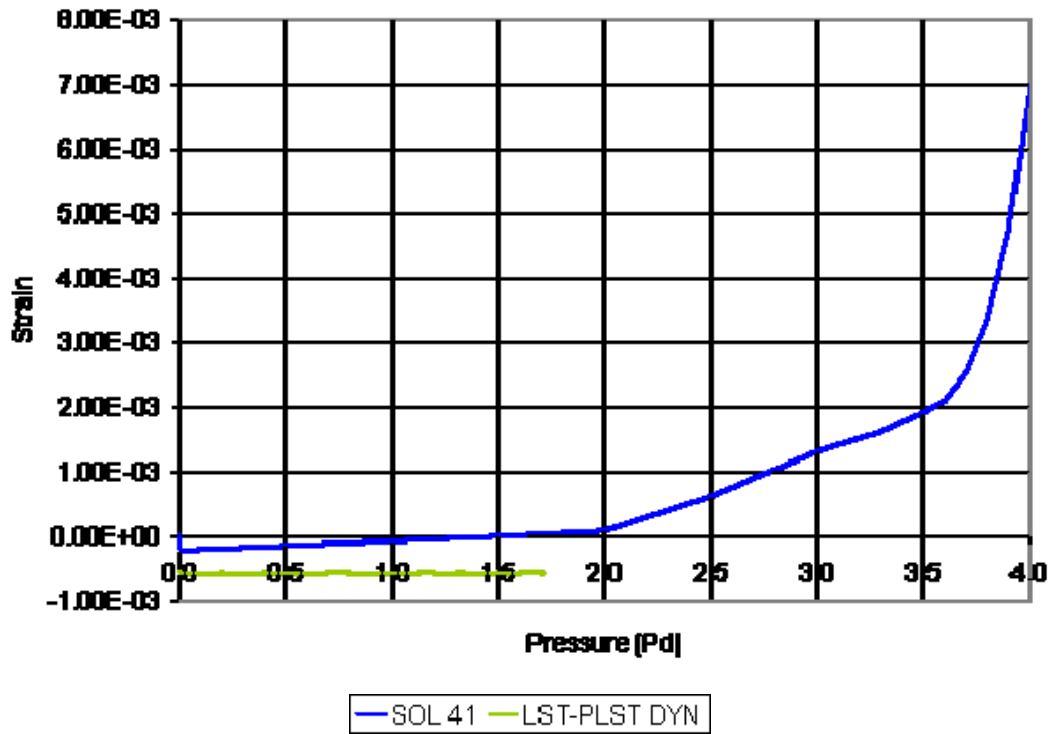


Figure C 67. Hoop liner strain at Standard output location 41.

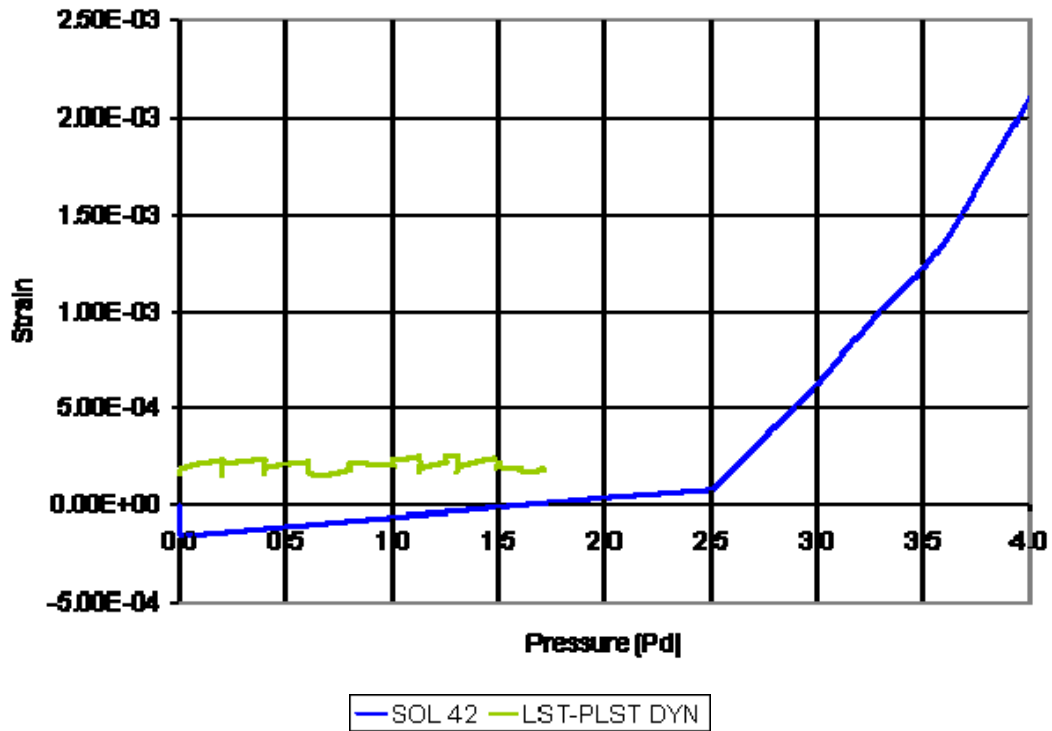


Figure C 68. Vertical liner strain at Standard output location 42.

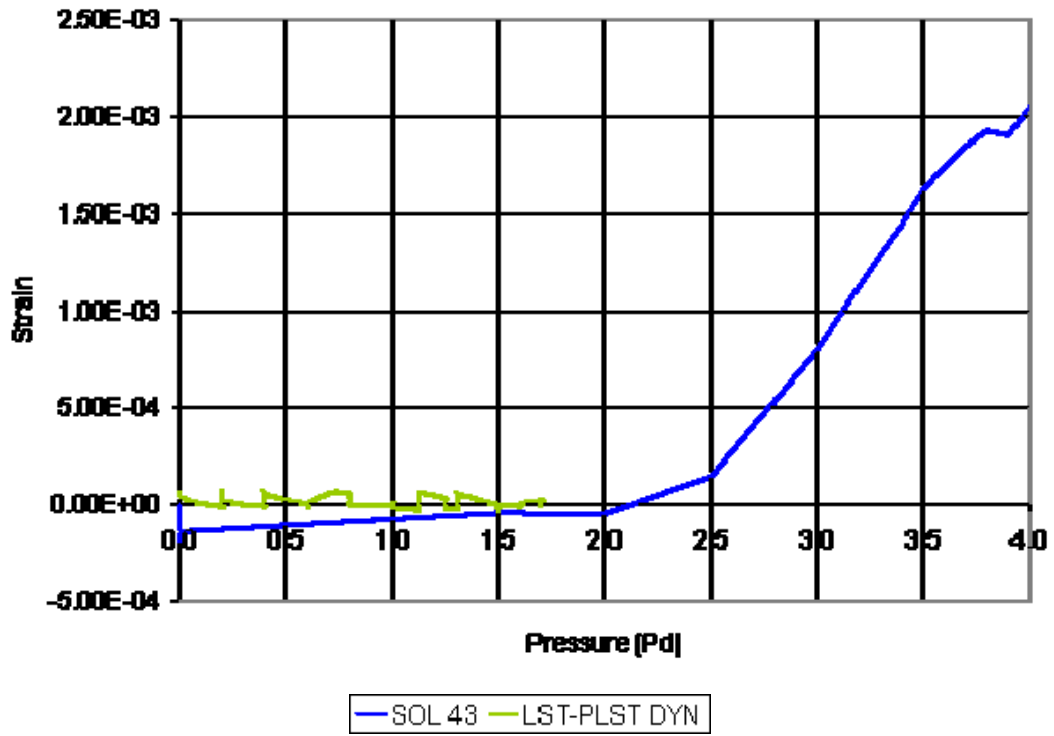


Figure C 69. Vertical liner strain at Standard output location 43.

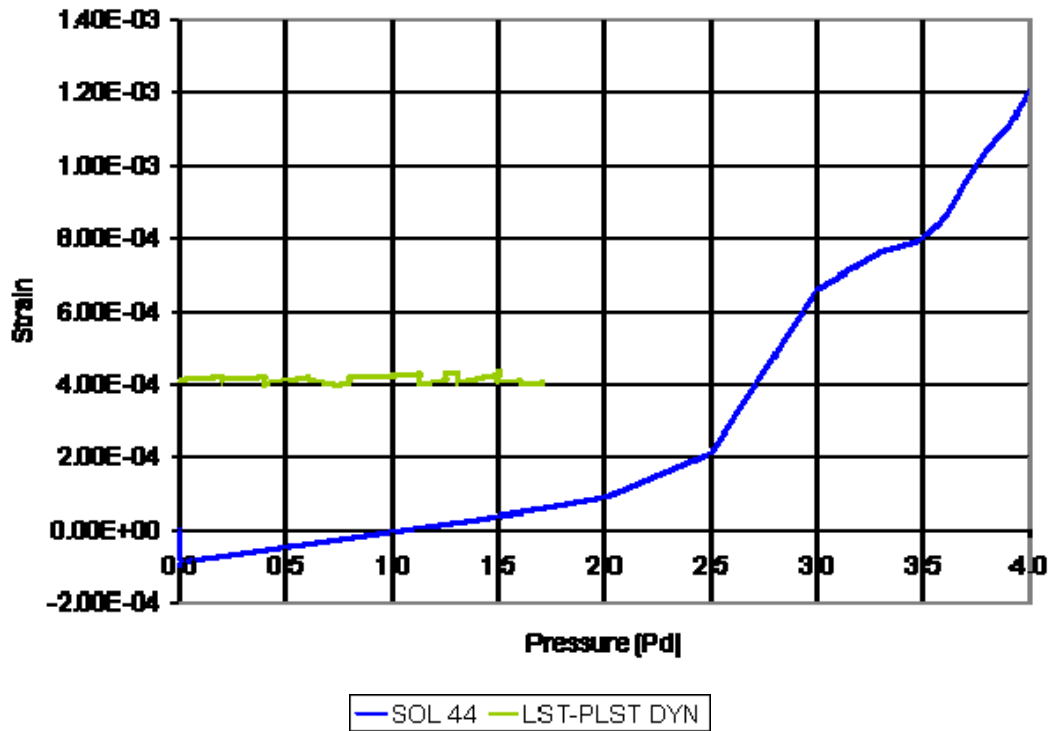


Figure C 70. Hoop liner strain at Standard output location 44.

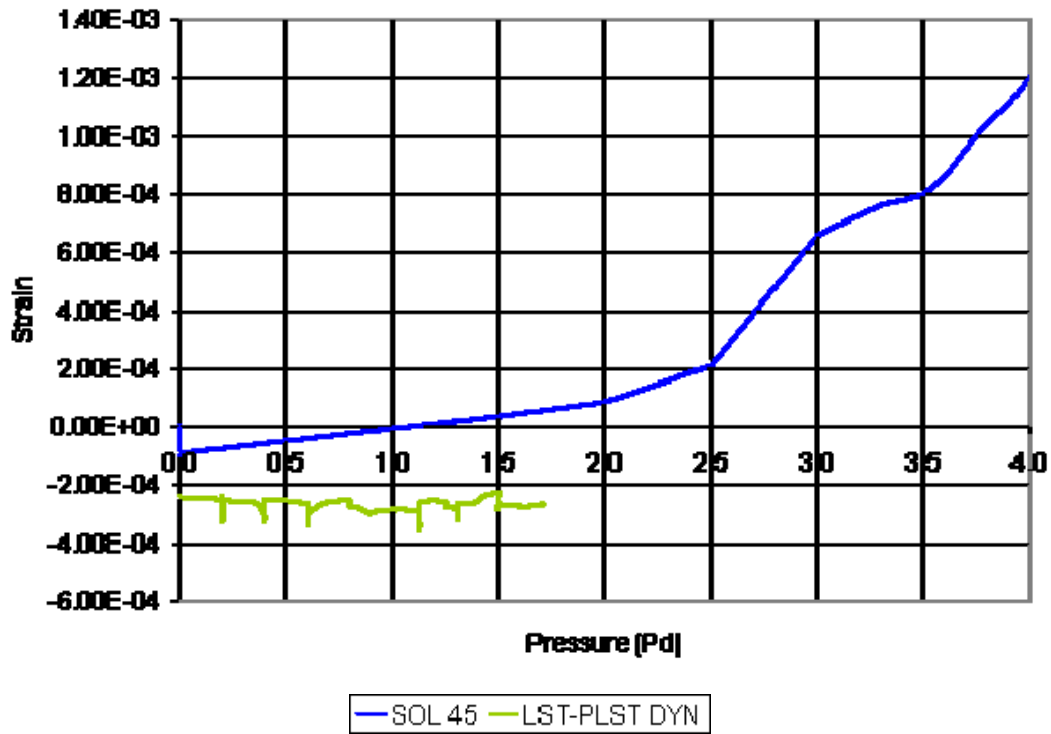


Figure C 71. Hoop liner strain at Standard output location 45.

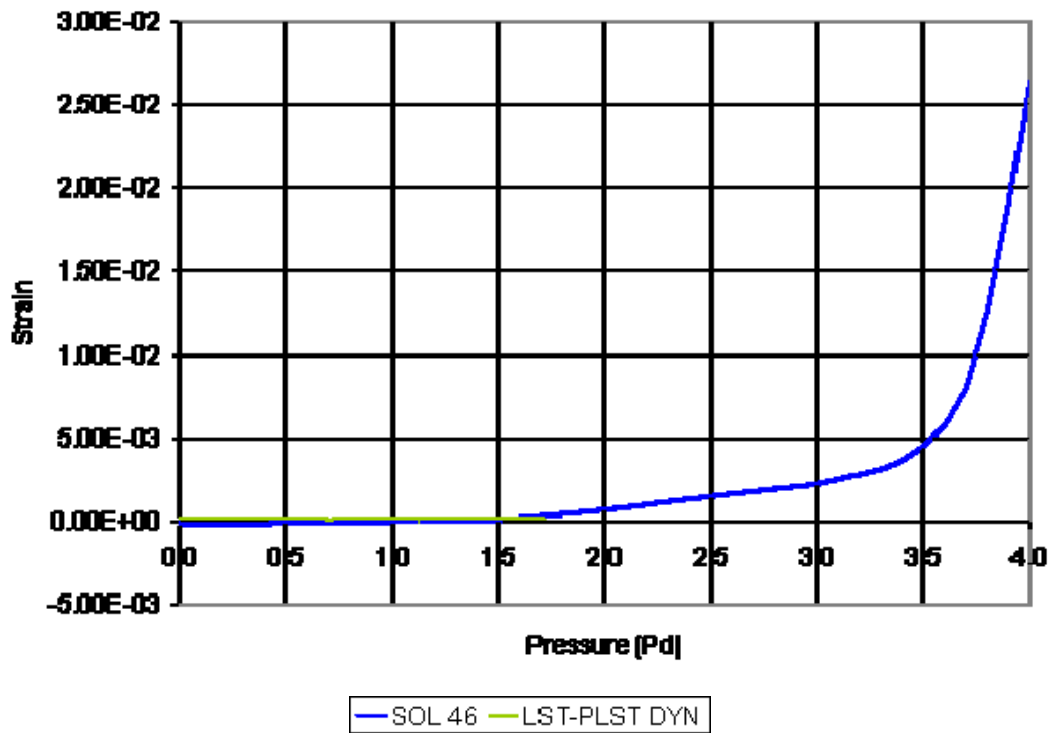


Figure C 72. Hoop liner strain at Standard output location 46.

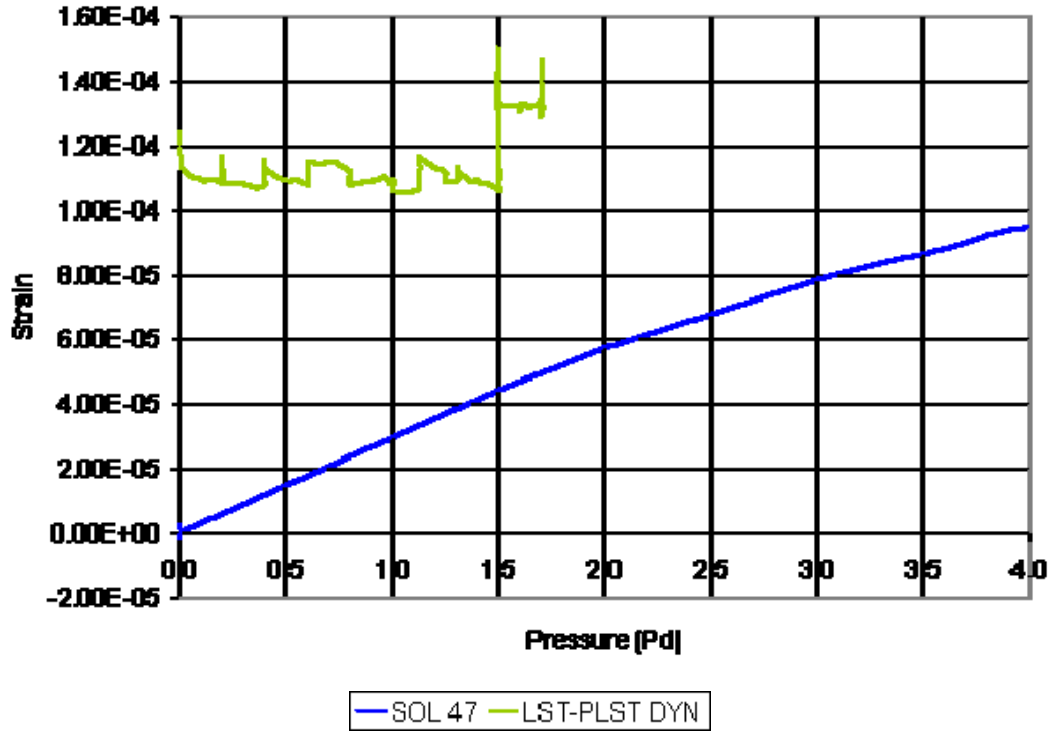


Figure C 73. Radial liner strain at Standard output location 47.

Tendon strains and forces

Figure C s 74 to 79 present the measured and simulated tendon strains at the standard output locations 48 to 53. Figure C s 80 and 81 present the measured and simulated tendon forces at the standard output locations 54 and 55. The simulation results appear to be in accordance with the test results.

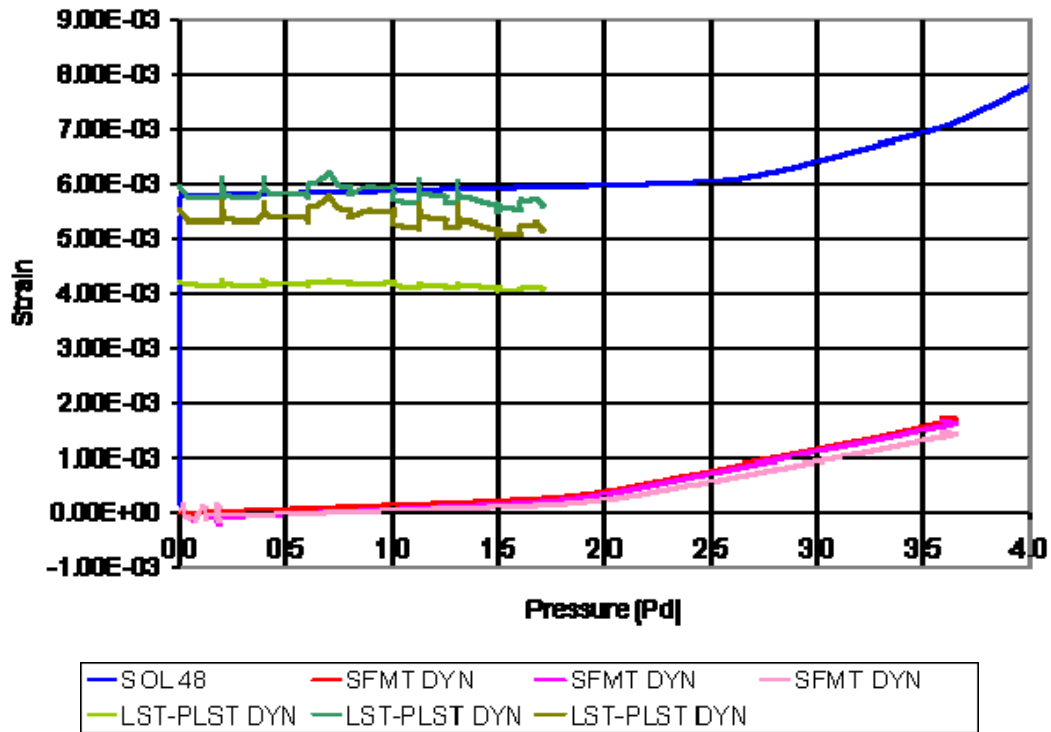


Figure C 74. Tendon strain at Standard output location 48.

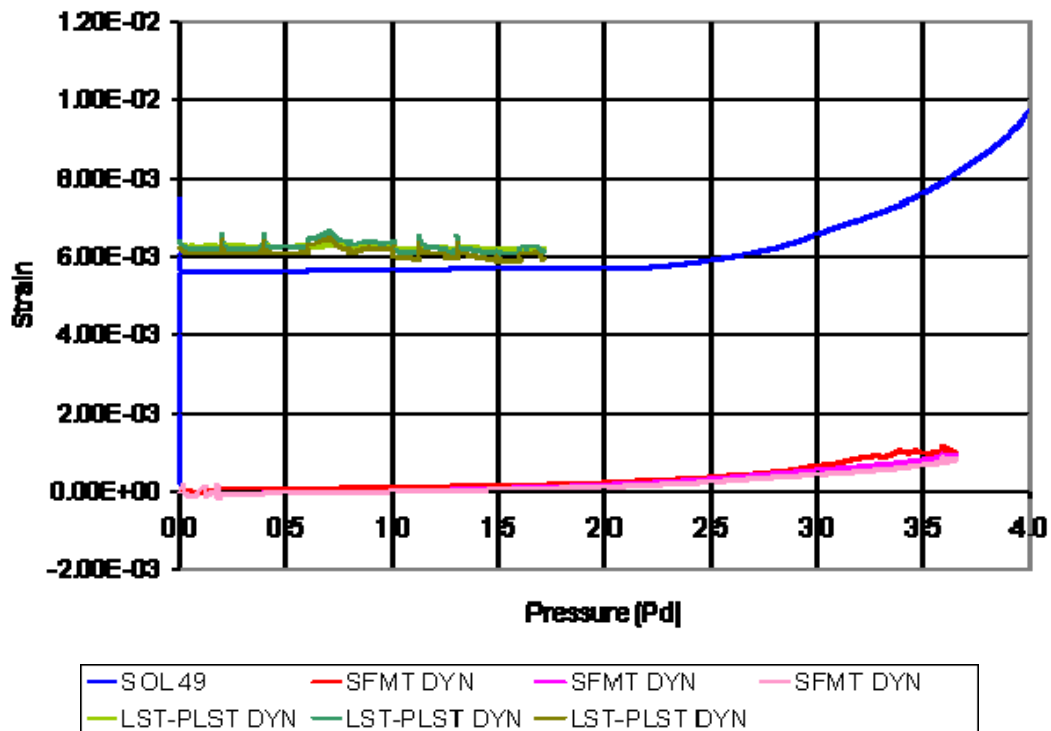


Figure C 75. Tendon strain at Standard output location 49.

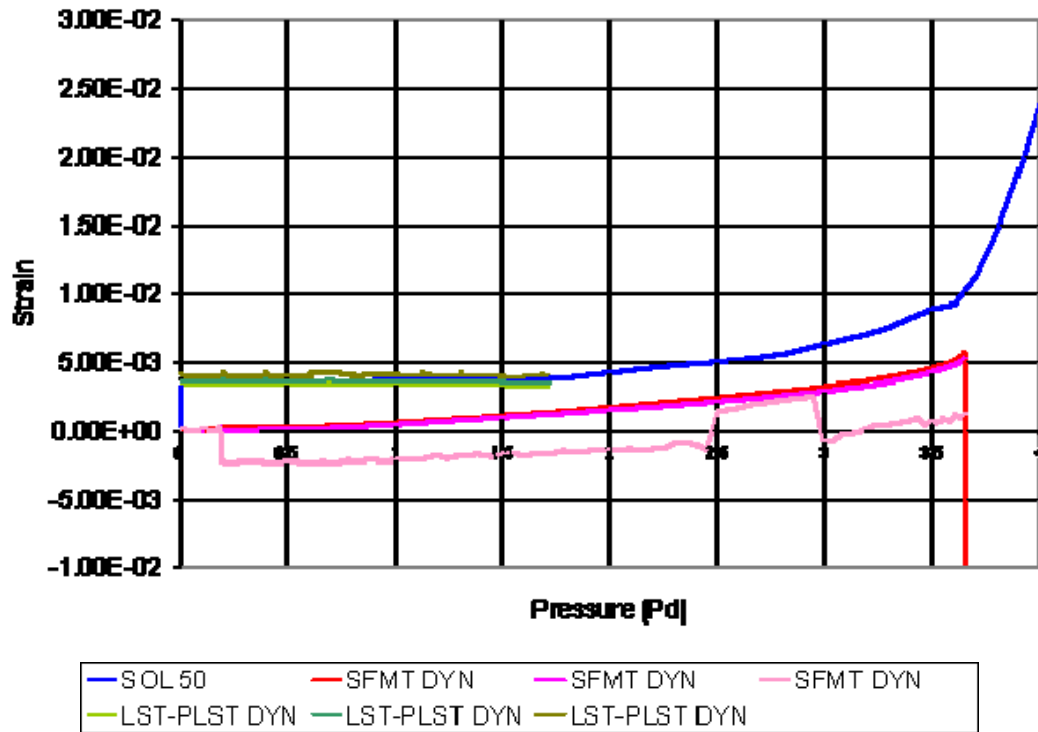


Figure C 76. Tendon strain at Standard output location 50.

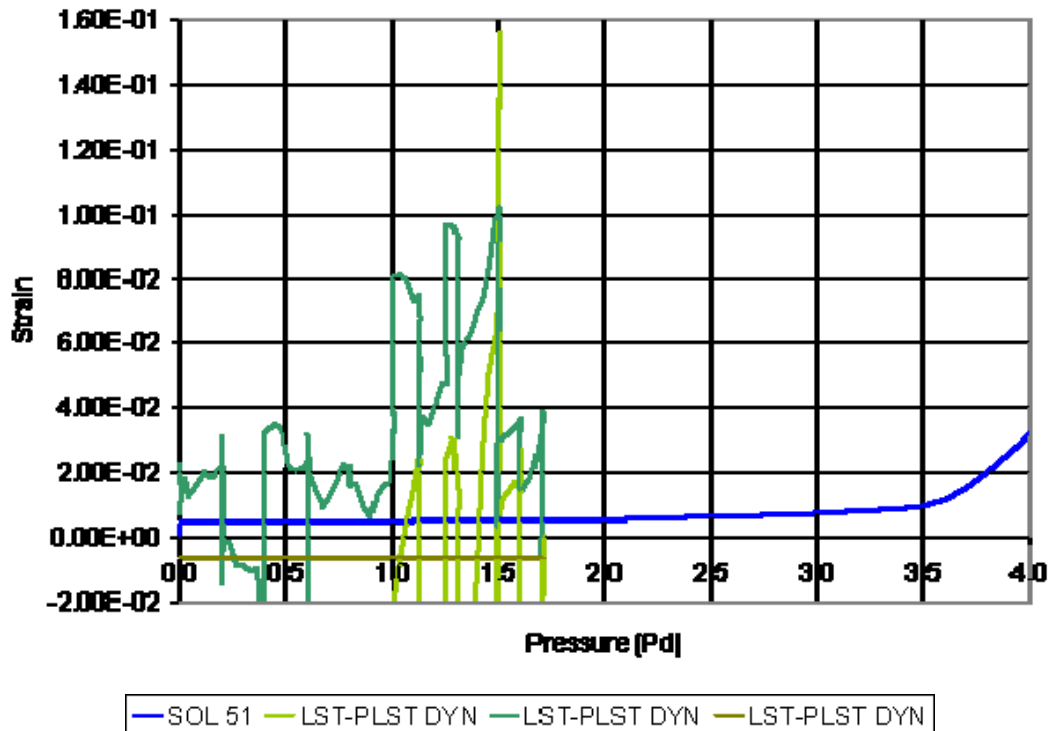


Figure C 77. Tendon strain at Standard output location 51.

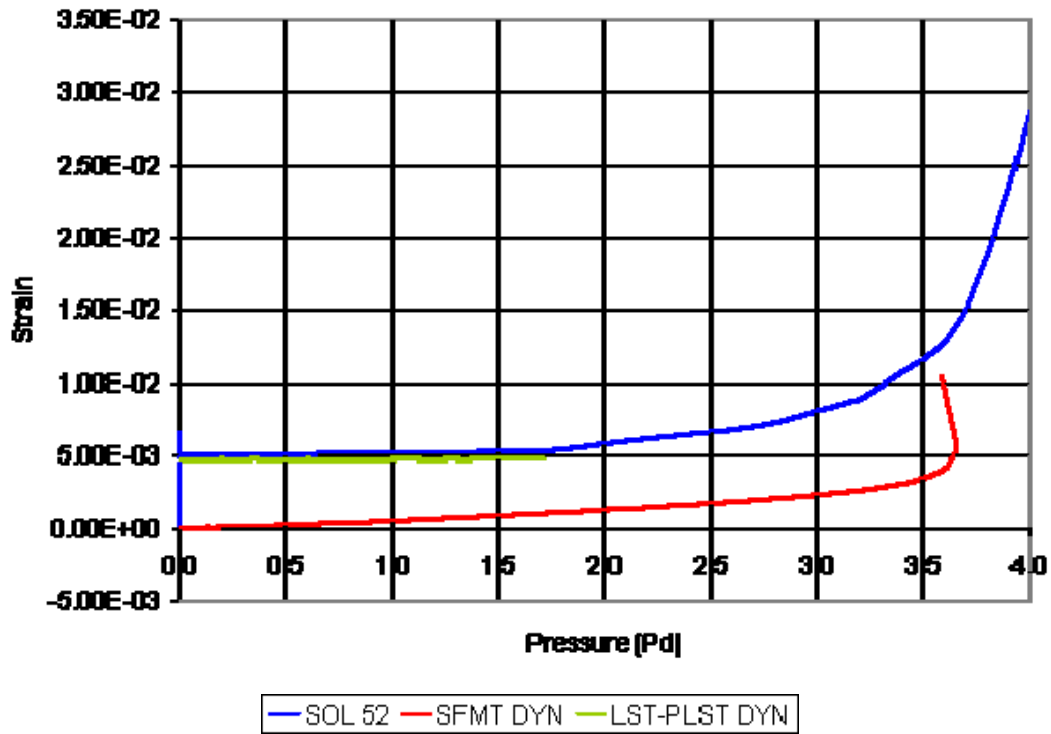


Figure C 78. Tendon strain at Standard output location 52.

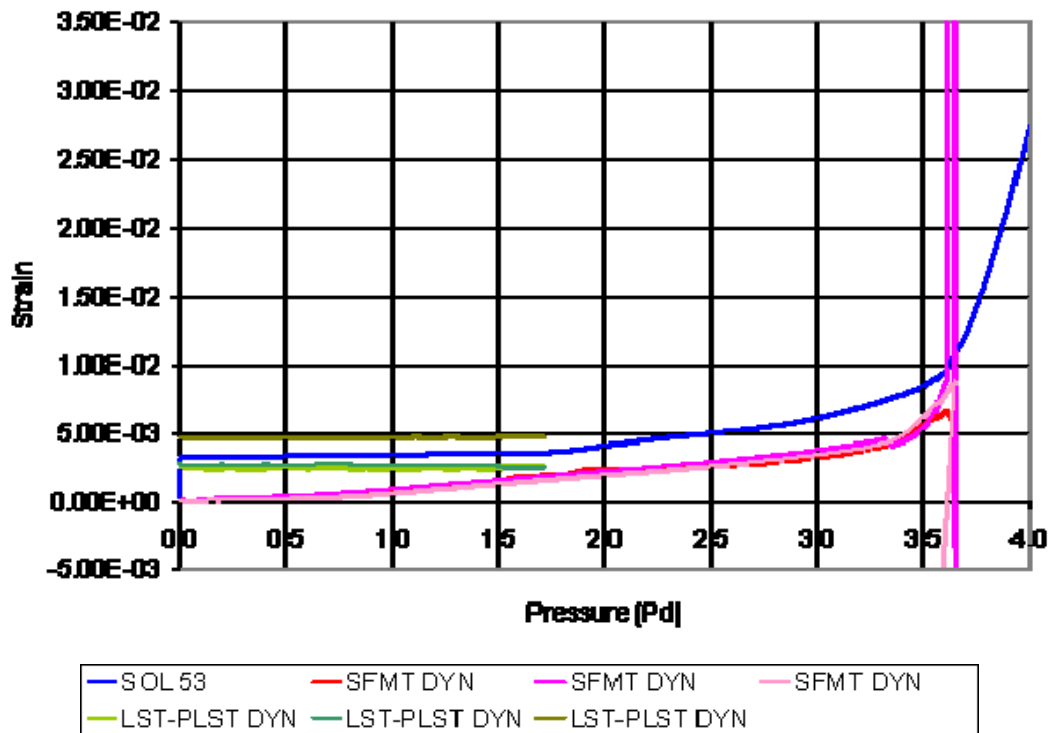


Figure C 79. Tendon strain at Standard output location 53.

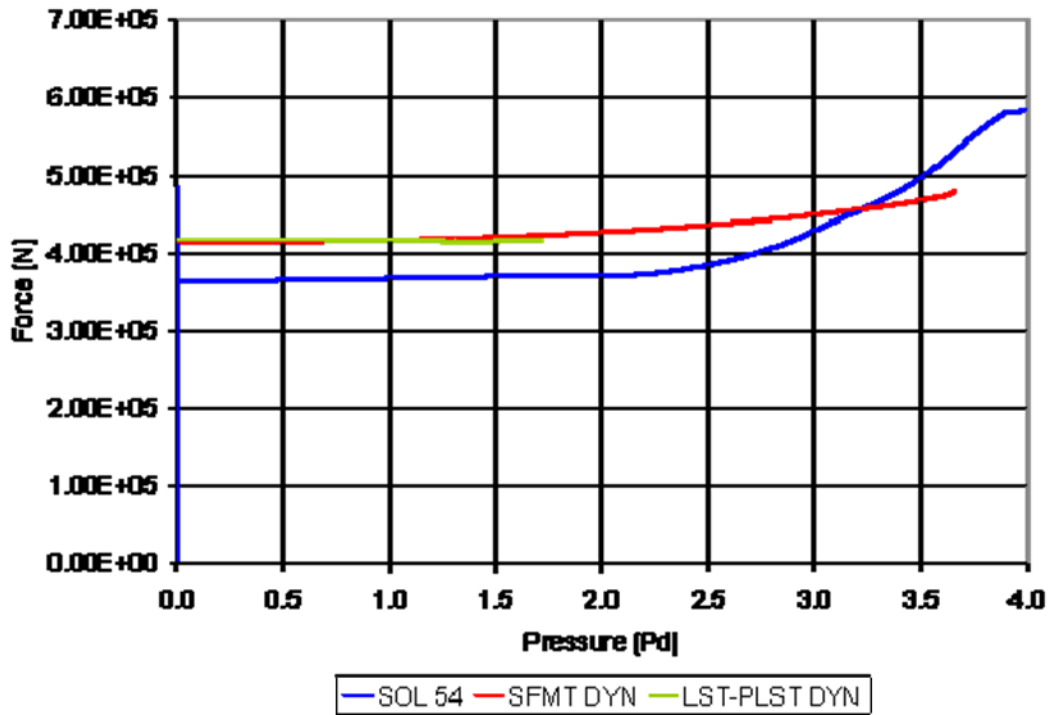


Figure C 80. Tendon force at Standard output location 54.

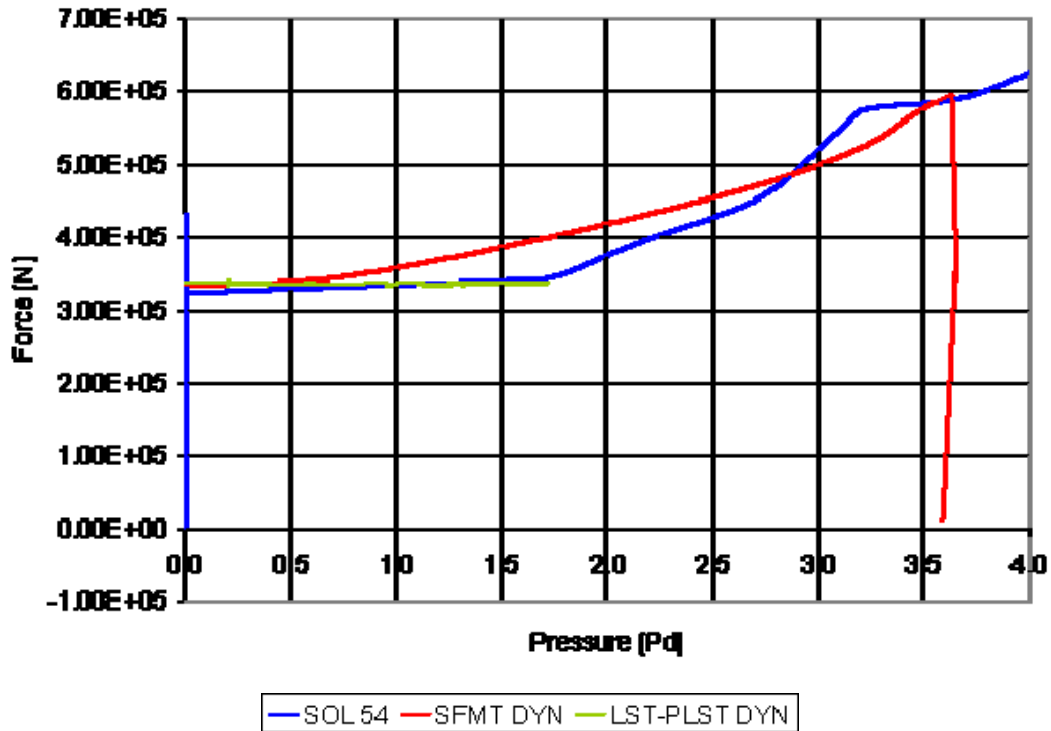


Figure C 81. Tendon force at Standard output location 55.

Peak strains in the liner

Figure C s 82 to 90 present the liner strains as the pressure increases. The maximum liner strains at rupture are near the equipment hatch and the airlock and around azimuth 0°.

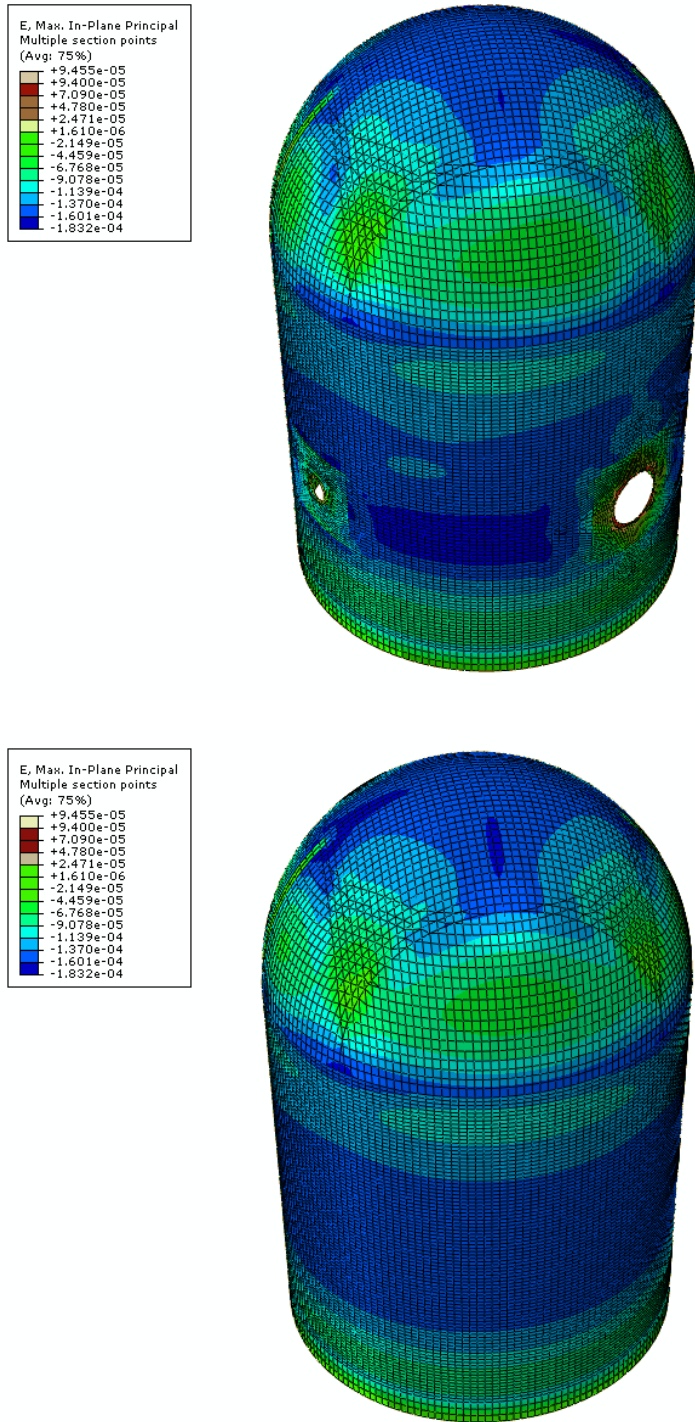


Figure C 82. Peak strains in the liner at applied pressure $P = 0.0 \times Pd$.

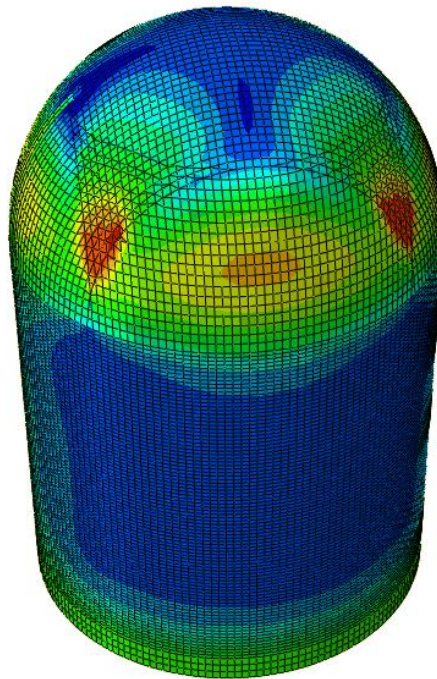
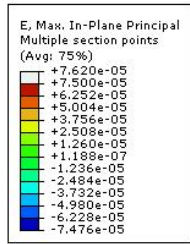
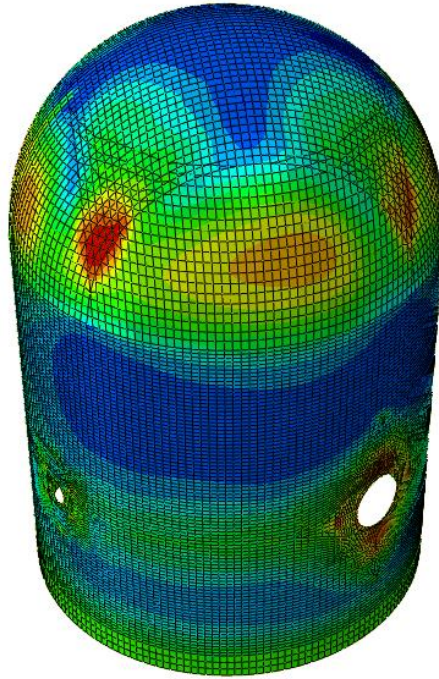
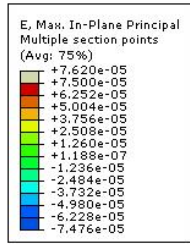


Figure C 83. Peak strains in the liner at applied pressure $P = 1.0 \times Pd$.

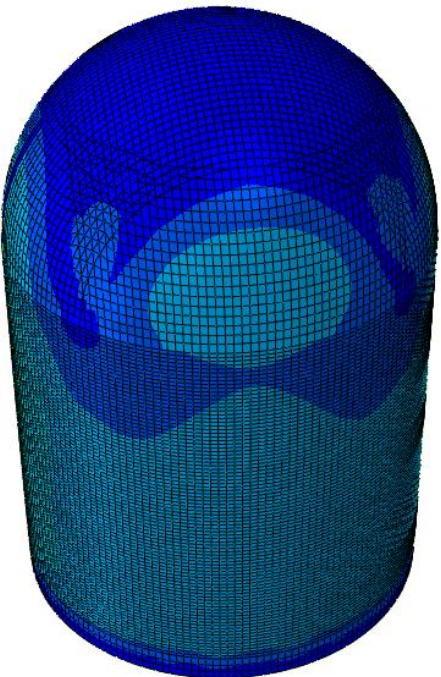
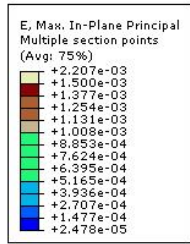
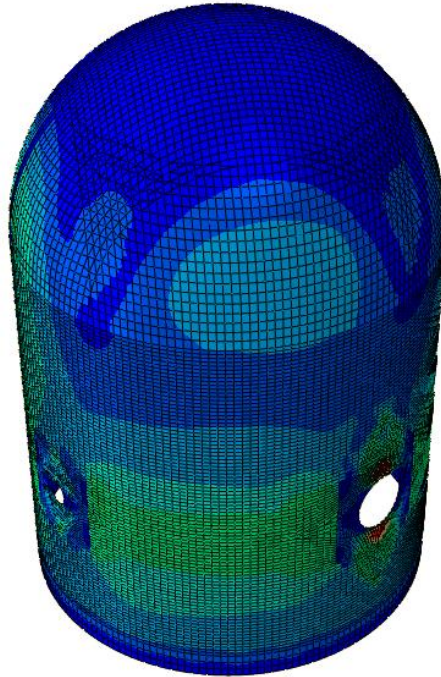
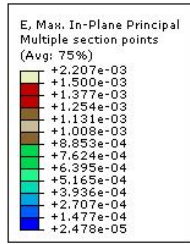


Figure C 84. Peak strains in the liner at applied pressure $P = 2.0 \times Pd$.

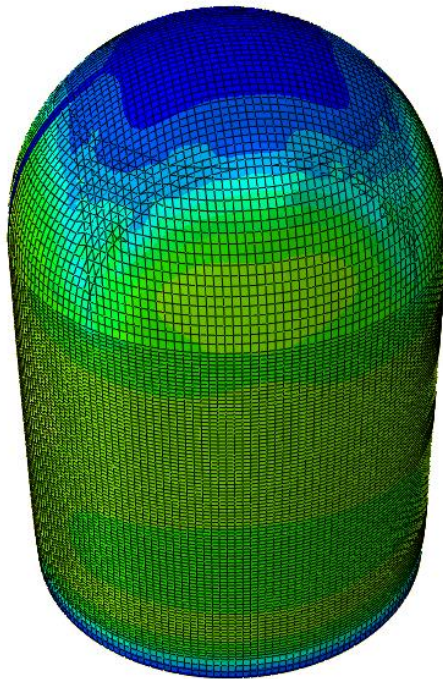
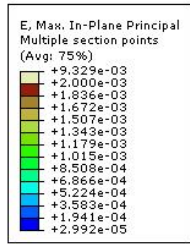
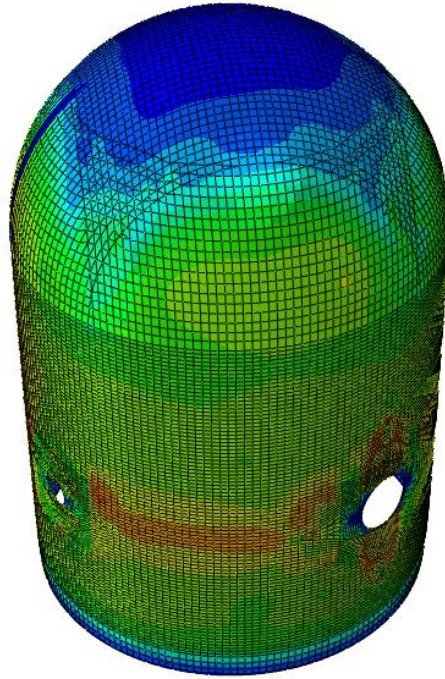
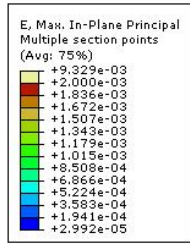


Figure C 85. Peak strains in the liner at applied pressure $P = 2.5 \times P_d$.

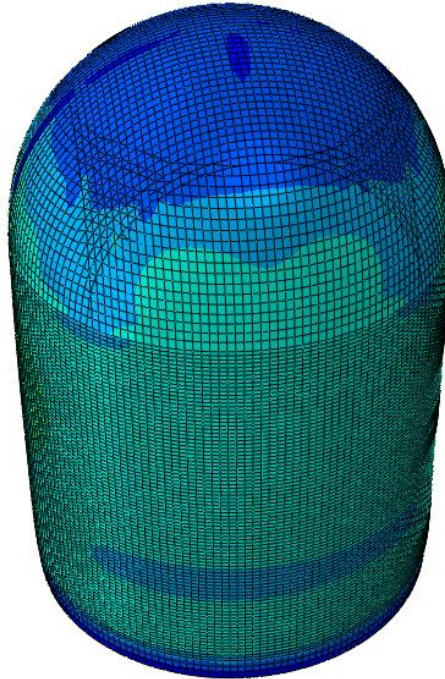
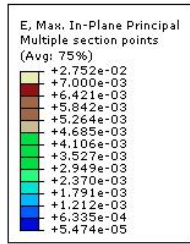
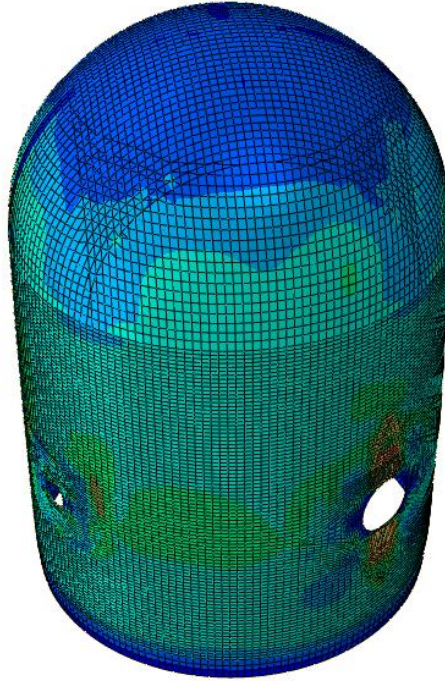
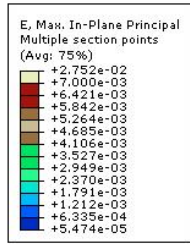


Figure C 86. Peak strains in the liner at applied pressure $P = 3.0 \times Pd$.

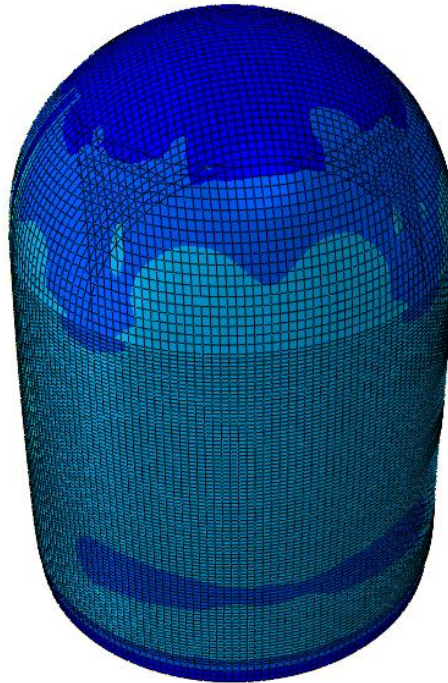
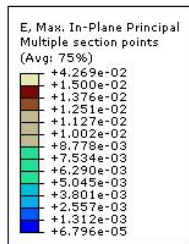
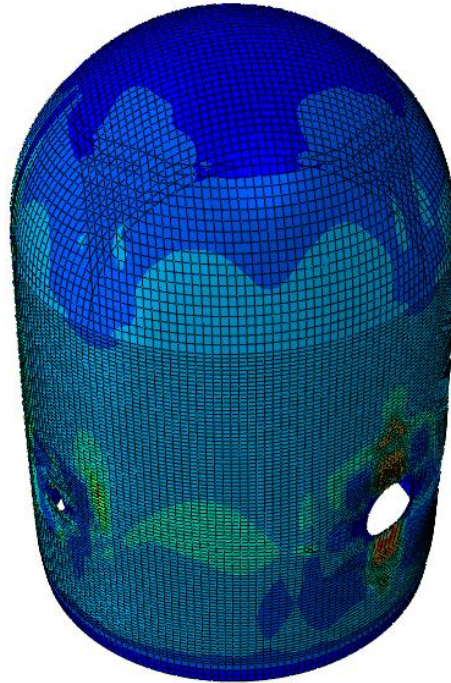
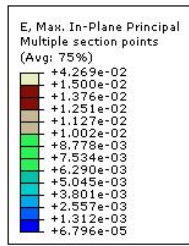


Figure C 87. Peak strains in the liner at applied pressure $P = 3.3 \times Pd$.

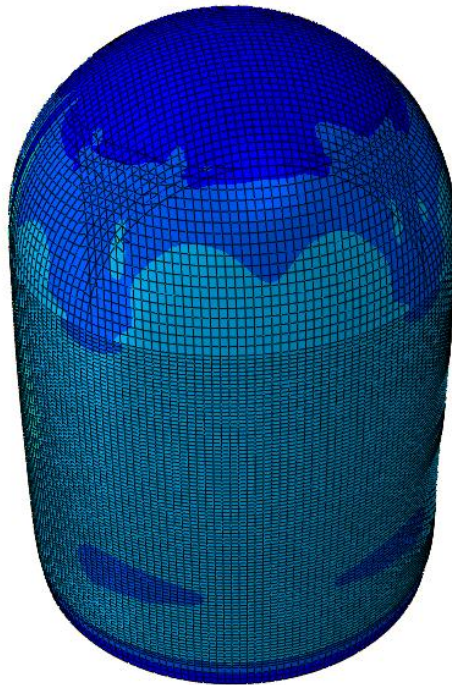
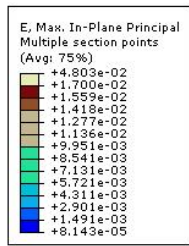
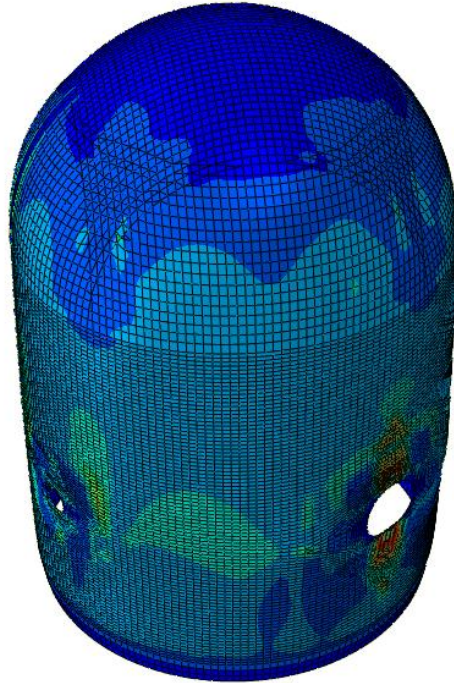
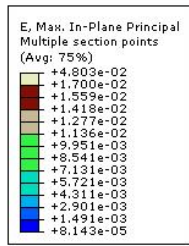


Figure C 88. Peak strains in the liner at applied pressure $P = 3.4 \times Pd$.

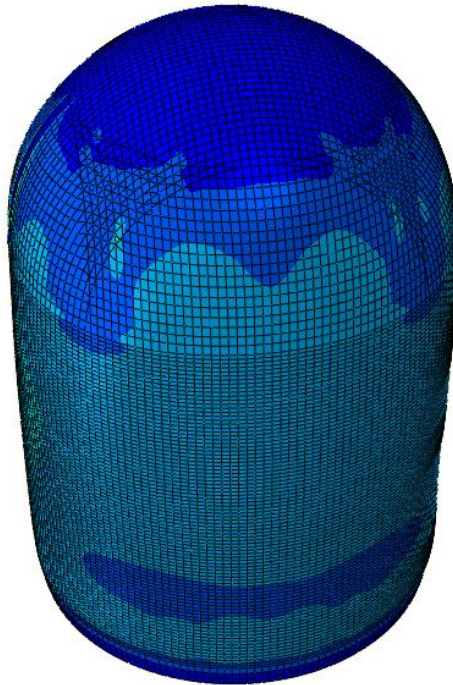
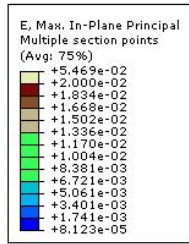
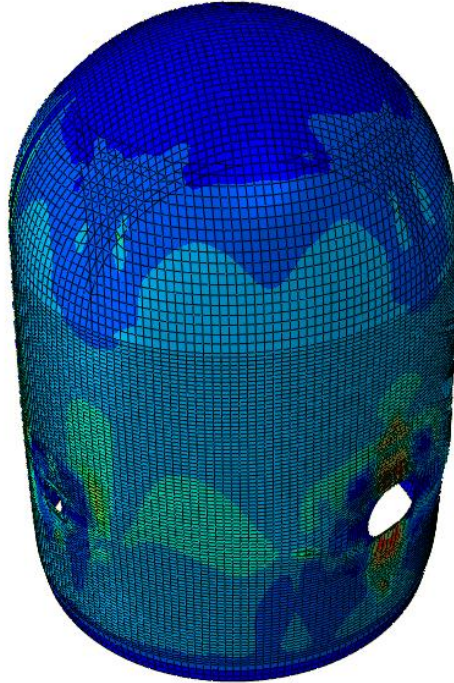
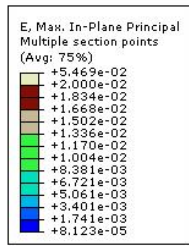


Figure C 89. Peak strains in the liner at applied pressure $P = 3.5 \times P_d$.

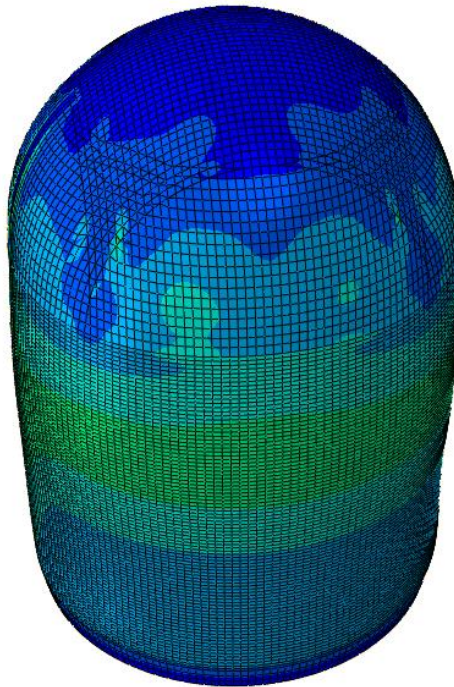
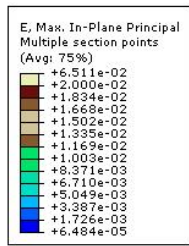
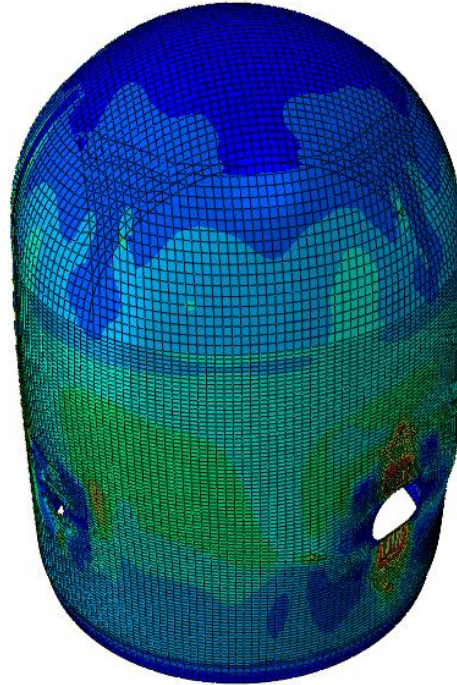
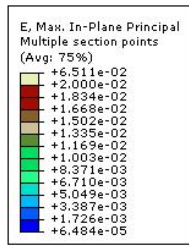


Figure C 90. Peak strains in the liner at applied pressure $P = 3.6 \times Pd$.

Strains near the penetrations

The simulated strains near the equipment hatch and the airlock are presented in Figure C s 92 and 94. The locations of the strain outputs are presented in Figure C s 91 and 93.

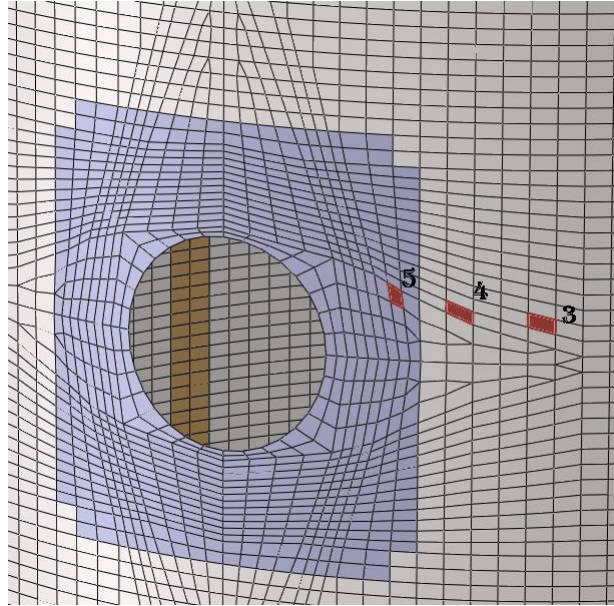


Figure C 91. Locations 3, 4 and 5 of the E/H.

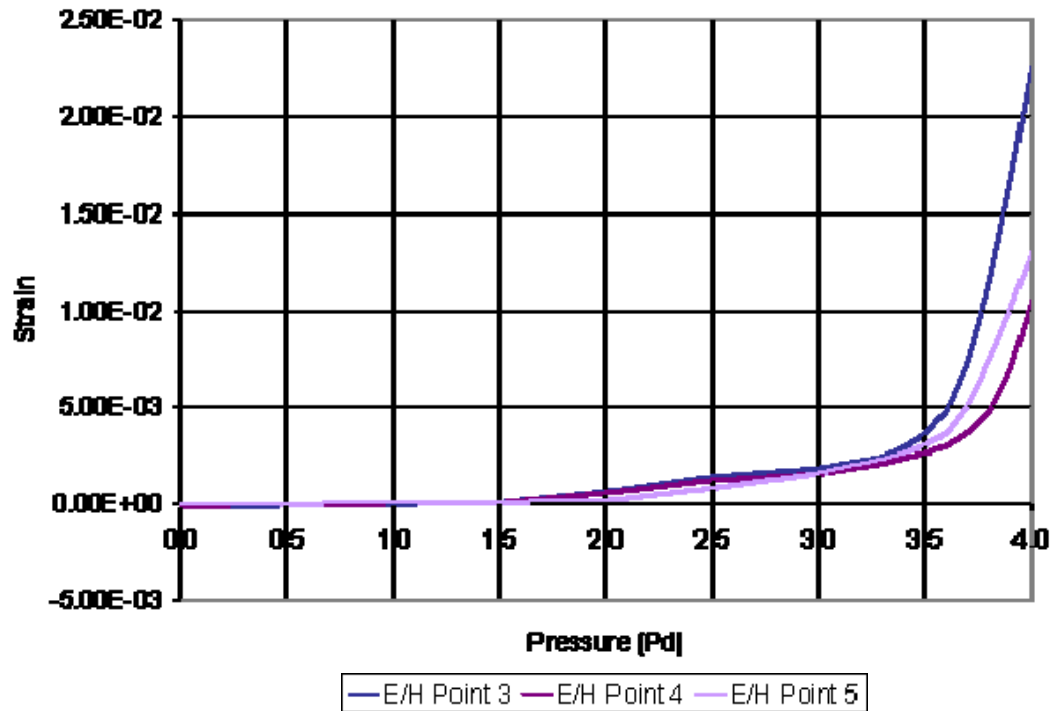


Figure C 92. Maximum in-plane principal strain at locations 3, 4 and 5 of the E/H as a function of pressure.

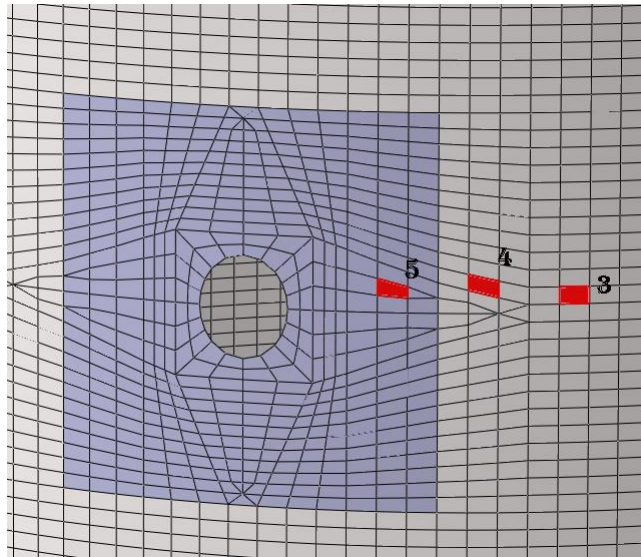


Figure C 93. Locations 3, 4 and 5 of the A/L.

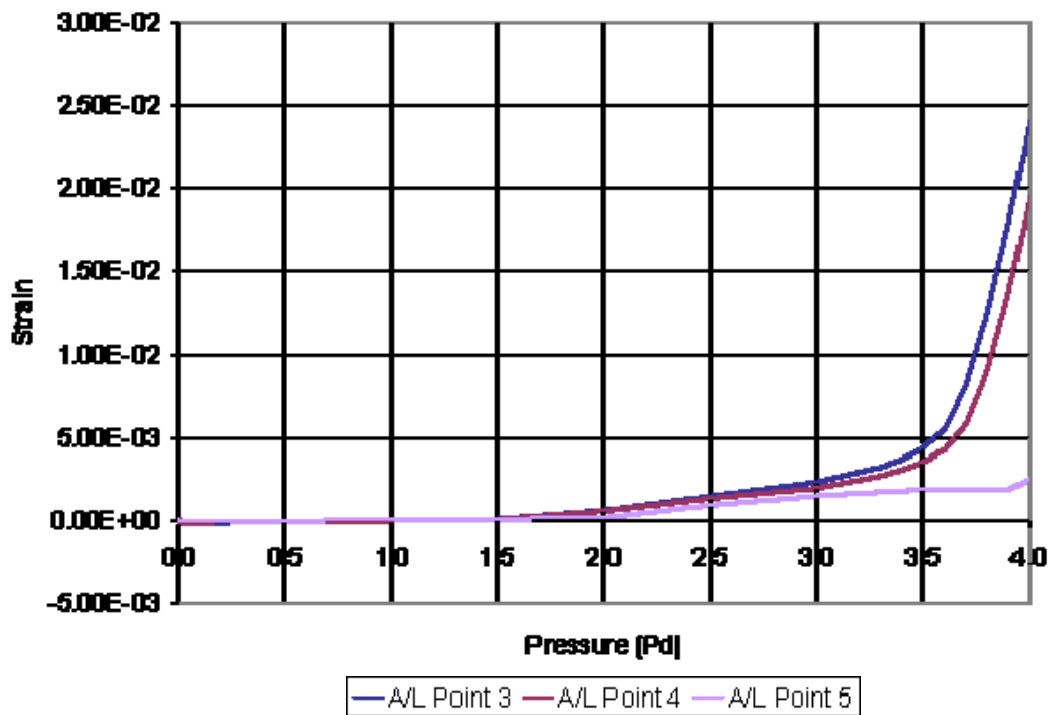


Figure C 94. Maximum in-plane principal strain at locations 3, 4 and 5 of the A/L as a function of pressure.

Global deformation at failure

The containment deformation at failure is presented in Figure C 95. From the figure it is seen that rupture occurs between A/L and E/H, which is in accordance with the test results.

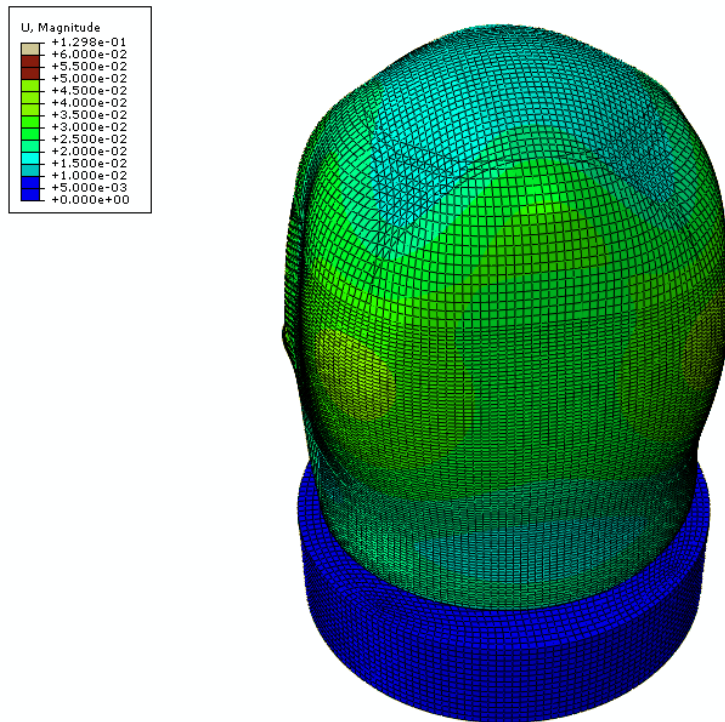
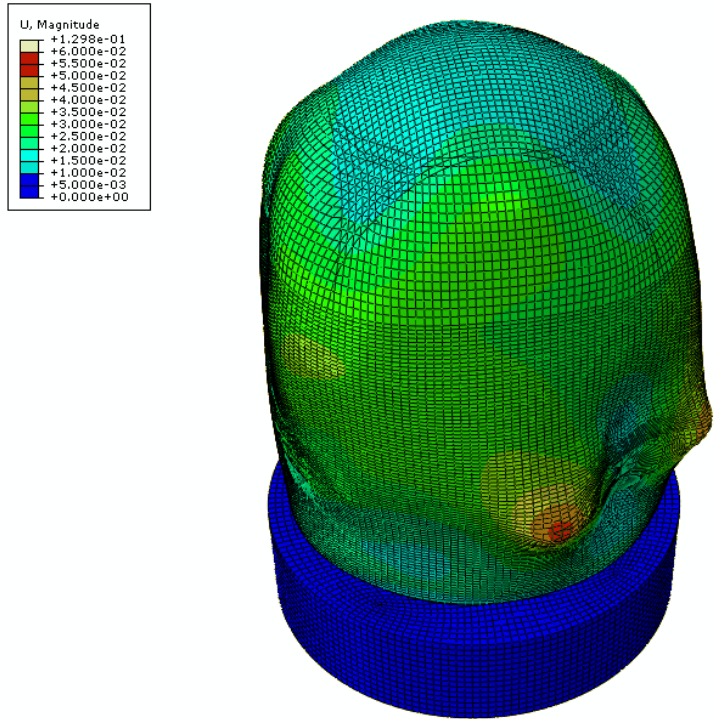


Figure C 95. Global deformation (x 50) at applied pressure $P = 3.5 \times P_d$.

Discussion

The displacement results show good agreement with the measurements. Calculated tendon forces are also satisfactory. The calculated strains, however, do not correspond to the measured values in all cases. This may be due to the used material models, the modelling of the rebar layers or the modelling of the liner-concrete interface. In addition, during the test there have been some difficulties with the strain measurements.

LINER FRACTURE NEAR THE EQUIPMENT HATCH

Model description

Submodeling

The liner behaviour near the equipment hatch is studied with the use of submodeling. A submodel is a more detail model of a part of a global model. The submodel drives boundaries (boundary conditions or stresses) from the analysis run for the global model.

In this study a more detail model of the liner of the equipment hatch is created. The boundary conditions of the submodel are obtained from Model 3. The FE-mesh of the submodel consists of two layers of reduced integrated solid brick elements. Element side length is ca. 5 cm. Extended finite element method (XFEM) is used. The submodel is presented in Figure C s 96 and 97.

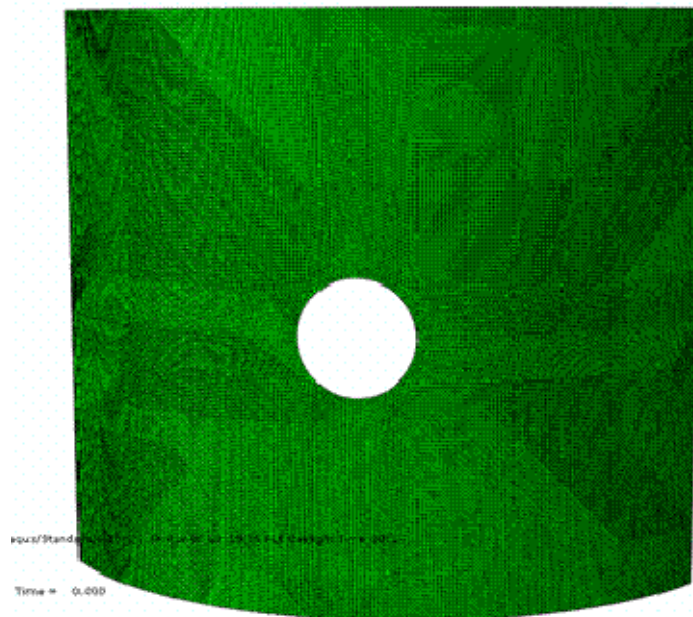


Figure C 96. Submodel of the E/H.

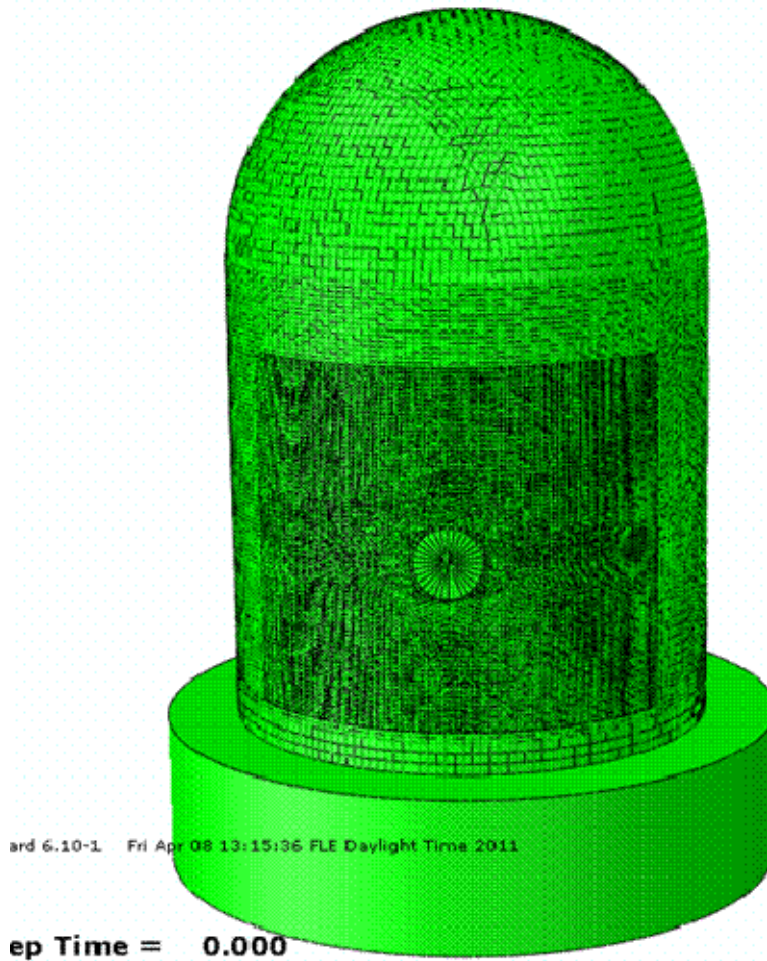


Figure C 97. Submodel of the E/H and the global model 3.

Fracture

The material model for the liner is the same as in model 3 with the exception that fracture is modelled. Fracture is modelled as a contact property. The same critical energy release rate is used for all modes, $J_{ICr} = J_{IICr} = J_{IIICr} = 61.32 \text{ kJ/m}^2$. Power law assumption is used: $(J_I / J_{ICr}) + (J_{II} / J_{IICr}) + (J_{III} / J_{IIICr}) \leq 1$. Crack is modelled to initiate when the maximum principal strain equals to 0.03. The crack growth criteria are presented in Figure C 98.

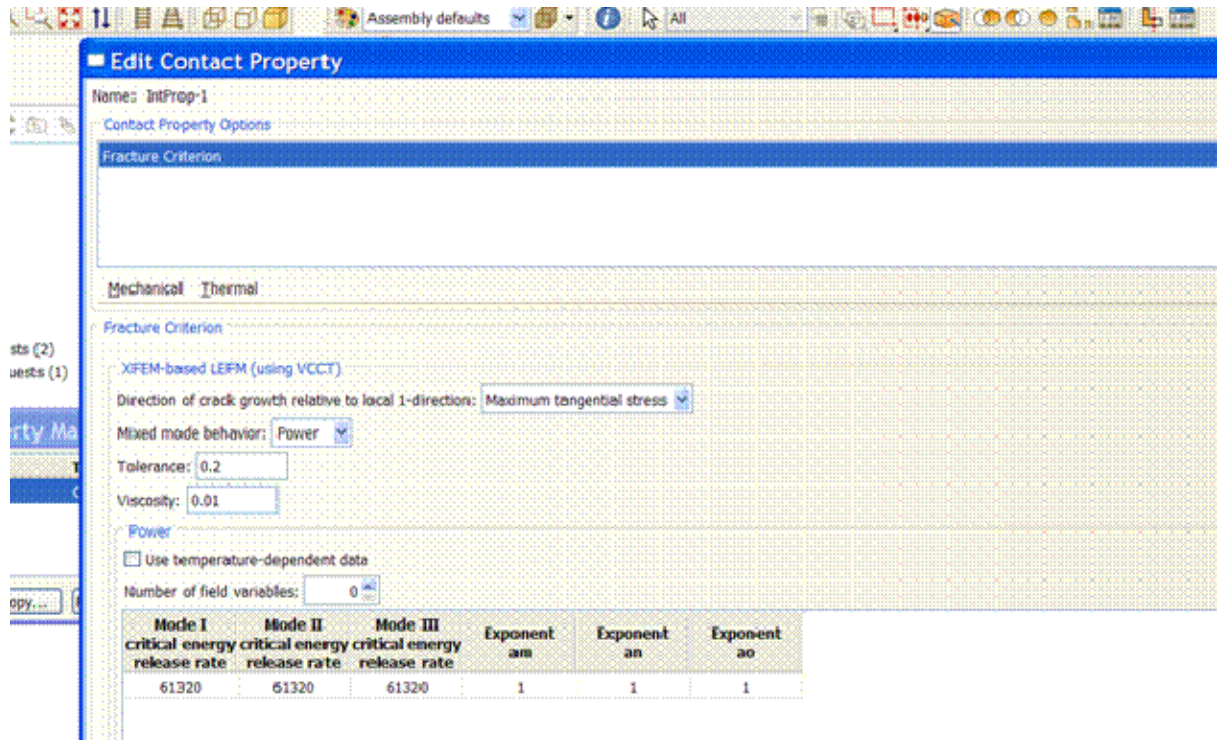


Figure C 98. Fracture criterion as a contact property.

Results

The crack propagation is presented in Figure C s 99 to 102.

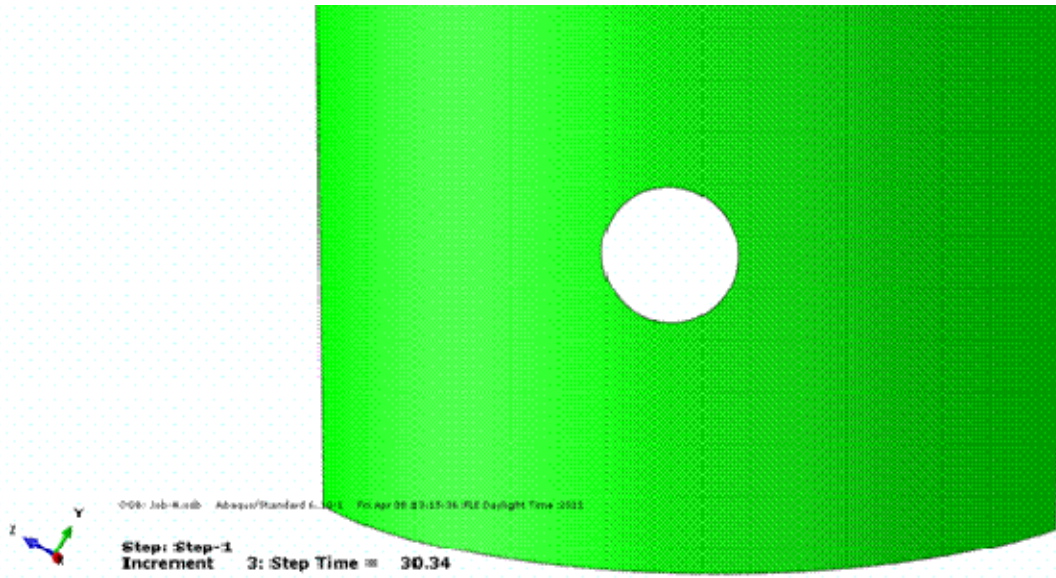


Figure C 99. Crack propagation. $P = 3.034$ Pd. No cracking.

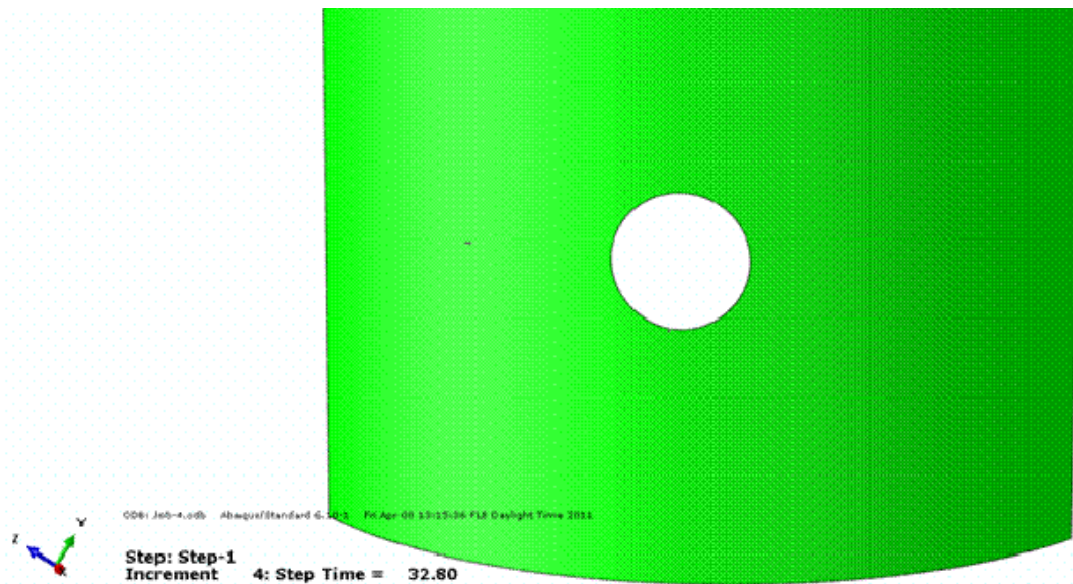


Figure C 100. Crack propagation. $P = 3.280$ Pd. Crack initiation.

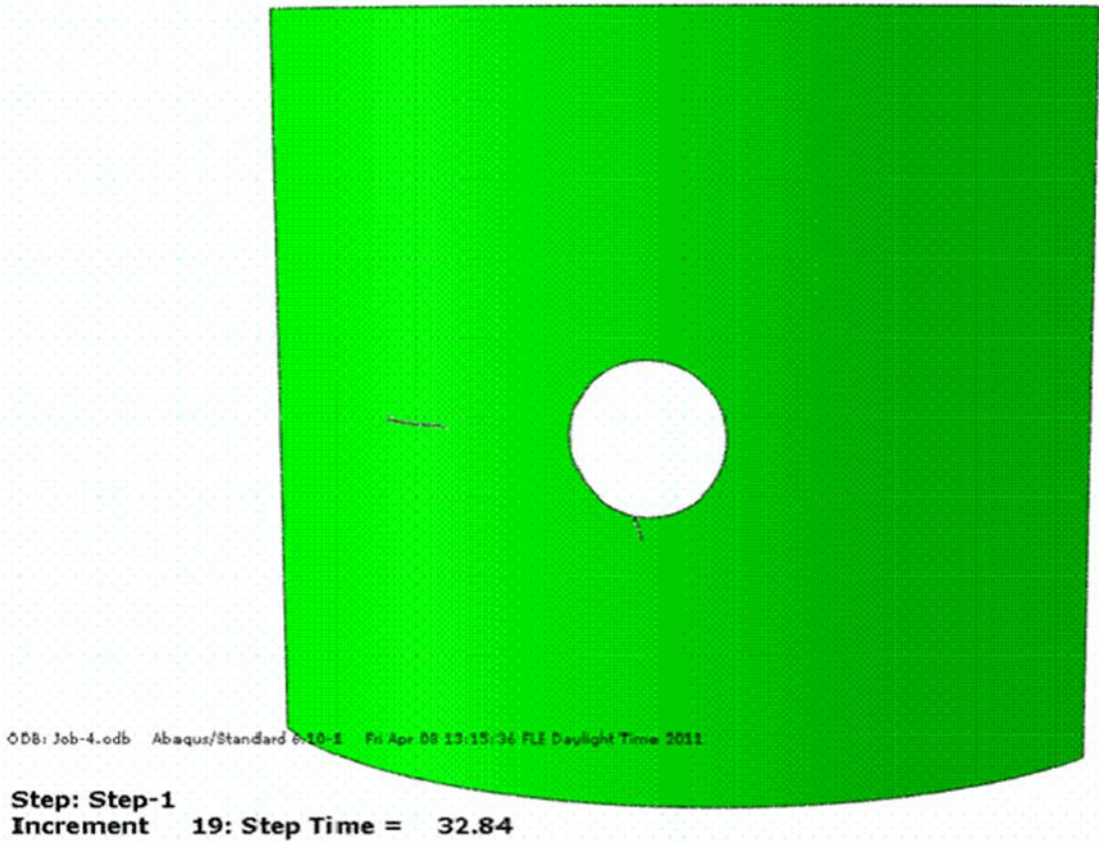


Figure C 101. Crack propagation. $P = 3.284 \text{ Pd}$

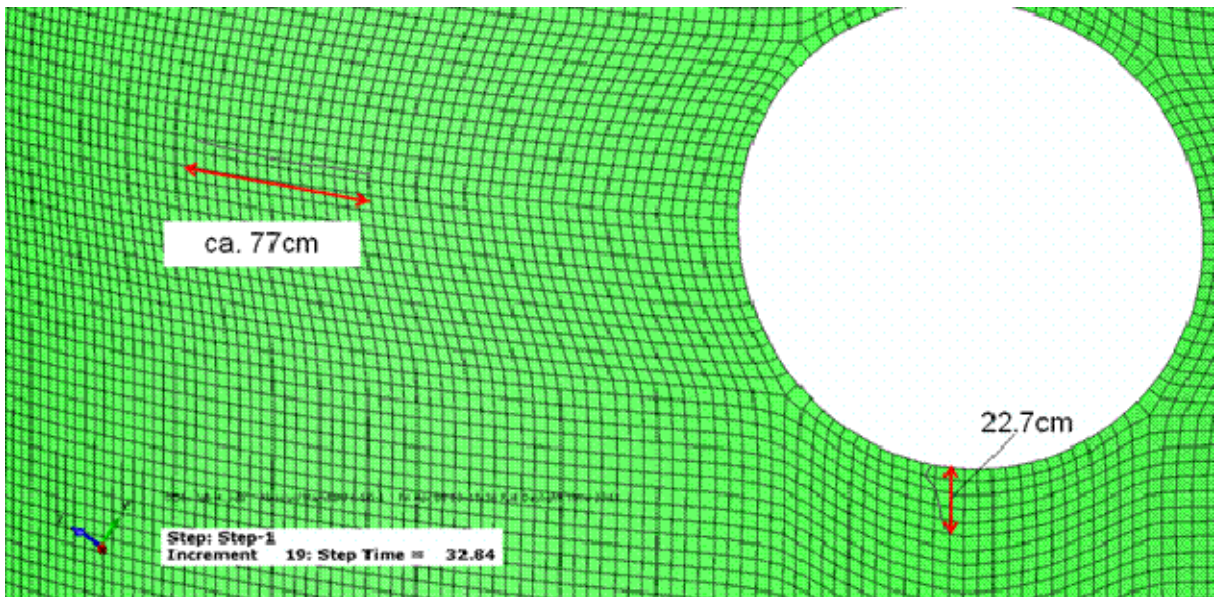


Figure C 102. Crack length at $P = 3.284 \text{ Pd}$

Discussion

A brief description is given on the use of submodeling in the study of the fracture of the E/H liner.

CONCLUSIONS

The Fortum participation to the first phase of the standard problem exercise on the performance of containment vessels under severe accident conditions is presented. The exercise consists of three models of which model 1 and model 3 are presented. In addition, some examinations representative of model 2 are given. The used modelling techniques are presented. The major results are given and compared to the test data.

In the Fortum participation, FE-method and shell element meshes are used. The tendons are modeled with slot connectors, and the liner is modeled as a skin layer on the concrete elements. The modelling of the tendons with slot connectors gives satisfactory results. The modelling of the liner, however, has not been as satisfactory. The tendon behaviour, the displacements of the global model and the model behavior at rupture are in accordance with the test results. The strain results are not as satisfactory, but the orders of magnitude are reasonable.

REFERENCES

- 1 Standard problem exercise on performance of containment vessel under severe accident conditions. Final Analysis Definition. White Paper to Define Analyses. 2010.
- 2 NUREG/CR-6810. Overpressurization Test of a 1:4-Scale Prestressed Concrete Containment Vessel Model. 2003.
- 3 P. Anderson. Standard problem exercise on performance of containment vessel under severe accident conditions (SPE). Meridional stress for Tendon behavior model (model 1). Scanscot Technology, 2010.

APPENDIX D NRC

The U.S. Nuclear Regulatory Commission (USNRC) and Sandia (with support from Moffatt & Nichol) are participating in a round robin analysis with the Atomic Energy Regulatory Board of India (AERB). This analysis is focused on the Standard Problem Exercise (SPE) No. 3, involving the structural analysis of a prestressed concrete containment vessel (PCCV), and examining local effects within the model. In July, 2010, Sandia presented a technical workshop in Mumbai on the NUPEC/NRC1:4-Scale Prestressed Concrete Containment Vessel Model test, which is the subject of the SPE.

SPE No. 3 has been broken into two parts: examining local effects, and developing pressure versus leakage relationships. M&N is performing the analyses for the SPE No. 3. During the first phase, the analyses are focusing on:

- Effects of containment dilation on prestressing force
- Slippage of prestressing cables
- Steel-concrete interface
- Fracture mechanics behavior
- Scatter in data of prestressed concrete properties

MODEL 1

We begin to study the first two of these effects using Model 1, the “Tendon Behavior Model”. The modeling assumptions, initial conditions, and analysis results are presented herein for 1). A pressure only analysis; and 2) a pressure + temperature (saturated steam condition) analysis.

Geometry and initial conditions

The Model 1 Geometry and Initial Conditions are described here and in Figure D 1 to 17. The model is illustrated in Figure D 1. It consists of two hoop tendons, so has a height of 225 mm (8-7/8”). Boundary conditions and pressure are applied as specified in the Figure.

The ABAQUS Standard FE program was used for the analysis. The minimum requirement for this task was a pressure analysis up to prediction of ultimate limit state. In a separate analysis, application of temperature effects has been conducted (though is optional for SPE participants). Simulation of friction and pressure-response related changes to tendon stress distribution has been included in the analysis.

The model includes concrete, tendons, rebar (hoop and shear reinforcement in the plane of the model), and liner. Vertical tendons and vertical rebar were not included in the model. Concrete was modeled with 8-node 3D solid elements, rebar was modeled with embedded subelements, tendons with two-node truss elements, and liner with 4-node shell elements, perfectly bonded to the concrete.

Analytical representation of losses is handled by a) the initial conditions applied to the tendons, and b) by the FE Model's representation of angular friction. In the problem definition, attempt was made to quantify the losses measured in the lead-up time to the test – the sum total of losses is measured and known. In an effort for all participants to begin their pressure analysis from the same basis, and same initial tendon stress distribution, the black lines (with dashed line anchor set), as shown in Figure D 2 and tabulated in Table D 1, are prescribed as the starting point for the exercise.

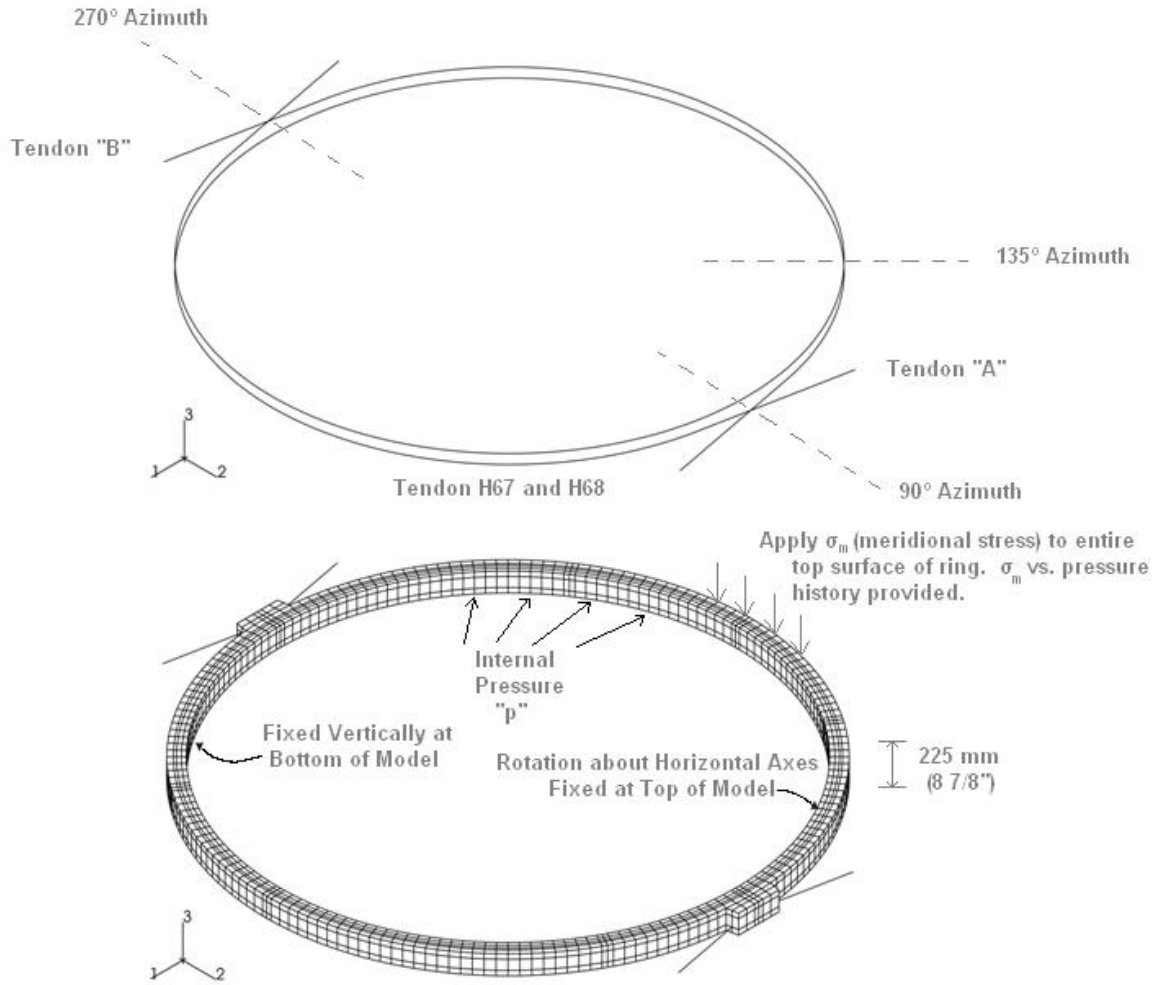


Figure D 1: Model 1 - Tendon Behavior Model, Representing Tendons H53 and H54, Elev. 6.579 m (Refer to Dwg. # PCCV-QCON-04)

Meridional Stress vs. Internal Pressure

The relation between the meridional stress (σ_m) and the internal pressure (p) at level 6.579 m is given below (as developed by SPE Participant, Scanscot).

$$\sigma_m = \text{dead load, prestress, internal pressure} = 7.02 - p * 8.27 \text{ MPa}$$

p in Mpa, (+) compression, (-) tension.

Table D 1: Tendon Stress Distribution for Standard Tendon Behavior Analysis (Includes Seating Losses and Assumed Linearly Varying with Azimuth In-Between Points)

Azimuth	Force (Newton)
355	334,625
315	381,526
270	323,648
180	230,512
90	323,648
45	381,526
5	334,625
-5	334,292

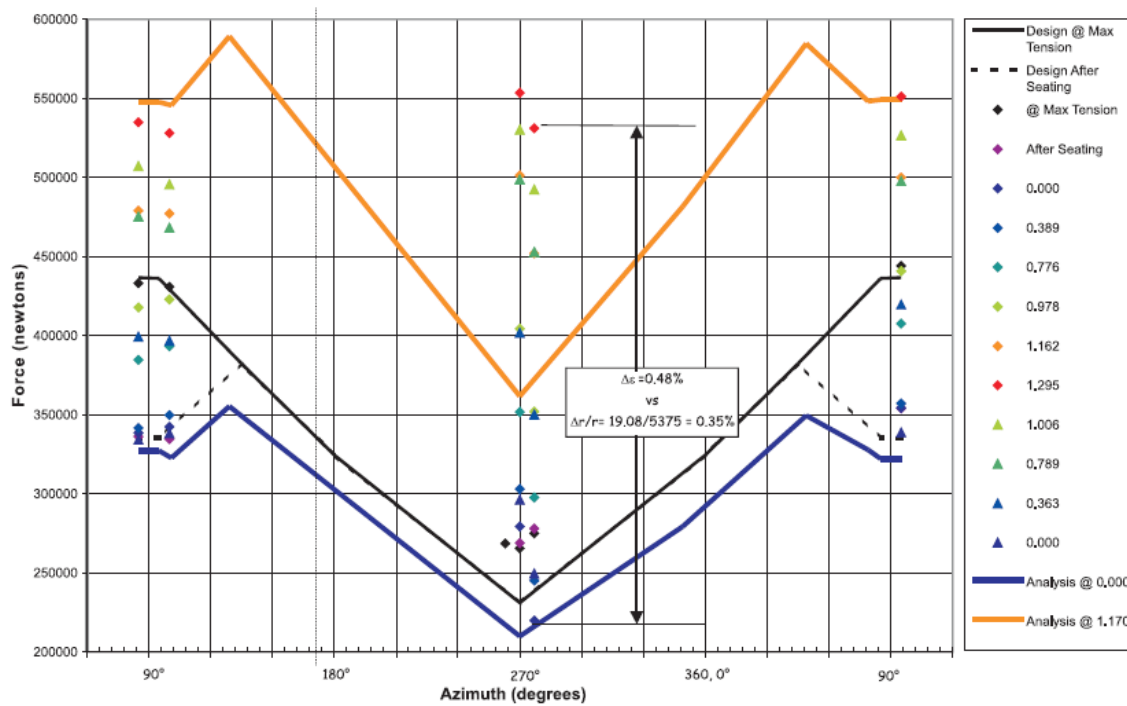


Figure D 2: H53 Tendon Force Comparisons to Pretest (From NUPEC/NRC PCCV test at SNL)

A more detailed calculation of tendon initial stress versus azimuth (including angular friction, wobble friction, and seating loss) was performed, with results shown in Figure D 3. This was the target stress distribution used in the Model 1 analysis.

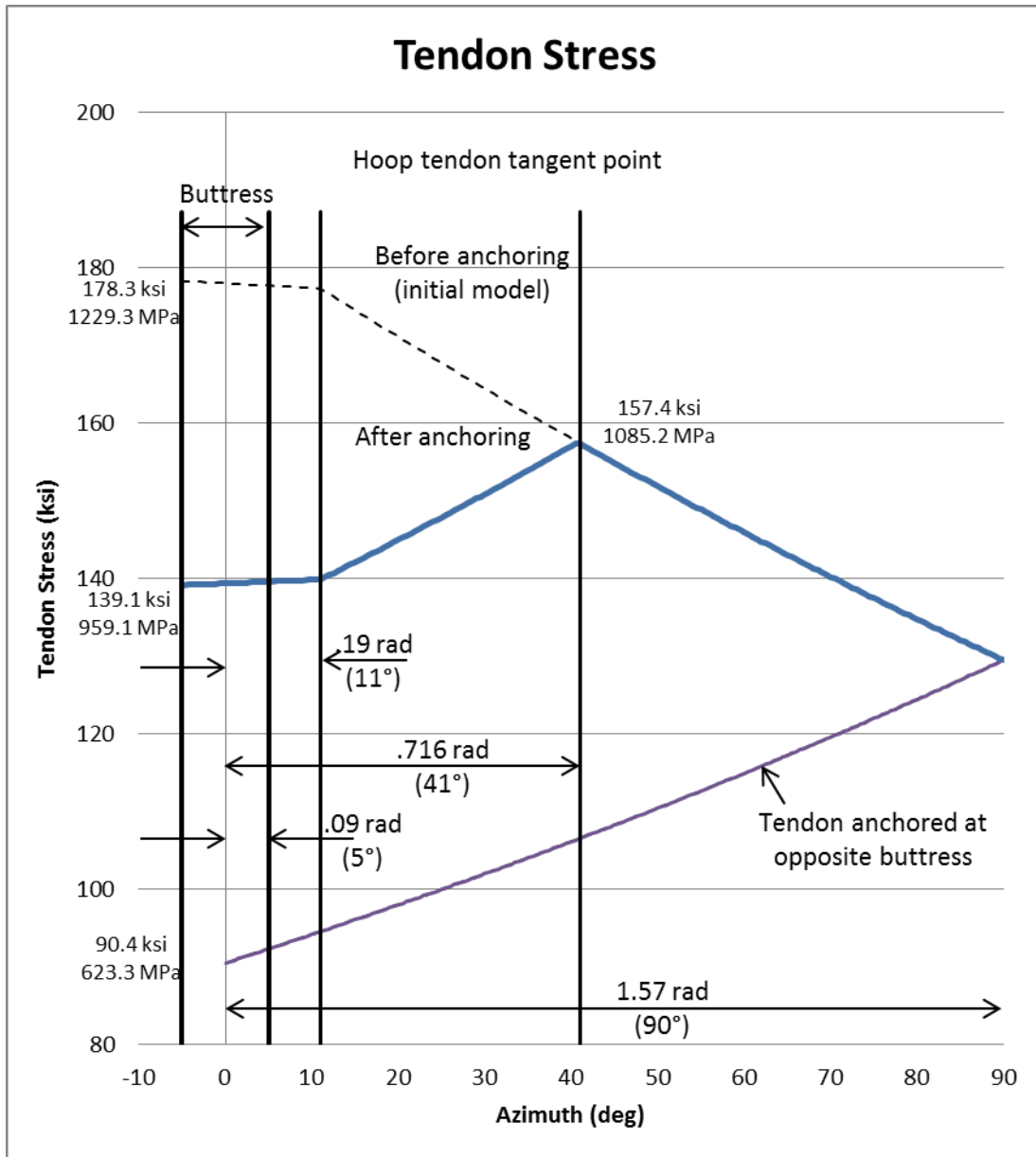


Figure D 3: Additional Information About Tendon Friction and Seating Losses

Material modeling

Tendon, rebar, and concrete material stress-strain assumptions were implemented which follow the stress-strain curves tabulated in Appendix 1 of NUREG/CR-6810. Concrete was simulated using the ABAQUS concrete “Damaged Plasticity” constitutive model. This model utilizes a smeared-cracking formulation in tension (where cracking occurs at the element integration points), and a compressive plasticity theory. Steel elements were simulated using ABAQUS Standard Plasticity. The stress-strain

inputs to these models consist of effective stress (Mises) and effective strain. The inputs are taken directly from the SPE Appendices, and are shown in Figures 4 through 8.

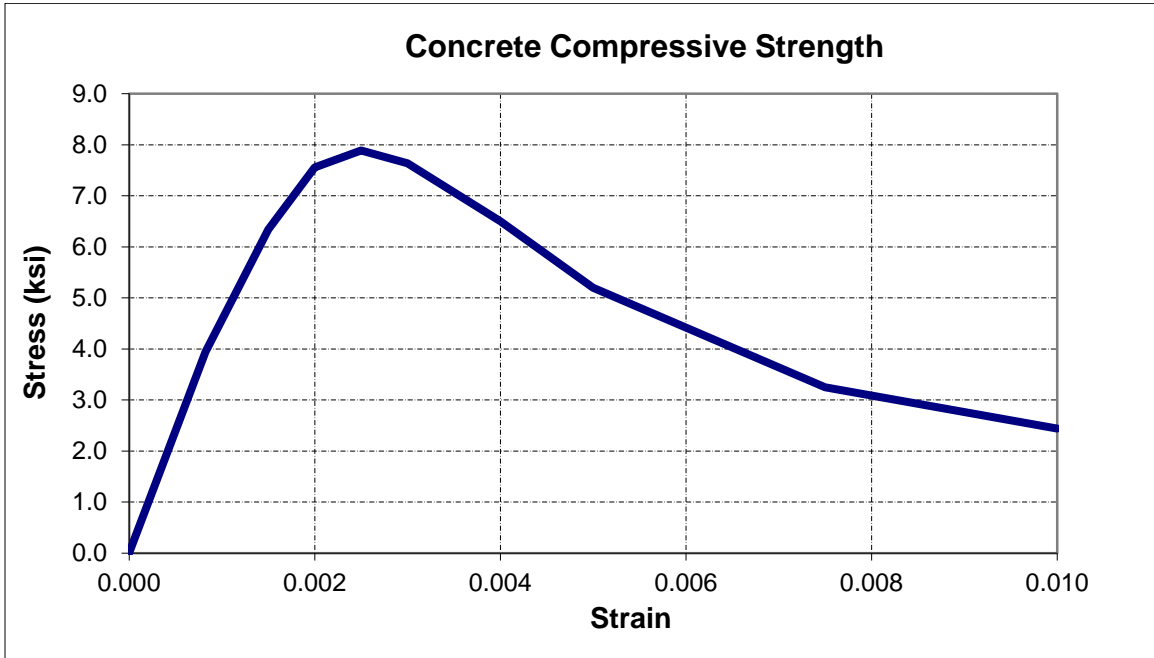


Figure D 4: Concrete Compression Curve

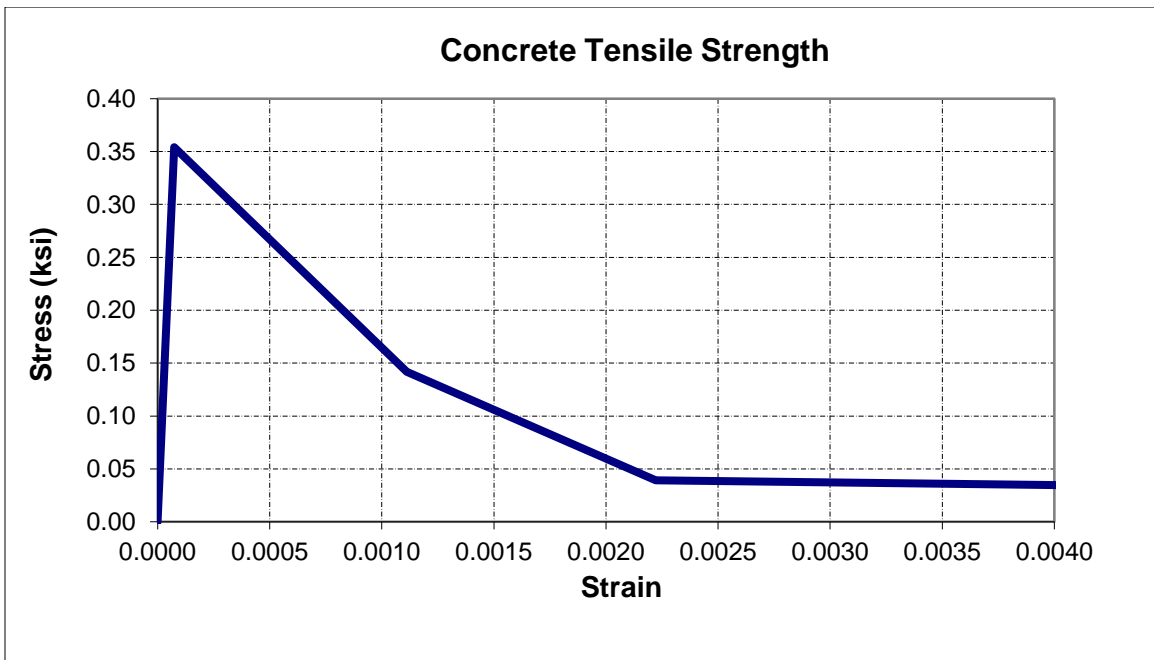


Figure D 5: Concrete Tension Curve

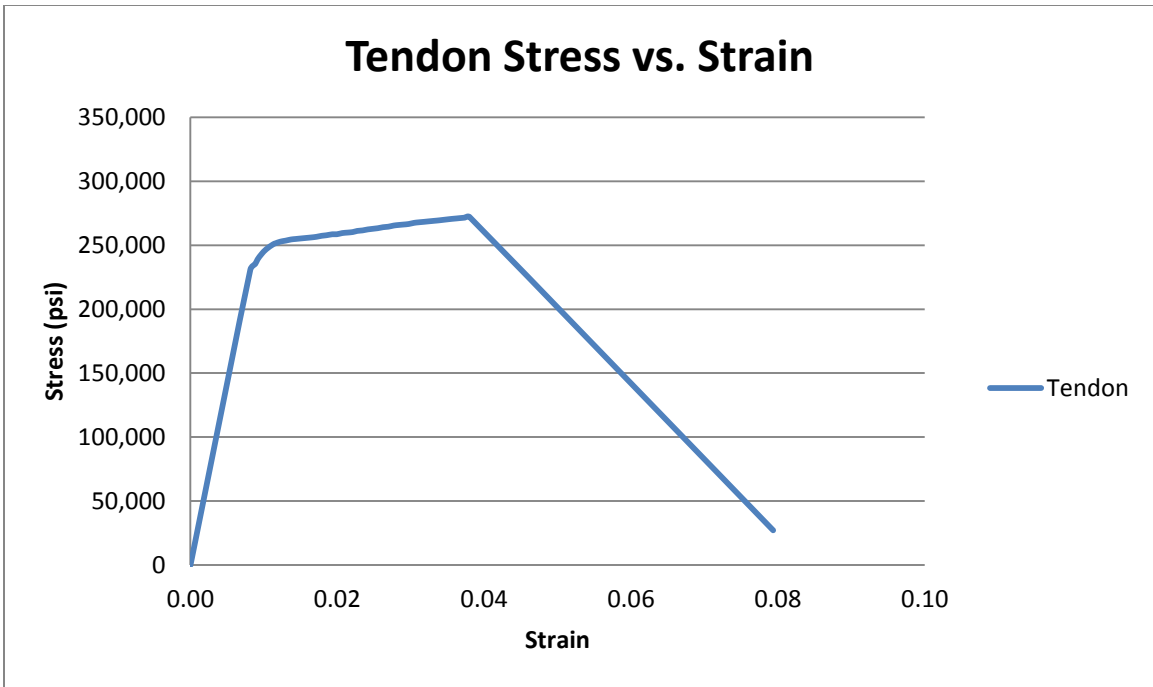


Figure D 6: Tendon Stress-Strain Curve

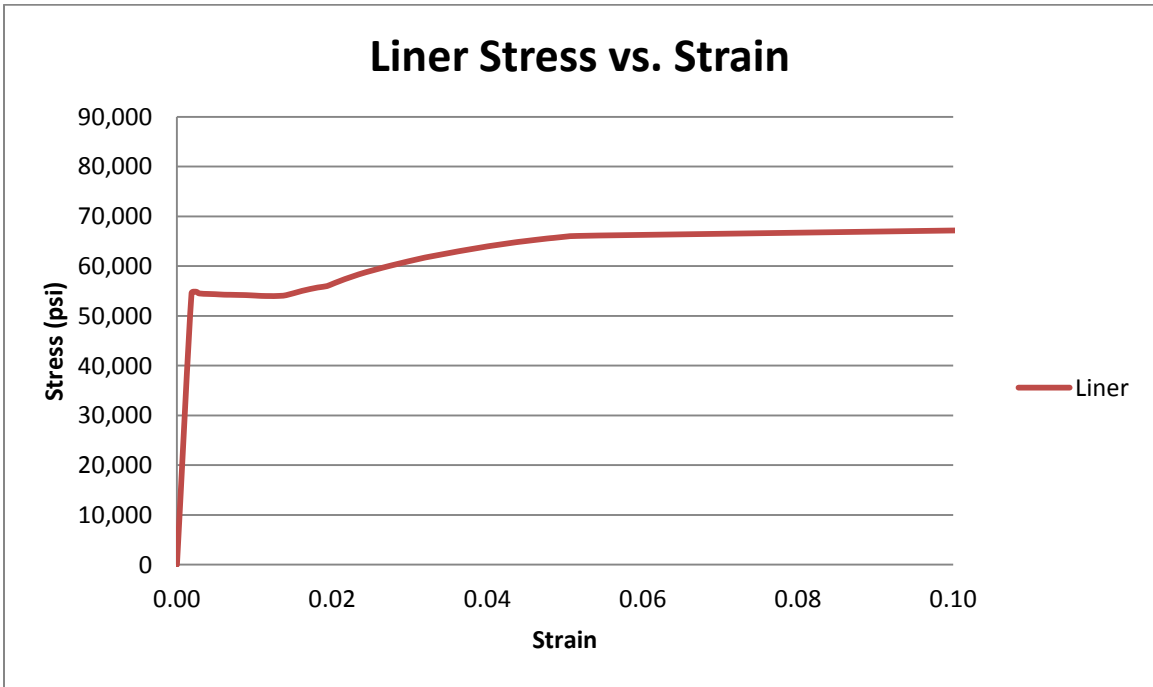


Figure D 7: Liner Stress-Strain Curve

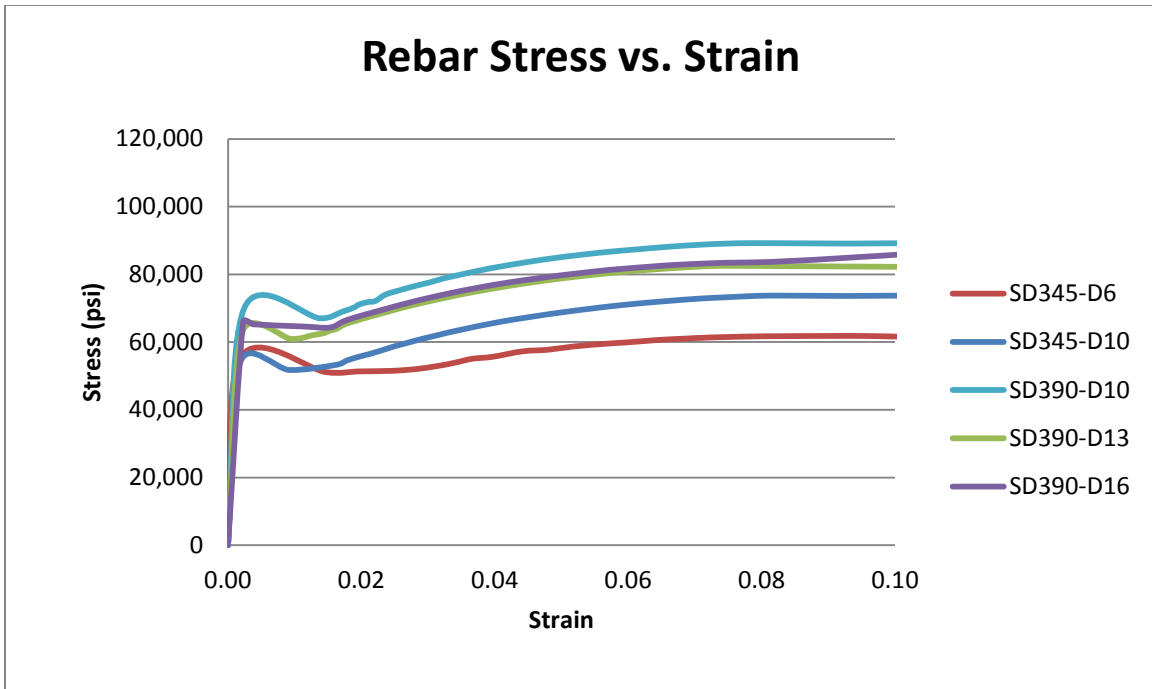


Figure D 8: Rebar Stress-Strain Curve

Failure criteria

The relevant failure criteria for Model 1 is Tendon failure. The rebar generally has higher ductility than the tendons, so it is not the controlling criteria. Model 1 is not focused on liner tear / leakage. Tendon Failure criteria for most activities related to the 1:4 Scale PCCV has been taken as the Tendon System Elongation (shown as strain) at Tendon rupture. There were different tests and different ways of measuring the strain/elongation, and these data are provided in the SPE package Appendix B, pages B-57 to B-60. A reasonable consensus has emerged through various PCCV Analysis and ISP-48 participants to use the average of the Tendon System Tests, or 3.8% as the Tendon Failure Criteria. One study focusing on prediction of the SFMT (Structural Failure Mode Test) suggested using 2% as a lower-bound criteria because this is the limit-by-Specification for the tendon system performance (and one tendon system test did show a premature failure at under 2% due to anchor slippage). For a global model analysis, making this assumption helped rationalize a tendon-failure-sequence scenario that agreed well with failure-sequence observations. However, tendon rupture at 2% is still considered to be a 'possible' but not 'best-estimate' failure strain. Best estimate failure strain remains at 3.8%.

Analysis results

The following lists the Required Output/Results for Model 1:

- Description of Modeling Assumptions and Phenomenological Models
- Description of Tendon Failure Criteria Used
- Pressure Milestones. Applied Pressure When:
 - Concrete Hoop Stress (at 135° azimuth) Equals Zero
 - Concrete Hoop Cracking Occurs (at 135° azimuth)
 - Tendon A Reaches 1% Strain (at 135° azimuth)
 - Tendon B Reaches 1% Strain (at 135° azimuth)
 - Tendon A Reaches 2% Strain (at 135° azimuth)

- Tendon B Reaches 2% Strain (at 135° azimuth)
- Deformed Shape and Tendon Stress Distribution at $P = 0$ (prestress applied); $1 \times P_d$; $1.5 P_d$; $2 P_d$; $2.5 P_d$; $3 P_d$; $3.3 P_d$; $3.4 P_d$; Ultimate Pressure
- Description of Observations About Tendon Force as a Function of Containment Dilation and Tendon Slippage

The model descriptions have been provided herein, and in Figure D 9 through 17. Figure D 9 and 10 show the FE model and tendon layout. Figure D 11 through 17 illustrate the rebar input to the model.

Figure D 11 shows the tendon connectivity to the buttresses. For this model the tendons are placed in contact with concrete using a “contact surface,” and friction equal to 0.21 is assigned, based on the ancillary testing performed for the 1:4 Scale PCCV. Prestress is prescribed by only applying initial stress to the single tendon element outside the concrete mesh (shown in Figure D 11), and allowing the FE solution to reach equilibrium. This procedure produced the initial stress profile shown in Figure D 18. The prestress condition (prior to application of pressure load) is reached in two solution steps:

1. Applied stress to tendon ends (call these the jacking elements); this produces the dark blue curve in Figure D 18.
2. Relaxing the stress in these ends by amount equal to the “anchor slip” (3.95 mm); this produces the red curve in Figure D 18. Tendon strains are shown in Figure D 19.

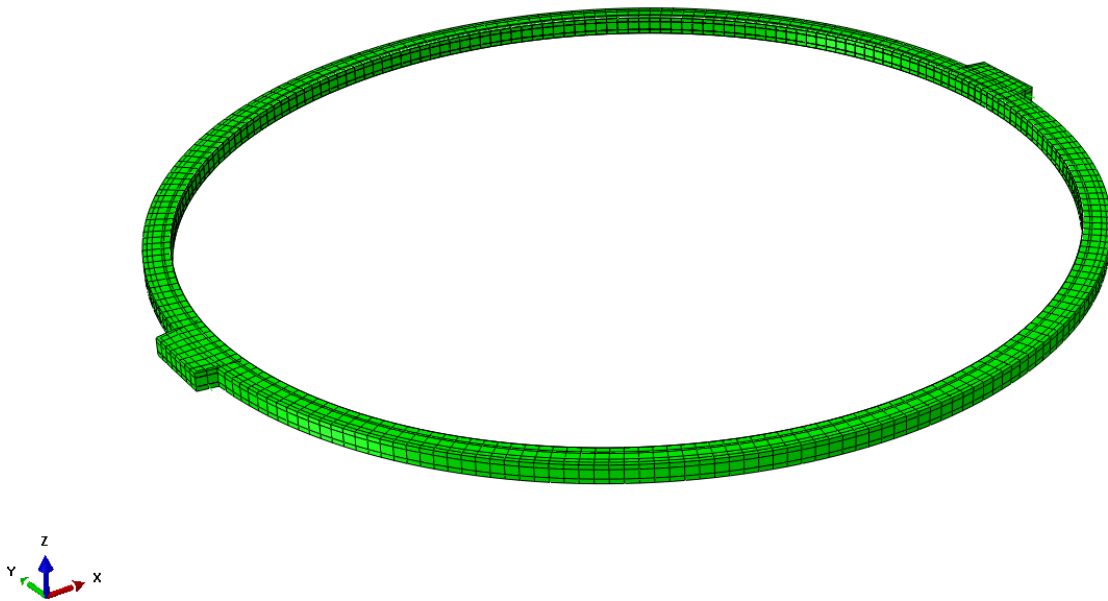


Figure D 9: Model-1 Abaqus Model

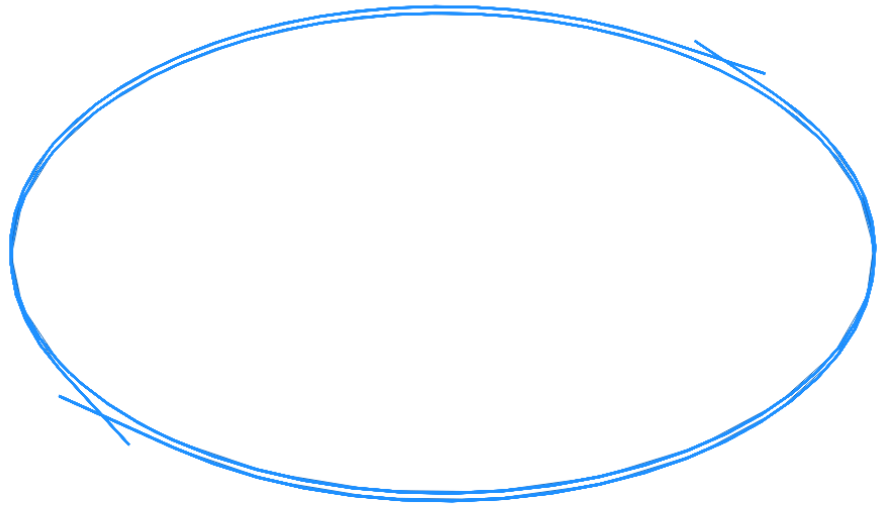


Figure D 10: Tendon Layout

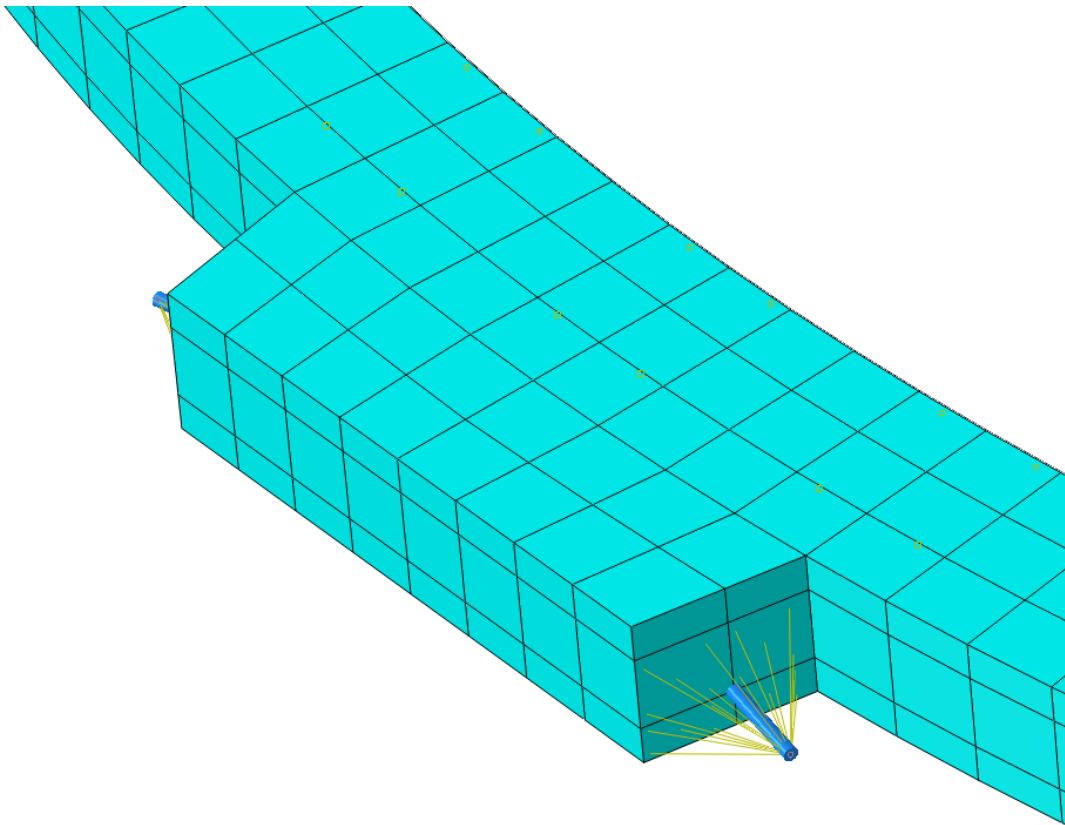


Figure D 11: Anchorage of Tendon to Concrete

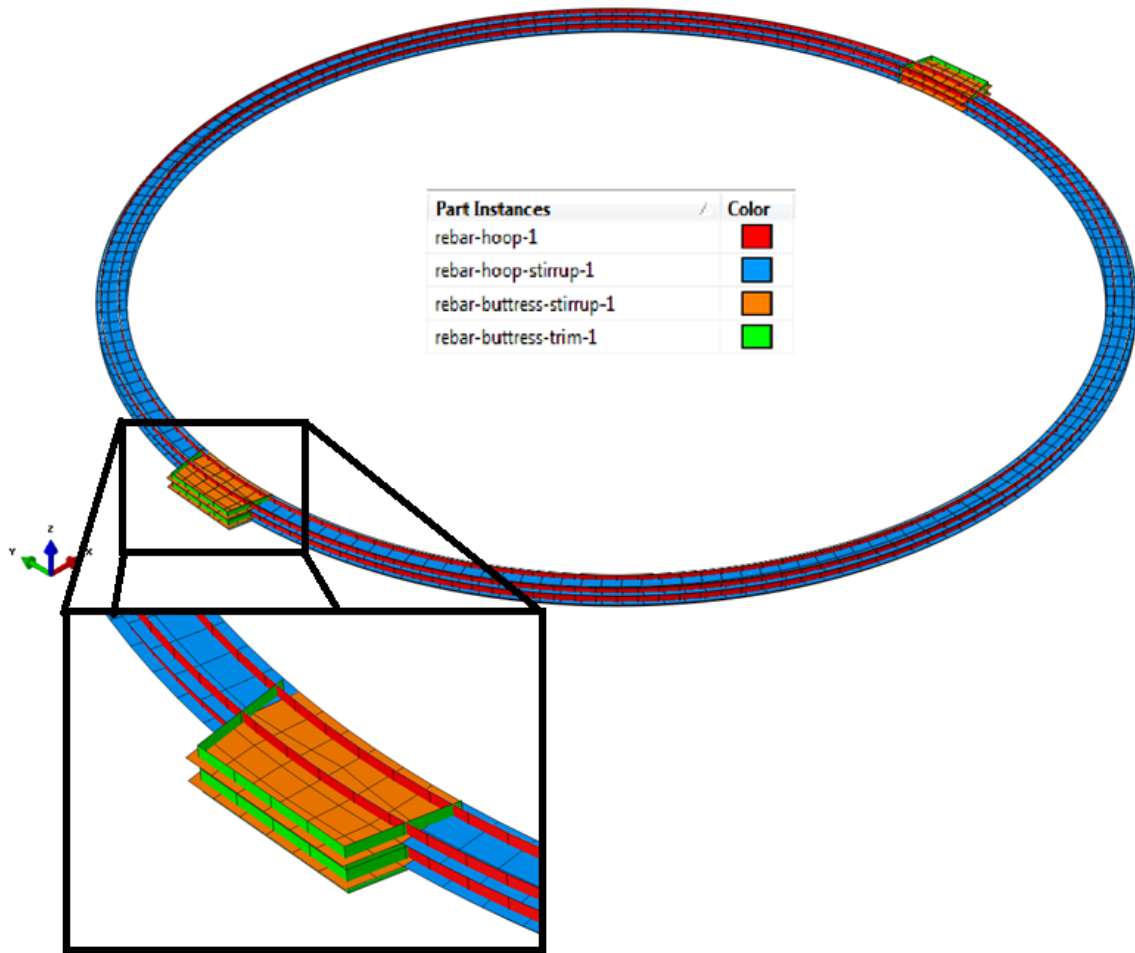


Figure D 12: Rebar Layers Embedded in Concrete

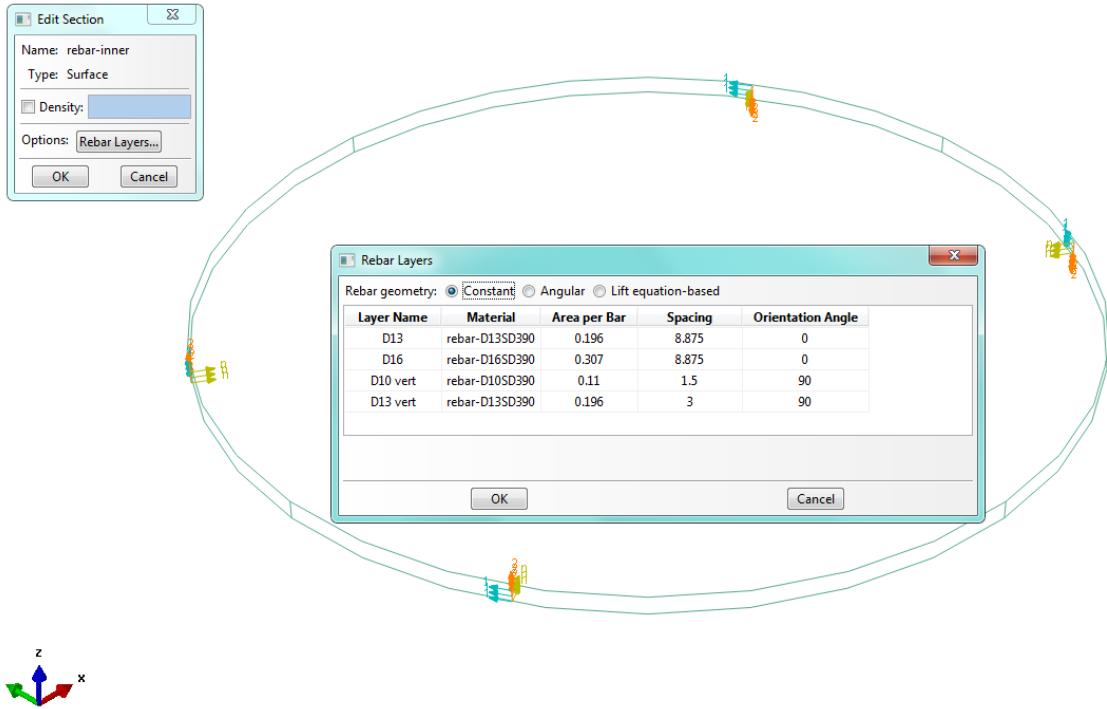


Figure D 13: Inner Hoop Rebar Layer

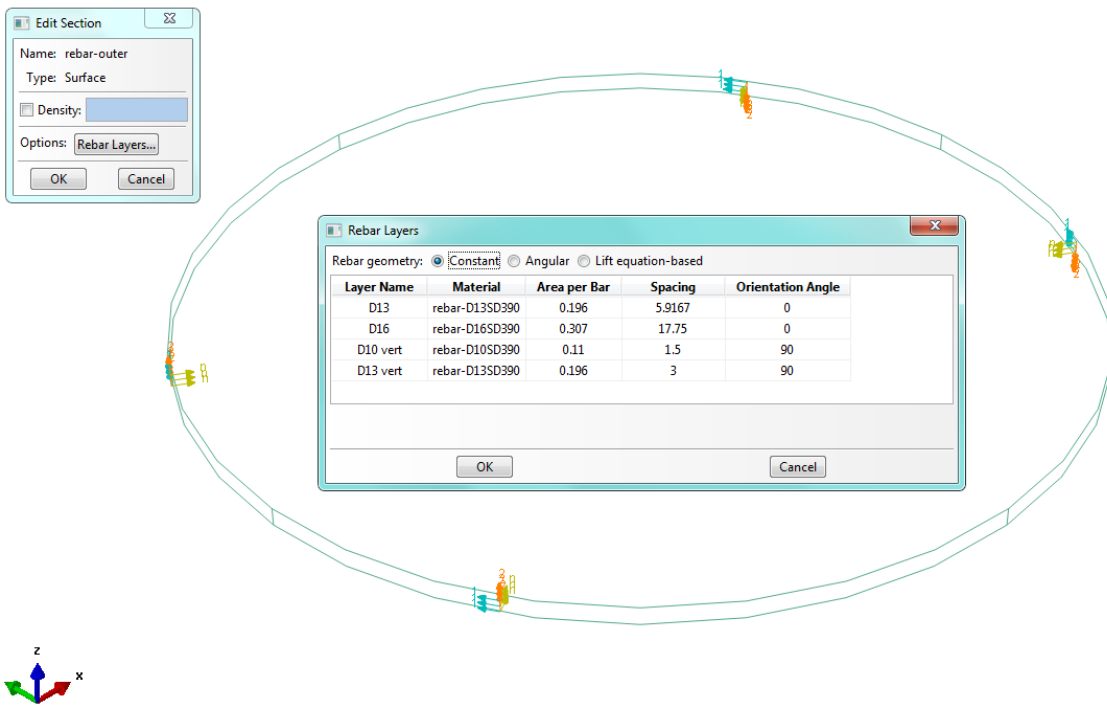


Figure D 14: Outer Hoop Rebar Layer

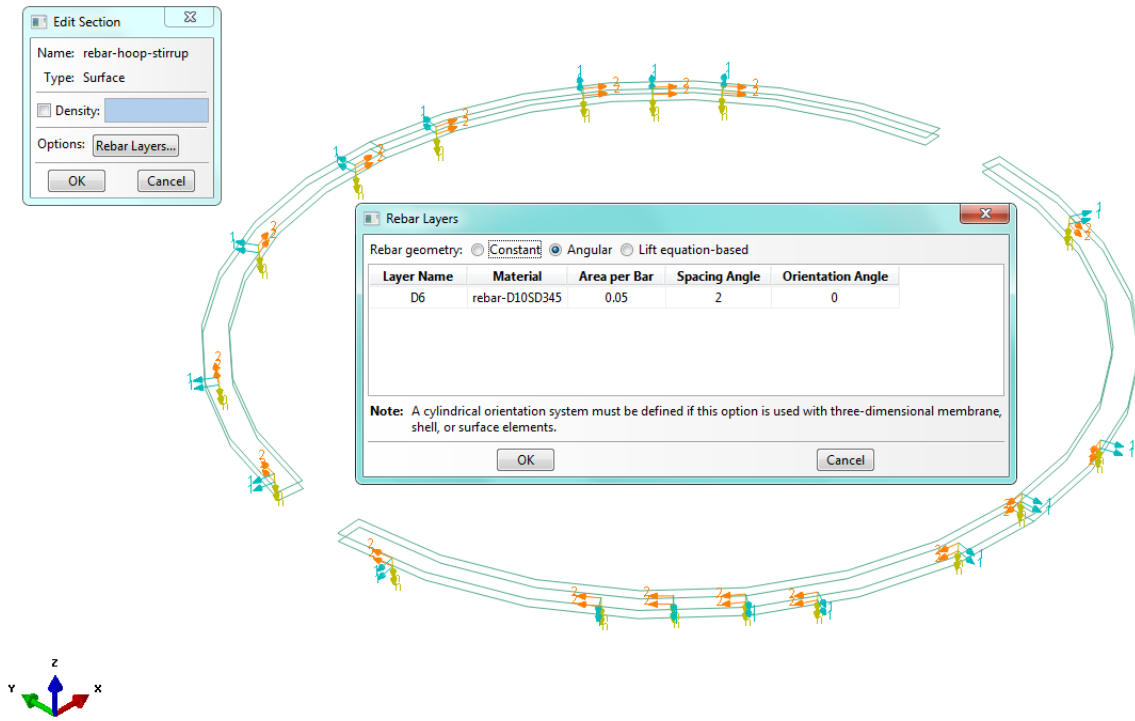


Figure D 15: Radial Ties - Rebar Layers

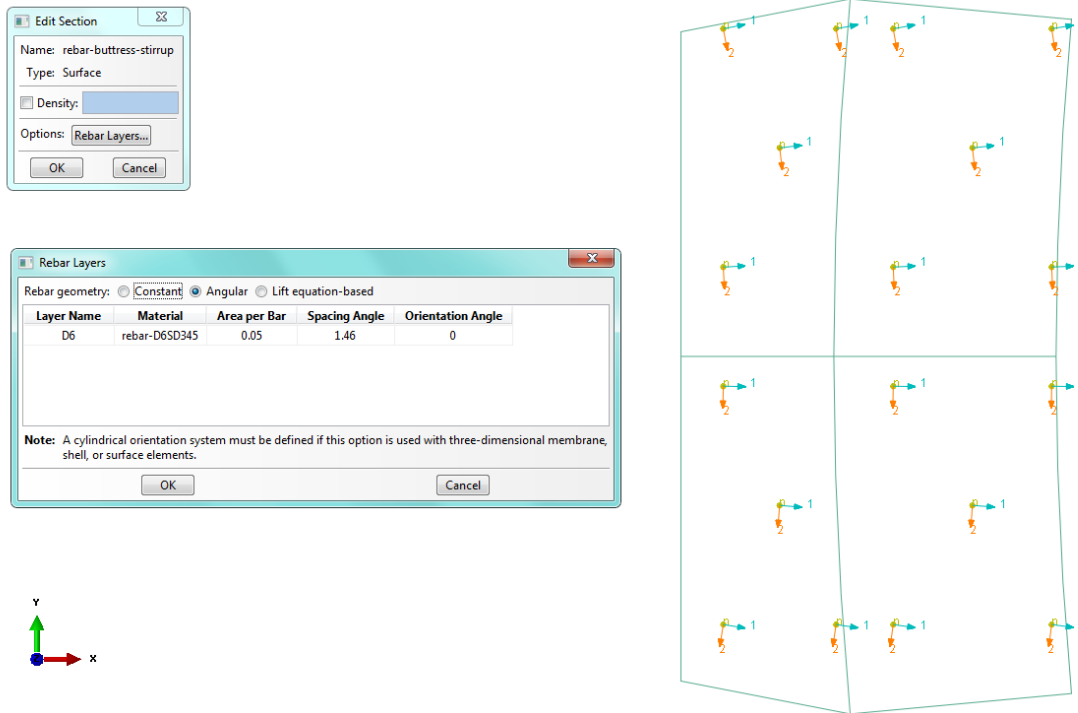


Figure D 16: Buttress Stirrup Layer (2 per buttress)

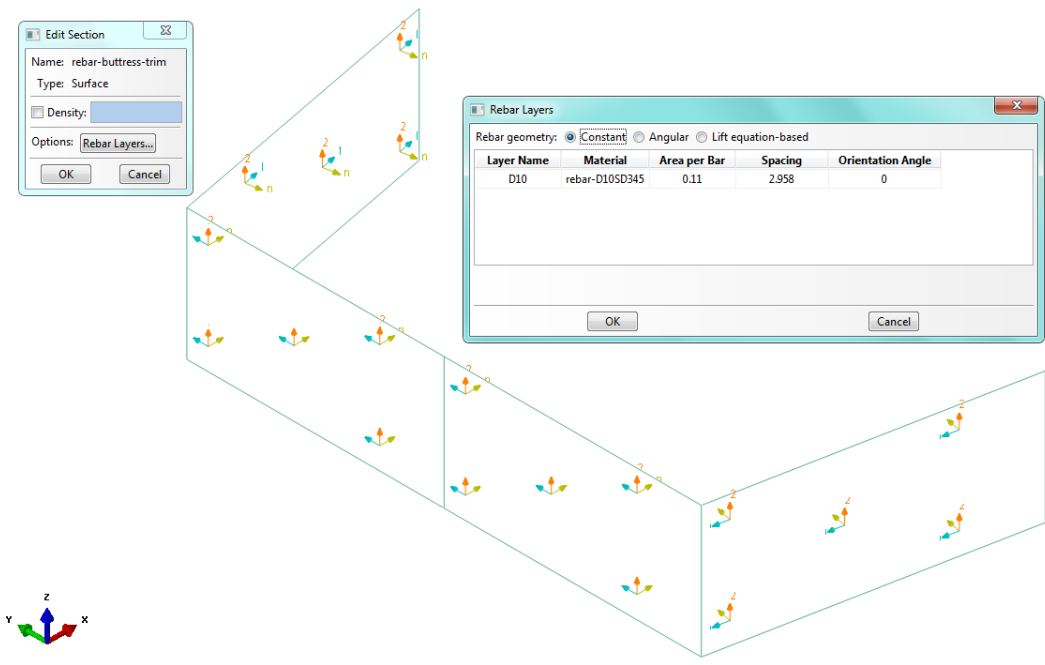


Figure D 17: Buttress Trim Bars Layer

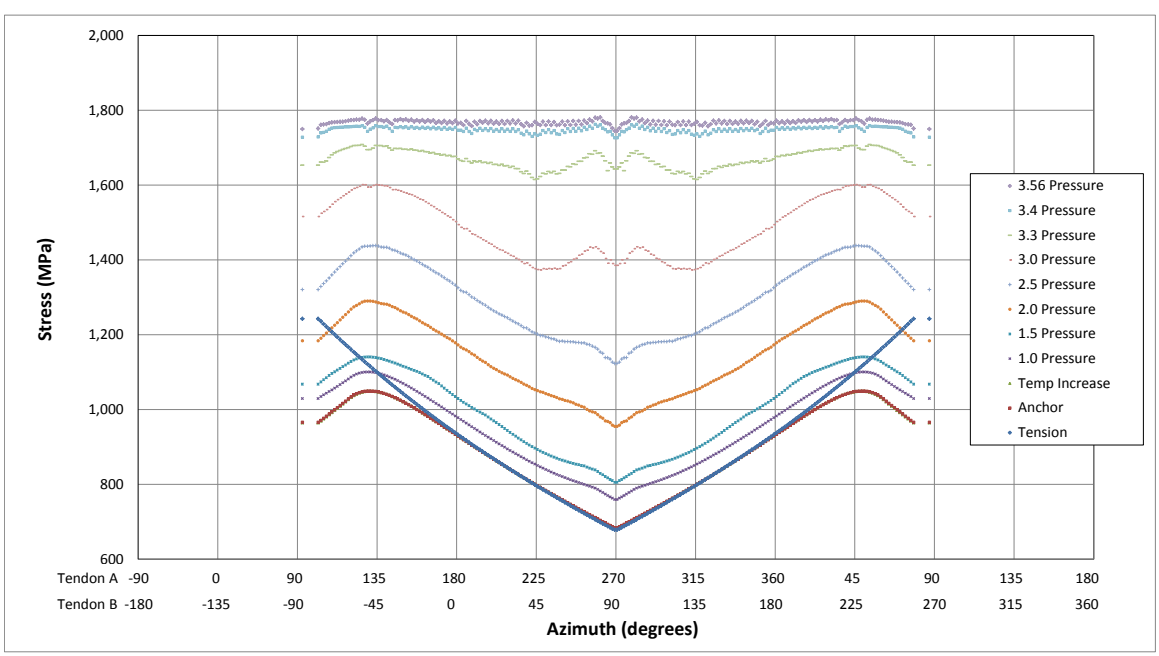


Figure D 18: Tendon Stress

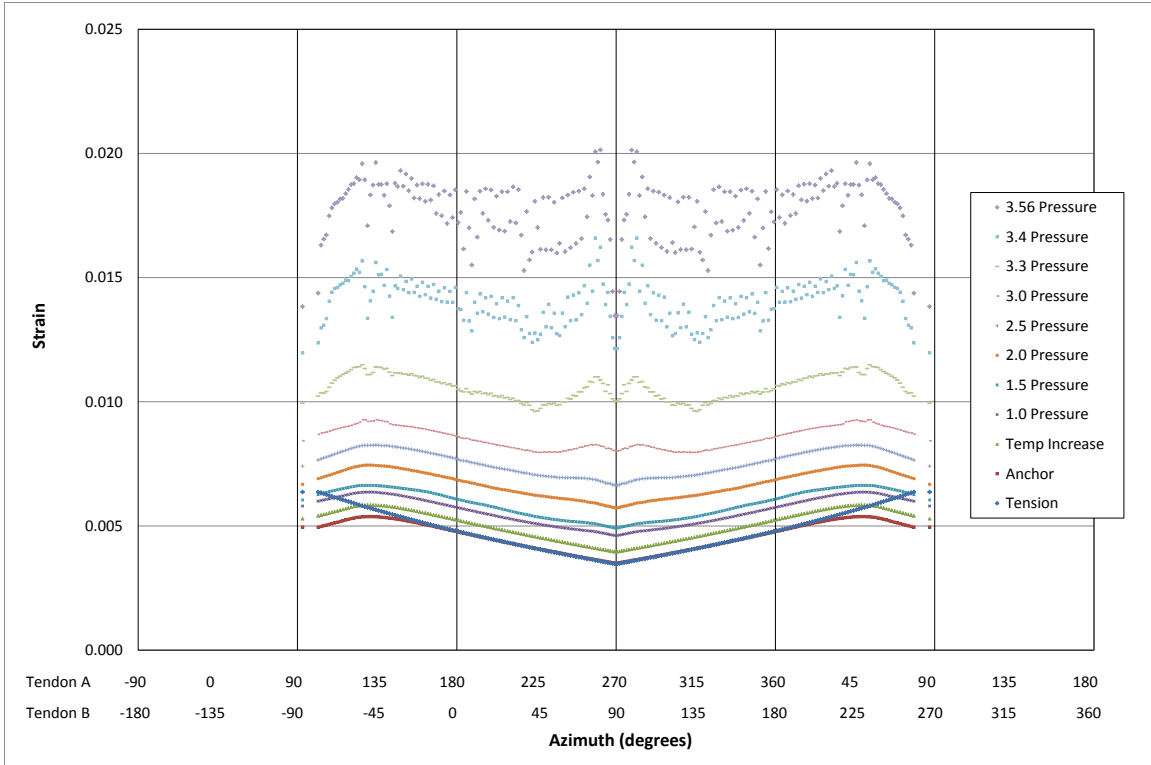


Figure D 19: Tendon Strain

Deformed Shapes at the required pressure milestones are shown in Figures 20 through 29. Radial Displacement versus Pressure at four different azimuths is shown in Figure D 30. Attempt has been made to compare to the test, and the agreement is reasonably good. In general, the test result “turns up” a little sooner than the analysis. This was a consistently observed conclusion from the post-test work, explained by the concrete being somewhat “pre-cracked” before the Limit State Test.

The results by pressure milestone are shown in Table D 1.

Table D 2: Results by Pressure Milestones – Pressure Only Case

Milestone	Pressure (MPa)	x Pd
Concrete Hoop Stress (at 135° azimuth) Equals Zero	0.562	1.433
Concrete Hoop Cracking Occurs (at 135° azimuth)	0.707	1.801
Tendon A Reaches 1% Strain (at 135° azimuth)	1.299	3.310
Tendon B Reaches 1% Strain (at 135° azimuth)	1.328	3.383
Tendon A Reaches 2% Strain (at 135° azimuth)	1.442	3.673
Tendon B Reaches 2% Strain (at 135° azimuth)	1.449	3.691

The 135-degree azimuth radial displacement (SOL #6) from the SFMT is also added to the plots. This shows reasonable agreement to the analysis at high pressures, but it can be noted that at low pressures, the SFMT data follows the path of a cracked and damaged structure, substantially different than the LST

or the analysis. The SFMT data is still valuable for the pressure response larger than $3.25xP_d$, because this is the maximum pressure reached by the LST.

Tendon Strains and Stresses versus Pressure are shown in Figure D 31 and 32. Liner Strain versus Pressure is shown in Figure D 33. The strains of Tendon A and Tendon B at 135-degree azimuth are shown, along with the peak strain "Anywhere" along the tendon. The peak strain tends to be located at near where the strain is maximum after prestress anchor set, i.e., azimuth 130-degrees. But the "peak" moves around somewhat as the tendons yield, reposition and slip relative to the concrete. Figure D 34 shows circumferential slip of tendons relative to the concrete. The peak slip is about 2 millimeters. This is an aspect of behavior which was a subject of speculation and study in 1999 and 2000 (post-test analysis), but the analyses of this era used "friction truss-tie" modeling to represent tendon friction. So in that earlier analysis work, it was difficult to estimate the amount of tendon slip occurring during the model pressurization. Now, using the contact surface method, such data as shown in Figure D 34 are conveniently available. This subject of tendon slippage, when and where it occurs during the vessel pressurization will be a good subject of discussion, comparison, and hopefully consensus during the current Standard Problem Exercise.

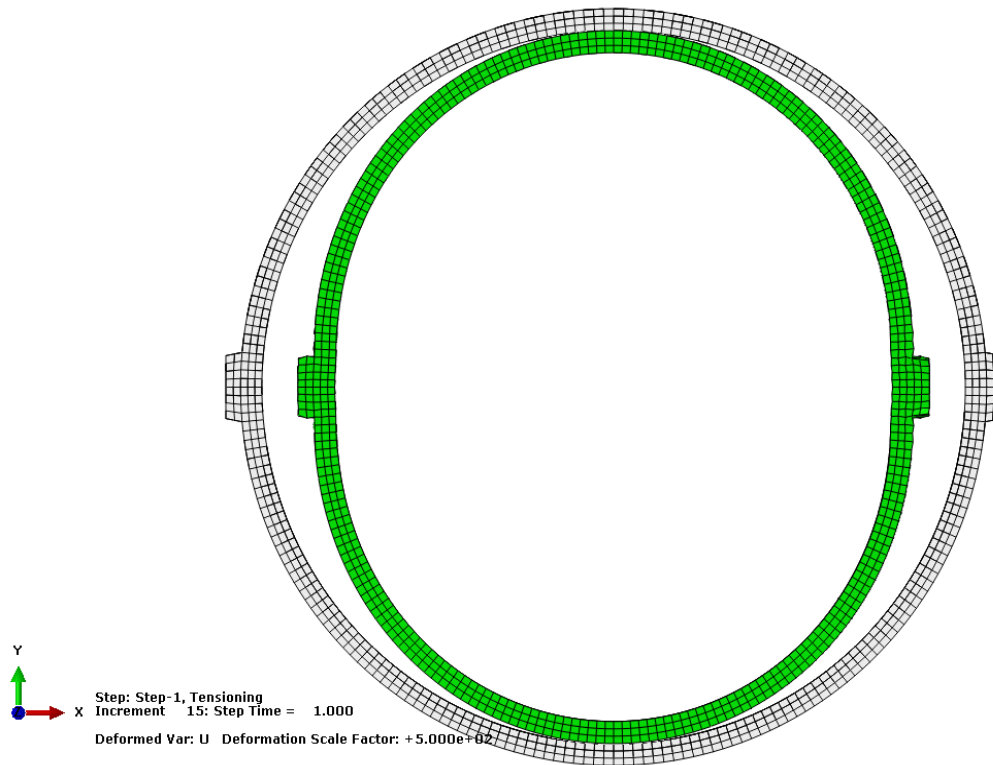


Figure D 20: Deformed Shape at Jacking (x500)

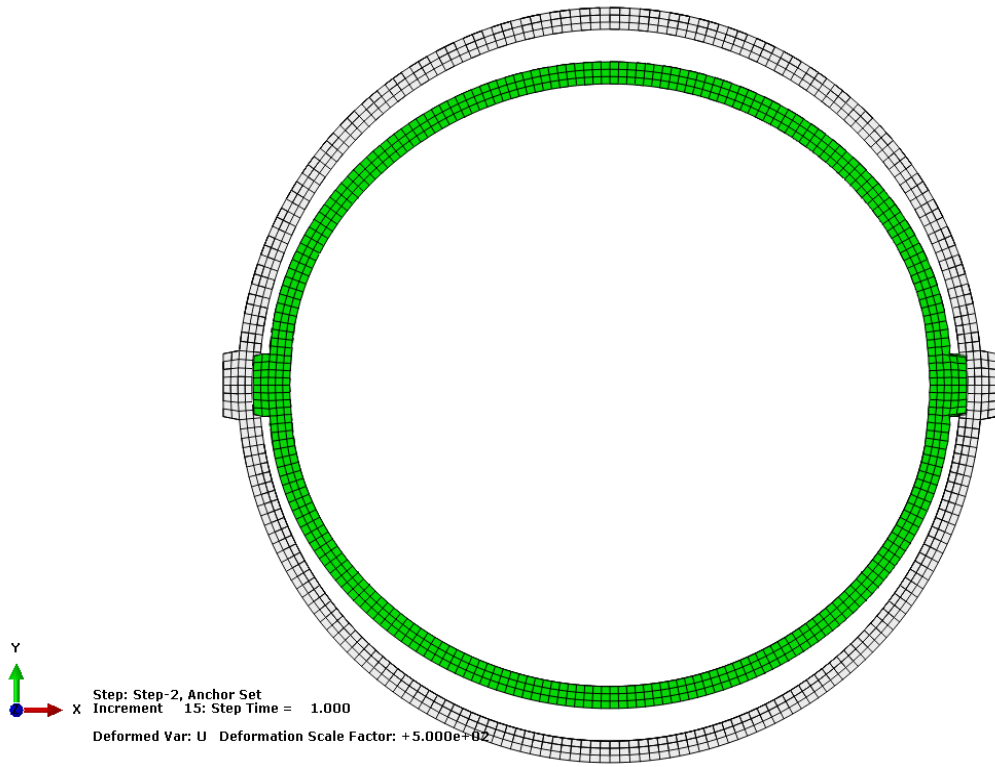


Figure D 21: Deformed Shape at Anchoring (x500)

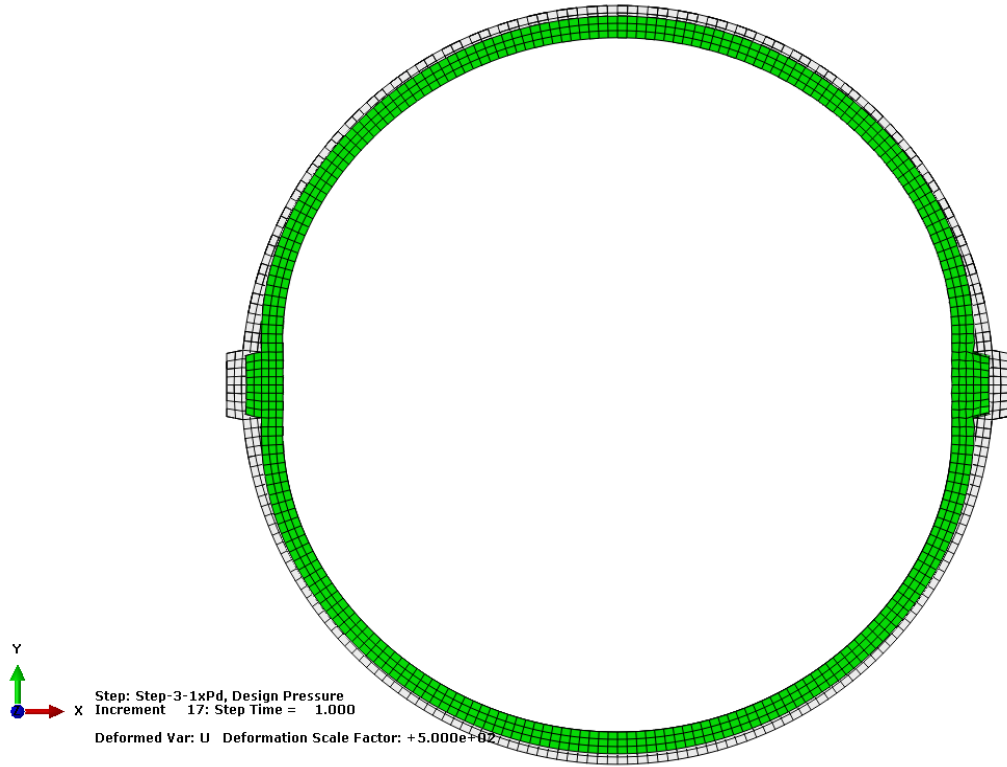


Figure D 22: Deformed Shape at Design Pressure (x500)

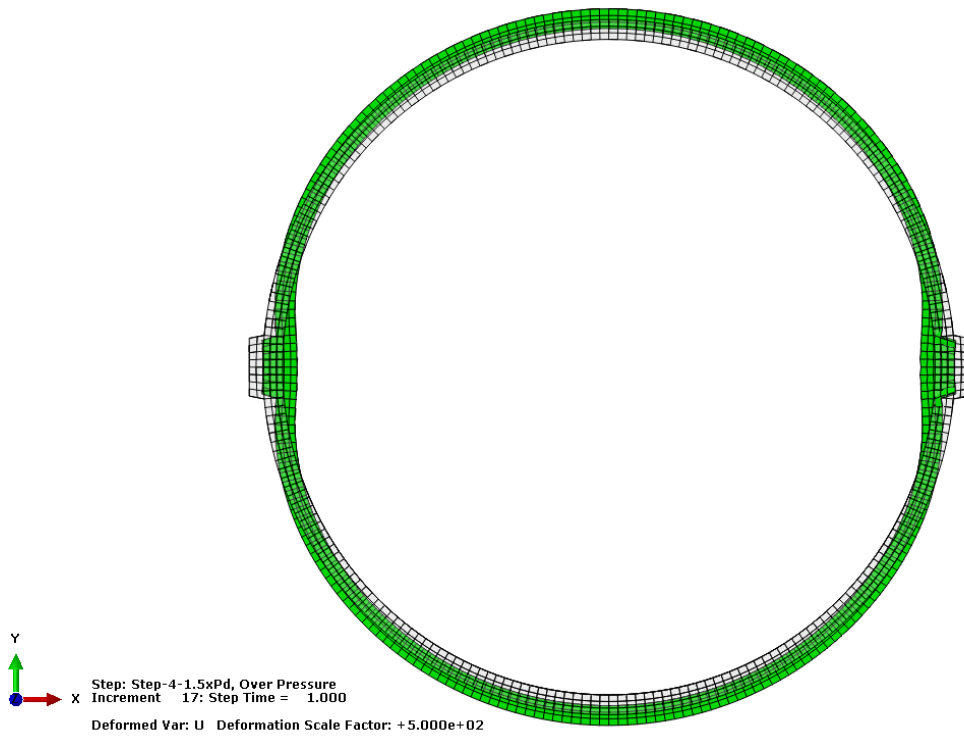


Figure D 23: Deformed Shape at 1.5 x Design Pressure (x500)

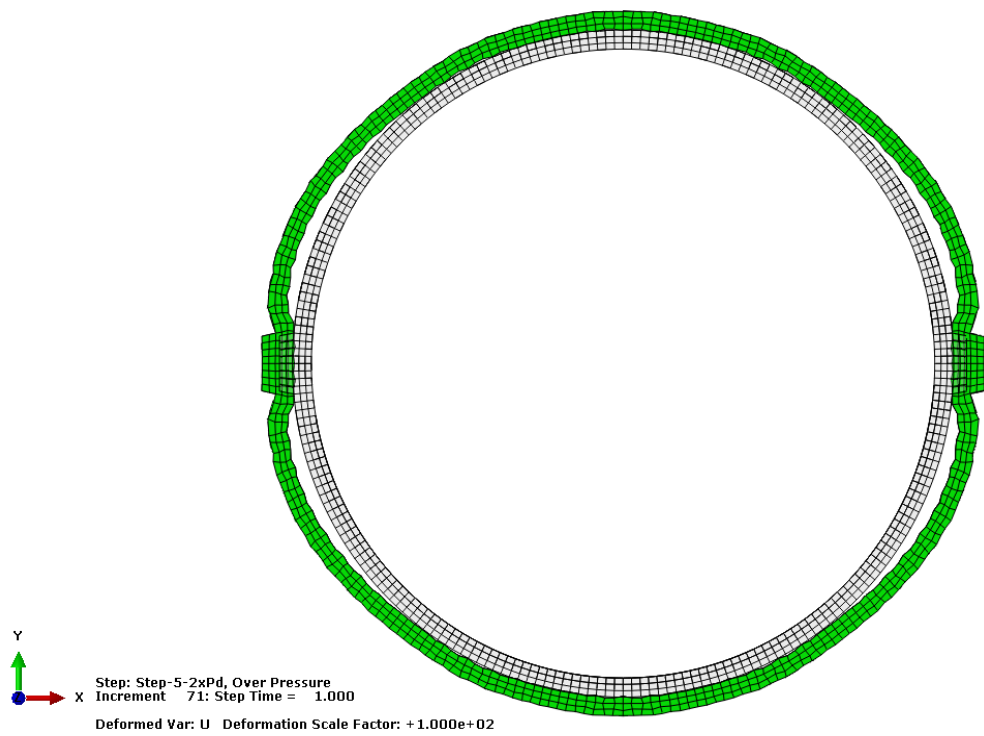


Figure D 24: Deformed Shape at 2.0 x Design Pressure (x100)

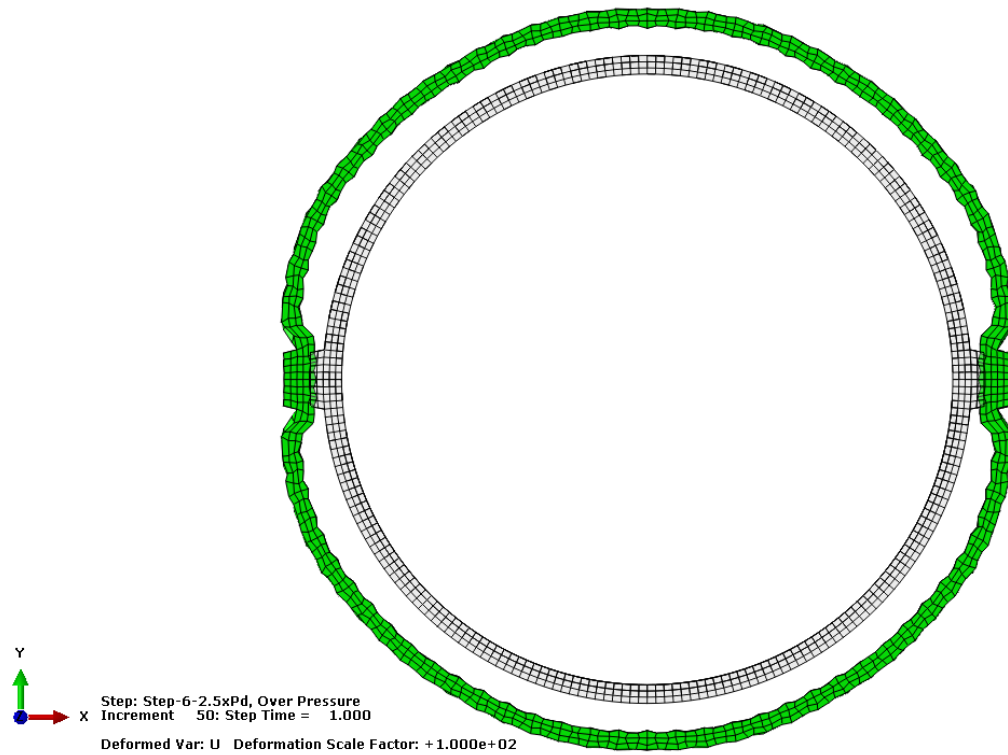


Figure D 25: Deformed Shape at 2.5 x Design Pressure (x100)

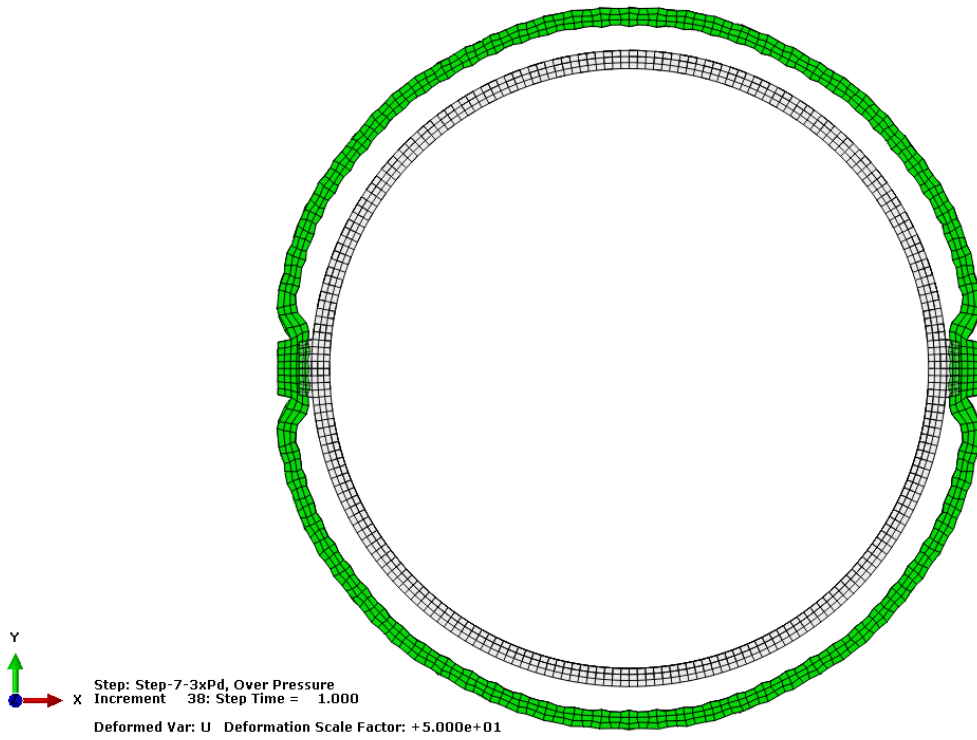


Figure D 26: Deformed Shape at 3.0 x Design Pressure (x50)

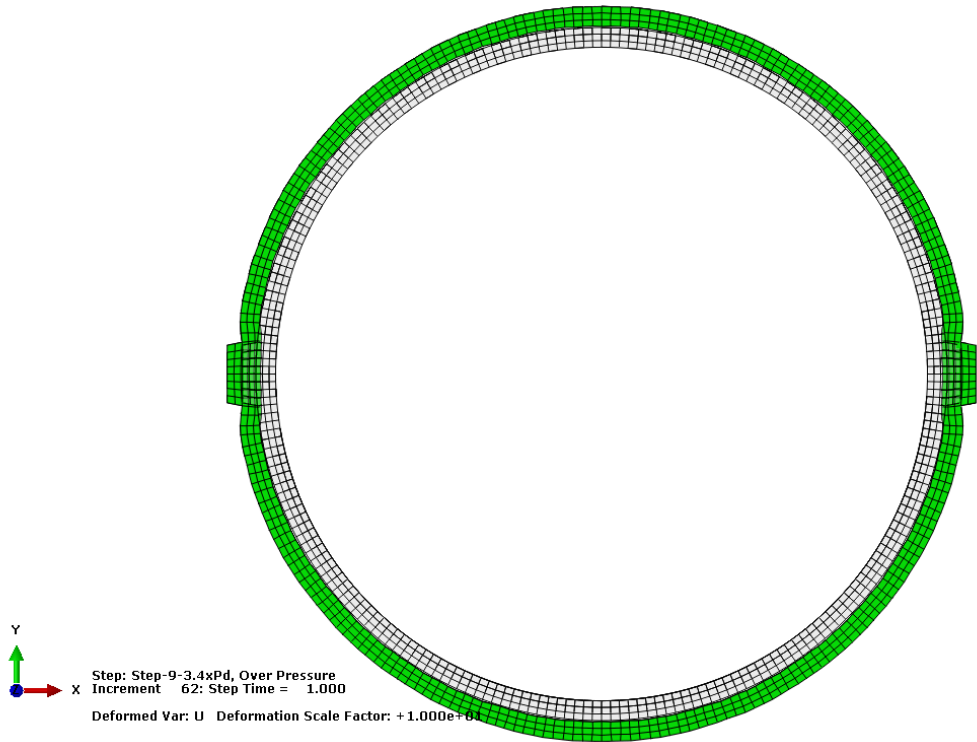


Figure D 27: Deformed Shape at 3.4 x Design Pressure (x10)

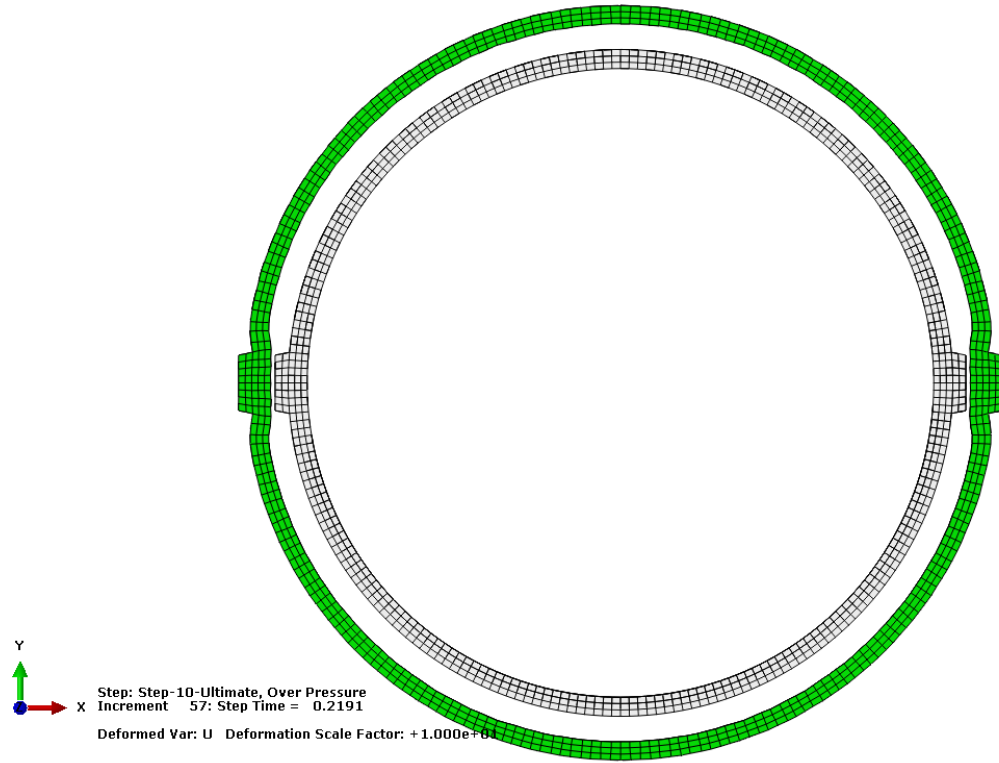


Figure D 28: Deformed Shape at 3.8 x Design Pressure (x10)

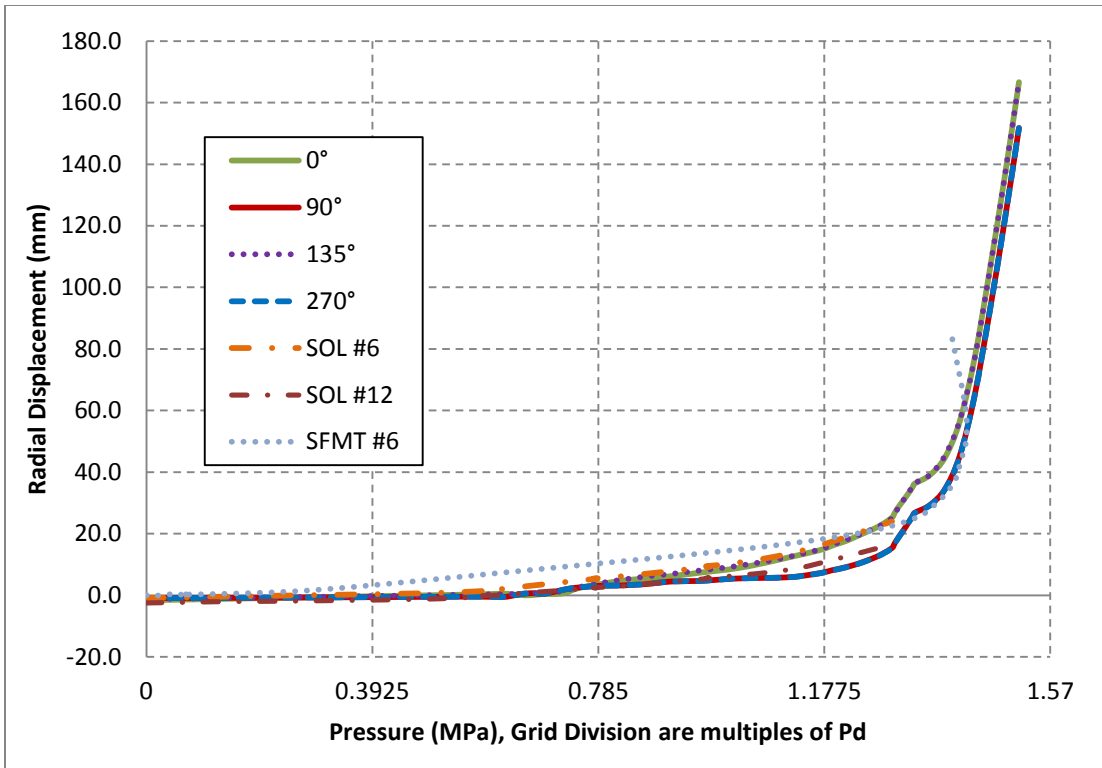


Figure D 29: Radial displacement versus pressure (full displacement range)

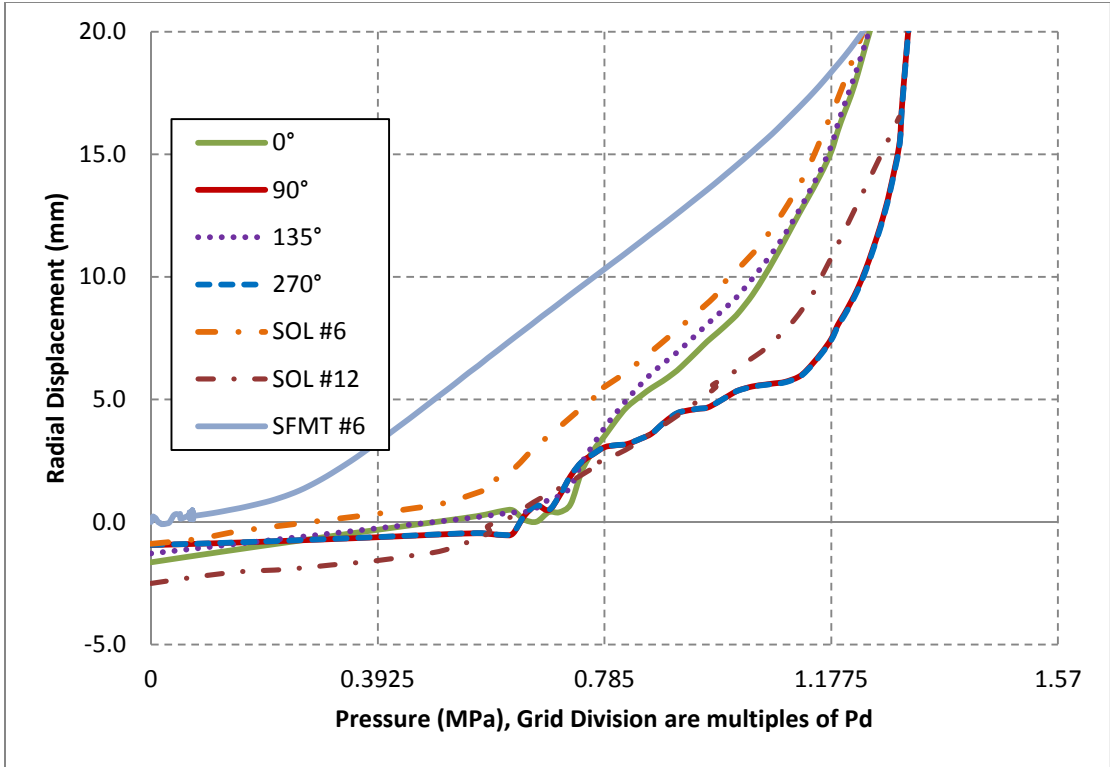


Figure D 30: Radial displacement versus pressure (reduced displacement range)

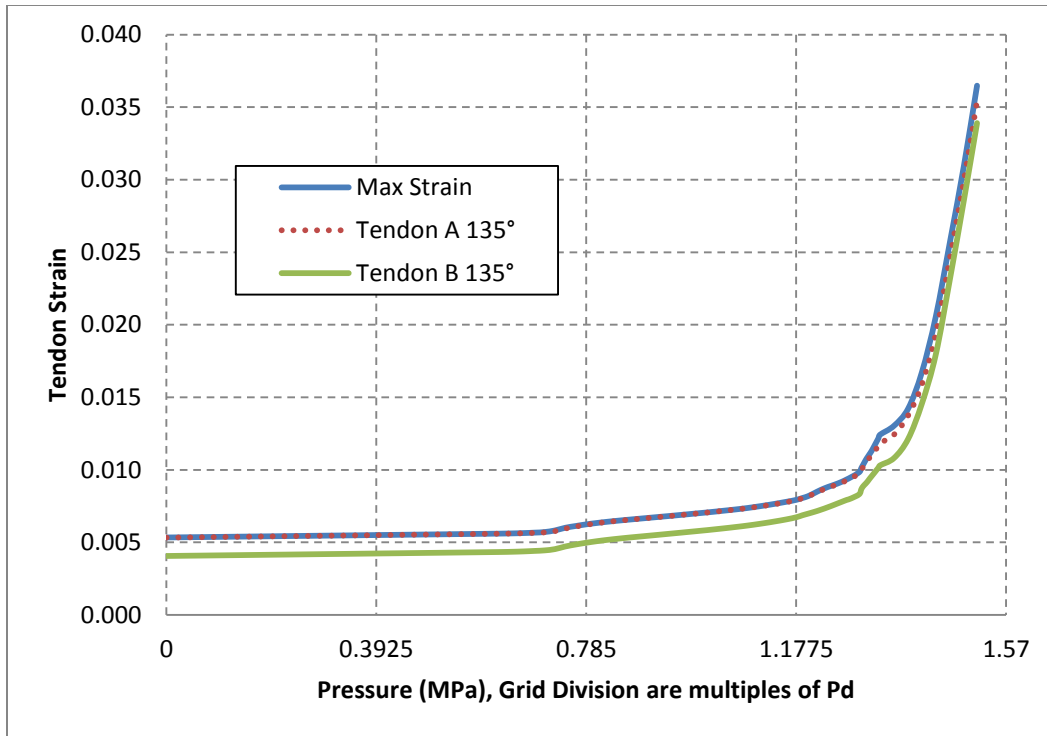


Figure D 31: Tendon strain versus pressure for standard output location at Azimuth: 135 degrees, Elevation : 6.20 Meters, Approx. Midheight (full strain range)

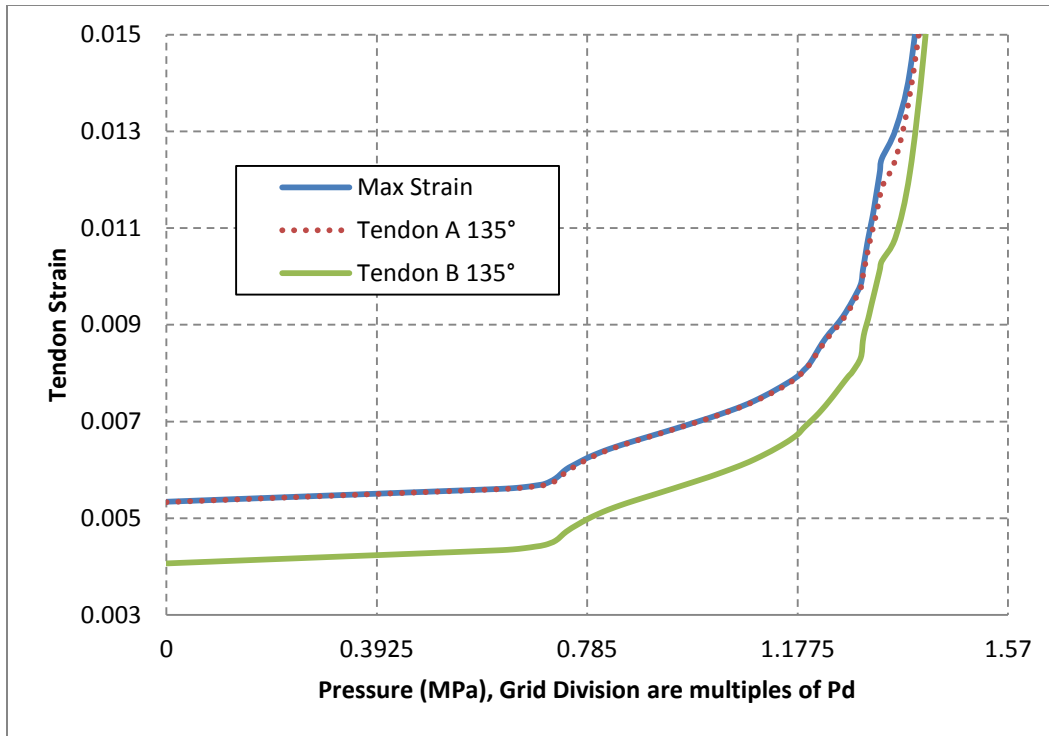


Figure D 32: Tendon strain versus pressure for standard output location at Azimuth: 135 degrees, Elevation : 6.20 Meters, Approx. Midheight (reduced strain range)

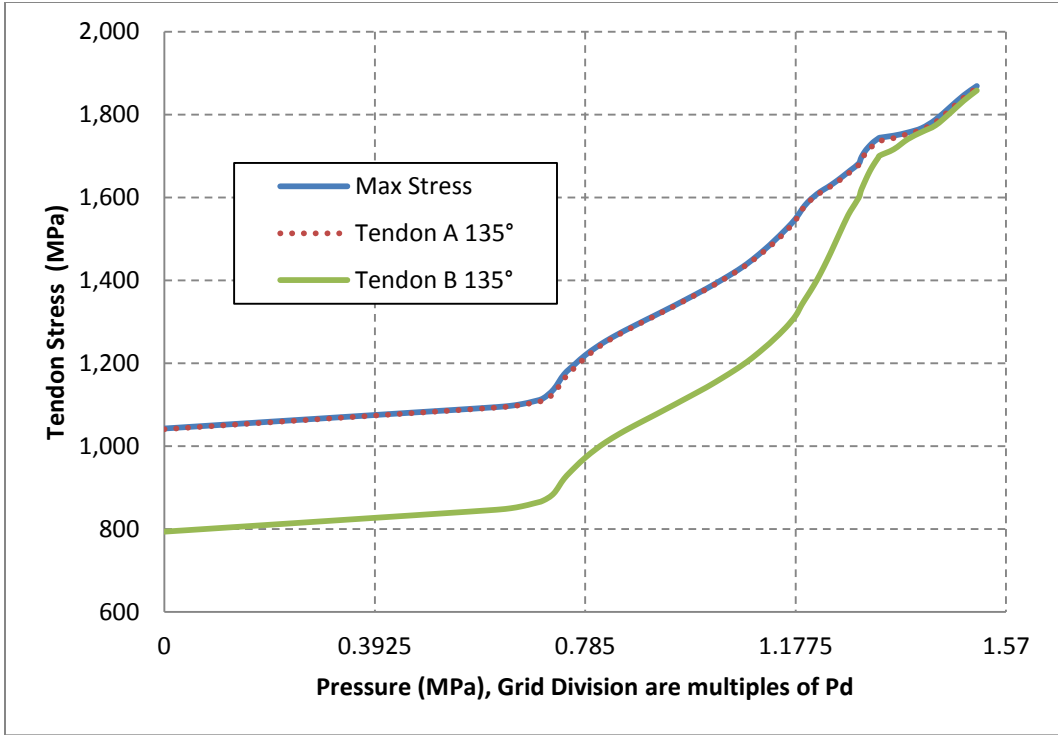


Figure D 33: Tendon stress versus pressure for standard output location at Azimuth: 135 degrees, Elevation : 6.20 Meters, Approx. Midheight

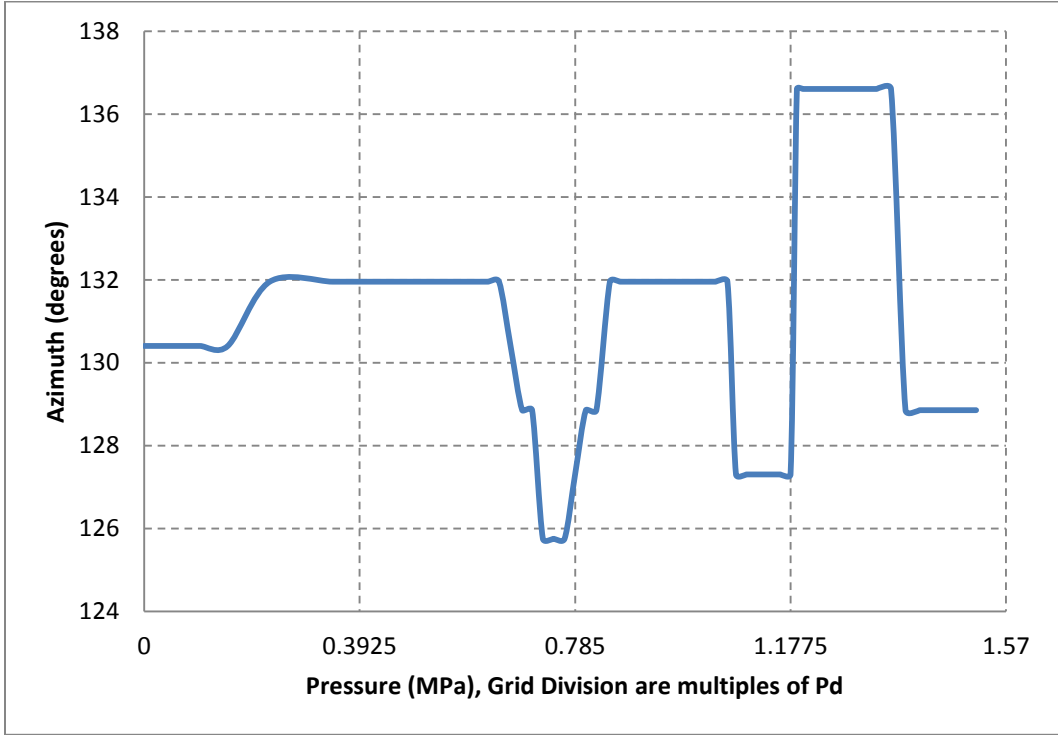


Figure D 34: Location of maximum tendon stress vs pressure

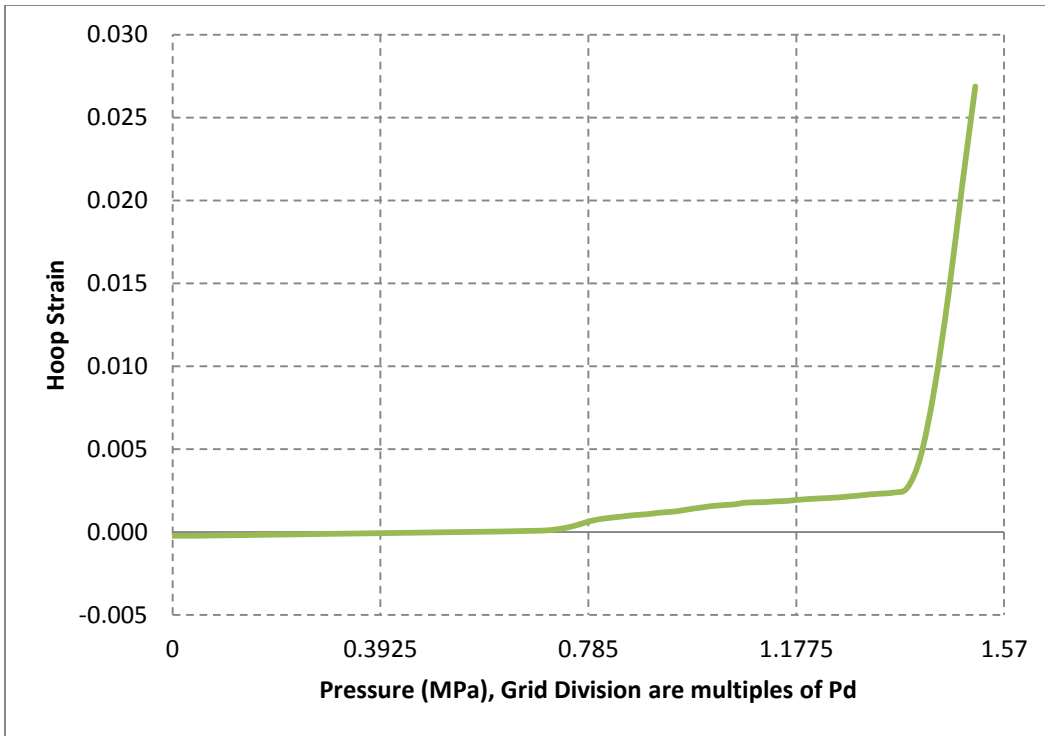


Figure D 35: Liner hoop strain versus pressure (full strain range)

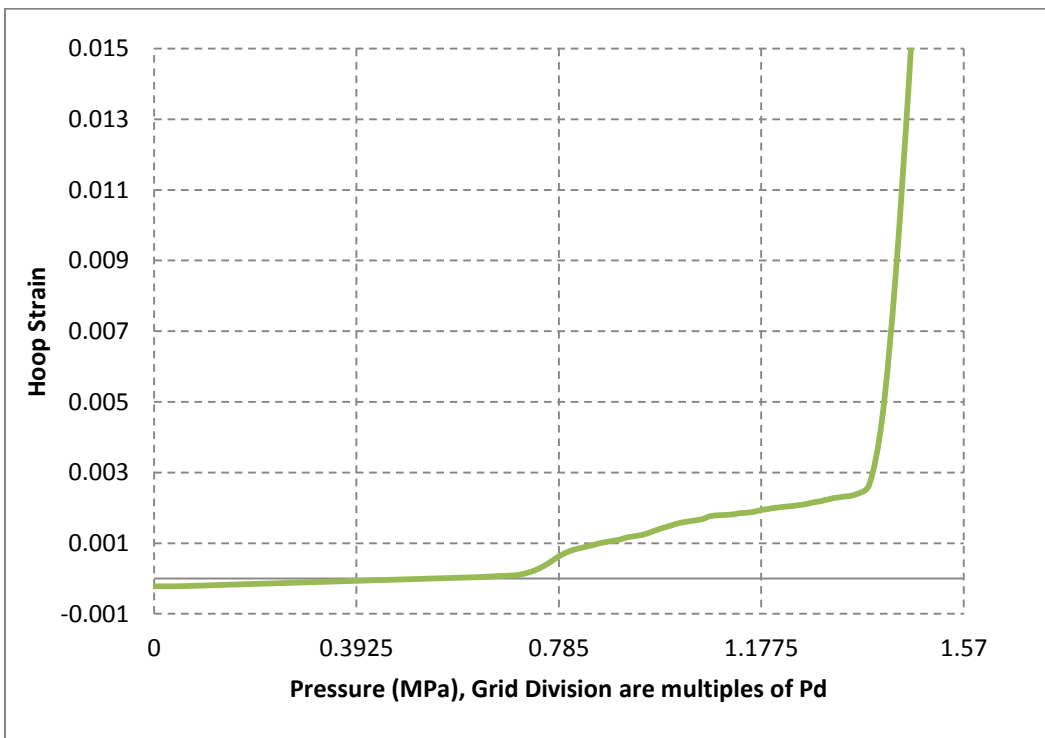


Figure D 36: Liner hoop strain versus pressure (reduced strain range)

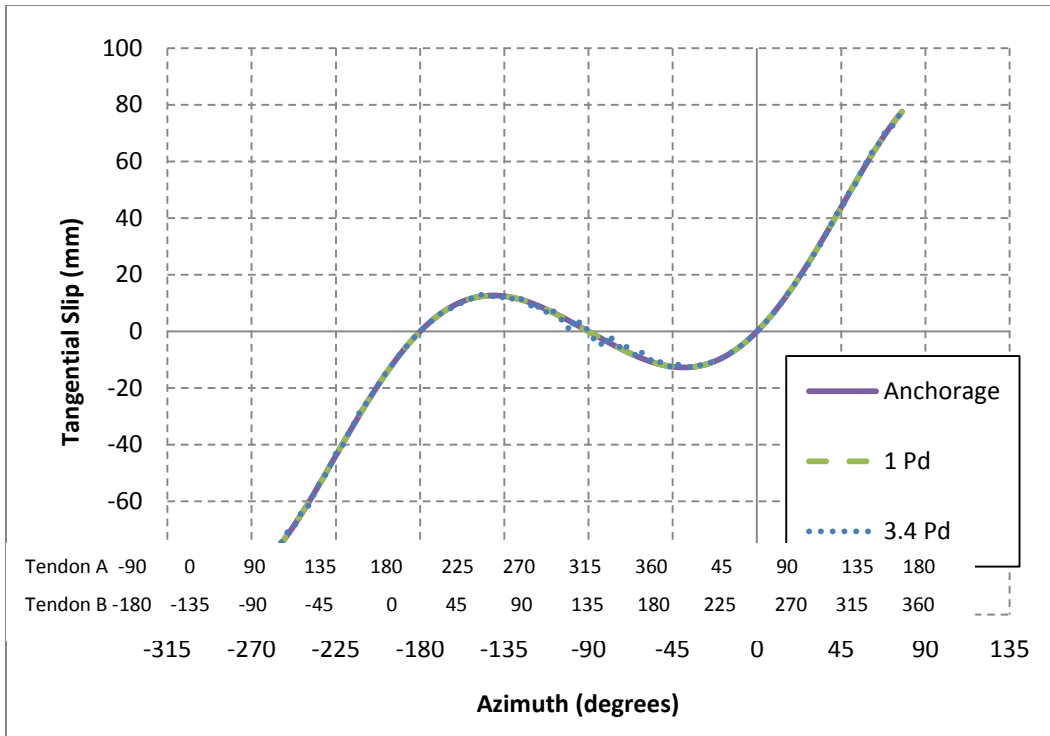


Figure D 37: Tendon slip versus location (full slip range)

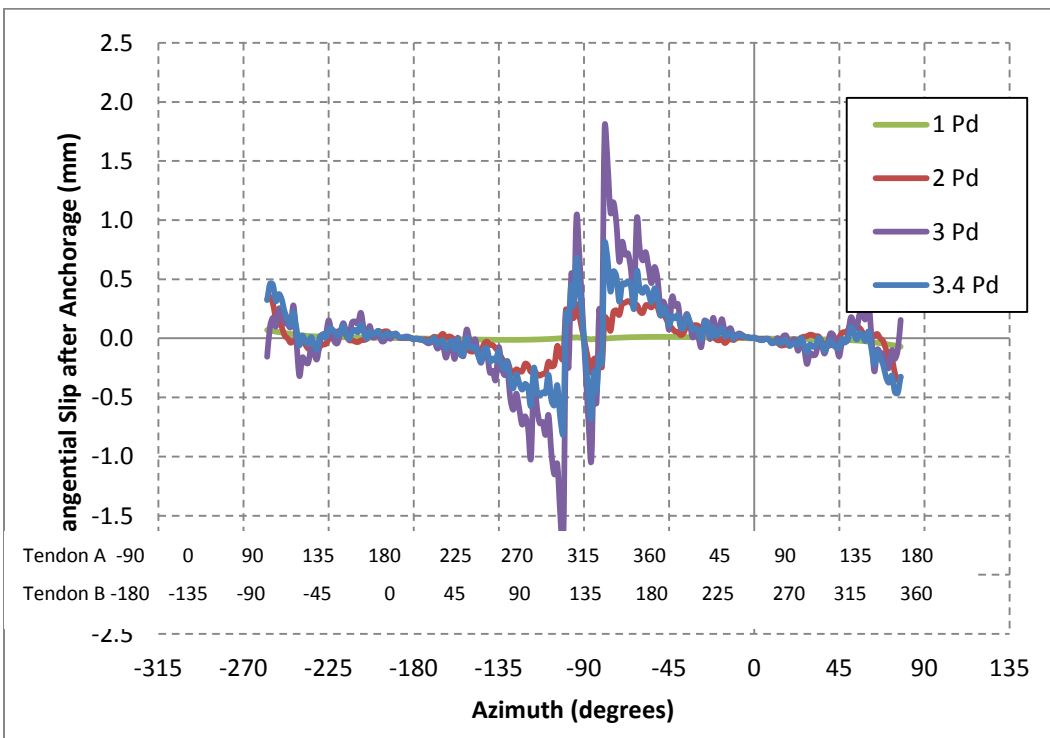


Figure D 38: Tendon slip versus location (reduced slip range)

As an optional exercise (per the SPE3 problem statement), we have also performed analysis for a pressure + temperature case. The case specified in the ISP-48 Exercise was adopted for this – namely, the ‘Saturated Steam’ condition for a PCCV. The ‘Case 2’ (postulated station-blackout scenario) can be studied in later tasks of the SPE3, but we think it is sufficiently illustrative of behavior to analyze Model 1 only for ‘Saturated Steam’. The pressure-temperature relationship applied to the inside face of the containment is shown in Figure D 35a. Based on work we performed during the ISP48 (available in the SPE3 references), we have temperature distribution results of thermal analysis through the thickness of the wall mid-height shown in Figure D 35b. These temperatures were applied to the nodes of Model 1 according to position through the thickness of the wall. Another effect which can be important to thermal analysis is degradation of material properties. The temperatures are not high enough to affect the steel, but they are getting high enough to affect concrete, as shown in the plot of Figure D 36 (also published and described in the ISP48 work). Based on these curves, the three layers of concrete elements through the thickness of Model 1 were assigned slightly degraded properties.

The analysis is then conducted similar to the pressure only analysis. The main difference is that after prestressing and anchor set, an additional equilibrium step is added where the temperature is raised to 80-degrees C. Then the temperature and pressure are increased together according to Figure D 35a.

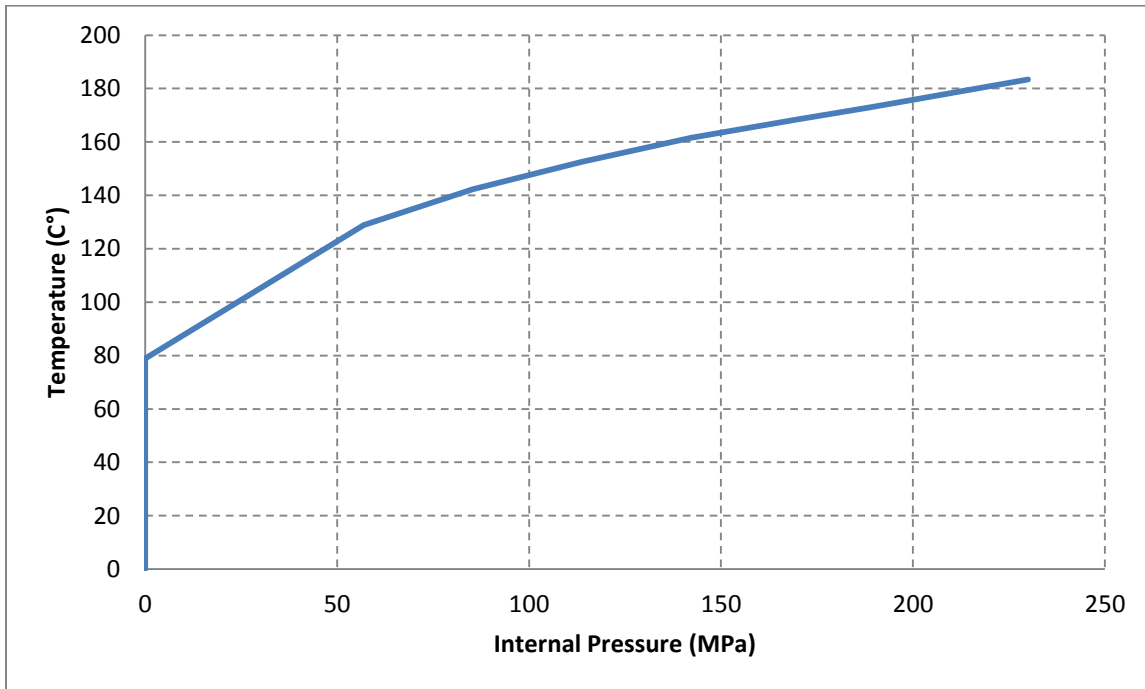


Figure D 39: Temperature change on internal face versus pressure

The results of the temperature + pressure case are provided in Figure D 37 through 41, in similar format as for the pressure only case. The results at pressure milestones are shown in Table D 2.

Table D 3: Results by Pressure Milestones – Pressure + Temperature Case

Milestone	Pressure (MPa)	x Pd
Concrete Hoop Stress (at 135° azimuth) Equals Zero	0.488	1.243
Concrete Hoop Cracking Occurs (at 135° azimuth)	0.705	1.797
Tendon A Reaches 1% Strain (at 135° azimuth)	1.237	3.150
Tendon B Reaches 1% Strain (at 135° azimuth)	1.296	3.301
Tendon A Reaches 2% Strain (at 135° azimuth)	1.402	3.571
Tendon B Reaches 2% Strain (at 135° azimuth)	1.415	3.606

ISP 48, Phase 3, Case 1, Section 2

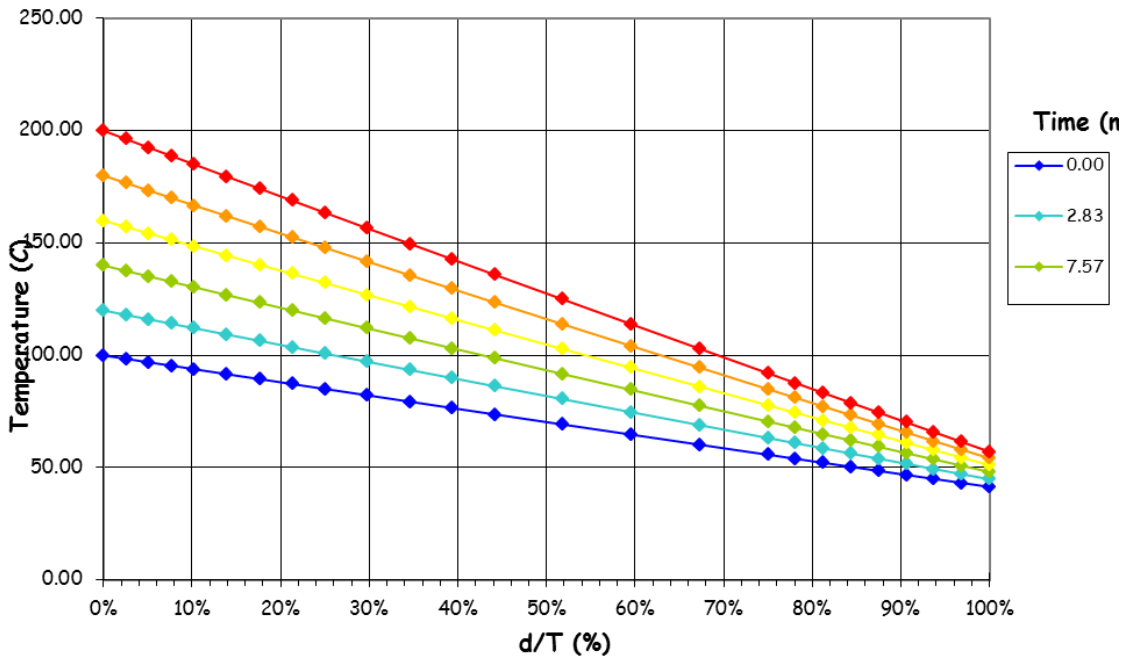


Figure D 40: Temperature variation through vessel wall (ambient temp = 21.1 C°)

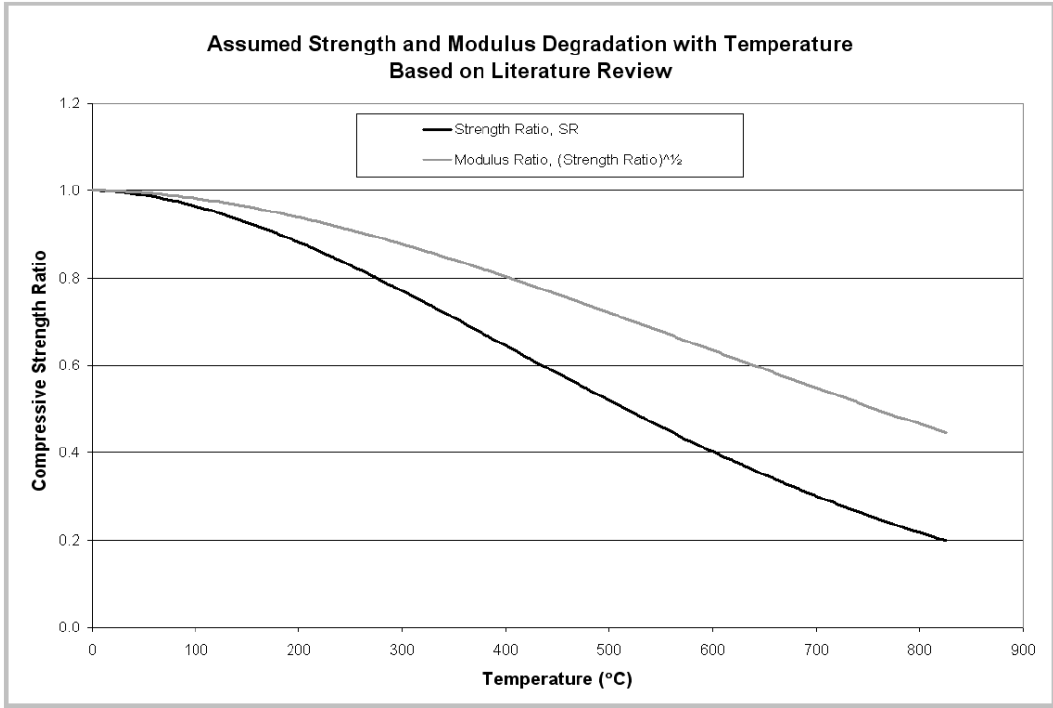


Figure D 41: Concrete Degradation with Change in Temperature

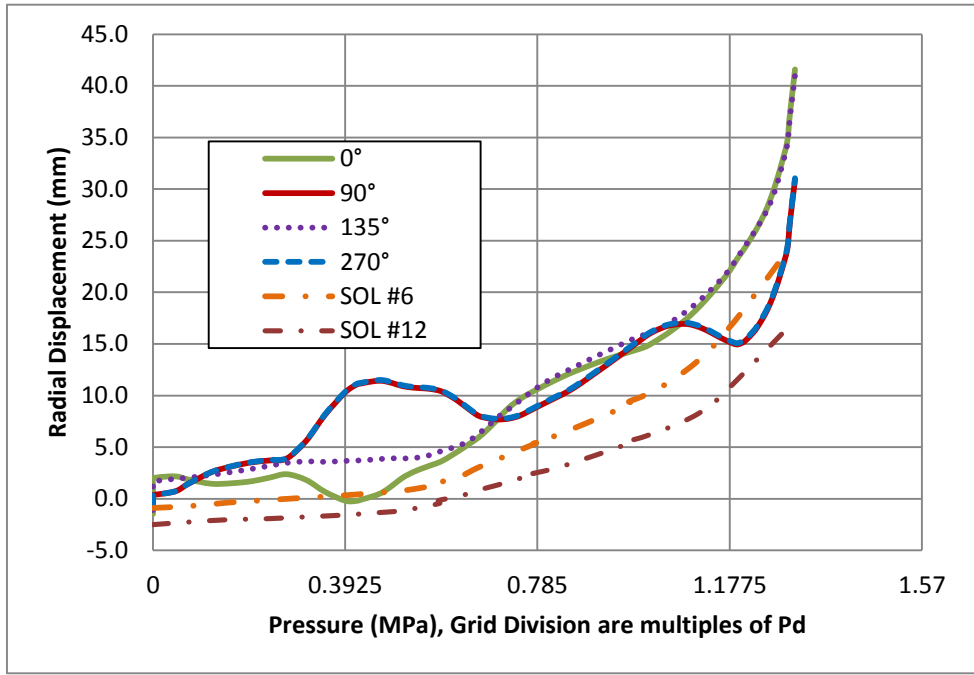


Figure D 42: Radial displacement versus pressure (full displacement range)

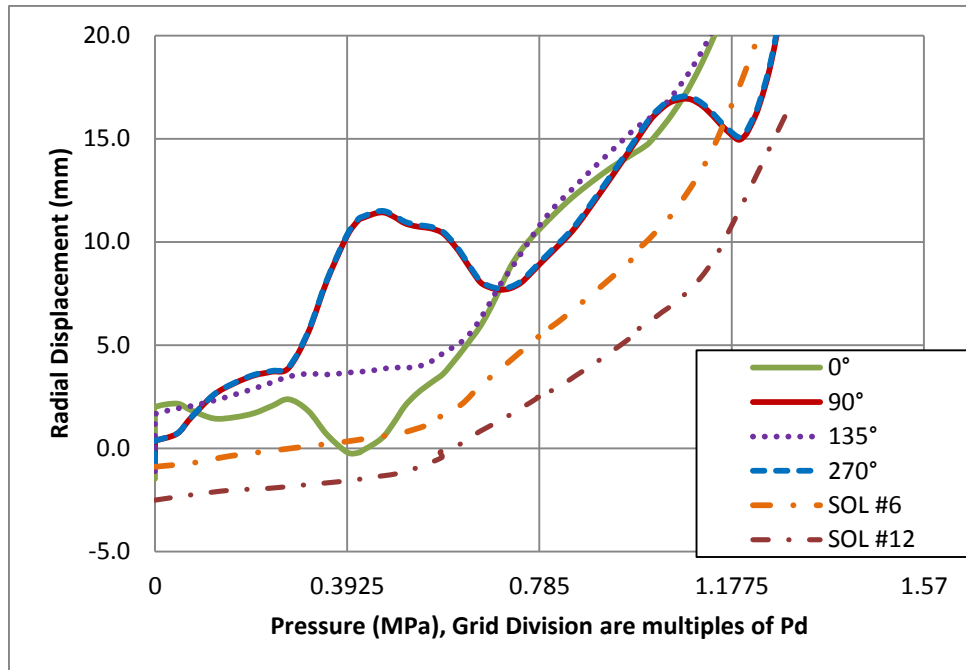


Figure D 43: Radial displacement versus pressure (reduced displacement range)

There are no significantly different conclusions in terms of ultimate limit state for the PCCV for the pressure + temperature case, but there is an interesting phenomena observed between approximately $1xPd$ and $2xPd$. During this range of response, the ovalized shape of the “ring” changes from being “dimpled” at the buttresses, to being ovalized outward at the buttresses. But at larger pressures, the shape of the ring, and the general magnitude of the displacements returns to a similar pattern as that of the pressure only analysis.

Another observed difference is that during pressurization, the tendon-slippage relative to the concrete reaches 3.2 mm, which is larger than the 1.8 mm observed for the pressure only analysis.

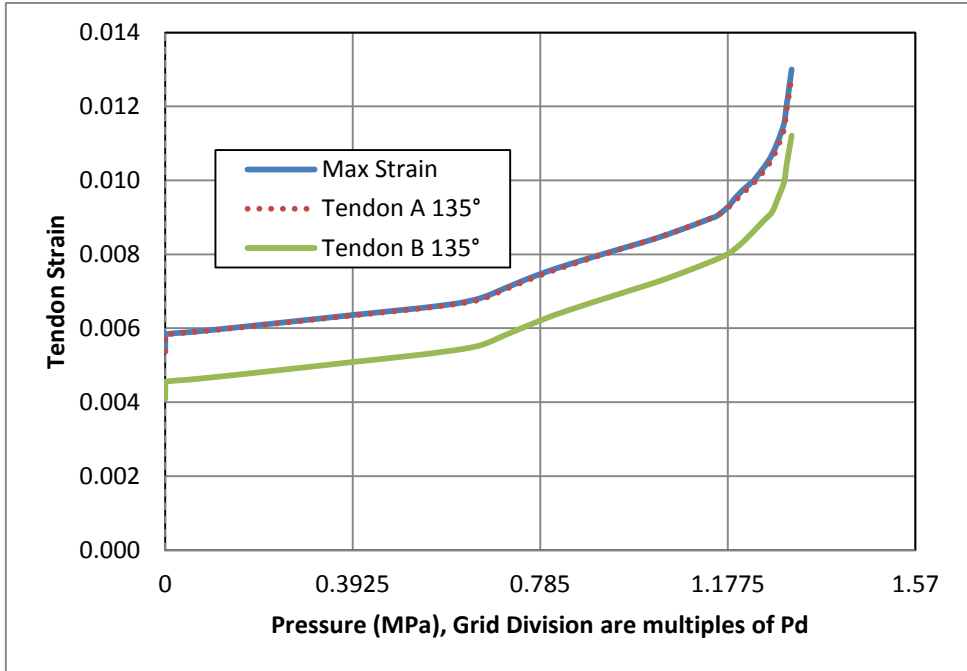


Figure D 44: Tendon strain versus pressure (full strain range)

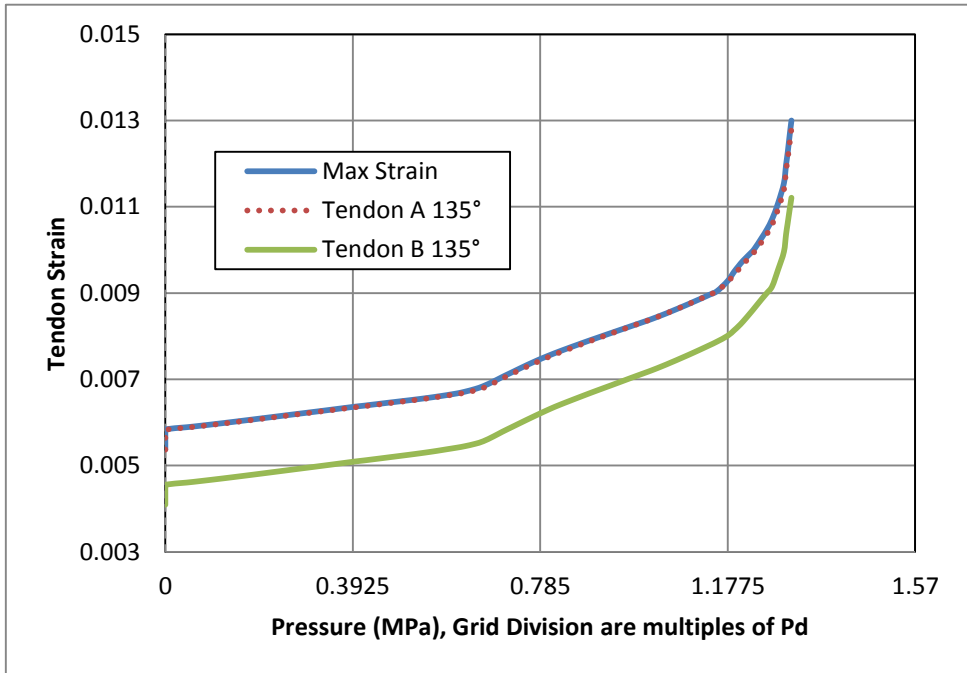


Figure D 45: Tendon strain versus pressure (reduced strain range)

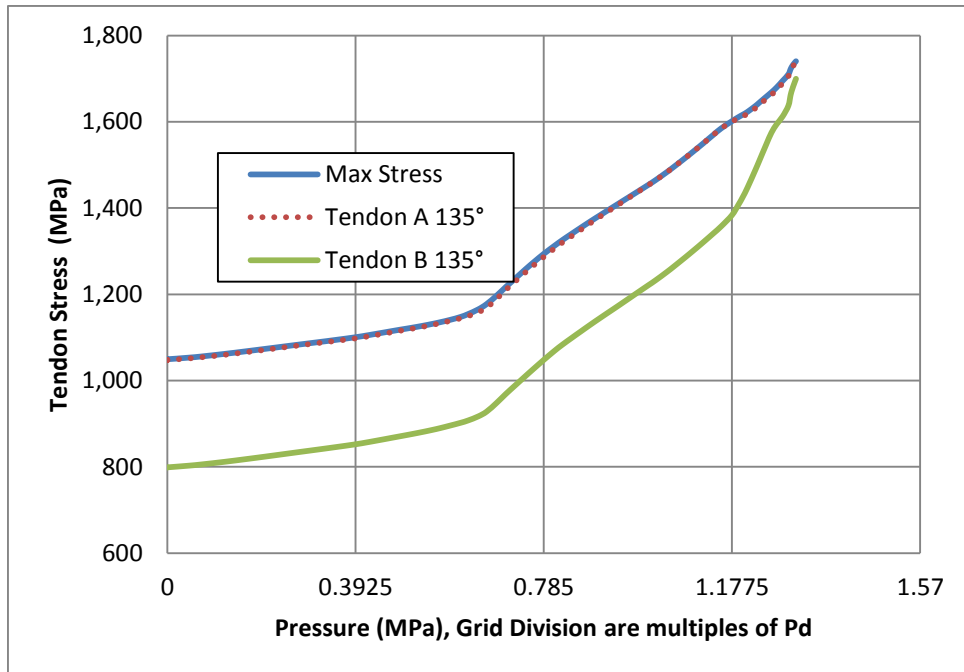


Figure D 46: Tendon stress versus pressure

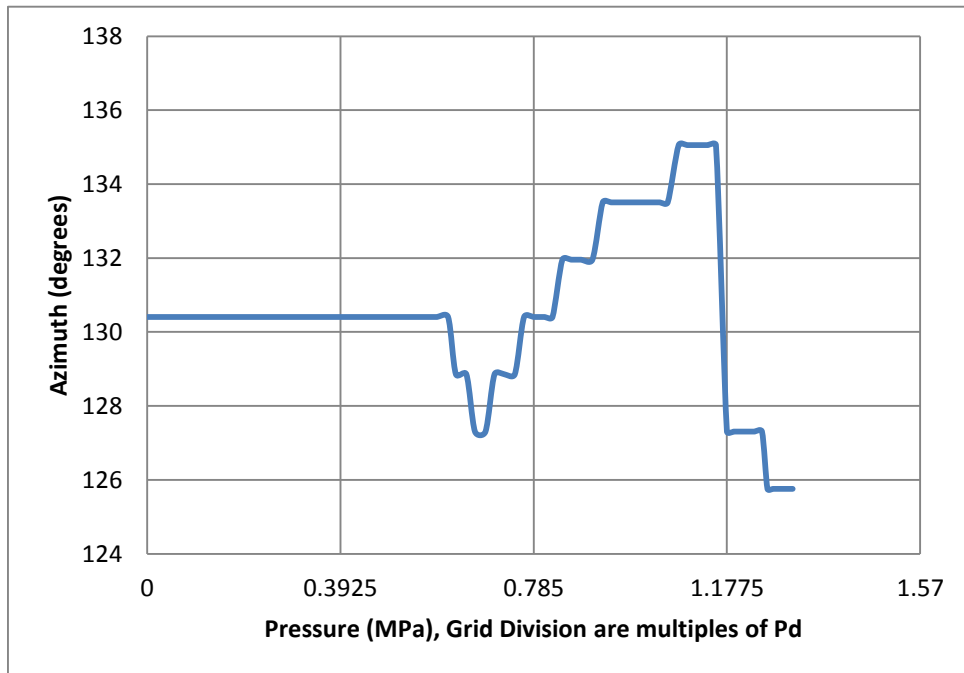


Figure D 47: Location of max tendon stress versus pressure

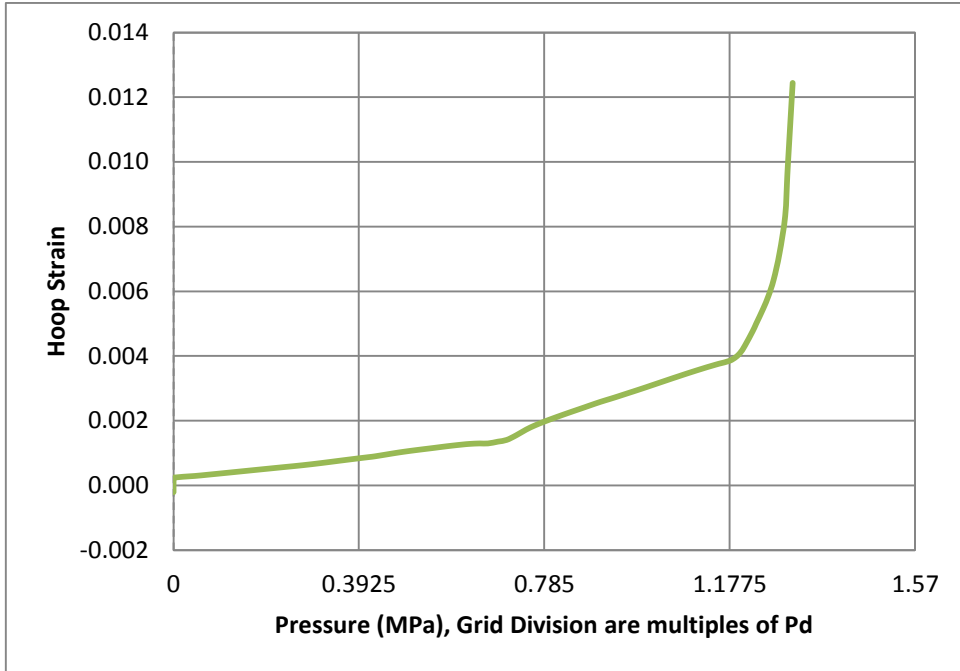


Figure D 48: Liner hoop strain at 135 degrees versus pressure (full strain range)

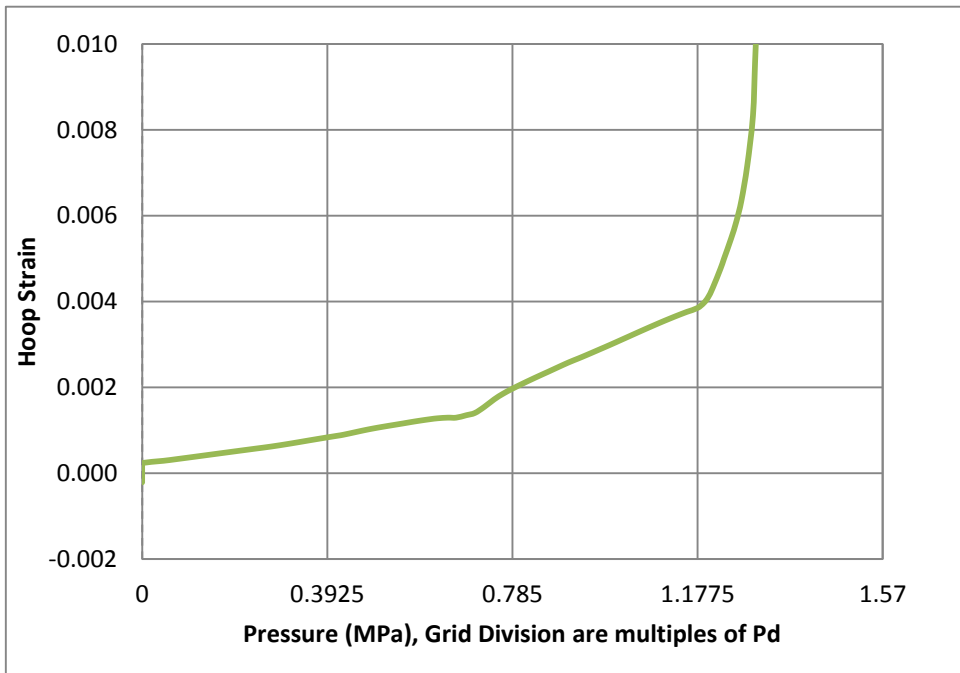


Figure D 49: Liner hoop strain at 135 degrees versus pressure (reduced strain range)

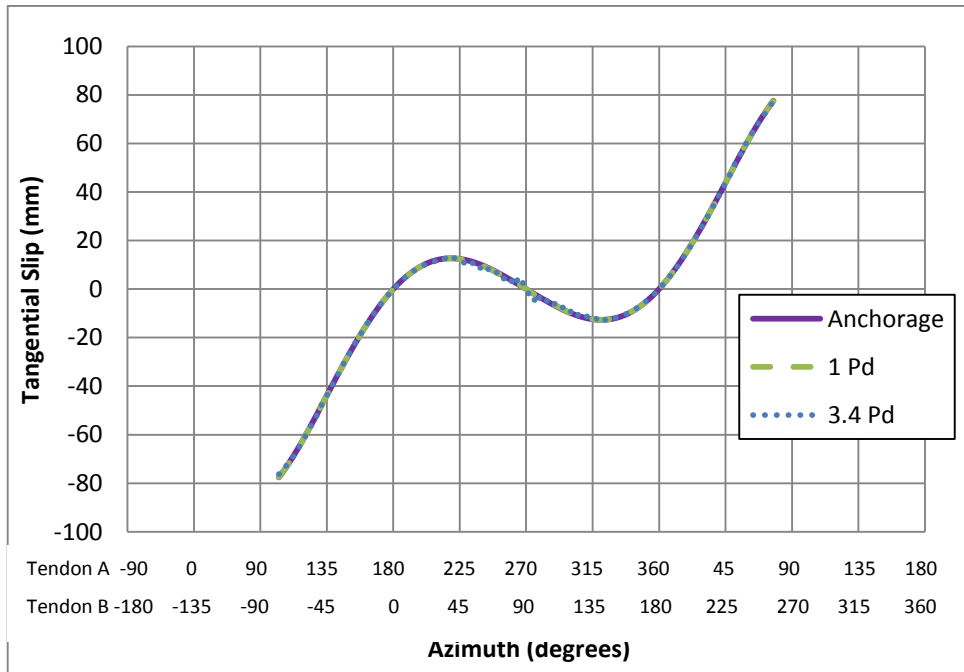


Figure D 50: Tendon slip versus location (full slip range)

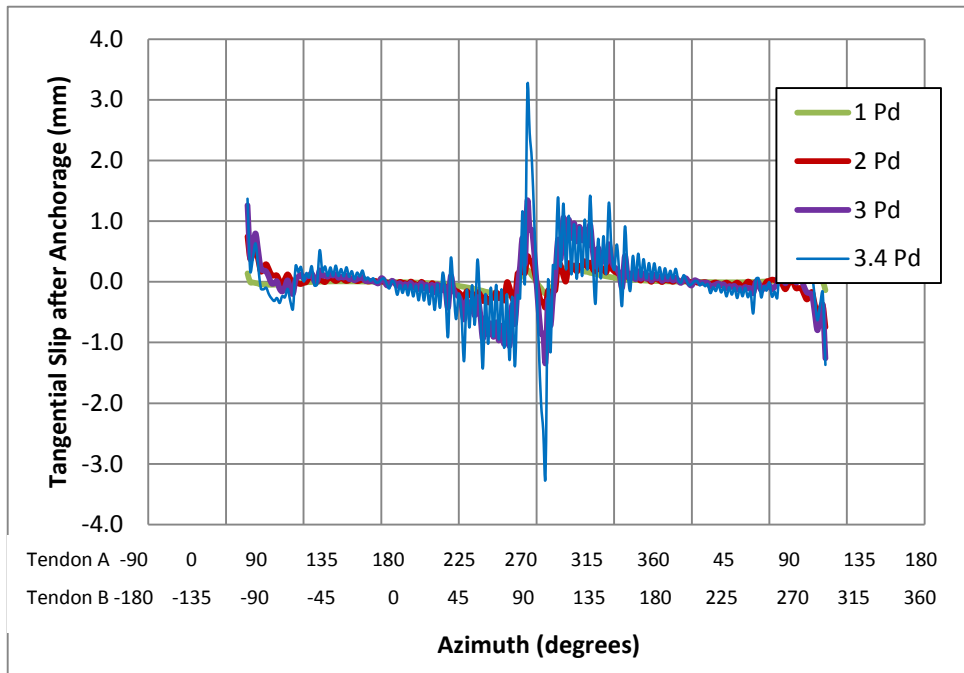


Figure D 51: Tendon slip versus location after anchorage

MODEL 2

This Tech Memo is second in a series following a similar report for Model 1, which studied the first two of these effects. With Model 2, a detailed model of the Equipment Hatch, we continue

studying the first two effects, and also begin to study the third and fourth of these effects, plus the ovalization of concrete versus steel and the displacement and leakage this could cause. The modeling assumptions, initial conditions, and analysis results are presented herein for a pressure only analysis. Temperature analysis was not part of the SPE for Model 2.

During the kick-off meeting, a third aspect of Steel-Concrete Interface was introduced: study of rebar stress-strain specified versus stress-strain characteristics in the FE model (because concrete can influence this representation). This will be addressed with Model 2 with a view toward applying lessons learned to final global analysis.

Geometry and initial conditions

The geometry and boundary condition assumptions of the local E/H model (Model 2) specified for all participants is shown in Figure D 1, 2, and 3. "D16", "D19", etc. refer to Diameter-16-millimeter, Diameter-19-millimeter size bars, as specified on the drawings and NUREG/CR-6810. The significance of the 358-degree and 0.2-degree azimuths (for example) is these are azimuths where changes in rebar size occur. Including these "step-downs" in reinforcing at the proper locations in the model is important to the analytical prediction.

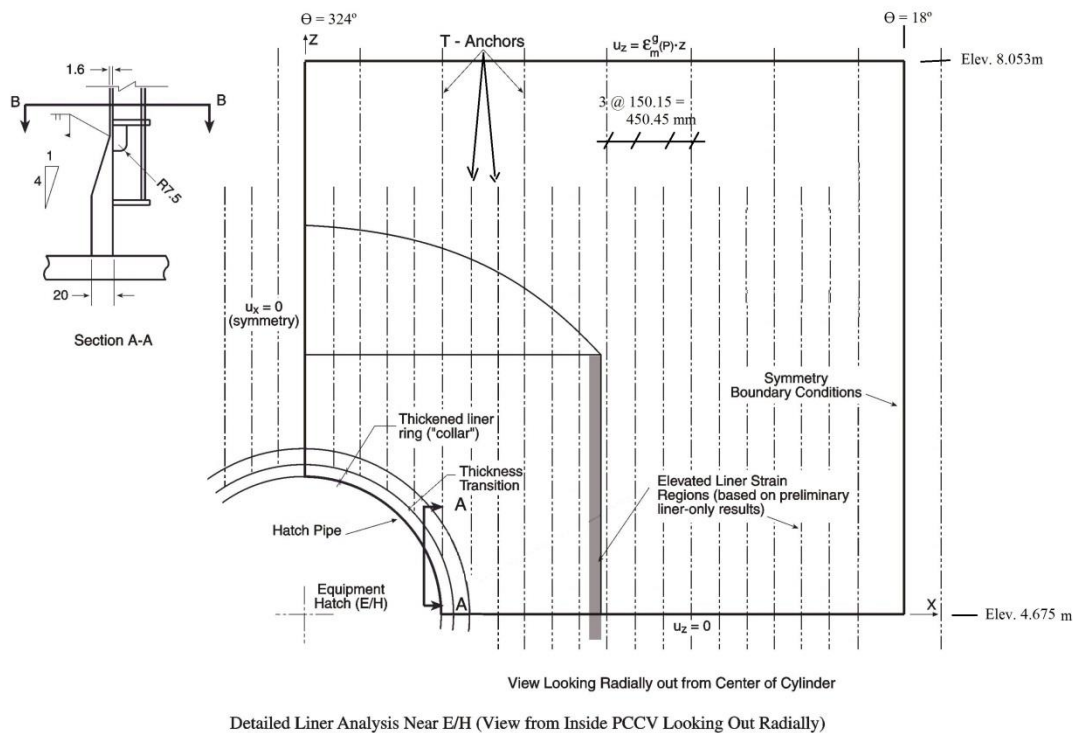


Figure D 52: Model 2 - Local E/H Model Geometry and Boundary Conditions

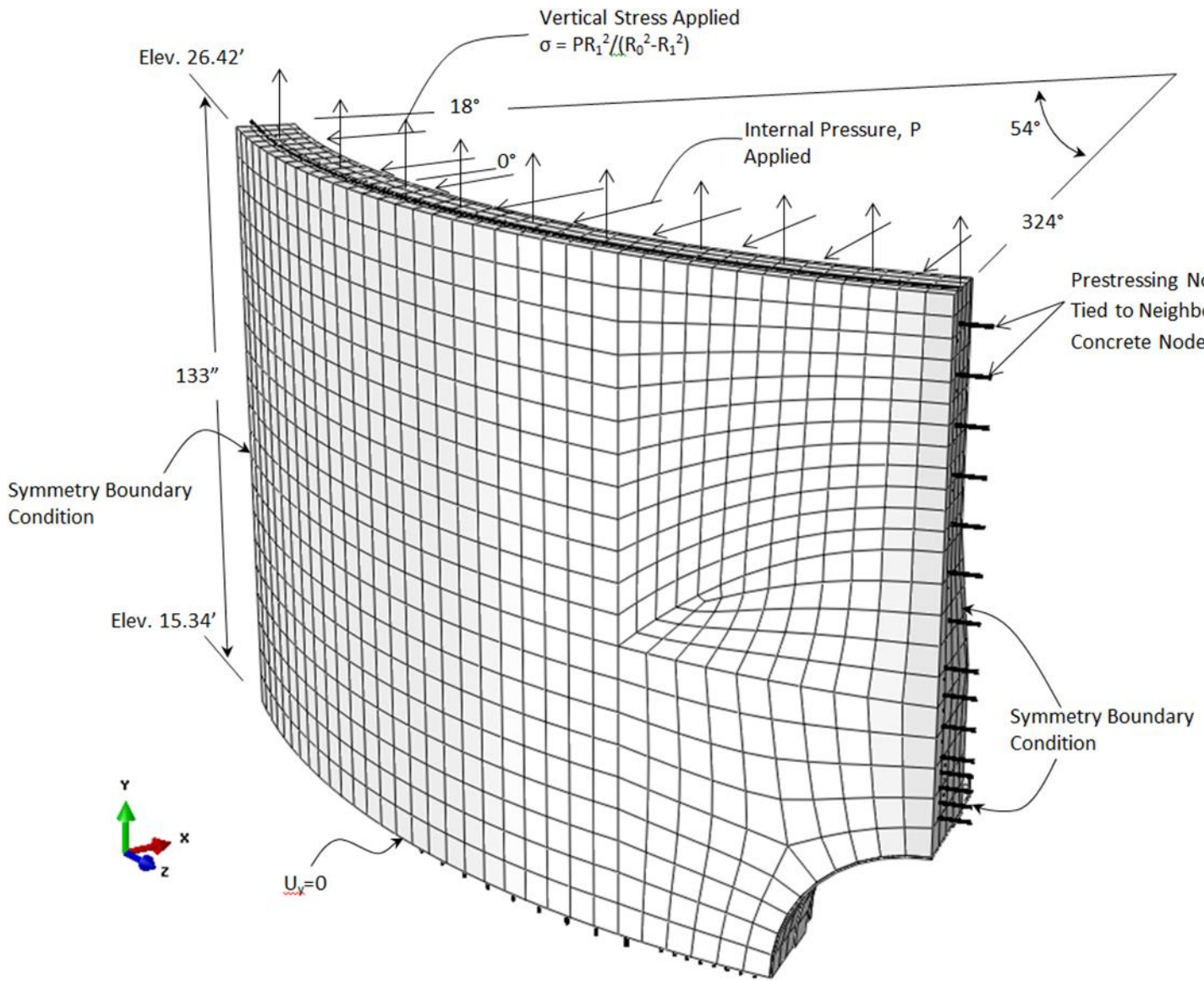


Figure D 53: Model 2 boundary conditions and geometry schematic

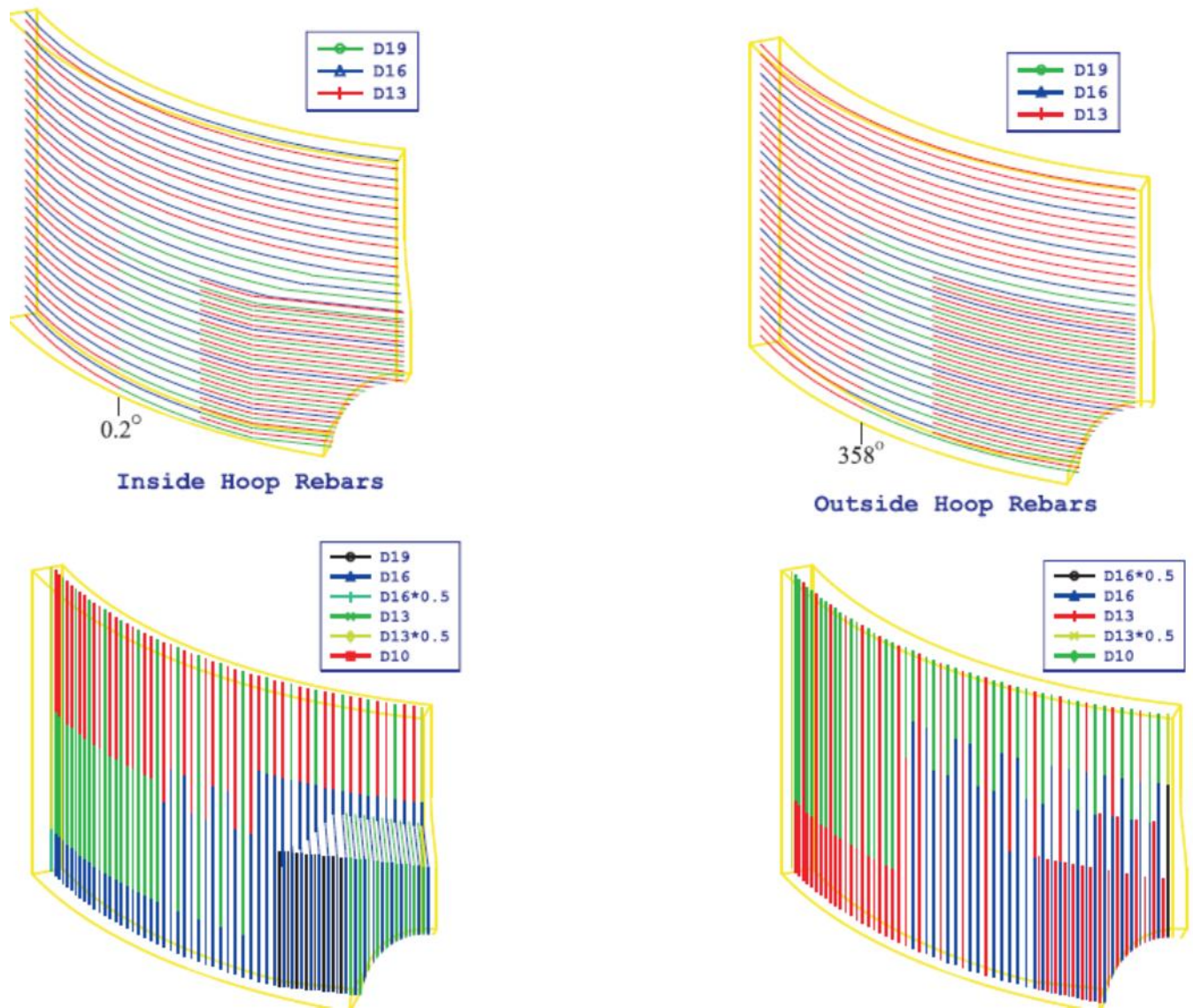


Figure D 54: Rebar Summary for Model 2 (Important to Simulating Strain Concentrations)

The boundary conditions of Model 2 are symmetry at the azimuth-324-degrees and Azimuth-18-degrees planes, and quasi-symmetry at the bottom and top of the model, i.e., $U_z = 0$ at the bottom, and the statically determinant meridional stress applied at the top (as indicated in Figure D 2). An additional required condition along the top of the model is that all nodes must stay in a plane, and the plane is not allowed to rotate about the tangential (theta) axis. Using this boundary condition allows the application of vertical prestress, without causing local distortions at the ends of the tendons at the top of the model. As a plane, the top of the model is still free to deform vertically, under the action of the meridional applied stress, and the model response.

The ABAQUS Standard FE program was used for the analysis. Simulation of friction and pressure-response related changes to tendon stress distribution has been included in the analysis. The model includes concrete, tendons (hoop and vertical), rebar (hoop, vertical, and shear reinforcement in the plane of the model), liner, and liner anchors. Vertical tendons and

vertical rebar were not included in the model. Concrete was modeled with 8-node 3D solid elements, rebar was modeled with embedded subelements, tendons with two-node truss elements, and liner with 4-node shell elements.

Analytical representation of losses was handled by a) the initial conditions applied to the tendons, and b) by the FE Model's representation of angular friction.

It should be noted that the tendons modeled in earlier work (NUREG/CR-6810) were represented "2 for 1", based on a simplifying FE modeling assumption. With more computational power available today, every tendon was modeled. The other important difference from the work performed ten years ago is the way the tendon friction was modeled. All the tendons, now modeled, are shown in Figure D 4.

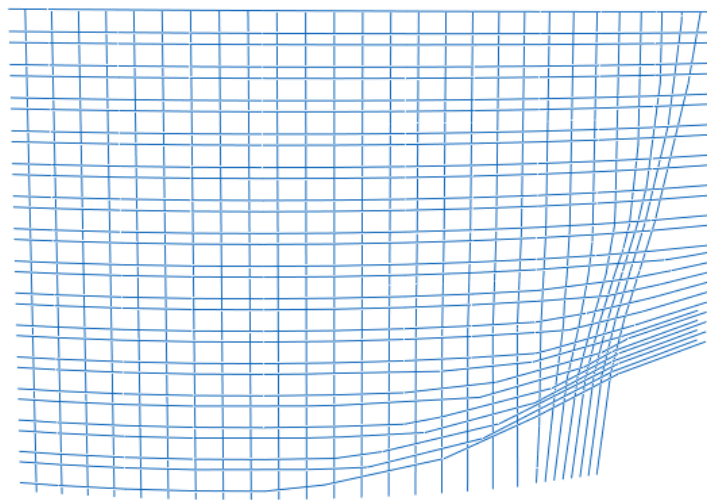


Figure D 55: Prestressing tendon geometry for Model 2

With the methodology followed in Model 1, this contact condition requires that the nodes of the tendon and the nodes of the concrete be coincident. With the complexity of the tendon geometry, making the concrete mesh compatible with the tendon mesh is extremely difficult and time consuming. Therefore, an innovative strategy was developed to facilitate the modeling of the tendon-concrete interaction - embedded shell elements were created, surrounding each tendon. (These are analogous to the "sheaths" or "ducts" of the tendons.) These elements are fully embedded into the concrete, while allowing the contact surface to be true to the 3d geometry and effectively modeling the actual conditions. The material properties of these embedded shell elements were chosen to make their contribution insignificant to the overall behavior.

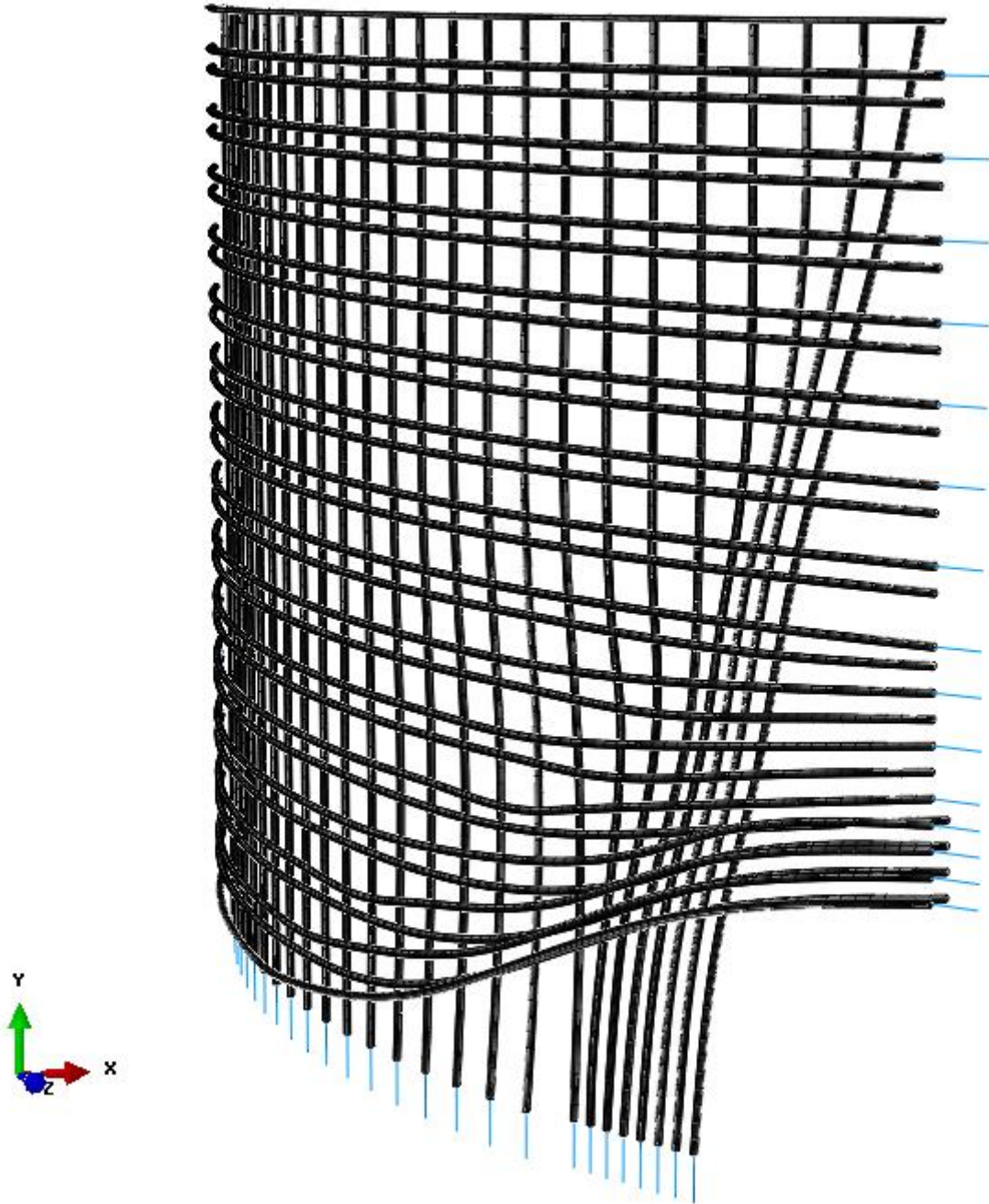


Figure D 56: Sheath elements along tendon with jacking elements

The interface shells were created with a finite element cross-section orthogonal to, and centered on, one end of the prestressing tendon. This profile is then swept along the length of the tendon and the shell is created. The finite section allows the shell to be embedded into the concrete all along the length of the shell, while the coincident nodes make the contact surface feasible. The geometry is shown in Figure D 57 and 58, and the analysis behavior shown in Figure D 59. In summary, friction and contact are simulated between the tendon elements and the “shell”, and

the “shell” is embedded in the concrete, but the modeling innovation allows the concrete to have dissimilar mesh from that of the tendon system.

Other aspects of the model are shown in Figure D 70 through 77. Figure D 70 shows how the primary component parts of the model, and how the penetration pipe and sleeve are modeled with a contact surface applied between the sleeve and the concrete. Figure D 60 shows the tendon sheaths and jacking elements. Figure D 59 through 64 show the concrete mesh, liner and penetration mesh, vertical and horizontal liner anchors, and the rebar subelements (hoop and vertical layers) with shear stirrups highlighted.

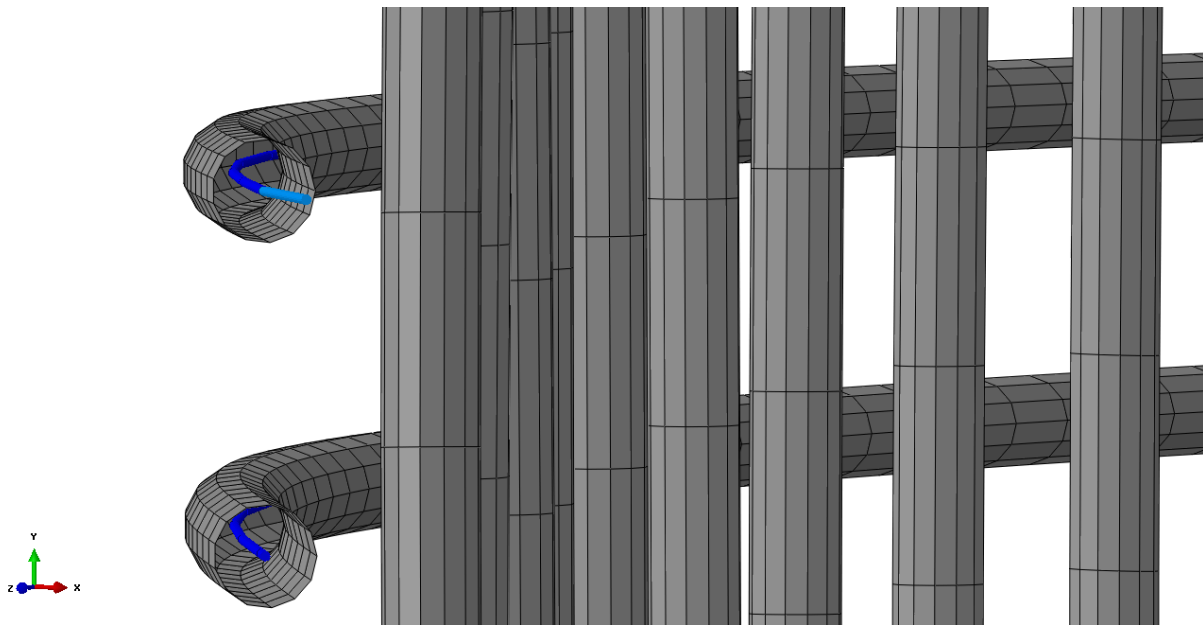


Figure D 57: Tendons inside duct

As with Model 1, the ends of the tendons have a ‘jacking element’ protruding out from the edge of the concrete mesh. For Model 2, the ‘jacking element’ was assigned only on one side of each tendon, the side closest to the buttress that the tendon is jacked from. The other end of each tendon was tied to the concrete face. Therefore, every other tendon on each face shows a jacking element, alternating with a tied element. This geometry set-up and methodology was very difficult to set up, and although there are some unavoidable edge effects which appear to influence the tendon stresses and strains of the end element, the tendon stress and strain distributions interior to these end elements appear to be very reasonable.

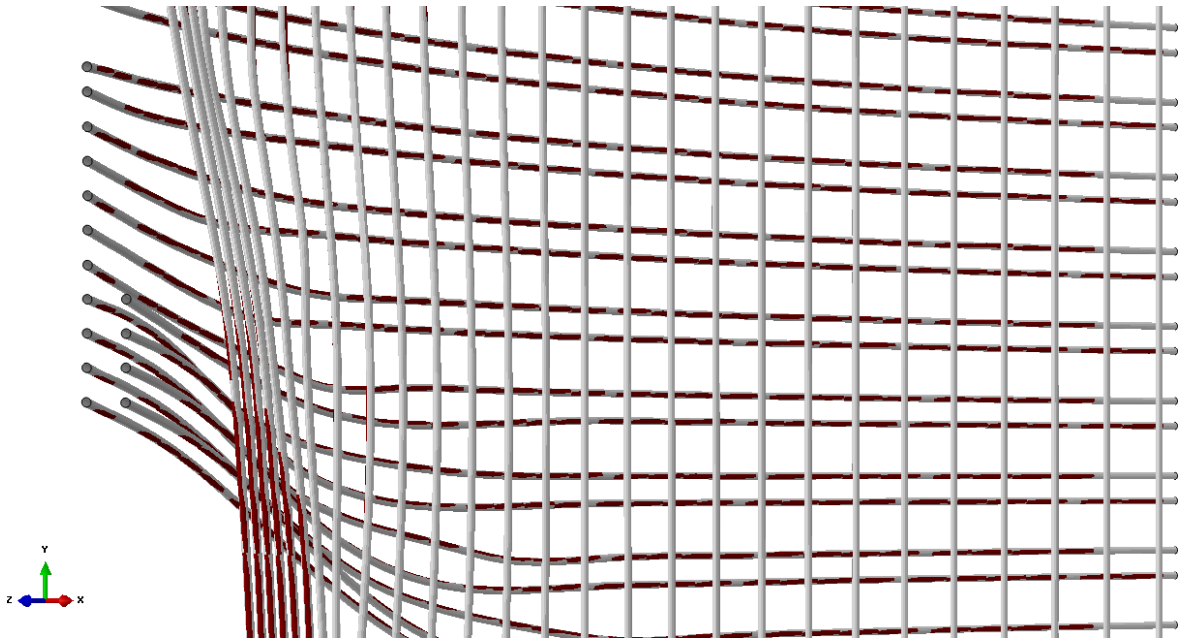


Figure D 58: Region of sheaths where tendons bear against the sheath shown in red

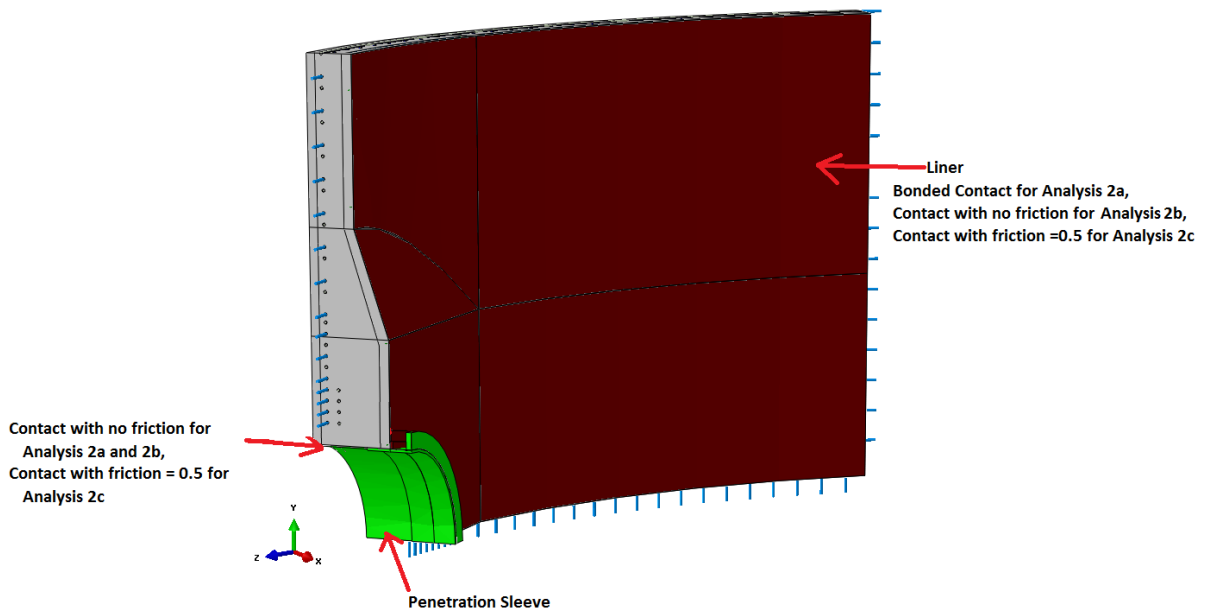


Figure D 59: Model overview

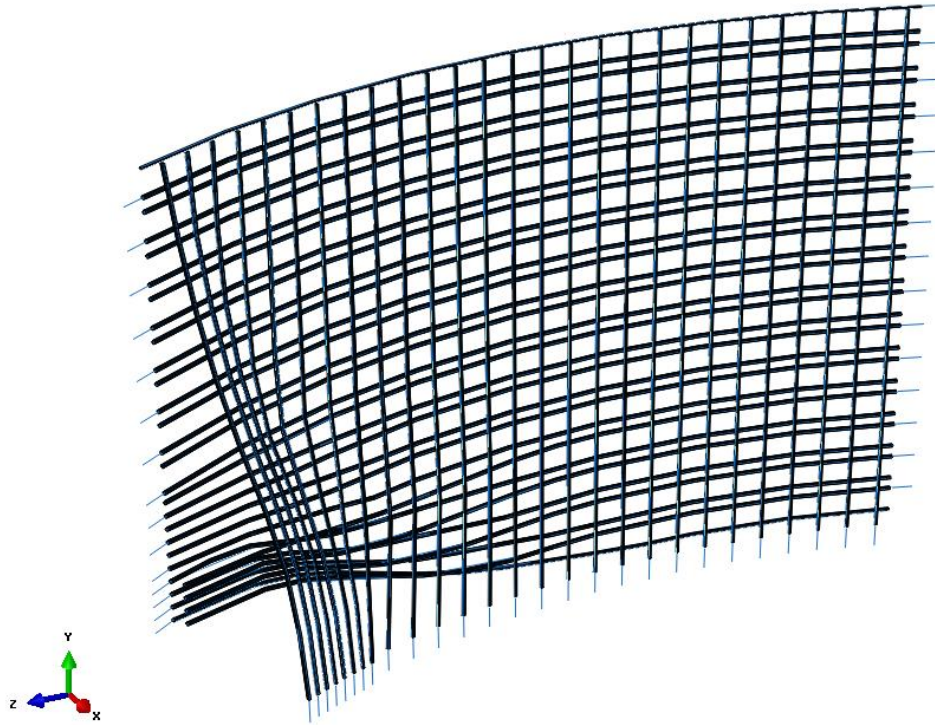


Figure D 60: Tendon sheaths with jacking elements shown

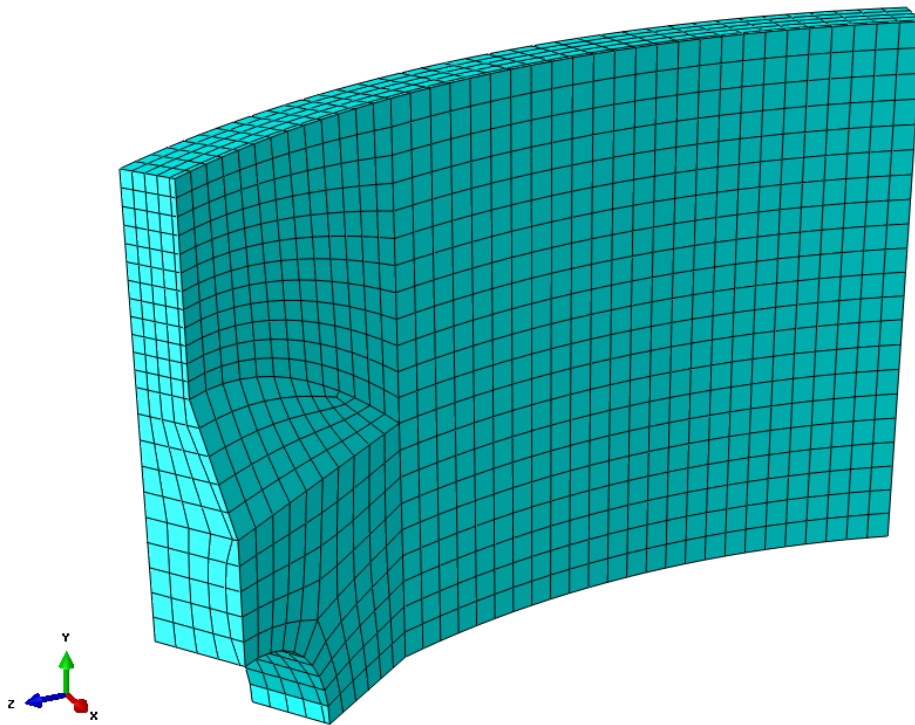


Figure D 61: Concrete mesh

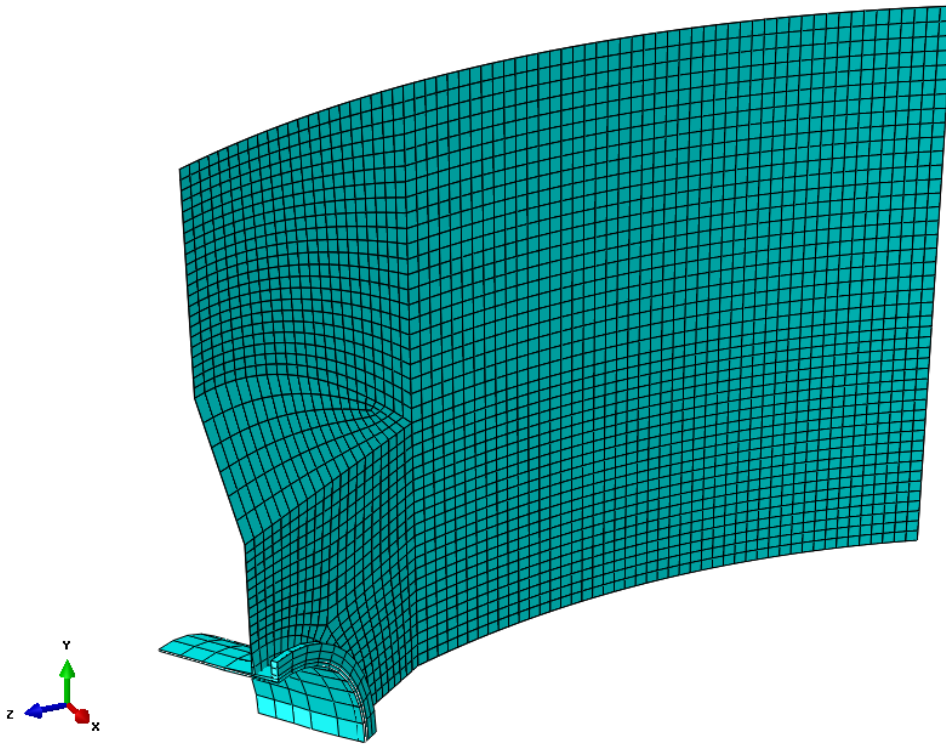


Figure D 62: Steel liner and penetration pipe mesh

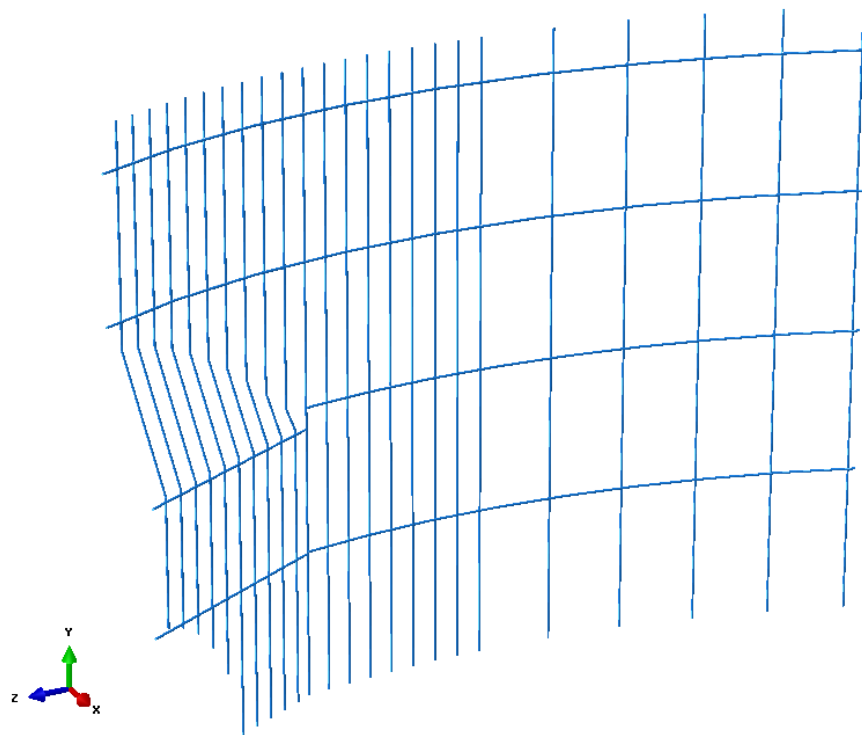


Figure D 63: Vertical and horizontal liner anchors

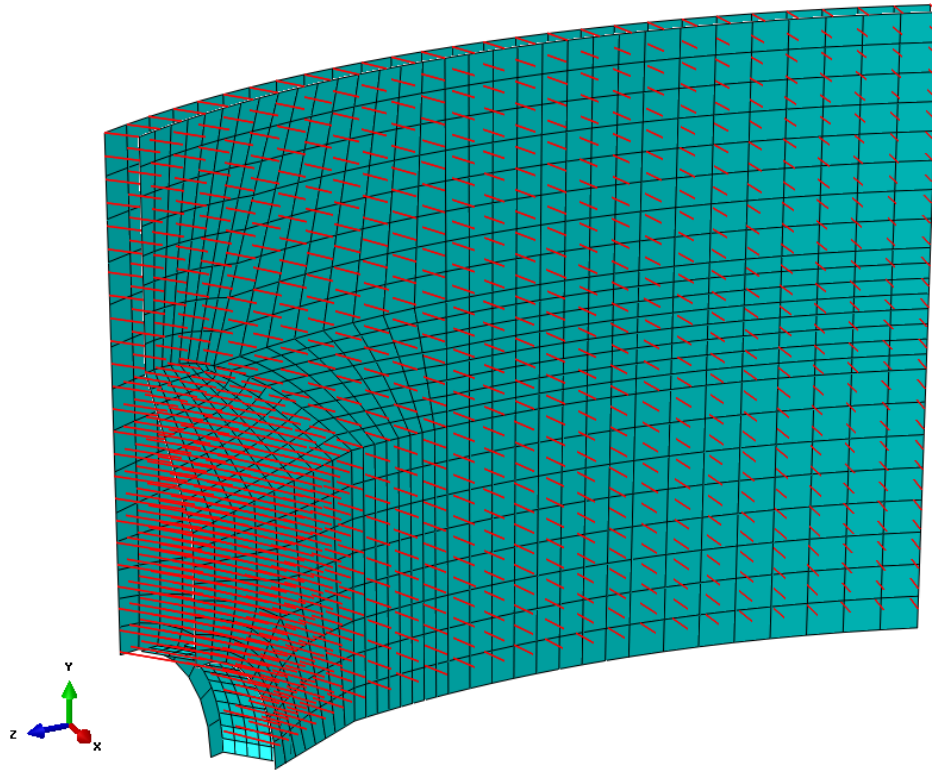


Figure D 64: Rebar subelemnts with stirrups highlighted

In the PCCV 1:4 scale model, several of the liner strain gages in the vicinity of the E/H showed elevated strains. Further, a number of tears were observed after the LST (as shown in Figure D 65). These strain gages (and possibly others), and the existence of tears #7, 8, 12, 13, 14, 15, and 18 are important to this SPE study model, and their locations are encompassed by it. The primary stress/strain concentration locations were observed to occur along two vertical lines: a) the juncture between the standard-thickness wall, and wall embossment (the thickened wall adjacent to the hatch), and b) along a vertical zone of material in the vicinity of 0-degree to 6-degree azimuth which corresponds to a “step-down” reduction in the steel area of the circumferential rebar (See Figure D 66). For this reason, it was important to represent the rebar areas in detail.

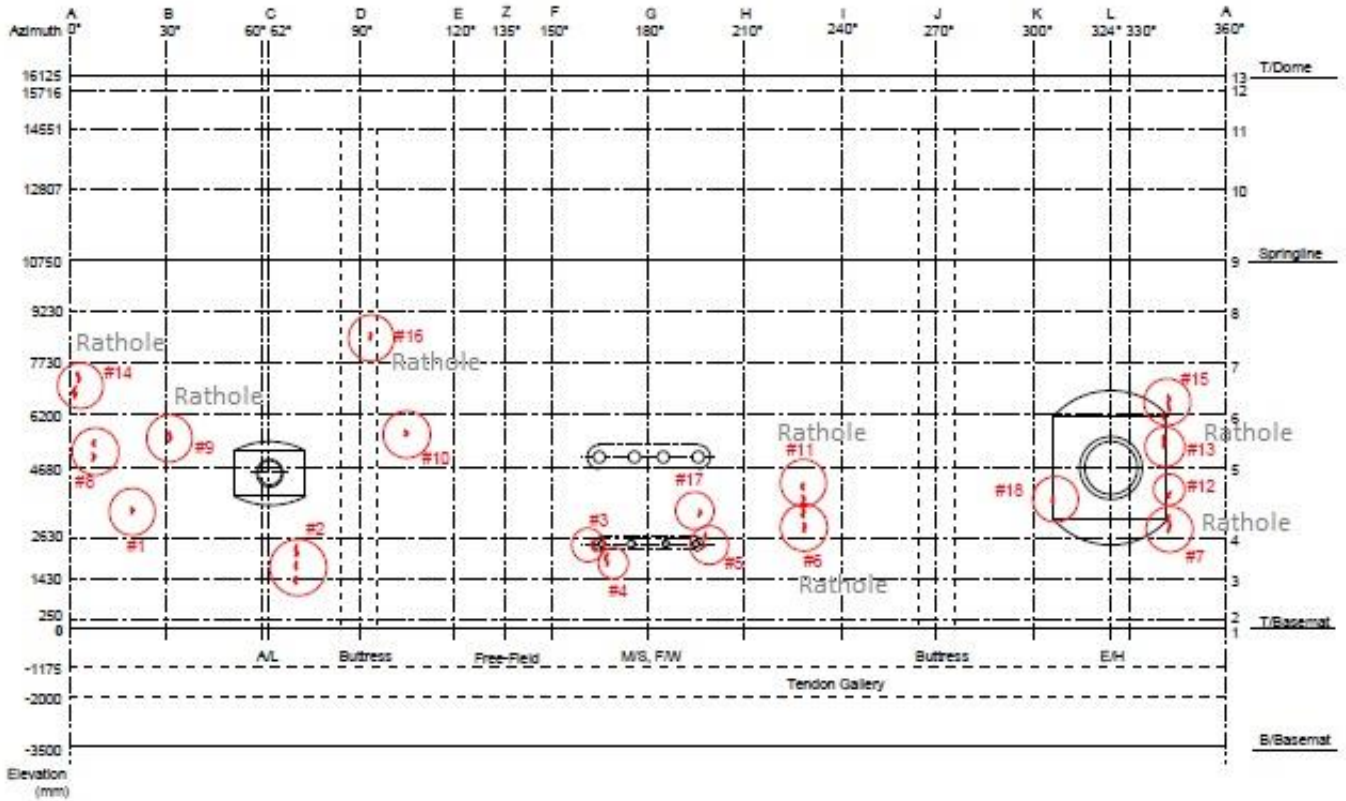


Figure D 65: Liner tear locations

Figure D 66 shows key locations for reporting the liner strain selected for the Model 2 Exercise. The objectives in choosing these locations are:

1. To choose a relatively long gage length over which to report strain in order to eliminate differences between analysts due to mesh size.
2. To focus on key aspects of liner-concrete interaction.
3. Establish a framework for a fracture-mechanics based liner failure prediction.

The locations are numbered 1 through 10, and the boundaries are defined by the liner anchors. This is logical, especially for the case where the liner slips freely between anchors because, for such a case, liner hoop strain will likely be nearly uniform between anchors. At the large anchor spacing, the gage length is, therefore, 450.45 mm. Analysts are requested to report 'averaged' circumferential strain values at Locations 1 through 10. Locations 1-4 and 6-9 have gage lengths of 450.45 mm, and Locations 5 and 10 straddle two anchor spaces, for a gage length equal to 300.30 mm.

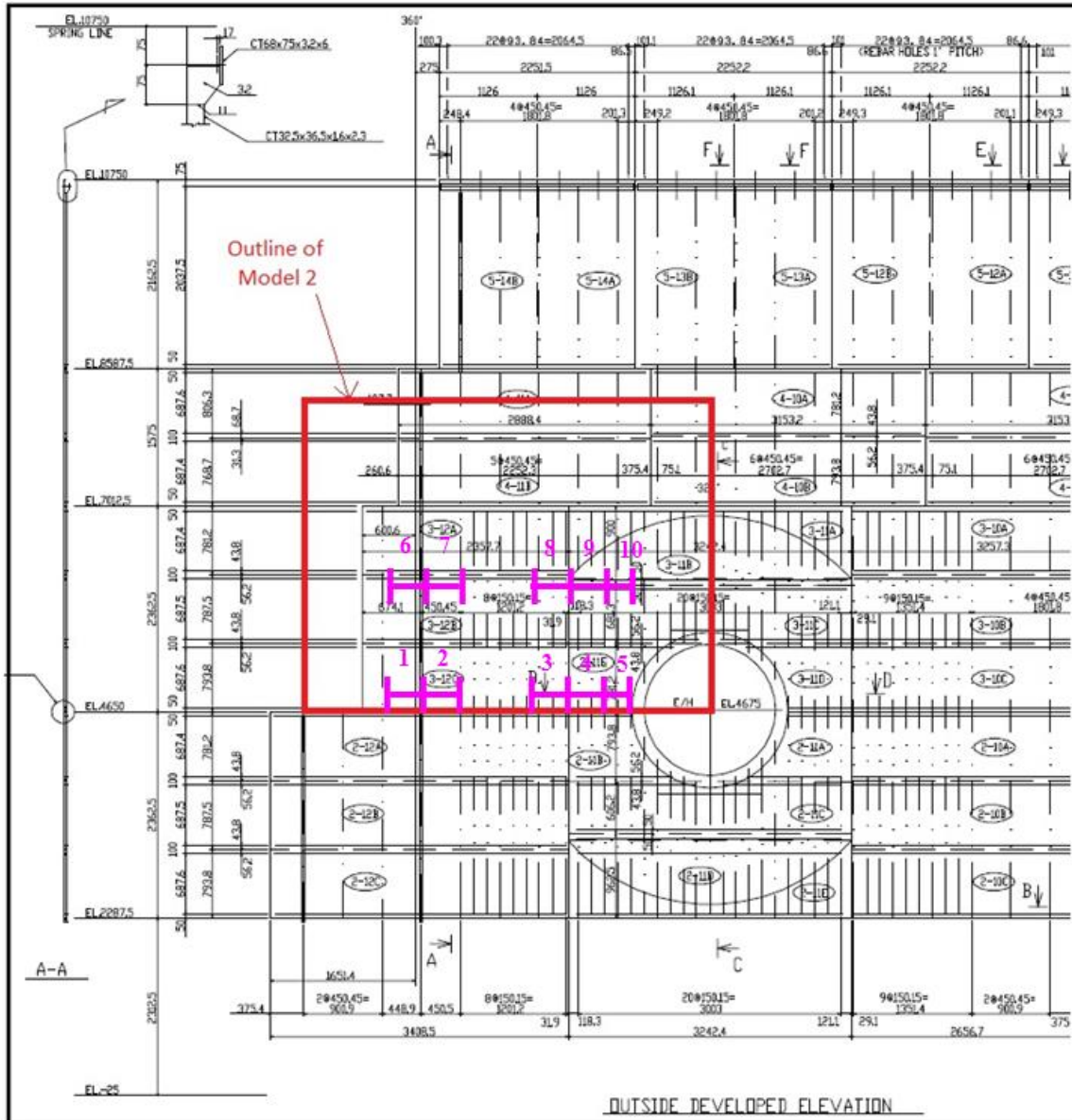


Figure D 66: Liner (E/H) View Showing Strain Reports (cut from Page A-28 of NUREG/CR-6810)

Meridional Stress vs. Internal Pressure

The relation between the meridional stress (σ_m) and the internal pressure (p) at level 6.579 m is given below (as developed by SPE Participant, Scanscot, but now modified because in Model 2, the vertical prestress is applied directly).

$$\sigma_m = \text{dead load, prestress, internal pressure} = 0.144 - p * 8.27 \text{ MPa}$$

p in Mpa, (+) compression, (-) tension.

Table D 4: Tendon Stress Distribution for Standard Tendon Behavior Analysis (Includes Seating Losses and Assumed Linearly Varying with Azimuth In-Between Points)

Azimuth	Force (Newton)
355	334,625
315	381,526
270	323,648
180	230,512
90	323,648
45	381,526
5	334,625
-5	334,292

A detailed calculation of tendon initial stress versus azimuth (including angular friction, wobble friction, and seating loss) was performed, with results shown in Figure D 67. This was the target stress distribution used in the Model 1 and Model 2 analysis.

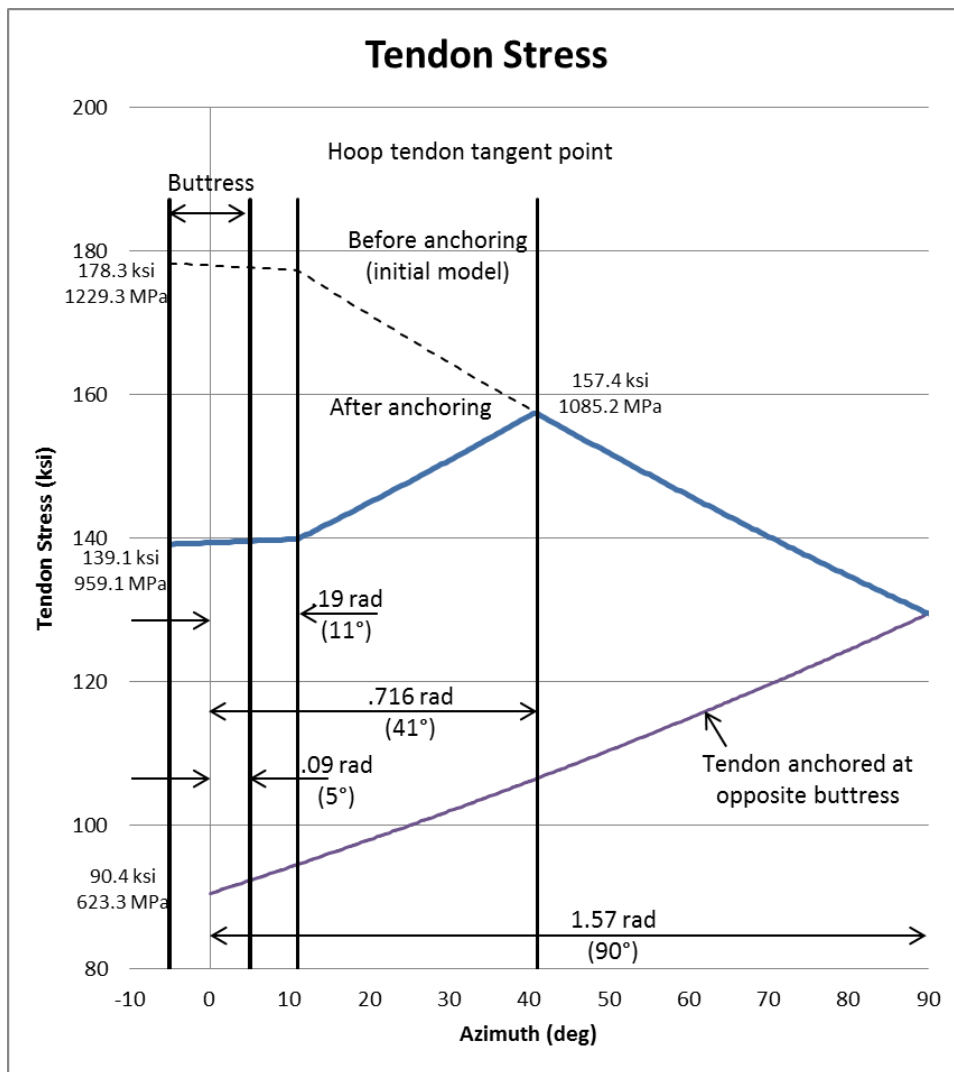


Figure D 67: Additional information about tendon friction and seating losses

Some tendons being jacked from 270° have additional losses as they sweep around the Equipment Hatch before reaching the region of Model 2. These tendons are assumed to have the same anchor stress after losses as the free-field hoop tendons. The paths of the tendons are used to determine the losses due to wobble and angular friction. Figure D 68 is an example of tendon H37; the same calculation was performed for all other tendons. For simplicity, the tendons being jacked from 90° are assumed to have negligible losses from the Personnel Airlock. A similar calculation was performed for the vertical tendons being jacked from the tendon gallery in the basemat. Table D 2 shows a summary of the tendons and their stress after losses.

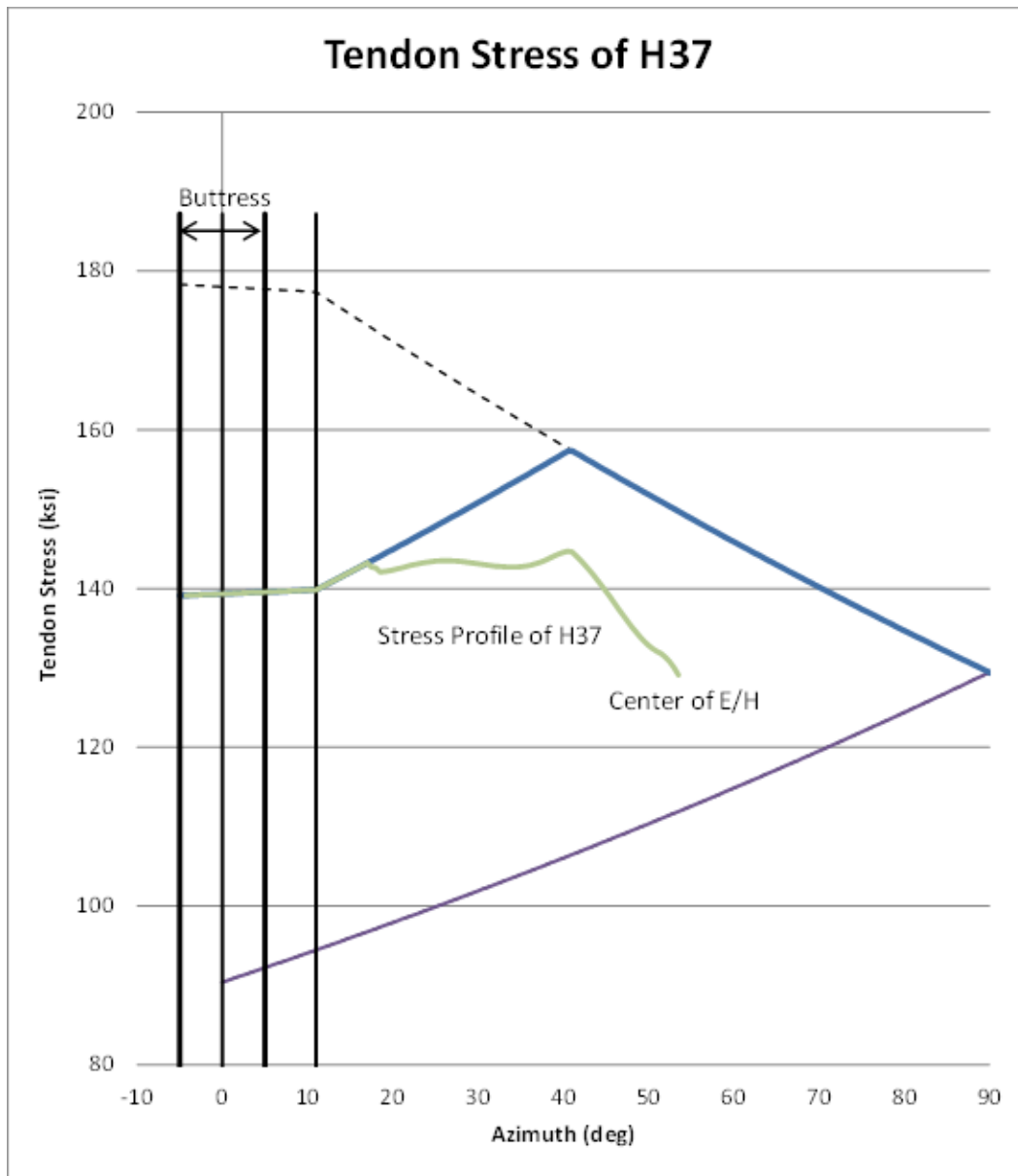


Figure D 68: Additional Information About Tendon Friction and Seating Losses

Table D 5: Tendon stress applied to jacking end of Model 2

Jacked from 270°		Jacked from 90°		Jacked from Basemat	
Tendon	Stress (MPa)	Tendon	Stress (MPa)	Tendon	Stress (MPa)
H37	890	H38	959	V59	1,130
H39	885	H40	959	V60	1,130
H41	873	H42	959	V61	1,130
H43	901	H44	959	V62	1,130
H45	962	H46	959	V63	1,130
H47	1,006	H48	959	V64	1,130
H49	1,015	H50	959	V65	1,130
H51	1,030	H52	959	V66	1,130
H53	1,030	H54	959	V67	1,130
H55	1,030	H56	959	V68	1,130
H57	1,030	H58	959	V69	1,130
H59	1,030	H60	959	V70	1,130
H61	1,030	H62	959	V71	1,130
H63	1,030	H64	959	V72	1,117
H65	1,030	H66	959	V73	1,102
				V74	1,090
				V75	1,076
				V76	1,065
				V77	1,054
				V78	1,057
				V79	968
				V80	978
				V81	968
				V82	968
				V83	948
				V84	950
				V85	943

For Model 2c, an estimate for the stiffness and strength of the liner anchors is needed to complete the desired simulation. Detailed local models for both the vertical and horizontal anchors were created to obtain force-versus-deflection curves. These values were then used to determine the stiffness of springs connecting the steel liner to the anchors. The local models and their results are shown in Figure D 69 through 74.

The length of the local models (in the direction of loading) was determined by the average spacing of the vertical anchors, which is approximately 5.9". The depth of the concrete was set to about 2-times the depth of the anchors (a little over 2-inches), approximately down to the first layer of reinforcement. This location provided a good point of fixity for the local model. The out-of-page thickness of the model was 1-inch. The geometry and deformed shape of the models can be seen in Figure D 69 and 70. Symmetry boundaries were used on the longitudinal faces of the concrete and the steel liner was allowed to translate. For the vertical anchor model, an additional boundary condition was applied to make the liner ends have the same displacement, to simulate the deformations caused by the neighboring anchor. The horizontal anchor model ignored this boundary due to the large spacing between anchors. The bottom and side faces were completely fixed. The contact, as well as separation, between the anchor/liner and concrete was explicitly modeled. For the anchor to concrete interaction, a friction coefficient of 0.5 was used. The friction between the liner and concrete was ignored due to the fact that we are not concerned with the force transfer between the two in these local models. As the liner was pulled, the anchor bore against and started crushing one side of the concrete while lifting off the other side.

At the end of each analysis, the strains in the liner, anchor, and concrete are plotted in Figure D 75 through 76. These show the liner has fully yielded at the anchor and the concrete is crushing. Figure D 75 and 76 show the force/deflection curves of the liner anchors per inch of anchor. The deflection was measured as the difference in displacement between the point where the anchor meets the liner and the centroid of the anchor, which is where they are located in the global model as beam elements. This data was converted to a bilinear curve to be used in the global model. Since this data was per inch of anchor, the spacing of the springs connecting the liner to the anchor beams needed to be determined to find their influence region. This came out to an average of about 2". The results of the local models were only applied in the direction perpendicular to the direction of the anchor. For the springs in the other directions, very stiff springs, the same as in model 2b, were used.

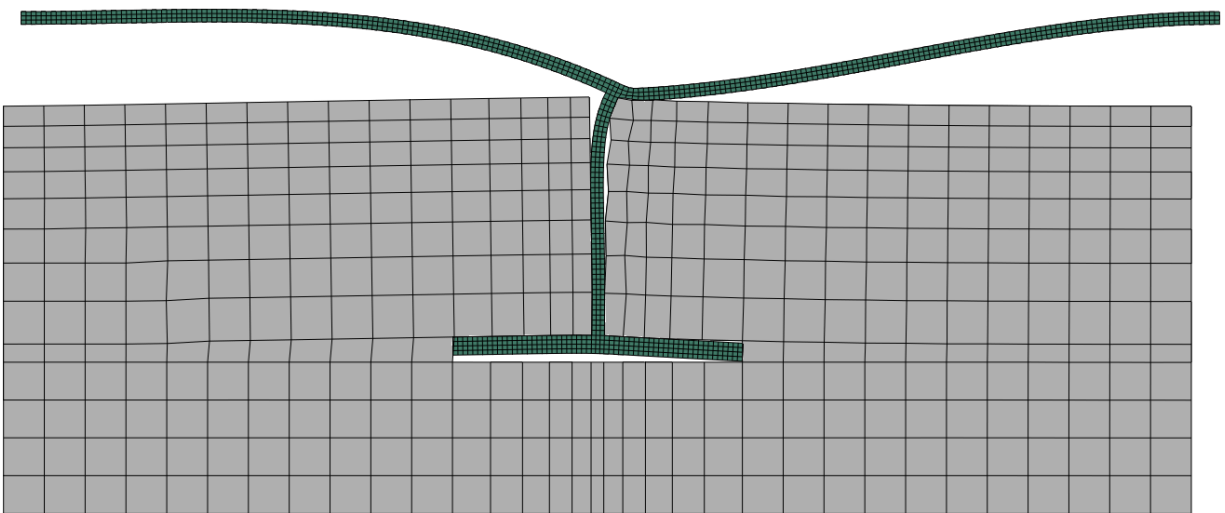


Figure D 69: Vertical Liner Anchor Local Model at 10x deformed shape

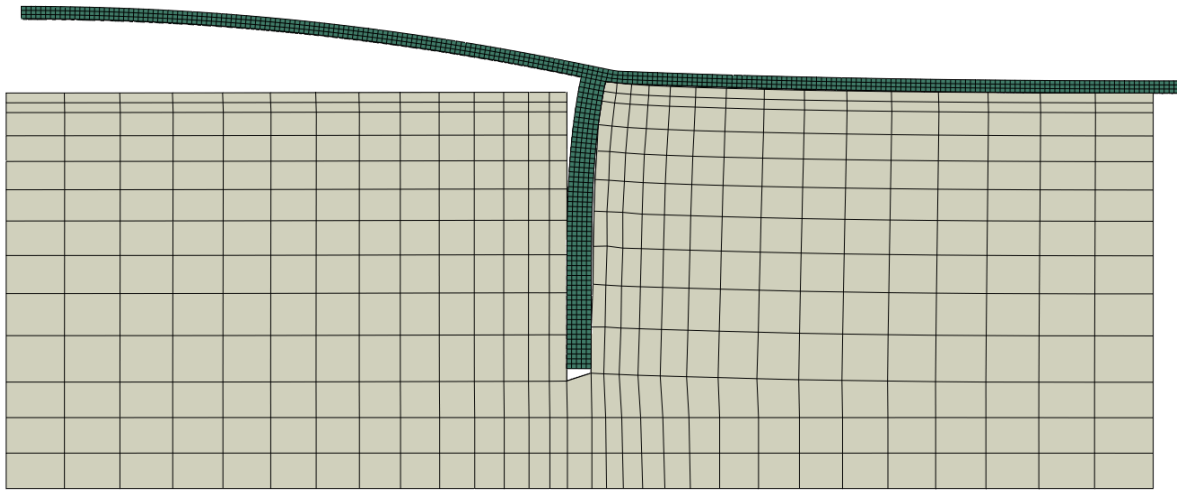


Figure D 70: Horizontal liner anchor local model at 10x deformed shape

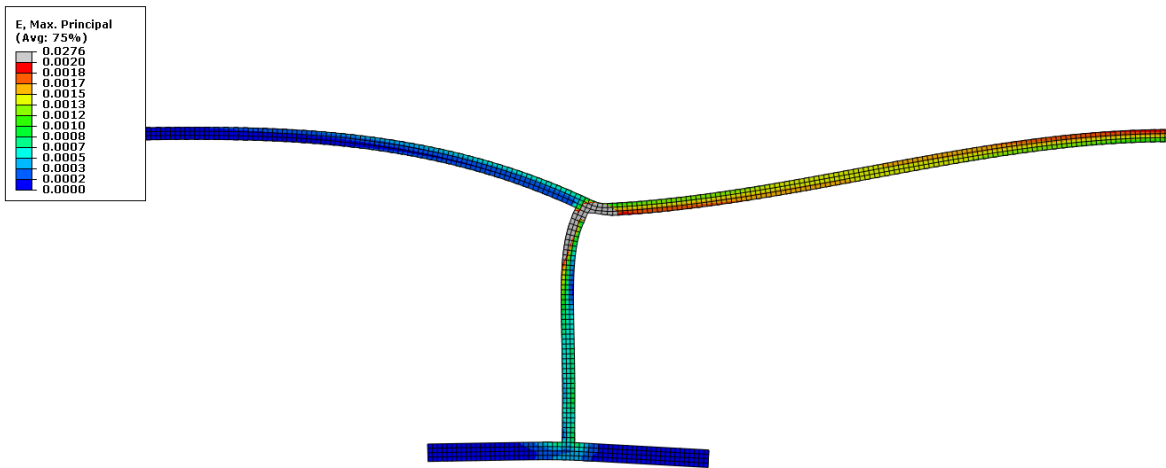


Figure D 71: Max principal strain in liner and vertical anchor

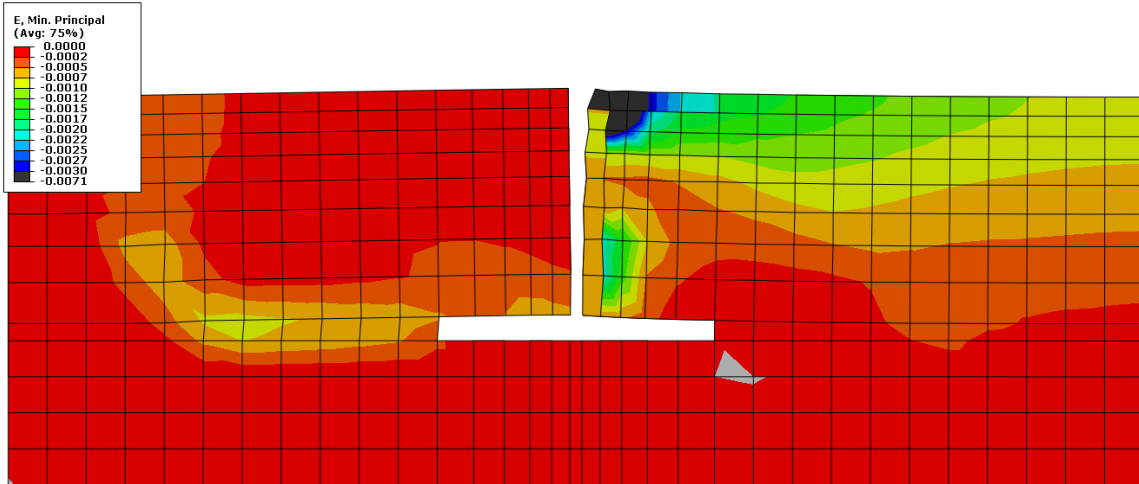


Figure D 72: Minimum principal strain in liner and vertical anchor

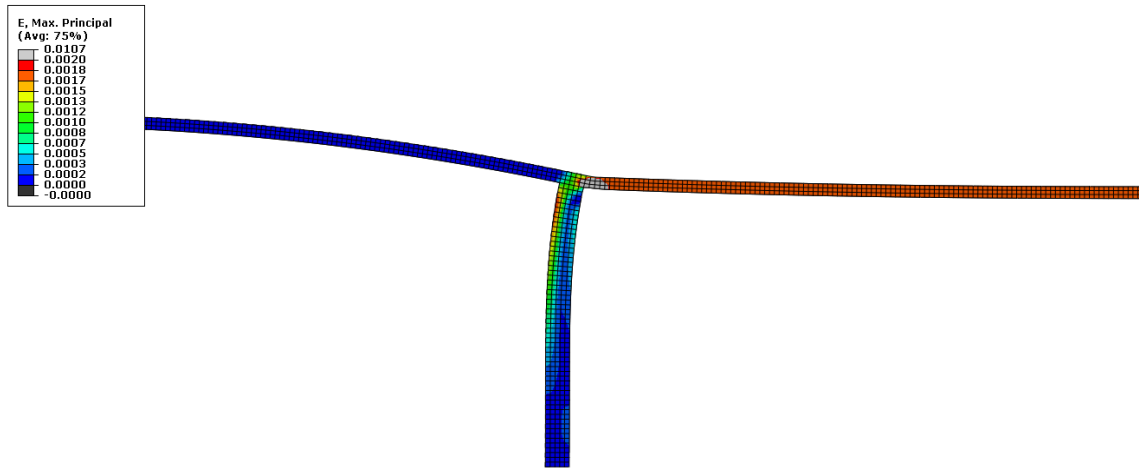


Figure D 73: Max principal strain in liner and horizontal anchor

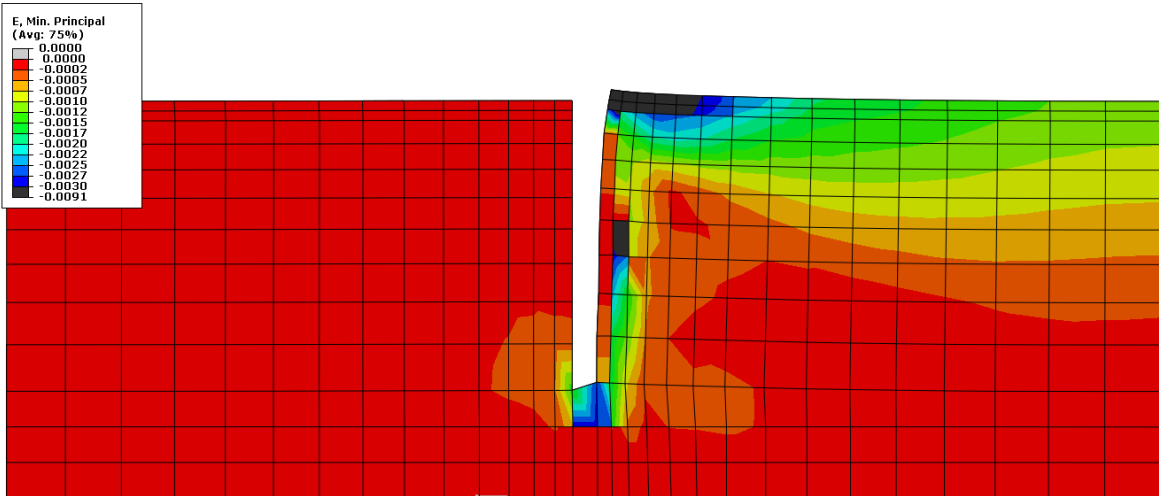


Figure D 74: Minimum principal strain in liner and vertical anchor

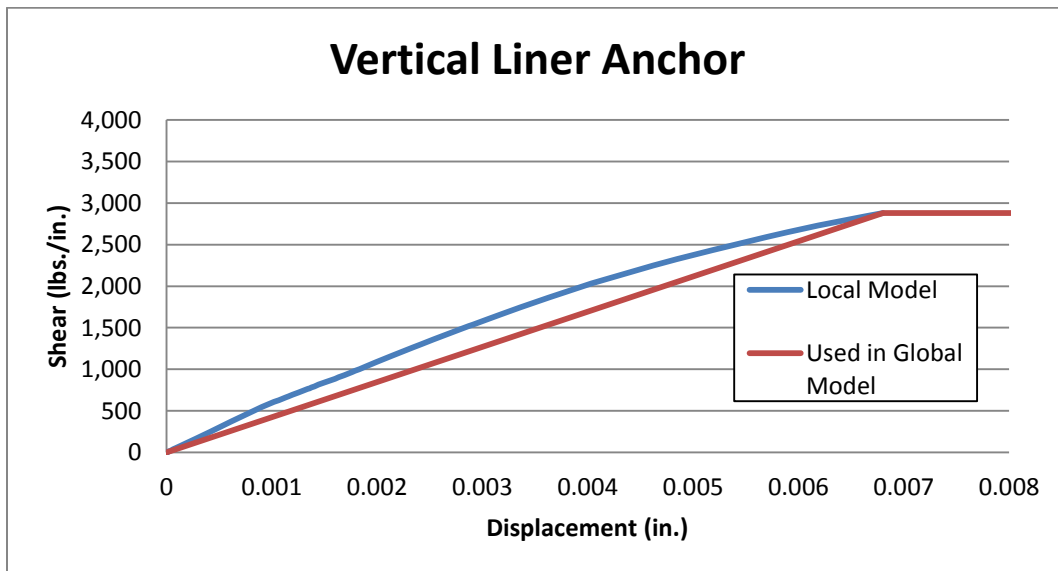


Figure D 75: Force deflection curve for vertical liner anchor

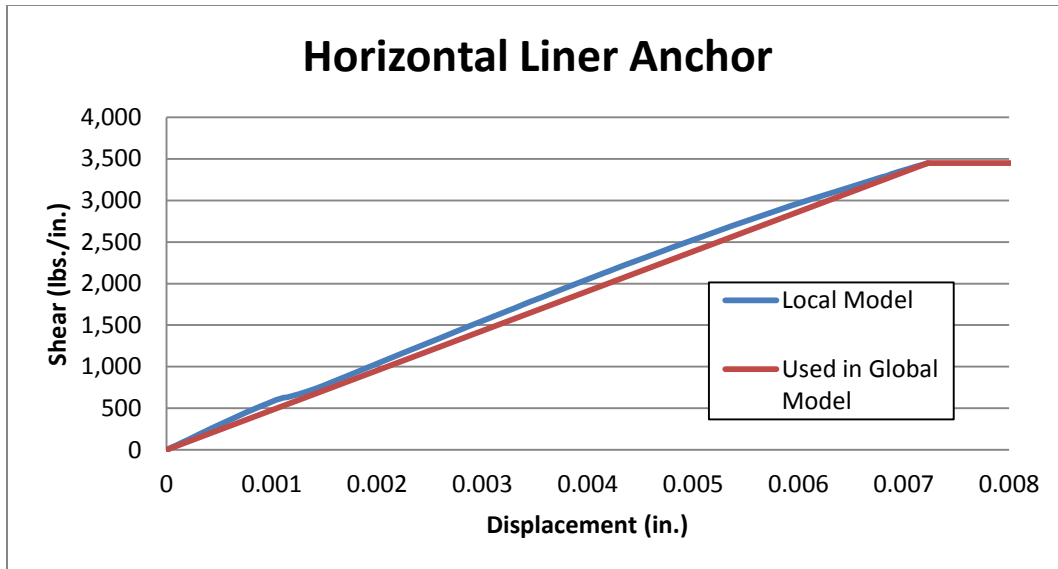


Figure D 76: Force deflection curve for horizontal liner anchor

Material modeling

Tendon, rebar, and concrete material stress-strain assumptions were implemented which follow the stress-strain curves tabulated in Appendix 1 of NUREG/CR-6810. Concrete was simulated using the ABAQUS concrete “Damaged Plasticity” constitutive model. This model utilizes a smeared-cracking formulation in tension (where cracking occurs at the element integration points), and a compressive plasticity theory. Steel elements were simulated using ABAQUS Standard Plasticity. The stress-strain inputs to these models consist of effective stress (Mises) and effective strain. The inputs are taken directly from the SPE Appendices, and are shown in our Model 1 report, so are not repeated here.

Failure Criteria

The relevant failure criteria for Model 1 was Tendon failure. The rebar generally has higher ductility than the tendons, so it is not the controlling criteria. Model 1 was not focused on liner tear / leakage. For Model 2, Tendon Failure criteria remains at 3.8% strain as for Model 1. But Model 2 is also focused on liner tear and leakage.

The steel material model used is an incremental plasticity model, i.e., an "incremental" theory where the mechanical strain rate is decomposed into elastic and a plastic (inelastic) parts. A key characteristic in this formulation is the yield surface, which is used to determine if the material responds purely elastically at a particular state of stress. We are using the Mises yield surface to define isotropic yielding. This is appropriate for all but the most extreme scenarios, e.g., sheet metal forming or welding, where the Hill yield surface (anisotropic yielding) or a porous metal plasticity model may be more appropriate.

Another important term is the flow rule, which in our case is associated plastic flow. Therefore, as yielding occurs, the inelastic deformation rate is in the direction of the normal to the yield surface (plastic deformation is volume invariant). The third aspect is the evolution law that defines how the yield and/or flow definitions change during inelastic deformation. We are using an isotropic hardening law, i.e., the yield surface changes size uniformly in all directions as

plastic straining occurs. A Stress vs. Strain curve is input to the program, but how it is implemented is not Uniaxial Stress vs. Uniaxial Strain, rather it is Effective (Von Mises) Stress versus Effective Plastic Strain. The Yield Surface grows (or contracts) as a function of the Effective Plastic Strain, and can shift the relationships of principal stresses and thereby influencing strain distribution after yielding occurs.

But it is important to note that even with sophisticated plasticity models, failure is typically predicted externally by the analyst, applying a strain failure criteria which takes into account the triaxiality of the stress state. We do this using the Davis Triaxiality Factor defined by the formulas shown below, and which have been the failure criteria of choice in nuclear containment analyses for many years.

Biaxial –stress based failure criteria

$$\mu = 2^{(1 - TF)}$$

Where μ is the ductility (reduction) ratio and TF is the Davis Triaxiality factor,

$$TF = \frac{\sqrt{2} (\sigma_1 + \sigma_2 + \sigma_3)}{\left[(\sigma_1 - \sigma_2)^2 + (\sigma_2 - \sigma_3)^2 + (\sigma_3 - \sigma_1)^2 \right]^{1/2}}$$

But when the third principal stress is zero or nearly zero, as in the case of TBT shell plates,

$$TF = \frac{(\sigma_1 + \sigma_2)}{(\sigma_1^2 - \sigma_1\sigma_2 + \sigma_2^2)^{1/2}}$$

For instance when $\sigma_1 = \sigma_2$, $TF = 2$ and the ductility ratio is 0.5; i.e., failure strain reduces to half its uniaxial value. For the last two decades, many containment analysts have used this criteria for predicting onset of liner tearing, but most have concluded that there is also extensive judgment involved in its application. Strains predicted by FE models can be highly dependent on the level of detail (and mesh refinement) included in the model. And, as was seen in the 1:4 Scale PCCV Model, the existence of flaws in the material (especially at weld seams) mean that tears might occur at strains significantly lower than the absolute ductility of the material. Time and budget permitting, we will try to be addressing these issues in the interpretation and conclusions of the current work.

Analysis results

To further the state-of-knowledge on the subject of liner-concrete slippage, Model 2 was analyzed with three sets of liner-concrete interaction assumptions (the third was optional):

- 2a. Liner Assumed Bonded (No-Slip) to Concrete
- 2b. Liner Only Connected to Concrete at Anchors, Free-Slip in Between
- 2c. Best Estimate Connection and Consideration of Friction

Required Outputs/Results for Model 2:

2.1 Description of Modeling Assumptions and Phenomenological Models

2.2 Description of Liner Failure Criteria Used

2.3 Pressure Milestones. Applied Pressure When:

2.3.1 Concrete Hoop Cracking Occurs, and Report Where

2.3.2 First Tendon Reaches 1% Strain, and Report Where

2.4 Deformed Shape and Liner Strain Distribution at $P = 0$ (prestress applied); $1 \times P_d$; $1.5 P_d$; $2 P_d$; $2.5 P_d$; $3 P_d$; $3.3 P_d$; $3.4 P_d$; Ultimate Pressure

2.5 Liner Strain Magnitudes (Hoop Direction) at Locations Indicated in Figure D 66

2.6 Ovalization: Plot Change in Diameter of Hatch and Adjacent Concrete, in Hoop Direction, Versus Pressure

2.7 Ovalization: Plot Change in Diameter of Hatch and Adjacent Concrete, in Meridional Direction, Versus Pressure

Deformed Shapes at pressure milestones of Prestress only, and Prestress plus Design Pressure are shown in Figure D 77 and 78. The deformed shapes for Analyses 2a, 2b, and 2c are nearly identical, so the 2b and 2c versions are not shown. In all three Analyses, the analyses could not be advanced further than $3.47xP_d$. Various analysis restart attempts were made, using modified convergence parameters, to no avail. Since this is well beyond the pressure reached in the LST ($3.25xP_d$), and nearly the pressure reached in the SFMT ($3.56xP_d$), we will accept this outcome and learn as much as we can from the results. The results of some pressure milestones are shown in Table D 3.

Table D 6: Results by pressure milestones

Milestone	Pressure (MPa)	$x P_d$
Zero Concrete Hoop Stress (at 0° azimuth)	0.534	1.36
Concrete Hoop Cracking Occurs (at 0° azimuth)	0.585	1.49
Tendon A and B Reach approx.1% Strain (at 0° azimuth)	1.362	3.47

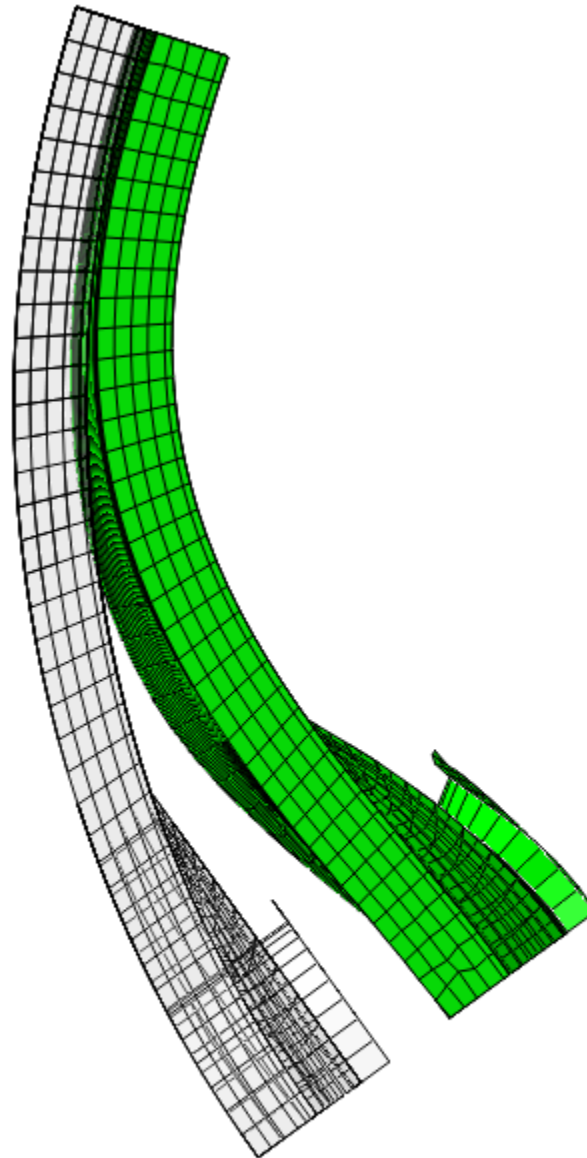
Minimum Principal Stress (in concrete) at Prestress is shown in Figure D 79, and Max Principal Stress is shown in Figure D 80. The minimum principal stresses are interesting because they show the distribution of pre-compression that occurs in the concrete. As expected by the vessel designers, the precompression is fairly uniform away from the E/H penetration, but not very uniform near and around the hatch. In fact the inner concrete surface near the hatch receives only a relatively low level of prestress (less than 270 psi compression).

Figure D 81 through 90 show stresses in tendons for the pressure milestones – Prestress, 1.0, 1.5, 2.0, 2.5, 3.0, 3.3, 3.4, and $3.47xP_d$. Figure D 92 through 107 includes stress and strain. The strain distribution shows a significant band of elevated strain occurring in the model in the vicinity of the 0-degree to 6-degree azimuth, which was the azimuth where ultimate failure occurred in the SFMT of the 1:4 Scale Model. There are also high strains observed at the end

elements (especially at the element immediately adjacent to the jacking elements described earlier); these are judged to be unavoidable artifacts of the boundary conditions of the model.

Figure D 92 through 107 show maximum principal strains in the liner at applied pressures of Prestress, 1.0, 1.5, 2.0, 2.5, 3.0, 3.3, 3.4, and 3.47xPd. In all cases, there is a boundary-effect at the far right edge of the model that we believe is an unavoidable artifact of working with a sub-model of the full structure. But just a few elements in from the edges, we believe provide reliable solution information. The yield strain for the liner is 0.0018. Pockets of yielding begin to occur at 2.5xPd, and become widespread by 3.0xPd. The first yielding occurs in a small area adjacent to the liner thickness transition near the hatch, and in larger areas between 0-degrees and 18-degrees azimuth. Note that near 0-degrees is where a transition occurs in the hoop rebar area density. Beginning at 3.0xPd, some of these areas are reaching strains of 0.004 to 0.005. These elevated strain zones are somewhat more prevalent in Model 2b and 2c than in Model 2a. By 3.3xPd, many of the elevated liner strain zones are reaching 0.01, and by 3.47xPd, 0.014 to 0.017, or nearly 2% strain. These trends agree reasonably well with observed behaviors from the 1:4 Scale Model Test. It should be noted that we have chosen a mesh-size of 2"-3" for modeling the liner, and with this mesh-size, we would not anticipate predicting as large of localized liner strains as may occur at an individual strain gage. But later in this Tech Memo, we show how by extracting strains and displacements between liner anchors (as shown in Figure D 66) for further submodel evaluation (using fracture mechanics theory or strain-based failure criteria) which will predict higher (much more localized) strains near liner discontinuities.

The final topic addressed in the results is ovalization of the penetration sleeve, and the resulting separation between pipe and concrete. On this subject, we found differences in diameters (both horizontal and vertical) between the pipe and concrete are not uniform through the thickness, thus the SPE specification for plotting change in diameter may need further clarification. To provide more insight about this, we have plotted the separation gap between the penetration surface and the concrete surface in Figure D 108 through 131. These plots show no significant separation until approximately 2.5xPd, but then separations of 0.03 inch, 0.08 inch, 0.12 inch, 0.14 inch, and 0.16 inch for 2.5xPd, 3.0xPd, 3.3xPd, 3.4xPd, and 3.47xPd, respectively. In all cases, Model 2a showed slightly more separation than Model 2b and 2c, and the maximum separation occurs at approximately the 2 o'clock position of the E/H penetration.



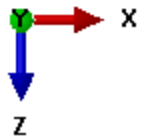
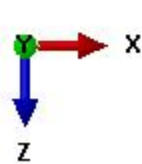
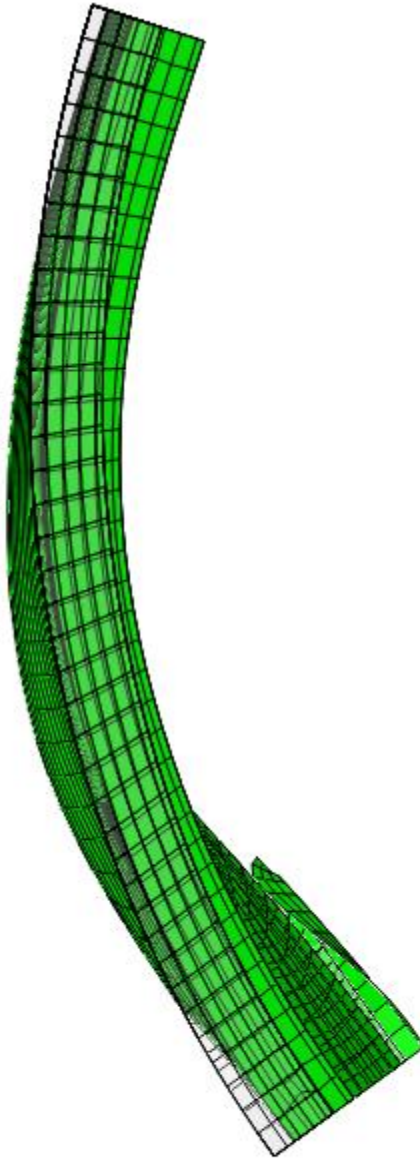
 Step: Temp Adjustment 2, Temperature Applied to Tendons 2
Increment 14: Step Time = 1.000
Deformed Var: U Deformation Scale Factor: +5.00e+02

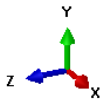
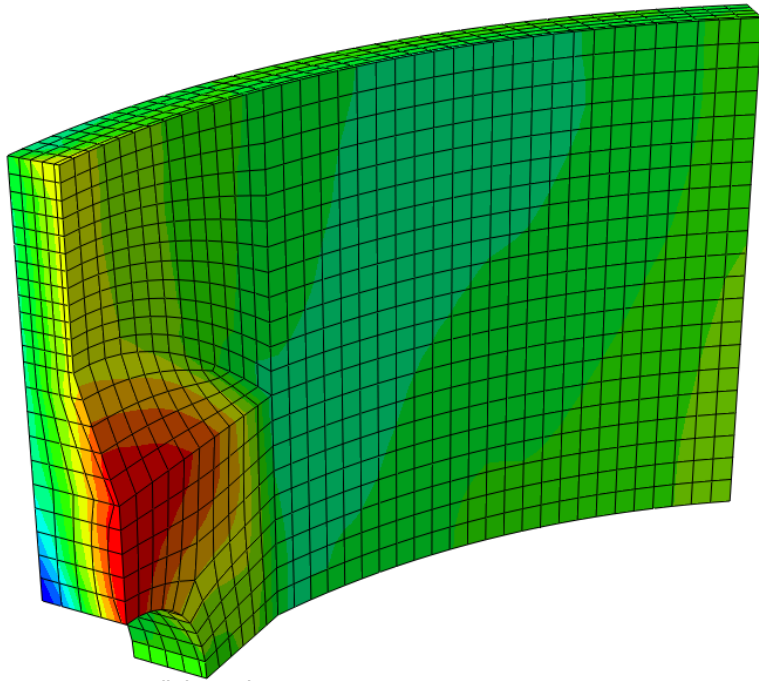
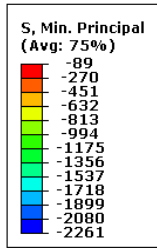
Figure D 77: Top View of Deformed Shape with Prestress Only (disp. x 500)



Step: Pressure, Pressure
Increment 8: Step Time = 0.2463

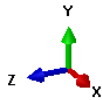
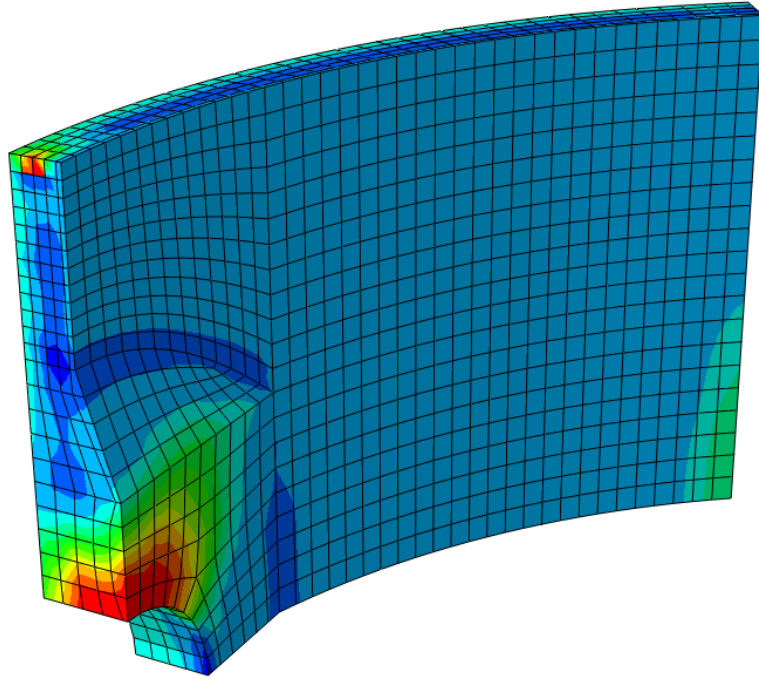
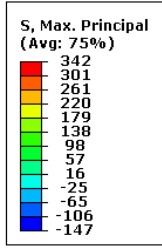
Deformed Var: U Deformation Scale Factor: +5.00e+02

Figure D 78: Top View of Deformed Shape Under Design Pressure, Pd (disp. x 500)



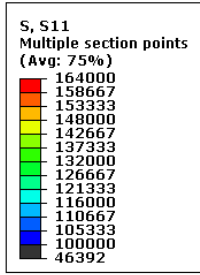
Step: Temp Adjustment 2, Temperature Applied to Tendons 2
 Increment 14: Step Time = 1.000
 Primary Var: S, Min. Principal
 Deformed Var: U Deformation Scale Factor: +1e+00

Figure D 79: Min Principal Stress (psi) in Concrete Under Prestress Only



Step: Pressure, Pressure
 Increment 8: Step Time = 0.2463
 Primary Var: S, Max. Principal
 Deformed Var: U Deformation Scale Factor: +1e+00

Figure D 80: Max Principal Stress (psi) in Concrete Under Pd



Step: Temp Adjustment 2, Temperature Applied to Tendons 2
 Increment 14: Step Time = 1.000
 Primary Var: S, S11
 Deformed Var: U Deformation Scale Factor: +1e+00

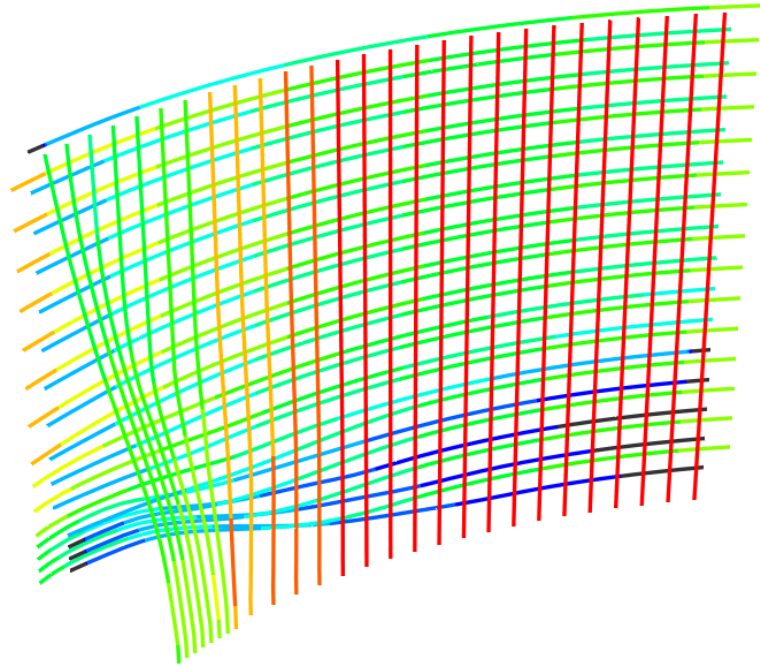
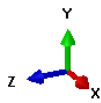
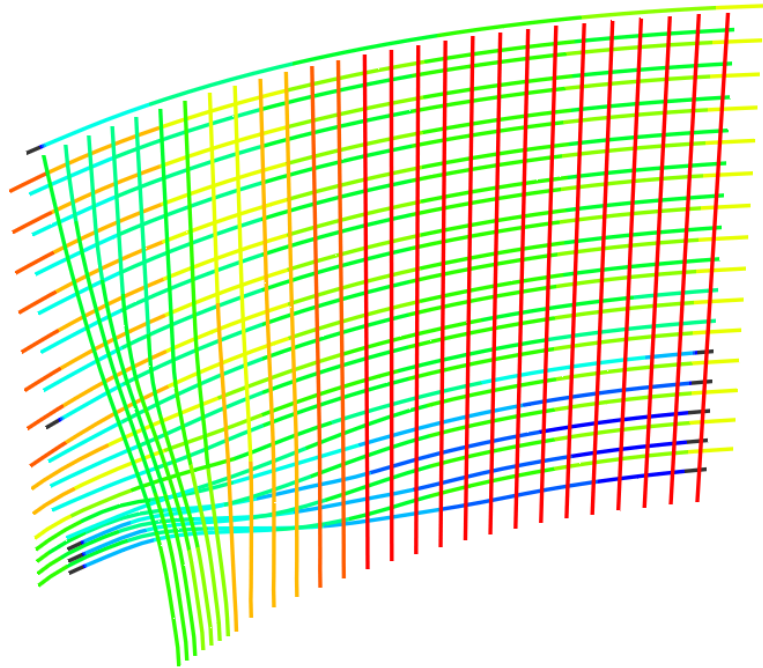
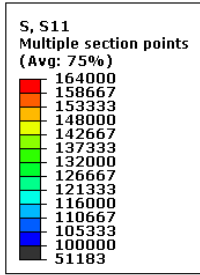
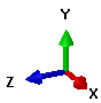
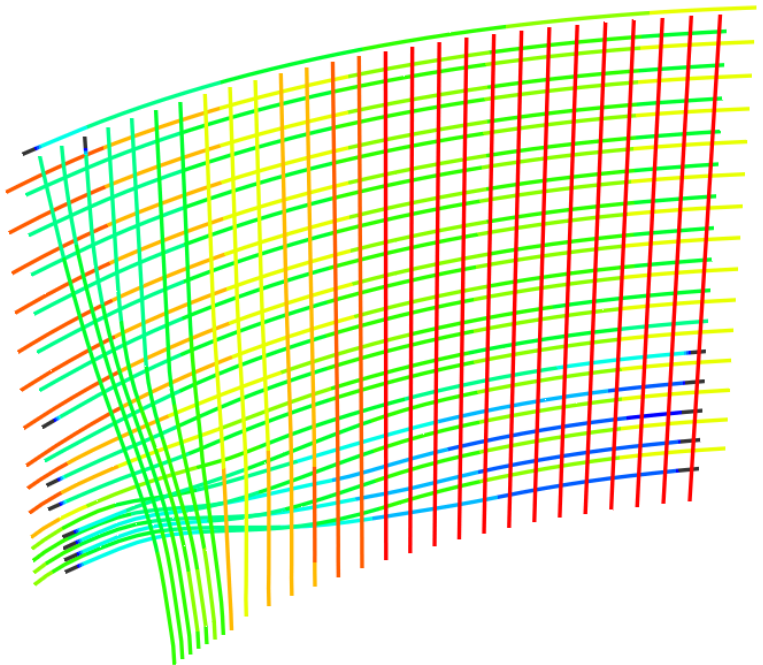
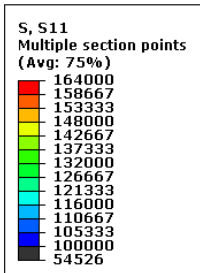


Figure D 81: Tendon Stresses (psi) After Prestress Only



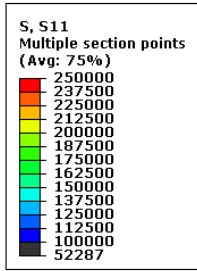
Step: Pressure, Pressure
Increment 8: Step Time = 0.2463
Primary Var: S, S11
Deformed Var: U Deformation Scale Factor: +1e+00

Figure D 82: Tendon Stresses (psi) with 1.0 x Pd



Step: Pressure, Pressure
Increment 14: Step Time = 0.3718
Primary Var: S, S11
Deformed Var: U Deformation Scale Factor: +1e+00

Figure D 83: Tendon Stresses (psi) with 1.5 x Pd



Step: Pressure, Pressure
Increment 65: Step Time = 0.5000
Primary Var: S, S11
Deformed Var: U Deformation Scale Factor: +1e+00

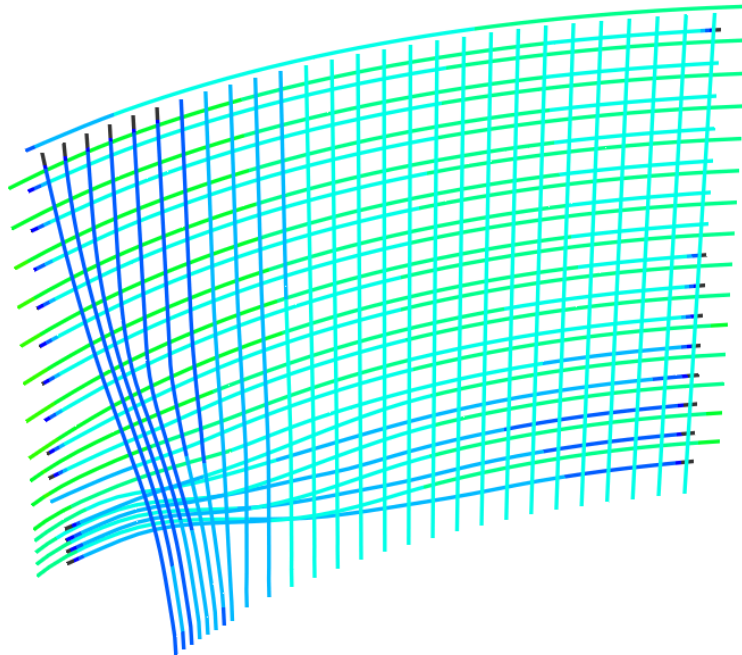
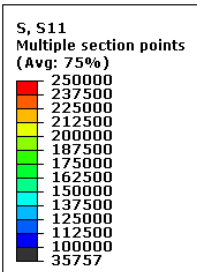


Figure D 84: Tendon Stresses (psi) with 2 x Pd (Note Different Contour Limits)



Step: Pressure, Pressure
Increment 110: Step Time = 0.6241
Primary Var: S, S11
Deformed Var: U Deformation Scale Factor: +1e+00

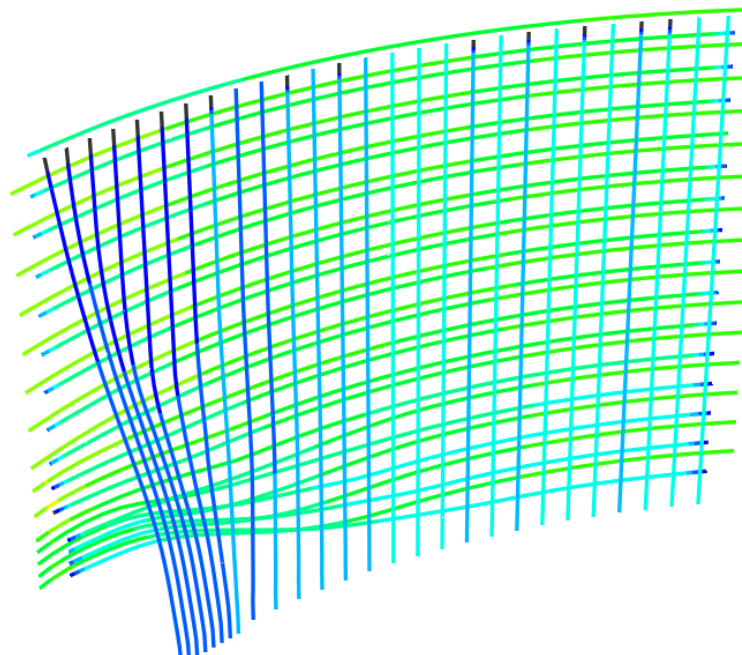
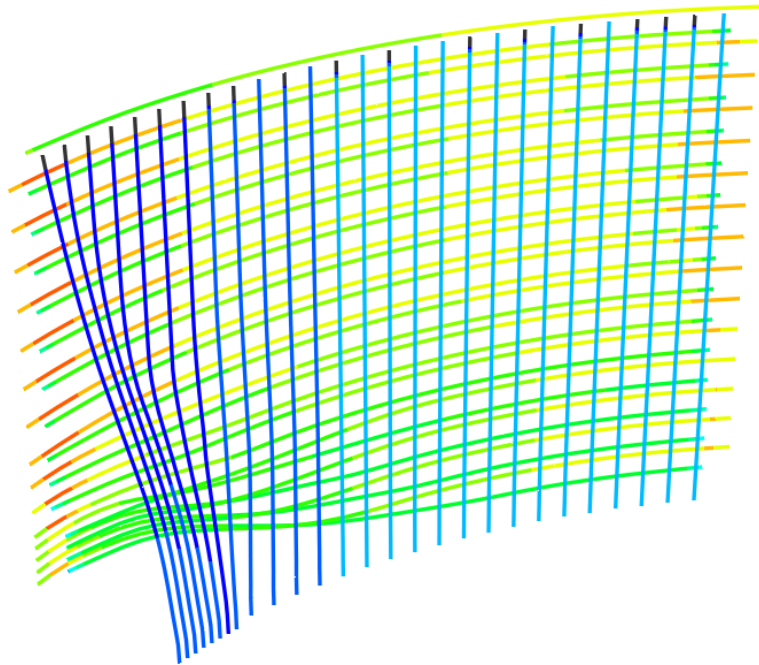
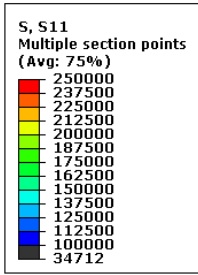
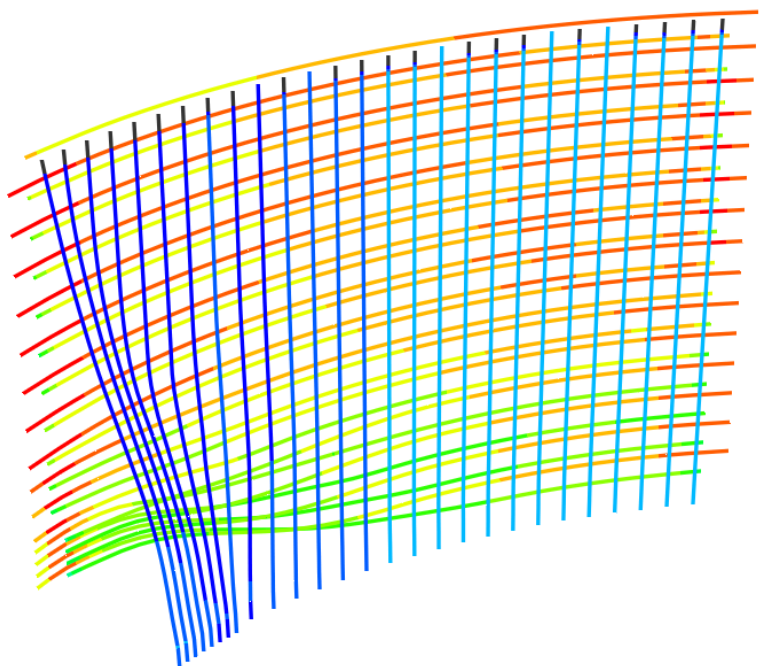
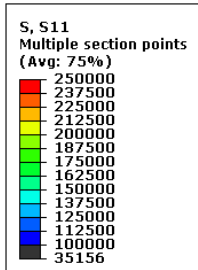


Figure D 85: Tendon Stresses (psi) with 2.5 x Pd



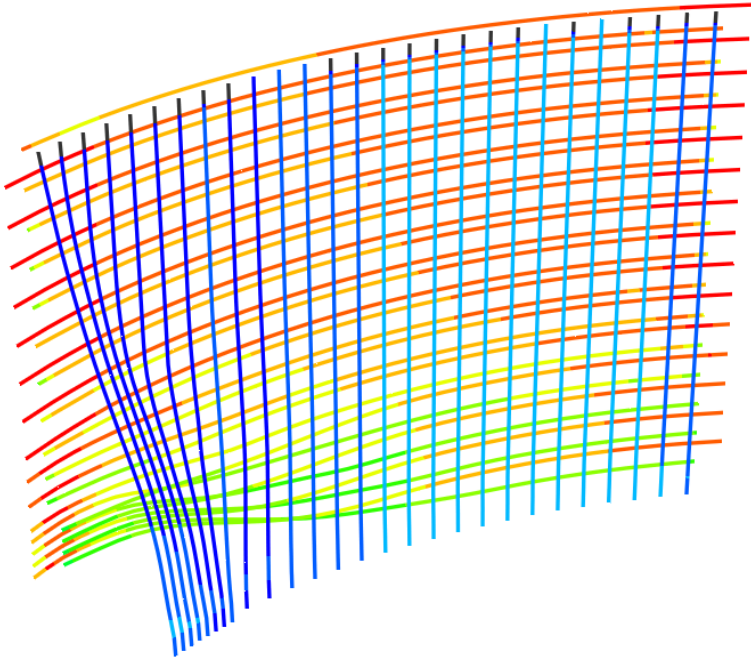
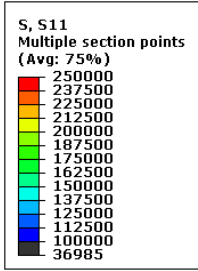
Step: Pressure, Pressure
Increment 162; Step Time = 0.7498
Primary Var: S, S11
Deformed Var: U Deformation Scale Factor: +1e+00

Figure D 86: Tendon Stresses (psi) with 3 x Pd



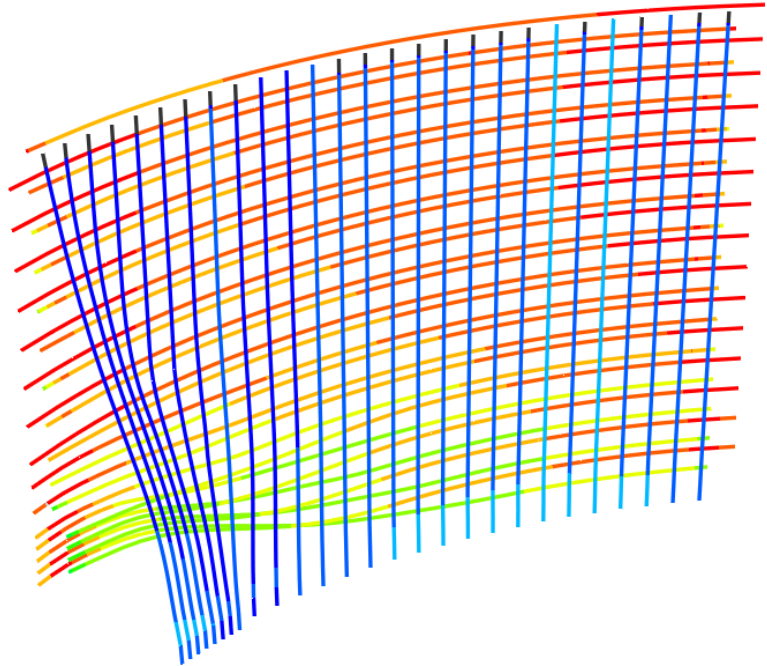
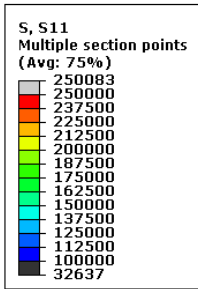
Step: Pressure, Pressure
Increment 209; Step Time = 0.8254
Primary Var: S, S11
Deformed Var: U Deformation Scale Factor: +1e+00

Figure D 87: Tendon Stresses (psi) with 3.3 x Pd



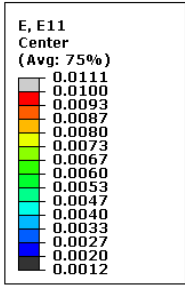
Step: Pressure, Pressure
Increment 240: Step Time = 0.8494
Primary Var: S, S11
Deformed Var: U Deformation Scale Factor: +1e+00

Figure D 88: Tendon Stresses (psi) with 3.4 x Pd



Step: Pressure, Pressure
Increment 300: Step Time = 0.8672
Primary Var: S, S11
Deformed Var: U Deformation Scale Factor: +1e+00

Figure D 89: Tendon Stresses (psi) with 3.47 x Pd



Step: Pressure, Pressure
 Increment: 300; Step Time = 0.8672
 Primary Var: E, E11
 Deformed Var: U - Deformation Scale Factor: +1.0000e+00

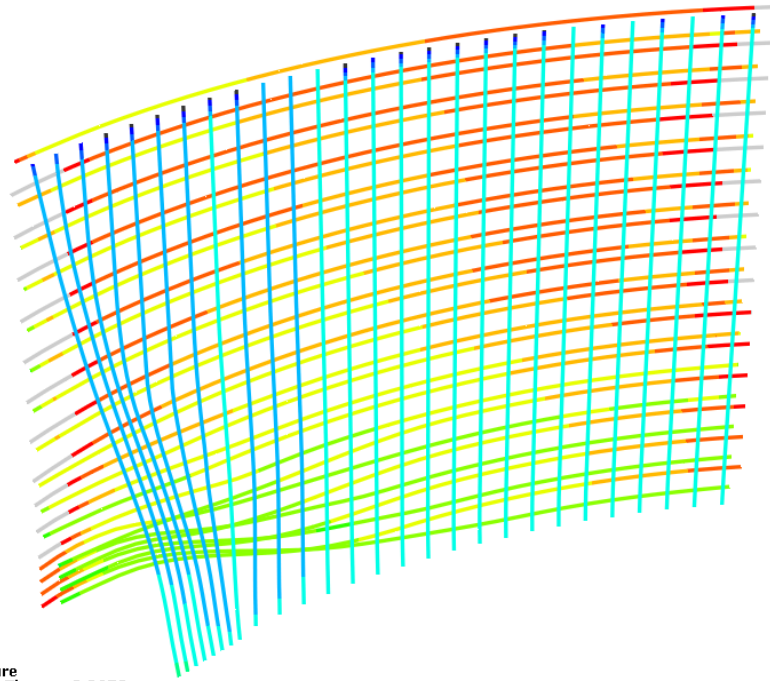
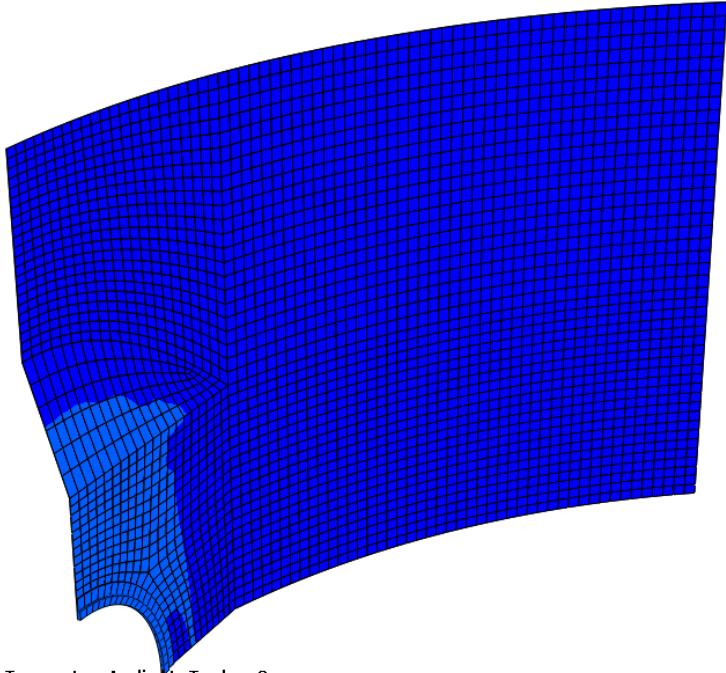
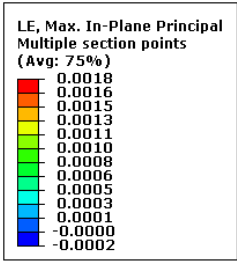
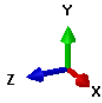
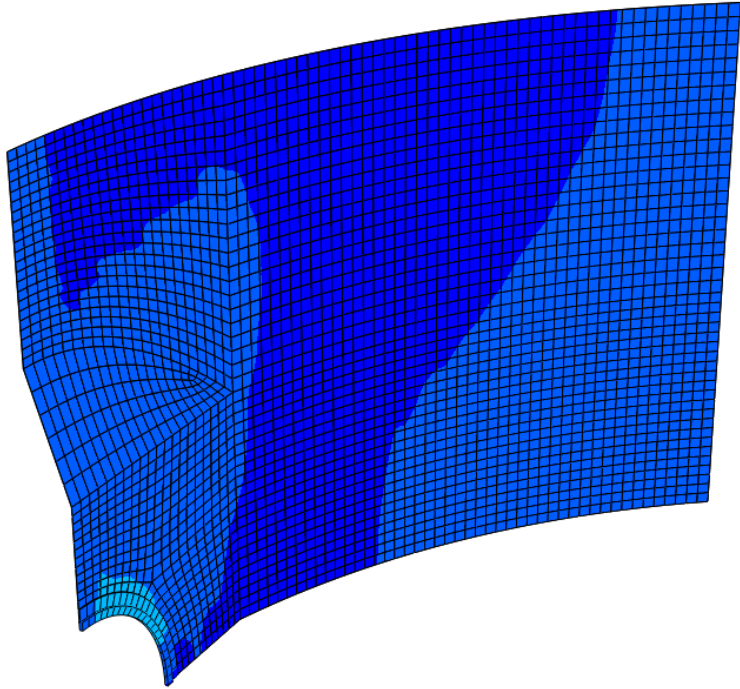
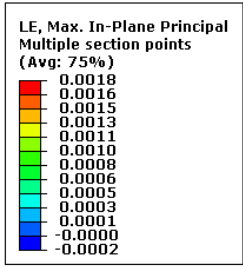


Figure D 90: Tendon Strain with 3.47 x Pd



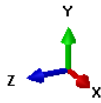
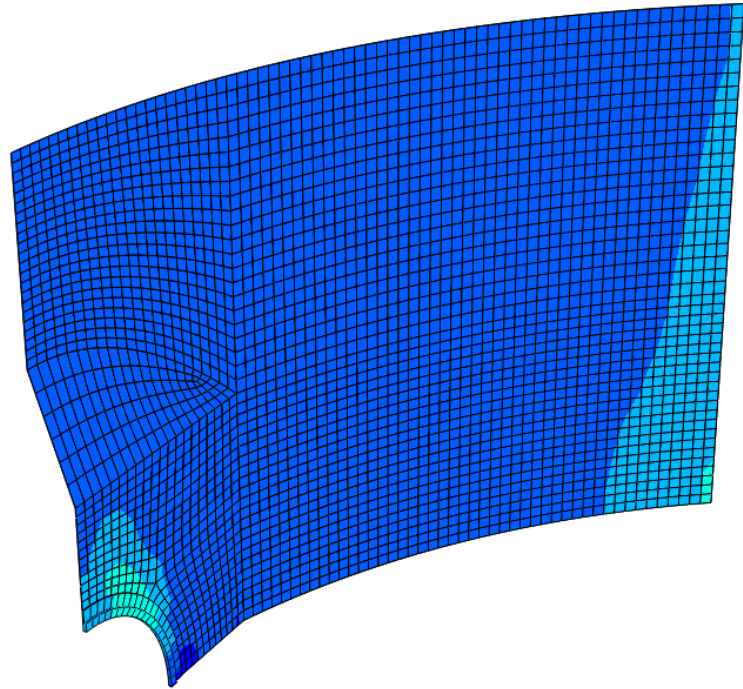
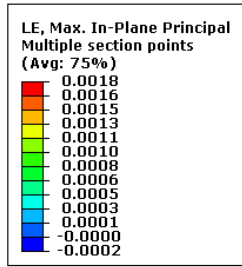
Step: Temp Adjustment 2, Temperature Applied to Tendons 2
 Increment 14: Step Time = 1.000
 Primary Var: LE, Max. In-Plane Principal
 Deformed Var: U Deformation Scale Factor: +1.0000e+00

Figure D 91: Liner Max Principal Strains at Prestress



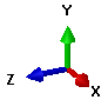
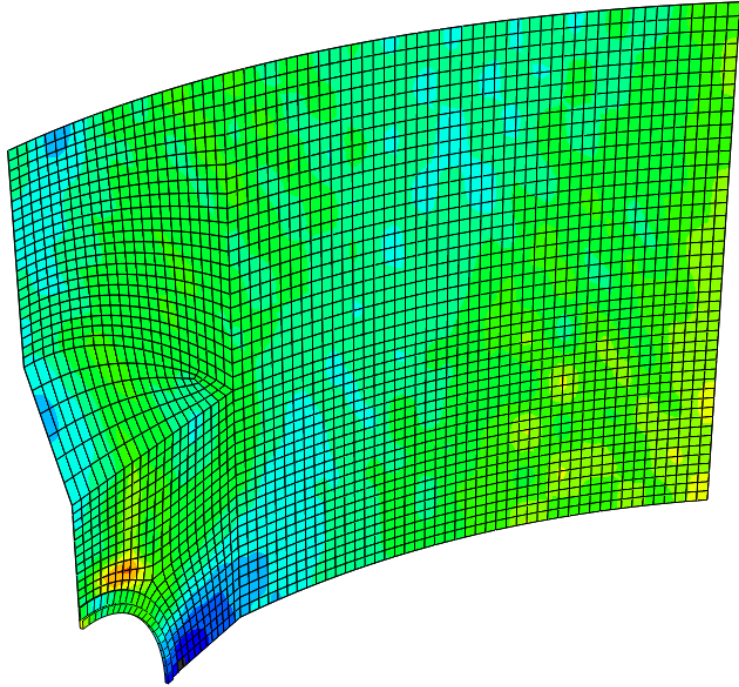
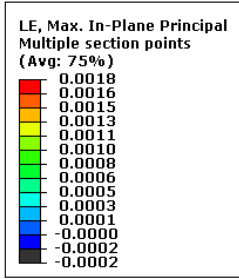
Step: Pressure, Pressure
 Increment 8: Step Time = 0.2463
 Primary Var: LE, Max. In-Plane Principal
 Deformed Var: U Deformation Scale Factor: +1.0000e+00

Figure D 92: Liner Max Principal Strains at 1.0 x Pd



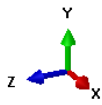
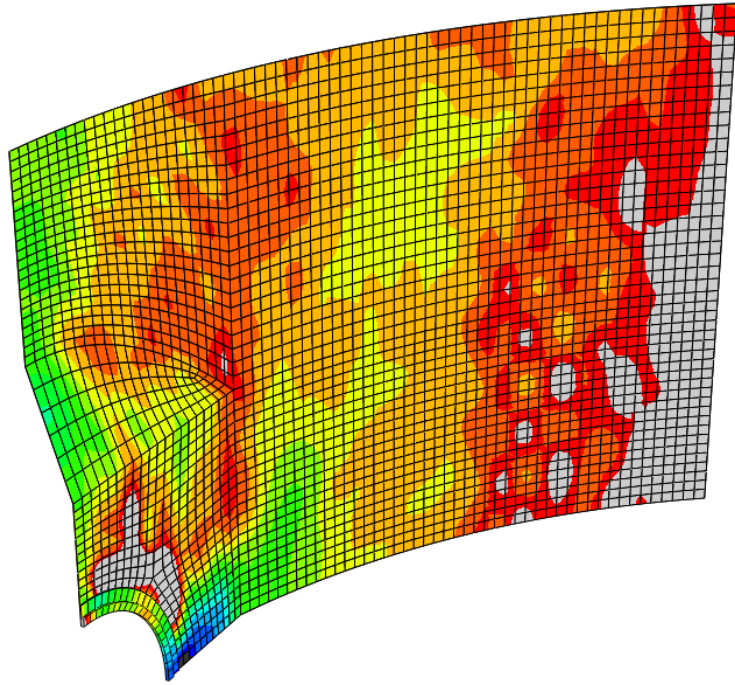
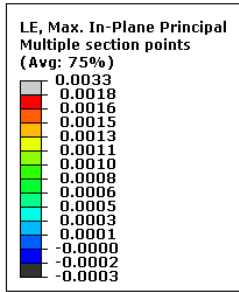
Step: Pressure, Pressure
Increment 14: Step Time = 0.3718
Primary Var: LE, Max. In-Plane Principal
Deformed Var: U Deformation Scale Factor: +1.0000e+00

Figure D 93: Liner Max Principal Strains at 1.5 x Pd



Step: Pressure, Pressure
 Increment 65: Step Time = 0.5000
 Primary Var: LE, Max. In-Plane Principal
 Deformed Var: U Deformation Scale Factor: +1.0000e+00

Figure D 94: Liner Max Principal Strains at 2.0 x Pd



Step: Pressure, Pressure
 Increment: 110; Step Time = 0.6241
 Primary Var: LE, Max. In-Plane Principal
 Deformed Var: U Deformation Scale Factor: +1.0000e+00

Figure D 95: Liner Max Principal Strains at 2.5 x Pd

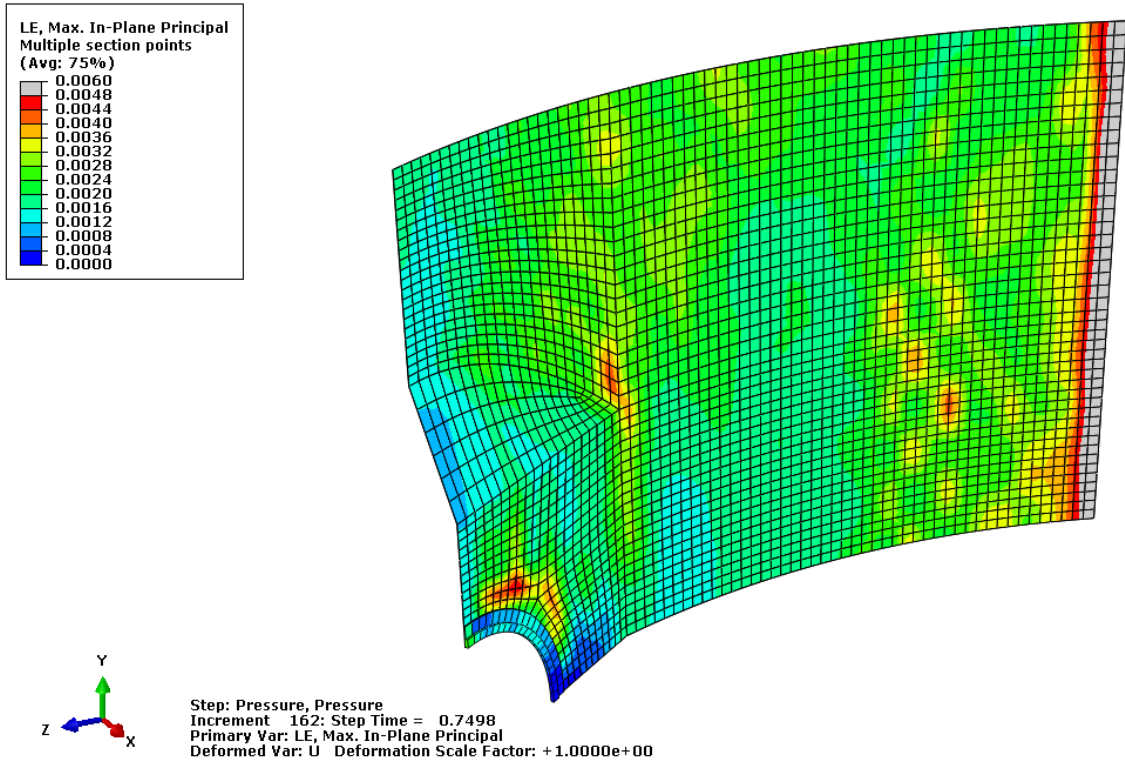


Figure D 96: Liner Max Principal Strains at 3.0 x Pd for Model 2a (note change in contour limits)

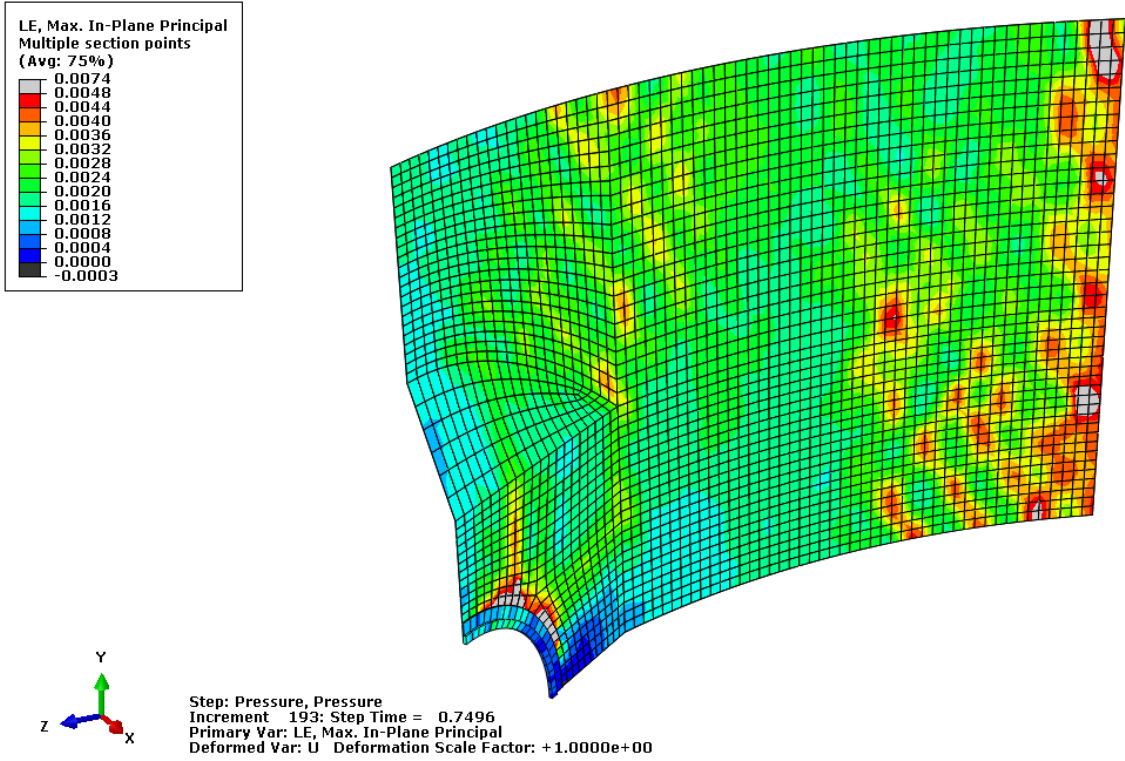


Figure D 97: Liner Max Principal Strains at 3.0 x Pd for Model 2

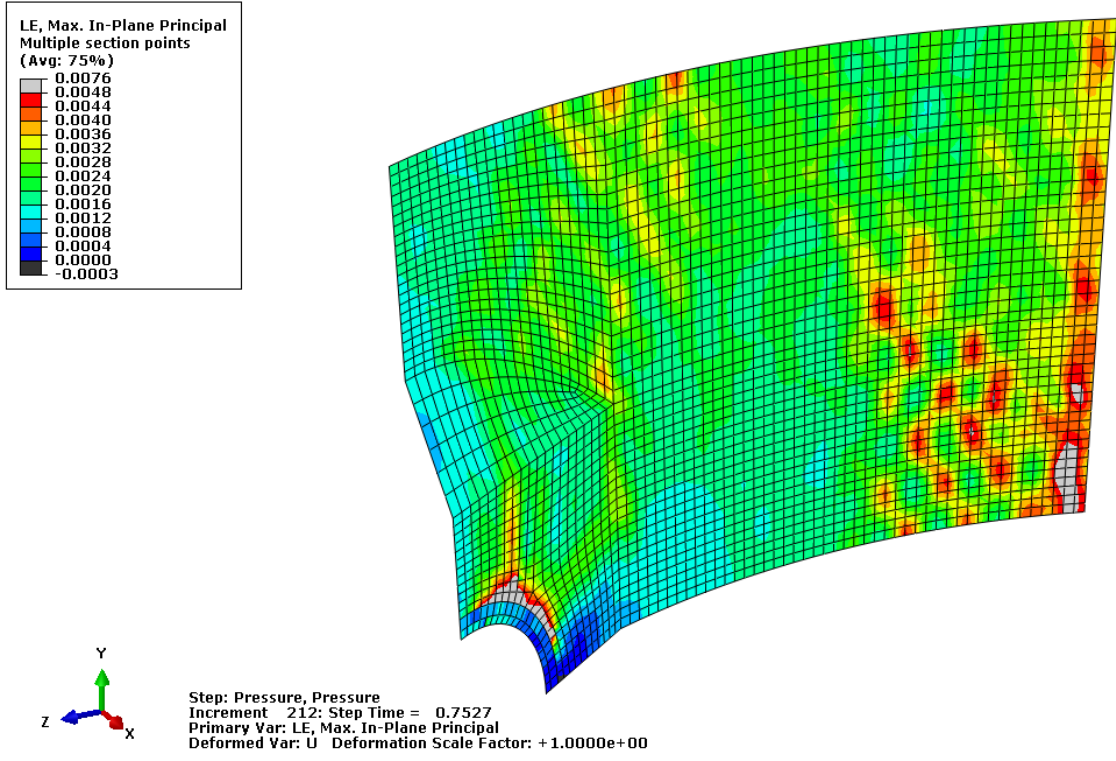


Figure D 98: Liner Max Principal Strains at 3.0 x Pd for Model 2c

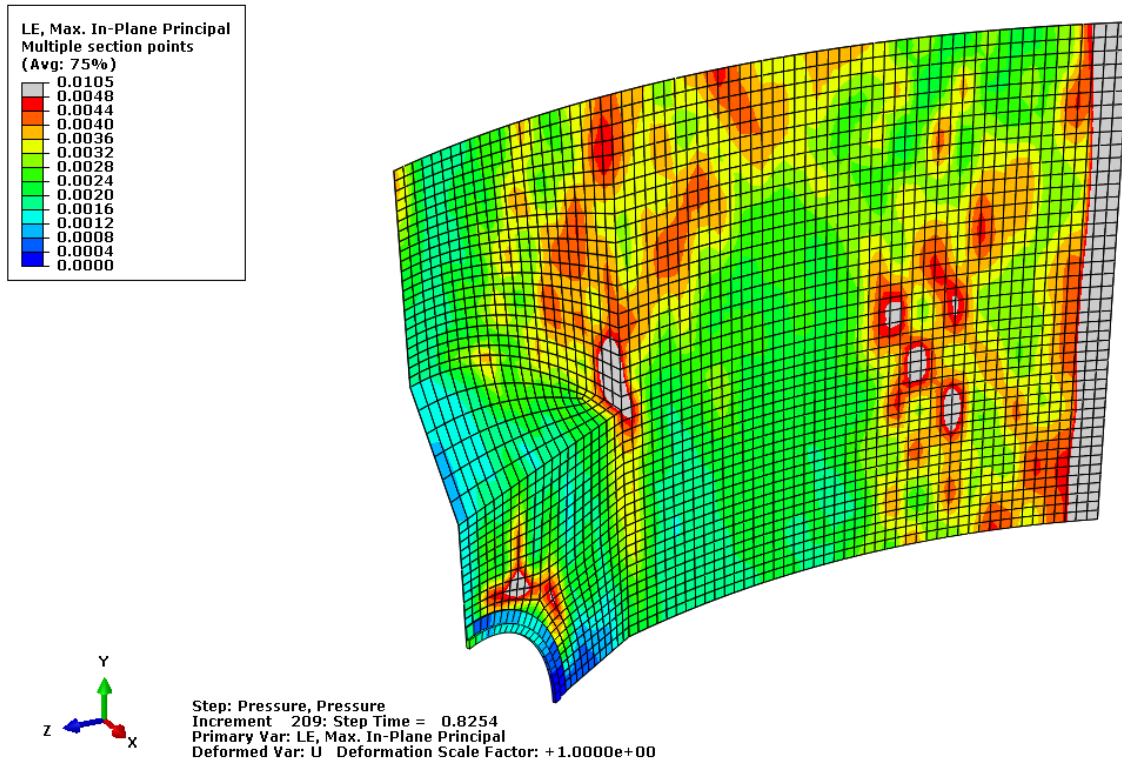


Figure D 99: Liner Max Principal Strains at 3.3 x Pd for Model 2a

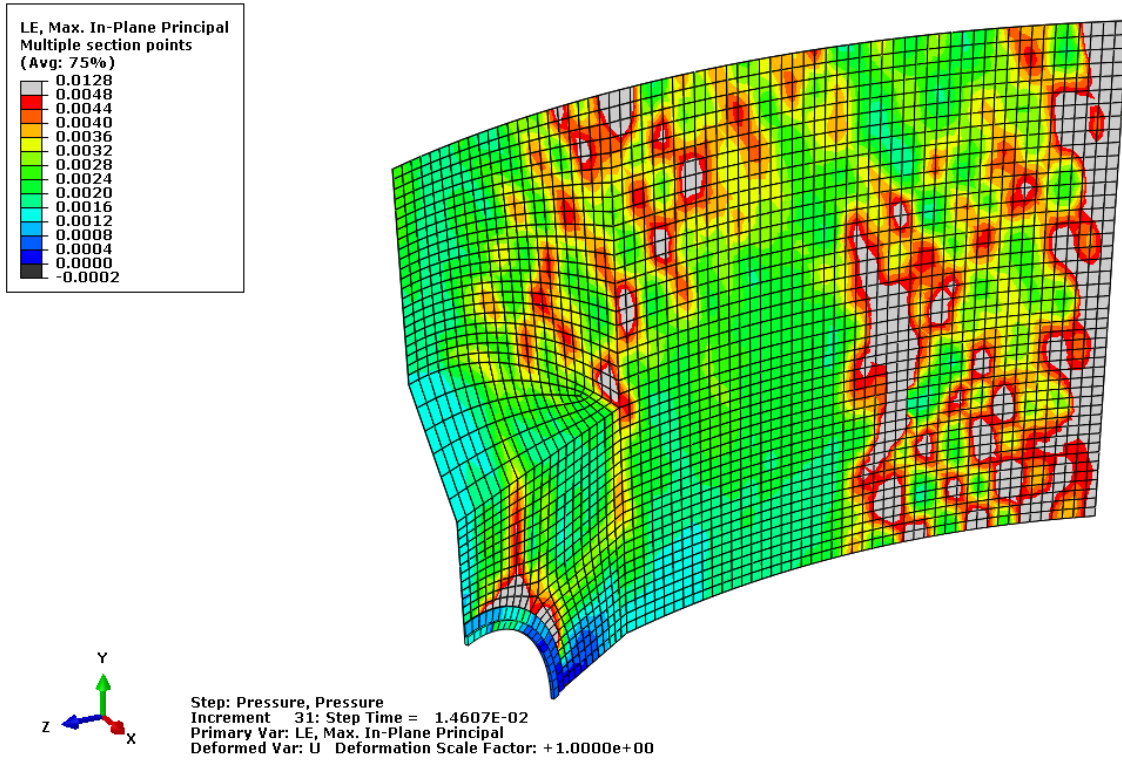


Figure D 100: Liner Max Principal Strains at 3.3 x Pd for Model 2b

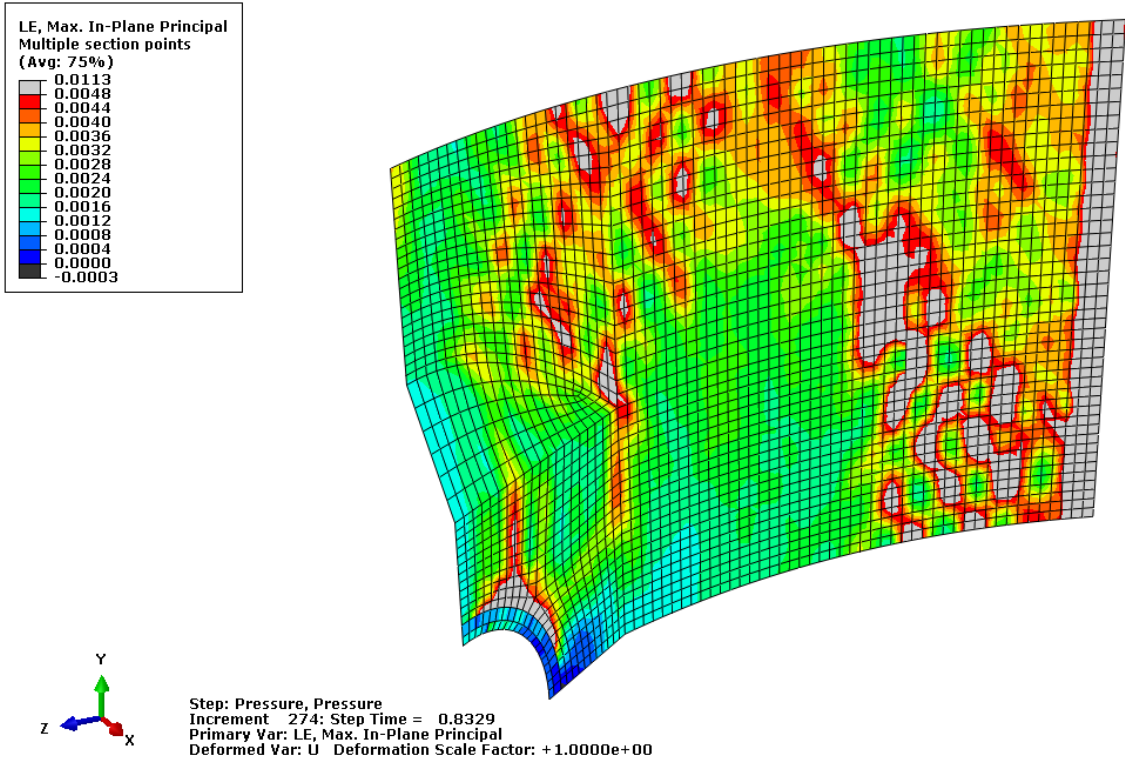


Figure D 101: Liner Max Principal Strains at 3.3 x Pd for Model 2c

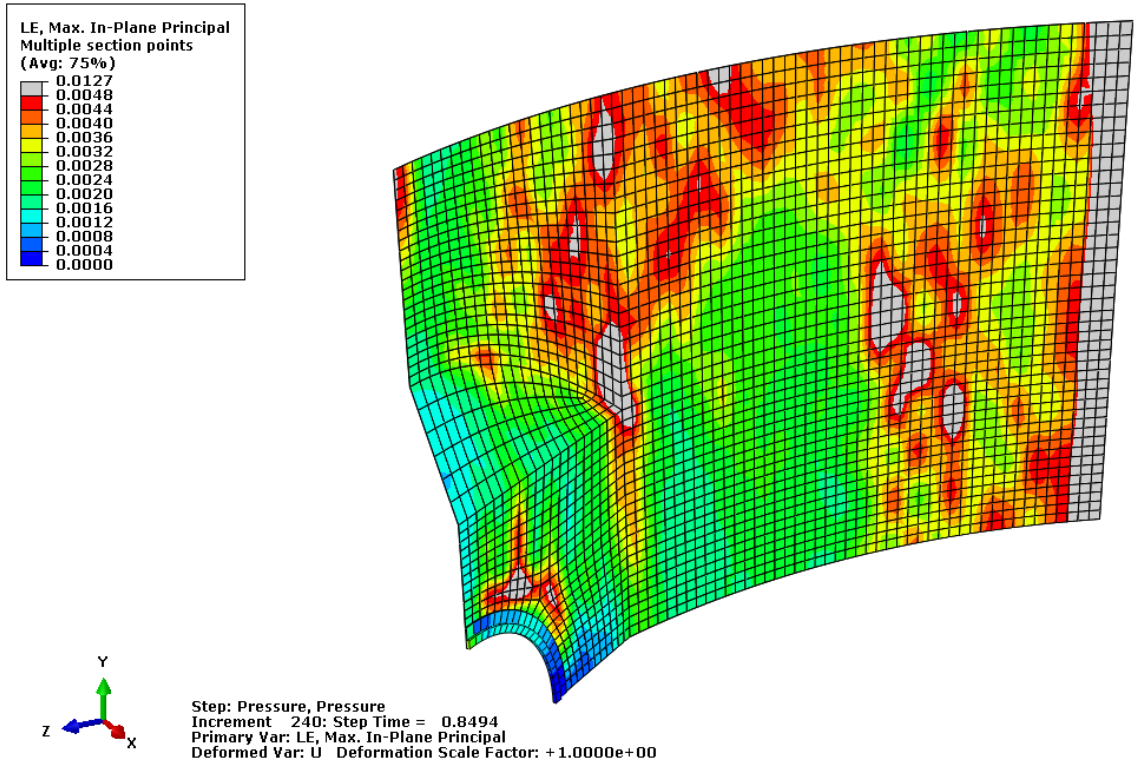
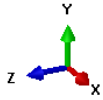
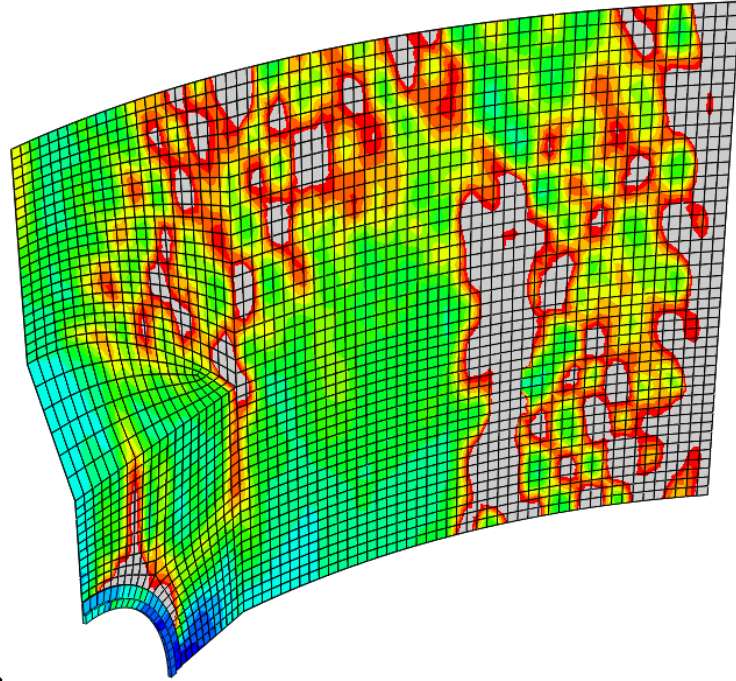
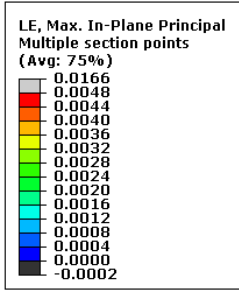


Figure D 102: Liner Max Principal Strains at 3.4 x Pd for Model 2a



Step: Pressure, Pressure
 Increment: 70; Step Time = 3.8795E-02
 Primary Var: LE, Max. In-Plane Principal
 Deformed Var: U Deformation Scale Factor: +1.0000e+00

Figure D 103: Liner Max Principal Strains at 3.4 x Pd for Model 2b

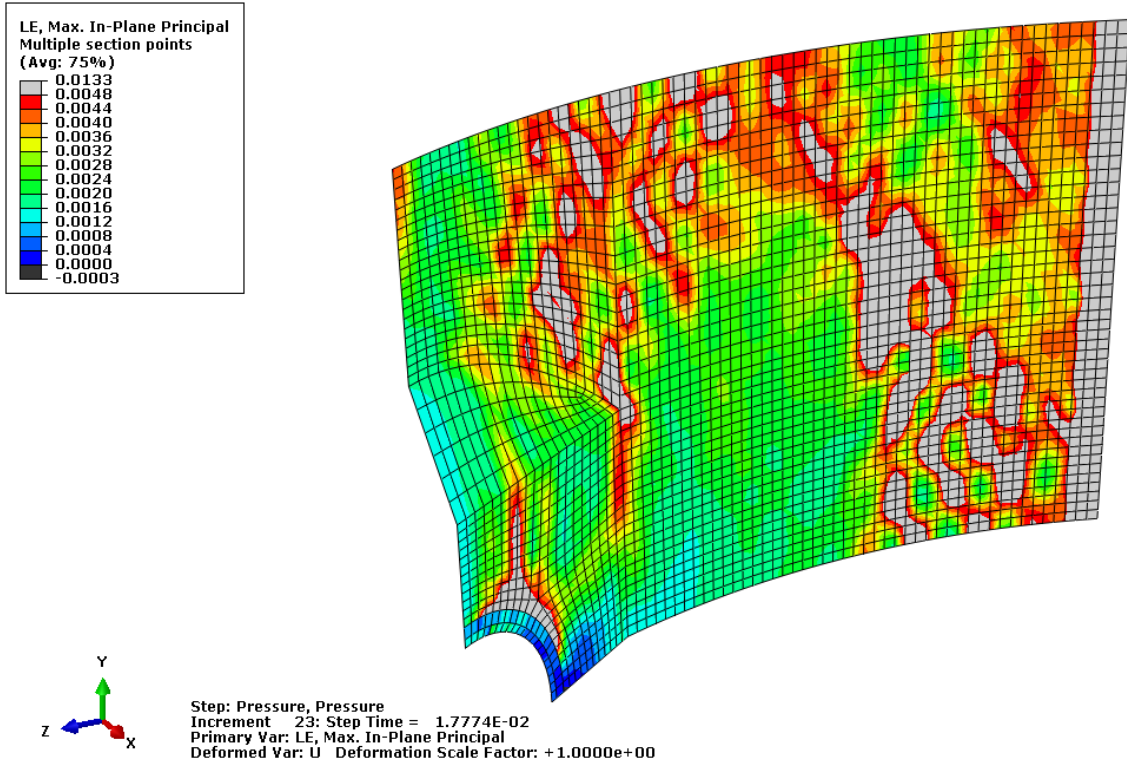
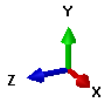
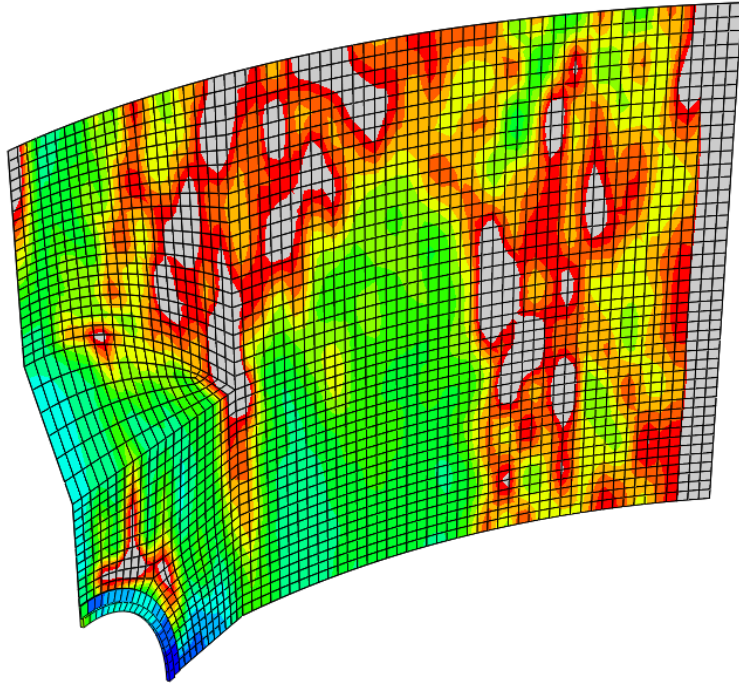
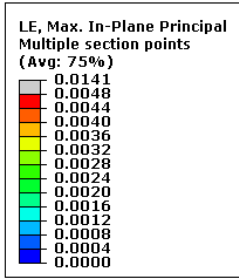


Figure D 104: Liner Max Principal Strains at 3.4 x Pd for Model 2c



Step: Pressure, Pressure
 Increment 300; Step Time = 0.8672
 Primary Var: LE, Max. In-Plane Principal
 Deformed Var: U Deformation Scale Factor: +1.0000e+00

Figure D 105: Liner Max Principal Strains at 3.47 x Pd for Model 2a

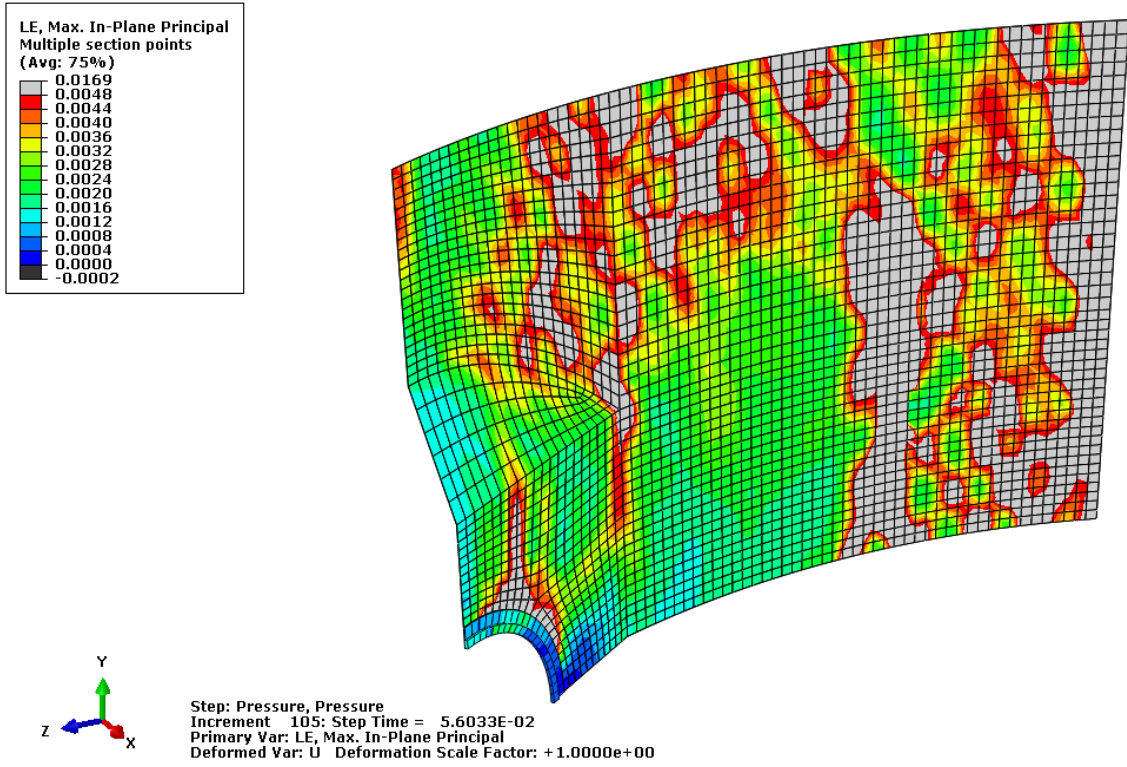


Figure D 106: Liner Max Principal Strains at 3.47 x Pd for Model 2b

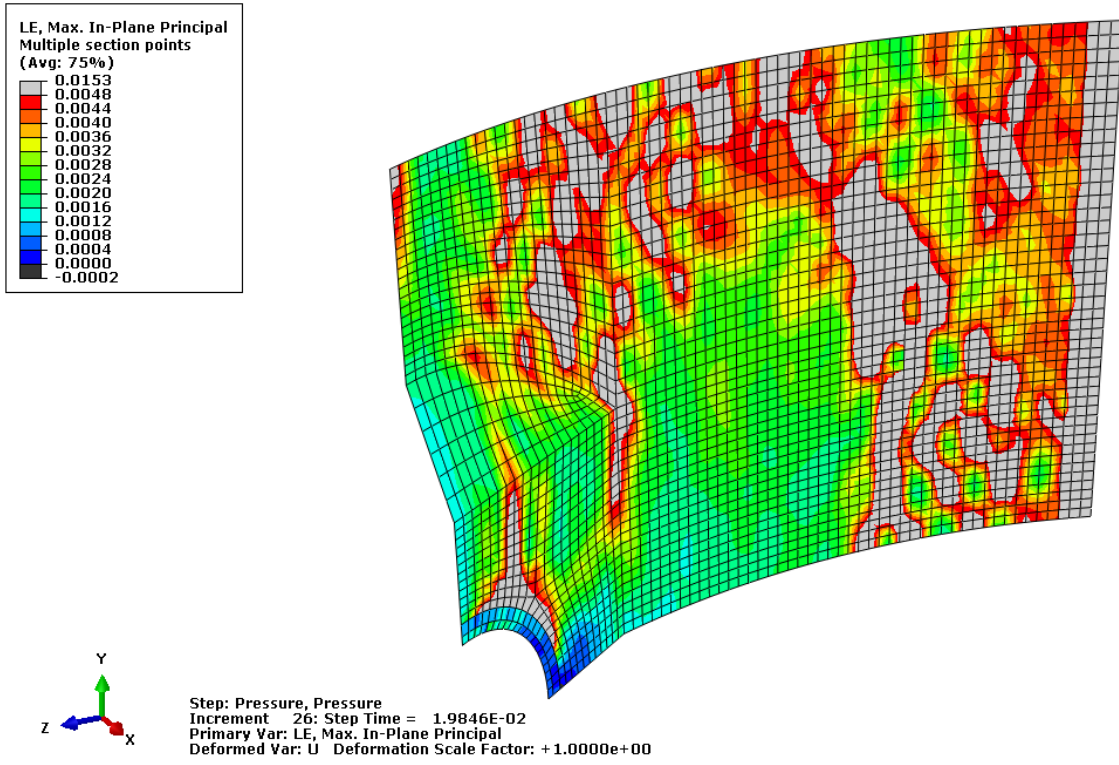


Figure D 107: Liner Max Principal Strains at 3.47 x Pd for Model 2c

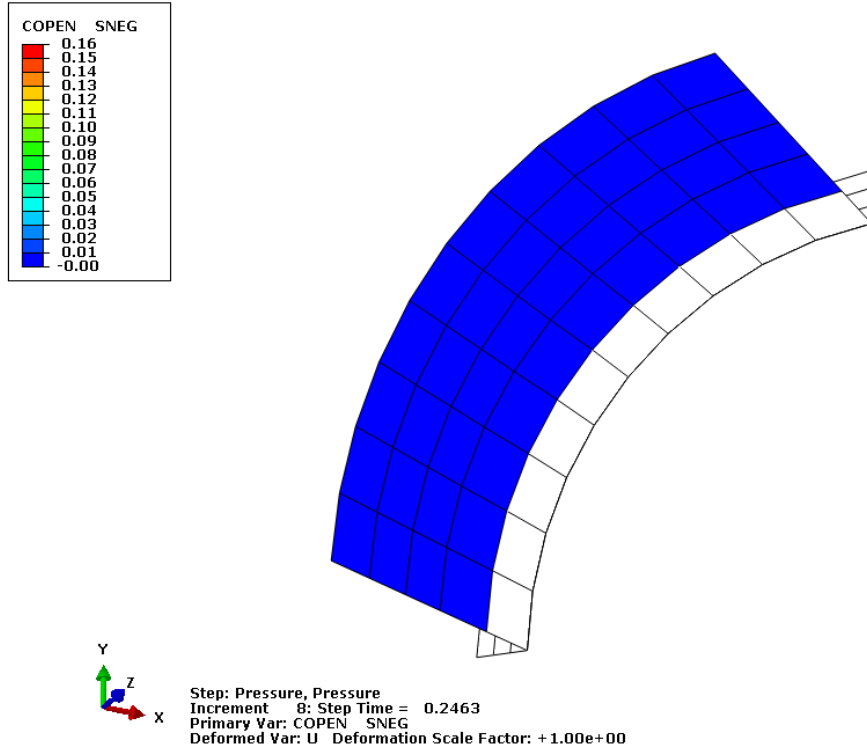


Figure D 108: Pipe Separation from Concrete (in.) at 1.0 x Pd for Model 2a

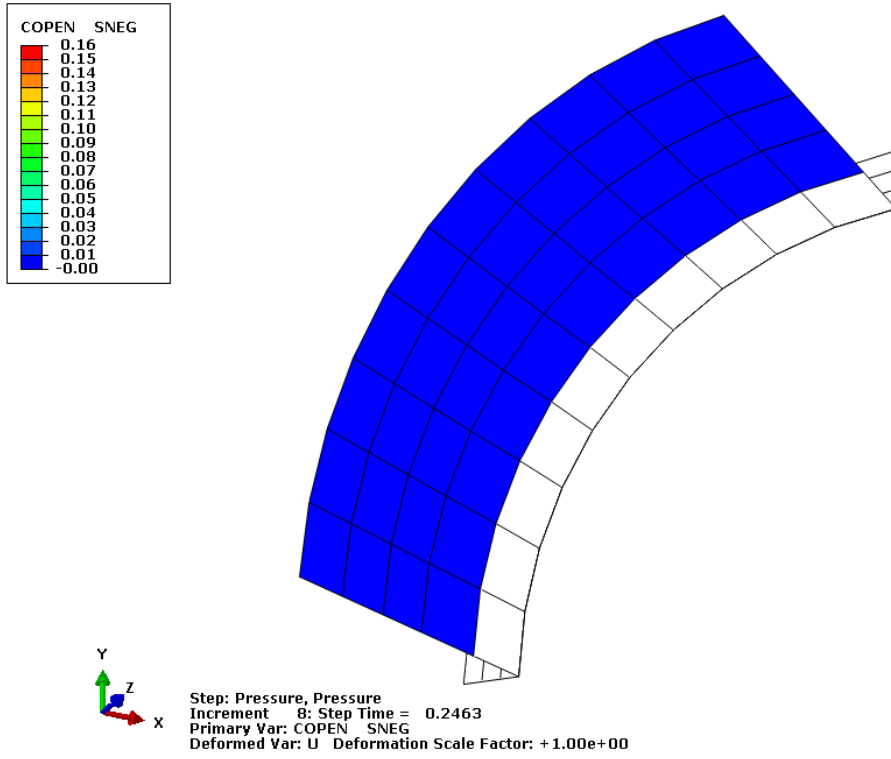


Figure D 109: Pipe Separation from Concrete (in.) at 1.0 x Pd for Model 2b

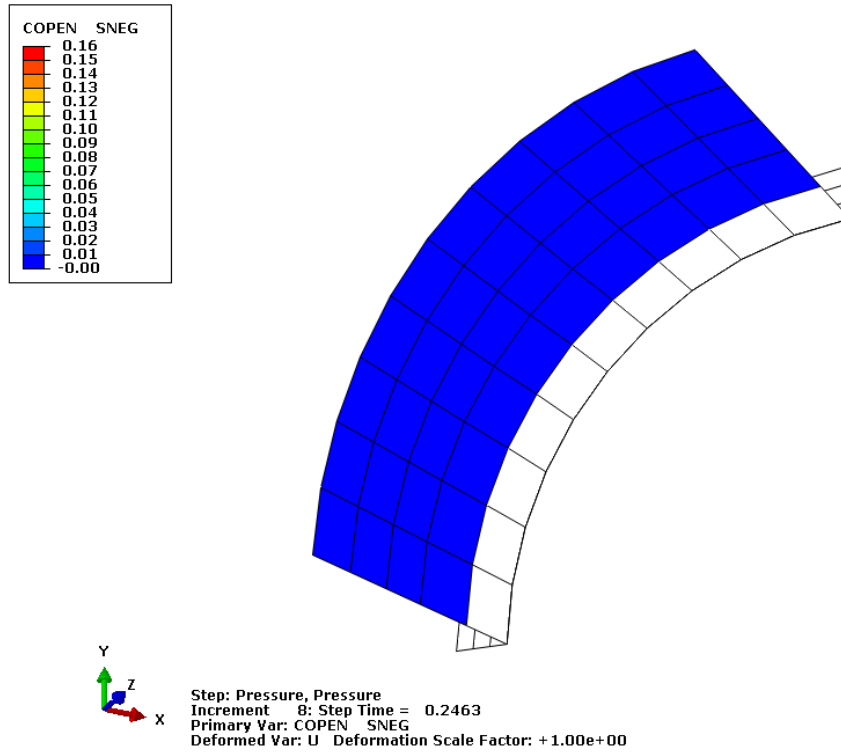


Figure D 110: Pipe Separation from Concrete (in.) at 1.0 x Pd for Model 2c

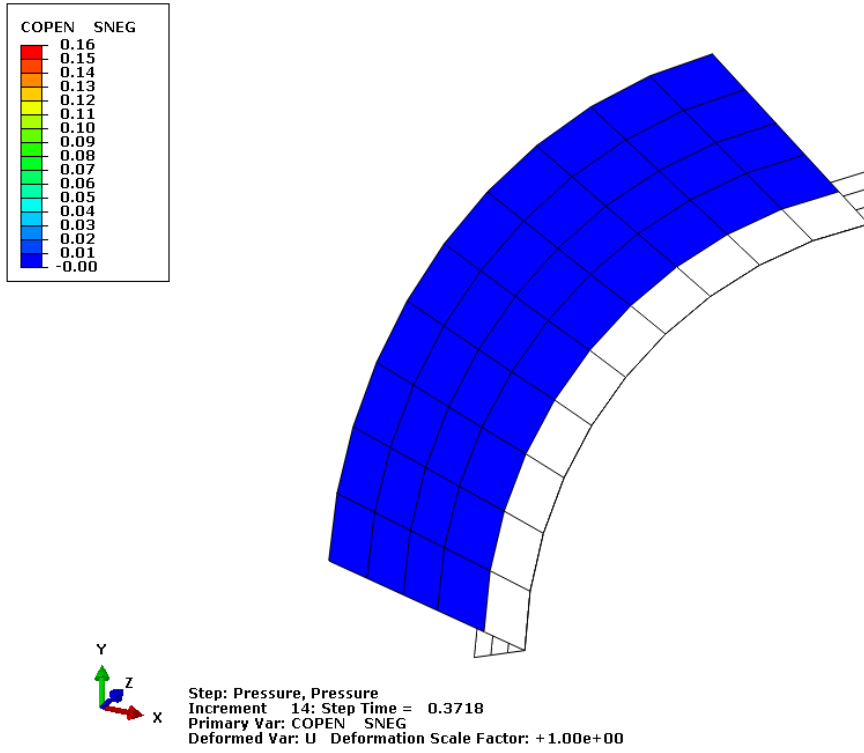


Figure D 111: Pipe Separation from Concrete (in.) at 1.5 x Pd for Model 2a

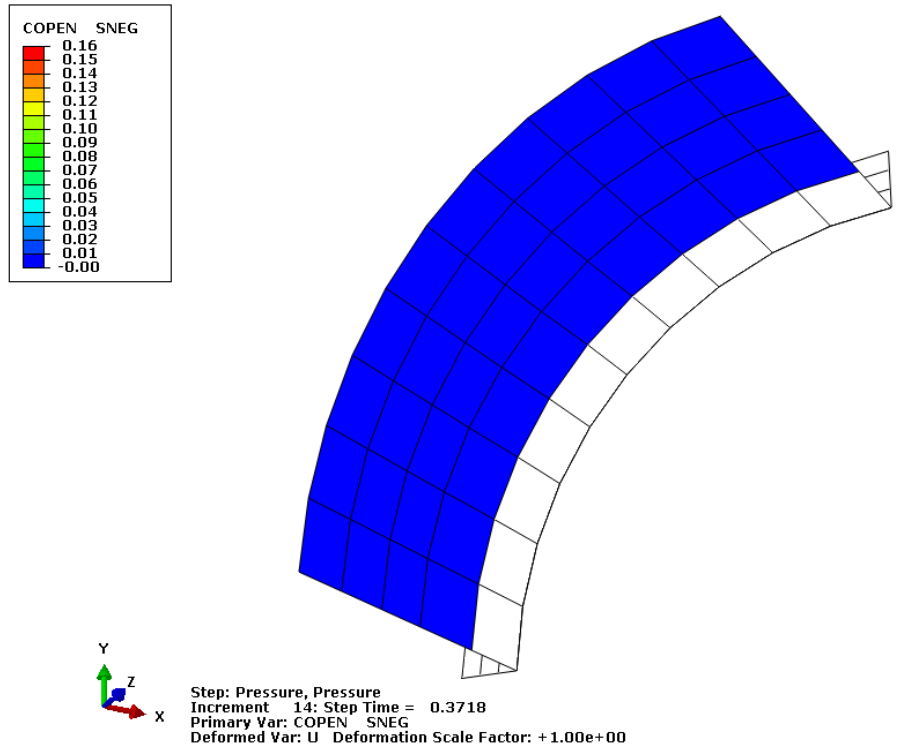


Figure D 112: Pipe Separation from Concrete (in.) at 1.5 x Pd for Model 2b

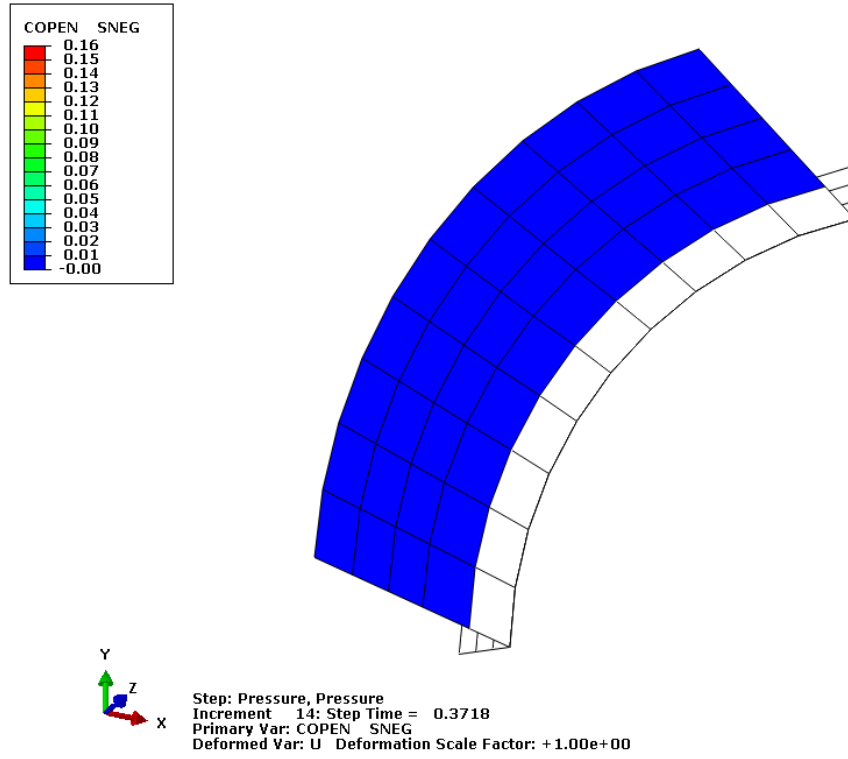


Figure D 113: Pipe Separation from Concrete (in.) at 1.5 x Pd for Model 2c

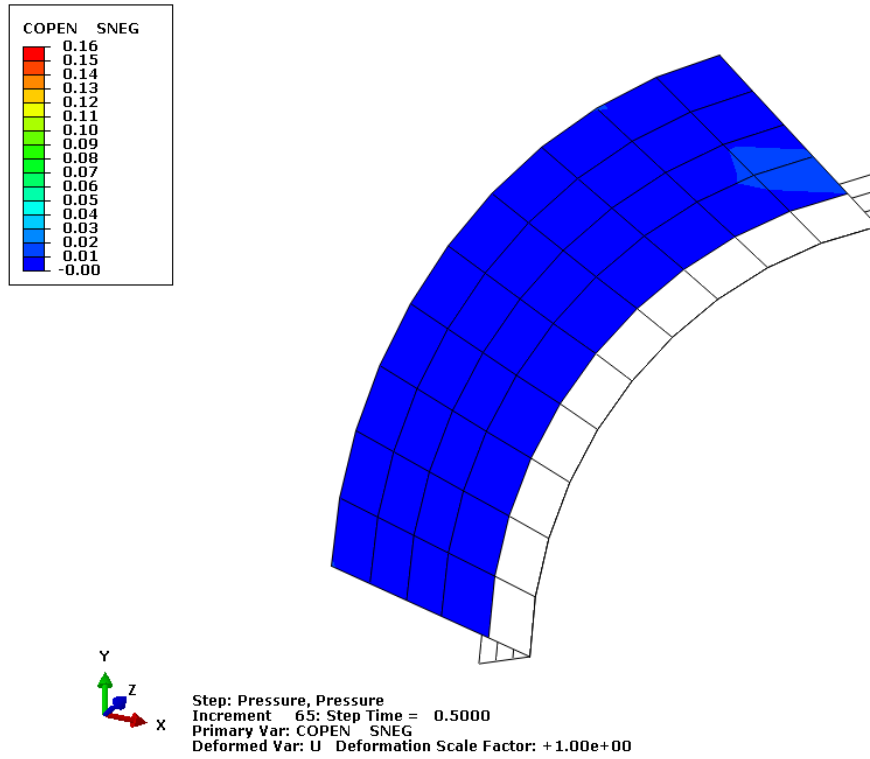


Figure D 114: Pipe Separation from Concrete (in.) at 2.0 x Pd for Model 2a

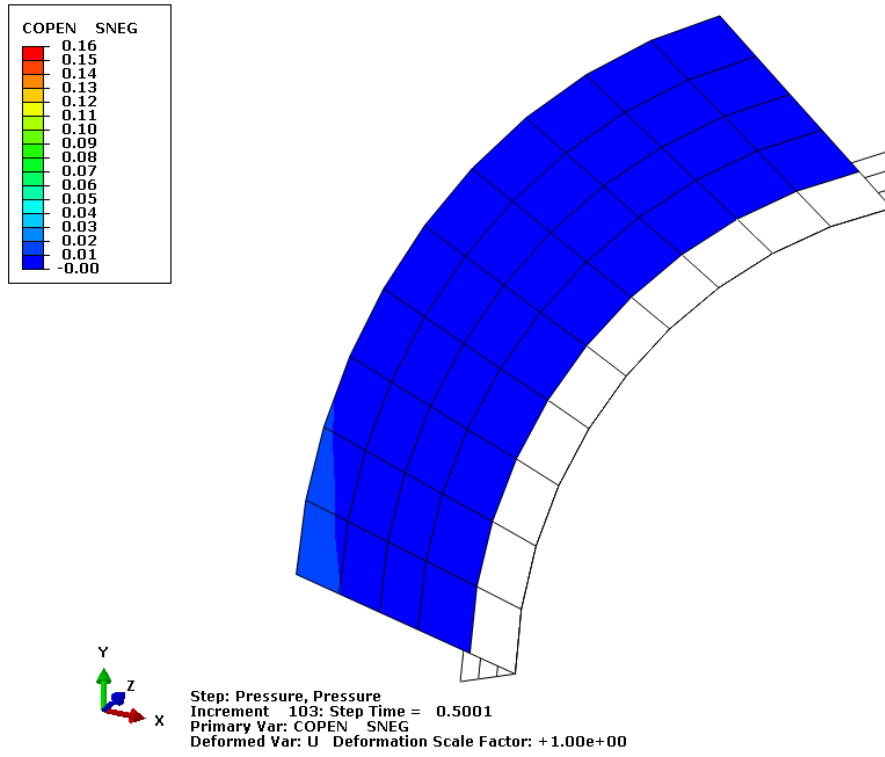


Figure D 115: Pipe Separation from Concrete (in.) at 2.0 x Pd for Model 2b

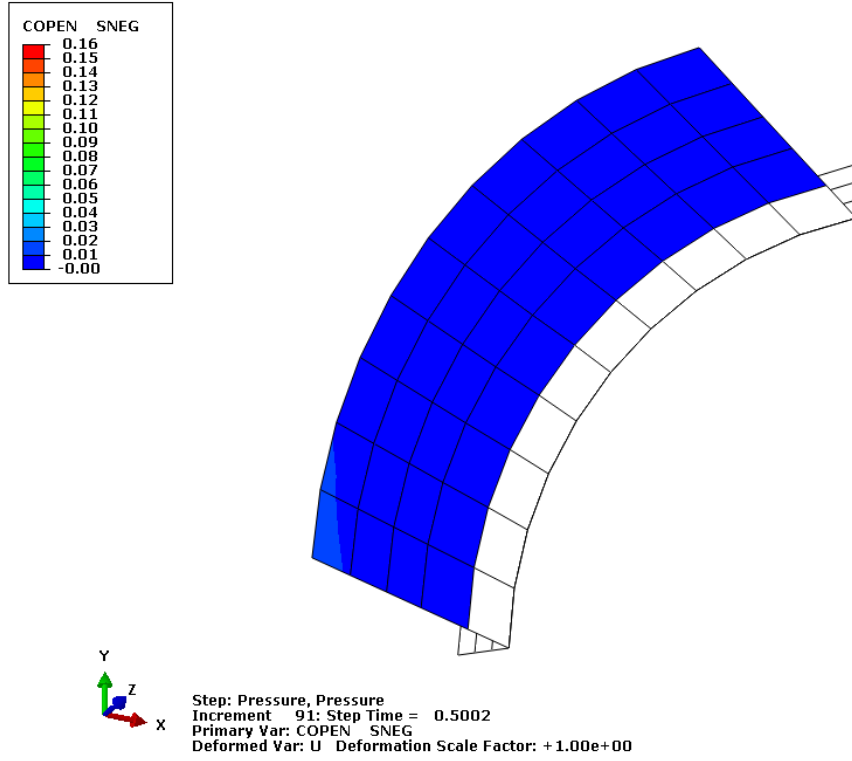


Figure D 116: Pipe Separation from Concrete (in.) at 2.0 x Pd for Model 2c

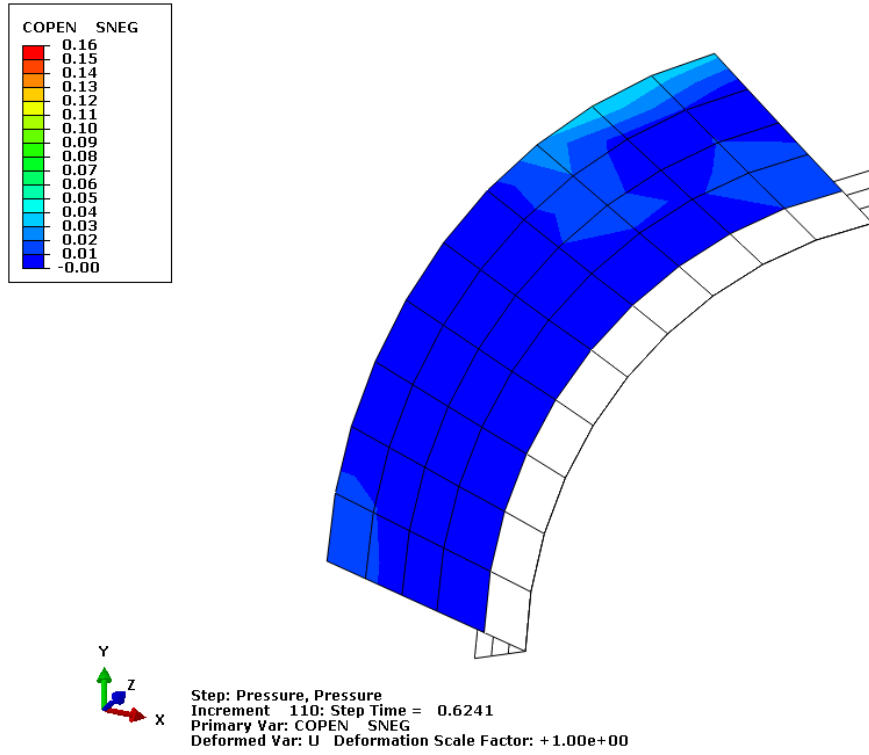


Figure D 117: Pipe Separation from Concrete (in.) at 2.5 x Pd for Model 2a

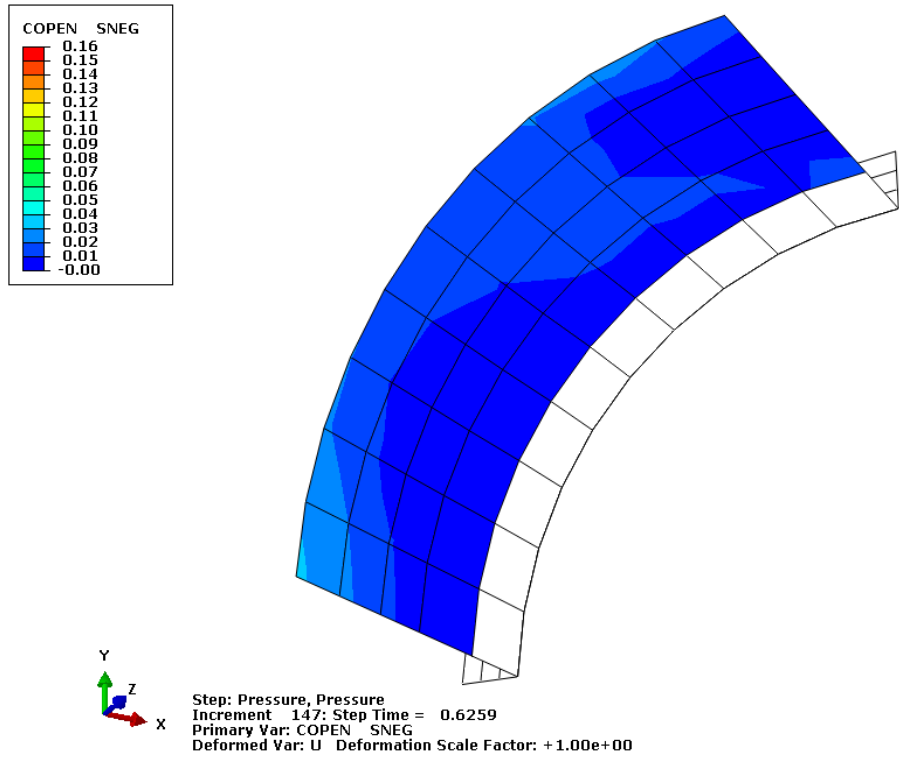


Figure D 118: Pipe Separation from Concrete (in.) at 2.5 x Pd for Model 2b

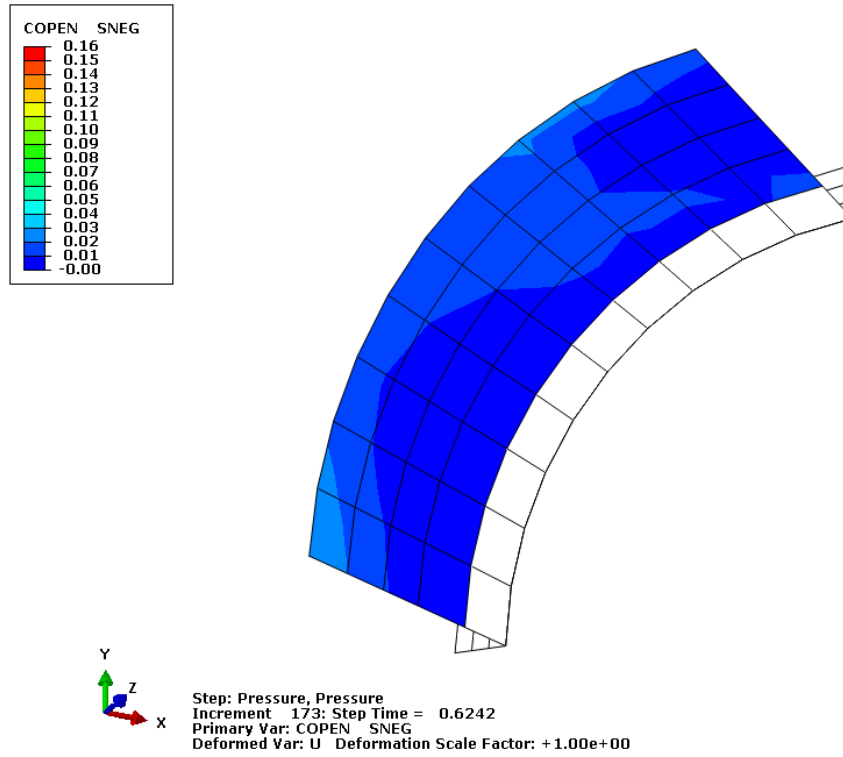


Figure D 119: Pipe Separation from Concrete (in.) at 2.5 x Pd for Model 2c

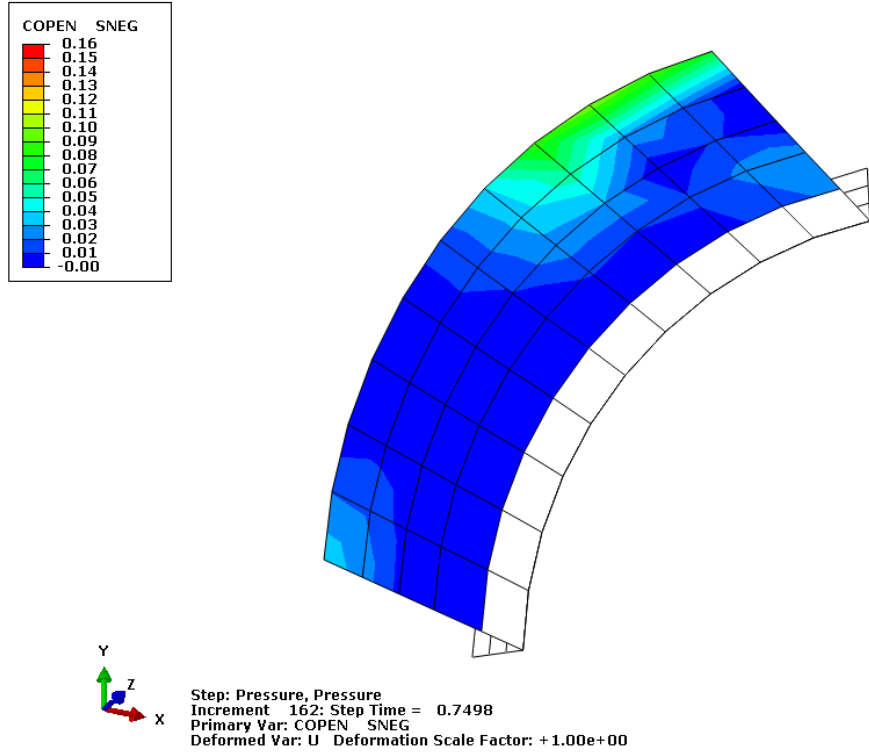


Figure D 120: Pipe Separation from Concrete (in.) at 3.0 x Pd for Model 2a

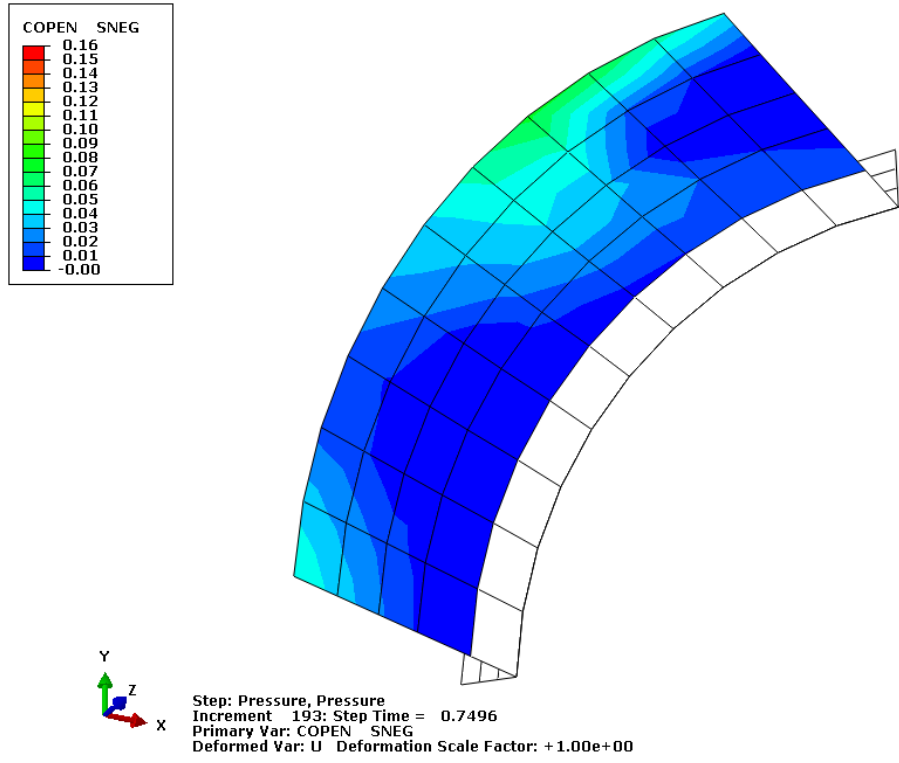


Figure D 121: Pipe Separation from Concrete (in.) at 3.0 x Pd for Model 2b

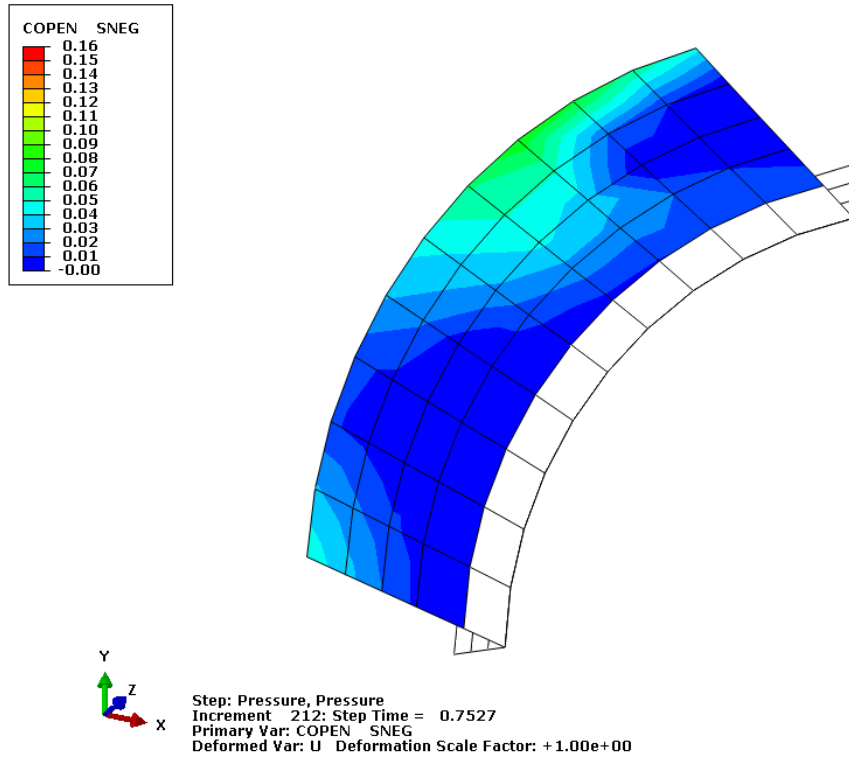


Figure D 122: Pipe Separation from Concrete (in.) at 3.0 x Pd for Model 2c

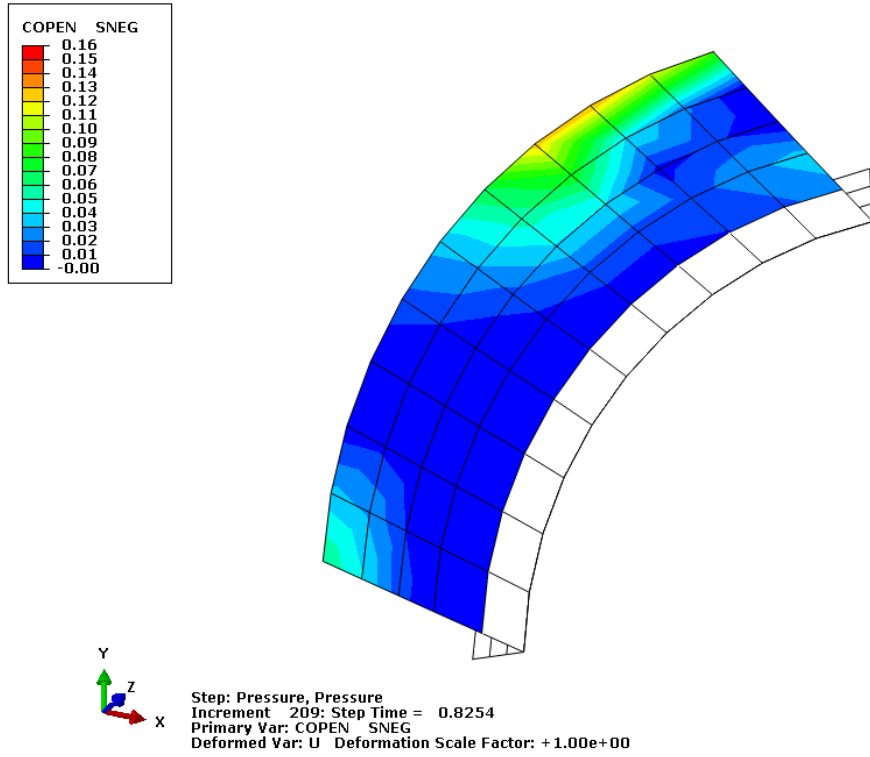


Figure D 123: Pipe Separation from Concrete (in.) at 3.3 x Pd for Model 2a

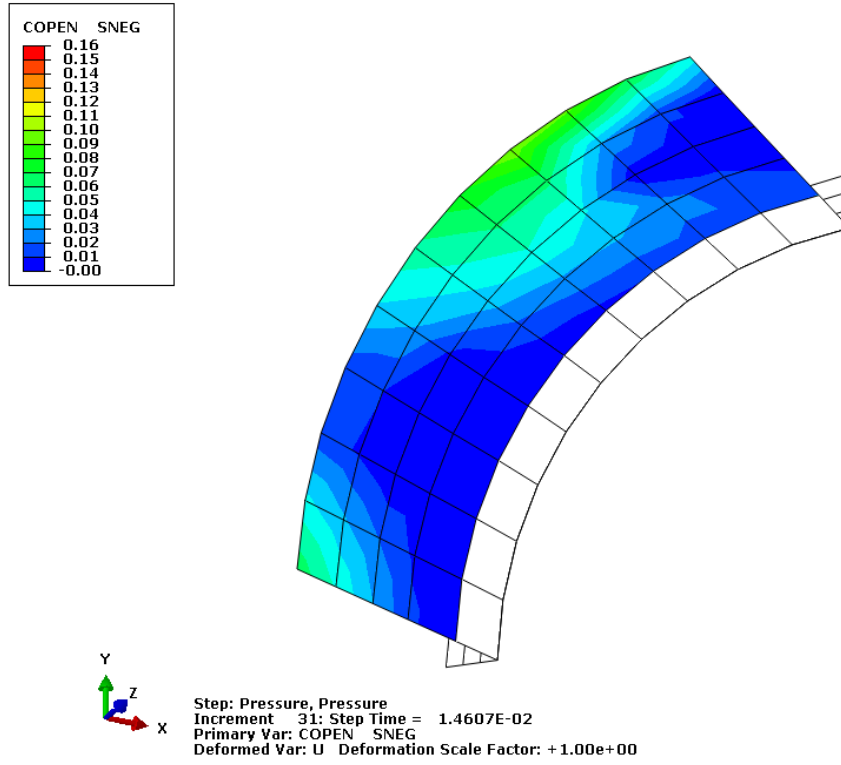


Figure D 124: Pipe Separation from Concrete (in.) at 3.3 x Pd for Model 2b

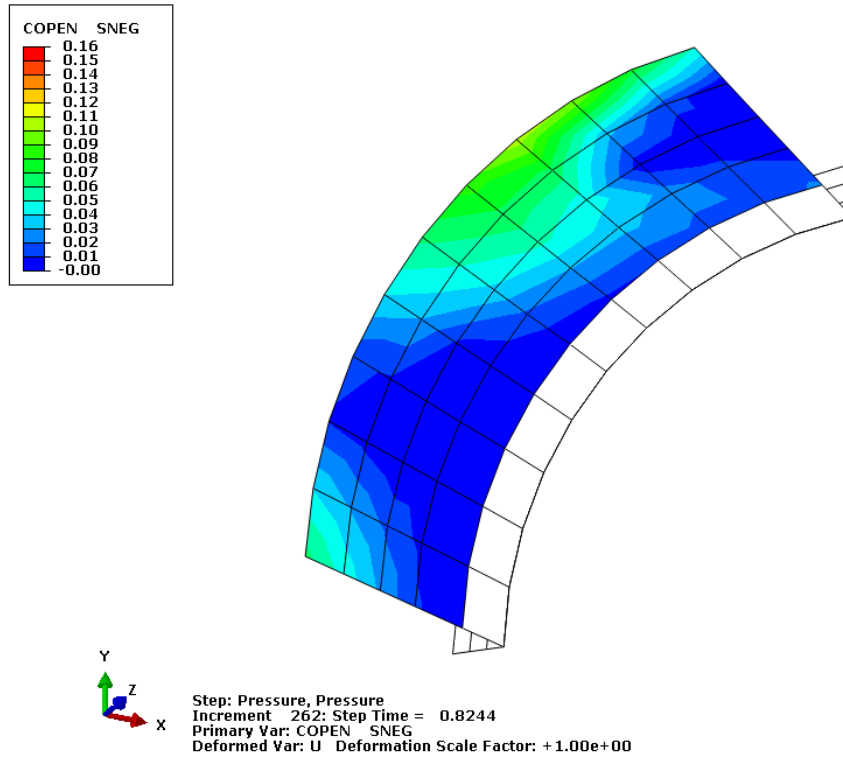


Figure D 125: Pipe Separation from Concrete (in.) at 3.3 x Pd for Model 2c

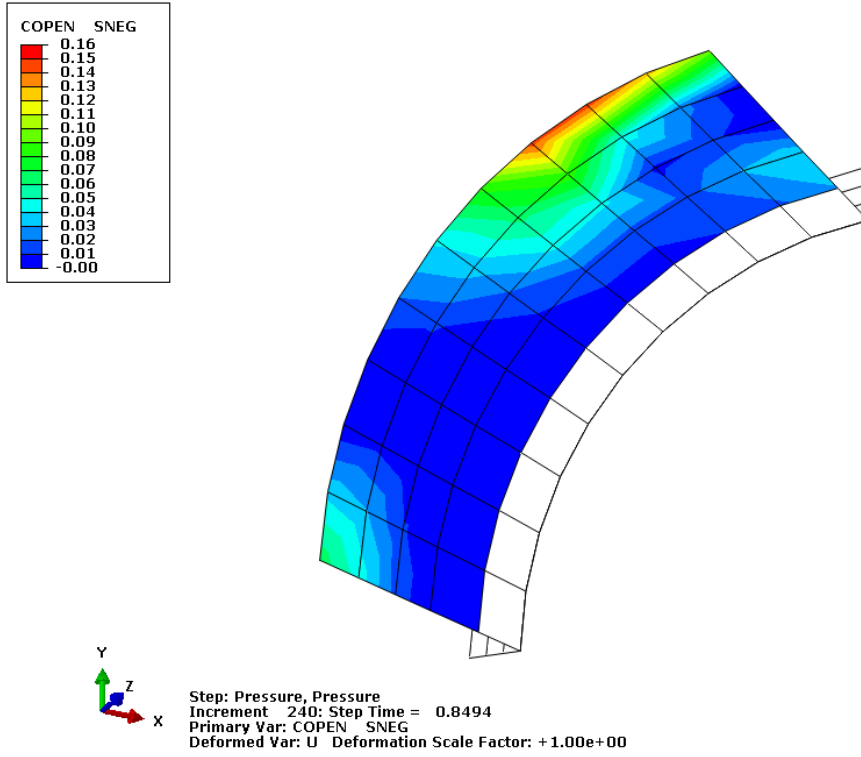


Figure D 126: Pipe Separation from Concrete (in.) at 3.4 x Pd for Model 2a

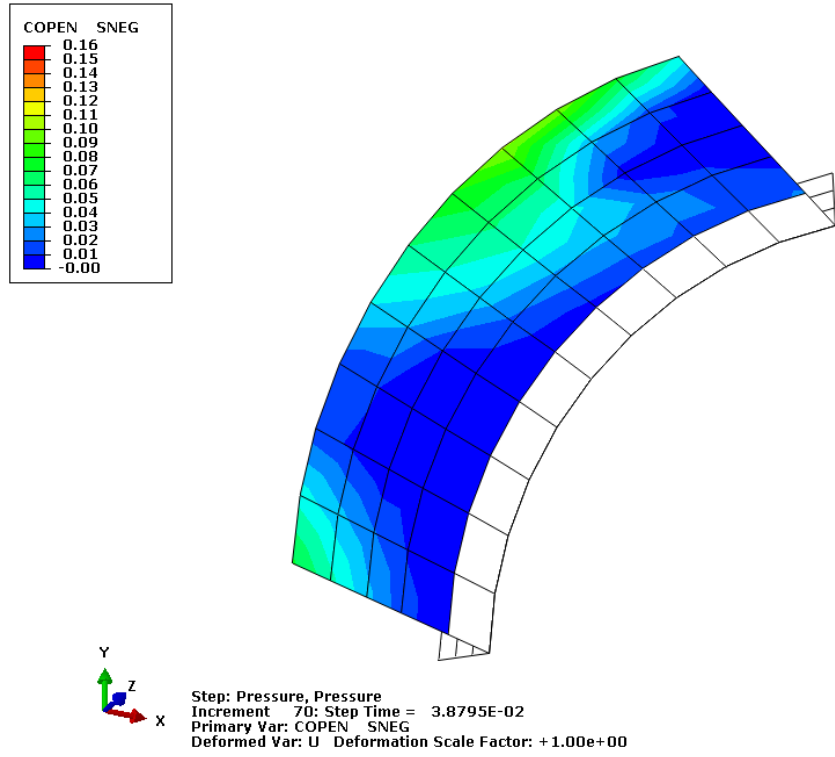


Figure D 127: Pipe Separation from Concrete (in.) at 3.4 x Pd for Model 2b

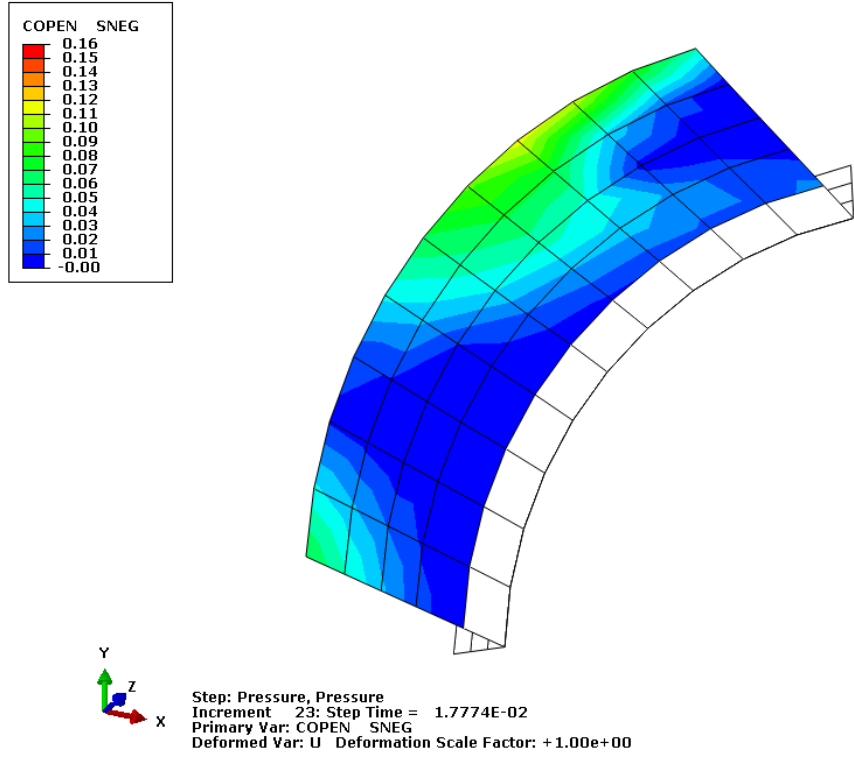


Figure D 128: Pipe Separation from Concrete (in.) at 3.4 x Pd for Model 2c

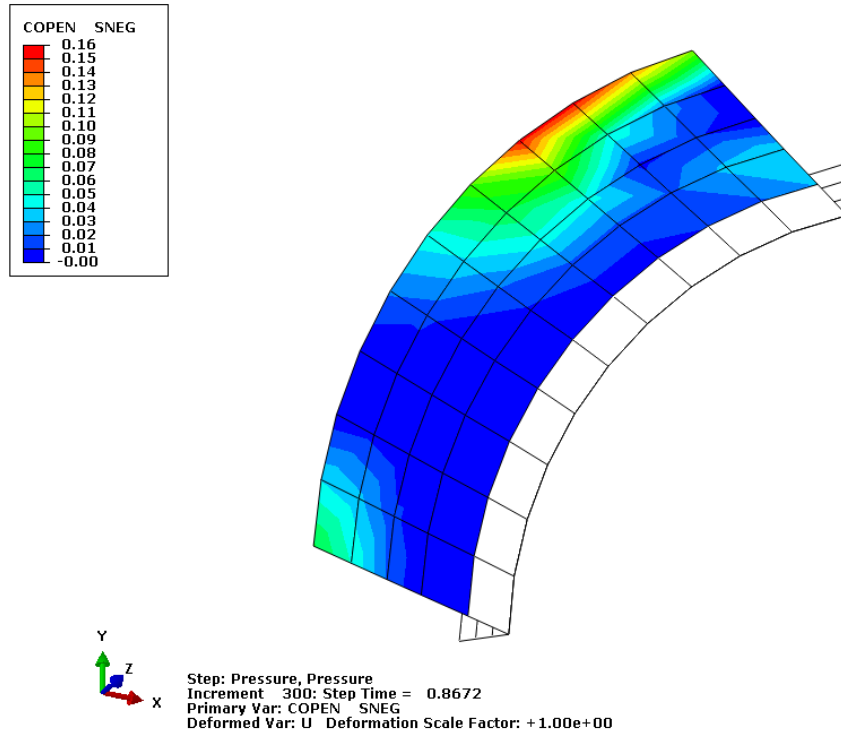


Figure D 129: Pipe Separation from Concrete (in.) at 3.47 x Pd for Model 2a

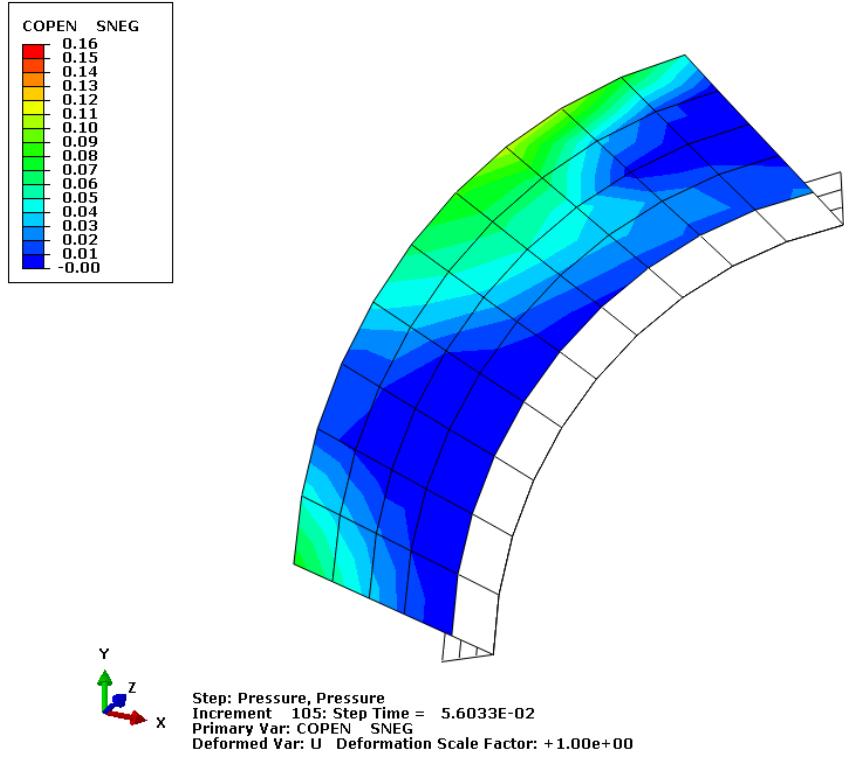


Figure D 130: Pipe Separation from Concrete (in.) at 3.47 x Pd for Model 2b

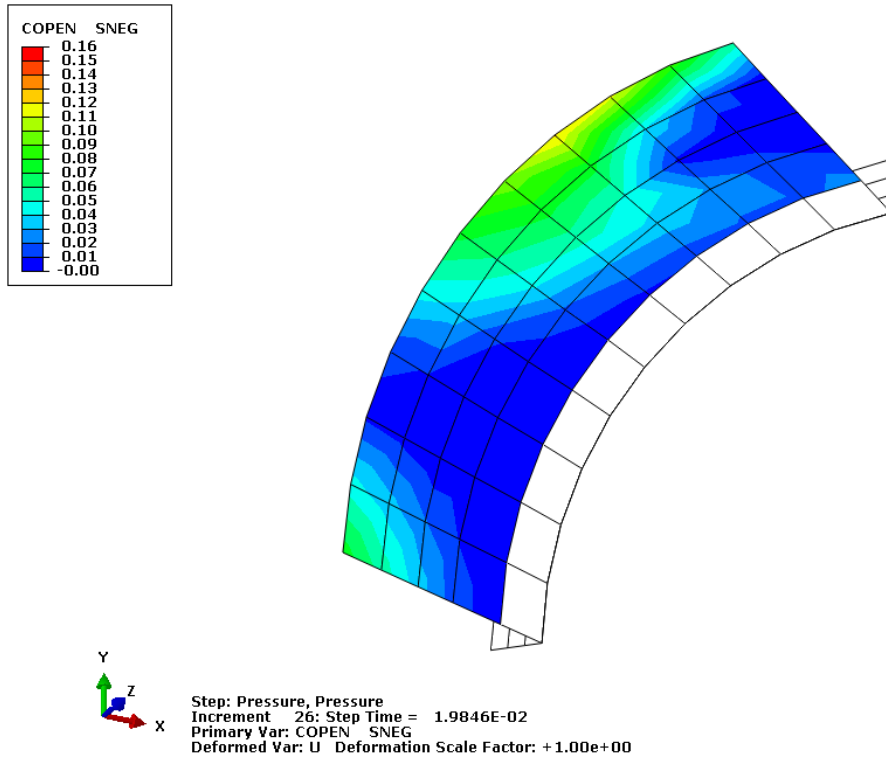


Figure D 131: Pipe Separation from Concrete (in.) at 3.47 x Pd for Model 2c

Failure prediction

The state-of-the-art for predicting tearing for steel shells comprised of plates, weld seams, stiffeners and other details, consists of two fundamental types of failure criteria:

1. strain-based failure criteria applied to unflawed steel material and components (described earlier in this tech memo);
2. fracture-based failure methods applied to postulated flaws, which are commonly found in welded steel shell structures

Both are highly relevant to PCCV liners, but both have different information requirements about the material, the strain state, and the conditions surrounding a potential crack. Failure Criteria Type 2 is more demanding in terms of information required. But for PCCVs, it may be a better predictor of “failure,” because it guides the prediction of failure size, while Criteria Type 1 does not. Further, investigation of the PCCV’s welding records show that weld flaws were prevalent.

Fractures are possible, and strain conditions sufficient to cause fracture, occur at potentially hundreds of locations. It would be inconceivable to analyze all possible locations. What is needed is an approximate procedure, or “transfer function”, for correlating J-based fracture prediction to strains in the PCCV Liner. The following outlines such a procedure. Ultimately, this also leads to prediction of liner tear lengths and opening areas versus strain in the liner. The final step from prediction of J for a typical “flawed” piece of liner, to prediction of specific numbers and sizes of cracks, requires the addition of a statistical assessment of the existence of flaws. This can also be done in a systematic way, but for the SPE, will not be addressed until Phase 2.

A preliminary set of detailed analyses was performed here as part of the Model 2 work, to better demonstrate development of strain-to-J-mapping, although the work has not been extended to prediction of crack size – this also will be addressed in Phase 2. The methodology requires basic understanding of calculation of the “J-Integral” shown in Figure D 132 and 133, and the concept of $J_{critical}$ as a toughness measure in the material.

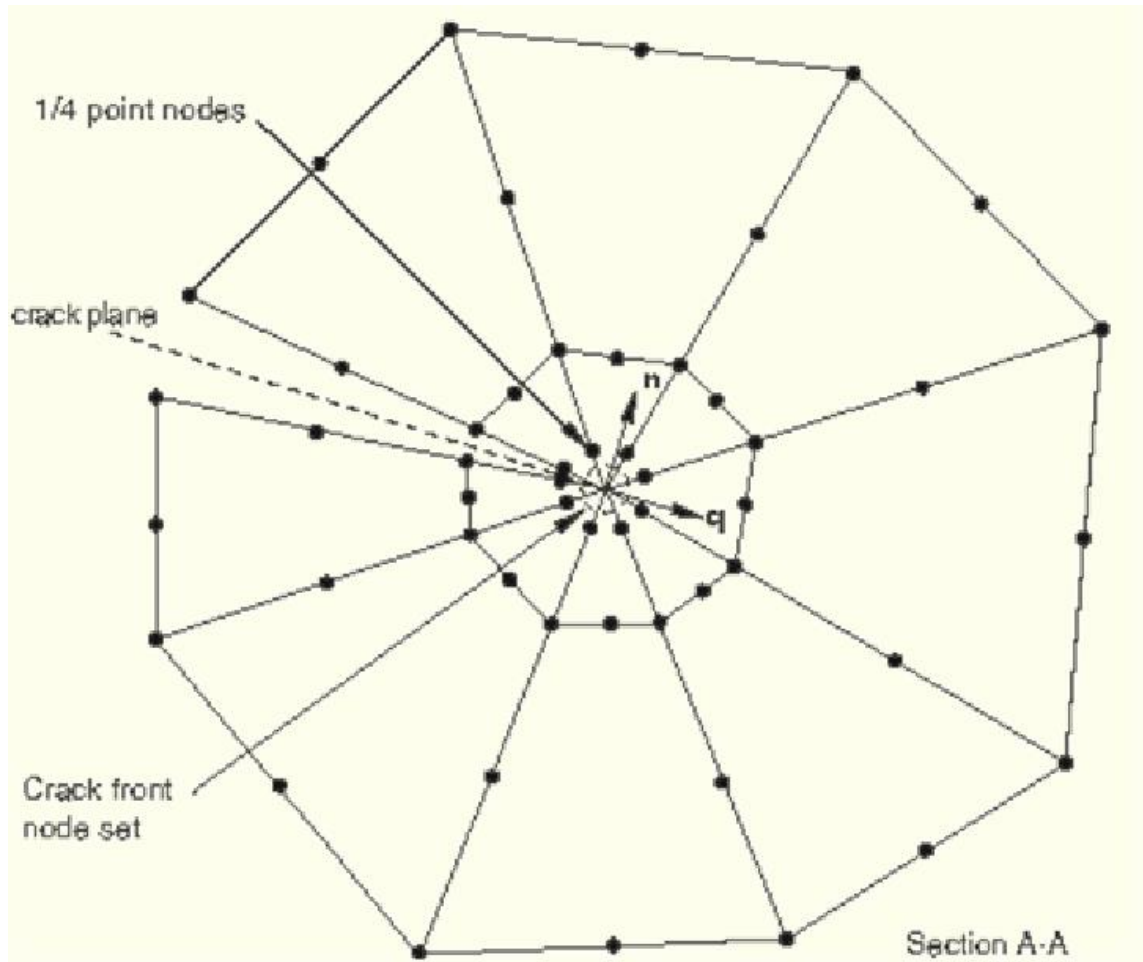


Figure D 132: Crack Modeling for Use In Strain-to-J-Mapping

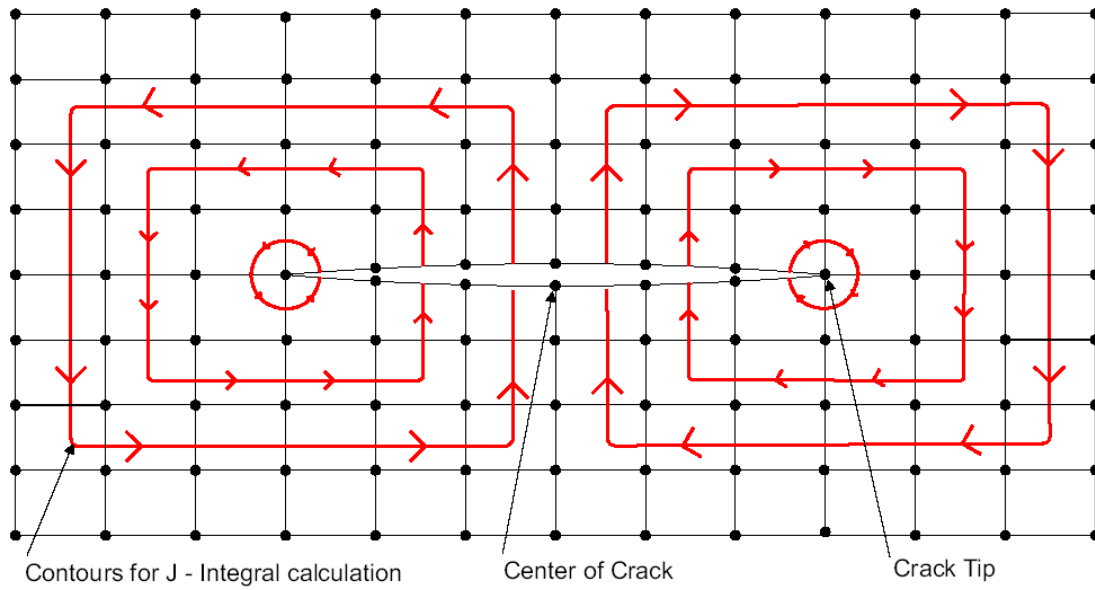


Figure D 133: Crack FE Modeling for Development of J-to-Strain-Mapping

Two fracture models have been developed as simple, separate FE models with extremely fine mesh (element size of 0.01-inch), appropriate to embedding small initial cracks into the models, calculating J-integrals, and (in Phase 2) propagating these cracks. The models developed for post-processing results of the Model 2 series are shown in Figure D 134 through 137. Guidance for selecting these models comes from the post-processing of ‘average strains’ at the locations defined in Figure D 138 through 140. These strains are shown in Figure D 141 and 142. The fracture models then consider two particular conditions where local liner strain concentrations will be particularly significant – a vertical seam weld, straddled by a horizontal stiffener, with or without presence of a vertical T-anchor. In fracture mechanics work, it is typical to assume a ‘flaw’ size that is equal to the thickness of the material (in our case 1/16”). If a single-crack tip J-integral study is performed, then the 1/16” flaw length is assigned to the crack. If a double-ended crack is used (for the sake of applying strain conditions from a continuous segment of material, then the two 1/16” crack tips are placed end to end, for a total two-ended crack of 1/8”.

The fracture submodels have a standardized length. In the case of the PCCV, it is the length between liner anchors. This length would become a gage-length for strain mapping, and it should be relatively immune to differences between analysts that occur due to mesh size in Models 2 or 3 of the SPE. It can be defined or viewed in different ways: the integration of strain from the crack to the edge of the fracture submodel, or the differential longitudinal displacement of the shell nodes in the FE model – divided by the gage length, or the integration of strain across the gage length of the FE model. Using this gage length to define a strain measure common to the fracture geometry, the fracture analysis results can be cast in terms of J versus strain.

The ‘averaged strains’ plotted in Figure D 138 through 140 are applied to the ends of the local fracture models as displacement boundary conditions versus pressure. It is interesting to note that for Model 2c (which we believe represents the best simulation of liner-concrete interaction phenomena), the largest strains are observed at Locations 6, 8, and 1. This tends to agree with

observed locations of liner distress around the E/H Region. The largest strains (Location 6) are applied to the fracture analyses. The results of the fracture analyses are shown in Figure D 141 and 142. Note that the spread of plasticity from the crack tip out into the previously non-yielded material occurs along paths at an angle between 30 and 45 degrees to the vertical line. This is not surprising since plasticity spreads according to a Mises Yield condition which in two (or three) dimensions, trends along lines of maximum octahedral shear stress.

The crack propagation threshold needs to be established, but say for example it is $J_{cr} = 350$ in-lb/in²; values such as this come from fracture toughness testing. (Typical J_{cr} values for Grade 50 ksi carbon steels can range from as low as 50-100 in-lb/in² to as high as 600-800 in-lb/in² but based on some recent work on another project, $J_{cr} = 350$ in-lb/in² was found to be a reasonable median value. (In Phase 2 of the SPE work, we will need to dig into the post-test Metallurgical studies in order to refine estimates for J_{cr} .)

With this established, the liner “failure” prediction is straight-forward. Figure D 143 shows that J_{cr} is reached when the “averaged strain” (between anchors) is 0.0028. This corresponds to a pressure of approximately 2.7 Pd (by cross referencing to Figure D 140). So applying this methodology directly to the PCCV would say that a small flaw in the liner would first begin to grow (and leak substantially) at a pressure of 2.7 Pd. The conclusion from this is similar to observations made during the PCCV testing. (In fact, the first detectable leak in the PCCV model was at 2.5 Pd, and was likely associated with a weld flaw – perhaps a lower toughness value would provide a direct explanation and tie-in to the current Model 2 result.) Such predictions for onset of tearing, AND predictions of the length of tears will be conducted in the Phase 2 work.

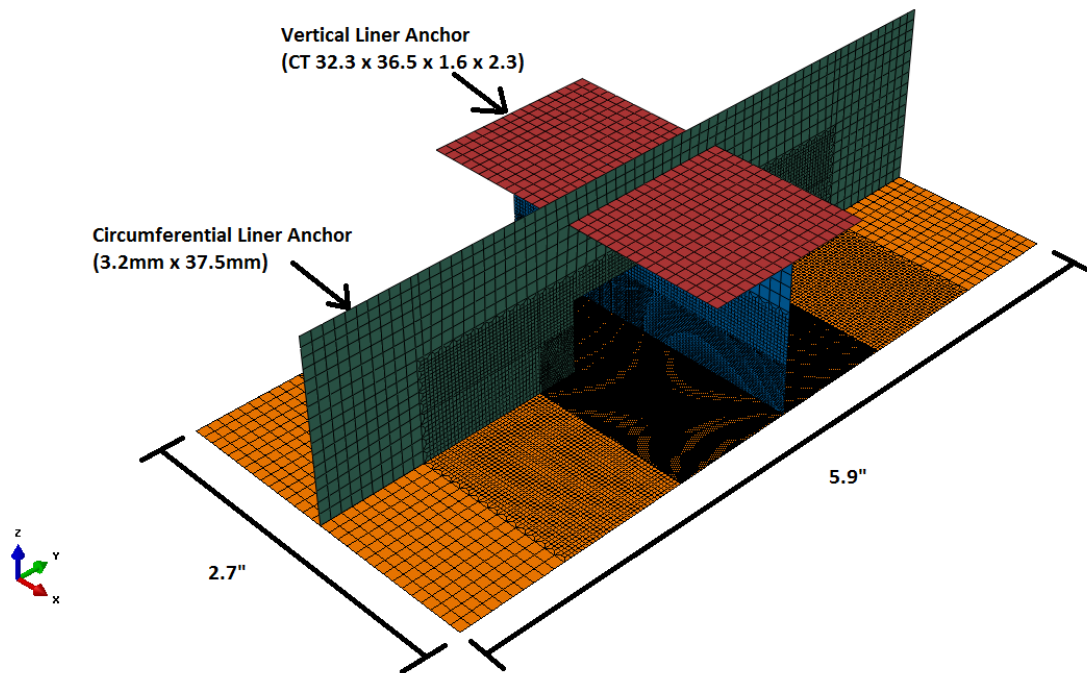


Figure D 134: Dimensions of Fracture Model 1 (Same for Fracture Model 2)

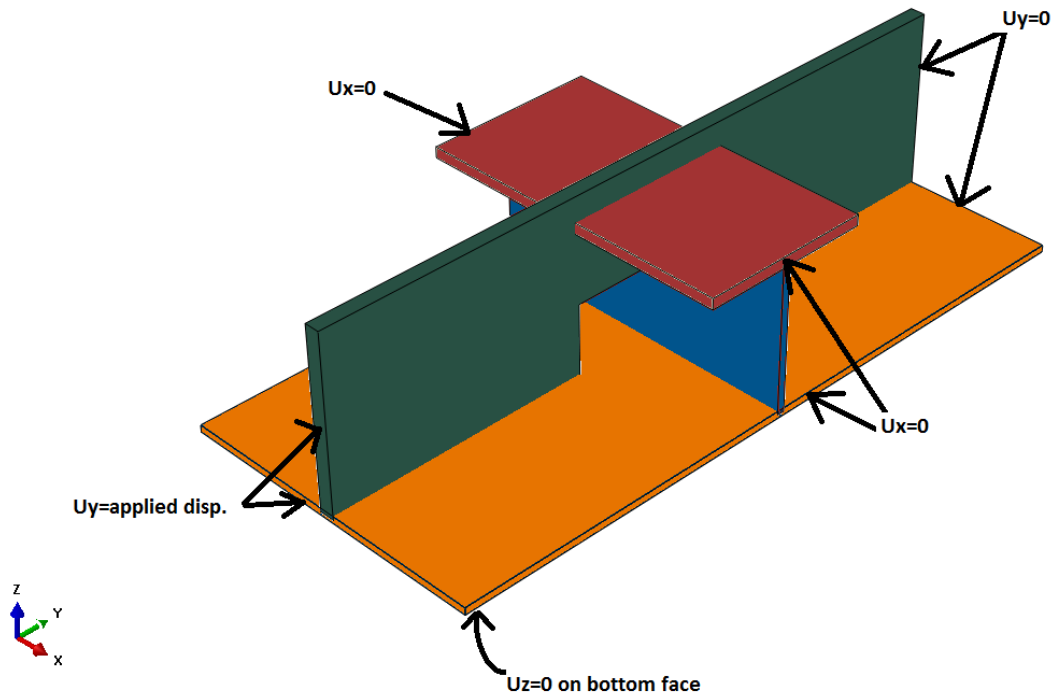


Figure D 135: Boundary Conditions Applied to Fracture Model (shell thickness rendered)

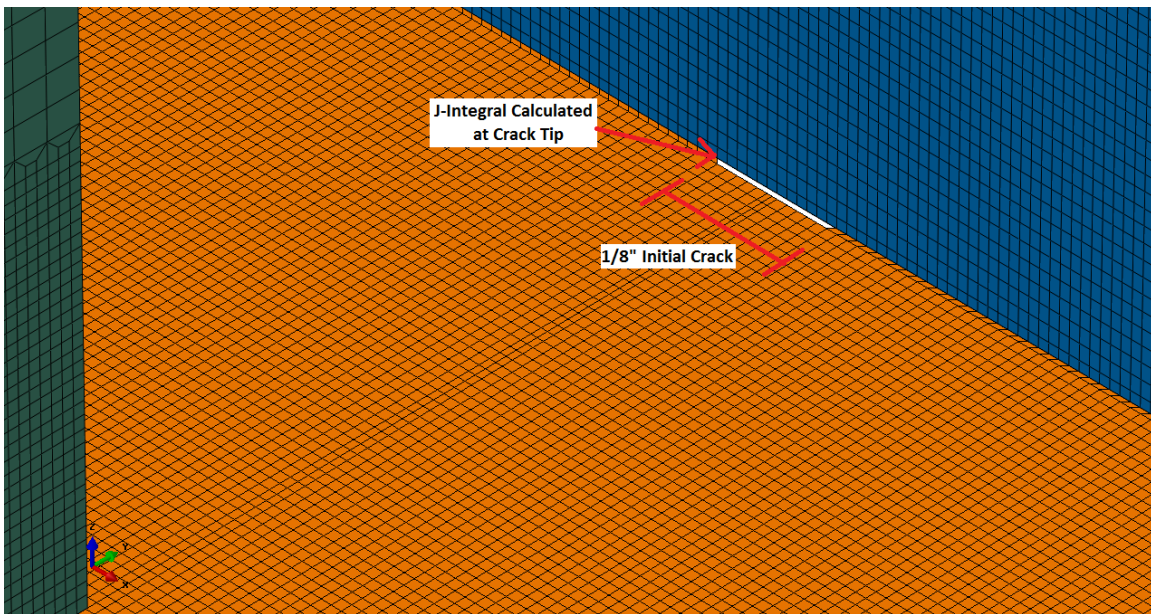


Figure D 136: Crack Size and Location on Fracture Model 1

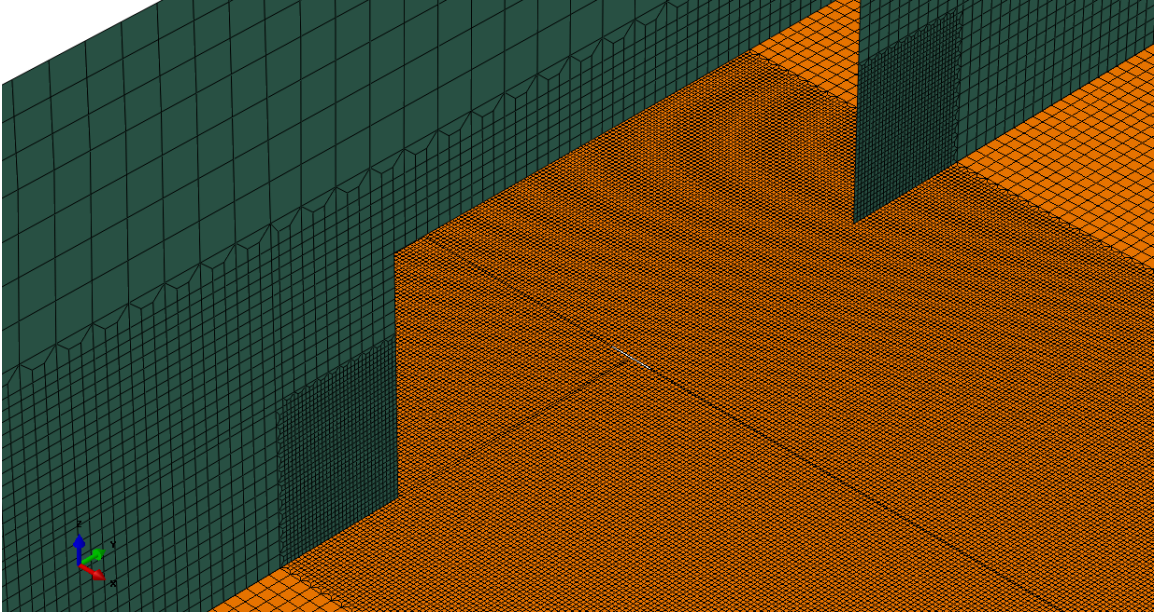


Figure D 137: Fracture Model 2 (Same as Fracture Model 1 with Vertical Liner Anchor Removed)

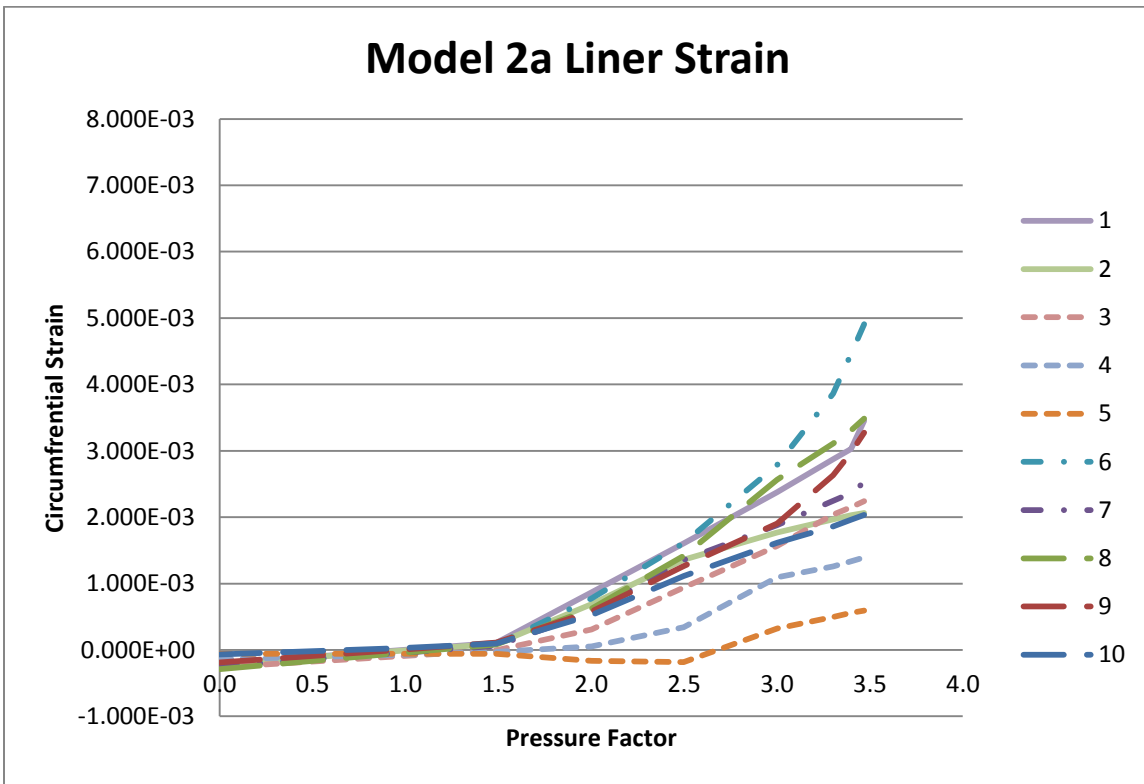


Figure D 138: Circumferential Strain at Specified Locations vs. Multiples of Design Pressure for Model 2a

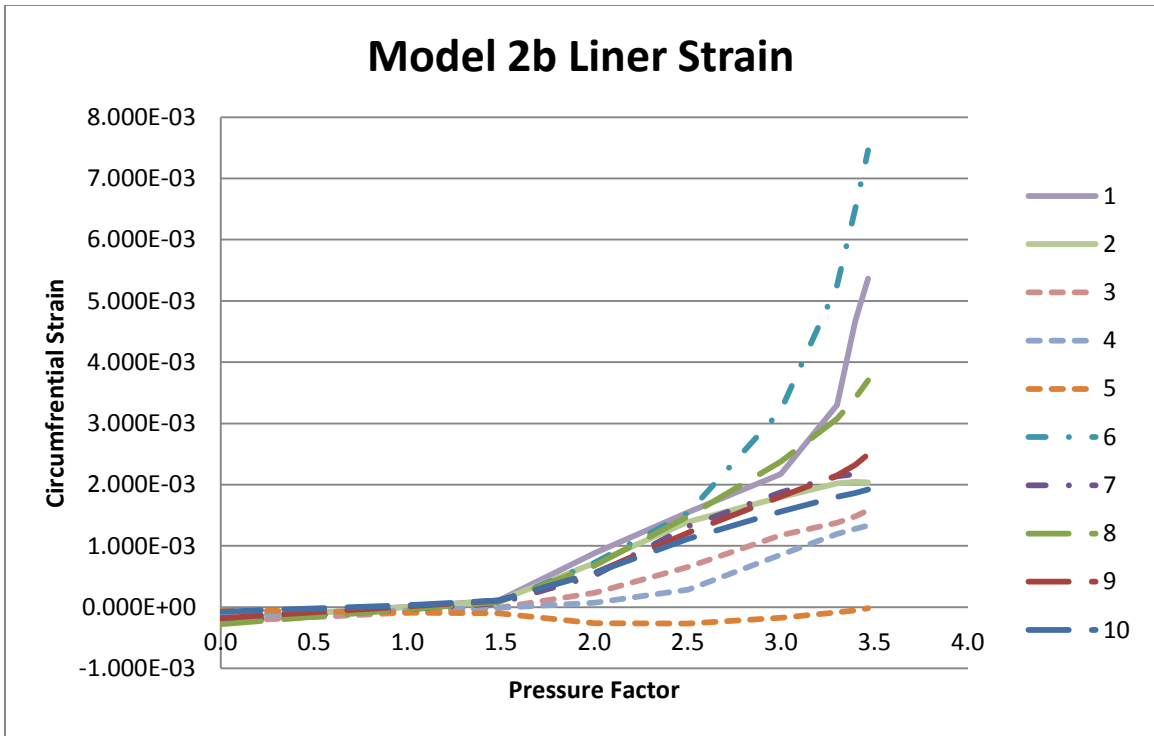


Figure D 139: Circumferential Strain at Specified Locations vs. Multiples of Design Pressure for Model 2b

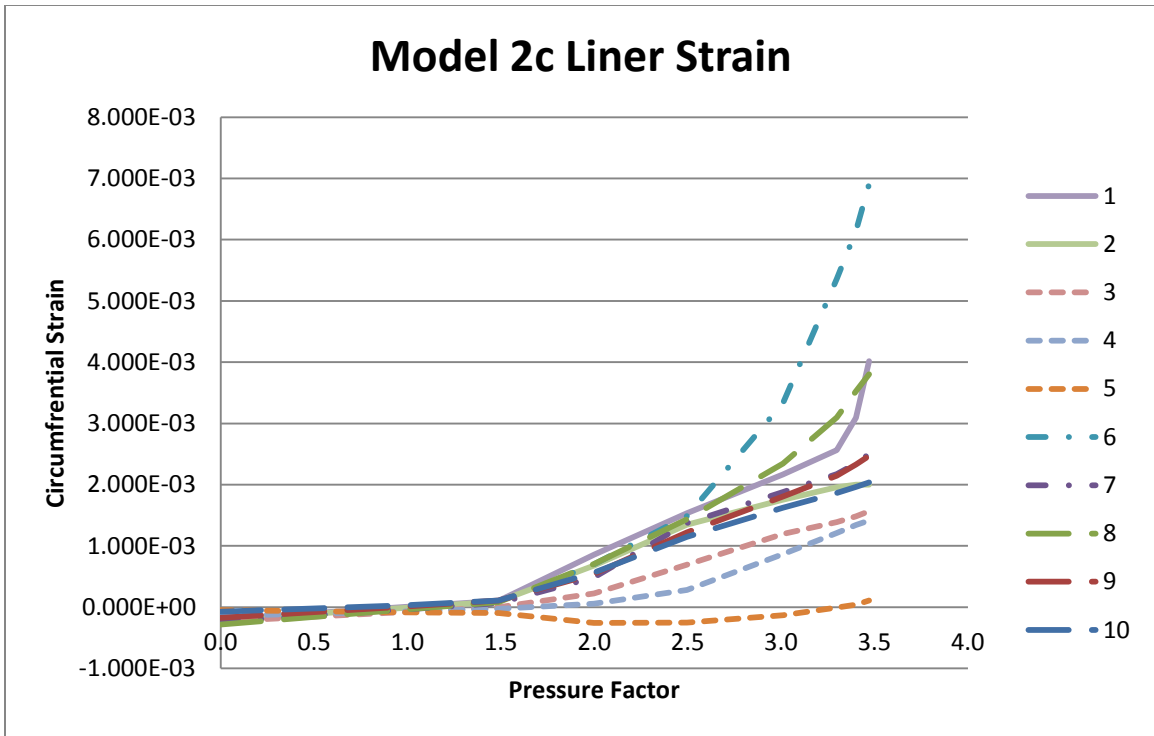


Figure D 140: Circumferential Strain at Specified Locations vs. Multiples of Design Pressure for Model 2c

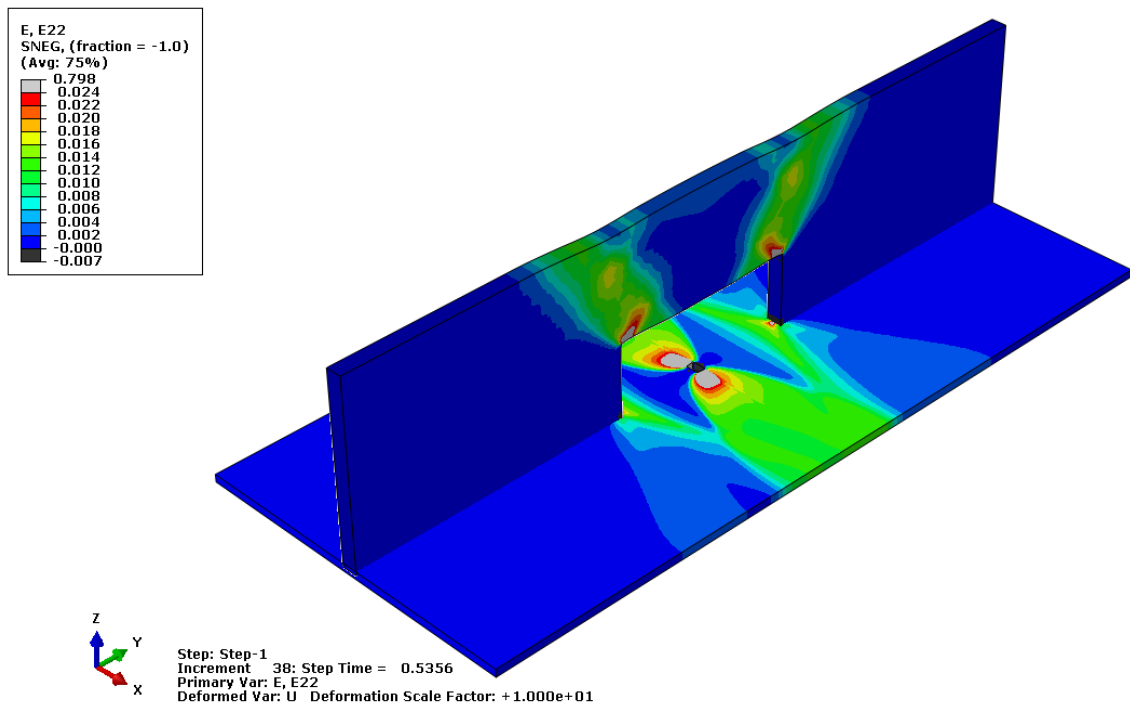


Figure D 141: Circumferential Strain in Model 1 with Average Strain of 0.00372 (Vertical Liner Anchor not Displayed for Clarity)

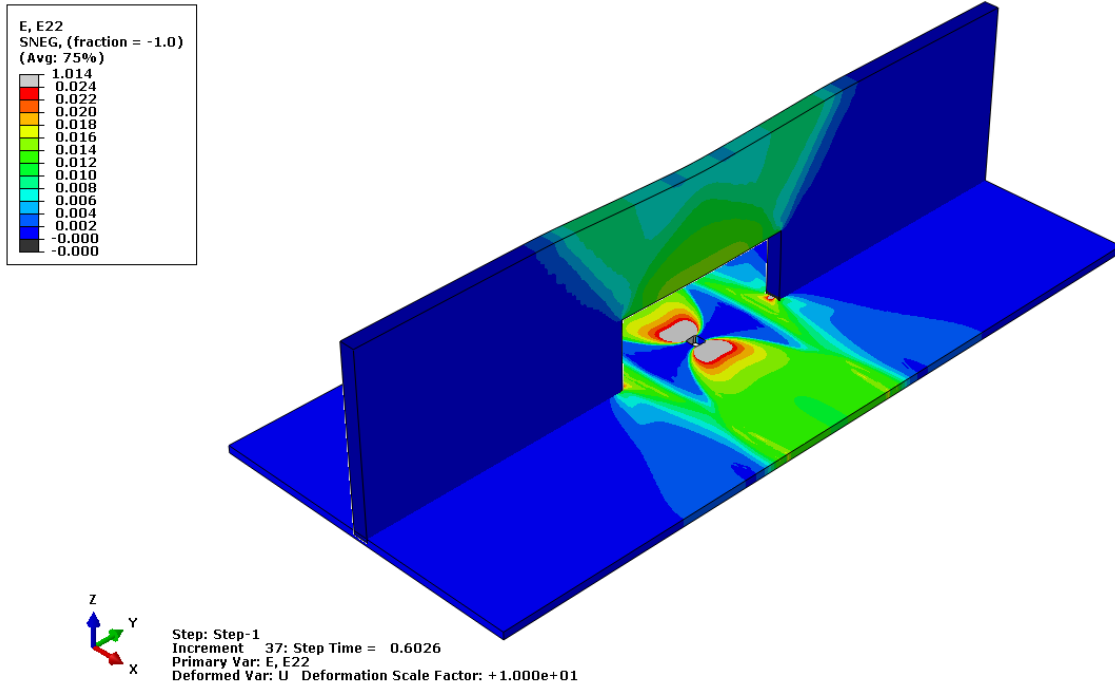


Figure D 142: Circumferential Strain in Model 2 with Average Strain of 0.00419

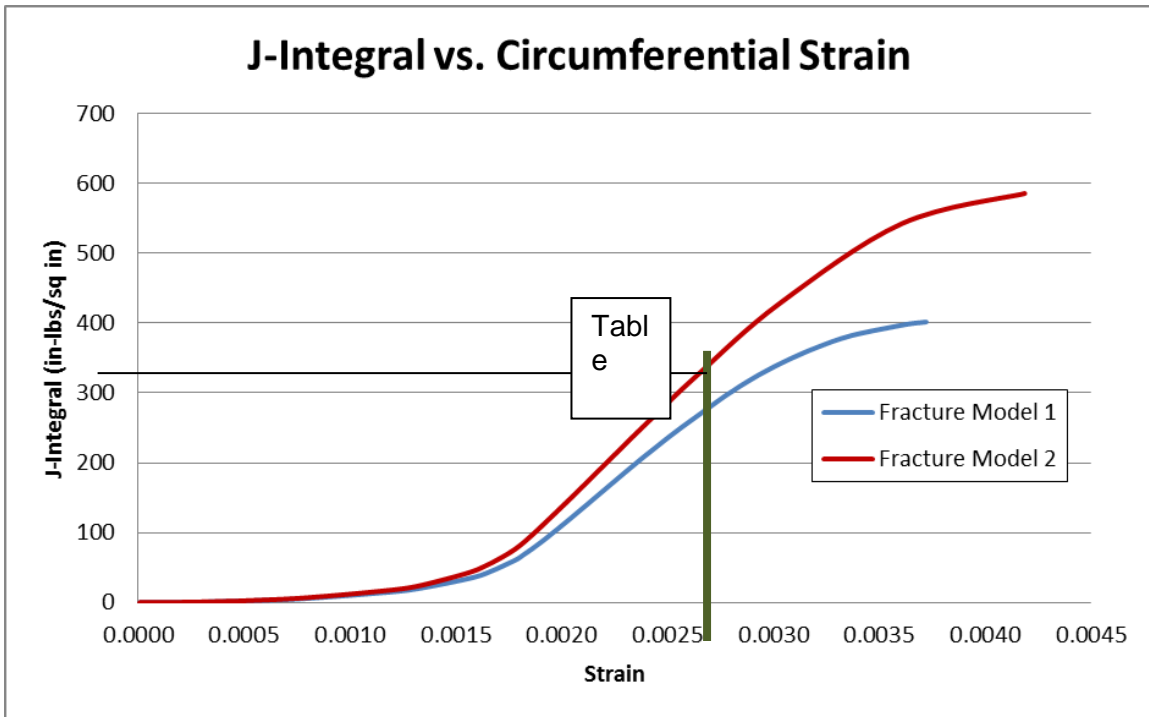


Figure D 143: J-integral vs. Circumferential Strain in Fracture Model 1 and 2

MODEL 3

This Tech Memo is third in a series following similar reports for Models 1 and 2, which studied the first two of these effects. With Model 3, a relatively detailed global 3D model, we apply lessons learned from Models 1 and 2, and to the extent possible with the larger mesh-size, continue studying all effects under consideration. The modeling assumptions, initial conditions, and analysis results are presented herein for a pressure only analysis. At this time, and in preparation for the April 13-14 Meeting, we will focus on the pressure analysis, and will address the temperature analysis at a later date.

Geometry and initial conditions

The geometry and boundary condition assumptions of Model 3 are shown in Figure D 144 through 152. The geometry is as specified in the SPE-3 problem statement, and on the drawings and NUREG/CR-6810.

The ABAQUS Standard FE program was used for the analysis as described herein. Simulation of friction and pressure-response related changes to tendon stress distribution has been included in the analysis. The model includes concrete, tendons (hoop and vertical), rebar (hoop, vertical), and liner. Shear reinforcement was not included in the model, since the structure wall was represented by shell elements. Vertical tendons and vertical rebar were included. Concrete was modeled with 4-node shell elements (for which through-wall shear response is approximated by elastic shell theory), and rebar was modeled with embedded subelements, tendons with two-node beam elements, and liner with 4-node shell elements, overlain onto the same nodes as the concrete shell nodes, but offset by the appropriate eccentric dimension.

Analytical representation of losses was handled by the FE Model's representation of friction, as described below. Every tendon was modeled, and each tendon had a "jacking element" (similar to the methodologies developed in Model 1 and Model 2) protruding from the tendon end zone.

Due to the much greater size and complexity of Model 3, the tendon-concrete interaction methodology followed in Model 1, was modified as follows. Every node of the tendons has a matching reference node that shares the same space. These reference nodes are tied to the surface of the concrete, and then transfer forces and displacements directly to the concrete. Connector elements are used to constrain the tendon nodes to the reference nodes. ABAQUS provides a selection of connector types, and the "SLOT" type has been selected. Slot connectors allow the tendon nodes to move only in one direction relative to the reference node. This direction is assigned to be the initial tangential direction along the tendon. The connector elements are able to solve for the frictional resistance by taking the force normal to the direction of motion and determine whether sticking or slipping occurs. The traction and normal forces exerted by the tendons are transferred directly to the concrete through the reference nodes.

The advantage of using slot connector elements over the contact surfaces used in Model 1 and 2 is the simplicity of the interaction. Although each connector adds to the number of elements in the model, it is much less than the elements needed to make tendon ducts as in Model 2. With simplicity come limitations however. As stated above, the tendon nodes can only move in one direction that is assigned before the analysis begins. As the tendons slip and move, the line of motion does not. With the contact surfaces, the interaction between the tendon and ducts adjusts for the new position the nodes are in for each analysis increment. For the detailed model focusing on a smaller region, this is desirable and feasible to do. For the global model

however, the assumption of small displacement theory can be anticipated to not affect the global behavior significantly. (This is a philosophy that was also followed in earlier, global pre-test and post-test analysis of the 1:4 Scale PCCV.)

Figure D 144 shows the general outline of the Model 3 FE Mesh. The wall-base juncture occurs at the correct location, geometrically, but since shell elements are aligned with mid-thicknesses of structural elements, wall-base juncture is separated by half the thickness of the basemat. This juncture is appropriately tied with translational and rotational constraints (“rigid links” as shown in Figure D 148). Figure D 145 and 146 show the actual element mesh, including color coding of different rebar mesh densities. Figure D 147 shows the Equipment Hatch thickness assigned to each element by the ABAQUS mesh generator.

Figure D 149 and 150 show the tendon “jacking elements” (or “nubs”) employed in the model. These elements have elastic properties, and all of the prestressing is applied through these elements by applying temperature contraction to them. Then the stresses distribute all the way around the vessel in the tendons (during solution equilibrium iterations), similar to how the ‘real world’ tendons are stressed. During the prestressing step, the ends of the jacking elements are rigid-linked to the nearest concrete node. More than a dozen different schemes jacking, anchor set, and nodal connectivity were attempted over a period of several weeks before one that was deemed satisfactory was finalized. The analysis sequence simulation for tendon jacking is illustrated in Figure D 151 through 153, and the steps are as described on pages D 122 through D 124.

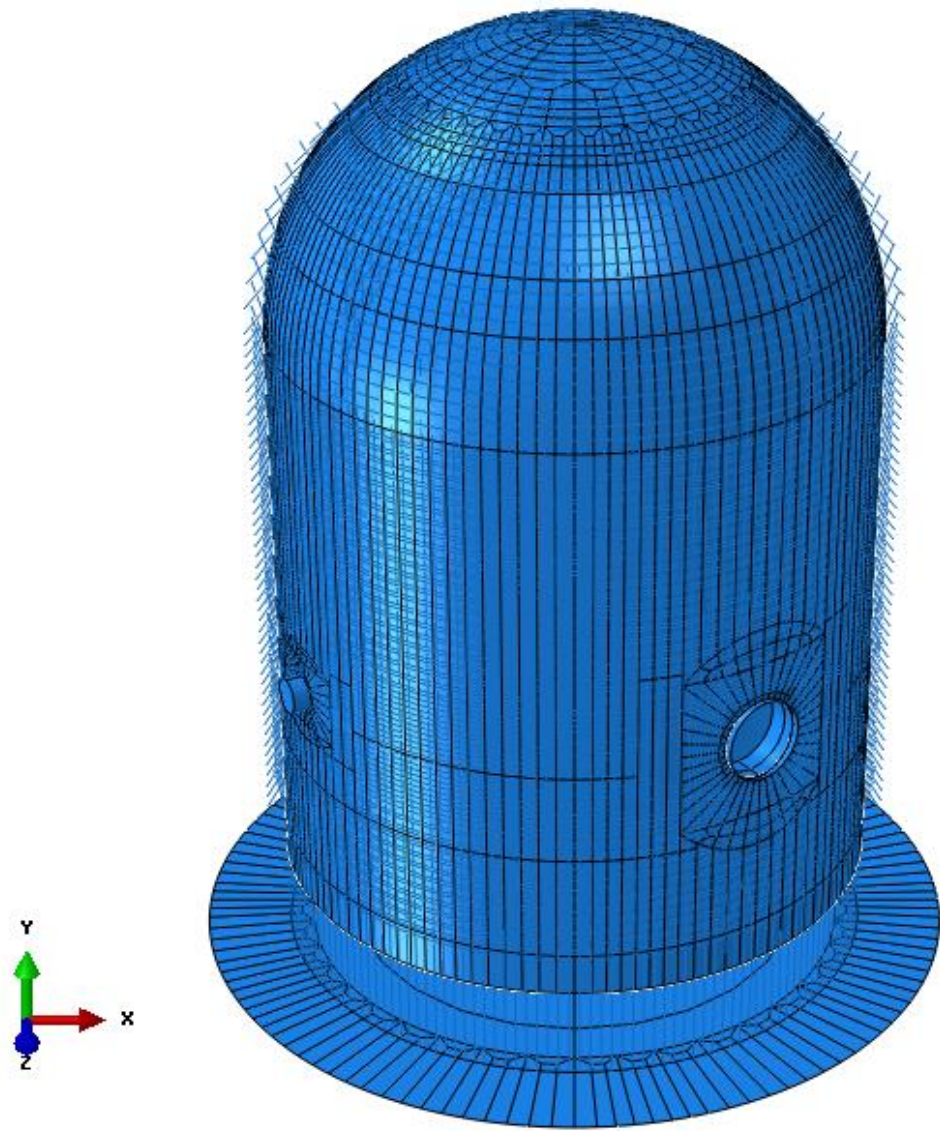


Figure D 144: Model 3 Overview

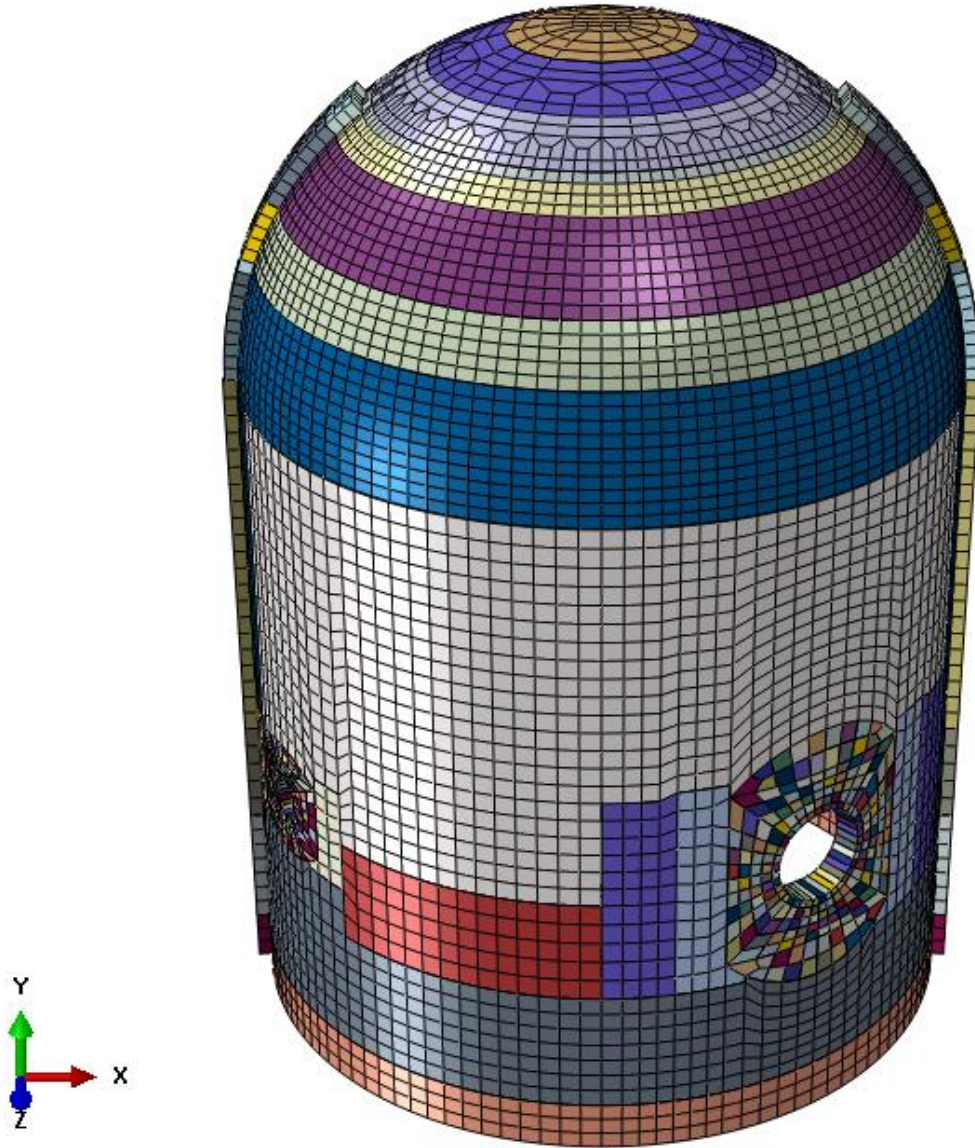


Figure D 145: Meshed Concrete Vessel with Various Section Assignments. Variations due to Rebar Layers and Concrete Thickness. Thickness of Shell Element Rendered in Abaqus.

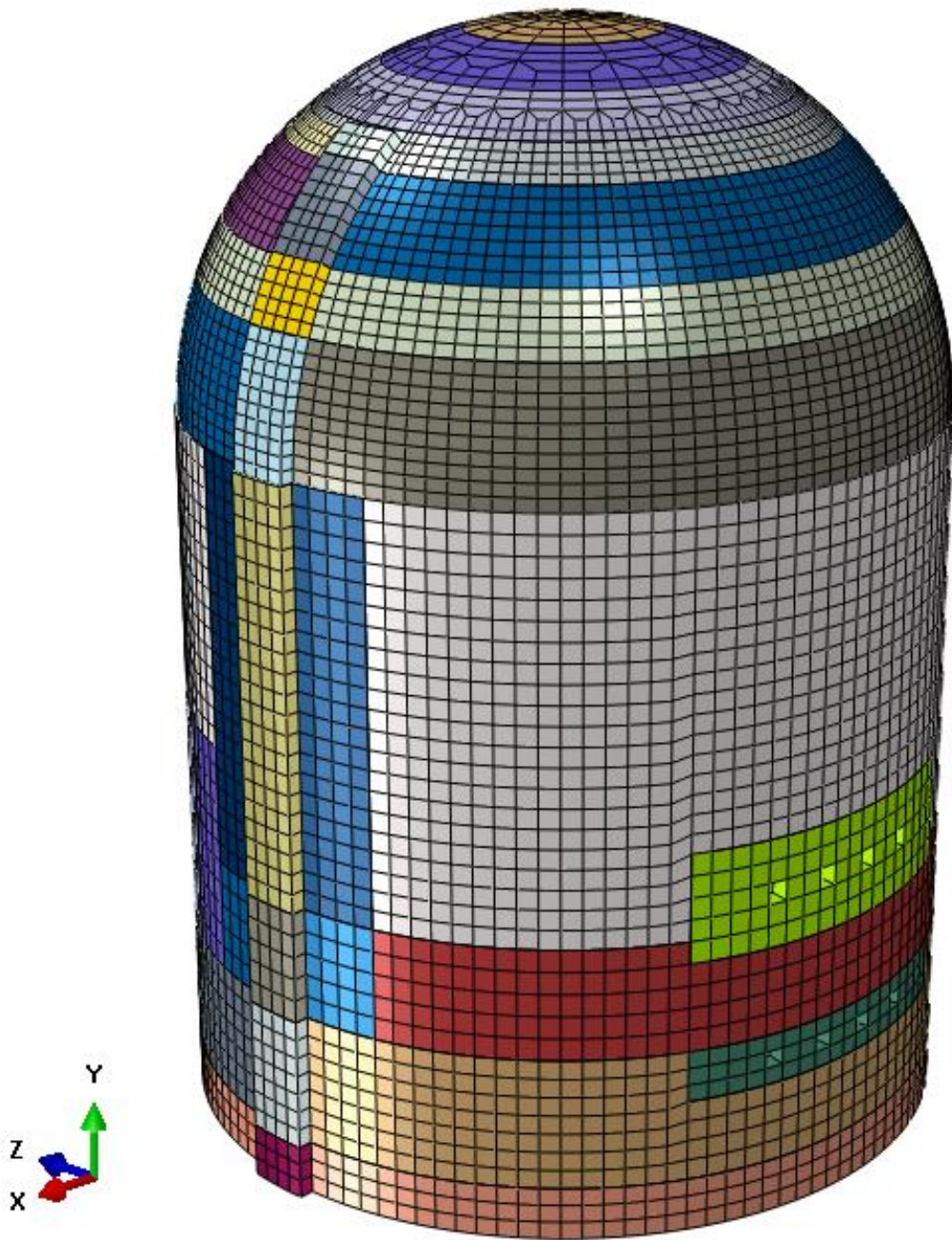


Figure D 146: Meshed Concrete Vessel with Various Section Assignments. View of M/S and F/W

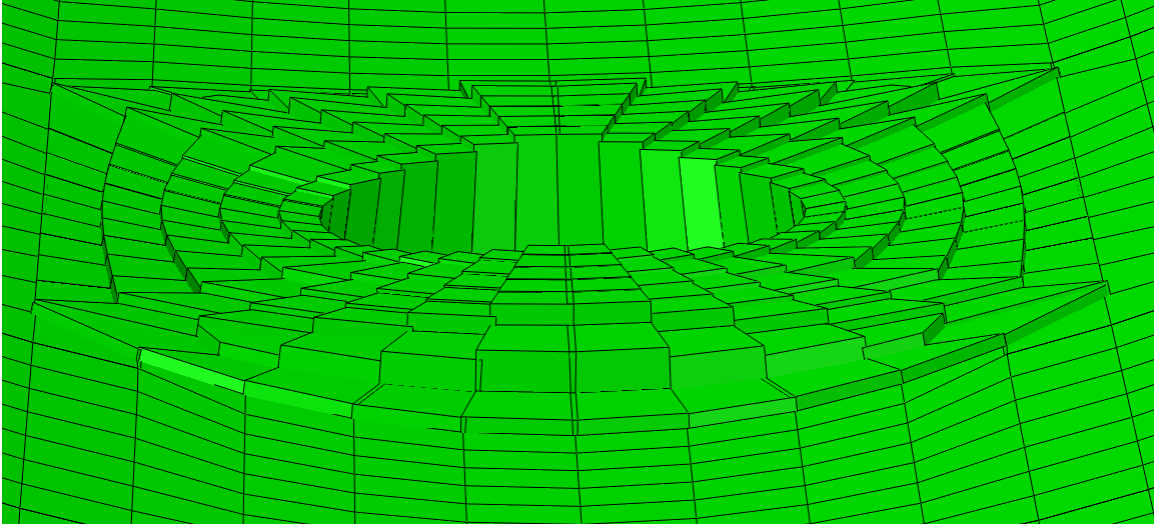


Figure D 147: Equipment Hatch Thickness Assigned to Center of Each Element. Air Lock Similar

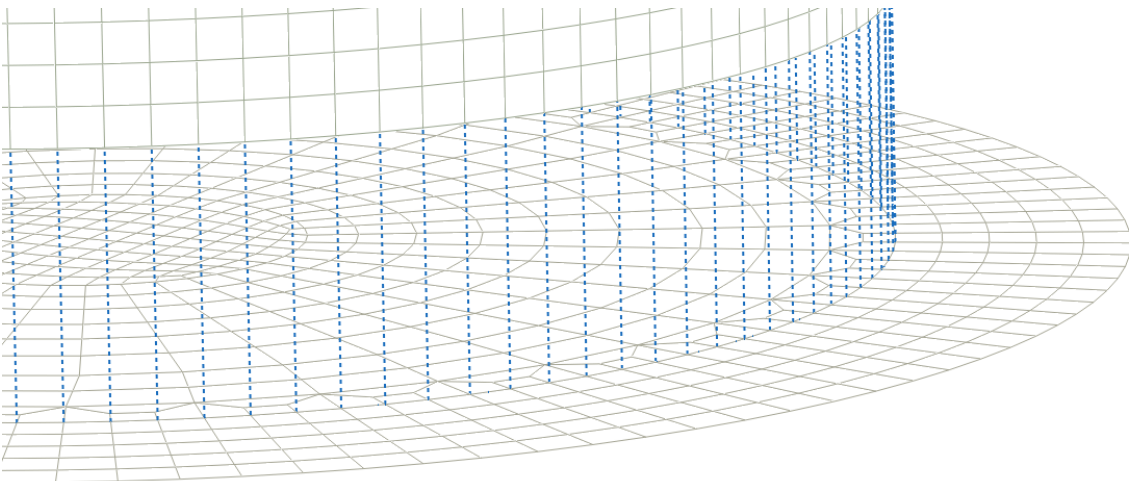


Figure D 148: Rigid links from Bottom of Vessel to Basemat Elements

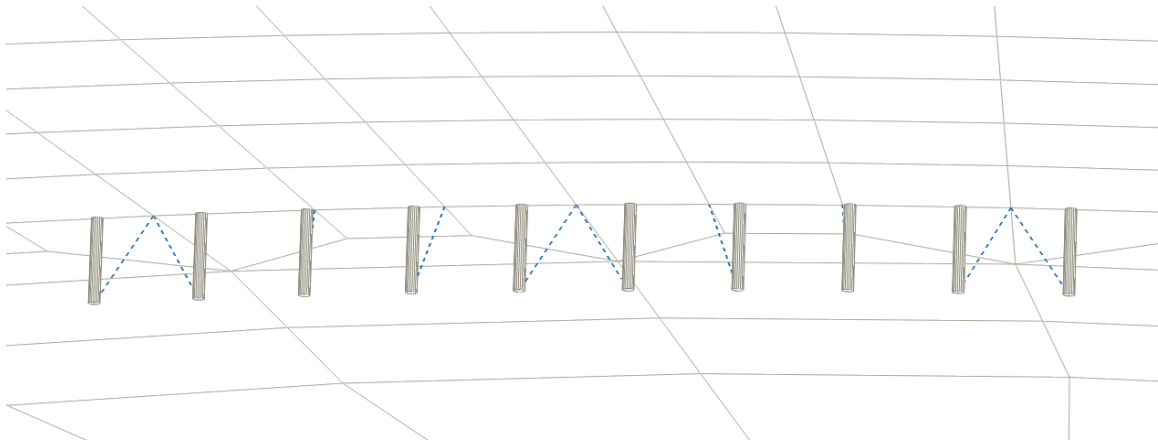


Figure D 149: Vertical Tendon Jacking Element Ends Rigid Linked to Closest Basemat Node

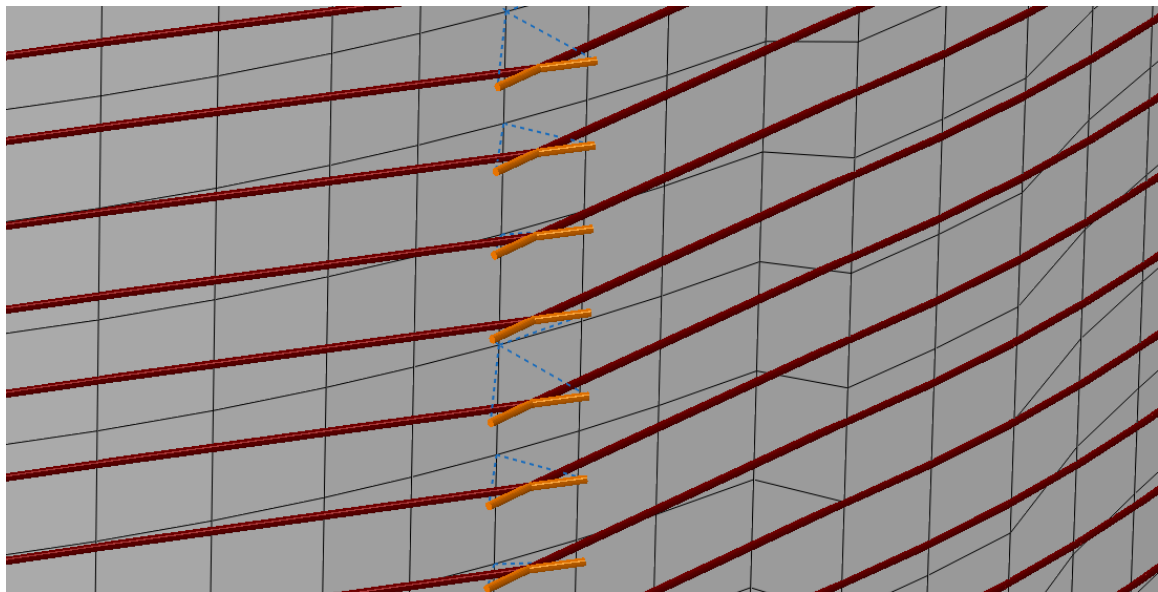


Figure D 150: Hoop Tendon Jacking Element Ends Tied to Closest Buttress Center Node

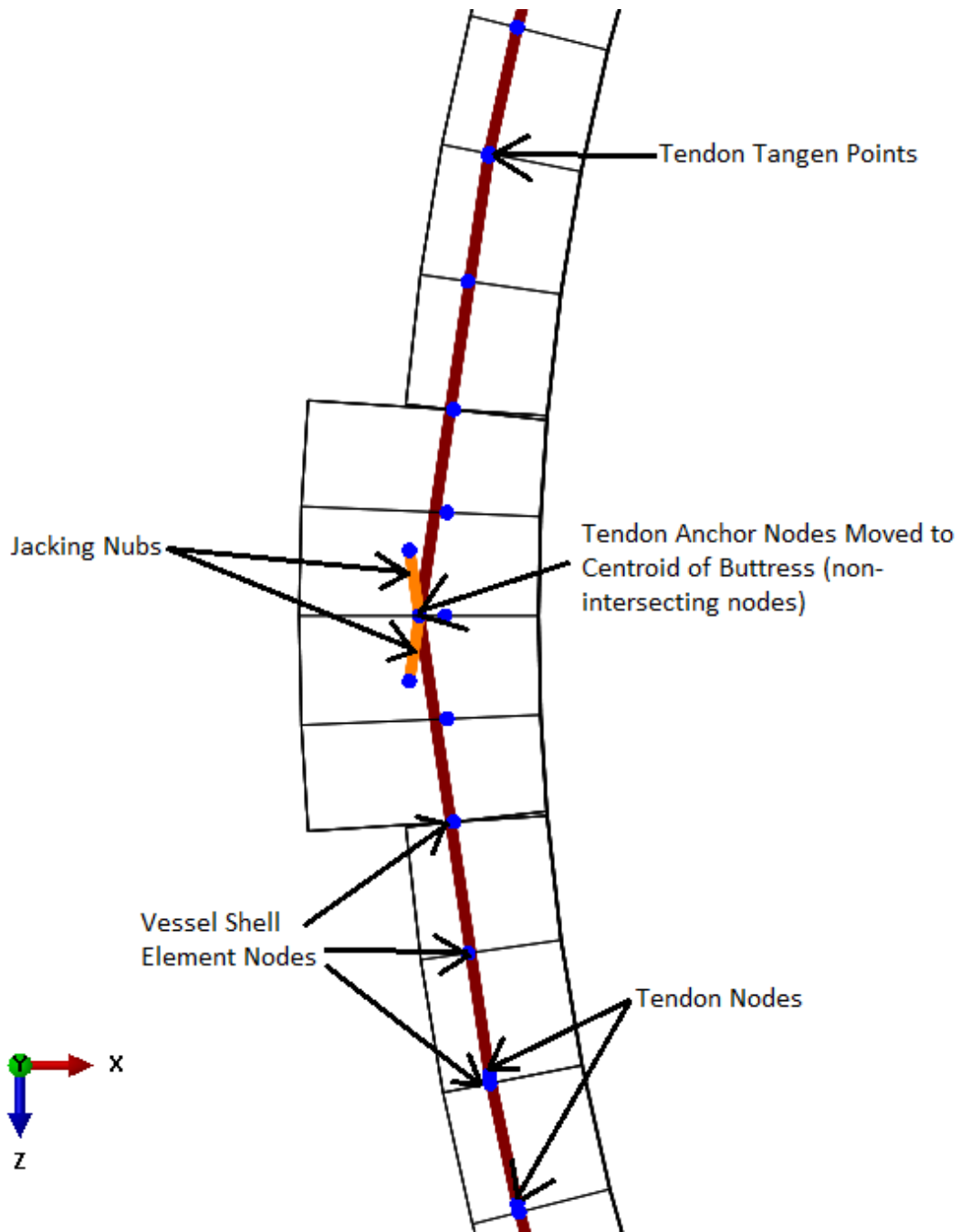


Figure D 151: Hoop Tendon Jacking Elements (“nubs”) and Tendon Nodes Shown Relative to Concrete

Nodes in the Buttress Region

(Figure D 151) the outer ends of the jacking elements “nubs” are mathematically “tied” to a concrete node in the center of the buttress; the limitations of shell element representation of the buttress zone caused problems and unrealistic behavior when these nodes were tied to the exterior buttress nodes (because in fact, no node exists at the exact, exterior jack location). It

was also found optimal, to slightly adjust the path of the tendon end to intersect the centroid of the buttress shell elements. The next tendon nodes moving inward from the ends are 1) located at the center of the buttress (when the tendon is in the undeformed position), and 2) at the tendon “tangent” point, i.e., when the tendon (as-built in the structure) begins its curvature around the concrete cylinder. This node is the first point where the “SLOT” constraints with friction begin;

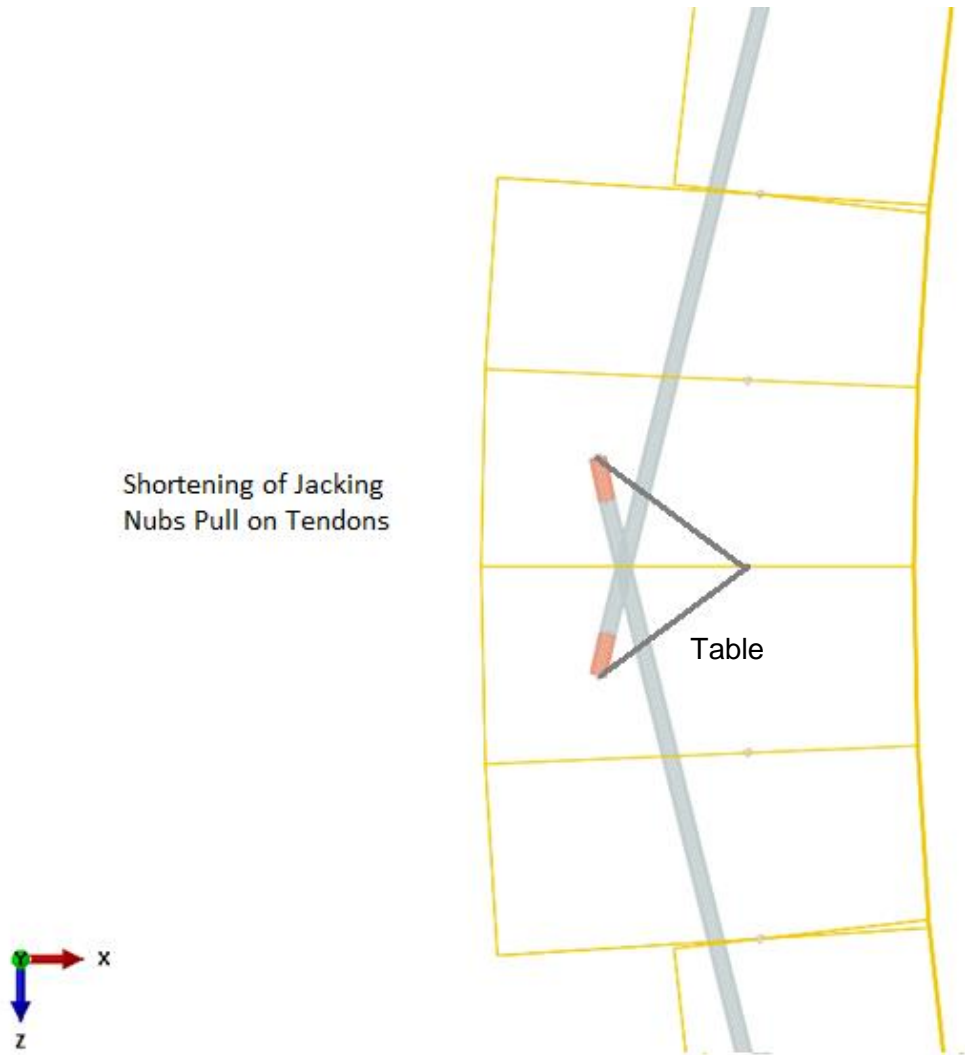


Figure D 152: Deformed Shape of Hoop Tendon Anchor System After “Jacking Loading Step”

At the end of the jacking solution step (Figure D 152), the anchor-set step is conducted. Within this solution step, the ties from the ends of the “nubs” are removed, the tendon “nub” elements are removed, and new ties (in the deformed position) are “birthed” between the new tendon-ends and the center node of the concrete buttress. The final configuration at the end of anchoring is shown in Figure D 153 This procedure is quite analogous to what occurs during

construction. The tendon “nub” is the part of the tendon that is pulled out beyond the face of the concrete and essentially no longer exists for purposes of the completed structure (and in fact in some prestressing applications, it is simply cut off).

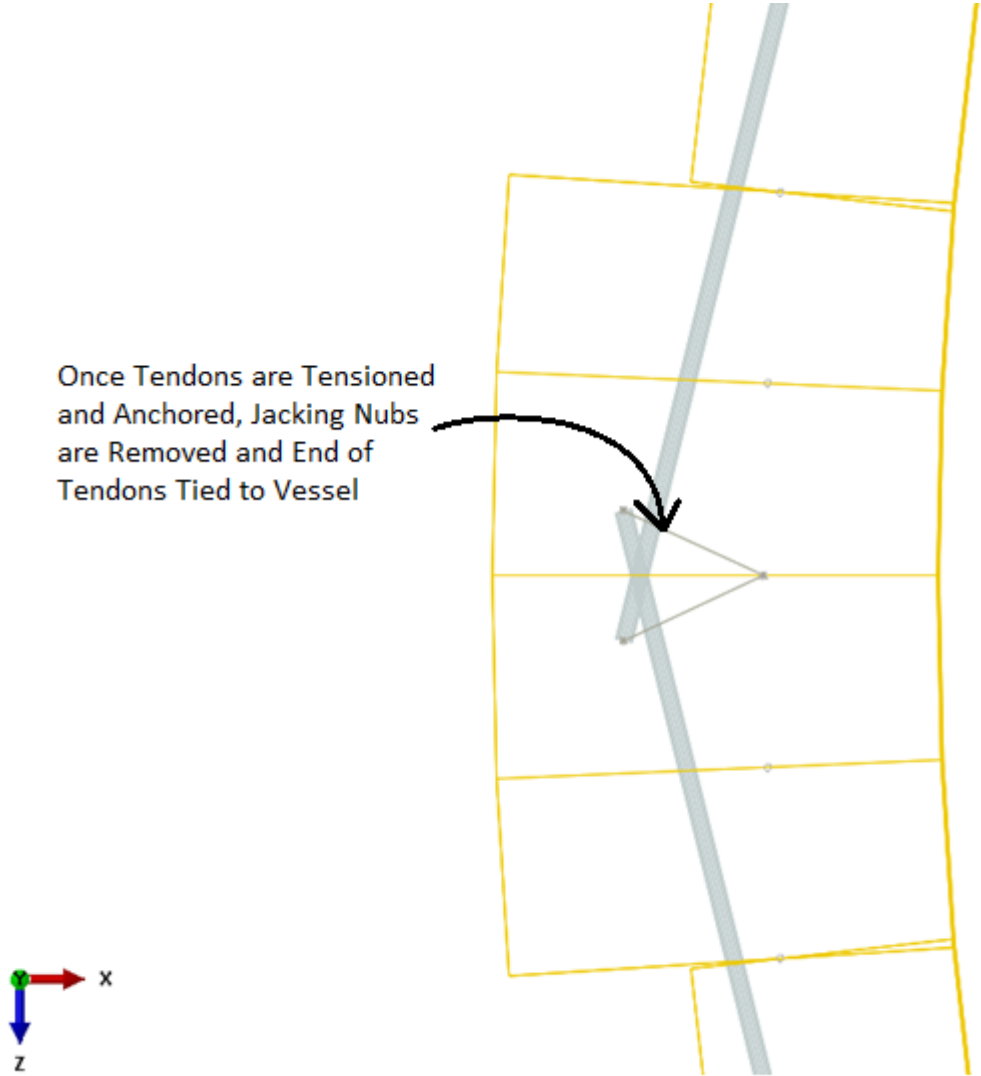


Figure D 153: Deformed Shape of Hoop Tendon System After “Anchor Set Step”

Figure D 154 and 155 show the Hoop and Vertical Tendon Layout. Every tendon was modeled in Model 3.

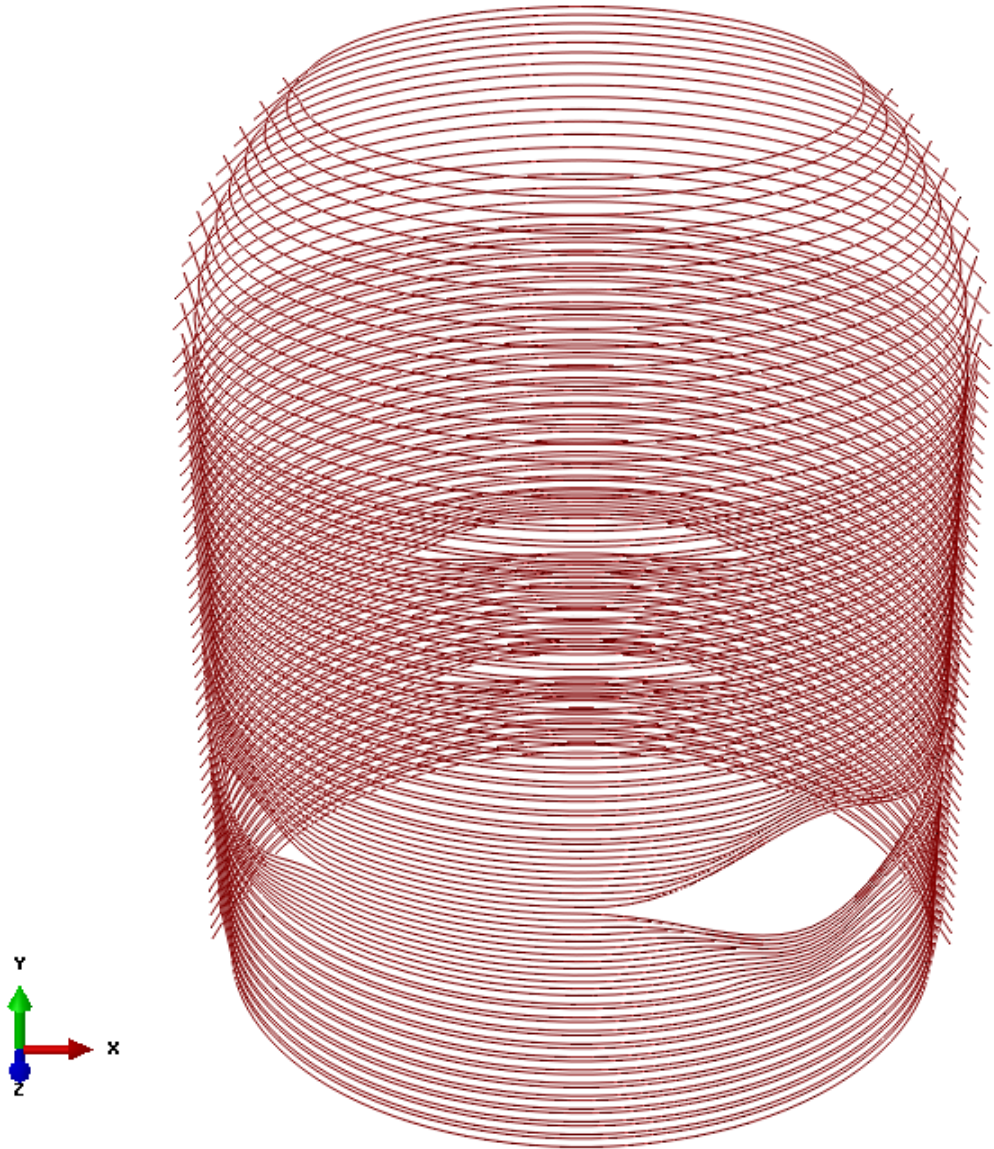


Figure D 154:Hoop tendon layout

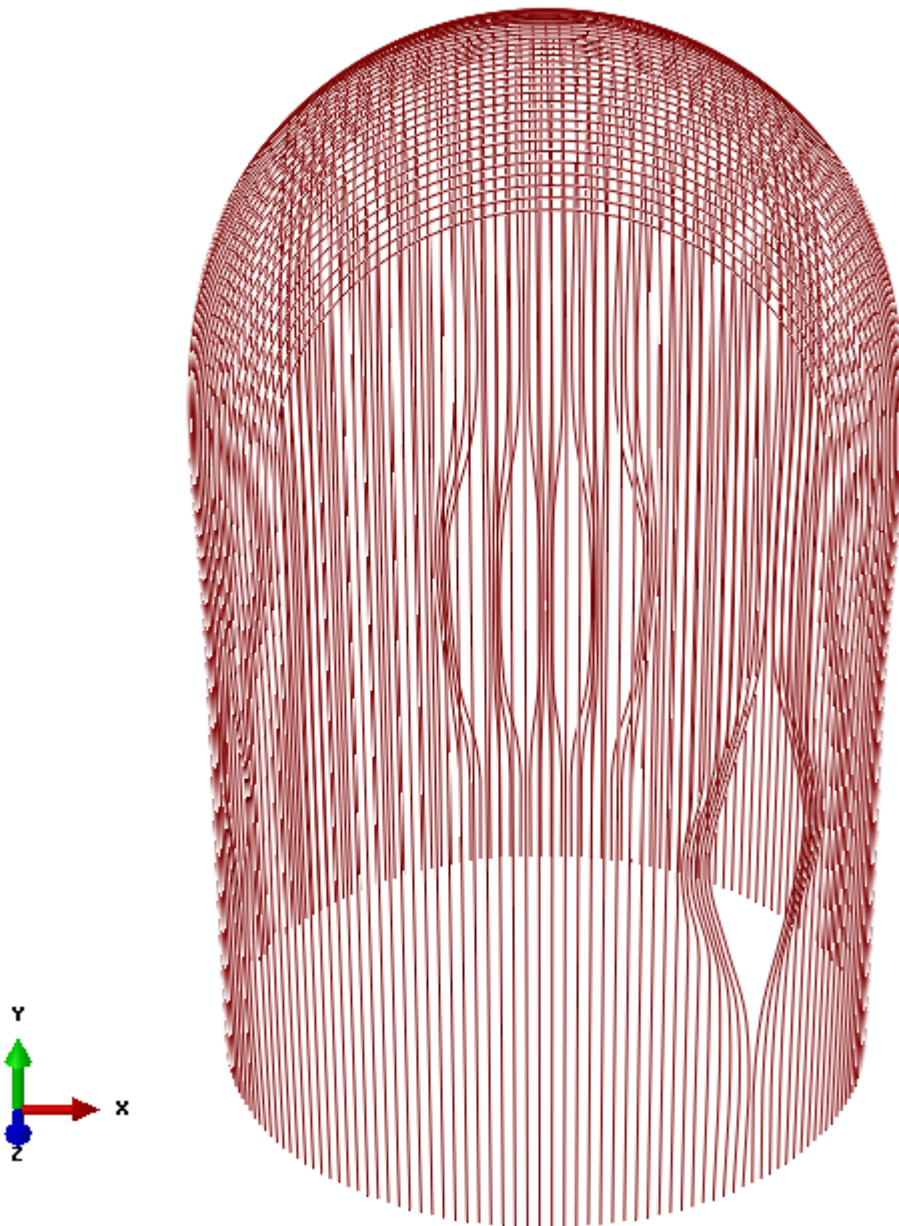


Figure D 155: Vertical tendon layout

In the PCCV 1:4 scale model, many liner strain gages showed elevated strains, and a number of tears were observed after the LST (as shown in Figure D 156 and 157). These strain gages (and possibly others), and the existence of tears #1 through #16 are important to the SPE studies. In the SFMT, stress/strain concentration locations were observed to occur along the vertical line in the vicinity of 0-degree to 6-degree azimuth which corresponds to a “step-down” reduction in the steel area of the circumferential rebar. For this reason, it is important to represent the rebar areas in significant detail.

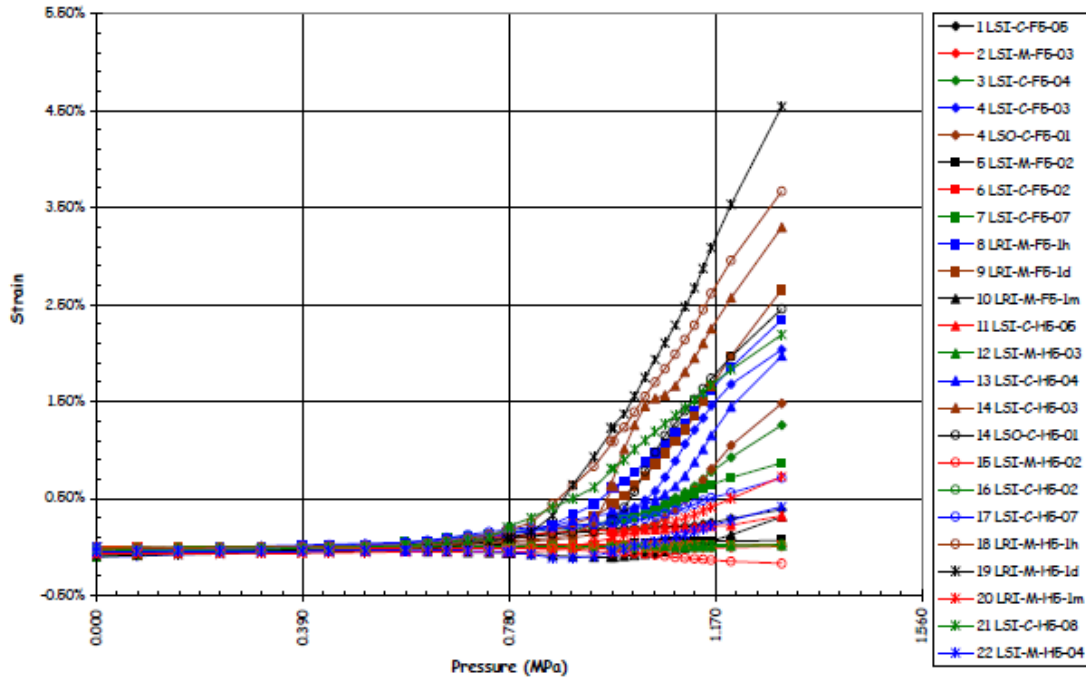


Figure D 156: Liner Strains (DOR) at M/S (Ref. D-SN-P-220)

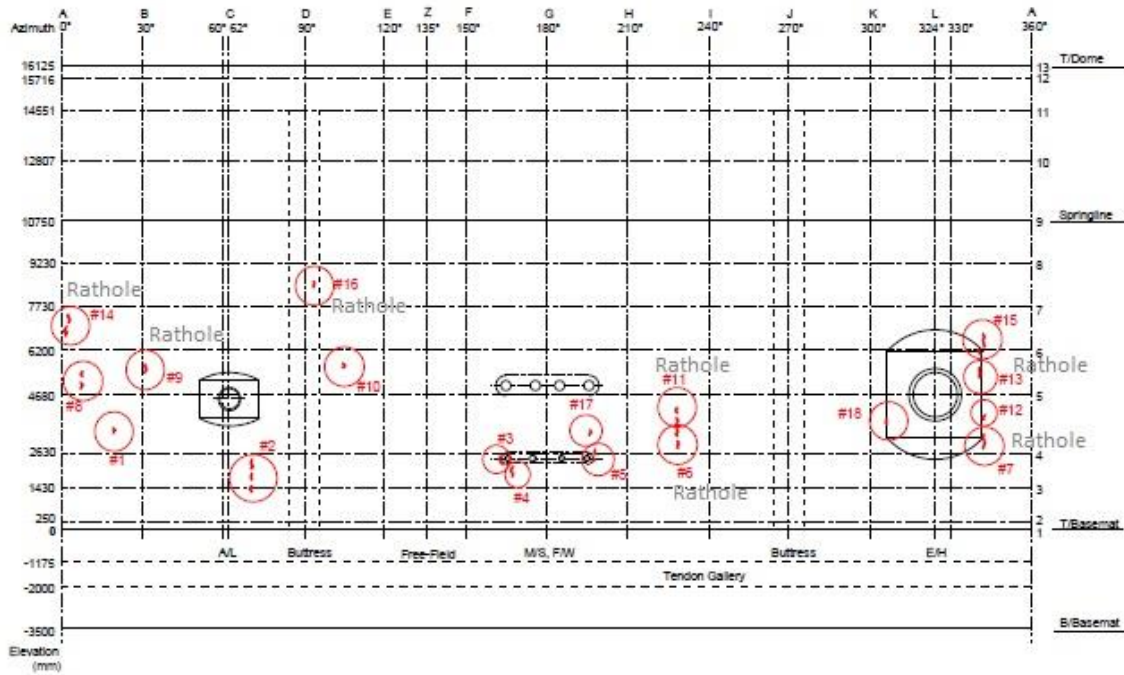


Figure D 157: 1:4 Scale PCCV Observed Liner Tear Locations

Table D 7: Tendon Stress Distribution for Standard Tendon Behavior Analysis (Includes Seating Losses and Assumed Linearly Varying with Azimuth In-Between Points)

Azimuth	Force (Newton)
355	334,625
315	381,526
270	323,648
180	230,512
90	323,648
45	381,526
5	334,625
-5	334,292

A detailed calculation of tendon initial stress versus azimuth (including angular friction, wobble friction, and seating loss) was performed, with results shown in Table D 1 and Figure D 158. This was the target stress distribution used in the Model 1 and Model 2 analysis.

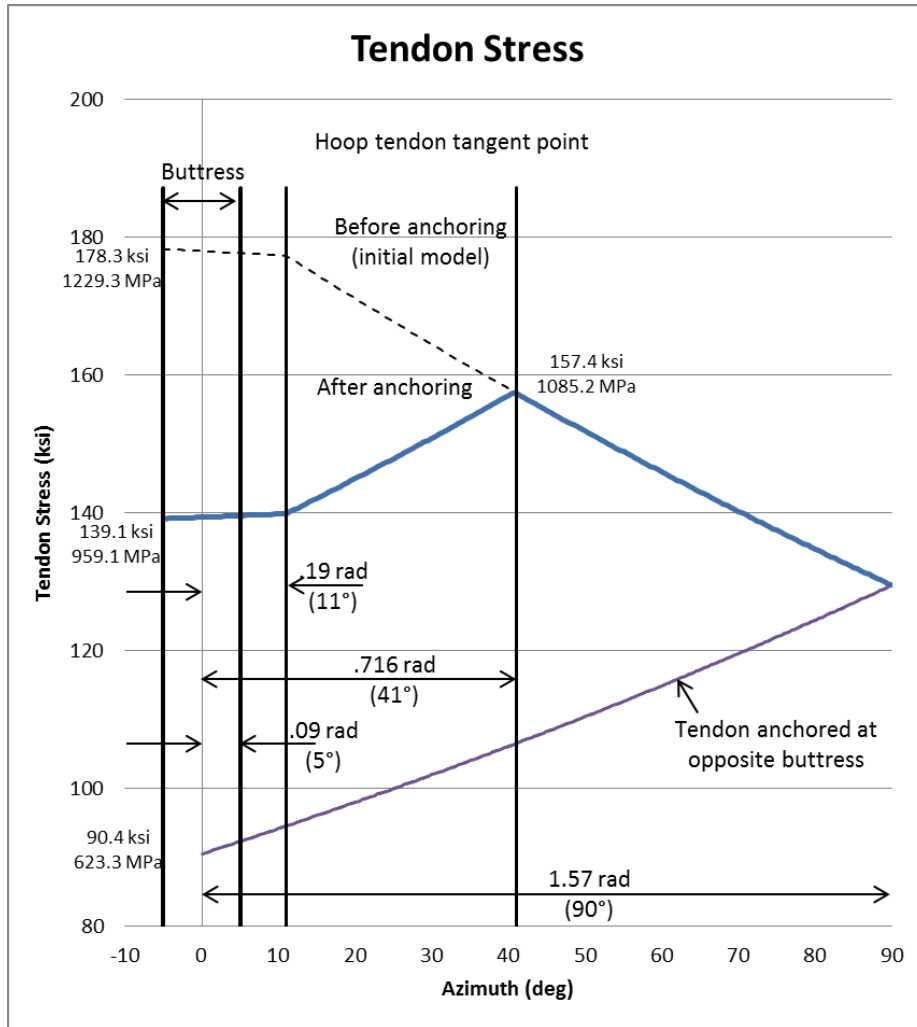


Figure D 158: Additional Information About Tendon Friction and Seating Losses

Material modeling

Tendon, rebar, and concrete material stress-strain assumptions were implemented which follow the stress-strain curves tabulated in Appendix 1 of NUREG/CR-6810. Concrete was simulated using the ABAQUS concrete “Damaged Plasticity” constitutive model. This model utilizes a smeared-cracking formulation in tension (where cracking occurs at the element integration points), and a compressive plasticity theory. Steel elements were simulated using ABAQUS Standard Plasticity. The stress-strain inputs to these models consist of effective stress (Mises) and effective strain. The inputs are taken directly from the SPE Appendices, and are shown in our Model 1 report, so are not repeated here.

Failure criteria

The relevant failure criteria for Model 1 was Tendon failure. The rebar generally has higher ductility than the tendons, so it is not the controlling criteria. Model 1 was not focused on liner tear / leakage. For Model 2, Tendon Failure criteria remains at 3.8% strain as for Model 1. But Model 2 is also focused on liner tear and leakage.

The steel material model used is an incremental plasticity model, i.e., an "incremental" theory where the mechanical strain rate is decomposed into elastic and a plastic (inelastic) parts. A key characteristic in this formulation is the yield surface, which is used to determine if the material responds purely elastically at a particular state of stress. We are using the Mises yield surface to define isotropic yielding. This is appropriate for all but the most extreme scenarios, e.g., sheet metal forming or welding, where the Hill yield surface (anisotropic yielding) or a porous metal plasticity model may be more appropriate.

Another important term is the flow rule, which in our case is associated plastic flow. Therefore, as yielding occurs, the inelastic deformation rate is in the direction of the normal to the yield surface (plastic deformation is volume invariant). The third aspect is the evolution law that defines how the yield and/or flow definitions change during inelastic deformation. We are using an isotropic hardening law, i.e., the yield surface changes size uniformly in all directions as plastic straining occurs. A Stress vs. Strain curve is input to the program, but how it is implemented is not Uniaxial Stress vs. Uniaxial Strain, rather it is Effective (Von Mises) Stress versus Effective Plastic Strain. The Yield Surface grows (or contracts) as a function of the Effective Plastic Strain, and can shift the relationships of principal stresses and thereby influencing strain distribution after yielding occurs.

But it is important to note that even with sophisticated plasticity models, failure is typically predicted externally by the analyst, applying a strain failure criteria which takes into account the triaxiality of the stress state. We do this using the Davis Triaxiality Factor defined by the formulas shown below, and which have been the failure criteria of choice in nuclear containment analyses for many years.

Biaxial –stress based failure criteria

$$\mu = 2^{(1 - TF)}$$

Where μ is the ductility (reduction) ratio and TF is the Davis Triaxiality factor,

$$TF = \frac{\sqrt{2} (\sigma_1 + \sigma_2 + \sigma_3)}{[(\sigma_1 - \sigma_2)^2 + (\sigma_2 - \sigma_3)^2 + (\sigma_3 - \sigma_1)^2]^{1/2}}$$

But when the third principal stress is zero or nearly zero, as in the case of TBT shell plates,

$$TF = \frac{(\sigma_1 + \sigma_2)}{(\sigma_1^2 - \sigma_1\sigma_2 + \sigma_2^2)^{1/2}}$$

For instance when $\sigma_1 = \sigma_2$, TF = 2 and the ductility ratio is 0.5; i.e., failure strain reduces to half its uniaxial value. For the last two decades, many containment analysts have used this criteria for predicting onset of liner tearing, but most have concluded that there is also extensive judgment involved in its application. Strains predicted by FE models can be highly dependent on the level of detail (and mesh refinement) included in the model. And, as was seen in the 1:4 Scale PCCV Model, the existence of flaws in the material (especially at weld seams) mean that

tears might occur at strains significantly lower than the absolute ductility of the material. Time and budget permitting, we will try to be addressing these issues in the interpretation and conclusions of the current work.

Analysis results

Following the guidelines set forth in the SPE Problem Statement there are the following

Required Outputs/Results for Model 3:

- 1.1 Description of Failure Prediction Model or Criteria Selected for Use
- 1.2 Assumptions Made In Geometric Modeling, and Model Description
- 1.3 A subset of the response information defined by the “55 standard output locations” of the 1:4 Scale PCCV round-robin exercise; subset is to be determined later, but participants should plan models accordingly. At a minimum, the displacement transducer/data plots portion of the 55 Standard Output Locations are required.
- 1.4 Contour Plot of Peak Strains in the Liner During the LST at the pressure milestones: $P = 0$ (prestress applied); $1 \times P_d$; $1.5 P_d$; $2 P_d$; $2.5 P_d$; $3 P_d$; $3.3 P_d$; $3.4 P_d$; Ultimate Pressure
- 1.5 Average Strains Over 450.45 mm Regions as were shown in **Error! Reference source not found.**, locations 3, 4, 5, but with similar locations adjacent to all other penetrations, plotted as a Function of Pressure. The intent is for these strains to be over a standardized gage length, which is defined by the spacing between liner anchors.)
- 1.6 A subset of the response information defined by the “55 standard output locations” of the 1:4 Scale PCCV round-robin exercise; see below for the specific list.
- 1.7 Contour Plots of Peak Strains in the Liner During the LST at the pressure milestones: $P = 0$ (prestress applied); $1 \times P_d$; $1.5 P_d$; $2 P_d$; $2.5 P_d$; $3 P_d$; $3.3 P_d$; $3.4 P_d$; Ultimate Pressure
- 1.8 Average Strains Over 450.45 mm Regions as were shown in **Error! Reference source not found.**, locations 3, 4, 5, but with similar locations adjacent to all other penetrations, plotted as a Function of Pressure. The intent is for these strains to be over a standardized gage length, which is defined by the spacing between liner anchors.)

For direct comparison amongst participants, it was also requested to plot (Using Excel)

- Liner Strain Magnitudes (Hoop Direction) at Locations Indicated in Figure 11 (of SPE problem statement), versus pressure
- Tendon stress distribution at $P = 0$ (prestress applied); $1 \times P_d$; $1.5 P_d$; $2 P_d$; $2.5 P_d$; $3 P_d$; $3.3 P_d$; $3.4 P_d$; Ultimate Pressure for
 - Hoop Tendons # H35, H53, H68
 - Vertical Tendon # V37 and V46
- Plots of response versus pressure for Standard Output Locations:
 - 1-15 (displacements)
 - 22-29 (rebar strains)
 - 36-42 (liner strains)

48-55 (tendon strains and stresses)

(see Table D 4-1 in NUREG/CR-6809 for exact locations and definitions of SOL's)

The results of some pressure milestones are shown in Table D 2.

Table D 8: Results by Pressure Milestones at 6.2 m

Milestone	Pressure (MPa)	x Pd
Zero Concrete Hoop Stress (at 0° azimuth)	0.498	1.27
Concrete Hoop Cracking Occurs (at 0° azimuth)	0.624	1.59
Tendon A Reach approx.1% Strain (at 0° azimuth)	1.299	3.31
Tendon B Reach approx.1% Strain (at 0° azimuth)	1.274	3.25

Deformed shapes of the full model are shown in Figure D 159 and 160 for, respectively, the a) after prestress and tendon anchorage step, b) at pressurization of 3.6 Pd, which is incipient failure of the vessel.

A series of “plan-view” slice deformed shapes are shown in Figure D 161 through 168, at a Model Elevation of 4.68 meters. Based on rough comparisons to the test data these shapes and the magnitude of the displacements are in reasonably good agreement with observations from the LST and SFMT.

A series of global plots of Maximum Principal Strains are shown for the Liner, and for the Concrete Mid-thickness of the Vessel in the Plot Series, Figure D 169 and 177. Studying the liner strain plots for pressures of 3.0Pd, 3.3Pd, 3.4Pd, and 3.6Pd, and comparing to known behaviors from the 1:4 Scale PCCV LST and SFMT, it can be concluded that many similar liner strain “hot spots” exist in the analysis as were observed in the test. For example, a) near 0-degrees azimuth, cylinder midheight, b) on either side of the E/H embossment, c) on either side of the other penetrations (A/L, M/S, and F/W penetrations). One significant exception to this agreement is the observed significant liner strain in the vicinity of the buttresses. This phenomena was observed to minor extent in the test, and not to the extent shown in the analysis. This has been of some concern to us in developing Model 3, and remained an issue as we fine-tuned our modeling strategy for the tendon anchors at the buttresses. But we have concluded that the shell modeling approach, and the strategy of attaching the tendon end to a single concrete node, will tend to cause somewhat larger strains in this vicinity than in the actual structure. Thus there remain some trade-offs in accuracy to choosing shell elements and element size which are manageable for completing 3D global analysis. The elevated strains near the buttress are not so prevalent for the mid-thickness strains of Figure D 178 through 186.

Figure D187 through 190 show hoop tendon stresses, Figure D 191 through 192 show vertical tendon stresses, and Figure D 194 through 211 show hoop tendon strains. The stress distribution plots show that the friction modeling strategy for Model 3 is very effective, and the stress distributions after jacking and after anchorage are in reasonable agreement with design expectations and with observations and measurements from the test. The hoop tendon strain contours indicate that at 3.6Pd, the largest tendon strains occur in the 0-6 degree midheight zone of the cylinder and in the 135-degree zone of the cylinder, and that these strains are reaching 1.73%. In the SFMT, the first tendon failures were observed to occur in the 0-6-degree

midheight zone of the cylinder, and it has been inferred (though not directly measured) that the tendon strains were of approximately this magnitude (approximately 2%) when the first tendons ruptured. (The reader can refer to the Post-Test Analysis report for further discussion of this.)

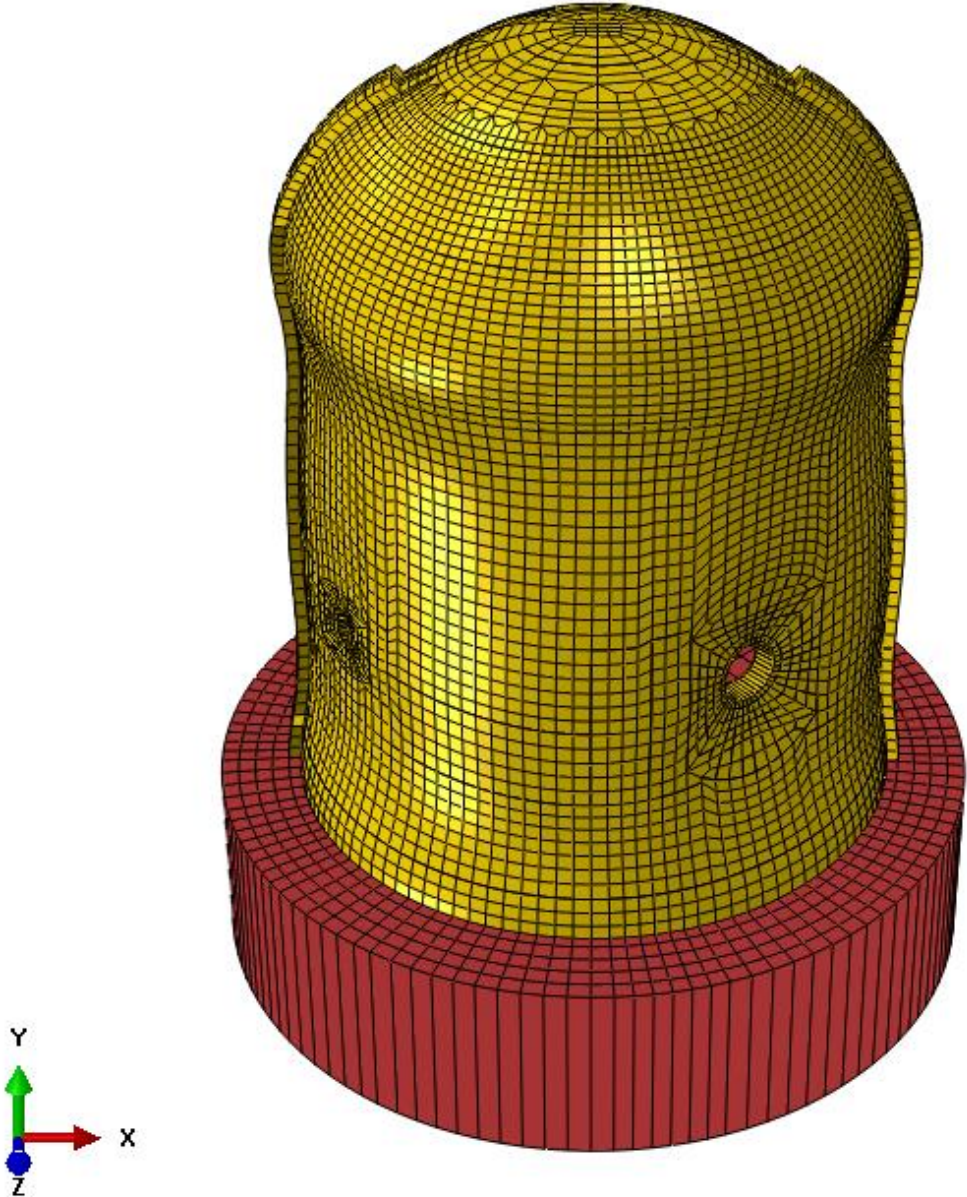


Figure D 159: Deformed Shape after Tendon Anchorage. Deformation Scale x 500

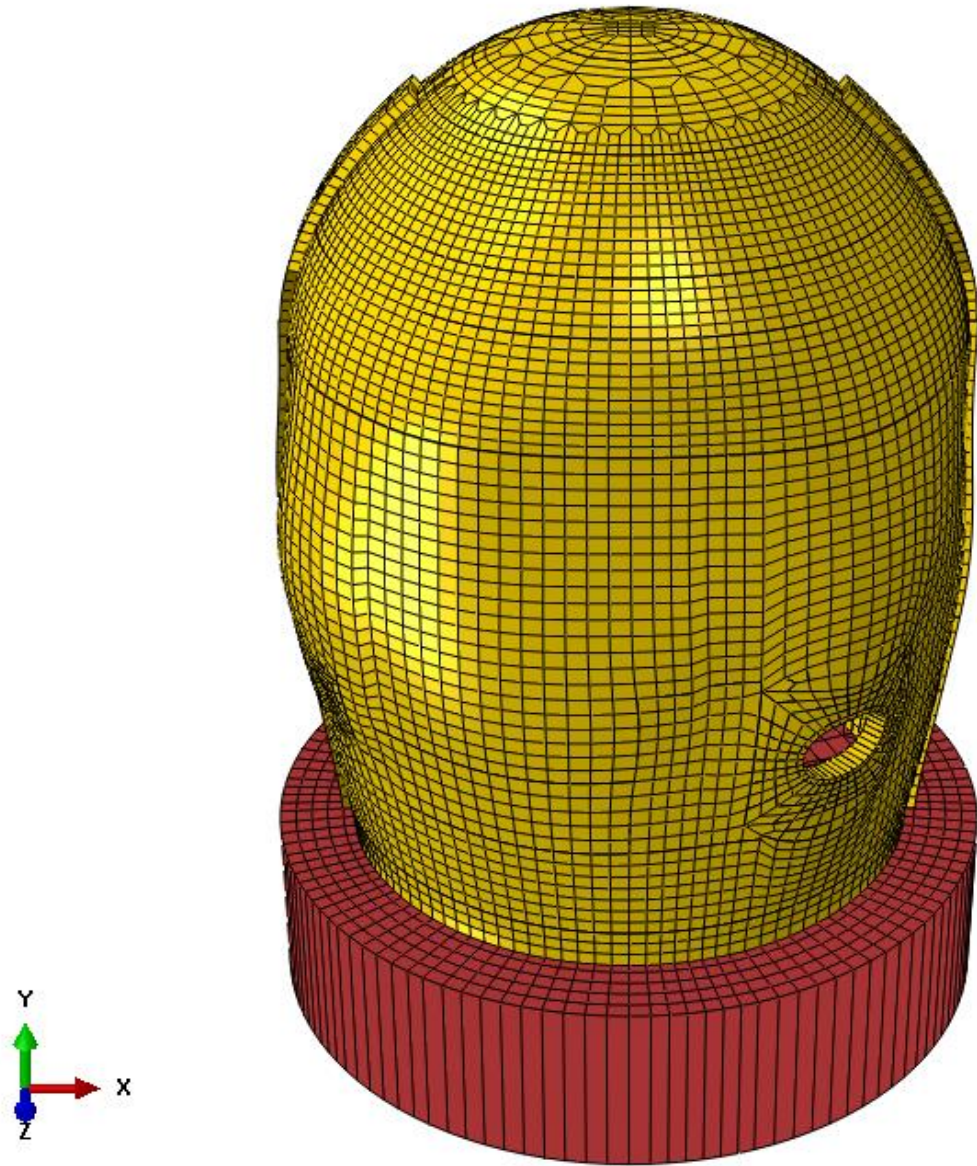


Figure D 160: Deformed Shape at 3.6 x Pd. Deformation Scale x 20

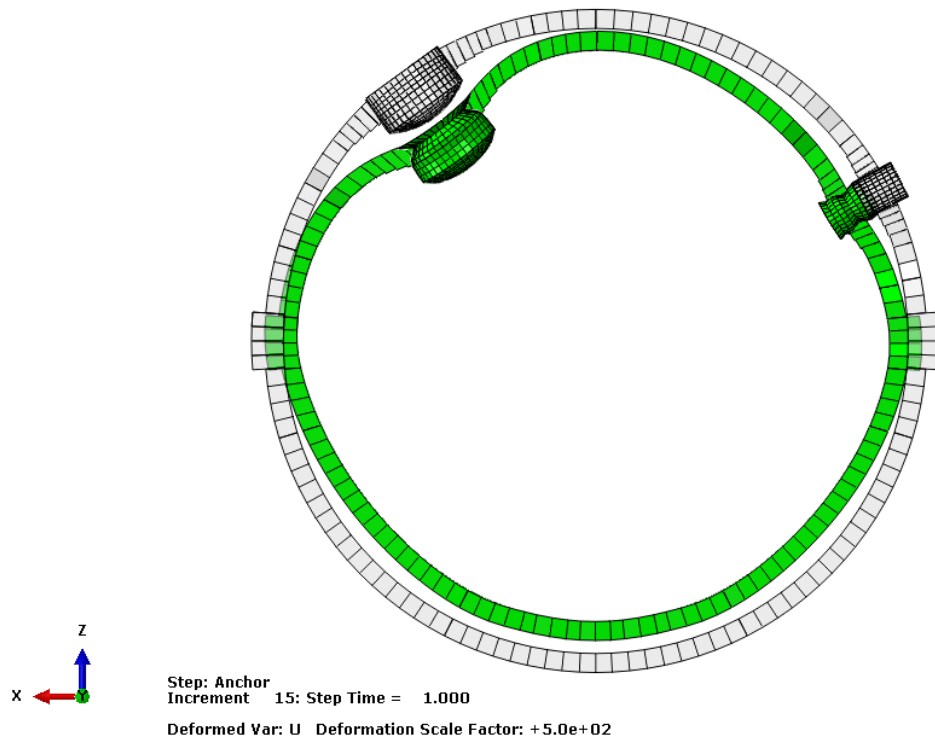


Figure D 161: Deformed Shape at Anchoring at Elev. 4.68 m (15'-4 1/16") (x500)

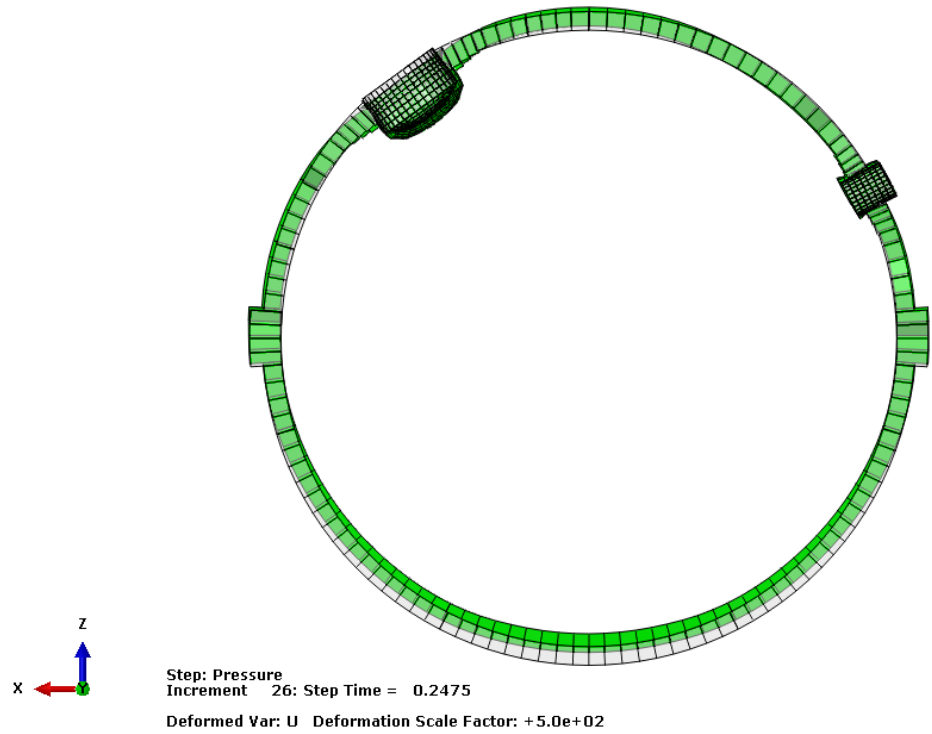
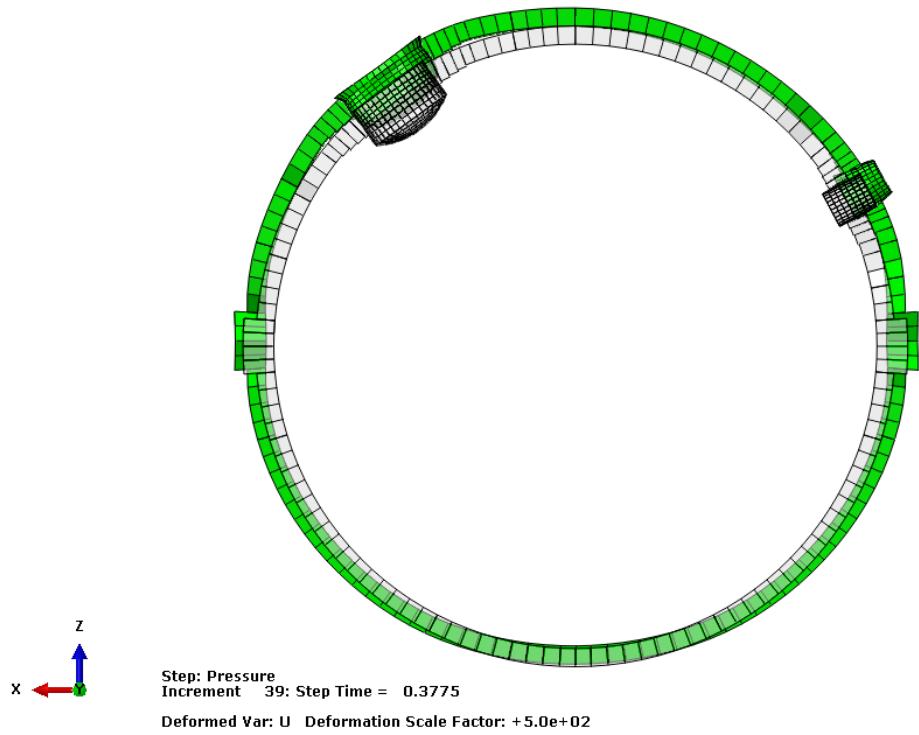
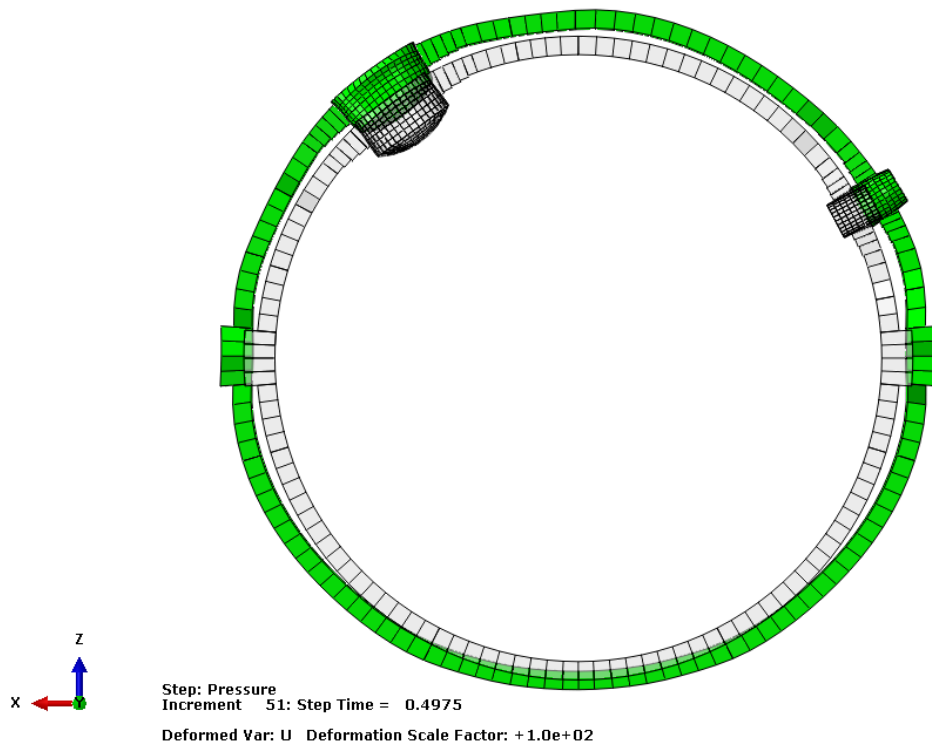


Figure D 162: Deformed Shape at Design Pressure at Elev. 4.68 m (15'-4 1/16") (x500)



**Figure D 163: Deformed Shape at 1.5 x Design Pressure at Elev. 4.68 m (15'-4 1/16")
(x500)**



**Figure D 164: Deformed Shape at 2.0 x Design Pressure at Elev. 4.68 m (15'-4 1/16")
(x100)**

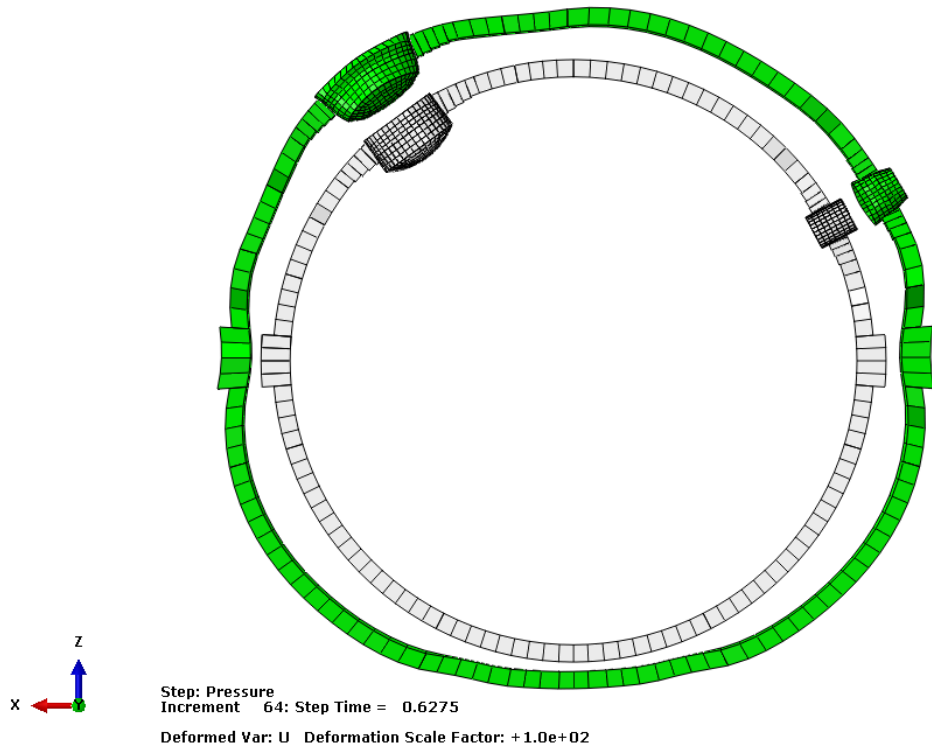


**Figure D 165: Deformed Shape at 2.5 x Design Pressure at Elev. 4.68 m (15'-4 1/16")
(x100)**

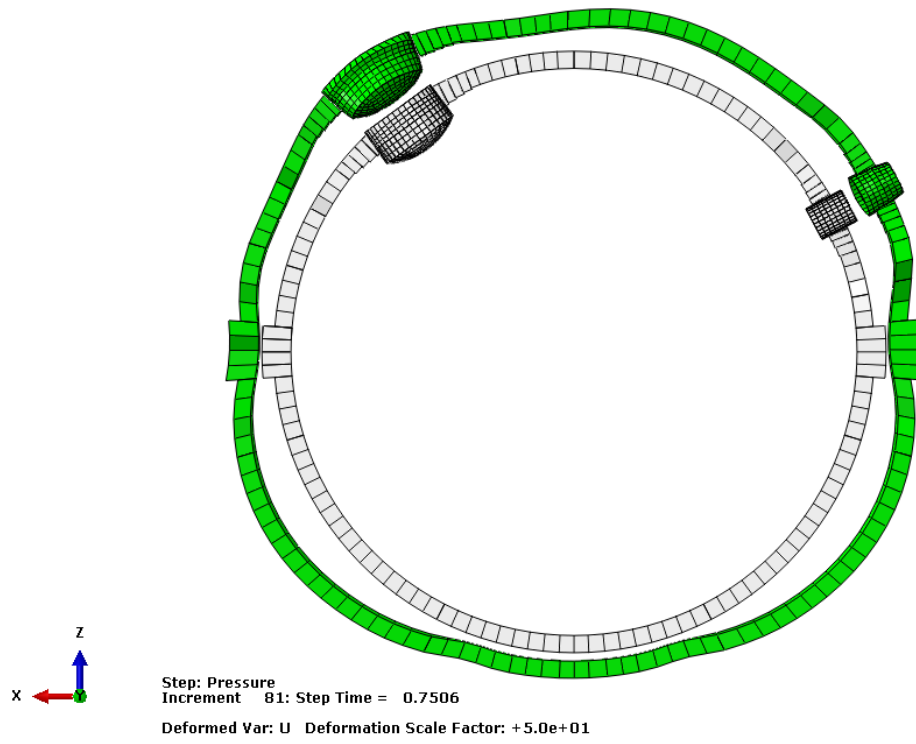


Figure D 166: Deformed Shape at 3.0 x Design Pressure at Elev. 4.68 m (15'-4 1/16") (x50)

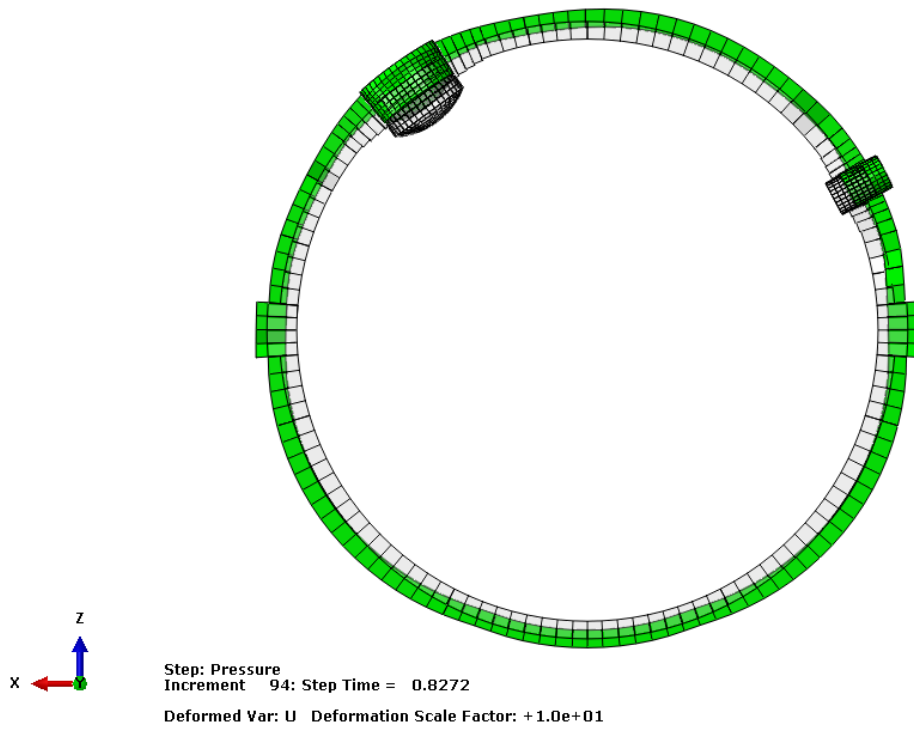


Figure D 167: Deformed Shape at 3.4 x Design Pressure at Elev. 4.68 m (15'-4 1/16") (x10)

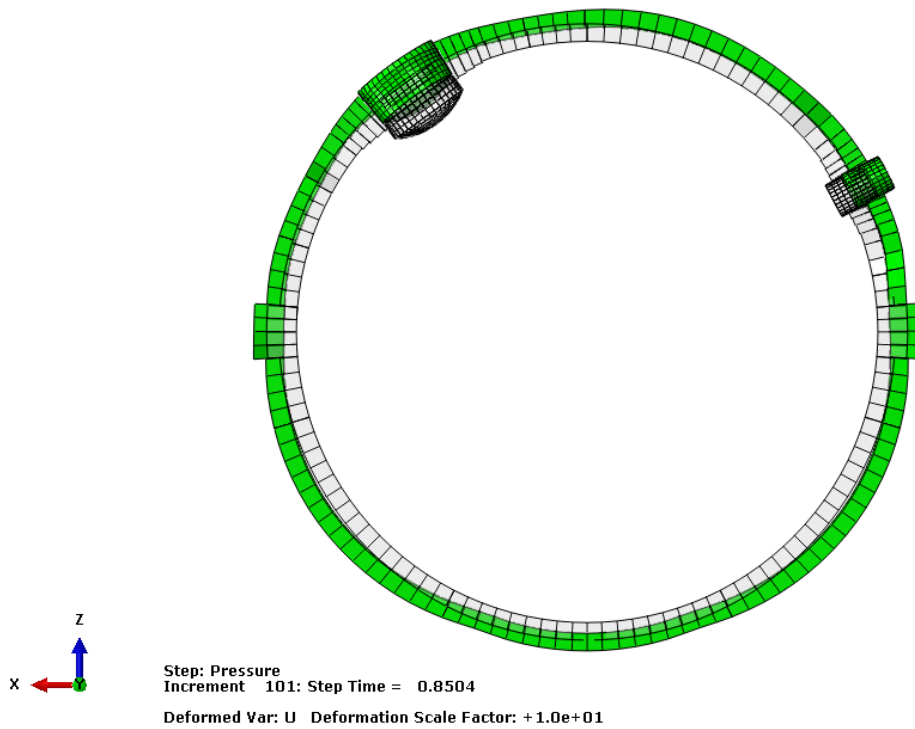
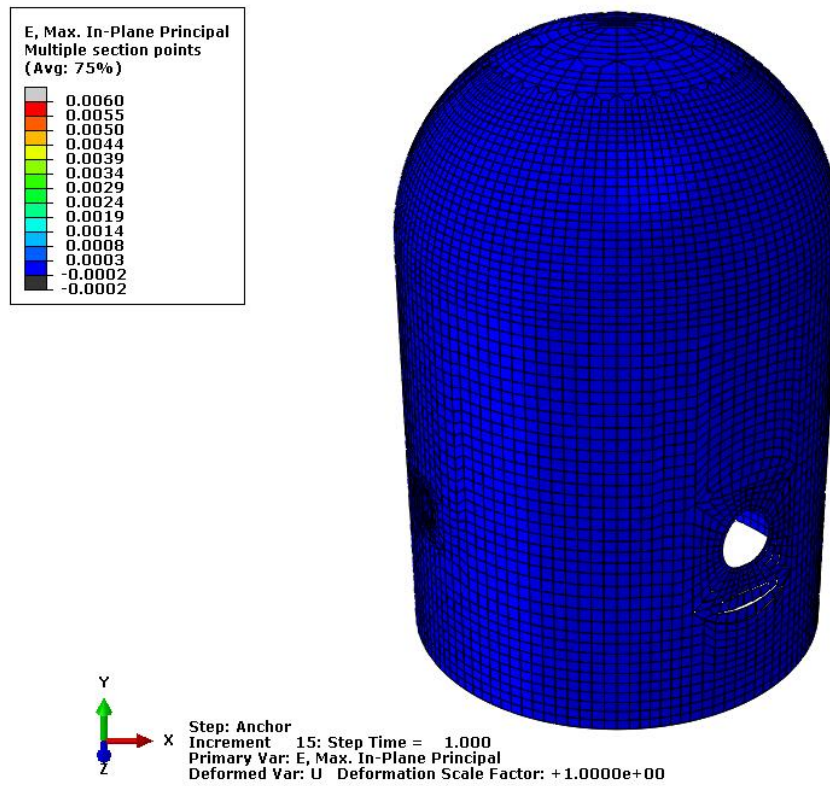


Figure D 168: Deformed Shape at 3.6 x Design Pressure at Elev. 4.68 m (15'-4 1/16") (x10)



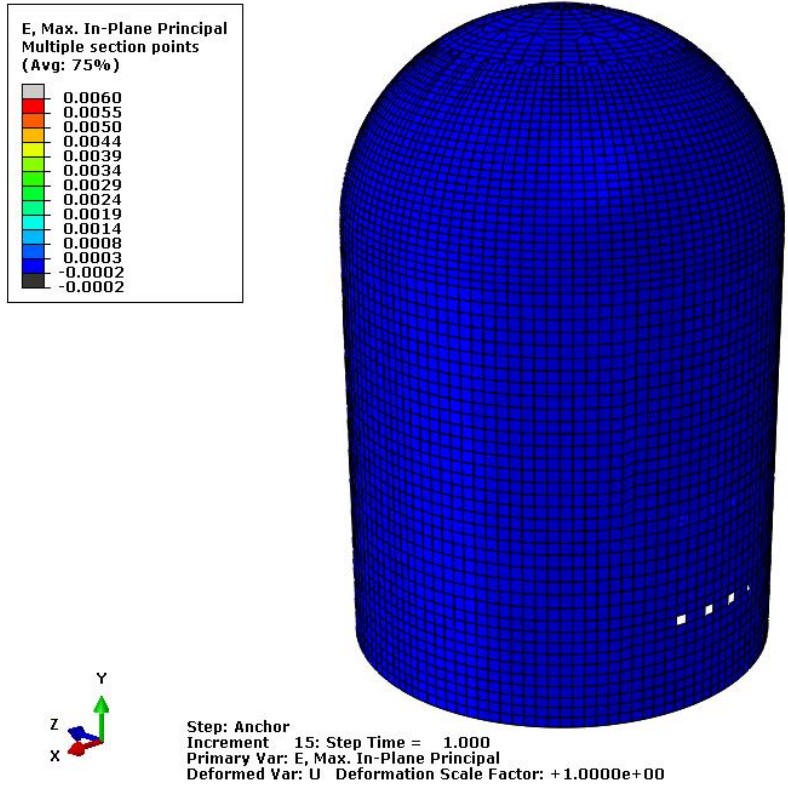
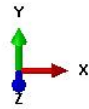
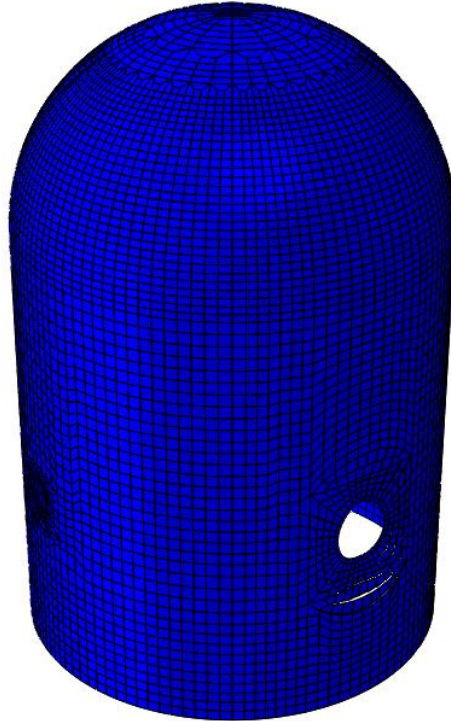
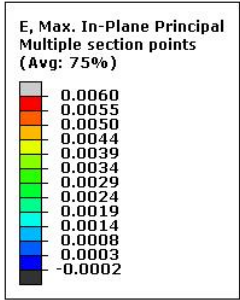


Figure D 169: Max Principal Strain in Liner at Jacking



Step: Pressure
 Increment 26: Step Time = 0.2475
 Primary Var: E, Max. In-Plane Principal
 Deformed Var: U Deformation Scale Factor: +1.0000e+00

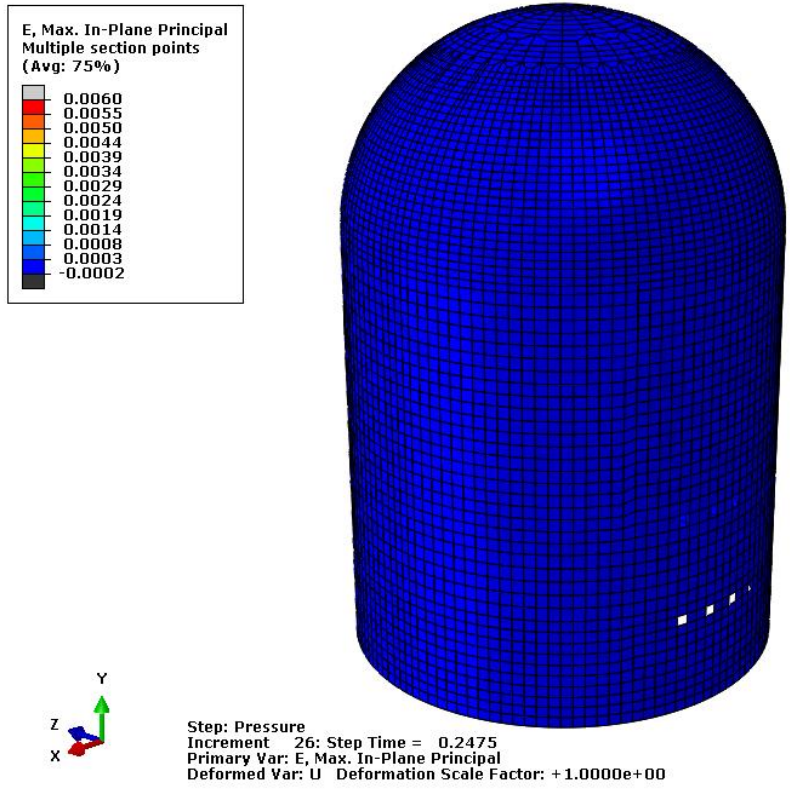
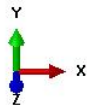
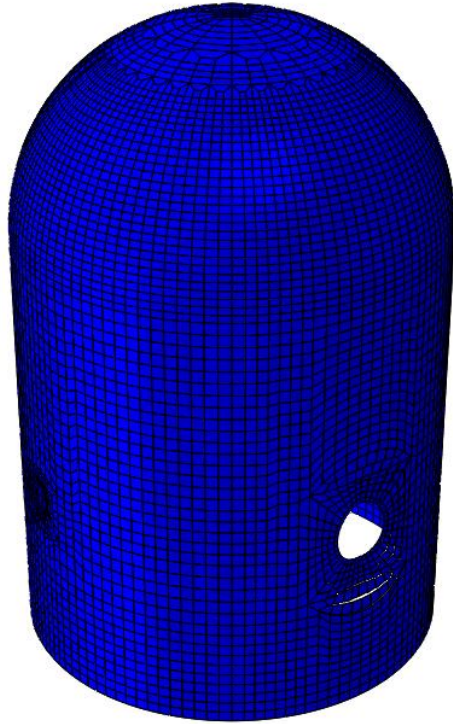
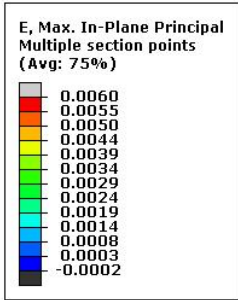


Figure D 170: Max Principal Strain in Liner at 1.0 x Pd.



Step: Pressure
Increment 39: Step Time = 0.3775
Primary Var: E, Max. In-Plane Principal
Deformed Var: U Deformation Scale Factor: +1.0000e+00

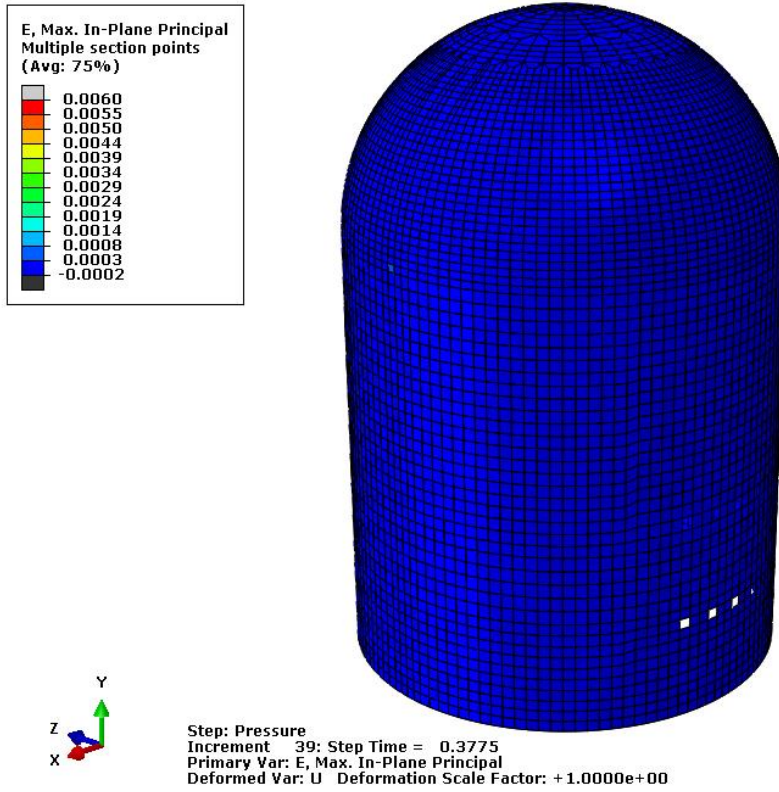
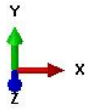
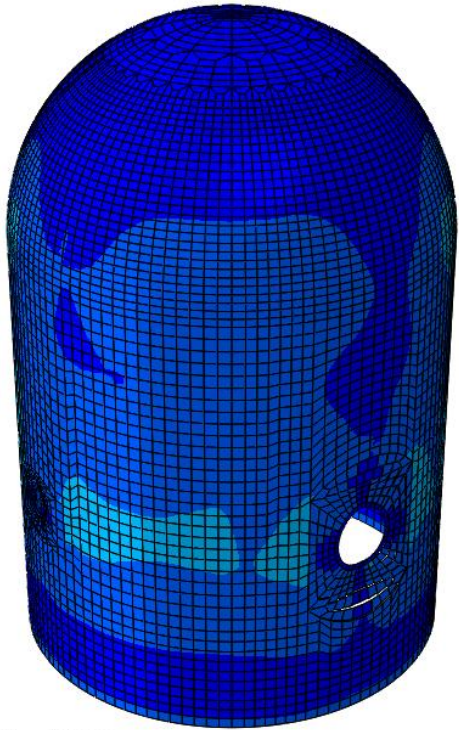
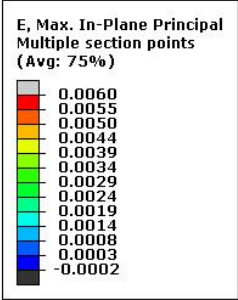


Figure D 171: Max Principal Strain in Liner at 1.5 x Pd.



Step: Pressure
 Increment 51: Step Time = 0.4975
 Primary Var: E, Max. In-Plane Principal
 Deformed Var: U Deformation Scale Factor: +1.0000e+00

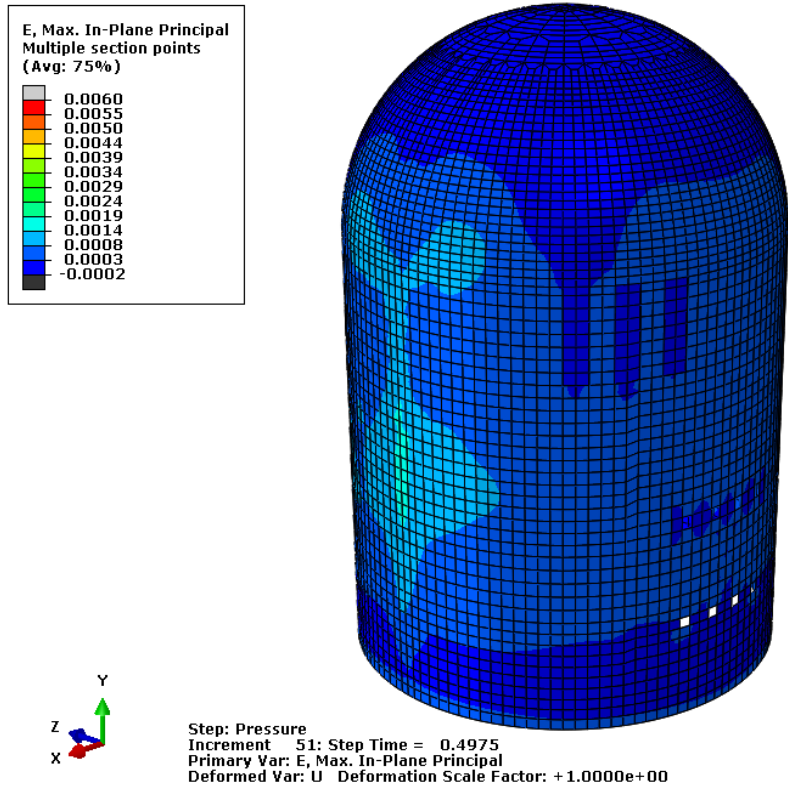
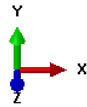
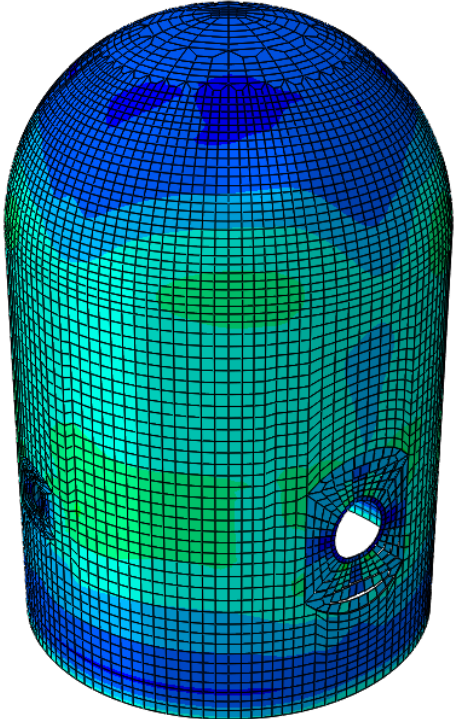
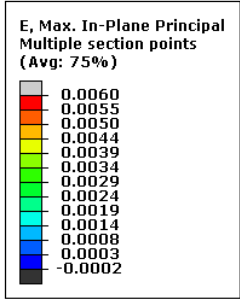


Figure D 172: Max Principal Strain in Liner at 2.0 x Pd.



Step: Pressure
Increment 64; Step Time = 0.6275
Primary Var: E, Max. In-Plane Principal
Deformed Var: U Deformation Scale Factor: +1.0000e+00

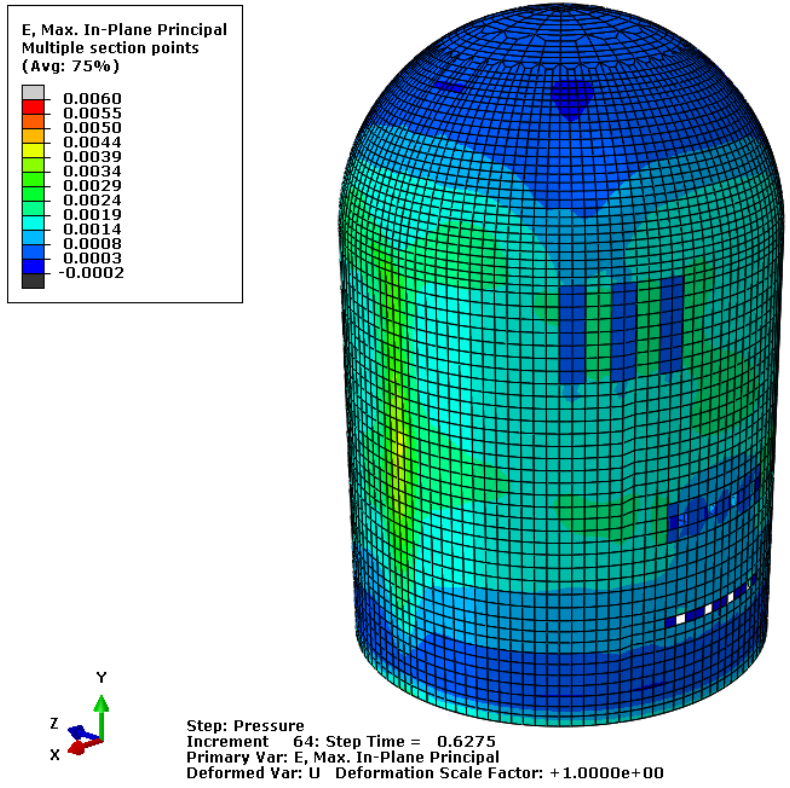
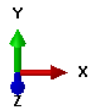
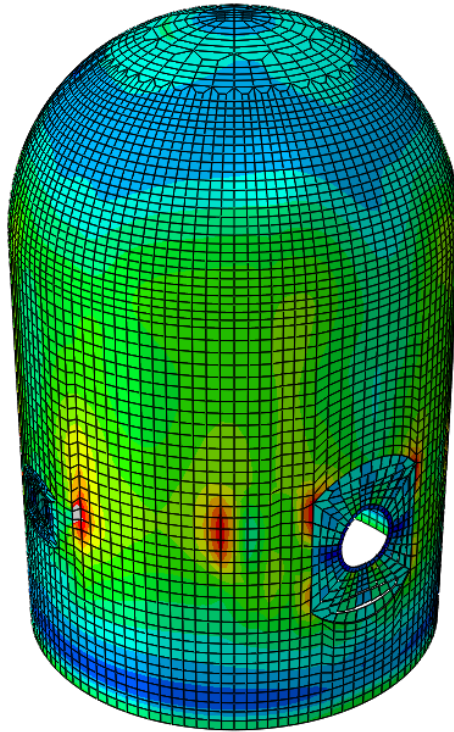
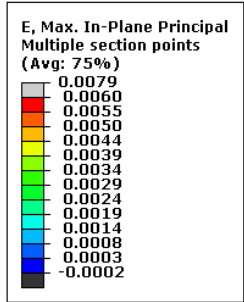


Figure D 173: Max Principal Strain in Liner at 2.5 x Pd.



Step: Pressure
 Increment B1: Step Time = 0.7506
 Primary Var: E, Max. In-Plane Principal
 Deformed Var: U Deformation Scale Factor: +1.0000e+00

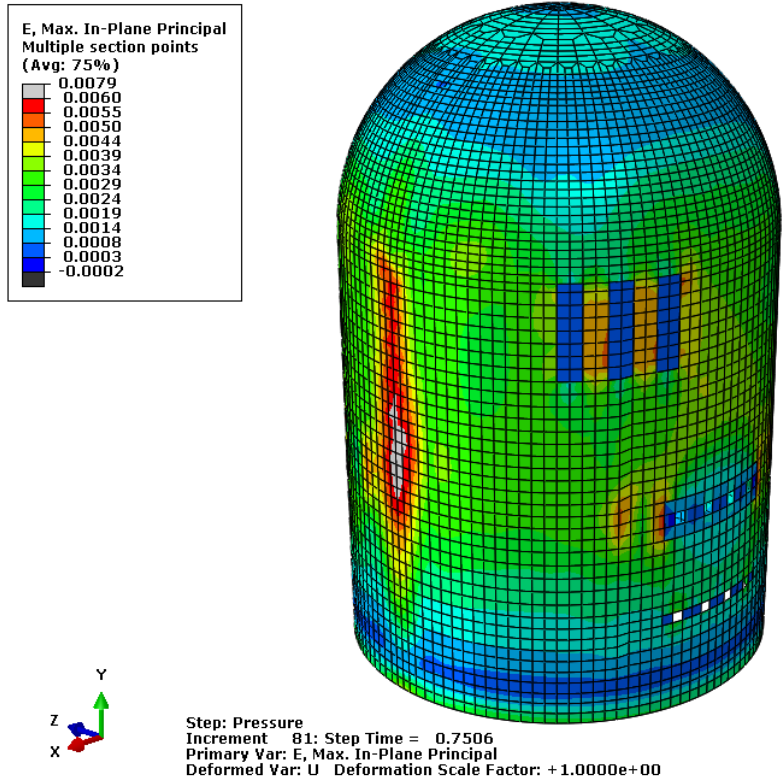
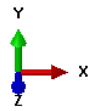
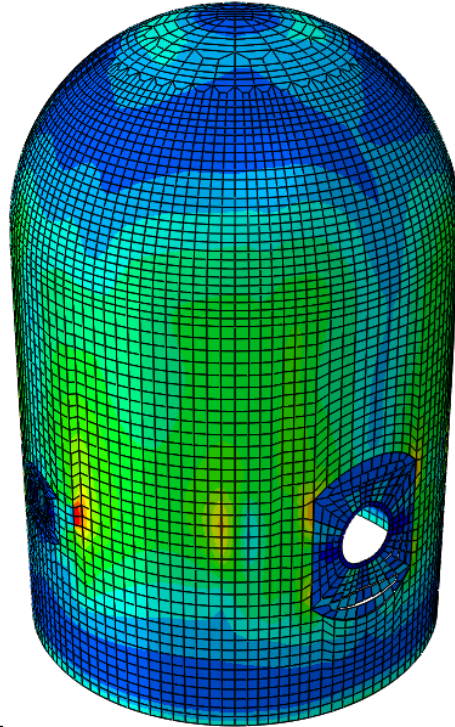
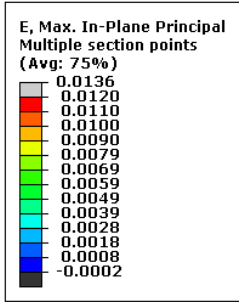
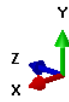
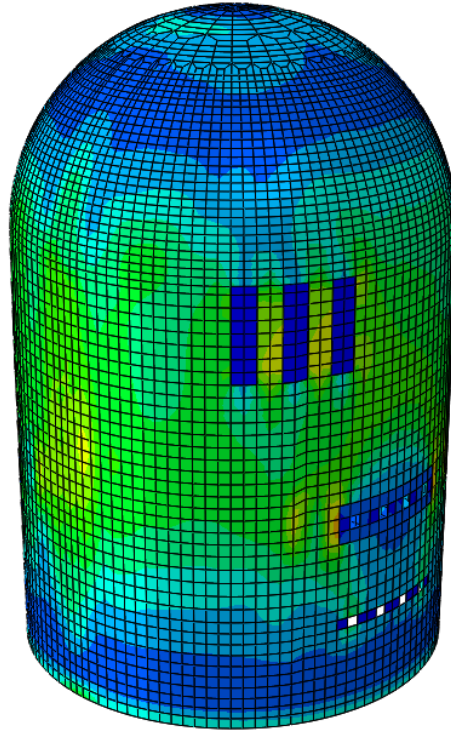
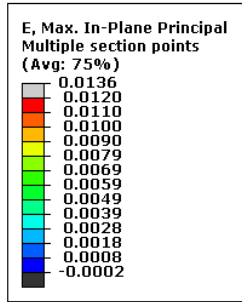


Figure D 174: Max Principal Strain in Liner at 3.0 x Pd.

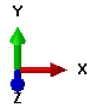
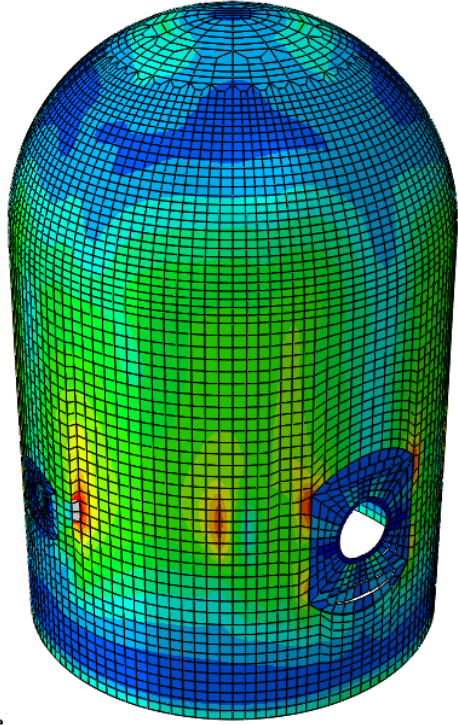
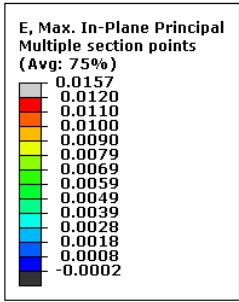


Step: Pressure
 Increment 94: Step Time = 0.8272
 Primary Var: E, Max. In-Plane Principal
 Deformed Var: U Deformation Scale Factor: +1.0000e+00



Step: Pressure
Increment 94: Step Time = 0.8272
Primary Var: E, Max. In-Plane Principal
Deformed Var: U Deformation Scale Factor: +1.0000e+00

Figure D 175: Max Principal Strain in Liner at 3.3 x Pd. (Higher Contour Color Limits)



Step: Pressure
 Increment 101: Step Time = 0.8504
 Primary Var: E, Max. In-Plane Principal
 Deformed Var: U Deformation Scale Factor: +1.0000e+00

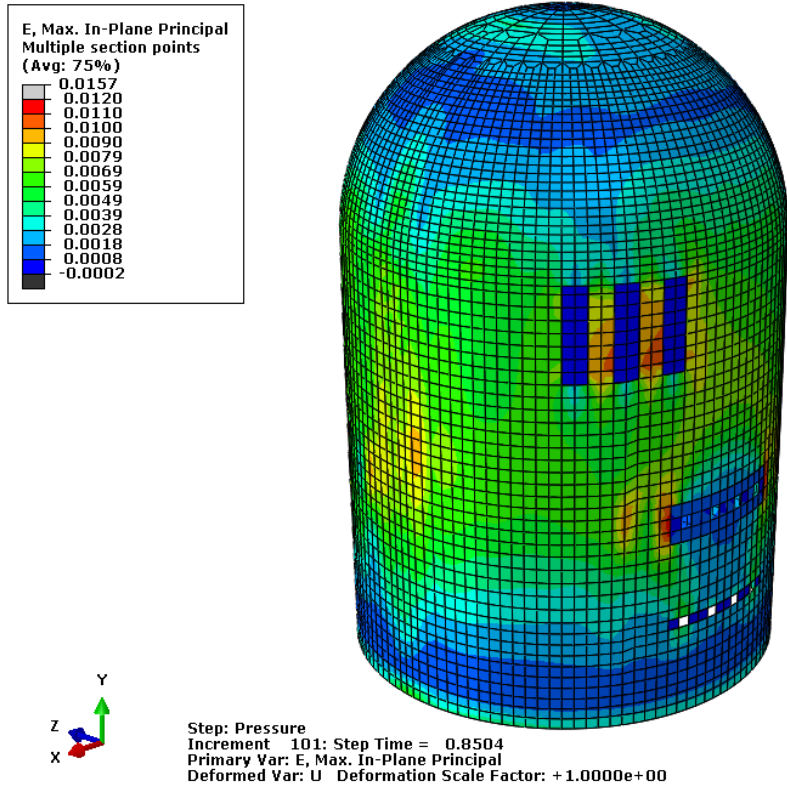
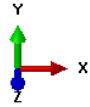
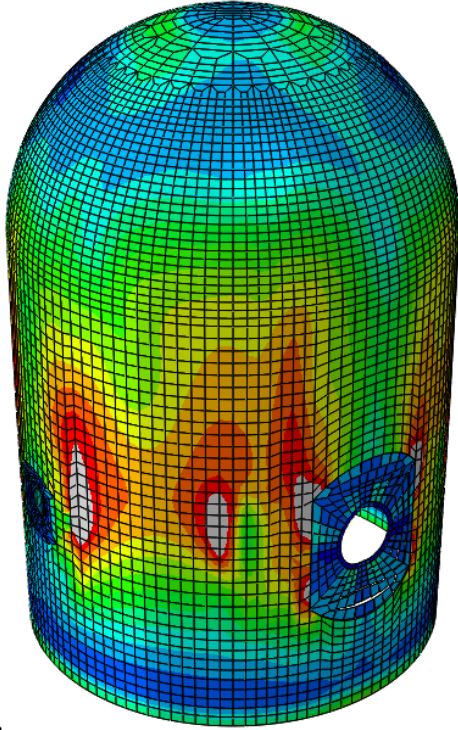
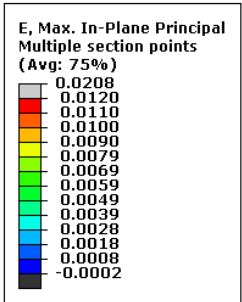


Figure D 176: Max Principal Strain in Liner at 3.4 x Pd.



Step: Pressure
Increment 113: Step Time = 0.8992
Primary Var: E, Max. In-Plane Principal
Deformed Var: U Deformation Scale Factor: +1.0000e+00

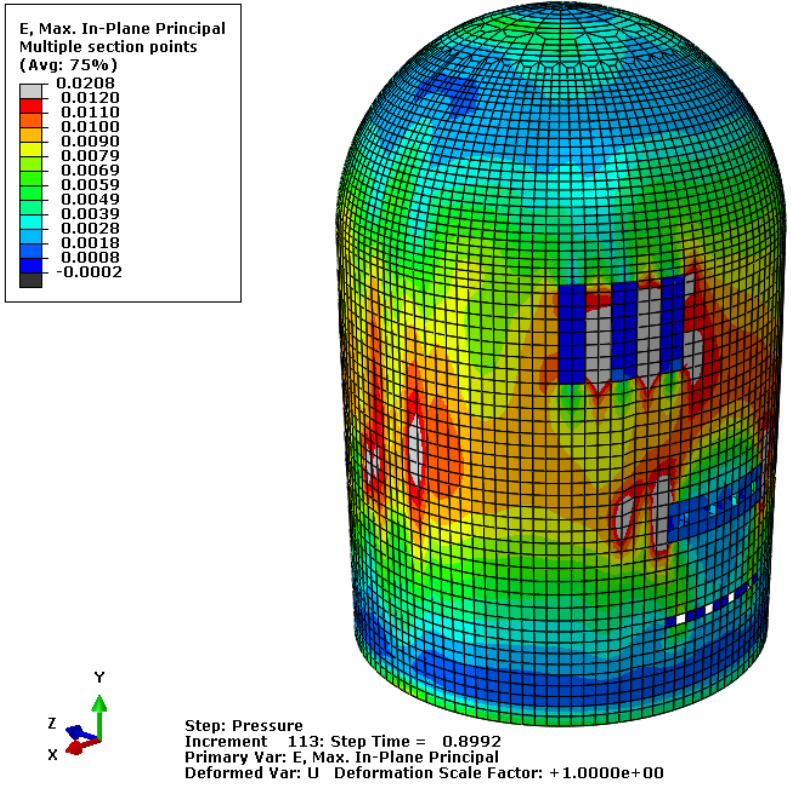
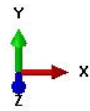
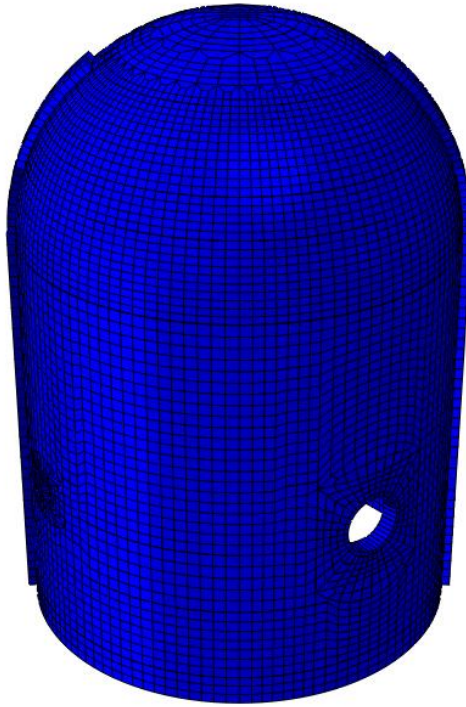
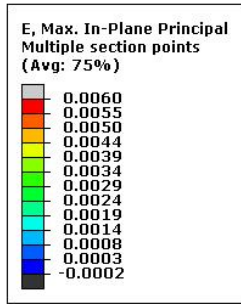


Figure D 177: Max Principal Strain in Liner at 3.6 x Pd.



Step: Anchor
Increment 15: Step Time = 1.000
Primary Var: E, Max. In-Plane Principal
Deformed Var: U Deformation Scale Factor: +1.0000e+00

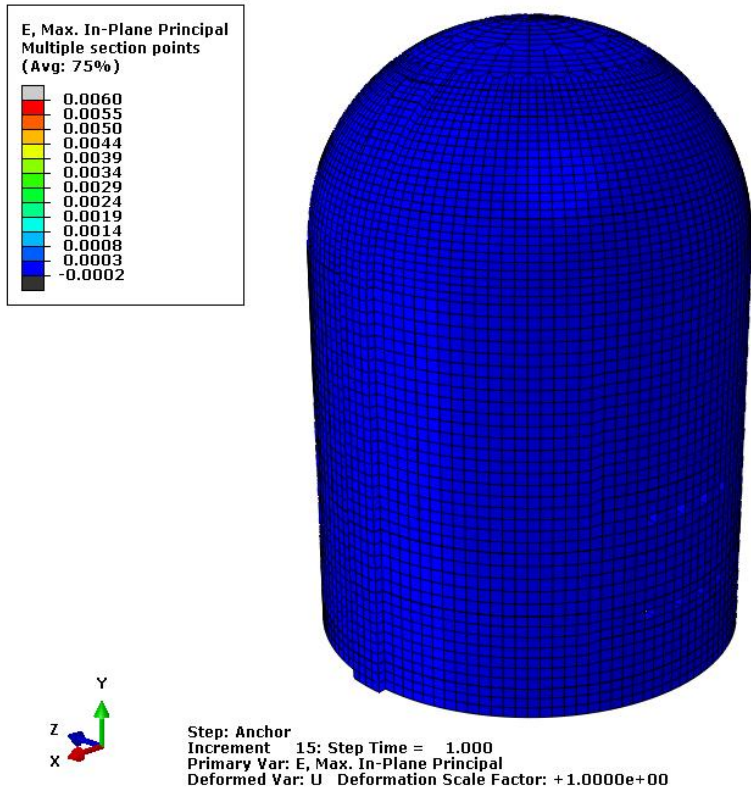
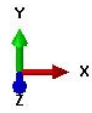
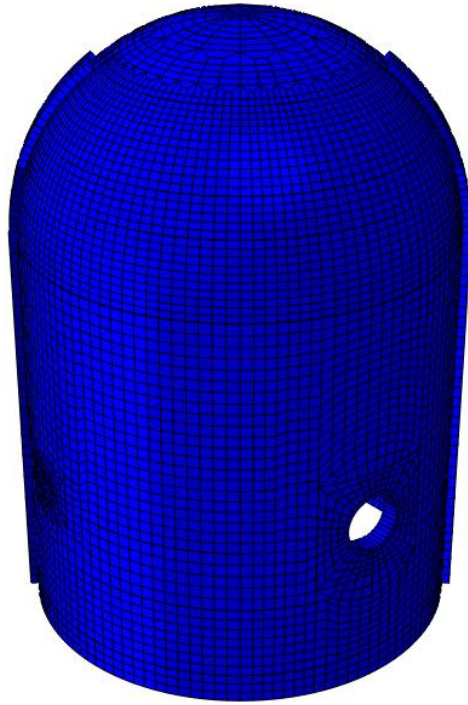
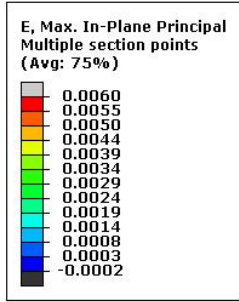


Figure D 178: Max Principal Membrane Strain in Concrete at Anchorage of Jacking



Step: Pressure
 Increment 26: Step Time = 0.2475
 Primary Var: E, Max. In-Plane Principal
 Deformed Var: U Deformation Scale Factor: +1.0000e+00

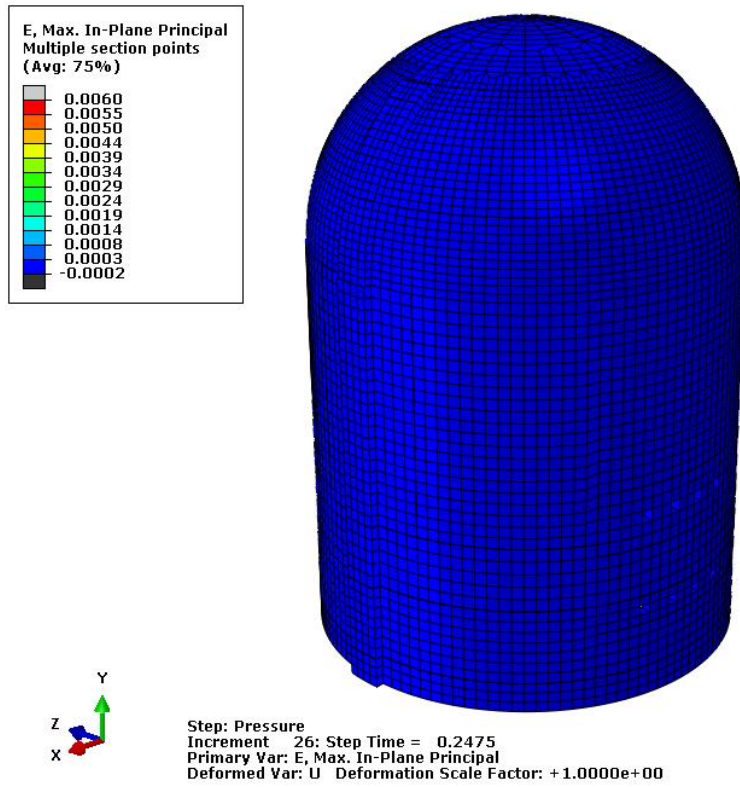
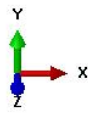
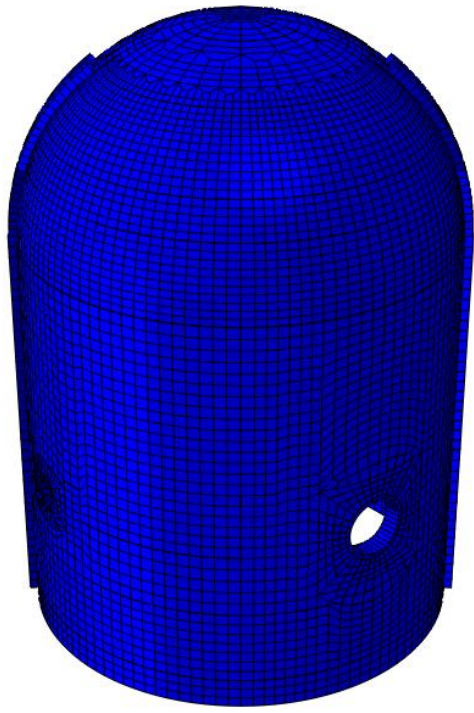
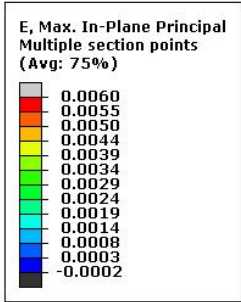


Figure D 179: Max Principal Membrane Strain in Concrete at 1.0 x Pd.



Step: Pressure
 Increment 39: Step Time = 0.3775
 Primary Var: E, Max. In-Plane Principal
 Deformed Var: U Deformation Scale Factor: +1.0000e+00

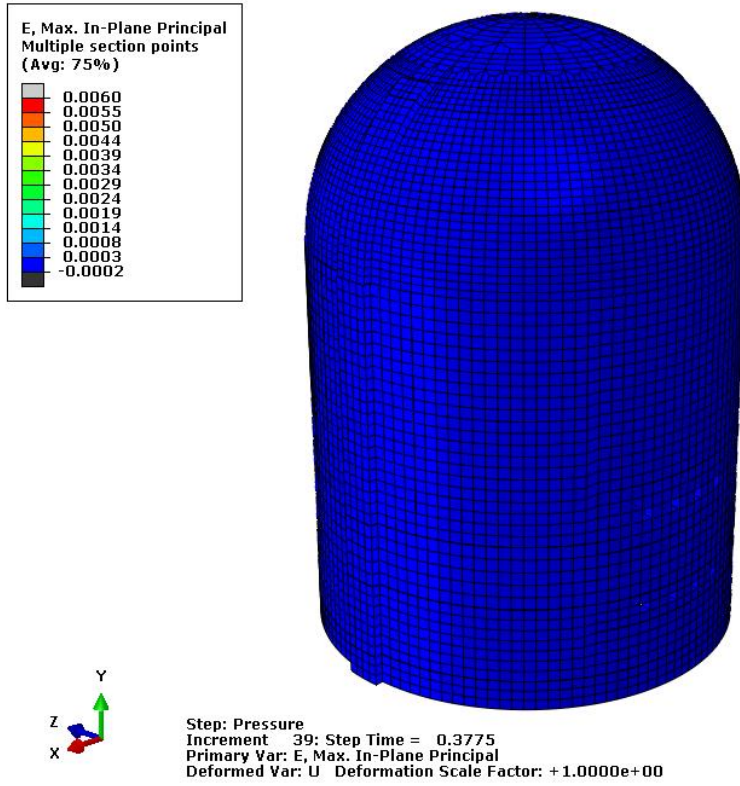
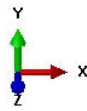
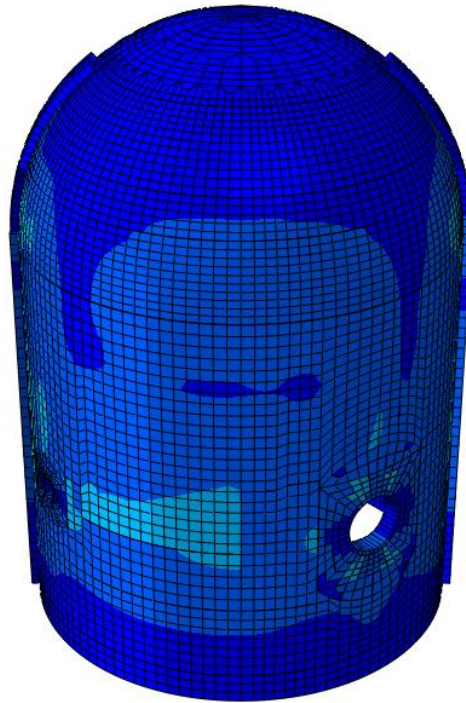
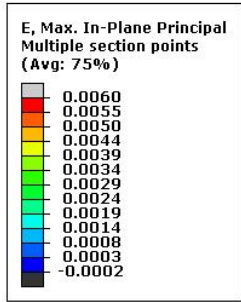


Figure D 180: Max Principal Membrane Strain in Concrete at 1.5 x Pd.



Step: Pressure
 Increment 51: Step Time = 0.4975
 Primary Var: E, Max. In-Plane Principal
 Deformed Var: U Deformation Scale Factor: +1.0000e+00

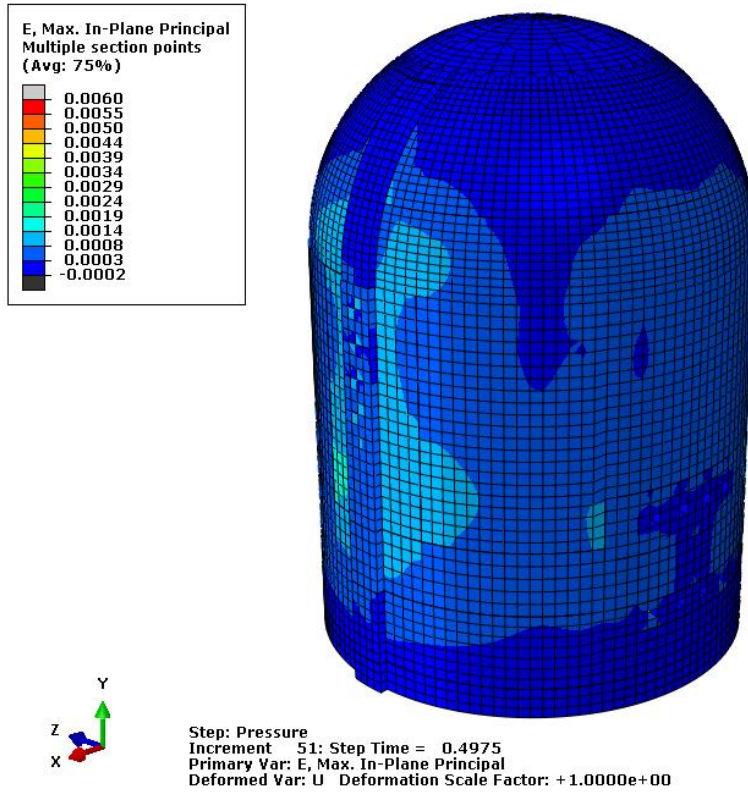
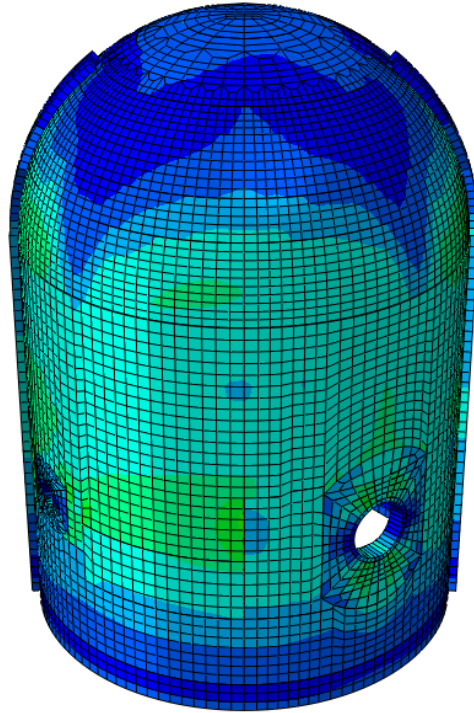
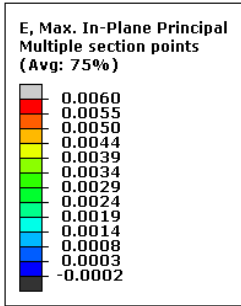


Figure D 181: Max Principal Membrane Strain in Concrete at 2.0 x Pd.



Step: Pressure
 Increment 64: Step Time = 0.6275
 Primary Var: E, Max. In-Plane Principal
 Deformed Var: U Deformation Scale Factor: +1.0000e+00

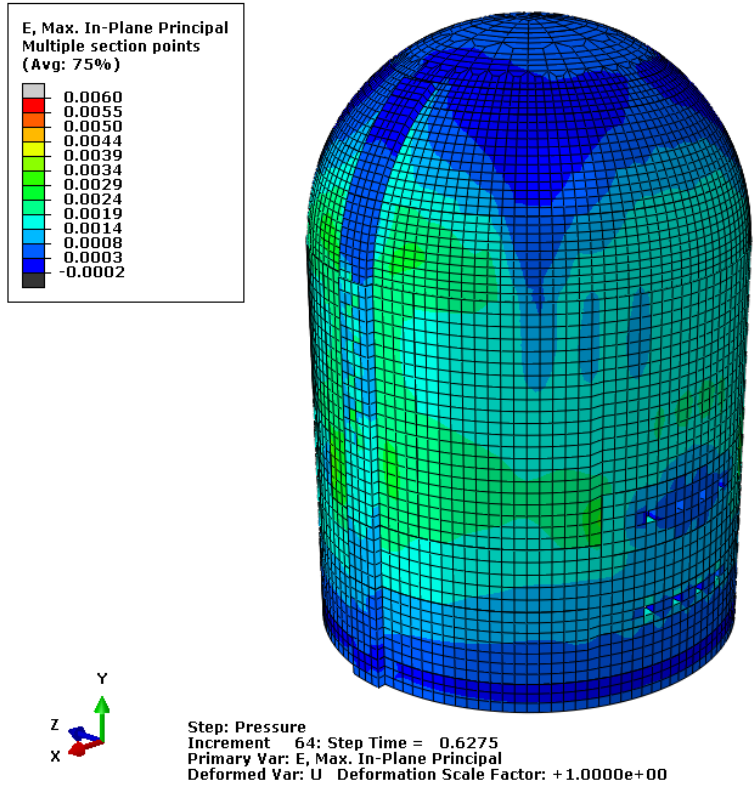
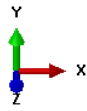
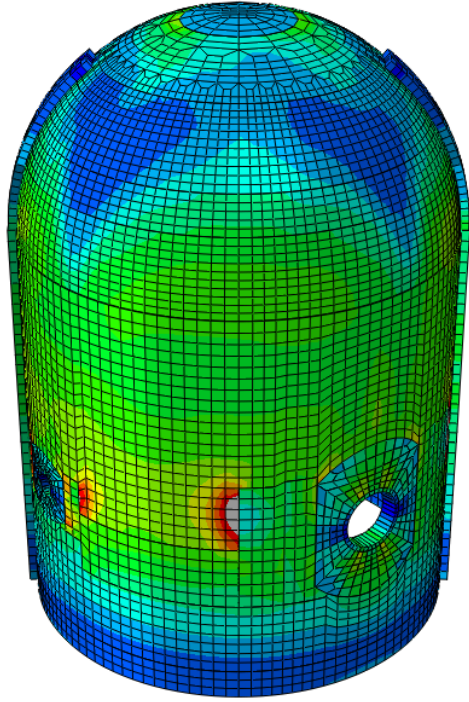
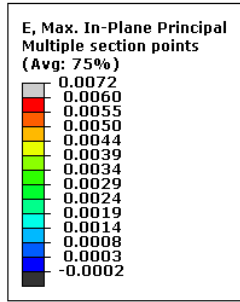


Figure D 182: Max Principal Membrane Strain in Concrete at 2.5 x Pd.



Step: Pressure
 Increment 81: Step Time = 0.7506
 Primary Var: E, Max. In-Plane Principal
 Deformed Var: U Deformation Scale Factor: +1.0000e+00

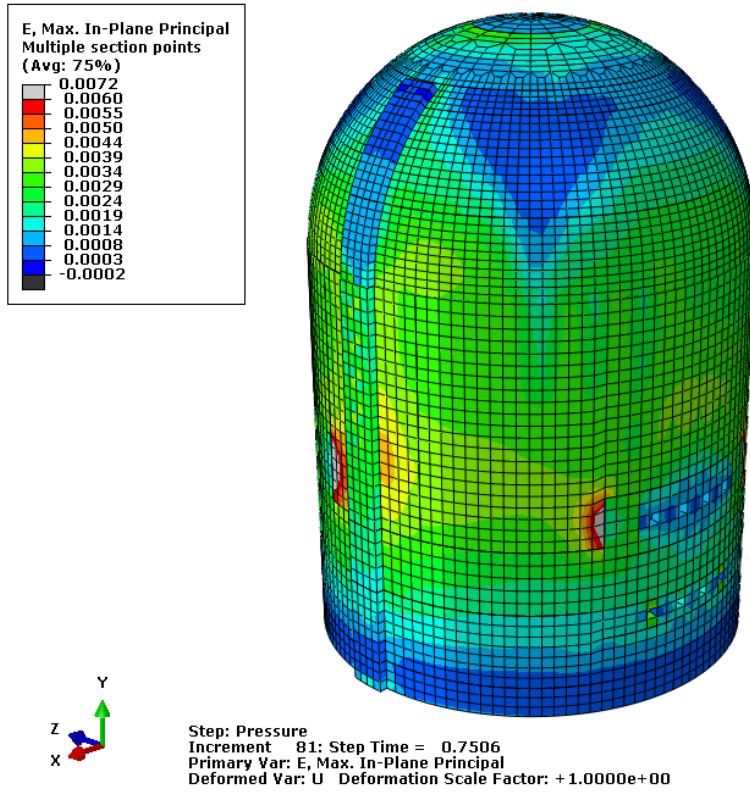
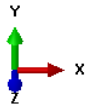
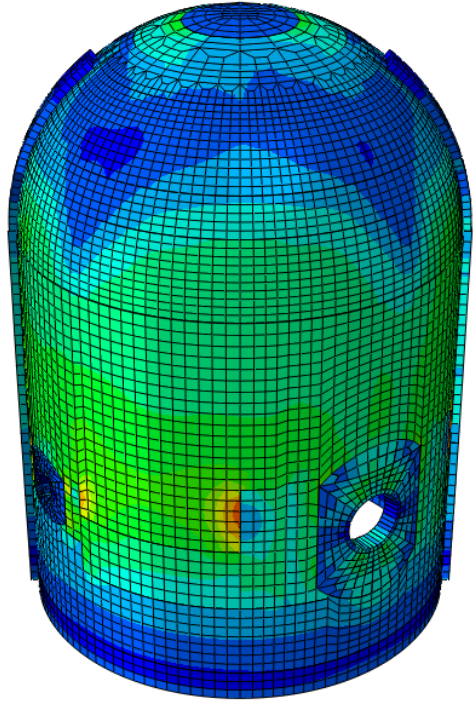
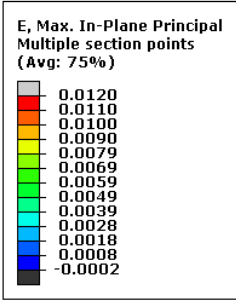


Figure D 183: Max Principal Membrane Strain in Concrete at 3.0 x Pd.



Step: Pressure
Increment 94: Step Time = 0.8272
Primary Var: E, Max. In-Plane Principal
Deformed Var: U Deformation Scale Factor: +1.0000e+00

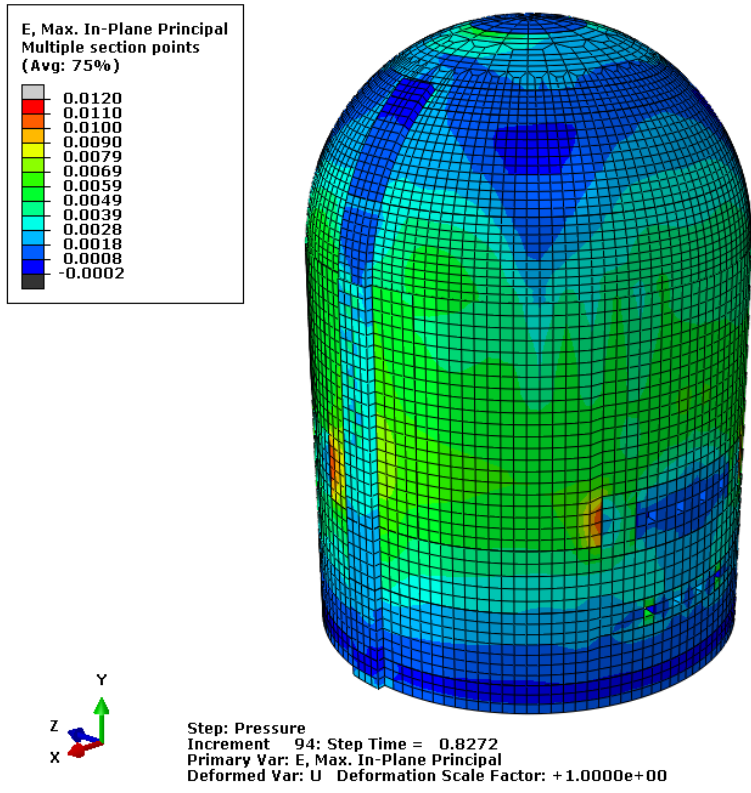
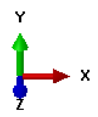
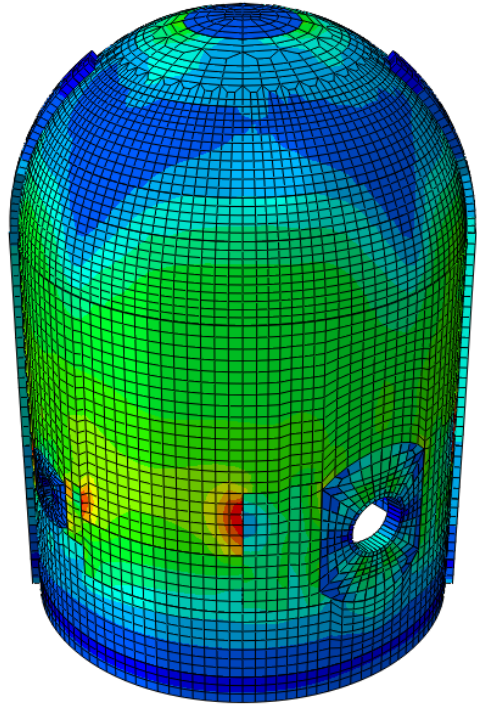
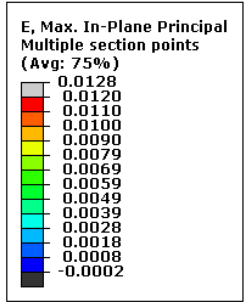


Figure D 184: Max Principal Membrane Strain in Concrete at 3.3 x Pd.



Step: Pressure
Increment 101: Step Time = 0.8504
Primary Var: E, Max. In-Plane Principal
Deformed Var: U Deformation Scale Factor: +1.0000e+00

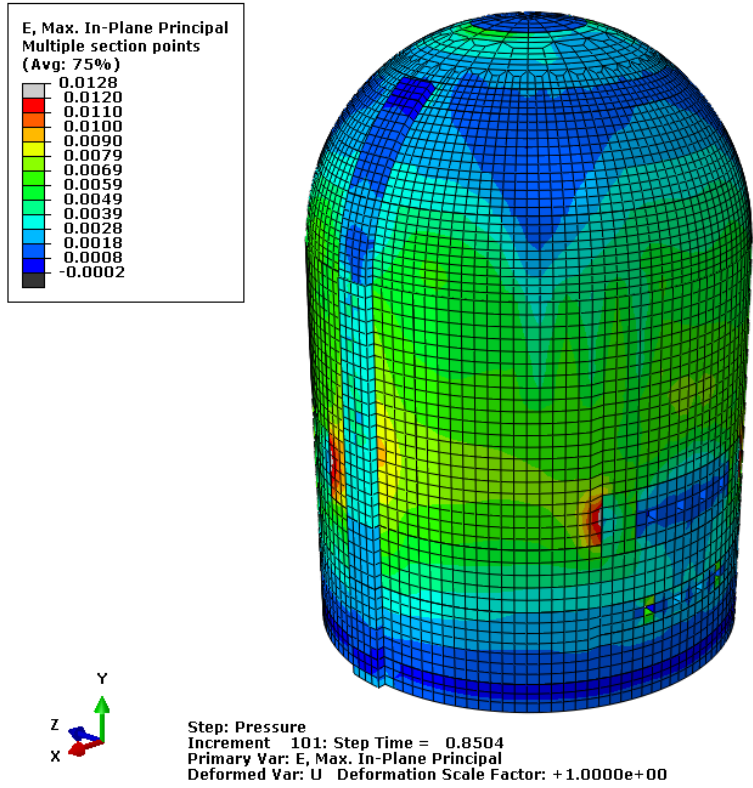
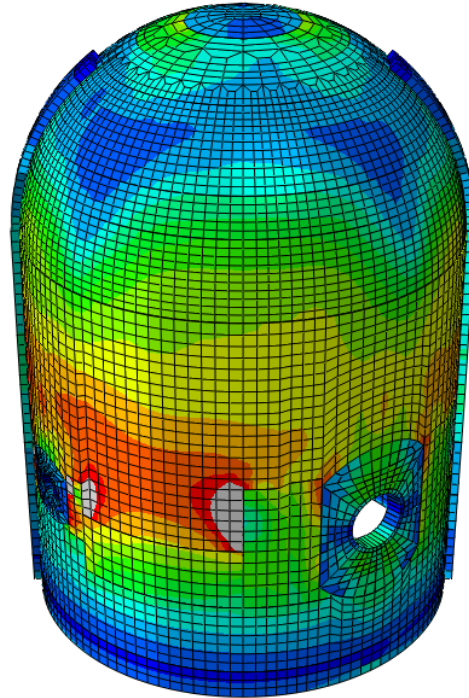
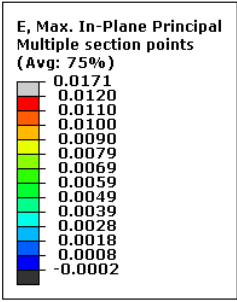


Figure D 185: Max Principal Membrane Strain in Concrete at 3.4 x Pd.



Y
X
Z

Step: Pressure
Increment 113: Step Time = 0.8992
Primary Var: E, Max. In-Plane Principal
Deformed Var: U Deformation Scale Factor: +1.0000e+00

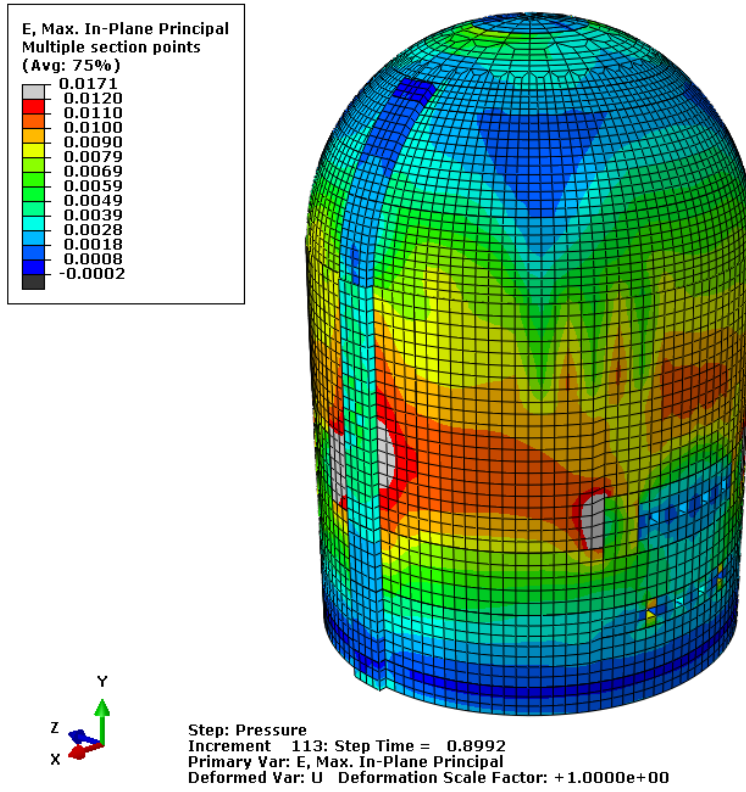
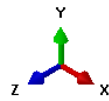
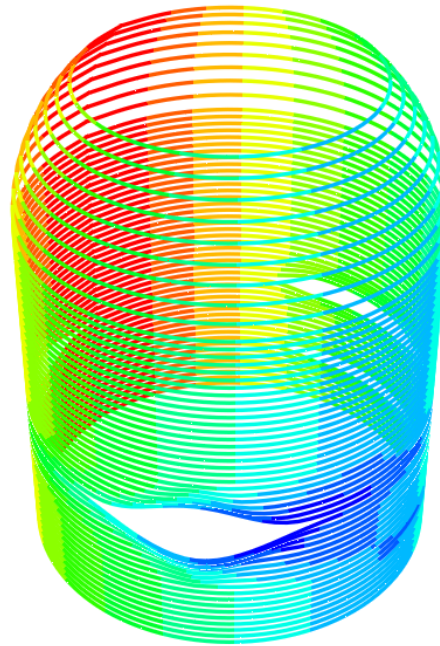
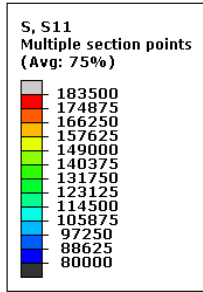
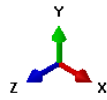
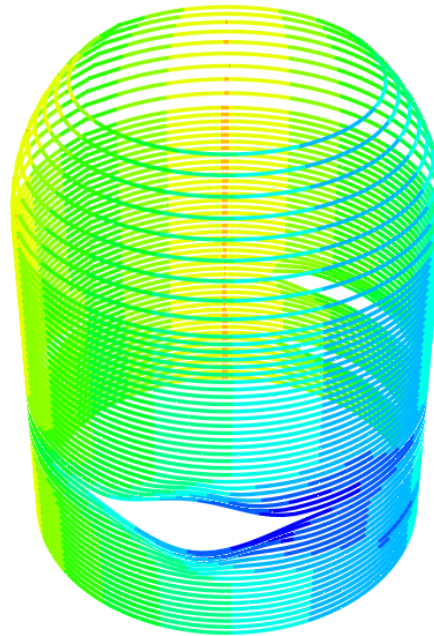
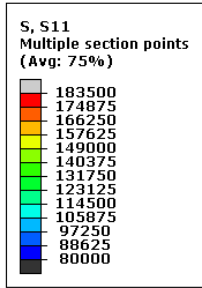


Figure D 186: Max Principal Membrane Strain in Concrete at 3.6 x Pd.



Step: Jacking-finish
Increment 24: Step Time = 1.000
Primary Var: S, S11
Deformed Var: U Deformation Scale Factor: +1e+00

Figure D 187: Stress in Hoop Tendons Anchored at 90° after Jacking before Anchorage.



Step: Anchor
Increment 15: Step Time = 1.000
Primary Var: S, S11
Deformed Var: U Deformation Scale Factor: +1e+00

Figure D 188: Stress in Hoop Tendons Anchored at 90° after Anchorage.

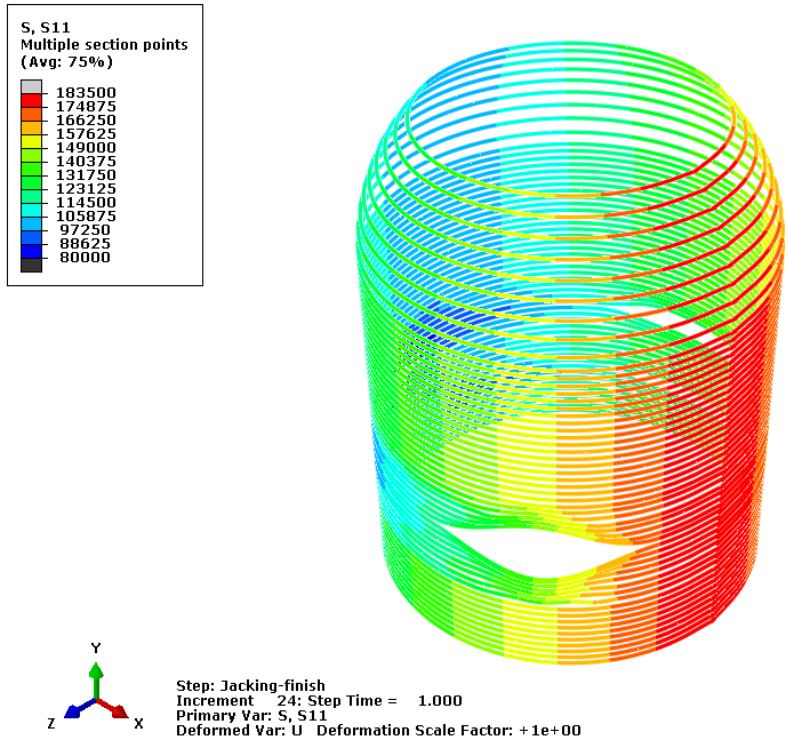
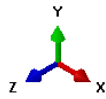
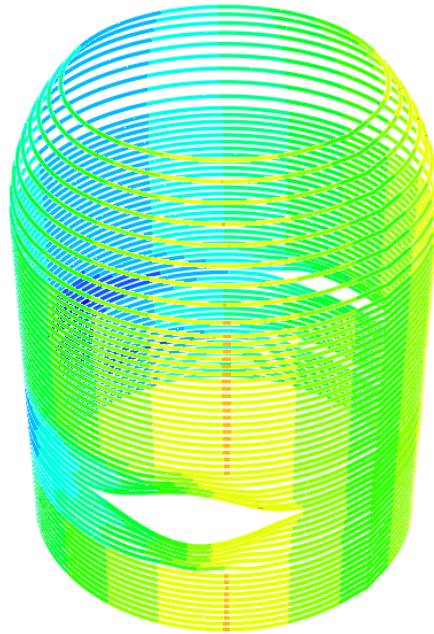
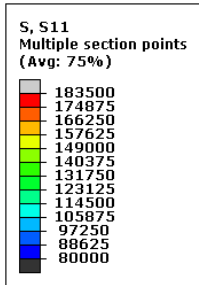
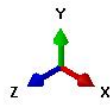
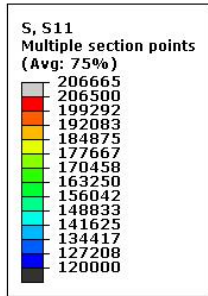


Figure D 189: Stress in Hoop Tendons Anchored at 270° after Jacking before Anchorage.



Step: Anchor
Increment 15: Step Time = 1.000
Primary Var: S, S11
Deformed Var: U Deformation Scale Factor: +1e+00

Figure D 190: Stress in Hoop Tendons Anchored at 270° after Anchorage.



Step: Jacking-finish
Increment 24: Step Time = 1.000
Primary Var: S, S11
Deformed Var: U Deformation Scale Factor: +1e+00

Figure D 191: Stress in Vertical Tendons after Jacking before Anchorage

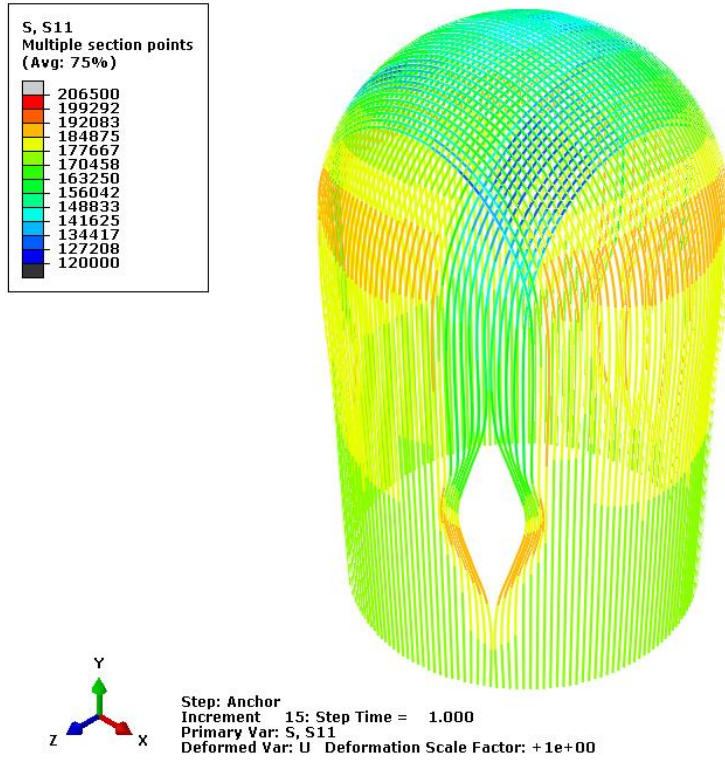


Figure D 192: Stress in Vertical Tendons after Anchorage

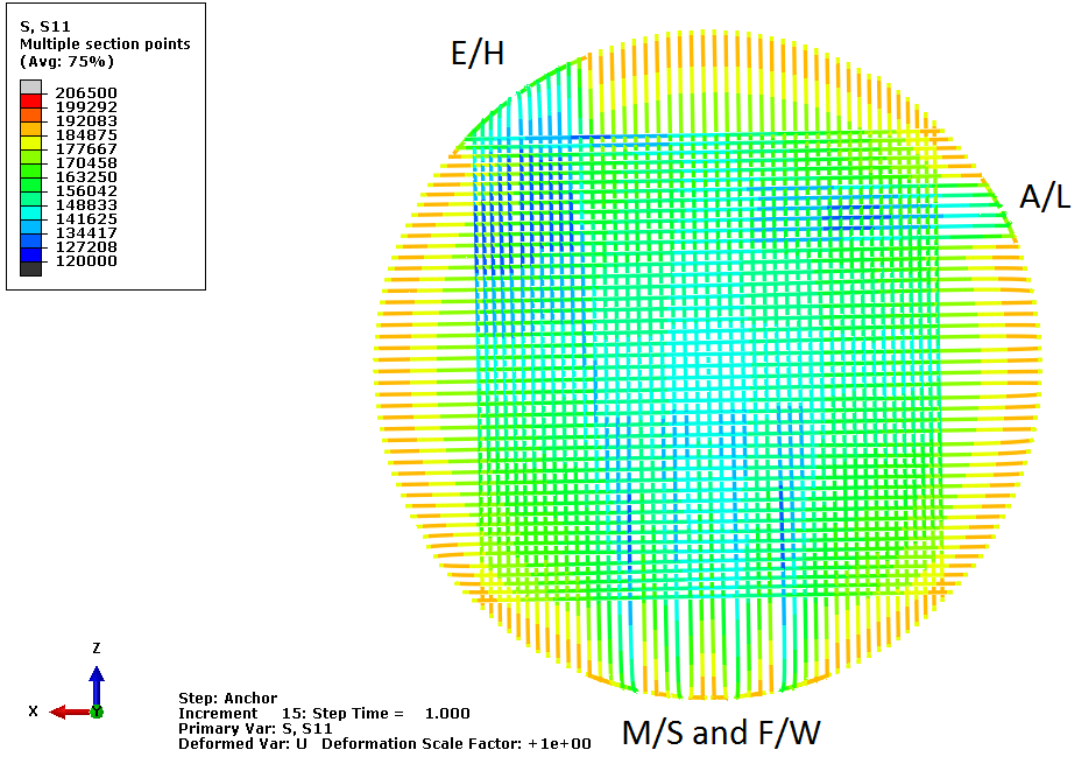
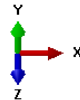
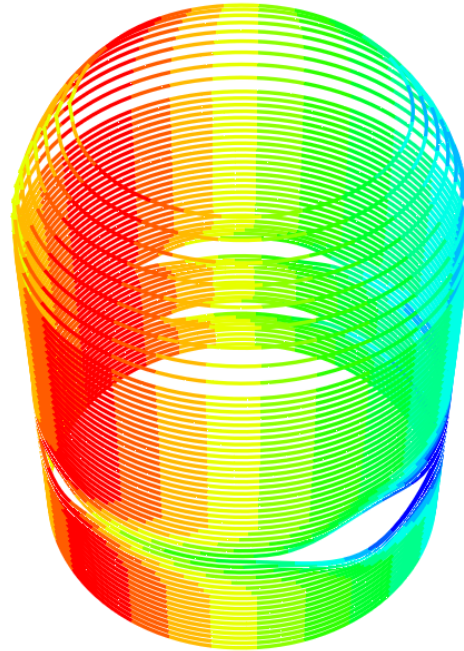
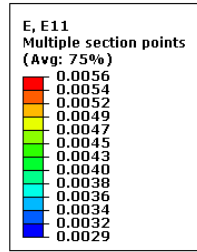
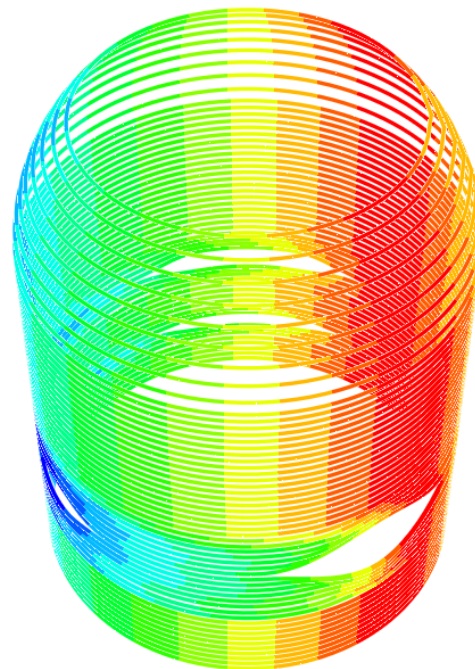
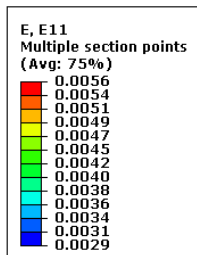


Figure D 193: Stress in Vertical Tendons in Dome after Anchorage



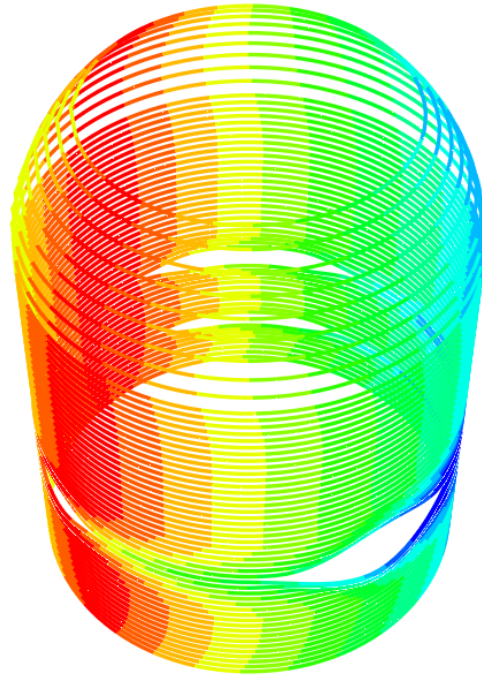
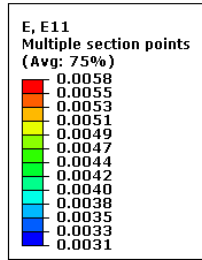
Step: Anchor
 Increment 15: Step Time = 1.000
 Primary Var: E, E11
 Deformed Var: U Deformation Scale Factor: +1.0000e+00

Figure D 194: Strain in Hoop Tendons Anchored at 90° after Anchorage



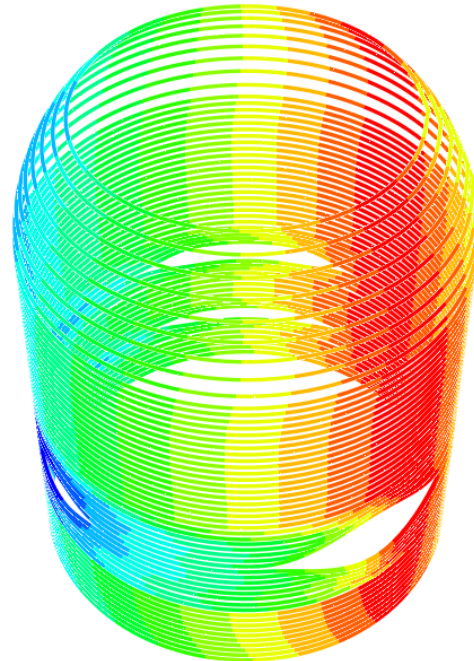
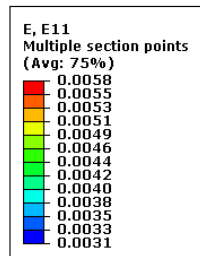
Step: Anchor
 Increment 15: Step Time = 1.000
 Primary Var: E, E11
 Deformed Var: U Deformation Scale Factor: +1.0000e+00

Figure D 195: Strain in Hoop Tendons Anchored at 270° after Anchorage



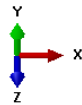
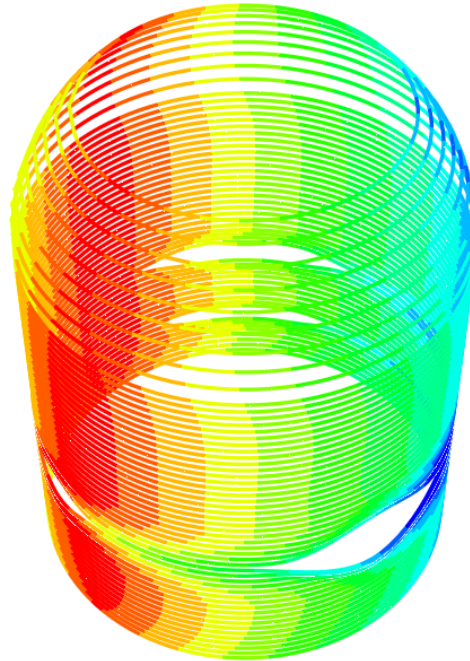
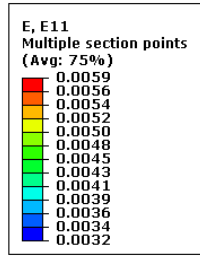
Step: Pressure
Increment 26: Step Time = 0.2475
Primary Var: E, E11
Deformed Var: U Deformation Scale Factor: +1.0000e+00

Figure D 196: Strain in Hoop Tendons Anchored at 90° at 1.0 x Pd



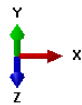
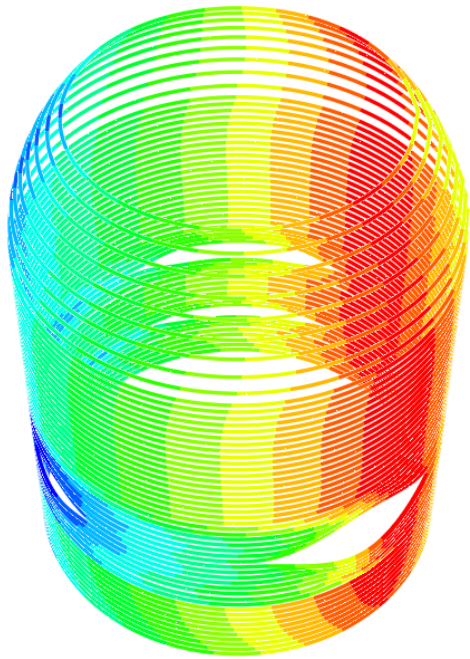
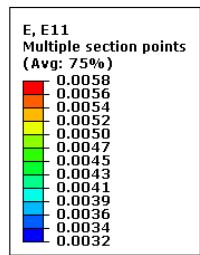
Step: Pressure
Increment 26: Step Time = 0.2475
Primary Var: E, E11
Deformed Var: U Deformation Scale Factor: +1.0000e+00

Figure D 197: Strain in Hoop Tendons Anchored at 270° at 1.0 x Pd



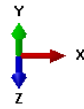
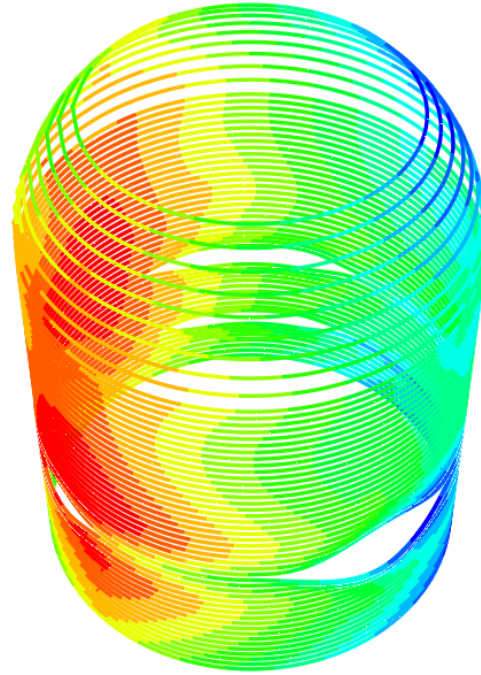
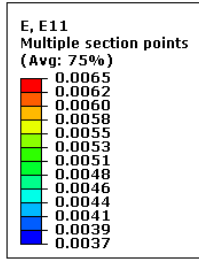
Step: Pressure
 Increment 39: Step Time = 0.3775
 Primary Var: E, E11
 Deformed Var: U Deformation Scale Factor: +1.0000e+00

Figure D 198: Strain in Hoop Tendons Anchored at 90° at 1.5 x Pd



Step: Pressure
 Increment 39: Step Time = 0.3775
 Primary Var: E, E11
 Deformed Var: U Deformation Scale Factor: +1.0000e+00

Figure D 199: Strain in Hoop Tendons Anchored at 270° at 1.5 x Pd.



Step: Pressure
Increment 51: Step Time = 0.4975
Primary Var: E, E11
Deformed Var: U Deformation Scale Factor: +1.0000e+00

Figure D 200: Strain in Hoop Tendons Anchored at 90° at 2.0 x Pd.

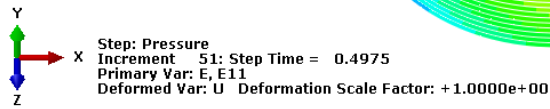
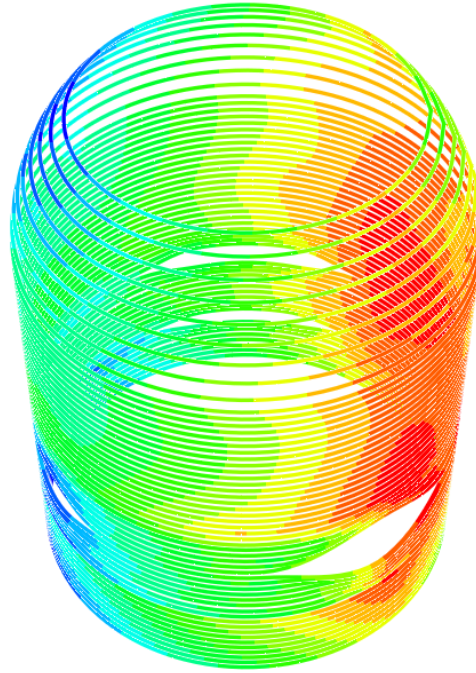
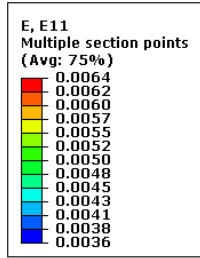
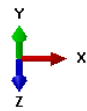
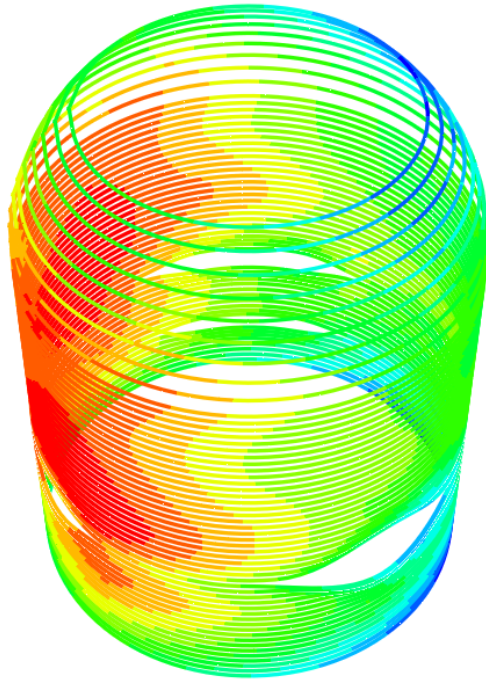
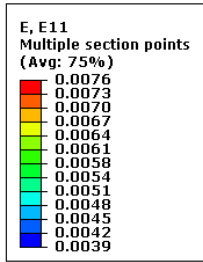
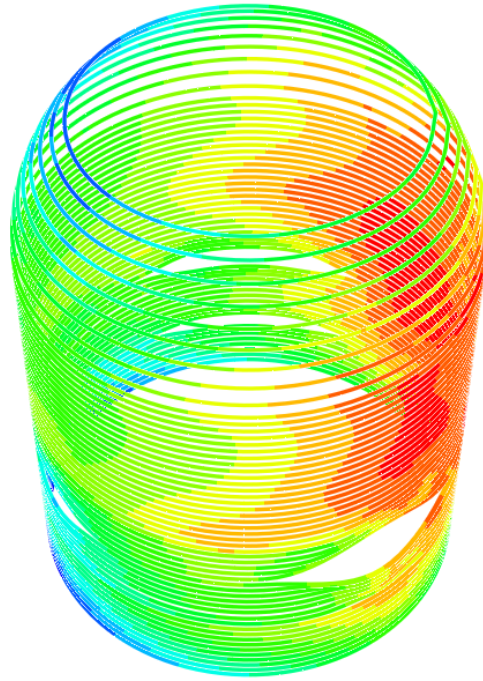
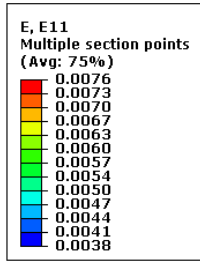


Figure D 201: Strain in Hoop Tendons Anchored at 270° at 2.0 x Pd



Step: Pressure
Increment 64: Step Time = 0.6275
Primary Var: E, E11
Deformed Var: U Deformation Scale Factor: +1.0000e+00

Figure D 202: Strain in Hoop Tendons Anchored at 90° at 2.5 x Pd.



Step: Pressure
Increment 64: Step Time = 0.6275
Primary Var: E, E11
Deformed Var: U Deformation Scale Factor: +1.0000e+00

Figure D 203: Strain in Hoop Tendons Anchored at 270° at 2.5 x Pd.

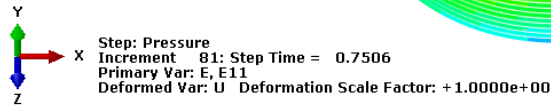
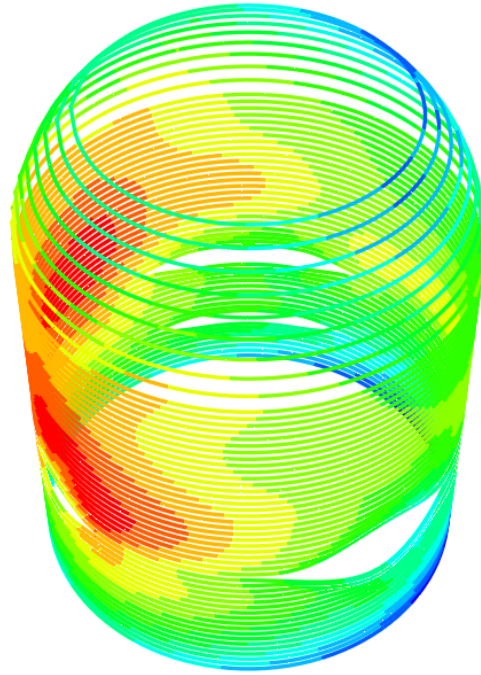
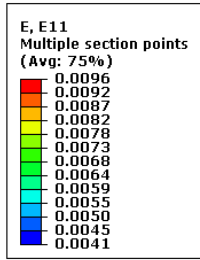
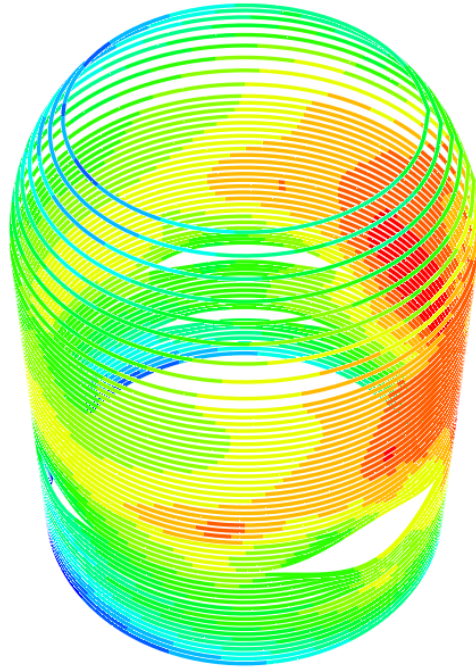
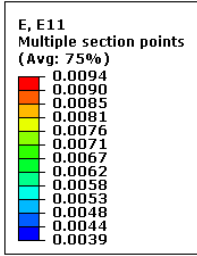


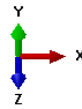
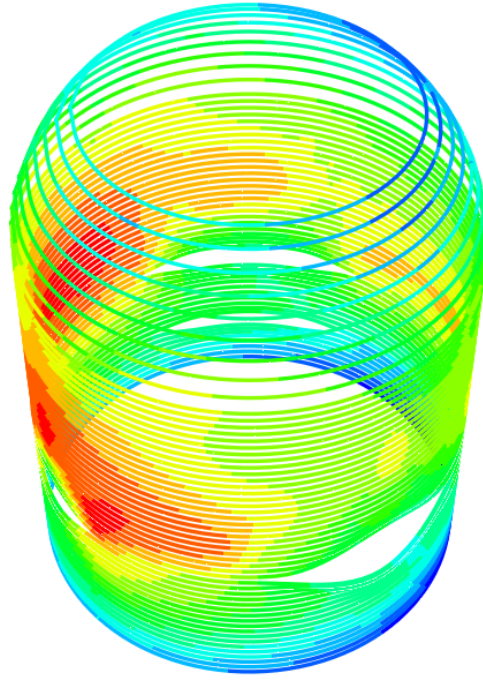
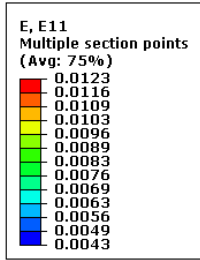
Figure D 204: Strain in Hoop Tendons Anchored at 90° at 3.0 x Pd.



Y
X
Z

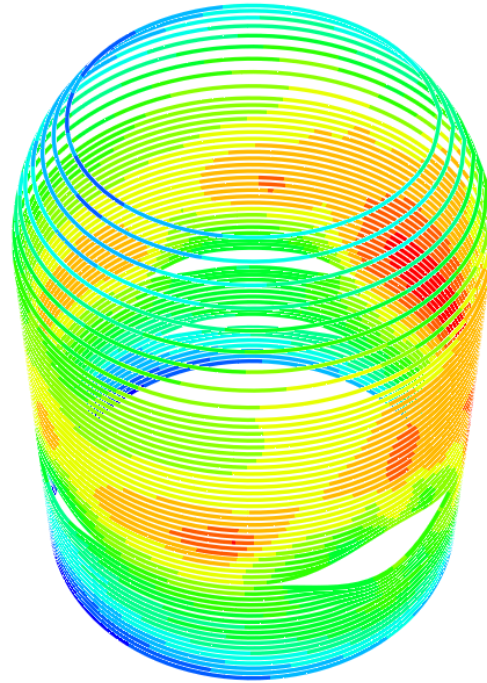
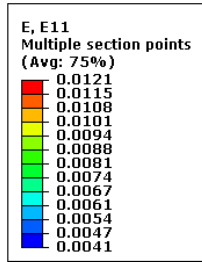
Step: Pressure
Increment 81: Step Time = 0.7506
Primary Var: E, E11
Deformed Var: U Deformation Scale Factor: +1.0000e+00

Figure D 205: Strain in Hoop Tendons Anchored at 270° at 3.0 x Pd.



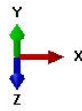
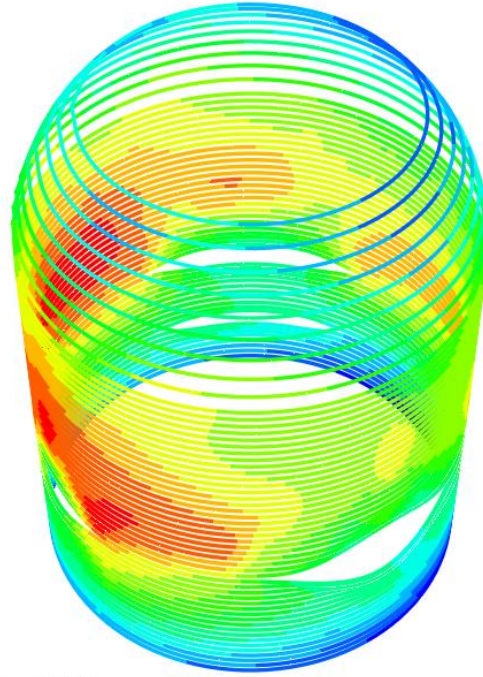
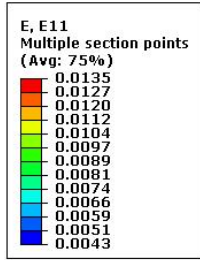
Step: Pressure
Increment 94; Step Time = 0.8272
Primary Var: E, E11
Deformed Var: U Deformation Scale Factor: +1.0000e+00

Figure D 206: Strain in Hoop Tendons Anchored at 90° at 3.3 x Pd.



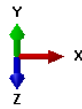
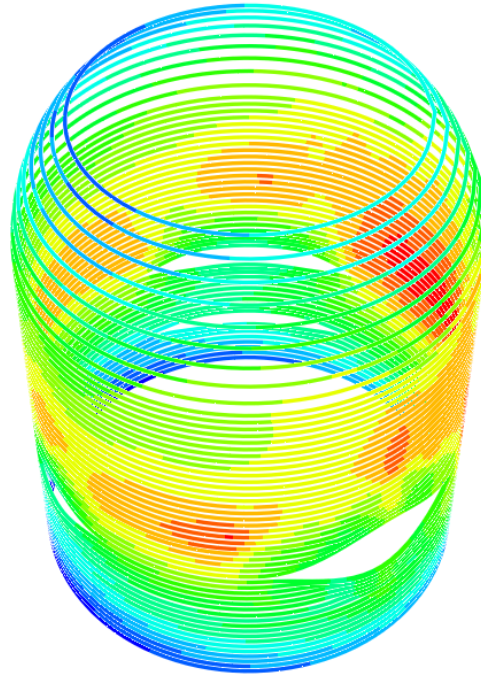
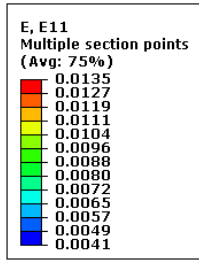
Step: Pressure
Increment: 94: Step Time = 0.8272
Primary Var: E, E11
Deformed Var: U Deformation Scale Factor: +1.0000e+00

Figure D 207: Strain in Hoop Tendons Anchored at 270° at 3.3 x Pd.



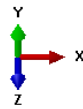
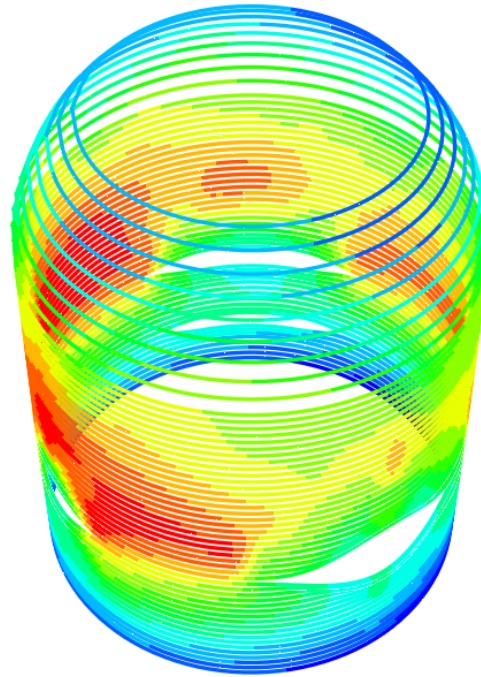
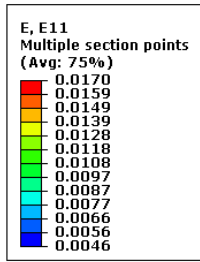
Step: Pressure
Increment 101: Step Time = 0.8504
Primary Var: E, E11
Deformed Var: U Deformation Scale Factor: +1.0000e+00

Figure D 208: Strain in Hoop Tendons Anchored at 90° at 3.4 x Pd



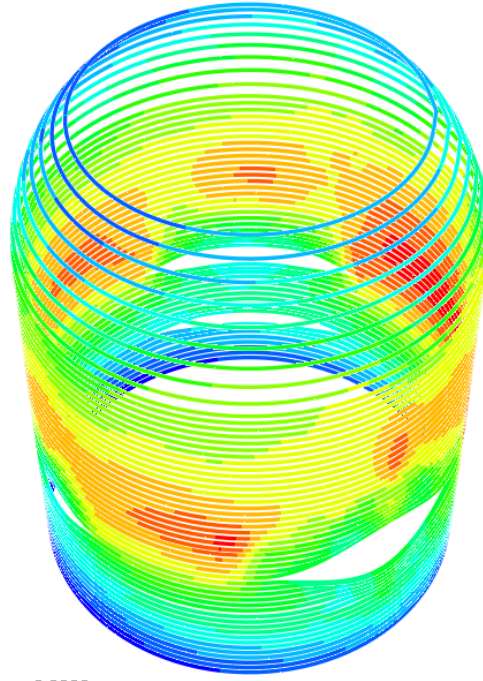
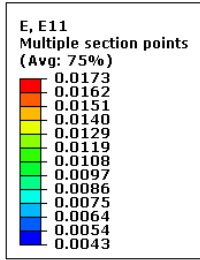
Step: Pressure
Increment 101: Step Time = 0.8504
Primary Var: E, E11
Deformed Var: U Deformation Scale Factor: +1.0000e+00

Figure D 209: Strain in Hoop Tendons Anchored at 270° at 3.4 x Pd.



Step: Pressure
Increment 113: Step Time = 0.8992
Primary Var: E, E11
Deformed Var: U Deformation Scale Factor: +1.0000e+00

Figure D 210: Strain in Hoop Tendons Anchored at 90° at 3.6 x Pd.



Y
X
Z

Step: Pressure
Increment 113: Step Time = 0.8992
Primary Var: E, E11
Deformed Var: U Deformation Scale Factor: +1.0000e+00

Figure D 211: Strain in Hoop Tendons Anchored at 270° at 3.6 x Pd.

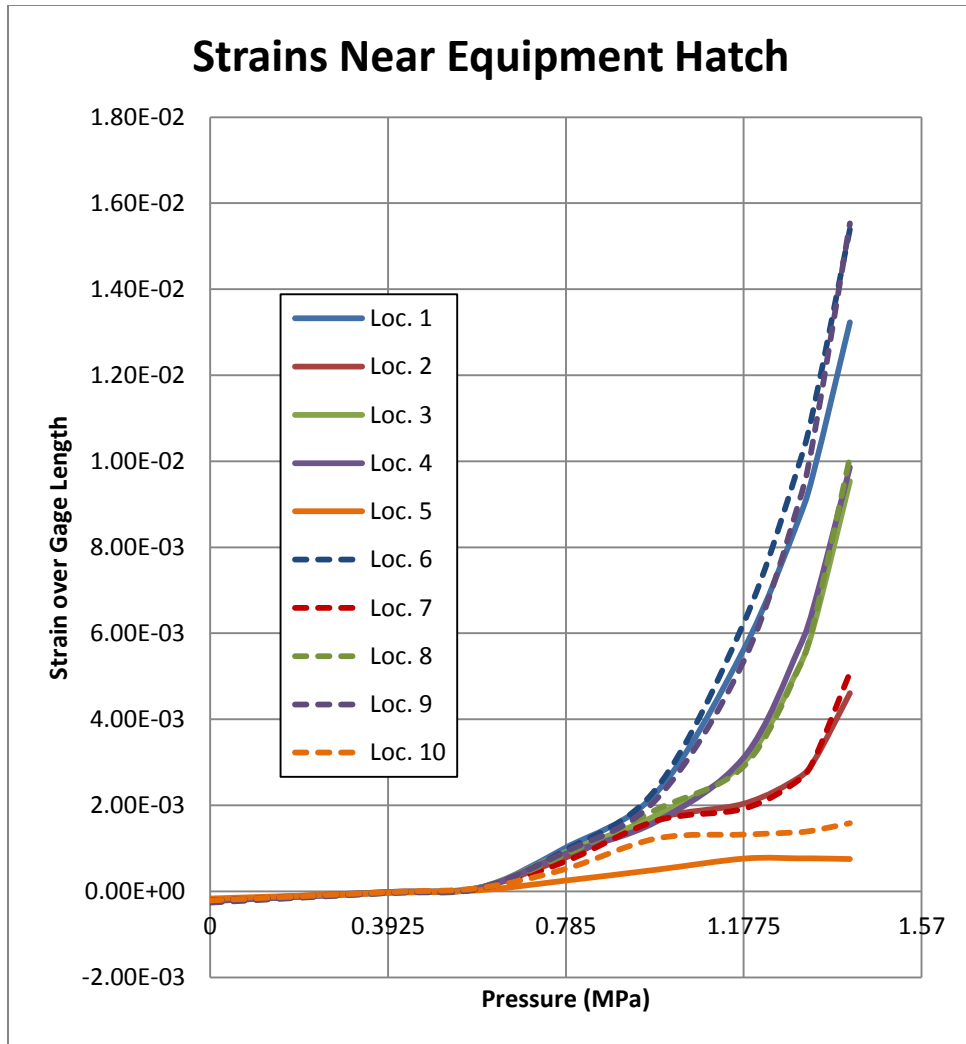


Figure D 212: Strains over Selected Gage Length Near E/H

Figure D 212 through 216 show strains over selected gage lengths near the penetrations, as requested of the analysts in the SPE instructions. The reference frame defining these locations was shown in Figure D 66 of the Model 2 Report (repeated herein on the next page). It should be noted that with the coarser mesh, and based on observations of where the highest strains are located, the locations “3, 4, 5” and locations “8, 9, 10” were shifted slightly so that locations 5 and 10 are on the embossment of the E/H and A/L (or on the thickened liner plate of the M/S and F/W penetrations), and locations 3, 4, and 8, 9 are adjacent to the embossments. The elevated strains tend to occur adjacent to the embossments, not ON the embossments. These strains can ultimately be compared to those shown in the Model 2 report, and to the Liner Fracture Assessments which were conducted for Model 2 (more for demonstration purposes than for an exhaustive study). In that report, it was shown that at selected gage lengths in the vicinity of liner strain concentrations (like welds and anchors), liner strains of 0.003 may be sufficient to create a tear. Such strain levels are shown to exist in the global Model 3 analysis, and they exist at locations which did indeed exhibit liner tearing in the 1:4 Scale PCCV model test.

After Figure D 217, we plot the requested Standard Output Locations (SOLs) from Model 3 Analysis compared to the 1:4 Scale PCCV Model LST (and in a few cases where data is available, also the SFMT). For curves labeled “DOR” 1, 2, 3, etc., these refer to Data of Record 1, 2, 3, and the 1, 2, 3 refer to the fact that there are multiple gages at or near the designated location.

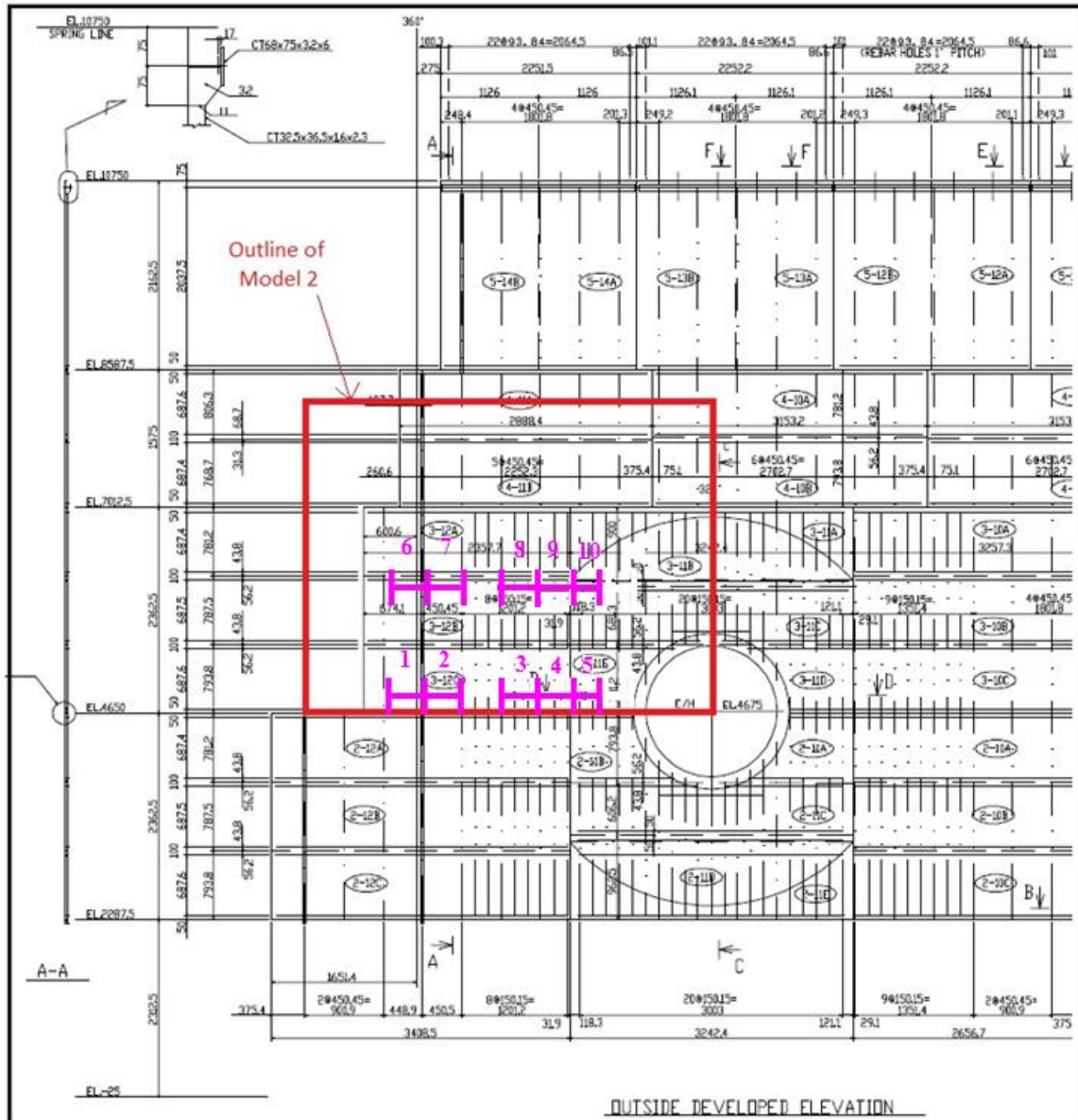


Figure D 213: Liner (E/H) View Showing Strain Reports (cut from Page A-28 of NUREG/CR-6810)

While in the coming weeks leading up to the April Meeting of SPE participants, we will be reviewing the SOL comparisons in detail, preliminarily, it can be observed that for most of the fundamental response quantities such as midheight displacement of the cylinder (at free-field, buttress, and E/H, for example), the analysis compares well to the test measurements. Some of the response quantities which are 1) very small, or 2) have limitations based on the shell

element modeling employed, such as displacements at the wall-base juncture, show some noticeable differences between analysis and test. Exploring these similarities and differences will be a subject of discussion at the April Meeting.

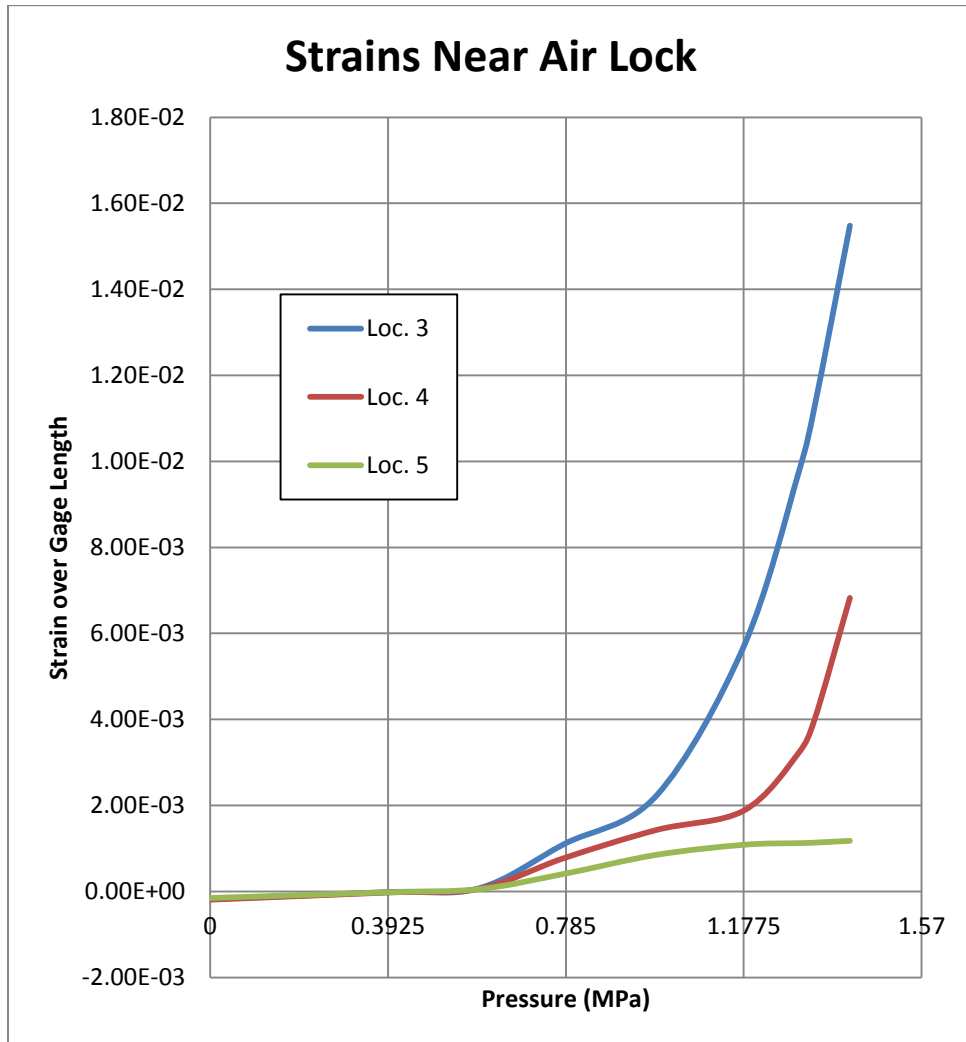


Figure D 214: Strains over Selected Gage Length Near A/L

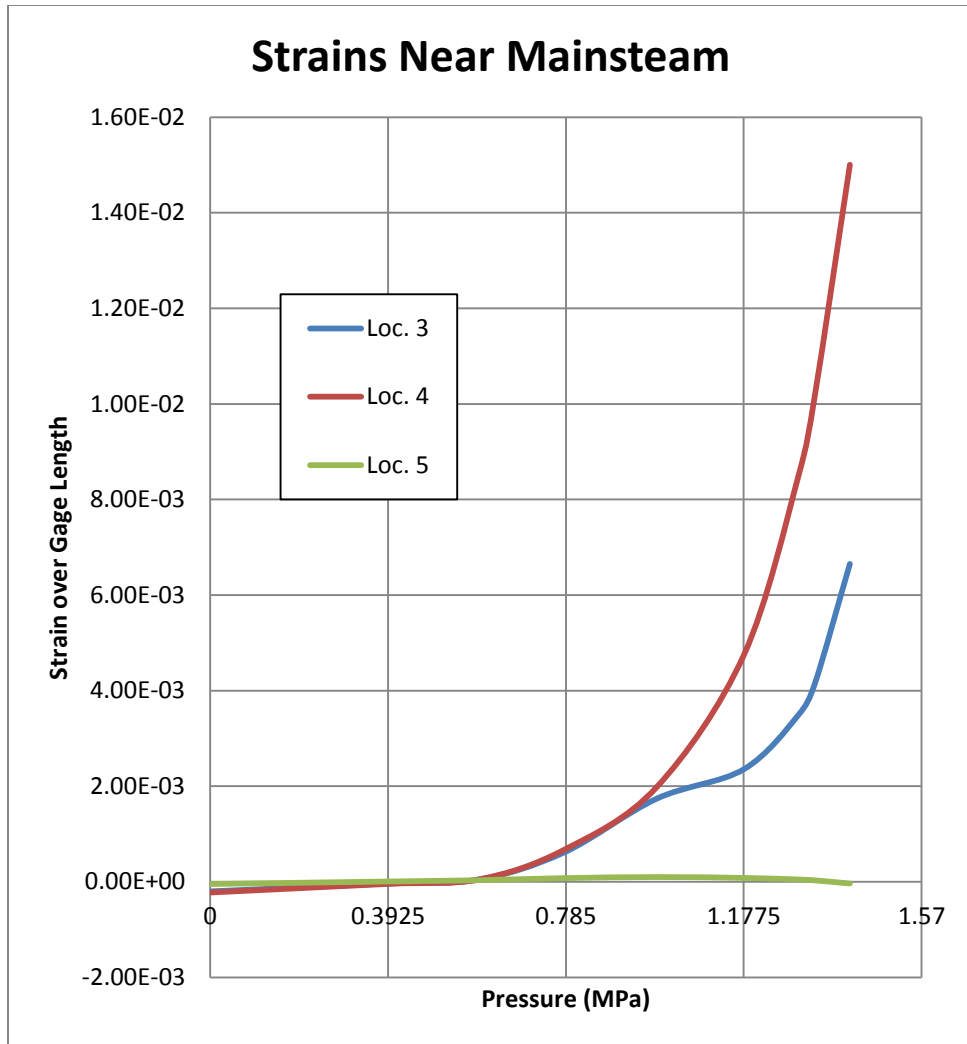


Figure D 215: Strains over Selected Gage Length Near M/S

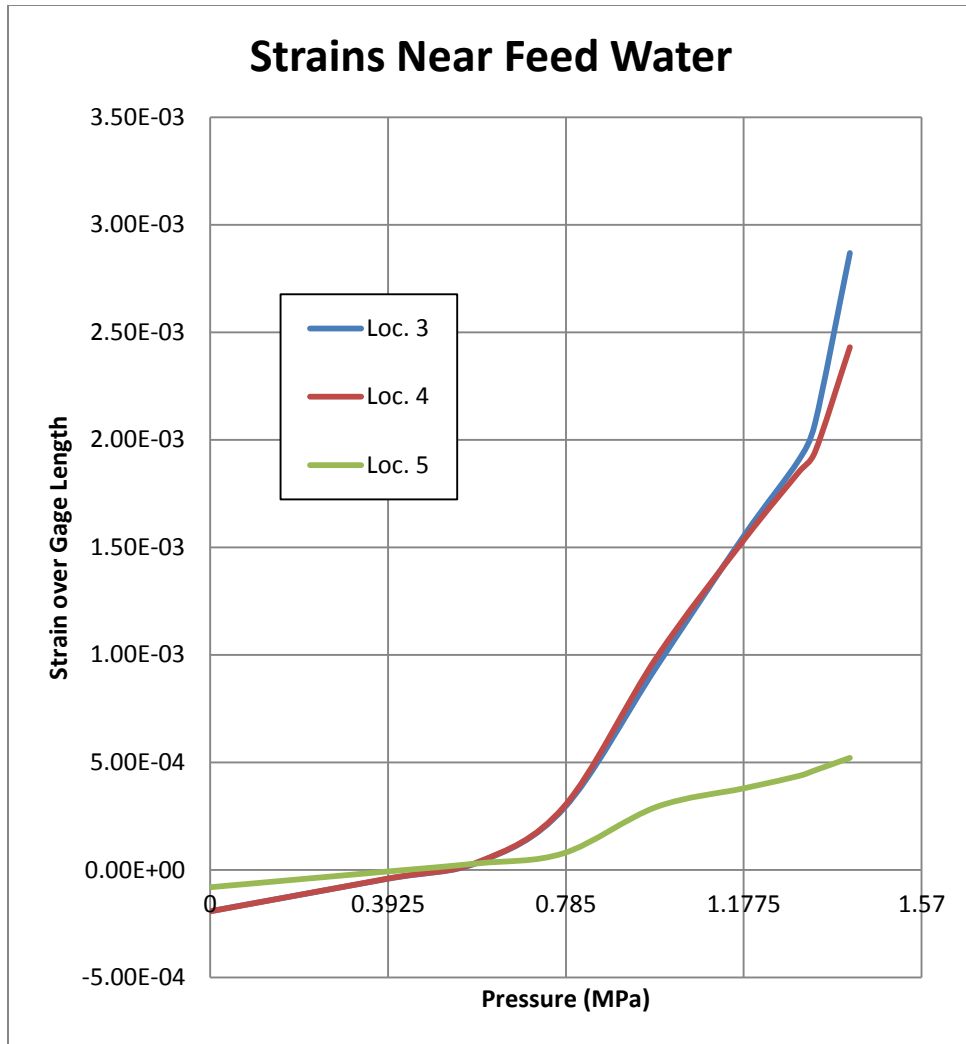


Figure D 216: Strains over Selected Gage Length Near F/W

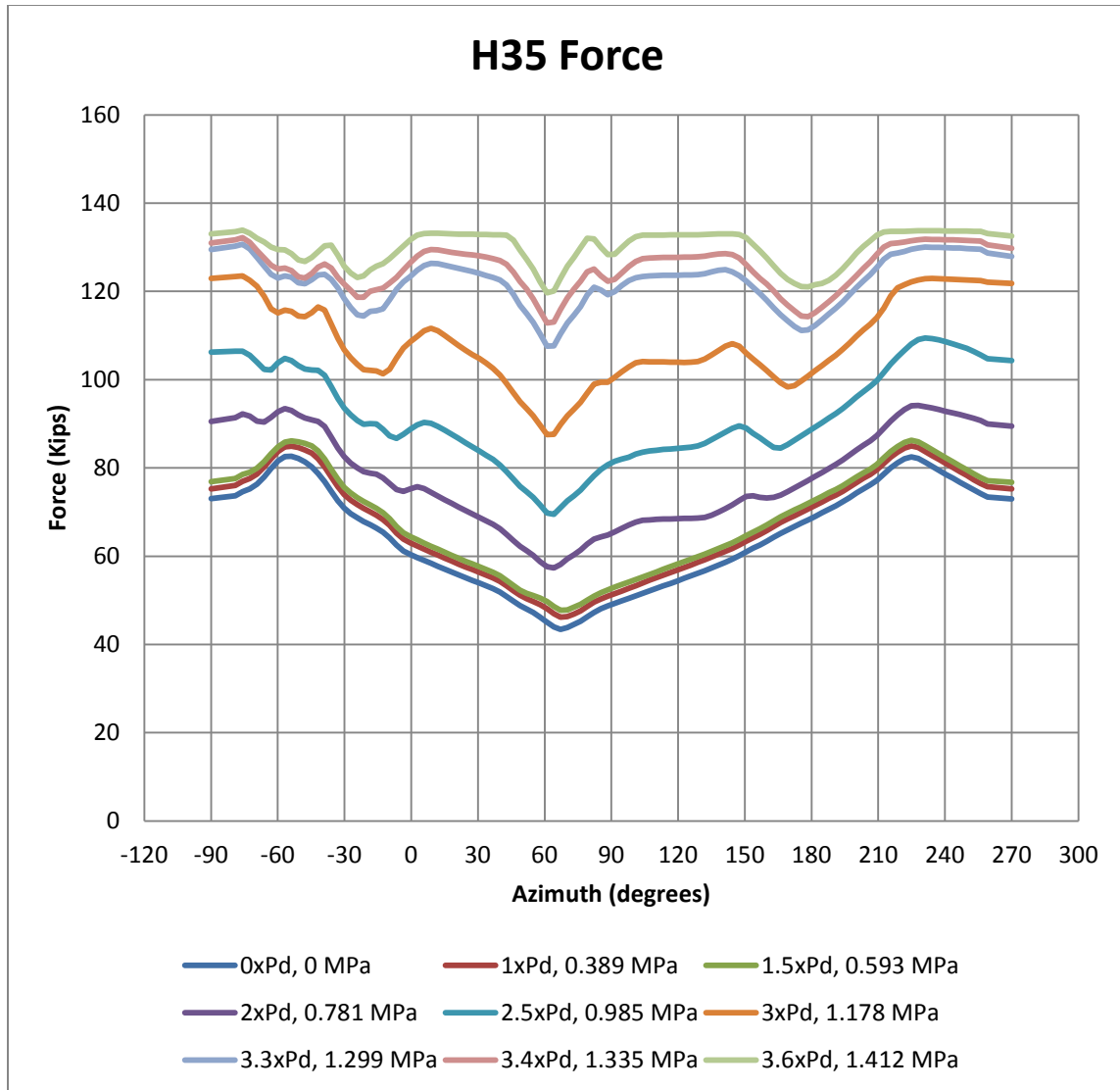


Figure D 217: Abaqus Analysis – Hoop Tendon H35 Force

Figure D 217 through 269 show tendon stress profiles for the four most comprehensively instrumented tendons in the 1:4 Scale PCCV model test. While it is difficult to compare the results precisely due to the limited number of instruments on the tendons, for the hoop tendons, in particular, the trends agree well between the analysis and test. For the vertical tendons the general stress levels and effects of friction show similar trends, but there are some differences in stress distribution observed in the dome, between the analysis and the test measurements, especially for Tendon V37. (For Tendon V46, the trends between analysis and test, even in the dome look reasonably similar.)

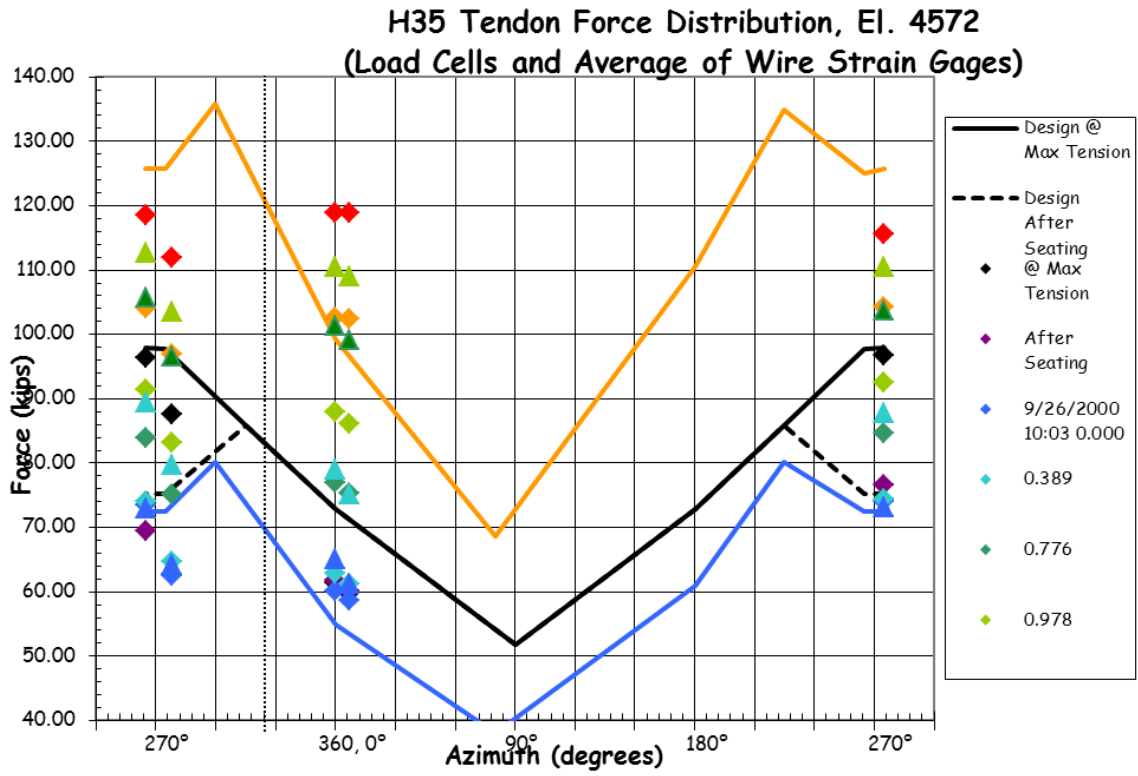


Figure D 218: LST Test – Hoop Tendon H35 Force

SFMT - H35 Tendon Force Distribution, El. 4572
 (Load Cells and Average of Wire Strain Gages)

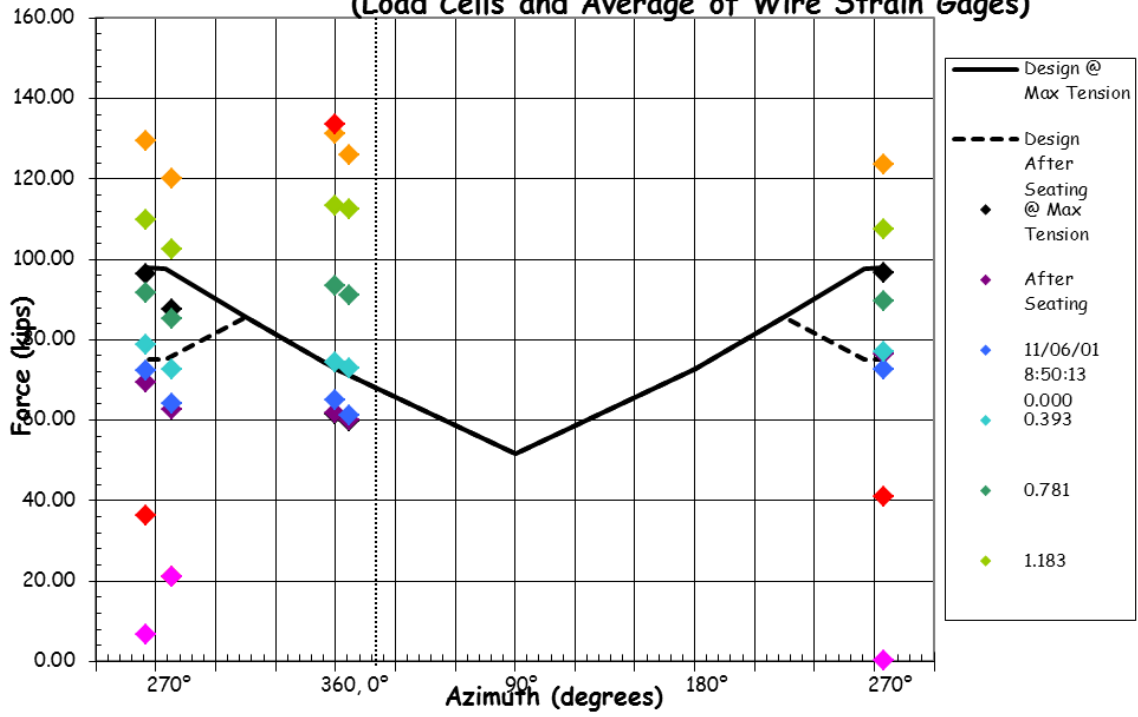


Figure D 219: SFMT Test – Hoop Tendon H35 Force

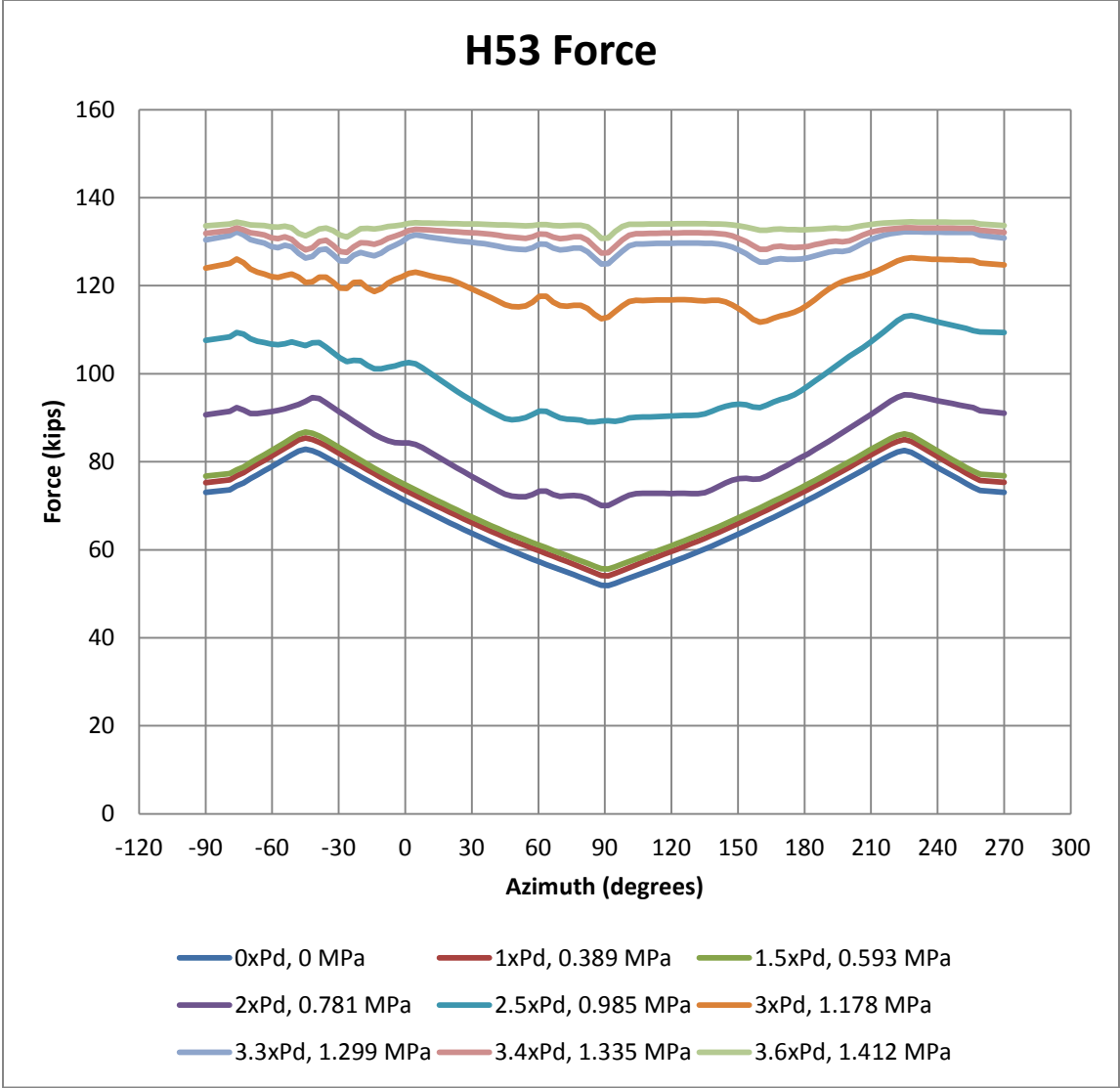


Figure D 220: Abaqus Analysis – Hoop Tendon H53 Force

LST - H53 Tendon Force Distribution, El. 6579
 (Load Cells and Average of Wire Strain Gages)

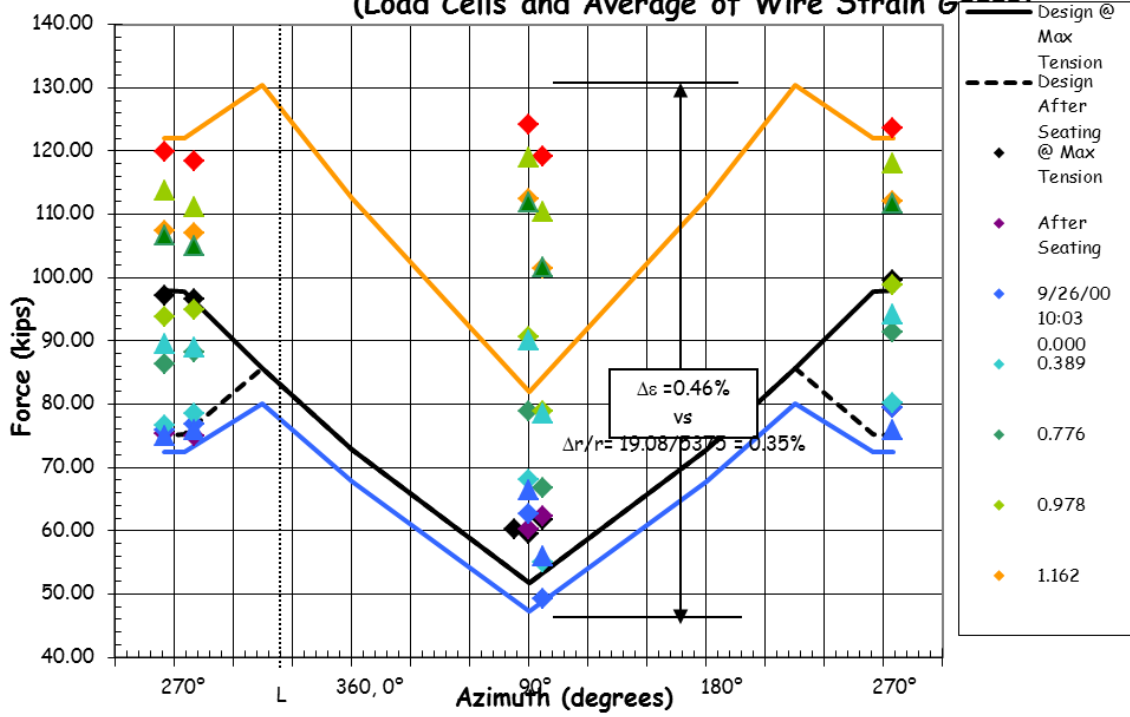


Figure D 221: LST Test – Hoop Tendon H53 Force

SFMT - H53 Tendon Force Distribution, El. 6579 (Load Cells and Average of Wire Strain Gages)

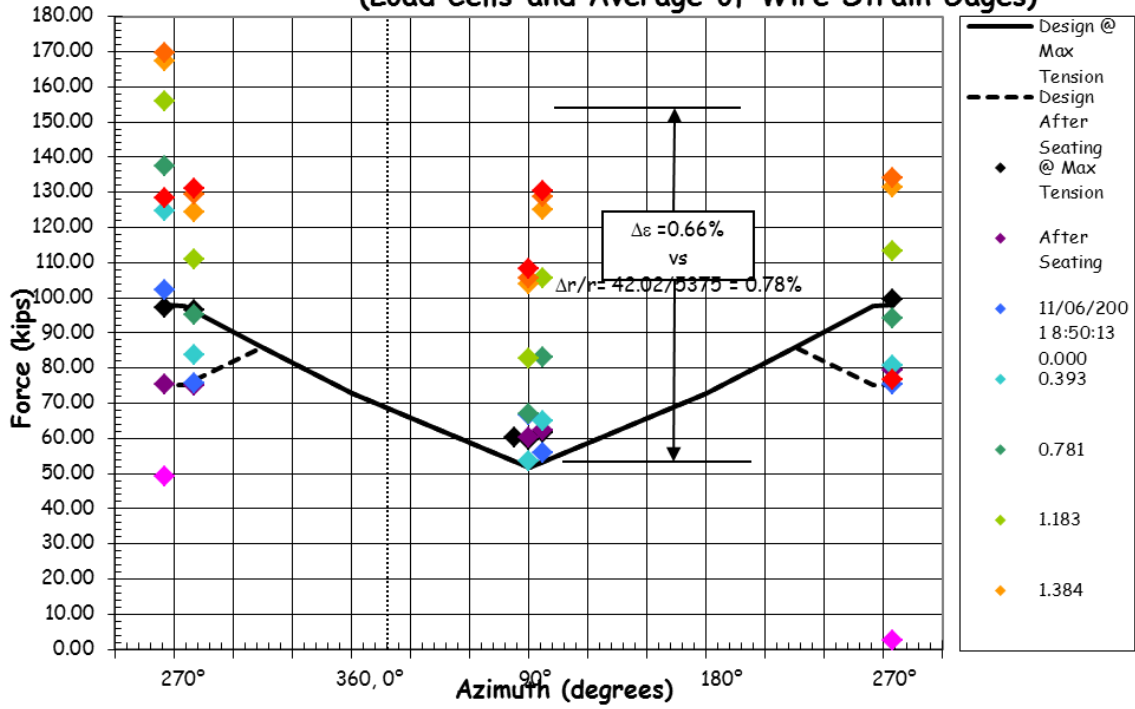


Figure D 222: SFMT Test – Hoop Tendon H53 Force

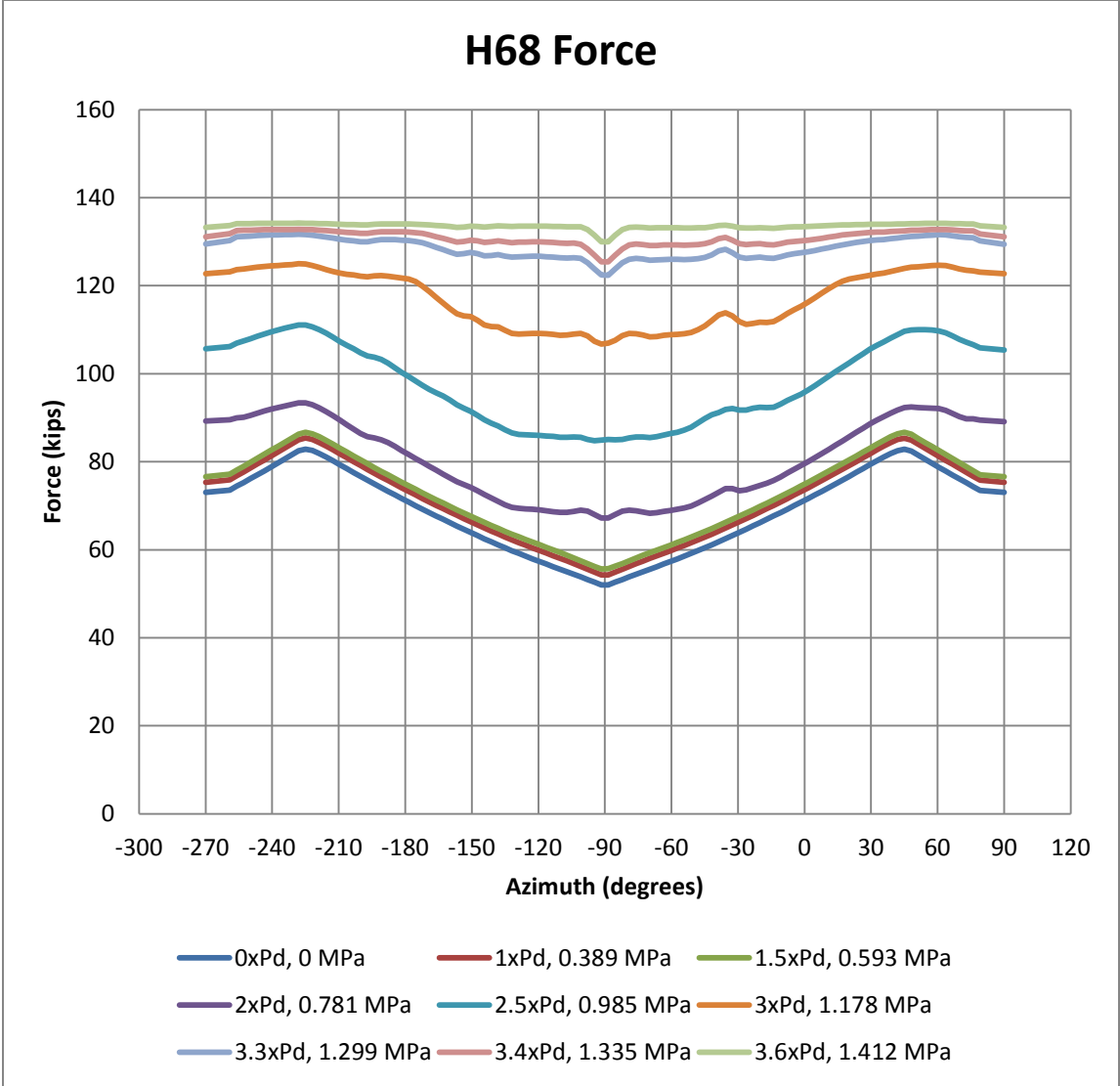


Figure D 223: Abaqus Analysis – Hoop Tendon H68 Force

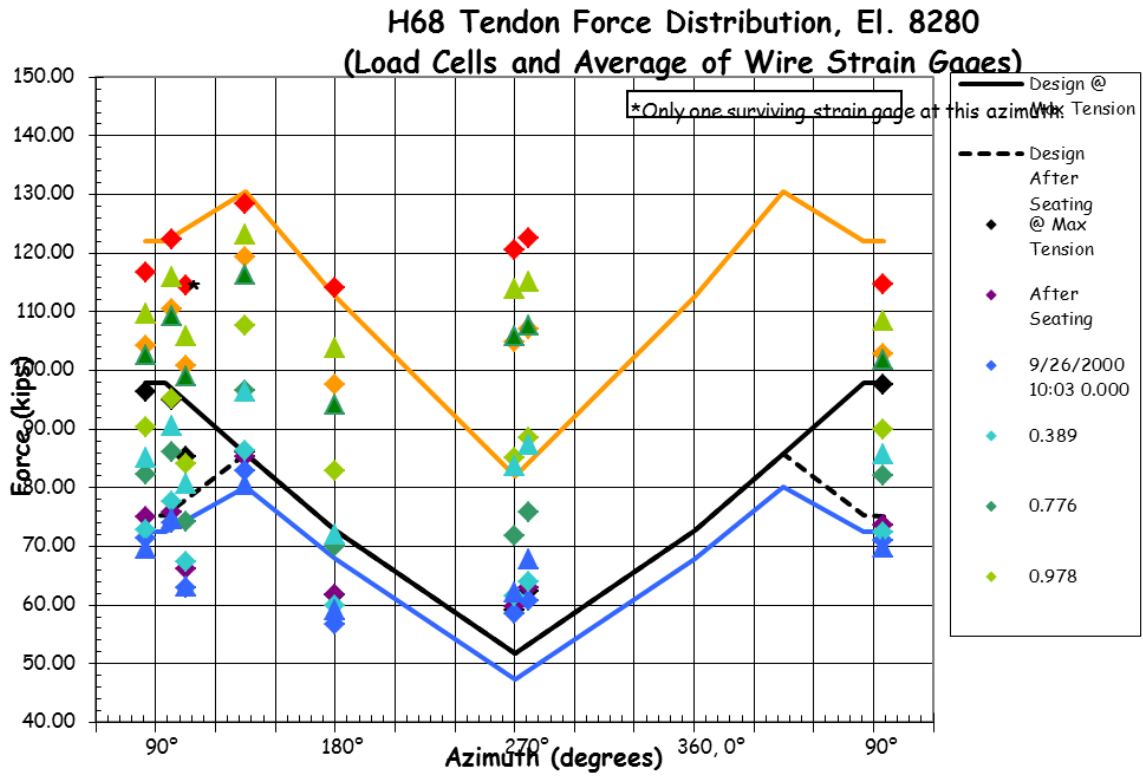


Figure D 224: LST Test – Hoop Tendon H68 Force

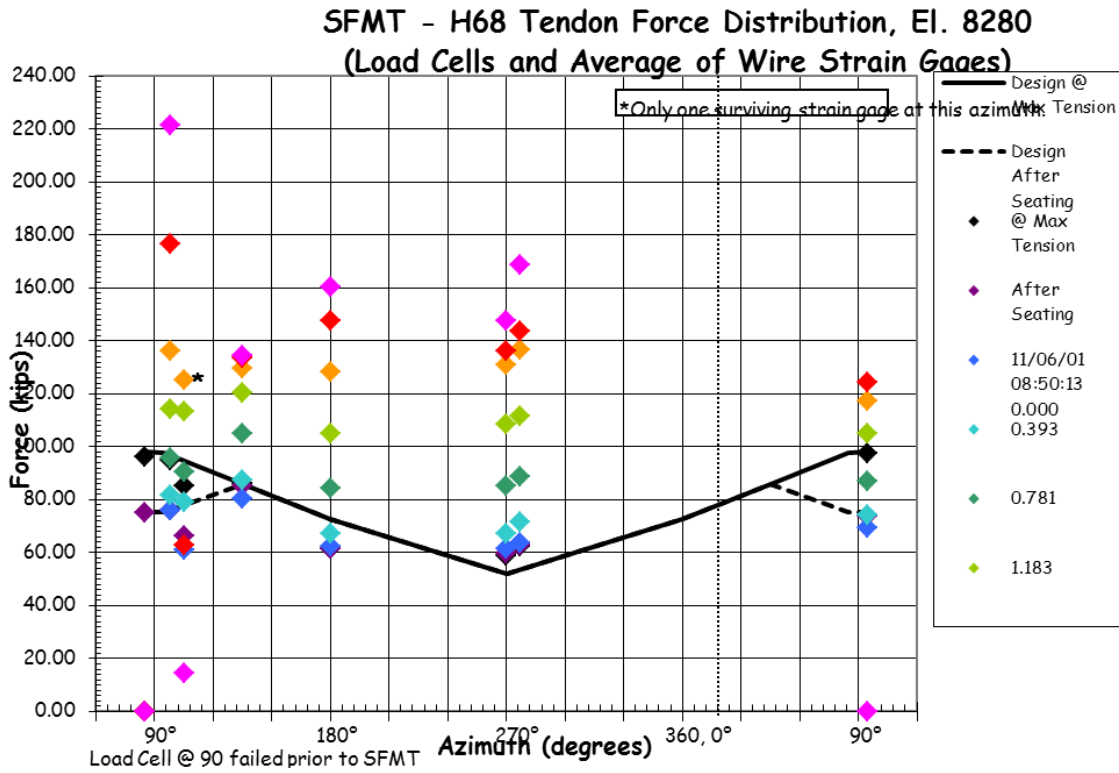


Figure D 225: SFMT Test – Hoop Tendon H68 Force

V37 Force - Unbonded

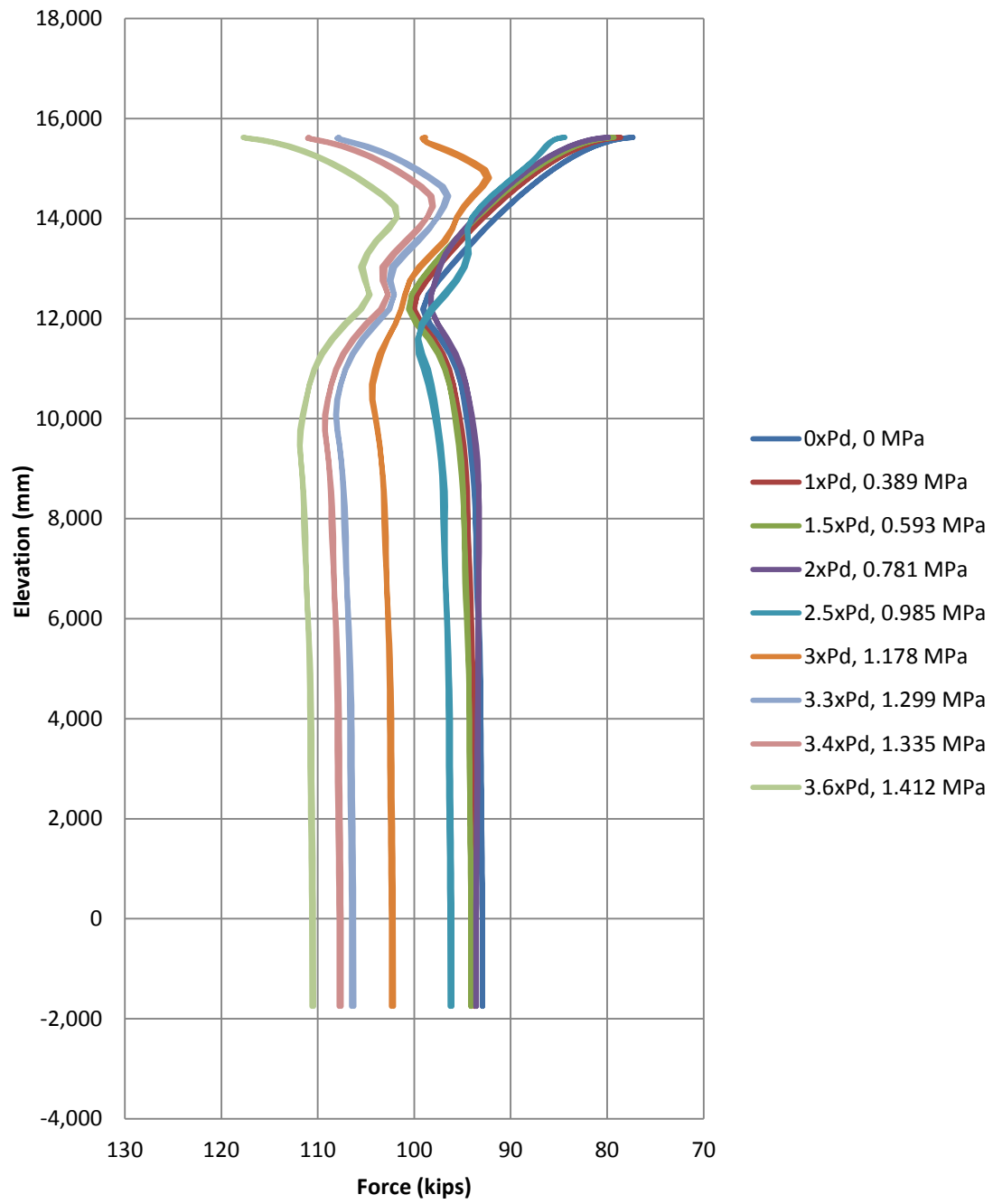


Figure D 226: Abaqus Analysis – Hairpin Tendon V37 Force

V37 Tendon Force Distribution @ AZ. 240 (Load Cells and Average of Wire Strain Gages)

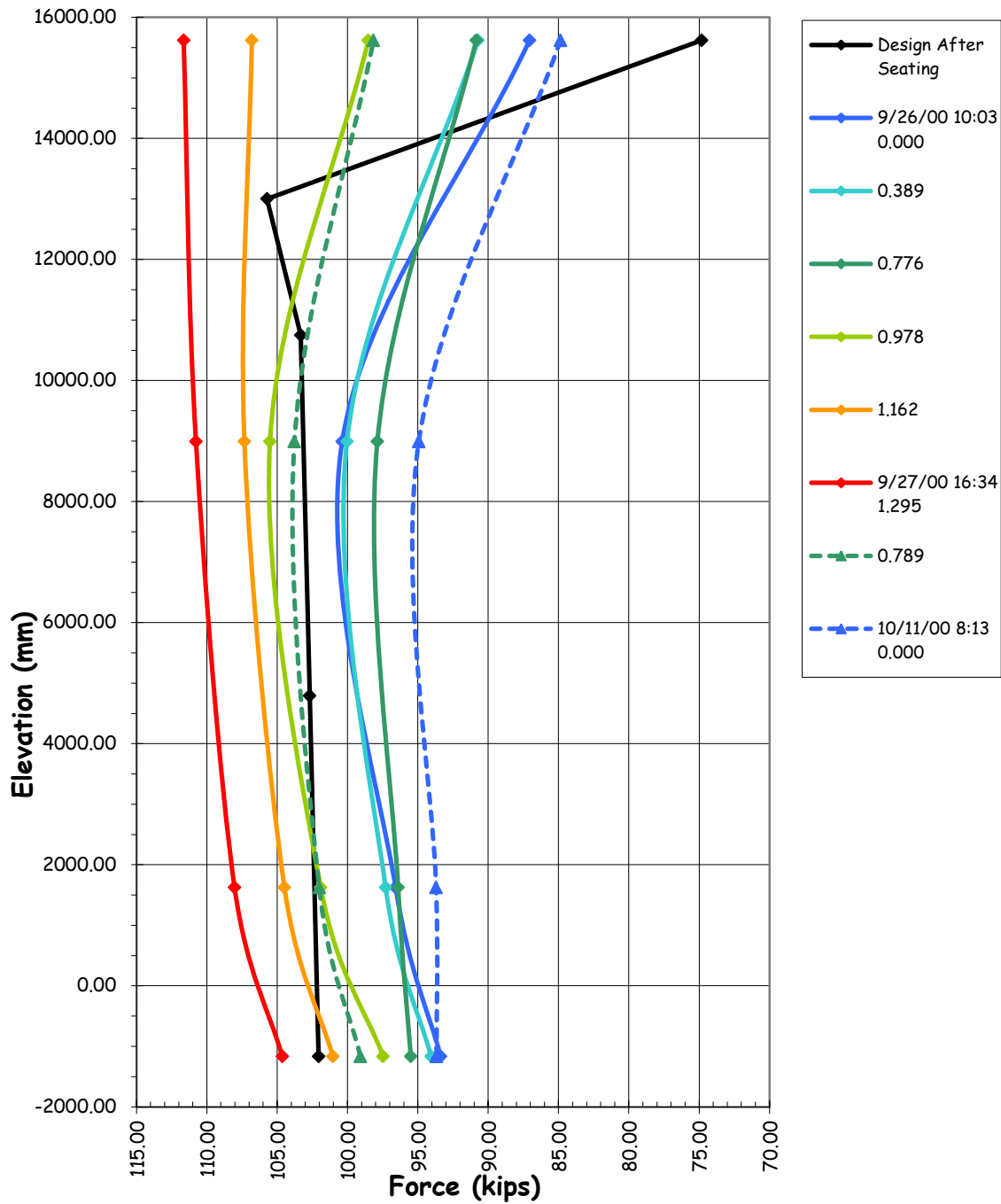


Figure D 227: LST Test – Hairpin Tendon H37 Force

SFMT-V37 Tendon Force Distribution @ AZ. 240

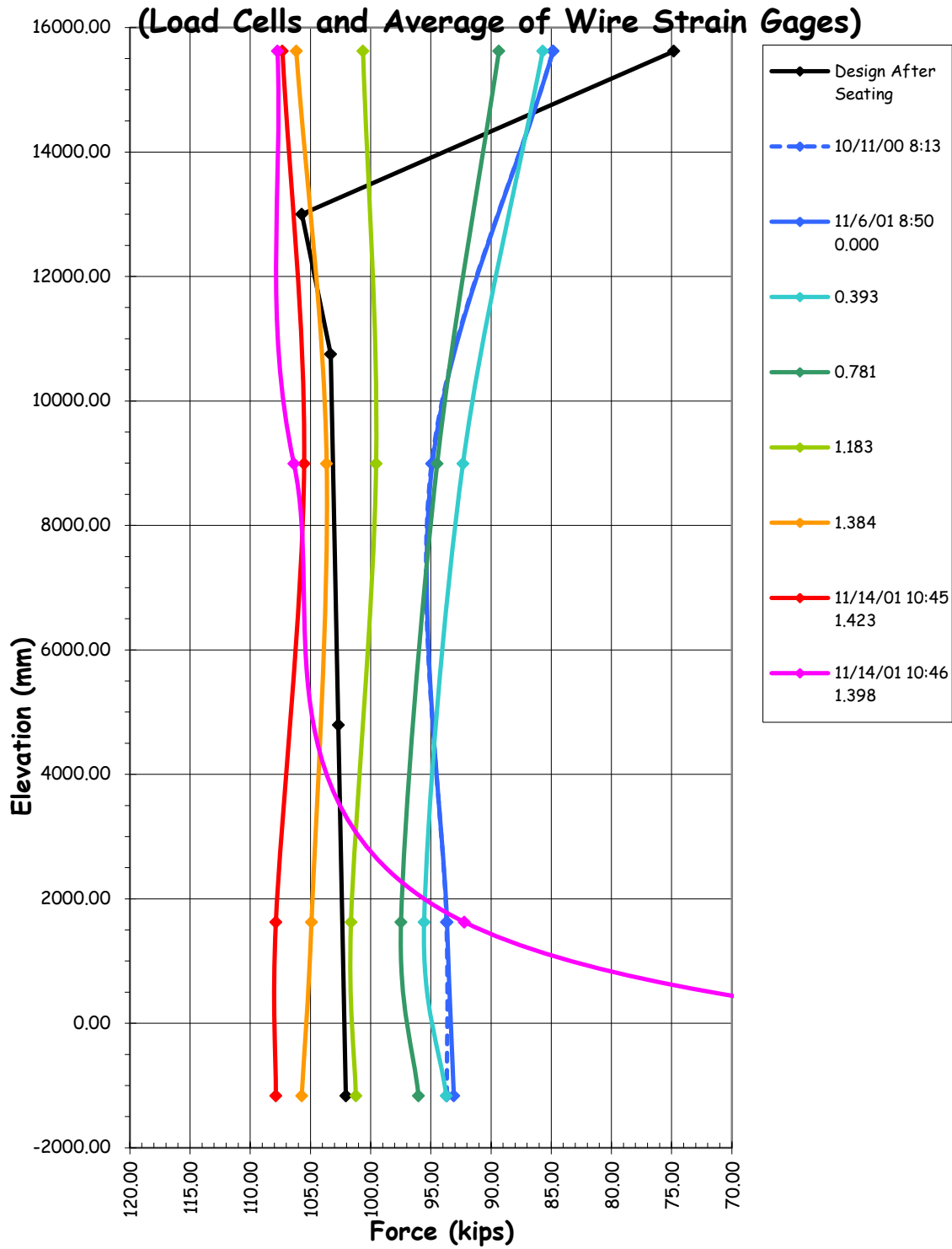


Figure D 228: SFMT Test – Hairpin Tendon H37 Force

V46 Force - Unbonded

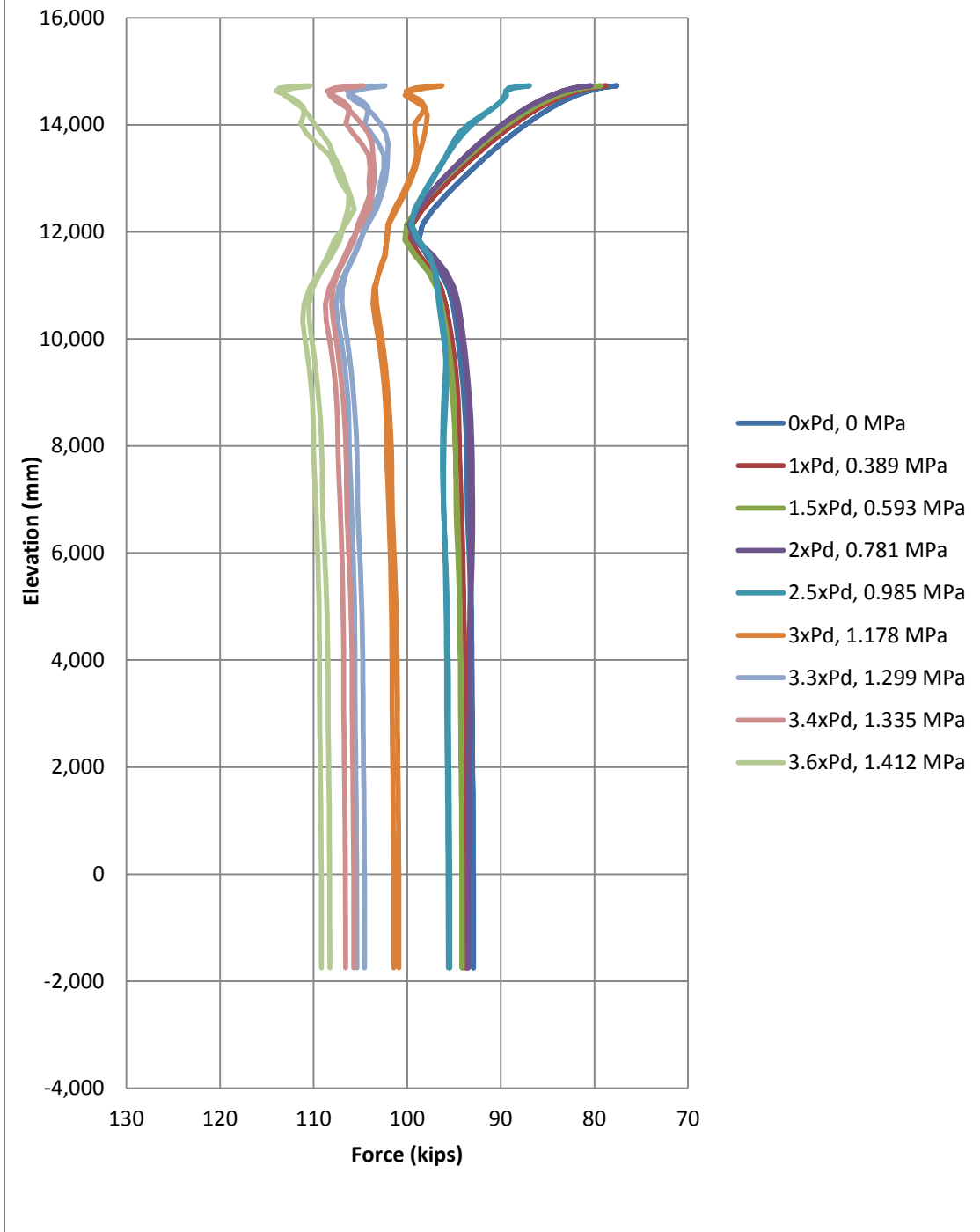


Figure D 229: Abaqus Analysis – Hairpin Tendon V46 Force

V46 Tendon Force Distribution @ AZ. 135 (Load Cells and Average of Wire Strain Gages)

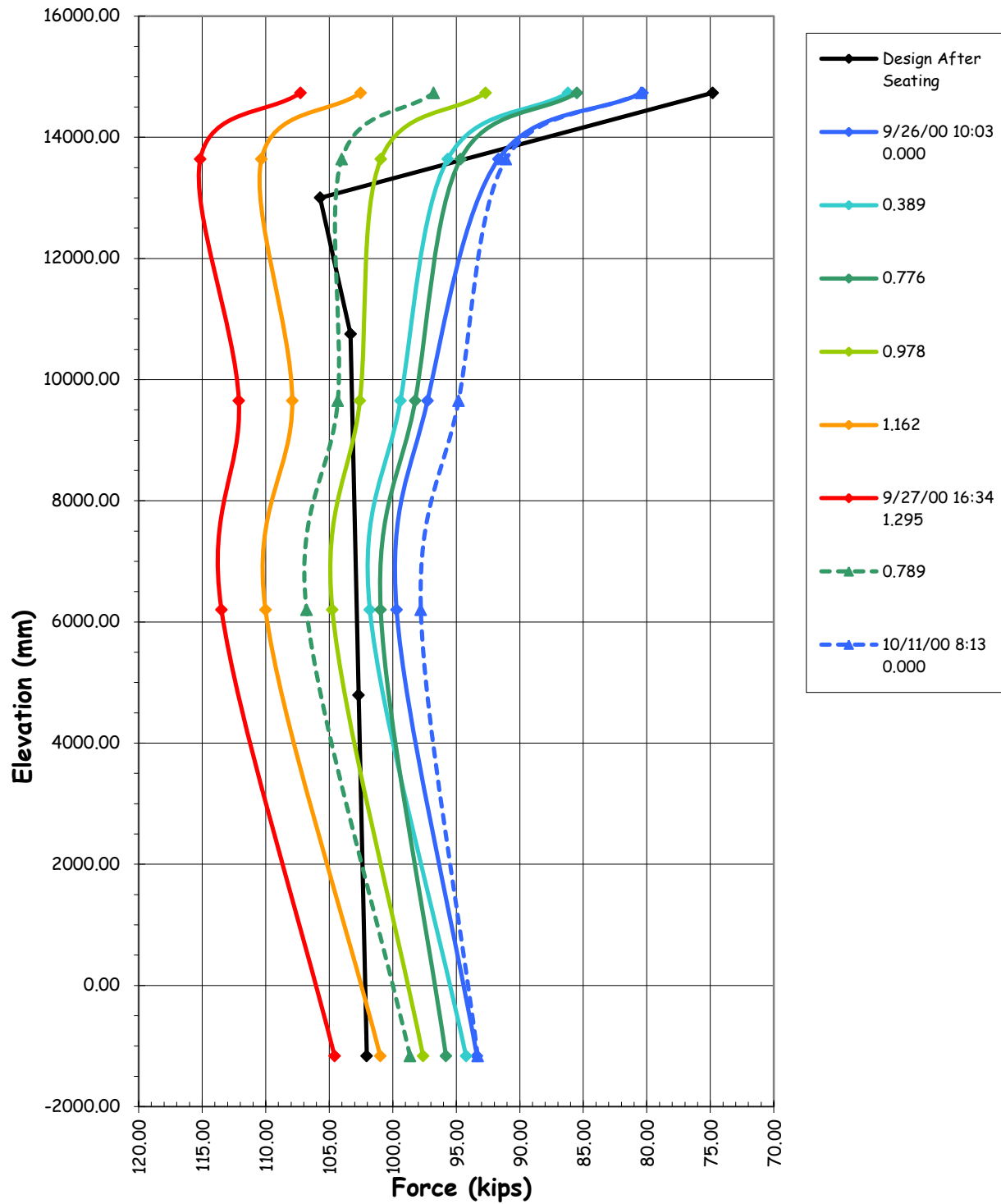


Figure D 230: LST Test – Hairpin Tendon H46 Force

SFMT-V46 Tendon Force Distribution @ AZ. 135 (Load Cells and Average of Wire Strain Gages)

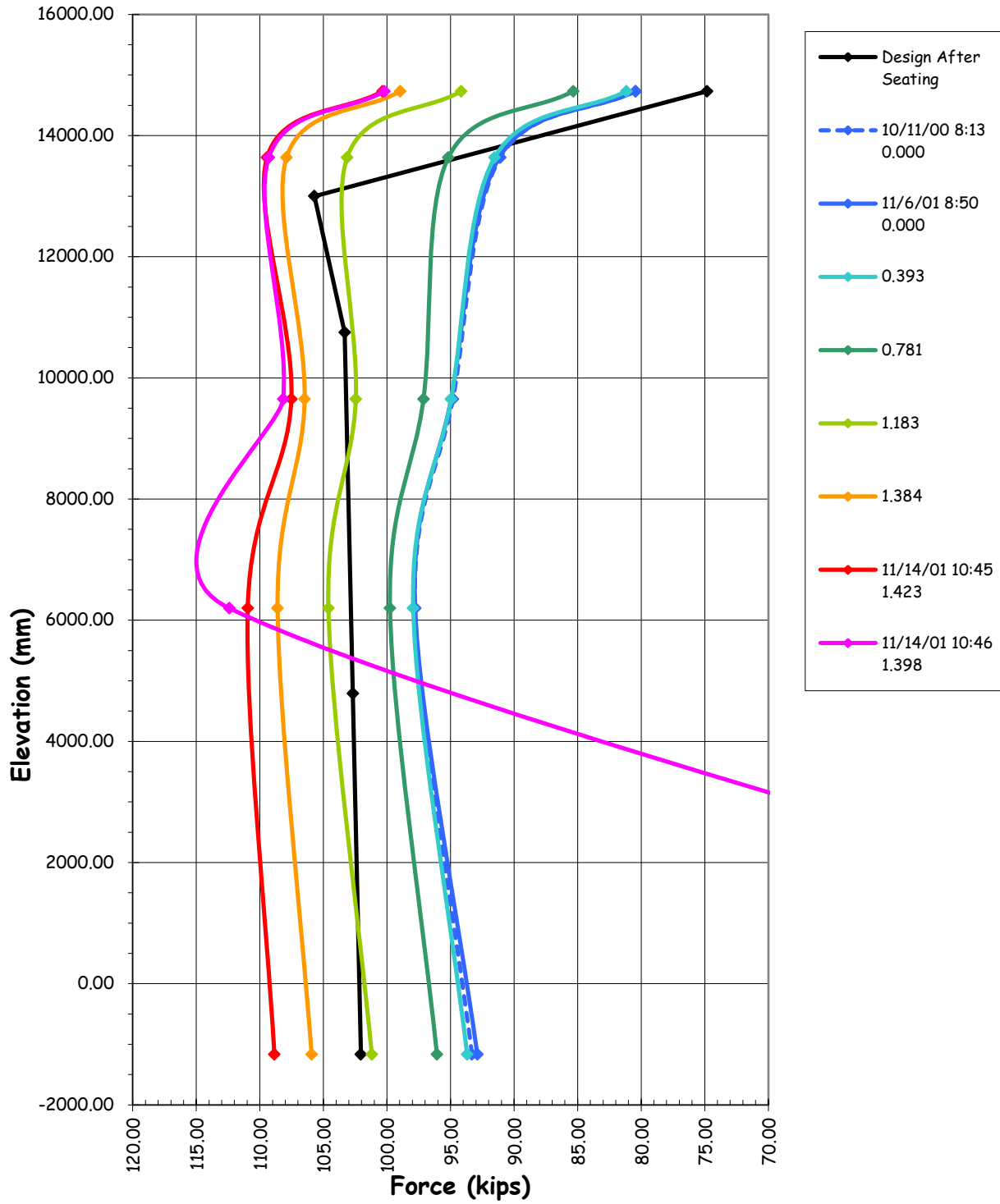


Figure D 231: SFMT Test – Hairpin Tendon H46 Force

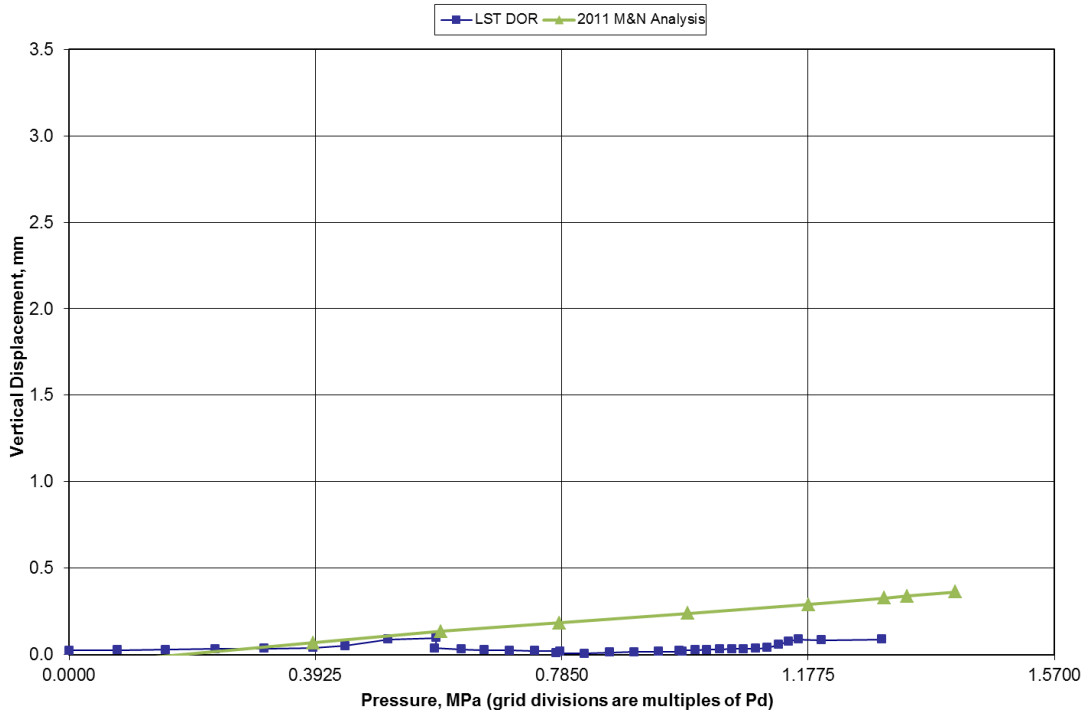


Figure D 232: Standard output location #1. Azimuth: 135 degrees, Elevation, 0.00 meters, top of Basemat

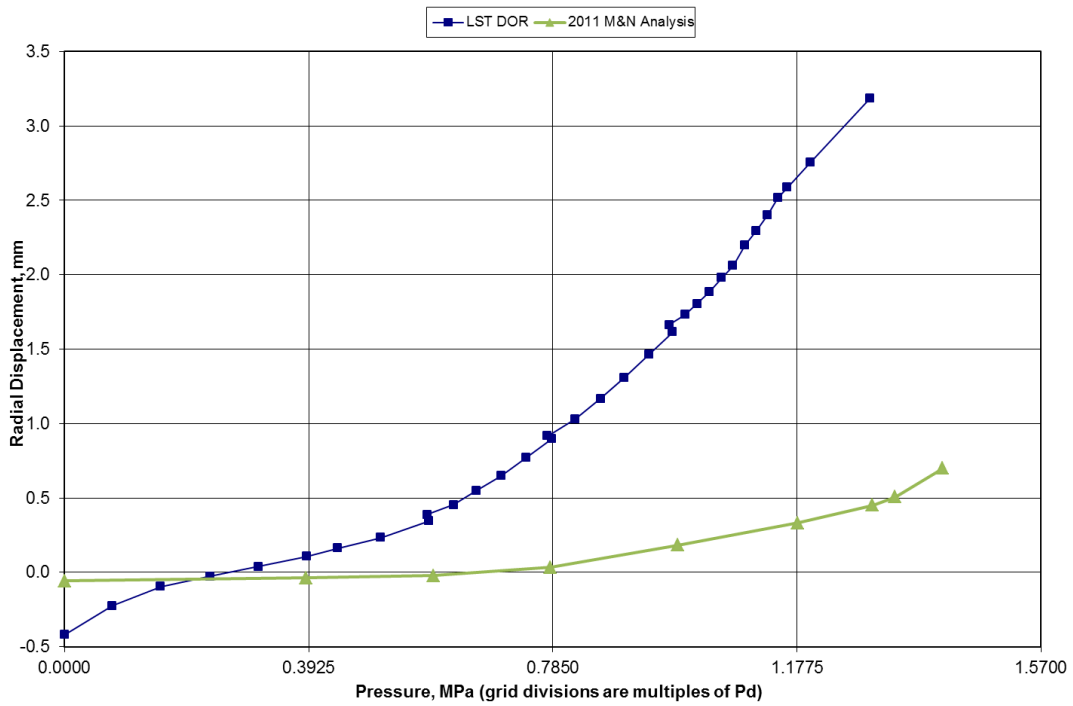


Figure D 233: Standard output location #2. Azimuth: 135 degrees, Elevation: 0.25 meters, Base of cylinder

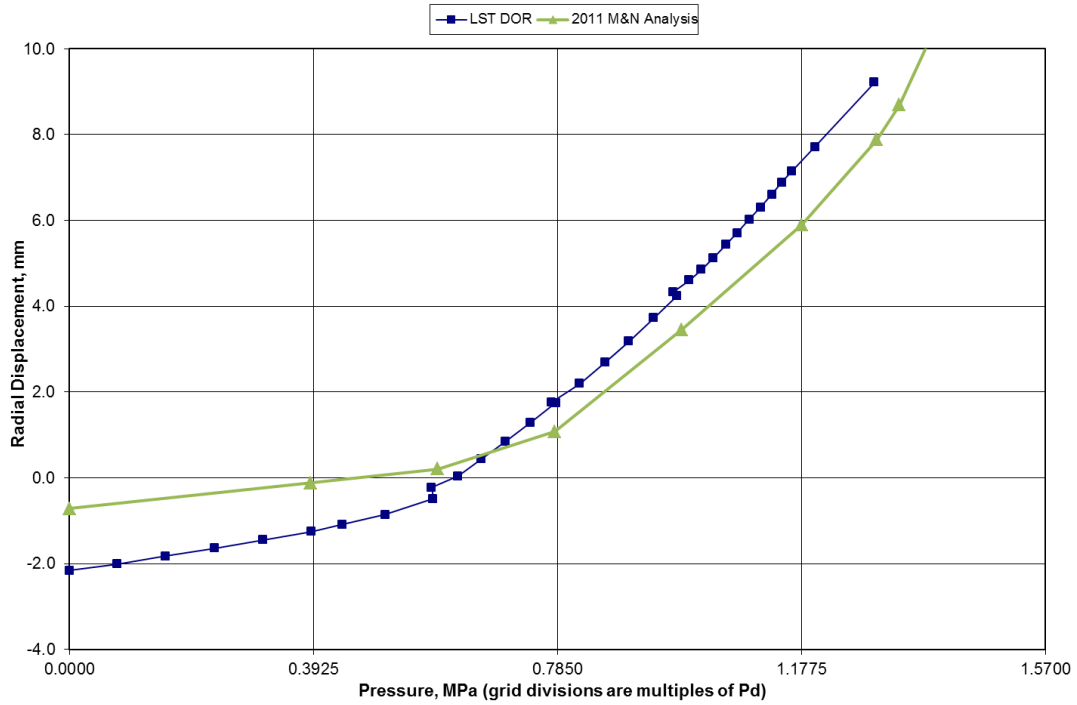


Figure D 234: Standard output location #3. Azimuth: 135 degrees, Elevation: 1.43 meters, Base of cylinder

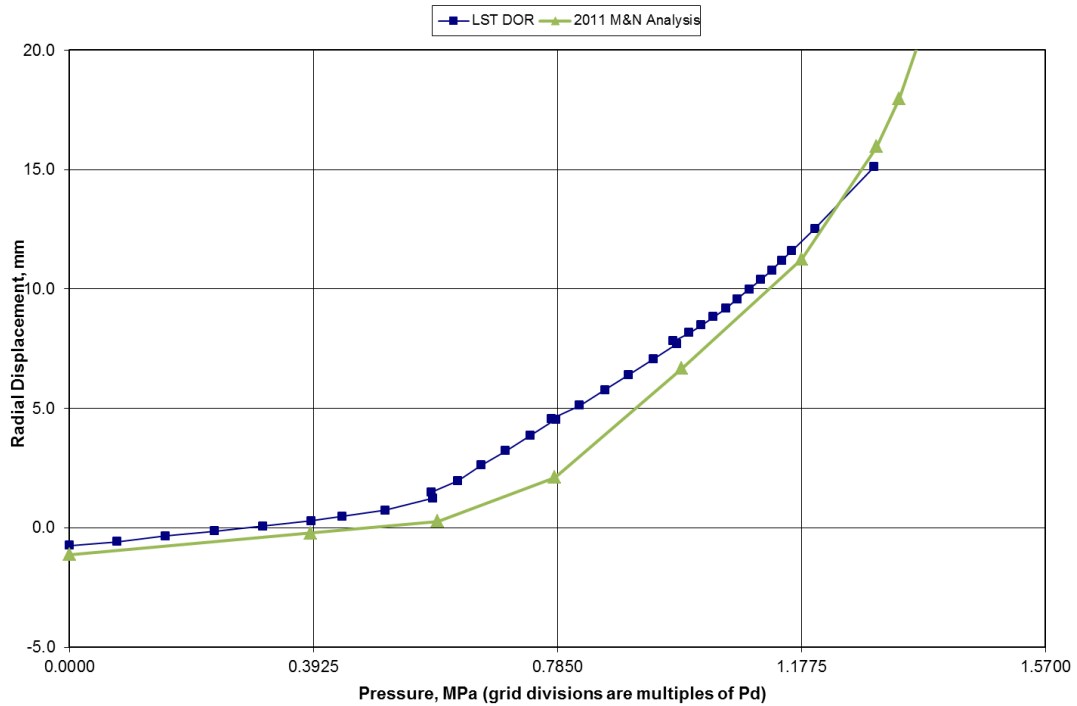


Figure D 235: Standard output location #4. Azimuth: 135 degrees, Elevation: 2.63 meters, Base of cylinder

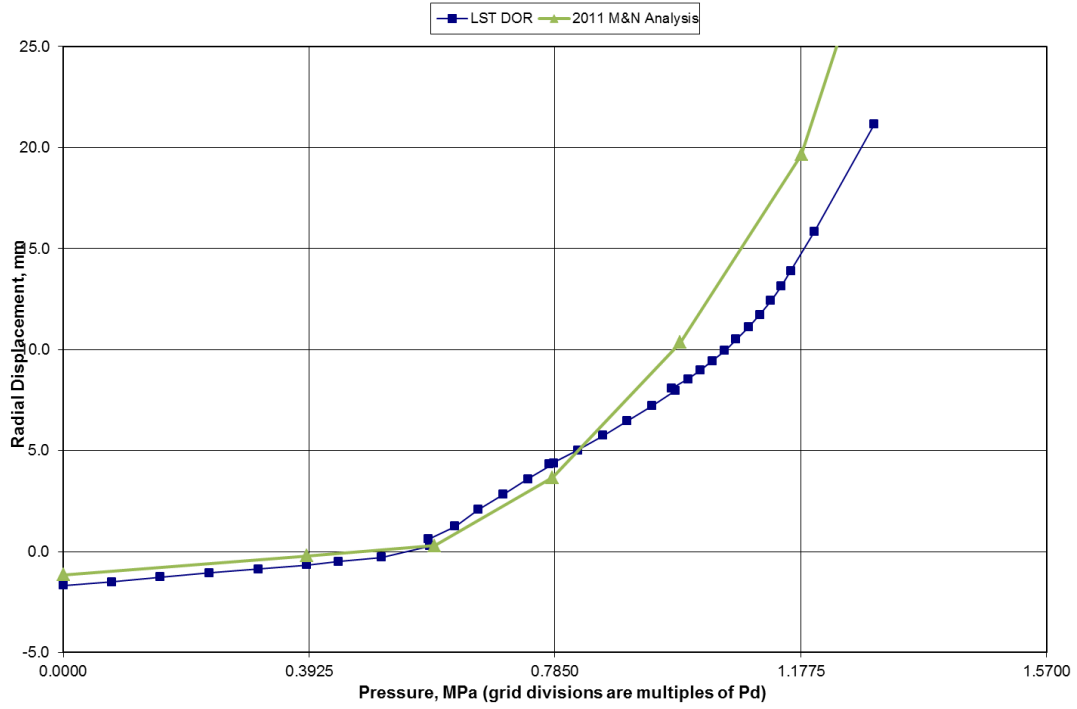


Figure D 236: Standard output location #5. Azimuth: 135 degrees, Elevation 4.68 meters, E/H elevation.

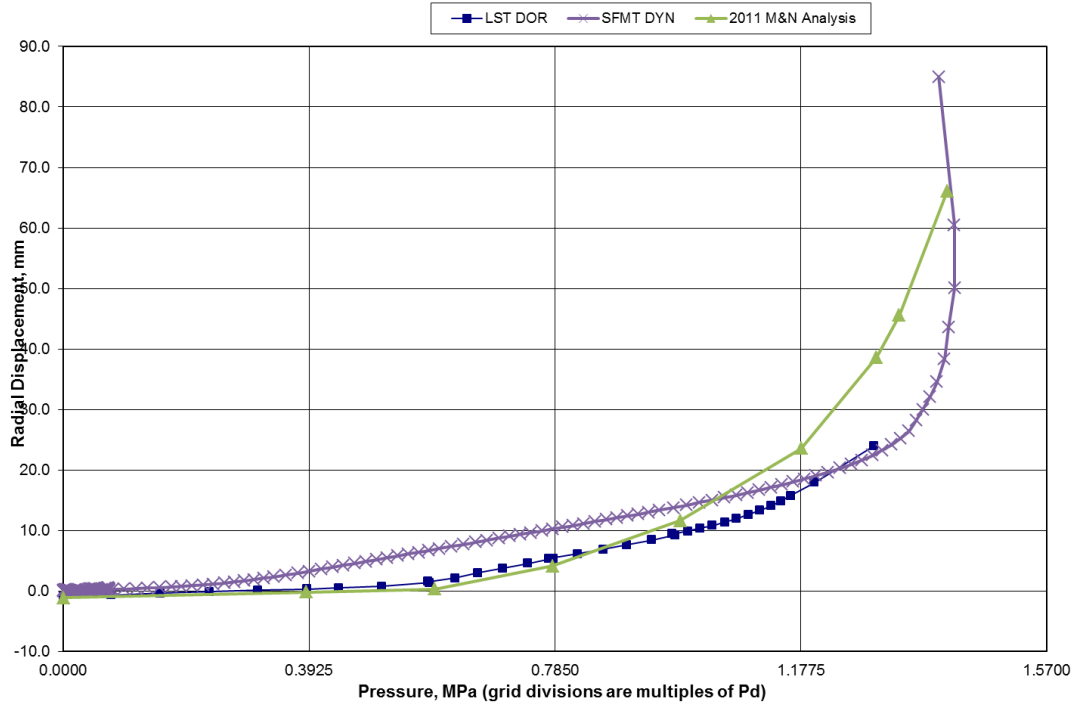


Figure D 237: Standard output location #6. Azimuth: 135 degrees, Elevation: 6.20 meters, Base of cylinder

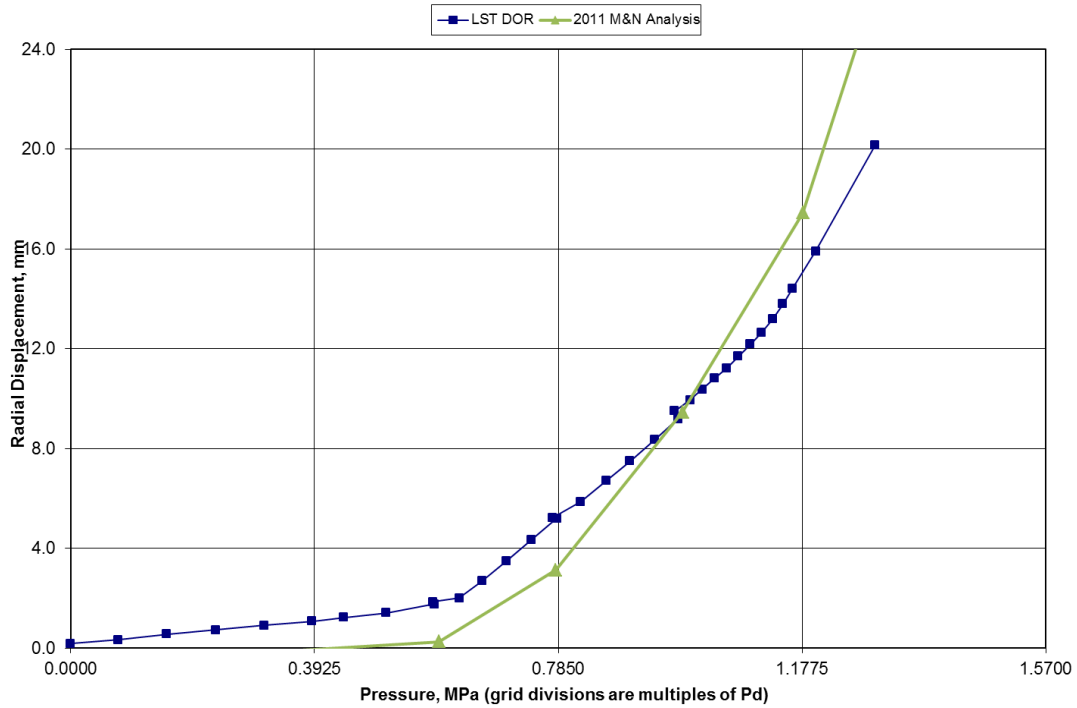


Figure D 238: Standard output location #7. Azimuth: 135 degrees, Elevation: 10.75 meters, Springline

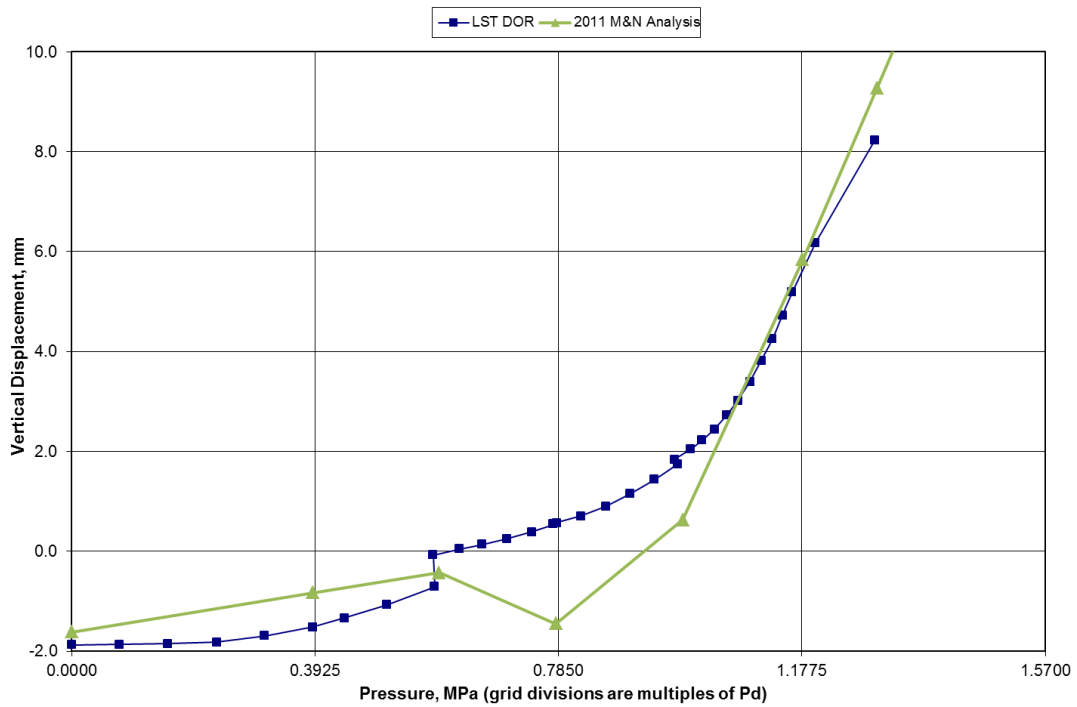


Figure D 239: Standard output location #8. Azimuth: 135 degrees, Elevation: 10.75 meters, Springline

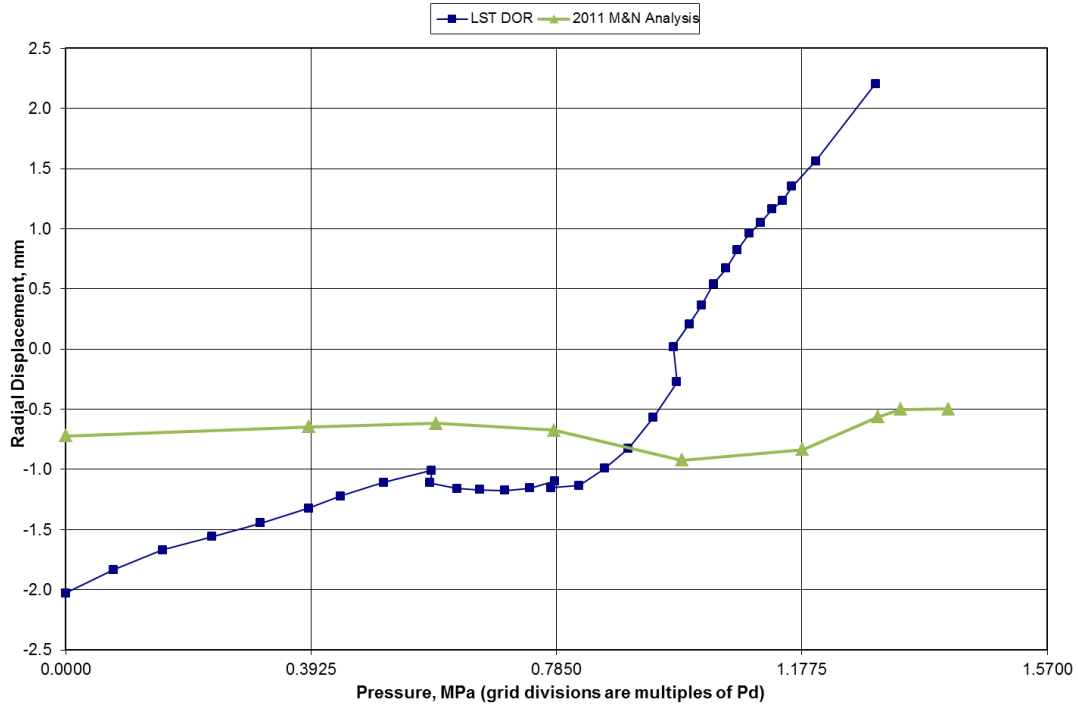


Figure D 240: Standard output location #9. Azimuth: 135 degrees, Elevation: 14.55 meters, Dome 45 deg

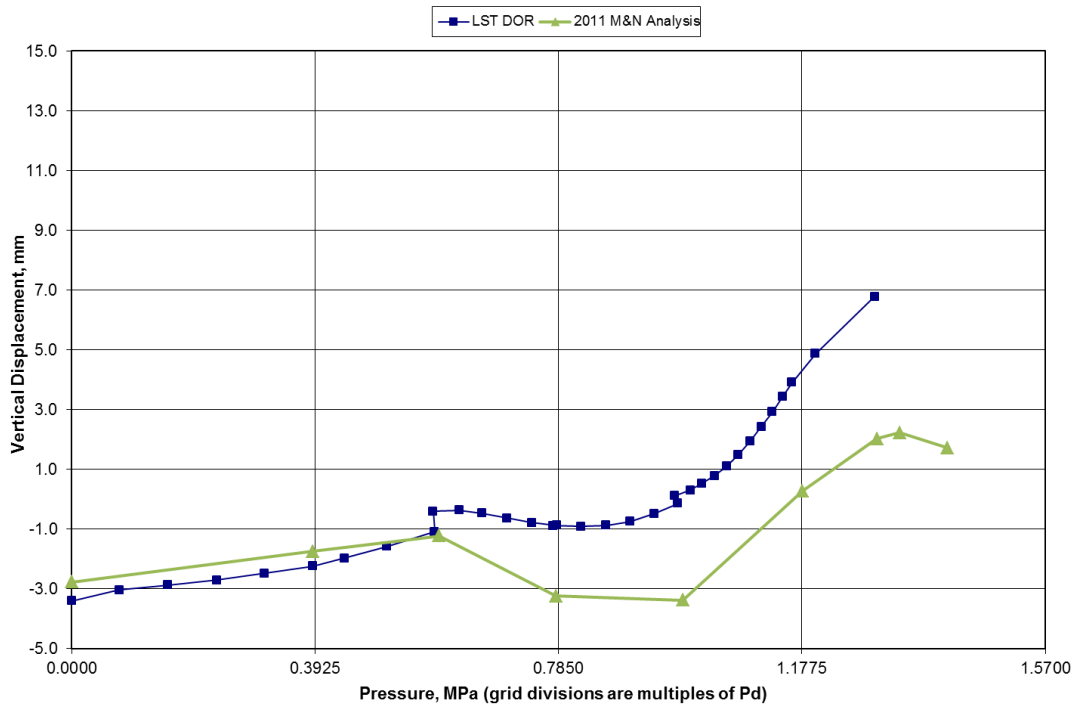


Figure D 241: Standard output location #10. Azimuth: 135 degrees, Elevation: 14.55 meters, Dome 45 deg

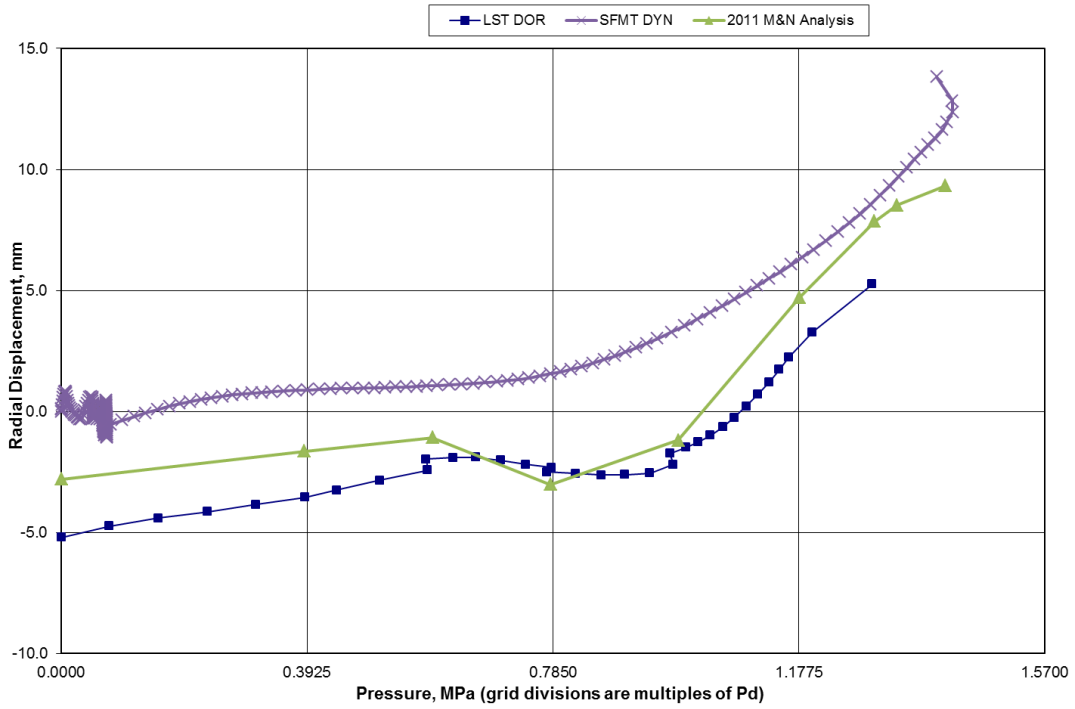


Figure D 242: Standard output location #11. Azimuth: Apex, Elevation: 16.13 meters

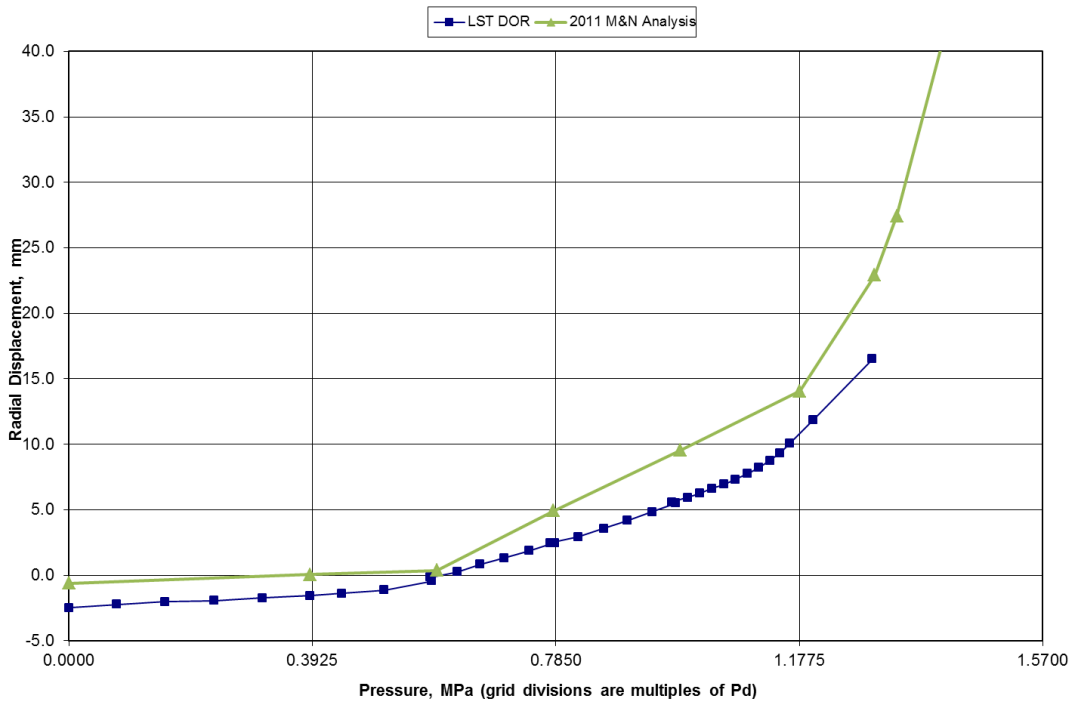


Figure D 243: Standard output location #12. Azimuth: 90 degrees, Elevation: 6.2 meters, Midheight at buttress

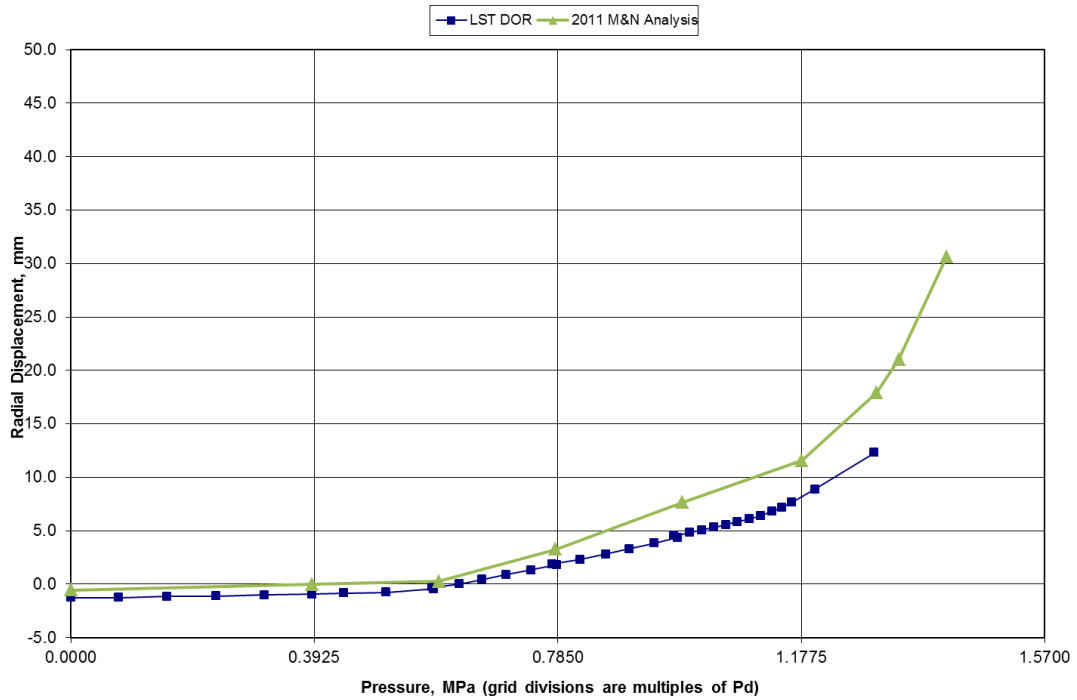


Figure D 244: Standard output location #13. Azimuth: 90 degrees, Elevation: 10.75 meters, Springline at buttress

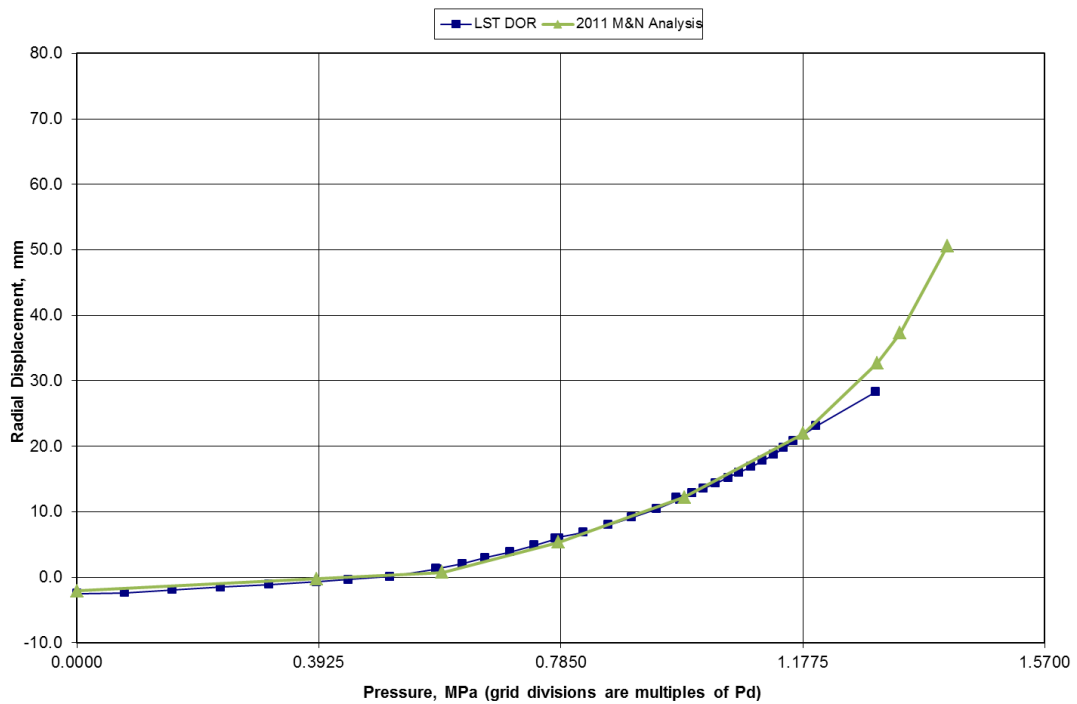


Figure D 245: Standard output location #14. Azimuth: 334 degrees, Elevation: 4.675 meters, Center of E/H

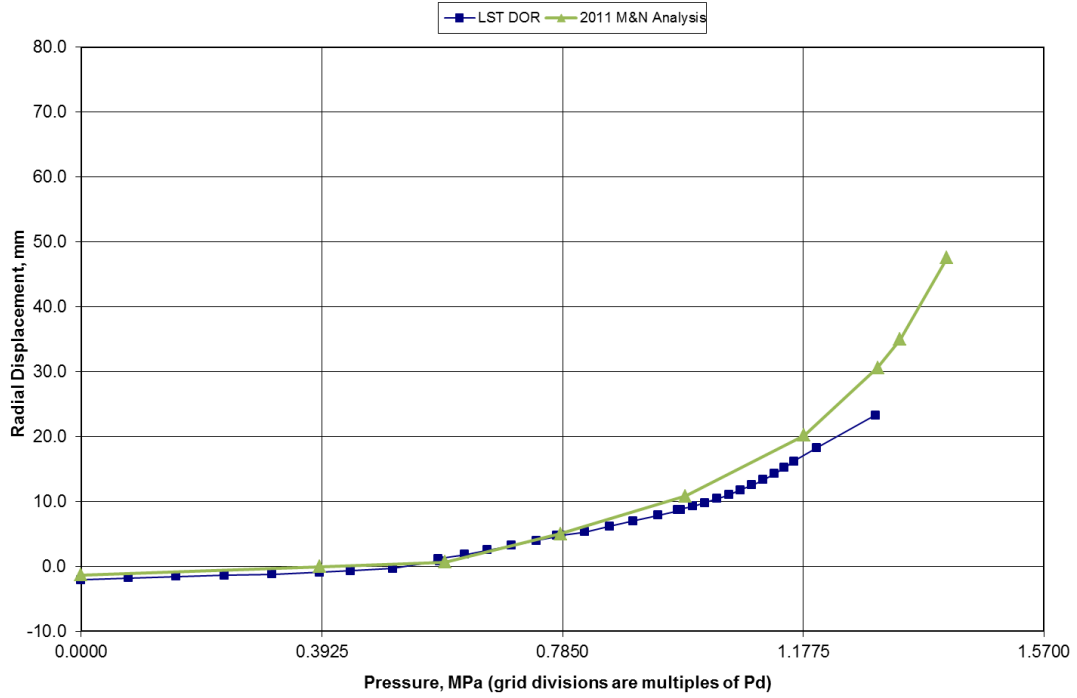


Figure D 246: Standard output location #15. Azimuth: 66 degrees, Elevation: 4.25 meters, Center of A/L

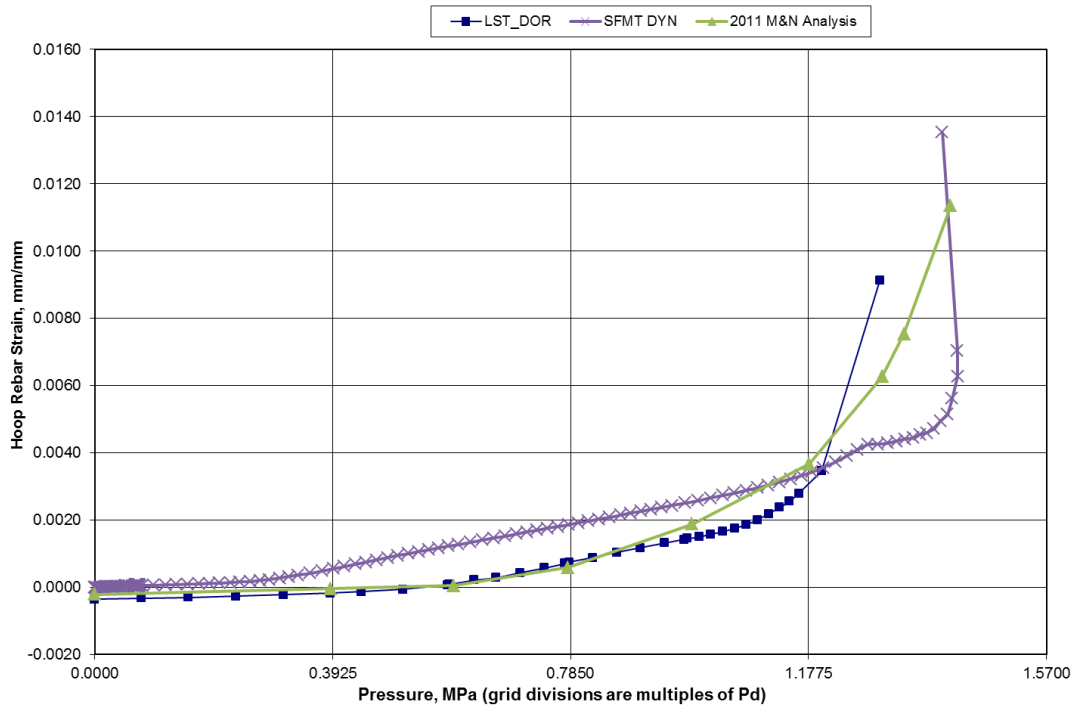


Figure D 247: Standard output location #22. Azimuth: 135 degrees, Elevation: 6.20 meters, Outer rebar layer, Midheight

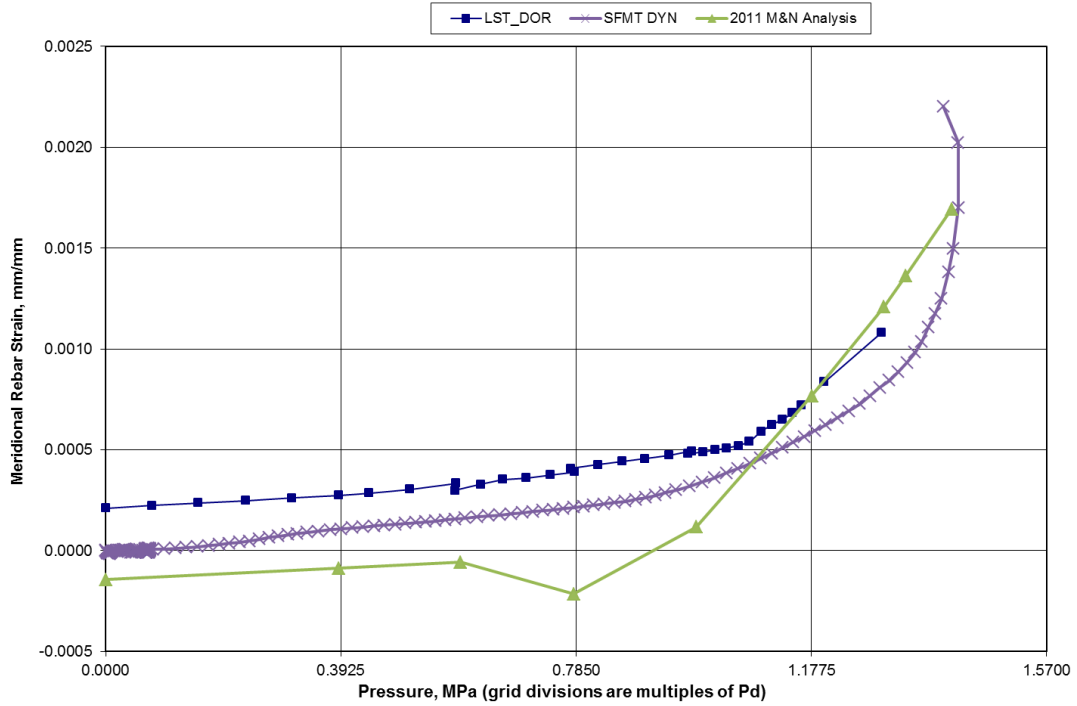


Figure D 248: Standard output location #23. Azimuth: 135 degrees, Elevation: 6.20 meters, Outer rebar layer, Midheight

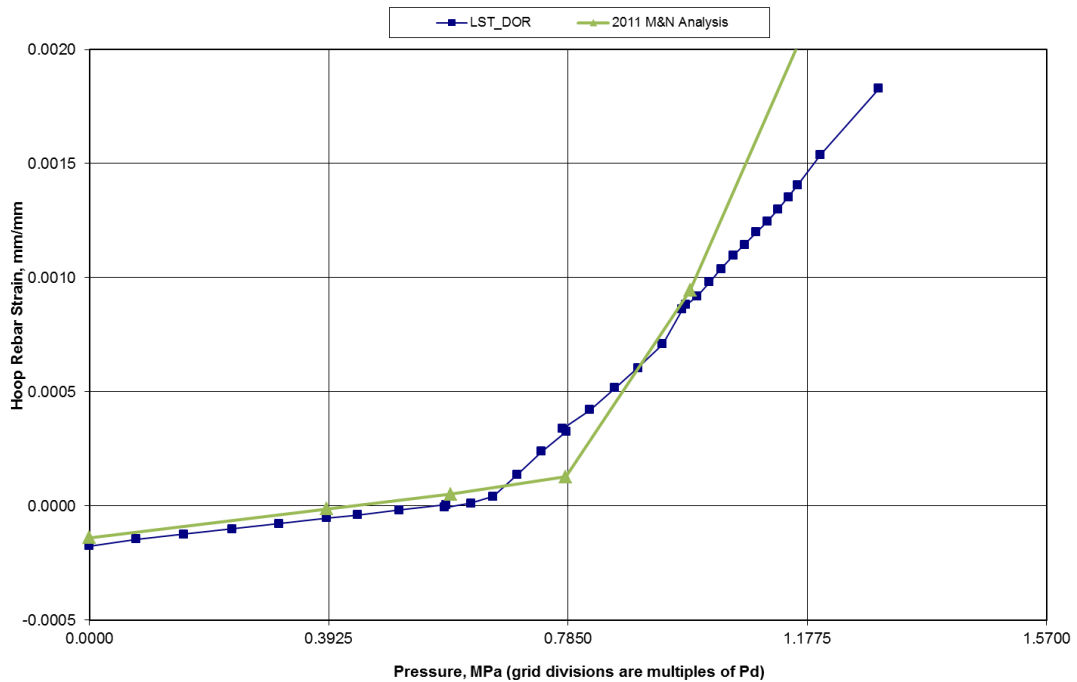


Figure D 249: Standard output location #24. Azimuth: 135 degrees, Elevation: 10.75 meters, Outer rebar layer, Springline

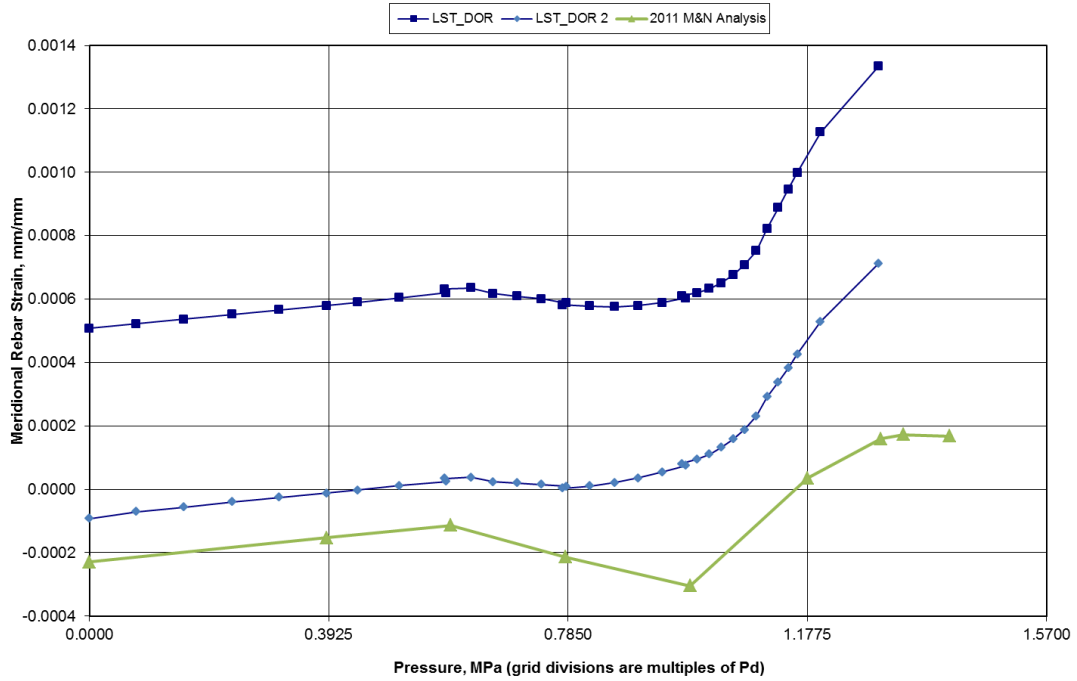


Figure D 250: Standard output location #25. Azimuth: 135 degrees, Elevation: 10.75 meters, Inner rebar layer, Springline

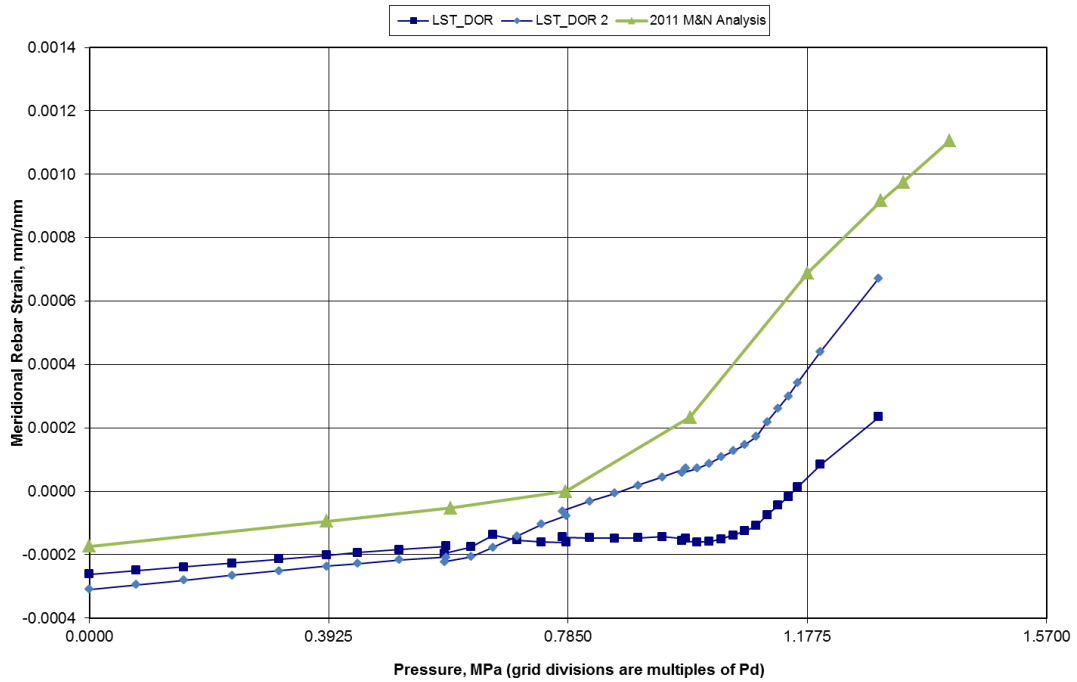


Figure D 251: Standard output location #26. Azimuth: 135 degrees, Elevation: 10.75 meters, Outer rebar layer, Springline

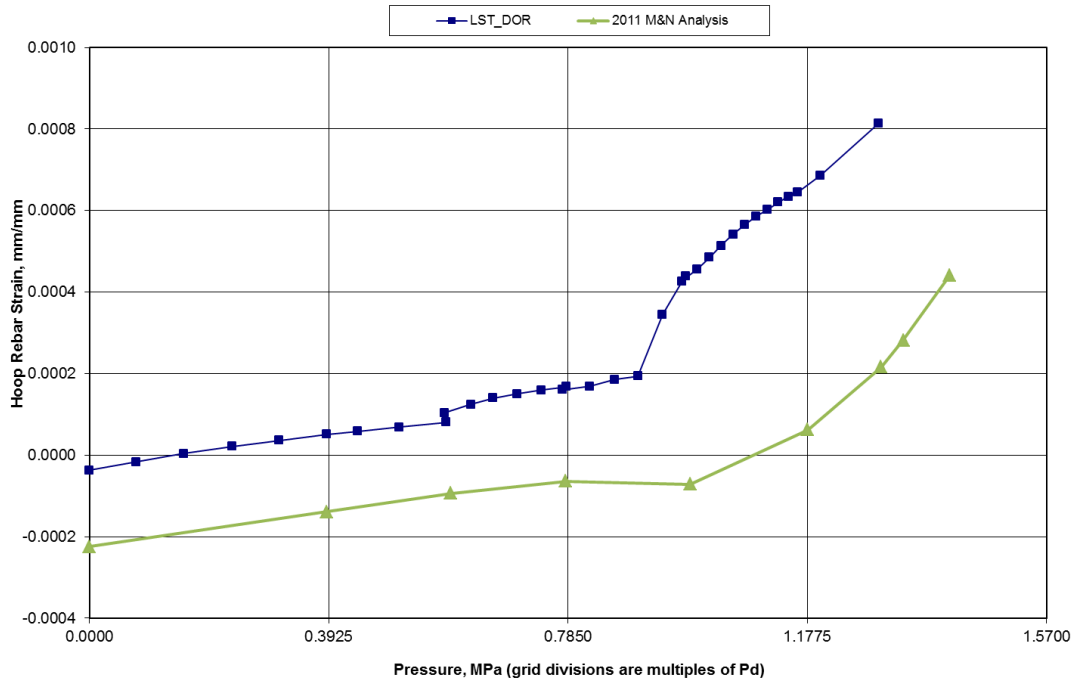


Figure D 252: Standard output location #27. Azimuth: 135 degrees, Elevation: 14.55 meters, Outer rebar layer, Dome 45 deg

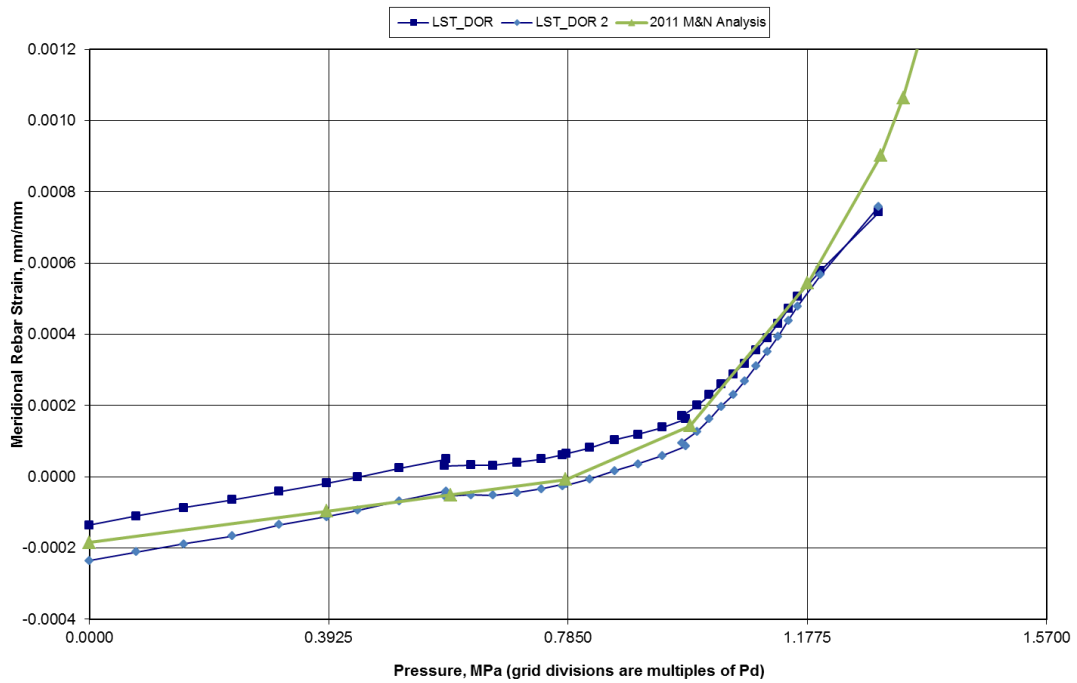


Figure D 253: Standard output location #28. Azimuth: 135 degrees, Elevation: 14.55 meters, Inner rebar layer, Dome 45 deg

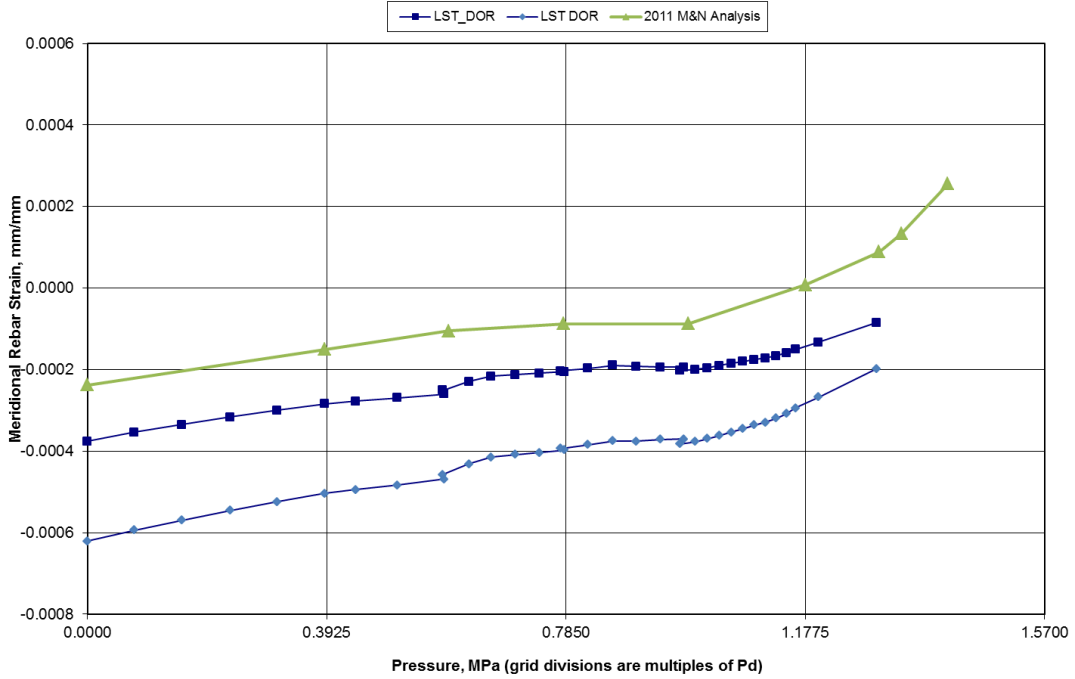


Figure D 254: Standard output location #29. Azimuth: 135 degrees, Elevation: 14.55 meters, Outer rebar layer, Dome 45 deg

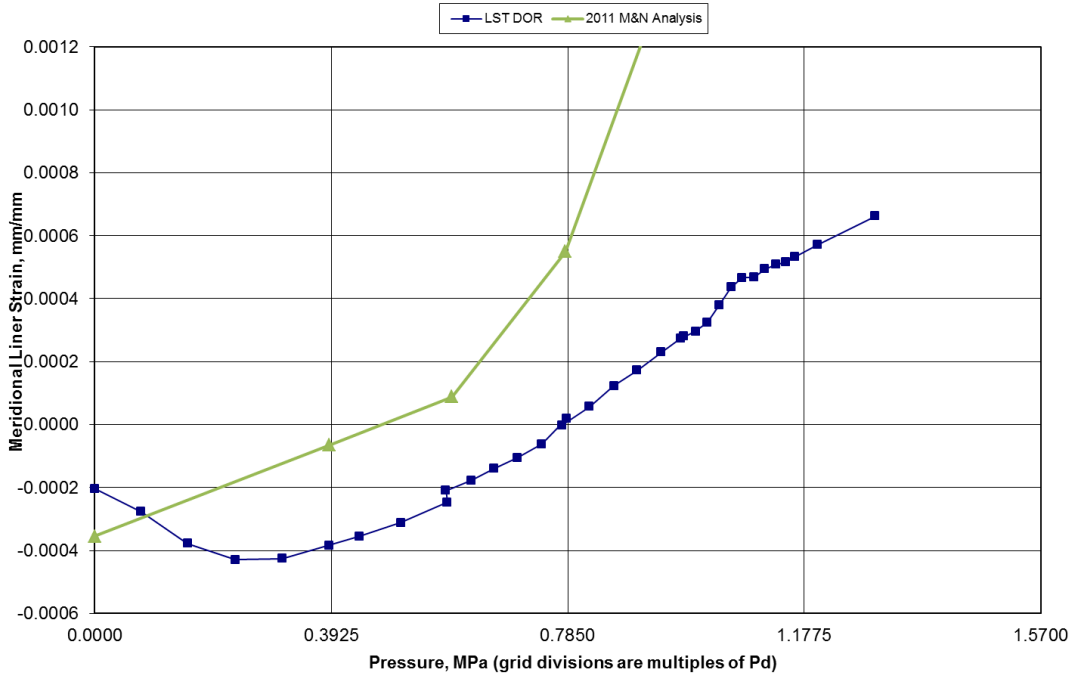


Figure D 255: Standard output location #36. Azimuth: 135 degrees, Elevation: 0.25 meters, Inside liner surface, Base of cylinder

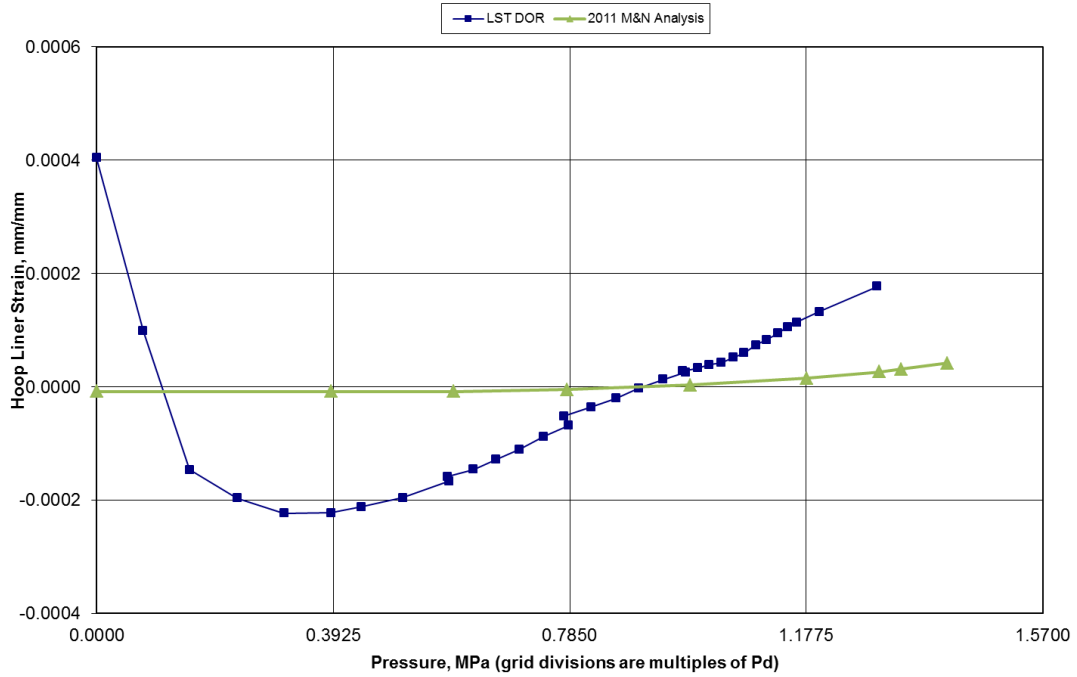


Figure D 256: Standard output location #37. Azimuth: 135 degrees, Elevation: 0.25 meters, Inside liner surface, Base of cylinder

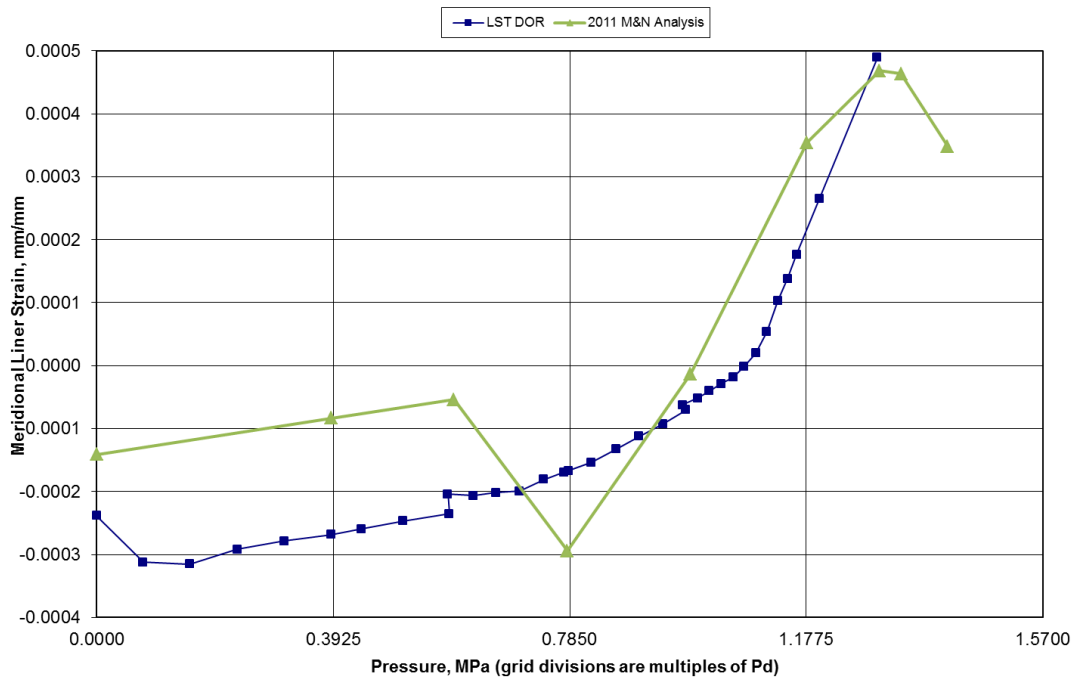


Figure D 257: Standard output location #38. Azimuth: 135 degrees, Elevation: 6.20 meters, Inside liner surface, Midheight

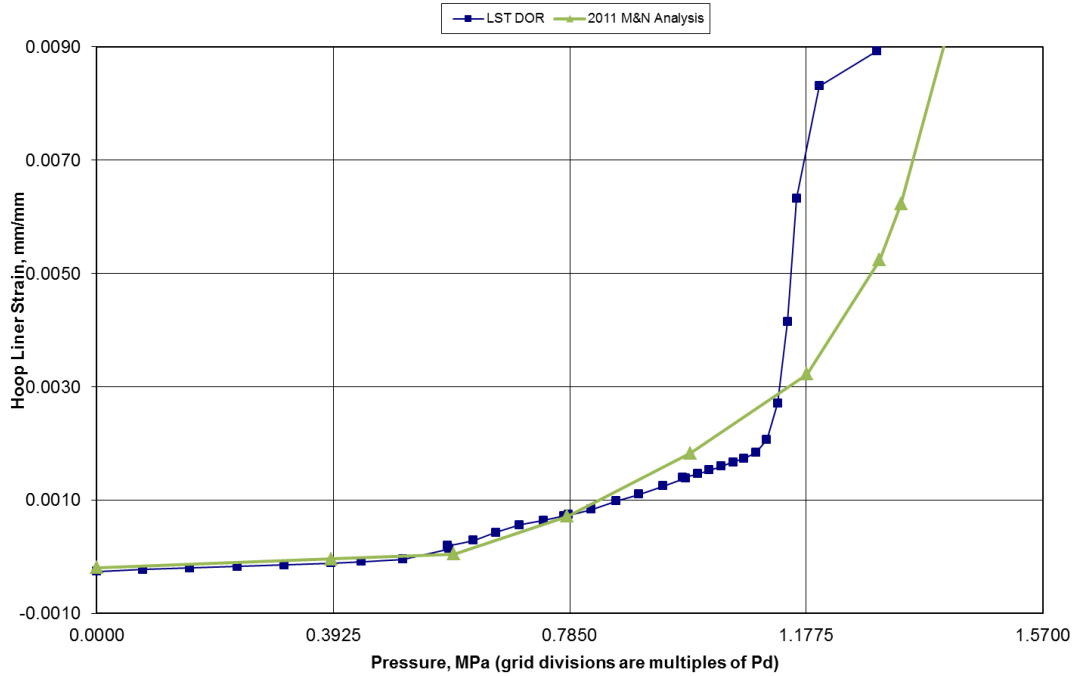


Figure D 258: Standard output location #39. Azimuth: 135 degrees, Elevation: 6.20 meters, Inside liner surface, Midheight

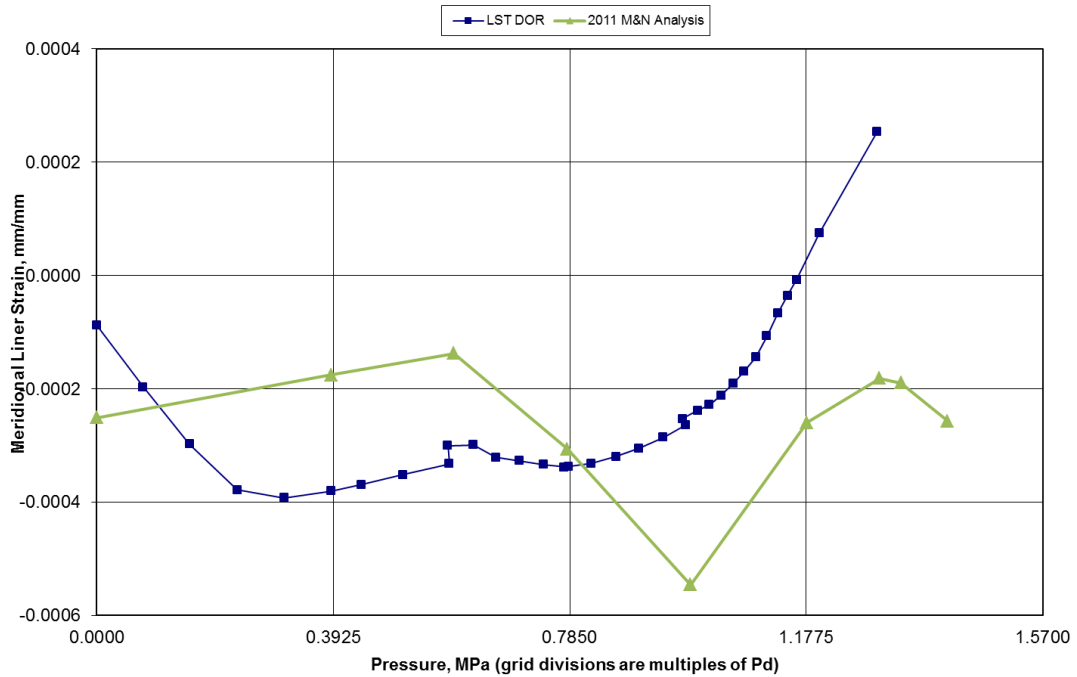


Figure D 259: Standard output location #40. Azimuth: 135 degrees, Elevation: 10.75 meters, Inside liner surface, Springline

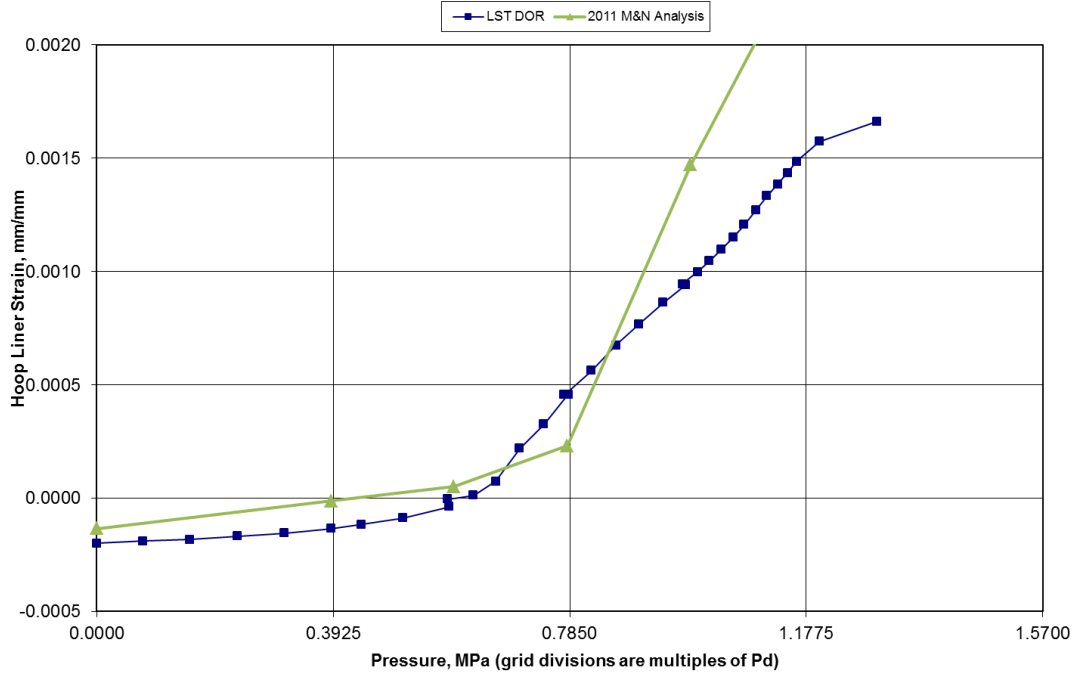


Figure D 260: Standard output location #41. Azimuth: 135 degrees, Elevation: 10.75 meters, Inside liner surface, Springline

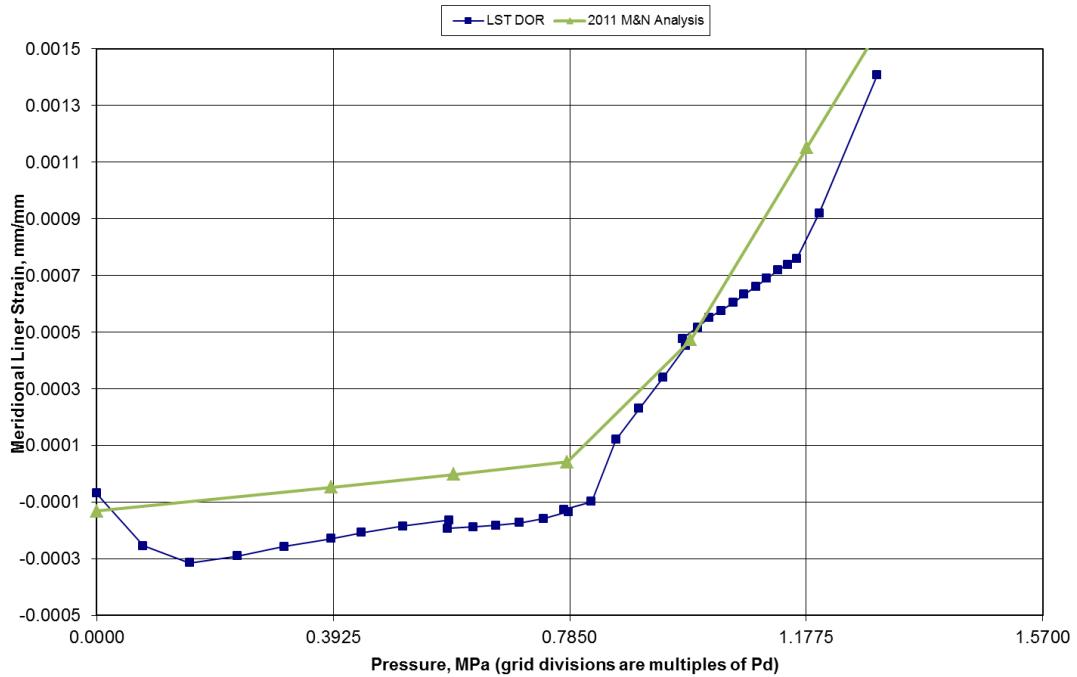


Figure D 261: Standard output location #42. Azimuth: 135 degrees, Elevation: 16.13 meters, Inside liner surface, Dome apex

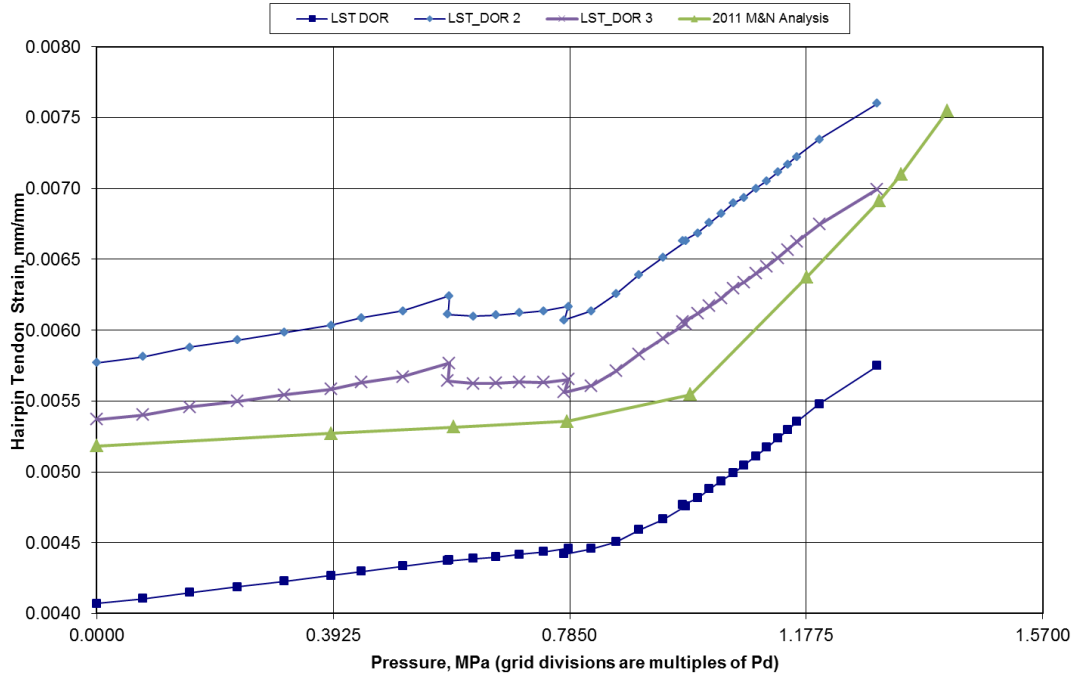


Figure D 262: Standard output location #48. Azimuth: 135 degrees, Elevation: 15.6 meters, Tendon V37, Tendon apex

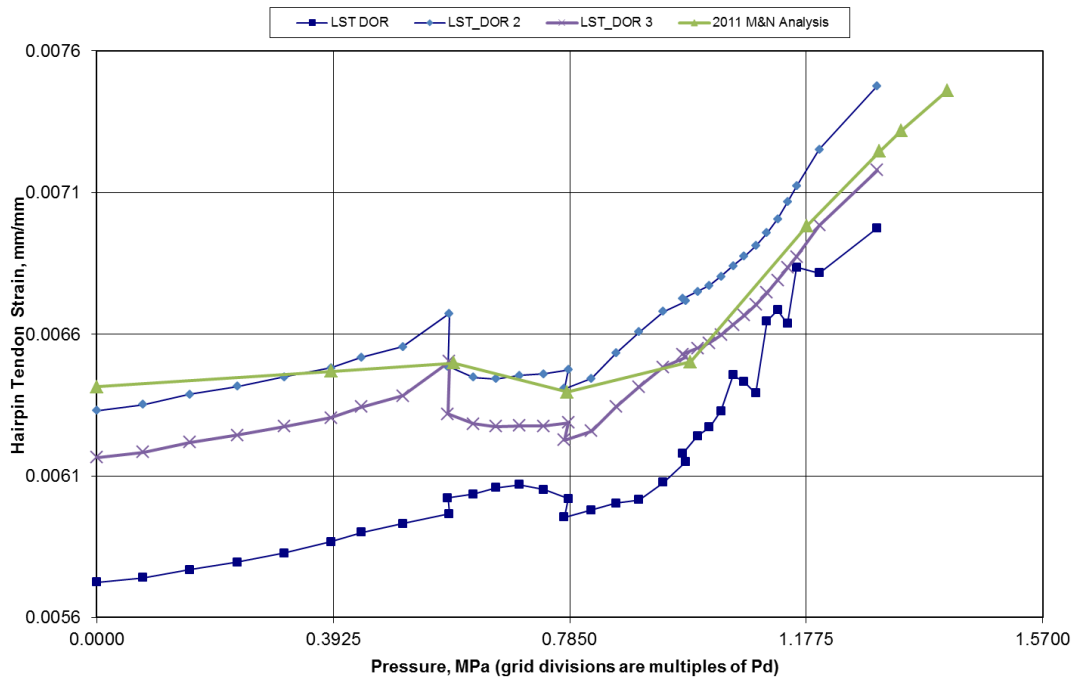


Figure D 263: Standard output location #49. Azimuth: 135 degrees, Elevation: 10.75 meters, Tendon V46, Tendon springline

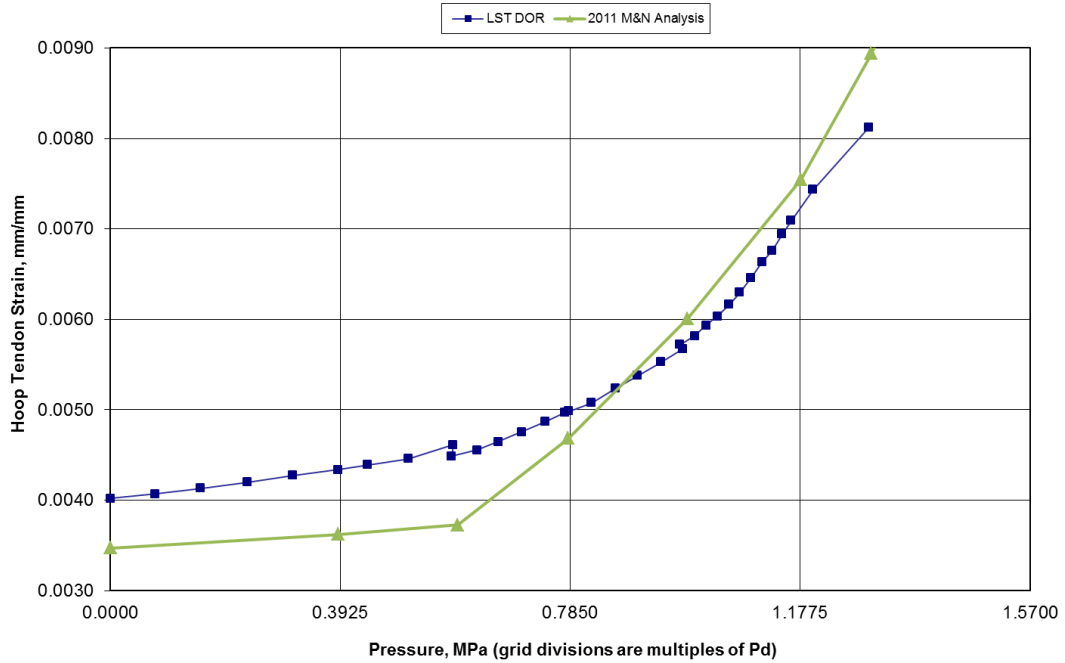


Figure D 264: Standard output location #50. Azimuth: 90 degrees, Elevation: 6.58 meters, Tendon H53, Mid-tendon

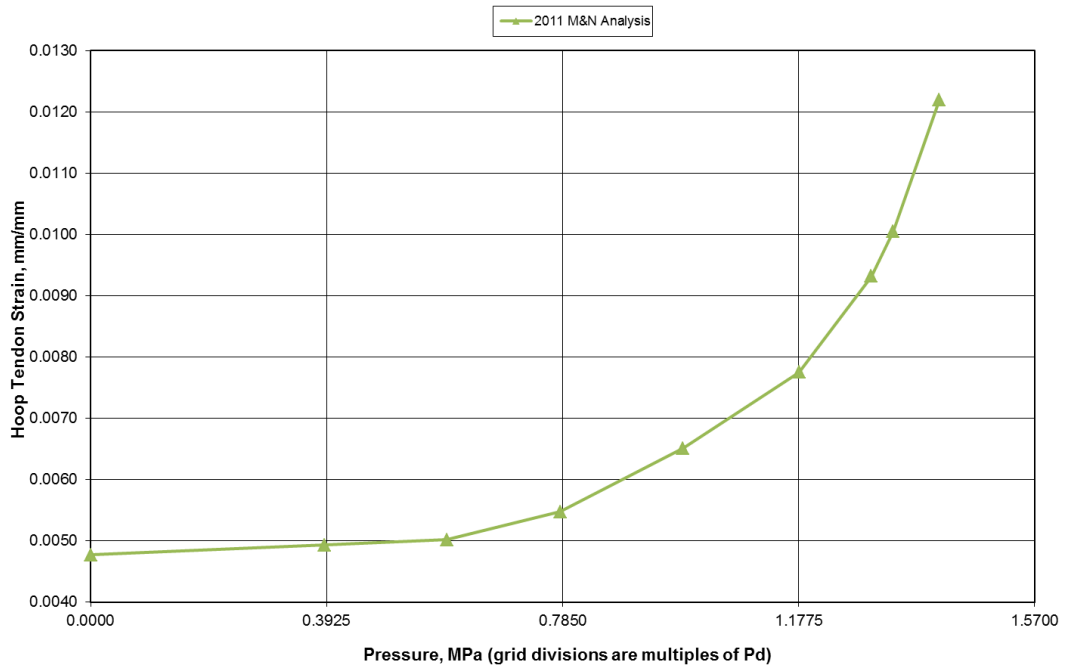


Figure D 265: Standard output location #51. Azimuth: 180 degrees, Elevation: 6.58 meters, Tendon H53, 1/4-tendon

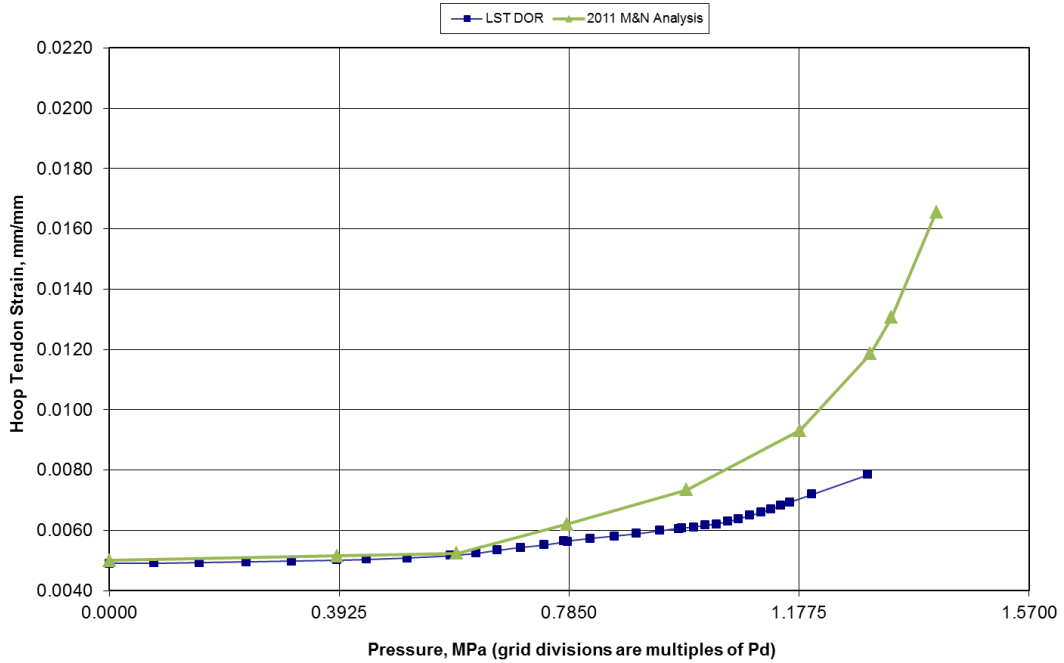


Figure D 266: Standard output location #52. Azimuth: 280 degrees, Elevation: 6.58 meters, Tendon H53, Tendon near buttress

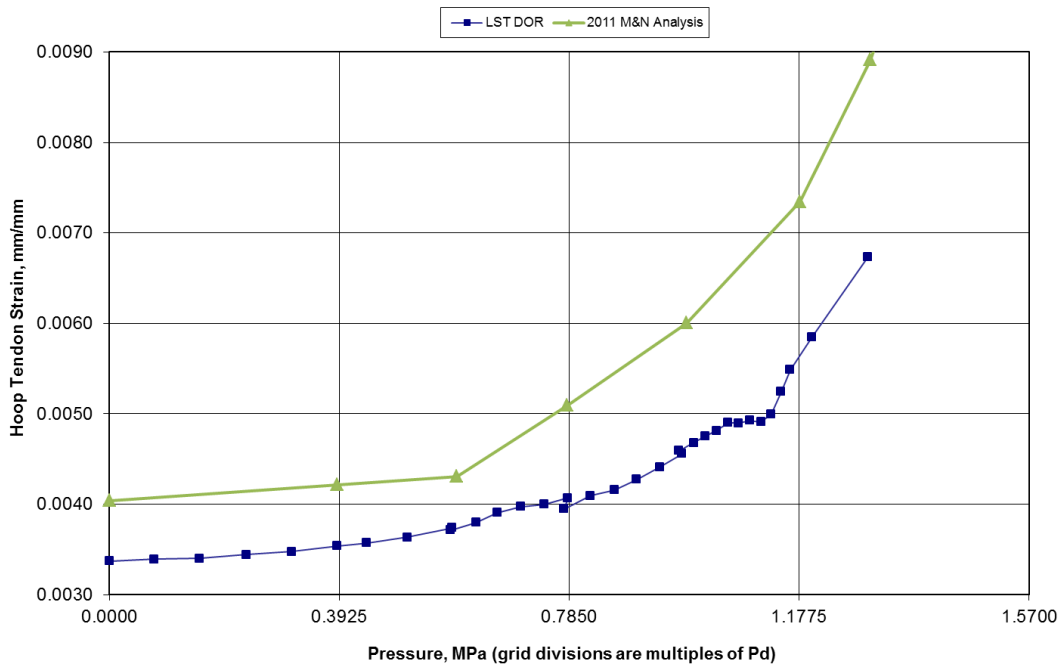


Figure D 267: Standard output location #53. Azimuth: 0 degrees, Elevation: 4.57 meters, Tendon H53, Tendon between E/H and A/L

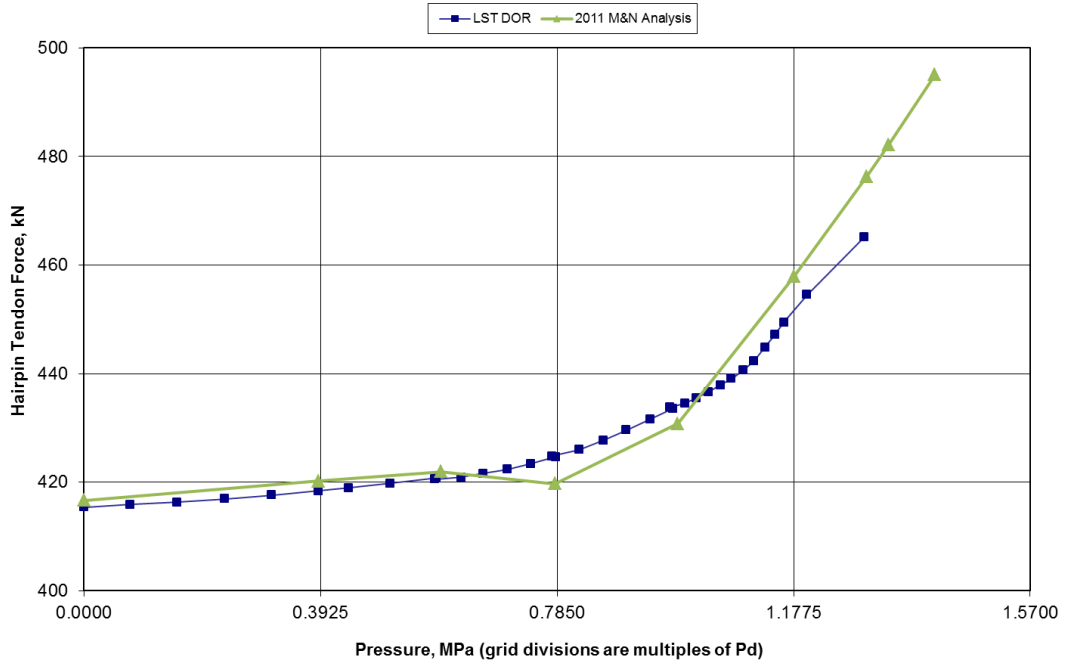


Figure D 268: Standard output location #54. Azimuth: 241 degrees, Elevation: -1.16 meters, Tendon V37, Tendon gallery

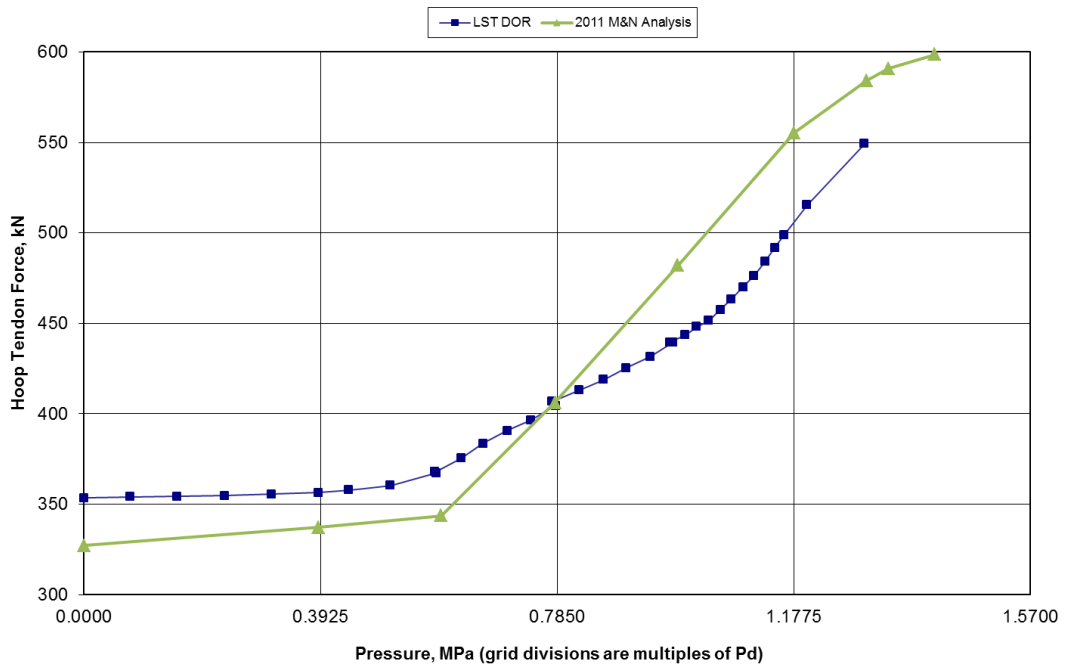





Figure D 269: Standard output location #55. Azimuth: 275 degrees, Elevation: 6.58 meters, Tendon H53, At buttress

APPENDIX E SANSCOTT

Report		Ref.: 10503/R-01		Edition: 1	
STANDARD PROBLEM EXERCISE PERFORMANCE OF CONTAINMENT VESSEL UNDER SEVERE ACCIDENT CONDITION (PHASE 1)					
<p>Abstract</p> <p>The reactor containment constitutes an important safety barrier between the reactor and the surrounding environment. The main purpose of the containment structure is to ensure tightness at the high overpressure that could occur at an internal accident. At severe accidental conditions, generating overpressure load beyond the design pressure, the response of the containment structures becomes highly non-linear.</p> <p>This report summarizes studies intended to be included in the Standard Problem Exercise on the performance of containment vessels under severe accident conditions (SPE). To verify and validate analytic studies performed in SPE results from a pressurization test carried out on a ¼ scale containment model is used.</p> <p>The main objective of this report is to explain the effects of structural interaction between containment steel components and cracked concrete. Also the failure mechanism of the steel liner and the effect of variation in input parameters are considered. Four specific studies are presented regarding; prestressing tendon behavior, containment global response, liner behavior near penetrations and the influence of structural parameter variation.</p> <p>The <i>prestressing tendon behavior study</i> considers the interaction between horizontal tendons and the containment structure. In the scale model test it was observed that the tendon force was equalized during pressurization. This behavior is also found in this study and the main redistribution is concluded to be caused by local tendon yielding in combination with sliding between tendon and duct.</p> <p>The containment <i>global response study</i> considers the global structural response during pressurization with focus on the behavior near the equipment hatch. It is observed in the analysis results that the expansion in containment midheight mainly depends on the hoop stiffness of the structure. It is also found that for load levels exceeding around two times the design pressure the stiffness in midheight only depends on included steel components, since the concrete is completely cracked. At very high pressure levels the radial displacement increases rapidly in regions where general tendon yielding occurs. It is concluded that tendons with general high initial tendon force (low friction loss) will yield before tendons with low initial tendon force (high friction loss). This fact could be important to observe considering the "leak before break" behavior of reactor containments.</p> <p>The <i>liner behavior study</i> considers the detailed liner behavior of the steel liner near the equipment hatch. It is shown that the highest strain level occurs in the vertical fold close to the equipment hatch when the liner is straightened out during pressurization. In general, the non-linear plastic behavior of the liner is concluded to be very sensitive to the detailed design and the interaction between concrete and liner.</p> <p>The <i>structural parameter variation study</i> considers the influence of variation in input data of the containment global expansion. The main scatter in midheight expansion is concluded to originate from the variation in prestress. It is also concluded that the total coefficient of variation (COV) of the midheight expansion is around 7.5%.</p>					
Edition	Date	Author	Reviewed by	Approved by	
1	2011-03-31	Patrick Anderson / Oscar Elison Torulf Nilsson / Björn Svärd	Ola Jovall	Ola Jovall	
					

Report 10503/R-01

PERFORMANCE OF CONTAINMENT VESSEL UNDER SEVERE ACCIDENT CONDITION (PHASE 1)

LIST OF CONTENTS

PAGE

Abstract.....	E-6
Introduction	E-8
Background.....	E-8
Scope	E-9
Outline of report	E-10
Containment scale model test.....	E-11
General.....	E-11
Structural outline	E-12
General	E-12
Steel liner	E-13
Anchors and stiffeners	E-14
Liner near penetration E/H.....	E-15
Penetrations [9]	E-16
Pre-stressing tendons.....	E-16
Reinforcing steel.....	E-20
Concrete.....	E-20
Instrumentation and material testing	E-21
Material testing	E-21
Containment model instrumentation	E-22
Pressurization test	E-22
Test operations.....	E-22
General results	E-23
Methods of analysis.....	E-24
General.....	E-24
Model principals	E-25
Software	E-25
Input parameters and FE-implementation.....	E-25
General.....	E-25
Concrete	E-26

FE-implementation	E-26
Material parameters.....	E-27
Compressive strength.....	E-28
Tensile strength	E-28
E-modulus	E-28
Fracture energy	E-29
Reinforcement	E-29
FE-implementation	E-29
Material parameters.....	E-30
Yield strength	E-30
Ultimate strength	E-31
Ultimate elongation.....	E-31
E-modulus	E-31
Stress strain curve.....	E-31
Steel liner.....	E-32
FE-implementation	E-32
Material parameters.....	E-32
Yield strength	E-32
Ultimate strength	E-32
Ultimate elongation.....	E-32
E-modulus	E-33
Stress strain curve.....	E-33
Liner anchorage	E-33
Prestress.....	E-34
FE-implementation	E-34
Material parameters	E-35
Yield strength	E-35
Ultimate strength	E-35
Ultimate elongation.....	E-36
E-modulus	E-36
Stress strain curve.....	E-36
Initial tendon force	E-36
Long-term effects	E-39
Geometry.....	E-41
Prestressing tendon behavior	E-41
General.....	E-41
FE-model.....	E-42

Concrete structure and liner	E-42
Tendon system.....	E-43
Reinforcement.....	E-45
Finite element model size	E-46
Analysis	E-46
Method.....	E-46
Pre-stress	E-46
Seating	E-46
Long-term effects	E-46
Creep	E-46
Relaxation	E-47
Pressure load.....	E-47
Results and evaluation.....	E-48
Initial steps	E-48
Displacement.....	E-48
Tendon force	E-49
Pressurization step.....	E-51
Displacement.....	E-51
Tendon system.....	E-53
Concrete and reinforcement	E-57
Liner strain.....	E-59
Tendon slip.....	E-59
Summary	E-61
Containment global response	E-62
General.....	E-62
FE-model	E-62
Layout	E-62
Concrete structure	E-63
Steel liner	E-64
Tendon system.....	E-65
Rebar reinforcement.....	E-67
Load and boundary conditions.....	E-69
Finite element model size	E-69
Results and evaluation.....	E-70
Global displacement.....	E-70
Liner deformation at standard output locations	E-70

Liner deformation at pressure milestones	E-70
Strains in concrete structure	E-74
Strains in steel liner	E-74
Strains in liner at standard output locations	E-74
Strains in liner at pressure milestones	E-74
Tendons system	E-75
Strains and forces in tendons at standard output locations	E-75
Tendon force distribution during pre-stressing	E-75
Tendon force distribution at pressure milestones	E-78
Summary	E-81
Liner behavior near equipment hatch.....	E-81
General.....	E-81
FE-model	E-82
Steel liner	E-82
Liner anchors.....	E-83
Submodel boundary conditions	E-84
Finite element model size	E-85
Results and evaluation.....	E-85
General	E-85
Displacement and contact	E-86
Liner strain	E-89
Liner strain in the outgoing fold.....	E-90
Liner anchor	E-91
Summary	E-92
Liner failure mechanism.....	E-93
General.....	E-93
Initiation of liner failure	E-93
Size of liner failure	E-94
Structural model	E-94
Analyses.....	E-97
Convergence	E-97
LEFM analyses.....	E-97
Non-linear analyses.....	E-98
Influence of structural parameter variation.....	E-99
General.....	E-99

Numerical simulation E-100

 Structural model E-100

 Input parameters E-101

 Results E-102

Statistical evaluation E-103

Summary E-104

Conclusions E-104

 General..... E-104

 Prestressing tendon behavior..... E-105

 Containment global response..... E-105

 Liner behavior near equipment hatch..... E-106

 Influence of structural parameter variation E-107

Referenses E-107

Tension stiffening effect..... E-110

Evaluation of loss of prestressing force E-114

Results of tendon behavior model E-118

Global model deformation at standard output loc..... E-127

Global model liner strains E-140

Global model Strains in concrete structure E-149

Results for region near equipment hatch E-156

ABSTRACT

The reactor containment constitutes an important safety barrier between the reactor and the surrounding environment. The main purpose of the containment structure is to ensure tightness at the high overpressure that could occur at an internal accident. At severe accidental conditions, generating overpressure load beyond the design pressure, the response of the containment structures becomes highly non-linear.

This report summarizes studies intended to be included in the Standard Problem Exercise on the performance of containment vessels under severe accident conditions (SPE). To verify and validate analytic studies performed in SPE results from a pressurization test carried out on a $\frac{1}{4}$ scale containment model is used.

The main objective of this report is to explain the effects of structural interaction between containment steel components and cracked concrete. Also the failure mechanism of the steel liner and the effect of variation in input parameters are considered. Four specific studies are presented regarding; prestressing tendon behavior, containment global response, liner behavior near penetrations and the influence of structural parameter variation.

The *prestressing tendon behavior study* considers the interaction between horizontal tendons and the containment structure. In the scale model test it was observed that the tendon force was equalized during pressurization. This behavior is also found in this study and the main redistribution is concluded to be caused by local tendon yielding in combination with sliding between tendon and duct.

The containment *global response study* considers the global structural response during pressurization with focus on the behavior near the equipment hatch. It is observed in the analysis results that the expansion in containment midheight mainly depends on the hoop stiffness of the structure. It is also found that for load levels exceeding around two times the design pressure the stiffness in midheight only depends on included steel components, since the concrete is completely cracked. At very high pressure levels the radial displacement increases rapidly in regions where general tendon yielding occurs. It is concluded that tendons with general high initial tendon force (low friction loss) will yield before tendons with low initial tendon force (high friction loss). This fact could be important to observe considering the "leak before break" behavior of reactor containments.

The *liner behavior study* considers the detailed liner behavior of the steel liner near the equipment hatch. It is shown that the highest strain level occurs in the vertical fold close to the equipment hatch when the liner is straightened out during pressurization. In general, the non-linear plastic behavior of the liner is concluded to be very sensitive to the detailed design and the interaction between concrete and liner.

The *structural parameter variation study* considers the influence of variation in input data of the containment global expansion. The main scatter in midheight expansion is concluded to originate from the variation in prestress. It is also concluded that the total coefficient of variation (COV) of the midheight expansion is around 7.5%.

INTRODUCTION

Background

The reactor containment constitutes an important safety barrier between the reactor and the surrounding environment. The main purpose of the containment structure is to ensure tightness at the high overpressure that could occur at an internal accident. In many countries it is and has been a common practice to design nuclear containments with an outer concrete structure and an inner sealing consisting of a tight-welded steel liner. The outer concrete constitutes the load bearing part that may be prestressed. The liner is securing the tightness of the containment and has in general no intended bearing function.

At severe accidental conditions, generating overpressure load beyond the design pressure, the response of the containment structures becomes highly non-linear. The nonlinear response originates mainly from concrete cracking and yielding of steel components. The need of verifying the containment load-bearing capacity and leak-tightness in the non-linear range sets high demands on the engineering simulations.

Due to the difficulties related to verifying the non-linear performance, reference tests have been carried out, both overpressurization tests on containment scale models and tests on large wall specimens. Two containment scale model tests have been carried out at Sandia National Laboratories (SNL). The first scale test (Sandia 1:6) was performed in 1987 where a 1/6 scale model of a reinforced containment was pressurized (see [1] and [2]). The second scale test (Sandia 1:4) was performed in year 2000 and in this test a 1/4 scale model of a prestressed containment was pressurized (see [3]). Several experimental studies have been conducted for large scale specimens. An extensive experimental program sponsored by Electric Power Research Institute (EPRI) was performed in the late eighties (see [4] and [5]). In these program full-scale or nearly full-scale flat panels, representing the containment wall were tested. The main purpose with the EPRI program was to study the influence of discontinuities and the interaction between the liner and concrete wall.

In the SPE¹ project [6], which this report is a part of, round robin exercises are performed in order to compare structural analysis results with test data from the Sandia 1:4 test (see [3]). The SPE round robin exercise follows up the experiences from previous round robin analyses in the ISP 48² project [7]. In the ISP 48 project the main focus was on the global structural behavior and the ultimate capacity. Generally the SPE project will continue the work in the ISP 48 project and focus on the detailed behavior for e.g. prestressing tendons and liner.

The SPE final objective is to determine the containment leakage as function of the internal pressure. The round robin exercise of the SPE project is divided in two work phases. In *phase one*, which is described in this report, focus is on examination of local effects including; containment dilation on prestressing force, slippage of prestressing cables, liner-concrete interaction, liner failure mechanisms, and the use of nominal versus in-situ conditions. *Phase two* includes two distinct parts. In the first part the leak rate as a function of pressure is examined relative to the Sandia 1:4 test results, incorporating lessons learned from phase one.

¹ Standard Problem Exercise on the performance of containment vessels under severe accident conditions

² International Standard Problem 48, Containment Capacity.

In the second part methods are developed for predicting leakage as function of pressure and temperature in the probabilistic space.

Scanscot Technology has for almost twenty years carried out reactor containment investigations for the nuclear power industry in Sweden and worldwide, using advanced finite element analysis methods. Scanscot had the opportunity to participate in the ISP 48 project¹ where important findings related to the reactor containment global response were found. The SPE project gives the opportunity to follow up the ISP 48 work and develop methods for predicting the detailed containment behavior.

Other research work related to containment integrity and the Sandia ¼ scale model test has been conducted in a PhD project at University of Lund (see Anderson (2007) [8]). The work regarding the steel liner in this PhD project, summarized in Anderson and Jovall (2007) [9], considers liner-concrete interaction and detailed behavior near penetrations. This work is strongly related to the main objectives in the SPE project [6] and the scope of this report.

Our participation in the SPE project has been possible due to financial support from the Swedish / Finnish nuclear power industry and the Swedish Radiation Safety Authority (SSM).

Scope

The overall scope of the SPE project is to increase the knowledge of the nonlinear response of containment structures exposed to high internal overpressure. This report summarizes studies intended to be included in the SPE project phase 1 round robin exercise (see [6]).

The main focus in this report is to explain the effects of structural interaction between containment steel components and cracked concrete. Also the failure mechanism of the steel liner and the effect of variation in input parameters are discussed.

Four specific studies are presented (see Chapter 5 to 9);

- The scope of the *first study* is to explain the interaction between horizontal tendons and the containment structure. The study is carried out by using a FE-model describing a horizontal slice of containment wall. (SPE 1.1-1.2 see [6])
- The scope of the *second study* is to describe the global structural response during pressurization with focus on the behavior near the equipment hatch (penetration E/H). In this study a FE-model describing the whole containment model structure is used. The displacement results from this model, in the region of the equipment hatch, are used as boundary conditions for the liner studies in the third study (see below).
- The scope of the *third study* is to explain the detailed liner behavior of the steel liner near the equipment hatch. Focus is on explaining the liner tears observed in the containment model test. A detailed FE-model describing the steel liner and the interaction with the concrete structure is used. Also the failure criteria of the liner is discussed where the size of a tear in a

¹ Thanks to financial support from Swedish / Finnish nuclear power industry and the Swedish Radiation Safety Authority.

general liner field is evaluated by fracture-based failure methods. (SPE 1.3-1.4 see [6])

- The scope of the *forth study* is to describe the influence of variation in input data and to evaluate the effects on containment structural behavior. In this study focus is on the global expansion of the containment. As built measurements on material parameters, prestress, geometry etc. are used to evaluate the statistical characteristics of the input data. (SPE 1.5 see [6])

Outline of report

The next chapter (Chapter 2) describes the general outline, materials, pressurization, etc. of the containment scale model test (Sandia 1:4), which is used as reference test in this report. In the following chapter (Chapter 3) the principal analysis technique and used FE-software is described. The evaluation of input parameters and material models are given in Chapter 4, where both the best estimate values for the deterministic FE-analyses and the variation of the input are estimated. In Chapter 5 the tendon interaction with the concrete structure is analyzed with a horizontal slice model. The global model and analysis results are described in Chapter 6. In Chapter 7 the analysis of the liner close to the equipment hatch is presented and in Chapter 8 liner failure criteria is discussed. Effects due to statistical variation in the input parameters are studied in Chapter 9, where the variation in radial displacement in containment midheight is studied. Finally, in Chapter 10 the main conclusions are presented.

CONTAINMENT SCALE MODEL TEST

General

The Nuclear Power Engineering Corporation (NUPEC) of Japan and the U.S. Nuclear Regulatory Commission (NRC) jointly funded a Cooperative Containment Research Program at Sandia National Laboratories (SNL), USA, from July, 1991 through December, 2002.

As a part of this program, a ¼ scale model of a pre-stressed concrete containment vessel (PCCV) was constructed and pressurized up to failure. The prototype for the model is the containment building of unit 3 at the Ohi Nuclear Power Station in Japan, an 1127 MW Pressurized Water Reactor (PWR) unit. The design accident overpressure, p_{da} , of both the prototype and the model containment is 0.39 MPa.

The objectives of the model containment test were to;

- study aspects of the severe accident loads on containment vessels
- observe the model failure mechanisms
- obtain structural response data up to failure for comparison with analytical models

The model incorporated all structural parts important for containment integrity, including all large penetrations (like equipment hatch, personal air lock and pipe penetration). During pressurization the structural response was monitored, giving information on displacements, liner, rebar, concrete and tendon strains and tendon anchor forces. In addition, acoustic monitoring, video and still photography were used to monitor the structural behavior.

Milestones in the construction and testing of the model containment include the following;

12 February 1997	First Basemat Pour
19 June 1997	First Liner Panel Installed
15 April 1999	Final Dome Pour
8 March-3 May 2000	Prestressing
25 June 2000	Construction Completed
12-14 September 2000	Structural Integrity and Integrated Leak Rate Test
27-28 September 2000	Limit State Test
14 November 2002	Structural Failure Mode Test
3 May 2002	Demolition and Site Restoration Completed

This chapter gives a brief overview of the structural system, important structural components and the pressurization test of the containment scale model. A detailed description is given in [3].

Structural outline

General

The scale model can be divided into three main structural parts, basemat, cylindrical wall and dome (see Figure E 2.1).

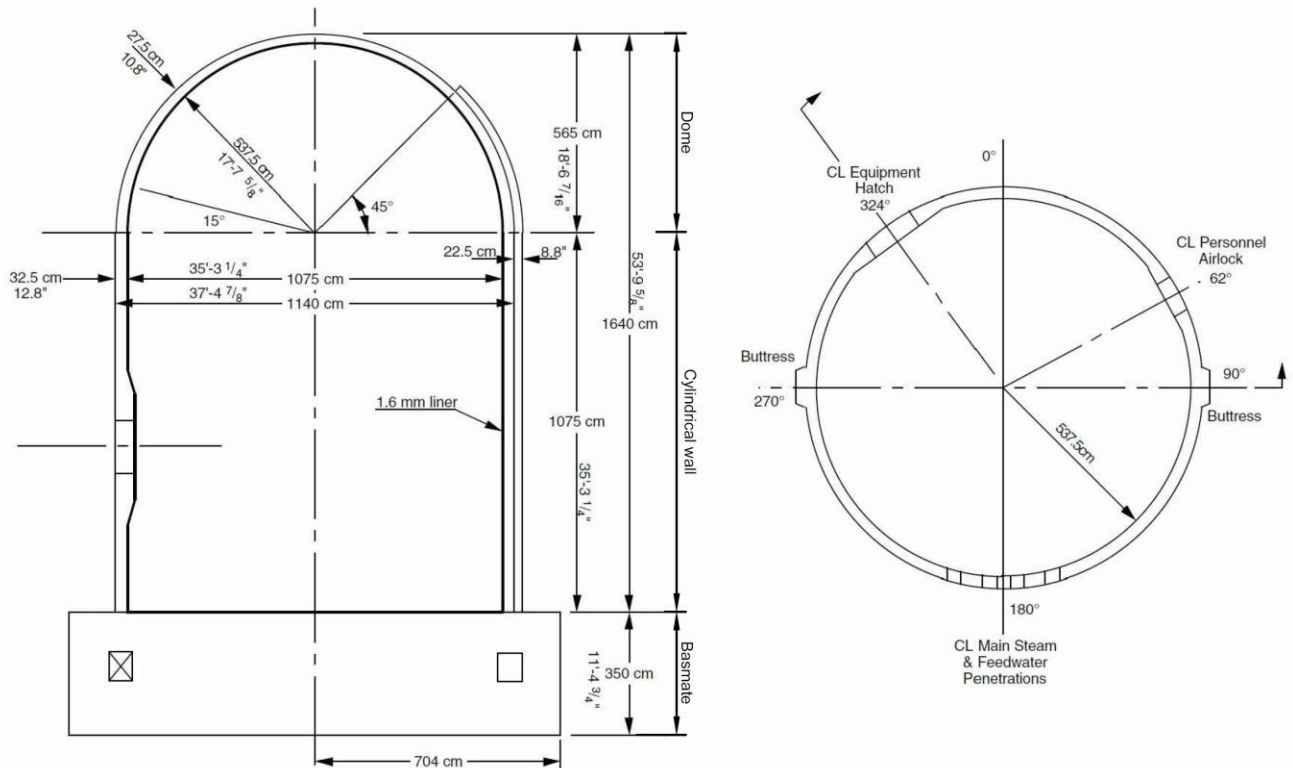


Figure E 2.1 Model containment, main structural parts and dimensions [3].

The *basemat* consists of a 3.5 m thick reinforced concrete slab on a 0.3 m thick mudmat of concrete, cast on an approximately 8 m thick engineered backfill. The steel liner is welded on steel profiles which are cast into the upper side of the basemat. The basemat includes the tendon gallery, situated underneath the cylindrical wall, where the vertical wall tendons are tensioned and anchored.

The *containment wall* has a nominal thickness of 0.325 m and is locally thickened at the major penetrations (see Figure E 2.1 and Figure E 2.7). The wall is prestressed in both the vertical and horizontal directions. Prestressing buttresses are located at 90 and 270 degrees, where the hoop tendons are anchored. The buttresses runs along the containment outside halfway up on the dome (see Figure E 2.1). The wall includes conventional reinforcement bars at the inner and outer side of the wall. The steel liner is placed on the inside of the wall and is anchored to the concrete by means of mechanical anchors, see Section 2.2.2. All penetrations through the containment are situated in the cylindrical wall, see Section 2.2.3. A general vertical cross-section through the containment wall is shown in Figure E 2.2.

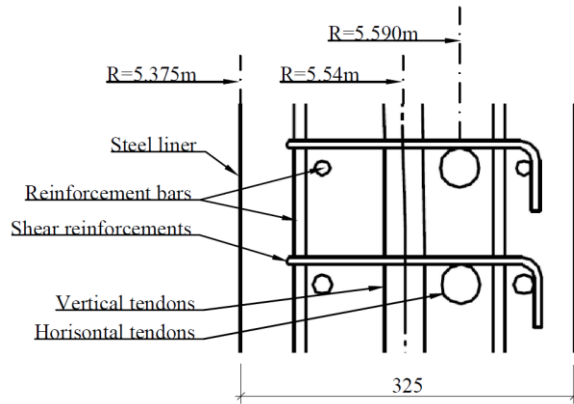


Figure E 2.2 General arrangement of structural components in containment wall (vertical cross section).

The nominal *dome* thickness is 0.275 m. At the connection to the wall the thickness is gradually increased to 0.325 m, in order to match the thickness of the wall. The vertical tendons in the wall are continued throughout the dome, constituting an orthogonal pattern of tendons (see Figure E 2.9 and Figure E 2.10). Hoop tendons are placed in the dome except for the uppermost part. The dome also includes conventional reinforcement bars. The steel liner is placed on the inside of the dome and anchored to the concrete by mechanical anchors, see section 2.2.2. In Figure E 2.3 the tendon arrangement in the dome is shown.



Figure E 2.3 Arrangement of tendons in the dome [3].

Steel liner

The steel liner is fabricated from mild carbon steel and the nominal liner thickness for the prototype containment is 6.4 mm, i.e. 1.6 mm for the scale model containment. The as-built liner is 1.8 mm where the extra 0.2 mm provides fabrication allowance. Material properties for the liner are described in Section 4.4. The nominal yield and failure strength is 230 and 420 MPa respectively.

Panels with different sizes were prefabricated, where liner components like vertical T-anchors and horizontal stiffeners were shop welded onto the liner panels. The liner panels were transported to the construction site including; liner anchors, stiffeners, pipe casing, etc. At site

the liner panels were welded together and used as inner formwork for the concrete wall and dome.

These stiffeners had no structural function after the model containment construction was completed. The plates were welded together at site. At penetrations, locally thickened plates were used, connected to the penetration assemblies.

Anchors and stiffeners

The vertical T-anchors (see Figure E 2.4), continuously welded to the liner, anchors the liner to the concrete. The horizontal stiffeners (see Figure E 2.4) have no intended structural function, they are only intended to stiffening the liner panels during transport and at the construction phase. However, the horizontal stiffeners will prevent the liner to slide vertically in relation to the concrete. The vertical anchors will both prevent the liner to separate from and slide in relation to the concrete (see Section 4.4).

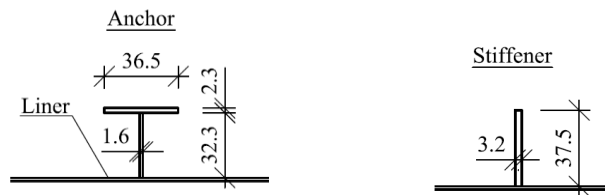


Figure E 2.4 Liner anchoring and stiffener details.

The vertical anchors are positioned with a distance of 0.45 m, except regions near discontinuities where they are more closely spaced (distance 0.15 m). The 0.15 m distance represents the accurate scaling from the full-scale containment, while the 0.45 m is three times the accurate scaling (was used to reduce costs). The liner anchor layout is presented in Figure E 2.5. The vertical T-anchors are not extended into the dome. Here the liner is instead anchored to the dome with small stud-type anchors.

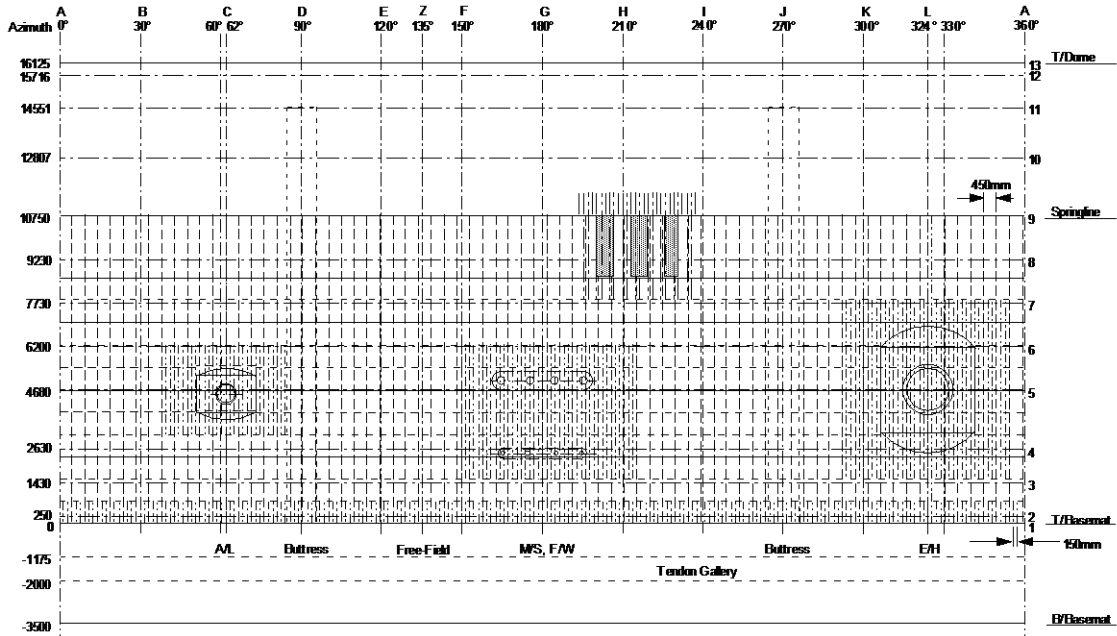


Figure E 2.5 Liner anchor layout [3].

Liner near penetration E/H

In this report special attention is paid to the steel liner in the region near the equipment hatch, penetration E/H (see Chapter 7). The arrangement of anchors and stiffeners in the region of penetration E/H is shown in Figure E 2.6. Near the penetration hole the liner was welded to a thicker steel plate (20 mm thick, 125 mm wide). The left side of Figure E 2.6 show detailed sketches of the region near the vertical fold where liner tears occurred during the pressurization test (also see Section 2.4 and Chapter 7).

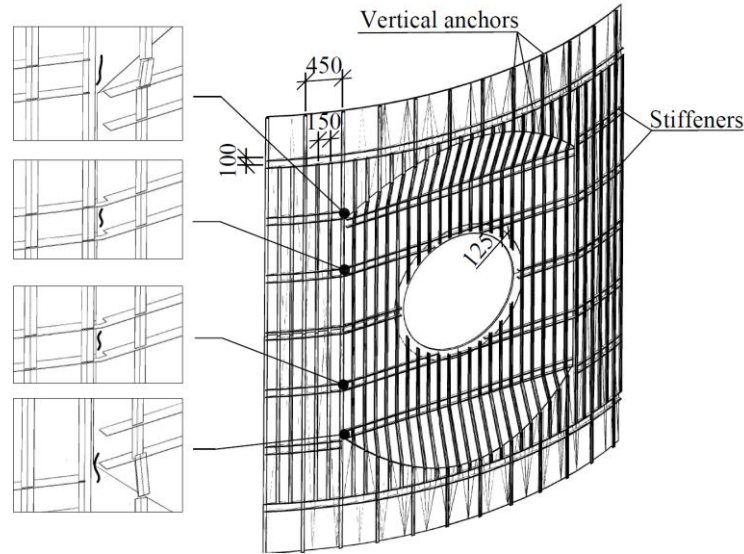


Figure E 2.6 Arrangement of liner anchors and stiffeners near penetration E/H (left sketches, regions where tears occurred) [9].

Penetrations [9]

There are several penetrations through the model containment; the equipment hatch (E/H), the personnel airlock (A/L), the main steam (M/S) and the feedwater (F/W) penetrations. All penetrations are placed in the cylindrical wall, the layout of the penetrations is shown in Figure E 2.7. The E/H and A/L penetration assemblies are 1:4-scale functional representations, while the M/S and F/W penetrations only includes the penetration sleeve and reinforcing plates.

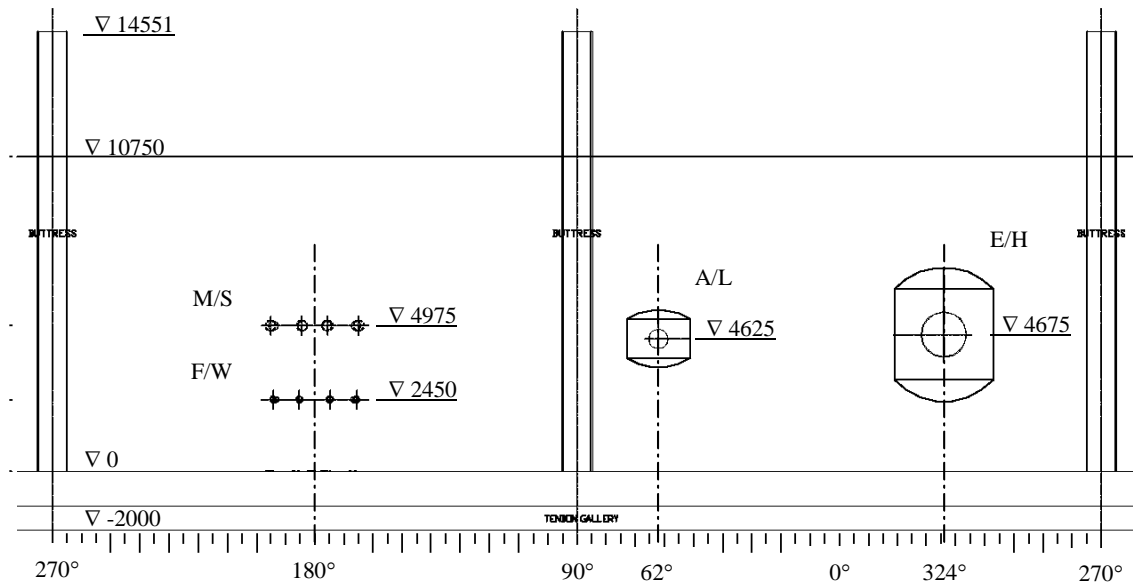


Figure E 2.7 Major penetrations through containment, cylindrical part (elevation) [3].

Pre-stressing tendons

The cylindrical wall and the dome are prestressed using unbonded tendons. The tendon consists of three, 13.7 mm seven wire strands with nominal yield strength (0.2% permanent elongation) and failure strength of 1580 and 1850 MPa respectively (see also Section 4.5.2). The tendon cross-section area is 339.3 mm². The tendons are post tensioned and placed in metal ducts, normally 35 mm in diameter. The tendons are of VSL type where the tendon strands are fixed in the tendon anchor by wedges (see Figure E 2.8).

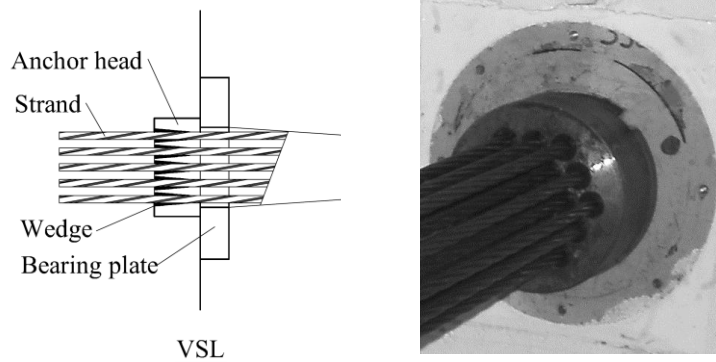
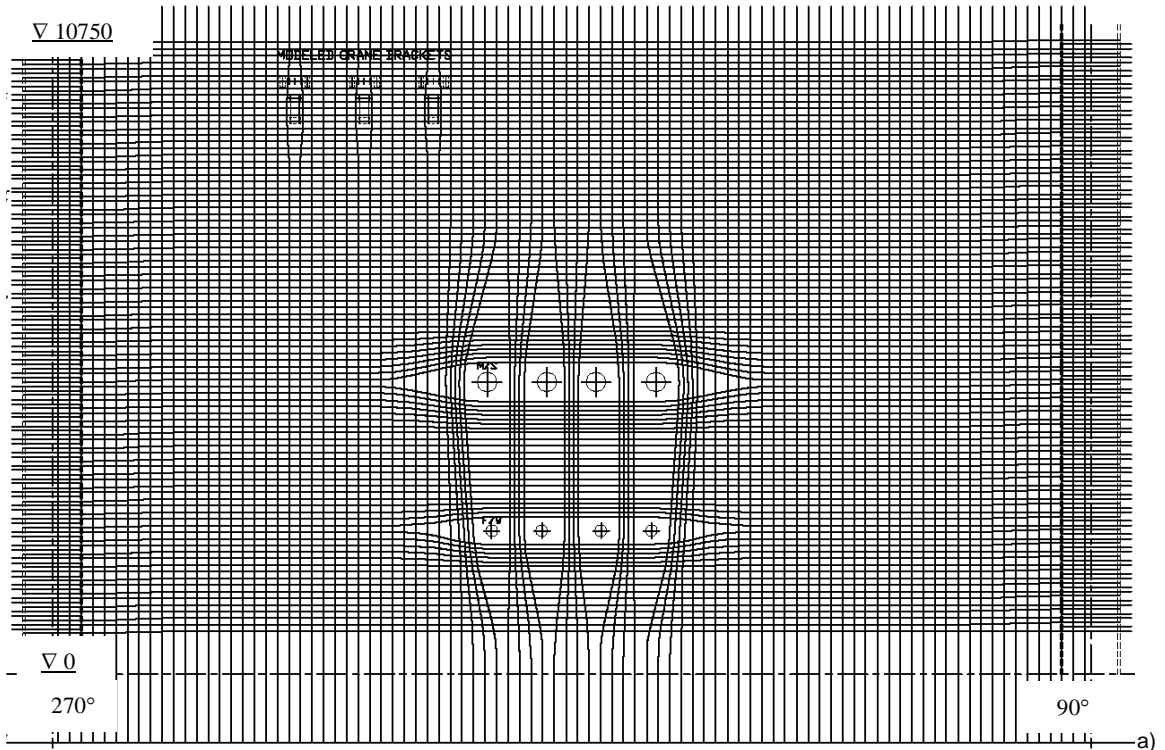


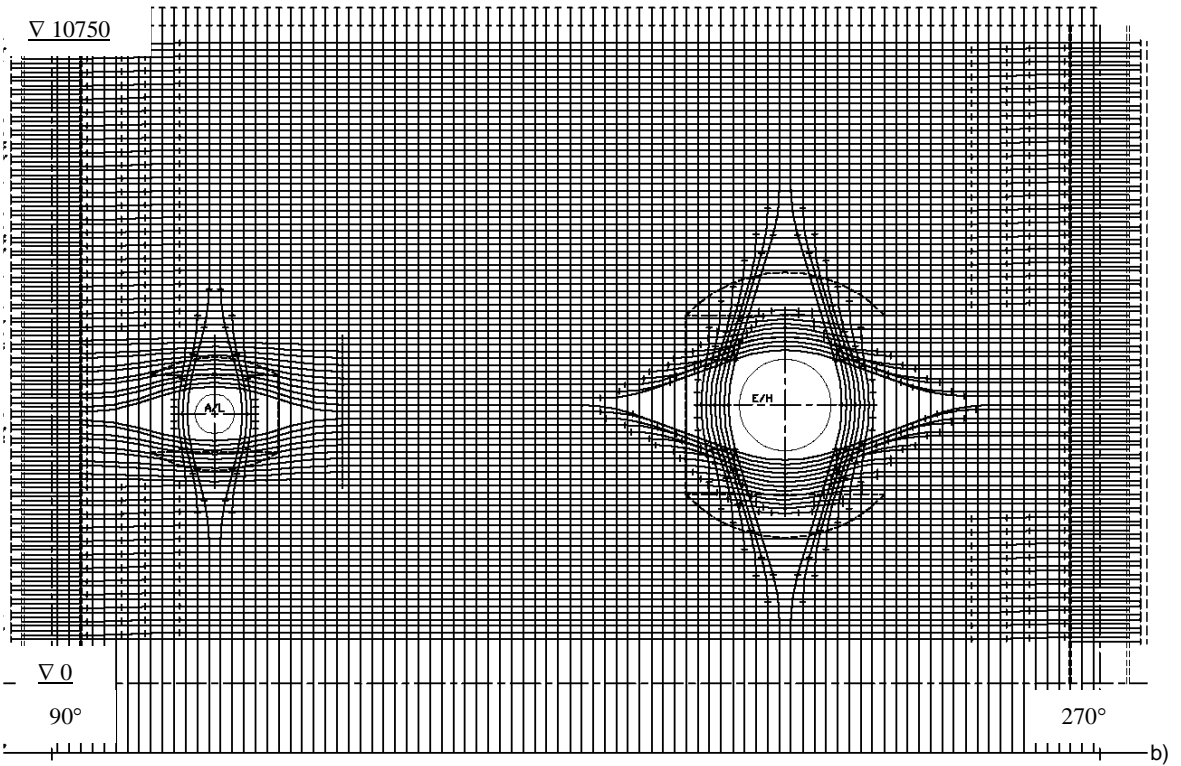
Figure E 2.8 Typical VSL anchor [8].

The tensioning of the tendons is carried out with hydraulic jacks simultaneously in both ends of the tendons. The tendons are tensioned up to a certain force value and then seated by fixing the tendon strands into the tendon anchor by wedges. During the seating the tendon strand will slip and the end force will decrease. The tendons are tensioned according to a specific schedule to avoid unbalanced prestress during construction and to equalize the effects of elastic loss of prestress.

The hoop tendons consist of 360° tendons anchored in each side of the buttress. Every second horizontal tendon is anchored at buttress 90° and 270° respectively. The vertical tendons in the wall and dome are tensioned and anchored in the basemat tendon gallery (see Figure E 2.1). In general the distance between horizontal tendons is 0.115 m in the containment wall and 0.245 m in the dome. Vertical tendons are arranged with a general distance of 0.195 m. The tendon layout in the cylindrical wall is shown in Figure E 2.9 and Figure E 2.10.



Pre-stressing tendon arrangement in cylindrical wall, elevation, outside containment, 270° - 90°



Pre-stressing tendon arrangement in cylindrical wall, elevation, outside containment, 90° - 270°

Figure E 2.9 Pre-stressing tendon arrangement, cylindrical part (elevation) [3].

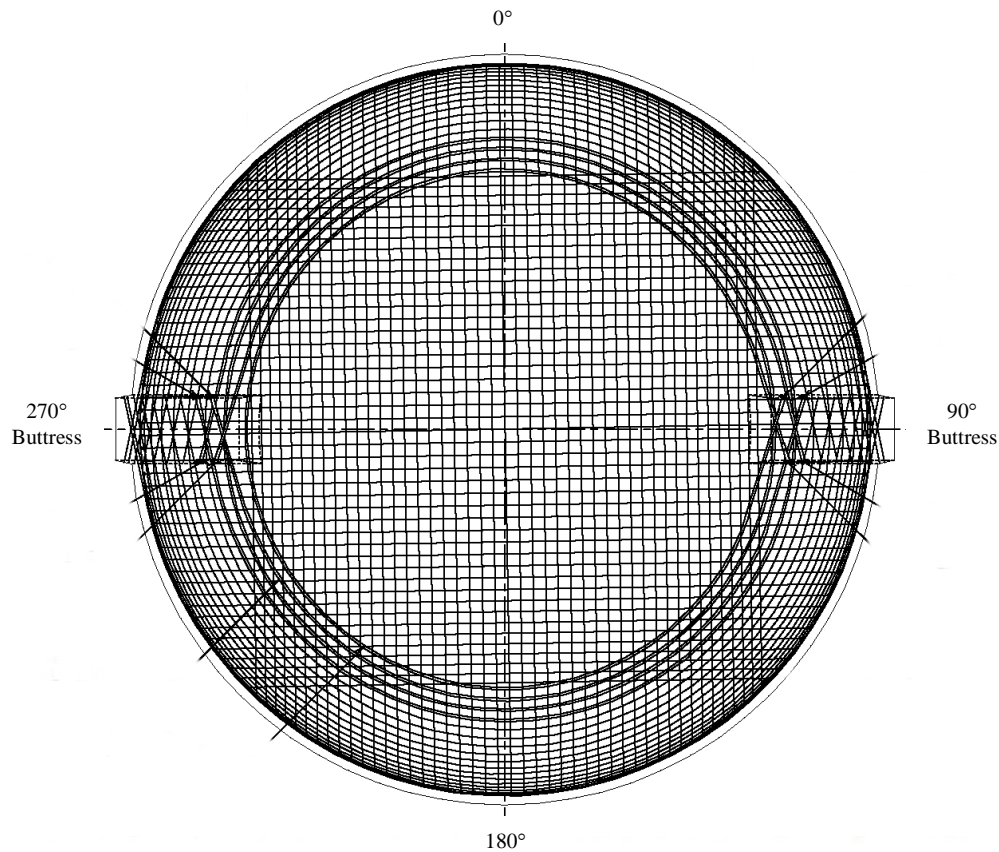


Figure E 2.10 Prestressing tendon arrangement, dome (plan view from above) [3].

Reinforcing steel

All structural parts are in general reinforced with an orthogonal net of longitudinal reinforcement bars, both in the in- and outside (see Figure E 2.2). All structural parts also includes shear reinforcement (radial ties). The carbon steel bars have bar diameters between 10 and 22 mm and a general nominal yield strength of 390 MPa (bar properties, see section 4.3). Additional reinforcement is used around penetrations, near the wall-basemat junction and at tendon anchoring zones, i.e. tendon gallery and buttresses.

Concrete

Two different nominal concrete strengths where used, 30 MPa for the majority of the basemat and 45 MPa for the wall and dome as well as above the basemat tendon gallery (concrete properties, see section 4.2). Concrete lifts and strengths are shown in Figure E 2.11.

The concrete mix used is air-entrained and contains flyash and superplasticizer. Maximum aggregate size is 10 mm.

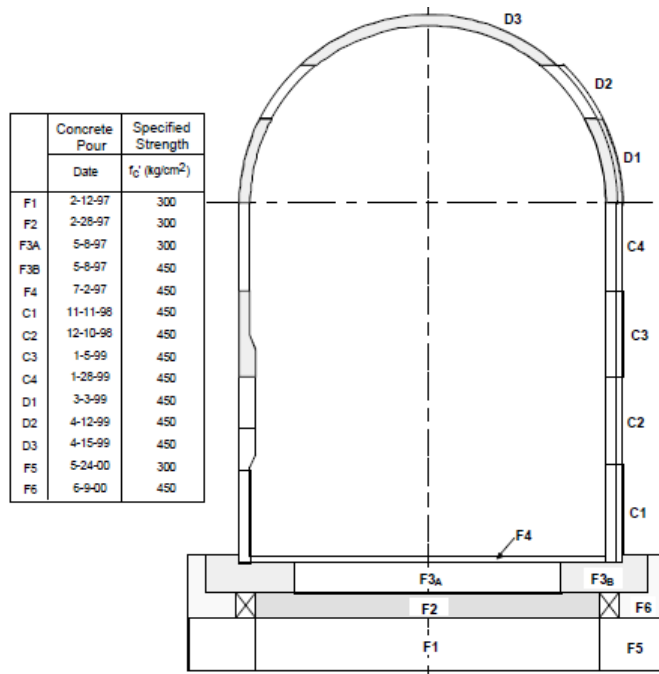


Figure E 2.11 Concrete quality and cast stages [3].

Instrumentation and material testing

Material testing

An extensive material testing program was carried out in connection to the scale model test (see [3]). Properties of all the containment model materials, except for the concrete, were determined from tests prior to construction. Model concrete properties were determined by testing standard specimens cast during the concreting operations.

For steel components (rebar, tendons and liner) standard tensile tests were conducted. In general the yield strength, failure strength and E-modulus were evaluated from these tensile tests.

Concrete tests were conducted according to ASTM standards and specimens were cast from nearly every truck of concrete placed in the model. Compression tests of cylinders were carried out at seven, 28, and 91 days. 91-day strengths were compared to the specified design strengths. More extensive concrete property tests were conducted around the time the model was being tested by pressurization. These tests included compression tests, split cylinder tensile strength and since prediction of concrete cracking was one main objective limited number of direct tension tests were conducted. Also other types of tests were conducted like tests to determine modulus of elasticity and Poisson ratio. Due to unexpected low strength for some compression tests also a limited number of creep tests were conducted.

In Chapter 4 material properties from test data are evaluated where the best estimate values and scatter in measuring data is estimated.

Containment model instrumentation

To record the structural response, extensive instrumentation was installed. Displacement transducers measured the global behavior both radially and vertically. Strain gauges installed at strategic locations on steel components (at reinforcement, tendons, liner etc.) was measuring the local strain behavior. For a large number of tendons load gauges measured tendon anchorage force during prestressing and the pressurization test. An acoustic monitoring system was used in order to indicate the location of tendon wire breaks, concrete cracking, liner tearing (leakage) etc. Also other types of instrumentation, measuring temperatures and internal pressure during the tests, were used.

A detailed description of the instrumentation of the containment model is given in [3].

Pressurization test

Test operations

The decision was to perform a static, pneumatic over-pressurization test at ambient temperature. The limit state test (LST) was terminated following a functional failure, i.e. equilibrium leakage was reached and no gross structural failure occurred. Subsequently it was decided to re-pressurize the model containment, prior to demolition, in an attempt to create a global structural failure (Structural Failure Mode Test, SFMT).

Prior to the limit state test (LST), pressure tests at lower levels were conducted. The pressure history for all tests performed is given in Figure E 2.12 below. The over-pressurization studies in this report correspond to the limit state test (LST).

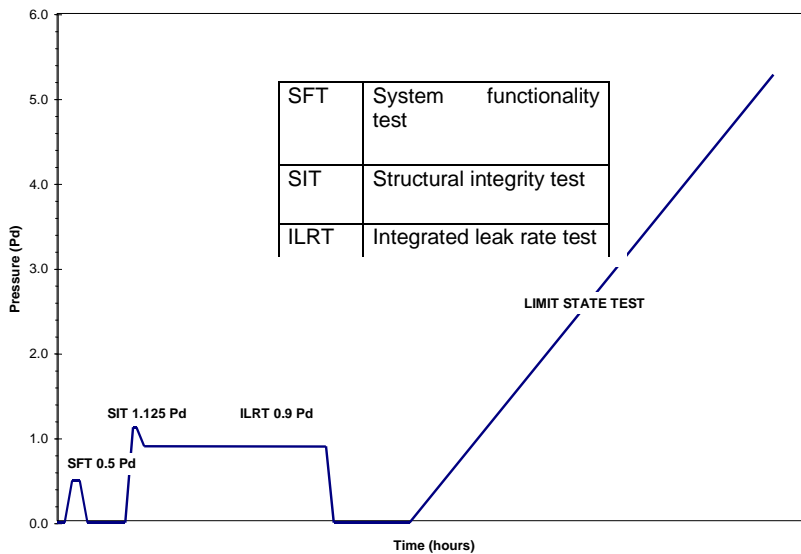


Figure E 2.12 Pressurization of the containment model [3].

A detailed presentation of the overpressurization test is given in [3].

General results

The limit state test was started the 27th of September 2000 and finalized the day after. Figure E 2.13 show the midheight radial displacement at different angles. The start displacement is negative due to prestressing and displacement increases almost linearly up to around 1.5 times p_d (0.59 MPa). At this pressure the concrete can be assumed to start cracking and after this pressure the displacement will increase more rapidly. At 2 times p_d the average displacement is around 3.5 mm, at 3 times p_d around 17.0 mm and finally at 3.3 times p_d around 22.5 mm.

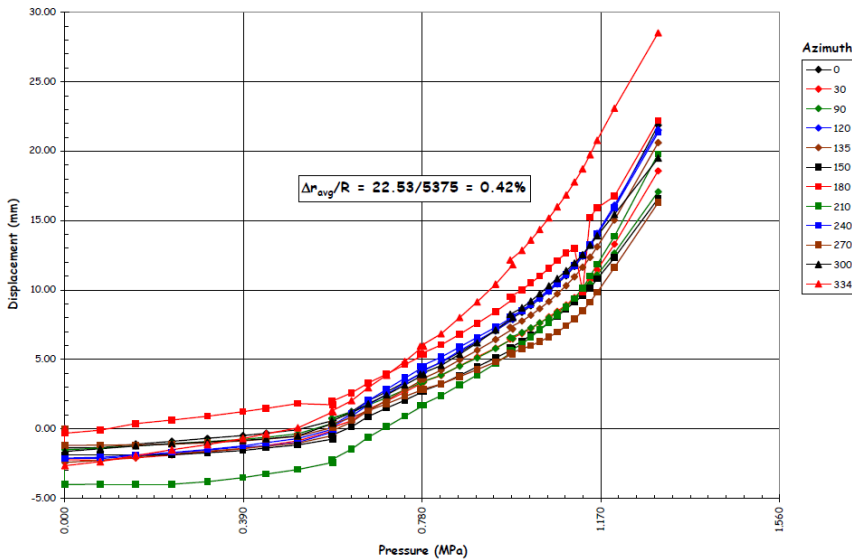


Figure E 2.13 Measured radial displacement at midheight (el 4680 mm) [3].

Figure E 2.14 shows a stretch-out sketch of the cylindrical part of the containment model seen from the inside, where liner tears that occurred during the test are indicated. At the overpressurization test, the first leak was detected at an internal pressure 2.5 times p_d (0.98 MPa). At 3.3 times p_d the leak rate exceeded the capacity of the pressurization system and the sources of the leak was a number of tears found in the post-test inspection (see Figure E 2.14). The acoustic monitoring system detected the first leak near the penetration E/H. Four tears were found close to the vertical bend line between the embossment and the general curved wall. The detailed location of these tears is also indicated in Figure E 2.6. In Chapter 7 a detailed study of the region near penetration E/H is presented with focus on the liner behavior.

At the construction stage the liner was grinded in connection with welding, which resulted in localized areas with thinner liner. It was concluded that in the region of almost all tears the liner had been grinded and the liner thickness was reduced up to 50% in some cases⁴. In the region of tear #7 and #15 (see Figure E 2.14) the liner grinding was concluded to be extensive, between 25 and 50% reduction. The liner grinding was less in the area of tear #12 and #13 and it was concluded that liner tear #12 was the most likely to be caused by a “true structural effect”.

⁴ Do not reflect the full-scale case. A 50% reduction of the model liner thickness corresponds to a 12.5% reduction for the prototype containment liner.

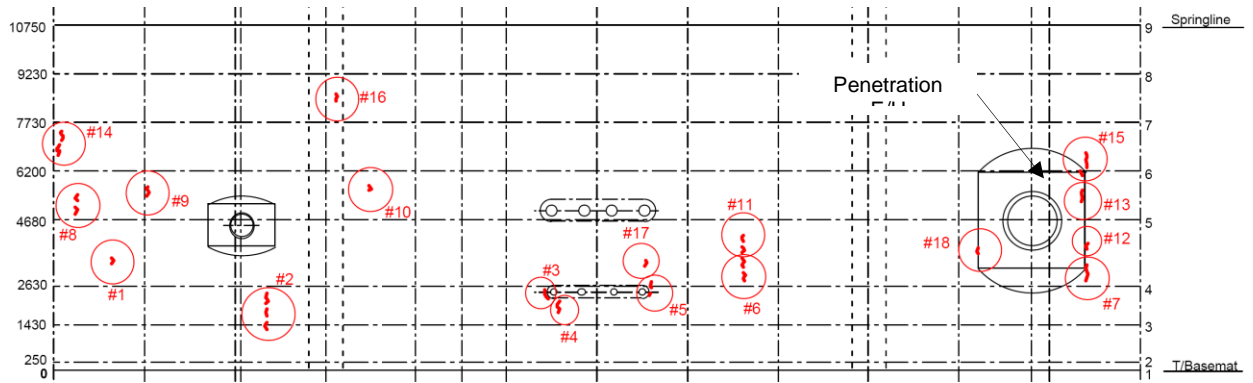


Figure E 2.14 Stretched-out sketch, liner in the cylindrical part [3].

METHODS OF ANALYSIS

General

In principal three major levels of analysis approaches are used when utilizing the finite element technique for studying the structural behavior of a prestressed concrete reactor containment;

1. Global analysis
2. Local analysis at critical areas
3. Detailed studies of the leak-tightness integrity

These levels are exemplified in Figure E 3.1 by the study of the equipments hatch region presented in this report.

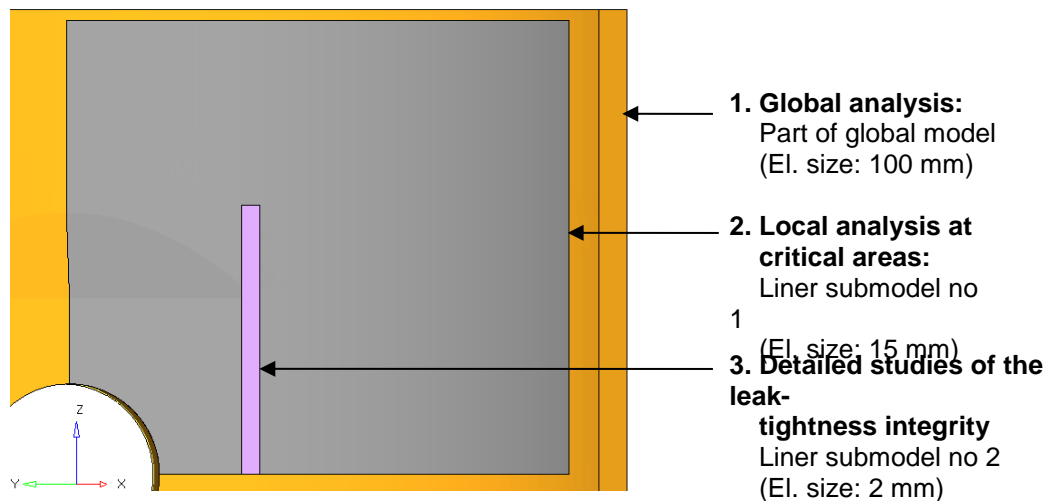


Figure E 3.1 FE-modeling levels

Modeling and analysis technique for containment structures were studied in the ISP48 project (see [7]). In the report⁵ by Scanscot Technology included in ISP48 report [7] (appendix L) investigations considering different modeling aspects are presented. Different parametric studies were conducted considering solver technique, mesh size, constitutive models of concrete, load rate and modeling of prestressing. These studies are considered and the general guidelines for modeling technique proposed in the ISP48 report are followed in studies presented in this report.

Model principals

The objective of this project is to simulate the behavior of the containment model pressurized up to failure. With the aim of describing the pressurization event the analyses are carried out using non-linear material models. To be able to simulate the interaction between concrete and steel components non-linear contact definitions are utilized.

As described above different FE-model levels are used to be able to describe the detailed response of especially the steel liner. So called submodeling technique is utilized where a specified interface on the global model is defined and used as a displacement load for the sub model. As the liner can be seen as more or less displacement controlled the liner is especially suitable to describe with submodeling technique.

In general best estimate values (average) are used as input data for the analyses. In Chapter 4 the input parameters to be used in the analyses are discussed. For most of the needed input parameters specific test data and measurements are available.

Software

In the global analysis and tendon studies, the finite element program Abaqus/Explicit version 6.9 has been used. Liner submodels have been performed with Abaqus/Standard version 6.9. For pre- and post processing both Abaqus/CAE and Altair/HyperMesh have been used.

INPUT PARAMETERS AND FE-IMPLEMENTATION

General

In this chapter input parameters used in the analyses are defined. Nominal values, average and the variation in the parameters are presented. The variation found in tests is compared with expected variation according to JCSS [15]. In general average or “best estimation” values are used as input in the FE-analysis (Chapter 5 to 7). The influence of variation in input parameters is evaluated in Chapter 9.

Also the general parameter implementation in FE-models is discussed here. The full description of the specific FE-models is presented in the chapter for each study (see Chapter 5 to 9).

⁵ Scanscot Technical report 03402/TR-01, “ISP 48: Posttest analysis of the NUPEC/NRC 1:4-scale prestressed concrete containment vessel model”, ed 2, 2005-02-23.

Concrete

FE-implementation

The concrete is described by solid elements and the used material model for the concrete is the so-called brittle cracking model in Abaqus [16]. For this model linear elastic behavior is assumed for compression and for tensile stresses up to the tensile strength of the concrete. For stresses exceeding the concrete tensile strength cracked concrete behavior is assumed. The used model is a so-called smeared crack model which represents the discontinuous brittle behavior of concrete. This material model do not track individual cracks, the effect of cracks enters into analysis by the way in which the cracks affect the structural stiffness. The fracture energy required to form a unit area of crack surface is used in this material model to decide if the crack will propagate in the structure. An important benefit of the brittle cracking model in Abaqus is that the crack orientation is considered. The principal stress-displacement curve used in the analyses is shown in Figure E 4.1 (see e.g. [10]).

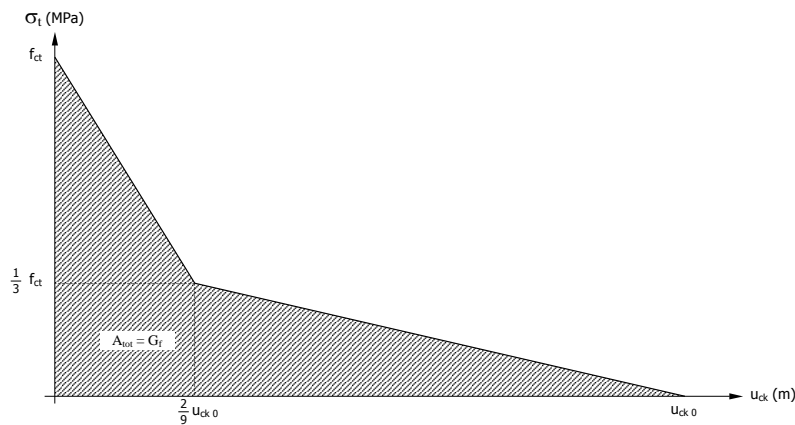


Figure E 4.1 Principal stress-displacement curve [10] (crack width vs. tensile stress).

Using this material model the material parameters needed to be defined is the, E-modulus, tensile strength and fracture energy. Even if the used material model does not describe compressive failure, also the compressive strength is needed to verify that compressive stress is acceptable. However, for the load case studied in report (internal overpressure) the main failure modes will be related to tensile loading of the structure and the compressive stress will be moderate. The stress-displacement curve used in the analyses in this report is shown in section 4.2.2.4.

In this report the global expansion of the containment due to pressurization is important. It is therefore important to describe the reduction of stiffness due to concrete cracking (tension softening) as well as the increase of stiffness due to concrete between cracks (tension stiffening) in a correct way. To verify the tensioning stiffening effect of the chosen concrete model a study is presented in Appendix A1 where results from a simple FE model is compared with results from an empirical model presented in Belarbi and Hsu [11].

The reduced shear stiffness in cracked concrete is in the brittle cracking model described by a so-called shear retention factor. This factor is implemented in the brittle cracking model as reduction of the shear modulus in elements exceeding the crack strain. The main shear transfer

mechanism in reinforced concrete is aggregate interlocking and dowel action. The dowel action is depending on the reinforcement arrangement. In Kolmar and Mehlhorn [12] it is concluded that the reinforcement ratio is the most important parameter defining the shear stiffness of cracked concrete. Near the basemat large shear force together with horizontal concrete cracks could occur and therefore is the reduction of shear stiffness aimed to be described properly here. In the lower part of the containment wall, (near the basemat) the average vertical reinforcement is ratio above 3%. The shear reduction curve used in the analyses is shown in Figure E 4.2 together with the curve by Kolmar [13] (the expression by Kolmar is only valid up to 2% reinforcement ratio). To avoid numerical problems the retention factor used in the analyses is in general exceeding Kolmar (see Figure E 4.2). This difference is assumed to have small effects on the analysis results presented in this report.

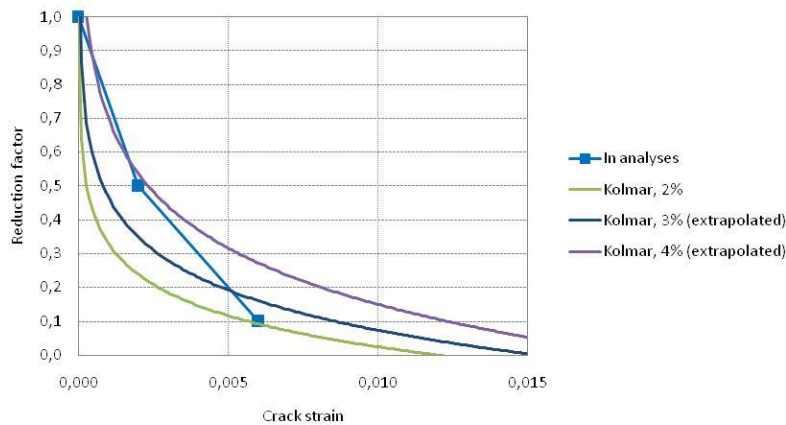


Figure E 4.2 Shear retention factor.

Material parameters

The containment wall and the basemat close to the wall are constructed of concrete with the nominal concrete strength of around 44 MPa (see Figure E 2.11).

Concrete tests were conducted according to ASTM standards. Compression tests of cylinders were carried out at 7, 28, and 91 days. 91-day strengths were compared to the specified design strengths. Around the time of the model limit state test a more comprehensive test was conducted. These tests included compression tests, split cylinder tensile strength and since prediction of concrete cracking was one main objective limited number of direct tension tests also were carried out.

The compressive strength, tensile strength, E-modulus and fracture energy are evaluated below from the test data presented in the Sandia 1:4 report [3], appendix B. The evaluation is made for samples taken from concrete in the wall and dome (cast stages C1-D3) and the evaluation are based on the tests made in connection to the limit state test.

Compressive strength

The average compressive strength (f_{cm}) at the time of limit state test⁶ is around 60 MPa.

⁶ Specimens cured at approximately 1,5 year. Totally 12 tests.

In Model Code (1990) [14] the concrete compressive strength dependency of age can be evaluated based on the 28 day strength. The compressive strength value at the time of the limit state test according to Model Code (1990) [14] is 58 MPa⁷ which is close to 60 MPa.

The coefficient of variation (COV) evaluated from the test results at the time of the limit state test is around 13 %. In JCSS [15] the statistical variation for different structural parameters are given and for compressive strength of concrete COV = 6 % is given. The variation in the measured compressive strength seems to be larger than what is normally assumed. All concrete parameters are assumed to be distributed according to the log-normal distribution (see JCSS [15]).

Tensile strength

The average tensile strength (f_{ctm}) can be evaluated in three different ways using the test data. The tensile strength can be evaluated from splitting tests, direct tension tests and also from the compressive strength tests.

- Seven splitting tests were carried out and the average split tensile strength ($f_{ct,sp}$) is 3.5 MPa with a COV of 8 %. According to Eurocode 2 the tensile strength evaluated from splitting tests should be taken as $0.9f_{ct,sp}=3.2$ MPa
- Five direct tension tests were carried out and the average tensile strength evaluated from these tests is 2.1 MPa with a COV of 12 %.
- Totally 12 compressive strength tests were carried out (see section 4.2.2.1) and the average compressive strength (f_{cm}) is 60 MPa with a COV of 13 %. Different relations between compressive and tensile strength are given in the literature. In JCSS [15] tensile strength evaluated from compressive strength should be taken as $f_{ctm} = 0.3 * f_{cm}^{2/3} = 4.6$ Mpa.

Depending on which test method that is used different tensile strength are determined (3.2, 2.1 and 4.6 MPa). In the analyses $f_{ctm} = 2.1$ MPa evaluated from the direct tensile tests is used.

The COV evaluated from the test result is around 10%. In JCSS [15] COV = 30 % is recommended for the tensile strength.

E-modulus

Seven different tests were carried out at the time of the limit state test to evaluate the E-modulus. The E-modulus can also be evaluated from the compressive strength tests.

The “direct” E-modulus tests give an average E-modulus (E_{cm}) of 26.8 GPa and a COV of 7%.

Different relations between compressive strength and E-modulus are given in the literature. In JCSS [15] the average E-modulus, evaluated from compressive strength, should be taken as $E_{cm} = 10500 * f_{cm}^{1/3} = 41$ GPa.

Depending on which test method that is used, different E-modulus is determined (26.8 and 41.0 GPa). In the analyses $E_{cm} = 26.8$ GPa is used.

⁷ Based on the measured average strength at 28 days (43 MPa) assuming slow curing cement. The measured average strength at 91 days is around 52 MPa

The COV evaluated from the test result is below 10%. In JCSS [15] a COV of 15 % is recommended for the E-modulus.

Fracture energy

No specific tests for evaluating the fracture energy (G_f) are performed. In Model Code [14] an expression is given which is based on the compressive strength and maximum aggregate size. According to Model Code [14] can the fracture energy be estimated as $G_f = \alpha_f (f_{cm}/f_{cmo})^{0.7}$, where α_f is a factor depending on the aggregate size and f_{cmo} is specified to 10 MPa.

According to the expression above the fracture energy for the specific concrete is $G_f = 25 (60/10)^{0.7} = 88 \text{ N/m}$.

No specific information about the statistical variation of the fracture energy is found. It is assumed that the COV is at least as evaluated for the other concrete parameters i.e. between 10 and 15 %.

The fracture energy together with the tensile strength specifies the principal stress-displacement curve given in Figure E 4.1. The curve used in the analyses is given below (see Figure E 4.3).

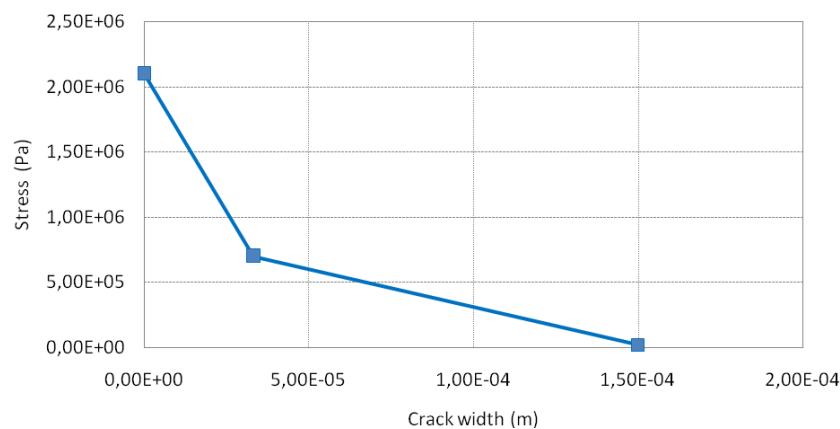


Figure E 4.3 Stress-displacement curve (crack width vs. tensile stress).

Reinforcement

FE-implementation

The reinforcement bars of the containment model are modeled with shells elements with orthotropic properties. The reinforcement elements are connected to the concrete elements by the Abaqus option Embedded Element. The used material model, for all steel components in the analyses, is elasto-plastic using Von Mises yield criteria. The principal uni-axial stress strain curve, used for all mild steel components in the analyses, is shown in Figure E 4.4.

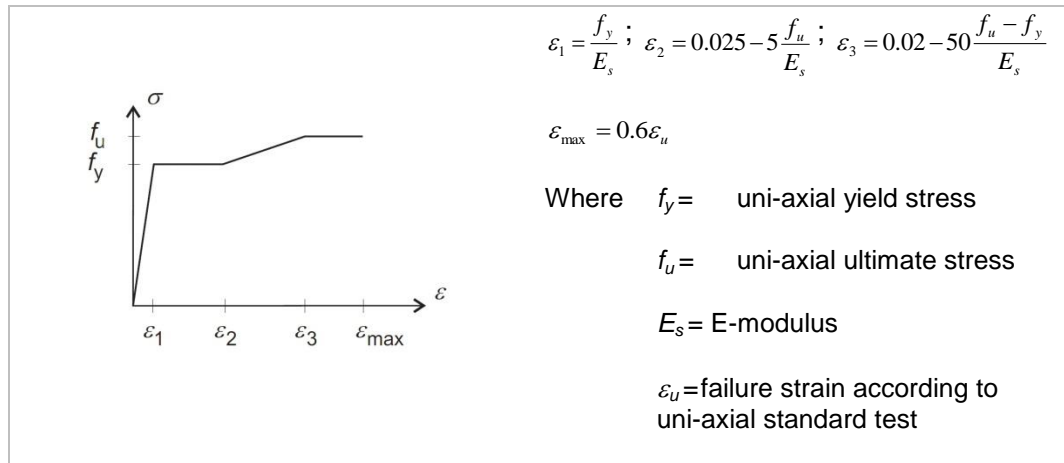


Figure E 4.4 Principal uni-axial Stress-strain curve according to the Swedish building code BSK 07 [17].

Material parameters

The reinforcement bars in the containment wall and dome has a nominal yield strength of around 390 MPa.

In general has three tensile tests has been carried out for each bar diameter ($\phi 10$, $\phi 13$, $\phi 16$, $\phi 19$ and $\phi 22$). The general test was made for bar specimens however, some standard dumbbell⁸ tests were also made. Test data are given for the yield strength, ultimate strength, maximum elongation and E-modulus.

The test data for bar specimens are evaluated below. As no clear dependency between different bar diameters can be seen in the test data, all test data are evaluated together. Data from dumbbell specimen tests are excluded from the evaluation below. The average values for the dumbbell specimens are in general higher than the average values evaluated from bar specimens.

All reinforcement material parameters are assumed to be distributed according to the normal distribution (see JCSS [15]).

Yield strength

The average yield strength (f_{ym}) evaluated from the bar specimens is around 460 MPa with a COV of 3.5%.

In JCSS [15] the statistical variation is separated for variation between different mills, between batches (within a mill) and within a batch. It is assumed that all tested reinforcement in the containment model comes from the same batch. According to JCSS [15] the standard deviation within a batch can be taken as 8 MPa (correspond to a COV of around 2 %). Slightly higher COV was evaluated from the tests (see above).

⁸ Standard shape on test specimen, tests give "pure material" properties.

Ultimate strength

The average ultimate strength (f_{um}) evaluated from the bar specimens is around 645 MPa with a COV of 4.3%.

The total statistical variation is assumed to be slightly larger for the ultimate strength than for the yield strength, according to JCSS [15]. No specific “within batch” values are given. However, the COV could be assumed to be low, say less than 3%. Slightly higher COV was evaluated from the tests.

Ultimate elongation

The average ultimate strain (ε_{um}) evaluated from the bar specimens is around 0.21 with a COV of around 12 %.

No expected values for the COV for this parameter are found in the literature. The COV evaluated from tests is quite high for a steel material parameter.

E-modulus

The average E-modulus (E_{sm}) evaluated from the bar specimens is around 185 GPa with a COV of 1.8%.

In the JCSS [15] the statistical variation of the E-modulus is assumed to be very small and the parameter is recommended to be seen as deterministic.

Stress strain curve

Figure E 4.5 shows the uni-axial stress strain curve used in the analyses, based on the evaluated average values above.

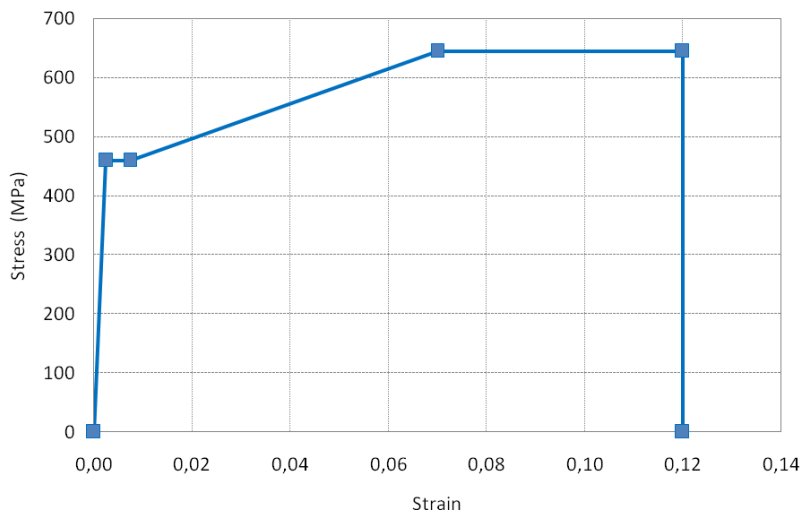


Figure E 4.5 Reinforcement uni-axial stress-strain used in analyses.

Steel liner

FE-implementation

The liner is modeled with shells elements. Depending of the model level (see Chapter 3) the liner is either rigidly connected to the concrete elements or connected by connectors representing the liner anchor profiles. The principal liner material model is the same as for the reinforcement (see Figure E 4.4).

Material parameters

The steel liner has a nominal yield strength of around 230 MPa.

Three tensile tests have been carried out in each direction (vertical and hoop direction). Test has been made for both pure liner specimens and for welded specimens. Only test for pure liner specimens are used for evaluating the material parameters. Welds in the liner will reduce the ultimate elongation and this reduction is discussed in Chapter 8, concerning liner failure criteria. Test data are given for the; yield strength, ultimate strength, maximum elongation and E-modulus.

The test data for liner specimens are evaluated below. As no clear difference between different directions (vertical and hoop direction) can be seen in the test data, all test data are evaluated together.

All liner material parameters (structural steel) are assumed to be distributed according to the log-normal distribution (see JCSS [15]).

Yield strength

The average yield strength (f_{ym}) evaluated from the liner specimens is around 383 MPa with a COV of 3 %.

It is assumed that all liner in the containment model comes from the same batch. According to JCSS [15] the COV within a batch can be taken as around 2%.

Ultimate strength

The average ultimate strength (f_{um}) evaluated from the liner specimens is around 498 MPa with a COV of 0.3%.

The total statistical variation is assumed to be less for the ultimate strength than for the yield strength, according to JCSS [15]. No specific “within batch” values are given. However, the COV could be assumed to be low, say around 1%.

Ultimate elongation

The average ultimate strain (ε_{um}) evaluated from liner specimens is around 0.33 with a COV of around 1 %.

No expected values for the COV for this parameter are found in the literature.

E-modulus

The average E-modulus (E_{sm}) evaluated from the liner specimens is around 220 GPa with a COV of 2.6%.

In the JCSS [15] the statistical variation of the E-modulus is assumed to be very small and the parameter is recommended to be seen as deterministic.

Stress strain curve

Figure E 4.6 shows the uni-axial stress strain curve used in the analyses, based on the evaluated average values above.

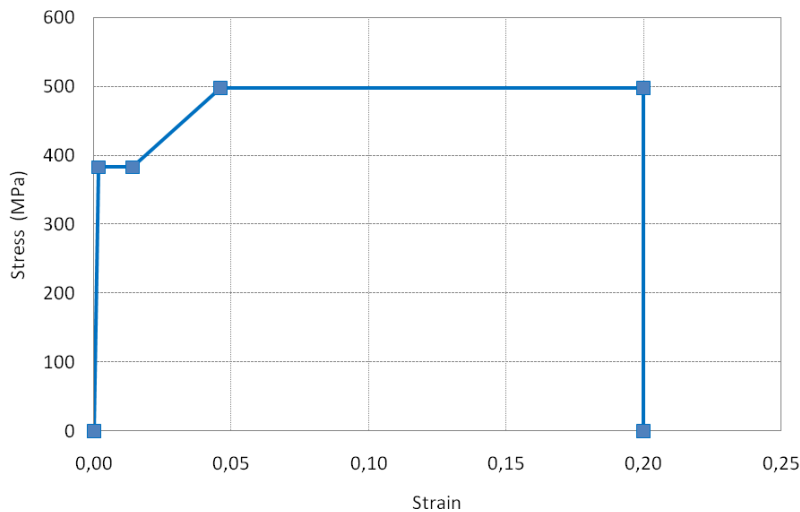


Figure E 4.6 Liner uni-axial stress-strain curve used in analyses.

Liner anchorage

Both vertical anchors and horizontal stiffeners are included in the models in this report (see Section 4.4.1 and Chapter 7). No tests are carried out to find the shear stiffness and a capacity for liner anchors within the Sandia $\frac{1}{4}$ project. The shear stiffness used in this report refers to analytical calculations made by one SPE participant, presented in [18]. Earlier experience at Scanscot, carrying out analytical calculations for liner anchors, is that analytical models gives higher initial stiffness than test results shows. In order to take this into account calculations are made with both high shear stiffness according to [18] and low shear stiffness according to tests presented in a Bechtel study [19]. In the Bechtel study [19] the tested anchors are full size anchors (L-steels), however the initial stiffness from these tests are much lower than the shear stiffness found in analytical studies [18].

Another factor that could give lower shear anchors stiffness is the fact that the concrete, at pressure levels of interest, is highly cracked. The appearance of concrete cracks due to high horizontal tensile force will most likely decrease the initial stiffness for the vertical anchors. However, the ultimate strength of the anchor profiles will probably not be significantly influenced as ultimate strength mostly depend on the steel properties.

The shear force-displacement curves used in this report are shown in Figure E 4.7 where the high values refers to analytical calculations in [18] and low values refer to a Bechtel test report [19]. The same yield force value, found in the analytical calculation [18], is used for both the high and low stiffness curves.

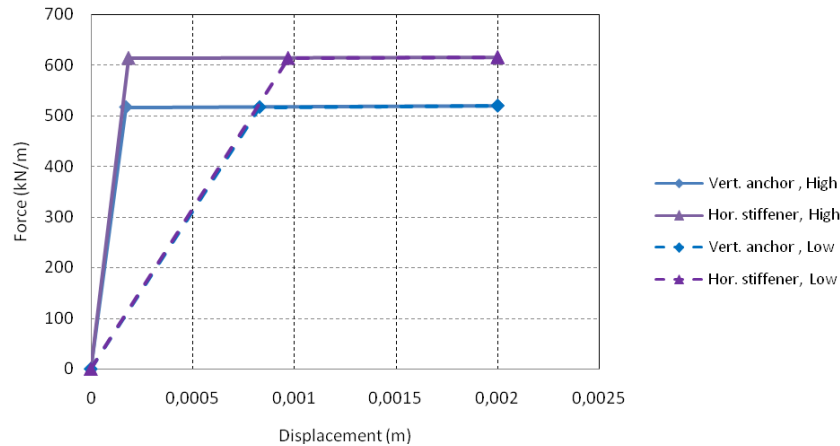


Figure E 4.7 Shear force - displacement curve for vertical anchors and horizontal stiffeners.

In the normal direction the vertical anchors are assumed to be very stiff and the horizontal stiffeners are assumed to be free to move.

Prestress

FE-implementation

The tendons are modeled one by one with truss elements. A contact formulation is used to modeling the interaction between the tendon truss in concrete structure and the tendons (see Chapter 5, 6 and ISP48 report [7], appendix L). The tensioning of the tendons is simulated by connectors at the tendon ends, where force controlled connectors are tensioning the tendon and displacement controlled connectors simulating the anchor slip. Both vertical and horizontal tendons are modeled by the same technique.

The used material model is elasto-plastic using Von Mises yield criteria. The principal uni-axial stress strain curve, used for the cold formed steel tendons, is shown in Figure E 4.8. The curve used in analysis is the modified curve for tendons (see Figure E 4.8), which is based on the curve for single strands given in the Swedish building code BBK 04 [20].

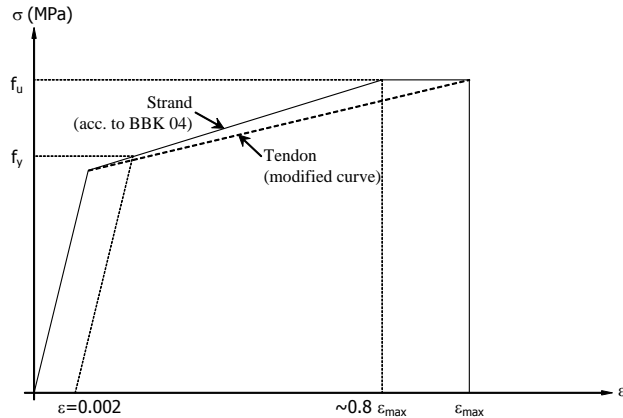


Figure E 4.8 Principal uni-axial Stress-strain curve.

Material parameters

The tendon has a nominal yield strength (at 0.2% permanent elongation) of around 1580 MPa.

Three different tests methods have been carried out; tendon strand material test, tendon system test and tendon strand calibration test (see [3] appendix b). The tendon strand calibration test is used in general to evaluate input for the analyses in this report, however for maximum elongation (ϵ_{max}) the tendon system test results has been used. The maximum elongation for the tendon test is shown to be significantly lower for the full tendon test than for single strand tests. This is probably due to the different anchorage in these tests and in the full tendon tests the most realistic anchorage is used. Other parameters like yield and ultimate strength do not differ significantly between the different test methods.

The material properties are evaluated from totally 7 tests (tendon strand calibration test) except for the ultimate elongation which is evaluated from 3 test (tendon system test).

All tendon material parameters (structural steel) are assumed to be distributed according to the normal distribution (see JCSS [15]).

Yield strength

The average yield strength (at 0.2% permanent elongation) evaluated from the strand specimens is around 1690 MPa with a COV of 0.1 %. (average yield force 191 kN/strand)

It is assumed that all strands in the containment model come from the same manufacturer. Harrop (1985) [21] gives some data for seven wire strands and according to this paper the COV for the yield strength is 2.3% (given for the 0.1% permanent elongation).

Ultimate strength

The average failure strength evaluated from the strand specimens is around 1860 MPa with a COV of 0.4 %. (average yield force 210 kN/strand)

The COV for the ultimate strength is 1.3% according to Harrop (1985) [21].

Ultimate elongation

The average ultimate strain evaluated from tendon tests is around 0.038 with a COV of around 3.7 %.

The COV for the ultimate elongation is 5.4 % according to Harrop (1985) [21].

E-modulus

The average E-modulus evaluated from the strand specimens is around 191 GPa with a COV of 1.5%.

In the JCSS [15] the COV of the E-modulus is assumed to be around 2 %.

Stress strain curve

Figure E 4.9 shows the tendon strain curve used in the analyses. Based on the evaluated average values above.

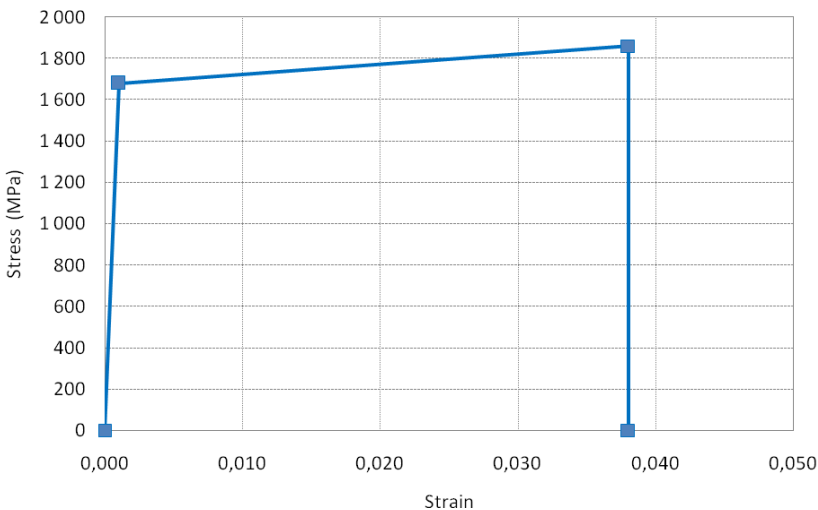


Figure E 4.9 Tendon stress-strain curve used in analyses.

Initial tendon force

The initial force along the tendons is in principal depending on; the maximum tension force (F_o), the slip at anchorage (Δd) and the curvature of the tendon duct (friction between tendon and duct). In the analysis the tendons are first tensioned to the maximum tension force (F_o) and after this the slip at anchorage (Δd) are simulated. In Figure E 4.10 and Figure E 4.11 the principal force distribution for horizontal and vertical tendons are shown.

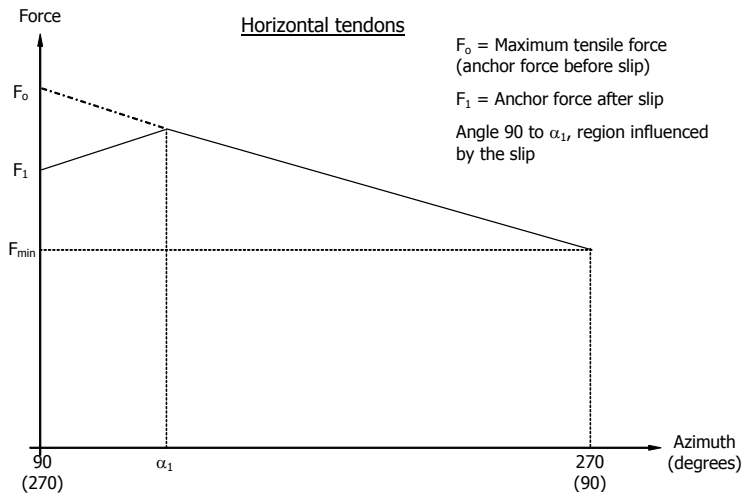


Figure E 4.10 Principal force distribution along horizontal tendons.

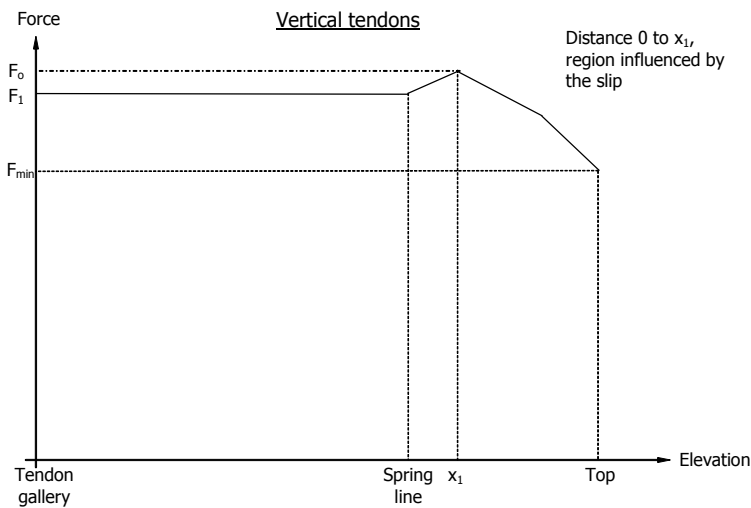


Figure E 4.11 Principal force distribution along vertical tendons.

The maximum tension force (F_o) is in general the target value at the tensioning operation. The force after slip (F_i) will be more unsure as it depends on both the size of the slip and the tendon curvature (friction) near the anchor. In the analysis the average maximum tension force and average slip measured at tensioning is used as input, see Table E 4.1. The end force after slip as well as the force along the tendon will be given from the analysis. All tendons are tensioned simultaneously in the analysis (in both ends), i.e. the real tensioning sequence is not simulated (no elastic loss will be included).

Table E 4.1 Average prestressing parameters.

	Horizontal tendons	Vertical tendons
Max. tension force (F_0)	427 kN	481 kN
Slip at anchorage (Δd)	3.95 mm	4.90 mm

Normally the force along a tendon due to friction loss is describe by the exponential function below

$$F(\alpha) = F_0 e^{-(\mu\alpha+kx)}$$

where F_0 is the force at the tensioning end of the tendon, μ is the friction coefficient, α is the cumulative angle, k is the wobbling coefficient and x is the length from the tensioning end.

The friction between tendon and duct was measured and it was concluded that the average friction coefficient was 0.18 for horizontal tendons and 0.22 for vertical tendons. In the analyses a friction coefficient of 0.22 is used in general.

Figure E 4.12 shows the approximate force distribution of two overlapping tendons and the corresponding average force (tendons not influenced by penetrations). The force in tendon 1 and 2 is calculated by the exponential expression above with analysis input parameters ($F_0=427$ kN, $\Delta d=3.95$ mm and $\mu=0.22$). It can be concluded from Figure E 4.12 that the average horizontal tendon force will have low values in the region near the buttresses.

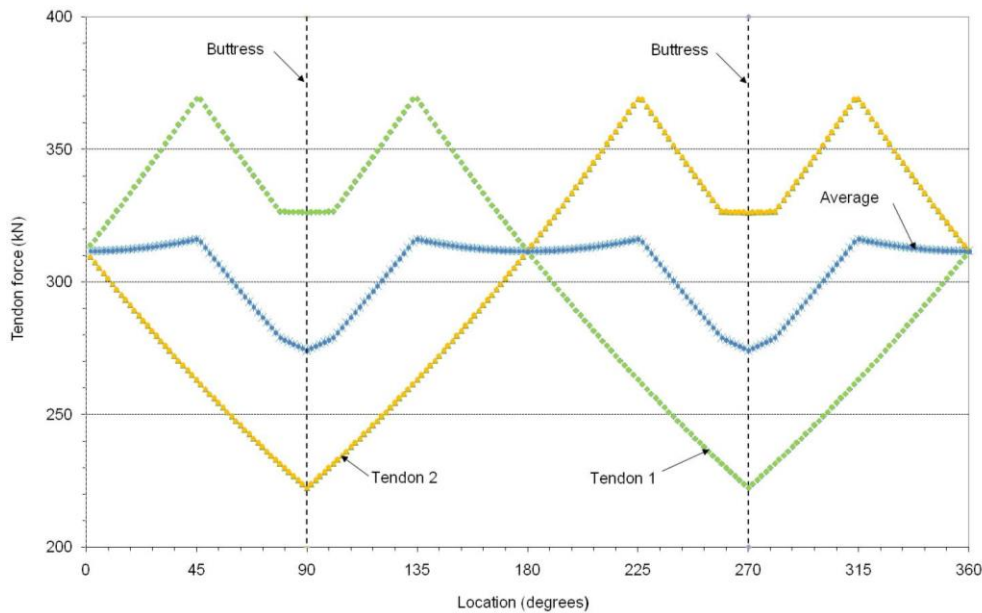


Figure E 4.12 Approximate tendon force distribution along hoop tendons.

In JCSS [15] the statistical variation in prestress is discussed. The COV for prestress is given for initial conditions and for long-term conditions. Initially the statistical variation in prestress includes losses due to elastic shortening of concrete, friction, short-term relaxation of

prestressing steel and anchorage slip. The COV of the initial prestress is assumed to be between 4 and 6 % according to JCSS [15]. The COV in prestress measured by anchor load cells at a number of horizontal and vertical tendons is around 6 and 4% respectively (also see Figure E 4.13). This value gives an indication of the force variation between tendons. The prestress in a specific part of the structure is dependent of the force in a large number of tendons (see Anderson et. al. [22]) and therefore is the variation in force between tendons less significant for the prestress level in the structure. However, the variation in initial prestress according to JCSS [15] (see above) include factors which could be assumed to influence all or a large number of tendons. Therefore is the COV of the initial prestress assumed to be quite large, say around 6%.

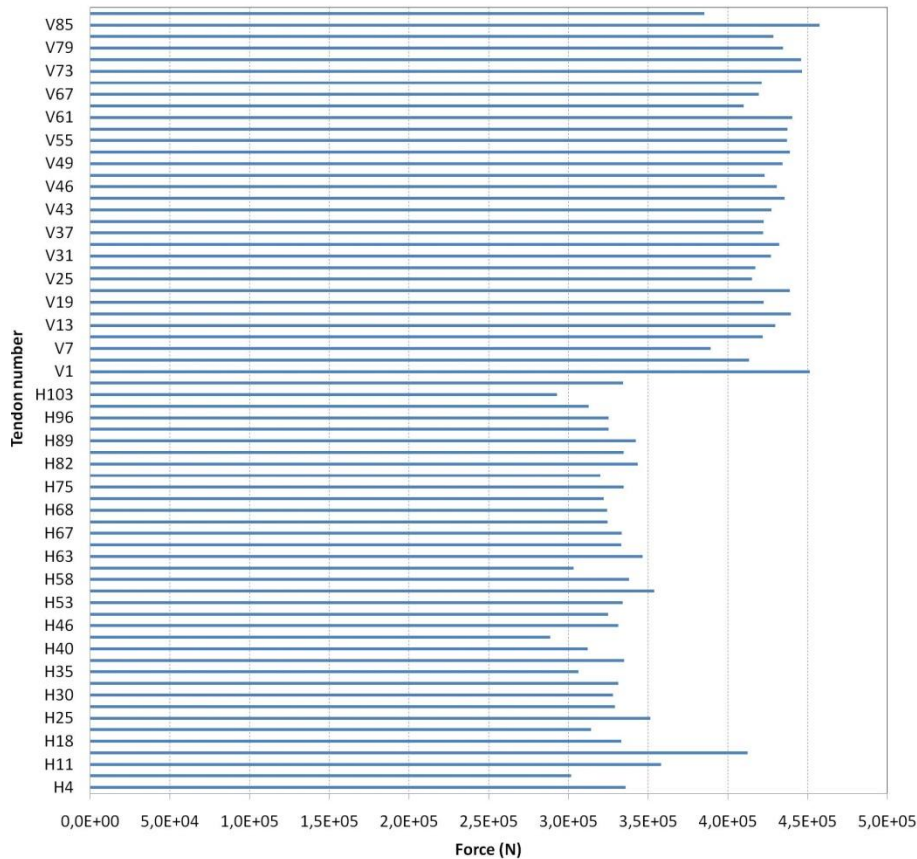


Figure E 4.13 Measured tendon force after prestressing (from load cells in both ends of each tendon).

Long-term effects

Important dates considering long-term effects are

- Average concreting of containment wall and dome, February 1999.
- Average prestressing of containment wall and dome, April 2000
- Limit state test, September 2000

Three different long-term mechanisms will affect the prestress, creep together with shrinkage for the concrete structure and relaxation for the steel tendons.

Results from the load cells mounted on the end anchors of a number of tendons are available for dates after the prestressing and just before the limit state test. The average measured tendon end force indicates that the loss of force during the approximately six months between prestressing and limit state test is small (less than 1% for both vertical and horizontal tendons). However, there are difficulties regarding measure loss of force at the tendon end anchor. Due to friction along the tendon the average force along the tendon can decrease more than the end force (see Anderson et. al. [23]).

Creep and shrinkage tests were performed for standard specimens casted from the same type of concrete as used for the containment model wall and dome. These tests were carried out during approximately one year and the results are given in [6].

Expected long-term effects (according to ACI 209 [24]) together with measured creep and shrinkage are shown in Table E 4.2. The test values are much higher than the values according to the ACI 209 [24]. The details of the test method and the drying conditions are not fully described. The calculation according to ACI 209 is made according to the drying conditions valid for a general field of the containment model wall. The drying conditions (volume / surface ratio) of the test specimens are probably much less favorable than in the containment model, which could explain the difference in Table E 4.2.

Table E 4.2 Expected long-term loss from shrinkage, creep and relaxation.

	Acc. to standard ¹		Acc. to measurements ³	
	Strain	Loss	Strain	Loss
	(μ m/m)		(μ m/m)	
Shrinkage after 20 months	150	3.3%	850 ⁴	18.7%
Creep after 6 months (μ strain)	170	3.7%	730	15.8%
Relaxation after 6 months (μ strain)	85 ²	1.8%	-	-

1) Acc. to ACI 209 [24]

2) Acc. to PCI journal [25]

3) Test results acc to [6] Table E 2.

4) Extrapolated value

5) Corresponding relative loss of force (assuming an initial average force of 300 kN)

The shrinkage given in Table E 4.2 is given for the whole period between casting and the limit state test. However, it is only the part of the shrinkage that take place after the prestressing that will reduce the prestress. In the analysis it is assumed that all shrinkage will occur before prestressing, i.e. only creep and relaxation will influencing the prestress. In the analysis the values calculated according to standards in Table E 4.2 will be used. In the local model presented in Chapter 5 the loss is applied as temperature load on concrete and tendon elements. In the global model the prestressing is applied as a 5% decrease of maximum tension force (F_0).

As discussed in the previous section the COV for the initial prestress can be assumed to be around 6% (see JCSS [15]). The COV for prestress after long time is of course assumed to have a higher COV (up to 9% according to JCSS [15]). Due to the short period between prestressing and evaluation in this case the COV for initial force is assumed to be valid, i.e. the total COV for prestress is assumed to be 6%.

Geometry

Measurements were made of the containment model inner radius, see Figure E 4.14. It can be concluded that the measured radius in the cylindrical wall part is close to design radius (5.375 m). The COV of the measured radius is around 0.1%.

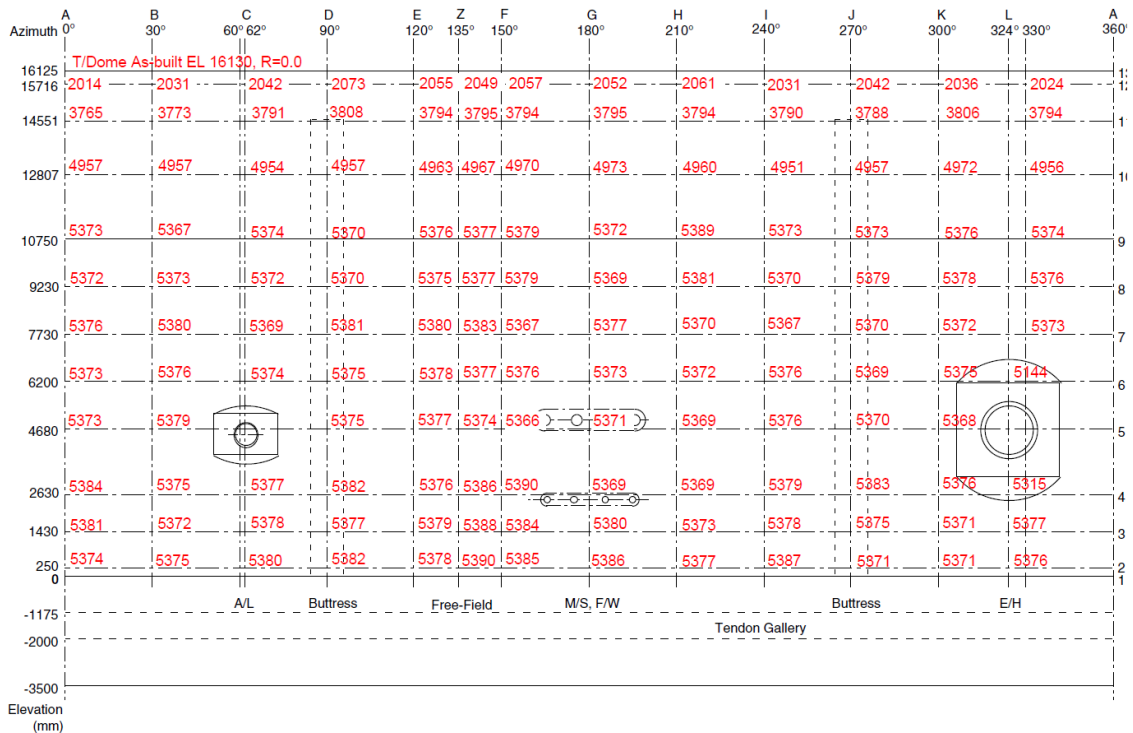


Figure E 4.14 Measured radius for inside of containment model (before LST) [3].

PRESTRESSING TENDON BEHAVIOR

General

In this chapter is model and analyses regarding pre-stressing tendon behavior, SPE part 1.1-1.2 described (see [6]). The main purpose of this study is to explain the interaction between horizontal tendons and the containment structure. Measurement on tendons in the containment scale model indicated redistribution of force occurred during pressurization of the structure.

Figure E 5.1 shows the outline of the fundamental tendon behavior model as described in [6]. The model contains a 225 mm high part of an undisturbed containment wall with two hoop

tendons included. The two hoop tendons, A and B, are anchored at the buttresses at 90° and 270° respectively. The bottom of the model is fixed in the vertical direction whereas a vertical stress is applied to the top surface to account for the vertical pre-stress force in the containment wall.

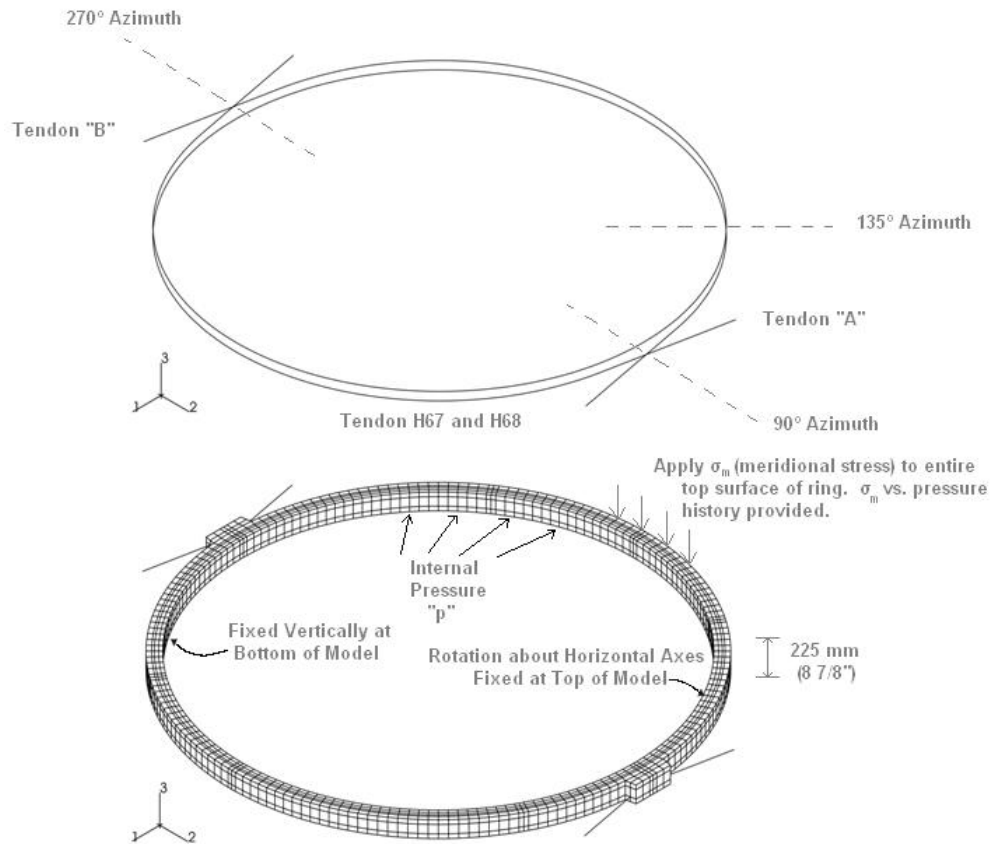


Figure E 5.1 Model 1, Tendon Behavior Model, Representing Tendons H53 and H54 [6].

FE-model

Concrete structure and liner

Figure E 5.2 shows the FE-model of the tendon behavior model. The concrete parts of the model are modeled with eight node solid elements with reduced integration, denoted C3D8R in Abaqus [16]. Each node of the solid elements has three translational degrees of freedom. The material parameters used for the concrete material are described in Section 4.2.2 (same as in the global 3D-model, see Section 6.2).

The liner is modeled with four node shell elements with reduced integration, denoted S4R in Abaqus [16]. Each node of the liner has three translational and three rotational degrees of freedom. The liner is modeled as fixed to the inside of the concrete wall. The material parameters used for the liner are described in Section 4.4.2 (same as in the global 3D-model, see Section 6.2). The steel liner thickness is set to the nominal value of 1.6 mm.

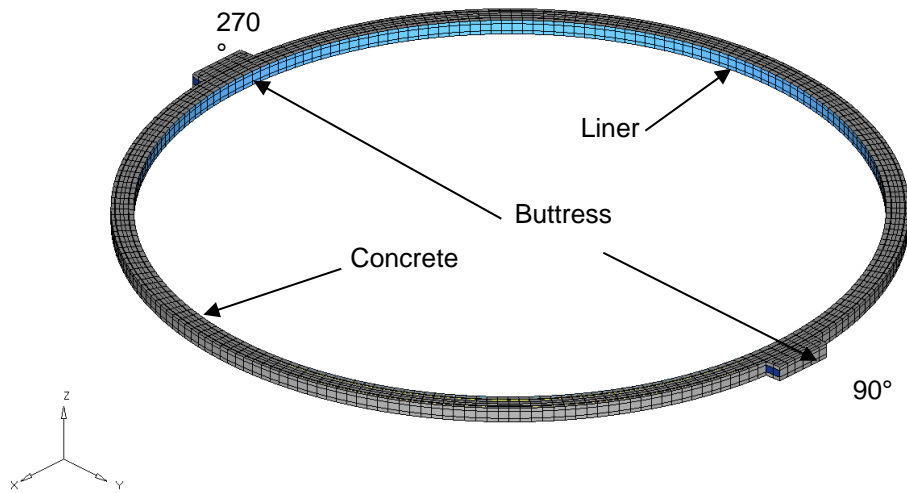


Figure E 5.2 FE-modeling of tendon behavior model.

Tendon system

In Figure E 5.3 is the modeling of the prestressing tendons shown. The tendons are modeled individually with trusses which are two node elements that only can transmit axial forces. The element type is denoted T3D2 in Abaqus [16]. Tendon A is anchored in the buttress at 90° and tendon B at the buttress at 270°. The material parameters used for the tendons are described in Section 4.5.2 (same as in the global 3D-model, see Section 6.2).

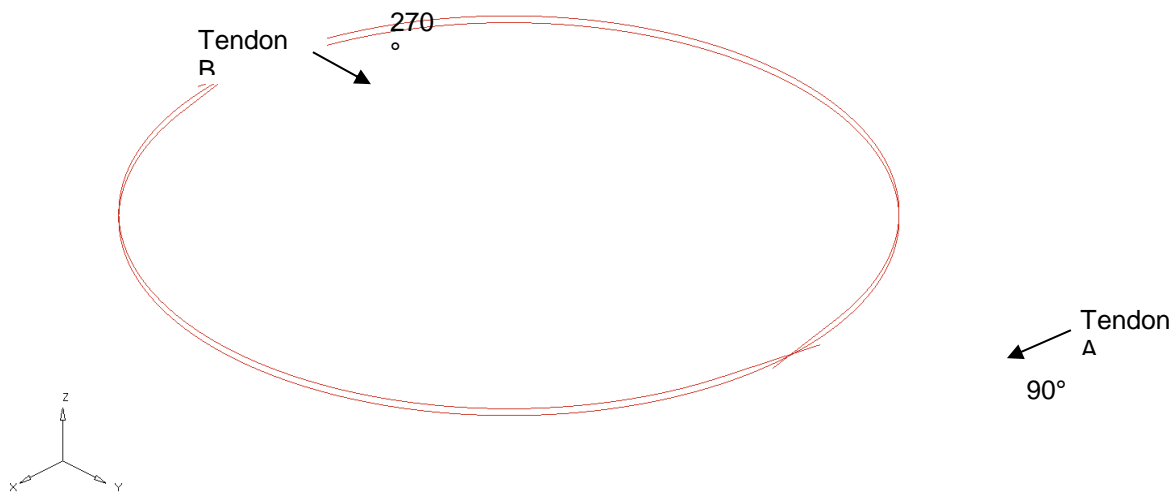


Figure E 5.3 FE-modeling of tendons.

The connection of the tendon to the buttress is handled with a connector element that acts between the end node of the tendon and a node on the buttress, see Figure E 5.1. The prestressing is applied by prescribing a force or a motion of the connector which results in a tension force in the tendon and a compressive force on the anchor plate. A local coordinate system is

defined for the connector which implies that only forces in the axial direction of the tendon are transmitted.

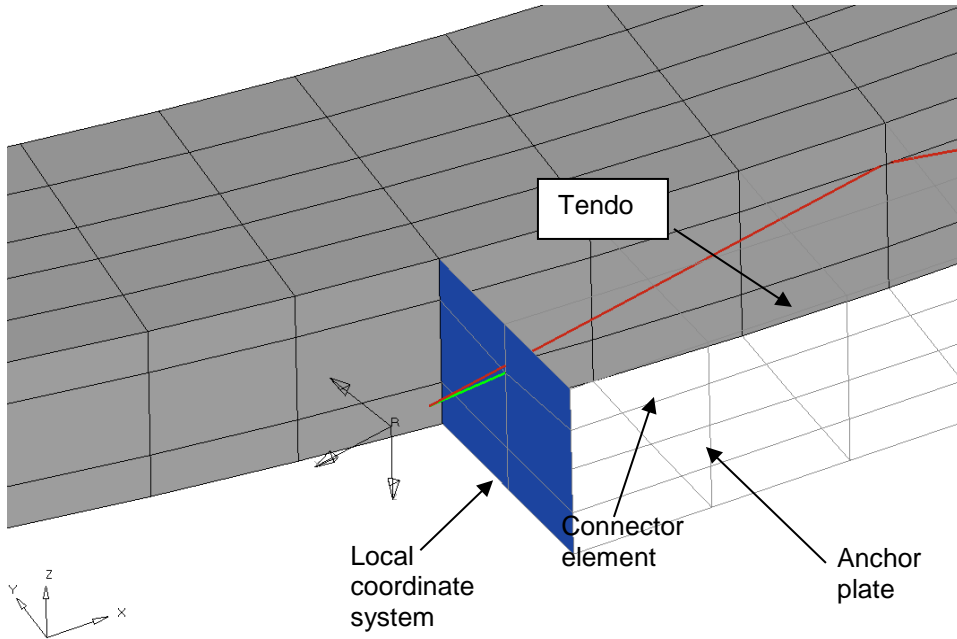


Figure E 5.4 Connection of tendons to buttress.

Since the tendons are uninjected it is important to simulate the contact behavior between tendons and concrete in a sufficient way. A contact formulation is created to model the interaction between the tendons and the concrete. The faces of one concrete element row are situated on radius 5.574 m (inner radius of tendon duct). These faces are included in a contact surface, see Figure E 5.5. For the tendons are node based surfaces created. The penalty contact algorithm in Abaqus [16] is used in the contact formulation. A friction coefficient of 0.22 has been used in the analysis (see Section 4.5.3).

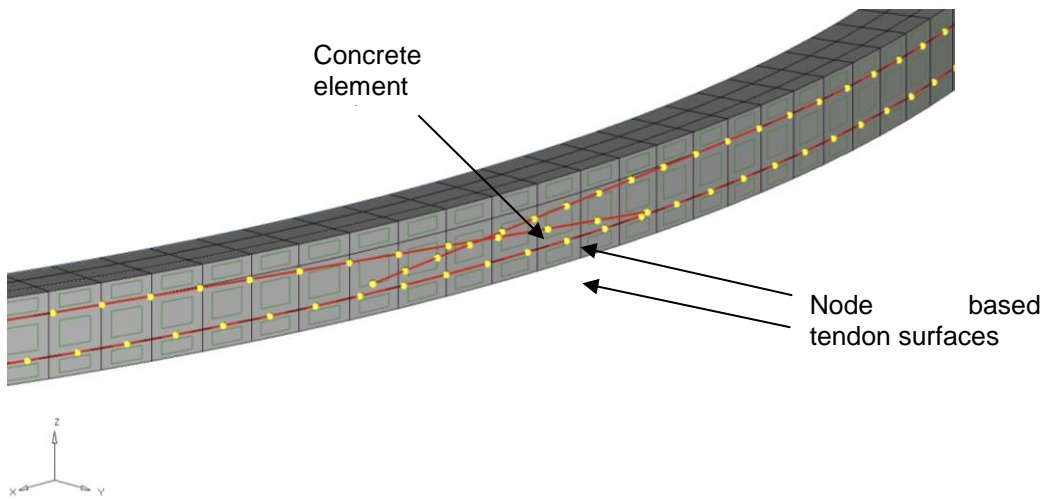


Figure E 5.5 Contact surfaces between tendons and concrete at radius 5.574 m.

Reinforcement

In Figure E 5.6 is the reinforcement shown that is included in the model. Only hoop reinforcement has been included in the cylindrical part of the containment wall. The vertical reinforcement, and vertical tendons, is not necessary for the analyses performed in this study.

The hoop reinforcement on the inside and outside of the wall is modeled with the rebar layer technique available in Abaqus [16]. The rebars are modeled as layers in surface elements by defining cross-section, spacing and orientation of the specific reinforcement. The layer only takes forces in the specified direction.

In Table E 5.1 are the properties of the modeled reinforcement presented. Figure E 5.6 shows the modeling of the reinforcement with surface elements. The material parameters used for the modeled reinforcement are described in Section 4.3.2 (same as in the global 3D-model, see Section 6.2).

Table E 5.1 Properties of rebar layers in model.

Reinforcement	Cross section [mm ²]	Spacing [mm]
Inner hoop rebars	162.65	112.7
Outer hoop rebars	144.7	112.7
Buttress	155.46	100.0

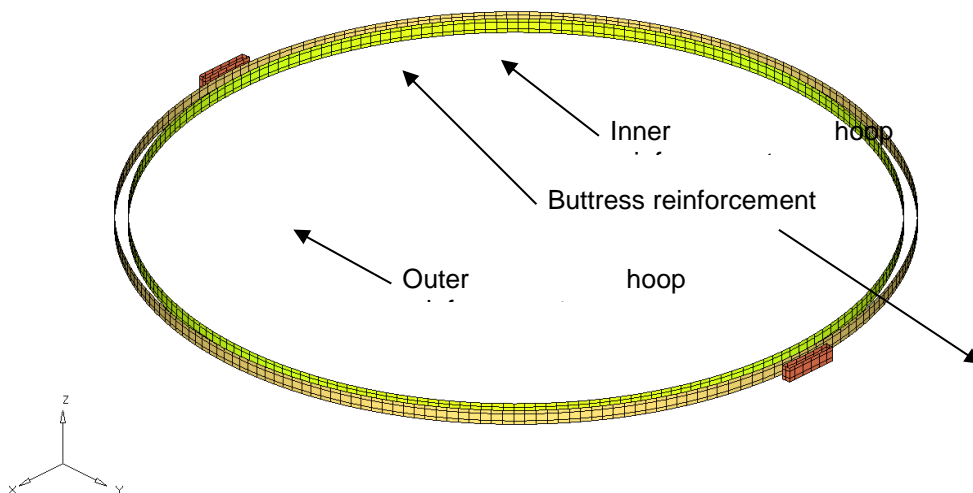


Figure E 5.6 FE-modeling of reinforcement.

Finite element model size

The size of the tendon behavior model is shown below.

- Number of elements: ~ 6000
- Number of nodes: ~ 7900
- Number of degrees of freedom: ~ 26500

Analysis

Method

The analyses in this study are performed with Abaqus/Explicit dynamic solver with automatic incrementation. The step times used has been chosen to avoid any dynamic behavior.

Pre-stress

A maximum pre-stressing tension force of 427 kN has been used in the analyses in this section. This is the average value of the max tension force for the horizontal tendons, se Section 4.5.3. The tendons are tensioned simultaneously in both ends by applying a force to the connectors that couples the tendons to the anchor plates.

The analysis time of the pre-stressing step is 1.0 s.

Seating

A slip at the anchorage of the horizontal tendons of 3.95 mm has been used in the analyses, se Section 4.5.3. The slip is applied simultaneously in both ends by applying a motion to the connectors that couples the tendons to the anchor plates.

The analysis time of the seating step is 1.0 s.

Long-term effects

The two long term effects which has been considered in the analyses is creep in the concrete structure and relaxation in the pre-stressing tendons. Shrinkage of the concrete has not been considered since it is assumed to have negligible effect on the results of this study (see Section 4.5.4).

Creep

Creep of concrete has been considered by applying a decreasing temperature load to the concrete parts which with results in shrinkage of the structure. The creep strain applied to the concrete structure has been chosen to -170 ($\mu\text{m}/\text{m}$), see Table E 4.2.

The analysis time of the creep step is 1.0 s.

Relaxation

Relaxation in the pre-stressing tendons has been considered by applying an increasing temperature load to the tendons which results in an expansion of the tendons. The relaxation strain applied to the tendons has been chosen to 85 ($\mu\text{m}/\text{m}$), see Table E 4.2.

The analysis time of the relaxation step is 1.0 s.

Pressure load

The internal overpressure load is applied on the inside of the liner with a load velocity of 125 kPa/s.

The analysis time of the pressure load step is 12 s.

Results and evaluation

In this section are results presented from the analyses of the prestressing tendon behavior model.

Initial steps

In this chapter are the results of the initial analysis steps presented. In the first four steps are tensioning and seating loss in tendons, creep in concrete and relaxation in tendons simulated.

The deformed shape of the tendon behavior model is shown in Appendix A3, Figure E A3.1- Figure E A3.5.

Displacement

In Figure E 5.7 is the radial displacement shown for azimuth 90° , 135° and 180° for the four initial steps.

It can be noticed that the inward radial displacement after applied max tension force is larger in the area of the buttresses which is reasonable since the pre-stressing force is largest in the ends of the tendons, also see Appendix A3. After seating the containment somewhat regains its original cylindrical shape with just a little larger radial displacement at the buttresses. After the creep step the whole structure has contracted. The relaxation step results in a small expansion of the model.

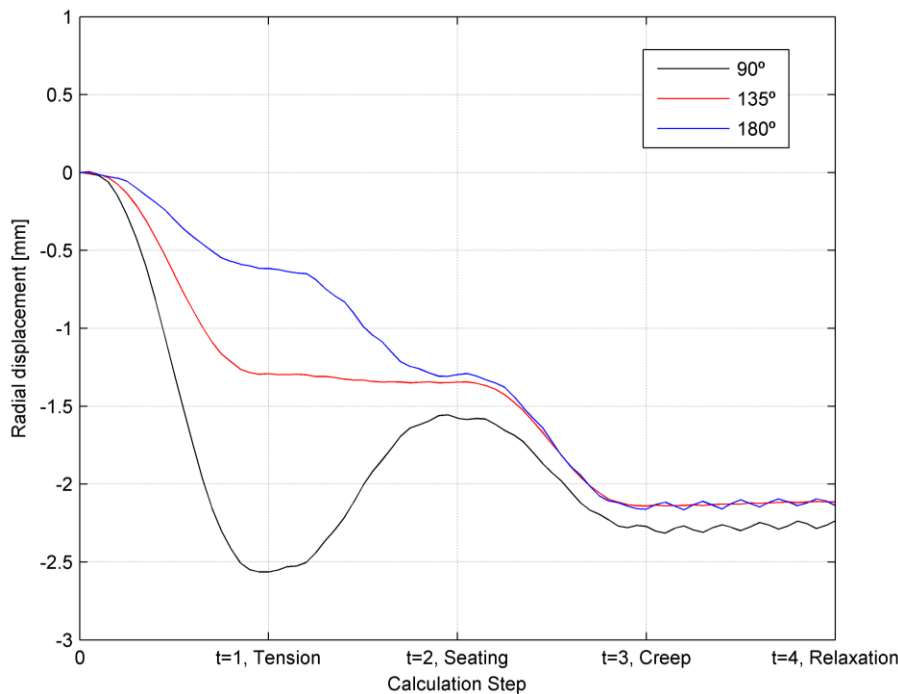


Figure E 5.7 Radial displacement at azimuth 90° , 135° and 180° for tension, seating, creep and relaxation step.

Tendon force

Figure E 5.8 shows the force in tendon A (anchored at 90°) shown along the circumference for the initial steps. The friction between the tendon and the concrete surface, results in a decreasing force from the point where the tendon tangents the concrete to the mid section of the cable.

The slip at anchorage (seating) results in a motion opposite to the tensioning direction. This results in a lowering of the force in the tendon in the area close to the anchorage, azimuth $90 \pm 37.5^\circ$. In Figure E 5.9 is the friction force direction shown after the seating step. The friction force changes direction in the region close to the buttress at the seating. The creep relaxation in the concrete structure results in a general lowering of the tendon force along the cable.

The force in tendon B (anchored at 270°) is exactly the same except that the cable is anchored at 270°.

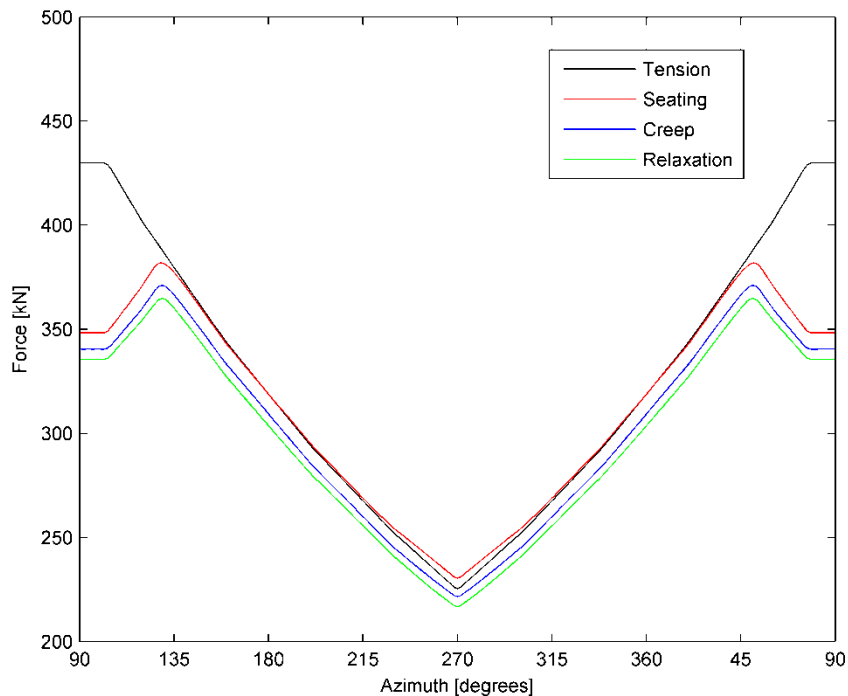


Figure E 5.8 Force variation along tendon A for tension, seating, creep and relaxation step.

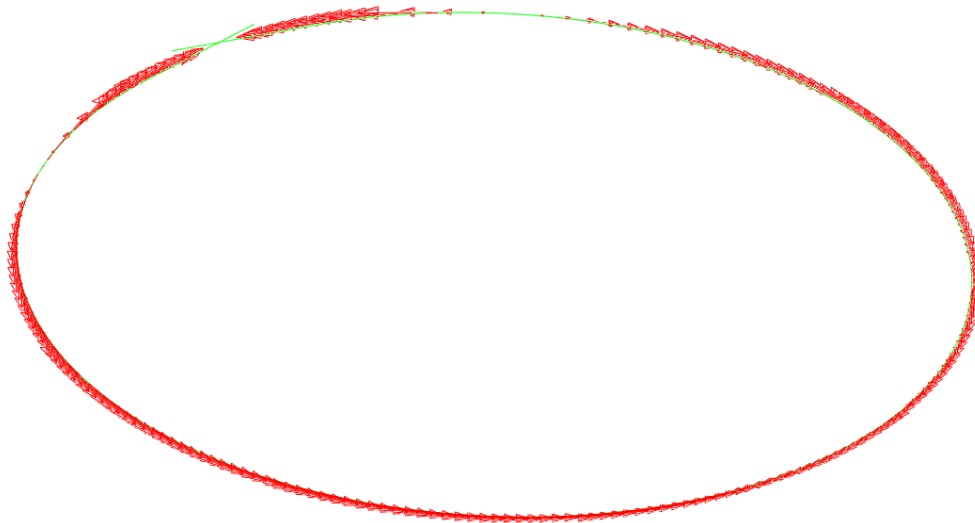


Figure E 5.9 Friction force directions after seating step.

In Figure E 5.10 is the mean pre-stress force along the circumference of the model shown. After applied max tension force, the mean tendon force is quite even along the circumference. The seating results in a lowered mean force at the buttresses $\pm 45^\circ$. The concrete creep and relaxation of the tendons lowers the force curve without any change of the shape.

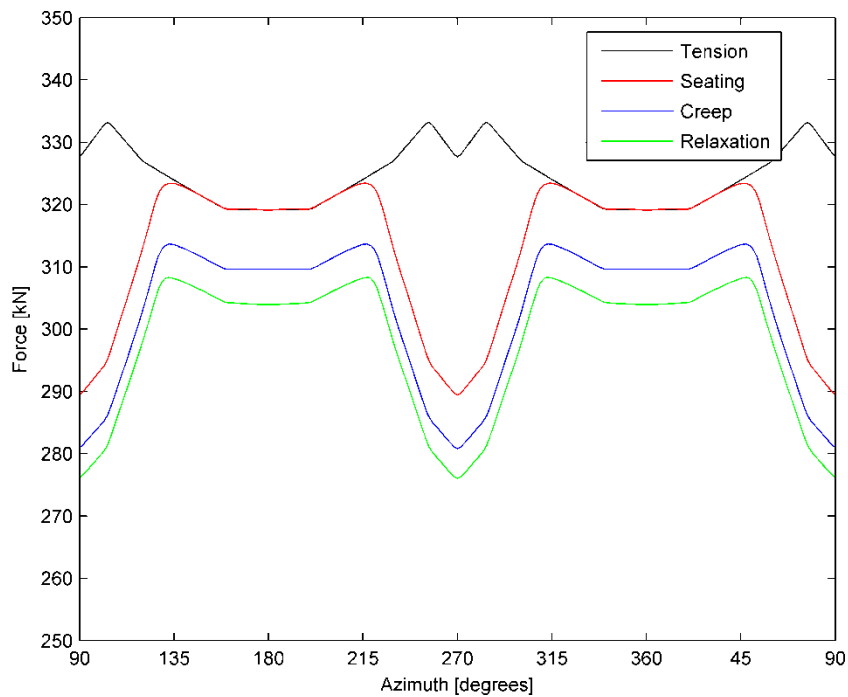


Figure E 5.10 Mean value of pre-stress along circumference for tension, seating, creep and relaxation step.

Pressurization step

In this chapter are the results of the pressurization step presented.

In Table E 5.2 are the pressure milestone results are shown.

Table E 5.2 Pressure Milestones for different occurrences.

Milestone	Pressure (MPa)	Pressure (p_d)
Concrete Hoop Stress (at 135° azimuth) Equals Zero	0.53	1.35
Concrete Hoop Cracking Occurs (at 135° azimuth)	0.63	1.61
Tendon A Reaches 1% Strain (at 135° azimuth)	1.28	3.25
Tendon B Reaches 1% Strain (at 135° azimuth)	1.31	3.34
Tendon A Reaches 2% Strain (at 135° azimuth)	1.37	3.49
Tendon B Reaches 2% Strain (at 135° azimuth)	1.375	3.50

In appendix A3, Figure E A3.6-Figure E A3.14, is the deformed shape of the model shown for pressure milestones up to ultimate pressure.

Displacement

Figure E 5.11 shows the radial displacement at azimuth 90°, 135° and 180° for the pressurization step. In the Figure E are the pressure levels at which cracking of concrete, yielding in reinforcement and yielding in pre-stressing tendons occur, marked with vertical green lines. Up to the pressure level when cracking of the concrete occurs, the radial displacement is very small. The first cracking is initiated close to the buttress which results in an increasing radial displacement in this position. As the pressure increases, the radial displacement at the buttress increases slower than in the other two positions. This is due to the high stiffness of the buttress and the large inwards acting resulting force of the tendon anchorage. When yielding is initiated in the reinforcement the radial displacement increases faster and the yielding in the tendons implies an even faster outward movement. When yielding of the tendons is all around the circumference, the radial displacement becomes very large.

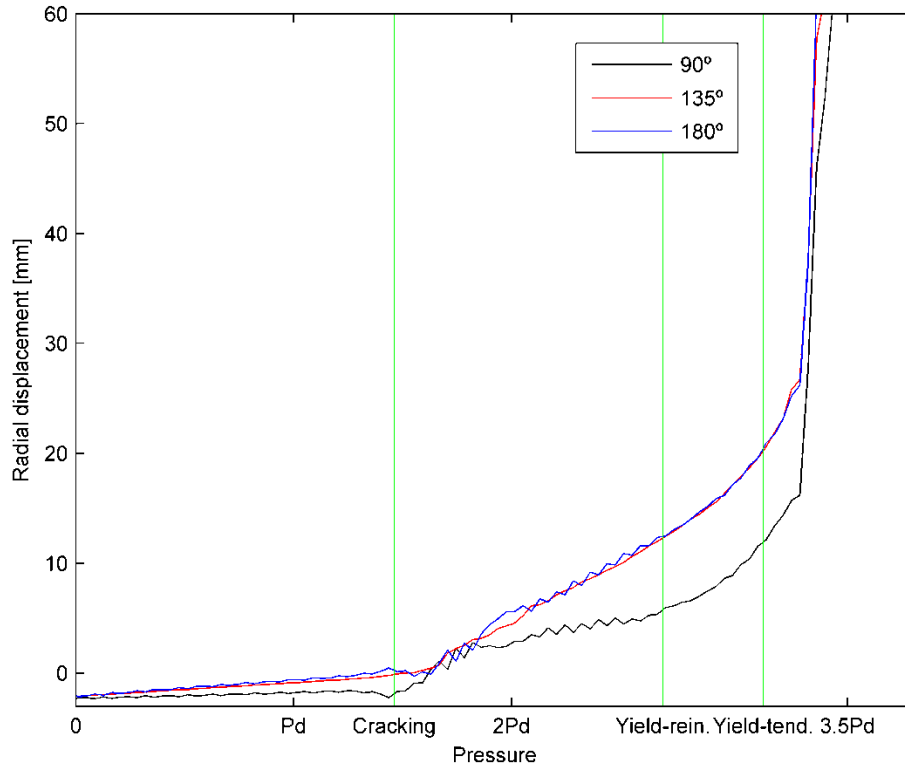


Figure E 5.11 Radial displacement at azimuth 90°, 135° and 180° for pressurization step.

In Figure E 5.12 is a comparison shown of the mean radial displacements of the tendon behavior model (TBM), the global 3D model (section 6) and the measurements of the Limit State Test, LST. For the tendon behavior model, the mean radial displacement has been calculated from all nodes on a path along the inner circumference. The curve for the global 3D model is the mean radial displacement of nodes along the circumference on elevation 4680. The LST curve is a mean of the displacement measurements on elevation 4680 during the LST measurements.

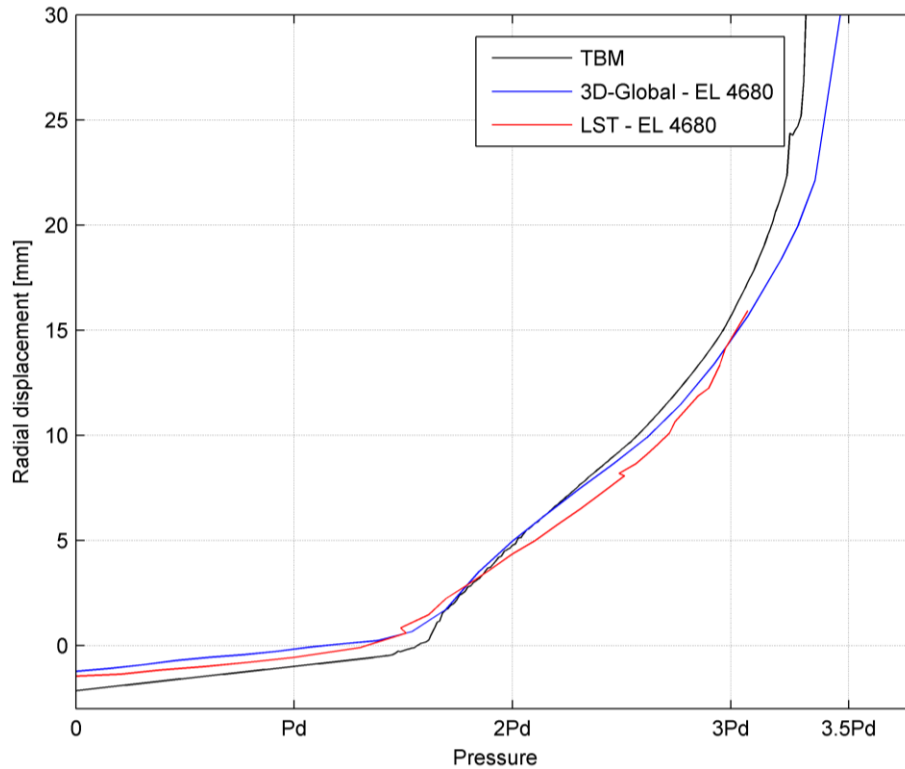


Figure E 5.12 Mean value of radial displacement during pressurization for tendon behavior model (TBM), global 3D model on elevation 4680, and measurements during LST for elevation 4680.

Tendon system

Figure E 5.13 shows the force in tendon A, anchored at 90°, along the circumference for the pressurization step. As can be seen is the increase in force small for a pressure up to $1.5p_d$. Between 1.5 and $2.0p_d$ is the force increased significantly. It is between these pressure values that cracking of the concrete takes place. The shape of the force variation along the tendon does not change significantly until the yield stress level is reached in parts of the tendon. When this occurs, at pressure exceeding $3.1p_d$, the force in the tendon is equalized along the circumference. When the pressure exceeds $3.6p_d$ the failure strain is reached in the tendon and the analysis is terminated.

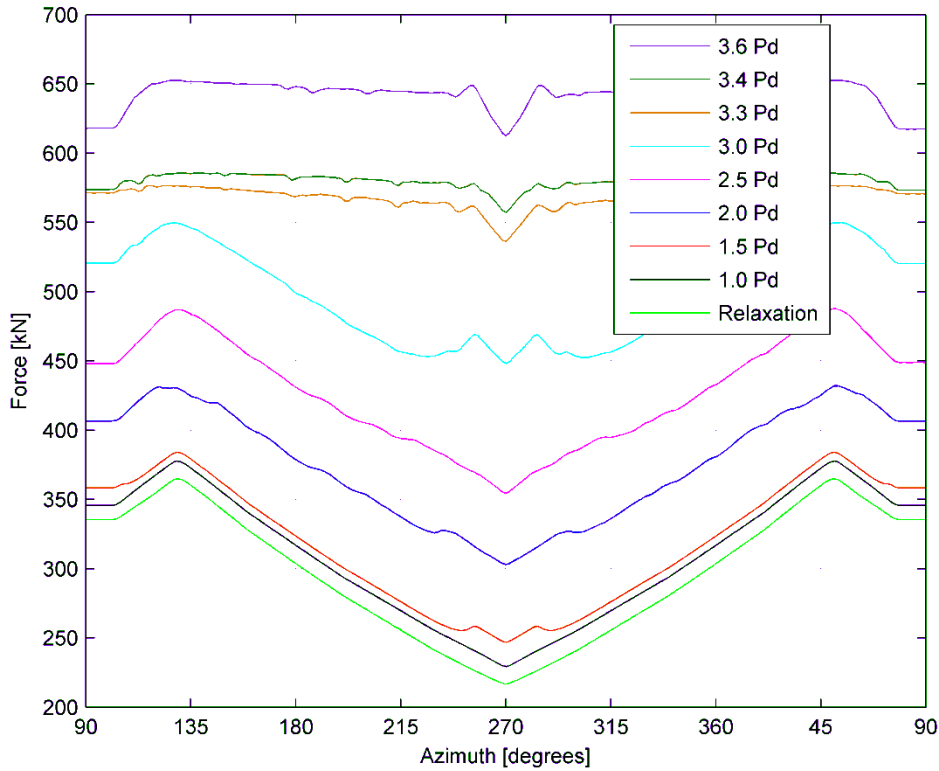


Figure E 5.13 Force variation along tendon A for pressurization step.

The equalization of the force along the tendon can be seen in Figure E 5.14 where the tendon force is plotted for pressure values between $3.0p_d$ and $3.3p_d$. The yield stress level is first reached at azimuth $\sim 125^\circ$ and 55° . The force in this position increases only slightly as the pressure increases. In areas where the force is lower, the force increase is much larger for the same increase in pressure level. The part of the tendon that is yielding increases with the pressure level and at $3.4p_d$ is it only in a small area around 270° that the yield stress is not exceed.

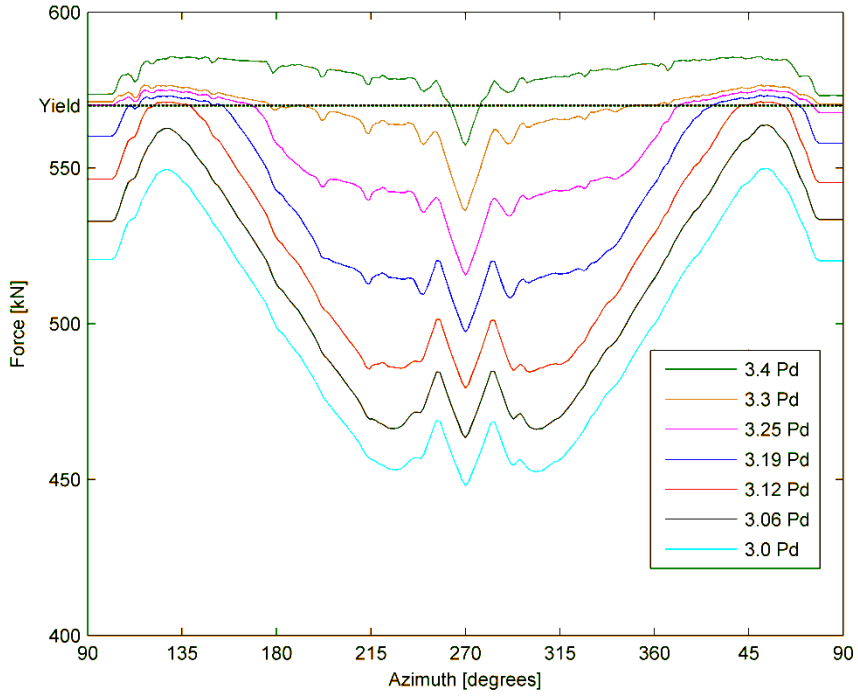


Figure E 5.14 Force variation along tendon A for pressure levels between 3.0 and 3.4 p_d .

In Figure E 5.15 is the mean value of the force in tendon A and B plotted along the circumference.

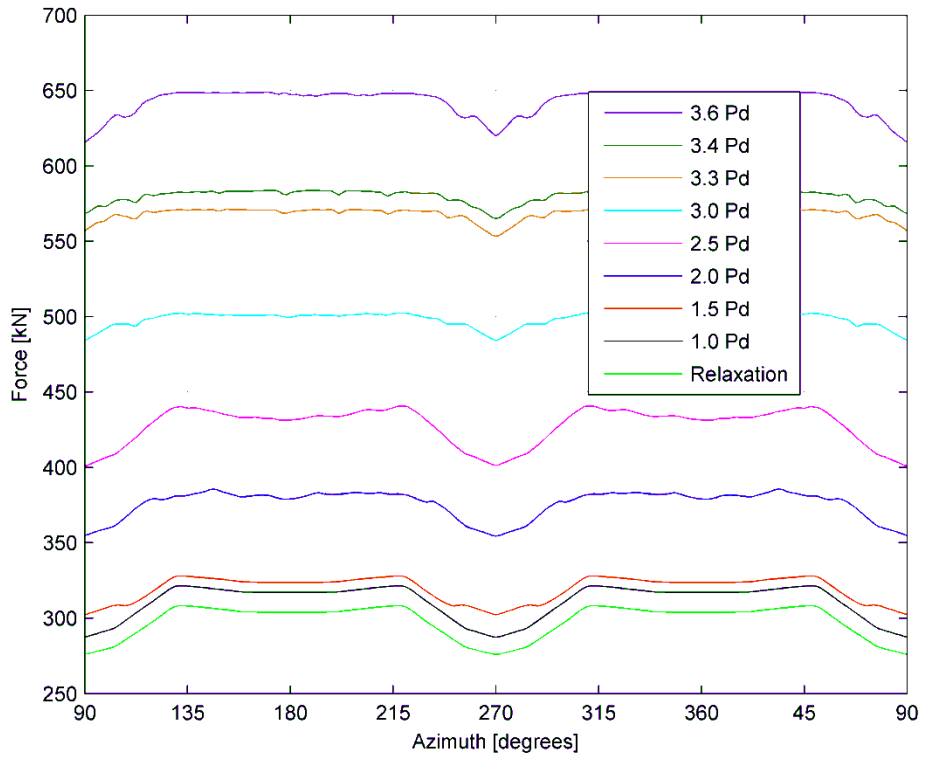


Figure E 5.15 Mean value of tendon force along circumference for pressurization step.

Figure E 5.16 shows the force in tendon A in the tendon behavior model together with the mean value of force in the even tendons from tendon 52 to tendon 68 in the global 3D model (elevation 6.48 to 8.28 m). As can be seen, the results are similar. A difference can be seen in the region near azimuth 315° which is the area where the large equipment hatch is situated in the global 3D model.

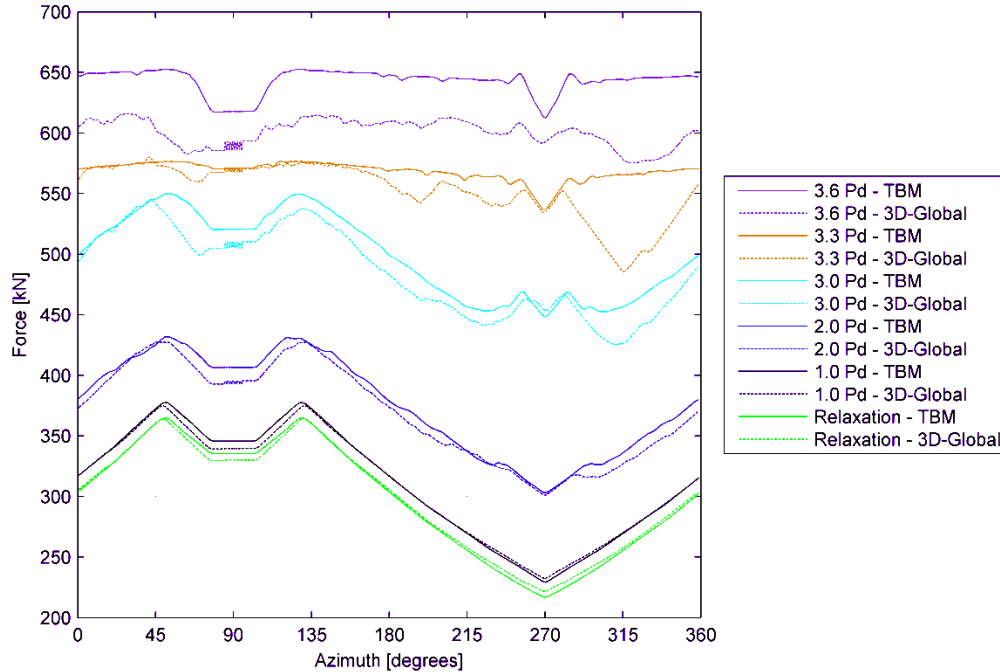


Figure E 5.16 Comparison of tendon force variation along circumference. Results of tendon A in tendon behavior model. Mean value of force in even tendons from tendon 52 to tendon 68 in global 3D model.

Figure E 5.17 shows a comparison of forces at the anchorage of the tendons. The force in the anchorage point of tendon A in the tendon behavior model is plotted. For the global 3D-model is the mean force at the anchorage point of tendon 52 to tendon 68 plotted (elevation 6.48 to 8.28 m). The mean value of the measured force in the anchorage of tendons 53, 58, 63 and 67 is also included in Figure E 5.17. As can be seen is the plotted force curves for the two FE-analyses very similar. The curve for the measured values of force during the LST shows also the same principle shape but with a somewhat lower stress increase.

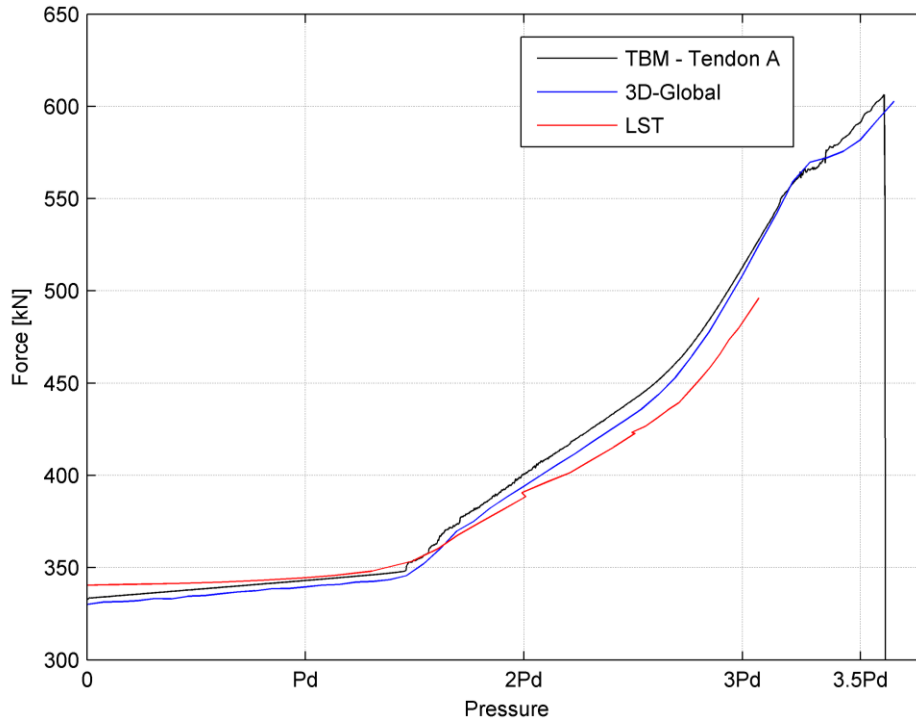


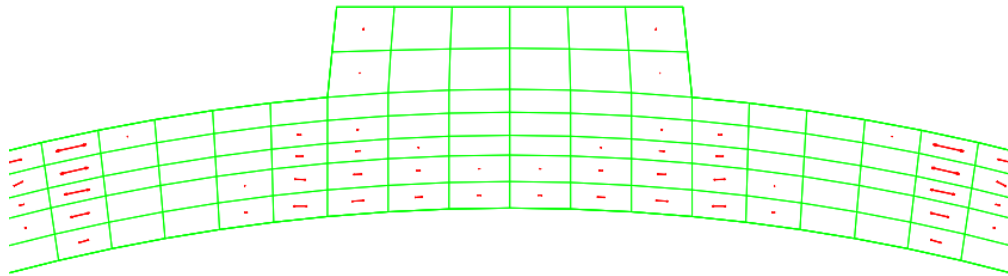
Figure E 5.17 Comparison of tendon force at the anchorage. Results of tendon A in tendon behavior model. Mean value of force in anchorage of tendons from tendon 52 to tendon 68 in global 3D model. Mean value of measured force in anchorage of tendons 53, 58, 63 and 67 from LST.

First yielding takes place in tendon A at $3.1p_d$. At azimuth 135° 1.0 % strain is reached for tendon A at pressure $3.25 p_d$ and for tendon B at pressure $3.34p_d$. At the pressure level $3.62p_d$ is the plastic failure strain 1.8% exceeded in the tendons.

Concrete and reinforcement

Figure E 5.18 shows a vector plot of the crack plane normals at increment of first occurrence of through-wall cracking, $1.47p_d$. The first cracking in the concrete occurs in the area close to the buttresses (azimuth 90 and 270°). At azimuth 135° does the first cracking occur at pressure a pressure of $1.61p_d$. At a pressure of $2.1p_d$ has cracking occurred all around the circumference. At $2.7p_d$ is the concrete completely cracked all around circumference, i.e. the concrete cannot transmit any forces. At this pressure level, is also the yield stress level in the reinforcement, inner and outer layer simultaneously, reached for the first time, see Figure E 5.19.

CRACKDIR, Max. Principal

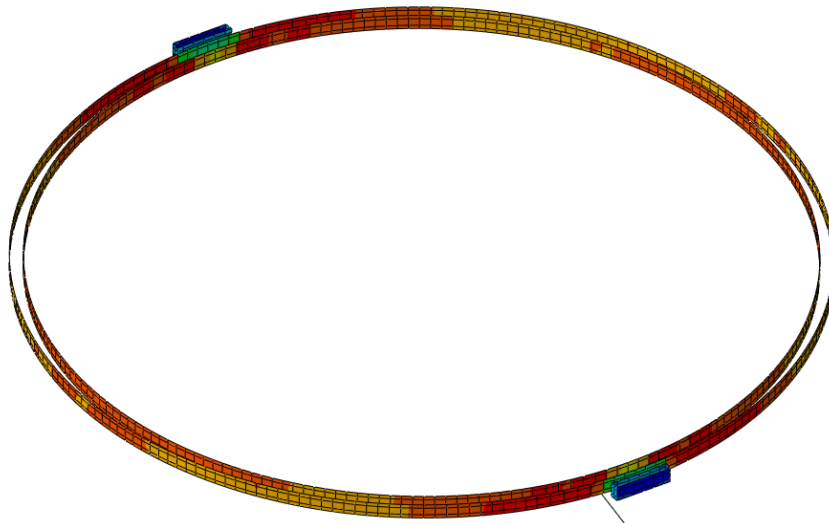


Y
X

Step: Step-5, Pressurization step
 Increment: 58779; Step Time = 0.5750
 Symbol Var: CRACKDIR, Max. Principal
 Deformed Var: U Deformation Scale Factor: +1.000e+00

Figure E 5.18 Vector plot of crack plane normals at 1.47p_d (maximum concrete strain ~-0.0012)

S, S11
 Multiple section points
 (Avg: 50%)
 +4.611e+08
 +4.110e+08
 +3.609e+08
 +3.108e+08
 +2.608e+08
 +2.107e+08
 +1.606e+08
 +1.105e+08
 +6.039e+07
 +1.030e+07
 -3.980e+07
 -8.989e+07
 -1.400e+08
 Max: +4.611e+08
 Elem: PART-1-1.40122
 Node: 40131



Z
Y
X

Max: +4.611e+08

Figure E 5.19 Stresses in reinforcement at increment of first yielding 2.7 p_d.

Liner strain

In Figure E 5.20 are the stresses in the liner shown for the increment when yielding first occurs, pressure $2.2p_d$.

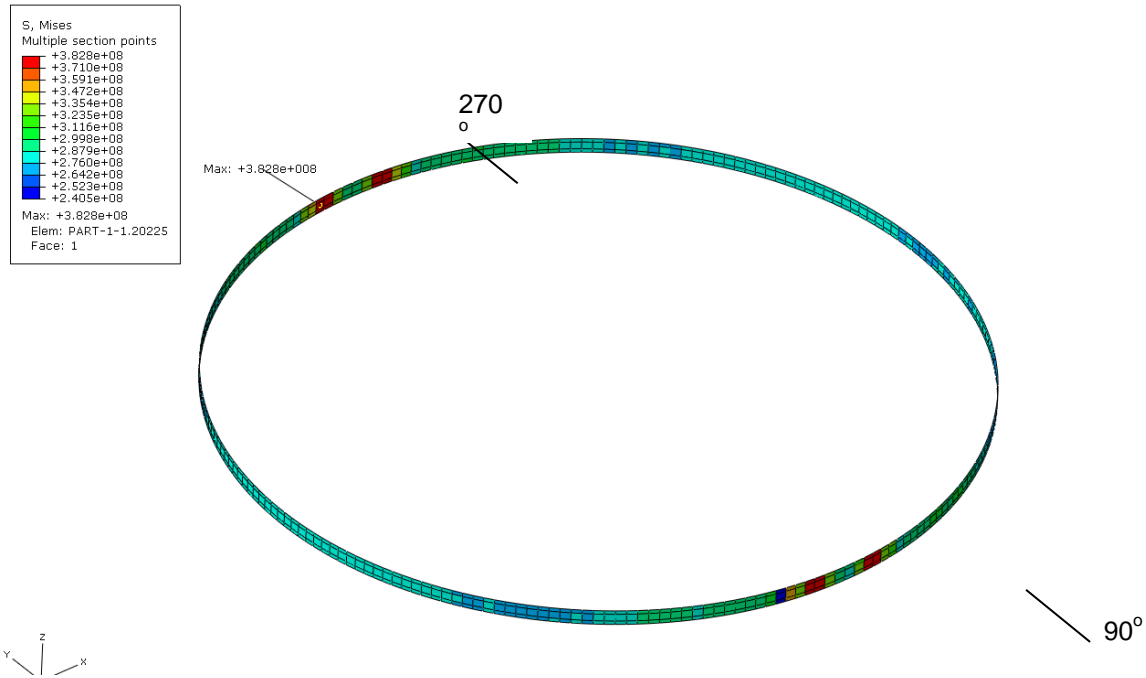


Figure E 5.20 Stresses in liner at increment of first yielding $2.2p_d$.

Tendon slip

In Figure E 5.21 is the total tangential slip of tendon A relative to the concrete along the tendon shown at $0p_d$. The slip at the tendon tangent point of the concrete, azimuth 100° , is approximately 85 mm. The slip decreases gradually to 0 mm at 270° . From 270° to the tangent point in the other end of tendon A, azimuth 80° , the tangential slip has negative values with a max slip of -85 mm.

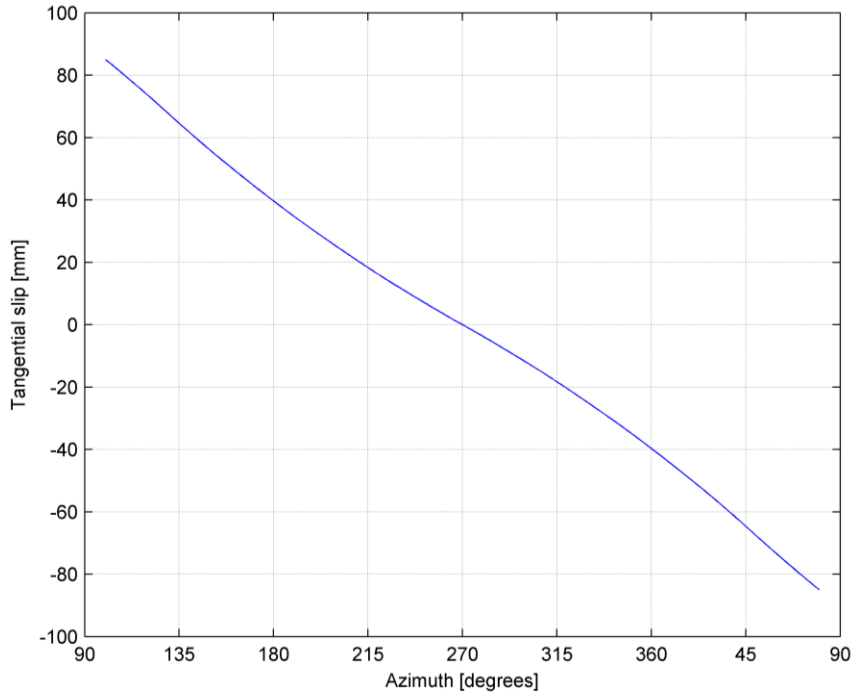


Figure E 5.21 Tangential slip along tendon A after relaxation step.

The additional tangential slip that occurs in the pressurization step is shown in Figure E 5.22. The slip is shown along tendon A for internal overpressure values of $1.0P_d$, $2.0P_d$, $3.0P_d$ and $3.4P_d$. In Figure E 5.13 is the tendon force along tendon A shown for the same pressure milestones as in Figure E 5.22. It can be seen in Figure E 5.22 that the additional tangential slip at $1.0p_d$ is very small. From pressure levels $1.0p_d$ to $2.0 p_d$ there is an increased slip of the tendon. It is also between these levels that cracking in the concrete is initiated and the force in the tendon starts to increase faster. The slip for the pressure levels above $2.0p_d$ is not increased especially except in the regions of the buttresses, 90° and 270° . The slip at 270° results in an increase of force in this region for tendon A. The slip at 90° does not result in any significant force redistribution in tendon A in this region. However, the force in tendon B is increased which can be seen as a more equalized mean force in this area, see Figure E 5.15.

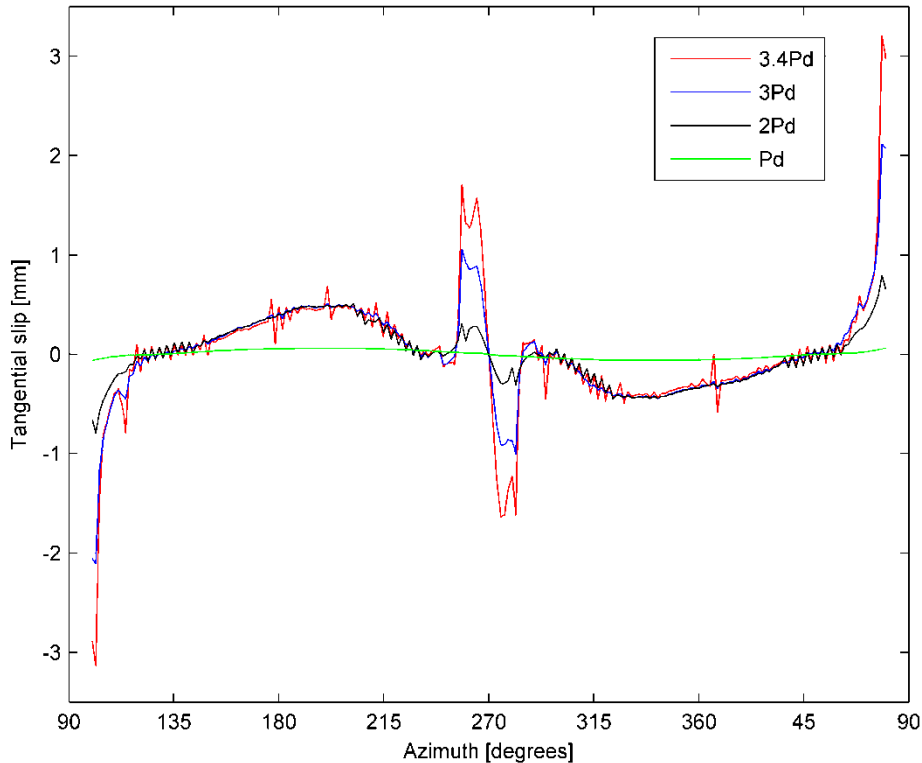


Figure E 5.22 Tangential slip along tendon A at pressure milestones relative to the slip after relaxation step.

Summary

The mean radial expansion during pressurization of the slice model, presented in this chapter, is shown to agree with the mean radial expansion evaluated from the 3D global model and the measurements (see Figure E 5.12). Also results for tendon force along tendons show good agreement between slice model and global 3D model (see Figure E 5.16).

Cracking in the concrete is initiated close to the buttresses which is logical since mean prestressing force is lowest in this region (see Figure E 5.15). It is also in the area close to the buttresses that yielding in the reinforcement and the liner is first initiated (see Figure E 5.19 and Figure E 5.20).

The slip of the tendons relative to the concrete is small for pressures up to $1.0p_d$ (see Figure E 5.22). When cracking of the concrete occurs the slip increases. For higher pressure levels, $>2.0p_d$, the slip increase is small except in the regions at the buttresses.

The main redistribution of tendon force during the pressurization step seems to take place after that some parts of the tendon reaches the yield limit (at $3.1p_d$), see Figure E 5.13. The yielding of the tendon together with the possibility of sliding is concluded to be the main reason for the redistribution of force observed in the scale model test [3].

CONTAINMENT GLOBAL RESPONSE

General

The experience and used modeling technique in Scanscot ISP 48 analyses (see [7] appendix L) are in general implemented in studies presented in this chapter.

An important purpose of the global model analysis is of course to describe the global response in accordance to the SPE request, like radial displacement, tendon behavior etc. (see [6]). However, in this report the global model is also utilized to show the detailed response near the equipment hatch (E/H). The global model deformation on the inner concrete surface, in the region of E/H is used as displacement load in the local model presented in Chapter 7. The detailing of the global model, in the region close to E/H, is therefore increased. In the E/H region the global FE-model has a higher element density and the geometry detailing of concrete, tendons, etc. is increased.

The structural layout of the containment model is described in Chapter 2. The modeling of the global FE-model is presented in Section 6.2. Average input parameters, according to Chapter 4, are used in the analysis.

FE-model

Layout

Figure E 6.1 shows the orientation of the finite element model with respect to the containment key plan in the drawings, see [3].

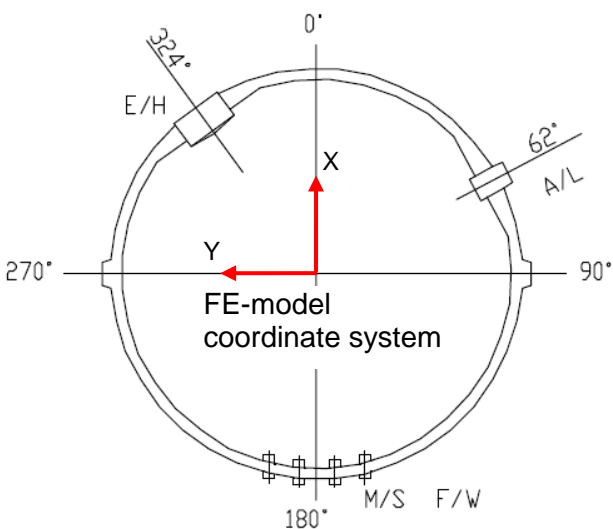


Figure E 6.1 The orientation of the finite element model with respect to the containment key plan in the drawings.

Concrete structure

The global 3D FE-model of the concrete structure is modeled with 8-node linear brick and 6-node linear triangular prism elements with reduced integration and hourglass control denoted C3D8R and C3D6R, respectively in Abaqus [16].

The part of the containment wall next to the equipment hatch (E/H), representing region of Model 2 in the SPE analysis definition [6], is modeled with a higher element density, see Figure E 6.2 and Figure E 6.3. The boundaries of the E/H part of the global model are governed by the deformation of the global containment model with an Abaqus mesh tie constraint which allows for rapid transitions in mesh densities within the model.

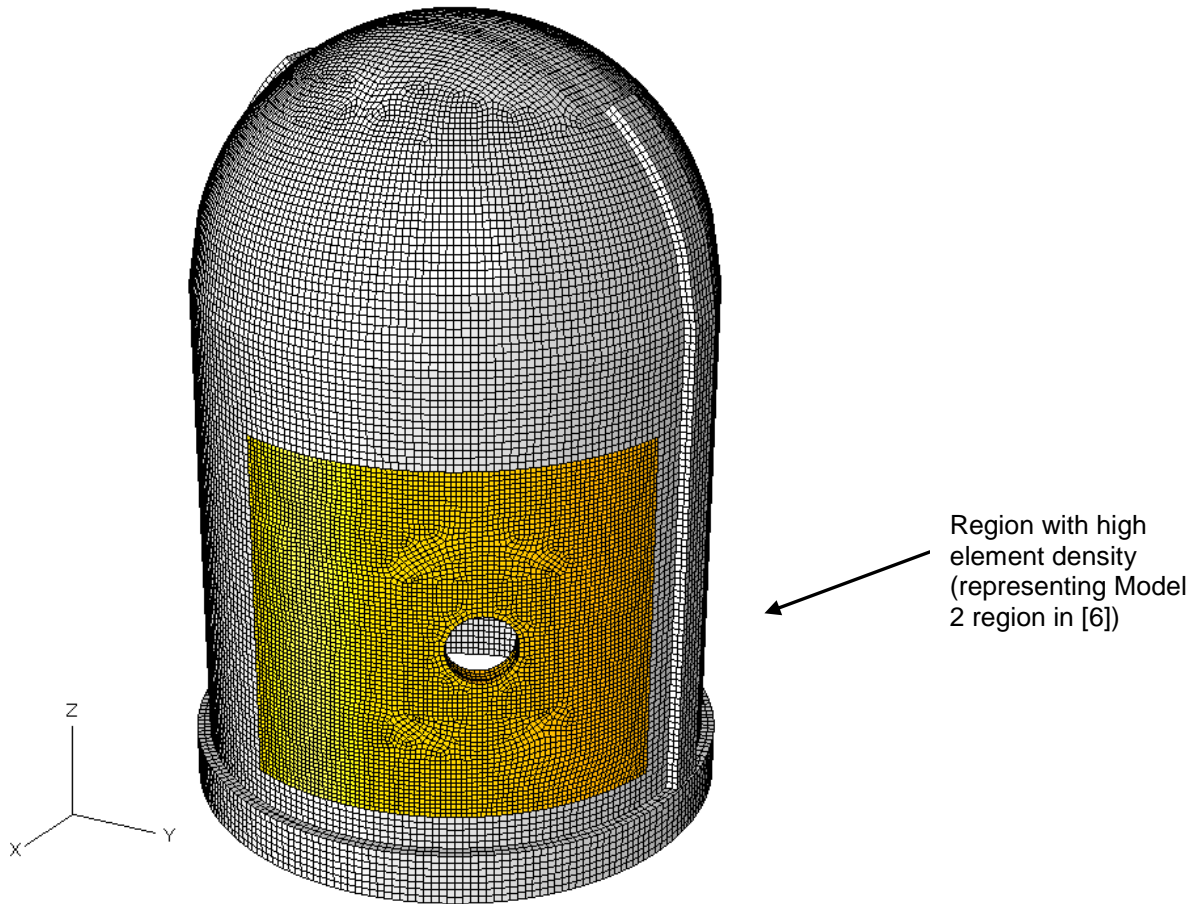


Figure E 6.2 Global FE-model, structural concrete parts.

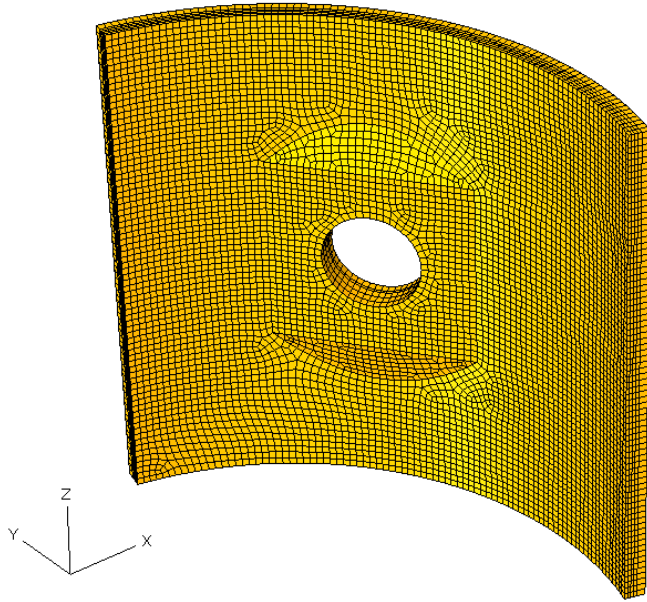


Figure E 6.3 Global FE-model, inside view of the structural concrete near E/H.

Steel liner

The steel liner on the inside of the concrete containment is modeled with 4-node shell elements with reduced integration and hourglass control denoted S4R in Abaqus [16]. The steel liner thickness is set to the nominal value of 1.6 mm.

The nodes of the steel liner model is equivalenced with the nodes on the inside surface of the concrete elements, see Figure E 6.2 and Figure E 6.3. Figure E 6.4 shows an outside view of the steel liner model including the penetration plates.

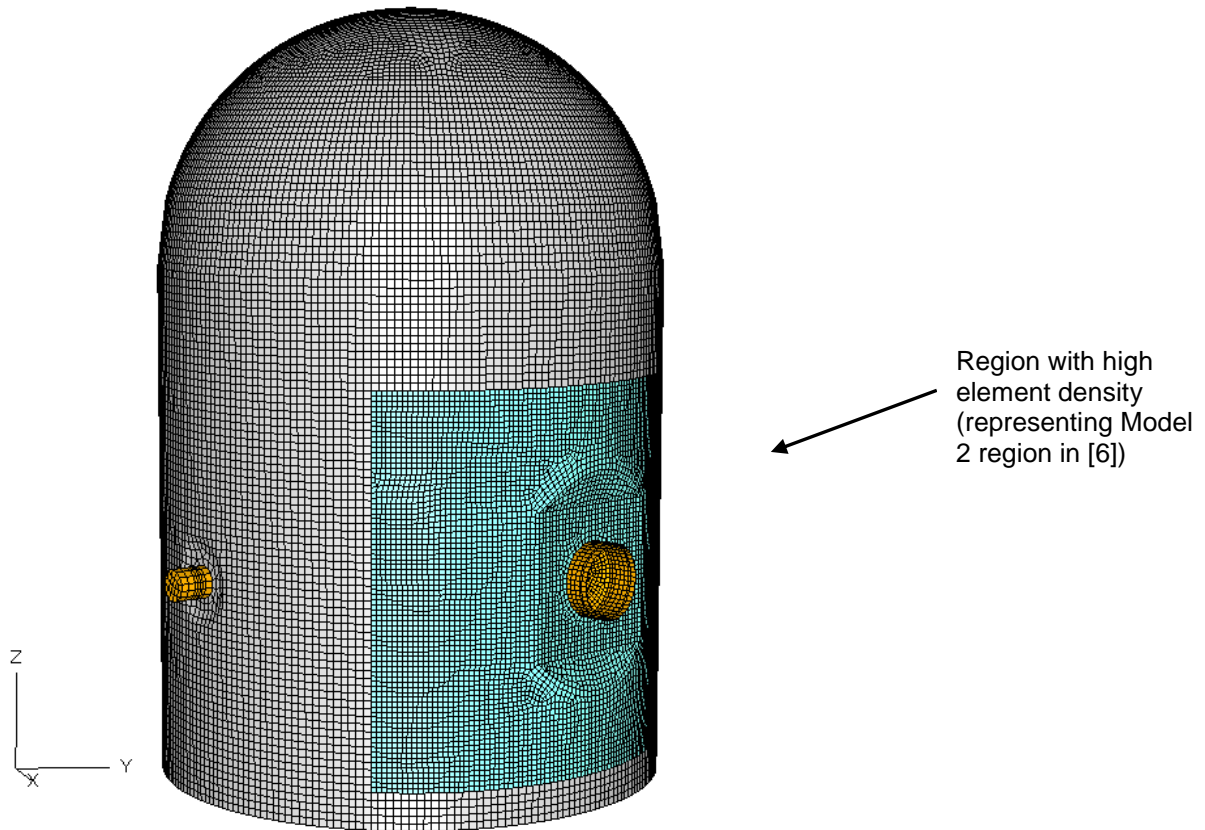


Figure E 6.4 Outside view of the steel liner model.

Tendon system

The vertical and horizontal unbonded tendons are modeled with 2-node linear 3D truss elements denoted T3D2 in Abaqus [16]. The same tendon modeling technique is used in this study as described for the model in the prestressing tendon behavior study, see Section 5.2.2. In Figure E 6.5 the geometrical layout of horizontal and vertical tendons in the global FE-model are shown.

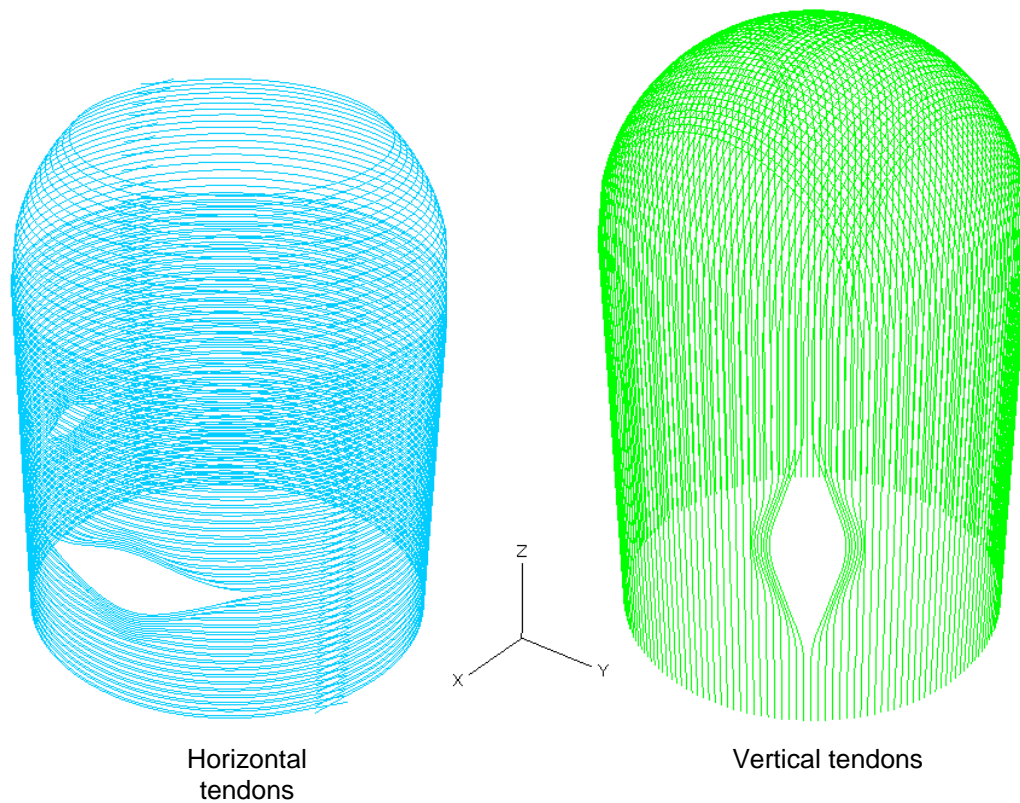


Figure E 6.5 Truss elements modeling the horizontal and vertical tendons in the global FE-model.

The inner surface of the tendon ducts are represented by element surfaces on solid element faces and on embedded shell elements, see Figure E 6.6. Node based surfaces are defined using the tendon truss elements. A finite-sliding contact formulation between the tendon surfaces and the surfaces representing the tendon ducts are defined. The contact definition allows arbitrary separation, sliding and rotation of the surfaces in contact.

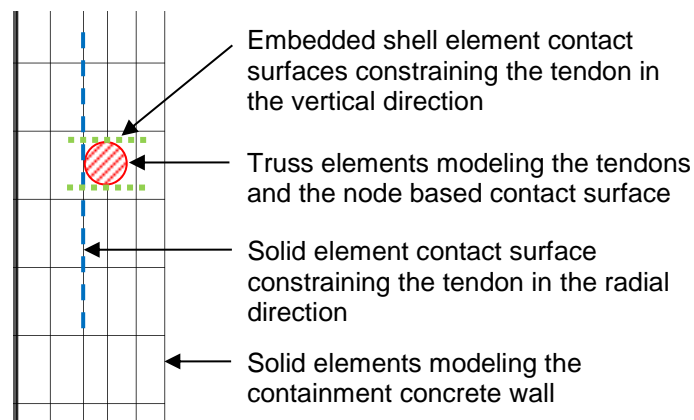


Figure E 6.6 Vertical section cut through the wall showing the technique of modeling the interaction between tendons and containment wall.

The prestressing of the tendons is modeled with the use of 2-node connector elements denoted CONN3D2 in Abaqus [16]. The connector elements connect the tendon ends to steel anchor plates modeled with 4-node shell element, see Figure E 6.7. The anchor plate shell element nodes are equivalenced with the containment wall solid mesh.

The tensioning and seating process are simulated in the analysis by stretching the elements representing the tendons with the connector elements up to the specified pre-stressing force before seating, see Section 4.5.3. The connectors relax the tendons with the specified seating losses in the following step, see Section 4.5.3.

This procedure gives rise to an un-evenly distributed tendon force along the length of the tendon, due to the friction specified in the contact definition, corresponding to the actual tendon force variation.

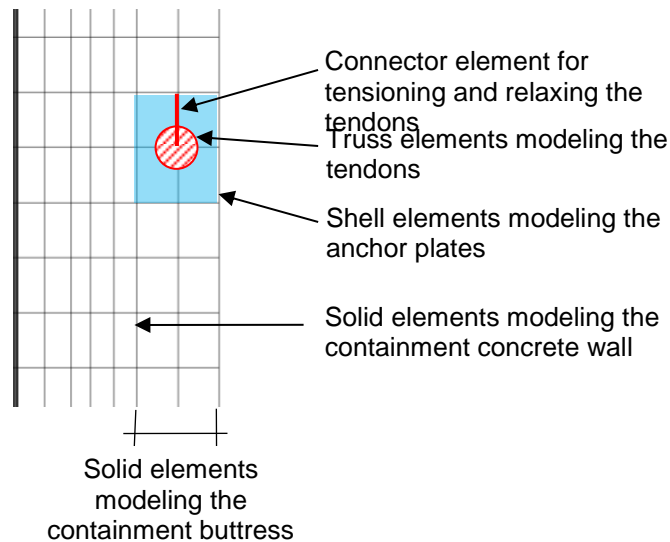


Figure E 6.7 Vertical section cut through the containment wall showing the technique of modeling the interaction between tendon and anchor plate.

Rebar reinforcement

The reinforcement is modeled using sets of 4-node membrane elements denoted M3D4R in Abaqus [16]. Each set of membrane elements represents an area with a specific amount of reinforcement and a specific direction of the reinforcement. I.e., for each set of membrane elements, the rebar cross-section area, the rebar spacing and the rebar orientation are specified using the rebar layer function in Abaqus [16]. The sets of membrane elements are embedded in the solid mesh constituting the concrete and are thus rigidly connected to the solid element mesh.

The reinforcement at the inner and outer rebar layers in the containment are in principle modeled as shown in Figure E 6.8 and Figure E 6.9. The different colors represent regions with different content of reinforcement.

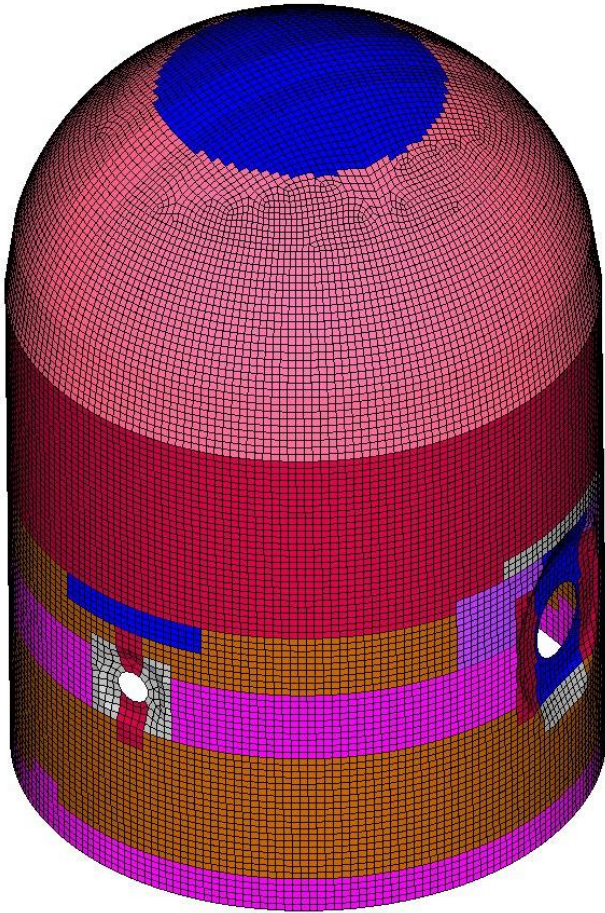


Figure E 6.8 Reinforcement regions, inner surface.

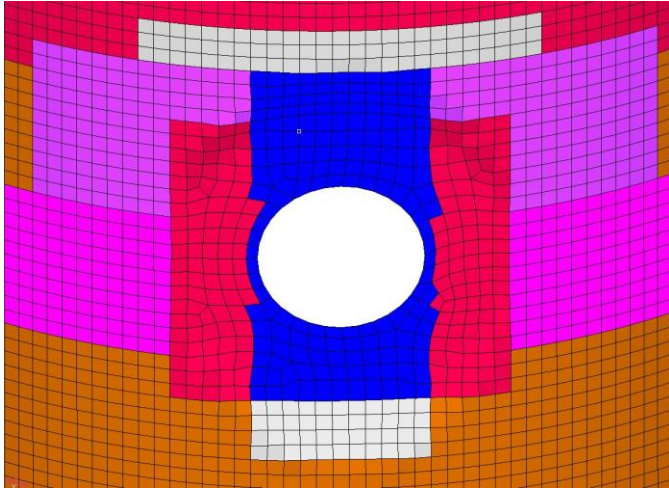


Figure E 6.9 Reinforcement regions, inner surface, around E/H.

Load and boundary conditions

Only a minor part of the basemat is included in the finite element model, the part between the cylindrical wall connection and the tendon gallery. The bottom and the vertical faces of the modeled basemat are constrained in both the vertical and the horizontal directions. Constrained nodes are shown in Figure E 6.10.

The load representing the inner pressure at the limit state test, see Section 2.4, is modeled by a pressure acting on the inside surfaces of the elements modeling the steel liner.



Figure E 6.10 Part of the containment model showing the basemat nodes, which are constrained in the vertical and horizontal directions.

Finite element model size

The size of the global finite element 3D model including the local E/H model is shown below.

- Number of elements: ~ 380 000
- Number of nodes: ~ 390 000
- Number of degrees of freedom: ~ 1 540 000

Results and evaluation

Global displacement

Liner deformation at standard output locations

The liner deformations at the standard output locations are shown in Appendix A4 in this report. The results are presented in plots where the output from the finite element model is compared with the measurements.

Liner deformation at pressure milestones

The liner deformation is presented for the sections shown in Figure E 6.11 below. The radial deformation of the containment wall is shown along the meridional sections A and C in Figure E 6.12 and Figure E 6.14, respectively. The radial deformation of the containment wall is shown along the hoop sections B and D in Figure E 6.13 and Figure E 6.15, respectively.

The deformations are shown for the predefined pressure milestones [6]. The ultimate pressure is taken to be $3.63p_d$ (1.41 MPa) as defined in [3].

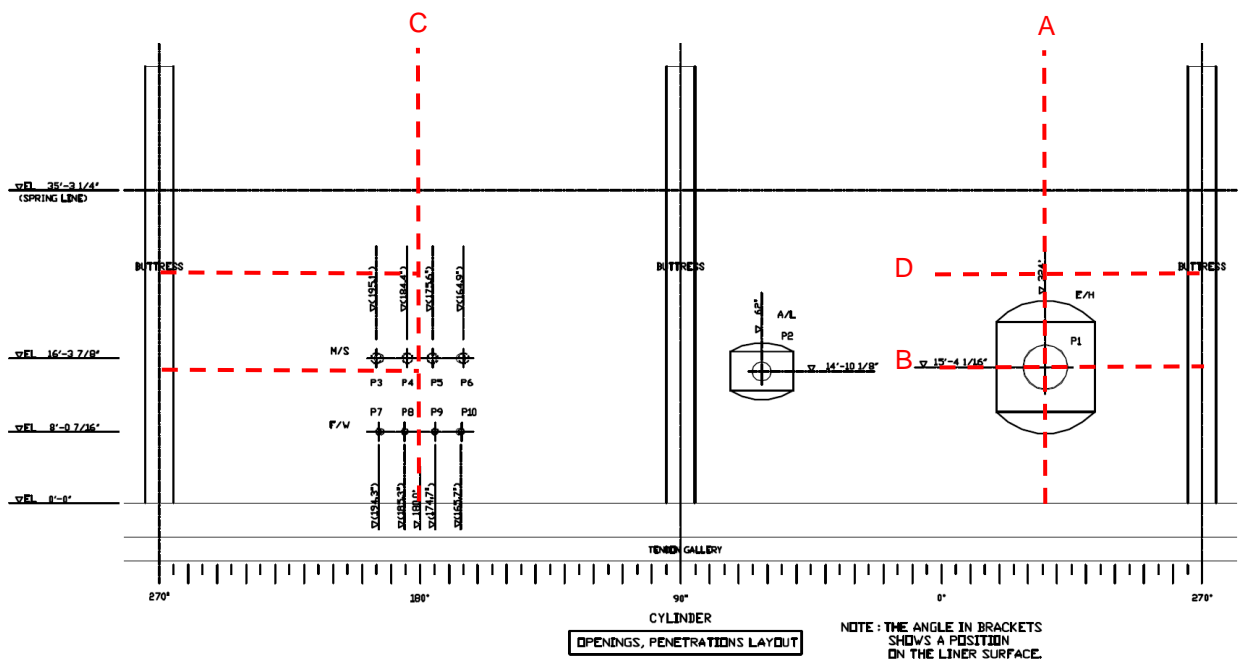


Figure E 6.11 Inside view of the containment liner showing the sections for which deformation output is presented.

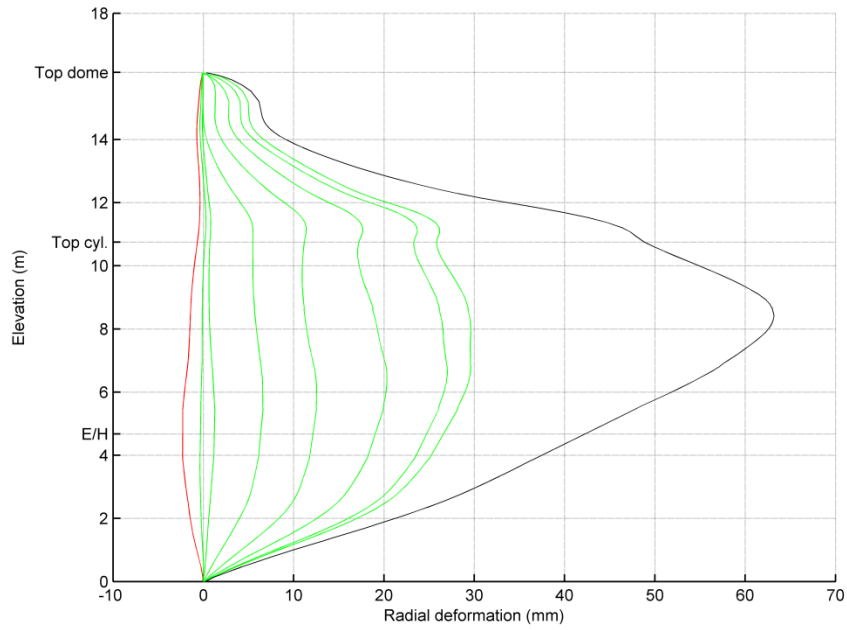


Figure E 6.12 Radial deformation of containment liner, section A, azimuth 324°.
Red curve: $0 \times P_d$
Green curves: $[1, 1.5, 2, 2.5, 3, 3.3, 3.4] \times P_d$
Black curve: 1.41 MPa

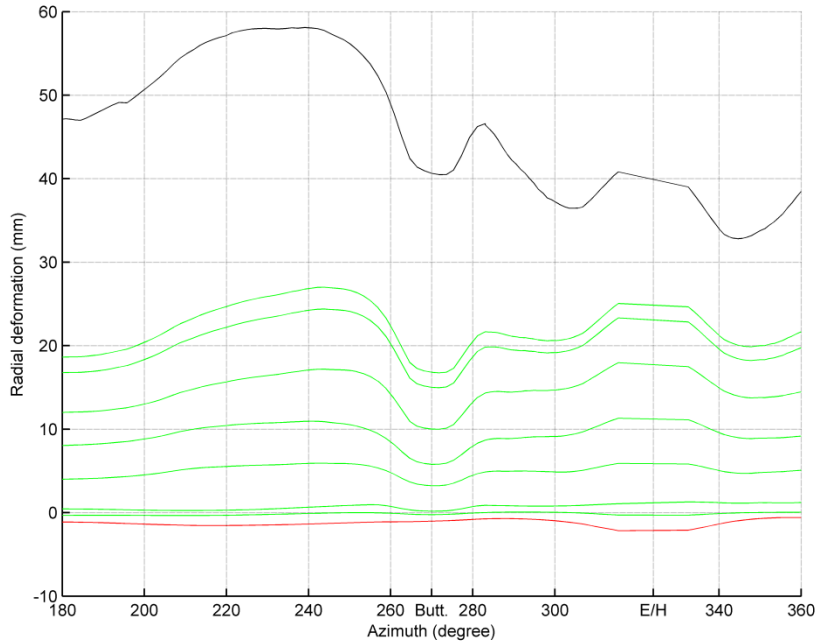


Figure E 6.13 Radial deformation of containment liner, section B, el 4.675 m.

Red curve: $0 \times P_d$
Green curves: $[1, 1.5, 2, 2.5, 3, 3.3, 3.4] \times P_d$
Black curve: 1.41 MPa

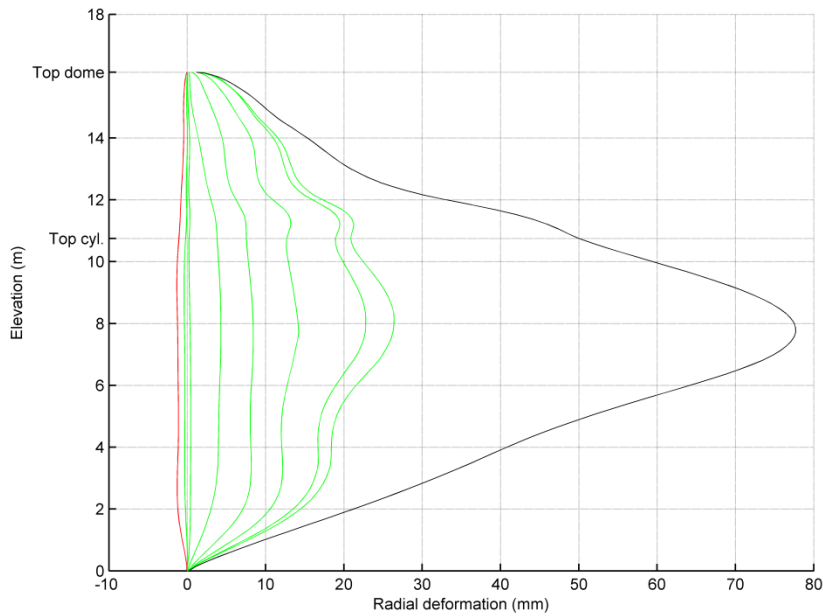


Figure E 6.14 Radial displacement of containment liner, section C, azimuth 180°.

Red curve: $0 \times P_d$
Green curves: $[1, 1.5, 2, 2.5, 3, 3.3, 3.4] \times P_d$
Black curve: 1.41 MPa

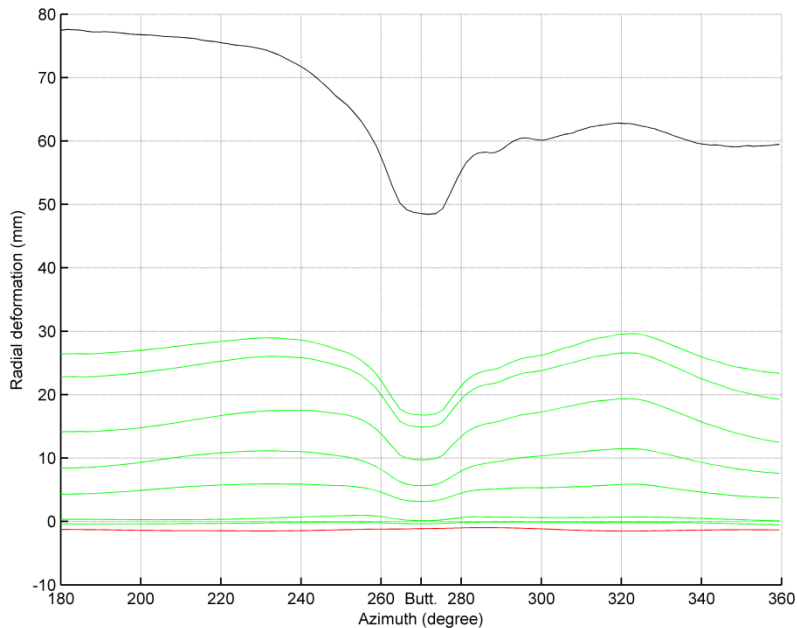


Figure E 6.15 Radial displacement of containment liner, section D, el 8.0 m.

Red curve: $0 \times P_d$
Green curves: $[1, 1.5, 2, 2.5, 3, 3.3, 3.4] \times P_d$
Black curve: 1.41 MPa

Strains in concrete structure

See appendix A6 for contour plots of concrete strains at pressures when:

1. Cracking is initiated ($1.23p_d$).
2. Crack strains are developed through entire cross-section of containment wall ($1.38p_d$).
3. Regions in containment wall are fully cracked ($1.54p_d$).
4. Regions in containment wall are fully cracked through entire cross-section of containment wall ($1.85p_d$).
5. The major part of the concrete containment wall is fully cracked and has no tensile strength in hoop direction ($2.31p_d$).

Strains in steel liner

Strains in liner at standard output locations

The liner strains at the standard output locations are shown in Appendix A4 in this report. The results are presented in plots where the output from the finite element model is compared with the measurements.

Strains in liner at pressure milestones

See appendix A5 for contour plots of liner strains at pressure milestones. Table E 6.1 below shows the maximum liner hoop strain at the pressure milestones.

Table E 6.1 Maximum hoop strains in steel liner at pressure milestones.

Milestone	Pressure (MPa)	Maximum hoop tension strain (‰)
$0 \times P_d$	0	0.0
$1 \times P_d$	~ 0.390	0.1
$1.5 \times P_d$	~ 0.600	0.6
$2 \times P_d$	~ 0.780	1.6
$2.5 \times P_d$	~ 0.990	4.1
$3 \times P_d$	~ 1.170	13.0
$3.3 \times P_d$	~ 1.290	17.4
$3.4 \times P_d$	~ 1.320	18.8
Ultimate [3]	~ 1.410	31.3

Tendons system

Strains and forces in tendons at standard output locations

The strains and forces in the tendons at the standard output locations are shown in Appendix A4 in this report. The results are presented in plots where the output from the finite element model is compared with the measurements.

Tendon force distribution during pre-stressing

Figure E 6.16 shows the forces in the tendons after tensioning and it can be seen that all horizontal tendons have a maximum tension force of approximately $427 \times 0.95 \approx 406$ kN as specified in sections 4.5.3 and 4.5.4.

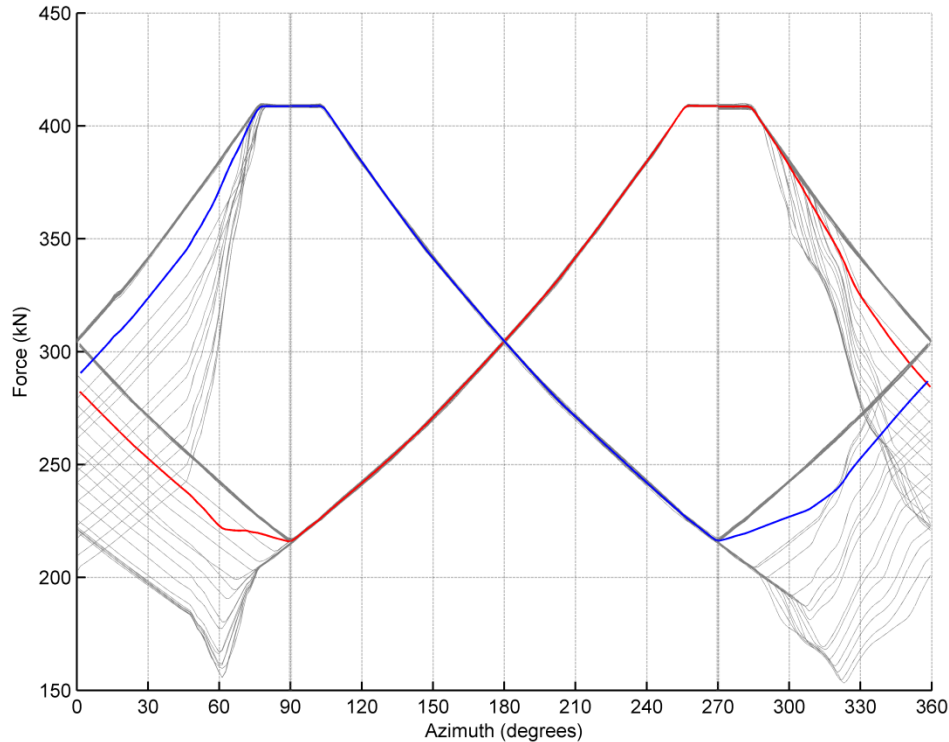


Figure E 6.16 Forces in horizontal tendons in the cylindrical part of cont. wall.

Analysis step: tensioning

Grey curves: tendon forces in each individual tendon

Blue curve: mean tendon force, anchoring at 90° azimuth

Red curve: mean tendon force, anchoring at 270° azimuth

The lowest force, for a horizontal tendon anchored at azimuth 90° without deflection in the vertical direction, should be according to the exponential function described in section 4.5.3:

$$F(270^\circ) = F_0 \times e^{-(\mu\alpha + kv)} = 406 \times 10^3 \times e^{-0.22 \times (270 - 90 - 15) \times (\pi / 180)} \approx 215 \text{ kN}$$

which corresponds to the tendon force at azimuth 270° in Figure E 6.16.

Note that in Appendix A2, a similar evaluation of tendon forces are presented for horizontal tendons with deflection in the vertical direction around the E/H and A/L penetrations.

Figure E 6.17 shows the forces in the tendons after seating and the maximum mean tendon force is now reduced to approximately 360 kN and at the tendon anchoring the force is reduced to approximately 330 kN. The minimum tendon force remains at the same force value as before seating.

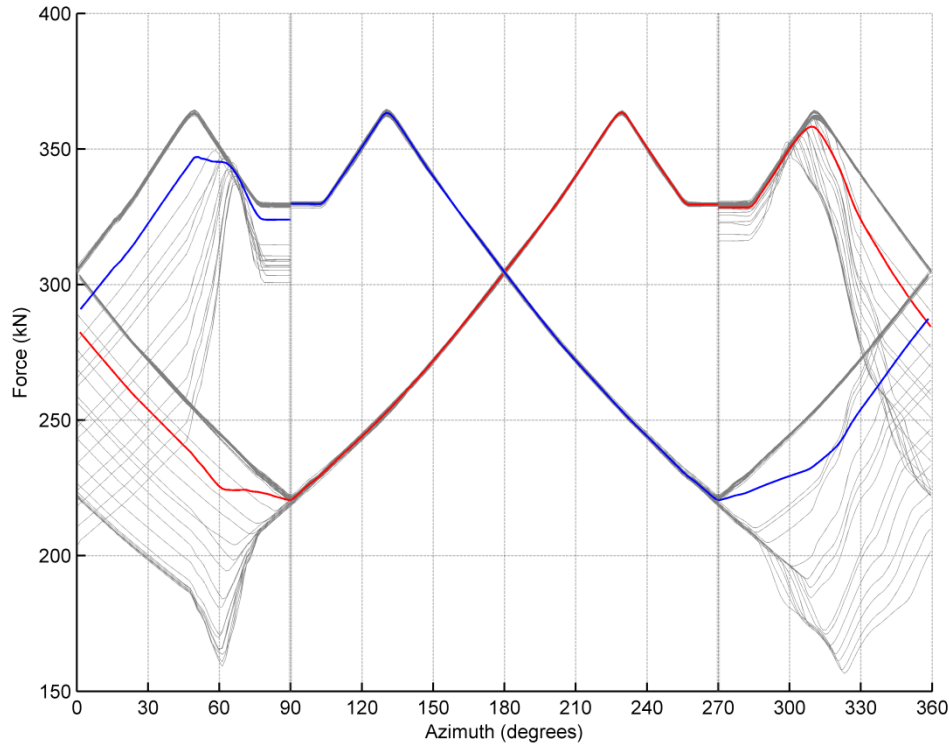


Figure E 6.17 Forces in horizontal tendons in the cylindrical part of cont. wall.

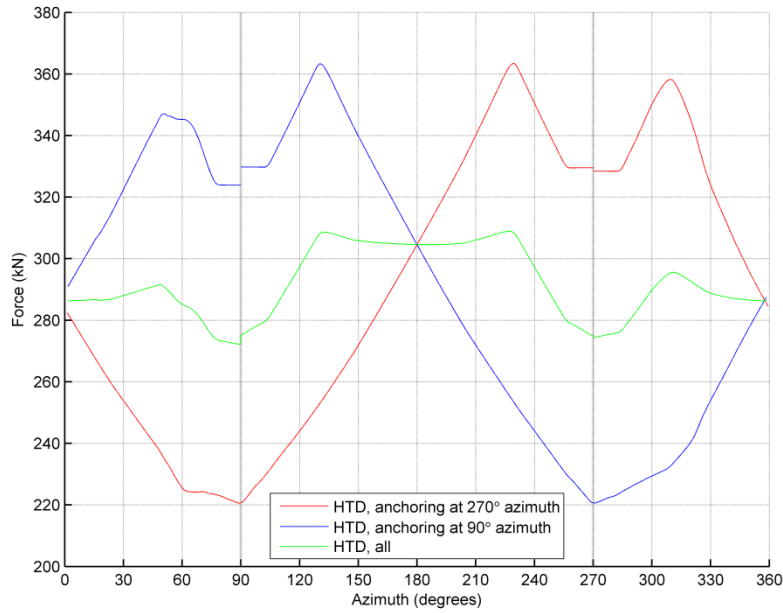
Analysis step: seating ($0 \times P_d$)

Grey curves: tendon forces in each individual tendon

Blue curve: mean tendon force, anchoring at 90° azimuth

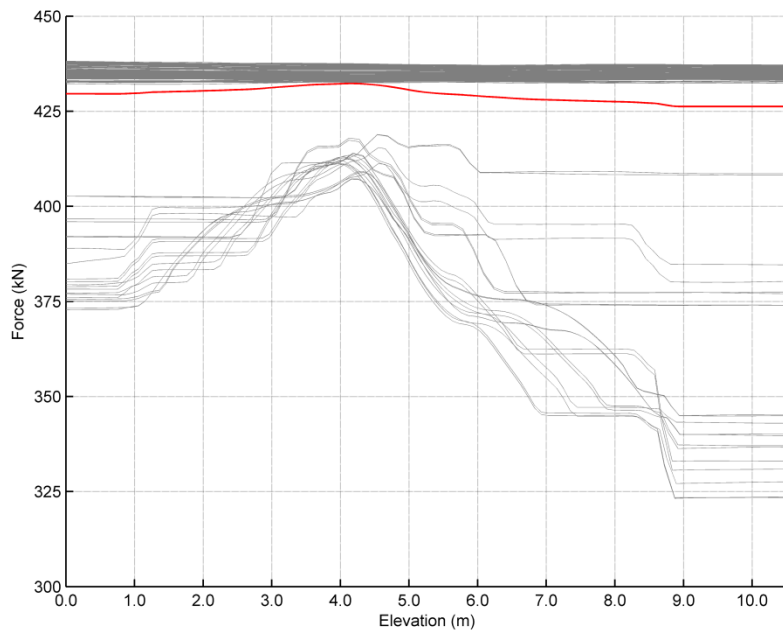
Red curve: mean tendon force, anchoring at 270° azimuth

Figure E 6.18 shows the mean forces along the tendon for all horizontal tendons anchored at azimuth 90° , for all horizontal tendons anchored at azimuth 270° and the mean value of those two curves. It can be seen that the highest mean tendon force is reached between azimuth 130 to 230° .



**Figure E 6.18 Mean forces in horizontal tendons in cylindrical part of cont. wall.
Analysis step: seating ($0 \times P_d$)**

Figure E 6.19 shows the forces in the vertical tendons after seating. The vertical tendons are plotted over elevation in cylindrical part of containment wall.



**Figure E 6.19 Forces in vertical tendons in cylindrical part of cont. wall.
Pressure: $0 \times P_d$ (after seating)
Grey curves: tendon forces in each individual tendon
Red curve: mean tendon force**

Tendon force distribution at pressure milestones

Figure E 6.20 shows the mean force in the horizontal tendons at the pressure milestones and the yield force limit and ultimate force limit are highlighted. It can be seen that the mean force of all horizontal tendons are below the yield force at all pressures.

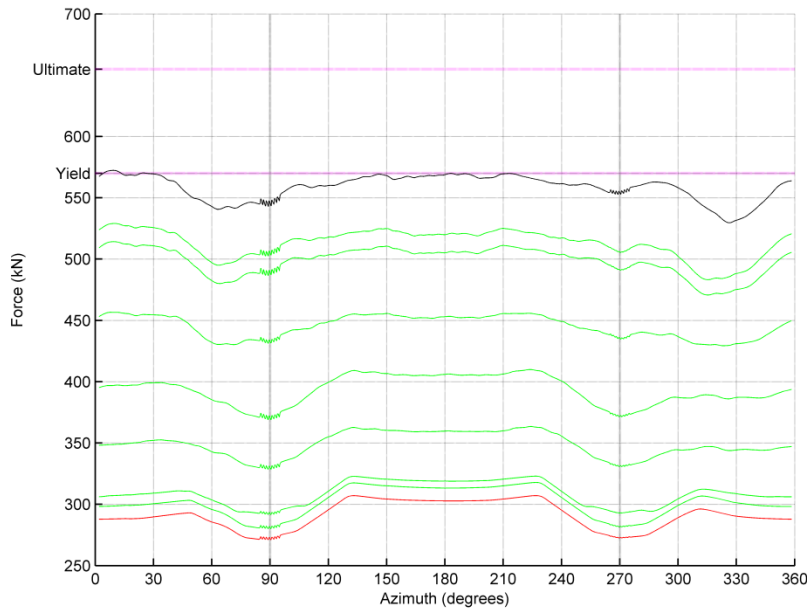


Figure E 6.20 Mean force of all horizontal tendons.

Red curve: $0 \times P_d$

Green curves: $[1, 1.5, 2, 2.5, 3, 3.3, 3.4] \times P_d$

Black curve: 1.41 MPa

However, it can be concluded from the deformation plots in Figure E 6.12 and Figure E 6.14 above, that the radial deformation of the containment varies a lot along the containment wall in the vertical direction. From the Figure Es it can be seen that the largest radial deformations occur approximately between elevation 6 m and 10 m.

In Figure E 6.21 below, the mean tendon forces for the horizontal tendons between elevation 6.4 m and 9.9 m are plotted and it can be seen that the forces reaches the yield limit at $3.4 P_d$. At 1.41 MPa the mean forces along the tendons are entirely in the plastic region

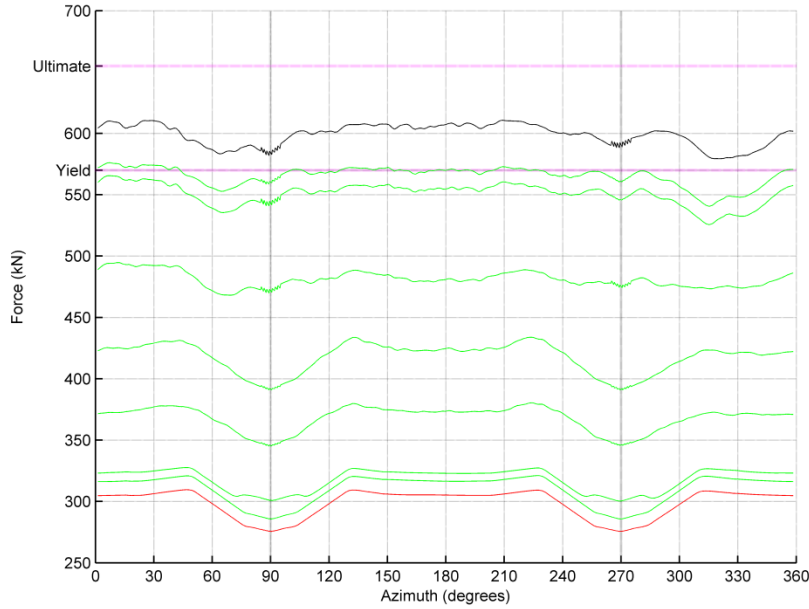


Figure E 6.21 Mean force of horizontal tendons No 51-82 (+6.4-+9.9).
Red curve: $0 \times P_d$
Green curves: $[1, 1.5, 2, 2.5, 3, 3.3, 3.4] \times P_d$
Black curve: 1.41 MPa

Figure E 6.22 shows the mean forces in the vertical tendons after seating, at $3.4p_d$ and at 1.41 MPa. It can be seen that none of the vertical tendons have forces that reaches the yield limit.

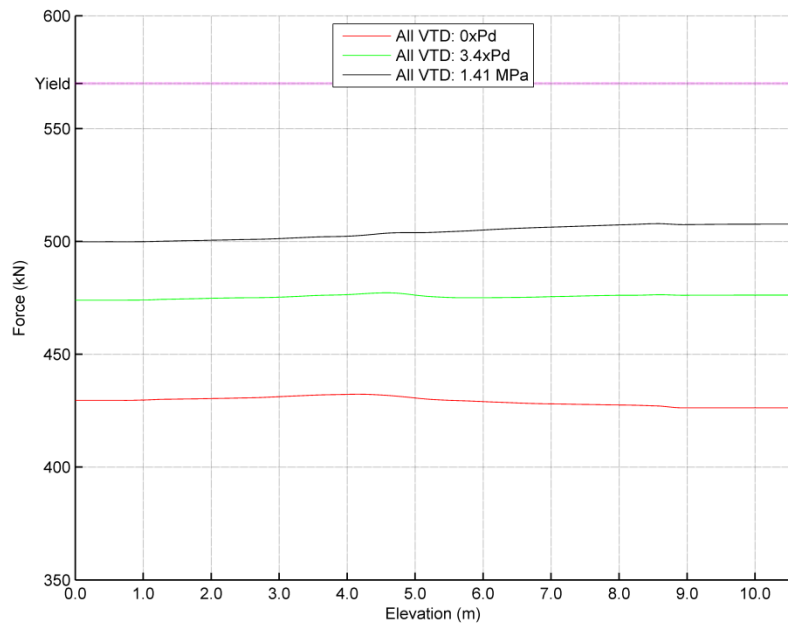


Figure E 6.22 Mean force of all vertical tendons over elevation in cylindrical part of containment wall.

Summary

The radial displacements at the predefined standard output locations in the finite element model compares well with the measured radial deformations, see Appendix A4. However, there is a discrepancy between the finite element model and the measurements regarding the vertical deformations at positions 1, 8 and 10. The difference at position 1 is probably due to the fact that the displacement gauge correctly measures zero displacement at elevation 0.0 m. At this level in the finite element model, the boundary conditions applied to the basemat allows for displacement in the vertical direction at the intersection between the containment cylindrical wall and the basemat. The radial displacement is also presented along vertical and horizontal sections along the steel liner, see Figure E 6.12 through Figure E 6.15. In these Figure Es it can be seen that at $1.0p_d$ (0.39 MPa), the radial displacement of the liner is approximately zero. At $3.4p_d$ the maximum radial displacement is approximately 30 mm at elevation 8 m and azimuth 324° .

Hoop strains in the concrete are presented at various pressures in Appendix A6. Crack strains are initially reached on the inside surface of the containment wall where the buttresses are situated. Maximum hoop strain is approximately 0.1 ‰ at $1.23p_d$. It can also be noted that at $2.31p_d$ the main part of the cylindrical containment wall is fully cracked and the concrete has no tensile strength in hoop direction. I.e., it is the rebar reinforcement and the tendons alone that continue to carry the pressure load up to the ultimate pressure. It is noted that the mean horizontal tendon forces are lowest at azimuth 90° and 270° , where the buttresses are placed. Also, in Figure E 6.13 and Figure E 6.15 it can be seen that there is a large dip in the radial displacement where the buttresses are placed and consequently bending strains will develop in this regions.

Liner hoop strains are presented as contour plots in Appendix A5 at the pressure milestones. It can be seen at $1.0p_d$ that almost the entire steel liner is subjected to compression strains. It is noted that in the regions of the buttresses the liner has developed tension strains in hoop direction. As anticipated from Figure E 6.13 and Figure E 6.15, the largest tension strains develop around the regions of the buttresses.

The horizontal tendons between elevation 6.4 m and 9.9 m have mean tendon forces beyond the yield limit at $3.4p_d$, see Figure E 6.21. No vertical tendons develop plastic strains up to the ultimate pressure of $3.63p_d$, see Figure E 6.22.

LINER BEHAVIOR NEAR EQUIPMENT HATCH

General

In this chapter the liner near the equipment hatch (E/H) is analyzed in detail. The principal method is described in Chapter 3, where two levels of submodels are used. In the first submodel the radial and vertical displacement, in liner locations fixed to the concrete structure (anchors and stiffeners), are driven by the global FE-model described in Chapter 6. In highly stressed regions of the liner the mesh density is increased and these regions are analyzed by a second submodel with boundaries driven by the first submodel.

The liner layout for the containment scale model is described in Section 2.2.2 and the liner FE-model is presented in Section 7.2 below. Average input parameters, according to Chapter 4, are

used in the analysis. To show the influence of liner anchor stiffness the liner model is analyzed for two different shear stiffness curves, see Section 4.4.3.

Liner buckling was observed in the containment scale model due to compression strains induced by the prestressing force. This phenomenon is not considered in the analyses presented in this chapter. To avoid numerical instability in the analyses, a constant pressure load is applied on the liner inner surface in the prestressing step. The actual pressure load is applied in the pressure load step in the analyses.

FE-model

Steel liner

The finite element submodel of the steel liner is modeled with 4-node shell elements with reduced integration denoted S4R in Abaqus [16]. The position of the finite element model in the global model is shown in Figure E 7.1.

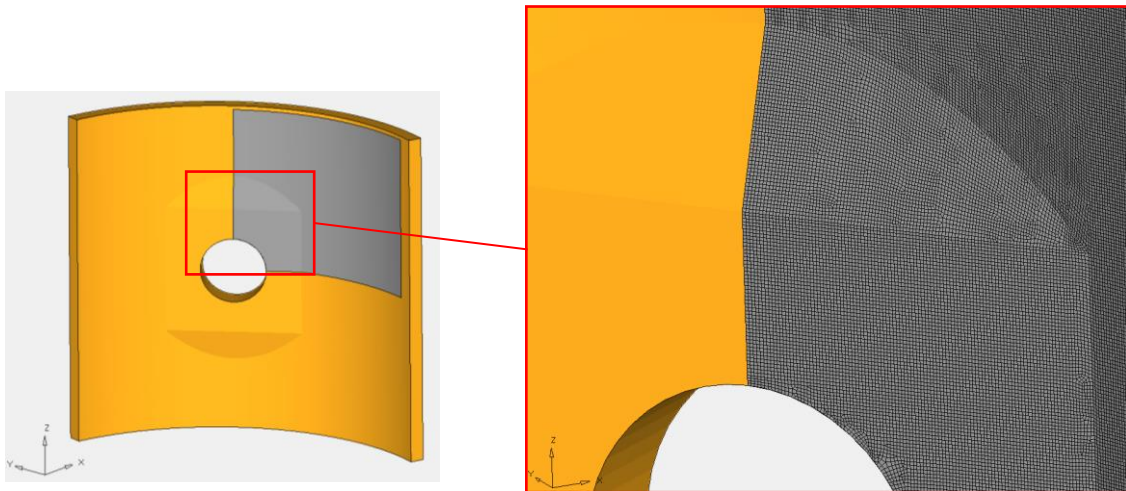


Figure E 7.1 Position of finite element submodel of liner in the global model.

The narrow liner field along the vertical bend line, outlined in Figure E 7.2 below, will straighten out between the vertical T-anchors when the containment wall expands due to the applied inner pressure. Consequently, high concentrations of stress and strain will develop in this region. Thus, a second submodel is generated modeling the liner field along the vertical bend line which is confined between the vertical T-anchors, see Figure E 7.2 below. This second submodel has an increased element density and the general element size is 2 mm.

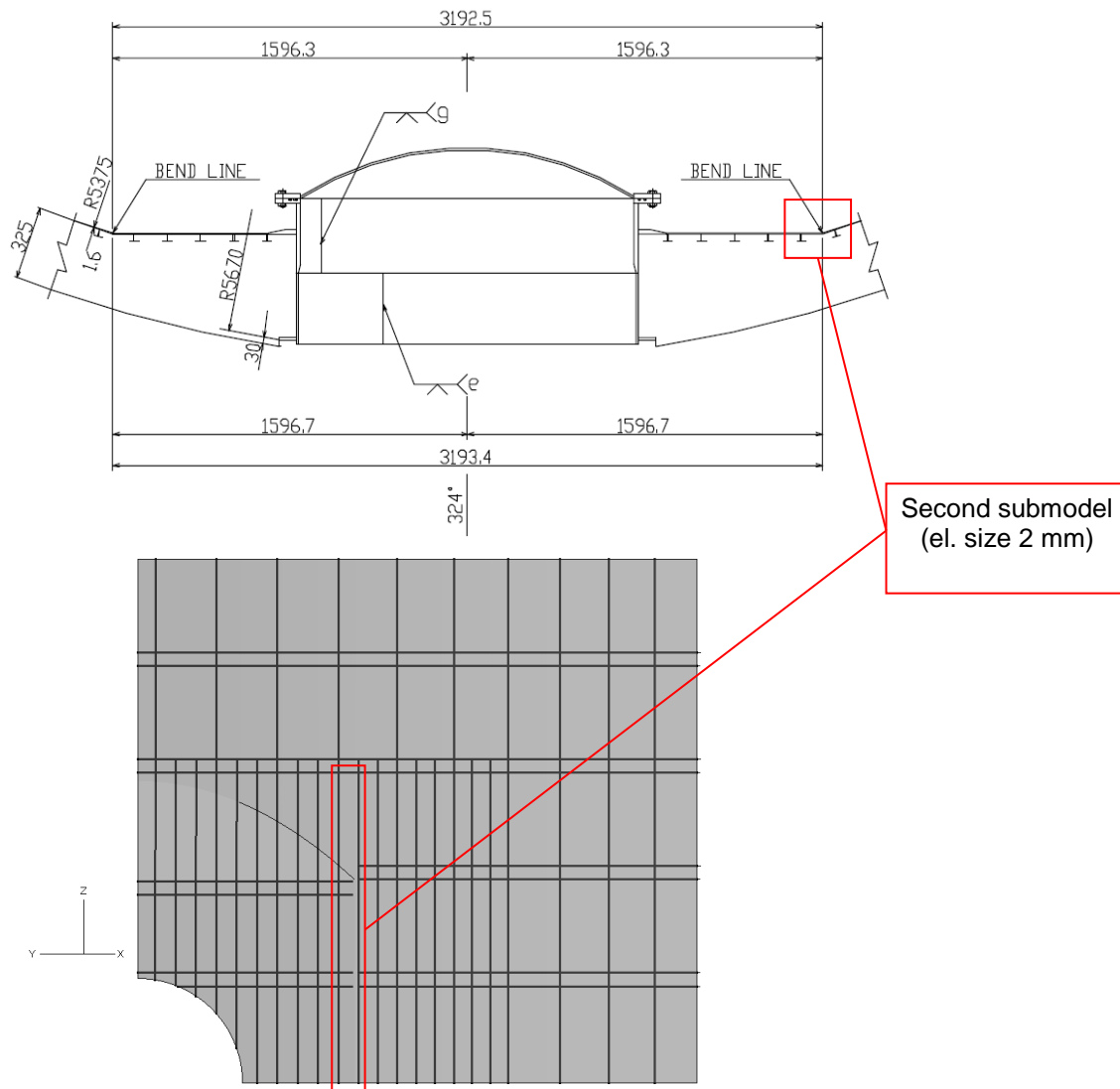


Figure E 7.2 Excerpt from liner drawing [3] showing a horizontal section through the equipment hatch (upper sketch). A view of the first submodel (element size 15 mm) is shown in the lower sketch, where the location of the second submodel is indicated.

Liner anchors

The liner is anchored to the concrete via vertical T-anchors which are grouted into the concrete, see Section 2.2.2.1. The T-anchors are modeled with 2-node connector elements denoted CONN3D2 in [16]. The T-anchors have an in-plane shear stiffness in the circumferential direction according to Section 4.4.3 in this report. The T-anchors are considered rigidly connected to the concrete in the radial and vertical directions.

Horizontal stiffeners are welded to the liner and also grouted into the concrete, see Section 2.2.2.1. The connection to the concrete is modeled with 2-node connector elements with an in-plane shear stiffness in the vertical direction according to Section 4.4.3. The horizontal stiffeners

are also modeled with shell elements denoted S4R in [16] to include the added stiffness to the liner. Figure E 7.3 shows the finite element liner submodel with horizontal stiffeners and with the connector elements highlighted in yellow.

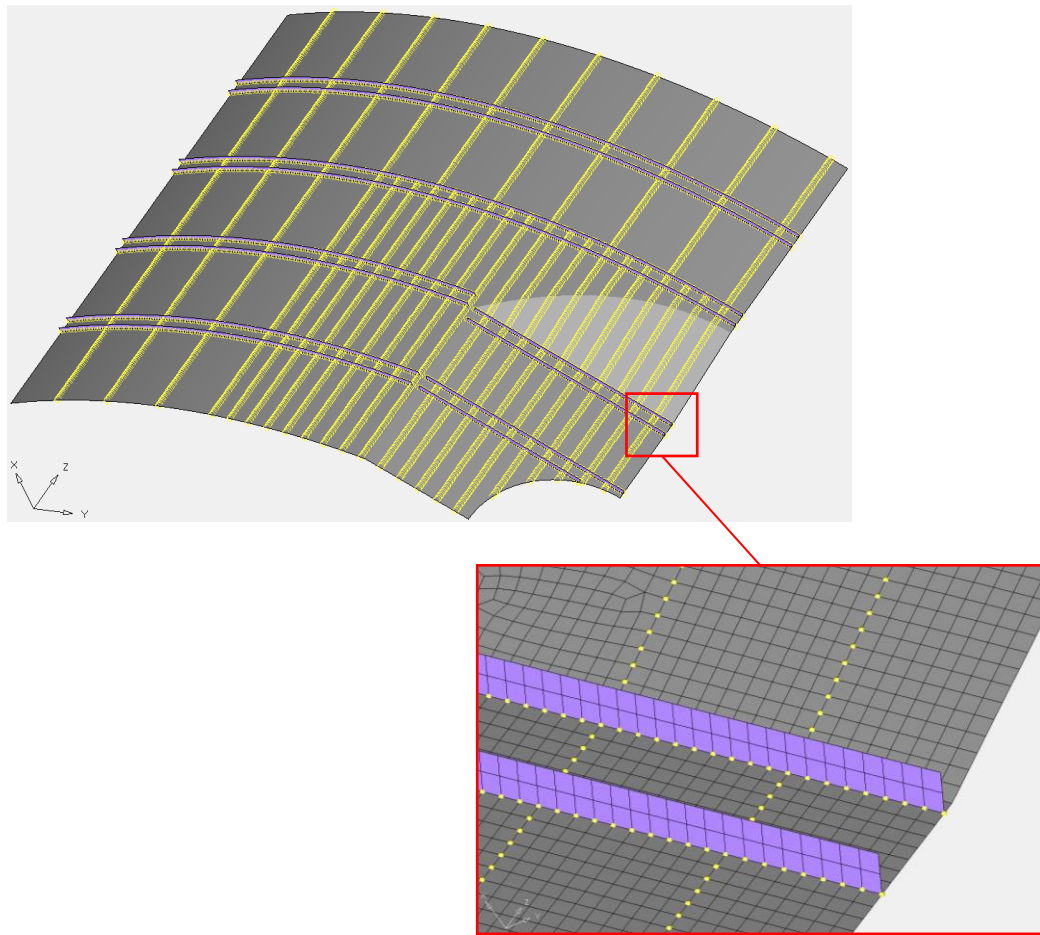


Figure E 7.3 Liner FE-model with connectors highlighted in yellow and horizontal stiffeners modeled with shell elements.

Submodel boundary conditions

The concrete wall in the submodel is described by shell elements at the same radius as the concrete inner surface. The liner model is connected via connector elements as described in Section 7.2.1 above. The interaction between the steel liner and the concrete wall inner surface is described with an element based contact surface. The friction coefficient is assumed to be zero and the contact formulation allows for arbitrary separation, sliding, and rotation of the surfaces.

The displacements, given from the global FE-model, govern all nodes of the shell elements describing the concrete inner surface in the submodel. The position of the liner submodel in the global model is shown in Figure E 7.1.

The first submodel with an element size of 15 mm (submodel 1) governs the boundary displacements of the second submodel (submodel 2) with an element size of 2 mm, see Figure E 7.4.

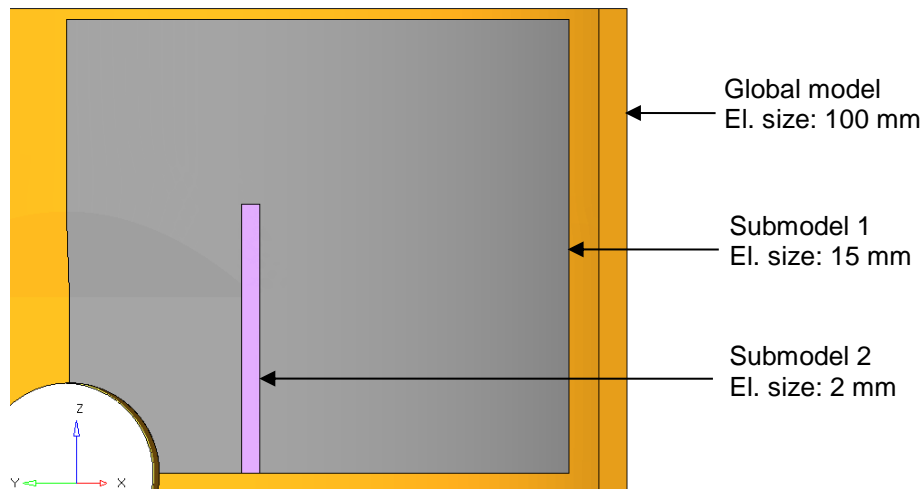


Figure E 7.4 Principal of liner submodel 1 and 2.

Finite element model size

The general element size in the first liner submodel is 15 mm and the element size for the second submodel is 2 mm, see Figure E 7.4 above. The size of the finite element submodel with a 15 mm element size is specified below:

- Number of elements: ~ 480 000
- Number of nodes: ~ 820 000
- Number of degrees of freedom: ~ 1 940 000

The size of the liner finite element submodel with a 2 mm element size:

- Number of elements: ~ 550 000
- Number of nodes: ~ 910 000
- Number of degrees of freedom: ~ 2 210 000

Results and evaluation

General

In this section the general results for the liner and the interacting structure near the equipment hatch (E/H) is presented. Focus is on liner strain and mechanisms generating elevated liner strain.

Requested output, asked for in [6], are presented in Appendix A7.

Displacement and contact

Figure E 7.5 and Figure E 7.6 show the radial and vertical displacement of the concrete surface in the region of the E/H liner model. The displacement is shown for the concrete part of the submodel, where all nodes are restrained by the displacement in the global model (see Section 7.2). The maximum radial displacement in this region agrees with the measured radial displacement in the E/H region (see Figure E 2.13).

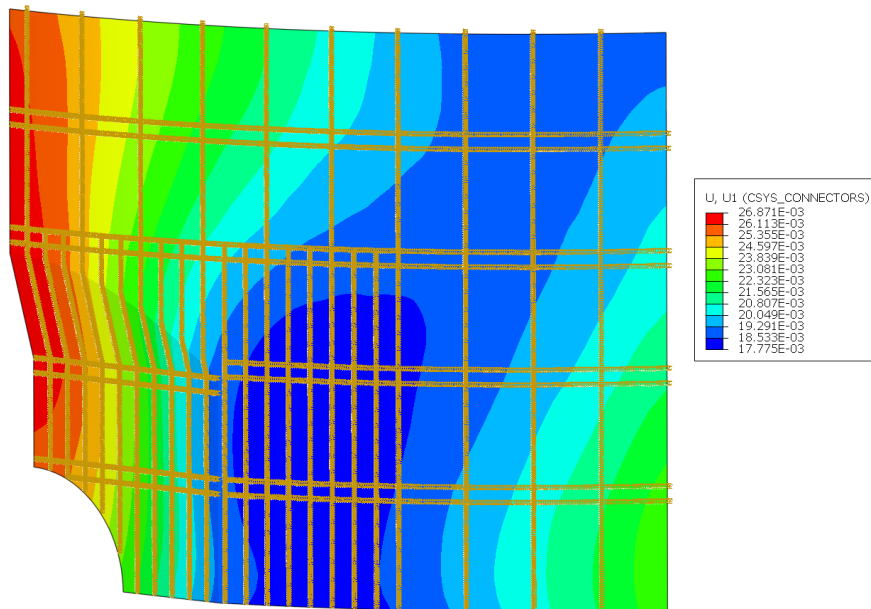


Figure E 7.5 Concrete inner surface, radial displacement at 1.29 MPa (3.3 p_d) in E/H region.

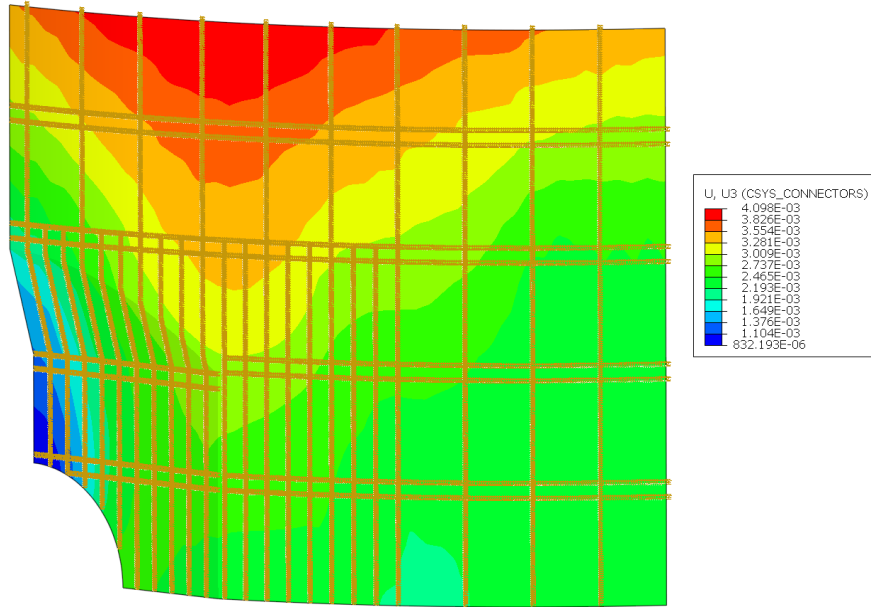


Figure E 7.6 Concrete inner surface, vertical displacement at 1.29 MPa (3.3 p_d) in E/H region.

Figure E 7.7 show the contact opening in the E/H region. In general the liner is in contact with the concrete wall. However, in border lines between the E/H embossment and the general curved containment wall (outgoing folds) the liner will be straighten out and separates from the concrete. This flexural behavior of the liner was also found in Anderson P. [28] where E/H of the Sandia $\frac{1}{4}$ model was investigated.

The size of the opening between concrete and liner strongly depends on the shear stiffness in the vertical liner anchors. Two different analyzes are carried out with different anchor shear stiffness values (see Section 4.4.3). The analysis with high shear stiffness gives a maximum contact opening of around 2.3 mm. The analysis with low shear stiffness gives a maximum contact opening of 3.2 mm. The shear displacement in connectors representing the anchor close to the vertical fold is given in Section 7.3.4.

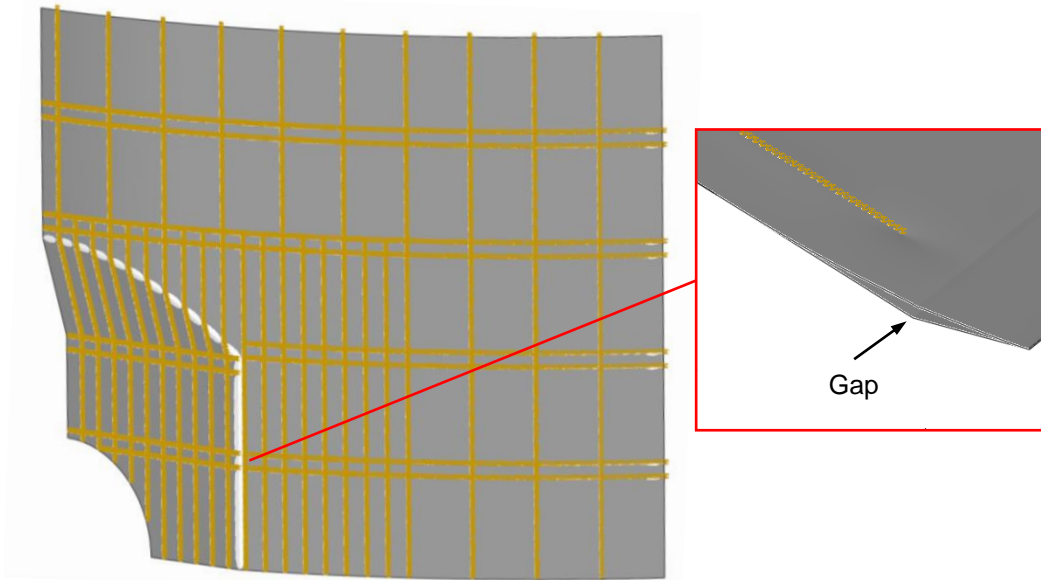


Figure E 7.7 Concrete inner surface, separation between concrete and liner at 1.29 MPa (3.3 p_d) in E/H region. White regions indicate where the liner has separated from the concrete.

Figure E 7.8 show the hoop sliding between concrete and liner. Sliding occurs especially in regions close to the outgoing folds and in regions where elevated concrete strain is indicated.

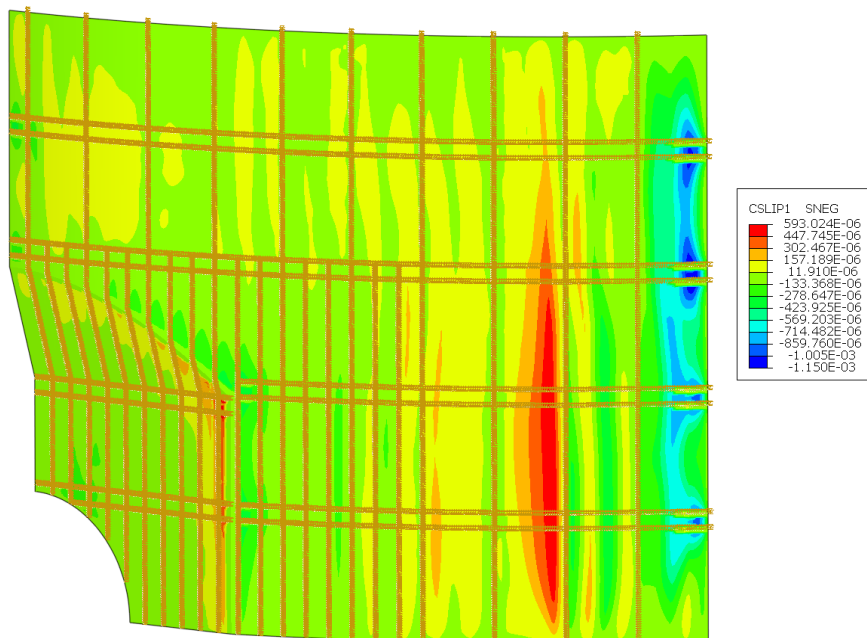


Figure E 7.8 Concrete inner surface, horizontal sliding between concrete and liner at 1.29 MPa (3.3 p_d) in E/H region (low anchor shear stiffness).

Liner strain

The liner strains are evaluated according to two different liner-concrete interaction assumptions, “bonded liner” and “free liner” (see SPE analysis definition, model 2 [6]). Liner strains for “bonded liner” are taken as equal to strain at the inner concrete surface and liner strains for “free liner” is evaluated from the liner model described in Section 7.2.

Figure E 7.9 show the strain at the inner concrete surface in the E/H region. Elevated strain can be seen in two regions (azimuth around 350° and around 5°) and the maximum strain in the hoop direction is around 1.5%. In the regions with elevated strain the horizontal reinforcement area is decreased. In the region close to the embossment (azimuth 300° to 350°) the horizontal reinforcement area is around 2.5 times the general reinforcement area. In the region just outside the embossment region (azimuth 350° to 5° and 285° to 300°) the horizontal reinforcement area is around 1.3 times the general reinforcement.

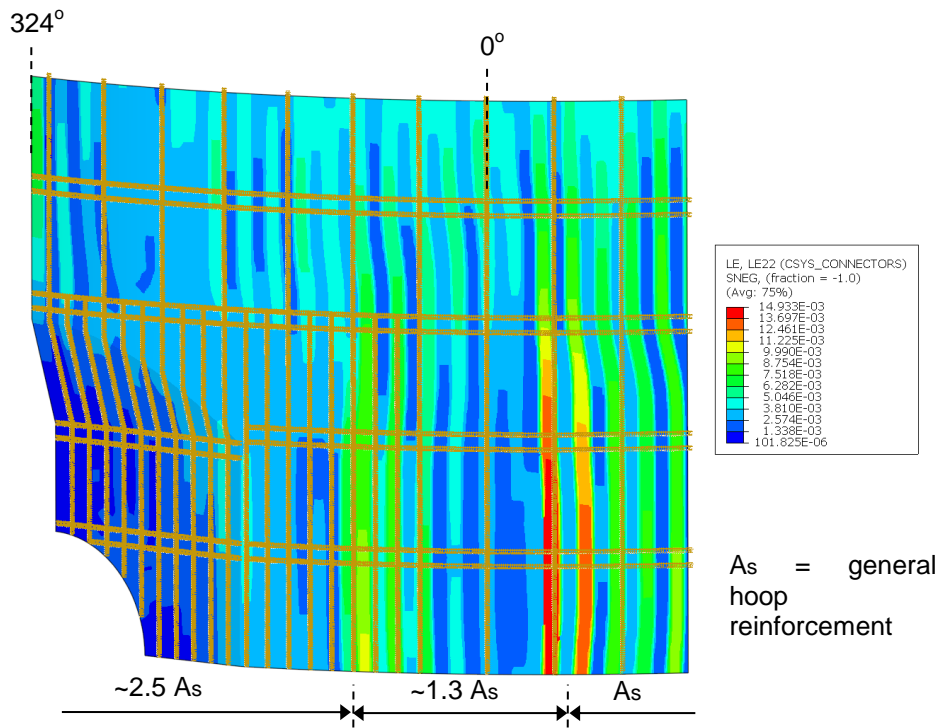


Figure E 7.9 Concrete inner surface, strain at 1.29 MPa (3.3 p_d) in hoop direction.

Figure E 7.10 shows the liner strain in the model where the liner is connected to the concrete by discrete connectors (see model description in Section 7.2). Elevated strains can be seen in the same regions as shown in Figure E 7.9 and the strain in these regions is around 0.8% (localized concrete strain is distributed between anchors).

However, elevated strain can also be observed in the region close to the outgoing fold which is straighten out during pressurization (see section 7.3.2). Due to the flexural behavior when the liner is straighten out the strain will increase locally in the fold and close to the nearest anchor

profile. To analyze the localized strain due to bending in the fold region a submodel with finer mesh is used. The results are presented in Section 7.3.3.1 below.

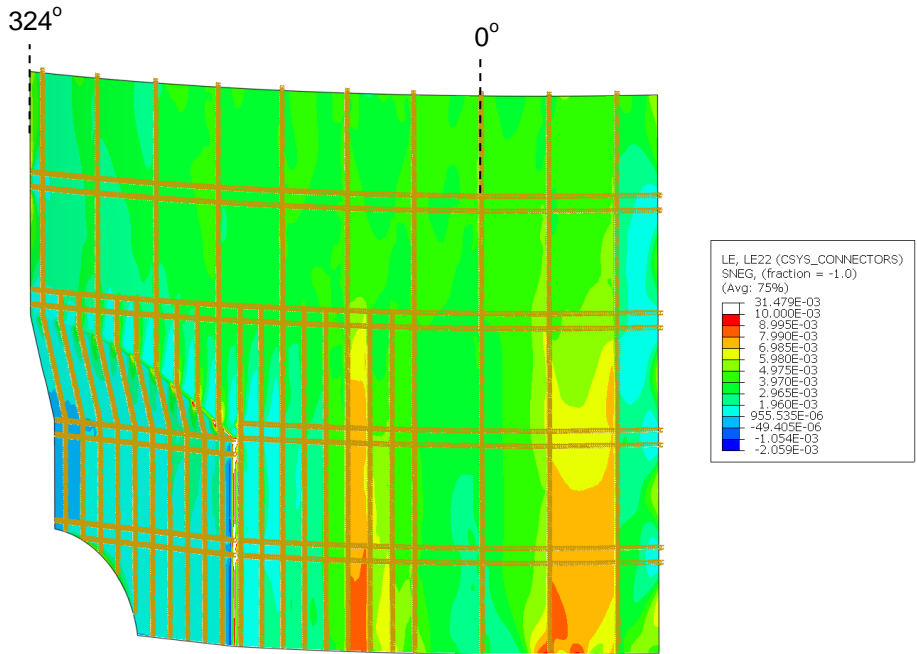


Figure E 7.10 Liner strain at 1.29 MPa (3.3 p_d) in hoop direction.

Liner strain in the outgoing fold

Figure E 7.11 show strain and displacement of the vertical fold analyzed by a detailed submodel. In the vertical fold the maximum tensile liner strain is around 5.7%. The highest strain values in the fold arise on the inside of the liner at the level of the horizontal stiffeners. The values presented here are given from the analysis with low anchor shear stiffness. High shear stiffness gives lower strain values, around 4.6%.

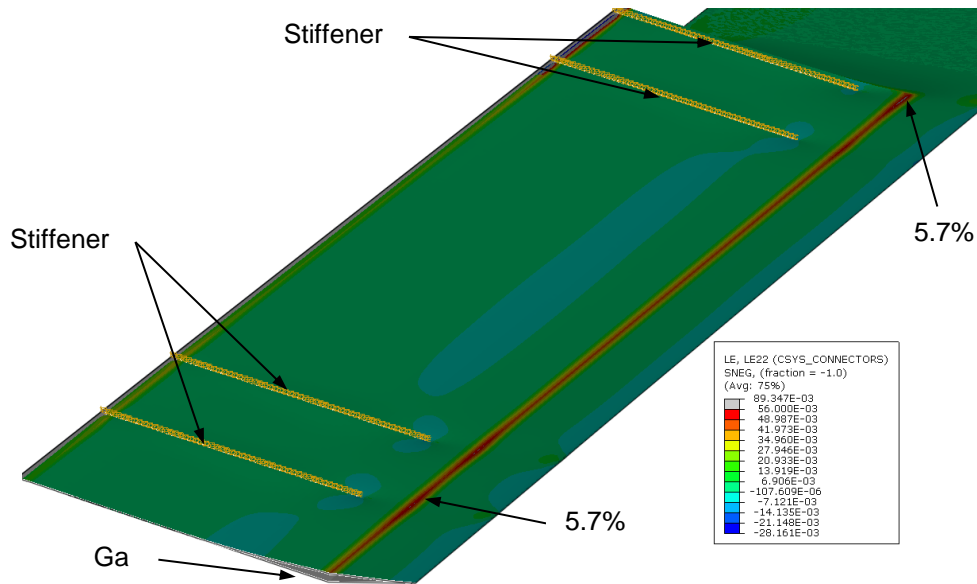


Figure E 7.11 Submodel 2, strain on liner inside at 1.29 MPa (3.3 p_d) in hoop direction.

Liner anchor

Figure E 7.12 shows the displacement in two connectors representing vertical anchor steels on each side of the vertical fold. Results from analysis with both stiff and soft anchors (see Section 4.4.3) are shown. The liner is sliding in the direction from the fold on both sides.

The liner part that contains the fold can be seen as a weak section and this causes an unbalance force in the anchor which causes the displacement in the anchors. If weaker shear stiffness is assumed, the anchor displacement increases and then also the liner strain in the fold increases.

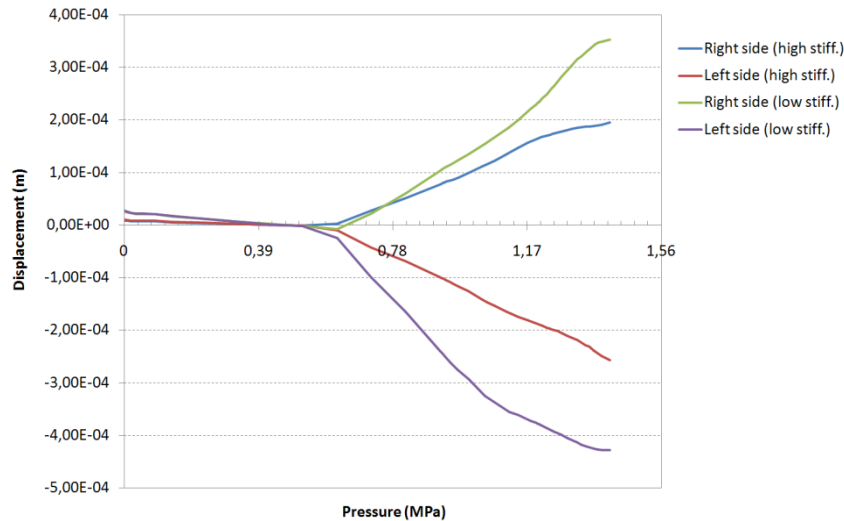


Figure E 7.12 Liner anchor shear displacement near to vertical bend line (both sides of bend line at around level +5500).

Summary

Three regions with elevated liner strain are found in the liner FE-model (see Figure E 7.10).

- Vertical fold between E/H embossment and general curved wall
- Along vertical line at azimuth $\sim 350^\circ$
- Along vertical line at azimuth $\sim 5^\circ$

The elevated strain along the vertical fold arises due to the flexural behavior when the liner is straightened out at high internal pressure. The strain level is concluded to strongly depend on the shear stiffness in the vertical anchors. Analyzes with two different shear stiffness values are carried out and for the weakest anchors the maximum tensile strain is 5.7% (see Figure E 7.11). The maximum strain in the vertical fold agrees with the location of tears found after the limit state test in the containment scale model (see Figure E 7.13).

The elevated strain found at azimuth 5° and 350° corresponds to the elevated concrete strain in the same region. The elevated concrete strain is concluded to be caused by the reduction hoop reinforcement in these regions. The maximum tensile liner strain found in this region is around 0.8% (see Figure E 7.10). The elevated strain at azimuth 5° agrees with the tears found after the limit state test in the containment scale model (see Figure E 2.6 and Figure E 7.13).

In Section 8 the failure strain is discussed. Two factors reducing the uni-axial failure strain are considered, biaxial stress state and welds. The failure strain level for the liner in the studied region is around 10% ($0.33 \times 0.5 \times 0.6$), assuming equal stress in vertical and horizontal direction.

The strain in the analysis is not reaching the failure strain according to Section 8. However, different factors not considered in the FE-models could generate elevated strain. As mentioned in [3] the liner thickness was reduced locally due to grinding which could localize the strain in these regions. Another factor which could increase the strain level locally is large concrete

cracks in combination with friction between concrete and liner. This effect is investigated in Anderson P. [29] and it is concluded that friction in combination with concrete cracks could give elevated strain especially for thin liners, as for the containment scale model.

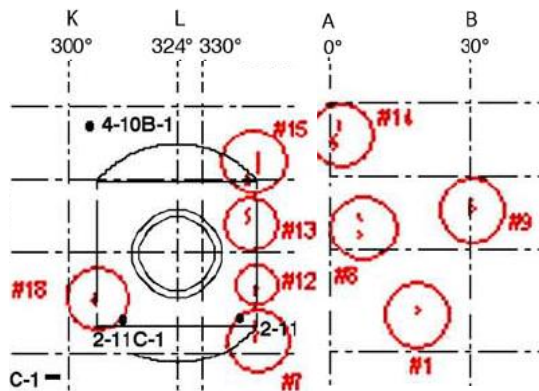


Figure E 7.13 Liner tears after limit state test in E/H region (extract from [3]).

LINER FAILURE MECHANISM

General

In this chapter the liner failure mechanism is discussed. To decide when a liner failure (liner tear) is initiated a ductility based criteria is utilized (see Section 8.2). The size of the failure can not be determined by a ductility based criteria. In Section 8.3 the failure size is studied by a method based on fracture mechanics. The size of a tear is evaluated for a general liner field with increasing displacement load. The study in Section 8.3 will be continued in phase 2 of the SPE project (see [6]), where focus is on containment leakage prediction.

Initiation of liner failure

The uniaxial ultimate elongation (ϵ_u) was measured in tensile tests and the average value was concluded to be 0.33 (see Section 4.4.2.3). The failure strain for the real structure is in this report assumed to be reduced due to welds and multi-axial stress state. In the pretest analysis for the Sandia 1:4 project [27] these two factors is considered.

An empirically based strain failure criterion is used where the liner stress state is taken into account. This criterion is based on Davis triaxiality factor TF , where the von Mises strain at failure (ϵ_f) is determined from the expression below.

$$\epsilon_f = \epsilon_u \times 2^{(1-TF)}$$

For the stress state of interest (no compressive membrane stresses and insignificant out of plane stress) TF is defined as

$$TF = \frac{\sigma_1 + \sigma_2}{\sqrt{\sigma_1^2 - \sigma_1\sigma_2 + \sigma_2^2}}$$

where σ_1 and σ_2 are principal stresses in the plane of the liner and tensile stresses are considered as positive.

If $\sigma_1 = \sigma_2$ the reduction of failure strain due to biaxial stress state is 50% according to the expression above.

Tensile tests on welded specimens were made within the Sandia 1:4 project and the results are presented in the Sandia ¼ report [3]. The test setup was identical to the tests made on virgin material, except for a weld orthogonal to the tensile direction. It is concluded in the Sandia ¼ pretest report [27] that there are only small effects of welding on the yield and ultimate strength, but the ultimate strain is highly influenced. Based on the tensile tests with welds, the reduction of failure strain near welds is assumed to be around 40% (see [27]).

Other factors, not captured by the FE-analyses, will also influence the liner failure. As described in Section Figure E A 2, the liner was grinded in connection with welding, which resulted in localized areas with thinner liner. This fact will of course influence the initiation of liner failure and have to be considered when the analysis results are evaluated and compared with the test results.

Size of liner failure

Structural model

In this section crack propagation is investigated. A finite element model of a simplified part of the liner is modeled as shown in Figure E 8.1. The structure has been simplified in a sense that two adjacent horizontal stiffeners are modeled as one stiffener and since the radius of curvature of the containment is large compared to the modeled part, plane stress conditions are assumed. Further, the liner is considered as detached from the concrete containment wall. The only contact is at the T-anchors and the stiffeners.

The analyzed section where a crack has been postulated is surrounded by unflawed sections in order to reduce boundary effects. The vertical T-anchors and the horizontal stiffeners are modeled as planar beam elements. The liner is modeled using plane stress elements. The size of the elements in the cracked section is 2x2 mm leading to approximately 87500 elements (depending on the size of the postulated crack). The number of elements in the surrounding unflawed sections is 14702.

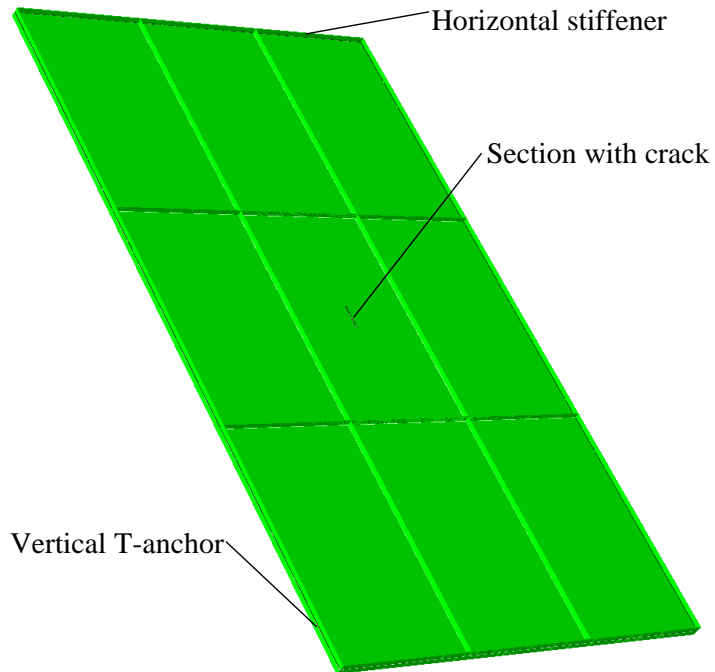


Figure E 8.1 Planar model of a part of the liner.

The boundary conditions are described in Figure E 8.2. Each section between T-anchors and stiffeners has the dimensions 450x780 mm. At $3.3p_d$ the average circumferential global strain of the containment is $\varepsilon_x = 0.42 \%$ and the average vertical strain is $\varepsilon_y = 0.1 \%$. The boundary conditions at $3.3p_d$ are prescribed as follows:

$$u_0 = 0 \cdot 450 \cdot 0.0042 = 0$$

$$u_1 = 1 \cdot 450 \cdot 0.0042 = 1.89 \text{ mm}$$

$$u_2 = 2 \cdot 450 \cdot 0.0042 = 3.78 \text{ mm}$$

$$u_3 = 3 \cdot 450 \cdot 0.0042 = 5.67 \text{ mm}$$

and

$$v_0 = 0 \cdot 780 \cdot 0.001 = 0$$

$$v_1 = 1 \cdot 780 \cdot 0.001 = 0.78 \text{ mm}$$

$$v_2 = 2 \cdot 780 \cdot 0.001 = 1.56 \text{ mm}$$

$$v_3 = 3 \cdot 780 \cdot 0.001 = 2.34 \text{ mm}$$

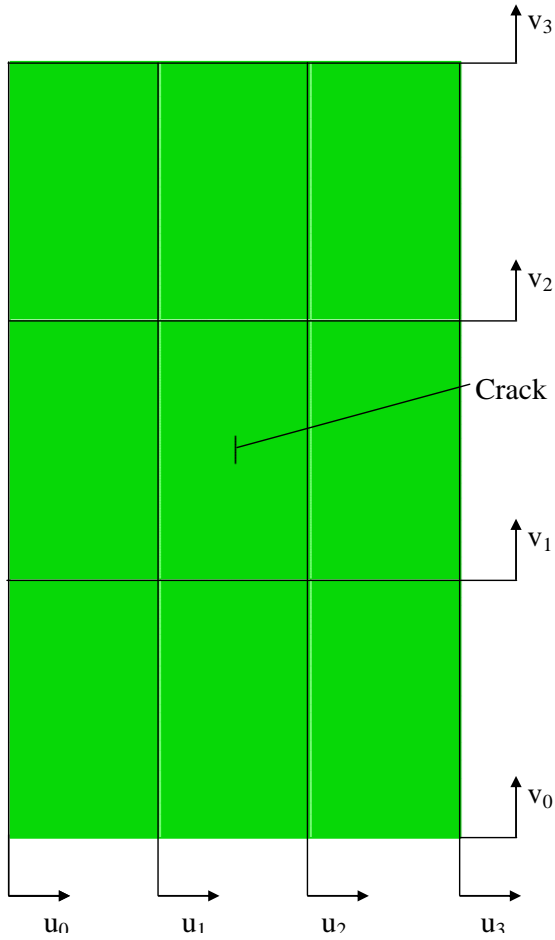


Figure E 8.2 Boundary conditions.

The model is analyzed using two material models. One linear elastic material model with a modulus of elasticity of $E = 220$ GPa and poisons ratio $\nu = 0.3$. The other material model is an isotropic von Mises plastic material model with a behavior as shown in Figure E 8.3.

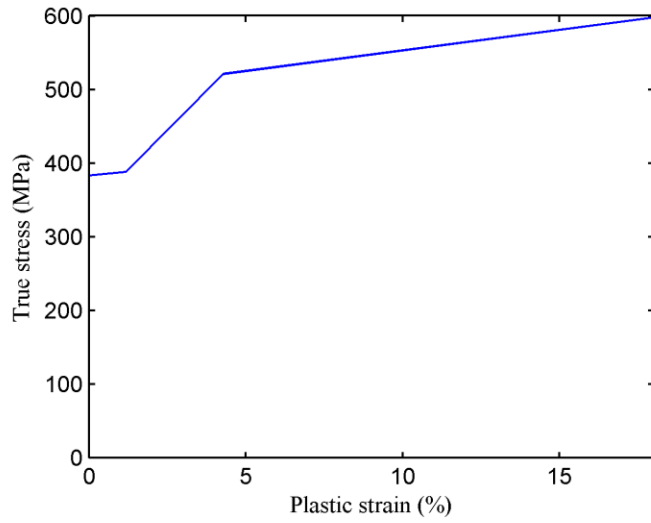


Figure E 8.3 Plastic material model.

The crack is modeled by removing elements from the mesh as shown in Figure E 8.4. A larger crack is created by simply removing more elements on each side of the crack.

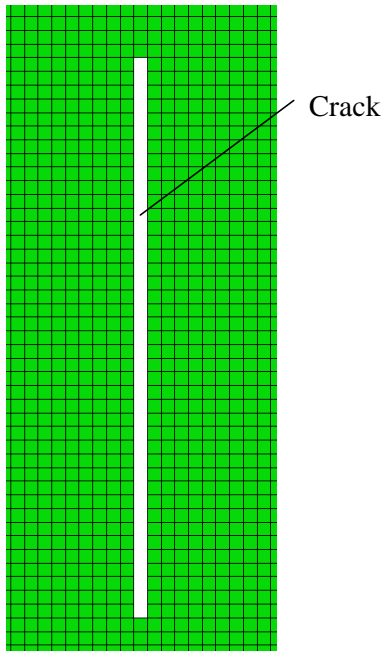


Figure E 8.4 Crack model.

Analyses

Convergence

In order to verify that the number of elements is sufficient for accurate calculation of the J-integral, the section with the crack is isolated and compared with linear handbook solutions. The simplified model is shown in Figure E 8.5.

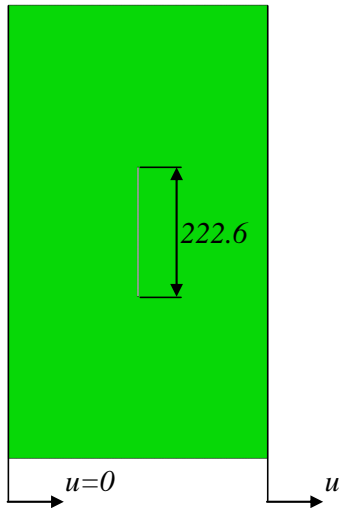


Figure E 8.5 Simplified model for convergence check.

The stress intensity factor K_I is calculated for a prescribed boundary displacement $u = 2.835$ mm with geometry and linear material parameters as given above. The finite element solution gives $K_I = 671 \text{ MNm}^{-3/2}$, and a handbook solution gives $K_I = 669 \text{ MNm}^{-3/2}$. This corresponds to a discrepancy of 0.3 %.

LEFM analyses

In order to achieve an estimate of critical crack length the stress intensity factor K_I is calculated. K_I can only be calculated for linear elastic materials. Linear Elastic Fracture Mechanics is commonly abbreviated LEFM.

In LEFM a crack propagates if K_I exceeds a critical value. This critical value, K_{cr} , is a material property denoted fracture toughness. The condition for crack propagation is:

$$K_I \geq K_{cr}$$

Typical values of fracture toughness of common steel materials are in the range 20-200 $\text{MNm}^{-3/2}$.

Although the liner experience global plastic deformation at approximately $\epsilon_x = 0.17$ % and $\epsilon_y = 0.04$ %, an estimate of K_I is determined for $\epsilon_x = 0.42$ % and $\epsilon_y = 0.10$ %.

The relation between the J -integral and the K factors under linear elastic plane stress conditions is:

$$J = \frac{K_I^2 + K_{II}^2}{E}$$

According to the SPE analysis definition [6] a typical value of J_{cr} is 61.3 kNm/m^2 (350 in-lb/in^2). Using $K_I = K_{cr}$ and $K_{II} = 0$, the corresponding fracture toughness is obtained as $K_{cr} = 116 \text{ MNm}^{-3/2}$.

By analyzing the FE-model as shown in Figure E 8.1 with linear elastic conditions for different crack lengths and comparing K_I with K_{cr} , a critical crack length is obtained to 10 mm. The corresponding value of K_I is $115 \text{ MNm}^{-3/2}$.

Non-linear analyses

Since the liner undergoes global plastic deformation at $3.3p_d$, non-linear fracture mechanics evaluation is needed which is introduced by using the material model shown in Figure E 8.3. The method used is to create a crack as shown in Figure E 8.4. The J -integral is calculated for the postulated crack. If the J -integral is larger than J_{cr} a new larger crack is created by removing elements on each side of the crack. A new analysis is then performed for the new postulated crack. It should be mentioned that each analysis is independent of each other. New larger cracks are postulated until the J -integral possibly decreases to J_{cr} .

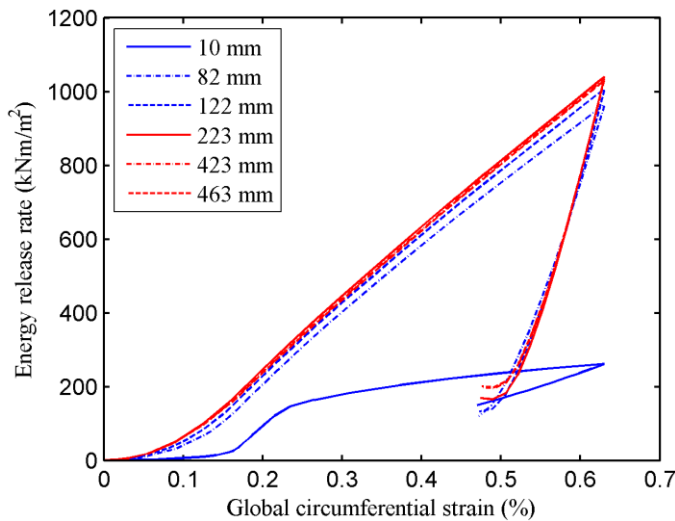


Figure E 8.6 J-integral versus strain and crack length.

The J -integral as a function of applied circumferential strain and crack length is presented in Figure E 8.6. The result reveals that the J -integral increase until the crack reaches 223 mm. Further increase of crack length leads to a slight decrease of the J -integral. The values obtained are however in great excess of the critical value $J_{cr} = 61.3 \text{ kNm/m}^2$. This indicates that no crack arrest is present, at least not until the crack reaches the stiffener or the T-anchor.

Further investigation needs to be performed. One mechanism which can have a great influence on the energy release rate is the friction between the liner and the concrete.

INFLUENCE OF STRUCTURAL PARAMETER VARIATION

General

The final objective of the SPE project is to develop methods for predicting leakage as function of pressure and temperature in the probabilistic space (see SPE Analysis Definition [6]).

Dameron et. al. [26] presents a methodology aimed to predict liner failure where uncertainties are taken into account (referred to in SPE [6]). The total peak strain (ϵ_p) for a specific discontinuity is in [26] proposed to be calculated according to the expression below,

$$\epsilon_{peak} = KB\epsilon_{global}$$

where K is the strain concentration factor, B is a factor taking the biaxial stress state into account and ϵ_{global} is the global strain in the region of the discontinuity. Each factor is evaluated separately for each specific locations and increasing internal pressure. Total peak strain (ϵ_{peak}) exceeding the uniaxial failure strain is defined as failure (followed by leakage).

Each parameter in the expression above includes both uncertainties in input data and model uncertainties. In the proposed methodology in [26] the included factors are assumed to be statistically independent random variables. The final total peak strain (ϵ_{peak}) is expressed as the product of average values ($KB\epsilon_{global}$) multiplied by a random variable with a unit average and a standard deviation including scattering from all three factors. A hypothetical example of the total peak strain (ϵ_{peak}) curve is shown in Figure E 9.1, where $P(\epsilon_p > \epsilon_{uf})$ represents the probability of liner failure for a certain pressure.

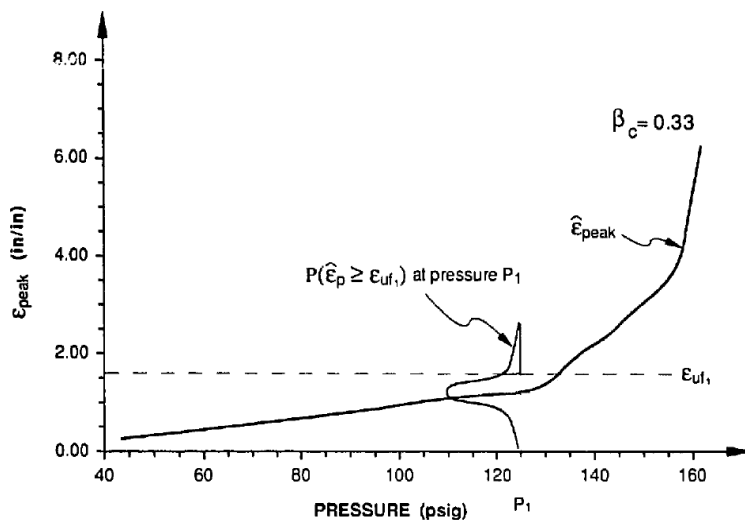


Figure E 9.1 Probabilistic definition of peak strain as function of the internal pressure.

In the study presented in this chapter focus is on evaluating the randomness in global strain (containment global expansion). The objective is to describe the variation in global strain at different pressure levels, due to uncertainties in input parameters. The evaluation will be carried out using a simple structural model describing the midheight expansion of the containment model. Variation in input parameters are described in Chapter 4 and the scatter in global strain are evaluated by a number of numerical simulations where the input parameters for each simulation are randomly selected (Monte Carlo simulation).

NUMERICAL SIMULATION

Structural model

The structural model describing the containment radial expansion can be seen as a horizontal slice affected by pure tensile load. Nonlinear behavior is considered for steel and concrete. The steel materials are approximated as ideal plastic and the concrete behavior after concrete cracking is described by a tensioning stiffening model described in [11]. The simulation is made up to yielding of the steel tendons, which corresponds to around 0.5 % global strain. If the tension stiffening effect of concrete is disregarded six different stress/strain states, with linear behavior in between, is described by the model. In Figure E 9.2 these stress/strain states are indicated, (1) zero pressure, (2) just before concrete cracking, (3) just after concrete cracking, (4) liner yielding, (5) reinforcement yielding and (6) tendon yielding. The tension stiffening effect is considered up to reinforcement yielding with a four piece linear curve (see Figure E 9.2).

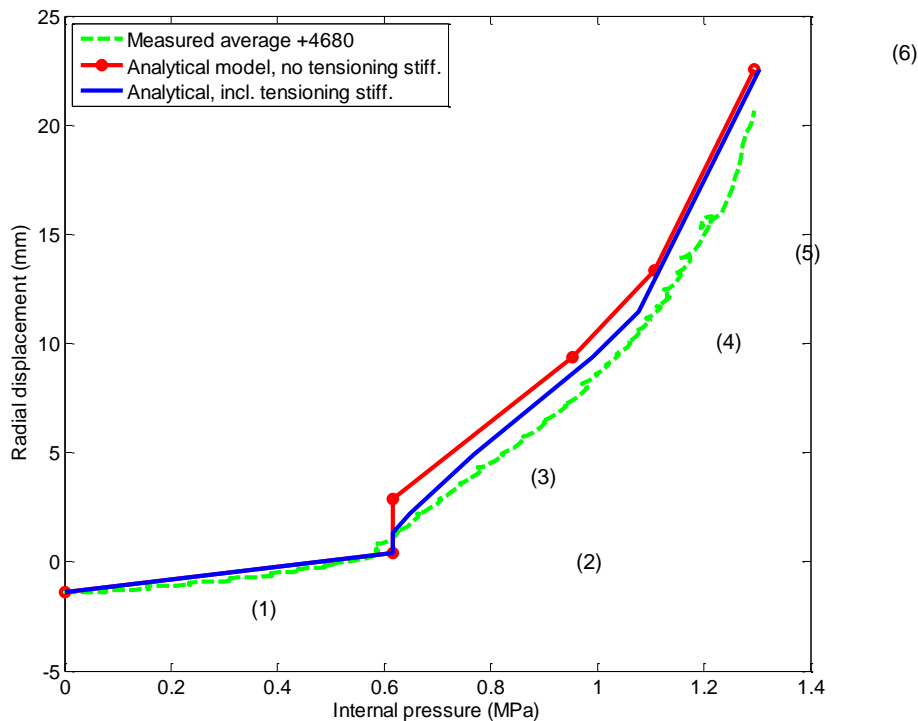


Figure E 9.2 Radial displacement vs. internal pressure for analytic “slice” model (with and without concrete tension stiffening) and measured displacement at +4680.

In Figure E 9.2 results from the analytical model, using average input parameters (see Table E 9.1), are compared with the average measured global radial displacement at midheight of the containment model. It can be concluded that the radial displacement show quite good agreement with the measured displacement. The structural model seems to capture the main characteristics in containment midheight and therefore should also the model be able to show the effect of variation in input parameters on the global displacement.

Input parameters

In Table E Table E 9.1 the statistic variables are summarized for each input parameter used in the numerical simulation presented in this chapter. In general the average value is evaluated from the tests or measurements in the containment model project. The coefficient of variation (COV) and the distribution type is in general taken from JCSS [15], also see Chapter 4.

Table E 9.1 Input parameters used in numerical simulation (see Chapter 4).

Input parameter		Average value	Coefficient of variation	Type of distribution
Concrete	Cross-section area	0.325 m ² /m	-	Deterministic
	E-modulus	26.8 GPa	15% ¹⁾	Log-normal
	Tensile strength	2.1 MPa	15% ¹⁾	Log-normal
Liner	Cross-section area	1800 mm ² /m	-	Deterministic
	E-modulus	220 GPa	-	Deterministic
	Yield strength	383 MPa	2%	Log-normal
Reinforcement	Cross-section area	2800 mm ² /m ³⁾	-	Deterministic
	E-modulus	185 GPa	-	Deterministic
	Yield strength	460 MPa	2%	Normal
Tendon	Cross-section area	2950 mm ² /m	-	Deterministic
	E-modulus	191 GPa	2%	Normal
	Yield strength	1690 MPa	2%	Normal
Prestress ²⁾ stress	Tendon initial	850 MPa	6%	Normal
Geometry	Radius	5.375 m	0.1%	Normal

1) All concrete parameters are assumed to have a COV of 15%.

2) Average tendon force along horizontal tendon.

3) General horizontal reinforcement.

Results

Figure E 9.3 show the results from 1000 simulations where input parameters are randomly selected according to statistical properties given in Table E 9.1. Before concrete cracking the variation in radial displacement is small. After cracking the variation increases and seems quite constant up to tendon yielding. The scatter in cracking pressure is large due to the large variation in prestress and concrete tensile strength. Considering the main objective, to predict liner failure and leakage, the radial displacement in the region of liner yielding and above is of interest. In the next section (Section 9.3) the scatter at the pressure 0.95 and 1.25 MPa is analyzed more in detail.

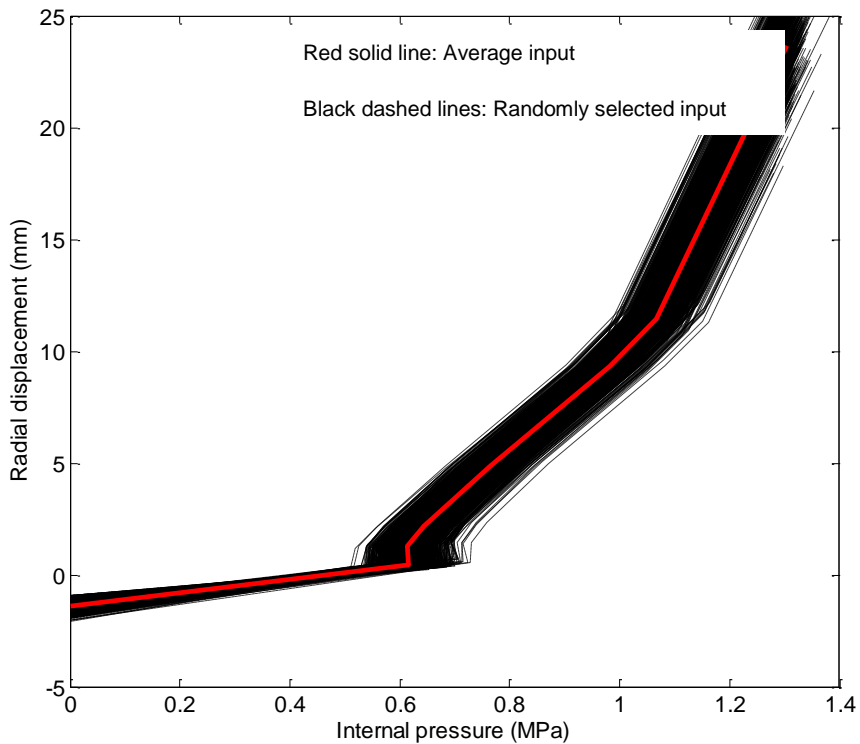


Figure E 9.3 Radial displacement vs. internal pressure for analytic slice model including tensioning stiffening effect.

The scatter shown in Figure E 9.3 originates from the variation described in the different input parameters (see Table E 9.1). To show the size of influence from different parameters the isolated variation from some parameters are shown in Figure E 9.4. It can be concluded from Figure E 9.4 that the main scatter in global displacement shown in Figure E 9.3 originates from prestress and to some extent also from concrete tensile strength.

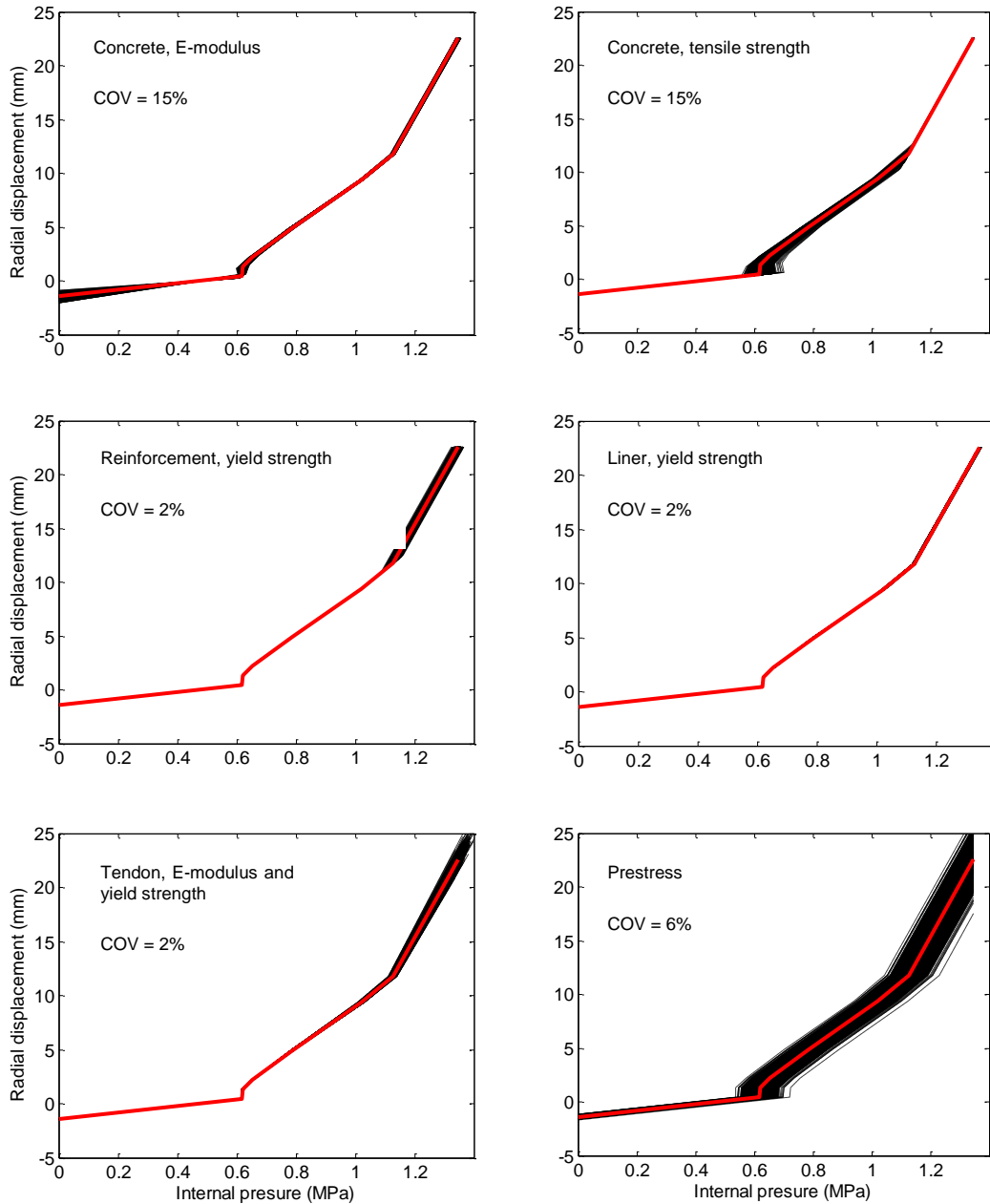


Figure E 9.4 Isolated variation for different input parameters. The parameter with included variation is given in each diagram where other parameters are kept constant.

Statistical evaluation

Results are evaluated at two pressure levels at 0.95 MPa (before liner yielding) and at 1.25 MPa (after reinforcement yielding). Histogram of the simulated displacement together with the analytical density function for the normal distribution function is shown in Figure E 9.5. It can be concluded from Figure E 9.5 that the normal distribution function fits well to the simulated values for the two pressure levels. If the displacement is showed in a normal probability plot it can be

seen that the results fits better to the normal than to the log-normal probability function. For the pressure levels studied in Figure E 9.5 the COV is 7.4% respectively 7.3%.

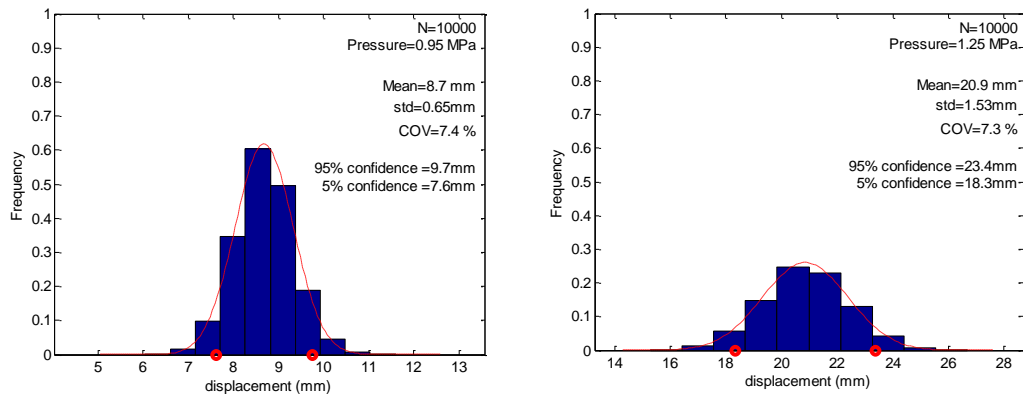


Figure E 9.5 Histogram of the simulated displacement together with the analytical density function. Red dots indicate the 5 and 95% confidence interval. (N = number of simulations, std = standard deviation).

Summary

The midheight displacement (global displacement) is evaluated by a simple analytical model describing horizontal slice affected by pure tensile load. A comparison between results from the analytical slice model and measured radial displacement show good agreement.

Statistical input data used in the simulations are given in Table E 9.1 (evaluated in Chapter 4) and the results are shown in Figure E 9.3. It is concluded that the scatter in midheight displacement increases after concrete cracking and is thereafter quite constant up to tendon yielding. The scatter is concluded to originate mainly from prestress and to some extent also from concrete tensile strength (see Figure E 9.4). The displacement result is evaluated at 0.95 and 1.25 MPa and it is concluded that the COV is around 7.5% at both these pressure levels.

CONCLUSIONS

This chapter presents the conclusions of the report. General conclusions are given in Section 10.1 and the specific conclusions from the four different studies are given in Section 10.2 to 10.5.

General

The overall scope of the SPE project is to increase the knowledge of the nonlinear response of containment structures exposed to high internal overpressure. In the SPE project, round robin exercises are performed in order to compare structural analysis results with test data from the Sandia 1:4 test (see [3]). The round robin exercises of the SPE project is divided in two work phases, where this report considers phase one.

The main objective of this report is to explain the effects of structural interaction between containment steel components and cracked concrete. Also the failure mechanism of the steel liner and the effect of variation in input parameters are considered. Four specific studies are

carried out regarding prestressing tendon behavior, containment global response, liner behavior near equipment hatch and the influence of structural parameter variation.

The global deformation in midheight parts of the containment is concluded to be more or less independent of the vertical stiffness of the structure. It is shown that the radial displacement of a horizontal slice model agrees well with the radial displacement in midheight of the global 3D-model and the measurements. It is also concluded, that for higher pressure levels (above $\sim 2.0p_d$) the concrete in hoop direction becomes nearly stress less. At high pressure levels the stiffness in midheight only depends on the steel components included in the wall cross section (liner and horizontal reinforcement / tendons).

Global deformation of the containment is shown to be highly influenced by the prestress level in the structure also after concrete cracking. It is therefore important to consider the prestress level when the risk of liner failure is evaluated.

The prestressing system is shown to influence the load level when the final global failure takes place. The final global failure in the 3D model is shown to occur just after a large number of tendons are yielding. In the tendon study it is shown that the force along the tendon will be equalized just before general tendon yielding occurs. Due to this, the load level when general tendon yielding arises will depend on the initial average prestress in the tendons. It is concluded that tendons with higher friction loss will yield later than tendons with low friction loss in the 3D model. This fact could be important to observe considering the “leak before break” behavior of reactor containments. Assuming the same prestress level in the containment structure, a structure with low tendon force along the tendons (high loss) will have higher probability for “leak before break” than a containment structure with high tendon force (low loss).

In the detailed study of the liner it is shown that the highest strain level occurs in the vertical fold close to the equipment hatch when the liner is straightened out during pressurization. In general, the non-linear plastic behavior of the liner is concluded to be very sensitive to the detailed design and the interaction between concrete and liner.

Prestressing tendon behavior

The scope of this study is to explain the interaction between horizontal tendons and the containment structure. The study is carried out by using a FE-model describing a horizontal slice of the containment wall.

It was observed in the scale model test that the initial force distribution along horizontal tendons seems to be equalized during pressurization. This behavior is also found in this study. A slight redistribution occurs at pressure levels up to around $3.0p_d$. However, the major redistribution in the model occurs at pressure levels exceeding $3.0p_d$, when some parts of the tendon starts to yield. At $3.3 p_d$ (end of limit state test) the force along the tendon is more or less equalized and all parts of the tendon is yielding. The main part of the redistribution in the tendon is concluded to be caused by local yielding in combination with the possibility for the tendon to slip.

Containment global response

The scope of this study is to describe the global structural response during pressurization with focus on the behavior near the equipment hatch. In this study an FE-model describing the whole containment model structure is used. The displacement results from this model, in the region of the equipment hatch, are used as boundary conditions for the liner studies.

The radial displacements at the predefined standard output locations in the finite element model are in general concluded to agree well with the measured radial displacement.

The maximum radial displacement, for pressure levels after general hoop concrete cracking ($\sim 1.6p_d$) up to the final limit state pressure ($3.3p_d$), is located close to the large penetrations (equipment hatch and airlock). At the final limit state pressure ($3.3p_d$) the maximum displacement in the global model is 27 mm. When the pressure is increased further the radial displacement suddenly increases more rapidly. At the pressure when the structure failure mode test is finalized ($3.62p_d$), the maximum radial displacement is around 80 mm. The maximum displacement for pressure levels above final limit state pressure ($3.3p_d$) occurs above the large penetrations (around elevation 8 m).

It is assumed that the radial displacement, for pressure levels below pressure $3.3p_d$, mainly is influenced by the prestress level. The maximum radial displacement for lower pressure levels is therefore located in the region of the large penetration where the general prestress level is low due to high friction loss. For pressure levels exceeding pressure $3.3p_d$, the large displacement occurs in regions where tendons are yielding. General yielding of tendons occur first in regions where the friction loss is small (due to the higher general initial force). The maximum displacement, at pressure levels above $3.3p_d$, occurs around elevation 8 m due to the relatively small friction loss for hoop tendons in this region.

Concrete hoop cracking are initiated at the pressure $1.23p_d$ and this cracking occurs in the lower part close to the buttresses. The initial through wall cracks occur between the equipment hatch and the personnel airlock, at the pressure level $1.38p_d$. At the pressure $1.53p_d$ some concrete regions has no hoop strength left (fully cracked). Above pressure $2.0p_d$ the concrete in large midheight regions can be assumed completely cracked with no concrete tensile stiffness left. At these high pressure levels the hoop stiffness in mid height can be assumed to only depend of the steel components.

Liner behavior near equipment hatch

The scope of this study is to explain the detailed liner behavior of the steel liner near the equipment hatch. Focus is on explaining the liner tears observed in the containment model test. A detailed FE-model describing the steel liner and the interaction with the concrete structure is used. Also the failure criteria of the liner is discussed where the size of a tear in a general liner field is studied by a fracture-based failure method.

Three regions with elevated liner strain are found in the FE-model

- Vertical fold between E/H embossment and general curved wall
- Along vertical line at azimuth $\sim 350^\circ$
- Along vertical line at azimuth $\sim 5^\circ$

The elevated strain along the vertical fold arises due to flexural behavior when the liner is straightened out at high internal pressure. Analyzes with two different anchor shear stiffness values are carried out and for the weakest anchors the maximum tensile strain is 5.7%. The maximum strain in the vertical fold agrees with the location of tears found after the limit state test.

The elevated liner strain found at azimuth 5° and 350° corresponds to the elevated concrete strain in the same region. The elevated concrete strain is concluded to be caused by the

reduction of hoop reinforcement in these regions. The maximum tensile liner strain found in this region is around 0.8%. The elevated strain at azimuth 5° agrees with the tears found after the limit state test.

The failure strain level for the liner in the studied region is evaluated to around 10% (reduced due to welds and biaxial stress). The strain in the analysis is not reaching the failure strain. However, different factors not considered in the FE-models could generate elevated strain;

- The liner thickness was concluded to be reduced locally due to grinding which could localize the liner strain generally.
- Large concrete cracks in combination with friction between concrete and liner could localize the liner strain.
- The shear stiffness in the vertical anchor profiles is difficult to define, especially for cracked concrete. The liner strain in the fold is concluded to strongly depend on the shear stiffness (low stiffness give elevated strain).

The size of the failure can not be determined by a ductility based criteria. A study based on fracture mechanics is presented with the purpose to evaluate the size of a tear in a general liner field of the scale model. It is estimated that a crack will propagate for an initial crack length that exceeds 10 mm. A realistic final crack length is not found. However, this study will be continued in phase 2 where e.g. the influence of friction between liner and concrete will be evaluated.

Influence of structural parameter variation

The scope of this study is to describe the influence of variation in input data and to evaluate the effects on containment structural behavior. In this study focus is on the global expansion of the containment. The midheight radial displacement is evaluated by a simple analytical model describing a horizontal slice affected by pure tensile load. A comparison between results from the analytical slice model and measured radial displacement shows good agreement.

It is concluded from this study that the scatter in displacement increases after concrete cracking and is thereafter quite constant up to tendon yielding. The scatter is concluded to originate mainly from prestress and to some extent also from scatter in concrete tensile strength. It is also concluded that the total COV of the global displacement is around 7.5% at pressure levels critical for the liner (pressure > $2.0p_d$).

REFERENCES

- [1] Horschel D.S. (1988), Design, construction, and instrumentation of a 1/6-scale reinforced concrete containment building. NUREG/CR-5083, U.S. Nuclear regulatory commission (NRC).
- [2] Horschel D.S. (1992), Experimental results from pressure testing a 1:6-scale nuclear power plant containment. NUREG/CR-5121, U.S. Nuclear regulatory commission (NRC).
- [3] Hessheimer M. F., Klamerus E. W., Lambert L. D. and Rightley G. S. (2003), Overpressurization test of a 1:4-Scale prestressed concrete containment vessel model NUREG/CR-6810, U.S. Nuclear regulatory commission (NRC).

- [4] Hanson N.W., Schults D.M., Roller J.J, Azizinamini A. and Tang H.T. (1987), Testing of large-scale concrete containment structural elements. Nuclear Engineering and Design, v100, pp. 129-149.
- [5] Hanson N.W., Schults D.M., Roller J.J, Azizinamini A. and Tang H.T. (1987), Testing of large-scale concrete containment structural elements. Nuclear Engineering and Design, v100, pp. 129-149.
- [6] SPE, Final Analysis Definition (2010, September), Standard Problem Exercise on performance of containment vessels under severe accident conditions.
- [7] ISP-48 (2005, August), International Standard Problem 48 Containment Capacity, Phase 1-3, OECD.
- [8] Anderson P. (2007), Structural Integrity of Prestressed Nuclear Reactor Containments, PhD thesis, Lund University.
- [9] Anderson P., Jovall O (2007), Increased plastic strains in containment steel liners due to concrete cracking and discontinuities in the containment structure, SMiRT 19th.
- [10] Petersson P-E. (1981), Crack growth and development of fracture zones in plain concrete and similar materials, PhD thesis, Lund University.
- [11] Belarbi A., Hsu T. (1994 July-August), Constitutive laws of concrete in tension and reinforcing bars stiffened by concrete. ACI structural journal.
- [12] Kolmar W. and Mehlhorn G. (1984 September), Comparison of shear stiffness formulation for cracked reinforced concrete elements. Proceeding of computer-aided analysis and design of concrete structures, Split.
- [13] Kolmar W. (1986), Beschreibung der kraftuebertragung über risse in nichtlinearen finite-element-berechnungen von stahlbetontragwerken. Ph.D thesis. Darmstadt University of Technology
- [14] CEB/FIP (1990) Model Code, Design code, Bulletin D' information, No. 203, CEB, Lausanne.
- [15] JCSS (2001), Probabilistic model code. Printed from www.jcss.ethz.ch
- [16] DS Simulia. Abaqus Analysis User's Manual Version 6.9. 2009.
- [17] Boverket, Byggavdelningen. Boverkets handbok om stålkonstruktioner, BSK 07. 2007. Karlskrona. (in Swedish)
- [18] Dameron R, Chang P, Bogage A (2010 January) PCCV SPE3 Model 2 Results - TECH MEMO.

- [19] Johnson T E and Wedellsborg B W (1972, December), Containment building liner plate design report, Bechtel Corporation, rev. 1.
- [20] Boverket. Boverkets handbok om betongkonstruktioner, BBK 04. 2004. Karlskrona. (in Swedish)
- [21] Harrop LP. (1985), Strength for ungrouted post-tensioned tendons. SMiRT, vol H.
- [22] Anderson P, Hansson M, Thelandersson S (2008), Reliability-based evaluation of the prestress level in concrete containments with unbonded tendons, Structural Safety, vol 29.
- [23] Anderson P, Berglund LE, Gustavsson J (2005), Average force along unbonded tendons; a field study at nuclear reactor containments in Sweden, Nuclear Engineering and Design, vol 235.
- [24] ACI Committee 209 (1992), Prediction of creep, shrinkage and temperature effects in concrete structures, ACI 209R-92.
- [25] PCI Committee of Prestress Losses (1975), Recommendations for estimating prestress losses, Journal of the prestressed concrete institute, v 20, n 4.
- [26] Dameron R.A., R.S. Dunham, Y.R. Rashid, and H.T. Tang (1991), Conclusions of the EPRI Concrete Containment Research Program, Nuclear Engineering and Design, 125.
- [27] Dameron R- A., Zhang, L., Rashid Y. R. and Vargas M. S. (2000), Pretest Analysis of a 1:4-Scale Prestressed Concrete Containment Vessel Model, NUREG/CR-6685.
- [28] Anderson P (2008), Analytic study of the steel liner near the equipment hatch in a 1:4 scale containment model, Nuclear Engineering and Design, vol 238.
- [29] Anderson P (2008), Concentration of plastic strains in steel liners due to concrete cracks in the containment wall, International Journal of Pressure Vessels and Piping, vol 85.

TENSION STIFFENING EFFECT

Model

In this appendix a brief study is presented showing the tensioning stiffening effect for a simple reinforced concrete test model loaded by pure tensile load. The test model is a 2D FE model where the concrete is described by plain strain element¹ and the reinforcement by truss elements¹ which are embedded by the concrete elements. The geometry, boundary conditions and mesh are shown in Figure E A1.1. The length of the model is 2 m and the width is 0.325 m (width same as containment model wall thickness). Two reinforcement bars are included as shown in Figure E A1.1 and the load (displacement load) is applied in the reinforcement left ends. The right reinforcement ends are fixed in the longitudinal direction and both concrete end edges are fixed in the transverse direction. The concrete and reinforcement material properties are given in Section 4.2 and 4.3. Three different mesh sizes (3, 6, 12 elements in transverse direction) and three different reinforcement ratios (1, 2, 3%) are analyzed.

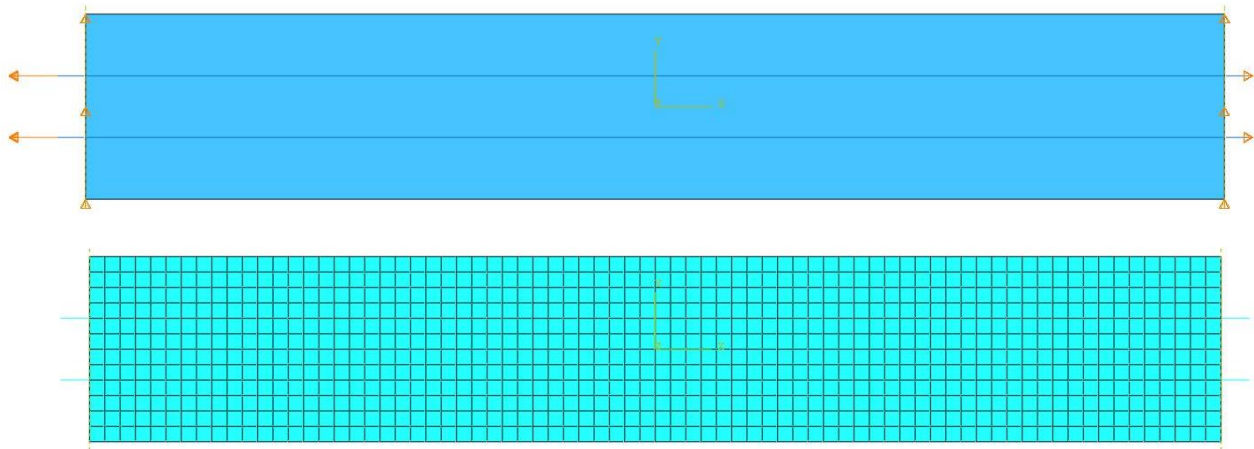
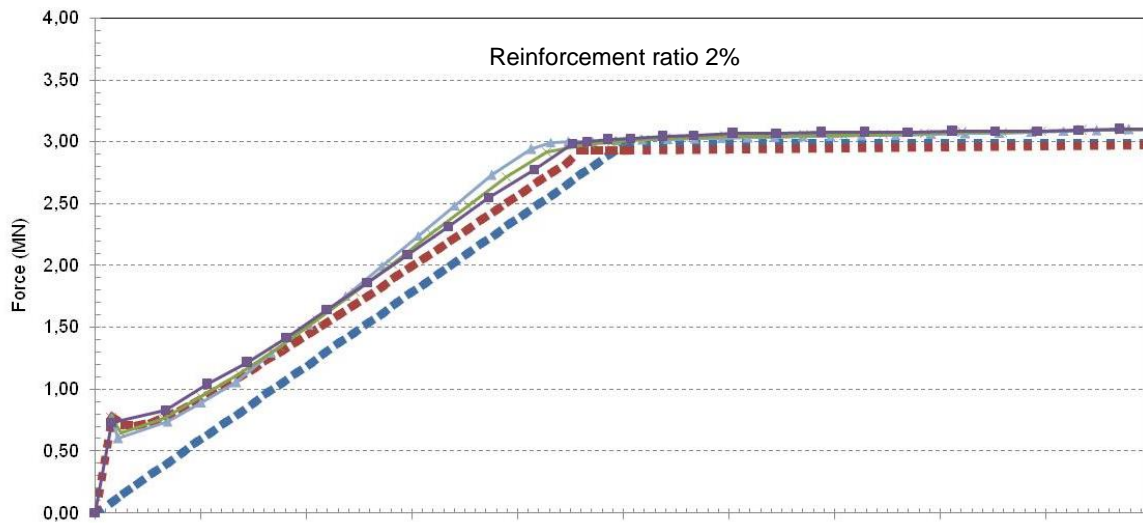
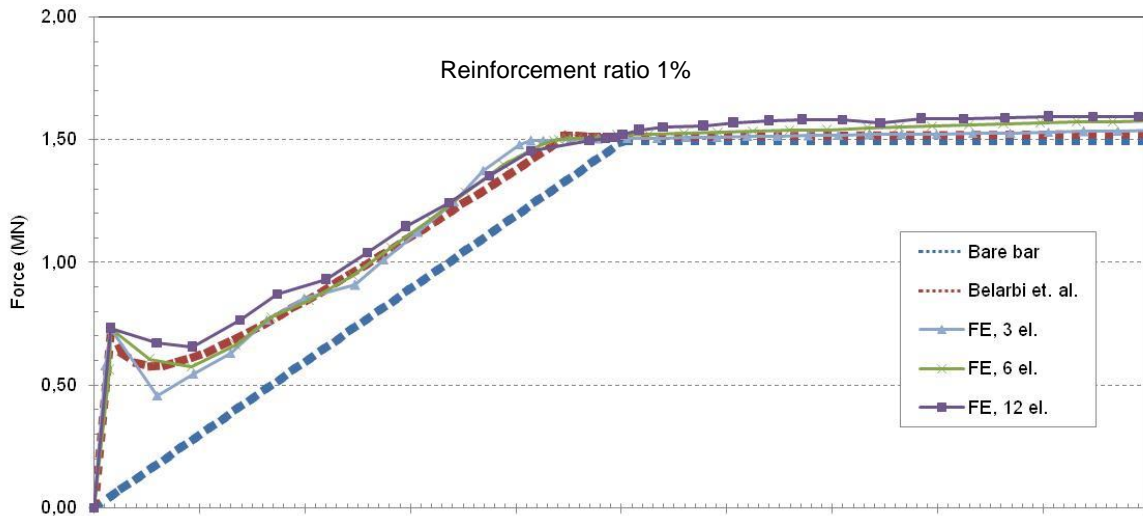


Figure E A1.1 Test model, geometry, boundary conditions and mesh (12 el.)

Results

Figure E A1.2 shows the average strain vs. total applied force for the totally nine different analyses. The results from the FE-analyses are compared with “bare bar” results (only reinforcement) and a tension stiffening model presented in Belarbi and Hsu [11]. It can be seen that the FE results for lower reinforcement ratio show better agreement with the model presented in [11] than higher ratio. For 2 and 3% ratio the FE-model show a slightly stiffer behavior than the model presented in [11], especially close to reinforcement yielding. The analysis with six and twelve elements gives more or less the same results, when the analysis with only three elements in the transference direction gives slightly different results.

¹ Abaqus/Explicit, plain strain elements CPE4R, Truss elements T2D2.



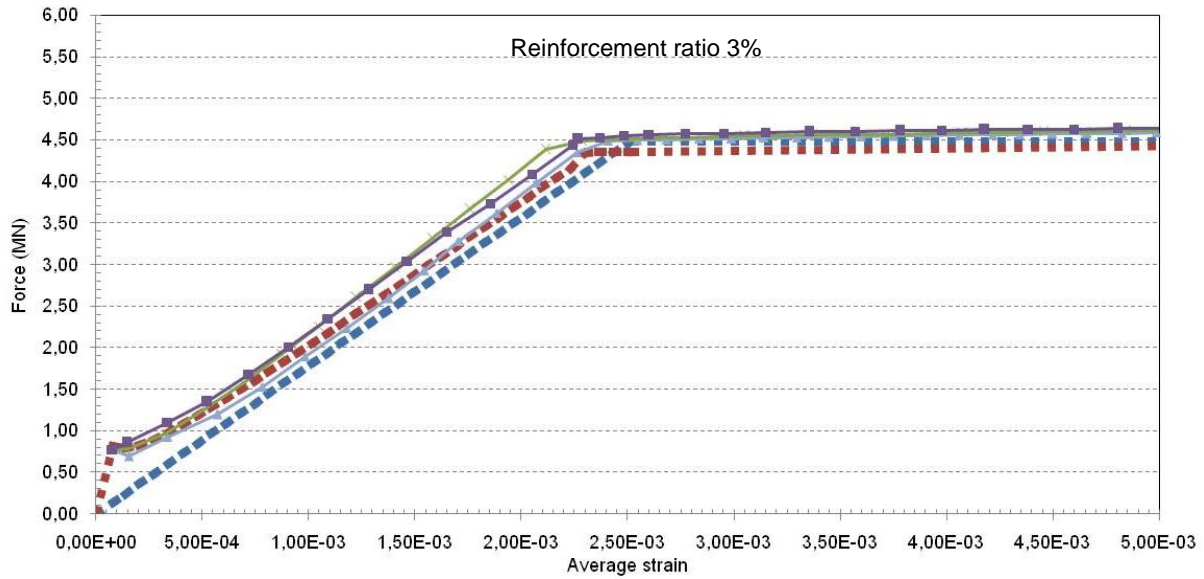


Figure E A1.2 Total force vs. average concrete strain from FE-models and reference models (observe, different force scale).

Figure E A1.3 show the concrete strain in the longitudinally direction at the load level just before reinforcement yielding. Grey regions in Figure E A1.3 have exceeded the strain level 0.56 % which corresponds to zero concrete stress (see Figure E 4.3). The average strain level is equal for each reinforcement ratio and the “pattern” of local strain (element strain) seems quite similar for all three reinforcement ratios.

Reinforcement ratio 1%

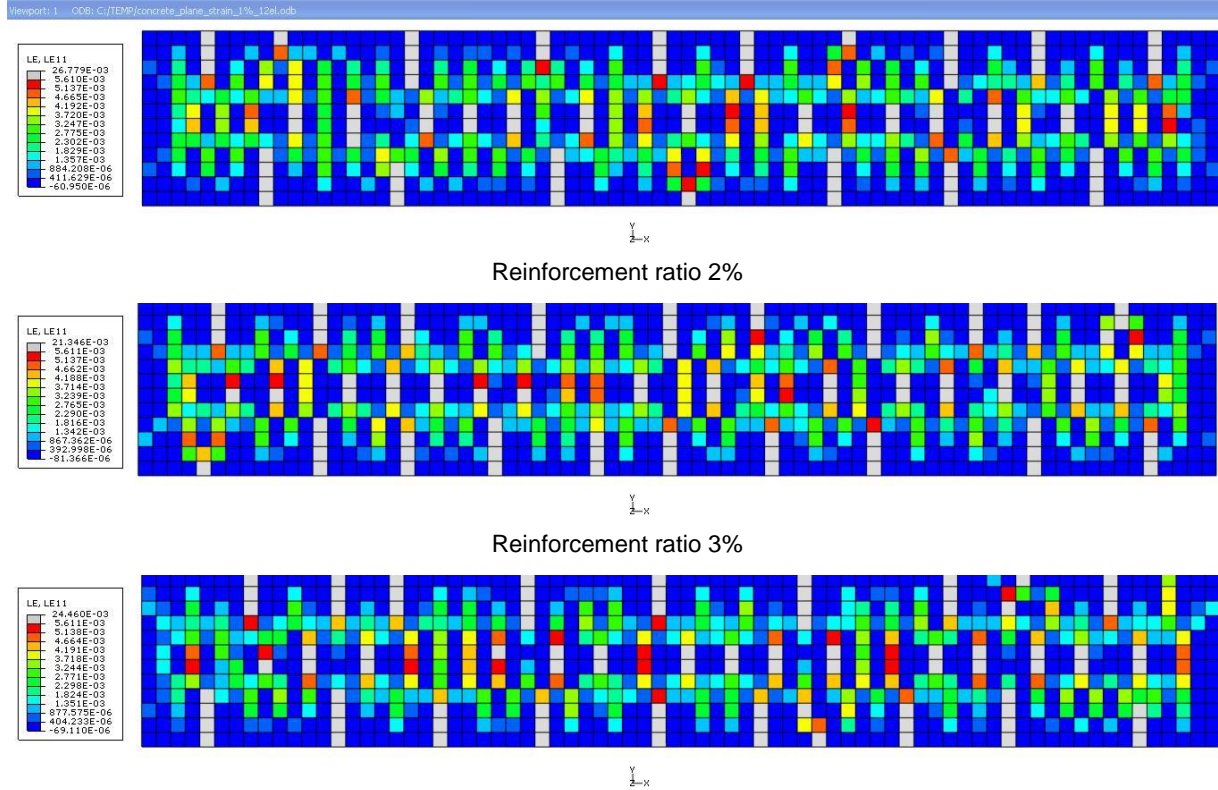


Figure E A1.3 Strain in longitudinal direction just before reinforcement yielding.

Conclusions

It can be concluded from the study in this appendix that the tension stiffening effect observed in the FE analysis results show quite good agreement with the results given from the model presented in Belarbi et. al. [11]. For higher reinforcement ratios (2 and 3%) the FE-model show a slightly stiffer behavior at strain levels near reinforcement yielding. The results from the analyses with only three elements in the transverse direction differ slightly from the results analyzed with finer mesh.

The used material model is concluded to describe the stiffness properties of cracked reinforced concrete with a sufficient precision for the studies presented in this report.

EVALUATION OF LOSS OF PRESTRESSING FORCE

In Figure E A2.1 forces along horizontal tendon No 38 and No 52 are plotted after tensioning. Tendon No 52 has no deflection in the vertical direction and tendon No 38 is deflected in the positive vertical direction around the A/L (not shown in Figure E) and the E/H penetrations.

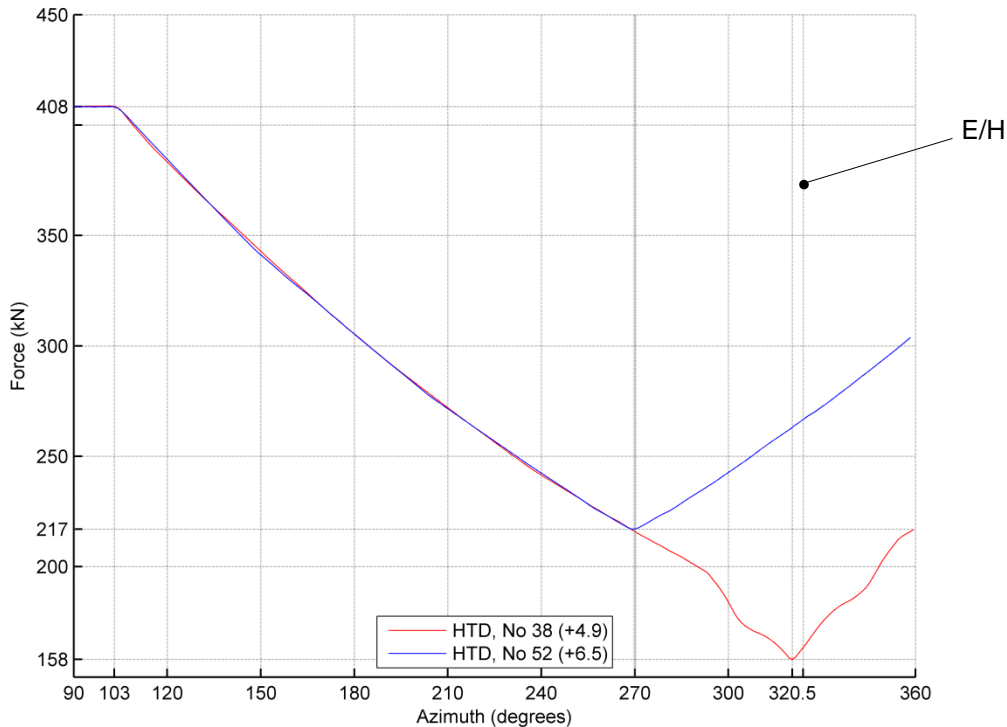


Figure E A2.1 Horizontal tendon forces in FE-model after tensioning.

The force along a tendon due to friction loss is described by the exponential function below, see also section 4.5.3 in this report:

$$F(\theta) = F_0 e^{-(\mu\alpha + kx)}$$

where F_0 is the force at the tensioning end of the tendon, μ is the friction coefficient, α is the cumulative angle, k is the wobbling coefficient and x is the length from the tensioning end.

In this evaluation the friction coefficient is set to 0.22 and the wobbling coefficient is set to zero.

Validation of pre-stressing force at azimuth 270° for horizontal tendon No 52:

$$F(270^\circ) = F_0 \times e^{-(\mu\alpha + kx)} = 408 \times 10^3 \times e^{-0.22 \times (270 - 103) \times (\pi / 180)} \approx 215 \text{ kN} \quad \text{OK!}$$

For horizontal tendon No 38, which is also deflected in the positive vertical direction, the accumulated angle α must include the accumulated angle in the horizontal plane and the vertical plane.

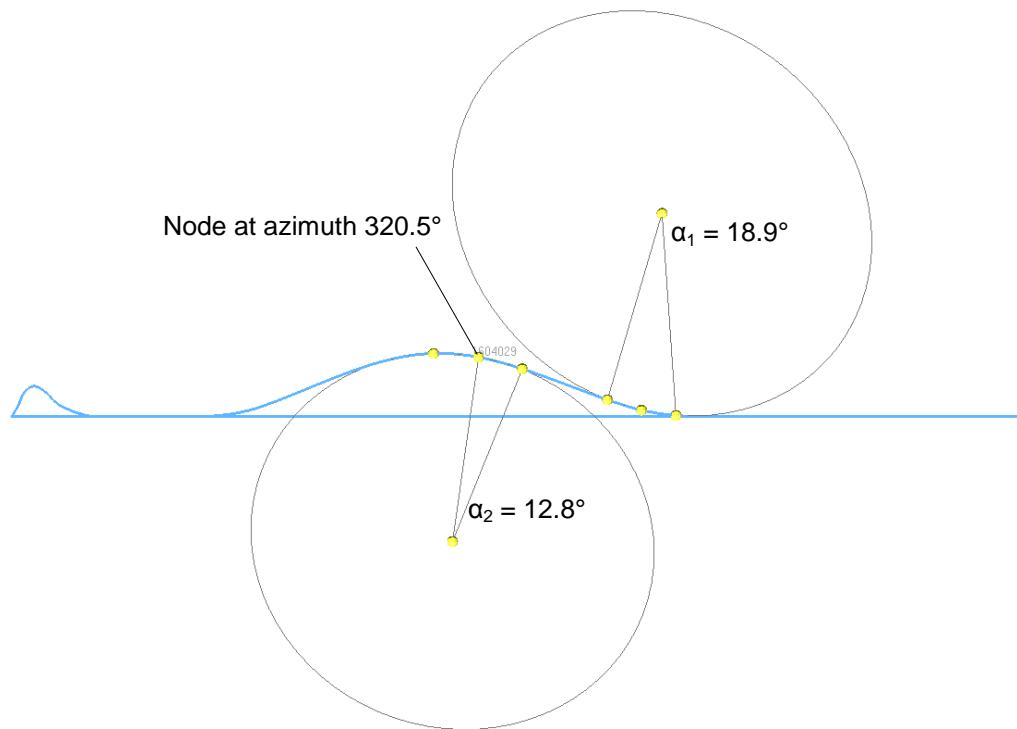


Figure E A2.2 Horizontal tendon No 38.

The accumulated angle is calculated according to Figure E A2.1 and Figure E A2.2:

$$\alpha = 320.5 - 103 + 18.9 + 12.8 = 249.2^\circ$$

The tendon force is calculated according to:

$$F(320.5^\circ) = F_0 \times e^{-(\mu\alpha + kx)} = 408 \times 10^3 \times e^{-0.22 \times 249.2 \times (\pi/180)} \approx 157 \text{ kN}$$

OK!

In Figure E A2.3 the forces along horizontal tendon No 52 is plotted before and after seating. The total area loss under the tendon force curve due to seating can be calculated according to [23]:

$$I_f = \Delta u \times E \times A$$

where Δu is the seating specified in section 5.3.3, E is the elastic modulus for the tendon steel specified in section 4.5.2.4 and A is the tendon cross-section area specified in section 2.2.4.

In the calculation of the pre-stress force after seating carried out below, the geometric assumption is made, that the area I_f is made up out of two identical rectangles and two identical triangles, see Figure E A2.3 below.

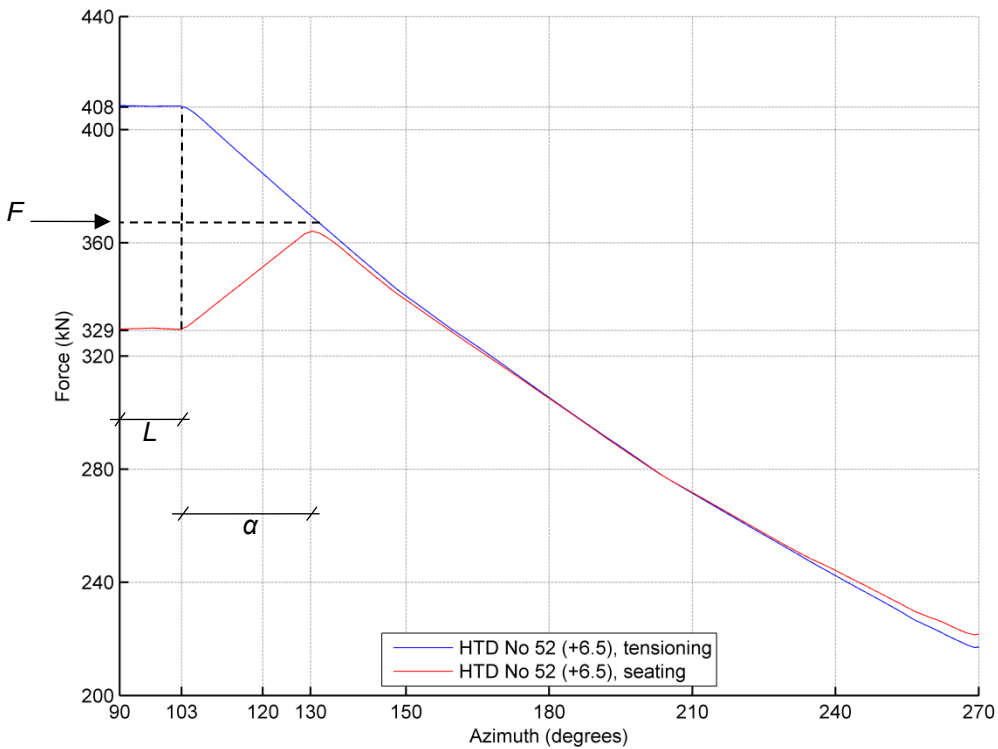


Figure E A2.3 Horizontal tendon forces in FE-model after tensioning and after seating.

Accordingly, the following equations can be set up:

$$\begin{cases} F = F_0 \times e^{-\mu \times \frac{\pi}{180} \times \alpha} \\ I_f = \Delta u \times E \times A \\ I_f = 2 \times \left[(F_0 - F) \times L + 0.5 \times (F_0 - F) \times \alpha \times \frac{\pi}{180} \times r \right] \end{cases}$$

where

F = maximum force after seating (unknown)

F_0 = tension force = 408 kN

μ = friction coefficient = 0.22

α = cumulated angle (unknown)

Δu = seating = 3.95E-3 m

E = elastic modulus = 191 GPa

A = tendon cross-section area = 339.3E-6 m²

L = length in FE-model of tendon from anchoring to bend = 1.75 m

r = radius of horizontal tendons in FE-model = 5.574 m

Solving the system of equations above with respect to the unknown variables:

$F \approx 367$ kN OK!

$\alpha \approx 28^\circ$ OK!

which gives an anchoring force after seating of:

$408 - 2 \times (408 - 367) = 326$ kN OK!

RESULTS OF TENDON BEHAVIOR MODEL

In Figure E A3.1 through Figure E A3.14 is the shape of the tendon behavior model shown from an above view. The deformed shape is shown after application of pre-stress, seating loss, creep in concrete and relaxation in the tendons in Figure E A3.2-Figure E A3.5.

Figure E A3.6 through Figure E A3.14 shows the deformed shape at pressure milestones.

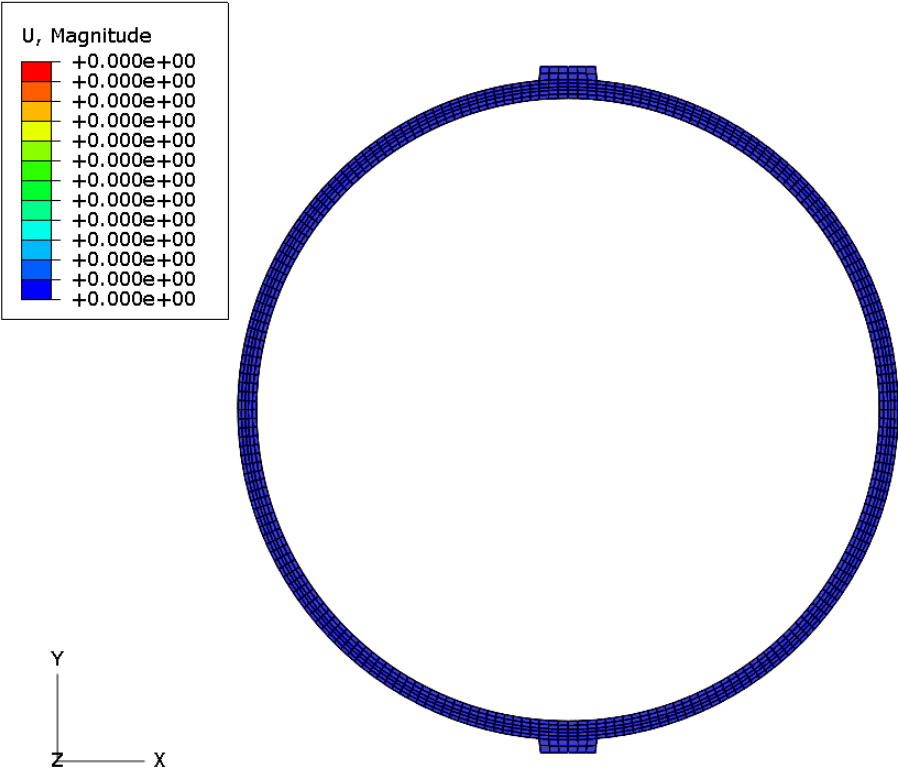


Figure E A3.1 Undeformed shape.

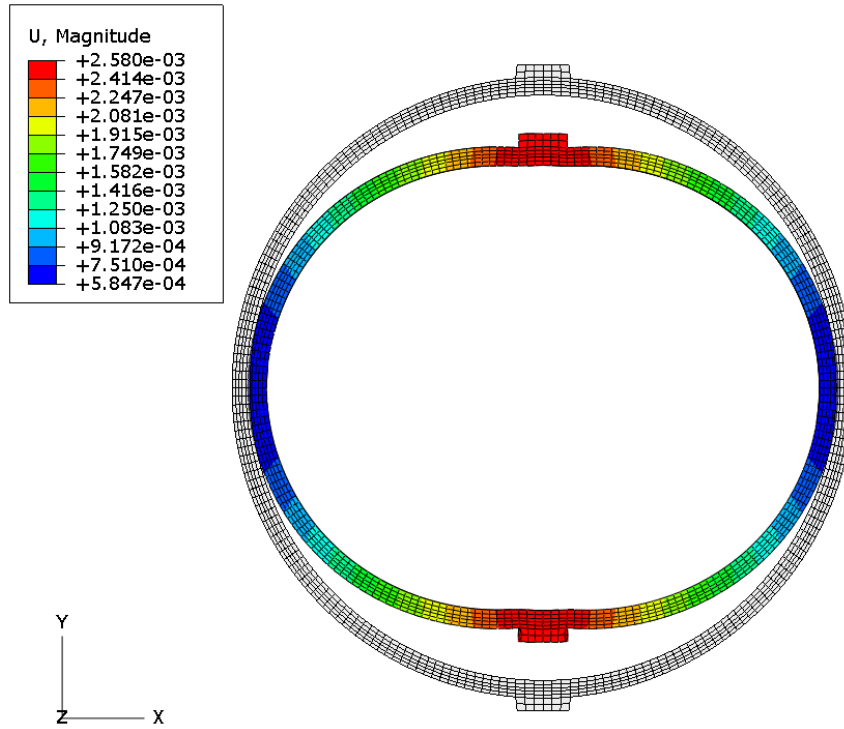


Figure E A3.2 Deformed shape after applied tension of tendons. Magnification factor 500.

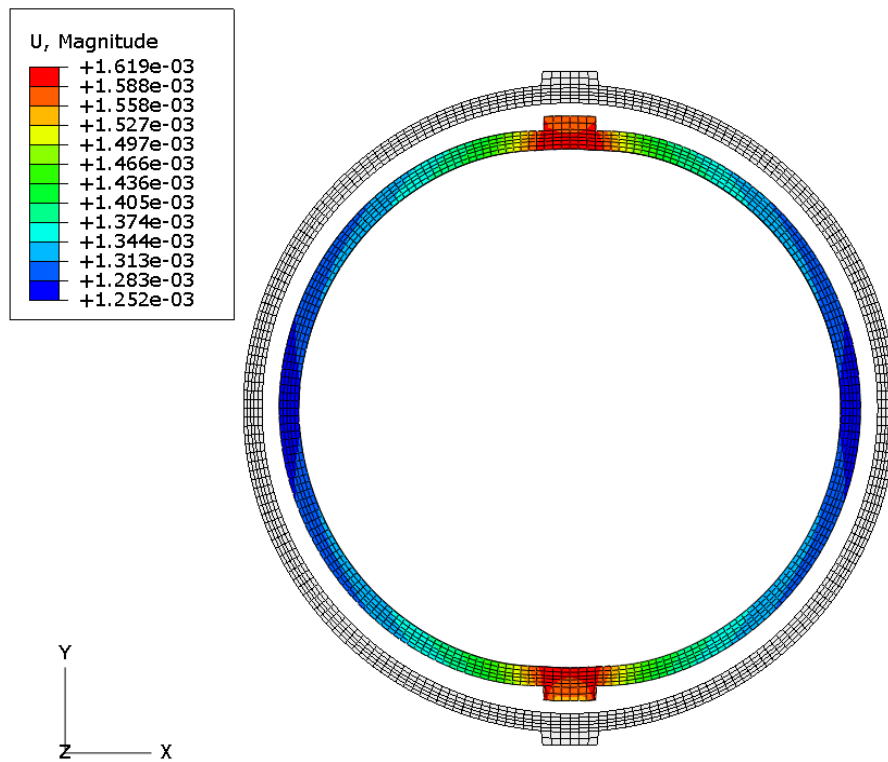


Figure E A3.3 Deformed shape after seating of tendons. Magnification factor 500.

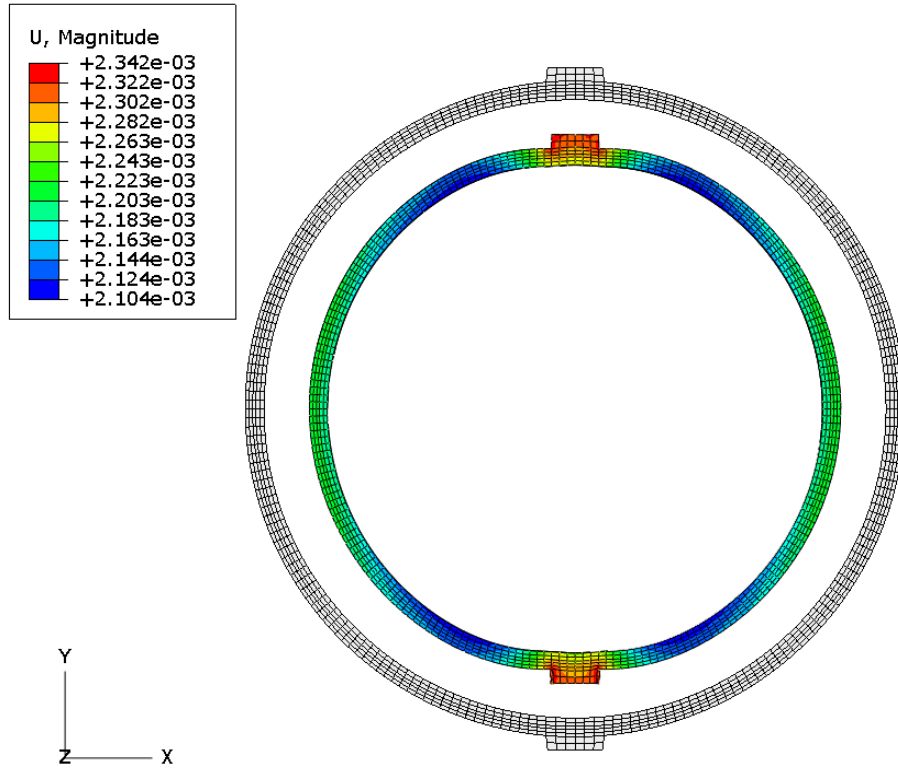


Figure E A3.4 Deformed shape after creep of concrete. Magnification factor 500.

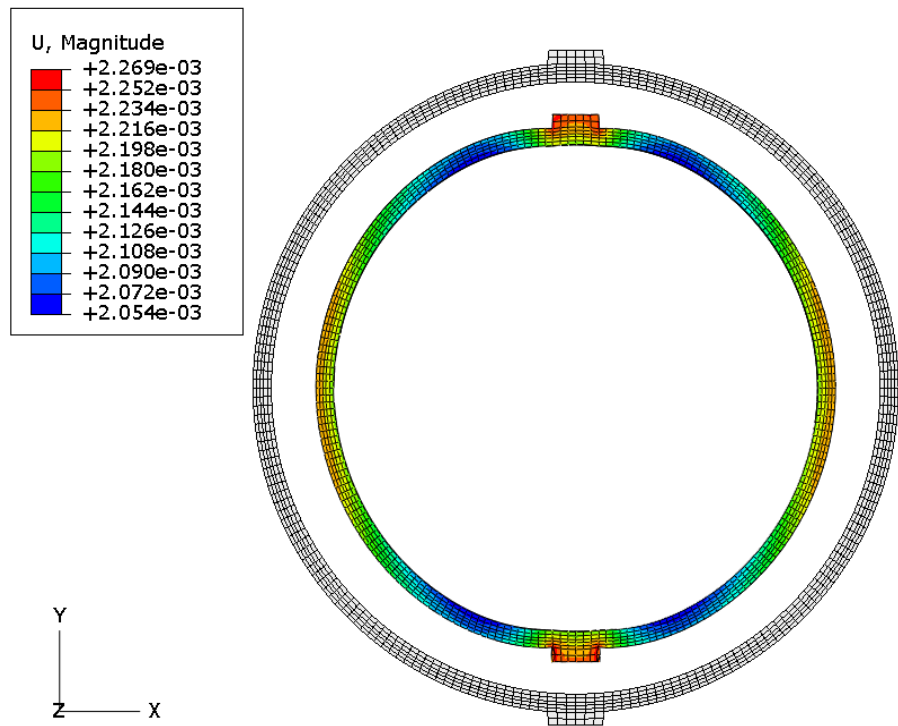


Figure E A3.5 Deformed shape after relaxation in tendons. Magnification factor 500.

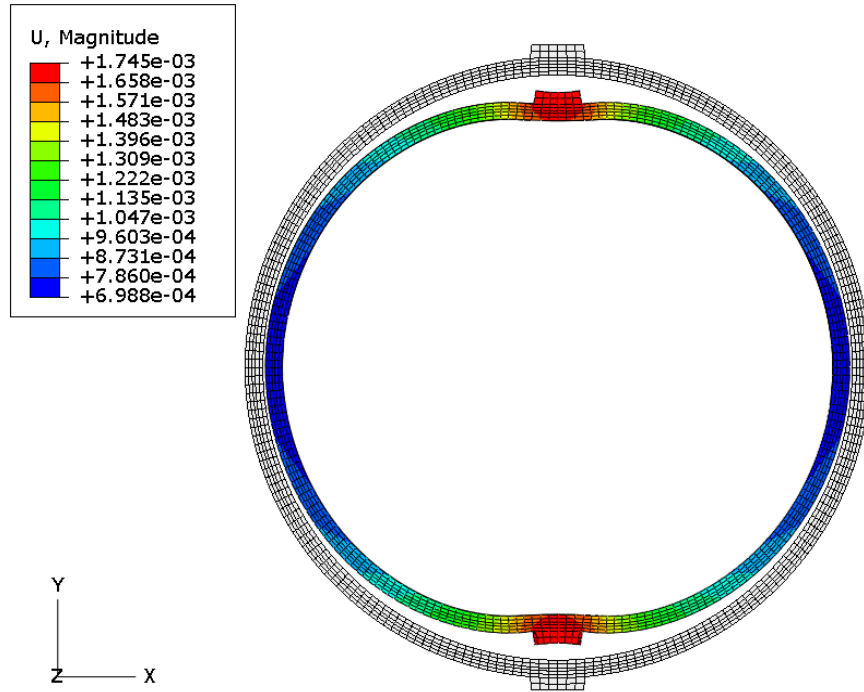


Figure E A3.6 Deformed shape at applied pressure $1.0 \times P_d$. Magnification factor 500.

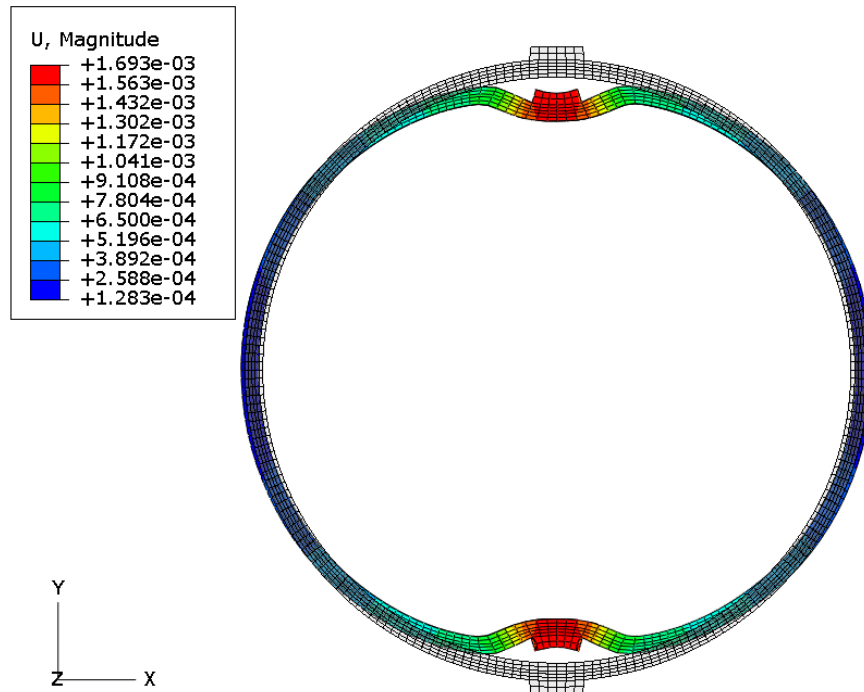


Figure E A3.7 Deformed shape at applied pressure $1.5 \times P_d$. Magnification factor 500.

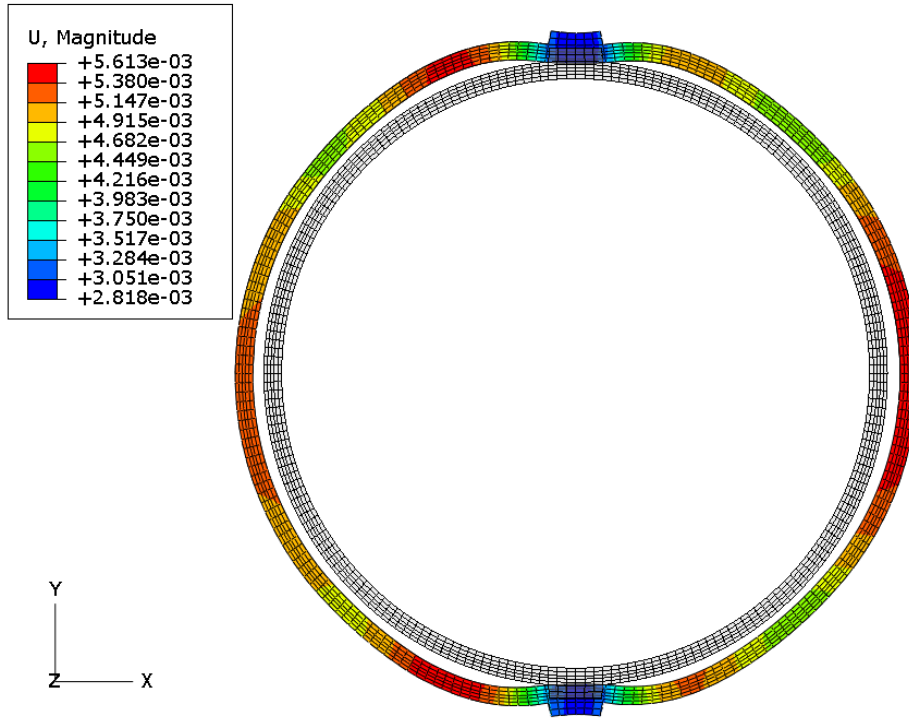


Figure E A3.8 Deformed shape at applied pressure $2.0 \times Pd$. Magnification factor 100.

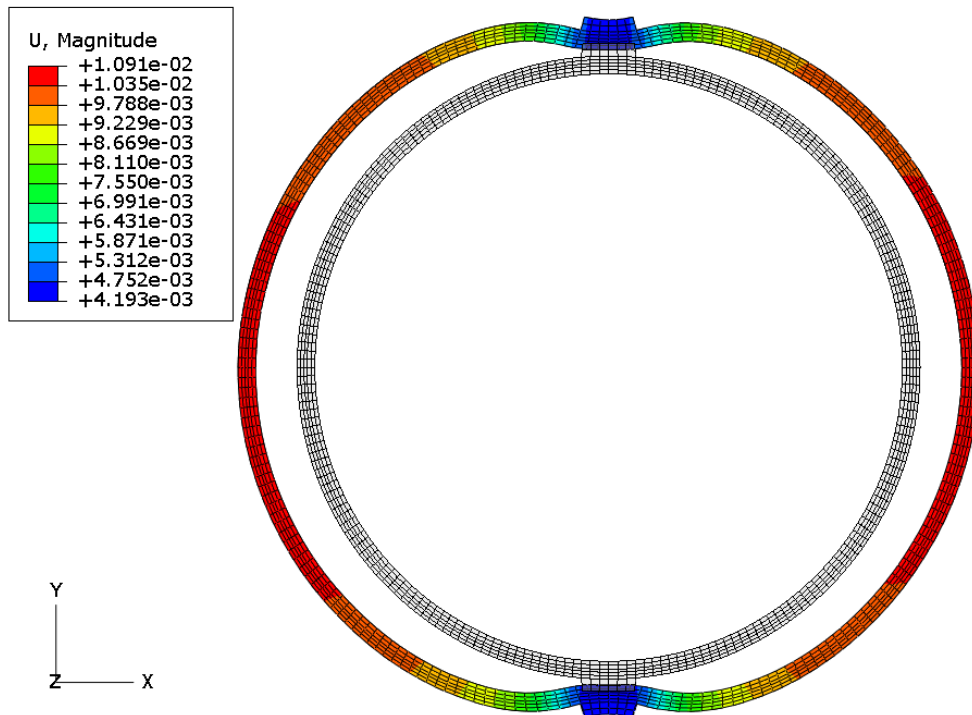


Figure E A3.9 Deformed shape at applied pressure $2.5 \times Pd$. Magnification factor 100.

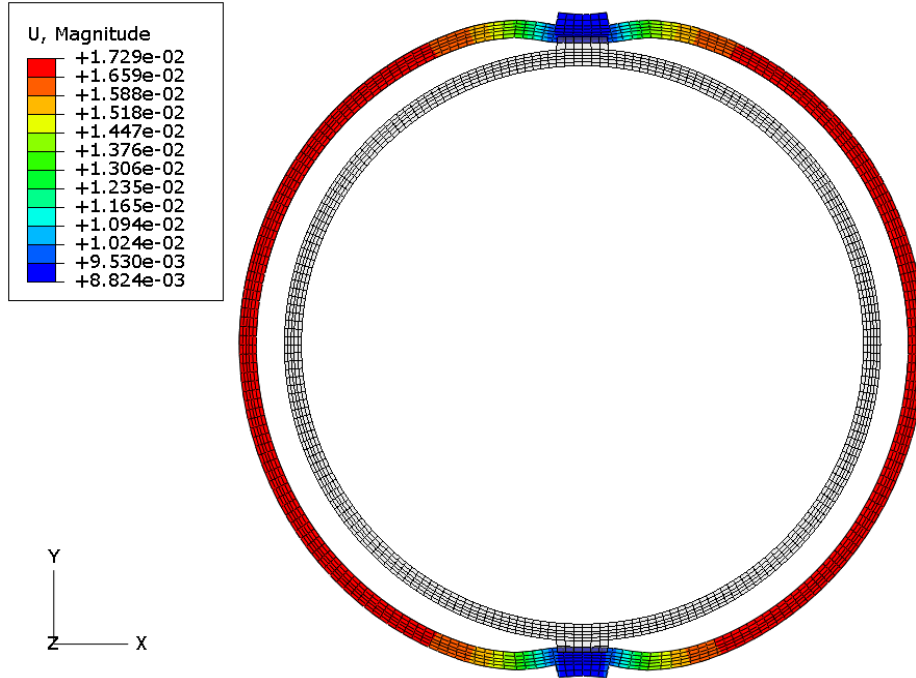


Figure E A3.10 Deformed shape at applied pressure $3.0 \times P_d$.
Magnification factor 50.

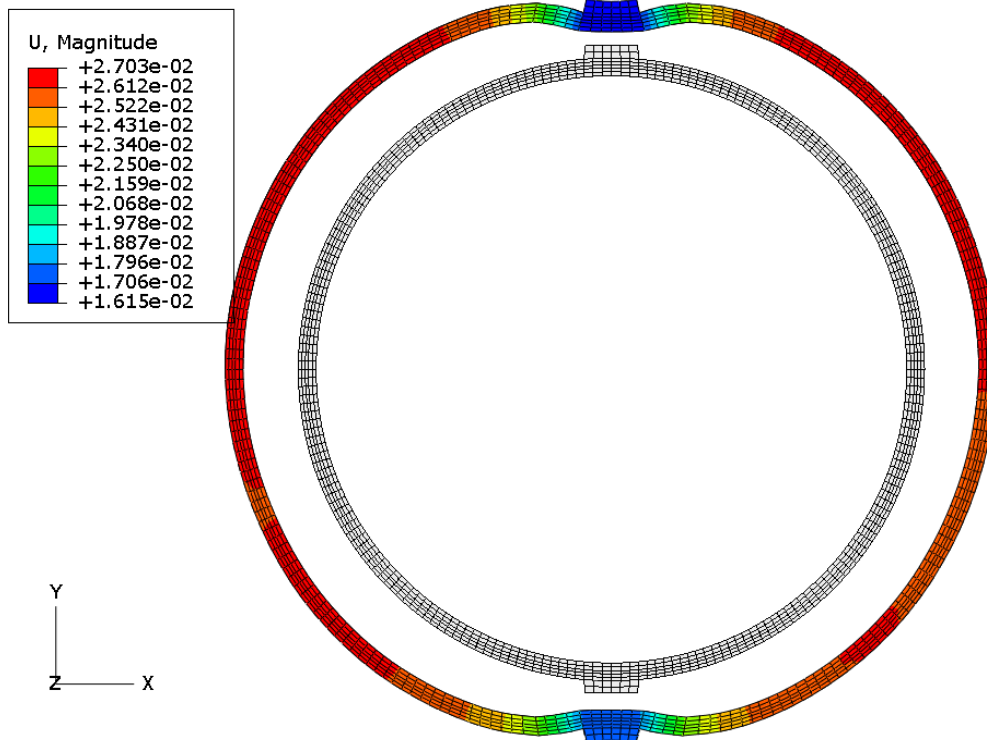


Figure E A3.11 Deformed shape at applied pressure $3.3 \times P_d$.
Magnification factor 50.

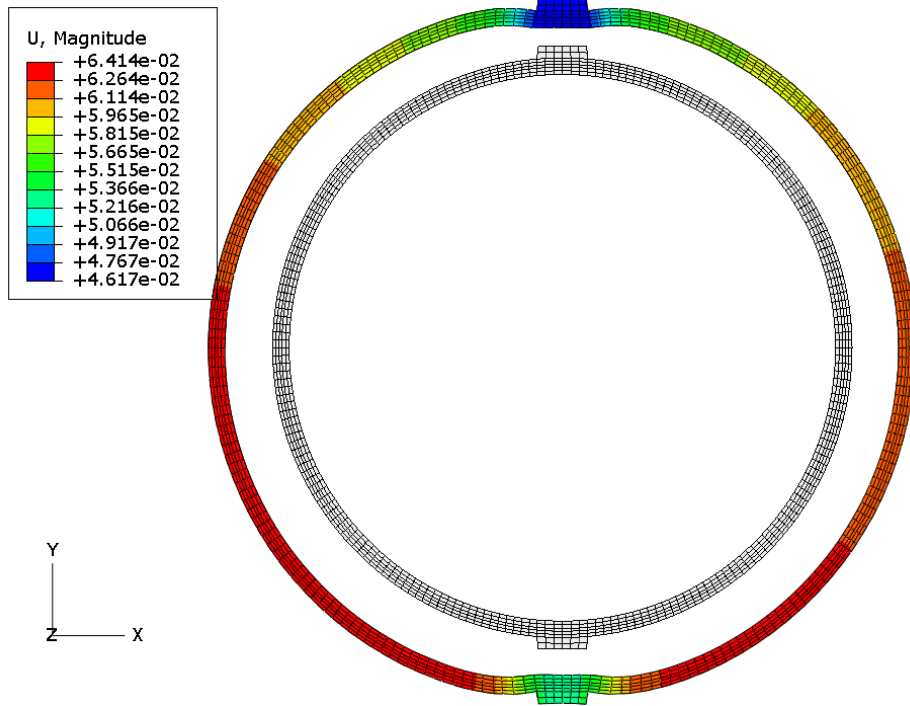


Figure E A3.12 Deformed shape at applied pressure $3.4 \times Pd$.
Magnification factor 20.

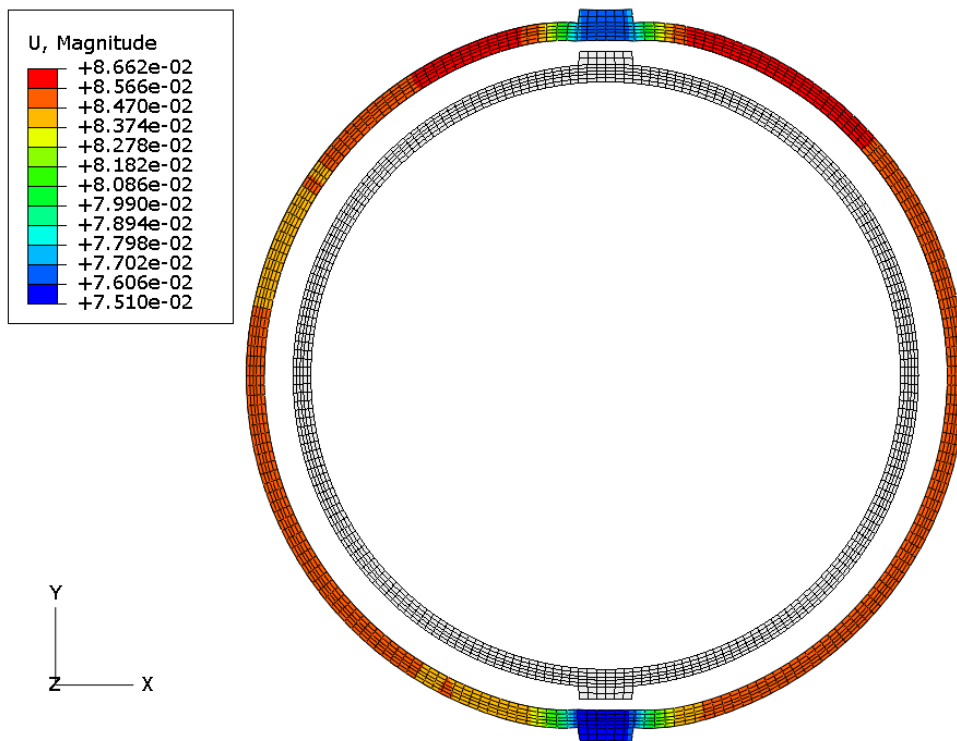


Figure E A3.13 Deformed shape at applied pressure $3.5 \times Pd$.
Magnification factor 10.

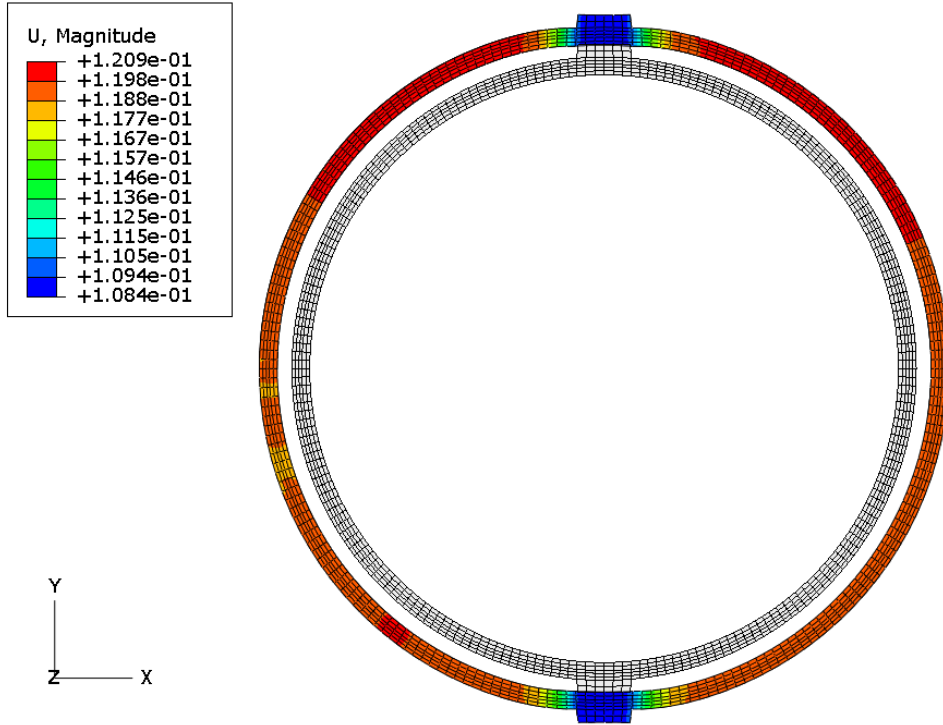


Figure E A3.14 Deformed shape at applied pressure $3.62 \times P_d$, ultimate pressure.
Magnification factor 5.

GLOBAL MODEL DEFORMATION AT STANDARD OUTPUT LOC.

Figure E A4.1 shows the position of the 55 standard output locations (SOL) on the inside of the containment liner. The standard output locations are also listed in Table E A4.1 below.

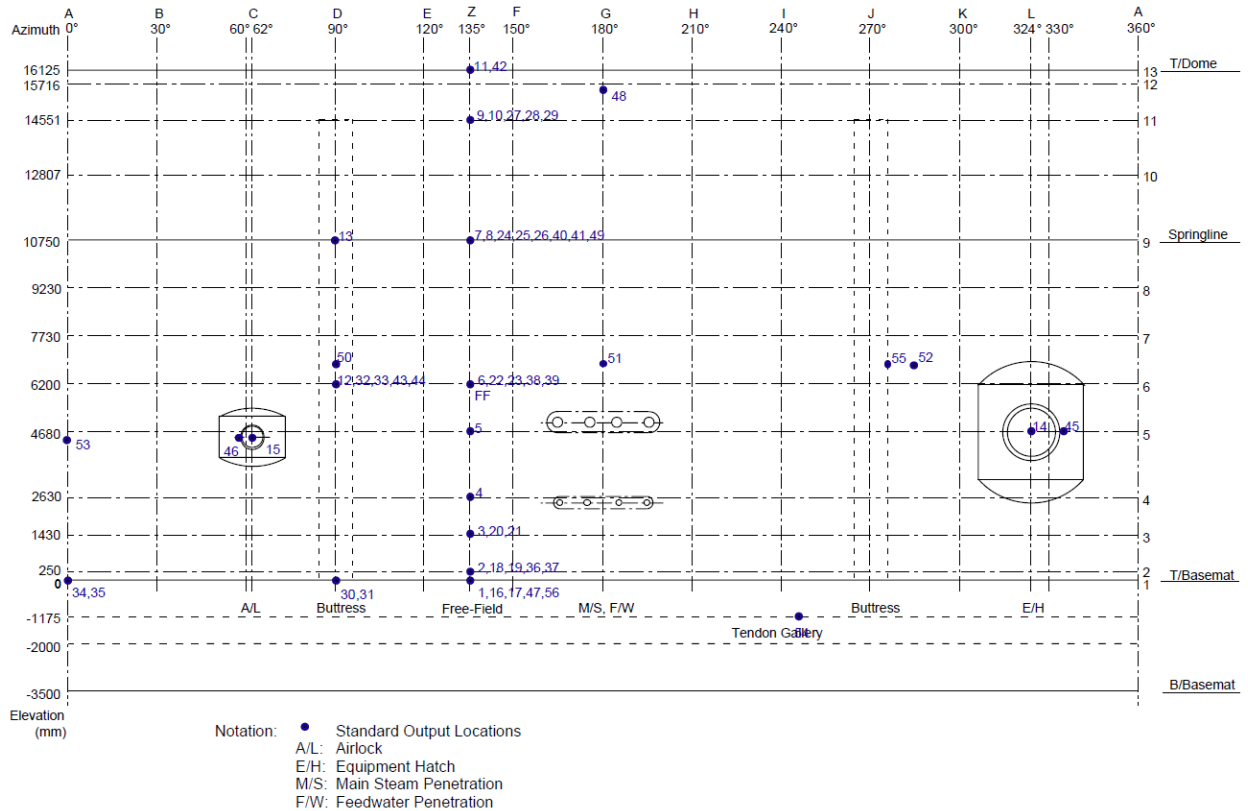


Figure E A4.1 The positions for the 55 standard output locations.

Pos. 2-7, 9 & 12-15 measures radial deformation

Pos. 1, 8, 10 & 11 measures vertical deformation

Pos. 36 - 42 measures meridional and hoop strains in liner

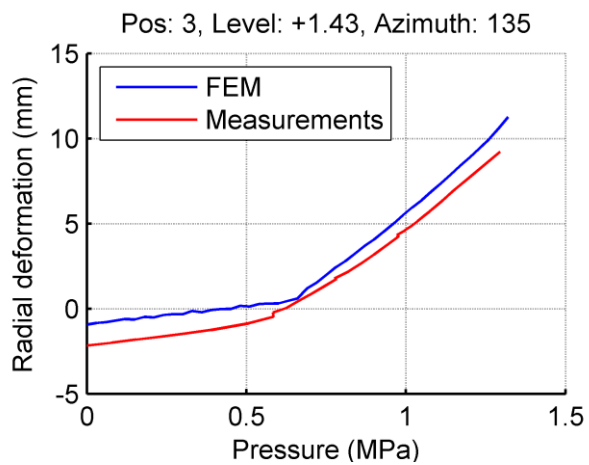
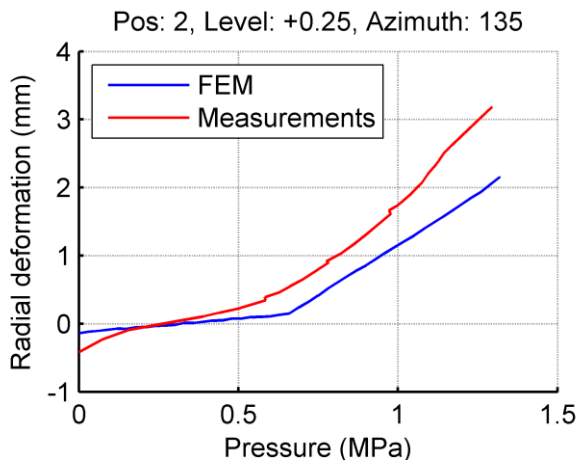
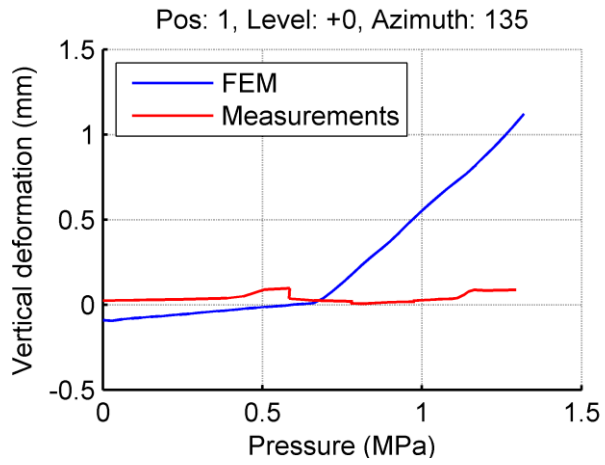
Pos. 48 - 53 measures strains in tendons

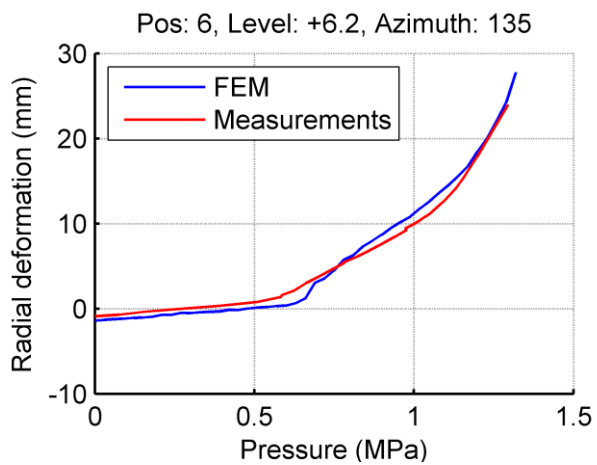
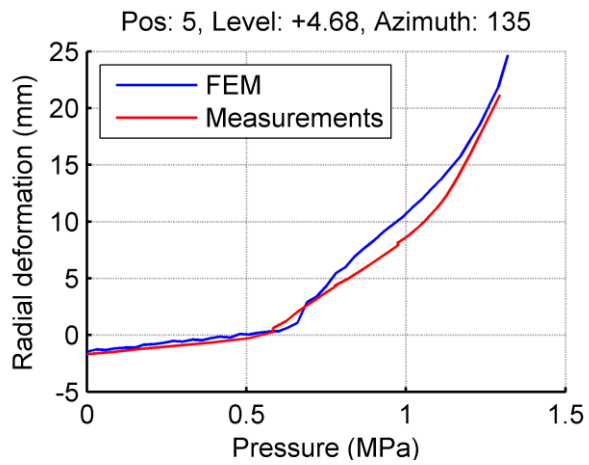
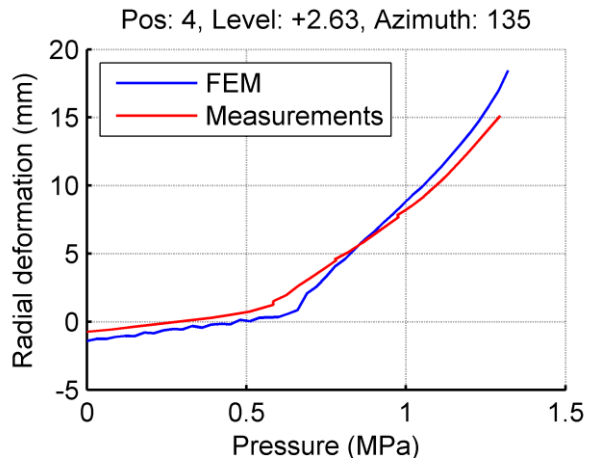
Pos. 54 - 55 measures tendon force at anchoring

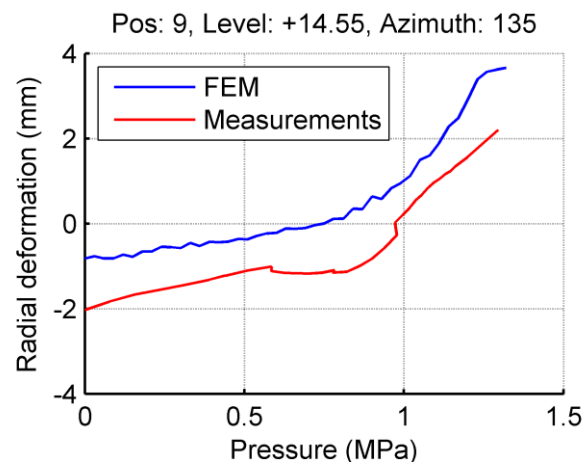
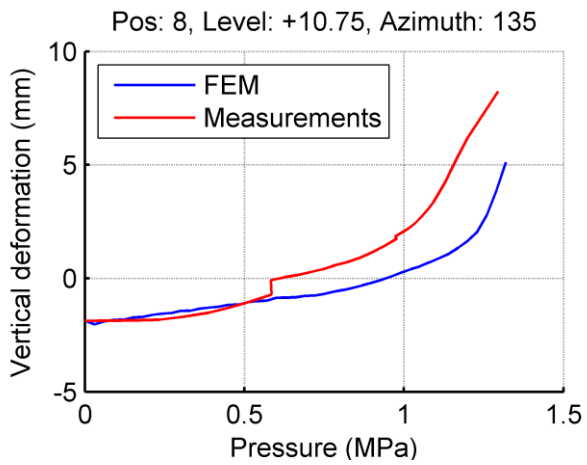
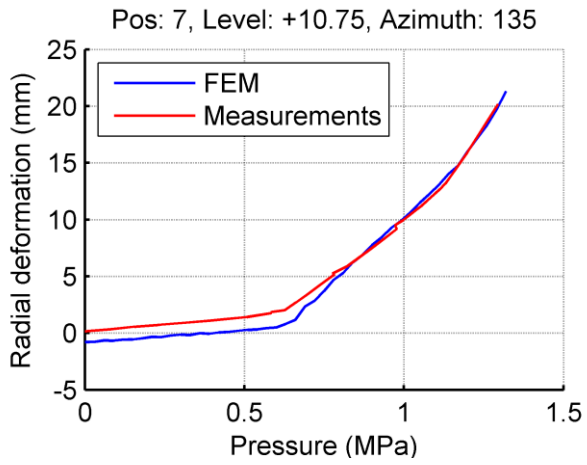
Table E A4.1 Description of the standard output locations, excerpt from [7].

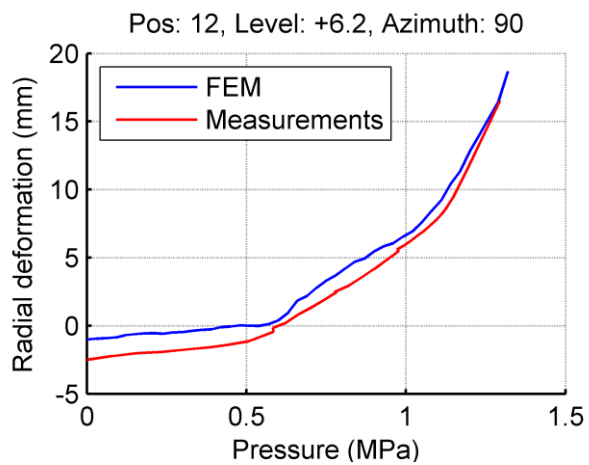
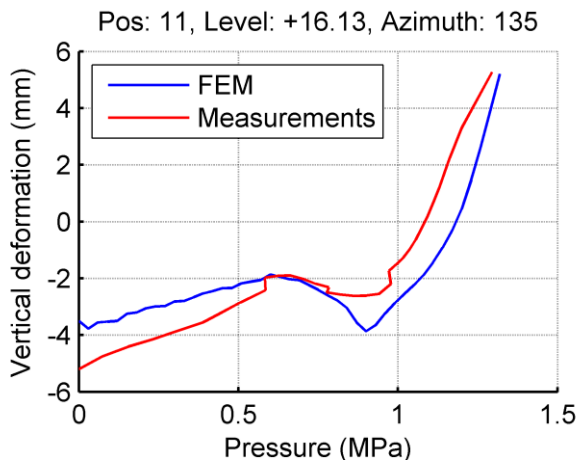
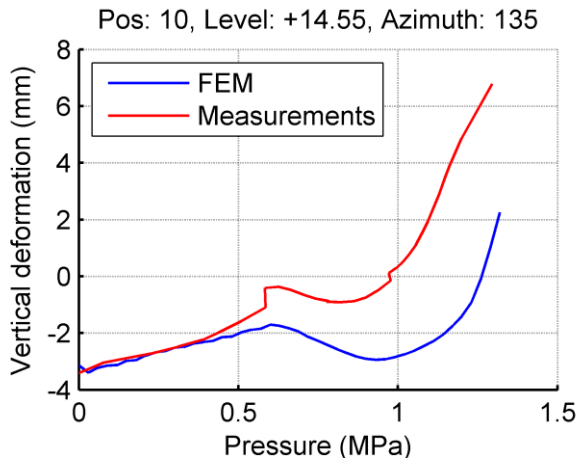
Loc. #	Type	Orientation	Az. (°)	EL. (m)	Comments	General Location
1	Displacement	Vertical	135	0.00	Outside Cylinder	Top of Basemat
2	"	Radial	135	0.25	Inside Liner Surface	Base of Cylinder
3	"	Radial	135	1.43	"	"
4	"	Radial	135	2.63	"	"
5	"	Radial	135	4.68	"	E/H elev.
6	"	Radial	135	6.20	"	Approximate Midheight
7	"	Radial	135	10.75	"	Springline
8	"	Vertical	135	10.75	"	"
9	"	Horiz.(Rad)	135	14.55	"	Dome 45 deg
10	"	Vertical	135	14.55	"	"
11	"	Vertical	135	16.13	"	Dome apex
12	"	Radial	90	6.20	"	Midheight @ Buttress
13	"	Radial	90	10.75	"	Springline @ Buttress
14	"	Radial	324	4.675	"	Center of E/H
15	"	Radial	62	4.525	"	Center of A/L
16	Rebar Strain	Meridional	135	0.05	Inner Rebar Layer	Base of Cylinder
17	"	Meridional	135	0.05	Outer Rebar Layer	"
18	"	Meridional	135	0.25	Inner Rebar Layer	"
19	"	Meridional	135	0.25	Outer Rebar Layer	"
20	"	Meridional	135	1.43	Inner Rebar Layer	"
21	"	Meridional	135	1.43	Outer Rebar Layer	"
22	"	Hoop	135	6.20	Outer Rebar Layer	Midheight
23	"	Meridional	135	6.20	Outer Rebar Layer	"
24	"	Hoop	135	10.75	Outer Rebar Layer	Springline
25	"	Meridional	135	10.75	Inner Rebar Layer	"
26	"	Meridional	135	10.75	Outer Rebar Layer	"
27	"	Hoop	135	14.55	Outer Rebar Layer	Dome 45 deg
28	"	Meridional	135	14.55	Inner Rebar Layer	"
29	"	Meridional	135	14.55	Outer Rebar Layer	"
30	"	Meridional	90	0.05	Inner Rebar Layer	Base of Cylinder @ Buttress
31	"	Meridional	90	0.05	Outer Rebar Layer	"
32	"	Hoop	90	6.20	Outer Rebar Layer	Midheight @ Buttress
33	"	Meridional	90	6.20	Outer Rebar Layer	"
34	Liner Strain	Meridional	0	0.010	Inside Liner Surface	Base of Cylinder
35	"	Meridional	0	0.010	Outside Liner Surface	"
36	"	Meridional	135	0.25	Inside Liner Surface	"
37	"	Hoop	135	0.25	"	"
38	"	Meridional	135	6.20	"	Midheight
39	"	Hoop	135	6.20	"	"
40	"	Meridional	135	10.75	"	Springline
41	"	Hoop	135	10.75	"	"
42	"	Meridional	135	16.13	"	Dome apex
43	"	Meridional	90	6.20	"	Midheight @ Buttress
44	"	Hoop	90	6.20	"	"
45	"	Hoop	332	4.675	"	10 mm from thickened plate
46	"	Hoop	59	4.525	"	10 mm from thickened plate
47	Base Liner	Radial	135	0.00	100 mm Inside Cyl.	FF Basemat Liner Strain
48	Tendon Str.	Hairpin	180	15.60	Tendon - V37	Tendon Apex
49	"	Hairpin	135	10.75	Tendon - V46	Tendon Springline
50	"	Hoop	90	6.58	Tendon - H53	Mid Tendon
51	"	Hoop	180	6.58	Tendon - H53	1/4 - Tendon
52	"	Hoop	225	6.58	Tendon - H53	1/8 - Tendon
53	"	Hoop	0	4.57	Tendon - H35	Tendon btwn E/H and A/L
54	Tendon Force	Hairpin	241	-1.16	Tendon - V37	Tendon Gallery
55	"	Hoop	275	6.58	Tendon - H53	@ Buttress

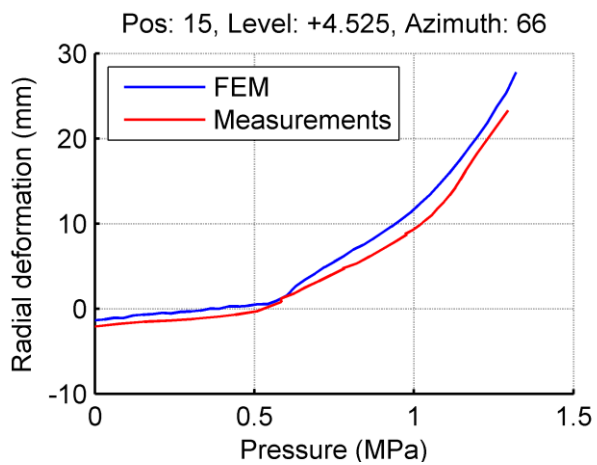
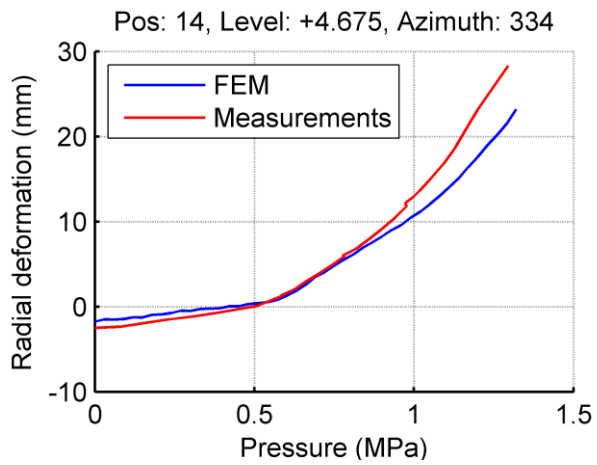
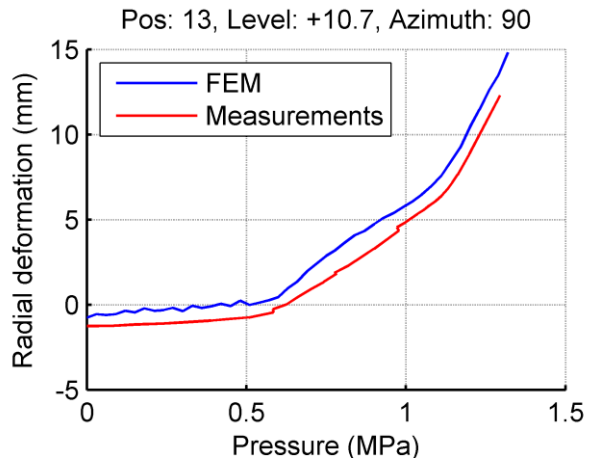
The plots below show the results in the global finite element model for SOL No 1 - 15, No 36 - 42 and No 48 - 55. The finite element model output is also compared to the measurements.

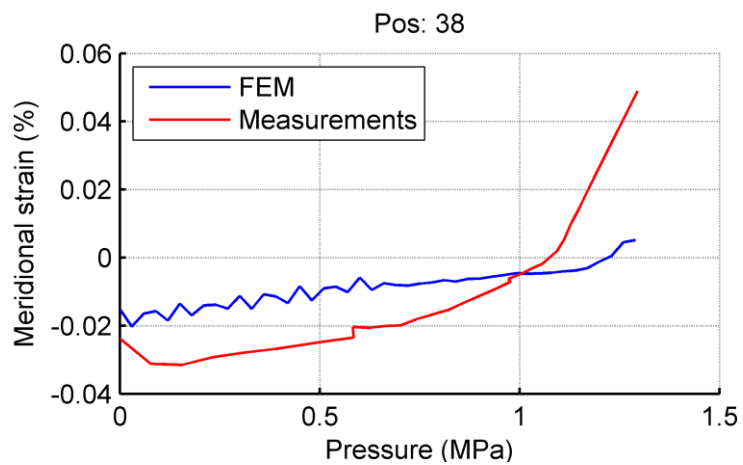
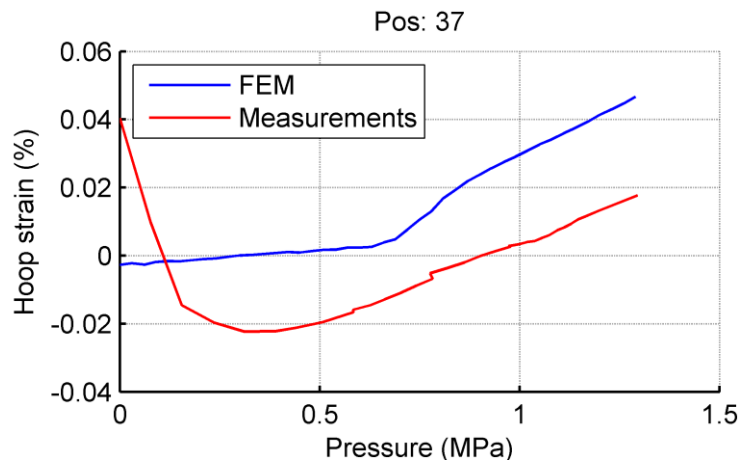
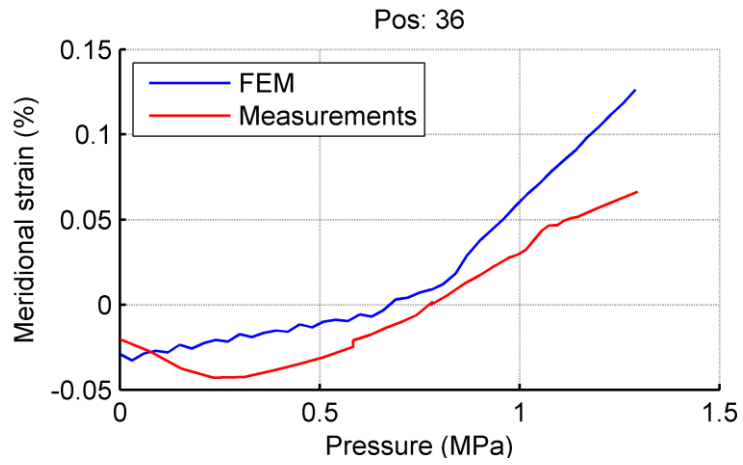


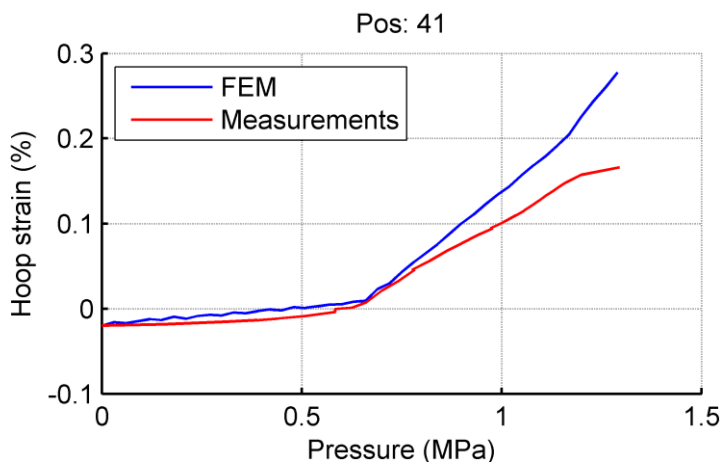
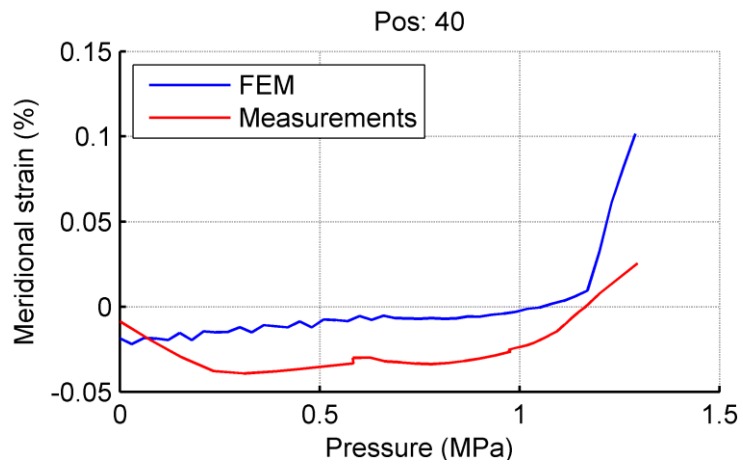
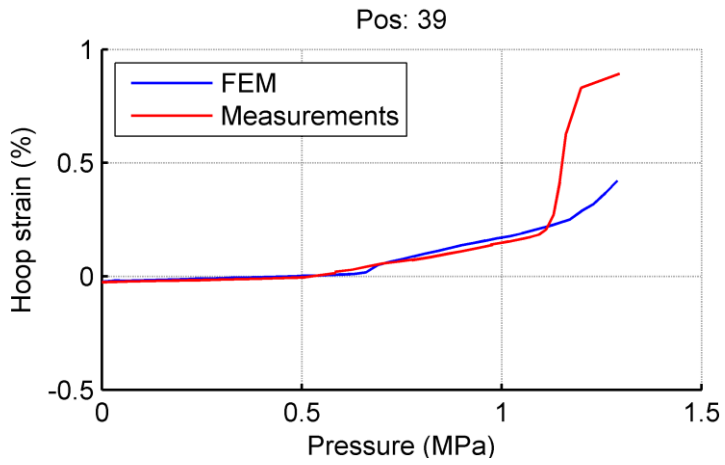


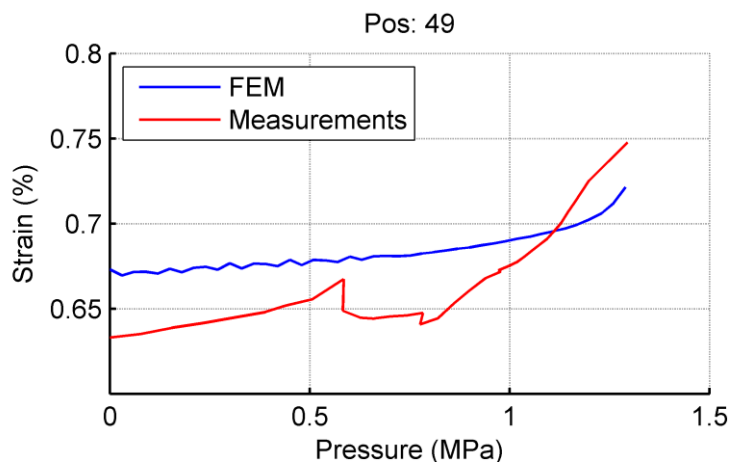
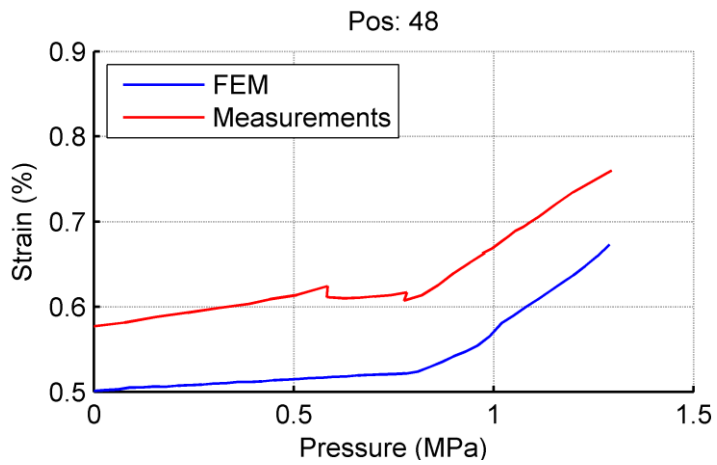
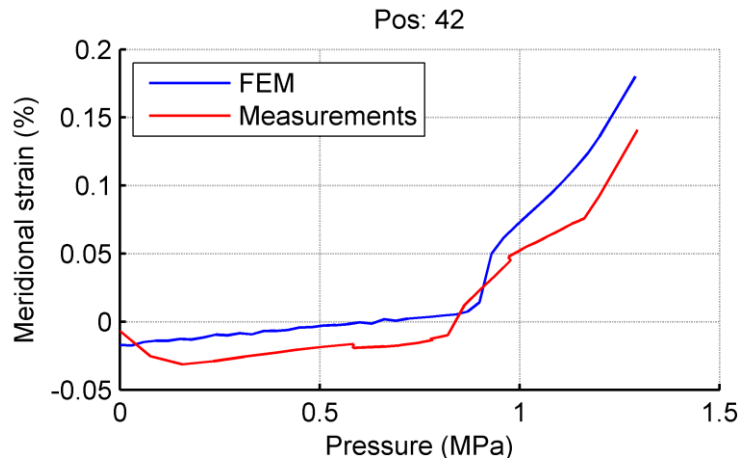


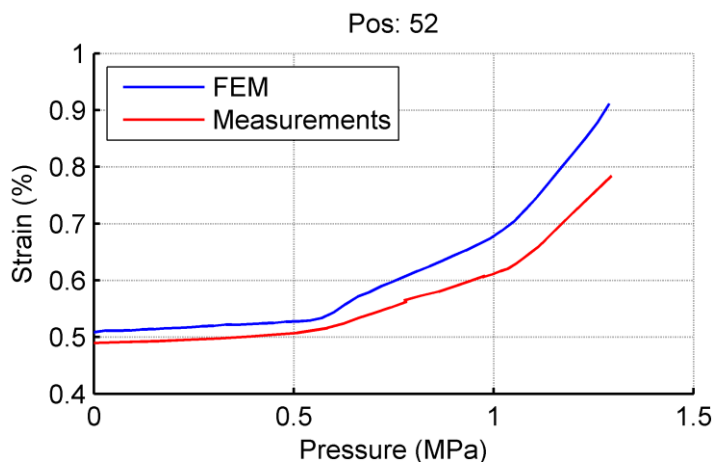
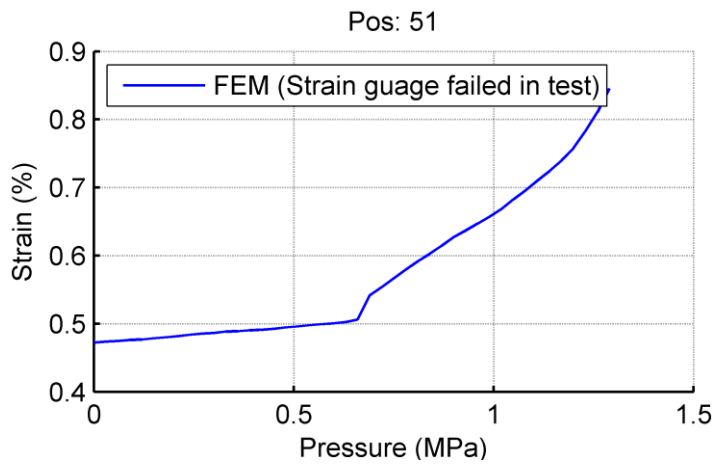
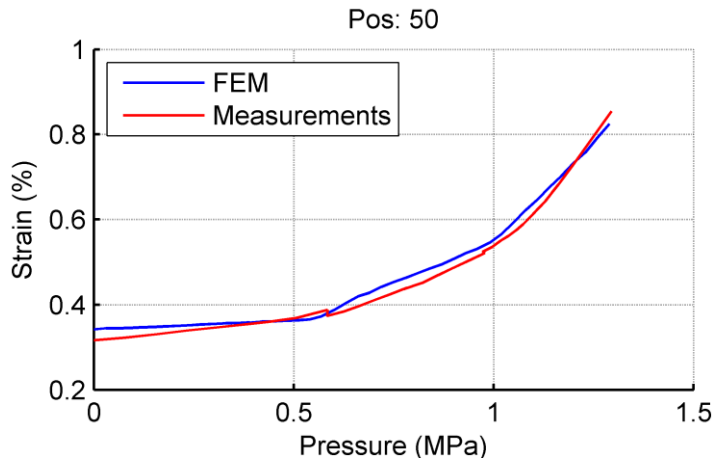


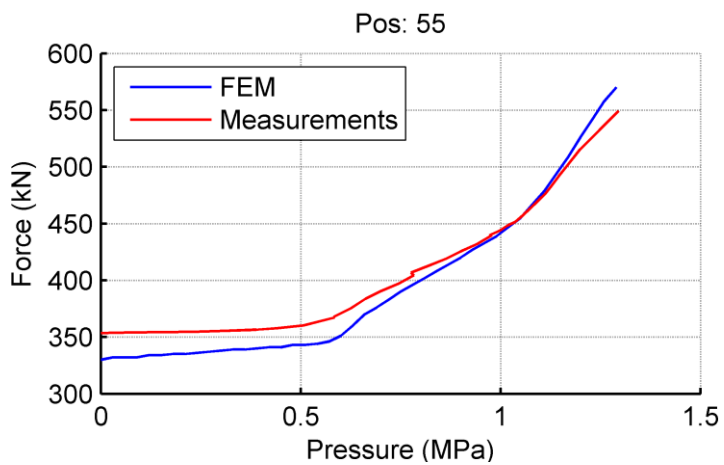
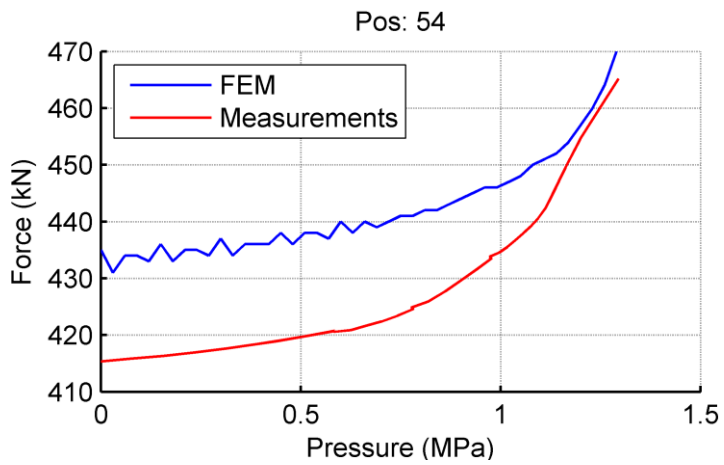
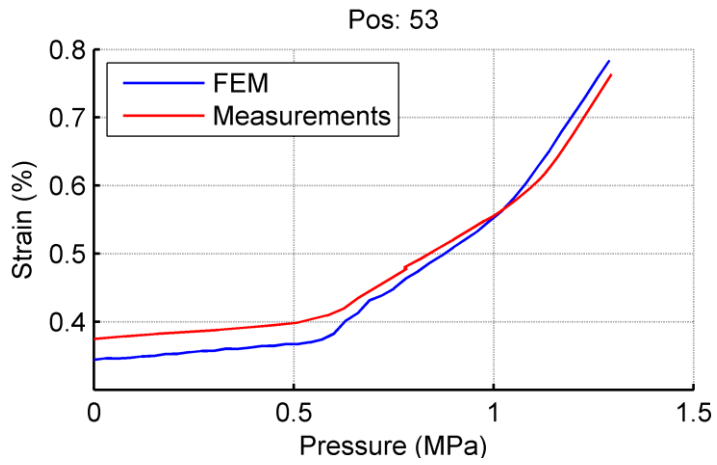












GLOBAL MODEL LINER STRAINS

Figure E A5.1 through Figure E A5.9 show maximum liner hoop strains at pressure milestones.

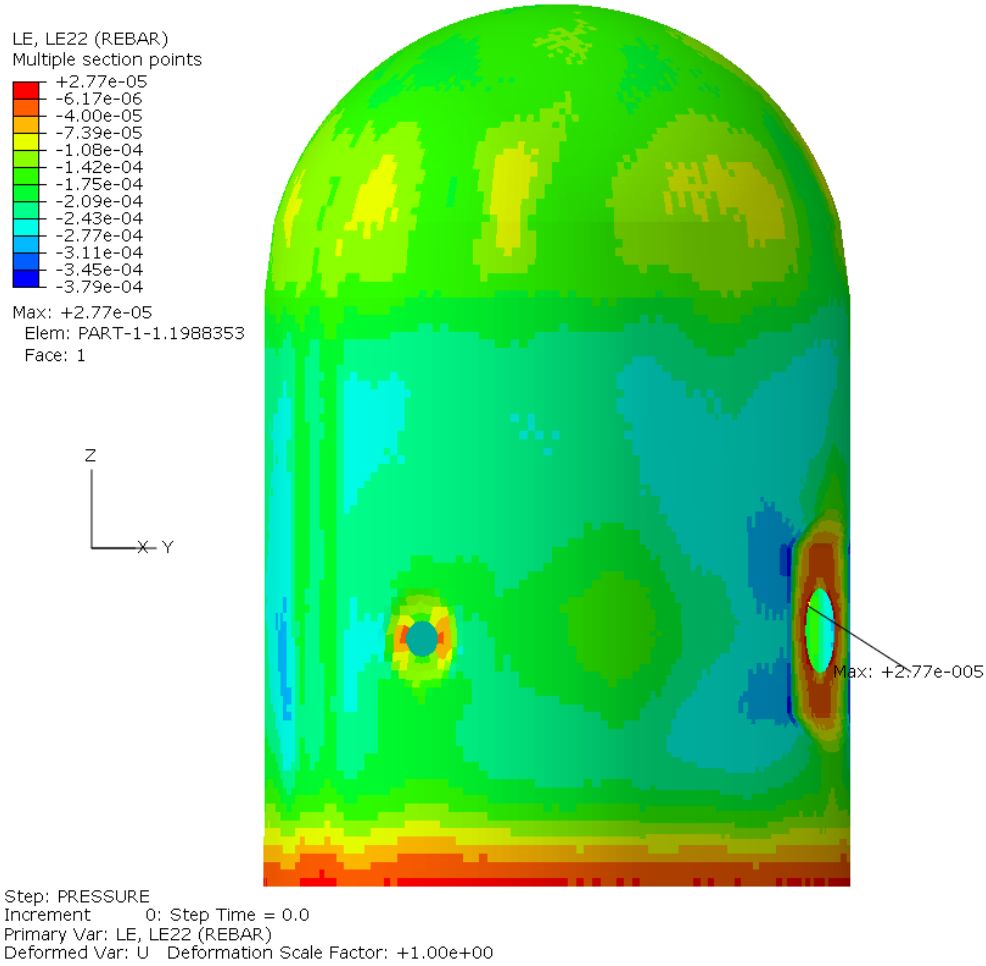


Figure E A5.1 Liner hoop strains, pressure = 0 MPa.

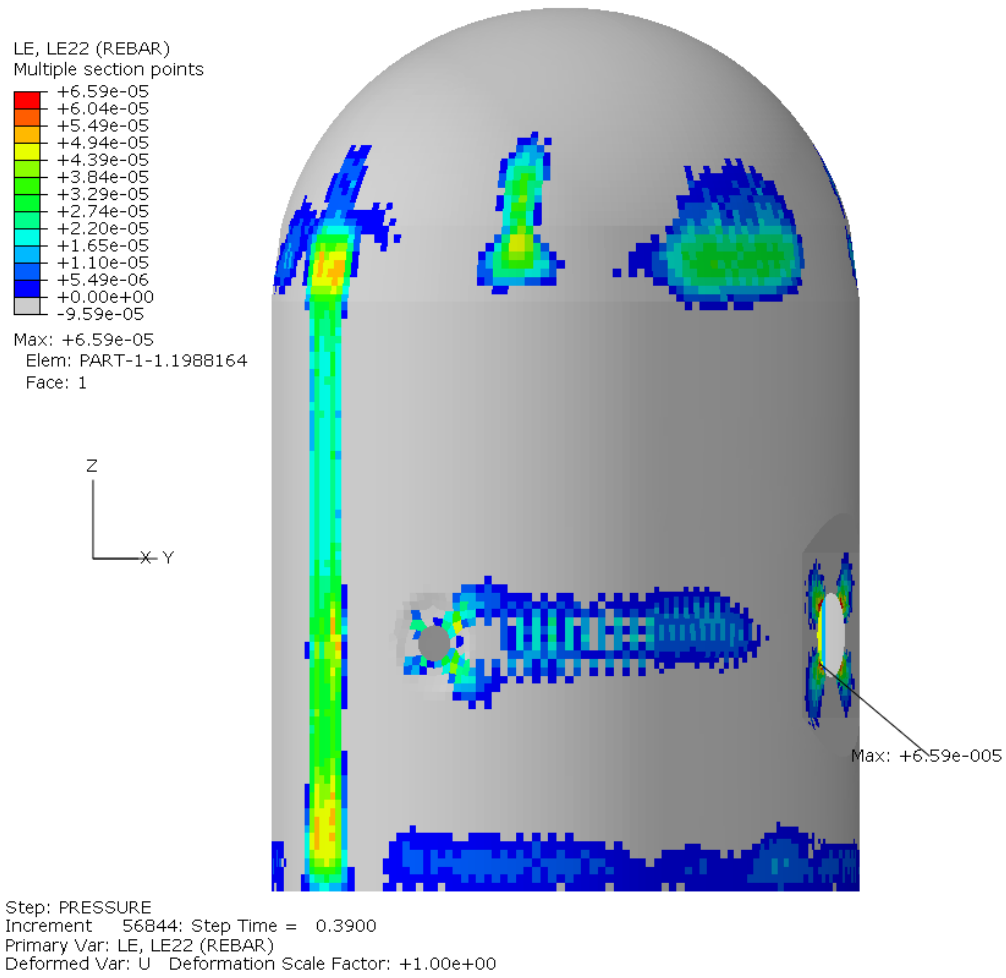


Figure E A5.2 Liner hoop strains, pressure = 0.390 MPa.

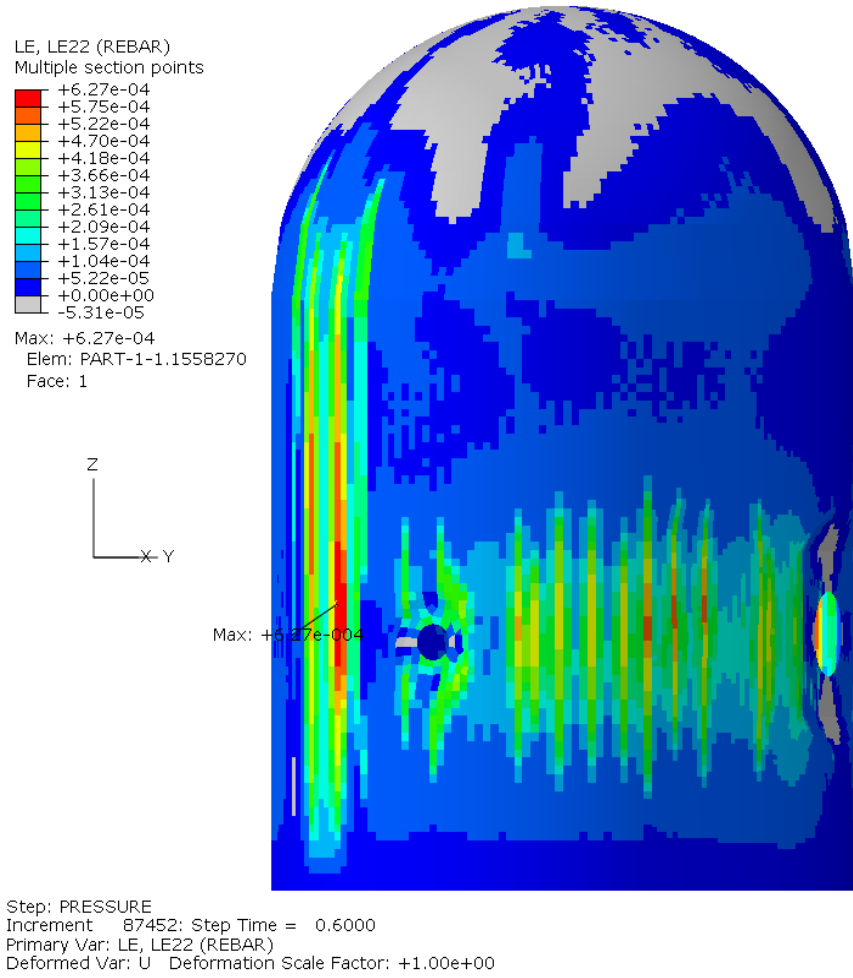


Figure E A5.3 Liner hoop strains, pressure = 0.600 MPa.

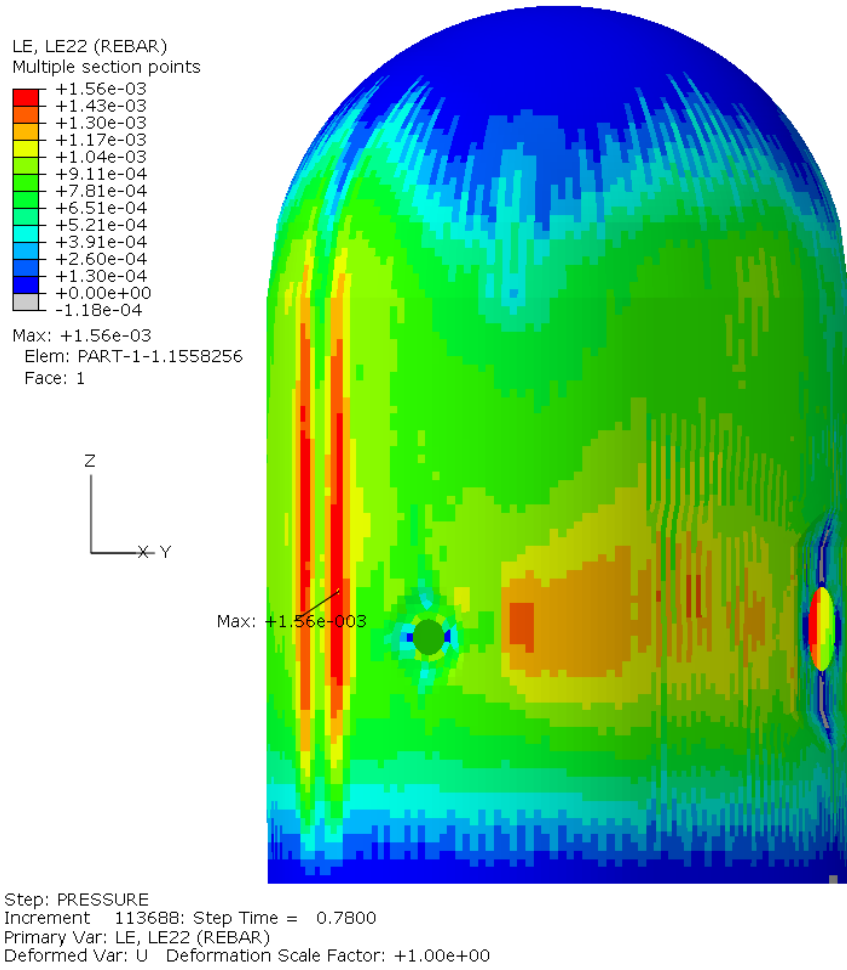


Figure E A5.4 Liner hoop strains, pressure = 0.780 MPa.

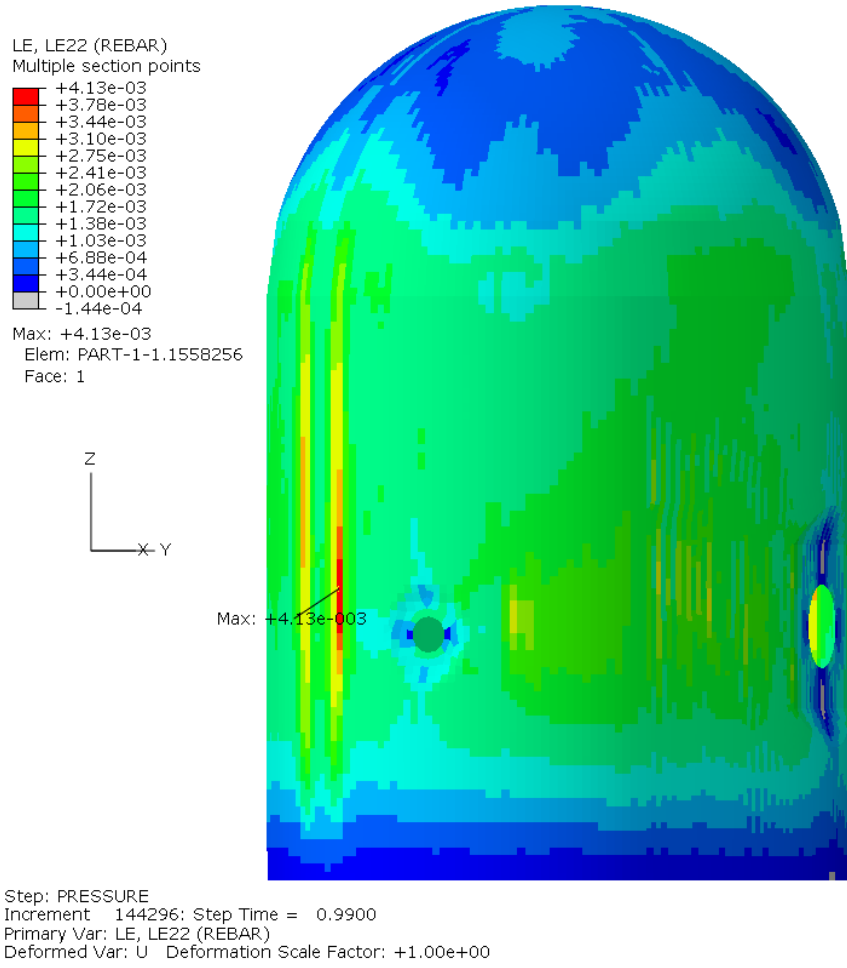


Figure E A5.5 Liner hoop strains, pressure = 0.990 MPa.

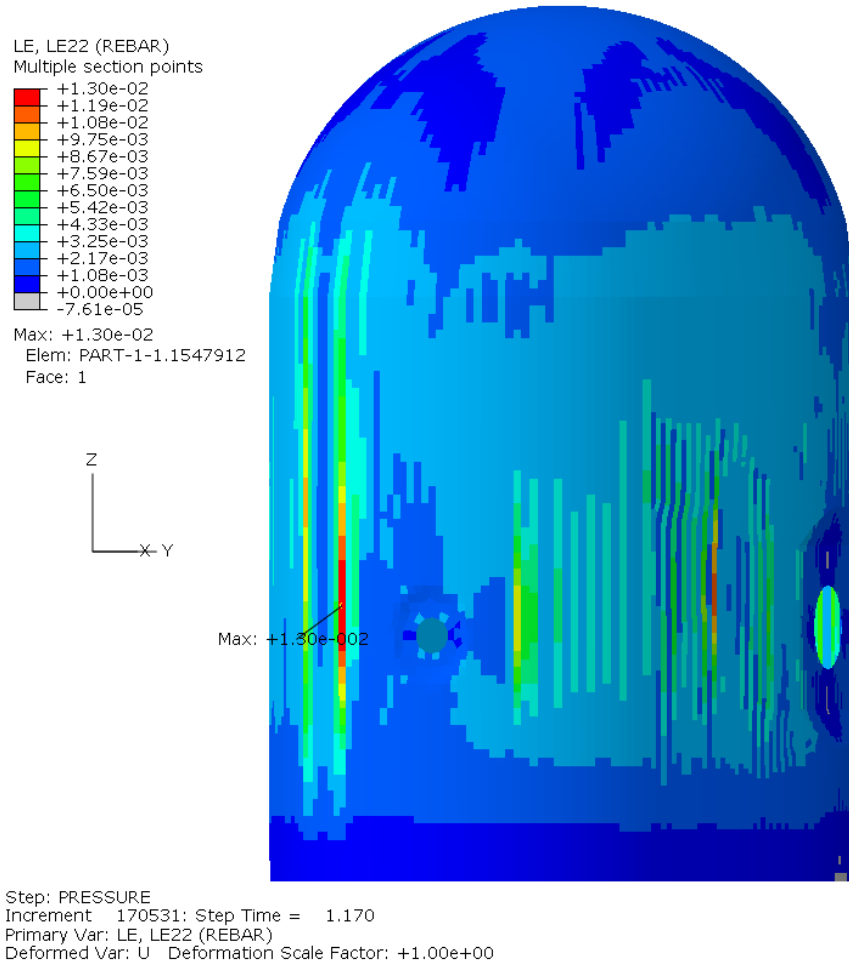


Figure E A5.6 Liner hoop strains, pressure = 1.170 MPa.

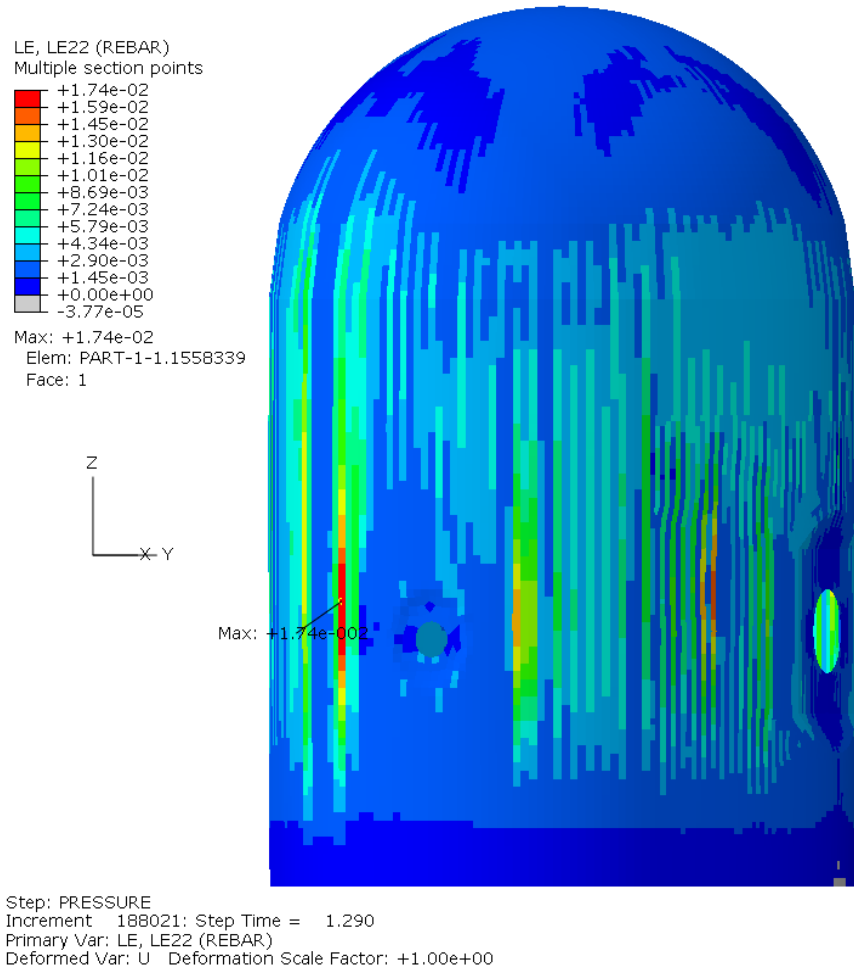


Figure E A5.7 Liner hoop strains, pressure = 1.290 MPa.

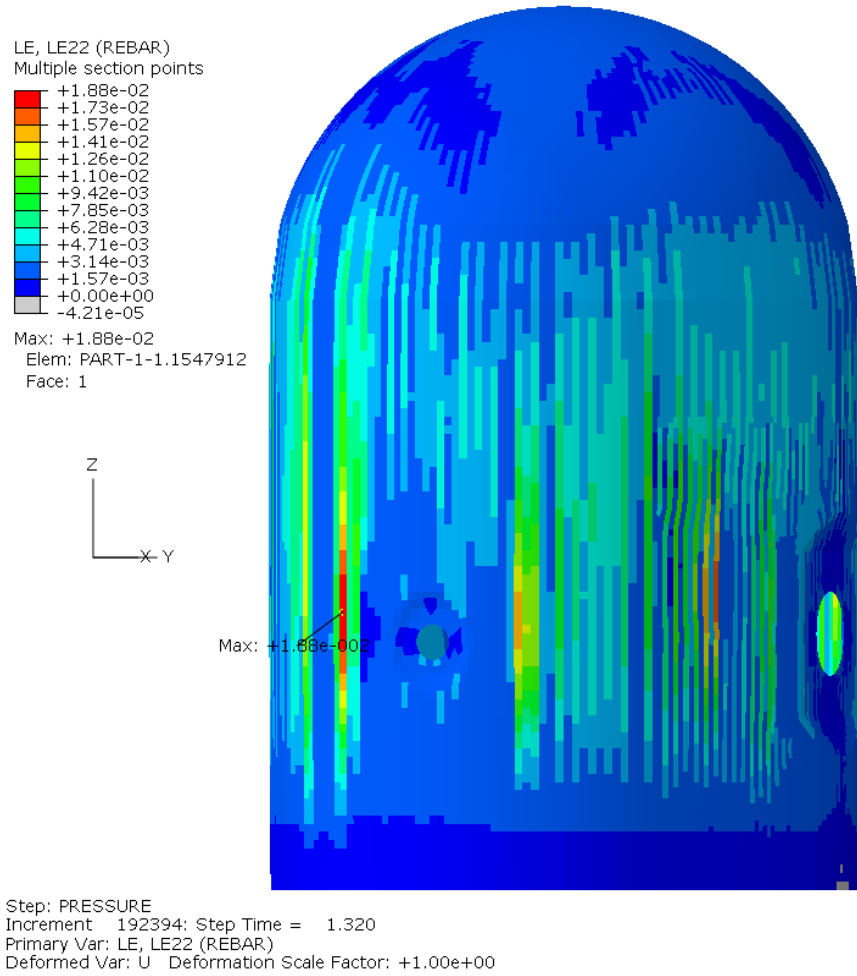
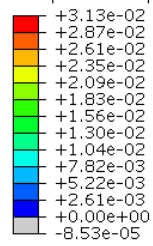
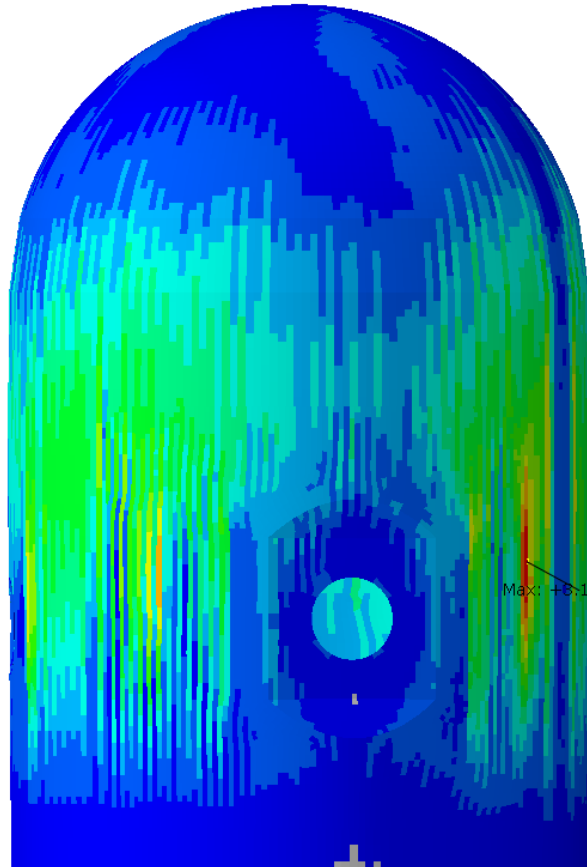
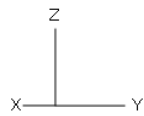


Figure E A5.8 Liner hoop strains, pressure = 1.320 MPa.

LE, LE22 (REBAR)
Multiple section points



Max: +3.13e-02
Elem: PART-1-1.1986544
Face: 1



Step: PRESSURE
Increment 205512: Step Time = 1.410
Primary Var: LE, LE22 (REBAR)
Deformed Var: U Deformation Scale Factor: +1.00e+00

Figure E A5.9 Liner hoop strains, pressure = 1.410 MPa.

GLOBAL MODEL STRAINS IN CONCRETE STRUCTURE

Figure E A6.1 through Figure E A6.3 below show regions where crack strains in hoop direction have developed. The strain limit where cracking is initiated is calculated below:

$$\sigma_t = 2.10 \times 10^6 \text{ Pa}$$

$$E = 26.8 \times 10^9 \text{ Pa}$$

$$\varepsilon_{elastic} = \frac{\sigma_t}{E} = 7.836 \times 10^{-5}$$

Figure E A6.4 through Figure E A6.6 show regions where the hoop strains has reached the point where the concrete has no tensile strength left, i.e. regions where the concrete is fully cracked. This strain limit is dependent on the element size and consequently two limits are used since one part of the global finite element model has a denser mesh, see Figure E 6.2 in this report. The strain limits where the concrete is assumed to be fully cracked is calculated below:

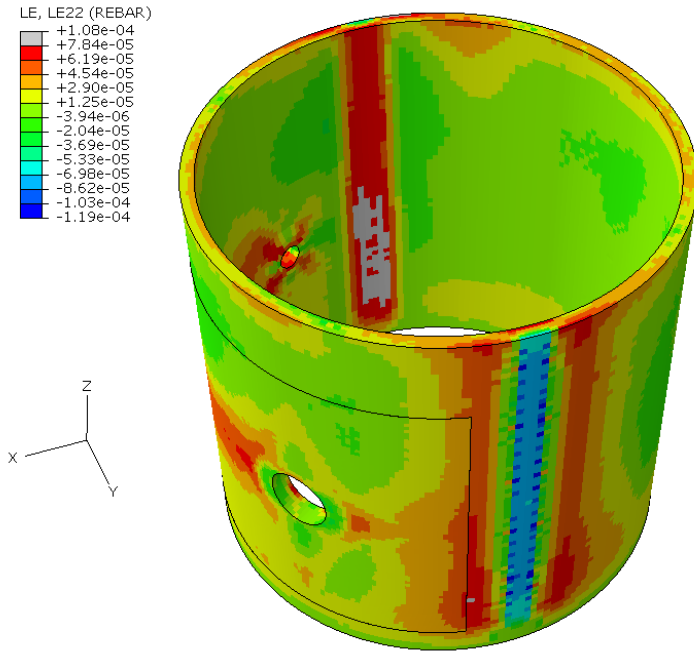
$$L_{element, model 3} \approx 0.158 \text{ m}$$

$$L_{element, model 2} \approx 0.104 \text{ m}$$

$$u_{c,0} = \text{crack width at zero tensile strength} = 0.00015 \text{ m}$$

$$\varepsilon_{\max,3} = \varepsilon_{elastic} + \frac{\Delta L}{L_{element}} = 7.836 \times 10^{-5} + \frac{0.00015}{0.158} \approx 10.27 \times 10^{-4}$$

$$\varepsilon_{\max,2} = \varepsilon_{elastic} + \frac{\Delta L}{L_{element}} = 7.836 \times 10^{-5} + \frac{0.00015}{0.104} \approx 15.24 \times 10^{-4}$$



Step: PRESSURE
 Increment 69962: Step Time = 0.4800
 Primary Var: LE, LE22 (REBAR)
 Deformed Var: U Deformation Scale Factor: +1.00e+00

**Figure E A6.1 Concrete hoop strains in the cylindrical part of the containment.
 Showing: initiation of crack strains.
 Grey region: crack strains.
 Pressure: 0.48 MPa.**

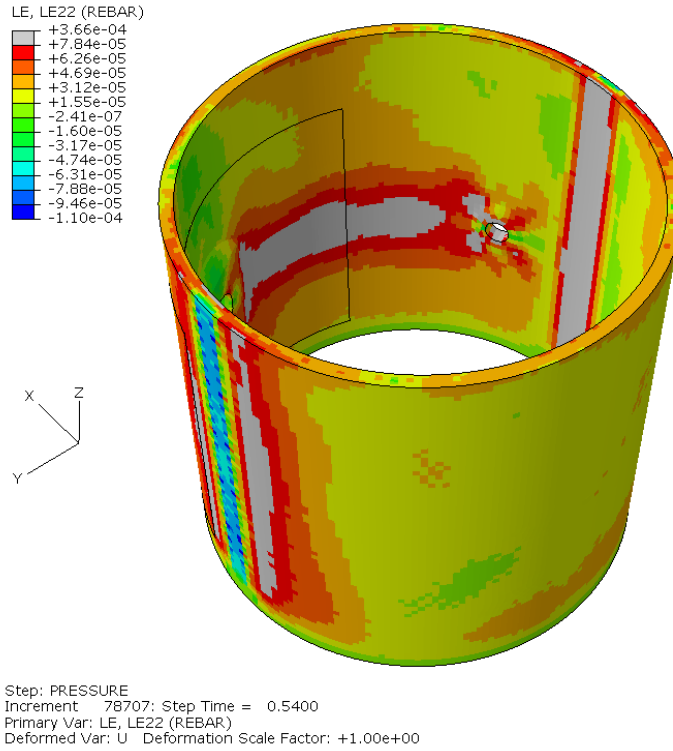


**Figure E A6.2 Concrete hoop strains in the cylindrical part of the containment.
Showing: crack strains developed through entire cross-section of containment wall, see
also Figure E A6.3.
Grey region: crack strains.
Pressure: 0.54 MPa.**

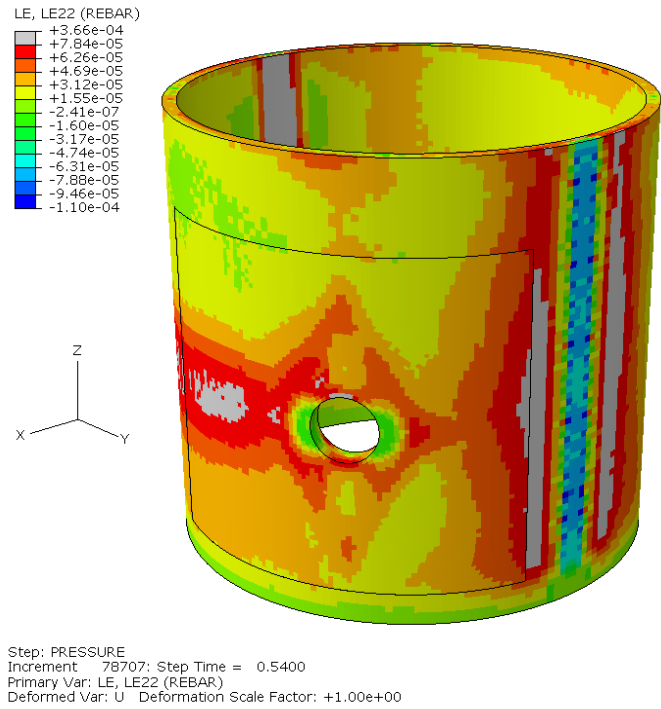
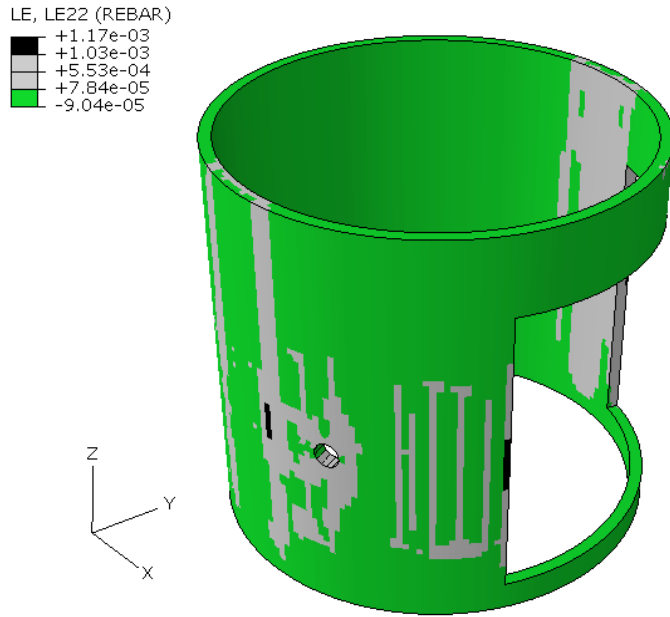


Figure E A6.3 Concrete hoop strains in the cylindrical part of the containment. Showing: crack strains developed through entire cross-section of containment wall, see also Figure E A6.2. Grey region: crack strains. Pressure: 0.54 MPa.



Step: PRESSURE
 Increment 87452: Step Time = 0.6000
 Primary Var: LE, LE22 (REBAR)
 Deformed Var: U Deformation Scale Factor: +1.00e+00

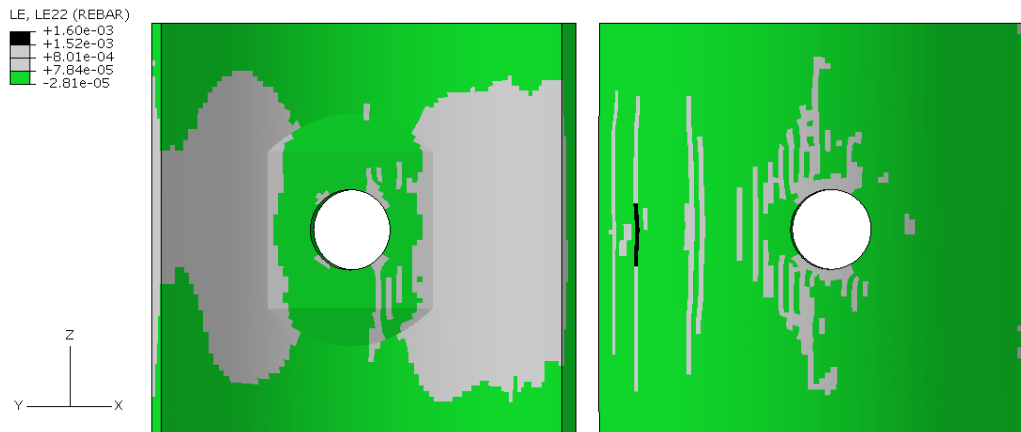
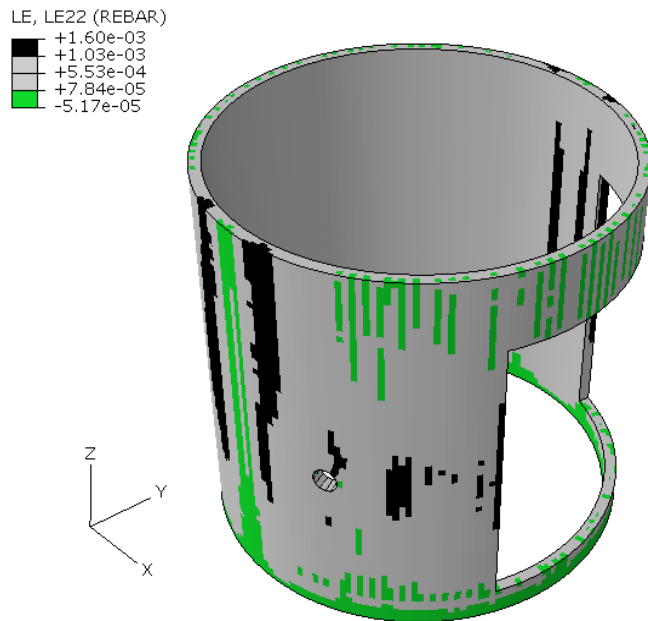


Figure E A6.4 Concrete hoop strains in the cylindrical part of the containment.
Showing: regions where the concrete has no hoop strength.
Green region: elastic concrete strains
Grey region: crack strains.
Black region: fully cracked concrete
Pressure: 0.60 MPa.



Step: PRESSURE
 Increment: 104943; Step Time = 0.7200
 Primary Var: LE, LE22 (REBAR)
 Deformed Var: U Deformation Scale Factor: +1.00e+00

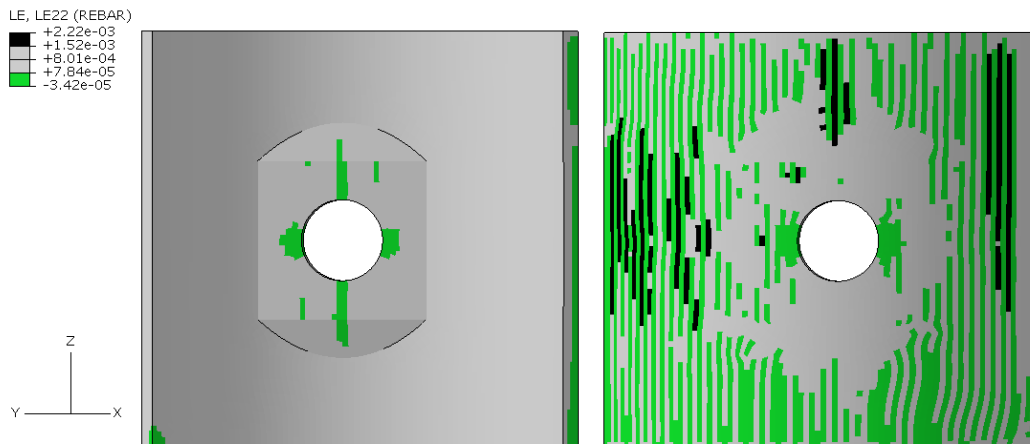
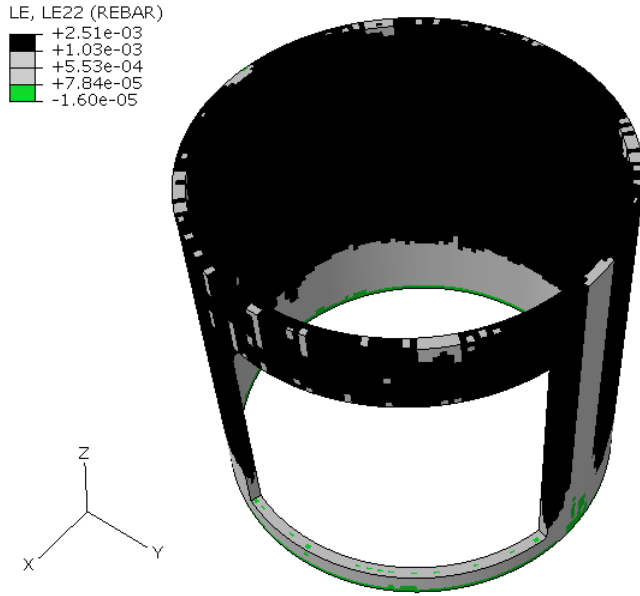


Figure E A6.5 Concrete hoop strains in the cylindrical part of the containment.
Showing: regions where the concrete has no hoop strength through entire cross-section of containment wall.
Green region: elastic concrete strains
Grey region: crack strains.
Black region: fully cracked concrete
Pressure: 0.72 MPa.



Step: PRESSURE
 Increment: 131178; Step Time = 0.9000
 Primary Var: LE, LE22 (REBAR)
 Deformed Var: U Deformation Scale Factor: +1.00e+00

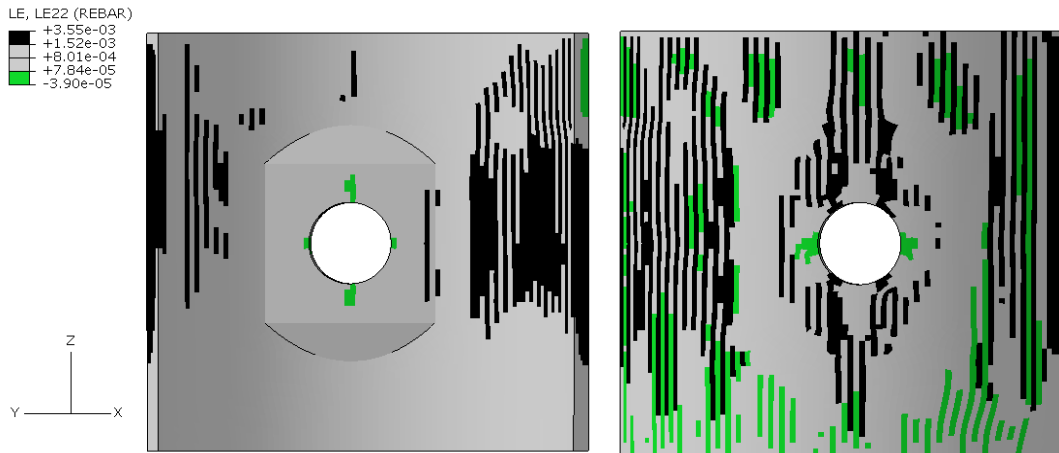


Figure E A6.6 Concrete hoop strains in the cylindrical part of the containment. Showing: pressure at which almost the entire containment wall is fully cracked.
Green region: elastic concrete strains
Grey region: crack strains.
Black region: fully cracked concrete
Pressure: 0.90 MPa.

RESULTS FOR REGION NEAR EQUIPMENT HATCH

In this appendix results requested in SPE analysis definition is presented (see page 19 in [6]). All results for the steel liner are analyzed with the model with low shear stiffness for the vertical anchors (see Section 4.4.3).

Concrete cracking

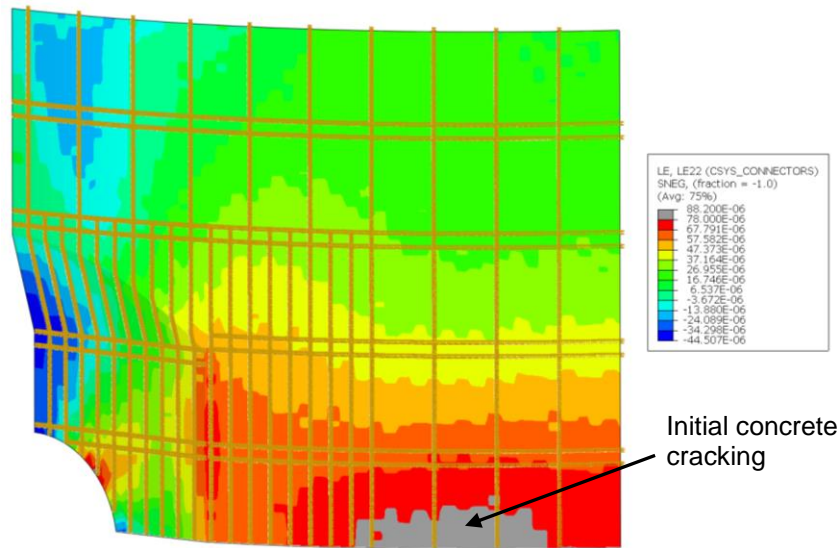


Figure E A7.1 Concrete inner surface, strain at 0.52 MPa, initial cracking in E/H region.

Tendon strain

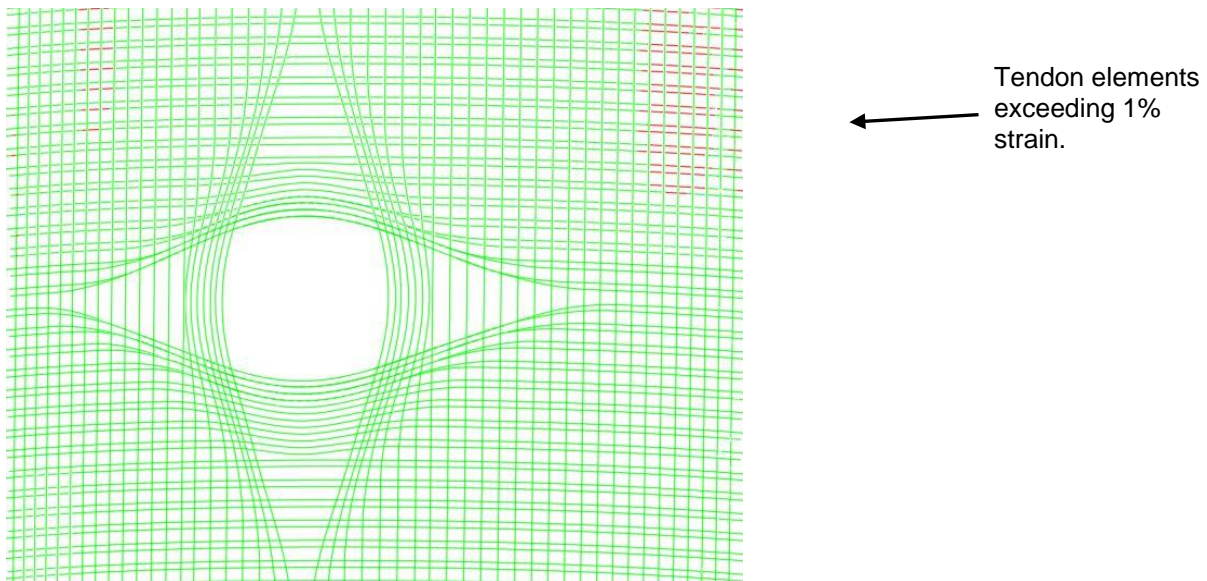


Figure E A7.2 Tendon strain at 1.32 MPa. Red color indicates tendon parts exceeding 1% strain in the E/H region.

Hoop liner strain contourplots (LE22)

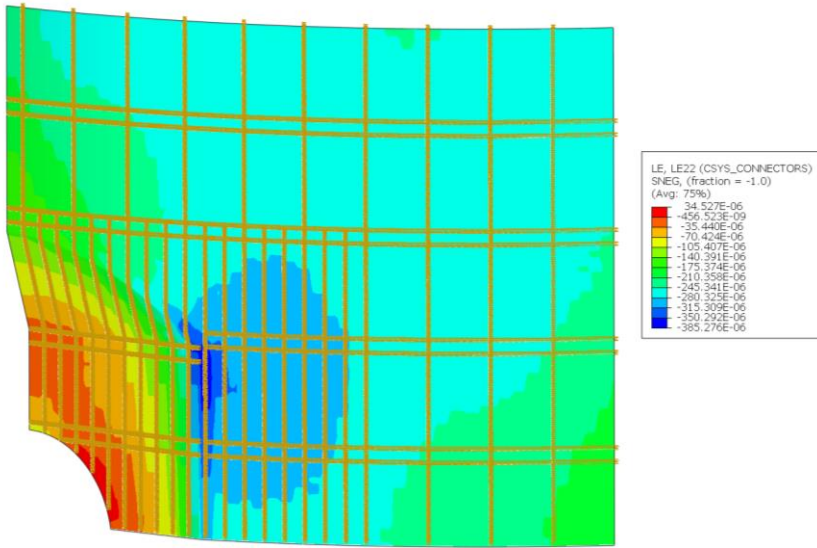


Figure E A7.3 Concrete inner surface, strain at 0 MPa (0 p_d) in E/H region.

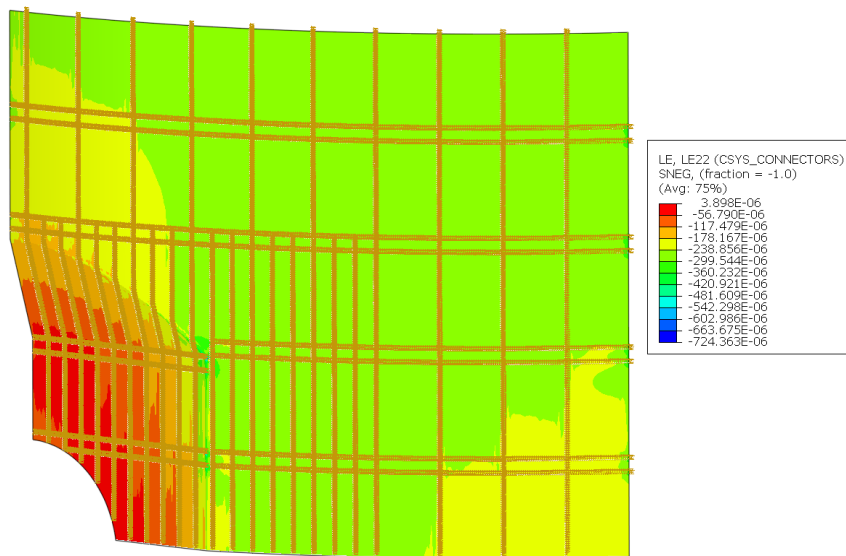


Figure E A7.4 Liner strain at 0 MPa (0 p_d) in E/H region.

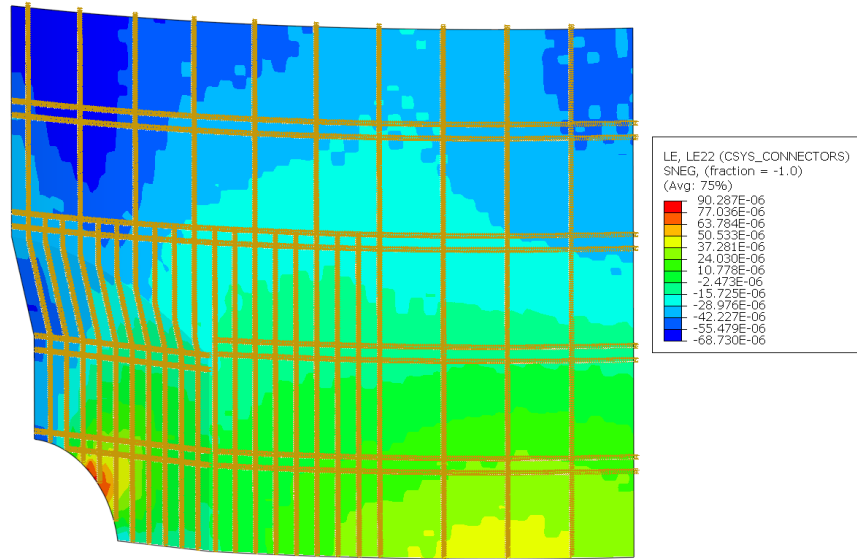


Figure E A7.5 Concrete inner surface, strain at 0.41 MPa ($\sim p_d$) in E/H region.

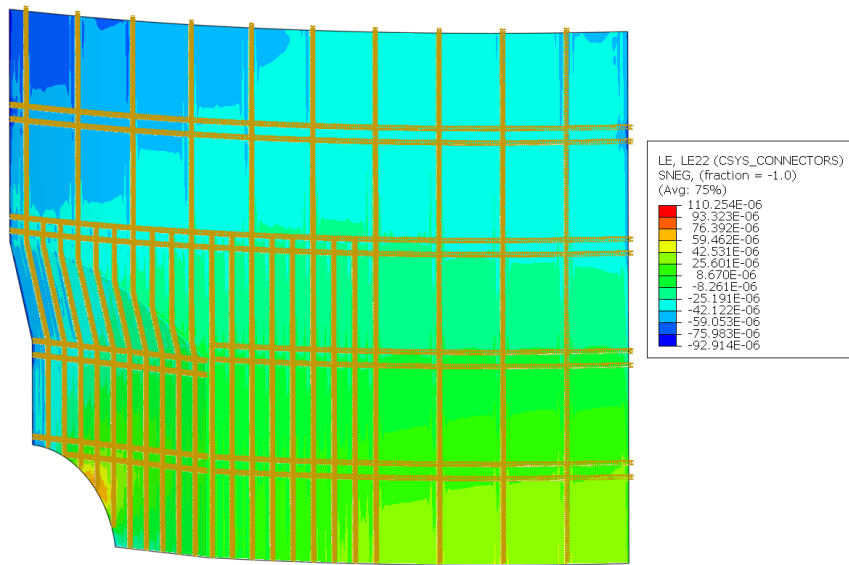


Figure E A7.6 Liner strain at 0.41 MPa ($\sim p_d$) in E/H region.

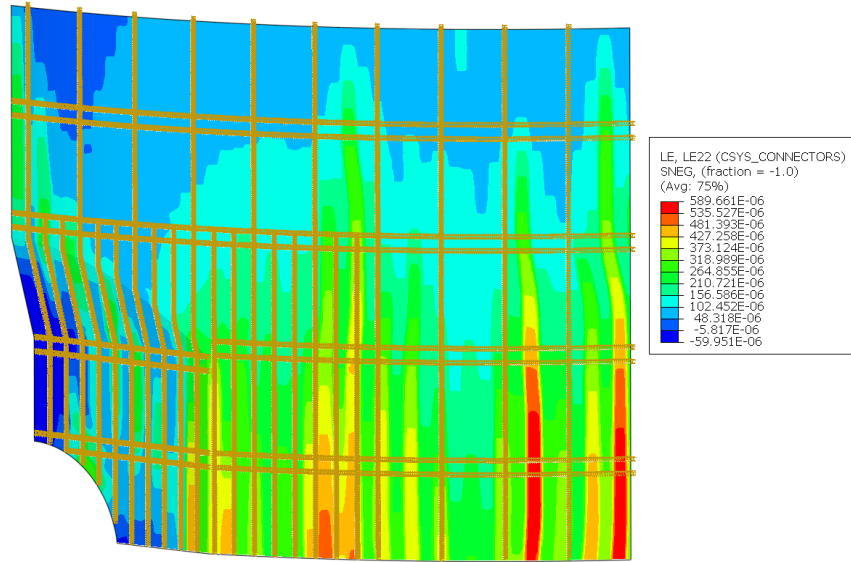


Figure E A7.7 Concrete inner surface, strain at 0.61 MPa (~1.5 p_d) in E/H region.

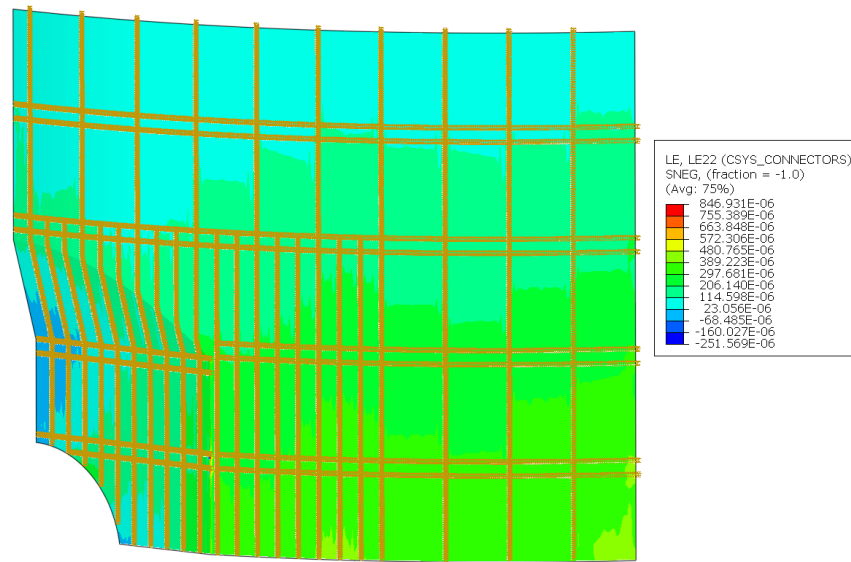


Figure E A7.8 Liner strain at 0.61 MPa (~1.5 p_d) in E/H region.

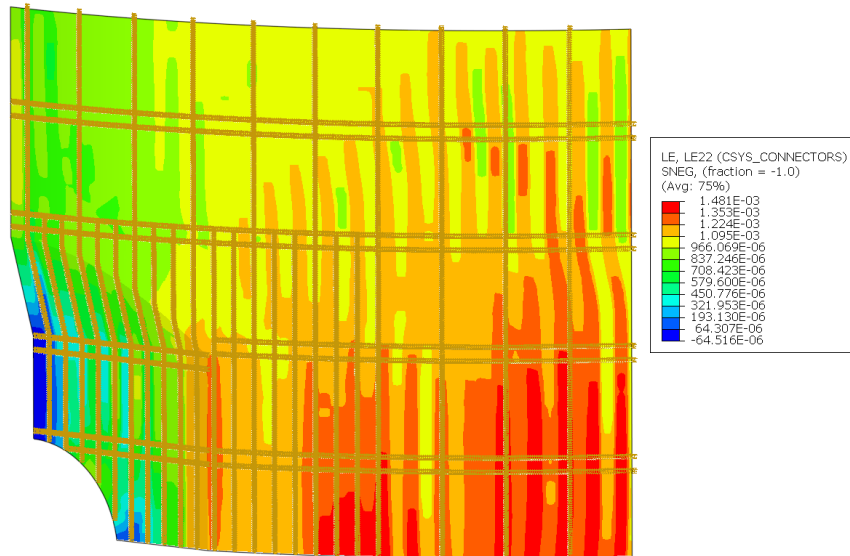


Figure E A7.9 Concrete inner surface, strain at 0.81 MPa (~2 p_d) in E/H region.

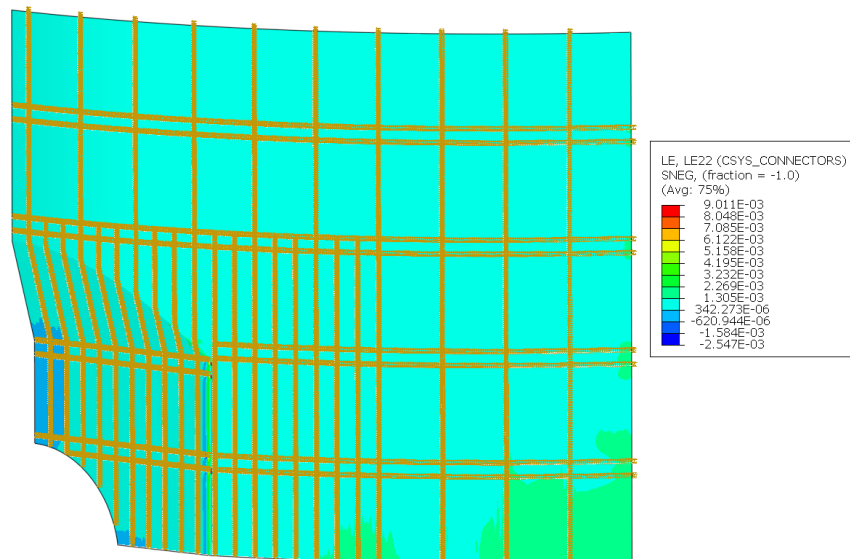


Figure E A7.10 Liner strain at 0.81 MPa (~2 p_d) in E/H region.

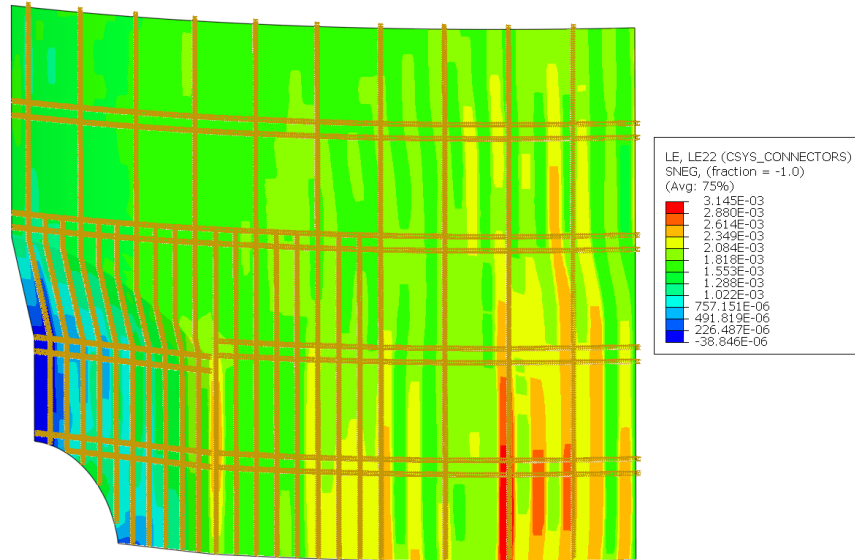


Figure E A7.11 Concrete inner surface, strain at 1.0 MPa (~2.5 p_d) in E/H region.

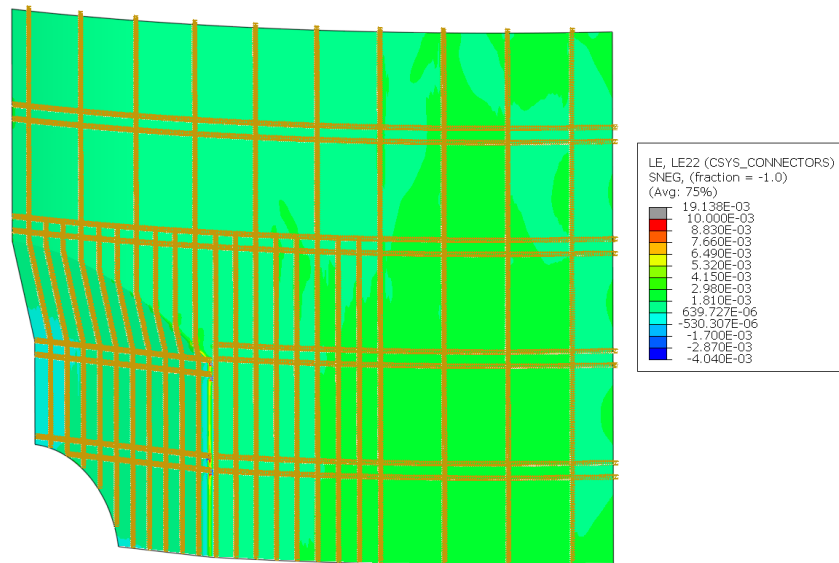


Figure E A7.12 Liner strain at 1.0 MPa (~2.5 p_d) in E/H region.

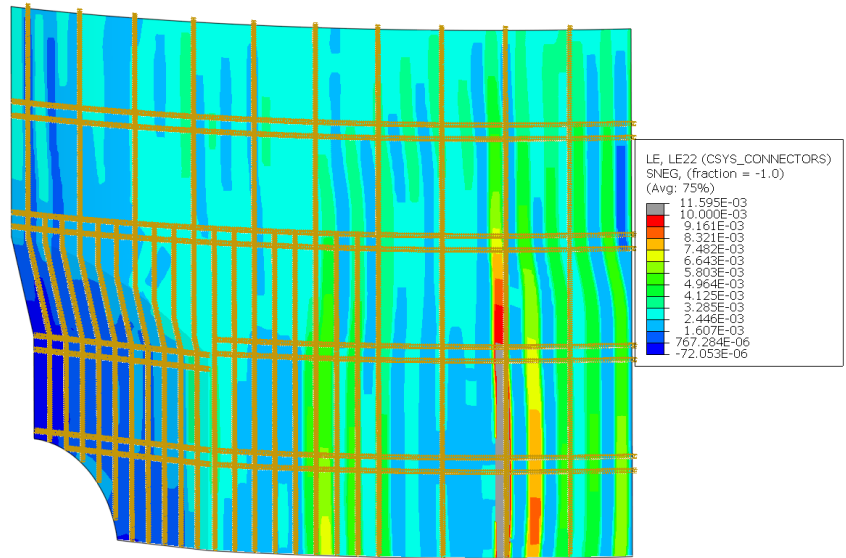


Figure E A7.13 Concrete inner surface, strain at 1.18 MPa (~3 p_d) in E/H region.

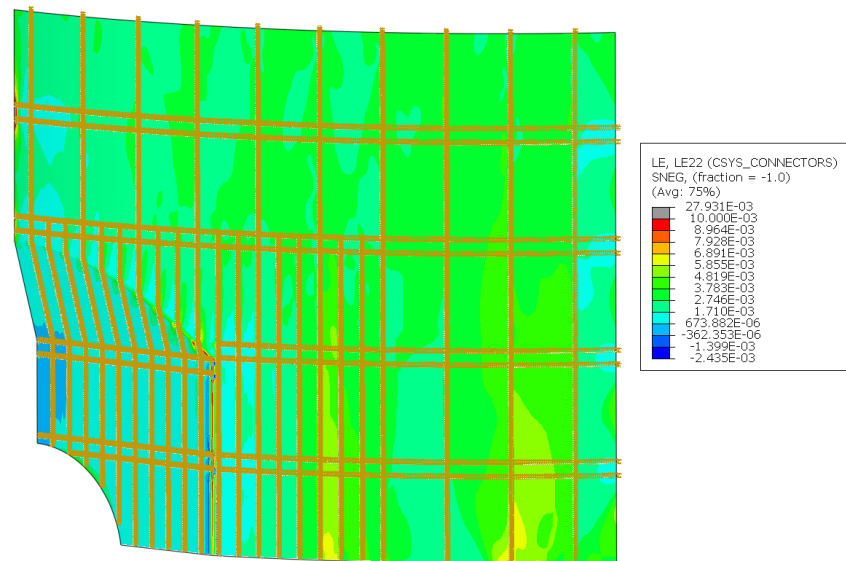


Figure E A7.14 Liner strain at 1.18 MPa (~3 p_d) in E/H region.

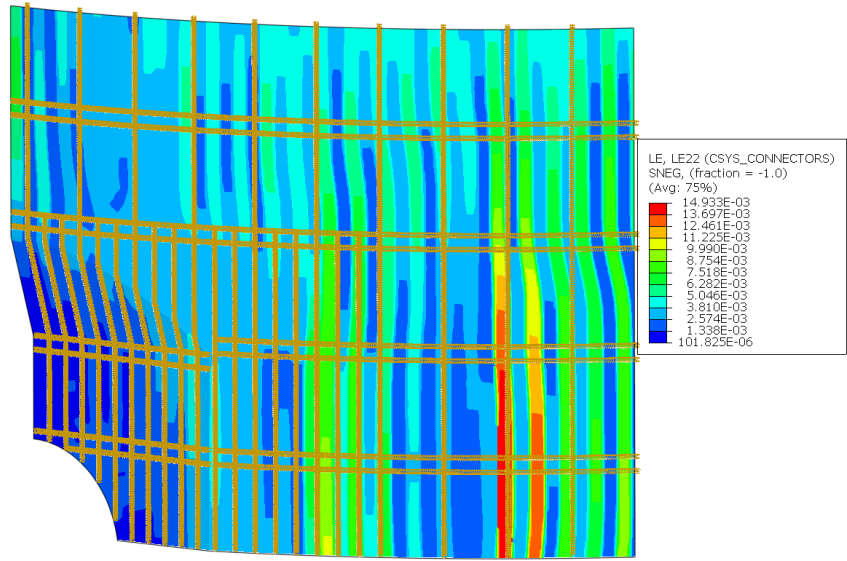


Figure E A7.15 Concrete inner surface, strain at 1.29 MPa (3.3 p_d) in E/H region.

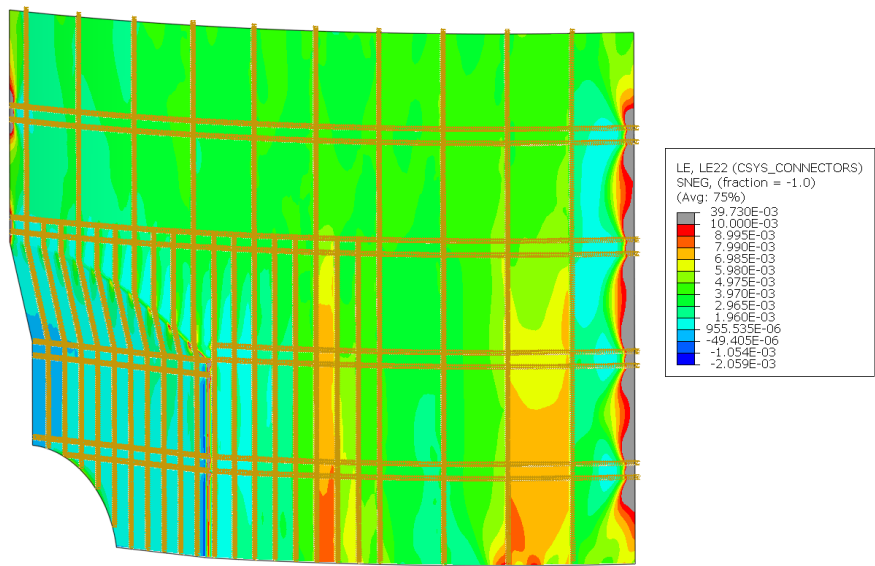


Figure E A7.16 Liner strain at 1.29 MPa (3.3 p_d) in E/H region.

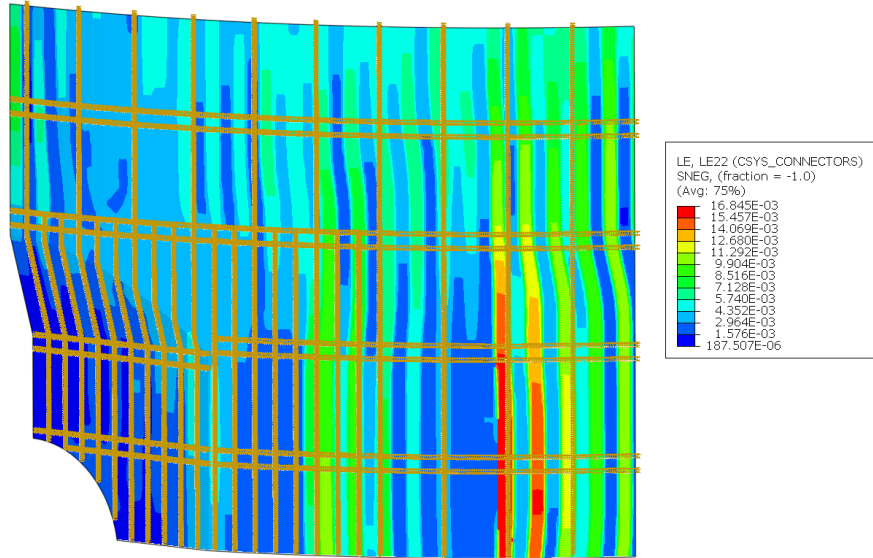


Figure E A7.17 Concrete inner surface, strain at 1.33 MPa (3.4 p_d) in E/H region.

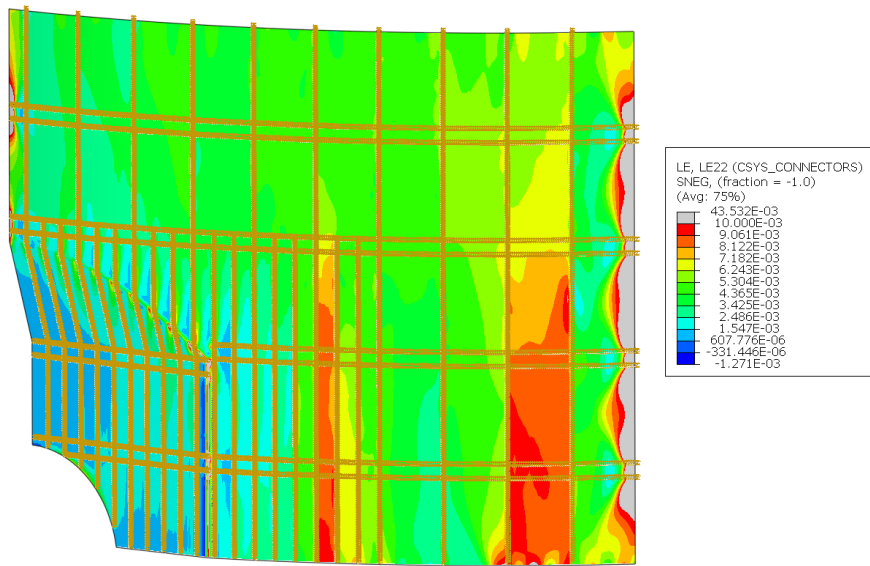


Figure E A7.18 Liner strain at 1.33 MPa (3.4 p_d) in E/H region.

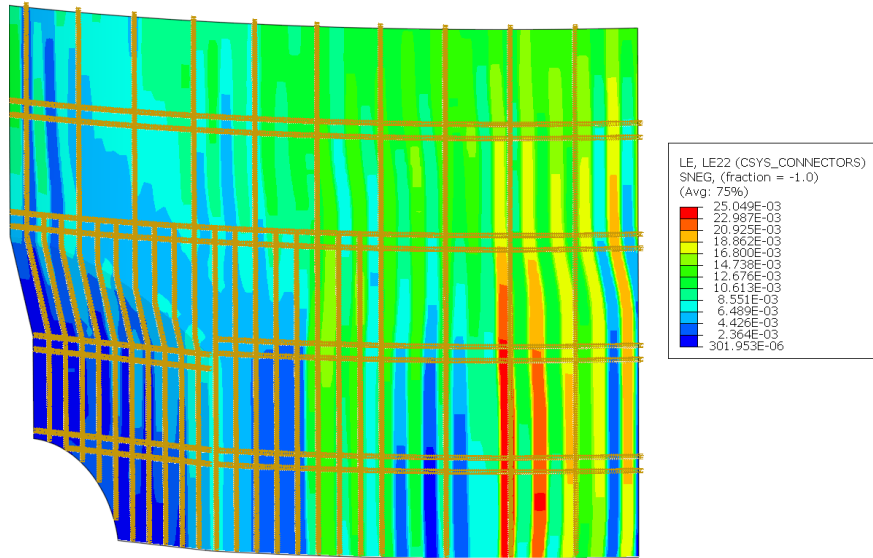


Figure E A7.19 Concrete inner surface, strain at 1.41 MPa in E/H region.

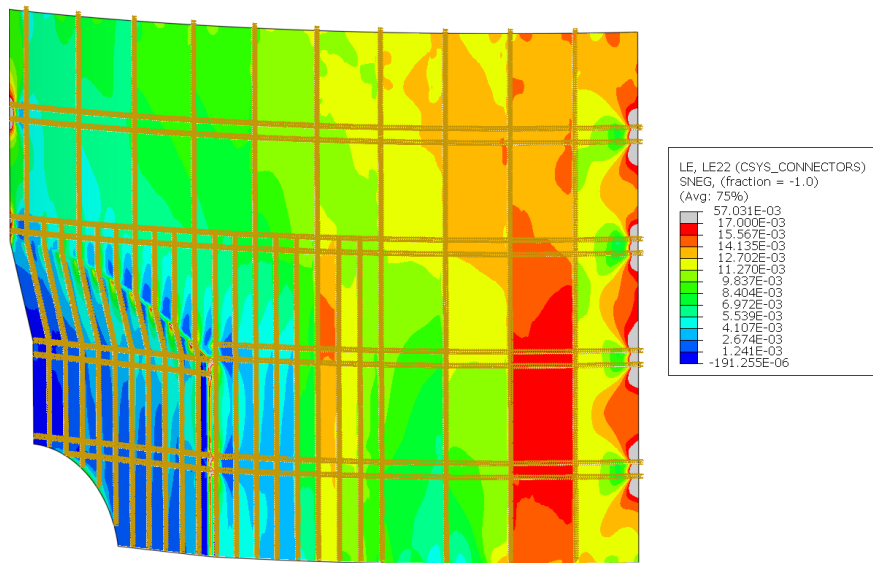


Figure E A7.20 Liner strain at 1.41 MPa in E/H region.

Hoop liner strain in locations defined in SPE analysis definition (see Figure E below)

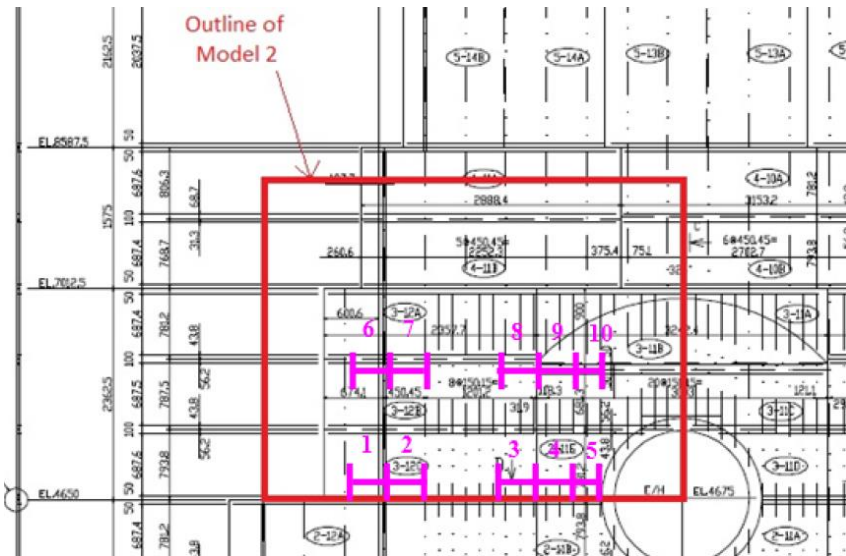


Figure E A7.21 Locations for requested liner output according to [6].

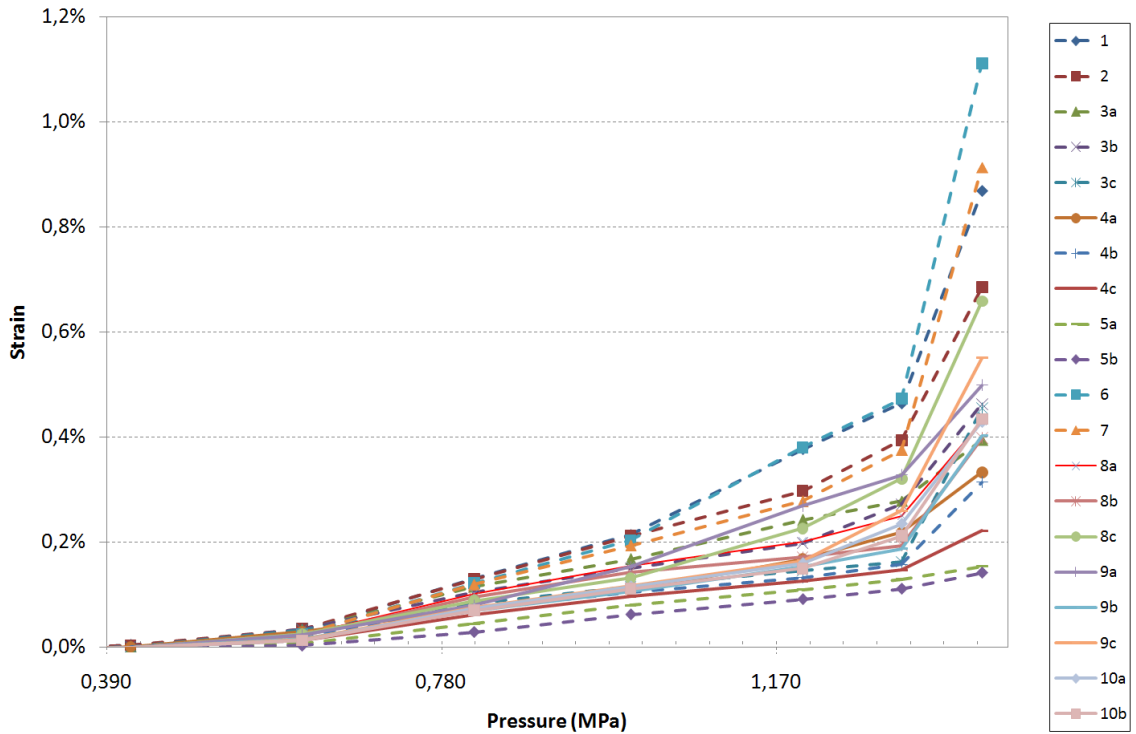


Figure E A7.22 Liner strain at in hoop direction in locations shown in Figure E above. Results for inside of the liner.